Effects of hadronic rescattering on multistrange hadrons in high-energy nuclear collisions

Shiori Takeuchi,[1,*] Koichi Murase,[1,2,3,†] Tetsufumi Hirano,[1,‡] Pasi Huovinen,[4,5,§] and Yasushi Nara[6,‖]

[1]*Department of Physics, Sophia University, Tokyo 102-8554, Japan*

[2]*Department of Physics, The University of Tokyo, Tokyo 113-0033, Japan*

[3]*Theoretical Research Division, Nishina Center, RIKEN, Wako 351-0198, Japan*

[4]*Institut für Theoretische Physik, Goethe-Universität, 60438 Frankfurt am Main, Germany*

[5]*Frankfurt Institute for Advanced Studies, 60438 Frankfurt am Main, Germany*

[6]*Department of International Liberal Arts, Akita International University, Yuwa, Akita-city 010-1292, Japan*

(Received 29 May 2015; published 16 October 2015)

We study the effects of hadronic rescattering on hadron distributions in high-energy nuclear collisions by using an integrated dynamical approach. This approach is based on a hybrid model combining $(3+1)$-dimensional ideal hydrodynamics for the quark gluon plasma (QGP) and a transport model for the hadron resonance gas. Since the hadron distributions are the result of the entire expansion history of the system, understanding the QGP properties requires investigating how rescattering during the hadronic stage affects the final distributions of hadrons. We include multistrange hadrons in our study and quantify the effects of hadronic rescattering on their mean transverse momenta and elliptic flow. We find that multistrange hadrons scatter less during the hadronic stage than nonstrange particles, and thus their distributions reflect the properties of the system in an earlier stage than the distributions of nonstrange particles.

DOI: 10.1103/PhysRevC.92.044907 PACS number(s): 25.75.Ld, 12.38.Mh, 24.10.Nz, 25.75.Dw

I. INTRODUCTION

Quark gluon plasma (QGP), strongly interacting matter composed of quarks and gluons, has been created in high-energy nuclear collisions at the Relativistic Heavy Ion Collider (RHIC) at Brookhaven National Laboratory (BNL) and the Large Hadron Collider (LHC) at CERN [1]. One of the main discoveries at the RHIC was that the QGP behaves like a nearly perfect fluid [2–7], and since then the transport properties of the QGP, especially its shear and bulk viscosity coefficients, have been under active investigation.

The QGP created in high-energy nuclear collisions expands, cools down, and turns into a hadron gas. Since hadrons scatter with each other via the strong interaction, information about the QGP stage is, in general, contaminated by rescatterings in the hadronic stage. To probe the QGP more directly, thermal photons and dileptons were proposed as penetrating probes [8,9]. Once emitted, photons and dileptons propagate to detectors without rescattering since they interact only electromagnetically and their mean free path is therefore longer than the typical size of the system. However, photons and dileptons are not perfect probes of the QGP either. They are emitted during all the stages of high-energy nuclear collisions such as the primary hard scatterings, pre-equilibrium stage, and late hadronic stage [10], and it is not possible to distinguish photons and dileptons emitted from the QGP from those originating from the other processes.

In this paper, we follow up the previous studies [11–17] about multistrange hadrons, and claim that their distributions allow us to probe the QGP immediately after hadronization. Multistrange hadrons, in particular ϕ mesons and Ω baryons, have small scattering cross sections with pions since they do not form any resonances unlike other hadrons. This is a unique property of the multistrange hadrons: Their distributions reflect the properties of the system mainly at a specific stage deep inside the fireball, unlike photons and dileptons, which come from all stages.

By using a hybrid model in which hydrodynamic description of the QGP fluid is followed by a hadronic cascade model, violation of the mass ordering of the differential elliptic flow parameter $v_2(p_T)$ was predicted [15]. This phenomenon was observed recently by the STAR Collaboration [18], which indicates that ϕ mesons are less affected by hadronic rescatterings and, consequently, that they are good probes deep inside the matter. In this paper, we investigate the hadronic rescattering effects on observables more systematically by employing an integrated dynamical approach which we have previously used to analyze various observables at the RHIC and the LHC energies [19]. In the previous study of the violation of mass ordering [15], a first-order phase transition model for the equation of state (EOS) was employed and only hadrons up to the mass of $\Delta(1232)$ were taken into account in the hadron phase. In the present paper, we use a more realistic equation of state [20] connecting a parametrized lattice QCD EOS at large temperatures to a hadron resonance gas EOS at low temperatures. The hadron resonance gas in the EOS contains all the resonances in the hadron cascade model JAM (Jet AA Microscopic transport model) [21] used as the last stage of the integrated dynamical approach. Hence, in addition to ϕ, we are able to investigate hadronic rescattering effects on heavier multistrange hadrons such as Ξ and Ω.

In the following we introduce the integrated dynamical model in Sec. II. We compare transverse momentum (p_T) spectra and p_T-differential elliptic flow parameters $v_2(p_T)$

*takeuchi@sophia.ac.jp
†murase@nt.phys.s.u-tokyo.ac.jp
‡hirano@sophia.ac.jp
§huovinen@th.physik.uni-frankfurt.de
‖nara@aiu.ac.jp

with the STAR data in Sec. III. After we confirm that we can reasonably reproduce the data by using this model, we discuss the hadronic rescattering effect in Sec. IV. In this section, we first revisit the violation of mass ordering of $v_2(p_T)$. We next focus on the mean transverse momentum $\langle p_T \rangle$ and p_T-averaged v_2 calculated with or without hadronic rescatterings and investigate how much these final observables reflect the information when the hydrodynamic stage finishes. We summarize our results in Sec. V.

II. THE MODEL

We describe the space-time evolution of high-energy nuclear collisions by use of an integrated dynamical approach on an event-by-event basis. We divide the whole reaction into three separate stages: Initial stage, hydrodynamic stage, and transport stage. The initial entropy-density distribution after the collision of energetic heavy nuclei is parametrized by using a Monte Carlo version of the Glauber model. The subsequent expansion of the matter is described by relativistic ideal hydrodynamics. When the system becomes sufficiently dilute due to strong expansion, we switch the description of the system from hydrodynamics to kinetic theory.

In the following we briefly overview each part of the model and the corresponding interfaces. For further details, see Ref. [19].

A. Hydrodynamics and equation of state

Hydrodynamics is a macroscopic description and an effective theory of the system's long wavelength/time behavior. The hydrodynamical equations of motion are obtained from the conservation of energy and momentum:

$$\partial_\mu T^{\mu\nu} = 0, \tag{1}$$

where $T^{\mu\nu}$ is the energy-momentum tensor. In the ideal fluid approximation, the energy momentum tensor can be decomposed as

$$T^{\mu\nu} = eu^\mu u^\nu - P(g^{\mu\nu} - u^\mu u^\nu), \tag{2}$$

where e, P, u^μ, and $g^{\mu\nu} = \mathrm{diag}(+1, -1, -1, -1)$ are energy density, pressure, flow velocity, and the Minkowski metric, respectively. To close the system of partial differential equations we need to know the EOS of the fluid to obtain pressure P as a function of energy density e. Once the EOS is known, the space-time evolution of thermodynamic quantities and flow velocity is determined for given initial conditions, i.e., energy-density distribution and flow field at initial time τ_0.

We ignore the baryon number and its continuity equation since at the collider energies, net baryon density at midrapidity is tiny. When we solve Eq. (1), temperature is not needed since it is merely a parameter to connect energy density and pressure. Nevertheless, we also follow the space-time evolution of temperature to decide where to switch from fluid to cascade. We employ the *s95p*-v1.1 parametrization for the EOS. The *s95p* parametrization [20] connects the lattice QCD based EOS [22] in the high-temperature region to a hadron resonance gas EOS in the low temperature region. The hadronic part of *s95p*-v1.1 contains the same hadronic species as the JAM hadronic cascade model [21] described in the next subsection.

We numerically solve Eq. (1) in the Milne coordinates (τ, η_s, x, y), which is appropriate for the description of the evolution at relativistic energies [23]. Here $\tau = \sqrt{t^2 - z^2}$ is longitudinal proper time, $\eta_s = \frac{1}{2}\ln[(t+z)/(t-z)]$ is space-time rapidity, and x and y are transverse coordinates perpendicular to the collision axis. In the numerical calculations, we employ the piecewise parabolic method [24], which is known to be able to describe shock waves. For details about this numerical algorithm, see also Ref. [25].

B. Particlization and hadronic cascade

We employ the hadronic cascade model JAM [21] to describe the space-time evolution of hadron gas after "particlization," i.e., after switching from fluid to particles. At the late stage of collisions, the system is too dilute to maintain equilibrium. We assume this happens around temperature, which we call the switching temperature $T_{\rm sw}$, and switch description from hydrodynamics to kinetic theory on the $T = T_{\rm sw}$ isosurface [13,26–31]. Within the current model, $T_{\rm sw}$ is a rather adjustable parameter which controls the final particle ratios. We choose $T_{\rm sw} = 155$ MeV to reproduce the observed p_T spectra of pions, kaons, and protons + antiprotons in the low-p_T region [19] at the full RHIC energy. At $T(x) = T_{\rm sw}$, we calculate the single-particle phase-space distributions $f_i(p,x)$ for all hadrons included in the EOS by employing the Cooper-Frye prescription [32]

$$f_i(p,x)d^3\boldsymbol{x}d^3\boldsymbol{p} = \frac{g_i}{(2\pi)^3 E}\frac{p\cdot\Delta\sigma d^3\boldsymbol{p}}{\exp(p\cdot u/T_{\rm sw})\pm 1}. \tag{3}$$

Here g_i is a degeneracy of the hadronic species i, $p^\mu = (E, \boldsymbol{p})$ is the four-momentum of a particle, and $\Delta\sigma_\mu$ is a normal vector of the $T(x) = T_{\rm sw}$ hypersurface. It is well known that at some momenta the Cooper-Frye formula (3) gives a negative contribution for the spacelike hypersurface element (or even the timelike hypersurface element with negative time component). These negative numbers correspond to incoming particles, which one cannot treat in the hadronic cascade model. So we just neglect these contributions and consider only outgoing particles. We sample particles by going through all the hypersurface elements and generate ensembles of hadrons on an event-by-event basis. Note that we do not oversample particles to gain statistics for each event. This means each hydrodynamic event corresponds to one ensemble of particles. Among all the calculations in the integrated dynamical approach, sampling particles from the particlization hypersurface is numerically the most expensive, which is crucial in event-by-event simulations. In Ref. [19], we discussed in detail how to sample particles and integrate the Cooper-Frye formula (3) over momentum at a smaller numerical cost.

In hadronic cascade models, experimental hadronic cross-section data are implemented when available. However, there are many hadronic scattering processes where data do not exist. In such a case, we use the additive quark model [33–36]

to describe the scattering cross section,

$$\sigma_{\rm tot}^{12} = \sigma_{\rm tot}^{NN} \frac{n_1}{3} \frac{n_2}{3} \left(1 - 0.4 \frac{n_{s1}}{n_1}\right) \left(1 - 0.4 \frac{n_{s2}}{n_2}\right). \quad (4)$$

Here $\sigma_{\rm tot}^{NN}$ is the total nucleon-nucleon cross section, n_i is the number of constituent quarks in a hadron, and n_{si} is the number of strange quarks in a hadron. Thus hadrons containing strange quark(s) have a relatively small total cross section in this model. Moreover, ϕ mesons and Ω baryons do not form resonances when scattering with pions and therefore have much smaller cross sections than nonstrange hadrons.

In the simulations, the dynamics of the system is described by a sum of incoherent two-body collisions. Two particles collide with each other if their minimum distance b in the center-of-mass frame is smaller than the distance given by the total cross section,

$$b < \sqrt{\frac{\sigma_{\rm tot}}{\pi}}. \quad (5)$$

This is a classical, geometrical interpretation of the two-body collision cross section.

Note that in JAM the properties of hadrons are those of free particles. The medium modifications of hadron properties such as a broadening and mass shift [37] have been extensively studied by various further developments of transport models such as the relativistic Vlasov-Uehling-Uhlenbeck (RVUU) model [38], the Hadron-String-Dynamics (HSD) [39] and Parton-Hadron-String-Dynamics (PHSD) [40] transport models, the Giessen Boltzmann-Uehling-Uhlenbeck (GiBUU) model [41], and Isospion Quantum Molecular Dynamics (IQMD) [42]. Nevertheless, since the main difference in the cross sections of multistrange particles and the other hadrons is due to the (non-)existence of resonance channels, we do not expect the in-medium modifications to significantly affect this difference, and the use of free particle properties to provide a conservative baseline is justified.

As mentioned, the interactions in JAM are described as two-particle scatterings, and multiparticle scatterings are not included. It has been argued that multipion fusion processes in particular would have a significant effect on the yields of proton-antiproton pairs [43], but subsequent calculations have shown that regeneration is a $\sim$10% level effect at the LHC [44,45]. Nevertheless, the multimeson fusion effects for Ω baryons are much smaller than for protons or Λ [46], and thus their inclusion would make the later-discussed differences between rescatterings of nonstrange and multistrange particles even larger.

As a default setting strong interactions and decays are simulated in JAM. However, we switch off the decay channels for ϕ mesons in the present study to investigate hadronic rescattering effects on ϕ mesons in an efficient way. Otherwise, we would need to perform mass reconstruction of ϕ mesons from two kaons after numerical simulations. Since the lifetime of ϕ mesons ($\sim$47 fm/c) [47] is somewhat larger than the typical lifetime of the system ($\sim$10 fm/c), the daughter kaons from ϕ meson decays (or lack of them) are not expected to affect the bulk evolution. As we will discuss in Sec. III, the yield of Λ measured by STAR contains the feed-down from electromagnetic Σ^0 decays. This process does not happen in the default setting in JAM and, therefore, is simulated separately when we analyze Λ spectra. We also have an option in JAM to deactivate all the hadronic rescatterings and/or resonance decays to investigate how these affect final observables.

C. Initial conditions

Once initial conditions for the hydrodynamic evolution are fixed, the subsequent evolution is determined, and we are able to obtain final particle distributions which can be compared with experimental data. The prethermalization stage between the first contact of colliding nuclei and the initial time of hydrodynamic evolution may be described by nonequilibrium field theory, although how exactly it could be done is one of the open issues in the physics of relativistic heavy-ion collisions. Thus, we do not even try to describe it and simply rely on the Monte Carlo (MC) Glauber [48] and the modified Brodsky-Gunion-Kuhn (BGK) models [29] to give the density distribution at τ_0 in the transverse plane and in the longitudinal direction, respectively. The MC Glauber model enables us to calculate the number density of participants and of binary collisions on an event-by-event basis. Our assumption is that the initial entropy density is proportional to a linear combination of these two densities. Even at very high collision energies the matter profile in the longitudinal direction depends on space-time rapidity, and boost invariance does not hold. Furthermore, in noncentral collisions the longitudinal density gradient at mid space-time rapidity may be nonzero due to the different thicknesses of the colliding nuclei at each transverse position. This can be deduced from (pseudo-)rapidity distribution of hadrons in $p(d)$-A collisions. In the modified BGK model a smooth initial longitudinal profile is parametrized by taking into account the difference in the local thickness of colliding nuclei. It is noted that we do not employ the Monte Carlo Kharzeev-Levin-Nardi model [49,50], which was used to calculate initial conditions in our previous hydrodynamic studies [19] since, in the present study, we focus on the hadronic rescattering effects on transverse dynamics, which are not supposed to be sensitive to the choice of initial conditions.

Assuming local thermalization, energy-density distribution $e(\tau = \tau_0, \eta_s, x, y)$ and pressure $P(\tau = \tau_0, \eta_s, x, y)$ are obtained from the entropy-density distribution through the *s95p*-v1.1 EOS. Initial flow velocity at τ_0 is supposed to be Bjorken's scaling flow [51], namely $u^\tau = 1$ and $u^x = u^y = u^{\eta_s} = 0$. Throughout this study, we fix $\tau_0 = 0.6$ fm/c. We choose initial parameters to reproduce the p_T distributions of pions, kaons, and protons + antiprotons in Au + Au collisions at $\sqrt{s_{NN}} =$ 200 GeV measured by the PHENIX Collaboration [52]. The centrality dependence of multiplicity is controlled by a fraction of soft (participants) and hard (binary collisions) component in the MC Glauber model, whereas the multiplicity in central collisions is fixed by the overall normalization parameter of the initial entropy distribution. On the other hand, as mentioned particle ratios are controlled by the switching temperature. The parameters controlling the shape of the rapidity distribution of particles are kept the same as in our previous study [19]. Since

here we concentrate on observables at midrapidity, we do not discuss them further.

In hydrodynamic simulations, one needs to convert the position distribution (a sum of δ functions in the transverse plane) of collision points in MC Glauber model to a hydrodynamic density distribution. In our model we obtain the density at a point x by counting the number of collision points or participants within radius $r_0 = \sqrt{\sigma_{\rm in}/\pi}$ around the point and divide by the inelastic cross section in $p + p$ collisions at $\sqrt{s_{NN}} = 200$ GeV, $\sigma_{\rm in}$. For further details, see Ref. [19].

III. SPECTRA AND FLOW

In this section, we compare invariant p_T spectra and differential elliptic flow parameter $v_2(p_T)$ of identified hadrons with experimental data from the STAR Collaboration. In the present study, we analyzed 0.6 million "minimum bias" events (defined as $N_{\rm part} \geqslant 2$ in the MC Glauber calculations for hydrodynamic initial conditions). Centrality is defined using an event distribution of the charged hadron multiplicity in $|\eta| < 0.5$ as done by the STAR Collaboration [53]. Note that error bars in the theoretical plots denote the statistical errors.

A. Transverse momentum spectra

In Figs. 1, 2, and 3, we show p_T distributions of identified hadrons around midrapidity in Au + Au collisions at $\sqrt{s_{NN}} =$ 200 GeV. For clarity, the results and the experimental data points are scaled up or down by a common factor.

Figure 1 shows the p_T spectra of (a) positive pions ($|\eta| < 0.5$) and (b) positive kaons ($|\eta| < 0.1$) compared with the STAR data ($|y| < 0.5$ for pions [54] and $|y| < 0.1$ for kaons [55]). The Jacobian between η and y is taken into account to obtain the invariant p_T spectra in our results. Even if we tuned the initial conditions and the switching temperature in the model using pion, kaon, and proton + antiproton p_T spectra from the PHENIX Collaboration in our previous study, the results are overall in good agreement with the STAR data, too.

In particular, the model reproduces the pion data up to $p_T \sim 3$ GeV/c in central (0–12%) collisions. Above this, our result gradually deviates from the data due to the appearance of (semi-)hard components such as recombination and jet fragmentation. The more peripheral the collision, the lower the p_T where our result begins to deviate from the data. Due to the limited p_T range of the data, the same behavior is not seen in the kaon spectra. If one looks at the pion spectrum in peripheral collisions (60–80% centrality) carefully, then one sees that experimental data are systematically larger than the results. This is because in peripheral collisions there is a small discrepancy between the PHENIX [52] and STAR [54] pion yields. Nevertheless, we did not further tune the parameters to reproduce the STAR data because we want to keep the same framework as in our previous study [19].

In Fig. 2, we compare the p_T spectra in $|\eta| < 0.5$ for (a) protons and (b) ϕ mesons with the STAR data [54,56]. Due to limited statistics, we do not show some data points of the proton spectra in high-p_T regions (above $p_T \sim 4$ GeV/c) in 20–40, 40–60, and 60–80% centrality. The proton spectra from STAR are corrected for the Λ and Σ^+ feed-down. Weak decays do not occur in the default setting in JAM, so we are able to compare our results directly with the STAR-corrected data. Since we neglect the baryon chemical potential in our model, our results for protons are slightly below the experimental data at some p_T range. Nevertheless, overall slopes are in good agreement with the data below $p_T \sim 3$ GeV/c. On the other hand, similarly to pions, deviation between the experimental

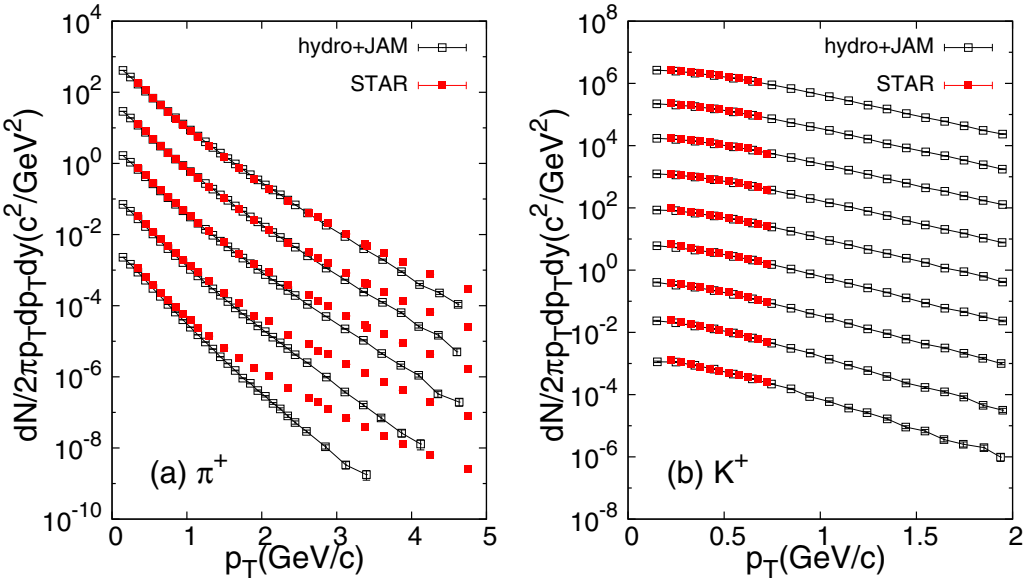

FIG. 1. (Color online) Transverse-momentum distributions of (a) π^+ ($|\eta| < 0.5$) and (b) K^+ ($|\eta| < 0.1$) obtained from the integrated dynamical approach (open square) compared with data from the STAR Collaboration [54,55] (filled square) for $\sqrt{s_{NN}} = 200$ GeV Au + Au collisions. From top to bottom, each spectrum shows the results of 0–12, 10–20, 20–40, 40–60, and 60–80% centrality multiplied by 10^n with $n = 0$ to -4 for pions and 0–5, 5–10, 10–20, 20–30, 30–40, 40–50, 50–60, 60–70, and 70–80% centrality multiplied by 10^n with $n = 5$ to -3 for kaons.

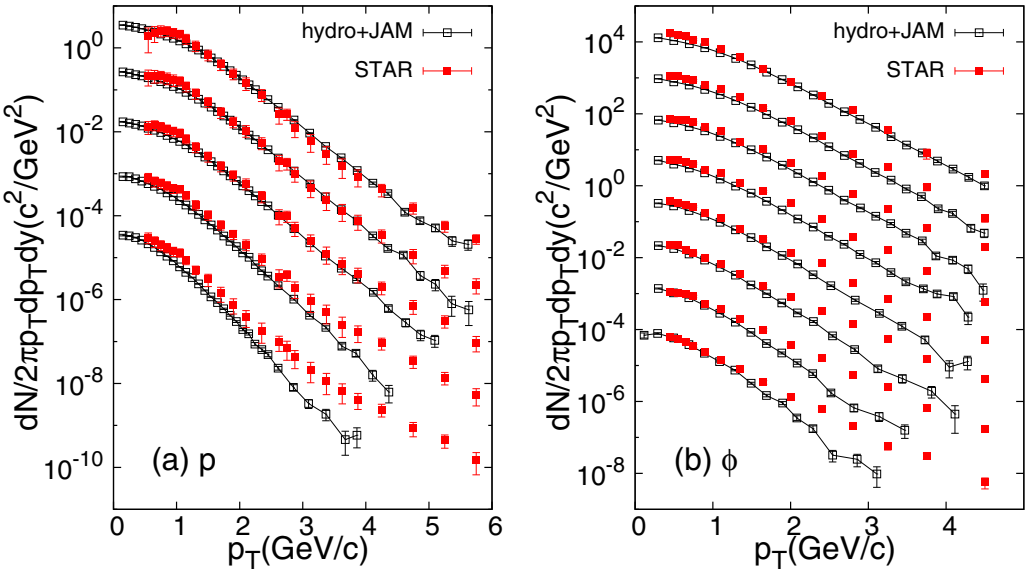

FIG. 2. (Color online) Transverse-momentum distributions of (a) protons and (b) ϕ mesons in $|\eta| < 0.5$ obtained from the integrated dynamical approach (open square) compared with data from the STAR Collaboration [54,56] (filled square) for $\sqrt{s_{NN}} = 200$ GeV Au + Au collisions. From top to bottom, each spectrum shows the results of 0–12, 10–20, 20–40, 40–60, and 60–80% centrality multiplied by 10^n with $n = 0$ to -4 for protons and 0–10, 10–20, 20–30, 30–40, 40–50, 50–60, 60–70, and 70–80% centrality multiplied by 10^n with $n = 4$ to -3 for ϕ mesons.

data and the results gradually increases with p_T, and the more peripheral the collision, the lower the p_T where this deviation appears. As mentioned in the previous section, we switch off the decays of ϕ mesons in the hadronic cascade to be able to analyze ϕ meson spectra directly without resorting to mass reconstruction from kaons. Tendencies seen in ϕ-meson spectra are similar to those in proton spectra.

Figure 3 shows the p_T spectra of strange baryons, (a) $\Lambda + \bar{\Lambda}$ ($|\eta| < 1.0$), (b) $\Xi + \bar{\Xi}$ ($|\eta| < 0.75$), and (c) $\Omega + \bar{\Omega}$ ($|\eta| < 0.75$), compared with the STAR data [57]. Similarly to the proton case, the more peripheral the collisions, the worse the agreement between experimental data and the results, especially above $p_T = 1.5$–2.0 GeV/c. As expected, the measured Λ and Ξ yields are larger than the calculated yields. We had chosen the switching temperature $T_{\rm sw}$ to reproduce the observed pion-to-kaon and pion-to-proton ratios, which leads to a lower temperature than the statistical model fit to all observed hadrons [58,59] and thus to lower yields of hyperons. On the other hand, it has been argued that the statistical model [60] with the common chemical freeze-out temperature does not reproduce the proton and Λ yields simultaneously at the LHC and RHIC energies [61]. It was claimed [44] that earlier switching from hydrodynamics to UrQMD at energy density $\sim$840 MeV/fm^3, which corresponds to higher temperature than $T_{\rm sw} = 155$ MeV, would be a key to resolve the issue, but our results do not improve significantly if we use higher switching temperature $T_{\rm sw} = 165$ MeV. It remains to be seen whether the origin of this discrepancy lies in a different description of the proton-antiproton annihilations in JAM and UrQMD cascades or in different expansion dynamics in collisions at RHIC and LHC energies.

Note that the experimental yield of Λ in STAR contains the feed-down from electromagnetic Σ^0 decays ($\Sigma^0 \to \Lambda + \gamma$) [62]. Since this is the dominant mode of Σ^0 decay with the branching ratio $\sim$100% and $c\tau = 2.22 \times 10^{-11}$ m [47], the feed-down correction of it is experimentally challenging. We simulate this decay in JAM and include this contribution in the final Λ spectra in Fig. 3(a). Since the mass of Σ^0 is close to that of Λ, the yield of the primordial Σ^0 is expected to be of the same order as the yield of the primordial Λ. The ratio of Σ^0 to Λ at switching temperature can be estimated as

$$\frac{n_{\Sigma^0}}{n_\Lambda} \approx \frac{\exp\left(-\frac{m_{\Sigma^0}}{T_{\rm sw}}\right)}{\exp\left(-\frac{m_\Lambda}{T_{\rm sw}}\right)} \sim 0.61. \quad (6)$$

After correcting for the effects of resonance decay and rescatterings, we find that the final particle ratio of Σ^0 to Λ is around 0.3. We have included both sources of Λ in our results, but in general this should be kept in mind when comparing theoretical results with the data.

Although the number of data points from STAR is limited for Ω baryons, their yields and slopes are consistent with our results. It is worth noticing here that the recent lattice QCD calculations suggest the existence of resonances in general [63],[1] or strange baryon resonances in particular [22], which have not been discovered yet.

Such resonances, whether they are of the Hagedorn type [65] or those predicted by quark models (see, e.g., Refs. [66,67]), would contribute to the yields of strange

[1]It is, however, unknown whether the difference between the lattice QCD and hadron resonance gas model trace anomalies indicates the inadequacy of the hadron resonance gas model [64] or the existence of so-far undiscovered resonance states [63].

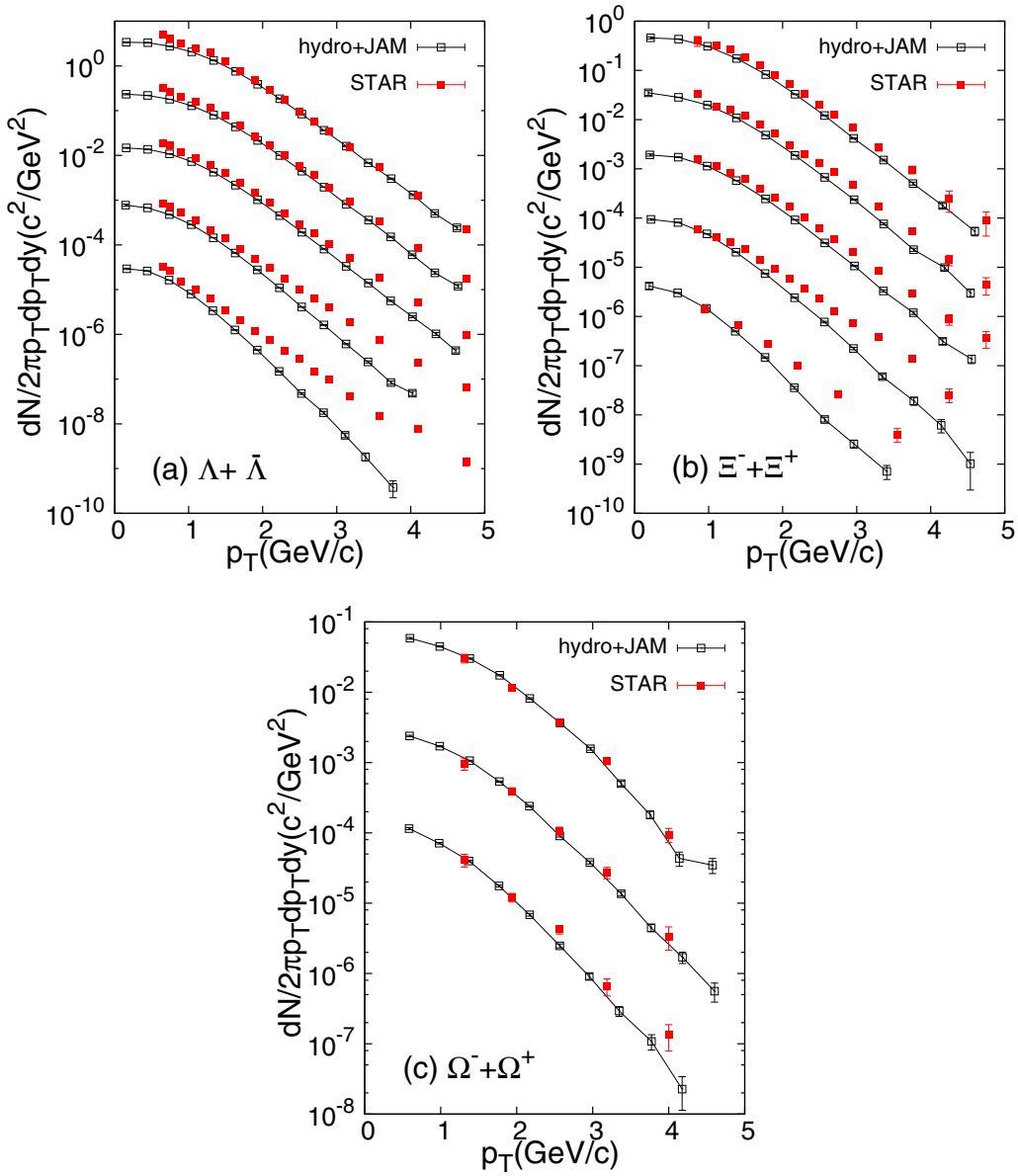

FIG. 3. (Color online) Transverse-momentum distributions of (a) Λ ($|\eta| < 1.0$), (b) Ξ ($|\eta| < 0.75$), and (c) Ω ($|\eta| < 0.75$) obtained from the integrated dynamical approach (open square) compared with data from the STAR Collaboration [57] (filled square) for $\sqrt{s_{NN}} = 200$ GeV Au + Au collisions. From top to bottom, each spectrum shows data of 0–5, 10–20, 20–40, 40–60, and 60–80% centrality multiplied by 10^n with $n = 0$ to -4 for Λ and Ξ and 0–5, 20–40, and 40–60% centrality multiplied by 10^n with $n = 0$ to -2 for Ω. Note that the p_T distributions of Λ include the contribution from Σ^0 decay, see the text for details.

hadrons, and might somewhat change the dynamics of the late hadronic stage [68–70]. Some of those resonances could be formed in the scattering of ϕ mesons or Ω baryons, but it is unknown whether such resonances would significantly affect the average scattering cross section of ϕ mesons and Ω baryons in temperatures below the switching temperature. Investigation of this possibility is beyond the scope of the present paper.

B. Elliptic flow

In Fig. 4 the two-particle cumulant $v_2(p_T)$ of pions, kaons, and protons in the midrapidity region ($|\eta| < 1.0$) are compared with STAR $v_2\{2\}$ data [71] at three centralities (10–20%, 30–40%, and 50–60%). For pions, we reasonably reproduce the experimental data for each centrality class. Due to the limited number of events, it is hard to obtain $v_2\{2\}$ with smaller statistical errors, and this would be especially difficult for protons. Thus some points with large error bars, in particular in the low-p_T region, are not shown in these figures for clarity. We also calculated $v_2\{\mathrm{RP}\}$ (not shown), namely v_2 with respect to the theoretically known reaction plane, to reduce the statistical errors and found that the $v_2\{\mathrm{RP}\}$ of pions, kaons, and protons from our model are in reasonable agreement with the STAR data in midcentral collisions. However, $v_2\{\mathrm{RP}\}$ lacks initial fluctuations of the event plane angle and, consequently,

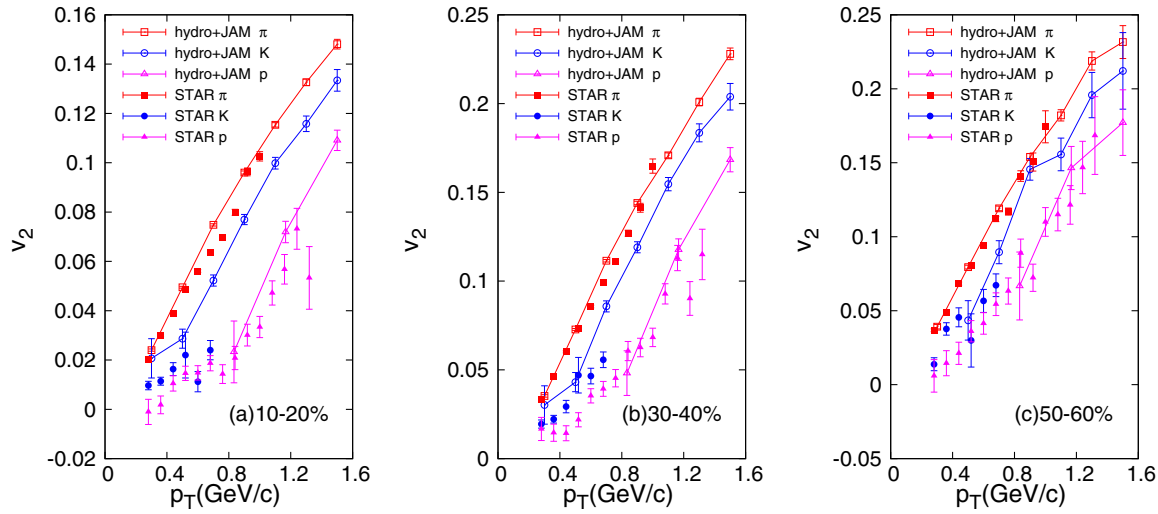

FIG. 4. (Color online) Transverse-momentum dependence of elliptic flow parameter $v_2\{2\}$ of pions (open square), kaons (open circle), and protons (open triangle) in $|\eta| < 1.0$ obtained from the integrated dynamical approach compared with $v_2\{2\}$ data from the STAR Collaboration [71] (filled symbol) for $\sqrt{s_{NN}} = 200$ GeV Au + Au collisions. Centrality classes are (a) 10–20%, (b) 30–40%, and (c) 50–60%.

is significantly smaller than the data in both central and peripheral collisions. It is noted that, from the MC Glauber model analysis, the fluctuation effect on eccentricity is large in central and peripheral collisions, but almost negligible in midcentral collisions. See, e.g., Fig. 3(a) in Ref. [72]. At the centralities shown in Fig. 4 clear mass ordering behavior among pions, kaons, and protons, namely larger v_2 for smaller mass at fixed p_T, is seen both in our results and in the STAR data.

In Fig. 5, we show the event plane $v_2(p_T)$ of ϕ, Λ, Ξ, and Ω at some centrality classes from the integrated dynamical approach. In comparison, STAR data from the event plane method $v_2\{\mathrm{EP}\}$ [56,73] are also shown in the figure. We calculate $v_2\{\mathrm{EP}\}$ by employing the η-subevent method using hadrons in $|\eta| < 1.0$ as done by the STAR Collaboration [73],

$$v_2\{\mathrm{EP}\} = \frac{1}{\mathcal{R}}\langle\cos[2(\phi_\pm - \Psi_{2,\mp})]\rangle. \tag{7}$$

The event plane angle $\Psi_{2,+}$ ($\Psi_{2,-}$) is defined for the particles with positive (negative) pseudorapidity. In the actual experimental analysis, a pseudorapidity gap of $|\Delta\eta| = 0.075$ between two subevents was introduced to suppress the nonflow effects [73]. We found, however, that introduction of the gap does not change final results within error bars in our analysis. The resolution factor in this case is calculated as $\mathcal{R} = \sqrt{\langle\cos[2(\Psi_{2,+} - \Psi_{2,-})]\rangle}$. In calculating the Q vector,

$$Q = \sum_j w_j \exp(2i\phi_j), \tag{8}$$

needed for the event plane angle

$$\Psi_{2,\pm} = \frac{1}{2}\tan^{-1}\frac{\mathrm{Im}Q}{\mathrm{Re}Q}, \tag{9}$$

a weight factor $w_j = \min\{p_{T,j}, 2\ \mathrm{GeV}/c\}$ was also introduced [73]. However, within statistical errors the results are similar to those obtained using $w_j = 1$. Therefore, we employ $w_j = 1$ in all the results shown in Fig. 5. For Λ and Ξ our results are systematically larger than the STAR data. For ϕ and Ω our results show similar behavior, but since the data have large errors, no firm conclusion can be made.

Our results of elliptic flow parameters for identified hadrons are systematically larger than the STAR data, which suggests that there is room for finite, but perhaps small, viscosity in the fluid-dynamical stage. However, we do not go into detail about the QGP viscosity since the purpose of the present study is to investigate the effects of rescattering in the late hadronic stage, which are not affected by the QGP viscosity nor by the initial state of the system.

IV. HADRONIC RESCATTERING EFFECTS

In this section, we investigate hadronic rescattering effects on final observables, in particular, how much final observables reflect the properties of the system at particlization in the integrated dynamical approach. If some observables do not change much during the late kinetic stage, then these observables can be utilized as "penetrating" probes. Namely, their distributions reflect the properties of the system immediately after hadronization and are not contaminated by later hadronic rescatterings. To quantify the effects of hadronic rescattering we perform simulations of nuclear collisions with the following three options in the hadronic cascade calculations: (I) full dynamical evolution (default), (II) deactivating hadronic rescatterings, and (III) deactivating both hadronic rescatterings and resonance decays. To simplify the calculations we calculate elliptic flow parameters with respect to the theoretically known reaction plane.

In Figs. 6(a) and 6(b), we show $v_2(p_T)$ of pions, kaons, protons, and ϕ mesons in minimum bias Au + Au collisions at $\sqrt{s_{NN}} = 200$ GeV from the integrated dynamical approach. Figure 6(a) represents the results without hadronic rescatterings [option (II)]. These results exhibit the mass ordering behavior, namely $v_2^\pi(p_T) > v_2^K(p_T) > v_2^p(p_T) > v_2^\phi(p_T)$ for $m_\pi < m_K < m_p < m_\phi$, in the low-$p_T$ region. In general, the

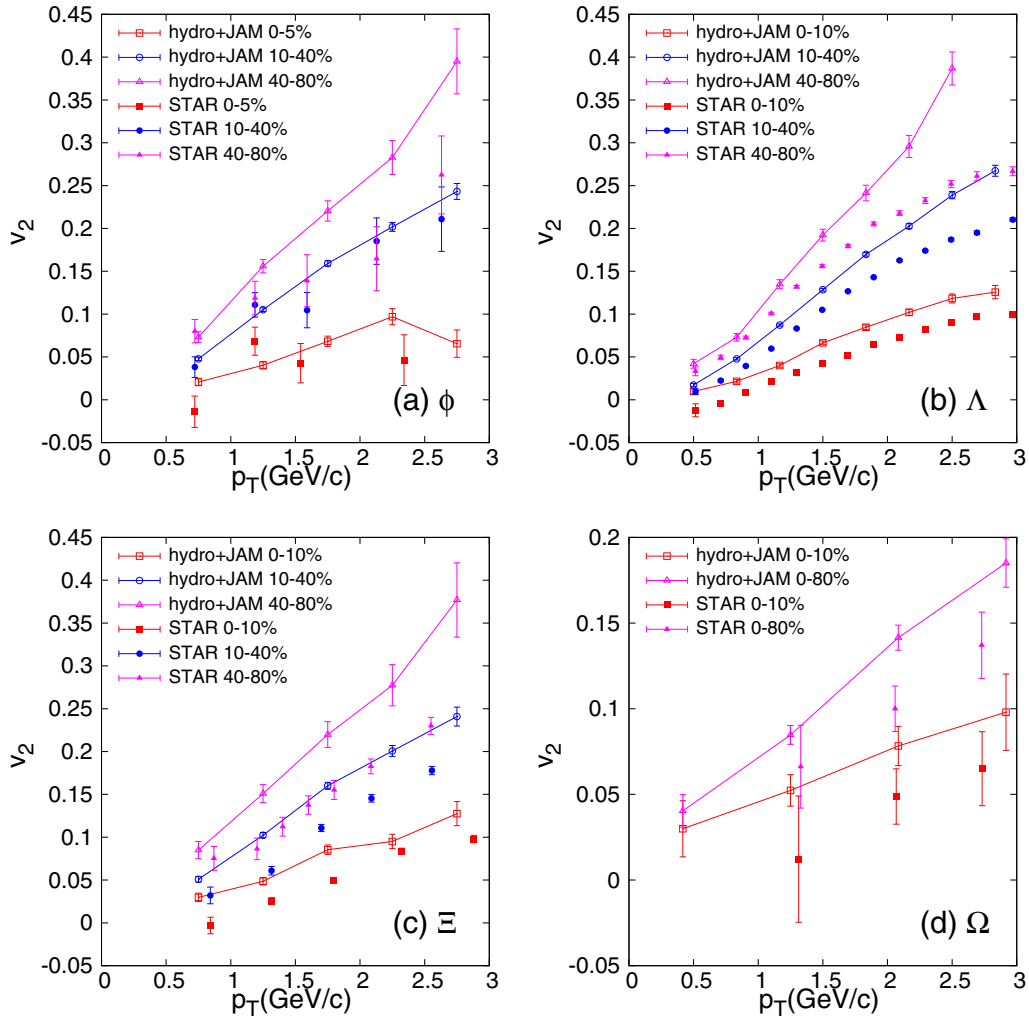

FIG. 5. (Color online) Transverse-momentum dependence of the elliptic flow parameter $v_2\{\mathrm{EP}\}$ of (a) ϕ mesons (0–5, 10–40, and 40–80% centrality), (b) Λ baryons (0–10, 10–40, and 40–80% centrality), (c) Ξ baryons (0–10, 10–40, and 40–80% centrality), and (d) Ω baryons (0–10 and 0–80% centrality) in $|\eta| < 1.0$ obtained from the integrated dynamical approach (open symbol) compared with data from the STAR Collaboration [56,73] (filled symbol) for $\sqrt{s_{NN}} = 200$ GeV Au + Au collisions.

mass ordering results from collective flow in which all the components of the fluid flow at a common fluid velocity [74]. On the other hand, Fig. 6(b) shows a violation of mass ordering between protons and ϕ mesons below $p_T \sim 1.5$ GeV/c: $v_2^p < v_2^\phi$ even though $m_p < m_\phi$. If one compares these two plots, $v_2^p(p_T)$ decreases below ~1.5 GeV/c during the hadronic rescattering stage. On the other hand, $v_2^\phi(p_T)$ stays almost unchanged during the hadronic rescattering stage. As a consequence, the order is inversed between protons and ϕ mesons. To see this behavior more clearly, we also show the ratio v_2^ϕ/v_2^p. Below 1 GeV/c, this ratio becomes clearly positive indicating the violation of mass ordering.

The violation of mass ordering was predicted in Ref. [15] and observed recently by the STAR Collaboration [18]. It should be noted that a larger switching temperature ($T_{\mathrm{sw}} =$ 169 MeV) and a first-order phase transition in the EOS were employed in the calculations of Ref. [15]. We confirm in the present study that the violation of mass ordering is also observed when a more realistic EOS from lattice QCD and a lower switching temperature ($T_{\mathrm{sw}} = 155$ MeV) are used.

We can interpret the violation of mass ordering as a result of the evolution of mean p_T and p_T-averaged v_2 during the late transport stage. The slope of the p_T differential v_2 can be approximated by the ratio of p_T-averaged v_2 to mean p_T [7],

$$\frac{dv_2(p_T)}{dp_T} \approx \frac{v_2}{\langle p_T \rangle}. \tag{10}$$

If $v_2(p_T)$ is linearly proportional to p_T, then it is easy to show that Eq. (10) holds exactly. Thus a change of slope in $v_2(p_T)$ due to hadronic rescatterings could be attributed to changes of v_2 and/or $\langle p_T \rangle$, which provides us with more intuitive understanding.

We next calculate $\langle p_T \rangle$ and p_T-averaged v_2 for each identified hadron in $|y| < 1$ in minimum-bias Au + Au collisions at $\sqrt{s_{NN}} = 200$ GeV with the three different options mentioned above. We show $\langle p_T \rangle$ and v_2 as functions of hadron mass in Figs. 7(a) and 7(b), respectively. Default results using option (I)

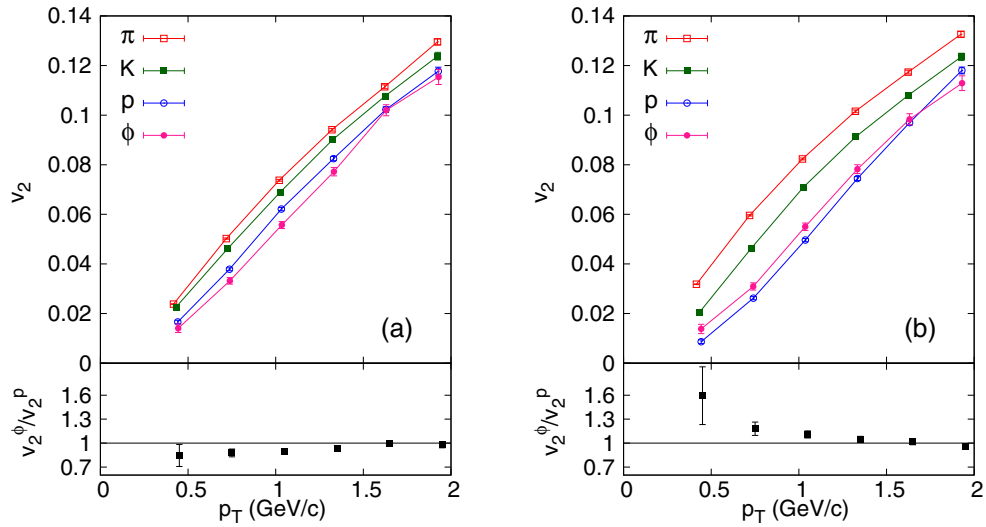

FIG. 6. (Color online) Transverse-momentum dependence of elliptic flow parameter v_2 for pions (open square), kaons (filled square), protons (open circle), and ϕ mesons (filled circle) in $|\eta| < 1.0$ obtained from the integrated dynamical approach (a) without hadronic rescattering and (b) with hadronic rescattering in minimum bias $\sqrt{s_{NN}} = 200$ GeV Au + Au collisions. The lower panels of the plots show the ratio of v_2^{ϕ} to v_2^{p}.

are shown with closed squares. To see the effect of hadronic rescatterings, we use option (II) in the hadronic cascade calculation. We also use option (III) to obtain the results excluding the contributions of both hadronic rescatterings and resonance decays. In the default option (I) in which both hadronic rescatterings and resonance decays are included, $\langle p_T \rangle$ is not a linear function of the hadron mass. By switching off hadronic rescatterings by employing option (II), we are able to extract the hadronic rescattering effects on evolution of mean p_T in the late hadronic stage. The difference of $\langle p_T \rangle$ between those with and without hadronic rescatterings are relatively smaller for π, ϕ, Ξ, and Ω than for the others. In order to confirm a pure flow effect we also calculate $\langle p_T \rangle$ with option (III) in which resonance decay contributions are also not included. As is well known in analysis using the blast-wave model [75], $\langle p_T \rangle$ is a linear function of the hadron mass in this case [76]. We also confirm that it is the case even in our fully dynamical calculations. p_T-averaged v_2 for the three options (I), (II), and (III) are compared with each other in Fig. 7(b). By comparing the results (I) and (II) one finds that, due to hadronic rescatterings, v_2 for hadrons other than pions increases little—by at most ∼6%—but v_2 for pions increases by ∼25% even though elliptic flow parameters are commonly believed to be sensitive to the early stage of the reaction. On

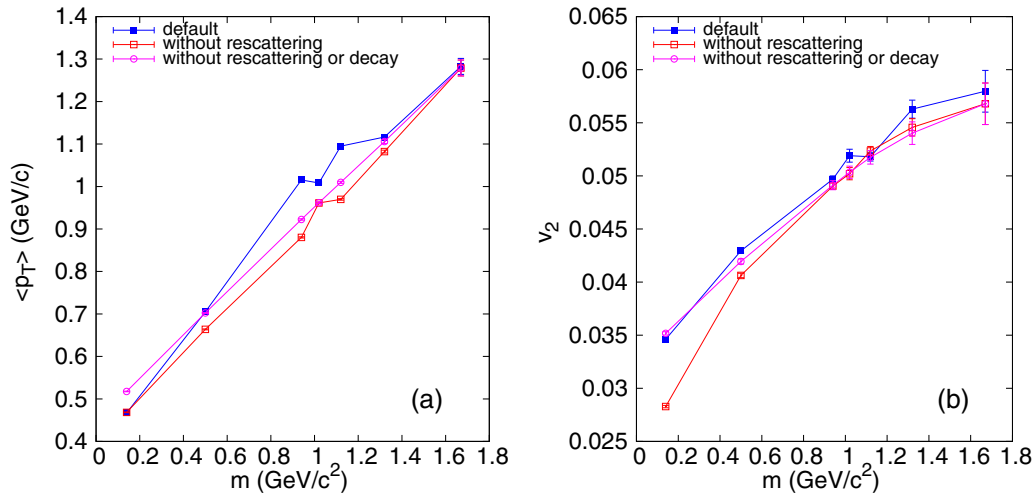

FIG. 7. (Color online) (a) Mean transverse momentum $\langle p_T \rangle$ and (b) p_T-averaged v_2 in minimum-bias $\sqrt{s_{NN}} = 200$ GeV Au + Au collisions around midrapidity ($|y| < 1.0$) obtained by the hybrid model as a function of the hadron mass. Each point represents the result for π, K, p, ϕ, Λ, Ξ, and Ω from left to right. Three lines show the results with different options, respectively: (I) full calculations with both resonance decays and hadronic rescsatterings (filled square), (II) calculations with resonance decays only (open square), and (III) calculations without resonance decays or hadronic rescatterings (open circle). Lines are to guide the eye.

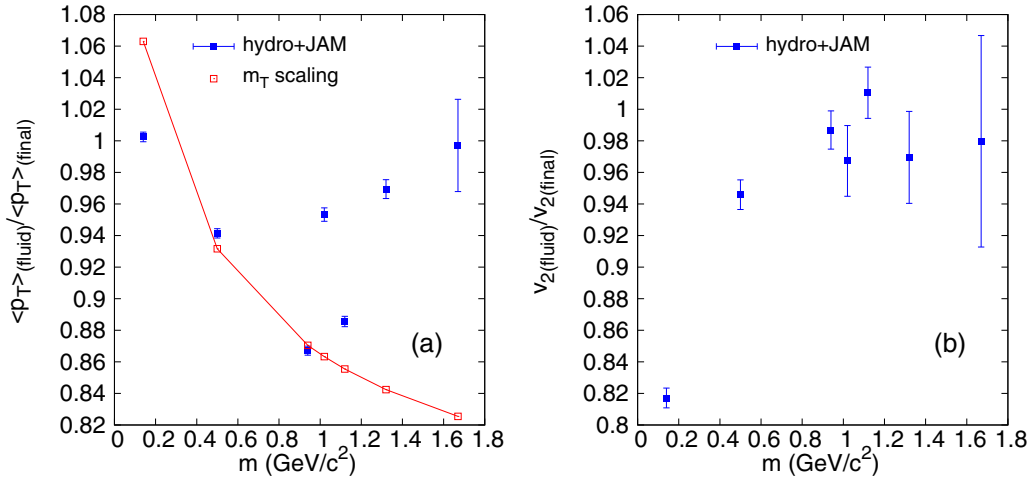

FIG. 8. (Color online) Ratio of observables at the fluid stage to the final ones in minimum bias $\sqrt{s_{NN}} = 200$ GeV Au + Au collisions in $|y| < 1.0$ obtained by use of the integrated dynamical approach (filled square) for (a) mean transverse momentum $\langle p_T \rangle$ and (b) p_T-averaged v_2. In comparison, the ratio of $\langle p_T \rangle$ obtained from a transverse mass scaling ansatz (open square) is also shown (see the text). Each point corresponds to a hadron as shown in the caption to Fig. 7.

the other hand, the effect of hadronic rescattering on pion mean p_T is almost absent [7]. It is interesting to note that the effect of resonance decays on pion v_2 is also significant, see Fig. 7(b). How resonance decays reduce pion v_2 was discussed in Ref. [77]. As we expected, neither $\langle p_T \rangle$ nor v_2 for multistrange hadrons is affected by hadronic rescatterings, but at least one of these two observables is affected for all other particles.

To see how much hadronic rescatterings affect the final observables, we show ratios of $\langle p_T \rangle$ and v_2 at particlization but after decays [option (II)] to the ones in the final state [option (I)] [78] for each identified hadron in Fig. 8. For comparison, we also show the ratio obtained from a m_T scaling ansatz (open square) [76] in the case of mean p_T. In this ansatz, one can parametrize the p_T distribution as

$$\frac{dN}{p_T dp_T} \propto \exp\left(-\frac{m_T}{T_{\rm eff}}\right), \tag{11}$$

$$T_{\rm eff} = T_f + \tfrac{1}{2} m v_f^2, \tag{12}$$

$$m_T = \sqrt{p_T^2 + m^2}, \tag{13}$$

where T_f, m, and v_f are freeze-out temperature, particle mass, and flow velocity, respectively. Parameters were chosen to reproduce the slope of the proton p_T spectrum in option (II) ($T_f = 0.155$ GeV and $v_f = 0.56$) and in option (I) ($T_f = 0.130$ GeV and $v_f = 0.71$). If all the particles interact strongly with each other and move at a common collective velocity during the hadronic stage, then mass ordering would appear. In fact, the result from the m_T scaling depends monotonically on particle mass, and pions, kaons, and protons follow this monotonic tendency obtained from m_T scaling ansatz. However, multistrange hadrons (including "hidden" strangeness) (ϕ, Ξ, and Ω) in the integrated dynamical approach deviate from the pattern. This means that multistrange hadrons freeze out earlier than other hadrons and do not participate in the radial flow during the transport stage. Multistrange hadrons couple weakly with the system consisting mostly of pions since they have small scattering cross sections and hardly rescatter with pions in the late hadronic stage.

Mean transverse momentum $\langle p_T \rangle$ for dominant constituents of the medium, namely pions, decreases during the hadronic rescattering stage since pdV work done in the longitudinal direction reduces the transverse energy per unit rapidity [79,80] but the number of pions is fixed. In this way,

$$\frac{\langle p_T \rangle_{\rm (fluid)}}{\langle p_T \rangle_{\rm (final)}} \approx \frac{(1/N_\pi)(dE_T/dy)_{\rm (fluid)}}{(1/N_\pi)(dE_T/dy)_{\rm (final)}} > 1. \tag{14}$$

In fact, the two parameter sets in the m_T scaling ansatz mentioned above are chosen to obey this inequality (14). As for v_2 in Fig. 8(b), about 20% of final v_2 of pions is generated during the late transport stage. In other words, only ~80% of final v_2 reflects elliptic flow generated during the fluid-dynamical stage. Obviously, this could depend on centrality (and perhaps collision energy) and the number can be regarded as an average value at the RHIC energy. Whereas hadronic rescatterings affect little final v_2 for the other hadrons. By combining these two results in Fig. 8, we conclude that multistrange hadrons are less affected by hadronic rescatterings and, therefore, can be used to probe the hadronization stage in high-energy nuclear collisions.

Coming back to violation of mass ordering in differential v_2 shown in Fig. 6 and also in Fig. 5 in Ref. [15], one can interpret this intriguing phenomenon as follows. For pions, p_T-averaged v_2 increases but $\langle p_T \rangle$ changes little in the hadronic stage, so the slope of $v_2^\pi(p_T)$ gets steeper, as seen from Eq. (10). On the other hand, for protons, p_T-averaged v_2 does not change so much, but $\langle p_T \rangle$ increases in the hadronic stage, so $v_2^p(p_T)$ decreases. However, for ϕ mesons, both p_T-averaged v_2 and $\langle p_T \rangle$ after the hydrodynamic stage are almost the same in the final state and, consequently, $v_2^\phi(p_T)$ is unchanged.

Finally, we show the normalized freeze-out time (defined as the longitudinal proper time τ of the last interaction in hadronic cascade simulations) distributions around midrapidity ($|y| < 1.0$) in minimum bias Au + Au collisions

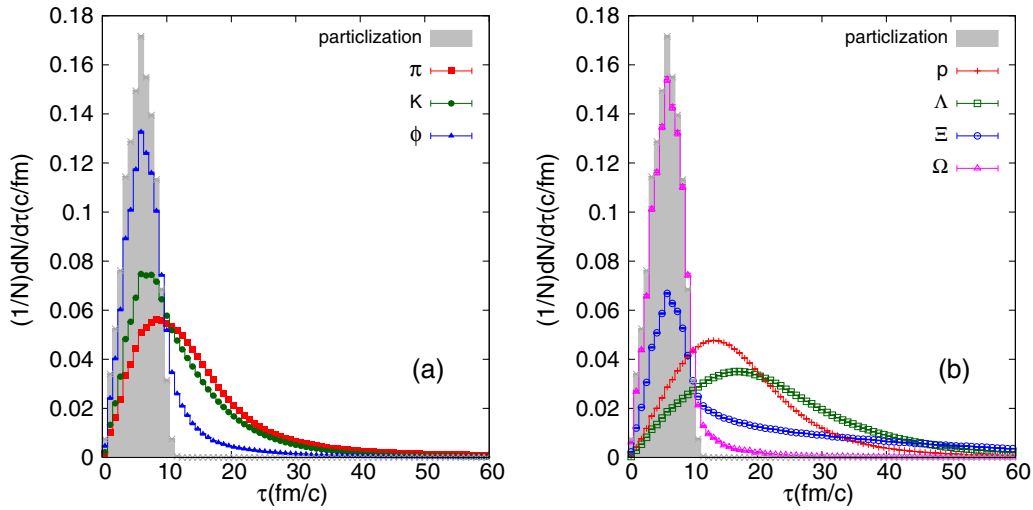

FIG. 9. (Color online) Normalized freeze-out time (τ) distributions for (a) mesons: π, K, and ϕ, and (b) baryons: p, Λ, Ξ, and Ω in $|y| < 1.0$ in minimum bias $\sqrt{s_{NN}} = 200$ GeV Au + Au collisions. The shaded areas correspond to normalized particlization time distributions of charged hadrons.

at $\sqrt{s_{NN}} = 200$ GeV. In Fig. 9 the results are shown in two panels, [Fig. 9(a)] for mesons and [Fig. 9(b)] for baryons, for clarity. The shaded areas represent the particlization time distribution for charged hadrons. Since the particlization time does not depend on scattering cross sections, it is almost equal for all hadrons within error bars. A prominent peak with small width is seen below $\tau = 10$ fm/c, corresponding to the time of particlization at different parts of the system. The freeze-out time distributions of ϕ and Ω do not differ from the particlization time distribution significantly, which reflects their small scattering cross sections. On the other hand, other hadrons have broader freeze-out time distributions. For Ξ, a peak also exists at an early time as for ϕ and Ω but its height is lower and the peak is accompanied by a broad tail. This is because Ξ has a contribution from long-living resonance $\Xi(1530)$ (decay width $\Gamma = 9.9$ MeV $\sim 1/(20$ fm/$c)$ [47]) whose decay forms a long tail in the freeze-out time distribution. So the primordial Ξ freezes out as early as do ϕ and Ω. These results support our findings above that multistrange hadrons freeze out just after the particlization due to fewer rescatterings in the late kinetic stage.

V. SUMMARY

We have studied the effects of the hadronic rescatterings especially on multistrange hadrons and claimed they can be used to probe the hadronization stage in high-energy nuclear collisions. We have employed an integrated dynamical model in which the ideal hydrodynamic model is combined with the hadronic cascade model, JAM, and confirmed that our model fairly reproduces the experimental data of p_T spectra and differential v_2 not only for pions, kaons, and protons but also for multistrange hadrons. Within this approach, we have simulated the hadronic stage with or without the rescatterings and compared the calculated mean transverse momentum and p_T-averaged v_2 in these two cases to investigate the hadronic rescattering effects. We have found that the multistrange hadrons are less affected by the rescatterings than nonstrange hadrons. Because of the small scattering cross sections, the multistrange hadrons do not fully participate in the radial flow during the hadronic stage and freeze out earlier than nonstrange hadrons. With these results we have shown how to interpret behaviors of mass ordering and its violation in $v_2(p_T)$. Changes of slope of $v_2(p_T)$ during the hadronic rescattering stage result from interplay between changes of mean p_T and p_T-averaged v_2. We have also showed the freeze-out time distributions for identified hadrons and confirmed that the multistrange hadrons freeze out soon after they are "particlized."

In future, we also plan to investigate the hadronic rescattering effects on observables for multistrange hadrons at the LHC energy. Although elliptic flow parameters are expected to be less affected by the hadronic rescatterings at the LHC, it would be important to quantify how much they do change and thus how much the observed v_2 at LHC reflects the QGP evolution.

ACKNOWLEDGMENTS

We acknowledge fruitful discussion with N. Xu. This work was supported by JSPS KAKENHI Grants No. 12J08554 (K.M.) and No. 25400269 (T.H.) and by BMBF under Contract No. 06FY9092 (P.H.).

[1] K. Yagi, T. Hatsuda, and Y. Miake, Cambr. Monogr. Part. Phys., Nucl. Phys., Cosmol. **23**, 1 (2005).
[2] U. W. Heinz and P. F. Kolb, Nucl. Phys. A **702**, 269 (2002).
[3] M. Gyulassy, arXiv:nucl-th/0403032 (2004).
[4] T. D. Lee, Nucl. Phys. A **750**, 1 (2005).
[5] M. Gyulassy and L. McLerran, Nucl. Phys. A **750**, 30 (2005).

[6] E. V. Shuryak, Nucl. Phys. A **750**, 64 (2005).
[7] T. Hirano and M. Gyulassy, Nucl. Phys. A **769**, 71 (2006).
[8] E. L. Feinberg, Nuovo Cimento A **34**, 391 (1976).
[9] E. V. Shuryak, Phys. Lett. B **78**, 150 (1978).
[10] E. L. Bratkovskaya, Nucl. Phys. A **931**, 194 (2014).
[11] A. Shor, Phys. Rev. Lett. **54**, 1122 (1985).
[12] H. van Hecke, H. Sorge, and N. Xu, Phys. Rev. Lett. **81**, 5764 (1998).
[13] S. A. Bass and A. Dumitru, Phys. Rev. C **61**, 064909 (2000).
[14] Y. Cheng, F. Liu, Z. Liu, K. Schweda, and N. Xu, Phys. Rev. C **68**, 034910 (2003).
[15] T. Hirano, U. Heinz, D. Kharzeev, R. Lacey, and Y. Nara, Phys. Rev. C **77**, 044909 (2008).
[16] M. He, R. J. Fries, and R. Rapp, Phys. Rev. C **85**, 044911 (2012).
[17] X. Zhu, F. Meng, H. Song, and Y. X. Liu, Phys. Rev. C **91**, 034904 (2015).
[18] M. Nasim (STAR Collaboration), Nucl. Phys. A **904-905**, 413c (2013).
[19] T. Hirano, P. Huovinen, K. Murase, and Y. Nara, Prog. Part. Nucl. Phys. **70**, 108 (2013).
[20] P. Huovinen and P. Petreczky, Nucl. Phys. A **837**, 26 (2010).
[21] Y. Nara, N. Otuka, A. Ohnishi, K. Niita, and S. Chiba, Phys. Rev. C **61**, 024901 (1999).
[22] A. Bazavov *et al.*, Phys. Rev. Lett. **113**, 072001 (2014).
[23] T. Hirano, Phys. Rev. C **65**, 011901(R) (2001).
[24] P. Colella and P. R. Woodward, J. Comput. Phys. **54**, 174 (1984).
[25] T. Hirano and Y. Nara, Prog. Theor. Exp. Phys. **2012**, 01A203 (2012).
[26] S. A. Bass, A. Dumitru, M. Bleicher, L. Bravina, E. Zabrodin, H. Stöcker, and W. Greiner, Phys. Rev. C **60**, 021902(R) (1999).
[27] D. Teaney, J. Lauret, and E. V. Shuryak, Phys. Rev. Lett. **86**, 4783 (2001).
[28] D. Teaney, J. Lauret, and E. V. Shuryak, arXiv:nucl-th/0110037 (2001).
[29] T. Hirano, U. W. Heinz, D. Kharzeev, R. Lacey, and Y. Nara, Phys. Lett. B **636**, 299 (2006).
[30] C. Nonaka and S. A. Bass, Phys. Rev. C **75**, 014902 (2007).
[31] H. Petersen, J. Steinheimer, G. Burau, M. Bleicher, and H. Stocker, Phys. Rev. C **78**, 044901 (2008).
[32] F. Cooper and G. Frye, Phys. Rev. D **10**, 186 (1974).
[33] H. Sorge, A. von Keitz, R. Mattiello, H. Stöcker, and W. Greiner, Z. Phys. C **47**, 629 (1990).
[34] H. Sorge, L. Winckelmann, H. Stöcker, and W. Greiner, Z. Phys. C **59**, 85 (1993).
[35] S. A. Bass *et al.*, Prog. Part. Nucl. Phys. **41**, 255 (1998).
[36] M. Bleicher *et al.*, J. Phys. G **25**, 1859 (1999).
[37] C. M. Ko, V. Koch, and G. Q. Li, Annu. Rev. Nucl. Part. Sci. **47**, 505 (1997).
[38] X. S. Fang, C. M. Ko, G. Q. Li, and Y. M. Zheng, Nucl. Phys. A **575**, 766 (1994).
[39] W. Cassing and E. L. Bratkovskaya, Phys. Rep. **308**, 65 (1999).
[40] W. Cassing, Eur. Phys. J. Spec. Top. **168**, 3 (2009).
[41] O. Buss, T. Gaitanos, K. Gallmeister, H. van Hees, M. Kaskulov, O. Lalakulich, A. B. Larionov, T. Leitner, J. Weil, and U. Mosel, Phys. Rep. **512**, 1 (2012).
[42] C. Hartnack, H. Oeschler, Y. Leifels, E. L. Bratkovskaya, and J. Aichelin, Phys. Rep. **510**, 119 (2012).
[43] R. Rapp and E. V. Shuryak, Phys. Rev. Lett. **86**, 2980 (2001).
[44] J. Steinheimer, J. Aichelin, and M. Bleicher, Phys. Rev. Lett. **110**, 042501 (2013).
[45] Y. Pan and S. Pratt, Phys. Rev. C **89**, 044911 (2014).
[46] P. Huovinen and J. I. Kapusta, Phys. Rev. C **69**, 014902 (2004).
[47] K. A. Olive *et al.* [Particle Data Group], Chin. Phys. C **38**, 090001 (2014).
[48] M. L. Miller, K. Reygers, S. J. Sanders, and P. Steinberg, Annu. Rev. Nucl. Part. Sci. **57**, 205 (2007).
[49] H.-J. Drescher and Y. Nara, Phys. Rev. C **75**, 034905 (2007).
[50] H.-J. Drescher and Y. Nara, Phys. Rev. C **76**, 041903 (2007).
[51] J. D. Bjorken, Phys. Rev. D **27**, 140 (1983).
[52] S. S. Adler *et al.* (PHENIX Collaboration), Phys. Rev. C **69**, 034909 (2004).
[53] C. Adler *et al.* (STAR Collaboration), Phys. Rev. Lett. **89**, 202301 (2002).
[54] B. I. Abelev *et al.* (STAR Collaboration), Phys. Rev. Lett. **97**, 152301 (2006).
[55] J. Adams *et al.* (STAR Collaboration), Phys. Rev. Lett. **92**, 112301 (2004).
[56] B. I. Abelev *et al.* (STAR Collaboration), Phys. Rev. C **79**, 064903 (2009).
[57] J. Adams *et al.* (STAR Collaboration), Phys. Rev. Lett. **98**, 062301 (2007).
[58] J. Cleymans, B. Kampfer, M. Kaneta, S. Wheaton, and N. Xu, Phys. Rev. C **71**, 054901 (2005).
[59] P. Huovinen, Eur. Phys. J. A **37**, 121 (2008).
[60] A. Andronic, P. Braun-Munzinger, and J. Stachel, Phys. Lett. B **673**, 142 (2009); **678**, 516(E) (2009).
[61] L. Milano (ALICE Collaboration), Nucl. Phys. A **904-905**, 531c (2013).
[62] C. Adler *et al.* (STAR Collaboration), Phys. Rev. Lett. **89**, 092301 (2002).
[63] A. Majumder and B. Muller, Phys. Rev. Lett. **105**, 252002 (2010).
[64] A. Wiranata, V. Koch, M. Prakash, and X. N. Wang, Phys. Rev. C **88**, 044917 (2013).
[65] R. Hagedorn, Nuovo Cimento Suppl. **3**, 147 (1965).
[66] U. Loring, B. C. Metsch, and H. R. Petry, Eur. Phys. J. A **10**, 395 (2001).
[67] U. Loring, B. C. Metsch, and H. R. Petry, Eur. Phys. J. A **10**, 447 (2001).
[68] C. Greiner, P. Koch-Steinheimer, F. M. Liu, I. A. Shovkovy, and H. Stoecker, J. Phys. G **31**, S725 (2005).
[69] J. Noronha-Hostler, J. Noronha, G. S. Denicol, R. P. G. Andrade, F. Grassi, and C. Greiner, Phys. Rev. C **89**, 054904 (2014).
[70] J. Noronha-Hostler and C. Greiner, arXiv:1405.7298 [nucl-th].
[71] J. Adams *et al.* (STAR Collaboration), Phys. Rev. C **72**, 014904 (2005).
[72] T. Hirano and Y. Nara, Phys. Rev. C **79**, 064904 (2009).
[73] B. I. Abelev *et al.* (STAR Collaboration), Phys. Rev. C **77**, 054901 (2008).
[74] P. Huovinen, P. F. Kolb, U. W. Heinz, P. V. Ruuskanen, and S. A. Voloshin, Phys. Lett. B **503**, 58 (2001).
[75] E. Schnedermann, J. Sollfrank, and U. W. Heinz, Phys. Rev. C **48**, 2462 (1993).
[76] H. Heiselberg and A. M. Levy, Phys. Rev. C **59**, 2716 (1999).
[77] T. Hirano, Phys. Rev. Lett. **86**, 2754 (2001).
[78] T. Hirano, P. Huovinen, and Y. Nara, Phys. Rev. C **83**, 021902 (2011).
[79] M. Gyulassy and T. Matsui, Phys. Rev. D **29**, 419 (1984).
[80] P. V. Ruuskanen, Phys. Lett. B **147**, 465 (1984).

Estimation of the shear viscosity at finite net-baryon density from $A + A$ collision data at $\sqrt{s_{NN}} = 7.7$–200 GeV

Iu. A. Karpenko,[1,2,*] P. Huovinen,[1,3] H. Petersen,[1,3,4] and M. Bleicher[1,3]

[1]*Frankfurt Institute for Advanced Studies, Ruth-Moufang-Straße 1, 60438 Frankfurt am Main, Germany*

[2]*Bogolyubov Institute for Theoretical Physics, Metrolohichna street, 14-b, 03680 Kiev, Ukraine*

[3]*Institute for Theoretical Physics, Goethe-Universität, Max-von-Laue-Straße 1, 60438 Frankfurt am Main, Germany*

[4]*GSI Helmholtzzentrum für Schwerionenforschung GmbH, Planckstrasse 1, 64291 Darmstadt, Germany*

(Received 12 February 2015; published 1 June 2015)

Hybrid approaches based on relativistic hydrodynamics and transport theory have been successfully applied for many years for the dynamical description of heavy-ion collisions at ultrarelativistic energies. In this work a new viscous hybrid model employing the hadron transport approach UrQMD for the early and late nonequilibrium stages of the reaction, and 3+1 dimensional viscous hydrodynamics for the hot and dense quark-gluon plasma stage, is introduced. This approach includes the equation of motion for finite baryon number and employs an equation of state with finite net-baryon density to allow for calculations in a large range of beam energies. The parameter space of the model is explored and constrained by comparison with the experimental data for bulk observables from Super Proton Synchrotron and the phase I beam energy scan at Relativistic Heavy Ion Collider. The favored parameter values depend on energy but allow extraction of the effective value of the shear viscosity coefficient over entropy density ratio η/s in the fluid phase for the whole energy region under investigation. The estimated value of η/s increases with decreasing collision energy, which may indicate that η/s of the quark-gluon plasma depends on baryochemical potential μ_B.

DOI: 10.1103/PhysRevC.91.064901 PACS number(s): 25.75.Ld, 25.75.Nq

I. INTRODUCTION

Ultrarelativistic heavy-ion collisions allow investigation of the properties of strongly interacting matter under extreme conditions. At high temperatures and/or high net-baryon densities a new state of matter, the so-called quark-gluon plasma (QGP), is formed. The two main goals of heavy-ion research are the exploration of the phase diagram of quantum chromodynamics and the determination of transport coefficients of this new state of matter.

The studies of high-energy heavy-ion collisions at the Large Hadron Collider (LHC) at CERN and the Relativistic Heavy Ion Collider (RHIC) at Brookhaven National Laboratory have revealed that the quark-gluon plasma behaves like an almost perfect fluid. In recent years, so-called hybrid approaches [1–5] based on (viscous) relativistic hydrodynamics for the hot and dense stage coupled to hadron transport approaches for the decoupling stage of the reaction have been applied with great success to extract average values of the shear viscosity over entropy ratio η/s. The results are very close to the conjectured universal limit of $\eta/s = \frac{1}{4\pi}$, based on the anti–de Sitter and conformal field theory (AdS-CFT) correspondence [6]. For example, the values extracted in Ref. [7] for collisions are $\eta/s = 0.12$ at RHIC and $\eta/s = 0.2$ at the LHC.

One expects the formation of partonic matter in heavy-ion collisions at ultrarelativistic energies (see, e.g., Ref. [8]). However, it is unknown at what collision energy the transition from hadronic to partonic matter sets in. In addition, as the collisions at lower energies probe the phase diagram at larger net-baryon densities, it may be possible to experimentally see signs of the theoretically predicted critical point [9] and the first-order phase transition beyond it. To investigate these questions the so-called beam energy scan (BES) programs at SPS (NA49, NA61 experiments) and at RHIC (STAR, PHENIX experiments) were started. One of the surprises of the stage I of the BES program at RHIC has been that the p_T-differential elliptic flow, $v_2(p_T)$, of charged hadrons does not change significantly when the collision energy is reduced from $\sqrt{s_{NN}} = 200$ to $\sim$20 GeV [10]. The large values of elliptic flow measured at $\sqrt{s_{NN}} = 200$ GeV collisions were taken as a sign of very low shear viscosity of the matter formed in these collisions. Thus, the large $v_2(p_T)$ measured in collisions at lower energy leads to the question of how η/s changes as function of net-baryon density and baryochemical potential μ_B [11].

Unfortunately, many of the hydrodynamical and hybrid models used to model collisions at full RHIC and LHC energies are not directly applicable to collisions at RHIC BES and CERN SPS energies or to collisions at even lower energies in the future at Facility for Antiproton and Ion Research (FAIR), Nuclotron-based Ion Collider Facility (NICA), and stage II of the BES program at RHIC. The simplifying approximations of boost invariance and zero net-baryon density are not valid, and different kinds of nonequilibrium effects play a larger role. To overcome these limitations, a novel hybrid approach has been developed. This approach is based on the Ultrarelativistic Quantum Molecular Dynamics (UrQMD) transport [12] for the nonequilibrium early and late stages and on a (3+1)-dimensional viscous hydrodynamical model [13] for the hot and dense stage of the reaction.

*karpenko@fias.uni-frankfurt.de

In this paper, this approach is applied to extract the shear viscosity coefficient over entropy density ratio of strongly interacting matter from the heavy-ion collision data at RHIC beam energy scan energies in the broad range $\sqrt{s_{NN}} =$ 7.7–200 GeV. The details of the model are explained in Sec. II, and the generic effects of finite shear viscosity on the hydrodynamical expansion are described in Sec. III. The sensitivity of particle yields and spectra to the parameters for the initial- and final-state transitions is explored in Sec. IV. Section V contains the main results of this work including the estimated values of the effective shear viscosity over entropy density ratio as a function of beam energy. Finally, the main conclusions are summarized and an outlook on future work is given in Sec. VI.

II. MODEL DESCRIPTION

Our hybrid approach combines the UrQMD transport model [12] for the early and late stages of the evolution with a dissipative hydrodynamical model, called VHLLE [13], for the hot and dense stage. The distinguishing features of the present model are that the fluid dynamical expansion is solved numerically in all three spatial dimensions without assuming boost invariance nor cylindrical symmetry, the equations of motion for finite net-baryon and charge densities are explicitly included, and, in contrast to the standard UrQMD hybrid approach (UrQMD-3.4 at urqmd.org) [3,14], dissipation in the form of shear viscosity is included in the hydrodynamical stage. Unlike our previous studies [17,18], event-by-event fluctuations are now included. The hadronic cascade operates with the full phase-space distribution of the final particles, which allows for a proper comparison to experimental data.

A. Prethermal phase

The UrQMD string or hadronic cascade is used to describe the primary collisions of the nucleons and to create the initial state of the hydrodynamical evolution. The two nuclei are initialized according to Woods-Saxon distributions and the initial binary interactions proceed via string or resonance excitations, the former process being dominant in ultrarelativistic collisions (including the BES collision energies). All the strings are fragmented into hadrons before the transition to fluid phase (fluidization) takes place, although not all hadrons are yet fully formed at that time; i.e., they do not yet have their free-particle scattering cross sections and thus do not yet interact at all. The hadrons before conversion to fluid should not be considered physical hadrons but rather marker particles to describe the flow of energy, momentum, and conserved charges during the pre-equilibrium evolution of the system. The use of UrQMD to initialize the system allows us to describe some of the pre-equilibrium dynamics and dynamically generates event-by-event fluctuating initial states for hydrodynamical evolution.

The interactions in the pre-equilibrium UrQMD evolution are allowed until a hypersurface of constant Bjorken proper time $\tau_0 = \sqrt{t^2 - z^2}$ is reached, since the hydrodynamical code is constructed using the Milne coordinates (τ, x, y, η), where $\tau = \sqrt{t^2 - z^2}$ [13]. The UrQMD evolution, however, proceeds in Cartesian coordinates (t, x, y, z), and thus evolving the particle distributions to constant τ means evolving the system until large enough time t_l in such a way that the collisional processes and decays are only allowed in the domain $\sqrt{t^2 - z^2} < \tau_0$. The resulting particles on $t = t_l$ surface are then propagated backwards in time to the $\tau = \tau_0$ surface along straight trajectories to obtain an initial state for the hydrodynamic evolution.

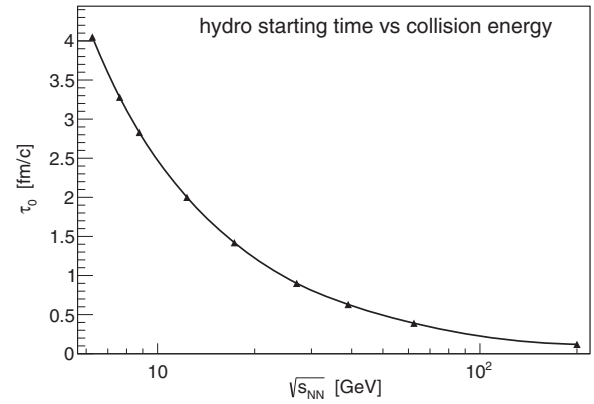

FIG. 1. The earliest possible starting time of the hydrodynamic evolution as a function of $\sqrt{s_{NN}}$ according to Eq. (1).

The lower limit for the starting time of the hydrodynamic evolution depends on the collision energy according to

$$\tau_0 = 2R/\sqrt{(\sqrt{s_{NN}}/2m_N)^2 - 1}, \tag{1}$$

which corresponds to the average time when two nuclei have passed through each other, i.e., all primary nucleon-nucleon collisions have happened. This is the earliest possible moment in time where approximate local equilibrium can be assumed. The τ_0 values calculated according to this formula are plotted in Fig. 1.

To perform event-by-event hydrodynamics using fluctuating initial conditions, every individual UrQMD event is converted to an initial-state profile. As mentioned, the hadron transport does not lead to an initial state in full local equilibrium and the thermalization of the system at $\tau = \tau_0$ has to be artificially enforced. The energy and momentum of each UrQMD particle at τ_0 is distributed to the hydrodynamic cells ijk assuming Gaussian density profiles

$$\Delta P^{\alpha}_{ijk} = P^{\alpha} C \exp\left(-\frac{\Delta x_i^2 + \Delta y_j^2}{R_\perp^2} - \frac{\Delta \eta_k^2}{R_\eta^2}\gamma_\eta^2 \tau_0^2\right), \tag{2}$$

$$\Delta N^{0}_{ijk} = N^{0} C \exp\left(-\frac{\Delta x_i^2 + \Delta y_j^2}{R_\perp^2} - \frac{\Delta \eta_k^2}{R_\eta^2}\gamma_\eta^2 \tau_0^2\right), \tag{3}$$

where Δx_i, Δy_j, $\Delta \eta_k$ are the differences between particle's position and the coordinates of the hydrodynamic cell $\{i, j, k\}$ and $\gamma_\eta = \cosh(y_p - \eta)$ is the longitudinal Lorentz factor of the particle as seen in a frame moving with the rapidity η. The normalization constant C is calculated from the condition that the discrete sum of the values of the Gaussian in all neighboring cells equals one. The resulting ΔP^{α} and ΔN^{0} are transformed into Milne coordinates and added to the energy, momentum,

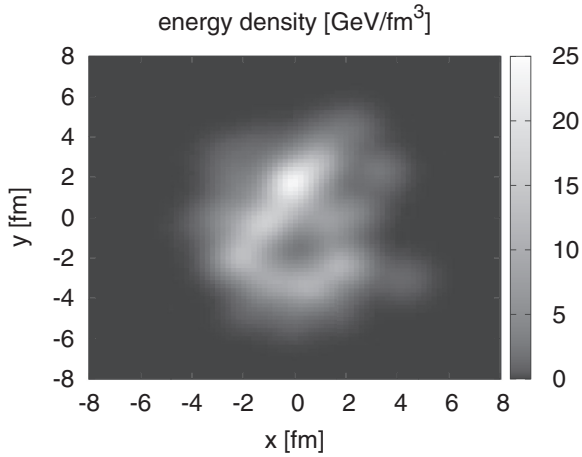

FIG. 2. An example of a fluctuating (single-event) initial energy density profile in the transverse plane at $\eta = 0$. The profile is obtained with $R_\perp = R_\eta = 1$ fm Gaussian smearing and corresponds to a 20–30% Au-Au collision at $\sqrt{s_{NN}} = 39$ GeV.

and baryon number in each cell. This procedure ensures that in the initial transition from transport to hydrodynamics energy, momentum and baryon number are conserved.

For the present study energy and momentum of the initial particles are converted at τ_0 into a perfectly equilibrated fluid, i.e., the initial values for the viscous terms in the energy-momentum tensor are set to zero: $\pi^{\mu\nu}(\tau_0) = \Pi(\tau_0) = 0$. In other words the $T^{0\mu}$ components of the energy-momentum tensor stay the same but the T^{ij} components change when we switch from UrQMD to the fluid. Thus, we do not consider how much the energy-momentum tensor of UrQMD deviates from the ideal fluid energy-momentum tensor but leave this topic for further studies.

One typical example of the initial energy density distributions in the transverse plane at midrapidity for one event is presented in Fig. 2. The parameters $R_\perp$ and R_η regulate the granularity of the initial state. At the same time they influence the initial entropy of the hydrodynamic evolution, while the total initial energy and momentum are always fixed to be equal to the energy and momentum of the pre-equilibrium UrQMD event. The dependence of the final results on these two parameters is discussed later in Sec. IV.

B. Hydrodynamic evolution

The (3+1)-dimensional viscous hydrodynamical code VH-LLE is described in full detail in Ref. [13]. We repeat here only its main features. The code solves the usual local energy-momentum conservation equations

$$\partial_{;\nu} T^{\mu\nu} = 0, \tag{4}$$

$$\partial_{;\nu} N^{\nu}_{\mathrm{B,Q}} = 0, \tag{5}$$

where N^{ν}_{B} and N^{ν}_{Q} are net baryon and electric charge currents respectively, and the semicolon denotes the covariant derivative. The calculation[1] is done in Milne coordinates (τ, x, y, η), where $\tau = \sqrt{t^2 - z^2}$ and $\eta = 1/2 \ln[(t+z)/(t-z)]$.

In the Israel-Stewart framework of causal dissipative hydrodynamics [19], the dissipative currents are independent variables. For the purpose of the present work we set the bulk viscosity to zero, $\zeta/s = 0$. We work in the Landau frame, where the energy diffusion flow is zero, and neglect the baryon and charge diffusion currents, which is equivalent to zero heat conductivity. For the shear stress evolution we choose the relaxation time $\tau_\pi = 5\eta/(Ts)$, the coefficient $\delta_{\pi\pi} = 4/3\tau_\pi$, and approximate all the other coefficients [20,21] by zero. For the shear-stress tensor $\pi^{\mu\nu}$ we obtain the evolution equation

$$\langle u^\gamma \partial_{;\gamma} \pi^{\mu\nu} \rangle = -\frac{\pi^{\mu\nu} - \pi^{\mu\nu}_{\mathrm{NS}}}{\tau_\pi} - \frac{4}{3} \pi^{\mu\nu} \partial_{;\gamma} u^\gamma, \tag{6}$$

where the brackets denote the traceless and orthogonal to u^μ part of the tensor and $\pi^{\mu\nu}_{\mathrm{NS}}$ is the Navier-Stokes value of the shear-stress tensor.

Another necessary ingredient for the hydrodynamic stage is the equation of state (EoS) of the medium. We use the chiral model EoS [22], which features correct asymptotic degrees of freedom—i.e., quarks and gluons in the high-temperature limits and hadrons in the low-temperature limits, crossover-type transition between confined and deconfined matter for all values of μ_B—and qualitatively agrees with lattice QCD data at $\mu_B = 0$.

The tests to confirm the accuracy of the code have been reported in Ref. [13]. In particular the solutions have been compared to the ideal Gubser solution [23] and to a numerical solution of dissipative hydrodynamics calculated using the VISH2+1 hydro code [24].

C. Particlization and hadronic rescattering

It is well known that hydrodynamics loses its validity when the system becomes dilute. To deal with this problem we apply the conventional Cooper-Frye prescription [25] to convert the fluid to individual particles at a hypersurface of constant local rest frame energy density and use the UrQMD cascade to describe the further evolution of these particles. This switching hypersurface is evaluated during the hydrodynamic evolution using the Cornelius routine [26], and as a default value for the switching density we use $\epsilon_{\mathrm{sw}} = 0.5$ GeV/fm^3, which in the chiral model EoS corresponds to $T \approx 175$ MeV at $\mu_{\mathrm{B}} = 0$. At this energy density the crossover transition is firmly on the hadronic side, but the density is still a little higher than the chemical freeze-out energy density suggested by the thermal models [27]. Thus the hadronic transport can take care of both chemical and kinetic decoupling of hadrons. We discuss the sensitivity of the results to the value of the switching density in Sec. IV.

[1]Typical grid spacing used in the calculations: $\Delta x = \Delta y = 0.2$ fm, $\Delta\eta = 0.05$–0.15, and time step $\Delta\tau = 0.05$–0.1 fm/c depending on the collision energy. A finer grid with $\Delta x = \Delta y = 0.125$ fm was taken to simulate peripheral collisions.

As given by the Cooper-Frye prescription, the hadron distribution on each point of the hypersurface is

$$p^0 \frac{d^3N_i(x)}{d^3p} = d\sigma_\mu p^\mu f(pu(x), T(x), \mu_i(x)). \quad (7)$$

The phase space distribution function f is usually assumed to be the one corresponding to a noninteracting hadron resonance gas in or close to the local thermal equilibrium. This is inconsistent with mean fields included in the chiral model EoS used during the evolution. To solve this inconsistency we evaluate the switching surface using the chiral model EoS, but use a free hadron resonance gas EoS to recalculate the energy density, pressure, flow velocity u^μ, temperature, and chemical potentials from the ideal part of the energy-momentum tensor and charge currents, and use these values to evaluate the particle distributions on the switching surface. For example, the above mentioned temperature of $T \approx 175$ MeV in chiral model EoS at zero baryon density and $\epsilon_{\rm sw} = 0.5$ GeV/fm^3 drops to $T \approx 165$ MeV in the free hadron resonance gas EoS. This procedure ensures that the total energy of the produced particles is reasonably close to the overall energy flow through the particlization hypersurface (up to negative contributions to the Cooper-Frye formula), although a small error arises since we use a different energy density to evaluate the position of the surface and the properties of the fluid on it.[2] We have checked that in a case of event-averaged initialization, this error is on the level of a few percent. In addition, the conservation of energy and momentum in the 3+1-dimensional numerical solution of the fluid-dynamical equations using Milne coordinates is slightly violated as discussed in Refs. [13,21].

To take into account the dissipative corrections to the distribution function f, we use the well-known Grad's 14-moment ansatz for a single-component system and assume that the correction is the same for all hadron species. We evaluate the particle distribution in the rest frame of the fluid at each surface element using the Cooper-Frye formula

$$\frac{d^3\Delta N_i}{dp^* d(\cos\theta) d\phi} = \underbrace{\frac{\Delta\sigma^*_\mu p^{*\mu}}{p^{*0}}}_{W_{\rm residual}} \underbrace{p^{*2} f_{\rm eq}(p^{*0}; T, \mu_i)}_{\rm isotropic} \times \underbrace{\left[1 + (1 \mp f_{\rm eq}) \frac{p^*_\mu p^*_\nu \pi^{*\mu\nu}}{2T^2(\epsilon + p)}\right]}_{W_{\rm visc}}. \quad (8)$$

The distribution function in Eq. (8) is expressed in terms of temperature and chemical potential(s), which implies a grand canonical ensemble. This allows to do the particle sampling independently on each surface element. To create an ensemble for particles, we perform the following steps at each element $\Delta\sigma_i$:

(a) First, the average number of hadrons of every sort is calculated:

$$\Delta N_i = \Delta\sigma_\mu u^\mu n_{\rm i,th} = \Delta\sigma^*_0 n_{\rm i,th}$$

(b) For a given $\langle N_{\rm tot}\rangle = \sum_i N_i$, the number of particles to be created is generated according to a Poisson distribution with a mean value $\langle N_{\rm tot}\rangle$.

(c) For each created particle, the type is randomly chosen based on the probabilities $N_i/N_{\rm tot}$.

(d) A momentum is assigned to the particle in two steps:
   (1) The modulus of the momentum is sampled in the local rest frame of the fluid, according to the isotropic part of Eq. (8), and the direction of momentum is picked randomly in 4π solid angle.
   (2) The correction for $W_{\rm residual}$ or $W_{\rm residual}W_{\rm visc}$ in Eq. (8) is applied via rejection sampling: A random number x in the range $[0, W_{\rm max}]$ is generated. If $x < W$, the generated momentum is accepted; if not, the momentum generating procedure is repeated.

(e) The particle momentum is Lorentz boosted to the center-of-mass frame of the system.

(f) The particle position is taken to be equal to the coordinate of the centroid of the corresponding surface element, except for the space-time rapidity of the particle, which is uniformly distributed within the longitudinal size of the volume element.

For the current study, no correction over the grand canonical procedure is made to effectively account for the exact conservation of the total baryon-electric charge, strangeness, and total energy-momentum for every sampled event.[3] As a result, these quantities fluctuate from event to event.

The generated hadrons are then fed into the UrQMD cascade. Since the cascade accepts only a list of particles at an equal Cartesian time as an input, the created particles are propagated backwards in time to the time when the first particle was created. The particles are not allowed to interact in the cascade until their trajectories cross the particlization hypersurface.

III. SENSITIVITY TO SHEAR VISCOSITY

The overall effects of shear viscosity on hydrodynamical expansion have been extensively discussed in the literature [24,30–32]. Here we show that the results from high energy collisions, e.g., entropy increase, enhancement of transverse and inhibition of longitudinal expansion, and suppression of anisotropies are also manifested in calculations at lower collision energies.

We have carried out event-by-event simulations for different collision energies, centralities, and two fixed values of shear viscosity: $\eta/s = 0$ (ideal hydro evolution) and $\eta/s = 0.2$. For these simulations we use the values of the Gaussian radii for the particles' energy/momentum deposition $R_\perp = R_\eta = 1$ fm

[2]The exact procedure suggested in Ref. [28] requires a numerical solution of a cubic equation for each surface element and is therefore too slow for event-by-event studies.

[3]For a suggested procedure to impose the conservation laws, see Ref. [26].

[see Eqs. (2) and (3)]. The initial time is chosen according to Eq. (1); however, for the collisions at energies equal or higher than $\sqrt{s_{NN}} = 27$ GeV we set $\tau_0 = 1$ fm/c.

To reduce the need for processing time, we use the so-called oversampling technique, as in Ref. [33]. For each collision energy, centrality, and parameter set we have created around 500 hydrodynamic events with randomly generated initial conditions. For each hydrodynamic event, or transition hypersurface, we generate $N_{\text{oversample}} = 50$–$100$ final-state events, which results in 25 000–50 000 events used to calculate observables. We have checked that the oversampling procedure does not significantly affect the final observables by creating 1000 or 10 000 hydrodynamic events, with $N_{\text{oversample}} =$ 20 and 2, respectively, for several parameter sets. In both cases, the calculated observables agreed within statistical errors.

The available experimental data set for the basic bulk hadron observables at the BES energies is inhomogeneous. (Pseudo)rapidity spectra of all charged hadrons for Au-Au collisions are available from the PHOBOS analysis [34] for $\sqrt{s_{NN}} = 19.6$, 62.4, and 200 GeV energies only. The p_T spectra are published for $\sqrt{s_{NN}} = 62.4$ GeV by the PHOBOS Collaboration [35] and for $\sqrt{s_{NN}} = 200$ GeV by the PHENIX Collaboration [36]. To cover the lower collision energies we use dN/dy and p_T spectra from the NA49 [29] Collaboration for Pb-Pb collisions at $E_{\text{lab}} = 40$ and 158 A GeV, which correspond to $\sqrt{s_{NN}} = 8.8$ and 17.6 GeV, and set up the simulations accordingly for Pb-Pb system. For the elliptic flow we compare to the STAR results at $\sqrt{s_{NN}} = 7.7$, 11.5, 19.6, 27, 39 GeV [10] and 200 GeV [37] collision energies. In the model we define the centrality classes as impact parameter intervals based on the optical Glauber model estimates [38,39].

The transverse momentum distributions of identified particles at $\sqrt{s_{NN}} = 8.8$ GeV ($E_{\text{lab}} = 40$ A GeV) collision, and (pseudo)rapidity distributions of identified or charged particles at collision energies $\sqrt{s_{NN}} = 8.8$–200 GeV are shown in Figs. 3 and 4, respectively. As can be seen, the inclusion of shear viscosity in the hydrodynamic phase hardens the p_T spectra and increases dN/dy (and similarly $dN/d\eta$) at midrapidity, squeezing the overall rapidity distribution. This effect can be attributed to the effect of shear viscosity on the strong longitudinal expansion of the system in the initial state for the hydrodynamic phase. Shear viscosity attempts to isotropize the expansion by decelerating it in the longitudinal direction and accelerating it in the transverse direction. The energy of the hydrodynamic system is always conserved, whereas additional entropy is produced during the viscous hydrodynamic evolution, which explains the increased total particle multiplicity. By comparing it to the experimental data one observes that $\eta/s = 0.2$ gives a good estimate of the rapidity and transverse momentum distributions at the lowest collision energy point $\sqrt{s_{NN}} = 8.8$ GeV ($E_{\text{lab}} =$ 40 A GeV), while overestimating $dN/d\eta$ at midrapidity for the rest of collision energies except for the highest energy, $\sqrt{s_{NN}} = 200$ GeV, where we underestimate the PHOBOS results.

In Fig. 5 the p_T-averaged elliptic and triangular flow coefficients v_2 and v_3 are shown as a function of collision energy. The flow coefficients are calculated using the event-plane method as described in Ref. [33], including the

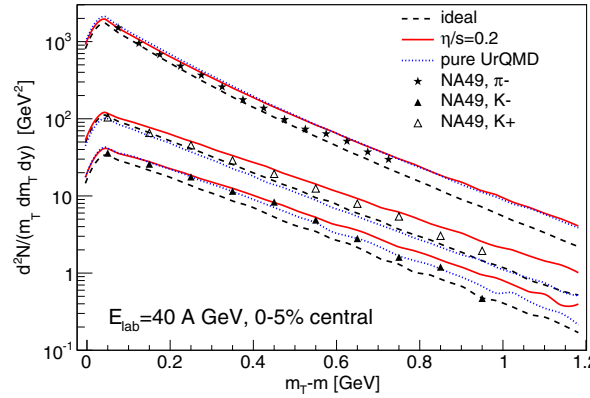

FIG. 3. (Color online) Transverse momentum spectra of negative pions, positive and negative kaons in $E_{\text{lab}} = 40$ A GeV ($\sqrt{s_{NN}} =$ 8.8 GeV) central Pb-Pb collisions. The experimental data from the NA49 Collaboration [29] are compared to the hybrid model calculations with $\eta/s = 0$ (dashed lines) and $\eta/s = 0.2$ (solid lines) in the hydrodynamic phase. The results from UrQMD model with no intermediate hydro phase (dubbed as "pure UrQMD") are shown with dotted lines.

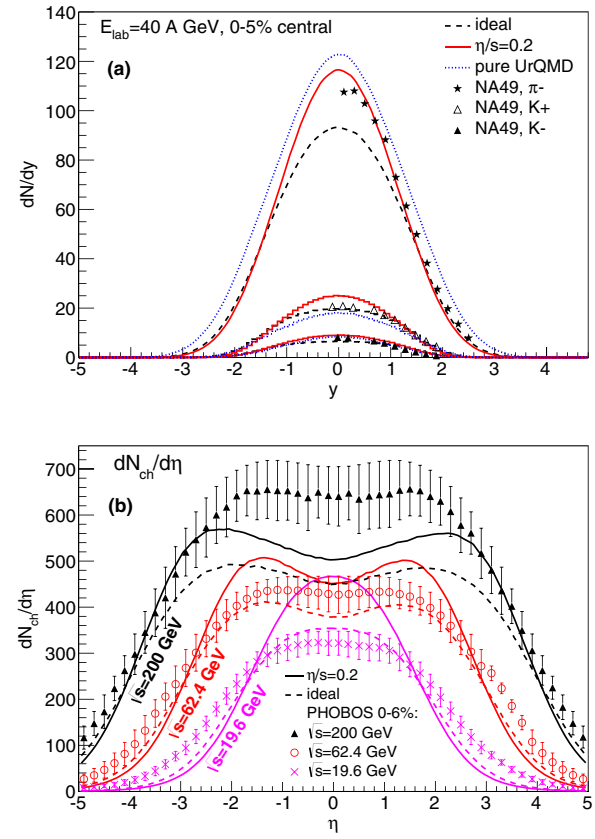

FIG. 4. (Color online) Pion and kaon dN/dy in $E_{\text{lab}} = 40$ A GeV ($\sqrt{s_{NN}} = 8.8$ GeV) central Pb-Pb collisions (top) and charged hadron $dN/d\eta$ distributions at $\sqrt{s_{NN}} = 19.6$, 39, 62.4, and 200 GeV central Au-Au collisions (bottom). The experimental data from the NA49 [29] and the PHOBOS Collaborations [34] are compared to the hybrid model calculations with $\eta/s = 0$ (dashed lines) and $\eta/s = 0.2$ (solid lines) in the hydrodynamic phase.

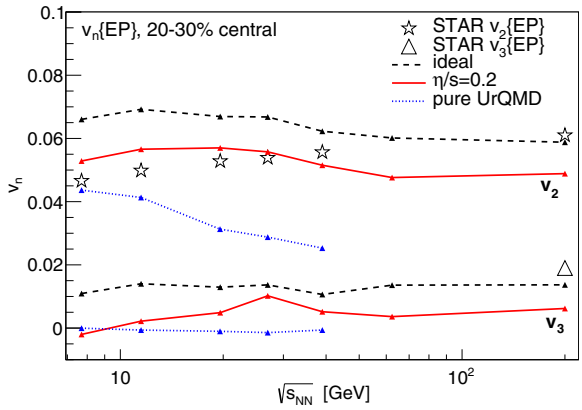

FIG. 5. (Color online) p_T integrated ($0.2 < p_T < 2.0$ GeV and $|\eta| < 1$) elliptic (v_2) and triangular (v_3) flows of all charged hadrons in 20–30% central Au-Au collisions as a function of collision energy, calculated with the event-plane method. The elliptic and triangular flow data is from the STAR Collaboration [10,40]. The solid line depicts the calculation with $\eta/s = 0.2$, the dashed line shows the calculation with $\eta/s = 0$, whereas the dotted line corresponds to the "pure" UrQMD calculation with no intermediate hydrodynamic stage.

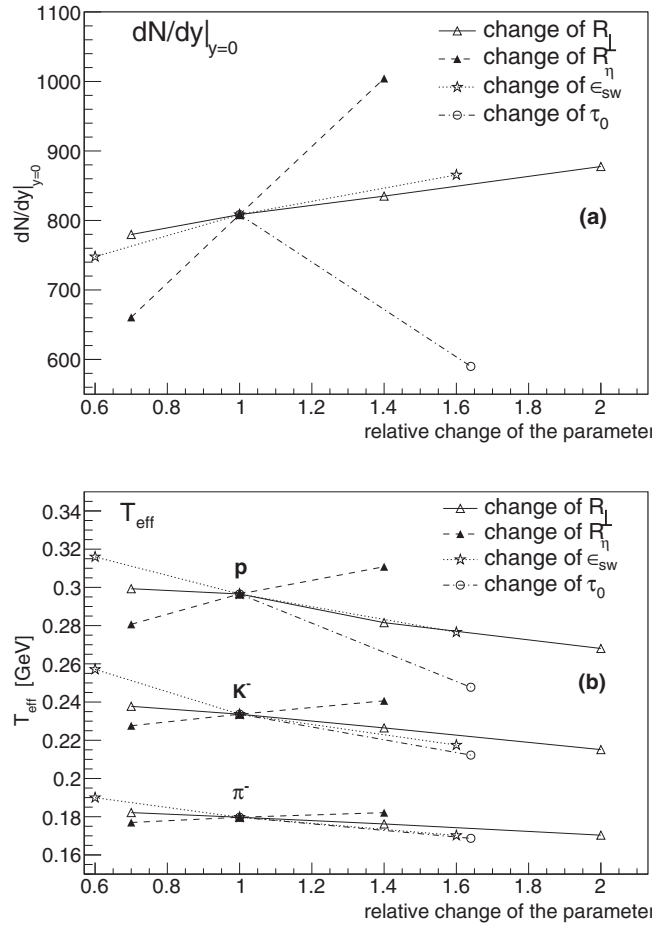

FIG. 6. Parameter dependence of the total yield at midrapidity (top) and the effective temperature of pion, kaon, and proton p_T spectra (bottom) in 0–5% central Au-Au collisions at $\sqrt{s_{NN}} = 19.6$ GeV.

event-plane resolution correction. As expected, the elliptic and triangular flow coefficients are suppressed by the shear viscosity. However, when comparing the results for $\eta/s = 0.2$ to the STAR experimental results at 20–30% centrality we find that the suppression is too weak for $\sqrt{s_{NN}} \lesssim 30$ GeV and too strong otherwise. The latter is consistent with the fact that the optimal value of η/s required to fit the elliptic flow data at $\sqrt{s_{NN}} = 200$ A GeV is $\eta/s = 0.08$ assuming the initial energy density profile from Monte Carlo–Glauber approach [41]. Another particular feature of both v_2 curves is that, in the region $\sqrt{s_{NN}} \approx 20$–62 GeV, the elliptic flow decreases as a function of $\sqrt{s_{NN}}$. If we do not limit the initial time τ_0 from below at energies $\sqrt{s_{NN}} > 25$ GeV, but take it directly from Eq. (1), we do not see this decrease, but v_2 increases monotonously with increasing collision energy. Thus we expect that the reason for the nonmonotonous behavior is in our choice for the initial time of the hydrodynamic evolution.

The results from the standard UrQMD cascade (without intermediate hydrodynamic phase) are also shown for comparison in Figs. 3 and 4 with dotted lines. One may conclude that whereas standard UrQMD does a good job for p_T spectra and rapidity distributions at the lowest energy, it clearly underestimates v_2 when the collision energy increases (which repeats the conclusion about the v_2 excitation function from Ref. [42], and later results from v_3 analysis in Ref. [14]). This is an indication of too large viscosity of the high-density medium and served historically as a motivation to introduce the intermediate hydrodynamic stage.

IV. INVESTIGATION OF PARAMETER SPACE

After investigating the generic influence of a finite shear viscosity during the hydrodynamic evolution on basic bulk observables, it is clear that we cannot fit all the available experimental data using the same set of parameters.[4] Thus we have to adjust the model parameters according to the collision energy before drawing any conclusions about the physical properties of the system.

In this section we study systematically the sensitivities of the particle yield at midrapidity, which is a measure for the final entropy, the effective slope parameter that measures the strength of the transverse expansion, and the anisotropic flow to the main parameters of the model. Due to the limited space, and to emphasize the main features of the dependencies, we restrict ourselves to one collision energy, $\sqrt{s_{NN}} = 19.6$ GeV, in the middle of the investigated range. Since the influence of shear viscosity was discussed above, we now concentrate on the remaining parameters of the model: the two Gaussian radii

[4]The internal parameters of UrQMD, e.g., particle properties and cross sections, are fixed by experimental data as explained in Ref. [15]. The effects of changes in resonance properties were studied in Ref. [16]. It was found that if the changes stay within experimentally acceptable limits, the effects on final particle distributions are small.

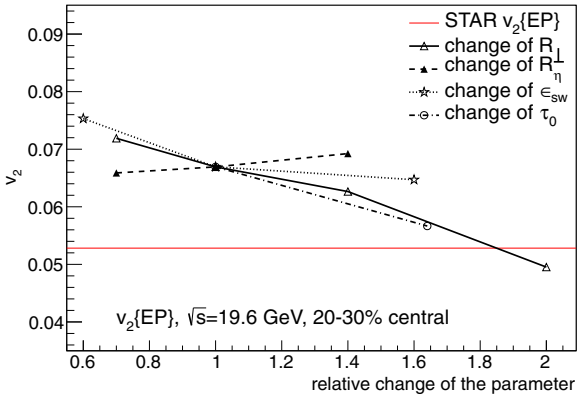

FIG. 7. (Color online) Parameter dependence of p_T integrated elliptic flow v_2 of charged hadrons in 20–30% central Au-Au collisions at $\sqrt{s_{NN}} = 19.6$ GeV. The experimental value of the elliptic flow is shown with a solid red (gray) line for comparison.

$R_\perp$ and R_η for the initial distribution of energy, momentum and charges, the starting time for the hydro phase τ_0, and the energy density $\epsilon_{\rm sw}$ when the switch to the hadronic cascade happens. The default case is $R_\perp = R_\eta = 1.0$ fm, $\tau_0 = 1.22$ fm/c [calculated according to Eq. (1)], $\eta/s = 0$ (for simplicity), and $\epsilon_{\rm sw} = 0.5$ GeV/fm^3. The dependencies are presented in Figs. 6 and 7, where each curve corresponds to the variation of only one of the parameters, while keeping the default values for the others. All values are normalized to their default values to allow a direct comparison to each other. The effective temperatures of the hadron spectra in the lower panel of Fig. 6 are defined as the parameter of the exponential fit,

$$\frac{dN}{m_T dm_T dy} = C \exp\left(-\frac{m_T}{T_{\rm eff}}\right),$$

where the $m_T - m$ range is 0.2–1 GeV for pions and protons and 0.05–1 GeV for kaons.[5] In general we do observe only a very weak dependence on the parameters, that is less than 10% for a 10% change in parameters. The observed dependencies can be summarized as follows:

(a) Increased $R_\perp$ smoothens the initial energy density profile in the transverse plane, which leads to smaller gradients and less explosive transverse expansion. The latter leads to a decrease of the effective temperature (inverse slope) $T_{\rm eff}$ of the p_T spectra; see Fig. 6, lower panel. Larger $R_\perp$ also results in decreased ellipticity and triangularity of an initial energy density profile, which is hydrodynamically translated into smaller final elliptic (v_2, see Fig. 7) and triangular (v_3) flow components.

(b) In a similar manner, the increase of R_η leads to shallower longitudinal gradients and weaker longitudinal expansion. Thus more energy remains at midrapidity to form stronger transverse expansion, which increases $T_{\rm eff}$ and v_2. On the other hand, larger R_η also results in larger initial entropy of the system, which considerably increases the final particle multiplicity; see Fig. 6, upper panel.

(c) Increased τ_0 has two effects:
   (1) It leads to a shorter lifetime of the hydrodynamic phase, as a result of longer prethermal phase.
   (2) At the same time τ_0 enters the Gaussian energy-momentum smearing profile. Thus its increase acts opposite to the increase of R_η.
   From the response of the observables to the increase of τ_0 we find that the second effect is stronger.

(d) Increased $\epsilon_{\rm sw}$ shortens the effective lifetime of the hydrodynamic phase. The shorter time to develop radial and elliptic flows is not fully compensated by the longer cascade phase, which results in the decrease of both final $T_{\rm eff}$ and final v_2. Since the total entropy is conserved in the ideal hydrodynamic expansion but increases in the cascade stage, the final particle multiplicity increases with the increase of $\epsilon_{\rm sw}$.

TABLE I. Schematical representation of the response (increase or decrease) of the observables to the increase of a particular parameter of the model.

	$R_\perp \uparrow$	$R_z \uparrow$	$\eta/s \uparrow$	$\tau_0 \uparrow$	$\epsilon_{\rm sw} \uparrow$
$T_{\rm eff}$	↓	↑	↑	↓	↓
dN/dy	↑	↑	↑	↓	↑
v_2	↓	↑	↓	↓	↓

The observed dependencies are schematically depicted in Table I, where the signs of the responses of the observables to the increase of a particular model parameter are shown. As for the magnitudes of the response, one can see from the plots that by varying the parameters of the initialization procedure one has a nearly linear influence on the final dN/dy, $T_{\rm eff}$, and v_2. From Fig. 7 one can see that by choosing a larger value of $R_\perp$ it is possible to approach the experimental value of v_2 with zero shear viscosity in the hydrodynamic phase. However, such value is inconsistent with the p_T spectra and charged particle multiplicity.

Investigating all the dependencies in detail allows us to choose parameter values which lead to a reasonable reproduction of the data. These values are shown in Table II. For reasons of simplicity we keep $\epsilon_{\rm sw} = 0.5$ GeV/fm^3 for all collision energies, since the other parameters provide enough freedom for adjustment. Note that since the model requires a lot of processing time to obtain results for each particular collision energy and centrality, it is at the moment impractical to provide χ^2-optimized values of the model parameters and their errors. Thus the parameters are adjusted manually based on a visual correspondence to the data. A full-fledged χ^2 fit to the data is planned for the future using a model emulator, as suggested in Refs. [43–45].

[5]Smaller $m_T - m$ range for pions and protons is taken since the lowest $m_T - m$ part of the spectrum has a different slope than the intermediate $m_T - m$ range.

TABLE II. Collision energy dependence of the model parameters chosen to reproduce the experimental data in the BES region and higher RHIC energies. Asterisks denote the values of starting time τ_0, which are adjusted instead of being taken directly from Eq. (1).

$\sqrt{s_{NN}}$ (GeV)	τ_0 (fm/c)	$R_\perp$ (fm)	R_η (fm)	η/s
7.7	3.2	1.4	0.5	0.2
8.8 (SPS)	2.83	1.4	0.5	0.2
11.5	2.1	1.4	0.5	0.2
17.3 (SPS)	1.42	1.4	0.5	0.15
19.6	1.22	1.4	0.5	0.15
27	1.0	1.2	0.5	0.12
39	0.9*	1.0	0.7	0.08
62.4	0.7*	1.0	0.7	0.08
200	0.4*	1.0	1.0	0.08

V. RESULTS FOR BULK OBSERVABLES

Finally, let us have a look at the results for bulk observables with the energy-dependent parameters for the hydrodynamic description (see Table II).

The (pseudo)rapidity spectra are presented in Fig. 8. One can see that whereas the parameters were adjusted to reproduce the total multiplicities, the resulting shapes of the pseudorapidity distributions are also in a reasonable agreement with the data. From the model results one can observe the change in shape from the single peak structure at $\sqrt{s_{NN}} < 20$ GeV to a doubly peaked distribution (or from a Dromedary to a Bactrian camel shape), which starts to form at $\sqrt{s_{NN}} = 39$ GeV. At higher collision energies we observe a shallow dip around zero pseudorapidity.

The p_T spectra of pions, kaons, and protons in collisions at $\sqrt{s_{NN}} = 62.4$, 17.6, and 8.8 GeV energies are shown in Fig. 9. In general the spectra and especially the p_T slopes are reproduced, which indicates that both the collective radial flow (generated in the hydrodynamic and cascade stages), and thermal motion are combined in the right proportion.

The elliptic and triangular flow coefficients for 20–30% central Au-Au collisions as a function of collision energy are presented in Fig. 10. As expected, the calculated values of the elliptic flow follow the data closely, since this quantity was used to fix the parameters. In contrast to that, triangular flow v_3 is calculated from the same simulated events, and thus can be considered as a prediction of the model. We expect that the nonmonotonous behavior of v_3 is an artifact of our fitting procedure, and more careful adjustment of the model parameters would further smoothen the behavior of $v_3(\sqrt{s})$.

The 20–30% centrality class was chosen because the elliptic flow signal is strongest around this centrality class. Also, at this centrality nonflow contributions from minijets, which are not included in the model, are small. The centrality dependence of elliptic flow at $\sqrt{s_{NN}} = 39$ GeV is shown in Fig. 11. The parameters are the same at all centralities. In peripheral collisions the model significantly undershoots the data. This is due to the smoothening procedure used to convert individual particles to the fluid-dynamical initial state. With the present smearing parameters the eccentricity of the system is too small in peripheral collisions, where the size of the entire system is comparable to the smearing radius.

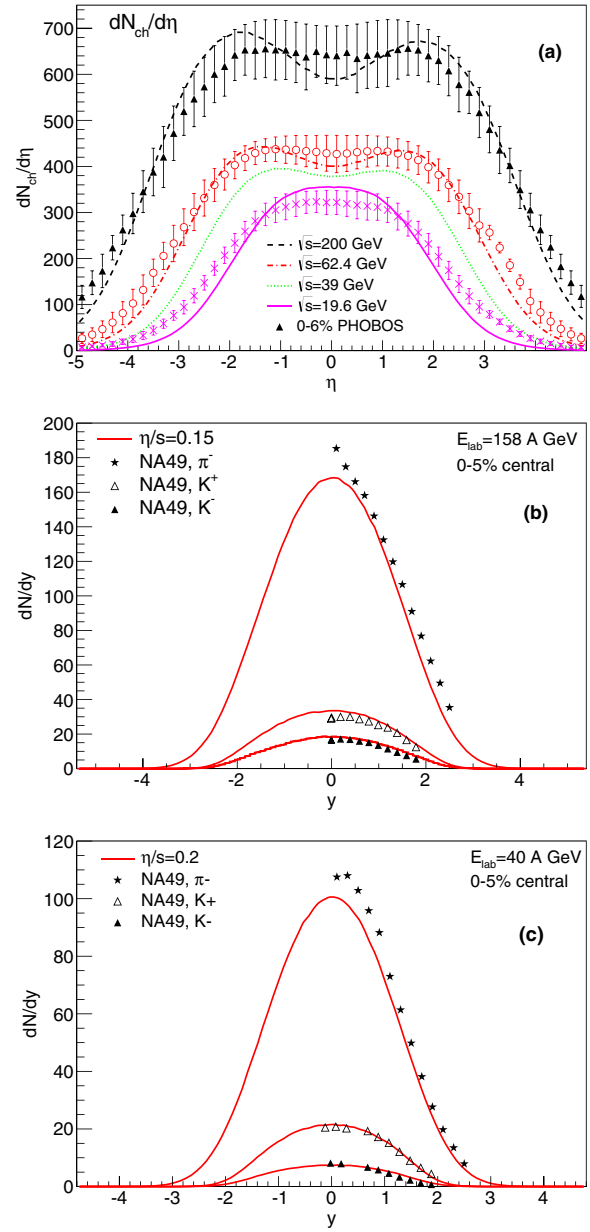

FIG. 8. (Color online) Pseudorapidity distributions of charged hadrons (top) in Au-Au collisions at $\sqrt{s_{NN}} = 19.6$, 39, 62.4, and 200 GeV energies, and rapidity distributions of identified hadrons in Pb-Pb collisions at $E_{\rm lab} = 158$ and 40 A GeV ($\sqrt{s_{NN}} = 17.6$ and 8.8 GeV) energies (middle and bottom panels, respectively). The calculations were done using the collision energy-dependent parameters listed in Table II. The data are from the PHOBOS [34] and the NA49 [29] Collaborations.

The most important conclusion from the adjustment procedure is that reproduction of the data requires an effective η/s which decreases as a function of increasing collision energy; see Table II and Fig. 12. In Fig. 12 one can also see an estimated error band around the optimal values of η/s. As mentioned, a proper determination of the error bars would require a χ^2

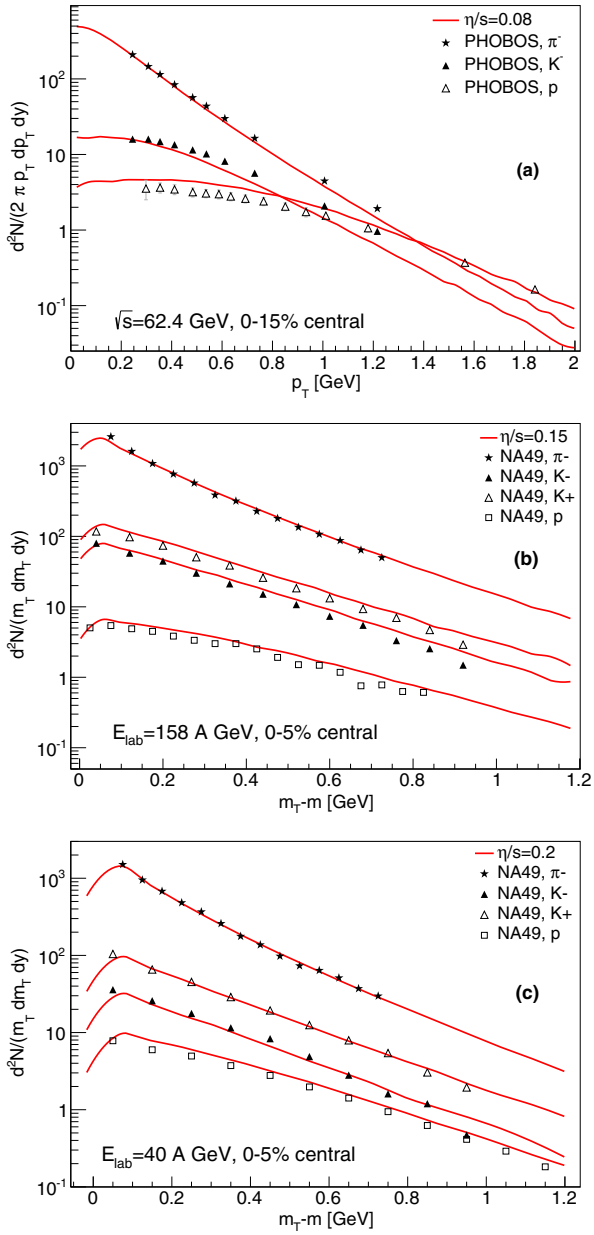

FIG. 9. (Color online) p_T spectra of identified hadrons in Au-Au collisions at $\sqrt{s_{NN}} = 62.4$ GeV energy (top) and in Pb-Pb collisions at $E_{\rm lab} = 158$ and 40 A GeV ($\sqrt{s_{NN}} = 17.6$ and 8.8 GeV) energies (middle and bottom panels, respectively). The model calculations were carried out using the collision energy-dependent parameters listed in Table II, and the data are from the PHOBOS and NA49 Collaborations [29,35,46].

fit. Currently the error band is estimated from the variations of two parameters of the model (η/s and R_T) which result in the same value of p_T integrated elliptic flow and a 5% variation in the slope of proton p_T spectrum, which is the most sensitive to a change in radial flow.

In the present calculations η/s is taken to be constant during the evolution of the system, and its value changes only

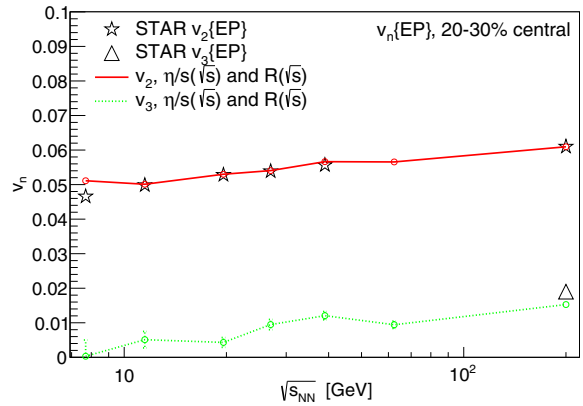

FIG. 10. (Color online) p_T integrated elliptic and triangular flow coefficients v_2 and v_3 as a function of collision energy. Both the experimental and calculated coefficients were evaluated using the event-plane method. The calculation was done using the collision energy-dependent parameters listed in Table II, and the data are from the STAR Collaboration [10,40].

with the collision energy. However, we expect that physical η/s depends on both the temperature and baryon chemical potential, and that η/s has a minimum around T_c and zero μ_b [47–50]. As the collision energy becomes smaller, the average baryon chemical potential in the system increases. This indicates that the physical value of η/s should increase with increasing μ_B.

In Ref. [51] it was argued that η/s is not an appropriate measure of the fluidity of the system. However, the measure of fluidity proposed in that paper, $L_\eta/L_n = (\eta n^{1/3})/(wc_s)$, where n is the total particle number density, w is enthalpy, and c_s is the speed of sound, is difficult to implement in the present fluid-dynamical calculation since n is not well defined in our

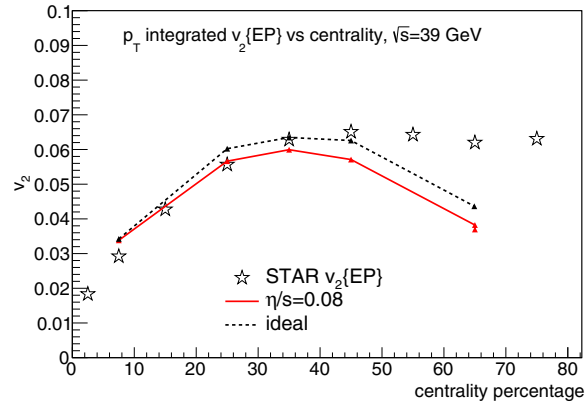

FIG. 11. (Color online) p_T integrated elliptic flow coefficient v_2 in $\sqrt{s_{NN}} = 39$ GeV Au-Au collisions as function of centrality. Both the experimental and calculated v_2 was evaluated using the event plane method. The calculation was done using the collision energy-dependent parameters listed in Table II, and the data are from the STAR collaboration [10].

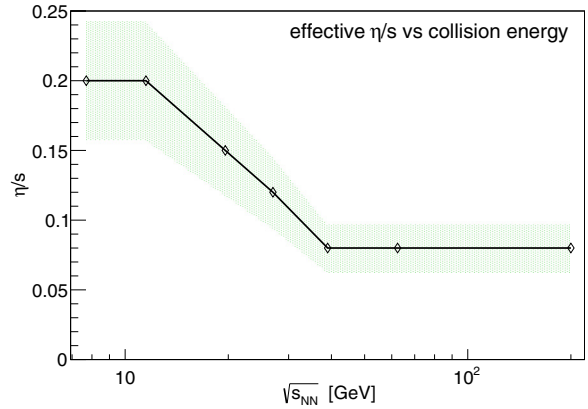

FIG. 12. (Color online) Effective values of shear viscosity over entropy density η/s used to describe the experimental data at different collision energies as shown in Table II. The green (gray) band represents an estimate of uncertainty in η/s resulting from the allowed variation of model parameters around their optimal values.

two-phase EoS. Instead, we use as an alternative measure of fluidity the combination $\eta T/w = \eta T/(\epsilon + P) = \eta/(s + \sum_\alpha \mu_\alpha n_\alpha/T)$, where n_α are the charge densities (baryon, strange, electric) and μ_α are the corresponding chemical potentials, and which approaches η/s in the limit of small charge densities. We have performed an additional round of simulations, keeping $\eta T/w = 0.08$ and $\eta/s = 0.08$ at all collision energies to see whether different measures of fluidity make any difference. The resulting elliptic and triangular flow coefficients are shown in Fig. 13. One can see that at all considered collision energies there is no visible difference in the elliptic flow coefficient between the $\eta/s = 0.08$ and $\eta T/w = 0.08$ cases. We have also checked that the two scenarios result in virtually same p_T spectra and dN/dy distributions. This indicates that the contribution from baryon-electric charge density to the entropy density does not induce baryon density dependence of the η/s ratio that is strong enough to affect the hydrodynamic evolution.

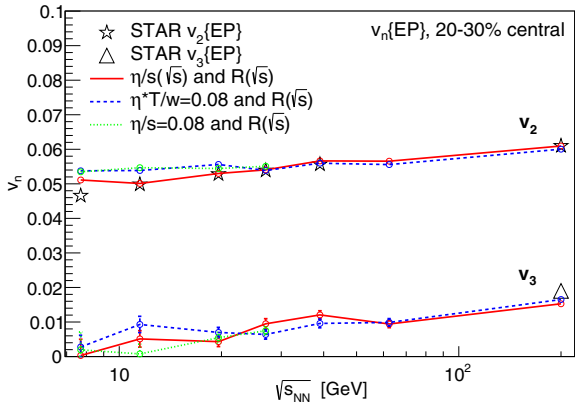

FIG. 13. (Color online) p_T integrated elliptic and triangular flow coefficients v_2 and v_3 as a function of collision energy. Solid red (gray) line represents the results from Fig. 10 obtained using collision energy-dependent η/s. Dashed (blue) and dotted (green) lines correspond to collision independent $\eta T/w = 0.08$ and $\eta/s = 0.08$, respectively. In all three cases the other model parameters were taken to depend on the collision energy as shown in Table II. The experimental data are from the STAR Collaboration [10,40].

VI. SUMMARY AND OUTLOOK

A hybrid model featuring a 3+1-dimensional viscous hydrodynamic phase with an explicit treatment of finite baryon and charge densities is introduced. The model employs a chiral model equation of state for the hydrodynamic stage. The initial and late nonequilibrium stages are modeled using the UrQMD hadron cascade on an event-by-event basis.

This hybrid model was applied to describe the dynamics of relativistic heavy-ion collisions at energies ranging from the lowest RHIC beam energy scan energy to full RHIC energy, $\sqrt{s} = 7.7$–200 GeV. After tuning the parameters, it was possible to reproduce the observed pseudorapidity and transverse momentum distributions of produced hadrons and their elliptic flow coefficients. The reproduction of the data requires a finite shear viscosity over entropy density ratio η/s, which depends on collision energy. This ratio was found to decrease from $\eta/s = 0.2$ to 0.08 as collision energy increases from $\sqrt{s_{NN}} = 7.7$ to 39 GeV, and to stay at $\eta/s = 0.08$ for $39 \leqslant \sqrt{s} \leqslant 200$ GeV. Since the average baryochemical potential at midrapidity decreases with increasing collision energy, the required collision energy dependence of the effective η/s indicates that the physical η/s ratio may depend on baryochemical potential and that η/s increases with increasing μ_B. It was also found that a constant and collision energy-independent $\eta T/w = 0.08$ and $\eta/s = 0.08$ in hydrodynamic phase yield quantitatively similar results. This indicates that the $\mu_B n_B$ term in entropy density does not induce the baryon density dependence of η/s required to reproduce the data when $\eta T/w$ is kept independent of collision energy.

In addition we have explored the parameter dependence of the model results and generally found a $<10\%$ variation of the results, when the individual parameters were varied by 10%. Of course, the proper evaluation of the effect of finite baryochemical potential on η/s would require reproducing all the data using the same temperature- and baryochemical-potential-dependent parametrization of η/s at all energies and centralities. This will be addressed in future studies.

ACKNOWLEDGMENTS

The authors acknowledge the financial support by the Helmholtz International Center for FAIR and Hessian LOEWE initiative. The work of P.H. was supported by BMBF under Contract No. 06FY9092. H.P. acknowledges funding by the Helmholtz Young Investigator Group VH-NG-822 from the Helmholtz Association and GSI. Computational resources have been provided by the Center for Scientific Computing (CSC) at the Goethe University Frankfurt.

[1] T. Hirano, U. W. Heinz, D. Kharzeev, R. Lacey, and Y. Nara, Phys. Lett. B **636**, 299 (2006).
[2] C. Nonaka and S. A. Bass, Nucl. Phys. A **774**, 873 (2006).
[3] H. Petersen, J. Steinheimer, G. Burau, M. Bleicher, and H. Stocker, Phys. Rev. C **78**, 044901 (2008).
[4] K. Werner, I. Karpenko, T. Pierog, M. Bleicher, and K. Mikhailov, Phys. Rev. C **82**, 044904 (2010).
[5] H. Song, S. A. Bass, and U. Heinz, Phys. Rev. C **83**, 024912 (2011).
[6] G. Policastro, D. T. Son, and A. O. Starinets, Phys. Rev. Lett. **87**, 081601 (2001); P. K. Kovtun, D. T. Son, and A. O. Starinets, *ibid.* **94**, 111601 (2005).
[7] C. Gale, S. Jeon, B. Schenke, P. Tribedy, and R. Venugopalan, Phys. Rev. Lett. **110**, 012302 (2013).
[8] M. Gyulassy and L. McLerran, Nucl. Phys. A **750**, 30 (2005).
[9] M. A. Stephanov, K. Rajagopal, and E. V. Shuryak, Phys. Rev. D **60**, 114028 (1999); Phys. Rev. Lett. **81**, 4816 (1998).
[10] L. Adamczyk *et al.* (STAR Collaboration), Phys. Rev. C **86**, 054908 (2012).
[11] G. S. Denicol, C. Gale, S. Jeon, and J. Noronha, Phys. Rev. C **88**, 064901 (2013).
[12] S. A. Bass, M. Belkacem, M. Bleicher, M. Brandstetter, L. Bravina, C. Ernst, L. Gerland, M. Hofmann *et al.*, Prog. Part. Nucl. Phys. **41**, 255 (1998); M. Bleicher *et al.*, J. Phys. G **25**, 1859 (1999).
[13] I. Karpenko, P. Huovinen, and M. Bleicher, Comput. Phys. Commun. **185**, 3016 (2014).
[14] J. Auvinen and H. Petersen, Phys. Rev. C **88**, 064908 (2013).
[15] H. Petersen, M. Bleicher, S. A. Bass, and H. Stocker, arXiv:0805.0567 [hep-ph].
[16] J. Gerhard, B. Bauchle, V. Lindenstruth, and M. Bleicher, Phys. Rev. C **85**, 044912 (2012).
[17] I. A. Karpenko, M. Bleicher, P. Huovinen, and H. Petersen, J. Phys. Conf. Ser. **509**, 012067 (2014).
[18] I. A. Karpenko, M. Bleicher, P. Huovinen, and H. Petersen, J. Phys. Conf. Ser. **503**, 012040 (2014).
[19] W. Israel, Ann. Phys. (Amsterdam, Neth.) **100**, 310 (1976); W. Israel and J. M. Stewart, *ibid.* **118**, 341 (1979).
[20] G. S. Denicol, H. Niemi, E. Molnar, and D. H. Rischke, Phys. Rev. D **85**, 114047 (2012).
[21] E. Molnar, H. Holopainen, P. Huovinen, and H. Niemi, Phys. Rev. C **90**, 044904 (2014).
[22] J. Steinheimer, S. Schramm, and H. Stocker, J. Phys. G **38**, 035001 (2011).
[23] S. S. Gubser, Phys. Rev. D **82**, 085027 (2010).
[24] H. Song and U. W. Heinz, Phys. Rev. C **77**, 064901 (2008); **78**, 024902 (2008).
[25] F. Cooper and G. Frye, Phys. Rev. D **10**, 186 (1974).
[26] P. Huovinen and H. Petersen, Eur. Phys. J. A **48**, 171 (2012).
[27] F. Becattini, J. Manninen, and M. Gazdzicki, Phys. Rev. C **73**, 044905 (2006).
[28] Y. Cheng, L. P. Csernai, V. K. Magas, B. R. Schlei, and D. Strottman, Phys. Rev. C **81**, 064910 (2010).
[29] S. V. Afanasiev *et al.* (NA49 Collaboration), Phys. Rev. C **66**, 054902 (2002).
[30] A. Muronga, Phys. Rev. Lett. **88**, 062302 (2002); **89**, 159901 (2002).
[31] R. Baier and P. Romatschke, Eur. Phys. J. C **51**, 677 (2007).
[32] D. Teaney, Phys. Rev. C **68**, 034913 (2003).
[33] H. Holopainen, H. Niemi, and K. J. Eskola, Phys. Rev. C **83**, 034901 (2011).
[34] B. Alver *et al.* (PHOBOS Collaboration), Phys. Rev. C **83**, 024913 (2011).
[35] B. B. Back *et al.* (PHOBOS Collaboration), Phys. Rev. C **75**, 024910 (2007).
[36] S. S. Adler *et al.* (PHENIX Collaboration), Phys. Rev. C **69**, 034909 (2004).
[37] J. Adams *et al.* (STAR Collaboration), Phys. Rev. C **72**, 014904 (2005).
[38] K. J. Eskola, K. Kajantie, and J. Lindfors, Nucl. Phys. B **323**, 37 (1989).
[39] D. Miskowiec, http://web-docs.gsi.de/misko/overlap/
[40] L. Adamczyk *et al.* (STAR Collaboration), Phys. Rev. C **88**, 014904 (2013).
[41] H. Song, S. A. Bass, U. Heinz, T. Hirano, and C. Shen, Phys. Rev. Lett. **106**, 192301 (2011); **109**, 139904 (2012).
[42] H. Petersen and M. Bleicher, Phys. Rev. C **79**, 054904 (2009).
[43] H. Petersen, C. Coleman-Smith, S. A. Bass, and R. Wolpert, J. Phys. G **38**, 045102 (2011).
[44] J. Novak, K. Novak, S. Pratt, J. Vredevoogd, C. E. Coleman-Smith, and R. L. Wolpert, Phys. Rev. C **89**, 034917 (2014).
[45] J. E. Bernhard, P. W. Marcy, C. E. Coleman-Smith, S. Huzurbazar, R. L. Wolpert, and S. A. Bass, Phys. Rev. C **91**, 054910 (2015).
[46] T. Anticic *et al.* (NA49 Collaboration), Phys. Rev. C **83**, 014901 (2011).
[47] L. P. Csernai, J. I. Kapusta, and L. D. McLerran, Phys. Rev. Lett. **97**, 152303 (2006).
[48] G. S. Denicol, T. Kodama, and T. Koide, J. Phys. G **37**, 094040 (2010).
[49] H. Niemi, G. S. Denicol, P. Huovinen, E. Molnar, and D. H. Rischke, Phys. Rev. Lett. **106**, 212302 (2011).
[50] H. Niemi, G. S. Denicol, P. Huovinen, E. Molnar, and D. H. Rischke, Phys. Rev. C **86**, 014909 (2012).
[51] J. Liao and V. Koch, Phys. Rev. C **81**, 014902 (2010).

PHYSICAL REVIEW C **91**, 024906 (2015)

Systematic investigation of negative Cooper-Frye contributions in heavy ion collisions using coarse-grained molecular dynamics

D. Oliinychenko,[1,2,*] P. Huovinen,[1,3,†] and H. Petersen[1,3,4,‡]

[1]*Frankfurt Institute for Advanced Studies, D-60438 Frankfurt am Main, Germany*

[2]*Bogolyubov Institute for Theoretical Physics, Kiev 03680, Ukraine*

[3]*Institut für Theoretische Physik, Goethe-Universität, D-60438 Frankfurt am Main, Germany*

[4]*GSI Helmholtzzentrum für Schwerionenforschung GmbH, Planckstr. 1, 64291 Darmstadt, Germany*

(Received 24 November 2014; published 17 February 2015)

In most heavy ion collision simulations involving relativistic hydrodynamics, the Cooper-Frye formula is applied to transform the hydrodynamical fields to particles. In this article the so-called negative contributions in the Cooper-Frye formula are studied using a coarse-grained transport approach. The magnitude of negative contributions is investigated as a function of hadron mass, collision energy in the range of $E_{\rm lab} = 5$–$160A$ GeV, collision centrality, and the energy density transition criterion defining the hypersurface. The microscopic results are compared to negative contributions expected from hydrodynamical treatment assuming local thermal equilibrium. The main conclusion is that the number of actual microscopic particles flying inward is smaller than the negative contribution one would expect in an equilibrated scenario. The largest impact of negative contributions is found to be on the pion rapidity distribution at midrapidity in central collisions. For this case negative contributions in equilibrium constitute 8–13% of positive contributions, depending on collision energy, but only 0.5–4% in cascade calculation. The dependence on the collision energy itself is found to be nonmonotonous with a maximum at 10–20A GeV.

DOI: 10.1103/PhysRevC.91.024906 PACS number(s): 24.10.Lx, 24.10.Nz, 02.70.Ns, 47.75.+f

I. INTRODUCTION

Relativistic hydrodynamics is now the standard approach for modeling ultrarelativistic heavy ion collisions at highest RHIC (Relativistic Heavy Ion Collider) and LHC (Large Hadron Collider) energies. These dynamical descriptions are either based on ideal [1,2] or dissipative hydrodynamics [3,4] and describe the entire expansion fluid dynamically. In so-called hybrid approaches [5,6] only the early hot and dense stage of the expansion is described using hydrodynamics and the later dilute stage is described by hadron transport.

Most of these models use a conceptually similar procedure: Given an initial condition, the hydrodynamic equations are solved in the whole forward light cone. Near the boundary of vacuum and at the late times of evolution hydrodynamics is not applicable any more, when the density is small and the mean free path is larger than the system size. Therefore, models switch to an off-equilibrium microscopic description in terms of particles in this region. In hybrid approaches particles can scatter, while other models allow only free-streaming and resonance decays. In any case, the most commonly used way to convert the fluid-dynamical fields to particles, a process that we call here "particlization," is by using the Cooper-Frye formula.

The Cooper-Frye formula assumes particlization to take place on an infinitesimally thin three-dimensional hypersurface in four-dimensional space-time. This hypersurface Σ is usually determined a posteriori from the hydrodynamical solution in the whole forward light cone, usually as a hypersurface of constant time, energy density, temperature, or Knudsen number. Particle distributions on an infinitesimal element of hypersurface, $d\Sigma$, are calculated using the following formula:

$$p^0 \frac{d^3N}{d^3p} = p^\mu d\sigma_\mu f(p), \tag{1}$$

where $f(p)$ is a distribution function and $d\sigma_\mu$ is a normal four-vector of hypersurface with length equal to the area of the infinitesimal surface element. This formula was obtained by Cooper and Frye [7] with the main feature that it respects four-momentum conservation. Though formula (1) is valid for any $f(p)$, the distribution function is usually assumed to be either the boosted thermal distribution $f(p) = f_0(p) = [\exp(\frac{p^\mu u_\mu - \mu}{T}) \pm 1]^{-1}$ (ideal fluid), or a distribution close to the boosted thermal distribution $f(p) = f_0(p) + \delta f(p)$ (viscous fluid), where $\delta f(p)$ is the dissipative correction. Here T, μ, and $u^\mu = \gamma(1, \boldsymbol{v})$ are temperature, chemical potential, and the flow velocity of the fluid, respectively.

There is, however, a conceptual problem with the Cooper-Frye formula. Where the surface is spacelike, i.e. its normal vector $d\sigma_\mu$ is spacelike, $p^\mu d\sigma_\mu < 0$ for some $\boldsymbol{p}$. Thus if $f(p) > 0$ for all p, as is the case for the thermal distribution, $\frac{d^3N}{d^3p} < 0$ for some $\boldsymbol{p}$. This can be easily seen in the local rest frame of a spacelike surface (which always exists since $v_{\rm surf} < c$ for spacelike surfaces), where $p^\mu d\sigma_\mu = \boldsymbol{p} \cdot \boldsymbol{n}$ and thus $\frac{d^3N}{d^3p} < 0$ for momenta directed inward the surface. On the other hand, for those timelike surfaces in which normal vector points toward the future (i.e., $d\sigma_0 > 0$), $\frac{d^3N}{d^3p} > 0$ for any $\boldsymbol{p}$. This can be also understood as follows: The surface is "escaping" faster than the speed of light, so no particle can cross it inward. (For a summary of the properties of timelike and spacelike surfaces, see Table I.)

*oliiny@fias.uni-frankfurt.de

†huovinen@th.physik.uni-frankfurt.de

‡petersen@fias.uni-frankfurt.de

TABLE I. Properties of surface elements. $g^{\mu\nu} = (1, -1, -1, -1)$. The normal vector is directed toward lower density. RF denotes reference frame, and $\frac{d^3N_{CF}}{d^3p}$ denotes particle distribution from the hypersurface element calculated using the Cooper-Frye formula.

Timelike surface	Spacelike surface
Timelike normal	Spacelike normal
$d\sigma^\mu d\sigma_\mu > 0$	$d\sigma^\mu d\sigma_\mu < 0$
$v_{\text{surf}} > c$	$v_{\text{surf}} < c$
$\exists$ RF: $d\sigma^\mu = (\pm dx\, dy\, dz, 0, 0, 0)$	$\exists$ RF: $d\sigma^\mu = (0, 0, 0, dt\, dx\, dy)$
$d\sigma_0 > 0 \Rightarrow \forall p^\mu$: $p^\mu d\sigma_\mu > 0$	$\exists p^\mu$: $p^\mu d\sigma_\mu < 0$
$d\sigma_0 > 0 \Rightarrow \forall p^\mu$: $\frac{d^3N_{CF}}{d^3p} > 0$	$\exists p^\mu$: $\frac{d^3N_{CF}}{d^3p} < 0$

If $\frac{d^3N}{d^3p}$ is interpreted as a phase-space density, negative values of it are clearly unphysical, but instead of giving a literal phase-space density, Cooper-Frye formula counts the world lines of particles crossing the surface element $d\Sigma$ and gives positive weight to particles moving "outward" and negative weight to particles moving "inward." Thus the negative values of $\frac{d^3N}{d^3p}$, the so-called negative Cooper-Frye contributions, refer to particles flying inward toward the hydrodynamical region, and which should thus be absorbed back to the fluid.

In pure hydrodynamical models, this poses a problem: Particlization takes place at freeze-out when rescatterings cease and particles stream free. Thus, once particles cross the particlization surface, there is nothing from where particles could scatter back toward the surface, and thus there should be no particles flying back. To avoid this problem, one could choose a completely timelike particlization hypersurface, for example, a hypersurface of a constant time without any negative contributions. However, it was shown [8] that particle spectra obtained in such an approach are dramatically different from spectra on a constant temperature hypersurface. Another way is to consider cutoff distribution [9]: $p^0 \frac{d^3N}{dp^3} = p^\mu d\sigma_\mu f(p)\Theta(p^\mu d\sigma_\mu)$. Such a prescription violates conservation laws, unless one adjusts temperature, chemical potentials, and flow velocity in the particle distribution $f(p)$ [10,11].

On the other hand, there is no such a problem in hybrid models. Particlization takes place where rescatterings are abundant, and thus it is natural to have particles flying back to the fluid-dynamical region. The problem is rather a practical one: What does the negative weight of a particle mean when one samples the particle distributions at particlization surface to create an initial state for the hadron transport? Usually one simply ignores them (see, e.g., Ref. [12]), which violates conservation laws. An attempt to include these negative weights to the hadron transport was recently made in Ref. [13]. Alternatively, if the transition from fluid to transport takes place in a region where hydrodynamics and transport are equivalent, the negative Cooper-Frye contributions coincide with the distribution of particles that backscatter to hydrodynamical region. Thus all one needs to do is to remove these particles from the cascade, but such removal is technically challenging, and the problem remains of how to find the region where hydrodynamics and transport lead to equal solutions—assuming that such a region exists at all! Thus the ultimate solution to the problem would be to construct a model, solving coupled hydrodynamical and kinetic equations with the kinetic model providing boundary condition for hydrodynamics. An attempt in this direction was undertaken by Bugaev [14–16], but these ideas have not yet been implemented in practice.

Fortunately, at high collision energies, the explosive expansion dynamics keeps the negative contributions on the level of a few percent. Emission of particles from timelike areas of surface where no negative contributions appear (so-called volume emission) is much larger than emission from spacelike areas (so-called surface emission), and as we discuss later, large flow velocity reduces negative contributions from spacelike surfaces. Nevertheless, there are very few studies that actually quote the values of negative contributions, and investigations at lower collision energies are lacking completely. In this article the negative contributions arising on the Cooper-Frye transition surface, assuming distribution functions in local equilibrium, are compared to the actual underlying microscopic dynamics to investigate the systematic differences between a transport and a hybrid approach.

Therefore, the aim of the current study is to compare the expected negative contributions in a locally equilibrated hydrodynamical approach with the actual number of particles that scatter back through a hypersurface in a coarse-grained microscopic transport approach. A constant energy density transition surface is constructed and negative Cooper-Frye contributions are compared to actual backscattered particles. In addition, the magnitude of negative contributions is calculated in a systematic way depending on hadron sort, collision energy, centrality, and choice of the transition surface. In Sec. II the framework for the calculation is explained. Section III shows results of tests of the numerical setup and sensitivity to internal parameters of the calculation. Finally, Sec. IV contains physical results: the quantification of Cooper-Frye negative contributions and their comparison to backscattered particles.

II. METHODOLOGY

Our calculation is based on the hadronic transport approach, Ultrarelativistic Quantum Molecular Dynamics (UrQMD 3.3p2) [17]. The degrees of freedom in UrQMD are hadrons, resonances up to a mass of 2.2 GeV, and strings. The implemented processes include binary elastic and inelastic scatterings, which mainly proceed via resonance formation and decays, or string excitation and fragmentation at higher collision energies. The UrQMD particles move along classical trajectories and scatter according to their free-particle cross sections. In our studies there are no long-range potentials and particle trajectories between collisions are always straight lines. Using UrQMD we simulate Au + Au collisions at laboratory frame energies $E_{\text{lab}} = 5$, 10, 20, 40, 80, and 160A GeV. This energy region is chosen because we expect UrQMD to provide a reasonable description of the collision dynamics at those energies and the Cooper-Frye negative contributions to become significant in this energy range.

The general procedure for our calculations is as follows:

(i) Generate many UrQMD events and coarse-grain them using a 3 + 1D space-time grid.
(ii) Find the local energy density in the Landau rest frame of each grid cell, $\epsilon_{\rm LRF}(t,x,y,z)$, and the collective flow velocity in each cell, $\boldsymbol{v}(t,x,y,z)$.
(iii) Construct the hypersurface Σ of a constant energy density $\epsilon_{\rm LRF}(t,x,y,z) = \epsilon_c$.
(iv) Calculate the particle spectra on Σ by using the Cooper-Frye formula and by counting the actual UrQMD particles that cross Σ. To obtain these spectra and to compare them to each other is the goal of the current work.

This procedure mimics switching from hydrodynamics to transport in a hybrid model, but here the "hydrodynamical" picture is obtained by averaging over particle distributions on a space-time grid. Since all the information is still available in the underlying microscopic approach we are able to compare the negative Cooper-Frye contributions to the spectrum of actual backscattered particles. In the following we explain all necessary details for each of these steps of the calculation.

A. Calculating physical quantities on a grid

To obtain the energy density in the Landau rest frame as a function of space-time, which is necessary to construct the Cooper-Frye transition surface, the energy momentum tensor and the net baryon current in the computational frame are calculated:

$$T^{\mu\nu}(t,x,y,z) = \frac{1}{\Delta x\Delta y\Delta z}\left\langle\sum\frac{p^\mu p^\nu}{p^0}\right\rangle_N, \tag{2}$$

$$j^\mu_B(t,x,y,z) = \frac{1}{\Delta x\Delta y\Delta z}\left\langle\sum\frac{p^\mu}{p^0}B\right\rangle_N, \tag{3}$$

where the sum is over all particles in each grid cell at the moment t, and B is the baryon number of each particle. Angular brackets denote averages over N UrQMD events. The cell sizes need to be small enough so that gradients of all relevant physical quantities within the cell are small. On the other hand, if the cell sizes are too small, one needs to generate infeasibly many events to damp statistical fluctuations of $T^{\mu\nu}$ components from cell to cell and obtain a smooth surface Σ. To satisfy these conditions and to ensure energy conservation precisely, we choose $\Delta x = \Delta y = 1$ fm, $\Delta z = 0.3$ fm, and time step $\Delta t = 0.1$ fm. For the highest collision energy, $E_{\rm lab} = 160A$ GeV, the gradients are larger, so even smaller grid sizes were taken: $\Delta x = \Delta y = 0.3$ fm and $\Delta z = 0.1$ fm. This choice is further discussed in Sec. III, where the sensitivity of results to the grid size is studied. Since even $N = 10\,000$ events does not provide enough statistics to obtain a smooth hypersurface, and increase of N is not feasible due to limited storage capacities, the individual particles are smeared by marker particles distributed according to a Gaussian distribution.

Every UrQMD particle with coordinates (t_p,x_p,y_p,z_p) and four-momentum p^μ is substituted by $N_{\rm split}$ particles with coordinates distributed with probability density $f(x,y,z) \sim \exp(-\frac{(x-x_p)^2}{2\sigma^2} - \frac{(y-y_p)^2}{2\sigma^2} - \gamma_z^2\frac{(z-z_p)^2}{2\sigma^2})$, where $\gamma_z = (1 - p^z/p^0)^{-1/2}$. These marker particles are attributed the 4-momentum and quantum numbers of the original particle divided by $N_{\rm split}$. In our calculation $N_{\rm split} = 300$ and $\sigma = 1$ fm. The sensitivity of our results to the width of the Gaussian is discussed in Sec. III. When this Gaussian smearing is applied, stable results are obtained with only $N = 1500$ events, which we employ for our calculations.

B. The hypersurface construction

After obtaining $T^{\mu\nu}$ in the computational frame, it has to be transformed to the Landau rest frame (LRF) in each cell. By definition, $T^{0i}_{\rm LRF} = 0$, i.e., the energy flow in the LRF is zero. To find the LRF we solve the generalized eigenvalue problem $(T^{\mu\nu} - \lambda g^{\mu\nu})h_\nu = 0$. The eigenvector corresponding to the largest eigenvalue is proportional to the 4-velocity of the LRF and the proportionality constant is fixed by the constraint that $\sqrt{u_\mu u^\mu} = 1$. After finding $T^{\mu\nu}_{\rm LRF}$ the hypersurface of constant Landau rest frame energy density is constructed where $T^{00}_{\rm LRF} \equiv \epsilon_{\rm LRF}(t,x,y,z) = \epsilon_c$, with ϵ_c a parameter that characterizes the hypersurface. In such a way we mimic the transition surface in hybrid models, which typically use $\epsilon_c = 0.3$–1 GeV/fm^3 [12]. The isosurface is constructed using the Cornelius subroutine [12], that provides a continuous surface without holes and avoids double counting of hypersurface pieces. The subroutine provides the normal 4-vectors $d\sigma_\mu$ of the hypersurface. The physical quantities on the grid, i.e., the energy, net baryon density, and the flow velocity, are linearly interpolated to the geometrical centers of the hypersurface elements.

C. Thermodynamic quantities

To apply the Cooper-Frye formula one needs the temperature T and chemical potentials on the surface, which do not exist in the microscopic picture. Strictly speaking they make sense only in the vicinity of thermal and chemical equilibrium, which may not be the case in our UrQMD simulation. Nevertheless, we take the LRF energy density and net baryon density to mean equilibrium densities—as is the case when deviations from equilibrium are small—and obtain temperature and chemical potentials from an ideal hadron resonance gas (HRG) equation of state (EoS) containing the same hadrons and resonances as UrQMD. Since our EoS assumes zero strangeness density, we impose this constraint as well, even if UrQMD itself allows local nonzero strangeness. In practice, this means solving the following coupled equations to find the temperature T, baryon chemical potential μ_B, and strangeness chemical potential μ_S:

$$\epsilon_{\rm LRF} = \sum_p \frac{g_p}{(2\pi)^3}\int\frac{d^3k\,\sqrt{k^2+m_p^2}}{e^{(\sqrt{k^2+m_p^2}-\mu_B B_p-\mu_S S_p)/T}\pm 1}, \tag{4}$$

$$n_B^{\rm LRF} = \sum_p \frac{g_p B_p}{(2\pi)^3}\int\frac{d^3k}{e^{(\sqrt{k^2+m_p^2}-\mu_B B_p-\mu_S S_p)/T}\pm 1}, \tag{5}$$

$$n_S^{\rm LRF} = \sum_p \frac{g_p S_p}{(2\pi)^3}\int\frac{d^3k}{e^{(\sqrt{k^2+m_p^2}-\mu_B B_p-\mu_S S_p)/T}\pm 1}. \tag{6}$$

Here $\epsilon_{\rm LRF} = T^{00}$ is the energy density in LRF, $n_B^{\rm LRF}$ is the baryon density in LRF, n_s is the strangeness density, and the sum runs over all hadron species that appear in UrQMD; m_p is the mass of a hadron p, g_p is its spin and isospin degeneracy factor, and B_p and S_p are its baryon number and strangeness, respectively.

D. Cooper-Frye and "by particles" calculations

After the hypersurface of constant LRF energy density Σ is obtained and T and μ are evaluated using the EoS, the Cooper-Frye formula is applied on the hypersurface. The spectrum from the Cooper-Frye formula is split into positive and negative parts:

$$\frac{dN^{+}_{CF}}{p_T dp_T d\varphi dy} = \frac{g}{(2\pi)^3}\int_\sigma \frac{\Theta(p^\mu d\sigma_\mu)\, p^\mu d\sigma_\mu}{e^{(p^\nu u_\nu-\mu)/T}\pm 1}, \quad (7)$$

$$\frac{dN^{-}_{CF}}{p_T dp_T d\varphi dy} = \frac{-g}{(2\pi)^3}\int_\sigma \frac{\Theta(-p^\mu d\sigma_\mu)\, p^\mu d\sigma_\mu}{e^{(p^\nu u_\nu-\mu)/T}\pm 1}. \quad (8)$$

To evaluate dN/dy or $dN/p_T dp_T$ the integrations are performed numerically, applying the 36×36 points Gauss-Legendre method to integrals transformed to finite limits.

For comparison with the Cooper-Frye calculation we count the actual microscopic (not marker) particles crossing the same hypersurface Σ that is used for Cooper-Frye calculations. Inward and outward crossings are counted separately. To find the point where a particle trajectory crosses Σ we use the fact that by construction the energy density $\epsilon > \epsilon_c$ inside the surface and $\epsilon < \epsilon_c$ outside of it. The energy density is interpolated to the particle trajectory to find the point where $\epsilon - \epsilon_c$ changes sign. Each of these crossings is counted as positive if the particle streams outward and as negative if the particle flies toward higher energy densities.

Both Cooper-Frye calculation and particle counting start at the same time $t_{\rm start}$, which depends on the collision energy. Following the prescription from hybrid models, we take $t_{\rm start} = \frac{2R}{v\gamma}$. This is the time two nuclei need to pass through each other. Numerical values are 8 fm/c for 5A GeV, 5.6 fm/c for 10A GeV, 4 fm/c for 20A GeV, 2.8 fm/c for 40A GeV, 2 fm/c for 80A GeV, and 1.4 fm/c for 160A GeV. The same $t_{\rm start}$ is used for all centralities.

III. SENSITIVITY TO INTERNAL PARAMETERS AND FULFILLMENT OF CONSERVATION LAWS

Besides physical parameters like the beam energy, $E_{\rm lab}$, and centrality of the collision controlled by the impact parameter b, our simulation contains internal parameters like grid spacing, the width of the smearing Gaussian σ, and the number of events N. Ideally, we should work in such a region of internal parameters, where our results are independent of them. To see how sensitive our results are to these internal parameters, the positive and negative contributions to the pion yield at midrapidity, $\frac{dN}{dy}|_{y=0}$, at different values of these parameters are evaluated.

The calculation is more sensitive to the grid spacing in the z direction, dz, than to the spacings in x and y directions, dx and dy, since gradients of $T^{\mu\nu}$ are largest in the longitudinal direction, although, as shown in Fig. 1(a), even the sensitivity to dz is weak over a reasonable range of values. The main motivation for choosing the grid spacing and time step comes in fact from the requirement of energy conservation, discussed later.

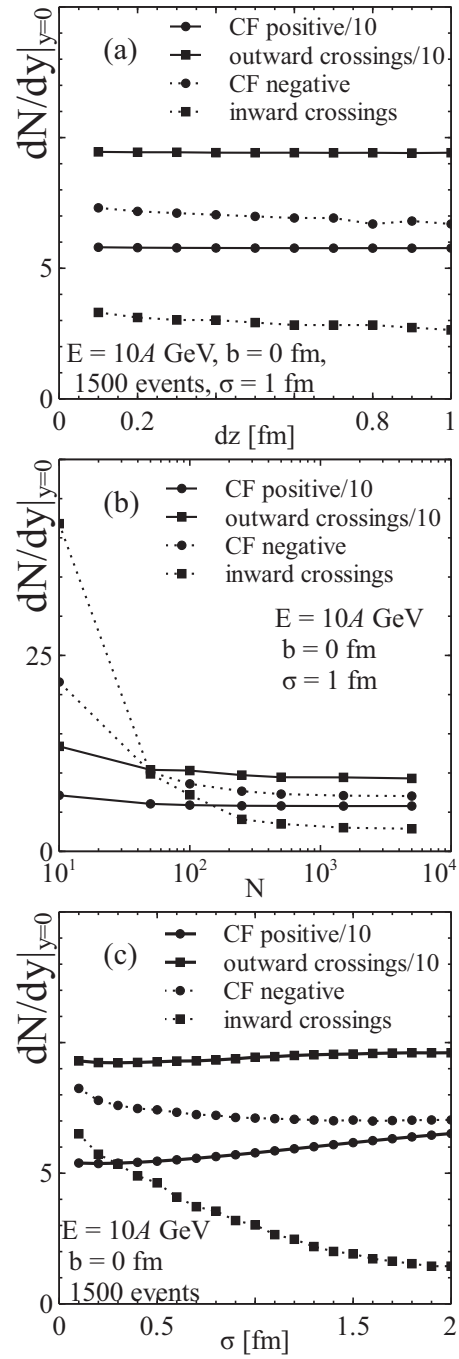

FIG. 1. Sensitivity of results to internal parameters of the simulation: grid spacing along the z axis, dz (a), number of events, N (b), and the width σ of Gaussian smearing (c).

The results are very sensitive to the small number of events [see Fig. 1(b)], but already $N = 500$ events provides sufficient statistics for stable results. To be on the safe side, we have analyzed $N = 1500$ events for our final results. Unfortunately,

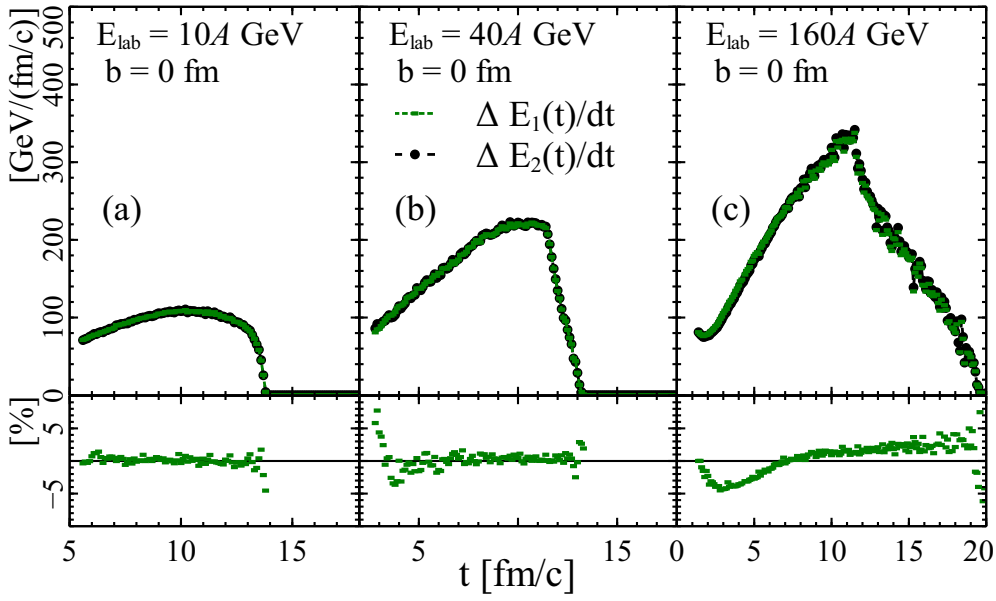

FIG. 2. (Color online) Energy flux through the surface at different times evaluated as actual flow, $\Delta E_1(t)/dt = \int_{t-dt}^{t} T^{\mu 0} d\sigma_\mu/dt$ (circles), and as a difference in energy within the surface at different times, $\Delta E_2(t)/dt = (E_{\rm in}(t) - E_{\rm in}(t-dt))/dt$ (rectangles). Lower panel shows the relative difference between these two measures in percent (%), and thus the conservation of energy in the calculation.

our results are not completely independent of the width σ of the Gaussian smearing, as shown on Fig. 1(c). The number of inward crossing UrQMD pions is most sensitive to σ. Two effects play a role here: At small σ the surface still has large statistical fluctuations and small-scale structures, "lumps" (see Fig. 2 of Ref. [18]), whereas at large σ Gaussian smearing pushes the transition surface further out in space. Further out, the densities are smaller, and the UrQMD particle distributions are further away from equilibrium so that especially the number of particles moving toward the center is strongly reduced. We choose $\sigma = 1$ fm as a reasonable value for our calculations, but keep in mind that varying σ in the range from 0.6 fm to 1.4 fm causes ∼20% difference in the number of inward crossings. We consider this a systematic error in our analysis, but fortunately this uncertainty does not affect our main conclusions.

To check that energy is conserved in the coarse-graining procedure, we evaluate the energy flow through the surface during the time step dt, $\Delta E_1(t) = \int_{t-dt}^{t} T^{\mu 0} d\sigma_\mu$, and compare it to the change in energy within the surface during the same time step, $\Delta E_2(t) = E_{\rm in}(t) - E_{\rm in}(t-dt)$, where $E_{\rm in}$ is total energy of particles inside the surface. Ideally $\Delta E_1(t) = \Delta E_2(t)$ for any dt, but finite cell sizes limit the precision and break the conservation of energy. The accuracy of $\Delta E_1 \approx \Delta E_2$ improves when grid spacing and time step are decreased. Figure 2 shows the energy flux through the surface and the relative difference between $\Delta E_1(t)$ and $\Delta E_2(t)$ in central collisions at energies $E_{\rm lab} = 10, 40$, and $160A$ GeV. To achieve better than 5% percent accuracy at all times, we use small grid spacing with $\Delta x = \Delta y = 1$ fm, $\Delta z = 0.3$ fm, and time step $\Delta t = 0.1$ fm/c in collisions with $E_{\rm lab} \leqslant 80A$ GeV, and an even finer grid with $\Delta x = \Delta y = 0.3$ fm, and $\Delta z = 0.1$ fm for collisions at $E_{\rm lab} = 160A$ GeV. When integrated over the whole collision time, the violation of energy conservation is less than 1% at all collision energies. We have done a similar check for the net baryon charge and obtained similar results.

IV. RESULTS AND DISCUSSION

Let us start by investigating the properties of the transition hypersurface itself as a function of beam energy. Figure 3 depicts the surface Σ in longitudinal direction along the x axis. We see that with increasing energy the lifetime of the system increases. This indicates longer lasting surface emission (from spacelike parts of the surface), which might lead to larger negative contributions. On the other hand, with increasing energy the longitudinal expansion leads to larger volume of the final volume emission (from timelike parts of the surface), which indicates smaller negative contributions. Thus we have two competing effects, and one has to carry out the actual calculation to find out how the negative contributions depend on energy.

Distributions of the (apparent) temperature of the hypersurface elements are shown on the right panel of Fig. 3. At each collision energy temperature distribution is rather narrow, which means that constant energy density surface approximately coincides with constant temperature surface. As well, the average temperature increases with increasing collision energy as expected from thermal model fits to particle yields [19].

In Fig. 4 we compare rapidity spectra of identified particles in $E_{\rm lab} = 40A$ GeV Au + Au collisions obtained by Cooper-Frye calculation and by counting of the microscopic particles. Even though, we are showing the results only for one collision energy, all results are qualitatively the same at all other energies. If UrQMD is close to equilibrium on a surface at $\epsilon_c = 0.3$ GeV/fm^3, both approaches should yield similar distributions. At midrapidity this is the case for nucleons, with

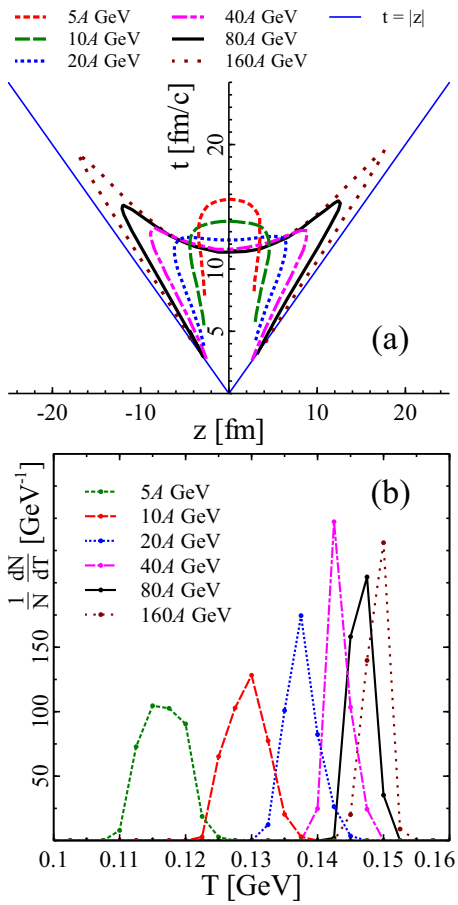

FIG. 3. (Color online) Upper panel: Hypersurface of constant LRF energy density $\epsilon(t,0,0,z) = \epsilon_c = 0.3$ GeV/fm^3. Lower panel: The fraction of hypersurface elements with (apparent) temperature T in central Au + Au collisions at the collision energy of $E_{\rm lab} = 5$, 10, 20, 40, 80, and 160A GeV.

a lesser accuracy for kaons. Δ, Λ, ρ, and η which are not shown in the figure depict a behavior similar to nucleons. However, the pion yields are wildly different, indicating that pions are—and thus the entire system is—far away from chemical equilibrium at least. To cancel the effect of nonequilibrium and to make the differences in momentum distributions visible, we consider not the absolute value of the negative contributions but the ratio of negative to positive ones, $(dN^-/dy)/(dN^+/dy)$ or $(dN^-/dp_T)/(dN^+/dp_T)$. From Fig. 4 it is also apparent that the magnitude of the negative contributions is always small compared to the positive ones, as expected.

The dependence of the ratio $(dN^-/dy)/(dN^+/dy)$ on the hadron type is illustrated in Fig. 5 by the Cooper-Frye results. Since for all cases the microscopic negative contributions of backstreaming particles are much smaller than the Cooper-Frye ones, we concentrate on showing the maximal effect. Surface temperature and velocity profiles are identical for all hadrons, so the plot demonstrates first of all the effect of particle mass. One can see that the average value of $(dN^-/dy)/(dN^+/dy)$ decreases with particle mass. This can be understood by considering a small volume of fluid in its rest frame, and a spacelike surface moving through it with a

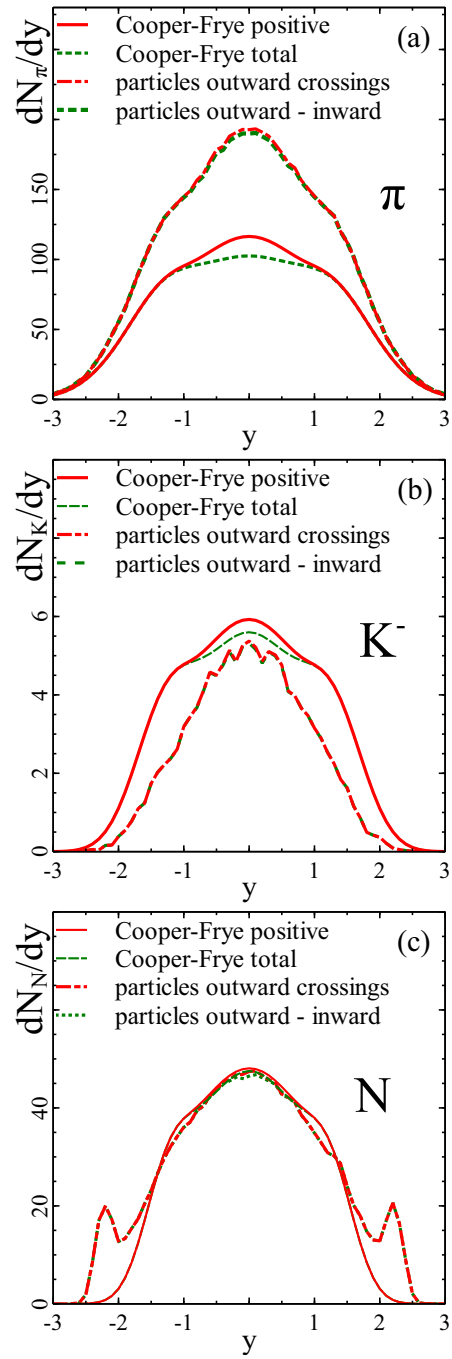

FIG. 4. (Color online) Rapidity distribution of identified particles obtained from Cooper-Frye formula on the surface Σ and from explicit counting of particles that cross the same surface. Positive contributions and the net distribution, i.e., positive-negative, are shown separately. $E_{\rm lab} = 40A$ GeV, central Au + Au collisions.

velocity $0 < v_{\rm surf} < c$ so that lower density, i.e., outside, is in the negative direction. To be counted as a negative contribution, a particle must enter the fluid, and thus have a larger velocity than the surface. Average thermal velocity decreases with increasing mass, and therefore as the particles are heavier, fewer of them cross the surface inward. Since relative negative contributions for pions are several times larger than for other hadrons, we consider only pions in the following.

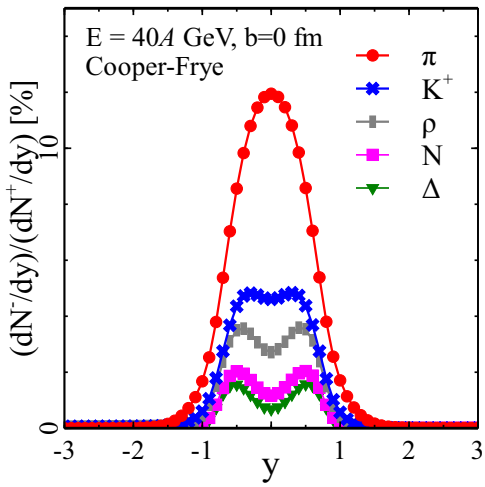

FIG. 5. (Color online) Rapidity distribution of the ratio of negative to positive contributions for different hadron species: pions (circles), K^+ (crosses), ρ (bars), nucleons (rectangles), and Δs (triangles). Cooper-Frye calculation in central Au + Au collisions at $E_{\rm lab} = 40A$ GeV.

As could be seen in Fig. 4, imposing equilibrium for Cooper-Frye calculation leads to a significantly larger negative to positive contribution ratio at midrapidity than the counting of UrQMD particles. As shown in Fig. 6 this holds for all the energies we have considered, showing that the system is out not only of chemical but also of kinetic equilibrium. Either the collective flow velocity of pions is different from the collective velocity of other particles [20,21] or the dissipative corrections to pion distribution are very large. We have also checked that the relative microscopic negative contributions are much smaller in UrQMD at all centralities, for all particle species, and on isosurfaces of energy density $\epsilon_c = 0.3$ and 0.6 GeV/fm^3.

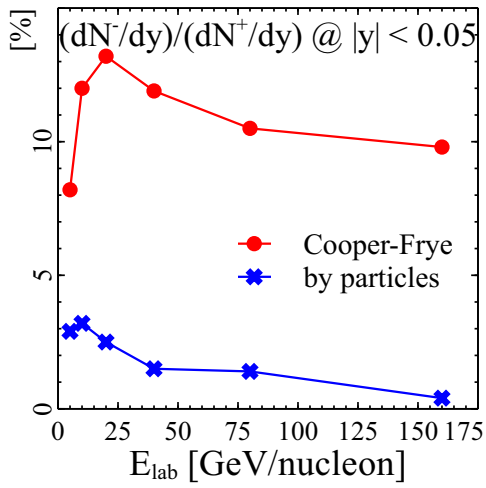

FIG. 6. (Color online) The ratio of negative to positive contributions on the $\epsilon(t,x,y,z) = \epsilon_c = 0.3$ GeV/fm^3 surface for pions at midrapidity in central Au + Au collisions at various collision energies. Circles depict Cooper-Frye result and rectangles the explicit counting of UrQMD particles.

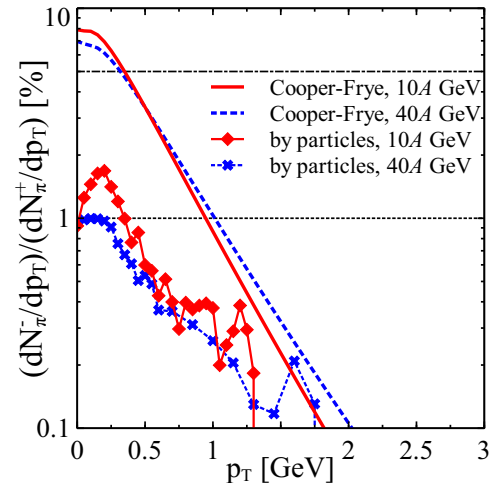

FIG. 7. (Color online) The ratio of negative to positive pion contributions as a function of transverse momentum at midrapidity in central Au + Au collisions at $E_{\rm lab} = 5$, 10, 20, 40, and 80A GeV.

On the other hand, the trend as a function of collision energy in Cooper-Frye and UrQMD calculations is the same: Both curves have a maximum at 10–20A GeV and then decrease with increasing energy. This behavior is a result of a complicated interplay of several factors: temperature, relative velocities between surface and fluid, and relative amounts of volume and surface emission, i.e., emission from the time- and spacelike parts of the surface. To gain some insight we consider all these factors separately. The same argument used to explain the sensitivity of negative contributions to particle mass also explains why larger temperature leads to larger negative contributions. Temperature on the constant density surface grows with increasing collision energy (see Fig. 3),

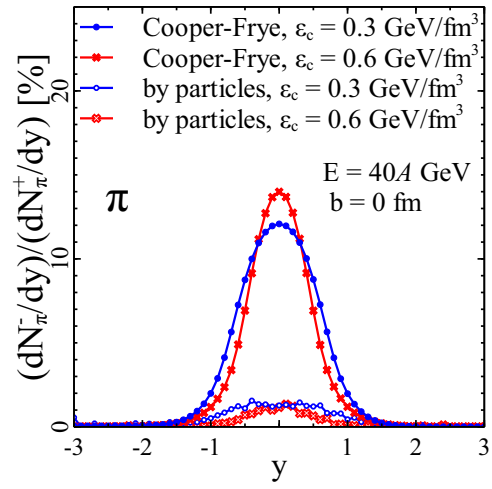

FIG. 8. (Color online) Rapidity distribution of the ratio of negative to positive contributions for pions on $\epsilon(t,x,y,z) = \epsilon_c = 0.3$ GeV/fm^3 (circles) and $\epsilon_c = 0.6$ GeV/fm^3 (crosses) surfaces in central Au + Au collisions at $E_{\rm lab} = 40A$ GeV. Full symbols correspond to Cooper-Frye calculation and open symbols to explicit counting of UrQMD particles.

which would lead one to expect an increase of negative contributions with increasing collision energy. On the other hand, larger relative velocity between the fluid and surface reduces the negative contributions (again the same argument), and we see that the average relative velocity increases with increasing collision energy. Finally, as argued when discussing Fig. 3, we have seen that as the collision energy increases, so does the fraction of volume emission, which, as mentioned, reduces the negative contributions.

It is instructive to evaluate the negative contributions as function of transverse momentum p_T as well, as shown in Fig. 7 for Cooper-Frye calculation and "by particles." One can see that the largest negative contributions are located at small p_T, which means that one can reduce the uncertainty caused by the negative contributions by a low p_T cut. Also as a function of transverse momentum, the amount of microscopically backward streaming particles is much smaller than in an equilibrium scenario.

When discussing Fig. 6 we mentioned that, independent of the energy density of the surface, the negative contributions

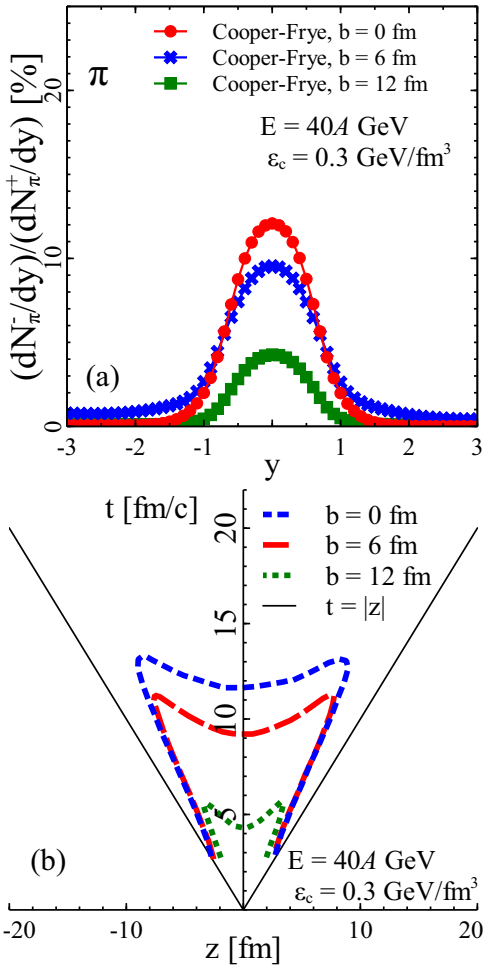

FIG. 9. (Color online) Upper panel: Rapidity distribution of the ratio of negative to positive contributions for pions in Au + Au collisions at $E_{\rm lab} = 40A$ GeV at various centralities: $b = 0$ (circles), $b = 6$ fm (crosses), and $b = 12$ fm (rectangles). Lower panel: hypersurfaces along the z axis in the same collisions at the same centralities.

are much smaller when counting the UrQMD particles. Furthermore, in Cooper-Frye calculations the strength of the negative contributions depends on the value of ϵ_c where the distributions are evaluated as shown in Fig. 8. Larger ϵ_c leads to larger negative contribution at midrapidity and lower at back- and forward rapidities. This result arises from interplay of two factors: larger temperature and smaller average $v_{\rm rel}$ for larger energy density. Quite surprisingly the negative contributions evaluated by counting the UrQMD particles are almost independent of the value of ϵ_c. This indicates that even in much higher temperature $T \sim 155-160$ MeV the microscopic system is not fully thermalized.

Dependence of the contribution ratio on centrality is shown in Fig. 9. The negative contributions decrease with decreasing centrality because as the collision is more peripheral, the fraction of timelike hypersurface elements increases. This behavior is illustrated in the right panel of Fig. 9. In the limit of very peripheral collisions the lifetime of the system becomes zero, and thus the surface is timelike everywhere and there are no negative contributions at all. Temperature and relative velocities appear to be less important factors in this case than relative amount of timelike and spacelike hypersurface elements.

Let us finally compare our results to previous studies. In Ref. [12] negative contributions were evaluated on the $\epsilon = 0.3$ GeV/fm^3 transition surface of a hybrid model at SPS and RHIC energies—$E_{\rm lab} = 160A$ GeV and $\sqrt{s_{\rm NN}} = 200$ GeV, respectively—and found to be around $(dN_\pi^-/dy)/(dN_\pi^+/dy) \simeq 13\%$ and 9% at $y = 0$. The negative contributions for $160A$ GeV are slightly larger than in our calculation. The reason for this discrepancy lies in the difference of the velocity profiles on the hypersurfaces: In hydrodynamics the average relative velocity between flow and surface is smaller than in our transport-based approach, which leads to larger negative contributions.

V. CONCLUSIONS

We have investigated negative Cooper-Frye contributions and backscattering using a coarse-grained molecular dynamics approach. Au + Au collisions at $E_{\rm lab} = 5$–$160A$ GeV energies have been simulated using UrQMD, and a hypersurface Σ of constant Landau rest frame energy density has been constructed. On this surface we have calculated two quantities: the ratio of Cooper-Frye negative to positive contributions, which assumes local thermal equilibrium, and the ratio of UrQMD particles crossing Σ inward to crossing Σ outward, which assumes no equilibrium.

We found that at all collision energies the ratio of inward- to outward-moving particles calculated counting the UrQMD particles is much smaller than the same ratio calculated assuming equilibrium, i.e., the Cooper-Frye negative to positive ratio. This finding poses a question for the construction of hybrid models and the treatment of freeze-out in hydrodynamical models: If the cascade leads to distributions nowhere near equilibrium, how are the hydrodynamical and cascade stages to be connected in a consistent fashion? On the other hand, this result shows that an ideal fluid dynamics hybrid approach contains the worst-case scenario for negative contributions

and even then they are on the order of maximum 15% for the pion yield at midrapidity. What remains to be seen, however, is whether we could get closer to the UrQMD result if we allowed dissipative corrections to the distribution function of Cooper-Frye, or whether the deviations from equilibrium are so large that dissipative expansion is not feasible.

The largest observed impact of negative contributions is to the pion rapidity spectrum at midrapidity in central collisions. In thermally equilibrated Cooper-Frye calculations it constitutes 8–13%, but only 0.5–4% in the counting of UrQMD particles. The Cooper-Frye value roughly agrees with the values obtained previously for hydrodynamics at 160 GeV. We found several systematic features in these ratios. They are smaller for larger hadron mass and therefore largest for pions. The relative negative contributions decrease as a function of collision energy and by going from central to peripheral collisions. On the other hand, they increase if a higher energy density is chosen as a surface criterion. The small-scale structures of the surface, its "lumpiness", play a significant role: If the surface is not smooth enough, both ratios can increase dramatically. Therefore, an interesting future study could compare single fluctuating events to the averaged result.

ACKNOWLEDGMENTS

This work was supported by the Helmholtz International Center for the Facility for Antiproton and Ion Research (HIC for FAIR) within the framework of the Landes-Offensive zur Entwicklung Wissenschaftlich-Oekonomischer Exzellenz (LOEWE) program launched by the State of Hesse. D.O. and H.P. acknowledge funding of a Helmholtz Young Investigator Group VH-NG-822 from the Helmholtz Association and GSI, and P.H. acknowledges support from BMBF under Contract No. 06FY9092. Computational resources have been provided by the Center for Scientific Computing (CSC) at the Goethe University of Frankfurt.

[1] P. F. Kolb and U. Heinz, in *Quark-Gluon Plasma 3*, edited by R. C. Hwa and X.-N. Wang (World Scientific, Singapore, 2004), p. 634.
[2] P. Huovinen and P. V. Ruuskanen, Ann. Rev. Nucl. Part. Sci. **56**, 163 (2006).
[3] U. W. Heinz and R. Snellings, Annu. Rev. Nucl. Part. Sci. **63**, 123 (2013).
[4] C. Gale, S. Jeon, and B. Schenke, Int. J. Mod. Phys. A **28**, 1340011 (2013).
[5] T. Hirano, P. Huovinen, K. Murase, and Y. Nara, Prog. Part. Nucl. Phys. **70**, 108 (2013).
[6] H. Petersen, J. Phys. G: Nucl. Part. Phys. **41**, 124005 (2014).
[7] F. Cooper and G. Frye, Phys. Rev. D **10**, 186 (1974).
[8] D. H. Rischke, Lect. Notes Phys. **516**, 21 (1999).
[9] K. A. Bugaev, Nucl. Phys. A **606**, 559 (1996).
[10] C. Anderlik, Z. I. Lazar, V. K. Magas, L. P. Csernai, H. Stocker, and W. Greiner, Phys. Rev. C **59**, 388 (1999).
[11] C. Anderlik *et al.*, Phys. Rev. C **59**, 3309 (1999).
[12] P. Huovinen and H. Petersen, Eur. Phys. J. A **48**, 171 (2012).
[13] S. Pratt, Phys. Rev. C **89**, 024910 (2014).
[14] K. A. Bugaev and M. I. Gorenstein, arXiv:nucl-th/9903072.
[15] K. A. Bugaev, Phys. Rev. Lett. **90**, 252301 (2003).
[16] K. A. Bugaev, Phys. Rev. C **70**, 034903 (2004).
[17] S. A. Bass *et al.*, Prog. Part. Nucl. Phys. **41**, 255 (1998); M. Bleicher *et al.*, J. Phys. G **25**, 1859 (1999).
[18] P. Huovinen, M. Belkacem, P. J. Ellis, and J. I. Kapusta, Phys. Rev. C **66**, 014903 (2002).
[19] A. Andronic, P. Braun-Munzinger, and J. Stachel, Phys. Lett. B **673**, 142 (2009).
[20] H. Sorge, Phys. Lett. B **373**, 16 (1996).
[21] S. Pratt and J. Murray, Phys. Rev. C **57**, 1907 (1998).

Influence of temperature-dependent shear viscosity on elliptic flow at backward and forward rapidities in ultrarelativistic heavy-ion collisions

E. Molnár,[1,2] H. Holopainen,[2] P. Huovinen,[2,3] and H. Niemi[4,5]

[1]*MTA-DE Particle Physics Research Group, H-4010 Debrecen, P.O. Box 105, Hungary*

[2]*Frankfurt Institute for Advanced Studies, Ruth-Moufang-Strasse 1, D-60438 Frankfurt am Main, Germany*

[3]*Institut für Theoretische Physik, Johann Wolfgang Goethe-Universität, Max-von-Laue-Strasse 1, D-60438 Frankfurt am Main, Germany*

[4]*Department of Physics, University of Jyväskylä, P.O. Box 35 (YFL), FI-40014 University of Jyväskylä, Finland*

[5]*Helsinki Institute of Physics, P.O. Box 64, FI-00014 University of Helsinki, Finland*

(Received 31 July 2014; revised manuscript received 12 September 2014; published 7 October 2014)

We explore the influence of a temperature-dependent shear viscosity over entropy density ratio η_s/s on the azimuthal anisotropies v_2 and v_4 of hadrons at various rapidities. We find that in Au + Au collisions at full Relativistic Heavy Ion Collider energy, $\sqrt{s_{\rm NN}} = 200$ GeV, the flow anisotropies are dominated by hadronic viscosity at all rapidities, whereas in Pb + Pb collisions at the Large Hadron Collider energy, $\sqrt{s_{\rm NN}} = 2760$ GeV, the flow coefficients are affected by the viscosity in both the plasma and hadronic phases at midrapidity, but the further away from midrapidity, the more dominant the hadronic viscosity becomes. We find that the centrality and rapidity dependence of the elliptic and quadrangular flows can help to distinguish different parametrizations of $(\eta_s/s)(T)$. We also find that at midrapidity the flow harmonics are almost independent of the decoupling criterion, but they show some sensitivity to the criterion at backward and forward rapidities.

DOI: 10.1103/PhysRevC.90.044904 PACS number(s): 25.75.Ld, 12.38.Mh, 24.10.Nz

I. INTRODUCTION

Determining the transport properties of the quark-gluon plasma (QGP) formed in ultrarelativistic nuclear collisions [1] is nowadays one of the main goals in high-energy nuclear physics. Fluid-dynamical models indicate a very low shear viscosity to entropy density ratio η_s/s,[1] when tuned to reproduce the azimuthal anisotropies of the transverse momentum distributions of observed hadrons. For recent reviews see, for example, Refs. [2–4]. The values favored by state-of-the-art calculations are in the vicinity of the conjectured lower limit for shear viscosity, $\eta_s/s = 1/(4\pi)$, based on the anti–de Sitter/conformal field theory (AdS/CFT) correspondence [5]. For example, the values found in Ref. [6] are $\eta_s/s = 0.12$ for collisions at the Relativistic Heavy-Ion Collider (RHIC) at Brookhaven National Laboratory and $\eta_s/s = 0.2$ at the Large Hadron Collider (LHC) at CERN.

The values quoted above were obtained by using a constant η_s/s ratio during the entire evolution of the system. For a physical system η_s/s depends at least on temperature [7] and on baryon density [8]. A constant value of η_s/s represents only an effective average over the entire space-time evolution of the system. The slightly larger effective η_s/s obtained for collisions at the LHC, i.e., at larger collision energy, thus may be interpreted as an indication of the temperature dependence of η_s/s [9,10]. Unfortunately, extracting the temperature dependence of η_s/s from the experimental data is a challenging problem.

In our previous works [11–13], we have studied the consequences of relaxing the assumption of a constant η_s/s. We found that the relevant temperature region where the shear viscosity affects the elliptic flow most varies with the collision energy. At the RHIC the most relevant region is around and below the QCD transition temperature, while for higher collision energies the temperature region above the transition becomes more and more important. To constrain the temperature dependence of η_s/s better, it would thus be necessary to find observables which are sensitive to the shear viscosity at different stages of the evolution of a single collision.

In this work we relax the assumption of boost invariance of our earlier works, solve the evolution equations numerically in all three dimensions, and study whether the azimuthal anisotropies have similar dependence on $(\eta_s/s)(T)$ at all rapidities. If not, the measurements of v_n at backward and forward rapidities could bring further constraints to $(\eta_s/s)(T)$.

We also approach the problem of extracting the temperature dependence of η_s/s in a fashion similar to that of Ref. [9]: We tune different parametrizations to reproduce the anisotropies at one collision energy and centrality and check whether anisotropies at different centralities, rapidities, and collision energies can distinguish between these parametrizations.

Furthermore, we check the sensitivity of our results to different decoupling criteria. To this end we carry out the calculations using a dynamical freeze-out criterion, i.e., freeze-out at constant Knudsen number [14–16], and compare the results to those obtained using the conventional freeze-out at constant temperature.

In the following we describe the structure and freeze-out in our (3+1)-dimensional dissipative fluid-dynamical model in Sec. II and the parameters in our calculations in Sec. III. Section IV contains the comparison of our results with experimental data, while in Secs. V and VI we discuss whether it is possible to distinguish the details of different parametrizations of $(\eta_s/s)(T)$, as well as the effects of a

[1]In this work η_s denotes the coefficient of shear viscosity, $\eta_{\rm ch}$ the pseudorapidity, and η the space-time rapidity.

dynamical freeze-out criterion. We summarize our results in Sec. VII.

Specific details of the fluid-dynamical equations are relegated to Appendix A. The numerical algorithm and details of our implementation and the numerical accuracy of our code are discussed in Appendices B, and C, respectively.

In this work we use natural units $\hbar = c = k = 1$.

II. FLUID DYNAMICS

A. Equations of motion

Relativistic fluid dynamics corresponds to the local conservation of energy-momentum and net-charge currents (if any),

$$\partial_\mu T^{\mu\nu} = 0, \quad \partial_\mu N_i^\mu = 0, \tag{1}$$

where $T^{\mu\nu}$ is the energy-momentum tensor and N_i^μ are the net-charge four-currents.

These macroscopic fields can be decomposed with respect to the fluid flow velocity defined by Landau and Lifshitz [17], $u^\mu = T^{\mu\nu}u_\nu/e$, as

$$T^{\mu\nu} = eu^\mu u^\nu - P\Delta^{\mu\nu} + \pi^{\mu\nu}, \tag{2}$$

$$N_i^\mu = n_i u^\mu + V_i^\mu, \tag{3}$$

where $e = T^{\mu\nu}u_\mu u_\nu$ and $n_i = N_i^\mu u_\mu$ are the energy and net-charge densities in the local rest frame, respectively, $P = -T^{\mu\nu}\Delta_{\mu\nu}/3$ is the isotropic pressure, and $V_i^\mu = N_i^\alpha \Delta_\alpha^\mu$ are the charge diffusion currents. The shear-stress tensor, $\pi^{\mu\nu} = T^{\langle\mu\nu\rangle}$, is the traceless and orthogonal part of the energy-momentum tensor. With the $(+,-,-,-)$ convention for the metric tensor $g^{\mu\nu}$, the projection tensor is $\Delta^{\mu\nu} = g^{\mu\nu} - u^\mu u^\nu$. The angular brackets $\langle\rangle$ denote an operator leading to the symmetric, traceless, and orthogonal to the flow velocity part of a tensor: $T^{\langle\mu\nu\rangle} = [\frac{1}{2}(\Delta_\alpha^\mu\Delta_\beta^\nu + \Delta_\beta^\mu\Delta_\alpha^\nu) - \frac{1}{3}\Delta^{\mu\nu}\Delta_{\alpha\beta}]T^{\alpha\beta}$.

Landau's matching condition allows one to associate the rest-frame densities with their equilibrium values, $e = e_0(T,\{\mu_i\})$ and $n_i = n_{i,0}(T,\{\mu_j\})$. The difference between the isotropic and equilibrium pressures defines the so-called bulk viscosity, $\Pi = P - P_0$.

Equations (2) and (3) can be closed by providing an equation of state (EoS), together with the equations determining the evolution of dissipative quantities $\pi^{\mu\nu}$, Π, and V_i^μ. These quantities represent the dissipative forces in the system as well as deviations from the local thermal equilibrium. In the Navier-Stokes approximation they are linearly proportional to the gradients of velocity and temperature, with proportionality coefficients for shear viscosity $\eta_s(T,\{\mu_i\})$, bulk viscosity $\zeta(T,\{\mu_i\})$, and charge diffusion $\kappa_i(T,\{\mu_j\})$ quantifying the transport properties of the matter.

It is well known that the bulk viscosity coefficient of a relativistic gas is about three orders of magnitude smaller than its shear viscosity coefficient, and it vanishes in the ultrarelativistic limit [18]. However, it is still important for relativistic systems around phase transitions; therefore, even if the bulk viscosity is negligible in the QGP-phase, it may be large near and below the phase transition [19]. A large bulk viscosity at those stages may or may not have a significant effect on the observables [20–25]. Since disentangling the effects of shear and bulk on the observed spectra is difficult, and beyond the scope of this work, we adopt the approach of Ref. [21]. We assume that bulk viscosity is large only in the vicinity of the QCD phase transition but due to the critical slowing down its effect is so small that it can be safely ignored.

At midrapidity the matter formed in ultrarelativistic collisions at the RHIC and at the LHC is to a good approximation net-baryon free, and thus in boost-invariant calculations it has been an excellent approximation to neglect all conserved charges. Since in this study we want to investigate the backward and forward rapidity regions of the system where net-baryon density is finite, in principle we should include the net-baryon current and baryon charge diffusion in the description of the system. However, the baryon charge diffusion in a QGP as well as in a hadron gas is largely unknown at the moment. Also, at low values of net-baryon density where the lattice QCD results [26,27] can be used, the effect of the finite density on the EoS is small [28]. Therefore, to simplify the description of the system, and to allow us to concentrate solely on the effects of shear viscosity on the spectra, we ignore the finite baryon charge in the fluid as well. Thus we are left with the shear-stress tensor $\pi^{\mu\nu}$ as the only dissipative quantity in the system.

In so-called second-order or causal fluid-dynamical theories by Müller and by Israel and Stewart [29–31], the dissipative quantities fulfill certain coupled relaxation equations. Here we recall the relaxation equation for the shear-stress tensor obtained from the relativistic Boltzmann equation [32–34],

$$\begin{aligned}\tau_\pi D\pi^{\mu\nu} = {} & 2\eta_s\sigma^{\mu\nu} - \pi^{\mu\nu} - \tau_\pi(\pi^{\lambda\mu}u^\nu + \pi^{\lambda\nu}u^\mu)Du_\lambda \\ & - \delta_{\pi\pi}\pi^{\mu\nu}\theta - \tau_{\pi\pi}\pi_\lambda^{\langle\mu}\sigma^{\nu\rangle\lambda} \\ & + 2\tau_\pi\pi_\lambda^{\langle\mu}\omega^{\nu\rangle\lambda} + \varphi_7\pi_\lambda^{\langle\mu}\pi^{\nu\rangle\lambda}.\end{aligned} \tag{4}$$

Here τ_π is the shear-stress relaxation time, $D\pi^{\mu\nu} = u^\alpha\pi^{\mu\nu}_{;\alpha}$ denotes the time derivative, θ is the expansion rate, $\sigma^{\mu\nu}$ is the shear tensor, and $\omega^{\mu\nu}$ is the vorticity. The other coefficients can be calculated self-consistently from microscopic theory and, for example, in case of an ultrarelativistic massless Boltzmann gas we obtain, in the 14-moment approximation, $\tau_\pi = \frac{5}{3}\lambda_{mfp}$, $\delta_{\pi\pi} = (4/3)\,\tau_\pi$, $\tau_{\pi\pi} = (10/7)\,\tau_\pi$, while $\varphi_7 = (9/70)\,/P_0$, where λ_{mfp} is the mean free path between collisions. For QCD these coefficients are mostly unknown; however, for high-temperature QCD matter the coefficients given above may be acceptable as a first approximation.

For the sake of simplicity we ignore the last two terms in Eq. (4). This is justified since the relative contribution of the φ_7 coefficient was shown to be negligible compared to the others [34]. Similarly, we have observed that the term proportional to the vorticity has little effect on the overall evolution of the system and is thus omitted from the final calculations shown here.

B. The freeze-out stage

During the fluid-dynamical evolution the system cools and dilutes due to the expansion, and consequently the microscopic rescattering rate of particles, $\Gamma \sim n\sigma \simeq \lambda_{mfp}^{-1}$, decreases, until the rescatterings cease and particles stream freely toward detectors. The transition from an (almost) equilibrated fluid

to free-streaming particles is a gradual process, but since implementing such a gradual process into a fluid-dynamical description is very complicated [35,36], it is usually assumed to take place on an infinitesimally thin space-time layer, on the so-called freeze-out surface. Therefore the total number of particles crossing the surface Σ, with a normal vector $d^3\Sigma_\mu$ pointing outward, leads to the following invariant distribution of particles emitted from the fluid, known as the Cooper-Frye formula [37]:

$$E\frac{d^3N}{d^3p} = \int_\Sigma d^3\Sigma_\mu(x)\, p^\mu f(x,p), \tag{5}$$

where $p^\mu = (E,\mathbf{p})$ denotes the four-momentum, while $f(x,p)$ is the phase-space distribution function of particles on the surface.

To apply the Cooper-Frye formula, we need an appropriate criterion for choosing the surface Σ. Since scattering rates strongly depend on temperature, the usual approach is to assume the freeze-out to take place on a surface of constant temperature or energy density. However, it has been argued that it would be more physical to assume that the freeze-out happens when the average scattering rate is roughly equal to the expansion rate of the system [38].

This latter, so-called dynamical freeze-out, criterion can be expressed in terms of the Knudsen number, Kn, which is the ratio of a characteristic microscopic time or length scale, such as λ_{mfp}, and a characteristic macroscopic scale of the fluid, such as the inverse of the local gradients, $L^{-1} \approx \partial_\mu$. In terms of the Knudsen number the dynamical freeze-out criterion is Kn ≈ 1, which has occasionally been used in ideal fluid calculations [15,16,39,40], but for viscous fluids it is more appropriate to use the relaxation times of dissipative quantities as the microscopic scale, since they appear naturally in the evolution equations for dissipative quantities [32].

In most of our calculations we use the conventional constant-temperature freeze-out, but to evaluate how sensitive our results are to the particular freeze-out criterion, and to the freeze-out description in general, we also do the calculations assuming freeze-out at constant Knudsen number. We take the relaxation time of shear stress, τ_π, as the microscopic scale and the inverse of the expansion rate of the system, θ^{-1}, as the macroscopic scale. Thus we get a local Knudsen number of

$$\mathrm{Kn} = \tau_\pi \theta. \tag{6}$$

Since the Knudsen number can be evaluated in many different ways [14], we do not insist on freeze-out at Kn $= 1$, but we treat the freeze-out Knudsen number as a free parameter chosen to reproduce rapidity and p_T distributions of experimental data. To avoid pathologies encountered in Refs. [14,15], we also require that the dynamical freeze-out takes place below a temperature of $T = 180$ MeV and above $T = 80$ MeV.

To evaluate the distributions on the freeze-out surface, we assume that the distribution of particles for each species i, i.e., $f_i(x,p)$, is given by the well-known Grad's 14-moment ansatz, which includes corrections δf_i (shear viscosity only) to the local equilibrium distribution function as

$$f_i(x,p) \equiv f_{0i} + \delta f_i = f_{0i}\left[1 + (1 \mp \tilde{f}_{0i})\frac{p_i^\mu p_i^\nu \pi_{\mu\nu}}{2T^2(e+p)}\right], \tag{7}$$

where f_{0i} is the local equilibrium distribution function,

$$f_{0i}(x,p) = \frac{g_i}{(2\pi)^3}\left[\exp\left(\frac{p_i^\mu u_\mu - \mu_i}{T}\right) \pm 1\right]^{-1}, \tag{8}$$

and $\tilde{f}_{0i} = (2\pi)^3 f_{0i}/g_i$. We also include the contribution from all strong and electromagnetic two- and three-particle decays of the hadronic resonances up to a mass of 2 GeV to the final particle distributions.

The flow anisotropies are defined from a Fourier decomposition of the particle spectra as

$$E\frac{d^3N}{d^3p} = \frac{d^2N}{2\pi p_T dp_T dy_p}\left(1 + 2\sum_{n=1}^{\infty} v_n \cos n(\phi - \Psi_n)\right), \tag{9}$$

where $y_p = \frac{1}{2}\ln[(p^0 + p^z)/(p^0 - p^z)]$ is the rapidity of the particle, $p_T = \sqrt{p_x^2 + p_y^2}$ is its transverse momenta, and Ψ_n is the event plane for coefficient v_n. The Fourier coefficients $v_n = v_n(p_T, y_p)$ are the differential flow components. In this work the differential and integrated v_n are calculated by using the event-plane method.

III. PARAMETERS

We mostly implement the parametrization used in Refs. [11,13], but we retune the parameter values and generalize it for a (3+1)-dimensional non-boost-invariant case.

A. Equation of state

For the EoS we use the $s95p$-PCE-v1 parametrization of lattice QCD results at zero net-baryon density [41]. The high-temperature part of the EoS is given by the hotQCD Collaboration [42,43] and it is smoothly connected to the low-temperature part described as a hadron resonance gas, where resonances up to a mass of 2 GeV are included. The hadronic part includes a chemical freeze-out at $T_{\mathrm{chem}} = 150$ MeV where all stable particle ratios are fixed [44–46]. Since the construction of the EoS assumes that the entropy per particle is conserved after chemical freeze-out, the small (approximately 1%) entropy increase during the viscous hydrodynamical evolution below T_{chem} leads to a small increase in particle yields too.

B. Transport coefficients

As in our earlier works [11–13], we use four different parametrizations of the temperature-dependent shear viscosity over entropy ratio (see Fig. 1):

(1) LH-LQ, in which $(\eta_s/s)(T) = 0.08$ for all temperatures;
(2) LH-HQ, in which $(\eta_s/s)(T) = 0.08$ for the hadronic phase, while above T_{tr} the viscosity to entropy ratio

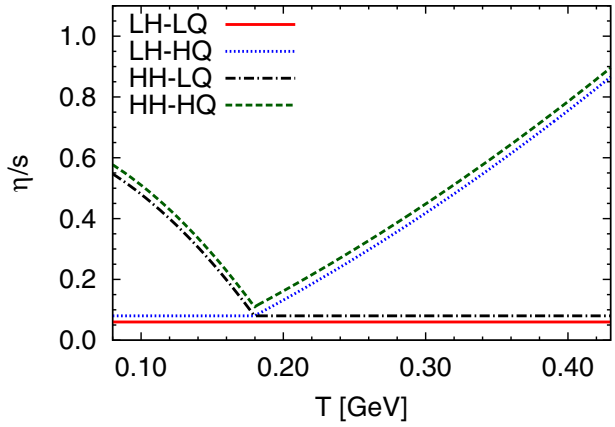

FIG. 1. (Color online) Different parametrizations of η_s/s as a function of temperature. The LH-LQ line has been shifted downward and the HH-HQ upward for better visibility.

increases according to

$$(\eta_s/s)(T)_{\rm QGP} = -0.289 + 0.288\,\frac{T}{T_{\rm tr}} + 0.0818\left(\frac{T}{T_{\rm tr}}\right)^2; \qquad (10)$$

(3) HH-LQ, in which, in the hadronic phase below $T_{\rm tr}$,

$$(\eta_s/s)(T)_{\rm HRG} = 0.681 - 0.0594\,\frac{T}{T_{\rm tr}} - 0.544\left(\frac{T}{T_{\rm tr}}\right)^2, \qquad (11)$$

while in the QGP-phase $(\eta_s/s)(T) = 0.08$; and

(4) HH-HQ, in which we use $(\eta_s/s)(T)_{\rm HRG}$ and $(\eta_s/s)(T)_{\rm QGP}$ for the hadronic and QGP phases, respectively.

Unless stated otherwise, the value of η_s/s at the transition temperature, $T_{\rm tr} = 180\,\text{MeV}$, is $(\eta_s/s)(T_{\rm tr}) = 0.08$. This is a close approximation to the lower bound conjectured in the framework of the AdS/CFT correspondence [5]. For all parametrizations the relaxation time for the shear-stress tensor is

$$\tau_\pi = 5\frac{\eta_s}{e+p}. \qquad (12)$$

For the sake of comparison, we also do the calculations using zero shear viscosity, i.e., for an ideal fluid.

C. The initial state

In this work we ignore the effects of event-by-event fluctuations [47,48], and we generalize a simple optical Glauber model [49] for a non-boost-invariant initial state. In different variants of the Glauber model the initial energy density in the transverse plane at midrapidity and at initial time τ_0 is given as a function of the density of binary collisions, $n_{\rm BC}(x,y,b)$, wounded nucleons, $n_{\rm WN}(x,y,b)$, or both:

$$e_T(\tau_0,x,y,b) = C_e(\tau_0)\, f(n_{\rm BC},n_{\rm WN}), \qquad (13)$$

where the normalization constant $C_e(\tau_0)$ is selected to reproduce the multiplicity measured in central collisions, and b is the impact parameter of the collision. In the following we use our BCfit parametrization [11,13], where the energy density depends solely on the number of binary collisions:

$$f_{\rm BC}(n_{\rm BC},n_{\rm WN}) = n_{\rm BC} + c_1 n_{\rm BC}^2 + c_2 n_{\rm BC}^3, \qquad (14)$$

and the coefficients c_1 and c_2 are chosen to reproduce the observed centrality dependence of multiplicity.

In the optical Glauber model, the density of binary collisions on the transverse plane is calculated from

$$n_{\rm BC}(x,y,b) = \sigma_{\rm NN} T_A(x+b/2,y)\, T_B(x-b/2,y), \qquad (15)$$

where $\sigma_{\rm NN}$ is the total nucleon-nucleon inelastic cross section, and $T_{A/B}$ is the nuclear thickness function. As a cross section we use $\sigma_{\rm NN} = 42$ mb at the RHIC [49,50] and $\sigma_{\rm NN} = 64$ mb at the LHC [51]. As usual, we define the thickness function as

$$T_A(x,y) = \int_{-\infty}^{\infty} dz\, \rho_A(x,y,z), \qquad (16)$$

where ρ_A is the Woods-Saxon nuclear density distribution,

$$\rho_A(\mathbf{r}) = \frac{\rho_0}{1+\exp[(r-R_A)/d]}, \qquad (17)$$

and $\rho_0 = 0.17$ fm^{-3} is the ground-state nuclear density and $d = 0.54$ fm is the surface thickness. The nuclear radii R_A are calculated from $R_A = 1.12A^{1/3} - 0.86/A^{1/3}$, which gives $R_{Au} \simeq 6.37$ fm and $R_{Pb} \simeq 6.49$ fm ($A_{Au} = 197$ and $A_{Pb} = 208$).

Unfortunately, there are very few theoretical constraints for the longitudinal structure of the initial state, since even the most sophisticated approaches to calculate the initial state from basic principles [52,53] are restricted to midrapidity. Here we follow the simple approaches shown in Refs. [54–56], and in a similar fashion we assume longitudinal scaling flow, $v_z = z/t$, i.e., $v_\eta = 0$, and a constant energy density distribution around midrapidity [57], followed by exponential tails in both backward and forward directions. We parametrize the longitudinal energy density distribution as

$$e_L(\eta) = \exp\left(-2c_\eta\sqrt{1+\frac{(|\eta|-\eta_0)^2}{2c_\eta\sigma_\eta^2}\Theta(|\eta|-\eta_0)} + 2c_\eta\right), \qquad (18)$$

where $\eta = \frac{1}{2}\ln[(t+z)/(t-z)]$ is the space-time rapidity, and $\Theta(x)$ is the Heaviside step function. Thus the normalized energy density distribution is

$$e(\tau_0,x,y,\eta,b) = e_T(\tau_0,x,y,b)\, e_L(\eta). \qquad (19)$$

We are aware that there are more sophisticated approaches in the literature [22,58–60], but since attempts to create more plausible longitudinal structures easily lead to a rapidity distribution of v_2 which strongly deviates from the observed one [54], we leave the detailed study of the longitudinal structures for a later work.

Due to entropy production in dissipative fluids, the different parametrizations of η_s/s lead to different entropy production and therefore different final multiplicity of hadrons. Because

most of the entropy is produced during the early stages of the expansion when the longitudinal gradients are largest [61], it is sufficient to adjust initial densities according to the entropy produced in the partonic phase. Further entropy production during the hadronic evolution turns out to represent only a small contribution in the final multiplicities and it is not corrected in our calculations.

At the RHIC, we used the following maximum energy densities, $e_0 = e(\tau_0,0,0,0)$:

(i) for an ideal fluid, $e_0 = 17.0$ GeV/fm^3,
(ii) for LH-LQ and HH-LQ, $e_0 = 15.8$ GeV/fm^3, and
(iii) for LH-HQ and HH-HQ, $e_0 = 14.9$ GeV/fm^3,

while at the LHC

(iv) for an ideal fluid, $e_0 = 57.5$ GeV/fm^3,
(v) for LH-LQ and HH-LQ, $e_0 = 54.5$ GeV/fm^3, and
(vi) for LH-HQ and HH-HQ, $e_0 = 49.5$ GeV/fm^3.

Note that these values are smaller than the ones given in Refs. [11,13]. The main reason for this is that we used different data to fit the centrality dependence, and we chose to fit the multiplicity as a function of centrality class, not as a function of number of participants, as was done in Refs. [11,13]. This leads to different values of c_1 and c_2 parameters, and, consequently, the maximum density in a head-on collision (which practically never happens) is different even if the energy density at midrapidity at impact parameters $b > 2$ fm is almost identical.

The parameters controlling the centrality dependence, c_1 and c_2 in Eq. (14), are $c_1 = -0.035$ fm^{-2} and $c_2 = 0.00034$ fm^{-4} at the RHIC and $c_1 = -0.02$ fm^{-2} and $c_2 = 0.000175$ fm^{-4} at the LHC. The parameters in Eq. (18) defining the longitudinal structure are $c_\eta = 4$ at the RHIC and $c_\eta = 2$ at the LHC, while $\eta_0 = 2.0$ for the constant-rapidity plateau for both. The width of the rapidity distribution is $\sigma_\eta = 1.0$ at the RHIC and $\sigma_\eta = 1.8$ at the LHC. The average impact parameters in each centrality class are given in Table I.

If not stated otherwise the fluid-dynamical evolution is started at $\tau_0 = 1$ fm/c proper time. The initial values for the transverse fluid velocity and shear-stress tensor are always set to zero. The value of the decoupling temperature or Knudsen number is indicated in the figures.

To obtain the final particle distributions we use the framework described in Ref. [62]. Thus we sample particle distributions to create "events" even if we are not doing event-by-event calculations, but we use conventional averaged initial states. The particle spectra and other measurables at the RHIC are obtained as an average over $N_{ev} = 100\,000$ events, where the sampling is done over $p_T = (0,5.4)$ GeV and $\eta_{\rm ch} = (-6.6,6.6)$ with $N_{p_T} = 36$ and $N_{\eta_{\rm ch}} = 22$ bins. At the LHC the particle multiplicity is $\simeq 2.5$ times larger than at the RHIC; hence we average over $N_{ev} = 40\,000$ events.

TABLE I. The average impact parameter b in each centrality class at the RHIC and the LHC.

Centrality (%)	RHIC b (fm)	LHC b (fm)
0–5	2.24	2.32
5–10	4.09	4.24
10–20	5.78	5.99
20–30	7.49	7.76
30–40	8.87	9.19
40–50	10.06	10.43

IV. RESULTS AND COMPARISONS TO DATA

A. Au + Au at $\sqrt{s_{\rm NN}} = 200$ GeV at the RHIC

We fix the parameters characterizing the initial state, Eqs. (13), (14), and (18), by comparison to the PHOBOS charged particle pseudorapidity distribution, $dN_{\rm ch}/d\eta_{\rm ch}$, at various centralities [63]. We present our results in Fig. 2, where the calculations are shown for 0%–5% centrality and for the average of 10%–20% and 20%–30% as well as 30%–40% and 40%–50% centralities. This is in order to facilitate a comparison to the data taken at 0%–6%, 15%–25%, and 35%–45% centralities. As required, the final multiplicity and pseudorapidity distribution are well reproduced at all centralities for all parametrizations of the temperature-dependent shear viscosity to entropy density ratio. Here we once again stress the importance of fixing the initial energy density to compensate for the entropy production for different η_s/s parametrizations. Otherwise, for fixed initial densities, the larger the effective viscosity, the larger the entropy production and thus the final multiplicity.

The kinetic freeze-out temperature, $T_{\rm dec}$, affects the charged particle pseudorapidity distribution very weakly. We have chosen $T_{\rm dec} = 100$ MeV by comparison to the pion, kaon, and proton p_T spectra measured by the PHENIX Collaboration [64], and we checked that, if we use $T_{\rm dec} = 140$ MeV, the pseudorapidity distributions are still within error bars and

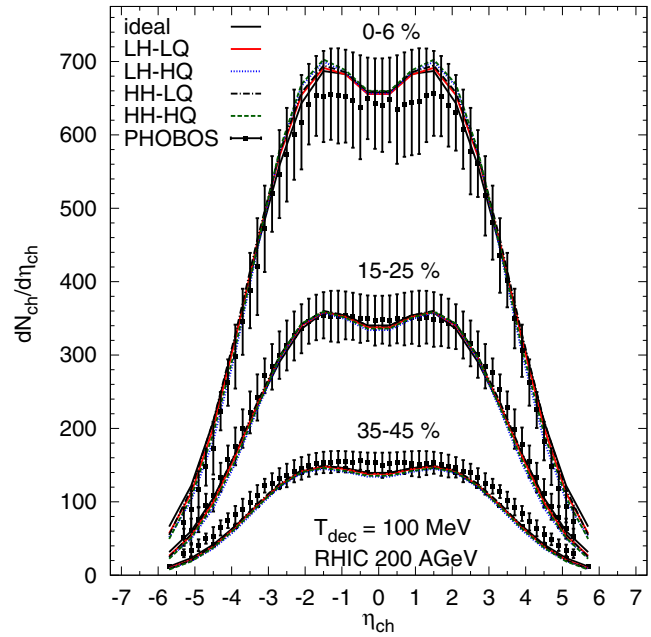

FIG. 2. (Color online) The charged particle pseudorapidity distribution $dN_{\rm ch}/d\eta_{\rm ch}$. Experimental data are from the PHOBOS Collaboration [63].

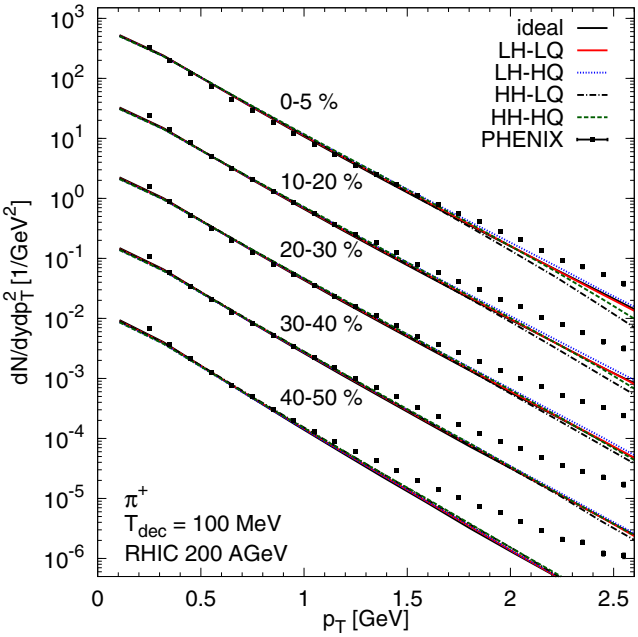

FIG. 3. (Color online) Transverse momentum spectra of positive pions at the RHIC. Experimental data are from the PHENIX Collaboration [64].

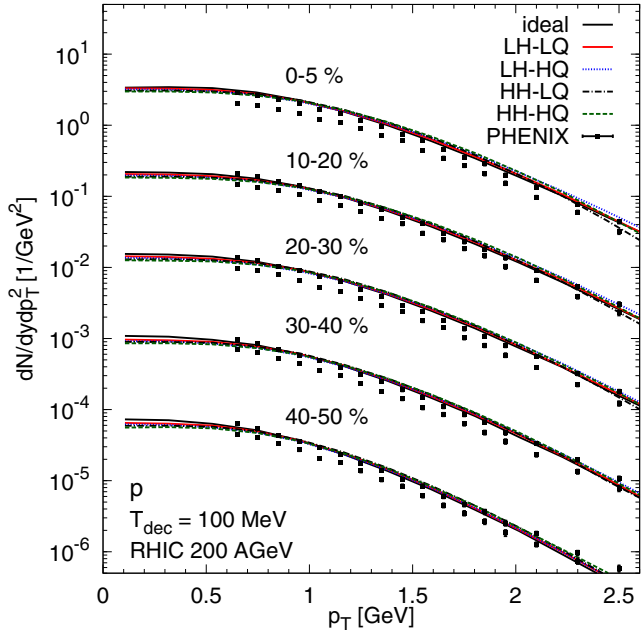

FIG. 5. (Color online) Transverse momentum spectra of protons at the RHIC. Experimental data for protons (upper) and antiprotons (lower) are from the PHENIX Collaboration [64].

that the change is on the same level as the differences due to different viscosities shown in Fig. 2. Such a weak dependence is not surprising: It is well known that, in a chemically frozen system, pion p_T distributions are weakly sensitive to the kinetic freeze-out temperature [65]. We now observe similar behavior in the longitudinal direction.

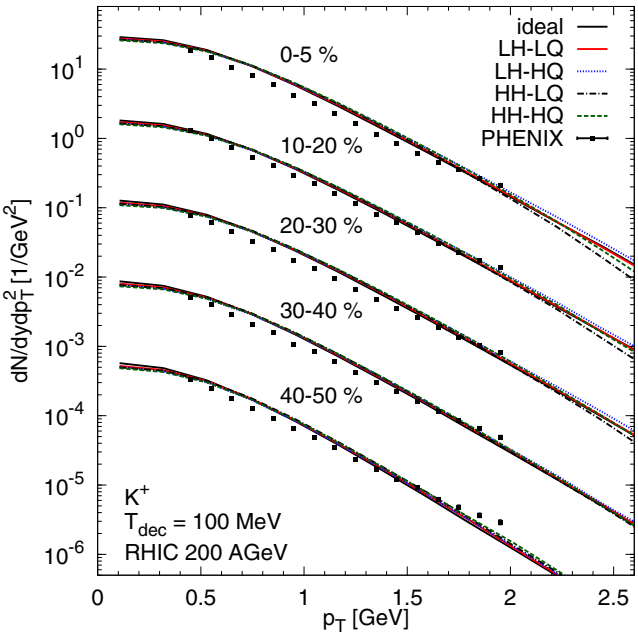

FIG. 4. (Color online) Transverse momentum spectra of positive kaons at the RHIC. Experimental data are from the PHENIX Collaboration [64].

In Figs. 3, 4, and 5 we present the p_T spectra of positive pions, kaons, and protons, respectively, corresponding to centrality classes, 0%–5%, 10%–20%($\times 10^{-1}$), 20%–30%($\times 10^{-2}$), 30%–40%($\times 10^{-3}$), and 40%–50%($\times 10^{-4}$). Here the multiplicative factors are applied (to both theoretical and experimental points) for better visibility. The experimental data are from the PHENIX Collaboration [64].

As seen before in viscous calculations (e.g., in Ref. [13]), the slopes of pion spectra are reasonably well reproduced up to $p_T \simeq 1.5$ GeV for semicentral collisions, but the agreement recedes with increasing impact parameter. The kaon yields are overpredicted at all centralities, whereas the fit to proton spectra is slightly better than the fit to kaons. Since we do not include a finite baryochemical potential in our calculation, we are consistently overestimating the yields of heavy particles, which might imply the need for even lower chemical freeze-out temperature.

The pion spectra become flatter with increasing freeze-out temperature; hence, for example, for $T_{\rm dec} = 140$ MeV the theoretical calculations are in a better agreement at larger momenta, but then we overestimate the spectra around $p_T \sim 1$ GeV. The slope of the proton spectra become steeper with increasing freeze-out temperature as well, and thus $T_{\rm dec} = 100$ MeV provides the best compromise.

As expected, after the initial densities are fixed to reproduce the yield, the slopes are practically unaffected by the different η_s/s parametrizations, and the corresponding δf_i in each case represents only a small correction compared to the thermal spectra.

In Figs. 6 and 7 the elliptic flow coefficient v_2 at various centralities is shown as a function of transverse momentum p_T and pseudorapidity $\eta_{\rm ch}$. In Fig. 6 the experimental data are from the STAR Collaboration [66], whereas in Fig. 7

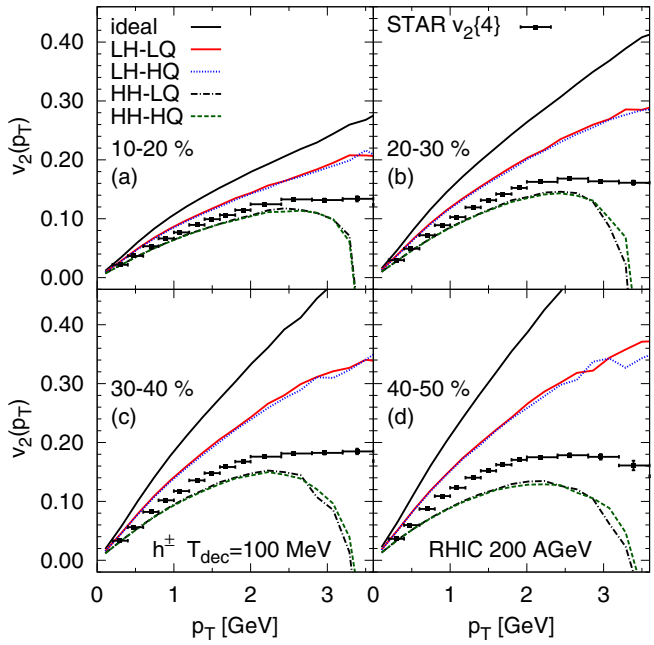

FIG. 6. (Color online) Charged hadron $v_2(p_T)$ at the RHIC. Experimental data are from the STAR Collaboration [66].

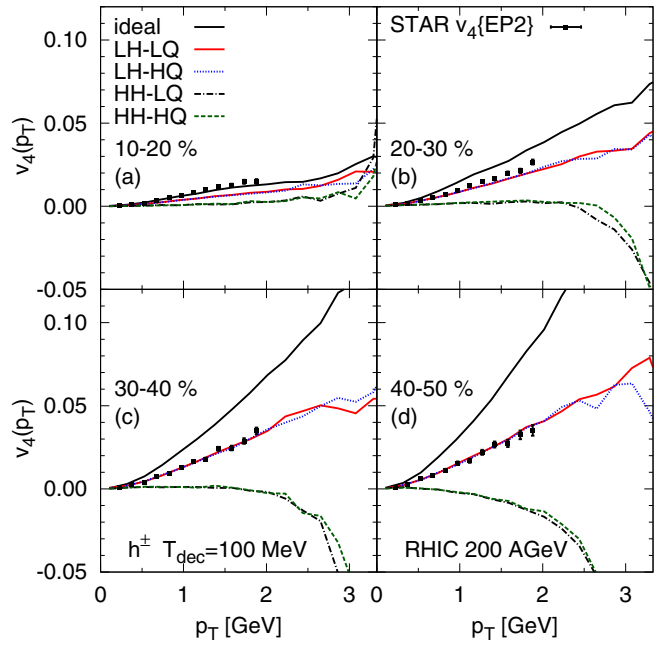

FIG. 8. (Color online) Charged hadron $v_4(p_T)$ at the RHIC. Experimental data are from the STAR Collaboration [68].

the average of 0%–5% and 10%–20% and of 10%–20% and 20%–30% events are compared to the data from the PHOBOS Collaboration for 3%–15% and 15%–25% centrality classes [67] and to the STAR Collaboration data in the 15%–25% centrality class [68].

As expected, the p_T differential elliptic flow coefficient shows the behavior reported in Refs. [11,13]: At the RHIC the elliptic flow coefficient is very sensitive to viscosity in the hadronic phase but independent of the high-temperature parametrization of the viscosity. The same observation also holds for the rapidity-dependent elliptic flow coefficient at all centrality classes. The dissipative reduction of v_2 is quite independent of rapidity, and thus we cannot reproduce the shape of $v_2(\eta_{\rm ch})$ very well. On the other hand, slightly larger hadronic viscosity would further reduce v_2, and our result would be very close to the ideal fluid + UrQMD hybrid calculation of Ref. [69].

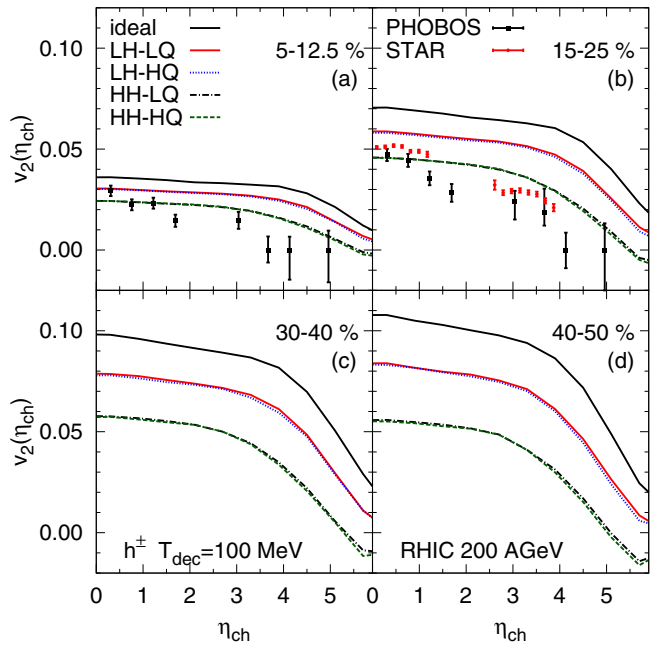

FIG. 7. (Color online) Charged hadron $v_2(\eta_{\rm ch})$ at the RHIC. Experimental data are from the PHOBOS [67] and STAR [68] Collaborations.

Similarly, the $v_4(p_T)$ and $v_4(\eta_{\rm ch})$ of charged hadrons in different centrality classes are compared to the experimental data from the STAR Collaboration [68] in Figs. 8 and 9. The v_4 coefficient, both as a function of transverse momentum and as a function of pseudorapidity, complies with the previously made observations about the elliptic flow coefficient. As we have reported earlier [12,13], v_4 is sensitive to viscosity at even later stages of the evolution than v_2, and a large hadronic viscosity is sufficient to turn $v_4(p_T)$ negative at quite low p_T. The comparison of Figs. 7 and 9 also shows the well-known fact that the larger the value of n, the stronger the viscous suppression of v_n [70,71]. Viscosity has only a weak effect on the shapes of $v_2(\eta_{\rm ch})$ and $v_4(\eta_{\rm ch})$, but quite interestingly the effect on the shapes is different for different coefficients: Increasing viscosity makes the (approximate) plateau in $v_2(\eta_{\rm ch})$ narrower but that in $v_4(\eta_{\rm ch})$ wider.

From Fig. 8 it is apparent that the $v_4(p_T)$ data favor the parametrizations with low hadronic viscosity, unlike $v_2(p_T)$. However, we have to remember that the experimental data were obtained by using different methods for v_2 and v_4, i.e., four-particle cumulant and mixed harmonic event-plane methods, whereas we use the event-plane method to evaluate all the harmonics. Another uncertainty is that event-by-event fluctuations cause a sizable fraction of v_4, but they are not included in our study. Thus we advise against drawing any

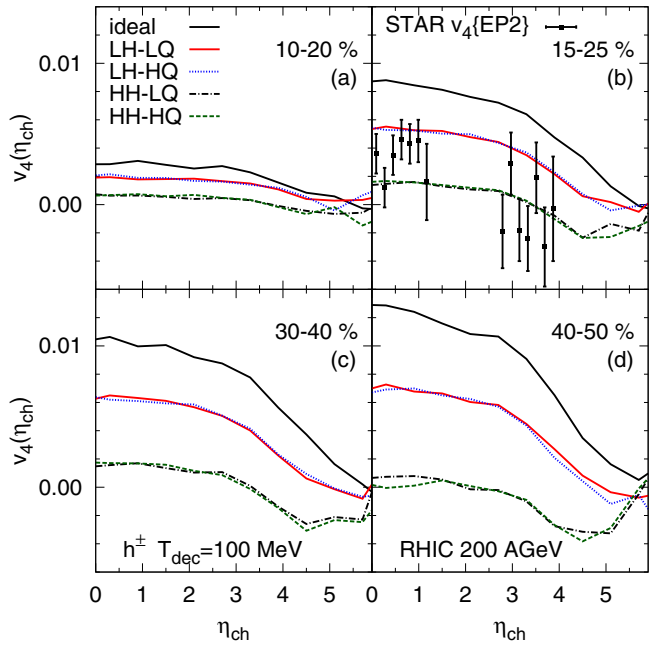

FIG. 9. (Color online) Charged hadron $v_4(\eta_{ch})$ at the RHIC. Experimental data are from the STAR Collaboration [68].

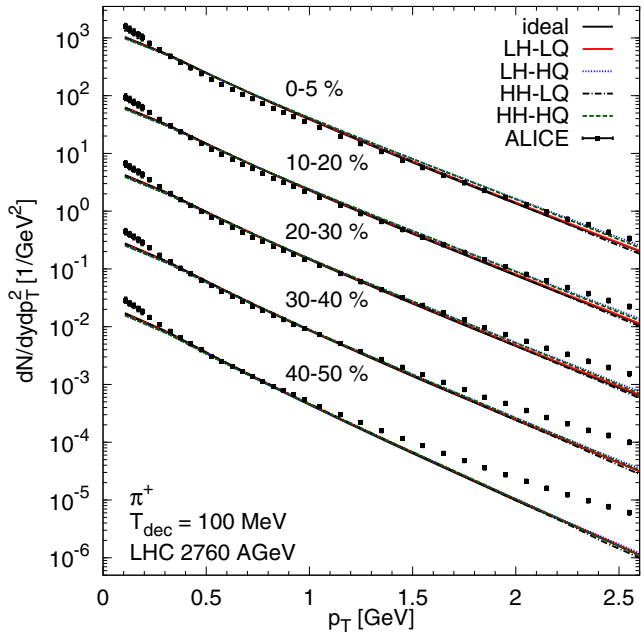

FIG. 11. (Color online) Transverse momentum spectra of positive pions at the LHC. Experimental data are from the ALICE Collaboration [73].

conclusions about the favored $(\eta_s/s)(T)$ from this particular result.

B. Pb + Pb at $\sqrt{s_{NN}} = 2760$ GeV at the LHC

As at the RHIC, we use the pseudorapidity distribution of charged particles to fix the initialization and the p_T distributions of identified particles to fix the kinetic freeze-out temperature.

In Fig. 10 the charged particle pseudorapidity distributions $dN_{ch}/d\eta_{ch}$ for different centrality bins are compared to the experimental data from the ALICE Collaboration [72]. The pseudorapidity distribution of charged particles reasonably matches the data for all centrality classes given in the figure. Similarly as for the RHIC we slightly overshoot the

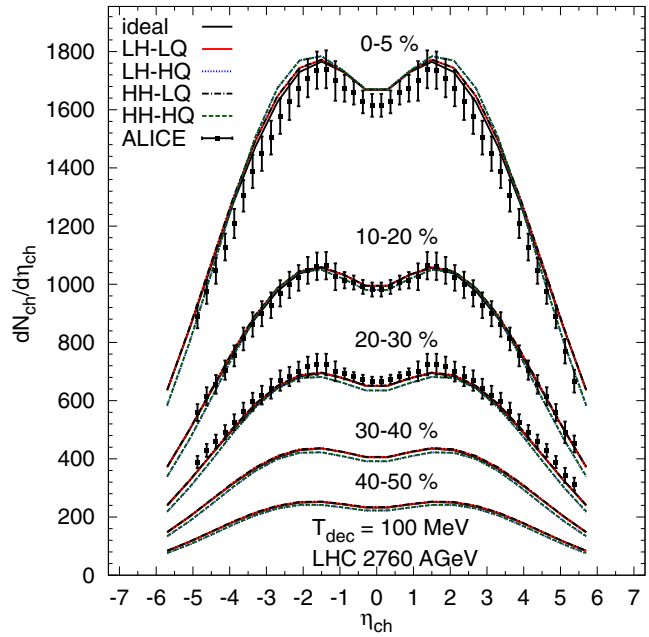

FIG. 10. (Color online) The charged particle pseudorapidity distribution $dN_{ch}/d\eta_{ch}$ at the LHC. Experimental data are from the ALICE Collaboration [72].

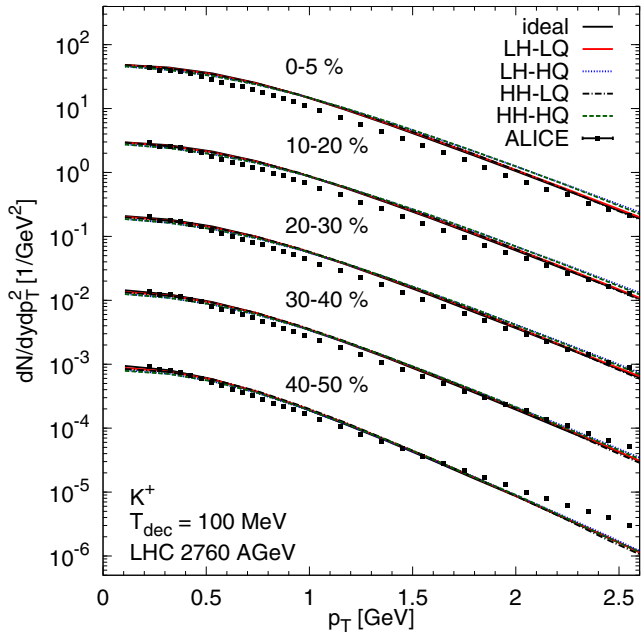

FIG. 12. (Color online) Transverse momentum spectra of positive kaons at the LHC. Experimental data are from the ALICE Collaboration [73].

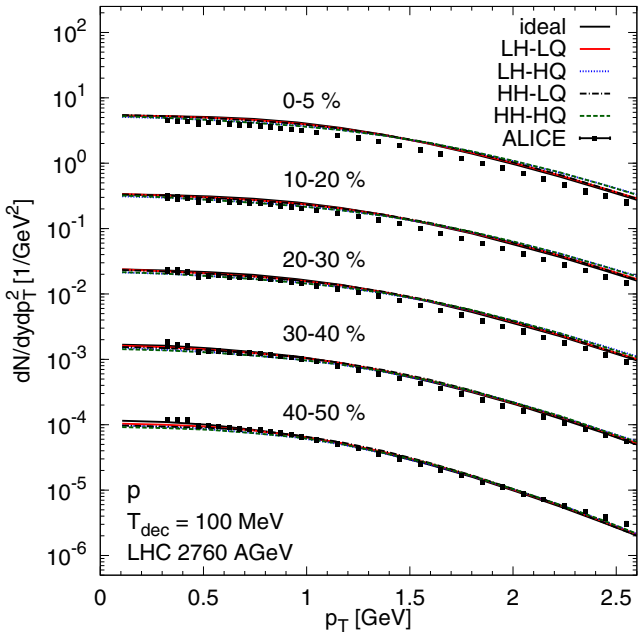

FIG. 13. (Color online) Transverse momentum spectra of protons at ALICE. Experimental data for protons and antiprotons are from the ALICE Collaboration [73].

experimental results at the LHC for the most central collisions while we undershoot for the peripheral ones. Moreover, as observed before, the pseudorapidity distributions of charged particles are insensitive to the chosen freeze-out temperature.

In Figs. 11, 12, and 13 we show the p_T spectra of positive pions, positive kaons, and protons corresponding to centrality classes, with multiplicative factors applied for

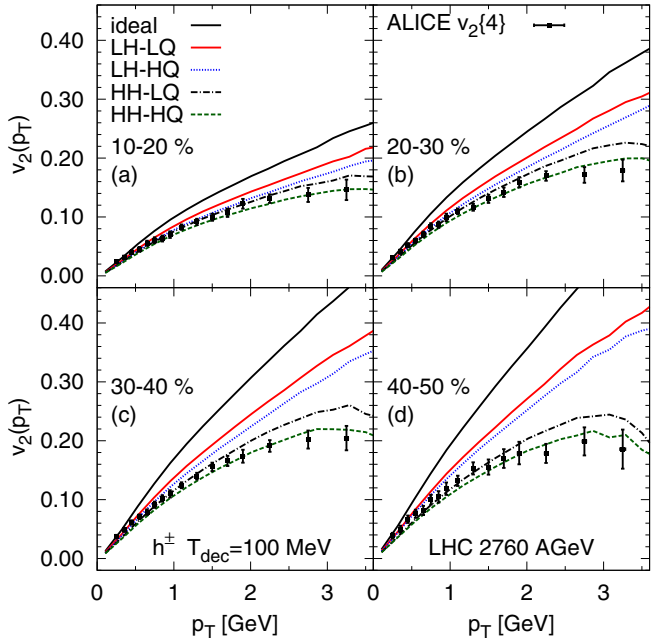

FIG. 14. (Color online) Charged hadron $v_2(p_T)$ at the LHC. Experimental data are from the ALICE Collaboration [75].

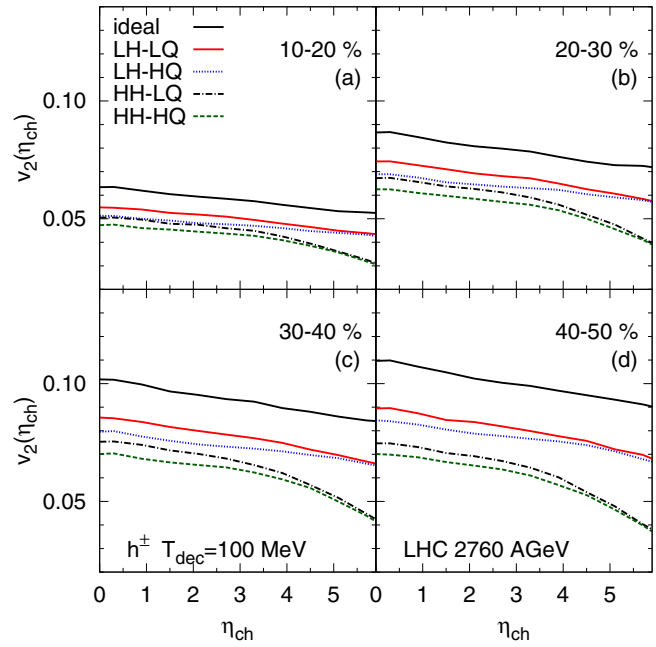

FIG. 15. (Color online) Charged hadron $v_2(\eta_{ch})$ at the LHC.

better visibility. The experimental data are from the ALICE Collaboration [73]. These distributions behave in a way similar to that of the RHIC results, and they are thus unaffected by the different η_s/s parametrizations. We note that, as in many other calculations [73,74], the low-p_T part of the pion distribution turned out to be very difficult to reproduce.

In Figs. 14 and 15 the elliptic flow coefficient v_2 is shown as functions of transverse momentum and pseudorapidity, respectively. In both figures the experimental data are from the ALICE Collaboration [75]. At the LHC viscous suppression

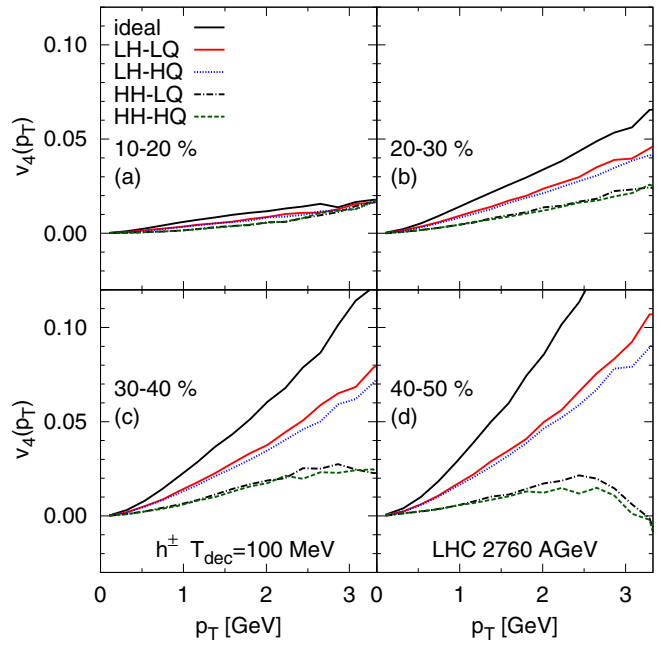

FIG. 16. (Color online) Charged hadron $v_4(p_T)$ at the LHC.

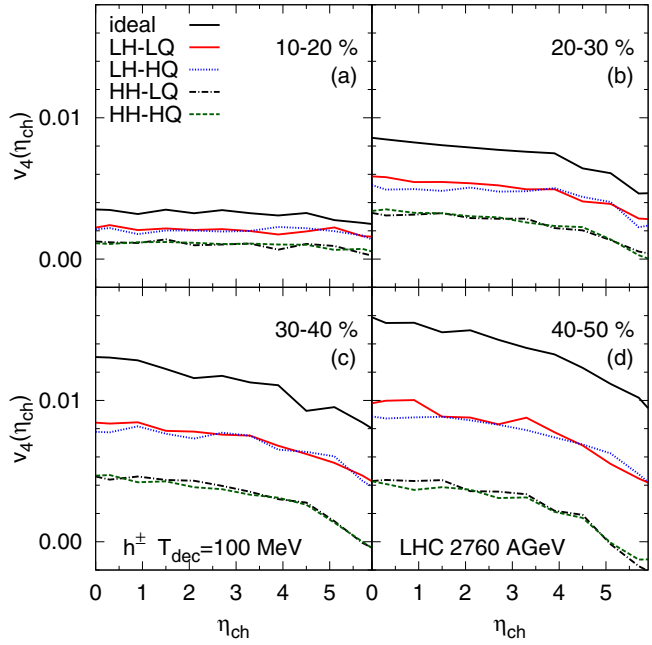

FIG. 17. (Color online) Charged hadron $v_4(\eta_{\rm ch})$ at the LHC.

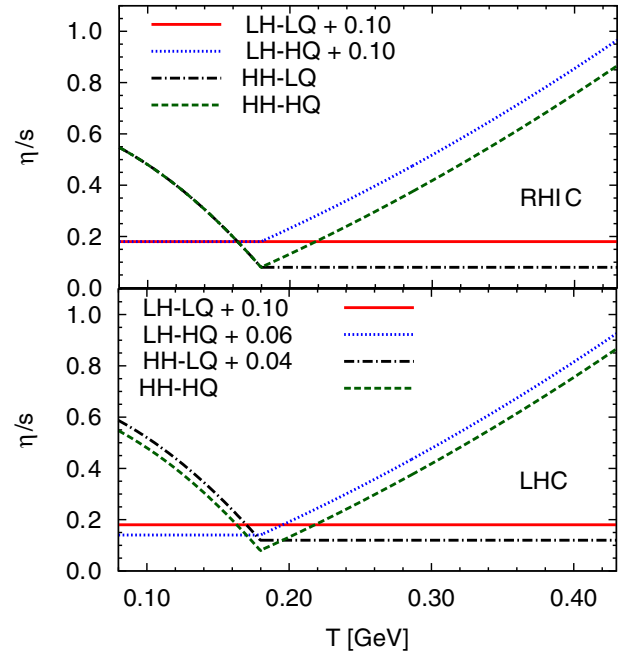

FIG. 18. (Color online) Parametrizations of $(\eta_s/s)(T)$ rescaled to lead to similar charged hadron $v_2(p_T)$ in central collisions at the RHIC (top) and the LHC (bottom).

of the elliptic flow is less dominated by the hadronic viscosity than at the RHIC. In central collisions at midrapidity, both QGP and hadronic viscosities affect v_2 equally: Large QGP viscosity may be compensated with a low hadronic viscosity and vice versa (compare LH-HQ with HH-LQ for 10%–20% and 20%–30% up to $p_T \leqslant 2$ GeV or $\eta_{\rm ch} \leqslant 2$). In peripheral collisions and at large rapidities, v_2 loses its sensitivity to QGP viscosity, and the system behaves like at the RHIC. Thus measuring v_2 at large rapidities at the LHC would provide an additional handle on the temperature dependence of the η_s/s ratio.

Finally, in Figs. 16 and 17 we present the v_4 coefficients as functions of p_T and $\eta_{\rm ch}$. As discussed in Refs. [12,13], v_4 is sensitive to viscosity at lower temperatures than is v_2. Therefore the behavior of v_4 at the LHC is similar to the behavior of v_4 and v_2 at the RHIC: The curves are grouped according to their hadronic viscosity, and they show no sensitivity to QGP viscosity. The suppression of v_4 at both the LHC and the RHIC is clearly sensitive to the hadronic viscosity (compare Fig. 8 with Fig. 16 and Fig. 9 with 17) and to the minimum value of η_s/s.

V. THE DISTINGUISHABILITY OF THE η_s/s PARAMETRIZATIONS

In the previous section we described how the sensitivity of v_2 and v_4 to QGP and hadronic shear viscosities depends on centrality, transverse momentum p_T, and pseudorapidity $\eta_{\rm ch}$. Now we use this observation to distinguish between different parametrizations of $(\eta_s/s)(T)$. We rescale our existing parametrizations in such a way that they all lead to almost identical p_T differential v_2 in central collisions, and we check whether the calculated v_2 and v_4 differ at other centralities and rapidities. Note that this procedure also tests the sensitivity of the flow coefficients to the minimum value of η_s/s and not only to its values above and below the transition temperature.

The new scaled parametrizations are shown in Fig. 18. At RHIC energies the value of the viscosity to entropy ratio for LH-LQ and LH-HQ is increased uniformly with $\Delta\eta_s/s = 0.1$ for all temperatures, while the other two parametrizations remain unchanged. Since the sensitivity to the temperature dependence of η_s/s is more complicated at the LHC, the required changes in parametrizations are $\Delta\eta_s/s = 0.1$ for LH-LQ, $\Delta\eta_s/s = 0.06$ for LH-HQ, and $\Delta\eta_s/s = 0.04$ for HH-LQ. The increase in η_s/s leads to larger entropy production, and thus to larger final multiplicities, which we have counteracted by rescaling the initial densities accordingly.

Note that since the LH-HQ and HH-LQ parametrizations require different rescalings at the RHIC and the LHC, they can be distinguished already by comparing $v_2(p_T)$ in central collisions at different energies, but LH-LQ and HH-HQ cannot. Furthermore, we want to check whether it is possible to distinguish LH-HQ and HH-LQ in collisions at the same energy by varying the centrality and rapidity.

In Figs. 19, 20, and 21 we present $v_2(p_T)$, $v_2(\eta_{\rm ch})$, and $v_4(p_T)$ at the RHIC using these new parametrizations. As required, in central collisions all parametrizations lead to similar $v_2(p_T)$—the differences due to different hadronic viscosity at very late stages of the evolution are compensated by the larger viscosity at and after the QCD transition region. However, when one moves to larger centralities, and thus to smaller systems, the region where v_2 is most sensitive to shear viscosity moves toward lower temperatures, and the parametrizations with different hadronic viscosities can be identified (see Fig. 19). The same, although weaker, phenomenon happens when we move to larger rapidities (see

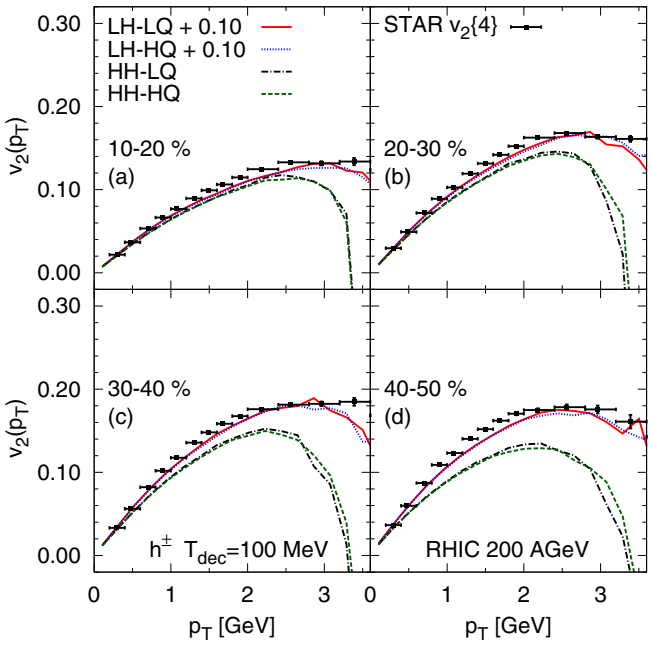

FIG. 19. (Color online) Charged hadron $v_2(p_T)$ at the RHIC. Experimental data are from the STAR Collaboration [66].

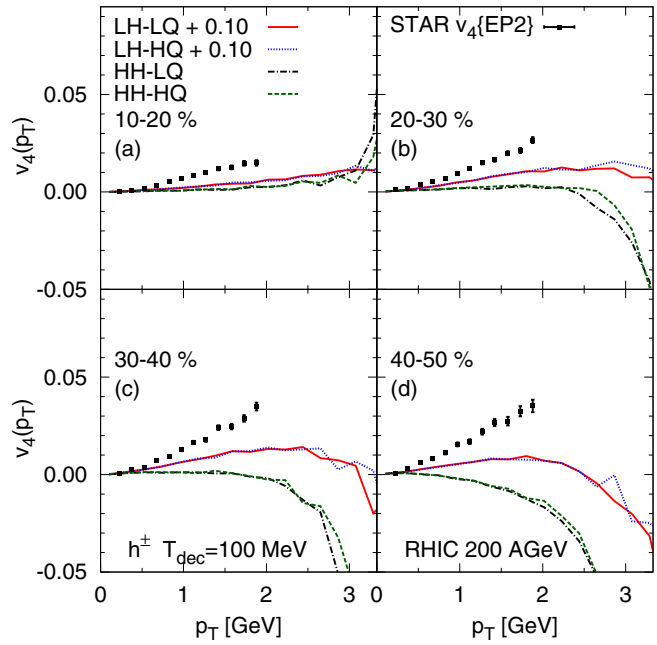

FIG. 21. (Color online) Charged hadron $v_4(p_T)$ at the RHIC. Experimental data are from the STAR Collaboration [68].

Fig. 20). Most of the sensitivity comes from the change in centrality, but, as seen in the 15%–25% centrality class [Fig. 20(b)], the difference at large rapidities increases faster than at midrapidity. On the other hand, the v_4 coefficient shows larger sensitivity than v_2: In central collisions all parametrizations are equal, but the difference increases with increasing fraction of cross section faster than for v_2. Note that none of the observables are sensitive to the plasma viscosity, but we have to study the collisions at the LHC to be able to distinguish, say, HH-LQ and HH-HQ parametrizations.

At the LHC we see slightly different behavior. In central collisions $v_2(p_T)$ is again the same for all parametrizations by construction, but the differences appear slowly and stay modest when we move toward more peripheral collisions (see Fig. 22). Again, in more peripheral collisions, the system is most sensitive to viscosity in lower temperatures, and $v_2(p_T)$ curves are

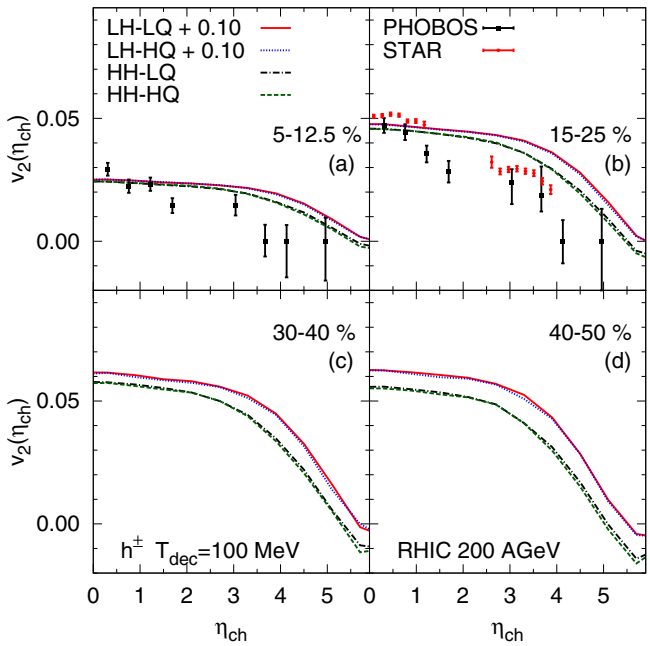

FIG. 20. (Color online) Charged hadron $v_2(\eta_{ch})$ at the RHIC. Experimental data are from the PHOBOS [67] and STAR [68] Collaborations.

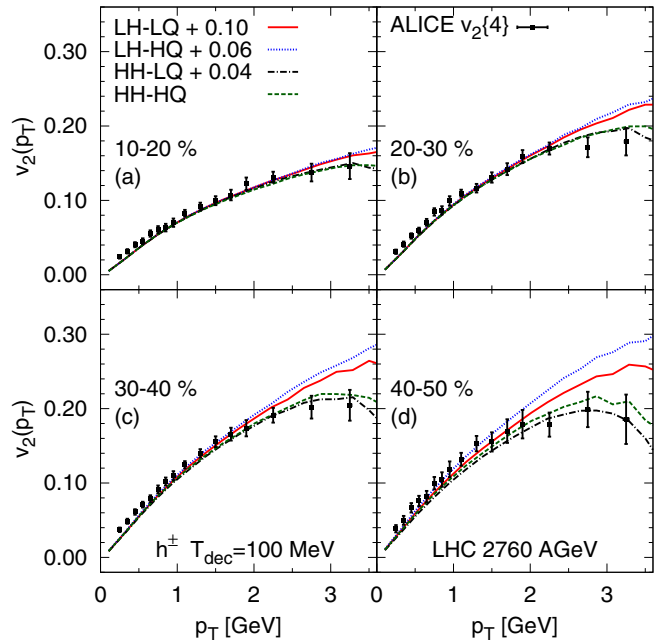

FIG. 22. (Color online) Charged hadron $v_2(p_T)$ at the LHC. Experimental data are from the ALICE Collaboration [75].

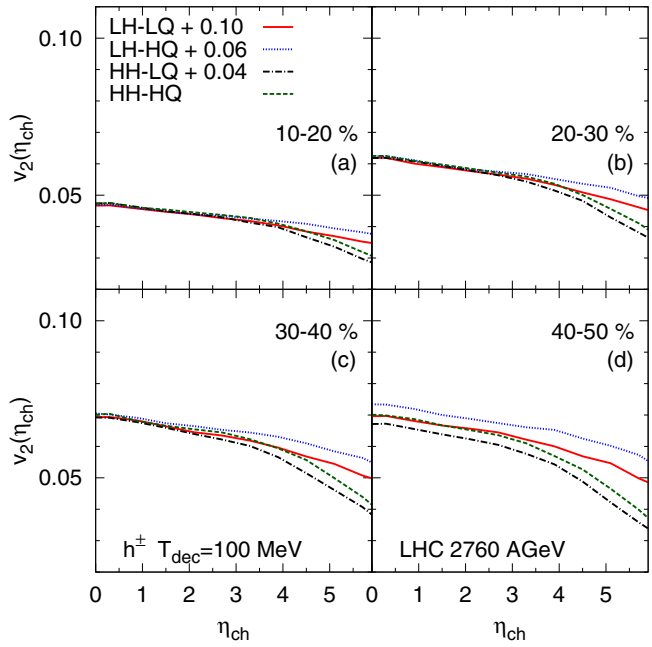

FIG. 23. (Color online) Charged hadron $v_2(\eta_{\rm ch})$ at the LHC.

ordered according to hadronic viscosity—the larger viscosity is at freeze-out, the lower is $v_2(p_T)$. In Fig. 15 the pseudorapidity distribution of v_2 showed clear sensitivity to shear viscosity. In that figure different parametrizations caused different v_2 already at midrapidity in central collisions. Now viscosity is scaled to remove this difference, and the sensitivity of the shape of $v_2(\eta_{\rm ch})$ to the viscosity is more visible. As one can see from Fig. 23, larger hadronic viscosity causes $v_2(\eta_{\rm ch})$ to drop slightly faster with increasing rapidity. The strongest difference is seen in $v_4(p_T)$, which is able to distinguish the new parametrizations at the LHC (see Fig. 24), but its resolving power at the LHC is weaker than at the RHIC (Fig. 21). Thus we conclude that differential measurements of the flow anisotropies as function of transverse momentum, pseudorapidity, and centrality can provide constraints for the temperature dependence of η_s/s, but the measurements at various energies are essential to constrain the parametrizations properly.

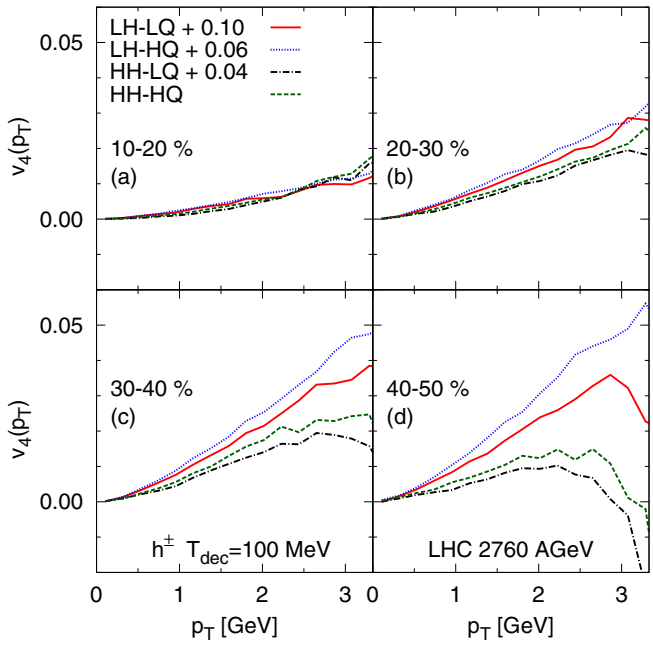

FIG. 24. (Color online) Charged hadron $v_4(p_T)$ at the LHC.

VI. DYNAMICAL FREEZE-OUT

To test the sensitivity of our results to the freeze-out criterion and the freeze-out description in general, we redo some of the calculations using the dynamical freeze-out criterion [38]. In these calculations we use only our HH-LQ and HH-HQ parametrizations for the shear viscosity, since the low value of η_s/s in a hadron gas leads to a very slowly increasing relaxation time and thus to unrealistically low temperatures, $\langle T\rangle \ll 80$ MeV, on the freeze-out surface when $\mathrm{Kn}_{\rm dec} \sim 1$. Since the Knudsen number can be based on many quantities [14], and since we do not know when exactly the hydrodynamical description should break down, we use the freeze-out Knudsen number as a free parameter chosen to fit the rapidity and p_T distributions.

Figures 25 and 26 show the charged particle pseudorapidity distributions at the RHIC and the LHC, respectively. As expected, the pseudorapidity distributions are only weakly dependent on the precise value of $\mathrm{Kn}_{\rm dec}$, but it turned out that our choice of Knudsen number and relaxation time lead to weak sensitivity of the p_T distributions to the value of $\mathrm{Kn}_{\rm dec}$ too. Nevertheless, we found that decoupling at constant Knudsen number $\mathrm{Kn}_{\rm dec} = 0.8$ leads to basically the same rapidity and p_T distributions as conventional decoupling at $T_{\rm dec} = 100$ MeV.

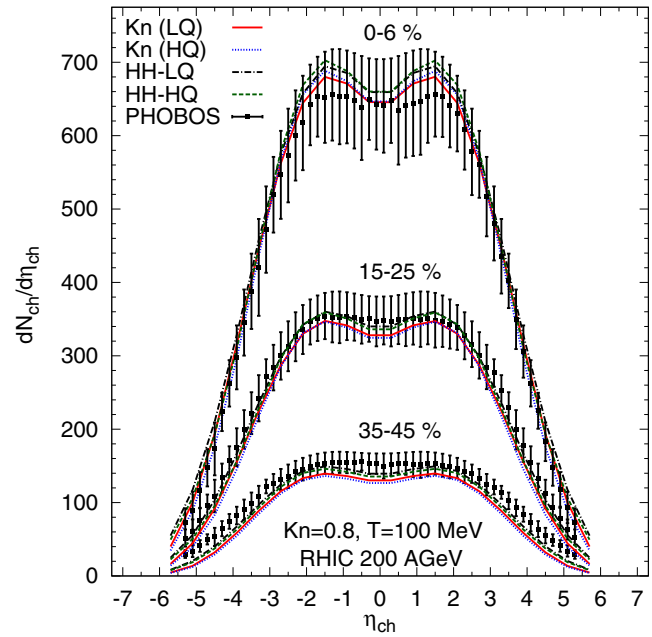

FIG. 25. (Color online) The charged particle pseudorapidity distribution $dN_{\rm ch}/d\eta_{\rm ch}$ at the RHIC obtained by using two different freeze-out criteria. Experimental data are from the PHOBOS Collaboration [63].

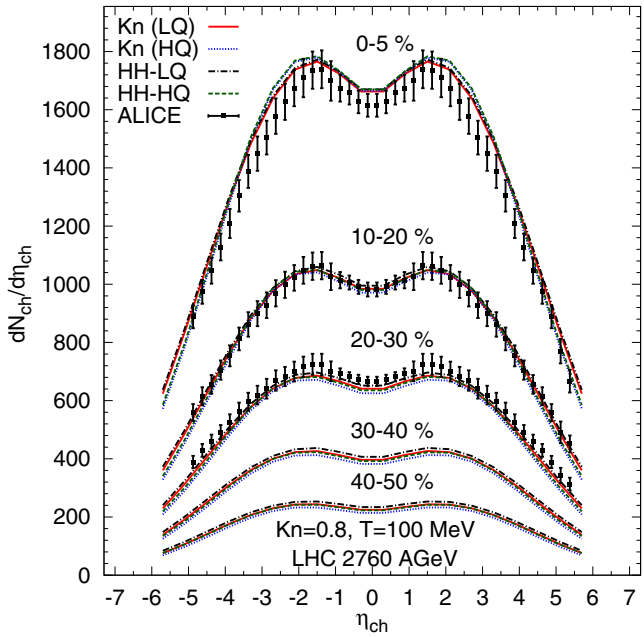

FIG. 26. (Color online) The charged particle pseudorapidity distribution $dN_{\rm ch}/d\eta_{\rm ch}$ at the LHC obtained by using two different freeze-out criteria. Experimental data are from the ALICE Collaboration [72].

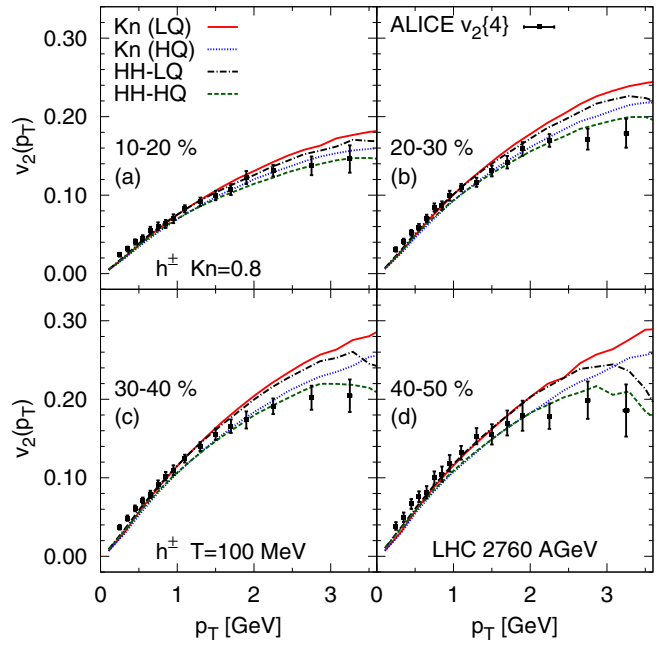

FIG. 28. (Color online) Charged hadron $v_2(p_T)$ at the LHC obtained by using two different freeze-out criteria. Experimental data are from the ALICE Collaboration [75].

The p_T differential v_2 of charged hadrons at the RHIC and the LHC is shown in Figs. 27 and 28, respectively. Unlike in Ref. [16], where both p_T distributions and anisotropies depended on the freeze-out criterion, we see that, once the freeze-out parameters are fixed to produce similar p_T distributions, the anisotropies become very similar. This is especially clear at the LHC. Below $p_T \sim 2$ GeV both criteria lead to identical $v_2(p_T)$, and the difference seen in the plots is due to the shear viscosity parametrization. At the RHIC both parametrizations lead to identical $v_2(p_T)$, and a weak sensitivity to the freeze-out criterion appears around $p_T \sim 1$ GeV. However, this sensitivity is too weak to be significant.

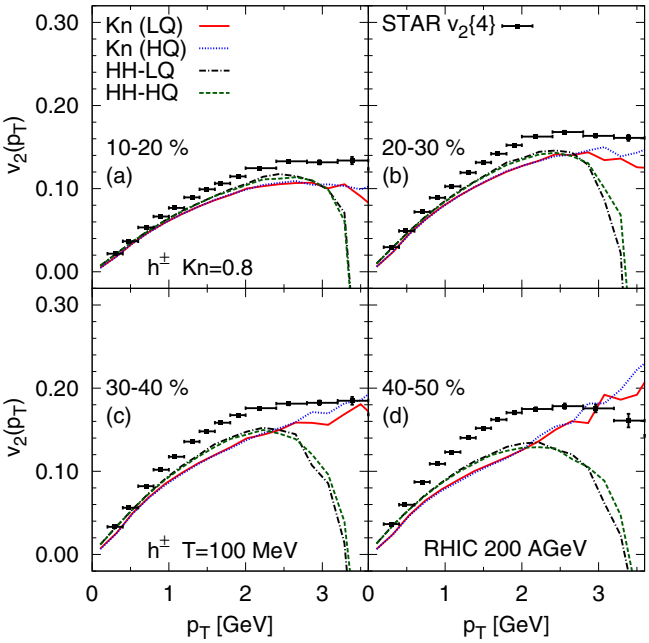

FIG. 27. (Color online) Charged hadron $v_2(p_T)$ at the RHIC obtained by using two different freeze-out criteria. Experimental data are from the STAR Collaboration [66].

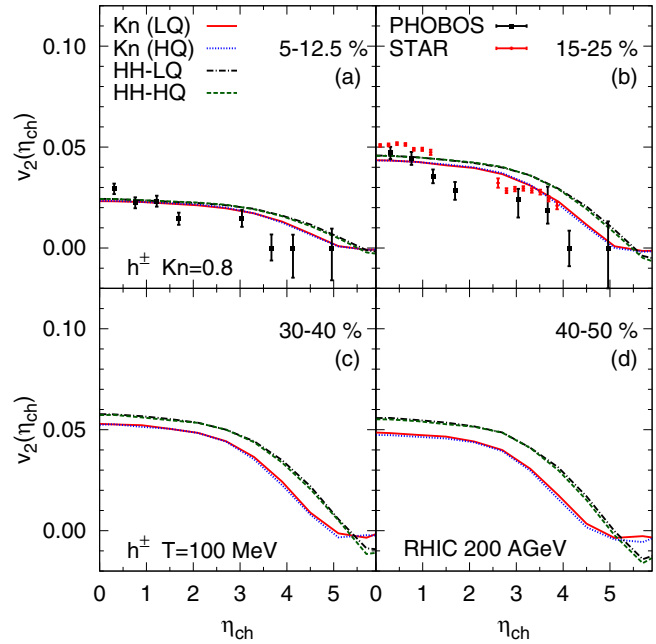

FIG. 29. (Color online) Charged hadron $v_2(\eta_{\rm ch})$ at the RHIC obtained by using two different freeze-out criteria. Experimental data are from the STAR Collaboration [66].

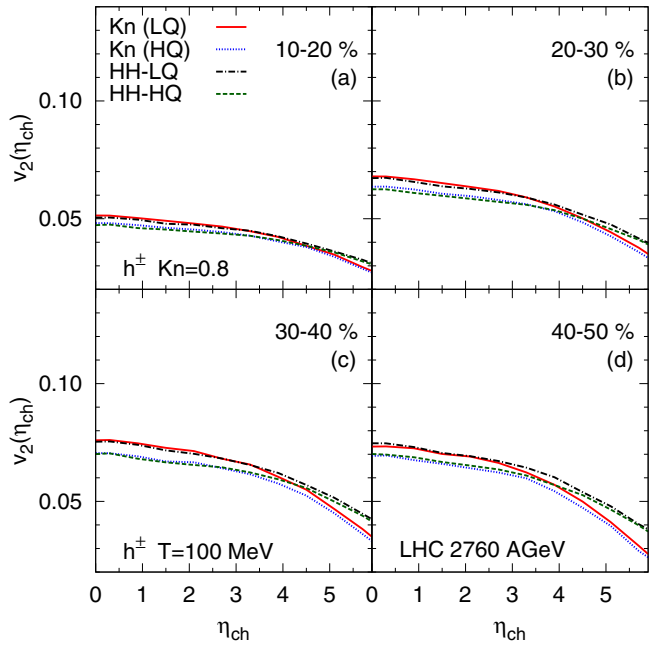

FIG. 30. (Color online) Charged hadron $v_2(\eta_{\rm ch})$ at the LHC obtained by using two different freeze-out criteria. Experimental data are from the ALICE Collaboration [75].

As a function of pseudorapidity v_2 shows more sensitivity to the freeze-out criterion (see Figs. 29 and 30). At both the RHIC and the LHC $v_2(\eta_{\rm ch})$ drops faster with increasing rapidity, when the dynamical freeze-out criterion is used. Also, with both freeze-out criteria the sensitivity to plasma viscosity disappears at large rapidities even at the LHC. This is again a manifestation of previously seen behavior: At large rapidities at the LHC, the system behaves like the system at the RHIC.

The rather weak dependence of anisotropies on the decoupling criterion means that at midrapidity fluid dynamical results are surprisingly robust against variations in the decoupling procedure. As well, this gives a reason to expect that the hybrid model results are sensitive only to the value of the switching criterion from fluid to cascade, not to the criterion itself. Since the fluid-dynamical results concerning the viscosity of the QGP are based on the analysis of anisotropies at midrapidity, this means that those results are not compromised by the freeze-out criterion. On the other hand, the sensitivity to the freeze-out description at high rapidities indicates that at lower collision energies the fluid-dynamical results may be sensitive to the freeze-out criterion even at midrapidity. Thus one has to pay extra attention to the freeze-out description of the collisions at $\sqrt{s_{\rm NN}} = 3$–9 GeV in the future Facility for Antiproton and Ion Research (FAIR) and Nuclotron-based Ion Collider Facility (NICA).

VII. CONCLUSIONS

We have studied the effects of temperature-dependent η_s/s on the azimuthal anisotropies of hadron transverse momentum spectra using genuinely (3+1)-dimensional viscous hydrodynamics. We have extended our previous studies [11,13] to backward and forward rapidities and explored the resolving power of differential measurements of v_2 and v_4 to distinguish between different parametrizations of $(\eta_s/s)(T)$.

In close to central collisions at the LHC energy, $\sqrt{s_{\rm NN}} = 2.76$ TeV, viscous suppression of elliptic flow at midrapidity is affected by both hadronic and QGP viscosities, but when one moves toward backward and forward rapidities, hadronic viscosity becomes more and more dominant—the system becomes effectively smaller and begins to behave like in collisions at the RHIC, $\sqrt{s_{\rm NN}} = 200$ GeV. Therefore, with large hadronic viscosity, v_2 tends to drop slightly faster with increasing rapidity, the effect being stronger in peripheral collisions. At both energies and at all rapidities v_4 is mostly suppressed by hadronic viscosity, but if we simultaneously change the minimum value of η_s/s, hadronic, and QGP viscosities, it is difficult to predict which coefficient at which collision energy is most sensitive to the changes. Nevertheless, the differential measurements of v_n as functions of transverse momentum, rapidity, centrality, and collision energy provide a way to distinguish different parametrizations of $(\eta_s/s)(T)$ and thus constrain the temperature dependence of the η_s/s ratio.

We also studied how sensitive our results are to the freeze-out criterion, and we found that, once the freeze-out parameters are fixed to reproduce p_T distributions, both decoupling at constant temperature and at constant Knudsen number lead to very similar anisotropies at midrapidity. Toward the large rapidities, v_2 tends to drop faster with the dynamical freeze-out criterion. This indicates that uncertainties in the decoupling description do not affect the present fluid-dynamical results regarding the anisotropies, but at lower collision energies the results may be more sensitive to the freeze-out criterion.

ACKNOWLEDGMENTS

This work was supported by the Helmholtz International Center for FAIR within the framework of the LOEWE program launched by the State of Hesse. The work of H. Niemi was supported by Academy of Finland Project No. 133005, the work of P. Huovinen by BMBF under Contract No. 06FY9092, and the work of H. Holopainen by the ExtreMe Matter Institute (EMMI). E. Molnár was partially supported by the European Union and the European Social Fund through project Supercomputer, the national virtual laboratory (Grant No. TAMOP-4.2.2.C-11/1/KONV-2012-0010), as well as by TAMOP 4.2.4.A/2-11-1-2012-0001 National Excellence Program (A2-MZPDÖ-13-0042).

APPENDIX A: EQUATIONS IN 3+1 DIMENSIONS

In the following, the components of four-vectors and tensors of rank-2 in four-dimensional space-time are denoted by Greek indices that take values from 0 to 3 while Roman indices range from 1 to 3. If not stated otherwise the Einstein summation convention for both Greek and Roman indices is implied.

First we recall the definitions of the covariant derivative of contravariant four-vectors and tensors of rank-2:

$$A^{\mu}_{;\alpha} = \partial_\alpha A^\mu + \Gamma^\mu_{\alpha\beta} A^\beta, \tag{A1}$$

$$A^{\mu\nu}_{;\alpha} = \partial_\alpha A^{\mu\nu} + \Gamma^\mu_{\alpha\beta} A^{\beta\nu} + \Gamma^\nu_{\alpha\beta} A^{\mu\beta}, \tag{A2}$$

where $\Gamma^\mu_{\alpha\beta} \equiv \Gamma^\mu_{\beta\alpha} = \frac{1}{2} g^{\mu\nu}(\partial_\beta g_{\alpha\nu} + \partial_\alpha g_{\nu\beta} - \partial_\nu g_{\alpha\beta})$ denotes the Christoffel symbol of the second kind and $\partial_\alpha = \partial/\partial x^\alpha$ denotes the four-derivative. For scalar quantities the covariant derivative reduces to the ordinary four-derivative, i.e., $(A^\mu A_\mu)_{;\alpha} = \partial_\alpha (A^\mu A_\mu)$.

Applying the definition of the transverse projection operator $\Delta^{\mu\nu} = g^{\mu\nu} - u^\mu u^\nu$ we can decompose the covariant derivative as the sum of the covariant time derivative D and spatial gradient ∇_α,

$$D A^{\mu_1 \cdots \mu_n} = u^\beta A^{\mu_1 \cdots \mu_n}_{;\beta}, \tag{A3}$$

$$\nabla_\alpha A^{\mu_1 \cdots \mu_n} = \Delta^\beta_\alpha A^{\mu_1 \cdots \mu_n}_{;\beta}; \tag{A4}$$

hence $A^{\mu_1 \cdots \mu_n}_{;\alpha} = u_\alpha D A^{\mu_1 \cdots \mu_n} + \nabla_\alpha A^{\mu_1 \cdots \mu_n}$, while for later use we also introduce the comoving or convective time derivative

$$d A^{\mu_1 \cdots \mu_n} = u^\beta \partial_\beta A^{\mu_1 \cdots \mu_n}. \tag{A5}$$

In the following, we summarize the equations of relativistic dissipative fluid dynamics in hyperbolic coordinates [i.e., (τ, x, y, η) coordinates] [57], where $\tau = (t^2 - z^2)^{-1/2}$ is the longitudinal proper time and $\eta = 1/2 \ln[(t+z)/(t-z)]$ is the space-time rapidity. The proper metric tensors are $g^{\mu\nu} = \mathrm{diag}(1, -1, -1, -\tau^{-2})$ and $g_{\mu\nu} = \mathrm{diag}(1, -1, -1, -\tau^2)$. Thus the only nonvanishing Christoffel symbols are $\Gamma^\eta_{\eta\tau} \equiv \Gamma^\eta_{\tau\eta} = \tau^{-1}$ and $\Gamma^\tau_{\eta\eta} = \tau$, and the gradient is $\partial_\mu = (\partial_\tau, \partial_x, \partial_y, \partial_\eta)$ while $\partial^\mu \equiv g^{\mu\nu}\partial_\nu = (\partial_\tau, -\partial_x, -\partial_y, -\tau^{-2}\partial_\eta)$. The inverse transformations to Minkowski coordinates with $g^{\mu\nu}_M \equiv \eta^{\mu\nu} = \mathrm{diag}(1, -1, -1, -1)$ are $t = \tau \cosh\eta$ and $z = \tau \sinh\eta$. Note that the hyperbolic coordinates are similar to the Milne coordinates that are spherically symmetric, i.e., $r \equiv \sqrt{x^2 + y^2 + z^2} = \tau \sinh\eta$.

The contravariant flow velocity is

$$u^\mu = \gamma(1, v_x, v_y, v_\eta); \tag{A6}$$

hence the covariant flow velocity is $u_\mu \equiv g_{\mu\nu} u^\nu = \gamma(1, -v_x, -v_y, -\tau^2 v_\eta)$, where the normalization condition $u^\mu u_\nu = 1$ leads to $\gamma = (1 - v_x^2 - v_y^2 - \tau^2 v_\eta^2)^{-1/2}$ as well as to $u^\mu u_{\mu;\nu} \equiv u_\mu u^\mu_{;\nu} = 0$.

The energy-momentum conservation equation in general coordinates is

$$T^{\mu\nu}_{;\mu} \equiv \frac{1}{\sqrt{g}} \partial_\mu (\sqrt{g}\, T^{\mu\nu}) + \Gamma^\nu_{\mu\beta} T^{\mu\beta} = 0, \tag{A7}$$

where $g \equiv -\det(g_{\mu\nu})$ is the negative determinant of the metric tensor, which in hyperbolic coordinates leads to $g = \tau^2$.

Henceforth the energy conservation equation leads to

$$\begin{aligned} &\partial_\tau T^{\tau\tau} + \partial_x(v_x T^{\tau\tau}) + \partial_y(v_y T^{\tau\tau}) + \partial_\eta(v_\eta T^{\tau\tau}) \\ &\quad = -\partial_x(v_x P - v_x \pi^{\tau\tau} + \pi^{\tau x}) - \partial_y(v_y P - v_y \pi^{\tau\tau} + \pi^{\tau y}) \\ &\qquad -\partial_\eta(v_\eta P - v_\eta \pi^{\tau\tau} + \pi^{\tau\eta}) - \frac{1}{\tau}(T^{\tau\tau} + \tau^2 T^{\eta\eta}), \end{aligned} \tag{A8}$$

while the momentum-conservation equation leads to

$$\begin{aligned} &\partial_\tau T^{\tau x} + \partial_x(v_x T^{\tau x}) + \partial_y(v_y T^{\tau x}) + \partial_\eta(v_\eta T^{\tau x}) \\ &\quad = -\partial_x(P - v_x \pi^{\tau x} + \pi^{xx}) - \partial_y(-v_y \pi^{\tau x} + \pi^{xy}) \\ &\qquad -\partial_\eta(-v_\eta \pi^{\tau x} + \pi^{x\eta}) - \frac{1}{\tau} T^{\tau x}, \end{aligned} \tag{A9}$$

$$\begin{aligned} &\partial_\tau T^{\tau y} + \partial_x(v_x T^{\tau y}) + \partial_y(v_y T^{\tau y}) + \partial_\eta(v_\eta T^{\tau y}) \\ &\quad = -\partial_x(-v_x \pi^{\tau y} + \pi^{xy}) - \partial_y(P - v_y \pi^{\tau y} + \pi^{yy}) \\ &\qquad -\partial_\eta(-v_\eta \pi^{\tau y} + \pi^{y\eta}) - \frac{1}{\tau} T^{\tau y}, \end{aligned} \tag{A10}$$

$$\begin{aligned} &\partial_\tau T^{\tau\eta} + \partial_x(v_x T^{\tau\eta}) + \partial_y(v_y T^{\tau\eta}) + \partial_\eta(v_\eta T^{\tau\eta}) \\ &\quad = -\partial_x(-v_x \pi^{\tau\eta} + \pi^{x\eta}) - \partial_y(-v_y \pi^{\tau\eta} + \pi^{y\eta}) \\ &\qquad -\partial_\eta\left(\frac{P}{\tau^2} - v_\eta \pi^{\tau\eta} + \pi^{\eta\eta}\right) - \frac{3}{\tau} T^{\tau\eta}. \end{aligned} \tag{A11}$$

The corresponding tensor components are defined according to the general definition of the energy-momentum tensor [Eq. (2)]:

$$T^{\tau\tau} = (e + P)\gamma^2 - g^{\tau\tau} P + \pi^{\tau\tau}, \tag{A12}$$

$$\begin{aligned} T^{\tau i} &\equiv (e + P)\gamma^2 v_i - g^{\tau i} P + \pi^{\tau i}, \\ &= v_i T^{\tau\tau} + P(g^{\tau\tau} v_i - g^{\tau i}) - v_i \pi^{\tau\tau} + \pi^{\tau i}, \end{aligned} \tag{A13}$$

$$\begin{aligned} T^{ij} &\equiv (e + P)\gamma^2 v_i v_j - P g^{ij} + \pi^{ij}, \\ &= v_i T^{\tau j} + P(g^{\tau j} v_i - g^{ij}) - v_i \pi^{\tau j} + \pi^{ij}. \end{aligned} \tag{A14}$$

A simplified but mathematically equivalent way of writing the equations of motion can be obtained by introducing scaled variables that absorb the $\sqrt{g}$ factor [76],

$$\tilde{T}^{\mu\nu} = \tau T^{\mu\nu}; \tag{A15}$$

hence we are led to the following τ-scaled equations:

$$\partial_\mu \tilde{T}^{\tau\mu} = -\tau \tilde{T}^{\eta\eta}, \tag{A16}$$

$$\partial_\mu \tilde{T}^{x\mu} = 0, \quad \partial_\mu \tilde{T}^{y\mu} = 0, \quad \partial_\mu \tilde{T}^{\eta\mu} = -\frac{2}{\tau} \tilde{T}^{\tau\eta}. \tag{A17}$$

For example, in special test cases with no transverse pressure and vanishing dissipation we can solve the energy-conservation equation exactly. We found that by solving the scaled equations we can achieve approximately $\mathcal{O}_5$ numerical precision, which is in comparison about two orders of magnitude more accurate than the numerical solution of the nonscaled equations of motion using the same time step. Note that the τ scaling from Eq. (A15) also affects the relaxation equations for the shear-stress tensor. Therefore the scaled quantities $\tilde{\pi}^{\mu\nu} = \tau \pi^{\mu\nu}$ result in $d\tilde{\pi}^{\mu\nu} - \tilde{\pi}^{\mu\nu}/\tau = \tau d\pi^{\mu\nu}$.

For a better understanding of what will follow, we introduce the notation $u^\mu = \gamma(1, \bar{\mathbf{v}}_i)$ for the contravariant flow velocity from Eq. (A6). Similarly, the covariant component is denoted as $u_\mu = \gamma(1, -\underline{\mathbf{v}}_i)$; thus $v^2 \equiv \bar{\mathbf{v}}_i \underline{\mathbf{v}}_i = v_x^2 + v_y^2 + \tau^2 v_\eta^2$ and $\gamma = \sqrt{1 - v^2}$.

In our case of interest, $g^{\tau\tau} = 1$, and the metric of space-time is diagonal, leading to $g^{\tau i} = 0$; thus we can introduce a simplified notation which mimics the ideal fluid relations, $E \equiv T^{\tau\tau} - \pi^{\tau\tau} = T_{\tau\tau} - \pi_{\tau\tau}$, $\bar{M}_i \equiv T^{\tau i} - \pi^{\tau i}$, and $\underline{\mathrm{M}}_i \equiv T_{\tau i} - \pi_{\tau i} = g_{\alpha\tau} g_{\beta i}(T^{\alpha\beta} - \pi^{\alpha\beta})$. Using this notation we obtain the

local rest frame energy density from Eqs. (A12) and (A13):

$$e \equiv T^{\tau\tau} - \pi^{\tau\tau} - (T^{\tau i} - \pi^{\tau i})\underline{\mathbf{v}}_i = E - \bar{M}_i \underline{\mathbf{v}}_i, \tag{A18}$$

while the expression for the velocity components from Eq. (A13) leads to

$$\bar{\mathbf{v}}_i \equiv \frac{T^{\tau i} - \pi^{\tau i}}{T^{\tau\tau} - \pi^{\tau\tau} + P} = \frac{\bar{M}_i}{E + P}. \tag{A19}$$

Now, similarly expressing the $\underline{\mathbf{v}}_i$ components we define the magnitude of the three-velocity as

$$v \equiv \sqrt{\bar{\mathbf{v}}_i \underline{\mathbf{v}}_i} = \frac{M}{E + P}, \tag{A20}$$

where $M \equiv (\bar{M}_i \underline{\mathrm{M}}_i)^{1/2} = \sqrt{\bar{M}_x^2 + \bar{M}_y^2 + \tau^2 \bar{M}_\eta^2}$. Using the latter two equations together we obtain

$$\bar{\mathbf{v}}_i = v \frac{\bar{M}_i}{M}. \tag{A21}$$

Therefore, with the help of Eq. (A18), Eq. (A20) can be solved by using a one-dimensional root search, whereas Eq. (A21) yields the individual velocity components.

In general, we can reduce the number of unknowns in the relaxation equations (4) by applying the orthogonality and tracelessness conditions of the shear-stress tensor. For example, by choosing π^{xx}, π^{yy}, π^{xy}, $\pi^{x\eta}$, and $\pi^{y\eta}$ as independent components, the other four components of the shear-stress tensor follow from the orthogonality $\pi^{\mu\nu} u_\nu = 0$:

$$\pi^{\tau\tau} = \pi^{\tau x} v_x + \pi^{\tau y} v_y + \tau^2 \pi^{\tau\eta} v_\eta, \tag{A22}$$

$$\pi^{\tau x} = \pi^{xx} v_x + \pi^{xy} v_y + \tau^2 \pi^{x\eta} v_\eta, \tag{A23}$$

$$\pi^{\tau y} = \pi^{xy} v_x + \pi^{yy} v_y + \tau^2 \pi^{y\eta} v_\eta, \tag{A24}$$

$$\pi^{\tau\eta} = \pi^{x\eta} v_x + \pi^{y\eta} v_y + \tau^2 \pi^{\eta\eta} v_\eta, \tag{A25}$$

whereas the last unknown component is available from the tracelessness condition $\pi^{\mu\nu} g_{\mu\nu} = 0$:

$$\begin{aligned}\pi^{\eta\eta} &\equiv \tau^{-2}(\pi^{\tau\tau} - \pi^{xx} - \pi^{yy}) \\ &= \tau^{-2}\left[\pi^{xx}\left(v_x^2 - 1\right) + \pi^{yy}\left(v_y^2 - 1\right) + 2\pi^{xy} v_x v_y \right. \\ &\quad \left. + 2\tau^2(\pi^{x\eta} v_x v_\eta + \pi^{y\eta} v_y v_\eta)\right] \big/ \left(1 - \tau^2 v_\eta^2\right).\end{aligned} \tag{A26}$$

Note that solving the above algebraic equations to obtain the remaining five components, instead of explicitly propagating all ten components of the shear-stress tensor, we introduce a small numerical error compared to the latter method. This is because the velocities entering into Eqs. (A22)–(A26) are given from the previous (half) time step, so we obtain different values with different methods. However, this difference usually becomes smaller as the number of time steps increases; hence this small numerical error is acceptable especially if the runtime is also reduced considerably.

For sake of completeness we write out all terms from the shear-stress relaxation equations explicitly. The relaxation equations for the chosen five independent components of the shear-stress tensor π^{xx}, π^{yy}, π^{xy}, $\pi^{x\eta}$, and $\pi^{y\eta}$ are

$$\tau_\pi d\pi^{xx} = 2\eta_s \sigma^{xx} - \pi^{xx} - I^{xx}, \tag{A27}$$

$$\tau_\pi d\pi^{yy} = 2\eta_s \sigma^{yy} - \pi^{yy} - I^{yy}, \tag{A28}$$

$$\tau_\pi d\pi^{xy} = 2\eta_s \sigma^{xy} - \pi^{xy} - I^{xy}, \tag{A29}$$

$$\tau_\pi d\pi^{x\eta} = 2\eta_s \sigma^{x\eta} - \pi^{x\eta} - \tau_\pi \frac{\gamma}{\tau}(\pi^{x\eta} + v_\eta \pi^{\tau x}) - I^{x\eta}, \tag{A30}$$

$$\tau_\pi d\pi^{y\eta} = 2\eta_s \sigma^{y\eta} - \pi^{y\eta} - \tau_\pi \frac{\gamma}{\tau}(\pi^{y\eta} + v_\eta \pi^{\tau y}) - I^{y\eta}. \tag{A31}$$

Here according to Eq. (4) we denoted

$$I^{\mu\nu} = I_1^{\mu\nu} + \delta_{\pi\pi} I_2^{\mu\nu} - \tau_\pi I_3^{\mu\nu} + \tau_{\pi\pi} I_4^{\mu\nu} - \varphi_7 I_5^{\mu\nu}, \tag{A32}$$

where

$$I_1^{\mu\nu} = (\pi^{\lambda\mu} u^\nu + \pi^{\lambda\nu} u^\mu) Du_\lambda, \tag{A33}$$

$$I_2^{\mu\nu} = \theta \pi^{\mu\nu}, \tag{A34}$$

$$I_3^{\mu\nu} = \pi^{\mu\lambda} \omega_\lambda^\nu + \pi^{\nu\lambda} \omega_\lambda^\mu, \tag{A35}$$

$$I_4^{\mu\nu} = \tfrac{1}{2} g_{\lambda\kappa}(\pi^{\mu\kappa}\sigma^{\nu\lambda} + \pi^{\nu\kappa}\sigma^{\mu\lambda}) - \tfrac{1}{3}\Delta^{\mu\nu}\pi_\beta^\alpha \sigma_\alpha^\beta, \tag{A36}$$

$$I_5^{\mu\nu} = g_{\lambda\kappa}\pi^{\mu\kappa}\pi^{\nu\lambda} - \tfrac{1}{3}\Delta^{\mu\nu}\pi_\beta^\alpha \pi_\alpha^\beta. \tag{A37}$$

The I_1 terms are

$$I_1^{xx} = 2\gamma v_x(\pi^{\tau x} Du_\tau + \pi^{xx} Du_x + \pi^{yx} Du_y + \pi^{\eta x} Du_\eta), \tag{A38}$$

$$I_1^{yy} = 2\gamma v_y(\pi^{\tau y} Du_\tau + \pi^{xy} Du_x + \pi^{yy} Du_y + \pi^{\eta y} Du_\eta), \tag{A39}$$

$$\begin{aligned} I_1^{xy} = \gamma[&(\pi^{\tau x} v_y + \pi^{\tau y} v_x) Du_\tau + (\pi^{xx} v_y + \pi^{xy} v_x) Du_x \\ &+ (\pi^{yx} v_y + \pi^{yy} v_x) Du_y + (\pi^{\eta x} v_y + \pi^{\eta y} v_x) Du_\eta], \end{aligned} \tag{A40}$$

$$\begin{aligned} I_1^{x\eta} = \gamma[&(\pi^{\tau x} v_\eta + \pi^{\tau\eta} v_x) Du_\tau + (\pi^{xx} v_\eta + \pi^{x\eta} v_x) Du_x \\ &+ (\pi^{yx} v_\eta + \pi^{y\eta} v_x) Du_y + (\pi^{\eta x} v_\eta + \pi^{\eta\eta} v_x) Du_\eta], \end{aligned} \tag{A41}$$

$$\begin{aligned} I_1^{y\eta} = \gamma[&(\pi^{\tau y} v_\eta + \pi^{\tau\eta} v_y) Du_\tau + (\pi^{xy} v_\eta + \pi^{x\eta} v_y) Du_x \\ &+ (\pi^{yy} v_\eta + \pi^{y\eta} v_y) Du_y + (\pi^{\eta y} v_\eta + \pi^{\eta\eta} v_y) Du_\eta], \end{aligned} \tag{A42}$$

where according to Eqs. (A3) and (A5) the proper time derivatives are given by $Du_\mu = du_\mu - \Gamma^\beta_{\mu\alpha} u^\alpha u_\beta$ and hence

$$Du_\tau \equiv Du^\tau = \gamma[\partial_\tau \gamma + v_x \partial_x \gamma + v_y \partial_y \gamma + v_\eta \partial_\eta \gamma] + \tau \gamma^2 v_\eta^2, \tag{A43}$$

$$\begin{aligned} Du_x \equiv -Du^x = -\gamma[&\partial_\tau(\gamma v_x) + v_x \partial_x(\gamma v_x) \\ &+ v_y \partial_y(\gamma v_x) + v_\eta \partial_\eta(\gamma v_x)], \end{aligned} \tag{A44}$$

$$\begin{aligned} Du_y \equiv -Du^y = -\gamma[&\partial_\tau(\gamma v_y) + v_x \partial_x(\gamma v_y) \\ &+ v_y \partial_y(\gamma v_y) + v_\eta \partial_\eta(\gamma v_y)], \end{aligned} \tag{A45}$$

$$\begin{aligned} Du_\eta \equiv -\tau^2 Du^\eta = -\gamma\tau^2[&\partial_\tau(\gamma v_\eta) + v_x \partial_x(\gamma v_\eta) \\ &+ v_y \partial_y(\gamma v_\eta) + v_\eta \partial_\eta(\gamma v_\eta)] - 2\tau\gamma^2 v_\eta. \end{aligned} \tag{A46}$$

Note that $Du_\tau \equiv du_\tau + \tau\gamma^2 v_\eta^2 = du^\tau + \tau\gamma^2 v_\eta^2$, $Du_x \equiv du_x = -du^x$, $Du_y \equiv du_y = -du^y$, and $Du_\eta \equiv du_\eta \neq du^\eta$, since $Du^\eta \equiv du^\eta + 2\tau^{-1}\gamma^2 v_\eta = -\tau^2 du_\eta$.

The I_3 terms are

$$I_3^{xx} = 2\left(\pi^{x\tau}\omega^x{}_\tau + \pi^{xy}\omega^x{}_y + \pi^{x\eta}\omega^x{}_\eta\right), \tag{A47}$$

$$I_3^{yy} = 2\left(\pi^{y\tau}\omega^y{}_\tau + \pi^{yx}\omega^y{}_x + \pi^{y\eta}\omega^y{}_\eta\right), \tag{A48}$$

$$I_3^{xy} = \pi^{x\tau}\omega^y{}_\tau + \pi^{y\tau}\omega^x{}_\tau + \pi^{xx}\omega^y{}_x + \pi^{yy}\omega^x{}_y + \pi^{x\eta}\omega^y{}_\eta + \pi^{y\eta}\omega^x{}_\eta, \tag{A49}$$

$$I_3^{x\eta} = \pi^{x\tau}\omega^\eta{}_\tau + \pi^{\eta\tau}\omega^x{}_\tau + \pi^{xx}\omega^\eta{}_x + \pi^{xy}\omega^\eta{}_y + \pi^{\eta y}\omega^x{}_y + \pi^{\eta\eta}\omega^x{}_\eta, \tag{A50}$$

$$I_3^{y\eta} = \pi^{y\tau}\omega^\eta{}_\tau + \pi^{\eta\tau}\omega^y{}_\tau + \pi^{yx}\omega^\eta{}_x + \pi^{\eta x}\omega^y{}_x + \pi^{yy}\omega^\eta{}_y + \pi^{\eta\eta}\omega^y{}_\eta, \tag{A51}$$

where the vorticities are defined most generally as

$$\begin{aligned}\omega^\mu{}_\nu &\equiv \tfrac{1}{2}\Delta^{\mu\alpha}\Delta^\beta{}_\nu(u_{\alpha;\beta} - u_{\beta;\alpha}) \\ &= \tfrac{1}{2}\left[g^{\mu\alpha}\left(\partial_\nu u_\alpha - u_\nu du_\alpha\right) - g^\beta_\nu(\partial^\mu u_\beta - u^\mu du_\beta)\right] \\ &\quad + \tfrac{1}{2}(g^{\mu\alpha}u_\nu - g^\alpha{}_\nu u^\mu)u^\beta\Gamma^\lambda_{\alpha\beta}u_\lambda.\end{aligned} \tag{A52}$$

Here we used the fact that the Christoffel symbols of the second kind are symmetric, $\Gamma^\mu_{\alpha\beta} = \Gamma^\mu_{\beta\alpha}$, with respect to the interchange of the two lower indices.

The different components of the vorticity are given as

$$\begin{aligned}\omega^\tau{}_x \equiv \omega^x{}_\tau &= \tfrac{1}{2}[\partial_\tau(\gamma v_x) + \partial_x\gamma] \\ &\quad + \tfrac{1}{2}\left[\gamma v_x d\gamma - \gamma d\left(\gamma v_x\right)\right] + \tfrac{1}{2}\tau\gamma^3 v_\eta^2 v_x,\end{aligned} \tag{A53}$$

$$\begin{aligned}\omega^\tau{}_y \equiv \omega^y{}_\tau &= \tfrac{1}{2}[\partial_\tau(\gamma v_y) + \partial_y\gamma] \\ &\quad + \tfrac{1}{2}[\gamma v_y d\gamma - \gamma d(\gamma v_y)] + \tfrac{1}{2}\tau\gamma^3 v_\eta^2 v_y,\end{aligned} \tag{A54}$$

$$\begin{aligned}\omega^\tau{}_\eta \equiv \tau^2\omega^\eta{}_\tau &= \tfrac{1}{2}[\partial_\tau(\tau^2\gamma v_\eta) + \partial_\eta\gamma] \\ &\quad + \tfrac{1}{2}[\tau^2\gamma v_\eta d\gamma - \gamma d(\tau^2\gamma v_\eta)] + \tfrac{1}{2}\tau^3\gamma^3 v_\eta^3\end{aligned} \tag{A55}$$

and

$$\begin{aligned}\omega^x{}_y \equiv -\omega^y{}_x &= \tfrac{1}{2}[\partial_y(\gamma v_x) - \partial_x(\gamma v_y)] \\ &\quad + \tfrac{1}{2}[\gamma v_y d(\gamma v_x) - \gamma v_x d(\gamma v_y)],\end{aligned} \tag{A56}$$

$$\begin{aligned}\omega^x{}_\eta \equiv -\tau^2\omega^\eta{}_x &= \tfrac{1}{2}[\partial_\eta(\gamma v_x) - \partial_x(\tau^2\gamma v_\eta)] \\ &\quad + \tfrac{1}{2}[\tau^2\gamma v_\eta d(\gamma v_x) - \gamma v_x d(\tau^2\gamma v_\eta)],\end{aligned} \tag{A57}$$

$$\begin{aligned}\omega^y{}_\eta \equiv -\tau^2\omega^\eta{}_y &= \tfrac{1}{2}[\partial_\eta(\gamma v_y) - \partial_y(\tau^2\gamma v_\eta)] \\ &\quad + \tfrac{1}{2}[\tau^2\gamma v_\eta d(\gamma v_y) - \gamma v_y d(\tau^2\gamma v_\eta)].\end{aligned} \tag{A58}$$

Note that the general expression of the vorticity given in Eq. (10) in Ref. [77] is missing the contribution of the Christoffel symbols compared to Eq. (A52) in this work. Therefore, the values for $\omega^\tau{}_x$, $\omega^\tau{}_y$, and $\omega^\tau{}_\eta$ given in Eqs. (C.22), (C.23), and (C.24) in Ref. [77] are also incorrect compared to these formulas.

The next term we need is given by

$$\begin{aligned}I_4^{xx} &= (\pi^{x\tau}\sigma^{x\tau} - \pi^{xx}\sigma^{xx} - \pi^{xy}\sigma^{xy} - \tau^2\pi^{x\eta}\sigma^{x\eta}) \\ &\quad + \frac{1}{3}\left(1 + \gamma^2 v_x^2\right)\pi^\alpha_\beta\sigma^\beta_\alpha,\end{aligned} \tag{A59}$$

$$\begin{aligned}I_4^{yy} &= \pi^{y\tau}\sigma^{y\tau} - \pi^{yx}\sigma^{yx} - \pi^{yy}\sigma^{yy} - \tau^2\pi^{y\eta}\sigma^{y\eta} \\ &\quad + \frac{1}{3}\left(1 + \gamma^2 v_y^2\right)\pi^\alpha_\beta\sigma^\beta_\alpha,\end{aligned} \tag{A60}$$

$$\begin{aligned}I_4^{xy} &= \frac{1}{2}(\pi^{x\tau}\sigma^{y\tau} + \pi^{y\tau}\sigma^{x\tau}) - \frac{1}{2}(\pi^{xx}\sigma^{yx} + \pi^{yx}\sigma^{xx}) \\ &\quad - \frac{1}{2}\left(\pi^{xy}\sigma^{yy} + \pi^{yy}\sigma^{xy}\right) - \frac{\tau^2}{2}(\pi^{x\eta}\sigma^{y\eta} + \pi^{y\eta}\sigma^{x\eta}) \\ &\quad + \frac{1}{3}\left(\gamma^2 v_x v_y\right)\pi^\alpha_\beta\sigma^\beta_\alpha,\end{aligned} \tag{A61}$$

$$\begin{aligned}I_4^{x\eta} &= \frac{1}{2}(\pi^{x\tau}\sigma^{\eta\tau} + \pi^{\eta\tau}\sigma^{x\tau}) - \frac{1}{2}(\pi^{xx}\sigma^{\eta x} + \pi^{\eta x}\sigma^{xx}) \\ &\quad - \frac{1}{2}(\pi^{xy}\sigma^{\eta y} + \pi^{\eta y}\sigma^{xy}) - \frac{\tau^2}{2}(\pi^{x\eta}\sigma^{\eta\eta} + \pi^{\eta\eta}\sigma^{x\eta}) \\ &\quad + \frac{1}{3}(\gamma^2 v_x v_\eta)\pi^\alpha_\beta\sigma^\beta_\alpha,\end{aligned} \tag{A62}$$

$$\begin{aligned}I_4^{y\eta} &= \frac{1}{2}(\pi^{y\tau}\sigma^{\eta\tau} + \pi^{\eta\tau}\sigma^{y\tau}) - \frac{1}{2}(\pi^{yx}\sigma^{\eta x} + \pi^{\eta x}\sigma^{yx}) \\ &\quad - \frac{1}{2}(\pi^{yy}\sigma^{\eta y} + \pi^{\eta y}\sigma^{yy}) - \frac{\tau^2}{2}(\pi^{y\eta}\sigma^{\eta\eta} + \pi^{\eta\eta}\sigma^{y\eta}) \\ &\quad + \frac{1}{3}(\gamma^2 v_y v_\eta)\pi^\alpha_\beta\sigma^\beta_\alpha.\end{aligned} \tag{A63}$$

The shear tensor is most generally defined as

$$\begin{aligned}\sigma^{\mu\nu} \equiv \nabla^{\langle\mu}u^{\nu\rangle} &= \frac{1}{2}\Delta^{\mu\alpha}\Delta^{\nu\beta}(u_{\alpha;\beta} + u_{\beta;\alpha}) - \frac{\theta}{3}\Delta^{\mu\nu} \\ &= \frac{1}{2}[g^{\mu\alpha}(\partial^\nu u_\alpha - u^\nu du_\alpha) + g^{\nu\beta}(\partial^\mu u_\beta - u^\mu du_\beta)] \\ &\quad - \Delta^{\mu\alpha}\Delta^{\nu\beta}\Gamma^\lambda_{\alpha\beta}u_\lambda - \frac{\theta}{3}\Delta^{\mu\nu},\end{aligned} \tag{A64}$$

whereas the expansion scalar is

$$\begin{aligned}\theta \equiv \nabla_\mu u^\mu &= \partial_\mu u^\mu + \Gamma^\lambda_{\lambda\mu}u^\mu \\ &= \frac{\gamma}{\tau} + \partial_\tau\gamma + \partial_x(\gamma v_x) + \partial_y(\gamma v_y) + \partial_\eta(\gamma v_\eta).\end{aligned} \tag{A65}$$

The various shear tensor components that we need to use are

$$\sigma^{\tau\tau} = -\tau\gamma^3 v_\eta^2 + [(\partial_\tau\gamma - \gamma d\gamma)] + (\gamma^2 - 1)\frac{\theta}{3}, \tag{A66}$$

$$\begin{aligned}\sigma^{\tau x} &= -\frac{1}{2}\left(\tau\gamma^3 v_\eta^2 v_x\right) + \frac{1}{2}\left[\partial_\tau\left(\gamma v_x\right) - \partial_x\gamma\right] \\ &\quad - \frac{1}{2}\left[\gamma v_x d\gamma + \gamma d\left(\gamma v_x\right)\right] + \gamma^2 v_x\frac{\theta}{3},\end{aligned} \tag{A67}$$

$$\begin{aligned}\sigma^{\tau y} &= -\frac{1}{2}\left(\tau\gamma^3 v_\eta^2 v_y\right) + \frac{1}{2}[\partial_\tau(\gamma v_y) - \partial_y\gamma] \\ &\quad - \frac{1}{2}[\gamma v_y d\gamma + \gamma d(\gamma v_y)] + \gamma^2 v_y\frac{\theta}{3},\end{aligned} \tag{A68}$$

$$\begin{aligned}\sigma^{\tau\eta} &= -\frac{\gamma^3 v_\eta}{2\tau}\left(2 + \tau^2 v_\eta^2\right) + \frac{1}{2}\left[\partial_\tau(\gamma v_\eta) - \frac{1}{\tau^2}\partial_\eta\gamma\right] \\ &\quad - \frac{1}{2}[\gamma v_\eta d\gamma + \gamma d(\gamma v_\eta)] + \gamma^2 v_\eta\frac{\theta}{3},\end{aligned} \tag{A69}$$

$$\sigma^{\eta\eta} = -\frac{\gamma}{\tau^3}\left(1+2\tau^2\gamma^2 v_\eta^2\right) - \frac{1}{\tau^2}\partial_\eta(\gamma v_\eta) - (\gamma v_\eta) d(\gamma v_\eta) + \left(\frac{1}{\tau^2}+\gamma^2 v_\eta^2\right)\frac{\theta}{3} \tag{A70}$$

and

$$\sigma^{xx} = -\left[\partial_x(\gamma v_x) + \gamma v_x d(\gamma v_x)\right] + \left(1+\gamma^2 v_x^2\right)\frac{\theta}{3}, \tag{A71}$$

$$\sigma^{yy} = -\left[\partial_y(\gamma v_y) + \gamma v_y d(\gamma v_y)\right] + \left(1+\gamma^2 v_y^2\right)\frac{\theta}{3}, \tag{A72}$$

$$\sigma^{xy} = -\frac{1}{2}\left[\partial_x(\gamma v_y) + \partial_y(\gamma v_x)\right] - \frac{1}{2}\left[\gamma v_y d(\gamma v_x) + \gamma v_x d(\gamma v_y)\right] + \gamma^2 v_x v_y \frac{\theta}{3}, \tag{A73}$$

$$\sigma^{x\eta} = -\frac{\gamma^3 v_x v_\eta}{\tau} - \frac{1}{2}\left[\partial_x(\gamma v_\eta) + \frac{1}{\tau^2}\partial_\eta(\gamma v_x)\right] - \frac{1}{2}\left[\gamma v_\eta d(\gamma v_x) + \gamma v_x d(\gamma v_\eta)\right] + \gamma^2 v_x v_\eta \frac{\theta}{3}, \tag{A74}$$

$$\sigma^{y\eta} = -\frac{\gamma^3 v_y v_\eta}{\tau} - \frac{1}{2}\left[\partial_y(\gamma v_\eta) + \frac{1}{\tau^2}\partial_\eta(\gamma v_y)\right] - \frac{1}{2}\left[\gamma v_\eta d(\gamma v_y) + \gamma v_y d(\gamma v_\eta)\right] + \gamma^2 v_y v_\eta \frac{\theta}{3}. \tag{A75}$$

The last contributions from Eq. (A32) are

$$I_5^{xx} = (\pi^{x\tau})^2 - (\pi^{xx})^2 - (\pi^{xy})^2 - (\tau\pi^{x\eta})^2 + \tfrac{1}{3}\left(1+\gamma^2 v_x^2\right)\pi_\beta^\alpha \pi_\alpha^\beta, \tag{A76}$$

$$I_5^{yy} = (\pi^{y\tau})^2 - (\pi^{yx})^2 - (\pi^{yy})^2 - (\tau\pi^{y\eta})^2 + \tfrac{1}{3}\left(1+\gamma^2 v_y^2\right)\pi_\beta^\alpha \pi_\alpha^\beta, \tag{A77}$$

$$I_5^{xy} = \pi^{x\tau}\pi^{y\tau} - \pi^{xx}\pi^{yx} - \pi^{xy}\pi^{yy} - \tau^2\pi^{x\eta}\pi^{y\eta} + \tfrac{1}{3}(\gamma^2 v_x v_y)\pi_\beta^\alpha \pi_\alpha^\beta, \tag{A78}$$

$$I_5^{x\eta} = \pi^{x\tau}\pi^{\eta\tau} - \pi^{xx}\pi^{\eta x} - \pi^{xy}\pi^{\eta y} - \tau^2\pi^{x\eta}\pi^{\eta\eta} + \tfrac{1}{3}(\gamma^2 v_x v_\eta)\pi_\beta^\alpha \pi_\alpha^\beta, \tag{A79}$$

$$I_5^{y\eta} = \pi^{y\tau}\pi^{\eta\tau} - \pi^{yx}\pi^{\eta x} - \pi^{yy}\pi^{\eta y} - \tau^2\pi^{y\eta}\pi^{\eta\eta} + \tfrac{1}{3}(\gamma^2 v_y v_\eta)\pi_\beta^\alpha \pi_\alpha^\beta. \tag{A80}$$

Furthermore, to evaluate the Cooper-Frye formula, Eq. (5), as well as the argument of the equilibrium distribution function, Eq. (8), we express the four-momenta of particles as

$$p^\mu = \left(m_T\cosh(y_p-\eta), p_x, p_y, \frac{m_T}{\tau}\sinh(y_p-\eta)\right), \tag{A81}$$

where m is the rest mass of the particle, $m_T = \sqrt{m^2+p_x^2+p_y^2}$ denotes the transverse mass, while y_p is the rapidity of the particle. Therefore, the nonequilibrium corrections to the spectra from Eq. (7) are given with an argument of

$$\begin{aligned}\pi^{\alpha\beta}p_\alpha p_\beta = {} & m_T^2[\cosh^2(y_p-\eta)\pi^{\tau\tau} + \tau^2\sinh^2(y_p-\eta)\pi^{\eta\eta}] \\ & +\left(p_x^2\pi^{xx} + 2p_x p_y \pi^{xy} + p_y^2\pi^{yy}\right) \\ & -2m_T\cosh(y_p-\eta)(p_x\pi^{\tau x} + p_y\pi^{\tau y}) \\ & +2\tau m_T\sinh(y_p-\eta)(p_x\pi^{x\eta} + p_y\pi^{y\eta}) \\ & -2\tau m_T^2\sinh(y_p-\eta)\cosh(y_p-\eta)\pi^{\tau\eta},\end{aligned} \tag{A82}$$

while using Eq. (C4) we obtain

$$p^\mu d^3\Sigma_\mu = \tau\Big[m_T\cosh(y_p-\eta)dxdyd\eta - p_x d\tau dyd\eta - p_y d\tau dxd\eta - \frac{m_T}{\tau}\sinh(y_p-\eta)d\tau dxdy\Big]. \tag{A83}$$

APPENDIX B: NUMERICAL METHODS

The conservation laws as well as the relaxation equations are solved using the well-known SHASTA (SHarp and Smooth Transport Algorithm) originally developed by Boris and Book [78] and later refined by Zalesak [79] and others [80]. This numerical algorithm solves equations of the conservation type with source terms:

$$\partial_t U + \partial_i(v_i U) = S(t,\mathbf{x}), \tag{B1}$$

where $U = U(t,\mathbf{x})$ is, for example, T^{00} or T^{0i}, while v_i is the ith component of three-velocity, and $S(t,\mathbf{x})$ is a source term; for more details see Refs. [77,81,82].

Because for smooth solutions (like in our case) the multidimensional antidiffusion limiter suffers from instabilities around the boundary caused by small ripples propagating into the interior [83], we further stabilized SHASTA by letting the antidiffusion coefficient $A_{\rm ad}$, which controls the amount of numerical diffusion, be proportional to

$$A_{\rm ad} = \frac{A_{\rm ad}^S}{(k/e)^2+1}, \tag{B2}$$

where $A_{\rm ad}^S = 0.125$ is the default value for the antidiffusion coefficient [78], e is the energy density in the local rest frame, and $k = 6\times10^{-5}$ GeV/fm^3 is a numerical parameter. In this way we increase the amount of numerical diffusion in the low-density region and $A_{\rm ad}$ goes smoothly to zero near the boundaries of the grid. In our cases of interest this neither affects the solution nor produces more entropy inside the decoupling surface.

It is also important to mention that in the (3+1)-dimensional case both the conservation and the relaxation equations are solved using SHASTA, employing the above-mentioned modification for the antidiffusion coefficient. Earlier, for the (2+1)-dimensional boost-invariant case, we used a simple centered second-order difference algorithm to solve the relaxation equations [13]. However doing so in the (3+1)-dimensional case does not always lead to stable solutions.

To further stabilize the numerical calculations (and also for ideal fluids) we used a smaller value for the antidiffusion coefficient in the transverse directions, $A_{\rm ad}^{x,y} = 0.105$, but kept $A_{\rm ad}^{\eta} = 0.125$ in the η direction. Decreasing the antidiffusion coefficient produces smoother solutions inside the decoupling hypersurface but also increases the numerical diffusion, which in turn may decrease the numerical accuracy. The reason we used a different coefficient in the longitudinal direction is to increase the accuracy; see the next section for more details.

The numerical calculations are done on a discretized spatial grid (including four boundary points in each direction as required by the algorithm) of $N_x \times N_y \times N_\eta$ cells with $N_x = N_y = 180$ while $N_\eta = 2 \times 120$ with $\Delta x = \Delta y = \Delta\eta = 0.15$ fm cell sizes. The time step is given from $\Delta\tau = \lambda\Delta x$, which for $\lambda = 0.4$ leads to $\Delta\tau = 0.06$ fm/c. Furthermore, the system is symmetric around the x and y directions, with exponentially interpolated boundary conditions for the conserved quantities (e.g., for Glauber-type initial conditions) and linearly interpolated boundary conditions for the shear-stress tensor (because the shear-stress tensor may change sign).

Finally, the freeze-out hypersurface is constructed at time intervals $\Delta\tau_{\rm CF} \equiv 5\Delta\tau = 0.3$ fm/c. The space is sampled uniformly in both the transverse and longitudinal directions, at $\Delta x_{\rm CF} \equiv 2\Delta x = 0.3$ fm distances.

The freeze-out hypersurface is calculated by using the CORNELIUS++ subroutine presented in Ref. [84] and its source code can be obtained from the Open Standard Codes and Routines (OSCAR) website [85].

APPENDIX C: REMARKS ON THE NUMERICAL ACCURACY

SHASTA solves the fluid dynamical equations up to some finite numerical accuracy. In most cases this means that in Cartesian coordinates the particle number and energy are conserved up to $\mathcal{O}_5$ accuracy. However, in (τ,x,y,η) coordinates, the expressions for the conserved quantities as well as the equations of motion change with additional source terms resulting from the nonvanishing Christoffel symbols.

As an example let us evaluate a conserved quantity at a given time or proper time; hence by comparing this initial value with one at a later time we can follow the accuracy of the fluid-dynamical solver during this time interval.

The total conserved charge $N_{\rm tot}$ across any given hypersurface is

$$N_{\rm tot} \equiv \int N^\mu d^3\Sigma_\mu = \int N^0 d^3\Sigma_0 + \int N^i d^3\Sigma_i. \tag{C1}$$

Here the hypersurface element $d^3\Sigma_\mu$ can be specified in any coordinate system according to the following general formula:

$$d^3\Sigma_\mu = -\epsilon_{\mu\nu\lambda\kappa}\frac{\partial\Sigma^\nu}{\partial u}\frac{\partial\Sigma^\lambda}{\partial v}\frac{\partial\Sigma^\kappa}{\partial w}dudvdw, \tag{C2}$$

where $\epsilon_{\mu\nu\lambda\kappa}$ is the Levi-Civita symbol.

For example, in Cartesian coordinates the hypersurface normal vector is $\Sigma_\mu^{(t,z)}(t,x,y,z)$, where $t = t(x,y,z)$; hence

$$\begin{aligned} d^3\Sigma_\mu^{(t,z)} &\equiv (dxdydz, -dtdydz, -dtdxdz, -dtdxdy) \\ &= \tau\left(\frac{\partial\tau}{\tau\partial\eta}\sinh\eta + \cosh\eta, -\frac{\partial\tau}{\partial x}, -\frac{\partial\tau}{\partial y},\right. \\ &\quad \left. -\frac{\partial\tau}{\tau\partial\eta}\cosh\eta - \sinh\eta\right)dxdyd\eta, \end{aligned} \tag{C3}$$

while in (τ,x,y,η) coordinates for $\Sigma_\mu^{(\tau,\eta)}(\tau,x,y,\eta)$ and $\tau = \tau(x,y,\eta)$ we obtain

$$d^3\Sigma_\mu^{(\tau,\eta)} = \tau(dxdyd\eta, -d\tau dyd\eta, -d\tau dxd\eta, -d\tau dxdy). \tag{C4}$$

If we are interested in the conserved current across constant time or proper time hypersurfaces then $d^3\Sigma_i^{(t,z)} = d^3\Sigma_i^{(\tau,\eta)} = 0$; hence in Cartesian coordinates we get

$$N_{\rm tot}(t) \equiv \int N^\mu d^3\Sigma_\mu^{(t,z)} = \gamma n_0 \int dxdydz, \tag{C5}$$

where $N^\mu \equiv n_0 u^\mu = \gamma n_0(1, v_x, v_y, v_z)$ is the conserved charge current. Similarly, Eq. (C1) leads to the total conserved charge at any proper-time hypersurface in hyperbolic coordinates,

$$N_{\rm tot}(\tau) \equiv \int N^\mu d^3\Sigma_\mu^{(\tau,\eta)} = \gamma n_0 \int \tau dxdyd\eta. \tag{C6}$$

To calculate how the total energy-momentum changes between two closed hypersurfaces, first we define the energy-momentum current across a hypersuface as

$$E_{\rm tot}^\mu \equiv \int T^{\mu\nu} d^3\Sigma_\nu = \int T^{\mu 0} d^3\Sigma_0 + \int T^{\mu i} d^3\Sigma_i. \tag{C7}$$

In Cartesian coordinates $E_{\rm tot}^\mu = (E_{\rm tot}^0, E_{\rm tot}^i)$, such that $E_{\rm tot}^0$ denotes the energy current while $E_{\rm tot}^i$ denotes the momentum current trough the hypersurface. Therefore the total energy current across a constant-t hypersurface is

$$E_{\rm tot}^0(t) \equiv \int T^{0\nu} d^3\Sigma_\nu^{(t,z)} = \int T^{00} dxdydz. \tag{C8}$$

The energy-momentum current across a constant-τ hypersurface in (τ,x,y,η) coordinates can also be calculated from Eq. (C7) together with the general transformation rules $E_{\rm tot}^\mu = (\partial x^\mu/\partial\hat{x}^\alpha)\,\hat{E}_{\rm tot}^\alpha$, where the position vectors are $x^\mu \equiv (t,x,y,z) = (\tau\cosh\eta, x, y, \tau\sinh\eta)$ and $\hat{x}^\mu \equiv (\tau,x,y,\eta)$. Thus the total energy across a constant-τ hypersurface is given by

$$\begin{aligned} E_{\rm tot}^0(\tau) &\equiv \int \cosh\eta\; T^{\tau\nu} d^3\Sigma_\nu^{(\tau,\eta)} + \int \tau\sinh\eta\; T^{\eta\nu} d^3\Sigma_\nu^{(\tau,\eta)} \\ &= \int (\cosh\eta\; T^{\tau\tau} + \tau\sinh\eta\; T^{\eta\tau})\,\tau dxdyd\eta. \end{aligned} \tag{C9}$$

Using the latter formulas we can check energy conservation from the initial time to the end using

$$\Delta E_{\rm tot}^0(t) = E_{\rm tot}^0(t_{\rm end}) - E_{\rm tot}^0(t_{\rm ini}). \tag{C10}$$

It turns out that by solving the fluid dynamical equations in Cartesian coordinates we can achieve $\Delta E_{\rm tot}^0(t) \approx \mathcal{O}_6$

numerical accuracy, while in hyperbolic coordinates $\Delta E^0_{\rm tot}(\tau) \approx \mathcal{O}_1$. This behavior is due to two different reasons.

First, the numerical algorithm is accurate only to finite precision, meaning that T^{00} or $T^{\tau\tau}$ is calculated correctly only up to the first six digits. However, due to the hyperbolic functions in Eq. (C9) the total energy of the system is given by a differently weighted sum over all cells (compared to Cartesian coordinates). These hyperbolic weights increase very rapidly as a function of η; hence even though the numerical error of the solver is acceptably small for SHASTA, the weighted sum over all cells in hyperbolic coordinates shows otherwise.

We have checked that for RHIC energies $\Delta E^0_{\rm tot}(\tau) < 2\%$ while at LHC energies this number can be as much as 20%. This is because $f(\eta)$ is much narrower at the RHIC than at the LHC. Similar results were also obtained in Ref. [86] using a different computational fluid-dynamical algorithm.

We also verified energy conservation inside the constant-temperature freeze-out hypersurface, and we found that in that case the energy is conserved at 1% accuracy, at both the RHIC and the LHC. This was expected since inside the $T = 100$ MeV freeze-out hypersurface the space-time rapidity of matter is $\eta < 10$.

[1] I. Arsene *et al.*, Nucl. Phys. A **757**, 1 (2005); B. B. Back *et al.*, *ibid.* **757**, 28 (2005); J. Adams *et al.*, *ibid.* **757**, 102 (2005); K. Adcox *et al.*, *ibid.* **757**, 184 (2005).

[2] U. W. Heinz and R. Snellings, Annu. Rev. Nucl. Part. Sci. **63**, 123 (2013).

[3] C. Gale, S. Jeon, and B. Schenke, Int. J. Mod. Phys. A **28**, 1340011 (2013).

[4] P. Huovinen, Int. J. Mod. Phys. E **22**, 1330029 (2013).

[5] G. Policastro, D. T. Son, and A. O. Starinets, Phys. Rev. Lett. **87**, 081601 (2001); P. K. Kovtun, D. T. Son, and A. O. Starinets, *ibid.* **94**, 111601 (2005).

[6] C. Gale, S. Jeon, B. Schenke, P. Tribedy, and R. Venugopalan, Phys. Rev. Lett. **110**, 012302 (2013).

[7] L. P. Csernai, J. I. Kapusta, and L. D. McLerran, Phys. Rev. Lett. **97**, 152303 (2006).

[8] G. S. Denicol, C. Gale, S. Jeon, and J. Noronha, Phys. Rev. C **88**, 064901 (2013).

[9] H. Song, S. A. Bass, and U. Heinz, Phys. Rev. C **83**, 054912 (2011); **87**, 019902 (2013).

[10] U. W. Heinz, J. Phys.: Conf. Ser. **455**, 012044 (2013).

[11] H. Niemi, G. S. Denicol, P. Huovinen, E. Molnár, and D. H. Rischke, Phys. Rev. Lett. **106**, 212302 (2011).

[12] H. Niemi, G. S. Denicol, P. Huovinen, E. Molnár, and D. H. Rischke, J. Phys. G **38**, 124050 (2011); Acta Phys. Polon. Suppl. **5**, 305 (2012).

[13] H. Niemi, G. S. Denicol, P. Huovinen, E. Molnár, and D. H. Rischke, Phys. Rev. C **86**, 014909 (2012).

[14] H. Niemi and G. S. Denicol, arXiv:1404.7327 [nucl-th].

[15] H. Holopainen and P. Huovinen, J. Phys.: Conf. Ser. **389**, 012018 (2012).

[16] H. Holopainen and P. Huovinen, J. Phys.: Conf. Ser. **509**, 012114 (2014).

[17] L. D. Landau and E. M. Lifshitz, *Fluid Dynamics*, 2nd ed. (Butterworth-Heinemann, London, 1987).

[18] C. Cercignani and G. M. Kremer, *The Relativisitic Boltzmann Equation: Theory and Applications* (Birkhäuser, New York, 2002).

[19] G. Torrieri, B. Tomasik, and I. Mishustin, Phys. Rev. C **77**, 034903 (2008).

[20] A. Monnai and T. Hirano, Phys. Rev. C **80**, 054906 (2009).

[21] H. Song and U. W. Heinz, Phys. Rev. C **81**, 024905 (2010).

[22] P. Bozek, Phys. Rev. C **85**, 034901 (2012).

[23] K. Dusling and T. Schäfer, Phys. Rev. C **85**, 044909 (2012).

[24] J. Noronha-Hostler, G. S. Denicol, J. Noronha, R. P. G. Andrade, and F. Grassi, Phys. Rev. C **88**, 044916 (2013).

[25] J. Noronha-Hostler, J. Noronha, and F. Grassi, Phys. Rev. C **90**, 034907 (2014).

[26] S. Borsanyi, Z. Fodor, S. D. Katz, S. Krieg, C. Ratti, and K. Szabo, J. High Energy Phys. 01 (2012) 138.

[27] A. Bazavov *et al.* (HotQCD Collaboration), Phys. Rev. D **86**, 034509 (2012).

[28] P. Huovinen, P. Petreczky, and C. Schmidt, Central Eur. J. Phys. **10**, 1385 (2012).

[29] I. Müller, Z. Phys. **198**, 329 (1967).

[30] I. Müller, Living Rev. Relativity **2**, 1 (1999).

[31] W. Israel and J. M. Stewart, Ann. Phys. (NY) **118**, 341 (1979).

[32] G. S. Denicol, H. Niemi, E. Molnár, and D. H. Rischke, Phys. Rev. D **85**, 114047 (2012).

[33] G. S. Denicol, E. Molnár, H. Niemi, and D. H. Rischke, Eur. Phys. J. A **48**, 170 (2012).

[34] E. Molnár, H. Niemi, G. S. Denicol, and D. H. Rischke, Phys. Rev. D **89**, 074010 (2014).

[35] L. P. Csernai, V. K. Magas, E. Molnár, A. Nyiri, and K. Tamosiunas, Eur. Phys. J. A **25**, 65 (2005); E. Molnár, L. P. Csernai, V. K. Magas, A. Nyiri, and K. Tamosiunas, Phys. Rev. C **74**, 024907 (2006); E. Molnár, L. P. Csernai, V. K. Magas, Z. I. Lazar, A. Nyiri, and K. Tamosiunas, J. Phys. G **34**, 1901 (2007).

[36] S. V. Akkelin, Y. Hama, I. A. Karpenko, and Y. M. Sinyukov, Phys. Rev. C **78**, 034906 (2008); I. A. Karpenko and Y. M. Sinyukov, *ibid.* **81**, 054903 (2010).

[37] F. Cooper and G. Frye, Phys. Rev. D **10**, 186 (1974).

[38] J. P. Bondorf, S. I. A. Garpman, and J. Zimanyi, Nucl. Phys. A **296**, 320 (1978).

[39] C. M. Hung and E. V. Shuryak, Phys. Rev. C **57**, 1891 (1998).

[40] K. J. Eskola, H. Niemi, and P. V. Ruuskanen, Phys. Rev. C **77**, 044907 (2008).

[41] P. Huovinen and P. Petreczky, Nucl. Phys. A **837**, 26 (2010).

[42] M. Cheng *et al.*, Phys. Rev. D **77**, 014511 (2008).

[43] A. Bazavov *et al.*, Phys. Rev. D **80**, 014504 (2009).

[44] H. Bebie, P. Gerber, J. L. Goity, and H. Leutwyler, Nucl. Phys. B **378**, 95 (1992).

[45] T. Hirano and K. Tsuda, Phys. Rev. C **66**, 054905 (2002).

[46] P. Huovinen, Eur. Phys. J. A **37**, 121 (2008).

[47] M. Luzum and H. Petersen, J. Phys. G **41**, 063102 (2014).

[48] L. Pang, Q. Wang, and X.-N. Wang, Phys. Rev. C **86**, 024911 (2012).

[49] M. L. Miller, K. Reygers, S. J. Sanders, and P. Steinberg, Annu. Rev. Nucl. Part. Sci. **57**, 205 (2007).

[50] B. Alver, M. Baker, C. Loizides, and P. Steinberg, arXiv:0805.4411 [nucl-ex].

[51] B. Abelev *et al.* (ALICE Collaboration), Phys. Rev. C **88**, 044909 (2013).
[52] B. Schenke, P. Tribedy, and R. Venugopalan, Phys. Rev. Lett. **108**, 252301 (2012); Phys. Rev. C **86**, 034908 (2012).
[53] R. Paatelainen, K. J. Eskola, H. Niemi, and K. Tuominen, Phys. Lett. B **731**, 126 (2014).
[54] T. Hirano, Phys. Rev. C **65**, 011901(R) (2001).
[55] C. Nonaka and S. A. Bass, Phys. Rev. C **75**, 014902 (2007).
[56] B. Schenke, S. Jeon, and C. Gale, Phys. Rev. C **82**, 014903 (2010).
[57] J. D. Bjorken, Phys. Rev. D **27**, 140 (1983).
[58] A. Adil and M. Gyulassy, Phys. Rev. C **72**, 034907 (2005).
[59] T. Hirano, P. Huovinen, K. Murase, and Y. Nara, Prog. Part. Nucl. Phys. **70**, 108 (2013).
[60] V. Vovchenko, D. Anchishkin, and L. P. Csernai, Phys. Rev. C **88**, 014901 (2013).
[61] A. Dumitru, E. Molnár, and Y. Nara, Phys. Rev. C **76**, 024910 (2007).
[62] H. Holopainen, H. Niemi, and K. J. Eskola, Phys. Rev. C **83**, 034901 (2011).
[63] B. B. Back *et al.* (PHOBOS Collaboration), Phys. Rev. Lett. **91**, 052303 (2003).
[64] S. S. Adler *et al.* (PHENIX Collaboration), Phys. Rev. C **69**, 034909 (2004).
[65] T. Hirano and M. Gyulassy, Nucl. Phys. A **769**, 71 (2006).
[66] Y. Bai, Ph.D. thesis, Nikhef and Utrecht University, Netherlands, 2007; A. Tang (STAR Collaboration), arXiv:0808.2144 [nucl-ex].
[67] B. B. Back *et al.* (PHOBOS Collaboration), Phys. Rev. C **72**, 051901 (2005).
[68] J. Adams *et al.* (STAR Collaboration), Phys. Rev. C **72**, 014904 (2005).
[69] T. Hirano, U. W. Heinz, D. Kharzeev, R. Lacey, and Y. Nara, Phys. Lett. B **636**, 299 (2006).
[70] B. Schenke, S. Jeon, and C. Gale, Phys. Rev. C **85**, 024901 (2012).
[71] B. H. Alver, C. Gombeaud, M. Luzum, and J.-Y. Ollitrault, Phys. Rev. C **82**, 034913 (2010).
[72] E. Abbas *et al.* (ALICE Collaboration), Phys. Lett. B **726**, 610 (2013).
[73] B. Abelev *et al.* (ALICE Collaboration), Phys. Rev. C **88**, 044910 (2013).
[74] V. Begun, W. Florkowski, and M. Rybczynski, Phys. Rev. C **90**, 014906 (2014).
[75] K. Aamodt *et al.* (ALICE Collaboration), Phys. Rev. Lett. **105**, 252302 (2010).
[76] P. F. Kolb, J. Sollfrank, and U. W. Heinz, Phys. Rev. C **62**, 054909 (2000).
[77] E. Molnár, H. Niemi, and D. H. Rischke, Eur. Phys. J. C **65**, 615 (2010).
[78] J. P. Boris and D. L. Book, J. Comput. Phys. A **11**, 38 (1973); D. L. Book, J. P. Boris, and K. Hain, *ibid.* **18**, 248 (1975).
[79] S. T. Zalesak, J. Comput. Phys. A **31**, 335 (1979).
[80] D. Kuzmin, R. Löhner, and S. Turek, *Flux-Corrected Transport: Principles, Algorithms, and Applications*, 2nd ed. (Springer, New York, 2012).
[81] A. Muronga, Phys. Rev. C **76**, 014909 (2007).
[82] E. Molnár, Eur. Phys. J. C **60**, 413 (2009).
[83] D. Kuzmin, M. Möller, and S. Turek, Comput. Methods Appl. Mech. Eng. **193**, 4915 (2004).
[84] P. Huovinen and H. Petersen, Eur. Phys. J. A **48**, 171 (2012).
[85] https://karman.physics.purdue.edu/OSCAR/
[86] I. Karpenko, P. Huovinen, and M. Bleicher, Comput. Phys. Commun. **185**, 3016 (2014).

Event-by-event distributions of azimuthal asymmetries in ultrarelativistic heavy-ion collisions

H. Niemi,[1] G. S. Denicol,[2,3] H. Holopainen,[4] and P. Huovinen[3,4]
[1]*Department of Physics, P.O.Box 35, FI-40014 University of Jyväskylä, Finland*
[2]*Department of Physics, McGill University, 3600 University Street, Montreal, Quebec H3A 2T8, Canada*
[3]*Institut für Theoretische Physik, Johann Wolfgang Goethe-Universität, Max-von-Laue-Str. 1, D-60438 Frankfurt am Main, Germany*
[4]*Frankfurt Institute for Advanced Studies, Ruth-Moufang-Str. 1, D-60438 Frankfurt am Main, Germany*
(Received 13 December 2012; published 2 May 2013)

Relativistic dissipative fluid dynamics is a common tool to describe the space-time evolution of the strongly interacting matter created in ultrarelativistic heavy-ion collisions. For a proper comparison to experimental data, fluid-dynamical calculations have to be performed on an event-by-event basis. Therefore, fluid dynamics should be able to reproduce, not only the event-averaged momentum anisotropies, $\langle v_n \rangle$, but also their distributions. In this paper, we investigate the event-by-event distributions of the initial-state and momentum anisotropies ϵ_n and v_n, and their correlations. We demonstrate that the event-by-event distributions of relative v_n fluctuations are almost equal to the event-by-event distributions of corresponding ϵ_n fluctuations, allowing experimental determination of the relative anisotropy fluctuations of the initial state. Furthermore, the correlation $c(v_2, v_4)$ turns out to be sensitive to the viscosity of the fluid providing an additional constraint to the properties of the strongly interacting matter.

DOI: 10.1103/PhysRevC.87.054901 PACS number(s): 25.75.Ld, 12.38.Mh, 24.10.Nz

I. INTRODUCTION

Relativistic dissipative fluid dynamics is the most widely employed model to describe the space-time evolution of the quark-gluon plasma (QGP) created in ultrarelativistic heavy-ion collisions. It was the success of fluid-dynamical models in describing the large azimuthal momentum anisotropies observed in heavy-ion collisions that led to our current picture of the QGP, as a strongly interacting fluid with one of the smallest shear viscosity to entropy density ratios, η/s, ever observed [1].

The azimuthal momentum anisotropy is characterized in terms of the coefficients v_n of the Fourier expansion of the single particle azimuthal distribution:

$$\begin{aligned} \frac{dN}{dyd\phi} &= \frac{dN}{dy}[1 + 2v_1\cos(\phi - \psi_1) \\ &\quad + 2v_2\cos[2(\phi - \psi_2)] + \cdots], \\ v_n &= \frac{\int d\phi \cos[n(\phi - \psi_n)]\frac{dN}{dyd\phi}}{\int d\phi \frac{dN}{dyd\phi}} = \langle \cos[n(\phi - \psi_n)] \rangle, \end{aligned} \tag{1}$$

where ψ_n is the event-plane angle, $\psi_n = (1/n)\arctan(\langle p_T \sin n\phi \rangle / \langle p_T \cos n\phi \rangle)$, and ϕ is the transverse momentum azimuthal angle. One of the main features of the fluid-dynamical description of the expansion is that the anisotropy originates from the azimuthal anisotropy of the initial density profile. In the literature this initial anisotropy is quantified in terms of coefficients $\epsilon_{m,n}$:

$$\epsilon_{m,n} = -\frac{\int dxdy\, r^m \cos[n(\phi - \Psi_{m,n})]\varepsilon(x, y, \tau_0)}{\int dxdy\, r^m \varepsilon(x, y, \tau_0)}, \tag{2}$$

where ε is the energy density, $r^2 = x^2 + y^2$, ϕ is now the spatial azimuthal angle, and $\Psi_{m,n}$ is the participant angle, defined as

$$\Psi_{m,n} = \frac{1}{n}\arctan\frac{\int dxdy\, r^m \sin(n\phi)\varepsilon(x, y, \tau_0)}{\int dxdy\, r^m \cos(n\phi)\varepsilon(x, y, \tau_0)} + \pi/n. \tag{3}$$

In the following we will concentrate on the anisotropies $\epsilon_{2,n}$, and use a shorthand $\epsilon_n \equiv \epsilon_{2,n}$.

In fluid-dynamical calculations, a linear relation between v_2 and ϵ_2 was found, i.e., $v_2 \propto \epsilon_2$ [2]. The proportionality coefficient was shown to depend, not only on the properties of the fluid such as the equation of state and viscosity, but also on the initial density, freeze-out temperature, and resonance content of the late hadronic state [2–4].

The initial conditions in these fluid dynamical calculations were always smooth, constructed as an average over infinitely many individual collisions of the particular centrality. It was thought that the use of this kind of averaged initial conditions would lead to a good description of observables which were averaged over many events. In other words, the anisotropy v_2 computed using the event-averaged initial condition was expected to be equal to the $\langle v_2 \rangle_{\rm ev}$ observed in the collisions, where $\langle \ldots \rangle_{\rm ev}$ corresponds to an average over all the events of the corresponding centrality class.

Recently, it has been realized that, in order to obtain a proper comparison with experimental data, fluid-dynamical calculations have to be performed on an event-by-event basis. This was first pointed out by Kodama *et al.* [5] almost ten years ago. However, this view only become widely accepted years later, after the work of Alver and Roland [6]. They showed that ϵ_3 and, consequently, v_3 are nonzero in a single event. This is in contrast to the traditionally used event-averaged initial conditions in fluid-dynamical models which had zero ϵ_3 and v_3. Furthermore, Alver and Roland demonstrated that such finite value of v_3 can be observed in heavy-ion collisions. This finding made $\langle v_3 \rangle_{\rm ev}$ as important observable as $\langle v_2 \rangle_{\rm ev}$ for probing the properties of the dense matter formed in heavy-ion collisions, and led to several works studying the behavior of

observables in an event-by-event fluid-dynamical description [7,9].

On the other hand, if fluid dynamics can be applied to describe individual ultrarelativistic heavy-ion collisions, it must be able to describe v_n in every collision, not only the average $\langle v_n \rangle_{\rm ev}$. Therefore it must be able to reproduce the distribution $\mathcal{P}(v_n)$ of v_n in an ensemble of events too. To confirm the applicability of fluid dynamics to describe the expansion stage of heavy-ion collisions, it is thus not enough to check whether the event-averaged values of v_n agree with the data, but one must also check whether their distributions, $\mathcal{P}(v_n)$, match what is experimentally observed. Recently, the distributions of v_2, v_3, and v_4 were measured at the LHC by the ATLAS collaboration [10]. Also, the first fluid-dynamical calculations of these distributions were performed by Gale *et al.* [11].

In this paper, we study the event-by-event probability distribution of the Fourier coefficients v_n, $P(v_n)$, and how they are correlated with the initial state anisotropies ϵ_n event by event. The goal of this paper is not to attempt a comparison with experimental data, but to explore how these distributions and correlations are affected by the fluid viscosity and initialization of the system. In this way, it will be possible to understand what can be learned by measuring such event-by-event distributions.

In the following we explain our fluid dynamical model in Sec. II, and show our results in Sec. III. Section III A is dedicated to an analysis of the event-by-event correlation between initial condition and flow anisotropy, while in Secs. III B and III C we show our results for probability distributions of scaled anisotropy δv_n, $P(\delta v_n)$, and linear correlation coefficients $c(v_n, v_m)$, respectively. In Sec. IV, we summarize our findings and make our conclusions.

II. MODEL

To generate the initial states event by event, we use a Monte Carlo Glauber model as implemented in Ref. [9]. In this model, nucleons are distributed into nuclei according to Woods-Saxon distribution. NN correlations and finite size effects are neglected since they have a negligible effect on the anisotropy coefficients [12]. In an event with a given impact parameter, nucleons from different nuclei are assumed to collide when their transverse distance d is small enough, i.e., when $d^2 < \sigma_{NN}/\pi$.

We consider two initial conditions, in which the initial entropy density, s, at $\tau_0 = 1$ fm, is evaluated as

$$s(x, y) = W \sum_{i=1}^{N_{\rm part,bin}} \exp\{-[(x - x_i)^2 + (y - y_i)^2]/(2\sigma^2)\}, \quad (4)$$

where x_i and y_i are the spatial coordinates of either wounded nucleons (initial condition sWN) or binary collisions (initial condition sBC), given by the Monte Carlo Glauber model. W is a normalization constant fixed to provide the observed multiplicity and $\sigma = 0.8$ fm is the spatial scale of a wounded nucleon or a binary collision. The centrality classes are determined according to the number of binary collisions (for initial condition sBC) or the number of participants (for initial condition sWN). The initial fluid velocity and shear-stress tensor are set to zero and we neglect the effects of bulk viscosity.

For the fluid-dynamical evolution, we use the model previously employed in Ref. [13]. We describe the time evolution of the fluid in the central rapidity region assuming boost invariance and a zero baryochemical potential. The equations of motion are given by the conservation laws for energy and momentum:

$$\partial_\mu T^{\mu\nu} = 0, \quad (5)$$

where $T^{\mu\nu} = (\varepsilon + p)u^\mu u^\nu - g^{\mu\nu} p + \pi^{\mu\nu}$, with ε, p, u^μ, and $\pi^{\mu\nu}$ being the energy density, the thermodynamic pressure, the fluid four-velocity, and the shear-stress tensor, respectively. We use the lattice QCD and hadron resonance gas based equation of state $s95p$-PCE-v1 [14] with chemical freeze-out at temperature $T_{\rm chem} = 150$ MeV. The evolution equation of the shear-stress tensor is given by transient relativistic fluid dynamics [15,16]:

$$\Delta^{\mu\nu}_{\alpha\beta}\tau_\pi D\pi^{\alpha\beta} + \pi^{\mu\nu} = 2\eta\sigma^{\mu\nu} - \frac{4}{3}\tau_\pi \pi^{\mu\nu}\theta - \frac{10}{7}\tau_\pi \Delta^{\mu\nu}_{\alpha\beta}\sigma^\alpha_\lambda \pi^{\beta\lambda} + \frac{74}{315\eta}\tau_\pi \Delta^{\mu\nu}_{\alpha\beta}\pi^\alpha_\lambda \pi^{\beta\lambda}, \quad (6)$$

where η is the shear viscosity coefficient, $D = u^\mu \partial_\mu$ is the comoving time derivative, $\sigma^{\mu\nu} = \Delta^{\mu\nu}_{\alpha\beta}\partial^\alpha u^\beta$ is the shear tensor, $\theta = \partial_\mu u^\mu$ is the expansion rate, and $\Delta^{\mu\nu}_{\alpha\beta} = (\Delta^\mu_\alpha \Delta^\nu_\beta + \Delta^\nu_\alpha \Delta^\mu_\beta - 2/3\Delta^{\mu\nu}\Delta_{\alpha\beta})/2$, with $\Delta^{\mu\nu} = g^{\mu\nu} - u^\mu u^\nu$. The transport coefficients of the nonlinear terms on the right-hand side of the Eq. (6) were taken in the massless limit, in the 14-moment

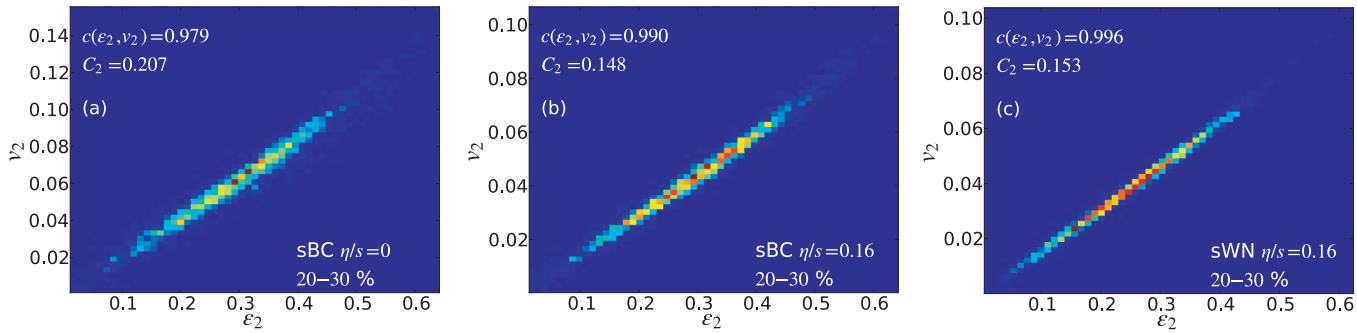

FIG. 1. (Color online) ϵ_2 and v_2 of pions in the 20–30% centrality class using different initializations and viscosities. (a) sBC and $\eta/s = 0$, (b) sBC and $\eta/s = 0.16$, and (c) sWN and $\eta/s = 0.16$.

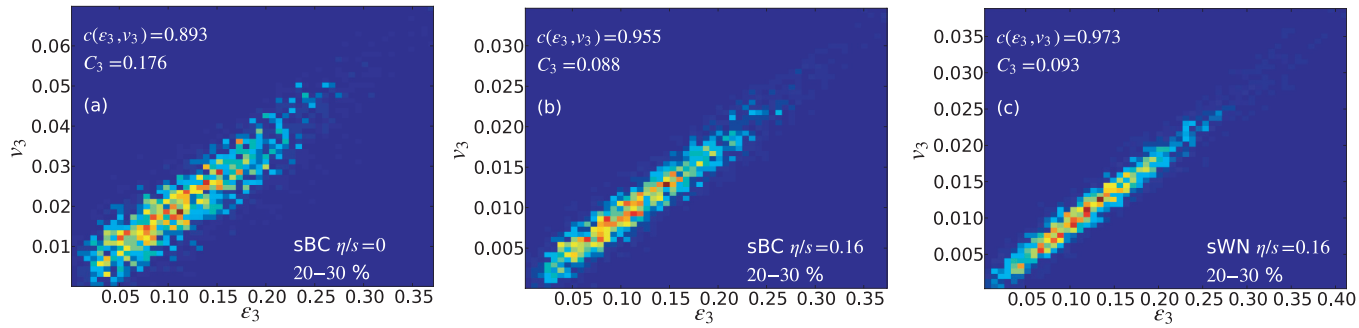

FIG. 2. (Color online) ϵ_3 and v_3 of pions in the 20–30% centrality class using different initializations and viscosities. (a) sBC and $\eta/s = 0$, (b) sBC and $\eta/s = 0.16$, and (c) sWN and $\eta/s = 0.16$.

approximation, and the relaxation time was assumed to be $\tau_\pi = 5\eta/(\varepsilon + P)$ [16,17]. Here, we have not included the nonlinear terms related to the vorticity tensor. Note that the last two terms in Eq. (6) were not included in our previous studies [13]. While such terms can have a significant effect on many observables, they are not relevant for the results discussed in this paper. We shall leave a detailed investigation of the effect of such terms to a future work. The equations of motion were solved numerically using the SHASTA algorithm, whereas the evolution equations for shear stress [Eq. (6)] were solved using simple finite differencing scheme. For more details see Refs. [13,18].

The hadron spectra are calculated with the Cooper-Frye freeze-out procedure [19] using the decoupling temperature $T_f = 100$ MeV, which was shown to give reasonable agreement with both the p_T spectrum and $\langle v_2 \rangle_{\rm ev}$ for pions at RHIC when a temperature-dependent η/s was used, see Ref. [13]. In this work, we use constant values of viscosity, $\eta/s = 0$ and 0.16. Nevertheless, the p_T spectrum and $\langle v_2 \rangle_{\rm ev}$ remain close to what is actually observed at RHIC. Since our main purpose is not the comparison to experimental observables, we adjusted only the initial entropy density to fit the observed multiplicity, but kept all the other parameters unchanged. Finally, we use Israel and Stewart's 14-moment ansatz for the dissipative correction to the local equilibrium distribution function,

$$\delta f_i = f_{0i} \frac{p_i^\mu p_i^\nu \pi_{\mu\nu}}{2T^2(\varepsilon + p)}, \tag{7}$$

where $f_{0i} = \{\exp[(u_\mu p_i^\mu - \mu_i)/T] \pm 1\}^{-1}$ is the local equilibrium distribution function, with the index i indicating different hadron species and p_i^μ the four-momentum of the corresponding hadron. After calculating the thermal spectra, we include the contribution from all two- and three-particle decays of unstable resonances up to 1.1 GeV mass.

It should be noted that because we do not generate particle ensembles at any point we always know the direction of the event plane and the magnitude of v_n exactly. Experimentally, one measures a finite number of particles, which smears the observed distribution of v_n. However, the final experimental result for the v_n distributions undergoes an unfolding procedure that is supposed to remove such a smearing [10]. Therefore, for a comparison with data, one can use the particle distributions computed with fluid dynamics without generating an ensemble of particles. A more detailed way would be to generate the particle ensembles and apply the same complicated unfolding procedure used by the experimentalist to obtain the v_n distribution, but this procedure would be an unnecessary complication for the purpose of this work.

III. RESULTS

In this work we consider Au + Au collisions at $\sqrt{s_{NN}} = 200$ GeV. All the results shown in this paper are for positively charged pions. For each centrality class a total of 2000 events were computed. The Fourier coefficients and the initial-state anisotropies were calculated according to

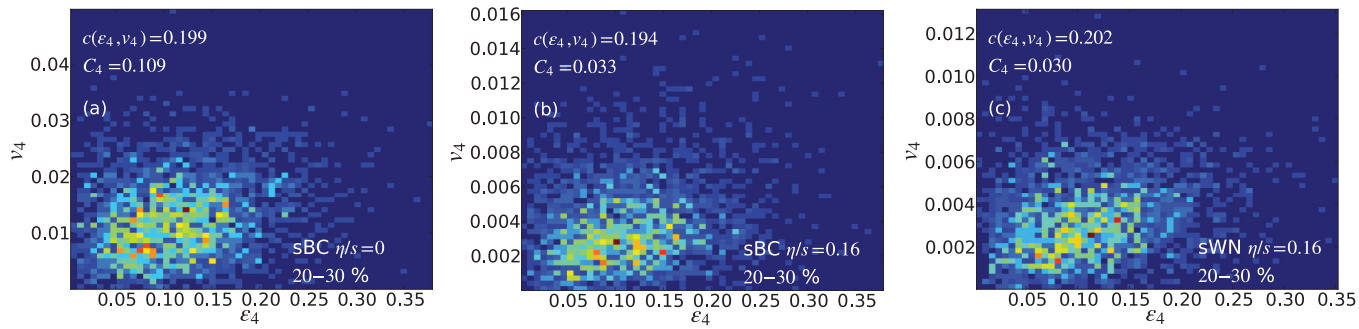

FIG. 3. (Color online) ϵ_4 and v_4 of pions in the 20–30% centrality class using different initializations and viscosities. (a) sBC and $\eta/s = 0$, (b) sBC and $\eta/s = 0.16$, and (c) sWN and $\eta/s = 0.16$.

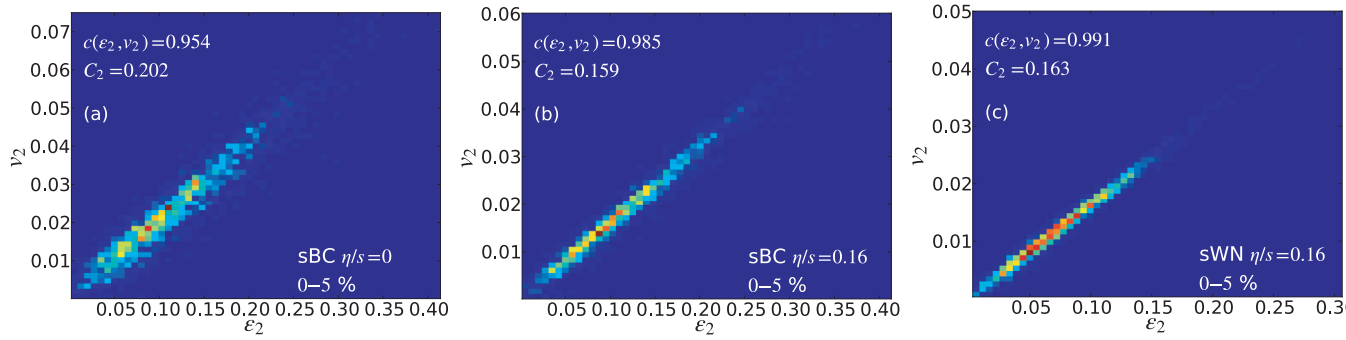

FIG. 4. (Color online) ϵ_2 and v_2 in the 0–5% centrality class using different initializations and viscosities. (a) sBC and $\eta/s = 0$, (b) sBC and $\eta/s = 0.16$, and (c) sWN and $\eta/s = 0.16$.

Eqs. (1) and (2), respectively. In the following, we consider two constant values for the shear viscosity to entropy density ratio, $\eta/s = 0$ and 0.16.

A. Correlations

As mentioned in the Introduction, it has been known for a long time that the event averaged v_2, and the eccentricity of the averaged initial state, ϵ_2 are approximately linearly related [2]. Similar relation has been found for ϵ_3 and the average v_3 but not for ϵ_4 and v_4 [20,21]. Here we study whether similar relations hold event-by-event by evaluating the linear correlation between the harmonics v_n and ϵ_n. We use the linear correlation coefficient,

$$c(a,b) = \left\langle \frac{(a - \langle a\rangle_{\rm ev})(b - \langle b\rangle_{\rm ev})}{\sigma_a \sigma_b} \right\rangle_{\rm ev}, \tag{8}$$

where σ_a is the standard deviation of the quantity a. This correlation function is 1 (-1) if a and b are linearly (antilinearly) correlated and zero in the absence of linear correlation. A similar study was done in Ref. [8], but using a slightly different definition of the correlator.

The two-dimensional histograms in Figs. 1–3 show the correlations between ϵ_2 and v_2, ϵ_3 and v_3, and ϵ_4 and v_4, respectively, for the 20–30% centrality class. To study the effect of both viscosity and initialization on these correlations, we show the correlations in three different cases: (a) sBC initialization with $\eta/s = 0$, (b) sBC initialization with $\eta/s = 0.16$, and (c) sWN initialization with $\eta/s = 0.16$.

As can be seen in these figures, the v_2 and v_3 coefficients display a strong linear correlation to their corresponding initial-state coefficients for all cases considered. This is confirmed by the values of the linear correlation coefficient $c(v_2, \epsilon_2) \sim c(v_3, \epsilon_3) \sim 1$, as shown in the figures (top left corner). As for any two variables we can write

$$v_n = C_n \epsilon_n + \delta_n, \tag{9}$$

where $C_n = \langle v_n\rangle_{\rm ev}/\langle \epsilon_n\rangle_{\rm ev}$, and consequently, $\langle \delta_n\rangle_{\rm ev} = 0$. The values of C_n are shown in Figs. 1 and 2. For $n = 2$ a linear relation, $v_2 = C_2\epsilon_2$, is approximately satisfied event by event with only $\sim$10% deviations from this relation at a given ϵ_2. On the other hand, an event-by-event linear relation between v_3 and ϵ_3 is not satisfied well, with v_3 deviating $\sim$50% from $v_3 = C_3\epsilon_3$ at a given ϵ_3.

In all the cases considered above, there is basically no linear correlation between ϵ_4 and v_4, see Fig. 3. At least one reason for this behavior is that there is also correlation between ϵ_2^2 and v_4, which can be of the same order or larger than $c(\epsilon_4, v_4)$: $c(\epsilon_2^2, v_4) = 0.40$ (sBC, $\eta/s = 0$), $c(\epsilon_2^2, v_4) = 0.69$ (sBC, $\eta/s = 0.16$), and $c(\epsilon_2^2, v_4) = 0.46$ (sWN, $\eta/s = 0.16$). This is a nonlinear effect triggered by the coupling between two different Fourier coefficients, i.e., $n = 2$ and $n = 4$, and a linear combination of these two components was found to be a good estimator for v_4 [22].

As expected, the proportionality coefficients C_n are sensitive to the value of the shear viscosity. This can be seen by comparing Figs. 1(a) and 1(b) $(n = 2)$, Figs. 2(a) and 2(b)

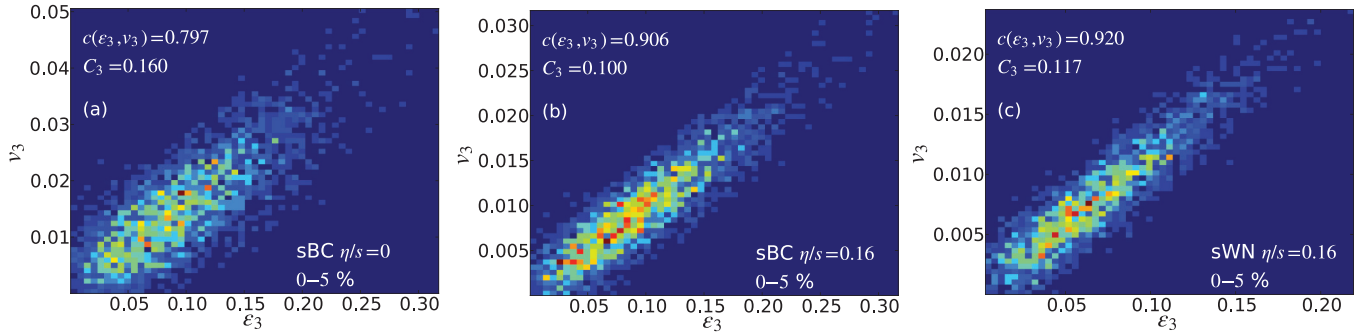

FIG. 5. (Color online) ϵ_3 and v_3 in the 0–5% centrality class using different initializations and viscosities. (a) sBC and $\eta/s = 0$, (b) sBC and $\eta/s = 0.16$, and (c) sWN and $\eta/s = 0.16$.

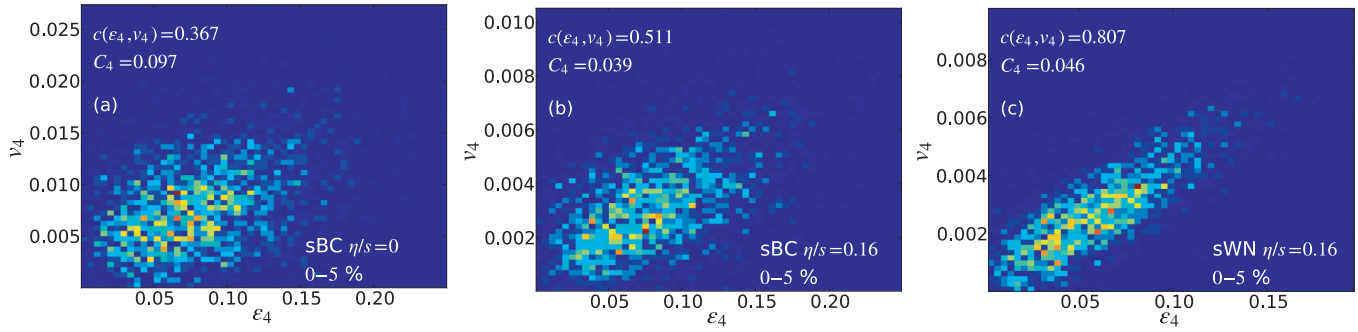

FIG. 6. (Color online) ϵ_4 and v_4 in the 0–5% centrality class using different initializations and viscosities. (a) sBC and $\eta/s = 0$, (b) sBC and $\eta/s = 0.16$, and (c) sWN and $\eta/s = 0.16$.

($n = 3$), and Figs. 3(a) and 3(b) ($n = 4$). In general, the higher Fourier coefficients are expected to be more sensitive to the viscosity [20]. This is also the case in our calculations, and is confirmed by comparing the relative changes in the coefficients C_2, C_3 and C_4.

Note that the proportionality constants C_n do not depend only on the intrinsic properties of the fluid, but also on the initial conditions. Again something to be expected, since in the calculations done using averaged initial conditions, the precise value of the proportionality depended on many details as discussed in the Introduction.

In Figs. 4 and 5 we show the two-dimensional histograms of ϵ_2 and v_2 and of ϵ_3 and v_3, respectively, in the 0–5% centrality class. We plot the same cases considered above: (a) sBC initialization with $\eta/s = 0$, (b) sBC initialization with $\eta/s = 0.16$, and (c) sWN initialization with $\eta/s = 0.16$. For $n = 2$ and $n = 3$ the linear correlation is still valid. Also, the effect of shear viscosity and initialization on C_n remain qualitatively the same. On the other hand, in Fig. 6 the correlation between ϵ_4 and v_4 in central collisions is drastically different from the correlation in the 20–30% centrality class. In the 0–5% centrality class the linear correlation coefficient $c(\epsilon_4, v_4)$ becomes much closer to 1 when compared to the peripheral case. It can be as large as ∼0.81 obtained for the sWN initialization with $\eta/s = 0.16$. This behavior is expected since in Ref. [22] it was shown that ϵ_4 becomes a better estimator for v_4 in central collisions.

We note that the definition of ε_n is not unique, but we could use, e.g., entropy density instead of energy density as a weight or use different powers of r in the definition. We have checked that these different definitions slightly change the numerical values of the correlators, and the proportionality constants C_n, but qualitatively the results are independent of the precise definition of ε_n.

B. Distributions of v_n

So far the event-averaged values of v_n have been extensively studied. In order to observe what can be learned by looking at v_n probability distributions, it is convenient to remove the average from the distributions, and study the relative fluctuations using the scaled variables

$$\delta v_n = \frac{v_n - \langle v_n \rangle_{\rm ev}}{\langle v_n \rangle_{\rm ev}}, \quad \text{and} \quad \delta\epsilon_n = \frac{\epsilon_n - \langle \epsilon_n \rangle_{\rm ev}}{\langle \epsilon_n \rangle_{\rm ev}}. \tag{10}$$

In this way changes in the probability distributions due to changes in the average values are removed.

It was shown in the previous subsection that v_n and ϵ_n have a strong linear correlation for $n = 2$ and 3. As discussed in the Appendix, if two variables are linearly correlated, and $\langle d \rangle = 0$, the variances of the relative distributions are equal. Since viscosity has only a small effect on the correlations of v_n and ϵ_n, we expect that $\sigma^2_{\delta v_n} \approx \sigma^2_{\delta\epsilon_n}$, independent of viscosity. In such a case the information about the fluid response to the initial geometry is contained in the coefficients C_n controlling the average $\langle v_n \rangle_{\rm ev}$, while the relative fluctuations of v_n originate

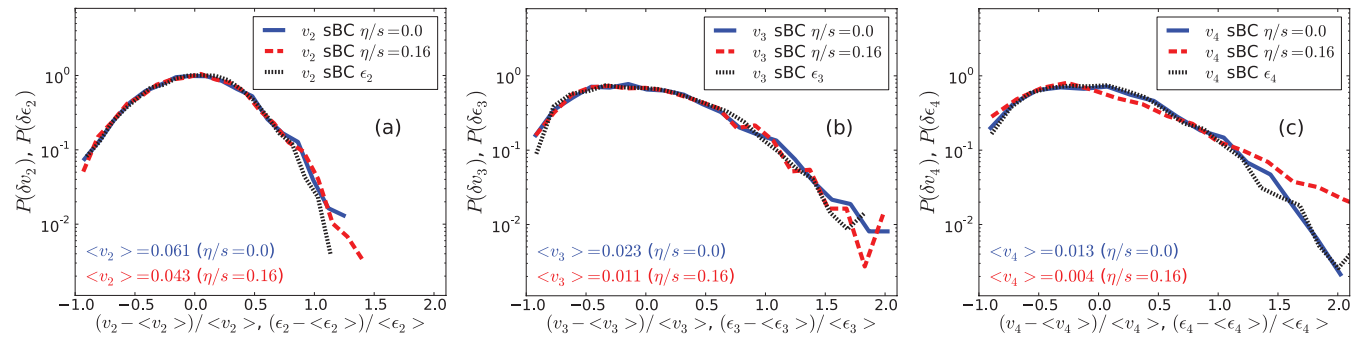

FIG. 7. (Color online) Probability distributions: (a) $P(\delta v_2)$ and $P(\delta\epsilon_2)$, (b) $P(\delta v_3)$ and $P(\delta\epsilon_3)$, and (c) $P(\delta v_4)$ and $P(\delta\epsilon_4)$, in the 20–30% centrality class with sBC initialization and two different values of η/s, $\eta/s = 0$, and $\eta/s = 0.16$.

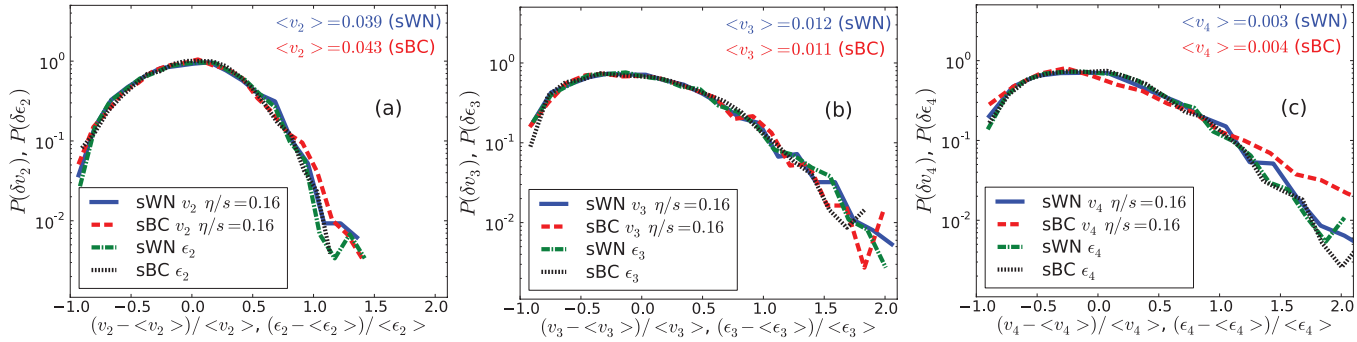

FIG. 8. (Color online) Probability distributions: (a) $P(\delta v_2)$ and $P(\delta\epsilon_2)$, (b) $P(\delta v_3)$ and $P(\delta\epsilon_3)$, and (c) $P(\delta v_4)$ and $P(\delta\epsilon_4)$, in the 20–30% centrality class with $\eta/s = 0.16$ and two different initial conditions, sBC and sWN.

from the relative fluctuations of ϵ_n and do not depend on viscosity of the fluid.

To test this assumption, and to see whether similarity extends beyond variances, we plot the probability distributions $P(\delta v_n)$ and $P(\delta\epsilon_n)$ in 20–30% centrality class in Fig. 7 using the sBC initialization and two values of viscosity, $\eta/s = 0$ and 0.16. As seen in panel (a) for $n = 2$ and in panel (b) for $n = 3$, not only the variances are similar, but the entire distributions are almost identical. Figure 7(c) depicts the relative distributions for $n = 4$, and surprisingly they are very similar even if v_4 and ϵ_4 are not linearly correlated. There are deviations only at the tail of the distribution. As discussed in the Appendix, lack of correlation leads to a large spread of possible values of v_4 at given ϵ_4 which tends to make δv_4 distribution wider, but this effect can be canceled by other terms. How these terms arise is an interesting question beyond the scope of this paper.

To check whether the similarity of $P(\delta v_n)$ and $P(\delta\epsilon_n)$ is only a coincidence based on the sBC initialization, we show in Fig. 8 the distributions using both sBC and sWN initialization, but using only one value of viscosity, $\eta/s = 0.16$. Again, panels (a), (b), and (c) depict cases with $n = 2$, 3, and 4, respectively. $P(\delta v_n)$ and $P(\delta\epsilon_n)$ are almost equal for both initializations. The distributions $P(\delta\epsilon_n)$ are also similar for both initializations, but this is because both Glauber-type initializations give rise to the same relative fluctuations of initial state anisotropies, see discussion in Ref. [23].

These results are valid in the 0–5% centrality class as well. We have also checked that $P(\delta v_n)$ is not sensitive to the freeze-out temperature within interval $100 < T_{\rm fo} < 160$ MeV. Thus the distribution of relative fluctuations of v_n could be the ideal observable to study the fluctuations of the initial geometry. If fluid dynamics provides a correct description of heavy-ion collisions, $P(\delta v_n)$ is a direct measurement of the initial state anisotropy fluctuations and can be compared directly to initial condition models, such as Monte Carlo Glauber or various implementations of color-glass condensate based initial conditions [24].

C. (v_n, v_m) linear correlations

We computed the linear correlation coefficients, $c(v_2, v_3)$, $c(v_2, v_4)$, and $c(v_3, v_4)$ as a function of the transverse momentum, p_T. We found that $c(v_2, v_3) \sim c(v_3, v_4) \sim 0$ and, therefore, are not *linearly* correlated. These correlations are shown in Figs. 9(a) and 9(b). We also show the values of the correlation coefficient between the integrated v_n's and of the coefficients ϵ_n in Table I. It should be noted that, even though both Glauber initializations used in this paper have the same relative anisotropy fluctuations, their correlations differ.

Figure 9(c) shows the correlation coefficient between v_2 and v_4 as a function of p_T. As can be read off from the figure, $c(v_2, v_4)$ depends strongly on η/s and, consequently, is sensitive to the properties of the QGP. It is strongly sensitive to the decoupling temperature as well, with the larger temperature

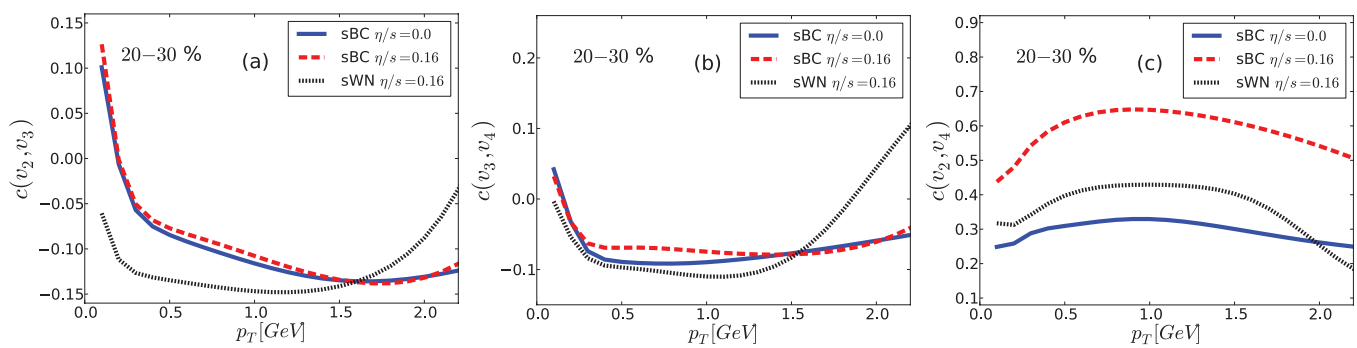

FIG. 9. (Color online) Correlations: (a) $c(v_2, v_3)$, (b) $c(v_3, v_4)$, and (c) $c(v_2, v_4)$, as function of transverse momentum in the 20–30% centrality class using different initializations and viscosities.

TABLE I. Linear correlation coefficients for p_T -integrated v_n's and ϵ_n's in the 20−30% centrality class.

	$c(\epsilon_2, \epsilon_3)$	$c(v_2, v_3)$	$c(\epsilon_2, \epsilon_4)$	$c(v_2, v_4)$	$c(\epsilon_3, \epsilon_4)$	$c(v_3, v_4)$
sBC $\eta/s = 0.0$	−0.09	−0.11	0.26	0.32	−0.03	−0.11
sBC $\eta/s = 0.16$	−0.09	−0.11	0.25	0.63	−0.03	−0.09
sWN $\eta/s = 0.16$	−0.15	−0.14	−0.04	0.42	0.03	−0.11

leading to weaker correlation, but the width of the hot spots [value of σ in Eq. (4)] affects the correlation only weakly. This correlation function is also strongly affected by the correlation between ϵ_2 and ϵ_4 in the initial state, i.e., initial conditions with different $c(\epsilon_2, \epsilon_4)$ lead to very different $c(v_2, v_4)$, see the dashed and dotted lines in Fig. 9(c). Overall, just like v_2 probes the fluid-dynamical response to an initial geometry (characterized by ϵ_2), $c(v_2, v_4)$ probes the fluid-dynamical response to correlations in the initial geometry [in this case characterized by $c(\epsilon_2, \epsilon_4)$].

In our investigations, $c(v_2, v_4)$ is the only correlation that was sensitive to both the fluctuations of the initial condition and the transport properties of the fluid. This correlation can thus be used as a further constraint to the fluid-dynamical models applied to heavy-ion collisions.

IV. CONCLUSIONS

In this paper, we studied the relation between v_n and ϵ_n in ultrarelativistic heavy-ion collisions using event-by-event fluid dynamics. We confirmed that the second and third Fourier coefficients have a strong linear correlation to the initial geometry of the collision. We showed that while the event-average Fourier coefficients, $\langle v_n \rangle_{\rm ev}$, $n = 2$, 3, and 4, are sensitive to the details of the fluid-dynamical evolution, their relative fluctuations, $\delta v_n = (v_n - \langle v_n \rangle_{\rm ev})/\langle v_n \rangle_{\rm ev}$, are determined solely by the fluctuations of the corresponding initial state anisotropy coefficients, with basically no sensitivity to the viscosity of the fluid. This makes the distribution of δv_n a direct probe of the initial condition of a heavy-ion collision, providing a direct and clean measurement of the distribution of the relative fluctuations of the initial anisotropy, i.e.,

$$P(\delta v_n) \simeq P(\delta \epsilon_n), \qquad n = 2, 3, 4. \tag{11}$$

Surprisingly, this relation was shown to be true even for the relative fluctuations of v_4, even though v_4 itself is not linearly correlated to ϵ_4.

Although the two different limits of the Glauber model considered here give rise to very similar relative fluctuations of ϵ_n [23], the different variants of the color glass condensate models lead to different relative fluctuations, see Refs. [10,11]. Therefore, by measuring the distributions of δv_n one can directly distinguish between these models.

Furthermore we found that the linear correlations between the flow harmonics v_n are not solely dominated by the initial conditions. Especially the correlation function $c(v_2, v_4)$ is sensitive to the viscosity of the fluid providing an additional constraint for the model when one tries to extract the viscosity coefficient from the data.

ACKNOWLEDGMENTS

The authors thank M. Gyulassy, J. Jia, D. H. Rischke, and W. A. Zajc for discussions. The work of H.N. was supported by Academy of Finland, Project No. 133005, G.S.D. by Helmholz Research School H-QM and by the Natural Sciences and Engineering Research Council of Canada, H.H. by the ExtreMe Matter Institute (EMMI), and P.H. by BMBF under Contract No. 06FY9092. We acknowledge CSC — IT Center for Science in Espoo, Finland, for the allocation of computational resources.

APPENDIX: RELATIVE WIDTHS OF CORRELATED DISTRIBUTIONS

A relation between variables ϵ and v (we omit the indexes n here) can be written as

$$v = k\epsilon + d. \tag{A1}$$

If we define

$$k = \frac{\sigma_v}{\sigma_\epsilon} c(\epsilon, v), \tag{A2}$$

where $c(\epsilon, v)$ is the linear correlator [Eq. (8)], ϵ and d are not linearly correlated, $c(\epsilon, d) = 0$. It also follows that

$$\sigma_d^2 = \sigma_v^2 (1 - c(\epsilon, v)^2), \tag{A3}$$

i.e., the stronger the linear (anti)correlation between ϵ and d, the narrower the distribution of d.

For the distributions of the scaled variables, $\delta x = (x - \langle x \rangle)/\langle x \rangle$, it holds that $\sigma_{\delta x} = \sigma_x/\langle x \rangle$, and that $\langle \delta x \rangle = 0$. The variance of δv can now be written as

$$\begin{aligned} \sigma_{\delta v}^2 &= \frac{1}{\langle v \rangle^2} \left[k^2 \sigma_\epsilon^2 + 2k\sigma_\epsilon \sigma_d c(\epsilon, d) + \sigma_d^2 \right] \\ &= \frac{\sigma_\epsilon^2}{\langle \epsilon \rangle^2} \left[\frac{\langle \epsilon \rangle^2}{\langle v \rangle^2} k^2 + \frac{\langle \epsilon \rangle^2}{\langle v \rangle^2} \frac{\sigma_d^2}{\sigma_\epsilon^2} \right] \\ &= \sigma_{\delta\epsilon}^2 \left[\frac{1}{\left(1 + \frac{\langle d \rangle}{k \langle \epsilon \rangle}\right)^2} + \frac{\langle \epsilon \rangle^2}{\langle v \rangle^2} \frac{\sigma_d^2}{\sigma_\epsilon^2} \right]. \end{aligned} \tag{A4}$$

As mentioned, if $c(\epsilon, v) \approx 1$, $\sigma_d \approx 0$, and the last term in Eq. (A4) is negligible. If also $\langle d \rangle \approx 0$, $\sigma_{\delta v} \approx \sigma_{\delta\epsilon}$. Roughly speaking the requirement $\langle d \rangle \approx 0$ means that when $\epsilon \to 0$, $\langle v \rangle \approx 0$—a requirement our distributions with $n = 2$ and 3 fulfill as seen in Figs. 1, 2, 4, and 5. On the other hand, the correlation is weak for $n = 4$ in the 20–30% centrality class. In that case the d distribution is wide, but $\langle d \rangle \neq 0$ as well, and the two terms in Eq. (A4) sum to approximately one, and the distributions of $\delta\epsilon$ and δv are equal even in that case.

[1] M. Gyulassy and L. McLerran, Nucl. Phys. A **750**, 30 (2005).
[2] P. F. Kolb and U. W. Heinz, in *Quark Gluon Plasma 3*, edited by R. C. Hwa and X.-N. Wang (World Scientific, Singapore, 2004), pp. 634–714.
[3] H. Song and U. W. Heinz, Phys. Rev. C **78**, 024902 (2008).
[4] P. Huovinen, in [2], pp. 600–633.
[5] C. E. Aguiar, Y. Hama, T. Kodama, and T. Osada, Nucl. Phys. A **698**, 639 (2002); O. Socolowski, Jr., F. Grassi, Y. Hama, and T. Kodama, Phys. Rev. Lett. **93**, 182301 (2004); R. Andrade, F. Grassi, Y. Hama, T. Kodama, and O. Socolowski, Jr., *ibid.* **97**, 202302 (2006); J. Takahashi, B. M. Tavares, W. L. Qian, R. Andrade, F. Grassi, Y. Hama, T. Kodama, and N. Xu, *ibid.* **103**, 242301 (2009).
[6] B. Alver and G. Roland, Phys. Rev. C **81**, 054905 (2010); **82**, 039903 (2010).
[7] B. Schenke, S. Jeon, and C. Gale, Phys. Rev. Lett. **106**, 042301 (2011); Phys. Lett. B **702**, 59 (2011); Phys. Rev. C **85**, 024901 (2012); Z. Qiu and U. W. Heinz, Phys. Lett. B **717**, 261 (2012); Z. Qiu, C. Shen, and U. Heinz, *ibid.* **707**, 151 (2012); H. Petersen, G.-Y. Qin, S. A. Bass, and B. Muller, Phys. Rev. C **82**, 041901(R) (2010); H. Petersen, V. Bhattacharya, S. A. Bass, and C. Greiner, *ibid.* **84**, 054908 (2011); H. Petersen, *ibid.* **84**, 034912 (2011); P. Bozek and W. Broniowski, *ibid.* **85**, 044910 (2012); Phys. Rev. Lett. **109**, 062301 (2012); P. Bozek, Phys. Lett. B **717**, 287 (2012); D. Teaney and L. Yan, Phys. Rev. C **86**, 044908 (2012); J. Jia and D. Teaney, arXiv:1205.3585 [nucl-ex]; D. Teaney and L. Yan, Phys. Rev. C **83**, 064904 (2011).
[8] A. K. Chaudhuri, Phys. Lett. B **713**, 91 (2012).
[9] H. Holopainen, H. Niemi, and K. J. Eskola, Phys. Rev. C **83**, 034901 (2011); Nucl. Phys. A **855**, 486 (2011); J. Phys. G **38**, 124164 (2011).
[10] J. Jia (ATLAS Collaboration), arXiv:1209.4232 [nucl-ex].
[11] C. Gale, S. Jeon, B. Schenke, P. Tribedy, and R. Venugopalan, Phys. Rev. Lett. **110**, 012302 (2013).
[12] M. Alvioli, H. Holopainen, K. J. Eskola, and M. Strikman, Phys. Rev. C **85**, 034902 (2012); PoS QNP (2012) 172.
[13] H. Niemi, G. S. Denicol, P. Huovinen, E. Molnar, and D. H. Rischke, Phys. Rev. C **86**, 014909 (2012); Phys. Rev. Lett. **106**, 212302 (2011).
[14] P. Huovinen and P. Petreczky, Nucl. Phys. A **837**, 26 (2010).
[15] W. Israel and J. M. Stewart, Phys. Lett. A **58**, 213 (1976); Ann. Phys. (NY) **118**, 341 (1979); Proc. Roy. Soc. London A **365**, 43 (1979).
[16] G. S. Denicol, H. Niemi, E. Molnar, and D. H. Rischke, Phys. Rev. D **85**, 114047 (2012).
[17] G. S. Denicol, T. Koide, and D. H. Rischke, Phys. Rev. Lett. **105**, 162501 (2010).
[18] E. Molnar, H. Niemi, and D. H. Rischke, Eur. Phys. J. C **65**, 615 (2010).
[19] F. Cooper and G. Frye, Phys. Rev. D **10**, 186 (1974).
[20] B. H. Alver, C. Gombeaud, M. Luzum, and J.-Y. Ollitrault, Phys. Rev. C **82**, 034913 (2010).
[21] Z. Qiu and U. W. Heinz, Phys. Rev. C **84**, 024911 (2011).
[22] F. G. Gardim, F. Grassi, M. Luzum, and J.-Y. Ollitrault, Phys. Rev. C **85**, 024908 (2012).
[23] W. Broniowski, P. Bozek, and M. Rybczynski, Phys. Rev. C **76**, 054905 (2007).
[24] A. Adil, H.-J. Drescher, A. Dumitru, A. Hayashigaki, and Y. Nara, Phys. Rev. C **74**, 044905 (2006); H.-J. Drescher and Y. Nara, *ibid.* **75**, 034905 (2007); **76**, 041903(R) (2007); Y. Nara, Prog. Theor. Phys. Suppl. **193**, 145 (2012); A. Dumitru and Y. Nara, Phys. Rev. C **85**, 034907 (2012); B. Schenke, P. Tribedy, and R. Venugopalan, Phys. Rev. Lett. **108**, 252301 (2012).

PAPER

Sensitivity of the elliptic flow to a temperature-dependent shear viscosity-to-entropy density ratio

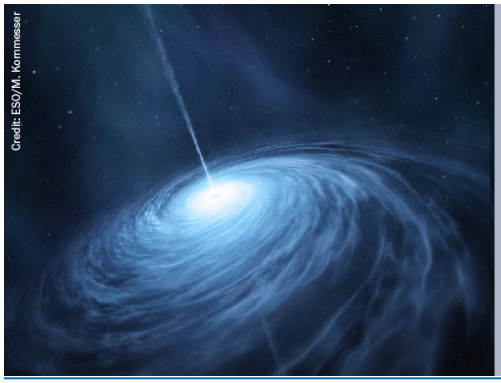

J. Phys. G: Nucl. Part. Phys. **38** (2011) 124050 (5pp) doi:10.1088/0954-3899/38/12/124050

Sensitivity of the elliptic flow to a temperature-dependent shear viscosity-to-entropy density ratio

H Niemi[1], G S Denicol[2], P Huovinen[2], E Molnár[1,3] and D H Rischke[1,2]

[1] Frankfurt Institute for Advanced Studies, Ruth-Moufang-Str. 1, D-60438 Frankfurt am Main, Germany
[2] Institut für Theoretische Physik, Johann Wolfgang Goethe-Universität, Max-von-Laue-Str. 1, D-60438 Frankfurt am Main, Germany
[3] MTA-KFKI, Research Institute for Particle and Nuclear Physics, H-1525 Budapest, PO Box 49, Hungary

E-mail: niemi@th.physik.uni-frankfurt.de

Received 7 July 2011
Published 10 November 2011
Online at stacks.iop.org/JPhysG/38/124050

Abstract
We investigate the effects of a temperature-dependent shear viscosity over entropy density ratio η/s, with a minimum near the phase transition, on the elliptic flow of hadrons in ultrarelativistic heavy-ion collisions at the RHIC and the LHC. We find that the suppression of the elliptic flow in Au+Au collisions at the RHIC is dominated by the viscosity in hadronic matter and in the phase transition region, but insensitive to the viscosity of the quark–gluon plasma (QGP). However, at the highest LHC energy, the elliptic flow becomes sensitive to the shear viscosity of the QGP and insensitive to the hadronic viscosity.

(Some figures may appear in colour only in the online journal)

1. Introduction

At present, most works aiming for the determination of the shear viscosity of strongly interacting matter assume a constant shear viscosity over entropy density ratio, η/s. However, this ratio can be a strongly varying function of temperature both in hadronic matter and in the quark–gluon plasma (QGP). In this work, we study the consequences of relaxing the assumption of a constant η/s on the elliptic flow of hadrons in Au+Au collisions at the RHIC and in Pb+Pb collisions at the LHC [1].

We model the spacetime evolution of the matter formed in heavy-ion collisions using the relativistic dissipative hydrodynamical theory of Israel and Stewart [2]. We assume longitudinal boost-invariance and neglect the net-baryon number. Essential inputs are the equation of state, the initial conditions and the transport coefficients. We consider here only the shear viscosity.

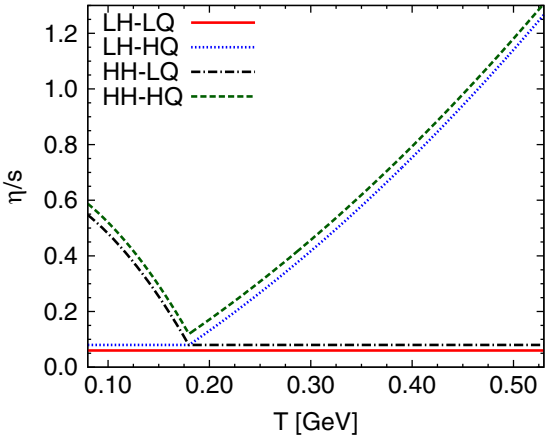

Figure 1. η/s parametrizations.

As equation of state we use the recent lattice parametrization of [3], with chemical freeze-out at $T = 150$ MeV. We take the initial energy density at $\tau_0 = 1.0$ fm (RHIC) and at $\tau_0 = 0.6$ fm (LHC) to be proportional to the density of binary nucleon–nucleon collisions in the transverse plane. The collision density is calculated by using the optical Glauber model. The maximum energy density is fixed to reproduce the measured multiplicity in the most central collisions [4, 5]. For $\sqrt{s_{NN}} = 5.5$ TeV Pb+Pb collisions we use the multiplicity predicted by the minijet + saturation model [6]. In order to compensate for different entropy production for different parametrizations of the shear viscosity, the initial energy density profiles are normalized differently for each parametrization of η/s. Freeze-out is calculated using the Cooper–Frye formula [7] on a constant-temperature hypersurface. The decoupling temperature is chosen to be $T_{\rm dec} = 100$ MeV.

For η/s, we consider the four different parametrizations shown in figure 1. Note that the minimum value of η/s is fixed to be $\eta/s = 0.08$ at $T = 180$ MeV for all parametrizations. The relaxation time in the Israel–Stewart formalism is taken to be $\tau_R = 5\eta/(e + p)$, where e and p are the local energy density and pressure, respectively.

2. Results

Figure 2 shows pion, kaon and proton spectra in the 0–5% most central $\sqrt{s_{NN}} = 200$ GeV Au+Au collisions at the RHIC. Our results are compared to PHENIX data [4]. All four η/s parametrizations give very similar results.

The elliptic flow coefficients, $v_2(p_T)$, for charged hadrons in four different centrality classes at the RHIC are shown in figure 3. The results are compared to STAR data [8]. We observe that the high-temperature part of η/s has practically no effect on the results. On the other hand, the viscous suppression of $v_2(p_T)$ is strongly enhanced if we increase the hadronic η/s. The same qualitative pattern is observed in all centrality classes, but the hadronic suppression is even stronger in more peripheral collisions. In these cases, the dominant contributions to the suppression are the viscous corrections to the hadron distribution functions.

Figure 4 shows $v_2(p_T)$ in $\sqrt{s_{NN}} = 2.76$ TeV Pb+Pb collisions at the LHC. The data are from the ALICE Collaboration [9]. In these collisions both hadronic and QGP viscosity have

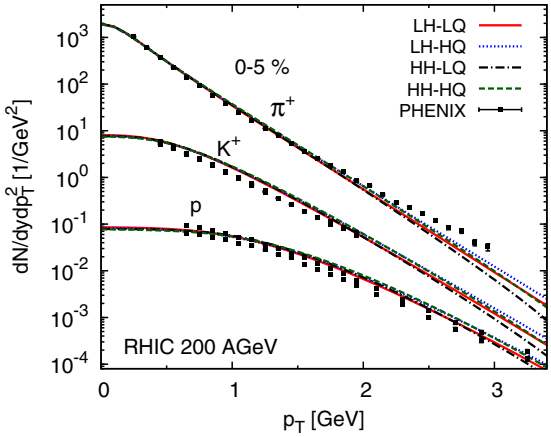

Figure 2. p_T-spectra at the RHIC.

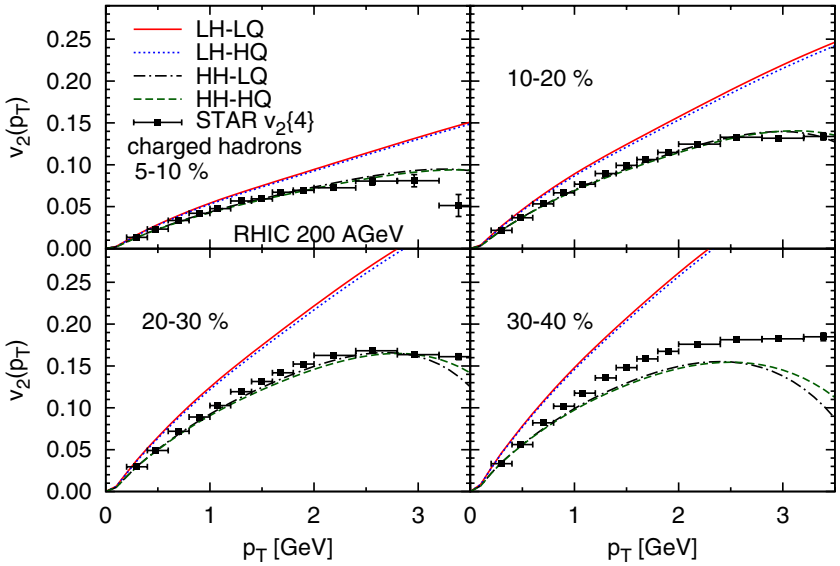

Figure 3. Centrality dependence of $v_2(p_T)$ in $\sqrt{s_{NN}} = 200$ GeV Au+Au collisions at the RHIC.

a similar impact. Only in the most peripheral collisions does the suppression by the hadronic viscosity begin to dominate over that from the QGP viscosity.

The elliptic flows in the 5–10% and 20–30% centrality classes are shown in figure 5 for $\sqrt{s_{NN}} = 5.5$ TeV Pb+Pb collisions. At the highest LHC energy the situation is reversed compared to collisions at the RHIC. In both centrality classes $v_2(p_T)$ is almost independent of the hadronic η/s, but sensitive to the high-temperature viscosity.

In summary, we have investigated the suppression of elliptic flow due to the shear viscosity. We found that the dominant temperature range that contributes to the suppression varies with the collision energy. At the RHIC the suppression is mostly because of hadronic η/s, while it is almost independent of the high-temperature η/s. In the highest energy collisions at the

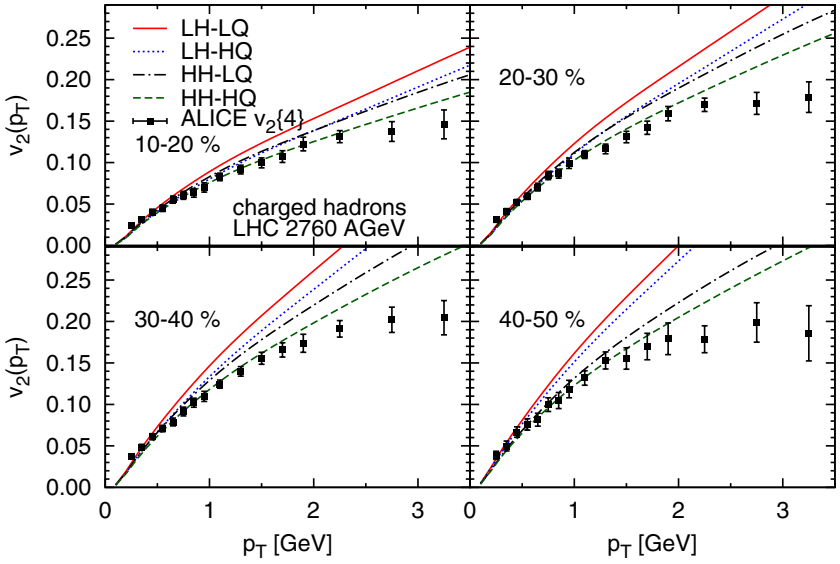

Figure 4. Centrality dependence of $v_2(p_T)$ in $\sqrt{s_{NN}} = 2.76$ TeV Pb+Pb collisions at the LHC.

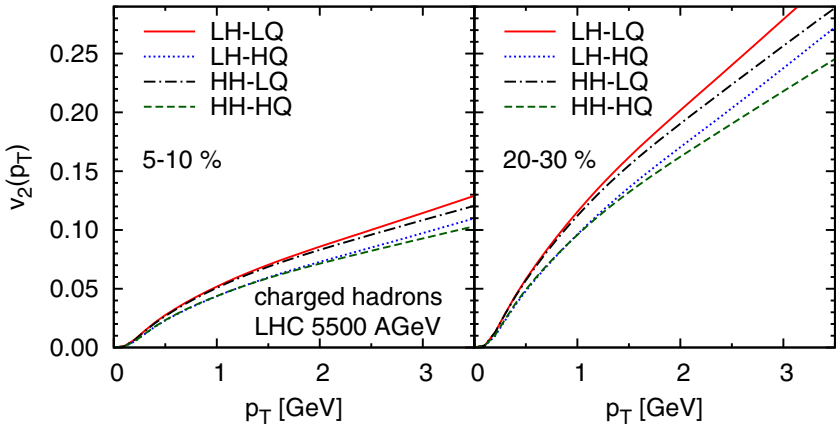

Figure 5. Centrality dependence of $v_2(p_T)$ in $\sqrt{s_{NN}} = 5.5$ TeV Pb+Pb collisions at the LHC.

LHC the situation is reversed: the elliptic flow is almost independent of the hadronic η/s, but sensitive to the high-temperature η/s. This opens the possibility of determining the temperature dependence of the shear viscosity from experimental data.

Acknowledgments

This work was supported by the Helmholtz International Center for FAIR within the framework of the LOEWE program launched by the State of Hesse. The work of PH and HN was supported by the Extreme Matter Institute (EMMI). PH is also supported by BMBF under contract no 06FY9092. EM is supported by OTKA/NKTH 81655 and the AvH foundation.

References

[1] Niemi H, Denicol G S, Huovinen P, Molnar E and Rischke D H 2011 *Phys. Rev. Lett.* **106** 212302
[2] Israel W and Stewart J M 1979 *Proc. R. Soc.* A **365** 43
Israel W and Stewart J M 1979 *Ann. Phys.* **118** 341
[3] Huovinen P and Petreczky P 2010 *Nucl. Phys.* A **837** 26
[4] Adler S S *et al* (PHENIX Collaboration) 2004 *Phys. Rev.* C **69** 034909
[5] Aamodt K *et al* (The ALICE Collaboration) 2010 *Phys. Rev. Lett.* **105** 252301
[6] Eskola K J *et al* 2005 *Phys. Rev.* C **72** 044904
[7] Cooper F and Frye G 1974 *Phys. Rev.* D **10** 186
[8] Bai Y 2007 *PhD Thesis* Nikhef and Utrecht University, The Netherlands
Tang A (STAR Collaboration) 2008 arXiv:0808.2144 [nucl-ex]
[9] Aamodt K *et al* (The ALICE Collaboration) 2011 *Phys. Rev. Lett.* **105** 252302

Equation of state at finite baryon density based on lattice QCD

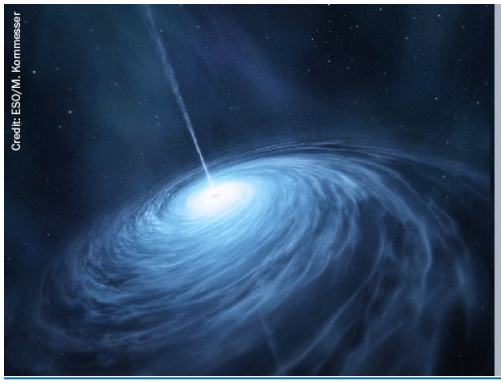

J. Phys. G: Nucl. Part. Phys. **38** (2011) 124103 (4pp) doi:10.1088/0954-3899/38/12/124103

Equation of state at finite baryon density based on lattice QCD

Pasi Huovinen[1] **and Péter Petreczky**[2]

[1] Institut für Theoretische Physik, Johann Wolfgang Goethe-Universität, 60438 Frankfurt am Main, Germany
[2] Physics Department, Brookhaven National Laboratory, Upton, NY 11973, USA

E-mail: huovinen@th.physik.uni-frankfurt.de

Received 30 June 2011
Published 10 November 2011
Online at stacks.iop.org/JPhysG/38/124103

Abstract
We employ the lattice QCD data on Taylor expansion coefficients to extend our previous parametrization of the equation of state to finite baryon density. When we take into account lattice spacing and quark mass dependence of the hadron masses, the Taylor coefficients at low temperature are equal to those of hadron resonance gas. Thus, the equation of state is smoothly connected to the hadron resonance gas equation of state at low temperatures. We also show how the elliptic flow is affected by this equation of state at the maximum SPS energy.

One of the methods to extend the lattice QCD calculations to non-zero chemical potential is Taylor expansion. In that approach, pressure is Taylor expanded in chemical potentials, and the Taylor coefficients are calculated on the lattice at zero chemical potential. In this contribution, we use the results of the most comprehensive lattice QCD analysis of the Taylor coefficients to date [1, 2] to construct a parametrization of an equation of state (EoS) for finite baryon density. As in our earlier parametrization of the EoS at zero chemical potential [3], we require that our parametrization matches smoothly to the hadron resonance gas (HRG) at low temperatures.

Taylor coefficients are simply derivatives of pressure with respect to baryon and strangeness chemical potential:

$$c_{ij}(T) = \frac{1}{i!j!}\frac{T^{i+j}}{T^4}\frac{\partial^i}{\partial\mu_B^i}\frac{\partial^j}{\partial\mu_S^j}P(T,\mu_B=0,\mu_S=0). \quad (1)$$

Purely baryonic and strange coefficients are related to quadratic and higher order fluctuations of conserved charges, whereas mixed derivatives of pressure give correlations of these charges. The second-order baryonic coefficient c_{20} is shown in the left panel of figure 1. The lattice result for c_{20}, as well as for all the other coefficients, is well below the HRG result obtained with physical masses (solid line). This discrepancy can largely be explained by the lattice discretization effects on hadron masses. When the hadron mass spectrum is modified

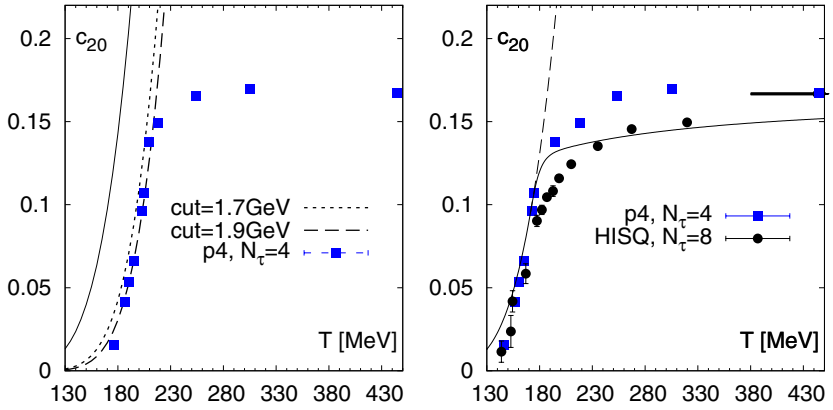

Figure 1. Left: the second-order baryonic Taylor coefficient c_{20} calculated on the lattice with p4 action [2] and compared with the HRG values with free particle (solid line) and lattice masses (dashed and dotted lines). Right: the parametrization (solid line) and HRG value (dashed) of the c_{20} coefficient compared with the shifted p4 data (see the text). The recent lattice result with the HISQ action [5] is also shown. The arrow depicts the Stefan–Boltzmann value of c_{20}.

(This figure is in colour only in the electronic version)

accordingly (for details see [4]), the HRG model reproduces the lattice data. The dashed and dotted curves in figure 1 refer to different treatment of baryonic resonances. We modify their masses in the same way as the ground-state baryons up to a threshold $m_{\rm cut}$, but keep the masses of heavier resonances in their physical values. The exact value of this threshold has only a small effect on c_{20}, but the difference between the HRG results and the HRG result with the modified hadron mass spectrum is significant. Interestingly, this difference can be accounted for by shifting the modified HRG result to lower temperature by 30 MeV. The situation is similar for other Taylor expansion coefficients [4], although the strange coefficients might favour slightly smaller shift. Based on this finding and because the lattice data agree so well with the modified HRG, we suggest that cutoff effects can be accounted for by shifting the lattice data by 30 MeV. We show the effect of such a shift in the right panel of figure 1, where we plot the HRG curve with physical masses (dashed line) and compare it with the lattice data, where all the points below 206 MeV temperature are shifted by 30 MeV and the 209 MeV point by 15 MeV. Now, the data points, which agreed well with the HRG curve with lattice masses, agree well with the HRG curve with physical masses. For further confirmation of this procedure we also plot the recent HISQ result of c_{20} [5] in figure 1 (right): at low temperatures the shifted p4 data agree with the HISQ data.

We parametrize the shifted data using an inverse polynomial of three (c_{20}), four (c_{11} and c_{02}) or five (fourth- and sixth-order coefficients) terms:

$$c_{ij}(T) = \frac{a_{1ij}}{T^{n_{1ij}}} + \frac{a_{2ij}}{T^{n_{2ij}}} + \frac{a_{3ij}}{T^{n_{3ij}}} + \frac{a_{4ij}}{T^{n_{4ij}}} + \frac{a_{5ij}}{T^{n_{5ij}}} + c_{ij}^{\rm SB}, \tag{2}$$

where $c_{ij}^{\rm SB}$ is the Stefan–Boltzmann value of the particular coefficient, and the powers n_{kij} are required to be integers between 1 and 42. As in our parametrization of the EoS at zero net baryon density [3], we match this parametrization to the HRG value at temperature $T_{\rm SW}$ by requiring that the Taylor coefficient and its first and second derivatives are continuous. Since the recent lattice data obtained using HISQ action [5] show that the second-order coefficients approach their Stefan–Boltzmann limits slowly, we require that their value is 95% of their Stefan–Boltzmann value at 800 MeV temperature. These constraints fix three (or four) of the

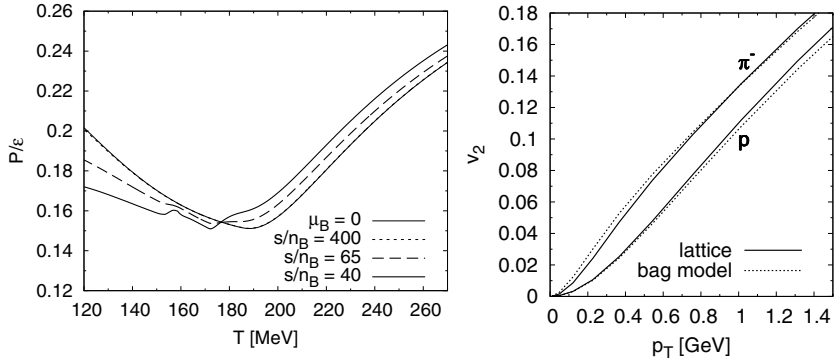

Figure 2. Left: pressure over energy density as a function of temperature on various isentropic curves with a constant entropy per baryon. Right: p_T-differential elliptic flow of pions (upper curves) and protons (lower curves) in an ideal fluid simulation of $\sqrt{s_{\rm NN}} = 17$ GeV Pb+Pb collisions at $b = 7$ fm.

parameters a_{kij}. The remaining parameters, including the switching temperatures, are fixed by a χ^2 fit to the lattice data. As an example, we show the parametrized c_{20} in the right panel of figure 1.

Once the coefficients are known, pressure can be written as

$$\frac{P}{T^4} = \sum_{ij} c_{ij}(T) \left(\frac{\mu_B}{T}\right)^i \left(\frac{\mu_S}{T}\right)^j, \tag{3}$$

and all the other thermodynamical quantities can be obtained from equation (3) by using the laws of thermodynamics. As pressure at $\mu_B = 0$, i.e. the coefficient c_{00}, we use our earlier parametrization $s95p$-v1 [3]. We describe the EoS in the left panel of figure 2 by showing the pressure to energy density ratio on various isentropic curves with a constant entropy per baryon. The curves at $s/n_B = 400$, 65 and 40 are relevant at collision energies $\sqrt{s_{\rm NN}} = 200$, 39 and 17 GeV, respectively. At $s/n_B = 400$ (dotted line), the EoS is basically identical to the EoS at $\mu_B = 0$ (thin solid line). This vindicates the common approximation of ignoring the finite net baryon density in the description of collisions at the full RHIC energy ($\sqrt{s_{\rm NN}} = 200$ GeV). At larger baryon densities, the effect of finite baryon density is no longer negligible. The larger the density, the stiffer the EoS above, and softer below the transition temperature. Furthermore, an additional structure begins to appear around the transition temperature with increasing density. This structure is mostly an unphysical artefact of our fitting procedure. We required the two first derivatives with respect to temperature to be continuous, but the speed of sound is proportional to the second derivative of the coefficients. Thus, in our parametrization, the derivative of the speed of sound is not continuous, and ripples may appear at a switching temperature of any coefficient. Nevertheless, when pressure is plotted as a function of energy density, these structures are hardly visible. Therefore, we do not expect them to affect the buildup of flow and the evolution of the system, and consider our parametrization a reasonable first attempt. The work to obtain a smoother and better constrained parametrization is in progress.

We illustrate the effect of the EoS on flow by studying the elliptic flow in the Pb+Pb collision at the full SPS collision energy ($\sqrt{s_{\rm NN}} = 17$ GeV). For simplicity, we use a boost invariant ideal hydrodynamical model to compare our lattice-based EoS to a bag model EoS with a first-order phase transition. We tune the calculation to reproduce the NA49 data

for negative hadrons and net protons in the most central collisions [6], and use freeze-out temperatures of $T_{\rm dec} = 130$ and 120 MeV for the lattice and bag model EoSs, respectively. Since it is very difficult to reproduce the elliptic flow data at SPS using ideal hydrodynamics, we do not try to fit the data. Instead, we calculate the p_T-differential v_2 of pions and protons at the fixed impact parameter of $b = 7$ fm, see the right panel of figure 2. At RHIC, the pion $v_2(p_T)$ is insensitive to the EoS, but the proton $v_2(p_T)$ shows a clear dependence on it [7]. However, at lower collision energy the behaviour is different: proton $v_2(p_T)$ is as insensitive to the EoS as the pion $v_2(p_T)$. This behaviour is supported by the early ideal fluid calculations of v_2: it was seen that at SPS both a bag model EoS and a purely hadronic EoS led to quite a similar $v_2(p_T)$ [8], but at RHIC a purely hadronic and lattice EoS led to a similar proton $v_2(p_T)$, whereas the bag model EoS lead to a smaller proton $v_2(p_T)$ [7].

To summarize, we have shown that a temperature shift of 30 MeV is a good approximation of the discretization effects in the lattice QCD data obtained using p4 action. We have constructed an EoS for finite baryon densities based on the HRG and lattice QCD data. At the full SPS energy ($\sqrt{s_{\rm NN}} = 17$ GeV), the p_T-differential elliptic flow is almost insensitive to the EoS. This is bad news for the experimental search of the critical point, since a change from a first-order phase transition to a smooth crossover does not cause an observable change in the flow.

Acknowledgments

This work was supported by BMBF under contract no 06FY9092 and by the US Department of Energy under contract DE-AC02-98CH1086.

References

[1] Miao C *et al* (RBC-Bielefeld Collaboration) 2008 *Proc. Sci.* (LATTICE2008) 172
[2] Cheng M *et al* 2009 *Phys. Rev.* D **79** 074505
[3] Huovinen P and Petreczky P 2010 *Nucl. Phys.* A **837** 26–53
[4] Huovinen P and Petreczky P 2010 *J. Phys.: Conf. Ser.* **230** 012012
[5] Bazavov A *et al* (HotQCD Collaboration) 2010 *J. Phys.: Conf. Ser.* **230** 012014
[6] Jones P G *et al* (NA49 Collaboration) 1996 *Nucl. Phys.* A **610** 188C–199C
[7] Huovinen P 2005 *Nucl. Phys.* A **761** 296–312
[8] Kolb P F, Huovinen P, Heinz U W and Heiselberg H 2001 *Phys. Lett.* B **500** 232–40

The QGP shear viscosity–elusive goal or just around the corner?

J. Phys. G: Nucl. Part. Phys. **38** (2011) 124045 (5pp) doi:10.1088/0954-3899/38/12/124045

The QGP shear viscosity – elusive goal or just around the corner?

Chun Shen[1], Steffen A Bass[2], Tetsufumi Hirano[3,4], Pasi Huovinen[5], Zhi Qiu[1], Huichao Song[6] and Ulrich Heinz[1]

[1] Department of Physics, The Ohio State University, Columbus, OH 43026, USA
[2] Department of Physics, Duke University, Durham, NC 27708, USA
[3] Department of Physics, Sophia University, Tokyo 102-8554, Japan
[4] Department of Physics, The University of Tokyo, Tokyo 113-0033, Japan
[5] ITP, J.W.Goethe-Universität, D-60438 Frankfurt am Main, Germany
[6] Lawrence Berkeley National Laboratory, Berkeley, CA 94720, USA

E-mail: heinz@mps.ohio-state.edu

Received 30 June 2011
Published 10 November 2011
Online at stacks.iop.org/JPhysG/38/124045

Abstract

With the new viscous hydrodynamic + hadron cascade hybrid code VISHNU, a rather precise ($\mathcal{O}(25\%)$) extraction of the quark gluon plasma (QGP) shear viscosity $(\eta/s)_{\rm QGP}$ from heavy-ion elliptic flow data is possible *if* the initial eccentricity of the collision fireball is known with $<5\%$ accuracy. At this point, eccentricities from initial state models differ by up to 20%, leading to an $\mathcal{O}(100\%)$ uncertainty for $(\eta/s)_{\rm QGP}$. It is shown that a simultaneous comparison of elliptic and triangular flow, v_2 and v_3, puts strong constraints on initial state models and can largely eliminate the present uncertainty in $(\eta/s)_{\rm QGP}$. The variation of the differential elliptic flow $v_2(p_T)$ for identified hadrons between RHIC and LHC energies provides additional tests of the evolution model.

(Some figures in this article are in colour only in the electronic version)

Prologue – how to measure $(\eta/s)_{\rm QGP}$. Hydrodynamics converts the initial spatial deformation of the fireball created in relativistic heavy-ion collisions into final state momentum anisotropies. Viscosity degrades the conversion efficiency $\varepsilon_x = \frac{\langle\langle y^2 - x^2\rangle\rangle}{\langle\langle y^2 + x^2\rangle\rangle} \rightarrow \varepsilon_p = \frac{\langle T^{xx} - T^{yy}\rangle}{\langle T^{xx} + T^{yy}\rangle}$ of the fluid; for a given initial fireball ellipticity ε_x, the viscous suppression of the dynamically generated total momentum anisotropy ε_p is monotonically related to the specific shear viscosity η/s. The observable most directly related to ε_p is the total charged hadron elliptic flow $v_2^{\rm ch}$ [1]. Its distribution in p_T depends on the chemical composition and p_T-spectra of the various hadron species; the latter evolve in the hadronic stage due to continuously increasing radial flow (and so does $v_2(p_T)$), even if (as expected at top LHC energy [2]) ε_p fully saturates in the quark gluon plasma (QGP) phase. When (as happens at RHIC energies) ε_p does not reach saturation before hadronization, dissipative hadronic dynamics [3] not only affects the distribution of ε_p over hadron species and p_T, but even the final value of ε_p itself, and thus of $v_2^{\rm ch}$ from which we

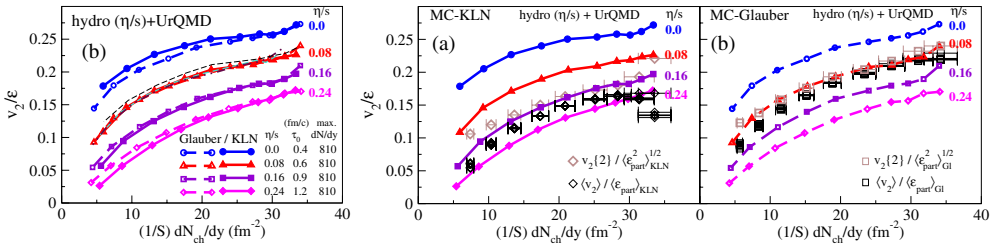

Figure 1. Centrality dependence of eccentricity-scaled elliptic flow [6].

want to extract η/s. To isolate the QGP viscosity $(\eta/s)_{\rm QGP}$, we therefore need a hybrid code that couples viscous hydrodynamics of the QGP to a realistic model of the late hadronic stage, such as `UrQMD` [4], that describes its dynamics microscopically. `VISHNU` [5] is such a code.

Extraction of $(\eta/s)_{\rm QGP}$ *from 200 A GeV Au+Au collisions at RHIC*. The left panel in figure 1 shows that such an approach yields a universal dependence of the ellipticity-scaled total charged hadron elliptic flow, $v_2^{\rm ch}/\varepsilon_x$, on the charged hadron multiplicity density per overlap area, $(1/S)(\mathrm{d}N_{\rm ch}/\mathrm{d}y)$, that depends only on $(\eta/s)_{\rm QGP}$ but not on the details of the initial state model that provides ε_x and S [6]. The pre-equilibrium flow and bulk viscous effects on these curves are small [6].

The QGP viscosity can be extracted from experimental $v_2^{\rm ch}$ data by comparing them with these universal curves. The right panels of figure 1 show this for MC-Glauber and MC-KLN initial state models [6]. In both cases, the slope of the data [7] is correctly reproduced (not true for ideal nor viscous hydrodynamics with constant η/s). Due to the $\sim$20% larger ellipticity of the MC-KLN fireballs, the magnitude of $v_{2,\rm exp}^{\rm ch}/\varepsilon_x$ differs between the two models. Consequently, the value of $(\eta/s)_{\rm QGP}$ extracted from this comparison changes by more than a factor of 2 between them. Relative to the initial fireball ellipticity, all other model uncertainties are negligible. Without constraining ε_x more precisely, $(\eta/s)_{\rm QGP}$ cannot be determined to better than a factor of 2 from elliptic flow data alone, irrespective of any other model improvements. Taking the MC-Glauber and MC-KLN models to represent a reasonable range of initial ellipticities, figure 1 gives $1 < 4\pi(\eta/s)_{\rm QGP} < 2.5$ for temperatures $T_{\rm c} < T < 2T_{\rm c}$ probed at RHIC.

`VISHNU` with $(\eta/s)_{\rm QGP}$=$\frac{1}{4\pi}$ for MC-Glauber and $\frac{2}{4\pi}$ for MC-KLN provides an excellent description of all aspects of soft ($p_T < 1.5$ GeV) hadron production (p_T-spectra and differential $v_2(p_T)$ for all charged hadrons together as well as for individual identified species) in 200 A GeV Au+Au collisions at all but the most peripheral collision centralities [8]. Such a level of theoretical control is unprecedented.

Event-by-event hydrodynamics of fluctuating fireballs. Figure 1 is based on the hydrodynamic evolution of a single smooth event-averaged initial profile ('single-shot hydrodynamics'). This overestimates the conversion efficiency v_2/ε [9, 10]. Figure 2 shows that event-by-event ideal fluid dynamical evolution of fluctuating fireballs reduces v_2/ε by a few percent [10]. The effect is only $\sim$ 5% for pions but larger for heavier hadrons. We expect it to be smaller in viscous hydrodynamics which dynamically dampens large initial fluctuations. A reduced conversion efficiency v_2/ε from event-by-event evolution will reduce the value of $(\eta/s)_{\rm QGP}$ extracted from $v_2^{\rm ch}$; based on what we see in ideal fluid dynamics, the downward shift for $(\eta/s)_{\rm QGP}$ will at most be of order 0.02–0.03.

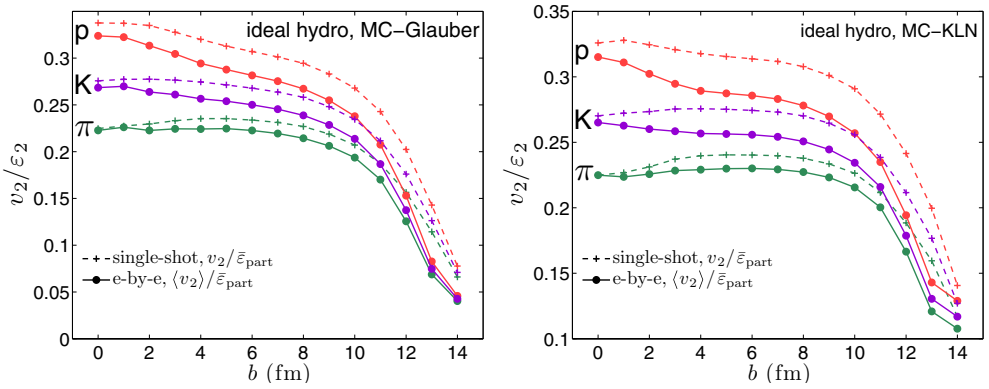

Figure 2. Eccentricity-scaled elliptic flow as a function of impact parameter for pions, kaons and protons from event-averaged ('single-shot', see the text) and event-by-event ideal fluid evolution of fluctuating initial conditions from the MC-Glauber (left) and MC-KLN (right) models.

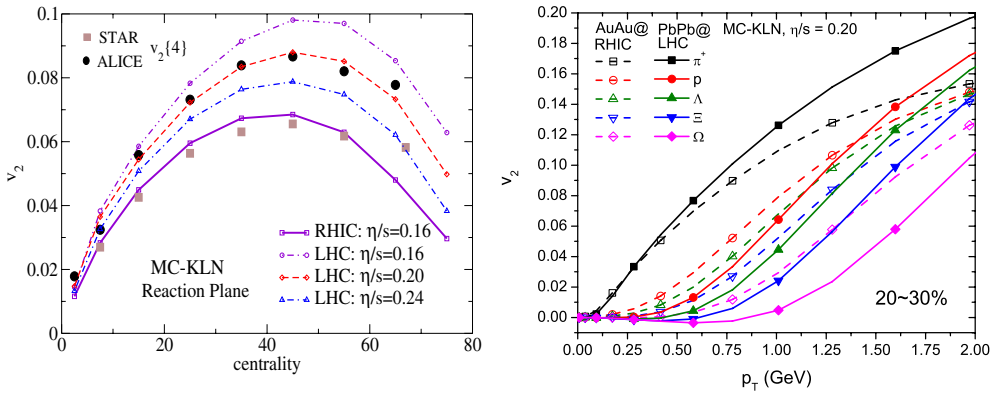

Figure 3. Total charged hadron elliptic flow as a function of centrality (`VISHNU`, left [12]) and differential elliptic flow for identified hadrons for 20–30% centrality (`VISH2+1`, right [11]) for 200 A GeV Au+Au collisions at RHIC and 2.76 A TeV Pb+Pb collisions at the LHC. Experimental data are from [13].

Predictions for spectra and flow at the LHC. The successful comprehensive fit of spectra and elliptic flow at the RHIC [8] allows for tightly constrained LHC predictions. Figure 3 shows such predictions for both pure viscous hydrodynamics `VISH2+1` [11] and `VISHNU` [12]. A straightforward extrapolation with fixed $(\eta/s)_{\rm QGP}$ overpredicts the LHC $v_2^{\rm ch}$ values by 10–15%; a slight increase of $(\eta/s)_{\rm QGP}$ from 0.16 to 0.20 (for MC-KLN) gives better agreement with the ALICE data [13]. However, at LHC energies v_2 becomes sensitive to details of the initial shear stress profile [11], and no firm conclusion can be drawn yet whether the QGP turns more viscous (i.e. less strongly coupled) at higher temperatures. The right panel shows that, at fixed $p_T < 1$ GeV, $v_2(p_T)$ increases from the RHIC to the LHC for pions but decreases for all heavier hadrons. The similarity at the RHIC and the LHC of $v_2^{\rm ch}(p_T)$ for the sum of all charged hadrons thus appears accidental.

Constraining initial state models by simultaneous measurement of v_2 and v_3. While the ellipticities ε_2 differ by about 20% between MC-KLN and MC-Glauber models, their

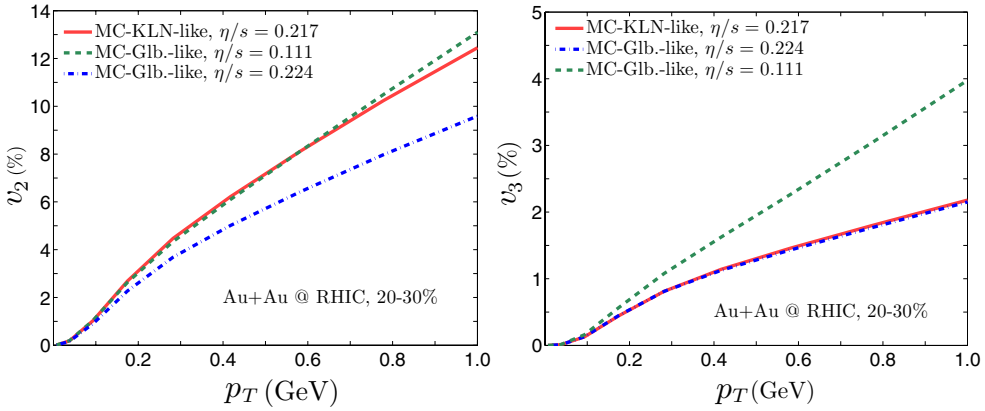

Figure 4. p_T-differential elliptic and triangular flow from viscous hydrodynamics for initial eccentricities from the MC-KLN and MC-Glauber models.

triangularities ε_3 (which are entirely due to event-by-event fluctuations) are almost identical [10]. This suggests us to use triangular flow v_3 (which is almost entirely [10] driven by ε_3) to obtain a model-independent measurement of $(\eta/s)_{\rm QGP}$. Figure 4 shows $v_2^\pi(p_T)$ and $v_3^\pi(p_T)$ for deformed Gaussian fireballs with average eccentricities ε_2 and ε_3 (with a random relative angle) taken from the fluctuating Glauber ('MC-Glauber-like') and KLN ('MC-KLN-like') models. It demonstrates that a given set of flow data requires shear viscosities that differ by a factor of 2 to reproduce $v_2(p_T)$, but the same shear viscosities in both models to reproduce $v_3(p_T)$. A good fit by both models to $v_2(p_T)$ produces dramatically different curves for $v_3(p_T)$ and vice versa. The figure illustrates the strong discriminating power for such simultaneous studies and gives hope for a much more precise extraction of $(\eta/s)_{\rm QGP}$ in the near future.

Acknowledgments

This work was supported by the US Department of Energy under grant nos DE-AC02-05CH11231, DE-FG02-05ER41367, DE-SC0004286 and (within the framework of the JET Collaboration) DE-SC0004104; by the Japan Society for the Promotion of Science through Grant-in-Aid for Scientific Research no 22740151; by the ExtreMe Matter Institute (EMMI); and by BMBF under project no 06FY9092. We gratefully acknowledge extensive computing resources provided to us by the Ohio Supercomputer Center. CS thanks the *Quark Matter 2011* organizers for support.

References

[1] Heinz U 2005 arXiv:nucl-th/0512051
[2] Hirano T, Heinz U, Kharzeev D, Lacey R and Nara Y 2007 *J. Phys. G: Nucl. Part. Phys.* **34** S879
[3] Hirano T, Heinz U, Kharzeev D, Lacey R and Nara Y 2006 *Phys. Lett.* B **636** 299
[4] Bass S A *et al* 1998 *Prog. Part. Nucl. Phys.* **41** 255
[5] Song H, Bass S A and Heinz U 2011 *Phys. Rev.* C **83** 024912
[6] Song H, Bass S A, Heinz U, Hirano T and Shen C 2011 *Phys. Rev. Lett.* **106** 192301
[7] Ollitrault J Y, Poskanzer A M and Voloshin S A 2009 *Phys. Rev.* C **80** 014904
[8] Song H, Bass S A, Heinz U, Hirano T and Shen C 2011 *Phys. Rev.* C **83** 054910

[9] Andrade R *et al* 2006 *Phys. Rev. Lett.* **97** 202302
Andrade R *et al* 2008 *Phys. Rev. Lett.* **101** 112301
[10] Qiu Z and Heinz U 2011 *Phys. Rev.* C (in press) arXiv:1104.0650
[11] Shen C, Heinz U, Huovinen P and Song H 2011 arXiv:1105.3226
[12] Song H, Bass S A and Heinz U 2011 *Phys. Rev.* C **83** 054912
[13] Aamodt K *et al* (ALICE Collaboration) 2010 *Phys. Rev. Lett.* **105** 252302

Influence of Shear Viscosity of Quark-Gluon Plasma on Elliptic Flow in Ultrarelativistic Heavy-Ion Collisions

H. Niemi,[1] G. S. Denicol,[2] P. Huovinen,[2] E. Molnár,[1,3] and D. H. Rischke[1,2]

[1]*Frankfurt Institute for Advanced Studies, Ruth-Moufang-Straße 1, D-60438 Frankfurt am Main, Germany*

[2]*Institut für Theoretische Physik, Johann Wolfgang Goethe-Universität, Max-von-Laue-Straße 1, D-60438 Frankfurt am Main, Germany*

[3]*MTA-KFKI, Research Institute for Particle and Nuclear Physics, H-1525 Budapest, P.O. Box 49, Hungary*

(Received 13 January 2011; published 26 May 2011)

We investigate the influence of a temperature-dependent shear viscosity over entropy density ratio η/s on the transverse momentum spectra and elliptic flow of hadrons in ultrarelativistic heavy-ion collisions. We find that the elliptic flow in $\sqrt{s_{\rm NN}} = 200$ GeV Au + Au collisions at RHIC is dominated by the viscosity in the hadronic phase and in the phase transition region, but largely insensitive to the viscosity of the quark-gluon plasma (QGP). At the highest LHC energy, the elliptic flow becomes sensitive to the QGP viscosity and insensitive to the hadronic viscosity.

DOI: 10.1103/PhysRevLett.106.212302 PACS numbers: 25.75.Ld, 12.38.Mh, 24.10.Nz

Ultrarelativistic heavy-ion collisions at the Relativistic Heavy-Ion Collider (RHIC) and the Large Hadron Collider (LHC) produce a hot and dense system of strongly interacting matter [1]. The subsequent expansion of the created matter has been shown to exhibit a strong degree of collectivity which reveals itself in the transverse momentum (p_T) spectra of finally observed hadrons. In particular, the observed large azimuthal anisotropy of the spectra, quantified by the so-called elliptic flow coefficient v_2, has been interpreted as a signal for the formation of a quark-gluon plasma (QGP) with very small viscosity in heavy-ion collisions at RHIC [2].

A first indication for the small viscosity of the QGP was the agreement between RHIC data and hydrodynamical calculations in the perfect-fluid limit, i.e., with zero viscosity [3]. An analysis of the elliptic flow at RHIC in the framework of relativistic dissipative hydrodynamics was performed in Refs. [4–6]. These works indeed indicate that the shear viscosity to entropy density ratio, η/s, has to be small in order to keep the agreement between the hydrodynamic simulations and experimental data.

Presently, most hydrodynamical simulations assume a constant, i.e., temperature-independent η/s. It has been claimed [6] that, in order to describe elliptic flow data, this value cannot be larger than 2.5 times the lower bound $\eta/s = 1/4\pi$ conjectured in the framework of the AdS/CFT correspondence [7]. A constant η/s is, however, in sharp contrast to the behavior observed in common liquids and gases, where η/s has a strong temperature dependence and, typically, a minimum near phase transitions. A similar behavior of η/s is expected for finite-temperature matter described by quantum chromodynamics (QCD) near the transition from hadronic matter to the QGP (the QCD phase transition) [8].

A natural question then is whether the temperature dependence of η/s has an effect on the collective flow of hadrons in heavy-ion collisions. In this work, we investigate this question in the framework of relativistic hydrodynamics. We consider a temperature-dependent η/s with a minimum near the QCD phase transition, and compare the results with those obtained for a constant η/s in either the hadronic phase, or the QGP phase, or both phases. Note that we do not attempt a detailed fit to the data in order to extract η/s. Rather, we are interested in the qualitative effects of different parametrizations for η/s on hadron spectra and elliptic flow.

Concerning the elliptic flow in Au + Au collisions at RHIC, we find little difference whether η/s is constant in the QGP phase or strongly increasing with temperature. In contrast, the elliptic flow values are highly sensitive to whether we use a constant or temperature-dependent η/s in the hadronic phase, corroborating the findings of Refs. [9,10]. On the other hand, we find that the sensitivity of the elliptic flow to the values of η/s in the high-temperature QGP increases with increasing collision energy, while the sensitivity to the hadronic viscosity decreases. At the highest LHC energy, the above conclusion for RHIC energies is reversed: the finally observable elliptic flow is dominated by the viscosity of the QGP and largely insensitive to that of the hadronic phase.

Fluid dynamics is determined by the conservation of energy, momentum, and charges like baryon number. Here, we are interested in the collective flow at midrapidity in heavy-ion collisions at RHIC and LHC energies. Consequently, we may neglect baryon number and assume longitudinal boost invariance [11]. We also need the constitutive relations for the dissipative currents. Here, we only consider the shear stress tensor $\pi^{\mu\nu}$, the evolution of which we describe in the approach of Israel and Stewart [12], $\langle D\pi^{\mu\nu}\rangle = \frac{1}{\tau_\pi}(2\eta\sigma^{\mu\nu} - \pi^{\mu\nu}) - \frac{4}{3}\pi^{\mu\nu}\partial_\lambda u^\lambda$, where $D = u^\mu\partial_\mu$, $\sigma^{\mu\nu} = \nabla^{\langle\mu}u^{\nu\rangle}$, and the angular brackets $\langle\,\rangle$ denote the symmetrized and traceless projection,

orthogonal to the fluid four-velocity u^μ. We have also taken the coefficient of the last term in the massless limit. For details, see Ref. [13].

We solve the conservation equations numerically by using the SHASTA algorithm, see, e.g., Ref. [13]. The relaxation equations for the components of $\pi^{\mu\nu}$ are solved by discretizing spatial gradients using centered second-order finite differences. We found that, in contrast to SHASTA, this method produces numerically stable solutions also for low-density matter at the edges of the system.

With longitudinal boost invariance, we need to specify the values of the energy-momentum tensor in the transverse plane at some initial time τ_0. We assume that the initial energy density profile is proportional to the density of binary nucleon-nucleon collisions as calculated from the optical Glauber model (model eBC in Ref. [14]). The initial transverse velocity and $\pi^{\mu\nu}$ are set to zero. The maximum energy densities ε_0 in central collisions (impact parameter $b = 0$) are chosen to reproduce the observed multiplicity in the 0%–5% most central $\sqrt{s_{\rm NN}} = 200$ GeV Au + Au collisions at RHIC [15] and $\sqrt{s_{\rm NN}} = 2.76$ TeV Pb + Pb collisions at LHC [16]. For the $\sqrt{s_{\rm NN}} = 5.5$ TeV Pb + Pb collisions at LHC we use the multiplicity predicted by the minijet + saturation model [17]. The initialization parameters are collected in Table I.

Our equation of state (EoS) is a recent parametrization of lattice-QCD data and a hadron resonance gas (s95p-PCE of Ref. [18]), with chemical freeze-out at a temperature $T_{\rm chem} = 150$ MeV implemented as in Ref. [19].

Hadron spectra are calculated by using the Cooper-Frye freeze-out description [20] with constant decoupling temperature $T_{\rm dec} = 100$ MeV, which will be shown below to give reasonable agreement with both the p_T spectrum and the elliptic flow coefficient for pions at RHIC. For the sake of simplicity, we include viscous corrections to the equilibrium distribution function f_0 as for Boltzmann particles, even though f_0 obeys the appropriate quantum statistics [21]:

$$f(x, p) = f_0 + \delta f = f_0\left[1 + \frac{p_\mu p_\nu \pi^{\mu\nu}}{2T^2(\varepsilon + p)}\right], \qquad (1)$$

where p is pressure and p^μ is the hadron four-momentum. Two- and three-body decays of unstable hadrons are included as described in Ref. [22]. We include resonances up to mass 1.7 GeV.

The shear viscosity to entropy density ratio is parametrized as follows. For the hadronic phase, it reproduces the results of Ref. [23]. In the QGP phase, η/s follows the lattice-QCD results of Ref. [24]. Then, η/s has to assume a minimum value at a certain temperature; in our case we take $\eta/s = 0.08$ at $T = 180$ MeV. This is the same parametrization as used in Ref. [25]. In total we have four cases, see Fig. 1: (LH-LQ) $\eta/s = 0.08$ for all temperatures, (LH-HQ) $\eta/s = 0.08$ in the hadron gas, and above $T = 180$ MeV η/s increases according to lattice-QCD data, (HH-LQ) below $T = 180$ MeV, η/s is that of a hadron gas, and above we set $\eta/s = 0.08$, (HH-HQ) we use a realistic parametrization for both the hadron gas and the QGP. For the relaxation time we use a result motivated by kinetic theory $\tau_\pi = 5\eta/(\varepsilon + p)$ [26].

TABLE I. Initialization parameters for different collisions.

$\sqrt{s_{\rm NN}}$ [GeV]	τ_0 [fm]	ε_0 [GeV/fm^3]	$T_{\rm max}$ [MeV]
200	1.0	24.0	335
2760	0.6	187.0	506
5500	0.6	240.0	594

Figure 2(a) shows the p_T spectrum of positive pions in the 0%–5% most central $\sqrt{s_{\rm NN}} = 200$ GeV Au + Au collisions at RHIC. Our calculations are compared to PHENIX data [15]. All the different parametrizations of η/s give similar agreement with the low-p_T pion spectra. For $p_T \gtrsim 1.0$ GeV, the parametrizations (LH-HQ) and (HH-HQ) start to give slightly flatter spectra. While the effect of the QGP viscosity on the p_T slopes is small for our comparatively long initialization time $\tau_0 = 1.0$ fm, it becomes more pronounced for smaller values of τ_0. On the other hand, the slopes of the spectra are almost independent of the hadronic viscosity and this conclusion remains true at least for $\tau_0 = 0.2$–1.0 fm.

Figures 2(b) and 2(c) show the spectra for $\sqrt{s_{\rm NN}} = 2.76$ TeV and 5.5 TeV Pb + Pb collisions, respectively. Here we observe a much stronger dependence of the p_T spectra on the high-temperature values of η/s, but the main reason for this is the earlier initialization time $\tau_0 = 0.6$ fm. On the other hand, the p_T spectra are independent of the hadronic viscosity also at LHC.

In Figs. 2(d)–2(f) we show the elliptic flow coefficients for charged hadrons in the 20%–30% centrality class for $\sqrt{s_{\rm NN}} = 200$ GeV Au + Au collisions and $\sqrt{s_{\rm NN}} = 2.76$ TeV and $\sqrt{s_{\rm NN}} = 5.5$ TeV Pb + Pb collisions, respectively. In Fig. 2(d) the results from the hydrodynamic simulations are compared to STAR 4-particle cumulant data [27] and in Fig. 2(e) to recent data from the ALICE Collaboration [28].

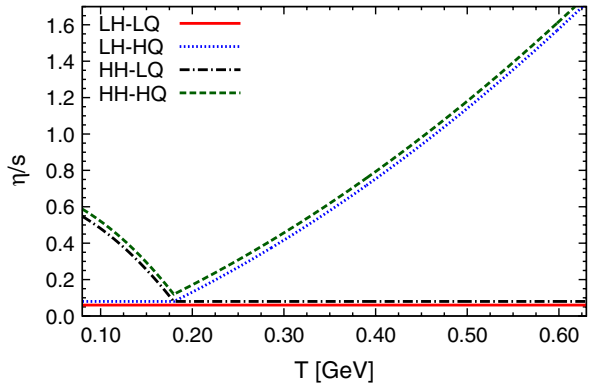

FIG. 1 (color online). Different parametrizations of η/s as a function of temperature. The (LH-LQ) line is shifted downwards and the (HH-HQ) line upwards for better visibility.

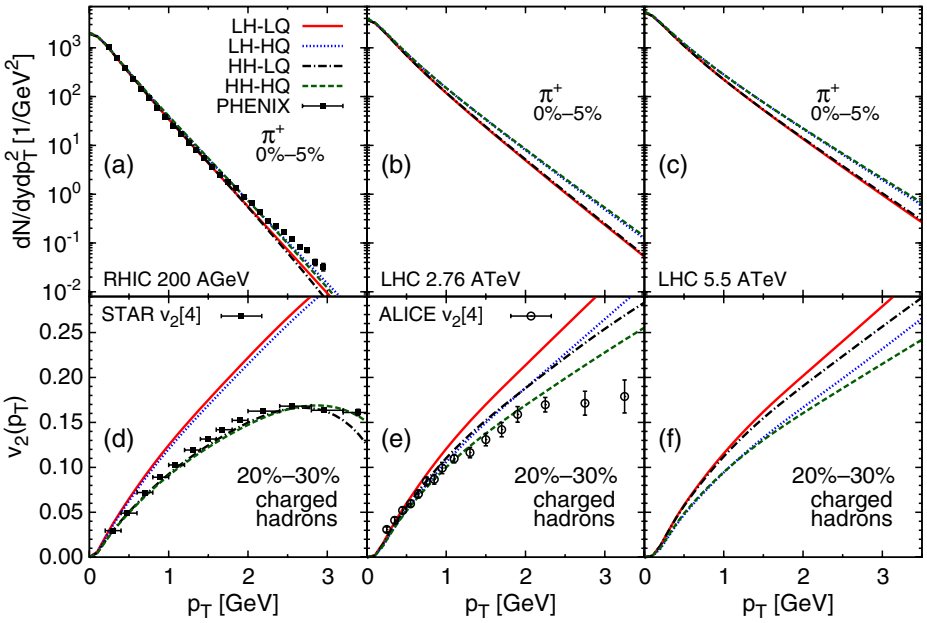

FIG. 2 (color online). Transverse momentum spectra of positive pions in the 0%–5% most central collisions and elliptic flow coefficients in the 20%–30% centrality class at RHIC and LHC. Different curves correspond to the different parametrizations of the temperature dependence of η/s. Data in panel (a) are from Ref. [15] and in panels (d) and (e) from Refs. [27,28].

We immediately see that, for RHIC, the four parametrizations for η/s produce values for the elliptic flow that fall into two classes. The curves are largely insensitive to the values of η/s in the QGP phase and follow the value of the viscosity in the hadron gas: the parametrizations (LH-LQ) and (LH-HQ) with constant η/s in the hadron gas result in larger $v_2(p_T)$ than the parametrizations (HH-LQ) and (HH-HQ) with realistic η/s in the hadron gas. We have confirmed the insensitivity to the values of η/s in the high-temperature QGP phase by decoupling the system at $T_{\rm dec} = 170$ MeV. In that case, $v_2(p_T)$ is largely independent of the η/s parametrization. The separation of curves occurs in the subsequent evolution in the hadronic phase. This shows that, within this model and at RHIC, viscous effects from the hadron gas dominate over viscous effects from the QGP, see also Refs. [9,10]. Because of the strong longitudinal expansion, the initial shear stress enhances the transverse pressure and thus the buildup of the flow anisotropy, but this is counteracted by the viscous suppression of anisotropies. Our simulations suggest that at RHIC these two effects cancel each other in the QGP phase.

The main reason for the hadronic suppression of $v_2(p_T)$ are the viscous corrections δf to the particle distribution function. Thus, the values of $\pi^{\mu\nu}$ on the decoupling boundary are significantly larger in the case with large hadronic η/s. On the other hand, the azimuthal anisotropies of the hydrodynamic flow field are quite similar in all cases. This is demonstrated in Fig. 3, where we plot $v_2(p_T)$ of pions at RHIC without δf. All curves are much closer to each other, indicating that the space-time evolution in the hadron gas is similar in all four cases.

We have tested that these conclusions are unchanged if we use different $\tau_0 = 0.2$–1.0 fm, different EoSs, e.g., with or without chemical freeze-out, use nonequilibrium initial conditions (the same nonzero initial $\pi^{\mu\nu}$ for all four cases), or shift the η/s parametrizations up by a constant value, such that η/s at $T = 180$ MeV is 5 times the AdS/CFT lower bound. Although $v_2(p_T)$ and the slopes of the p_T spectra change when we change the setup, the observed sensitivity of $v_2(p_T)$ on the viscosity around $T \sim 180$ MeV and below, rather than on the high-temperature QGP viscosity is quite generic at RHIC. If we increase η/s above $T = 200$ MeV by a factor of 10 in parametrization (HH-LQ), the elliptic flow is practically the same as shown in Fig. 2(d). This confirms that the value of η/s in the high-temperature QGP phase has no effect on the final observable $v_2(p_T)$ at RHIC, even though during the evolution the system spends approximately equal times above $T \sim 200$ MeV and between $T \sim 170$ and 200 MeV.

Interestingly, the sensitivity of $v_2(p_T)$ to the QGP viscosity increases with increasing collision energy, while the sensitivity to the hadronic viscosity decreases. This can be

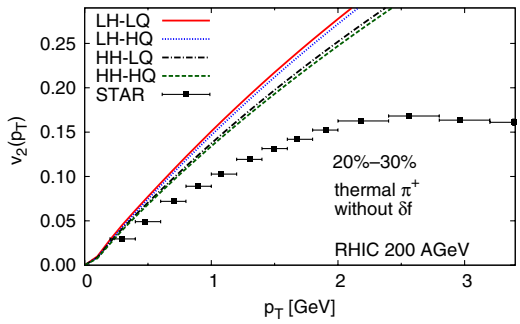

FIG. 3 (color online). Same as Fig. 2(d), but for elliptic flow of thermal (i.e., without decays) pions with $\delta f = 0$.

seen in Figs. 2(e) and 2(f), which show $v_2(p_T)$ for $\sqrt{s_{\rm NN}} = 2.76$ TeV and $\sqrt{s_{\rm NN}} = 5.5$ TeV Pb + Pb collisions, respectively.

At the highest LHC energy, the behavior of $v_2(p_T)$ is completely opposite to that at RHIC. It is almost independent of the hadronic viscosity, but sensitive to the QGP viscosity. In contrast to the RHIC case, at LHC the differences in $v_2(p_T)$ are mostly due to the difference in the transverse flow profiles (caused by the different QGP viscosities) and not due to the viscous corrections to the distribution function at freeze-out. The latter are much smaller than at RHIC: the magnitude of δf is the difference between the curves (LH-LQ) and (HH-LQ) or (LH-HQ) and (HH-HQ) in Fig. 2(f). We have also checked that $v_2(p_T)$ at low-p_T remains insensitive to the hadronic viscosity, even if we increase the hadronic η/s in such a way that it reaches $\eta/s = 1.0$ at $T = 100$ MeV, but keep the minimum of η/s fixed. The collisions at $\sqrt{s_{\rm NN}} = 2.76$ TeV are between these two extreme behaviors, as elliptic flow depends both on the hadronic and the QGP η/s.

There are several reasons why the effect of η/s on the elliptic flow at LHC is so different from that at RHIC: first, the longer lifetime of the QGP phase, which results in a stronger dependence of the transverse flow on the viscous properties of the QGP. Second, once the system decouples, it has much larger transverse size and velocity gradients are smaller. Subsequently, dissipative effects from the hadronic stage are smaller and have less effect on the observed $v_2(p_T)$.

In conclusion, we have investigated the effects of a temperature-dependent η/s on the hadron spectra and elliptic flow coefficients at $\sqrt{s_{\rm NN}} = 200$ GeV Au + Au collisions at RHIC and $\sqrt{s_{\rm NN}} = 2.76$ TeV and $\sqrt{s_{\rm NN}} = 5.5$ TeV Pb + Pb collisions at LHC. We found that in all cases the slopes of the p_T spectra of pions depend mainly on the high-temperature η/s, and hardly at all on the hadronic viscosity.

The effect of η/s on the differential elliptic flow $v_2(p_T)$ is more subtle. At RHIC energies, $v_2(p_T)$ is highly sensitive to the viscosity in hadronic matter and almost independent of the viscosity in the QGP phase. In contrast, at the highest LHC energy the opposite holds: elliptic flow is almost independent of the hadronic viscosity, but depends strongly on the QGP viscosity. Thus the extraction of an η/s value for the QGP, except for its value at the expected minimum around T_c, is basically impossible using the elliptic flow data at RHIC alone. On the other hand, a determination of the temperature dependence of η/s in the QGP phase from elliptic flow data seems to be possible at LHC. This could allow the observation of a possible transition from the strongly coupled plasma near T_c; see, e.g., Ref. [29], to the weakly coupled QGP.

This work was supported by the Helmholtz International Center for FAIR within the framework of the LOEWE program launched by the State of Hesse. The work of P. H. and H. N. was supported by the Extreme Matter Institute (EMMI). P. H. is also supported by BMBF under Contract No. 06FY9092. E. M. is supported by OTKA/NKTH 81655 and the AvH Foundation.

[1] I. Arsene *et al.*, Nucl. Phys. **A757**, 1 (2005); B. B. Back *et al.*, *ibid.* **A757**, 28 (2005); J. Adams *et al.*, *ibid.* **A757**, 102 (2005); K. Adcox *et al.*, *ibid.* **A757**, 184 (2005).
[2] M. Gyulassy and L. McLerran, Nucl. Phys. **A750**, 30 (2005).
[3] For a review see, for instance, P. Huovinen and P. V. Ruuskanen, Annu. Rev. Nucl. Part. Sci. **56**, 163 (2006).
[4] P. Romatschke and U. Romatschke, Phys. Rev. Lett. **99**, 172301 (2007); M. Luzum and P. Romatschke, Phys. Rev. C **78**, 034915 (2008); P. Bozek, Phys. Rev. C **81**, 034909 (2010).
[5] C. Shen *et al.*, Phys. Rev. C **82**, 054904 (2010).
[6] H. Song *et al.*, Phys. Rev. Lett. **106**, 192301 (2011).
[7] P. K. Kovtun, D. T. Son, and A. O. Starinets, Phys. Rev. Lett. **94**, 111601 (2005).
[8] L. P. Csernai, J. I. Kapusta, and L. D. McLerran, Phys. Rev. Lett. **97**, 152303 (2006).
[9] T. Hirano *et al.*, Phys. Lett. B **636**, 299 (2006).
[10] H. Song, S. A. Bass, and U. W. Heinz, Phys. Rev. C **83**, 024912 (2011).
[11] J. D. Bjorken, Phys. Rev. D **27**, 140 (1983).
[12] W. Israel and J. M. Stewart, Proc. R. Soc. A **365**, 43 (1979); Ann. Phys. (N.Y.) **118**, 341 (1979).
[13] E. Molnar, H. Niemi, and D. H. Rischke, Eur. Phys. J. C **65**, 615 (2009).
[14] P. F. Kolb *et al.*, Nucl. Phys. **A696**, 197 (2001).
[15] S. S. Adler *et al.* (PHENIX Collaboration), Phys. Rev. C **69**, 034909 (2004).
[16] K. Aamodt *et al.* (ALICE Collaboration), Phys. Rev. Lett. **105**, 252301 (2010).
[17] K. J. Eskola *et al.*, Phys. Rev. C **72**, 044904 (2005).
[18] P. Huovinen and P. Petreczky, Nucl. Phys. **A837**, 26 (2010).
[19] P. Huovinen, Eur. Phys. J. A **37**, 121 (2008).
[20] F. Cooper and G. Frye, Phys. Rev. D **10**, 186 (1974).
[21] D. Teaney, Phys. Rev. C **68**, 034913 (2003).
[22] J. Sollfrank, P. Koch, and U. W. Heinz, Z. Phys. C **52**, 593 (1991).
[23] J. Noronha-Hostler, J. Noronha, and C. Greiner, Phys. Rev. Lett. **103**, 172302 (2009).
[24] A. Nakamura and S. Sakai, Phys. Rev. Lett. **94**, 072305 (2005).
[25] G. S. Denicol, T. Kodama, and T. Koide, J. Phys. G **37**, 094040 (2010).
[26] G. S. Denicol, T. Koide, and D. H. Rischke, Phys. Rev. Lett. **105**, 162501 (2010).
[27] Y. Bai, Ph.D. thesis, Nikhef and Utrecht University, The Netherlands, 2007; A. Tang (STAR Collaboration), arXiv:0808.2144.
[28] K. Aamodt *et al.* (ALICE Collaboration), Phys. Rev. Lett. **105**, 252302 (2010).
[29] J. Liao and E. Shuryak, Phys. Rev. C **75**, 054907 (2007); Y. Hidaka and R. D. Pisarski, Phys. Rev. D **81**, 076002 (2010).

Dissipative effects from transport and viscous hydrodynamics

J. Phys. G: Nucl. Part. Phys. **35** (2008) 104125 (4pp) doi:10.1088/0954-3899/35/10/104125

Dissipative effects from transport and viscous hydrodynamics

Denes Molnar[1,2] **and Pasi Huovinen**[1]

[1] Physics Department, Purdue University, 525 Northwestern Avenue, West Lafayette, IN 47907, USA
[2] RIKEN BNL Research Center, Brookhaven National Laboratory, Upton, NY 11973, USA

Received 31 May 2008
Published 17 September 2008
Online at stacks.iop.org/JPhysG/35/104125

Abstract

We compare $2 \to 2$ covariant transport theory and causal Israel–Stewart hydrodynamics in a (2+1)-dimensional longitudinally boost-invariant geometry with RHIC-like initial conditions and a conformal $\varepsilon = 3p$ equation of state. The pressure evolution in the center of the collision zone and the final differential elliptic flow $v_2(p_T)$ from the two theories agree remarkably well for a small shear viscosity to entropy density ratio $\eta/s \approx 1/(4\pi)$, and also for a large cross section $\sigma \approx 50$ mb. A key to this agreement is keeping *all* terms in the Israel–Stewart equations of motion. Our results indicate promising prospects for the applicability of Israel–Stewart dissipative hydrodynamics at RHIC, provided the shear viscosity of hot and dense quark–gluon matter is indeed very small for the relevant temperatures $T \sim 200$–500 MeV.

(Some figures in this article are in colour only in the electronic version)

1. Introduction

Recent interest in heavy-ion physics has focused on constraining the transport properties of hot and dense nuclear matter using experimental data from RHIC. A particular open question is the effect of the conjectured 'minimal' shear viscosity $\eta = s/(4\pi)$ [1] on the dynamics and observables (s is the entropy density). Studies of dissipation require a suitable theory framework, in principle a non-equilibrium one. However, close to local equilibrium, one can also apply dissipative extensions of ideal (Euler) hydrodynamics [2–5].

The straightforward Navier–Stokes extension of relativistic ideal hydrodynamics with corrections linear in gradients leads to acausal behavior and instabilities. An improved formulation proposed by Mueller and later extended by Israel and Stewart [6] (IS) includes second derivatives, which alleviates the causality problem. However, that theory originates from an arbitrary truncation of the entropy current at quadratic order in dissipative corrections (shear and bulk stress, and heat flow), which is not a controlled approximation. Derivations of the IS equations from kinetic theory again rely on an arbitrary truncation of non-equilibrium corrections to the phase-space density at quadratic order in momentum (Grad's 14-moment

approximation). In contrast, rigorous (Chapman–Enskog) expansion in small gradients near local equilibrium results in Navier–Stokes theory.

Because of these uncertainties about the region of validity of Israel–Stewart theory, detailed cross-checks against a non-equilibrium approach are paramount. Here we report on a comparison against covariant transport theory, for conditions expected in Au + Au at $\sqrt{s_{NN}} \sim 200$ GeV at RHIC, and investigate the effect of small shear viscosities on the dynamics and differential elliptic flow $v_2(p_T)$.

2. Covariant transport and Israel–Stewart hydrodynamics

We solve the equations of motion of causal Israel–Stewart dissipative hydrodynamics

$$\partial_\mu T^{\mu\nu} = 0, \qquad \partial_\mu N^\mu = 0, \tag{1}$$

$$D\pi^{\mu\nu} = -\frac{1}{\tau_\pi}(\pi^{\mu\nu} - 2\eta\nabla^{\langle\mu}u^{\nu\rangle}) - (u^\mu\pi^{\nu\alpha} + u^\nu\pi^{\alpha\mu})Du_\alpha - \frac{1}{2}\pi^{\mu\nu}\left(\partial_\alpha u^\alpha + D\ln\frac{\beta_2}{T}\right) - 2\pi_\lambda^{\langle\mu}\omega^{\nu\rangle\lambda}, \tag{2}$$

$$T^{\mu\nu} \equiv (\varepsilon + p)u^\mu u^\nu - pg^{\mu\nu} + \pi^{\mu\nu}, \qquad N^\mu \equiv nu^\mu \tag{3}$$

in a (2 + 1)-dimensional longitudinally boost-invariant geometry. Here, ε, p, u^μ and n are the local energy density, pressure, flow velocity and particle density, respectively, $D \equiv u^\mu\partial_\mu$ and the $\langle\rangle$ brackets denote traceless symmetrization and projection orthogonal to the flow $A^{\langle\mu\nu\rangle} \equiv \frac{1}{2}\Delta^{\mu\alpha}\Delta^{\nu\beta}(A_{\alpha\beta} + A_{\beta\alpha}) - \frac{1}{3}\Delta^{\mu\nu}\Delta_{\alpha\beta}A^{\alpha\beta}$, $\Delta^{\mu\nu} \equiv g^{\mu\nu} - u^\mu u^\nu$, and $\nabla^\mu \equiv \Delta^{\mu\nu}\partial_\nu$. In the equation for the shear stress $\pi^{\mu\nu}$ we include the term with the vorticity tensor $\omega^{\mu\nu} \equiv (1/2)\Delta^{\mu\alpha}\Delta^{\nu\beta}(\partial_\beta u_\alpha - \partial_\alpha u_\beta)$ that follows from kinetic theory.

The numerical IS solutions are obtained with a modified version of the code used in [8]. Details of the algorithm will be published elsewhere. Covariant transport solutions are calculated via the MPC algorithm [9, 10].

To aid comparison with covariant $2 \to 2$ transport theory, we take an ideal gas equation of state of massless particles, $\varepsilon = 3p$, and keep particle number conserved. For our conformal system bulk viscosity vanishes, while heat flow is ignored for simplicity. The shear viscosity and shear stress relaxation time of the fluid are matched to the values from kinetic theory [6, 7]: $\eta \approx 6T/(5\sigma)$ and $\tau_\pi \equiv 2\beta_2\eta \approx 9\lambda_{\mathrm{MFP}}/5$ (because $\beta_2 = 3/4p$), where an isotropic two-body cross section is utilized for simplicity. We consider two scenarios: (i) a constant cross section and (ii) a cross section $\sigma \sim \tau^{2/3}$ growing with proper time $\tau \equiv \sqrt{t^2 - z^2}$. During the initial one-dimensional expansion stage $\eta/s \sim \tau^{2/3}$ grows in the former case, while in the latter case $\eta/s \approx$ const.

Initial conditions expected at RHIC for Au+Au at $\sqrt{s_{NN}} \sim 200$ GeV and impact parameter $b = 8$ fm are modeled through an initial density profile proportional to the (local) number of binary collisions for diffuse gold nuclei, normalized to $\mathrm{d}N/\mathrm{d}\eta(b = 0) = 1000$ to account for the observed $\mathrm{d}N_{ch}/\mathrm{d}\eta \approx 700$. The system is assumed to start from local thermal equilibrium ($\pi^{\mu\nu} = 0$) at a thermalization time $\tau_0 = 0.6$ fm with uniform initial temperature $T_0 = 385$ MeV.

3. Main results

Figure 1 compares the evolution of the transverse and longitudinal pressure from covariant transport (lines with symbols) and IS hydrodynamics (lines without symbols), averaged over

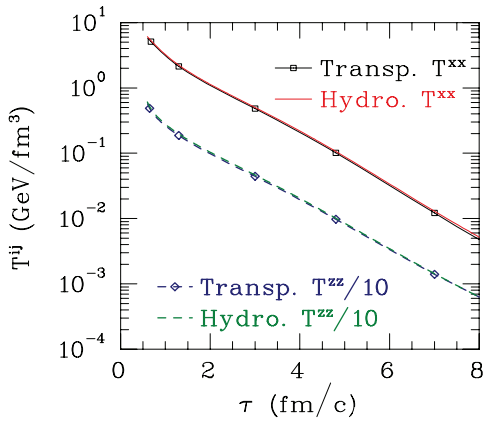

Figure 1. Proper time evolution of the average transverse (T^{xx}, solid) and longitudinal pressure (T^{zz}, dashed) in covariant transport (symbols) and causal Israel–Stewart hydrodynamics (no symbols) near the center of the collision zone ($r_T < 1$ fm) for RHIC-like initial conditions (see text) and $\eta/s \approx 1/(4\pi)$. For clarity, T^{zz} is divided by a factor of 10.

the center of the collision zone $r_T \equiv \sqrt{x^2 + y^2} < 1$ fm for $\eta/s \approx 1/(4\pi)$. At such a low shear viscosity, we find that IS hydrodynamics is a good approximation to covariant transport in the densest region of the collision.

In order to calculate momentum distributions, a freezeout prescription is necessary. Here we apply Cooper–Frye (sudden) freezeout

$$\frac{\mathrm{d}N}{\mathrm{d}y\,\mathrm{d}^2 p_T} = \int \mathrm{d}\sigma_\mu(x) p^\mu f(x, \vec{p}), \tag{4}$$

where f is the phase-space density corresponding to the local fluid variables and $\mathrm{d}\sigma_\mu$ is the local normal to the freezeout hypersurface. We choose a constant density hypersurface $n = 0.365\ \mathrm{fm}^{-3}$, which is the density of an ideal gas of massless gluons in chemical equilibrium at $T = 120$ MeV (three colors).

Figure 2(left) shows elliptic flow from IS hydrodynamics as a function of transverse momentum, for the $\eta/s \approx 1/(4\pi)$ scenario. The dashed curve corresponds to (4) with the local equilibrium ansatz $f_{\mathrm{eq}}(x, \vec{p}) = n(x)/[8\pi T^3(x)] \exp[-p^\mu u_\mu / T(x)]$ (we use Boltzmann statistics for consistent comparison with transport). This incorporates dissipative corrections to the evolution of the flow field, temperature and particle number density, but ignores non-equilibrium distortions of the local momentum distributions (i.e., assumes $\pi^{\mu\nu} = 0$). The solid curve is the result for

$$f(x, \vec{p}) = f_{\mathrm{eq}}(x, \vec{p}) \left[1 + \frac{p^\mu p^\nu \pi_{\mu\nu}(x)}{8n(x)T^3(x)}\right] \tag{5}$$

that properly takes the local shear stress into account. We find that relative to ideal hydrodynamics (dotted curve) dissipation reduces elliptic flow by ∼30%, even at such a low $\eta/s \approx 1/(4\pi)$. This reinforces an earlier kinetic theory estimate [11]. Unlike [5], we find that at least one-third of the reduction comes from corrections to the ideal hydrodynamic variables (the lower the p_T, the larger the fraction), while the remaining up to two-thirds come from shear stress altering the local momentum distributions.

Finally, we compare in figure 2(right) the differential elliptic flow $v_2(p_T)$ between covariant transport (squares) and IS hydrodynamics (dashed and solid). The dotted line is the ideal hydrodynamics reference. For $\sigma_{gg\to gg} \approx 47$ mb as in [10] we find excellent

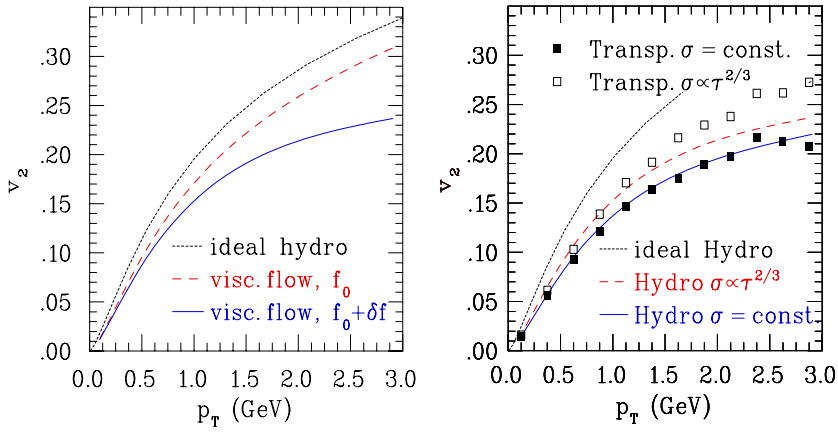

Figure 2. Left: elliptic flow as a function of p_T for Au + Au at $\sqrt{s_{NN}} \sim 200$ GeV and $b = 8$ fm from ideal hydrodynamics (dotted) and IS hydrodynamics with Cooper–Frye freezeout ignoring (dashed) or incorporating (solid) dissipative corrections to the local momentum distributions (see text) for $\eta/s \approx 1/(4\pi)$. Right: comparison of $v_2(p_T)$ from covariant transport (squares) and IS hydrodynamics (lines) for $\eta/s \approx 1/(4\pi)$ (open squares versus dashed), and $\sigma_{gg\to gg} \approx 47$ mb (filled squares versus solid). The ideal hydro reference is also shown (dotted).

agreement between transport and IS hydro (filled squares versus solid line). We also find good agreement for $\eta/s \approx 1/(4\pi)$ (open squares versus dashed line), for which IS hydro somewhat underpredicts the transport results at higher $p_T > 1.5$ GeV. We caution that the hydro results at high p_T are also sensitive to the freezeout prescription, which deserves further investigation.

We emphasize that, just like [2, 3], we solve the *full* set of equations that result from Israel–Stewart theory. For a system near *global* equilibrium, the first term in the second line of (2) can be dropped [6] because gradients are small. However, we have checked that these terms are important in our case, which has large gradients.

Acknowledgments

We thank RIKEN, Brookhaven National Laboratory and the US Department of Energy (DE-AC02-98CH10886) for providing facilities essential for the completion of this work.

References

[1] Kovtun P, Son D T and Starinets A O 2005 *Phys. Rev. Lett.* **94** 111601
[2] Muronga A 2002 *Phys. Rev. Lett.* **88** 062302
Muronga A 2002 *Phys. Rev. Lett.* **89** 159901 (erratum)
[3] Romatschke P and Romatschke U 2007 *Phys. Rev. Lett.* **99** 172301
[4] Song H and Heinz U W 2008 *Phys. Lett.* B **658** 279
[5] Dusling K and Teaney D 2008 *Phys. Rev.* C **77** 034905
[6] Israel W 1976 *Ann. Phys.* **100** 310
Israel W and Stewart J M 1979 *Ann. Phys.* **118** 349
[7] de Groot S R, van Leeuwen W A and van Weert Ch G 1980 *Relativistic Kinetic Theory—Principles and Applications* (Amsterdam: North-Holland) chapters V and VI
[8] Huovinen P 2005 *Nucl. Phys.* A **761** 296
[9] Molnar D and Gyulassy M 2000 *Phys. Rev.* C **62** 054907
[10] Molnar D and Huovinen P 2005 *Phys. Rev. Lett.* **94** 012302
[11] Molnar D 2008 arXiv:0806.0026

Annu. Rev. Nucl. Part. Sci. 2006. 56:163–206
doi: 10.1146/annurev.nucl.54.070103.181236

First published online as a Review in Advance on June 5, 2006

HYDRODYNAMIC MODELS FOR HEAVY ION COLLISIONS

P. Huovinen
Department of Physics, University of Virginia, Charlottesville, Virginia 22904 and Helsinki Institute of Physics, University of Helsinki, FIN-00014, Finland; email: ph4h@virginia.edu

P.V. Ruuskanen
Department of Physics, University of Jyväskylä, FIN-40014 Finland; email: vesa.ruuskanen@phys.jyu.fi

Key Words hydrodynamics, quark-gluon plasma, quark matter, elliptic flow, electromagnetic emission

■ **Abstract** Application of hydrodynamics for modeling of heavy ion collisions is reviewed. We consider several physical observables that can be calculated in this approach and compare them to the experimental measurements.

CONTENTS

1. INTRODUCTION

Quantum chromodynamics (QCD), the theory on strong interactions, has been tested extensively in hard, large-momentum transfer processes. In these processes, a large amount of energy or three-momentum is transferred to one (e.g., deep inelastic scattering) or few (jet production) quark and gluon constituents of initial hadrons. Owing to the asymptotic freedom property of QCD, the coupling strength is small. The time scale for this part is a small fraction of the time scale of the overall process. These two properties allow the factorization and perturbative treatment of the hard part of the process from the rest of the matrix element. This program has been very successful, and no clear discrepancies have been found between experimental results and theoretical calculations.

The goal of the experimental heavy ion program at ultrarelativistic energies is to study QCD in an environment very different from that encountered in hard processes, in a dense system of quarks and gluons. When the heavy ion program started two decades ago, the original goals were the production and study of dense, thermally equilibrated, strongly interacting matter, the quark-gluon plasma (QGP). Although this is still the highest priority, phenomena other than the formation of thermally equilibrated QGP also occur in dense partonic systems and can be studied in heavy ion collisions, e.g., the existence of a color glass condensate, which is related to the saturation of gluon occupation numbers in dense components of initial wave functions, may be important for the formation of the QGP, and may also have other observable effects (1). Also, the phenomenon of jet quenching, the loss of energy of a high-energy parton (quark or gluon) when it traverses a high-density parton system, should occur in the dense environment of heavy ion collisions, even when the system is not fully equilibrated.

The earlier experiments at Brookhaven National Laboratory and CERN-SPS provided clear evidence of collective phenomena in nuclear collisions. Recent results from experiments at the Relativistic Heavy Ion Collider (RHIC) at Brookhaven show that total multiplicities exceeding 1000 particles per unit rapidity, $dN/dy \gtrsim 1000$, are produced in central (head-on) collisions of gold nuclei at center-of-mass energies up to $\sqrt{s_{NN}} = 200$ GeV. Here, $\sqrt{s_{NN}}$ is the center-of-mass energy for a nucleon pair. The measured average transverse momentum is $p_T \gtrsim 0.5$ GeV, indicating a total energy per unit rapidity interval of $dE_T/dy \gtrsim 500$ GeV. At time τ after the nuclei have passed through one another, the volume occupied by the produced quanta in a rapidity interval Δy is $\Delta V = \tau \Delta y A_T$, or $\tau A_T = \tau \pi R_A^2$ for unit rapidity. At $\tau = 1$ fm/c, the above numbers imply (2) a particle density of ~ 10 fm^{-3} and an energy density of ~ 5 GeV fm^{-3}, well above different estimates and the results from lattice calculations of the energy density at which the phase transition from confined hadrons to unconfined quarks and gluons occur.

The subject of this review is the use of hydrodynamic modeling to describe the expansion and dilution of matter produced in nuclear collisions. One motivation for this is to formulate a framework to study different observable quantities and correlations among them. Obviously hydrodynamics alone does not suffice

because, first, at high energies, particle production can not be included and, second, only the properties of produced particles, not the hydrodynamic densities during the expansion, can be measured directly. Below we describe a possible dynamic scenario to calculate the production of initial matter. This provides the initial conditions for solving the hydrodynamic equations. Because the production dynamics is still not completely under control, sometimes it may be useful to use physically motivated parametrizations of initial conditions to study, for example, how the details of particle spectra depend on different features of initial conditions. The hydrodynamic description also needs another supplement. A link from hydrodynamical quantities to particle spectra is necessary at the end of expansion, when the particles become independent and fly to detectors.

The use of hydrodynamic concepts like temperature, pressure, and flow velocity cannot be strictly justified for matter formed in a heavy ion collision. Although the total number of particles produced is several thousand at RHIC and may be an order of magnitude more in the future ALICE experiments at the Large Hadron Collider (LHC) at CERN, they hardly form a macroscopic system in the proper thermodynamic sense. However, one can argue for partial equilibration and the formation of collective phenomena from the numbers given above. At initial particle densities of the order of 5–10 fm^{-3}, and even with modest estimates of cross sections of the order of 1–2 mb, mean free paths are $\lesssim$1 fm, much below the nuclear size $2R_A \gtrsim 10$ fm. Therefore, frequent collisions occur and momentum is transferred from denser regions toward less dense regions. In describing the main consequences of these secondary collisions, concepts like temperature and pressure are useful.

Although the use of hydrodynamics may be justified for some features of nuclear collisions, that need not be the case for others. Defining energy density and pressure in the usual way in terms of the local momentum distribution, one obtains for pressure of massless particles $P = \varepsilon/3$ for any isotropic momentum distribution $f(p)$, $p = |p| = E$. In this case, describing the buildup of collective motion or flow using hydrodynamics with $P = \varepsilon/3$ as the equation of state (EoS) could be a reasonable approach, even when the form of p dependence of $f(p)$ differs from that of the thermal equilibrium distribution, $f_{\mathrm{th}}(p)$. However, if $f(p)$ differs significantly from $f_{\mathrm{th}}(p)$, any conclusions based on the detailed momentum dependence of $f(p)$ would fail. This could well be the case at large momenta. Initial production is expected to contain a component that has an approximate power-law behavior at large momenta. It will take longer and require a larger volume than available to change this power behavior to the exponential form of thermal distribution. The observed behavior of high-p_T hadron spectra shows clearly that the high-momentum partons are not thermalized and that they suffer an energy loss while traversing the produced dense matter. Because the high-energy partons form only a small part of produced matter both in multiplicity and in transverse energy, a thermal equilibrium description can still be adequate for the bulk of the matter.

Keeping in mind all the reservations, we review the use of hydrodynamics in describing the heavy ion collisions at collider energies, and the calculation

of observable quantities. We compare the calculated results to the measurements mainly at RHIC, mentioning some results from the CERN-SPS. We also present examples of predictions for the future ALICE experiment at CERN.

2. HYDRODYNAMIC EXPANSION

Hydrodynamics is the theoretical framework describing the motion of fluid, a continuous, flowing medium. The equation of motion can be derived from kinetic equations. Hydrodynamic equations take the simplest form if local thermal equilibrium is assumed. In this treatment, there are no dissipative effects. To take such effects into account by approximation, small deviations from the local equilibrium are assumed. A linear treatment of deviations leads to a system of equations that contains the viscous coefficients, including heat conductivity in the case of conserved currents. For a review, see Reference 3. In most applications of hydrodynamics to heavy ion collisions, viscosity has been neglected. In studies with viscosity, results on global, integrated quantities do not differ qualitatively from those without viscosity. However, for example, transverse spectra at larger transverse momenta $p_T \gtrsim 1.5$ GeV may start to deviate clearly from ideal-fluid calculation (4–6). One should remember, though, that the viscous properties of strongly interacting matter are not well understood, and the approximations in the numerical work also introduce uncertainties.

Once the EoS is known and initial conditions are specified, the hydrodynamic equations determine the expansion of the fluid. In the context of describing heavy ion collisions, the use of these equations requires knowing the EoS of strongly interacting matter and knowing the primary production of particles. Detailed knowledge of microscopic processes is not required if a very strong assumption is taken: The expanding system stays in local thermodynamical equilibrium. This becomes of great practical importance if one wants to include in the hydrodynamic expansion the transition from quarks and gluons to hadrons. The complicated deconfinement or hadronization processes need not be known in microscopic detail; all that is necessary is the thermodynamic EoS as computed, for example, in lattice QCD.

2.1. Hydrodynamic Equations

The hydrodynamic equations

$$\partial_\mu T^{\mu\nu} = 0, \quad T^{\mu\nu} = (\varepsilon + P)u^\mu u^\nu - P g^{\mu\nu} \qquad 1.$$

express, in terms of the energy-momentum tensor $T^{\mu\nu}$, the conservation of energy and momentum in continuous, flowing matter. The quantities defining $T^{\mu\nu}$ are $\varepsilon =$ the energy density, $P =$ the pressure, and $u^\mu =$ the flow four-velocity, normalized to $u_\mu u^\mu = 1$ as usual. The simple form of $T^{\mu\nu}$ above holds for an ideal fluid.

In addition, if the system contains conserved densities n_i, such as those of charge and baryon number, their evolution is expressed by continuity

equations

$$\partial_\mu j_i^\mu = 0. \qquad 2.$$

With several conserved densities or nonzero viscous terms, the definition of u^μ is not unique. One can define the velocity in terms of one of the conserved currents by writing $j_i^\mu = n_i u_i^\mu$, where $n_i = \sqrt{(j_{i\mu} j_i^\mu)}$, or one can use the energy-momentum tensor to define the flow velocity. In the first case, usually referred to as the Eckart definition, there is no flow of charge Q_i in the local rest frame $u_i^\mu = (1, 0)$, the Eckart frame. For a nonideal fluid, the energy flow would usually be nonzero in the Eckart frame. A definition of the fluid velocity in terms of the energy-momentum tensor, referred to as the Landau definition, is such that the energy flow is zero in the local rest frame, but usually the flow of different charges does not vanish. Here, the only charge we consider is the baryon density. We also treat the matter in the final state as an ideal fluid, and thus the two choices for the flow velocity coincide. For a review, see Reference 3.

The only properties of the dynamics contained in Equations 1 and 2 are the conservation laws. However, the relations between the thermodynamic densities ε, P, and n_i, or alternatively their definitions in terms of temperature T and chemical potentials μ_i—e.g., $\varepsilon = \varepsilon(T, \mu_i)$—constituting the EoS, depend on the details of the dynamics among the constituents of the matter. The need for an EoS is obvious; Equations 1 and 2 contain five equations, whereas there are six quantities to be defined in them: three components of the velocity, and the energy density, pressure, and baryon-number density. For a nonideal flow, transport coefficients would enter into the expressions of the energy-momentum tensor and currents, and their derivation from theory requires the knowledge of microscopic dynamics in the same way as the derivation of EoS.

Most of the detailed hydrodynamical discussion below is limited to the situation of scaling longitudinal flow and invariance under longitudinal Lorentz boosts. This means that the longitudinal flow velocity is $v_z = z/t$, and hence, the flow rapidity is $\eta = \log[(t + z)/(t - z)]$, which is also often termed the space-time rapidity. If the initial densities are assumed to depend on t and z only through the longitudinal proper time $\tau = \sqrt{t^2 - z^2}$, e.g., $\varepsilon = \varepsilon(\tau, r)$, the expansion will evolve so that densities remain independent of η and the v_z will retain the scaling form $v_z = z/t$. In this situation the system is said to be boost-invariant (2).

Before discussing the EoS in more detail, we note that the most useful form of the EoS for solving the hydrodynamical equations is provided by the relations among the densities ε, P, and n_i when the hydrodynamical equations are written in the form of Equations 1 and 2. In this form, temperature and chemical potentials do not appear in the equations. For the calculation of observable quantities, such as hadron spectra or electromagnetic emission, relations among the above densities and the temperature and chemical potentials must be specified, as we discuss below.

The other ingredient that must be provided from outside into the hydrodynamic description are the initial conditions, e.g., in terms of initial energy distribution and velocity. From the physics point of view this is a very profound problem because

it involves not only the primary production dynamics, but also the question of thermalization of produced particles. We discuss first the initial conditions, then the EoS, and finally the calculation of physical observables.

2.2. Initial Conditions

As mentioned above, primary particle production cannot be formulated within the hydrodynamic framework in a realistic way in high-energy nuclear collisions. The dynamics of particle production is a separate problem and, if solved, it provides the initial conditions for the hydrodynamic expansion. Initial conditions specify the thermodynamic state of the matter and its velocity on an appropriate space-time boundary, which, for example, in the boost-invariant case discussed below, can be taken to be a constant, longitudinal proper-time surface $\tau = \sqrt{t^2 - z^2} = \tau_0$. From the point of view of the hydrodynamical calculation, the initial conditions can be provided either by a dynamical calculation of primary particle production or by a reasonable parametrization, with the parameters either given by physical arguments or fixed by comparing (some of) the results with experimental data.

There are different approaches to primary production, such as pQCD + final-state saturation (minijet) (7) and the color glass condensate model (8) based on the initial-state parton saturation (9). Both describe the produced matter as a parton system. Also, models based on string formation and decay, such as the DPMJET model (10), are used for the calculation of final hadron spectra. In such a model, a varying fraction of energy is in the form of color strings at an early stage of the collision, and they are not readily connected with a hydrodynamic description, which assumes particle-like constituents of matter. We do not consider string models further, but we describe briefly parton-based approaches to the primary production.

To illustrate different key factors that enter the determination of initial conditions from dynamical calculation of particle production, we consider a perturbative QCD calculation of parton production as an example. For such a calculation to converge, a cutoff must be provided on small momentum-transfer collisions. In this model, the cutoff is obtained from a saturation condition expressed in terms of the transverse nuclear geometry and the number of produced partons. At collider energies, the saturation scale turns out to be typically $p_{\rm sat} \sim 1 \ldots 3$ GeV, which is clearly larger than $\Lambda_{\rm QCD} \sim 0.2$ GeV. Because this cutoff is smaller than what is usually used in jet calculations, produced partons are often called minijets, as partons close to the cutoff dominate the production. In addition to the cutoff, the ingredients of the calculation are the parton-distribution functions of colliding nuclei and the parton-parton cross sections. These cross sections can be calculated from basic QCD theory, but parton distributions must be provided from other measurements.

The nuclear parton distributions are usually expressed in terms of parton distributions of nucleons that, however, are known to be modified in nuclei. The nuclear

modification factor $R_A(x, Q^2)$ is the nuclear parton distribution normalized to a single nucleon and divided by the parton distribution of a free nucleon.[1]

The perturbative QCD calculation of minijet production is a momentum-space calculation, as is the case in most production models. To define the initial spatial densities, a connection between the momentum of a produced parton and its space-time formation point is needed. At collider energies, the hard partons of the colliding nuclei are Lorentz contracted to a region on the order of $2R_A/\gamma_{\rm cm} \ll 1$ fm. We consider the collision region as a point in the longitudinal direction that allows us to assume that the rapidity of the minijet coincides with the space-time rapidity of the formation point $y = \eta = (1/2)\ln[(t+z)/(t-z)]$. We take the formation (proper) time to be the inverse of the saturation scale, $\tau_0 = 1/p_{\rm sat}$. Thus, the minijet matter forms along the hyperbola $t = \sqrt{(z^2 + \tau_0^2)}$ with initial longitudinal flow velocity $v_z(\tau_0) = z/t$. To determine the transverse distribution, we must start with a calculation of production cross section.

To obtain the initial conditions for baryon-number density and energy density, we first need the minijet cross sections for (anti)quarks and gluons and their first moments in transverse energy (momentum) in nucleon-nucleon collision, each calculated in a rapidity interval Δy and integrated in p_T from the saturation cutoff $p_T = p_{\rm sat}$ to its maximum value (11, 12):

$$\sigma_{\rm jet}(p_{\rm sat}, \sqrt{s}, \Delta y, A) = \int_{p_{\rm sat}}^{\sqrt{s}/2} dp_T \frac{d\sigma_{\rm jet}(\sqrt{s}, \Delta y, A)}{dp_T},$$

$$\sigma_{\rm jet}\langle E_T\rangle(p_{\rm sat}, \sqrt{s}, \Delta y, A) = \int_{p_{\rm sat}}^{\sqrt{s}/2} dp_T\, p_T \frac{d\sigma_{\rm jet}(\sqrt{s}, \Delta y, A)}{dp_T}.$$

The total number of minijets and the total amount of transverse energy in Δy in a nucleus-nucleus collision are obtained by multiplying the corresponding nucleon-nucleon cross section with the nucleon-nucleon luminosity of the collision (including an extra factor of two for the number of minijets). This is given by the overlap function $T_{AB}(b)$ of transverse densities $T_{A(B)}(s)$ of the colliding nuclei:

$$T_{AB}(\mathbf{b}) = \int d^2\mathbf{s} T_A(|\mathbf{b} - \mathbf{s}|) T_B(s) = T_{AB}(b),$$

$$T_A(\mathbf{s}) = \int_{-\infty}^{+\infty} dz \rho_A(z, \mathbf{s}) = T_A(s),$$

where $\mathbf{b}$ is the impact parameter and $\mathbf{s}$ is the transverse coordinate in nucleus A. For example, the number of partons (which can be defined only in lowest order because it is not an infrared-safe quantity at higher orders) produced in a central zero-impact-parameter collision of equal nuclei is

$$\Delta N_{AA} = T_{AA}(0)\sigma_{\rm jet}(p_{\rm sat}, \sqrt{s}, \Delta y, A) \qquad 3.$$

[1] In the actual calculation, protons and neutrons are treated separately.

in a rapidity interval Δy. A similar expression with $\sigma_{\rm jet}$ replaced by $\sigma_{\rm jet}\langle E_T\rangle$ gives ΔE_T, the transverse energy of minijets, in Δy.

Before discussing how to formulate the saturation condition to fix $p_{\rm sat}$, we notice that the average densities are obtained by dividing the total quantity with the volume that corresponds to the rapidity interval Δy, $\Delta V = \Delta z A_T = \tau_0 \Delta y\, \pi R_A^2$. This procedure, with densities averaged over the transverse plane, is easily generalized to local densities. The nucleon-nucleon luminosity in a transverse-area element $d^2\mathbf{s}$ is $T_A(|\mathbf{b}-\mathbf{s}|)T_B(s)d^2\mathbf{s}$, and the volume element is $dV = \Delta z\; d^2\mathbf{s} = \tau \Delta y\; d^2\mathbf{s}$, leading to (13)

$$n_{\rm pQCD}(\tau_0, \mathbf{s}) = \frac{dN}{\tau_0 \Delta y d^2\mathbf{s}} = \frac{2\sigma_{\rm jet}}{\tau_0 \Delta y} T_A(|\mathbf{b}-\mathbf{s}|)T_B(s) \qquad 4.$$

for the parton density and

$$\varepsilon_{\rm pQCD}(\tau_0, \mathbf{s}) = \frac{dE_T}{\tau_0 \Delta y d^2\mathbf{s}} = \frac{\sigma_{\rm jet}\langle E_T\rangle}{\tau_0 \Delta y} T_A(|\mathbf{b}-\mathbf{s}|)T_B(s) \qquad 5.$$

for the energy density. The densities depend on the cutoff scale through the cutoff dependence of cross sections.

The minijet cross sections above can be calculated separately for gluon, quark, and antiquark jets, allowing for the separate determination of the densities of quarks and antiquarks. From these cross sections the initial net baryon number density is obtained as $n_B = (n_q - n_{\bar q})/3$, which provides the initial condition for the net-baryon-number current that satisfies the conservation law (Equation 2).

Up to here, we have essentially discussed how to obtain from a boost-invariant momentum-space calculation of production cross sections, $\sigma_{\rm jet}$ and $\sigma_{\rm jet}\langle E_T\rangle$, the local densities n_B and ε. To close the calculation of minijet cross sections, the saturation momentum $p_{\rm sat}$ must be specified, and we do this by assuming that the parton (mainly gluon) production saturates when the wave functions of produced partons start to overlap.

In the transverse direction, the scale of the wave functions is $1/p_{\rm sat}$. The scale in the longitudinal direction is not as obvious, but we assume it is the same at the production time $\tau_0 = 1/p_{\rm sat}$. At this time, the volume occupied by particles in the rapidity interval Δy equals $\Delta V = \tau_0 \Delta y A_T$. At saturation, dividing this volume with the volume occupied by one jet, $V_{\rm jet}$, should equal the number of produced partons ΔN_{AA} in the rapidity interval Δy. This leads to the condition

$$\frac{\Delta N_{AA}(p_{\rm sat}, \sqrt{s}, \Delta y, A)}{\Delta y} \frac{\pi}{(p_{\rm sat})^2} = A_T = \pi R_A^2. \qquad 6.$$

To avoid introducing a rather arbitrary cutoff parametrization at the nuclear edges in transverse plane, we do not try to define the calculation of $p_{\rm sat}$ locally in the transverse plane. Instead, an effective value $p_{\rm sat}$, obtained from Equation 6 above, is used. Solving $p_{\rm sat}$ from this equation completes the calculation of primary production in the pQCD + saturation model. The initial energy densities at $1/p_{\rm sat}$

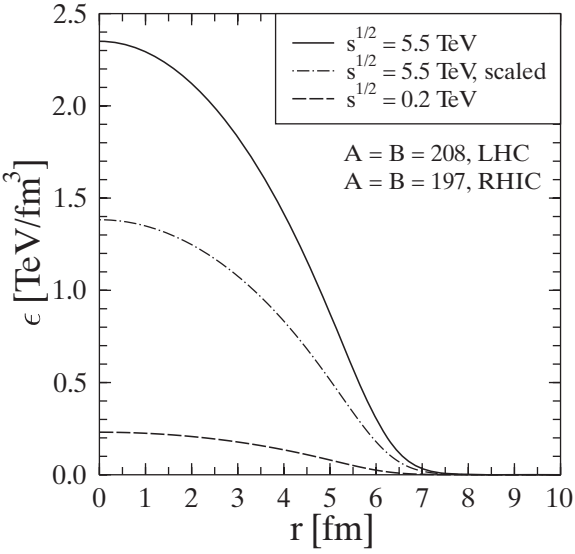

Figure 1 Transverse dependence of the initial energy distribution for a gold-on-gold collision at the Relativistic Heavy Ion Collider (RHIC) (*dashed line*) and lead-on-lead collision at the Large Hadron Collider (LHC) energy (*solid line*). The saturation scale is $p_{\rm sat} = 1.16$ GeV at RHIC and 2.03 GeV at LHC, with formation times of 0.170 fm/c and 0.100 fm/c, respectively. The dashed-dotted line shows the energy density at LHC if $\tau_i = 0.170$ fm/c is used, emphasizing the strong dependence of initial energy density on the assumed initial time.

at RHIC and LHC energies, $\sqrt{s_{NN}} = 200$ and 5500 GeV, respectively, are shown in Figure 1.

The above formulation of calculating the initial densities is applied in a central rapidity bin $|y| < \Delta y$. In the pQCD calculation, particle production depends on the rapidity through the parton distributions of colliding nuclei. However, when we use the results as initial conditions for the hydrodynamic calculation, we assume that boost-invariance is a good approximation at $y \approx 0$ and take the densities to give the boost-invariant initial conditions with no η dependence.

An attractive approach to particle production in heavy ion collisions at collider energies has been based on the assumption that the initial-state parton densities saturate and nonlinear dynamics becomes dominant (9). With increasing collision energy, the small-x partons, in particular the gluons, become the dominant part in the production, and their density in the initial wave function of the nucleus becomes so high that gluons interact coherently and their density saturates. The momentum below which gluons saturate is called the saturation scale, Q_s. It depends on the collision energy $\sqrt{s}$ and the mass number of the nuclei. From the point of view of the color fields, the high density or large occupation numbers of the field quanta

with momenta $\lesssim Q_s$ can be described as the formation of a color glass condensate. This part dominates the primary production at large $\sqrt{s}$ and can be treated in terms of a classical effective field theory (1, 8). Quantum corrections to the classical treatment have also been considered (14, 15; see also Reference 16 and references therein).

In the effective field theory approach to gluon production in AA collisions, when boost-invariance is assumed, a gauge can be chosen such that the problem can be formulated as a dimensionally reduced 2+1–dimensional theory. A numerical approach (17) with lattice regularization can be applied to the reduced theory.

The numerical calculations with lattice regularization started using SU(2) symmetry (18, 19) and other simplifications, such as cylindrical nuclei, but were soon formulated for SU(3) (20, 21) and realistic nuclear geometry. Also, local color neutrality in the transverse overlap region of the collision (21) was imposed and other smaller inconsistencies corrected, leading to a ratio of E_T/N, which is consistent with the physical interpretation of the saturation scale (22).

The lattice approach does not, however, give a value of the saturation scale itself; the overall normalization must be obtained from elsewhere. For RHIC phenomenology, the authors of Reference 21 suggest two sets of results, which, in light of the latest results of Reference 22, lead to the following qualitatively different descriptions of the final state:

1. In the case of a smaller scale μ, the total transverse energy $E_T \sim g_s^4 R_A^2 \mu^3$ produced from the classical fields roughly equals the experimentally measured result, whereas the number of initially produced partons ($N \sim g_s^2 R_A^2 \mu^2$) is only about half of the multiplicity of hadrons measured in the experiment. In this case, the only change in the final state is the fragmentation of partons to $\sim$2 hadrons on average. However, there would be no significant hydrodynamic evolution because this would reduce the transverse energy below the measured value. In this picture, which corresponds to the scenario suggested by Kharzeev & Levin (23), one would expect the photon and lepton-pair emission after the primary interactions to be very rare.
2. For a larger saturation scale, the number of partons is close to the measured number of hadrons, but the initially produced transverse energy is approximately 2.5 times bigger than the measured one (22). In this case, production must be followed by strong initial collective expansion in the longitudinal direction, allowing for a transfer of energy into the longitudinal motion. This case corresponds to the evolution suggested by pQCD + saturation + hydrodynamics calculation (13).

The energy dependence in the above models enters through the dependence of the saturation scales on the center-of-mass energy, leading, e.g., to the rather similar growth of multiplicity from RHIC to LHC in both models.

For a head-on, zero-impact-parameter collision, the produced system is cylindrically symmetric, all quantities depend only on τ and r, and the transverse flow is radial with no azimuthal dependence. We show results on hadron spectra displaying

effects from radial flow. However, a good test for the applicability of the hydrodynamic description of heavy ion collisions is provided by nonzero-impact-parameter collisions without cylindrical symmetry. In our example of the calculation of primary densities, the expressions (4, 5) hold also for nonzero-impact-parameter collisions. However, the determination of saturation scale becomes more involved, and a straightforward generalization of the saturation condition (Equation 6) leads the multiplicity to have a too-flat dependence on the number of participant nucleons, a possible measure of noncentrality of the collision (24).

Above, the transverse dependence of the initial densities is given by the number of collisions per unit transverse area: $n_{\mathrm{coll}}(\mathbf{b}, \mathbf{s}) \propto T_A(|\mathbf{b} - \mathbf{s}|)T_B(s)$. In another popular phenomenological approach, the initial densities are assumed to be proportional to the number of participants, also known as wounded nucleons, per unit transverse area.[2] In the eikonal Glauber model, this is defined as

$$n_{\mathrm{WN}}(\mathbf{s}; \mathbf{b}) = T_A\left(\mathbf{s} + \frac{1}{2}\mathbf{b}\right)\left[1 - \left(1 - \frac{\sigma T_B\left(\mathbf{s} - \frac{1}{2}\mathbf{b}\right)}{B}\right)^B\right] + T_B\left(\mathbf{s} - \frac{1}{2}\mathbf{b}\right)\left[1 - \left(1 - \frac{\sigma T_A\left(\mathbf{s} + \frac{1}{2}\mathbf{b}\right)}{A}\right)^A\right], \quad 7.$$

where σ is the nucleon-nucleon cross section. For a zero-impact-parameter collision, this indicates, except at the edges of the nuclei, a radial dependence approximately proportional to the sum of thickness functions $T_A(r)$ and $T_B(r)$. In the central region of the overlap area, the resulting density distribution is flatter than when the density is proportional to the number of collisions. This means smaller pressure gradients and slower evolution of transverse flow.

In the literature, both the proportionality to the number of binary collisions and to the number of participants has been used to fix either the initial entropy density or energy density. The proportionality constant is chosen to reproduce the measured final particle multiplicity in most central collisions. The centrality dependence of the multiplicity is then predicted by the model, but at RHIC, neither binary-collision scaling nor wounded-nucleon scaling reproduces the data. However, a linear combination of them does and is therefore used to describe the initial density distribution (25, 26).

We have not yet specified the initial transverse velocity $\mathbf{v}_T$. Usually this is taken to be zero. This choice is supported by the argument that the final state in each primary collision is randomly oriented in the transverse plane, and thus one expects the transverse-momentum average in any volume element to vanish. There is a slight flaw in this argument because the transverse density of produced partons is not constant, and this can lead to a nonzero momentum average in a

[2]Strictly speaking, wounded nucleons are nucleons that scatter inelastically, whereas participants are nucleons that scatter elastically or inelastically. In the recent literature this difference is usually ignored and both terms are used in the sense of participants.

(finite) volume element. However, comparison to experimental data shows that for agreement, only small initial transverse velocities are allowed. In the calculations shown below, $\mathbf{v}_T(\tau_0, \mathbf{r}) = 0$ has been used.

Because the use of hydrodynamics presumes thermal equilibrium, the time scale for thermalization after the primary production must be fixed. The dynamics of thermalization can be even more difficult to solve than that of primary production. Results of theoretical studies of thermalization have not yet converged. In the so-called bottom-up thermalization scenario (27), thermalization times are predicted to be long, of the order of 2–4 fm/c. A more recent idea of the role of instabilities in the expansion predicts much shorter thermalization times of order below 1 fm/c (28).

The thermalization time scale is an important issue because a hydrodynamic description of the elliptic flow can be achieved only if the thermalization time is short. In the numerical examples we provide below, we always use thermalization times below 1 fm/c. When showing results based on the minijet initial state, we use the production time scale as the thermalization time, $\tau_i = 1/p_{\rm sat}$.

2.3. The Equation of State of Strongly Interacting Matter

A major complication in the description of the evolution of the matter produced in a high-energy collision of nuclei is the change in the degrees of freedom. The dense initial-state parton matter expands and turns into a gas of hadrons and hadron resonances when dilute and cool enough. According to the present understanding, at large μ_B and small or moderate T, there exist different correlated phases, such as the phase with color-flavor locking (29). Nearing smaller μ_B, the transition between hadron resonance gas and QGP is believed to be of first order when μ_B is not too small. For two light quarks and one heavy quark, the phase boundary is conjectured to end at a critical point, and below that the transition is a rapid crossover. The quantitative theoretical information from QCD lattice simulations, which have recently been extended from the T-axis to finite chemical potential, supports this picture. There are also arguments in favor of the existence of strong correlations in the quark matter close to the phase boundary. These may explain the ideal-fluid behavior of QGP indicated by successful hydrodynamical explanation of elliptic flow. When matter is assumed to be in the state of noninteracting quarks and gluons, the ideal QGP, a simple ideal gas EoS of massless particles ($P = \varepsilon/3$) is often used to describe it. A more sophisticated but less usual way is to use parametrized lattice QCD results.

In heavy ion collisions at collider energies, the net-baryon number is small, with $\mu_B \lesssim 50$ MeV (30), indicating a crossover transition. Somewhat unexpectedly, from the point of view of hydrodynamic expansion, the difference between a weak first-order transition and a rapid crossover is not very significant, as long as the EoSs are relatively similar away from the transition region and the increase in entropy and energy densities around the critical temperature is sufficiently large and rapid (31). Upon a closer look this is not so surprising because the main

qualitative feature is a jump in the thermodynamical densities ε and s. The size of this jump depends essentially on the size of the change of the number of degrees of freedom. From the point of view of hydrodynamics, the rapid jump in ε combined with a slower change in pressure appears as a softening of the EoS. It is seen as a slowdown in the acceleration of the transverse flow in the transition region. Details differ for the two cases, but the final features of flow are quite similar and the quantitative differences in the final hadron spectra are small.

An interacting hadron gas can be described in good approximation as a gas of noninteracting hadrons and resonances. The inclusion of resonances mimics the effects of both attractive and repulsive interactions between hadrons reasonably well (32). However, the repulsive interaction between baryons at large net-baryon densities must be included as an additional mean field (33) or as an excluded volume correction (34) to give a reasonable phase-transition behavior between hadronic and partonic phases. A detailed account of constructing an EoS with a mean field can be found, for example, in Reference 35.

In calculations, we use an EoS with ideal QGP in the high-temperature phase and a hadron resonance gas with a mean field below the transition. A first-order transition is implemented by introducing a bag constant B into the QGP phase and connecting the two phases with a Maxwell construction. We use $N_f = 3$, and the bag constant B and mean field constant K are chosen to be $B^{1/4} = 243$ MeV and $K = 450$ MeV fm^3, respectively, giving $T_c = 167$ MeV for the transition temperature.

An additional complication in constructing an EoS of a hadron gas relevant for heavy ion collisions is the chemical composition of the hadron gas. The usual assumption of hydrodynamics is that of chemical equilibrium. This assumption is supported by thermal models that can reproduce the observed hadron abundances by assuming a thermal source in $T \approx 170$ MeV temperature. However, many studies have found that the p_T distributions of hadrons are better described by assuming a colder, flowing source in $T = 100$–140 MeV temperature. Thus, the assumption of chemical equilibrium between these temperatures is questionable. In many hydrodynamical calculations, this observation is simply ignored and chemical equilibrium is assumed to hold until kinetic freeze-out at $T = 100$–140 MeV. In such cases, one can reproduce the slopes of the hadron p_T spectra, but it is not possible to reproduce simultaneously both baryon and antibaryon yields.

One solution to this problem is the so-called single freeze-out model (36), in which a suitable choice of freeze-out surface allows one to fit the p_T spectra, even if the kinetic freeze-out temperature is taken to be the same $T \approx 165$ MeV as the chemical freeze-out temperature. As we show below, in the context of hydrodynamical models, a similar approach with $T = 150$ MeV can be used to reproduce, at least approximately, the hadron p_T distributions in most central collisions at RHIC energies (36a). Whether the anisotropies of particle distributions (see Section 3.3) can also be reproduced this way has not been tested so far.

Another solution to this problem is to assume two separate freeze-outs—chemical and kinetic—and to modify the EoS between these temperatures accordingly. In such an approach, the hadron yields are assumed to be fixed at some chemical freeze-out temperature, usually soon below or at the phase-transition temperature. These hadron yields are subsequently described as conserved currents, and each conserved hadron species is assigned a chemical potential. This way the yields of all hadron species can be reproduced separately, even if a low kinetic freeze-out temperature is used (37).

Such an EoS changes the buildup of collective motion—i.e., flow—very little because pressure as a function of energy density, $P = P(\varepsilon)$, is very similar to the chemical equilibrium EoS (38, 39). However, temperature as function of energy density changes radically, and when collective and thermal motion are folded to calculate observable particle distributions, the results differ (39, 40).

2.4. Transverse Flow

To illustrate the transverse flow, Figure 2 shows the boundaries of QGP and hadron gas, with the mixed phase between them. Also, three contours of temperature are depicted, as well as the flow lines with 1-fm intervals starting at τ_0. The initial conditions are those from the pQCD + saturation model at RHIC energy $\sqrt{s_{NN}} = 200$ GeV.

According to this calculation, the maximum lifetime of the plasma phase is 5 fm/c, and that of the mixed phase is ~8 fm/c. The flow lines show how the fluid elements accelerate and move. The slope of the flow line is related to the velocity of the fluid and the curvature to the acceleration. In the mixed phase, where the pressure is constant, flow lines are straight because there is no acceleration. At small r, gradients are small and the flow lines bend slowly. In particular, in a plasma, when r increases, the pressure gradient, and consequently the acceleration, increases, indicated by the faster bending of flow lines. Along the flow line starting at $r = 8$ fm/c, the densities are small even at τ_0, and this region is insignificant in calculating the spectra. For calculational reasons the initial densities are taken to go smoothly to zero, and the hydrodynamic equations are also solved at large values of r.

3. HADRON DISTRIBUTIONS AND CORRELATIONS

3.1. Freeze-out and the Calculation of Hadron Spectra

As matter expands, distances between particles become large, collisions cease, and momentum distributions freeze out. The condition for the freeze-out to occur is usually expressed locally in terms of the energy density or temperature reaching a given value. This determines a three-dimensional freeze-out surface $\sigma^\mu(x)$ in space-time. The prescription of Cooper & Frye (41) convolutes the flow with the

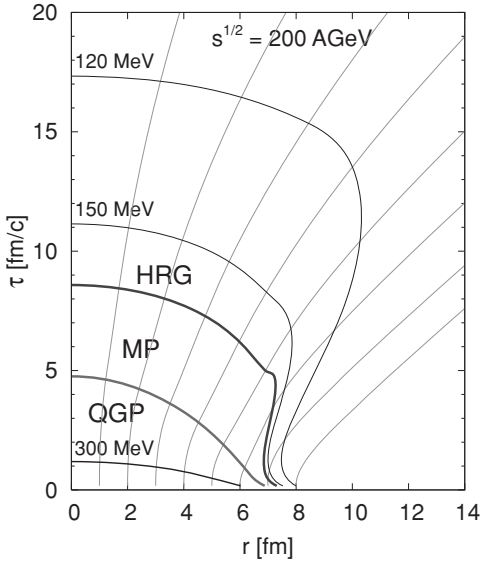

Figure 2 Temperature contours at 300 (in quark-gluon plasma, QGP), 150, and 120 MeV (in hadron resonance gas, HRG), and the boundaries of mixed phase (MP) with QGP and HRG at $T_c = 167$ MeV. Flow lines are also shown. Initial conditions are from a pQCD + saturation calculation at $\sqrt{s_{NN}} = 200$ GeV. Note that the slope of the flow line is related to the velocity and the curvature to the acceleration.

thermal motion along the freeze-out surface:

$$\pi \frac{dN}{d^3\mathbf{p}/E} = \frac{dN}{dy dp_T^2} = \pi \int_\sigma d\sigma_\mu(x) p^\mu f(x, p; T(x)) \qquad 8.$$

$$= \frac{g}{2\pi} \sum_{n=1}^{\infty} (\pm 1)^{n+1} \int_\sigma r\tau \left[-p_T I_1\left(n\gamma_r v_r \frac{p_T}{T}\right) K_0\left(n\gamma_r \frac{m_T}{T}\right) d\tau \right.$$

$$\left. + m_T I_0\left(n\gamma_r v_r \frac{p_T}{T}\right) K_1\left(n\gamma_r \frac{m_T}{T}\right) dr \right]. \qquad 9.$$

Equation 9 is valid for cylindrically symmetric, boost-invariant flow, with v_r the radial flow velocity, $\gamma_r = 1/\sqrt{1 - v_r^2}$, and K_i and I_i are Bessel functions of second kind.

The unstable particles are treated as follows: First, the spectra of all hadrons and hadron resonances are calculated using Equation 9. We then follow the chains of all possible two- and three-body decays and collect the spectra of final stable hadrons (42). Stable hadrons can either be interpreted as all those that do not decay through strong interactions, or we can follow the feed-downs via weak

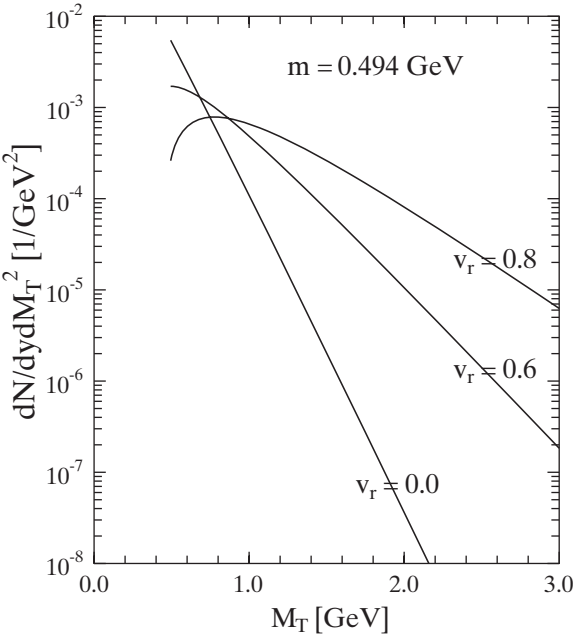

Figure 3 The effect of flow on the spectrum of kaons. Temperature is unchanged and the spectrum is shown for radially flowing matter at velocities $v_r = 0$, 0.6, and 0.8.

and electromagnetic decays, e.g., we can calculate the π^0 spectrum including both the π^0s at freeze-out and all the decays that lead to π^0s, and then study the photon spectrum from π^0 decays alone or from all decays with photons in the final state. Phenomenologically, an important case is that of feed-down nucleons from weak decays of strange hyperons. Here again, we can calculate, for example, the spectrum of Λs and then see how it contributes through weak decays to the spectrum of protons.

Before showing our results at RHIC and LHC energies, we discuss how the radial flow affects a spectrum. In Figure 3 we show the spectrum of kaons from matter at rest or flowing at velocities $v_r = 0.6$ and 0.8. We assume that the matter decouples at a fixed time so that only the second term in Equation 9 contributes. The temperature of the matter is the same in each case and is essentially the inverse of the logarithmic slope of the spectrum for $v_r = 0$. From the asymptotic properties of modified Bessel functions of second kind, it is clear that at large m_T the change in the slope, when v_r changes to a nonzero value, can be expressed by replacing the temperature T with an effective temperature $T_{\rm eff} = T\sqrt{(1+v_r)/(1-v_r)}$. For $v_r = 0.6$ the change is a factor of two, and for $v_r = 0.8$ a factor of three.

3.2. Transverse Momentum Spectra of Hadrons

Next we compare some of the hydrodynamical results (43) with the experimental transverse momentum spectra measured by the STAR (44–47), PHENIX (48–53), PHOBOS (54, 55), and BRAHMS (56–58) collaborations for the most central bins in Au + Au collisions at $\sqrt{s_{NN}} = 130$ and 200 GeV. The calculated spectra are obtained by using Equation 9 with the flow illustrated in Figure 2.

Note that a hydrodynamic calculation cannot describe the hadron spectra at large transverse momenta. At large p_T, the hydrodynamical calculation shows an approximate exponential behavior, whereas the tails of measured spectra essentially obey a power law. At RHIC, the transition from steep exponential to a shallower power behavior takes place at $p_T \sim 3$ GeV. The fraction of hadrons with $p_T \gtrsim 3$ GeV from all hadrons is small, and they originate from the fragmentation of high-energy partons, which suffer some energy loss in the dense medium of low-energy partons, but are not thermalized. We return to the interplay of the low-energy partons, which provide the main transverse energy and are assumed to thermalize, and the high-energy partons, which lose some fraction of energy in rescattering but require a much larger system for thermalization.

We start with the p_T spectra of identified hadrons at midrapidities. Figure 4 shows the PHENIX data collected for positive pions, kaons, and protons in the most central 5% of Au + Au collisions for $y = 0$ at $\sqrt{s_{NN}} = 130$ GeV (50). Similarly, in Figure 5, STAR (46), PHENIX (52), and BRAHMS (57, 58) data are shown at $\sqrt{s_{NN}} = 200$ GeV. Note the scaling factors 10 and 1000 for kaons and protons, respectively. An important issue of uncertainty in the calculation is the dependence of the results on the decoupling temperature. This is shown by plotting the results for freeze-out temperature $T_{\rm dec} = 150$ MeV (solid lines) and 120 MeV (dotted lines). Note that the normalization of the pion spectrum is almost independent of the decoupling temperature. Because pions provide the main contribution to the total multiplicity, $dN_{\rm tot}/dy$ depends only weakly on $T_{\rm dec}$. However, the multiplicity of heavier particles is very sensitive to $T_{\rm dec}$, as expected. The shape of all three spectra changes clearly with the decoupling temperature. This follows from the increase in flow velocity, characterized by the increase of the effect with the increasing mass of the particle. The aim of this calculation has not been to find a best fit to the data, but the results show that both the normalization and the slope of the data at momenta $p_T \lesssim 3$ GeV can be described quite well with a single $T_{\rm dec}$ in the neighborhood of 150 MeV.

For the identified particles in Figures 4 and 5, the measured spectra do not extend to large enough p_T to show clearly the deviation from the hydrodynamic results, with the exception of the proton spectra. If the decoupling temperature is 150 MeV to reproduce the normalization, the slope tends to be too steep. The proton yield from jet fragmentation, as explained in detail in Reference 43, does not seem to be large enough in the $p_T \sim 3 \ldots 5$ GeV region to bring the calculation into agreement with the data. In Figure 6, the spectra of two other heavy particles are shown, those of antilambdas and antiprotons. These show the same trend as protons,

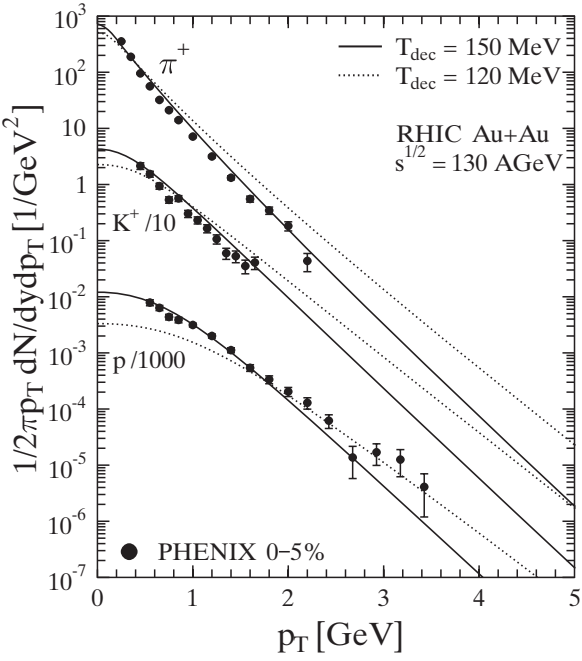

Figure 4 Transverse momentum spectra of positive pions, positive kaons, and protons at $y = 0$ in the most central 5% of Au + Au collisions at $\sqrt{s_{NN}} = 130$ GeV. The solid and dotted lines indicate our hydrodynamic results for freeze-out temperature $T_{dec} = 150$ MeV and $T_{dec} = 120$ MeV, respectively. The PHENIX data (50) is plotted with the given total error bars. Note the scaling factors 10 and 1000 for kaons and protons, respectively. Both the hydrodynamic result and the PHENIX data contain the feed-down contributions from hyperons. RHIC, Relativistic Heavy Ion Collider.

pointing to the need for separate chemical and kinetic decoupling when describing simultaneously the details of all spectra. Studies with separate chemical and kinetic decoupling, in which the stable particle numbers are fixed after chemical freeze-out, indeed show that the spectra of pions and kaons become almost independent of the kinetic decoupling temperature $T_{dec,kin}$, whereas the (anti)proton spectra widen with decreasing $T_{dec,kin}$ (39, 40). There are, however, claims in the literature that separate chemical and kinetic decoupling lead to a worse overall fit to the slopes of p_T distributions than what can be achieved by requiring chemical equilibrium until kinetic freeze-out (59, 60). Studies exploring the effects of initial time, the shape of initial distributions, and the value of $T_{dec,chem}$ while using two separate freeze-outs are needed to settle the issue.

The range between which hydrodynamics can be used to describe the hadron spectra is indicated clearly in Figure 7, which shows results from our hydrodynamical calculations and from a pQCD jet calculation, followed by an energy loss

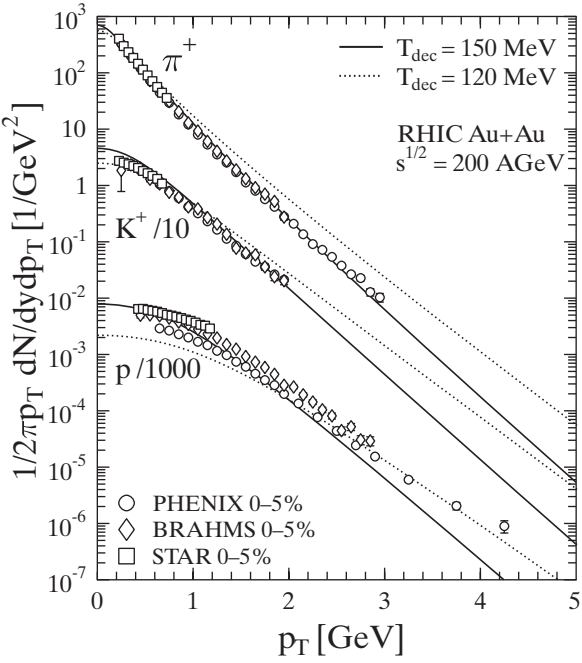

Figure 5 Transverse momentum spectra of positive pions, positive kaons, and protons at $y = 0$ in the most central 5% of Au + Au collisions at $\sqrt{s_{NN}} = 200$ GeV. The solid and dotted lines indicate our hydrodynamic results for freeze-out temperature $T_{dec} = 150$ MeV and $T_{dec} = 120$ MeV, respectively. The PHENIX data (52) and the BRAHMS data (57, 58) are shown with statistical errors, and the STAR data (46) with the given total error bars. The hydrodynamic calculation and the PHENIX data are without the hyperon feed-down contributions, whereas the STAR and BRAHMS data contain the feed-down. RHIC, Relativistic Heavy Ion Collider.

in the medium before the jet fragments into hadrons (see below). The STAR and PHOBOS data are plotted with the given total error bars, the PHENIX data by adding the given statistical and systematic errors in quadrature, and the BRAHMS data with the given statistical error bars.

The transverse spectrum up to ∼3 GeV is similar to that of the dominant pion component shown separately in Figure 5. It has the shape typical of the spectrum from hydrodynamic calculations, falling off roughly exponentially. In the region $p_T \sim 3 \ldots 4$ GeV, there is a large change in the slope, indicating a change in the overall production mechanism. The calculation of primary production proceeds through the hard and semihard interactions between the partons of the incoming nuclei, both in the case of initial conditions for hydrodynamical equations and the energy loss of the jets. In the hydrodynamic calculation, the produced partons are assumed to thermalize quickly and then undergo hydrodynamic expansion in local

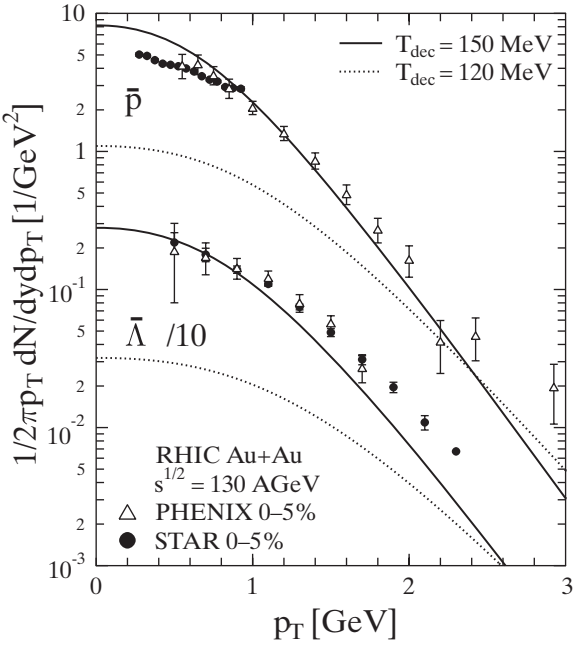

Figure 6 Transverse momentum spectra of antiprotons and antilambdas at $y = 0$ in the most central 5% of Au + Au collisions at $\sqrt{s_{NN}} = 130$ GeV. Our hydrodynamic results are for freeze-out temperature $T_{dec} = 150$ MeV (*solid line*) and $T_{dec} = 120$ MeV (*dotted line*), with hyperon feed-down contributions included, as in the PHENIX $\bar{p}$ (50) and $\bar{\Lambda}$ (51) data and the STAR data (47). RHIC, Relativistic Heavy Ion Collider.

thermal equilibrium until the freeze-out. In the calculation of jet fragmentation after energy loss, the produced high-energy partons are assumed to survive the thermalization, but lose energy when traversing the thermal medium formed by the lower-energy partons. When energy loss and fragmentation are taken into account, the original energy of the partons that fragment to hadrons of $p_T \gtrsim 3$ GeV must be of the order of ∼6 GeV or greater. It turns out that the contribution of partons with $p_T \gtrsim 4$ GeV to the production of (transverse) energy is less than 5%, justifying the assumption that all produced transverse energy is thermalized. The details of the jet-energy loss and fragmentation calculation are explained in References 43 and 61.

Although the two-component approach, hydrodynamically expanding thermal matter as the source of low-p_T hadrons and jet fragmentation after energy loss producing the high-p_T hadrons, seems reasonable and justified, adding them straightforwardly would be too naive. In the region of turnover from one mechanism to the other, both contribute, but part of the hadrons cannot be assigned to either component. Other mechanisms like recombination can also contribute in this region

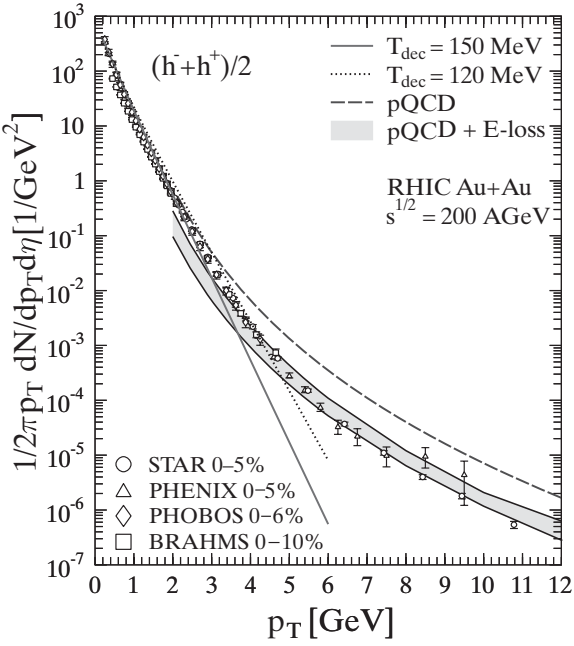

Figure 7 Transverse momentum spectra of charged particles at $\eta = 0$ (averaged over $|\eta| \leq 0.1$) in the most central 5% of Au + Au collisions at $\sqrt{s_{NN}} = 200$ GeV. Our hydrodynamic results are shown for $T_{dec} = 150$ MeV (*solid line*) and $T_{dec} = 120$ MeV (*dotted line*). The pQCD fragmentation results are shown with (*shaded band*) and without (*dashed line*, see text) energy losses. The data is taken by STAR (44), PHENIX (48), PHOBOS (54), and BRAHMS (56).

(61a). Accurate data in this area would be useful in understanding both the energy loss and thermalization of produced partons.

As an example of the dependence on the collision energy, $\sqrt{s_{NN}}$, Figure 8 shows an extension of the calculation to the CERN LHC, with $\sqrt{s_{NN}} = 5500$ GeV for the heavy ion collisions. In the calculation of initial conditions from the primary parton interactions, all parameters are fixed except for the collision energy. The saturation scale changes from $p_{sat} = 1.16$ GeV at RHIC energy to $p_{sat} = 2.03$ GeV at LHC. The total multiplicity increases from $dN_{tot}/dy \approx 1000$ at RHIC to 4500 at LHC. The initial thermal densities are higher and lead to longer expansion and stronger transverse flow at the decoupling. This is seen in the change of the region where the component of thermal particles goes over to the component of particles from jet fragmentation with energy loss. At RHIC the transition is centered around $p_T \sim 3$ GeV, whereas at LHC it is predicted to be $p_T \sim 5$ GeV. The larger p_T region where thermal particles dominate should also be seen in elliptic flow. At the present RHIC energies, the hydrodynamic predictions of elliptic flow start

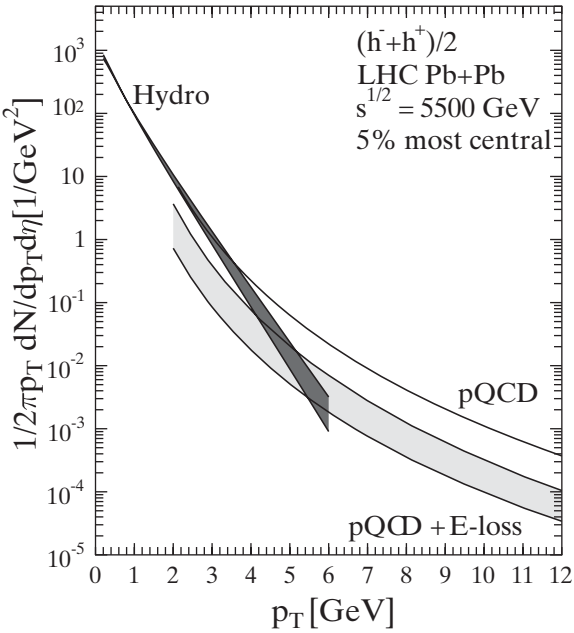

Figure 8 Predictions for the transverse momentum spectra of charged hadrons at $\eta = 0$ in the most central 5% of Pb + Pb collisions at Large Hadron Collider (LHC) energy $\sqrt{s_{NN}} = 5500$ GeV. The shaded band in the hydrodynamic results shows the freeze-out temperature interval 120–150 MeV. The solid curve labeled pQCD corresponds to the pQCD fragmentation results without energy losses. The shaded band labeled pQCD + E-loss describes the uncertainty in the pQCD fragmentation results with energy losses.

to overshoot the data above $p_t \sim 2$ GeV, but if the thermal component grows as predicted in Figure 8, the parameter of elliptic flow, v_2, should follow the hydrodynamical calculation to larger transverse momenta.

3.3. Elliptic Flow

The particle production in primary collisions is azimuthally isotropic, whereas the reaction zone in noncentral collisions is not, but has an elongated shape. If produced particles rescatter, the particles moving in the direction of the longer axis of the reaction zone are more likely to change their direction than the particles moving in the direction of the shorter axis. Therefore, the observed emission pattern of particles will be azimuthally anisotropic, and the more frequent the rescattering, the more anisotropic the particle distribution.

In this way, the anisotropy of the final particle distribution is a measurement of the frequency of rescatterings during the dense phase of the collision. This

anisotropy can be quantified as the coefficients of the Fourier expansion of the azimuthal particle distribution (62):

$$\frac{\mathrm{d}N}{\mathrm{d}y\mathrm{d}\phi_p} = \frac{\mathrm{d}N}{2\pi\mathrm{d}y}(1 + 2v_1\cos(\phi - \phi_R) + 2v_2\cos 2(\phi - \phi_R) + \cdots),$$

$$\frac{\mathrm{d}N}{\mathrm{d}y\mathrm{d}p_T\mathrm{d}\phi_p} = \frac{\mathrm{d}N}{2\pi\mathrm{d}y\mathrm{d}p_T}(1 + 2v_1(p_T)\cos(\phi - \phi_R) + 2v_2(p_T)\cos 2(\phi - \phi_R) + \cdots), \quad 10.$$

where ϕ_R is the azimuthal angle of the event plane (the plane spanned by the beam direction and the impact parameter). Assuming that the experimental uncertainties in event-plane reconstruction can be corrected for, each event can be rotated such that $\phi_R = 0$. The first and second coefficient of the expansion, v_1 and v_2, are usually referred to as directed and elliptic flow, respectively. Because the system is usually thinner in the direction parallel to the impact parameter, the in-plane direction, than in the out-of-plane direction, the value of v_2 is positive.

At midrapidity, all uneven coefficients are zero owing to symmetry. At SPS and RHIC energies, the directed flow, v_1, is expected to be very small and most of the experimental and theoretical interest has been directed toward measuring and analyzing the elliptic flow, v_2. Recently, the higher harmonics, v_4, v_6, and v_8 have also been measured (63–65).

In a hydrodynamic picture, the buildup of momentum anisotropies is easy to understand in terms of pressure gradients. The average pressure gradient between the center of the system and the surrounding vacuum is larger in the direction where the collision system is thinner. Therefore, the collective flow is stronger in that direction and more particles are emitted there than in the orthogonal direction, where the collision system is longer.

As mentioned above, the more the particles rescatter, the larger the observed anisotropy. Because hydrodynamics assumes practically infinite scattering rate and zero mean free path, it is often assumed to give an upper limit of anisotropy at fixed impact parameter (25). However, this upper limit depends on the EoS and, in principle, it is possible that hydrodynamical description with very soft EoS would give a smaller anisotropy than, for example, a microscopic cascade description (66).

If the freeze-out happens at the same temperature for all particle species, a signature of hydrodynamic flow is that the heavier the particle, the flatter the slope of its p_T spectrum. Similarly, the p_T-averaged elliptic flow v_2 increases when particle mass increases. However, the p_T-differential elliptic flow $v_2(p_T)$ has the opposite behavior: The heavier the particle, the smaller the anisotropy at fixed p_T. The apparent discrepancy has a simple explanation: v_2 is not an additive quantity, but when p_T-averaged v_2 is calculated from p_T-differential $v_2(p_T)$, the latter is weighted by the particle distribution. Thus, the flatter p_T distribution of a heavier particle weights more the high-p_T region, where $v_2(p_T)$ is larger. Therefore, even if $v_2(p_T)$ is smaller at all p_T for a heavier particle, the p_T-averaged v_2 can be larger

than v_2 for a light particle. Whether this happens in practice and how large the differences are depend on the details of the flow profile, i.e., expansion dynamics, and the resonance decays.

The mass ordering of the low-p_T anisotropy has its origin in the behavior of boosted particle distributions. As is well-known, transverse flow shifts the p_T distributions to larger values of p_T. In the extreme case in which the speed of the collective motion is the same everywhere, as in the case of a thin shell expanding with a velocity v, the particle distribution develops a maximum at some finite p_T [the so-called blast-wave peak (67)] and a local minimum at $p_T = 0$. The heavier the particle, the larger the p_T at the peak. Compared with a case without transverse flow, the particle yield is thus depleted at low p_T. The heavier the particle and the larger the flow velocity v_T, the larger the depletion. Correspondingly, if the flow velocity is larger in the in-plane than in the out-of-plane direction, the low-p_T depletion is larger for particles moving in the in-plane direction than the out-of-plane direction and the overall anisotropy, v_2, is reduced. This reduction and the range in which it occurs increase with the particle mass and average transverse flow velocity. In the extreme case of a thin expanding shell, this reduction can be so strong that it reverses the sign of the anisotropy and v_2 becomes negative. When the thin shell is replaced by a more realistic velocity profile, the peak in transverse-momentum distribution disappears. Similarly, a more realistic velocity distribution weakens the reduction of v_2 at low p_T, but the mass ordering of v_2 at low p_T remains. Whether some particles depict positive or negative v_2 at low p_T depends on the details of the flow velocity of the source.

For relativistic $p_T > m$, the particle mass does not play any role in the thermal distribution and, consequently, $v_2(p_T)$ of different particles converge. In a simple model in which the flow-velocity profile is replaced by its average value, $v_2(p_T)$ increases with p_T and approaches unity asymptotically. The details of the flow-velocity profile can change this behavior, but so far no hydrodynamical calculation has reproduced the experimentally observed saturation of elliptic flow.

3.3.1. CENTRALITY DEPENDENCE In a hydrodynamic description, the final anisotropy of particles is almost directly proportional to the geometrical anisotropy of the initial state (68). The proportionality is, however, nontrivial and depends on the applied decoupling criterion. When the impact parameter increases and the collision becomes more peripheral, the collision system becomes more and more elongated and its geometric anisotropy increases. We can thus expect the observed momentum anisotropy to increase as well. The data in Figure 9 shows increasing elliptic flow with decreasing centrality both at SPS and RHIC energies, but the magnitude of the flow differs from the hydrodynamical result. At SPS energy the data is consistently below the calculation, whereas at RHIC energy ($\sqrt{s_{NN}} = 200$ GeV in Figure 9) the data is reproduced up to semicentral collisions but is below the calculation at peripheral collisions.

The failure of hydrodynamics to describe the anisotropy in most peripheral collisions and at SPS energy is often explained by a lack of necessary

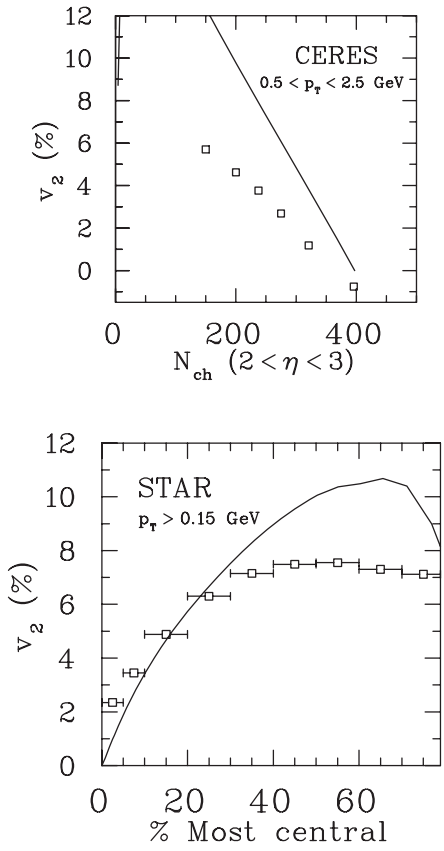

Figure 9 Elliptic flow v_2 of charged hadrons as a function of centrality at (*top panel*) Pb + Au collisions at $\sqrt{s_{NN}} = 17.3$ GeV measured by CERES (69) and at (*bottom panel*) Au + Au collisions at $\sqrt{s_{NN}} = 200$ GeV measured by STAR (64). Hydrodynamical calculations are taken from References 31 and 69. Note that the hydrodynamical results are not directly comparable because of different p_T cuts implemented.

thermalization owing to the small size and/or particle number of the collision system (70). An alternative explanation assumes that the initial partonic state is sufficiently thermalized, but the final hadronic state has such a large viscosity that it cannot be modeled using ideal-fluid dynamics (71). The latter approach has been tested using so-called hybrid models in which the plasma phase and phase transition are described using ideal hydrodynamics, but the hadron phase is described using a cascade model (60, 71–73). The centrality dependence of p_T-averaged elliptic flow at RHIC has been reproduced nicely using such a hybrid approach (60, 71), but the results for p_T differential v_2 at $\sqrt{s_{NN}} = 200$ GeV collision energy are not available at the time of this writing.

The beginning of this section argued that hydrodynamics leads to the largest possible anisotropy. However, at most central collisions at RHIC, the data tend to be above the hydrodynamical calculation. Fluctuations in the shape of the initial system may explain this. Owing to these fluctuations, the initial shape of some events in almost-central collisions can be in-plane elongated, even if the shape in most events is out-of-plane elongated. Thus, elliptic flow is negative in some events, but because experimental analysis measures the magnitude of the anisotropy, not its sign, elliptic flow is measured as positive in all events, and the measured value is larger than the average value. The initial state of a hydrodynamical calculation, however, is an average initial state in which fluctuations of the spatial anisotropy cancel each other and the calculated anisotropy is smaller than measured (74). Preliminary calculations in which the initial-state fluctuations are included favor this interpretation by leading to better reproduction of the data (75).

The general trend is that a stiffer EoS and a lower freeze-out temperature lead to larger p_T-averaged flow if nothing else in the model is changed. This also changes the single particle distributions. If these are still required to fit the data, additional changes are required. For example, a stiffer EoS usually necessitates a higher freeze-out temperature. The combined effect largely cancels and the final p_T-averaged anisotropy is almost unchanged in semiperipheral collisions in which a hydrodynamical description works best (31).

3.3.2. MOMENTUM AND PARTICLE SPECIES DEPENDENCE Hydrodynamic calculations at SPS and RHIC energies lead to anisotropy, which increases with increasing p_T and approaches unity asymptotically. Simple parametrizations of flow (so-called blast-wave models) also lead to this kind of behavior, which differs from experimental observations in which v_2 saturates at high p_T. At midrapidity, the agreement between the data and calculations depends on energy in the same way as for the centrality dependence: At SPS energies the calculations overestimate the data, whereas at RHIC energy a good agreement can be reached. The p_T range in which the data can be reproduced depends on the particle species. Charged hadrons and pions can be fit up to $p_T \approx 1.5$ GeV/c, whereas protons follow the calculations up to $p_T = 2.5$–3 GeV in minimum-bias collisions. This behavior is qualitatively similar to that seen in Figures 4 and 5 for transverse momentum spectra, where hydrodynamically calculated spectra fit the data up to $p_T \sim 3$ GeV.

A hydrodynamic description predicts a characteristic mass dependence of elliptic flow at low p_T. The higher the mass, the lower the v_2. How large this difference is depends on the details of the flow profile and therefore on the EoS. If chemical equilibrium in the hadronic phase is assumed, the differential anisotropy of pions can be well reproduced when the p_T spectra of pions is reproduced. In such a case, the proton $v_2(p_T)$ depicts sensitivity to the phase transition. If the phase transition takes place in a narrow temperature interval and has large latent heat, the proton differential anisotropy can almost be reproduced. If there is no phase transition, the calculated proton anisotropy is clearly above the data (31).

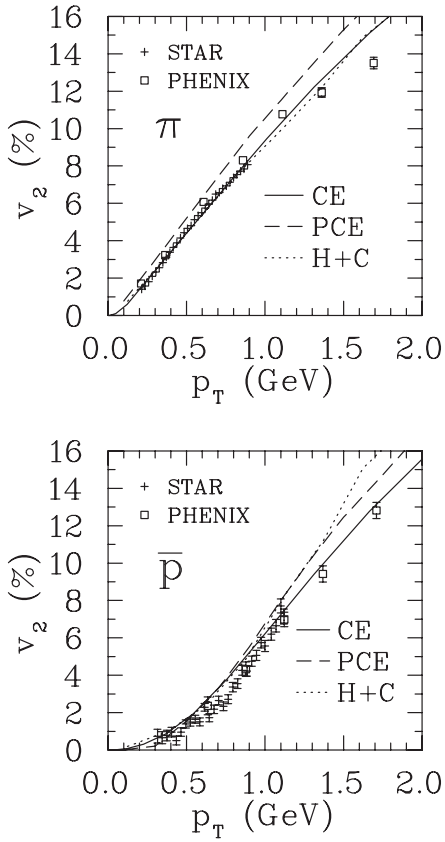

Figure 10 Pion (*top panel*) and antiproton (*bottom panel*) $v_2(p_T)$ at midrapidity in minimum-bias Au + Au collisions at $\sqrt{s_{NN}} = 200$ GeV. Hydrodynamical results are labeled CE for chemical-equilibrium result (31), PCE for chemical-nonequilibrium result (39, 60; T. Hirano, personal communication), and H + C for hydro + cascade hybrid model at $\sqrt{s_{NN}} = 130$ GeV energy (71). The data are taken by STAR (76) and PHENIX (77).

The status of strange particles is less satisfactory. Kaons and Λ-baryons show similar dependence on the EoS than protons, but the difference between the data and hydrodynamic calculation is larger than in the case of protons (31).

Unfortunately, it is not yet possible to use the apparent sensitivity of proton $v_2(p_T)$ to the EoS to quantitively constrain the EoS. If the requirement of chemical equilibrium is relaxed and one uses separate chemical and kinetic freeze-out temperatures, the fit to pion $v_2(p_T)$ is lost (see Figure 10 and Reference 39). However, if the hadronic phase is described using the RQMD transport model, as in Reference 71, for the $\sqrt{s_{NN}} = 130$ GeV collision energy, the yields are correct and the $v_2(p_T)$ is described as well as in the case of chemical equilibrium. Thus, there

is a considerable uncertainty in the description of the hadronic stage of the evolution, which makes it impossible to draw final conclusions about the EoS needed to describe the differential anisotropy.

Another uncertainty here is the effect of viscosity. The ability of ideal-fluid hydrodynamics to reproduce the v_2 data at RHIC has been interpreted to mean that the value of shear viscosity in QGP is particularly low (59, 78). However, viscosity has been estimated to decrease elliptic flow (4), and chemical nonequilibrium increases elliptic flow (39, 40). Hirano & Gyulassy have argued that the plasma has sufficiently low viscosity to allow its modeling using ideal hydrodynamics, but the dissipative effects in the hadronic phase are the reason for the failure of chemically nonequilibrium hydrodynamics to describe the data (59). This claim seems to be validated by the ability of hybrid models to describe the data, but final conclusions must wait for the complete results of hybrid calculations and the results of viscous calculations (5, 79).

3.3.3. PSEUDORAPIDITY DEPENDENCE The p_T-averaged elliptic flow has quite a strong dependence on pseudorapidity (76, 80–82). In a narrow region around midrapidity, $|\eta| < 1$, elliptic flow remains approximately constant (76, 83) but decreases strongly toward larger pseudorapidities. However, the charged particle multiplicity depicts a much wider plateau around midrapidity than does elliptic flow (84).

The purely hydrodynamic calculations have not reproduced the pseudorapidity dependence of elliptic flow, although the same calculations reproduce the multiplicity as a function of pseudorapidity (85, 39). However, a hybrid model that reproduces the centrality dependence of elliptic flow also gives a reasonable description of its pseudorapidity dependence (60). The failure of ideal-fluid hydrodynamics has been interpreted in the same way as in the case of centrality dependence—either as an incomplete thermalization of the system at large rapidities from the beginning (70) or as an effect of viscosity and incomplete thermalization at the late stage (60). There are also other open questions in the hydrodynamic treatment that may affect the results: The initial shape of the system, large deviations from boost-invariant flow, and different thermalization time and freeze-out temperature at different rapidities could all affect the final anisotropy and are mostly unexplored. It is therefore possible that the thermalized region where hydrodynamics works at RHIC energy is relatively narrow in rapidity, but final conclusions cannot be drawn yet.

3.4. Two-Particle Bose-Einstein Correlations

Information about the space-time structure of the system formed in a heavy-ion collision can be obtained by measuring the low-momentum correlations of identical particles. For bosons these correlations are called Bose-Einstein correlations, and the method for their interpretation is termed HBT interferometry, according to the originators of this method (86). Here we show only the basics of the HBT

formalism as applied to hydrodynamic models and its most important results. A detailed explanation about this technique can be found in Reference 87, and the present status is discussed in recent reviews (88, 89). HBT in hydrodynamical context is discussed more throughly in Reference 90.

Intensity interferometry is based on an analysis of the two-particle momentum correlation function,

$$C(\boldsymbol{q}, \boldsymbol{K}) = \frac{E_1 E_2 \frac{dN}{d^3 p_1 d^3 p_2}}{E_1 \frac{dN}{dp_1} E_2 \frac{dN}{dp_2}}, \qquad 11.$$

that is, the ratio of a two-particle distribution and a product of two one-particle distributions. The correlator is usually written in terms of the momentum difference between the two particles, $q = p_1 - p_2$, and their average momentum, $K = \frac{1}{2}(p_1 + p_2)$. If the particles are emitted independently (chaotic source) and propagate freely from the source to the detector, the two-particle distribution is not equal to the product of one-particle distributions. At small values of relative momentum q, it is larger than the product of one-particle distributions owing to quantum statistical (wave-function symmetrization) effects.

If there are no final-state interactions (or the spectra are corrected for them), the two-particle correlator $C(\boldsymbol{q}, \boldsymbol{K})$ is related to the emission function $S(x, K)$:

$$C(\boldsymbol{q}, \boldsymbol{K}) \approx 1 + \left| \frac{\int \mathrm{d}^4 x S(x, K) e^{\mathrm{i} q \cdot x}}{\int \mathrm{d}^4 x S(x, K)} \right|^2. \qquad 12.$$

The emission function $S(x, K)$ is the Wigner phase-space density of the emitting source. In the derivation of Equation 12 the emission function is assumed to be sufficiently smooth, i.e., $S(x, K) \approx S(x, K + \frac{1}{2}q)$ (see Reference 87). Because both p_1 and p_2 are on-shell, the average momentum K is, strictly speaking, off-shell. In practice, however, on-shell approximation for K is used: $K_0 \approx \sqrt{\boldsymbol{K}^2 + m^2}$.

In the hydrodynamic approach, the quantum-mechanical Wigner phase-space density is replaced by a classical phase-space density at the time of freeze-out. When Cooper-Frye formalism is applied, it is given by

$$S(x, K) = \frac{g}{(2\pi)^3} \int \frac{\mathrm{d}\sigma_\mu(x') K^\mu \delta^4(x - x')}{\exp\{[K \cdot u(x') - \mu(x')]/T(x')\} \pm 1}. \qquad 13.$$

It is not possible to define uniquely the source function $S(x, K)$ from the measured correlation function $C(\boldsymbol{q}, \boldsymbol{K})$. The experimental data of two-particle correlations are therefore presented using some ansatz for the the source function. Usually this is done using a Gaussian form for the correlator. If the collision system is further approximated to be boost-invariant, the correlator for central collisions can be written in a particularly simple form in terms of three HBT radii:

$$C(\boldsymbol{q}, \boldsymbol{K}) \approx 1 + \exp\left[-R_o^2(K_T) q_o^2 - R_s^2(K_T) q_s^2 - R_l^2(K_T) q_l^2\right]. \qquad 14.$$

In this so-called Bertsch-Pratt parametrization, the coordinate directions are defined in such a way that out- (R_o) and long-direction (R_l) are parallel to $\boldsymbol{K}_T$ and

beam, respectively, whereas the side-direction (R_s) is perpendicular to both $\boldsymbol{K}_T$ and beam. In a boost-invariant approximation, the radii depend only on the magnitude of K_T because the particle emission in central collisions does not depend on the azimuthal angle ϕ and boost-invariance means that there cannot be any rapidity dependence.

These radii do not correspond to the actual physical size of the source, but rather characterize so-called regions of homogeneity, the regions where particles with particular p_T are most likely emitted. For a Gaussian source, the HBT radii measure the following different combinations of space-time variances of the system (90):

$$R_s^2(K_T) = \langle \tilde{x}_s^2 \rangle (K_T), \qquad 15.$$

$$R_o^2(K_T) = \langle (\tilde{x}_o - \beta_\perp \tilde{t})^2 \rangle (K_T) \quad \text{and} \qquad 16.$$

$$R_l^2(K_T) = \langle \tilde{x}_l^2 \rangle (K_T), \qquad 17.$$

where $\beta_\perp = K_T/K^0$ is the transverse pair velocity and space-time coordinates $\tilde{x}$ are defined as distances from the effective source center $\tilde{x}^\mu(K_T) = x^\mu - \langle x^\mu \rangle (K_T)$, where brackets denote weighted averages over the source function $S(x, K)$:

$$\langle f(x) \rangle (K) = \frac{\int d^4x f(x) S(x, K)}{\int d^4x S(x, K)}. \qquad 18.$$

The radii are thus independent of the actual coordinates of the emission, but are sensitive to variances of the geometry.

Hydrodynamic calculations for RHIC energies predicted that a phase transition from a plasma to a hadron gas would increase the lifetime of the system (91). The long lifetime was predicted to increase the $\beta_\perp \tilde{t}$ term in Equation 16 and thus increase the R_o radius and make the ratio R_o/R_s large. The experimental data, however, shows no sign of this kind of effect and yields a ratio of $R_o/R_s \approx 1$.

Figure 11 shows some of the hydrodynamic calculations for the HBT radii at RHIC energy. Hydrodynamic calculations with assumed boost-invariance, chemical equilibrium, and a first-order phase transition (CE, solid line) tend to lead to a too small sideward radius R_s, too large outward and longitudinal radii R_o and R_l, respectively, and especially to a too large ratio R_o/R_s (25). Both R_o and R_l can be smaller if the system decouples sooner, i.e., in higher temperature, but such an approach leaves R_s basically unchanged and distorts the single particle spectra (26, 90). To a lesser extent, the same effect can be achieved by decreasing the initial time or increasing the transverse flow by a nonzero initial-velocity field, but neither of these approaches changes the too small R_s (25).

Another way to reduce the longitudinal radius R_l is to relax the boost-invariant approximation (39, 95). When this approach is used with an EoS with separate chemical and kinetic freeze-outs (PCE, dashed line), R_l is close to the data. Both R_o and R_s move closer to the data but are still too large and small, respectively. This approach also leads to problems with the elliptic anisotropy (see Section 3.3).

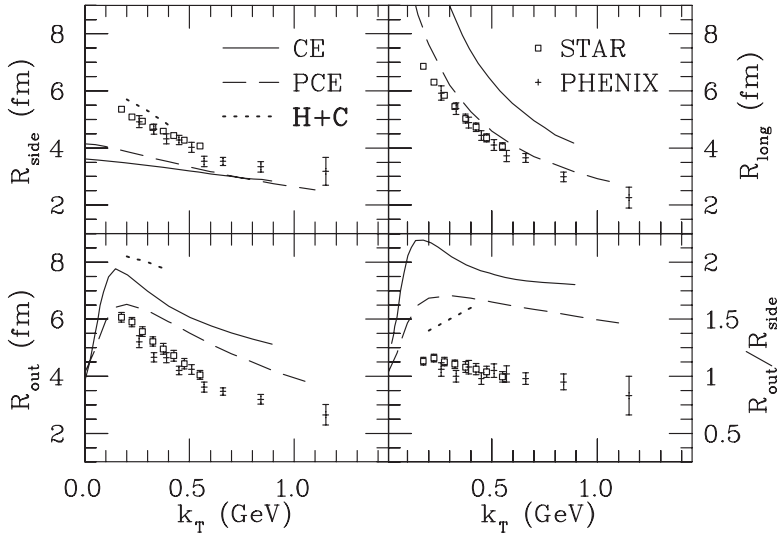

Figure 11 Pion source radii in Au + Au collisions at $\sqrt{s_{NN}} = 200$ GeV. Hydrodynamical results are labeled CE for boost-invariant chemical-equilibrium result (25), PCE for nonboost-invariant result with separate chemical and kinetic freeze-outs (39, 60; T. Hirano, personal communication), and H + C for hydro + cascade hybrid model (92). The data are taken by the STAR (93) and PHENIX (94) collaborations.

An approach that brings R_s close to the data chooses a wide but flat initial distribution (95), which leads to slower buildup of flow from an initially larger source. In that case, the problem is again R_o, which is too large. This is expected because R_o is sensitive to the lifetime of the system, which becomes relatively large in this approach.

One way to reduce the lifetime of the system and thus R_o is to change the EoS. As mentioned, one of the suggested signatures of a first-order phase transition is a long lifetime and large R_o. If one uses an EoS with a smooth crossover instead of a first-order phase transition, R_o decreases and R_s increases (96). Unfortunately, even in that case, no good fit to the data is achieved. It is also questionable how this change in EoS would affect the elliptic anisotropy (31).

Grassi et al. have suggested that the discrepancy between the data and calculations is due to too simple a treatment of freeze-out on a sharp hypersurface, and a more realistic continuous emission of particles would lead to better results (97). However, when this is accounted for effectively in hybrid models in which the hadronic stage is described using a cascade transport model, the results are even worse (92). The particles are emitted from larger, longer-lasting volume than in a simple hydrodynamic description, and correspondingly, R_s is larger and reproduces the data (H + C, dotted line in Figure 11). Unfortunately, the longer lifetime also leads to an even larger R_o.

Another possible reason for the discrepancy between the data and calculations is viscosity (4, 98). Initial calculations (5) show that it has the desired effects, but whether they are large enough remains to be seen. Again, the effect of viscosity on elliptic flow is large, and it is unknown if a viscous model could reproduce both the HBT radii and elliptic anisotropy.

4. ELECTROMAGNETIC EMISSION

All the observables described in the previous section are hadronic observables. By definition, the hadrons of the system interact with each other, and the distributions and yields of hadrons are fixed late in the evolution of the system, when interactions cease, the distributions and yields freeze out, and the particles decouple. Therefore, those observables characterize the properties of the particle-emitting source at the end of the system evolution, but not the history of the system during the evolution. In principle, it is possible to have very different dynamics, producing similar final states.

Possible observables that are sensitive to the entire evolution of the collision system are photon and lepton-pair distributions. Because these particles interact only electromagnetically, their mean free paths are much longer than those of hadrons. They can thus escape the collision system without rescattering and carry information about the conditions in which they were formed. However, the photon and dilepton spectra get contributions from all stages of the evolution, which makes it difficult to disentangle the signal coming from the hot, dense stage of the collision. To describe the different contributions to electromagnetic spectra, we follow the terminology of Reference 99:

1. Prompt photons and leptons are produced in the primary collisions of incoming partons;
2. thermal photons and leptons are emitted in the collisions of quarks and gluons during the plasma phase and in the collisions of hadrons in the hadronic phase;
3. decay photons and leptons are decay products of hadrons; and
4. direct photons and leptons are the sum of prompt and thermal photons.

The thermal photon production depends strongly on temperature via the factor $\exp(-p_T/T)$. Therefore, the early stage, when the matter is hottest, should dominate the photon emission, and the measurement of photon spectra should be an effective thermometer for the temperature achieved in the collision. However, prompt photons follow a power-law distribution p_T^{-n} and dominate at high p_T.

The hydrodynamic model can be used to calculate the thermal and decay contributions, but the prompt photons and leptons require a separate pQCD calculation. The calculation of decay photons is relatively straightforward, and it proceeds in the same way as the calculation of hadron spectra from resonance decays described

in Section 3.1. One calculates the distribution of hadrons at freeze-out and applies the relevant decay kinematics and branching ratios to get the spectra of decay photons and leptons. To calculate the thermal yield, the production rate of photons or leptons in a thermal system, $\mathrm{d}R/\mathrm{d}^3p(E, T, \mu)$, has to be integrated over the space-time volume of the system:

$$E\frac{dN}{d^3p} = \int d^4x \left\{ w(\varepsilon, \rho_\mathrm{B}) E \frac{dR^\mathrm{QGP}}{d^3p}(p \cdot u, T, \mu_\mathrm{B}) + [1 - w(\varepsilon, \rho_\mathrm{B})] E \frac{dR^\mathrm{HG}}{d^3p}(p \cdot u, T, \mu_\mathrm{B}) \right\}, \quad 19.$$

where the production in a plasma and in a hadron gas (HG) is written separately. The factor $w(\varepsilon, \rho_\mathrm{B})$, which expresses the volume fraction of plasma, is unity in the plasma phase, zero in HG, and between unity and zero in a mixed phase. Hydrodynamics provides the space-time evolution of the system, whereas the production rates in thermal matter are an input independent of hydrodynamics.

In the plasma phase, the photon production is dominated by the QCD Compton and annihilation reactions, $qg \to q\gamma$, $\bar{q}g \to \bar{q}\gamma$, and $q\bar{q} \to g\gamma$. In lowest order, the production rate due to these processes was calculated in References 100 and 101. However, some formally higher-order processes are strongly enhanced by collinear singularities and also contribute to order α_s (102, 103). The resummation of these contributions was shown to be possible and was carried out by Arnold et al. (104), completing the order α_s analysis of the photon-emission rate. A parametrization of the rate was also given in Reference 105.

The calculation of the photon-production rate in a hot hadron gas is less complete than the rate in a plasma owing to the multitude of different hadron species and photon-producing interactions and owing to the model dependence of the calculations (see References 99 and 106). The standard rate in the literature is the one calculated in Reference 100, where photon production in scattering and decay processes $\pi\pi \to \rho\gamma$, $\pi\rho \to \pi\gamma$, $\omega \to \pi\gamma$, and $\omega \to \pi\pi\gamma$ was calculated using pseudoscalar-vector Lagrangian, with coupling constants determined from free ρ and ω decays. These rates are often supplemented with a production rate via a_1 mesons from Reference 107.

The role of different channels in photon production was further studied using chiral Lagrangians (108). Unfortunately, it was not possible to fix the model parameters unambiguously in this work, which led to a factor of three uncertainty in the final rates. In the context of dilepton production, it was later possible to fix the model parameters much better (109), and this approach was used in a recent calculation by Turbide et al. (110). In that work, the study was extended to cover photon emission from heavier meson resonances, strange particles, and baryons. Another recent analysis of photon production from a hadron gas was done by Haglin (111), who studied the effect of strange particles and higher-order processes achieving a rate larger than the standard rate (100) by a factor of two at large q_T and by an order of magnitude at low q_T.

There are still uncertainties in the calculation of the photon-production rate in a hot hadron gas. Surprisingly, even after all the improvements in the calculations, the statement made in Reference 100 is still valid. At the same temperature, the production rate per unit volume in a plasma and a hot hadron gas is approximately equal, and they both "shine as brightly." However, the emission rate per unit entropy is larger in hadron gas.

The main contribution to dilepton production in plasma comes from the annihilation process $q\bar{q} \rightarrow l\bar{l}$. The rate calculated in lowest order in a baryon-free plasma can be found in textbooks (112) and was calculated for finite baryon chemical potentials in Reference 113. At small values of invariant lepton-pair mass, corrections on the order of $\alpha\alpha_s$ to this rate become important (114), but in a heavy ion collisions, lepton pairs from Dalitz decays of final mesons produce a larger background (115). Multiloop calculations similar to those done to calculate the photon rate have also been carried out for high-p_T pairs with small invariant mass (116). These calculations have resulted in rates somewhat larger than the first-order calculations. First attempts to calculate lepton production using a lattice-QCD formalism have also been done (117). The preliminary results are quite close to the perturbative rate, at least in some parts of the phase space.

The observation of large excess dileptons in the mass region below the ρ-meson mass in Pb + Au collisions at $\sqrt{s_{NN}} = 17.3$ GeV energy at the CERN-SPS (118) has fueled considerable theoretical interest in studying the lepton-pair emission in a hot hadronic gas (106, 119). The main problem of these studies has been whether and how the properties of mesons change in medium and how these changes are reflected in the rates. A rate calculated by Gale & Lichard (120) using free-particle properties is often used as a benchmark in comparisons with more sophisticated approaches. In the calculations of Rapp et al. (121) and Eletsky et al. (122), the basic assumption is that the spectral density of ρ meson changes in medium. These calculations are technically very different, but produce qualitatively similar rates (123). An alternative approach pursued by Brown & Rho (124) assumes that the ρ-meson mass decreases in the medium.

4.1. Photons at SPS

Direct photon production in $\sqrt{s_{NN}} = 17.3$ GeV Pb + Pb collisions at the CERN-SPS was measured by the WA98 collaboration (125). Several authors have compared this data with hydrodynamical calculations (126–130). All authors agreed that the photon spectrum could be explained if one assumes sufficiently hot ($T > 200$ MeV) initial state, but the required initial temperature varied largely from $T \sim 200$ MeV (127) to $T = 335$ MeV (126). The large difference is owing mainly to different assumptions in the calculations.

One factor that explains the largely varying initial temperature is the use of different rates in a hadron gas. Alam et al. (127) assumed in-medium modifications to hadron properties both in the EoS and in production rates that enhance the photon emission at lower temperatures, allowing cooler initial state. The full order α_S rate

for photon production in plasma was used only in the most recent paper (130), but at SPS energy the different rates in plasma cause significant differences in the final yield only at relatively large values of p_T.

The initial state of the system was also chosen in different ways in different calculations. Especially, the assumption of finite transverse flow velocity at the beginning of the hydrodynamic evolution leads to lower temperatures. Because the rates are proportional to $\exp(-p \cdot u/T)$, where p is the four momentum of the photon and u is the flow four-velocity, stronger transverse flow allows lower temperatures to produce equal yield at high p_T. Peressounko & Pokrovsky (128) argued the necessity of such an initial flow, and Alam et al. (127) and Chaudhuri (129) later studied its effects. It can be argued that gradients in initial particle production would lead to buildup of flow during thermalization, but it is very difficult to quantify how large flow velocities could build up this way. Peressounko & Pokrovsky also argued that the pion spectra especially necessitate the initial flow, but the authors of this review have not been able to fit the hadron spectra if initial transverse flow is assumed.

The hadron spectra were reproduced in References 128 and 130, and, when no initial transverse flow is assumed, also in Reference 127. In the other two calculations (126, 129), the initial state was only required to have the same entropy as the final-state particles. It is thus unknown whether these calculations are consistent with the hadron data.

With the exception of Reference 130, boost-invariant hydrodynamics was used in these calculations. If high initial temperature is required, this assumption leads to short initial, i.e., thermalization time, $\tau \sim 0.2$ fm/c (126). At SPS energy it can be argued that such a short initial time is ambiguous because the longitudinal extension of the colliding nuclei is larger than $c\tau_0$. This makes the application of boost-invariant expansion uncertain for times $\tau < 1$ fm/c. In Reference 130, this problem was solved by using nonboost-invariant hydrodynamics, where longitudinal geometry is explicit and the initial time does not appear. Also, the ambiguity in choosing the initial state was studied and it was shown that several EoSs and initial states reproduced both the hadron and photon data (130, 131).

To characterize the results, Figure 12 shows the photon spectrum calculated in Reference 130 and compares it with WA98 data. The calculation was done using two different EoSs (A and H) and two different initial states (IS 1 and IS 2). EoS A contains a phase transition from hadron gas to QGP at $T_c = 165$ MeV, whereas EoS H is a purely hadronic EoS. IS 1 has a very peaked initial density distribution in the longitudinal direction, whereas IS 2 has a flatter distribution (see Reference 131) and smaller maximum temperature, which is more consistent with the assumption of hadronic EoS. In both cases, the hadron spectra are reproduced and, as shown in the figure, the calculated photon spectrum is within the experimental error bars. Thus, the conclusion of the hydrodynamic studies of photon emission at the SPS is that a high-temperature initial state is needed to reproduce the measured photon spectra, but a phase transition to plasma is not necessarily required.

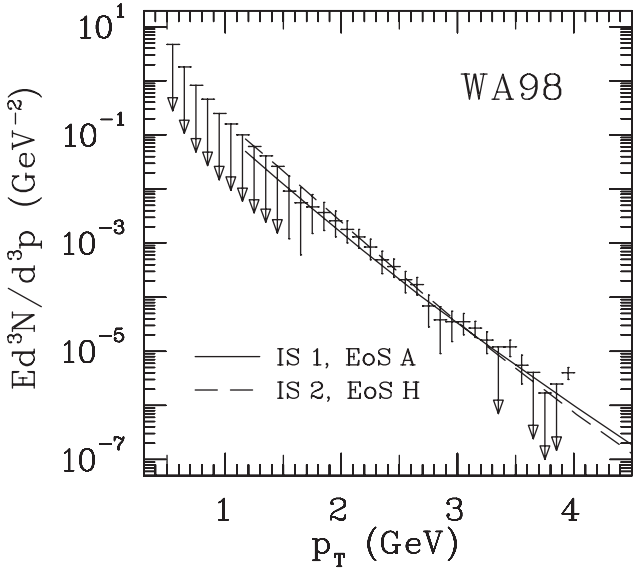

Figure 12 The sum of thermal photon emission at the SPS from hydrodynamic calculation (130) and prompt photon emission (132) compared with WA98 data (125).

4.2. Photons at RHIC

At the time of this writing, the situation of the photon data at RHIC is becoming very interesting: Preliminary data presented (133) at the latest Quark Matter 2005 meeting indicate a clear excess of photons over decay and prompt photons in the transverse-momentum range up to ∼3 GeV. Earlier measurements have been inconclusive owing to the large error bars, but the new method to extract the photon yield from the measurements of low-mass e^+e^- pairs appears more promising, and if the preliminary results are confirmed by the full analysis, these data offer a long-sought direct probe into the earliest moments of the collision.

Many authors have predicted the photon emission at RHIC and LHC (99, 103, 127, 134–139). Owing to uncertainties in the initial state, these predictions serve mostly as order-of-magnitude estimates, but they also address the question of whether the thermal photon yield would be larger than the prompt photon yield at any value of p_T. The initial conditions of more recent studies have been constrained to produce the total hadron multiplicity, and in Reference 99, the thermal photons are compared with the calculated yields of decay photons both from thermal pions and prompt pions from jet fragmentation. The measured spectrum of π^0's is compared with the calculations and the data are well described. The hydrodynamic calculations with the same initial conditions are also compared with other hadron data and the overall agreement is very good

(43). The perturbative QCD calculation to NLO in all quantities entering the calculation is supplemented with the energy loss of produced jets in the thermal matter.

The main conclusions from the studies in Reference 99, supported for the hadron observables by Reference 43, are as follows: The understanding of the hadron spectra in terms of hydrodynamic and pQCD calculations is quite good. This means that the photons from hadron decays are well under control when comparing different sources in the calculations. The other main sources of photons are prompt photons from primary interactions, including the photons from jet fragmentation, and the photons from secondary interactions in produced matter, the thermal photons.[3] These photon sources have quite distinct transverse-momentum dependence with the crossover from thermal photons to prompt photons taking place at around $p_T \sim 3$ GeV, the region where the behavior of the preliminary data also changes.

The simplest hydrodynamic calculations assume a scaling expansion in the longitudinal direction and ignore the transverse expansion. The first assumption can be argued to be reasonable in the central rapidity region because at RHIC energy, the Lorentz gamma factor is ∼100, indicating a time interval on the order of 0.1 fm/c for the nuclei to pass through one another. This is shorter than the shortest initial times used in the calculations. In the central rapidity region, the longitudinal components are not large and the acceleration of the longitudinal expansion is small, having little effect on the multiplicity density or the freeze-out time at $y \approx 0$ (141). Ignoring the transverse expansion cannot be justified, except for the photons emitted at the earliest times from the QGP. High-p_T photons from QGP are almost insensitive to flow because they are emitted when the system is hottest (139), but the strong flow at the late hadronic stages enhances the emission of high-p_T photons from hadron gas (127).

Predictions of the relative size of photon contributions at different values of p_T vary somewhat. For example, Srivastava (138) predicts that at RHIC energy, the photons from the QGP dominate at small values of p_T, i.e., $p_T < 1$ GeV, and the thermal photons at high p_T come mainly from the hadronic phase. More recent calculations lead to a conclusion that at RHIC multiplicity the plasma contribution dominates for $p_T > 3$, and at smaller transverse momenta the contribution from plasma and hadron gas are the same size, with the latter slightly larger at smallest momenta (134, 136). The rates used in the calculations are one reason for the difference: In Reference 138 older rates that do not include all order of α_S terms are utilitzed, whereas the newer calculations are based on such all-order-α_S (105) results. Also, note that the dependence of the plasma contribution depends strongly on the assumed thermalization time, τ_0. When comparing different predictions, the first detail to be checked is τ_0 (see Reference 99).

[3]More generally, the photons from secondary interactions among the produced particles can originate also from nonthermal processes, such as a high-energy quark producing photons when Compton scattering from a lower-energy thermal gluon (140).

Although the pQCD calculation of prompt photons is not entirely under control at small transverse momenta owing to the uncertainty in the photon fragmentation functions (see discussion in References 99 and 142), the photon yield from secondary collisions, i.e., the yield of the thermal photons, decreases more steeply and becomes negligible for $p_T \gtrsim 4$ GeV. In the calculations, thermal and prompt photons become comparable at around $p_T \sim 3$ GeV, and because of the difference in the slopes, the uncertainty in where the contributions cross is not large. At small momenta below 3 GeV, thermal photons dominate (134, 136), but it is not clear whether this contribution is so large that it can be isolated from the pion decay background.

Different contributions are compared with the preliminary photon data in Figure 13 (133). Here, initial times $\tau_0 = 0.2$ and 0.6 fm/c are used in the hydrodynamic calculation, which correspond to average initial temperatures $\langle T \rangle = 340$ and 250 MeV, respectively. In the prompt photon calculation, no intrinsic k_T is included because the same calculation for photon production in $p + p$ collisions at RHIC describes the data well. As indicated in Figure 13, the uncertainty in initial time causes more than an order of magnitude change in the thermal photon yield at high p_T.

In most calculations for thermal photons at RHIC and LHC, chemically equilibrated matter is assumed. However, it can be expected that the initial state is gluon dominated and quarks are suppressed compared to their equilibrium yields (143). This would lead to smaller emission rates at a given temperature, but the suppression of quarks means effectively smaller number of degrees of freedom and a larger temperature for a given entropy. Detailed calculations (99, 144) have indicated that these two effects largely cancel each other and that the final thermal spectra are quite similar in both equilibrium and nonequilibrium scenarios.

4.3. Dilepton Calculations

Like the photon measurements, the dilepton mass spectrum at the SPS collisions measured by the CERES (118, 145) and NA50 (146) collaborations has been compared to hydrodynamical calculations several times (35, 123, 127, 131, 147–150). The low-mass dilepton ($M_{ll} < m_\phi$) yield measured by CERES is dominated by emission from the late hadronic phase (see, e.g., Reference 149) and constrains only the properties of the hadronic stage of the evolution. All these calculations agree that if meson properties in vacuum are used (120), the thermal yield is not quite sufficient to explain the observed excess. Thus, the experimental data seem to require modifications in meson properties, but so far the mass resolution has not been good enough to differentiate between a change in mass and changes in spectral density. Recently, there have been new preliminary data with better mass resolution (151, 152), but the conclusions are still being debated (153).

Kvasnikova et al. (150) addressed the intermediate-mass ($m_\phi < M_{ll} < m_{J/\Psi}$) dilepton yield measured by NA50. In their calculation they found that the excess in lepton pairs in this mass region could be explained by thermal emission in the same

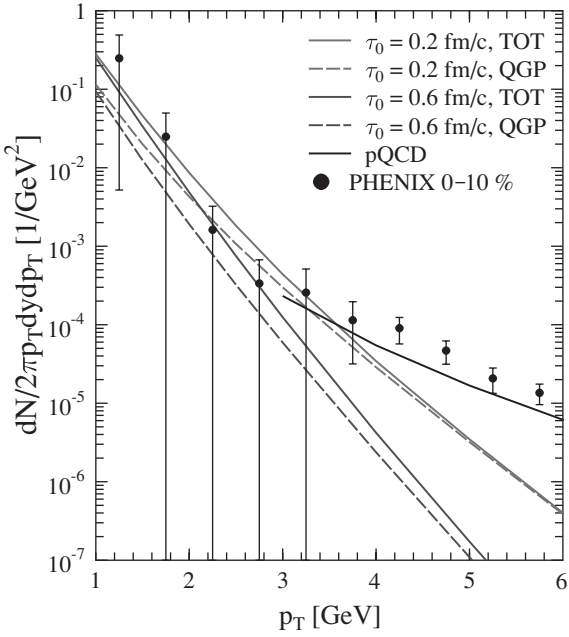

Figure 13 Thermal photon emission at the Relativistic Heavy Ion Collider from hydrodynamic calculation using two different initial times. Solid lines labeled TOT indicate the total yield of thermal photons, whereas dashed lines labeled QGP indicate emission from plasma. The pQCD calculation for prompt photons (99) and preliminary PHENIX data (133) are also shown.

way as in the low-mass region. Even if the intermediate-mass region is expected to provide a window for observing the emission from plasma (154), they found that a modest plasma contribution, ∼20%, was enough to fit the SPS data.

So far the genuinely hydrodynamic calculations of dilepton emission at RHIC have been rare, and different parametrizations for the space-time evolution of the system have been used instead (121). Medium modifications to meson properties depend on total baryon density, $\rho_{tot} = \rho_B + \rho_{\bar{B}}$. Because $\rho_{\rm tot}$ at RHIC is essentially the same as at the SPS, the low-mass dilepton spectrum at RHIC should show similar excess, as seen at the SPS (121).

At intermediate masses, the thermal yield is expected to be dominated by emission from plasma (155). However, owing to a larger $c\bar{c}$ production than at the SPS, the intermediate-mass dilepton yield can be dominated by correlated charm decays, unless the c quarks rescatter significantly in the medium or can be identified and subtracted. Isotropization of c-quark momentum distributions would soften the dilepton mass spectrum, leaving a mass range in which thermal emission dominates (155, 156). An additional source of lepton pairs at RHIC is the interaction

of jets with the surrounding dense plasma. According to recent calculations (157), the jet-plasma interactions may dominate over thermal dilepton emission at intermediate masses.

At the time of this writing there are no calculations in which all these contributions are taken into account and are folded with a realistic time evolution of the collision system. It will be interesting to see how the future data will look and if a plasma contribution is needed to explain the data. The PHENIX collaboration has recently shown the first preliminary data of low-mass dileptons at RHIC (158), but the present experimental uncertainties are too large to draw any conclusions. These experimental shortcomings are currently being addressed by a detector upgrade (159).

5. CONCLUDING REMARKS

Hydrodynamics provides a well-defined framework to study many experimentally accessible features of a heavy ion collision. Some parts of the collision, such as the primary particle production of final-state matter, lie outside hydrodynamics, and some features of hydrodynamics, such as the freeze-out of final hadrons, have grave uncertainties. Nevertheless, a hydrodynamic description has robust features such as the conservation laws, which are strictly enforced. The main assumption of hydrodynamics, the occurrence of frequent collisions in the final state, can also convincingly be argued for from the large observed multiplicity. Hydrodynamics describes the effects of collisions among the constituents, in particular the momentum transfer between adjacent regions, in terms of pressure that arises microscopically from momentum transfer in the collisions. This should be a good approximation as soon as the momentum distribution of constituents is approximately isotropic.

Hydrodynamics describes well the broadening and its mass dependence of hadron spectra resulting from the increase of transverse collective motion (flow). The collective motion can also be seen in the elliptic flow. At low transverse momenta, the observed elliptic flow can be described using hydrodynamics. Especially, the observed mass ordering is typical for a hydrodynamic description. These are partly genuine predictions of hydrodynamics because the amount of initial production is fixed from the total multiplicity. Once the hadronic observables are under control, the largest remaining uncertainty concerns the time scales of primary production and of (approximate) thermalization. Electromagnetic emission is very sensitive on these time scales, and the preliminary results on photon emission at RHIC may be the first indication that emission from the early moments of the collision can be resolved. The emission of lepton pairs around and below the ϕ-meson mass offers both a stringent test of the hydrodynamic description of the hadron phase and a tool to study the effects of medium on the properties of vector mesons. The amount of information that can finally be obtained on the properties of the expanding matter produced in the heavy ion collisions depends a good deal

on the progress in experimental measurements, but it is likely that hydrodynamics will remain an important tool for phenomenological studies for a long time.

ACKNOWLEDGMENTS

We would like to thank K. Eskola, H. Niemi, S.S. Räsänen, and T. Hirano for discussions regarding this review, H.N. and S.S.R. for help in preparing the figures, and T.H. for allowing us to show some of his unpublished results.

The *Annual Review of Nuclear and Particle Science* is online at http://nucl.annualreviews.org

LITERATURE CITED

1. McLerran LD. *Acta Phys. Polon. B* 30:3707 (1999)
2. Bjorken JD. *Phys. Rev. D* 27:140 (1983)
3. Rischke DH. arXiv:nucl-th/9809044
4. Teaney D. *Phys. Rev. C* 68:034913 (2003)
5. Muronga A, Rischke DH. arXiv:nucl-th/0407114
6. Muroya S, Sasaki N. *Prog. Theor. Phys.* 113:457 (2005)
7. Eskola KJ. *Nucl. Phys. A* 702:249 (2002)
8. McLerran L, Venugopalan R. *Phys. Rev. D* 49:2233 (1994); McLerran L, Venugopalan R. *Phys. Rev. D* 49:3352 (1994); McLerran L, Venugopalan *R. Phys. Rev. D* 50:2225 (1994)
9. Gribov LV, Levin EM, Ryskin MG. *Phys. Rep.* 100:1 (1983)
10. Ranft J. *Phys. Rev. D* 51:64 (1995)
11. Eskola KJ, Kajantie K, Ruuskanen PV, Tuominen K. *Nucl. Phys. B* 570:379 (2000)
12. Eskola KJ, Kajantie K, Lindfors J. *Nucl. Phys. B* 323:37 (1989)
13. Eskola KJ, Ruuskanen PV, Räsänen SS, Tuominen K. *Nucl. Phys. A* 696:715 (2001)
14. Kovchegov YV. *Phys. Rev. D* 54:5463 (1996)
15. Jalilian-Marian J, Kovner A, McLerran LD, Weigert H. *Phys. Rev. D* 55:5414 (1997)
16. Kovchegov YV, Tuchin K. *Phys. Rev. D* 65:074026 (2002)
17. Krasnitz A, Venugopalan R. *Nucl. Phys. B* 557:237 (1999)
18. Krasnitz A, Venugopalan R. *Phys. Rev. Lett.* 84:4309 (2000)
19. Krasnitz A, Venugopalan R. *Phys. Rev. Lett.* 86:1717 (2001)
20. Krasnitz A, Nara Y, Venugopalan R. *Phys. Rev. Lett.* 87:192302 (2001)
21. Krasnitz A, Nara Y, Venugopalan R. *Nucl. Phys. A* 717:268 (2003)
22. Lappi T. *Phys. Rev. C* 67:05490 (2003)
23. Kharzeev D, Levin E. *Phys. Lett. B* 523:79 (2001)
24. Kolb PF, et al. *Nucl. Phys. A* 696:197 (2001)
25. Heinz UW, Kolb PF. *Nucl. Phys. A* 702:269 (2002)
26. Heinz UW, Kolb PF. arXiv:hep-ph/0204061
27. Baier R, Mueller AH, Schiff D, Son DT. *Phys. Lett. B* 502:51 (2001)
28. Mrowczynski S. *Acta Phys. Polon. B* 37:427 (2006)
29. Rajagopal K. *Acta Phys. Polon. B* 31:3021 (2000)
30. Braun-Munzinger P, Magestro D, Redlich K, Stachel J. *Phys. Lett. B* 518:41 (2001)
31. Huovinen P. *Nucl. Phys. A* 761:296 (2005)
32. Venugopalan R, Prakash M. *Nucl. Phys. A* 546:718 (1992)
33. Kapusta JI, Olive KA. *Nucl. Phys. A* 408:478 (1983)

34. Rischke DH, Gorenstein MI, Stoecker H, Greiner W. *Z. Phys. C* 51:485 (1991)
35. Sollfrank J, et al. *Phys. Rev. C* 55:392 (1997)
36. Broniowski W, Florkowski W. *Phys. Rev. Lett.* 87:272302 (2001)
36a. Eskola KJ, Niemi H, Ruuskanen PV, Räsänen SS. *Phys. Lett. B* 566:187 (2003)
37. Bebie H, Gerber P, Goity JL, Leutwyler H. *Nucl. Phys. B* 378:95 (1992)
38. Teaney T. arXiv:nucl-th/0204023
39. Hirano T, Tsuda K. *Phys. Rev. C* 66:054905 (2002)
40. Kolb PF, Rapp R. *Phys. Rev. C* 67:044903 (2003)
41. Cooper F, Frye G. *Phys. Rev. D* 10:186 (1974)
42. Sollfrank J, Koch P, Heinz U. *Z. Phys. C* 52:593 (1991)
43. Eskola KJ, et al. *Phys. Rev. C* 72:044904 (2005)
44. Adams J, et al. (STAR Collab.) *Phys. Rev. Lett.* 91:172302 (2003)
45. Adler C, et al. (STAR Collab.) *Phys. Rev. Lett.* 89:202301 (2002)
46. Adams J, et al. (STAR Collab.) *Phys. Rev. Lett.* 92:112301 (2004)
47. Adler C, et al. (STAR Collab.) *Phys. Rev. Lett.* 89:092301 (2002)
48. Adler SS, et al. (PHENIX Collab.) *Phys. Rev. C* 69:034910 (2004)
49. Adcox K, et al. (PHENIX Collab.) *Phys. Rev. Lett.* 88:022301 (2002)
50. Adcox K, et al. (PHENIX Collab.) *Phys. Rev. Lett.* 88:242301 (2002)
51. Adcox K, et al. (PHENIX Collab.) *Phys. Rev. Lett.* 89:092302 (2002)
52. Adler SS, et al. (PHENIX Collab.) *Phys. Rev. C* 69:034909 (2004)
53. Adler SS, et al. (PHENIX Collab.) *Phys. Rev. Lett.* 91:072301 (2003)
54. Back BB, et al. (PHOBOS Collab.) *Phys. Lett.* B 578:297 (2004)
55. Back BB, et al. (PHOBOS Collab.) arXiv:nucl-ex/0401006
56. Arsene I, et al. (BRAHMS Collab.) *Phys. Rev. Lett.* 91:072305 (2002)
57. Bearden IG, et al. (BRAHMS Collab.) *Phys. Rev. Lett.* 94:162301 (2005)
58. Bearden IG, et al. (BRAHMS Collab.) *Phys. Rev. Lett.* 93:102301 (2004)
59. Hirano T, Gyulassy M. arXiv:nucl-th/0506049
60. Hirano T, et al. arXiv:nucl-th/0511046
61. Eskola KJ, Honkanen H, Salgado CA, Wiedemann UA. *Nucl. Phys. A* 747:511 (2005)
61a. Fries RJ. *J. Phys. G* 30:S853 (2004); Hwa RC. *Eur. Phys. J. C* 43:233 (2005)
62. Voloshin S, Zhang Y. *Z. Phys. C* 70:665 (1996)
63. Kolb PF. *Phys. Rev. C* 68:031902 (2003)
64. Adams J, et al. (STAR Collab.) *Phys. Rev. Lett.* 92:062301 (2004)
65. Poskanzer AM. *J. Phys. G* 30:S1225 (2004)
66. Molnar D, Huovinen P. *Phys. Rev. Lett.* 94:012302 (2005)
67. Siemens PJ, Rasmussen JO. *Phys. Rev. Lett.* 42:880 (1979)
68. Kolb PF, Sollfrank J, Heinz UW. *Phys. Rev. C* 62:054909 (2000)
69. Agakichiev G, et al. (CERES/NA45 Collab.) *Phys. Rev. Lett.* 92:032301 (2004)
70. Heinz U, Kolb PF. *J. Phys. G* 30:S1229 (2004)
71. Teaney D, Lauret J, Shuryak EV. arXiv:nucl-th/0110037
72. Bass SA, Dumitru A. *Phys. Rev. C* 61:064909 (2000)
73. Nonaka C, Bass SA. arXiv:nucl-th/0510038
74. Miller M, Snellings R. arXiv:nucl-ex/0312008
75. Hama Y, Kodama T, Socolowski OJ. *Braz. J. Phys.* 35:24 (2005)
76. Adams J, et al. (STAR Collab.) *Phys. Rev. C* 72:014904 (2005)
77. Adler SS, et al. (PHENIX Collab.) *Phys. Rev. Lett.* 91:182301 (2003)
78. Gyulassy M, McLerran L. *Nucl. Phys. A* 750:30 (2005); Shuryak EV. *Nucl. Phys. A* 750:64 (2005); Heinz UW. arXiv:nucl-th/0512051

79. Teaney DA. *J. Phys. G* 30:S1247 (2004); Chaudhuri AK, Heinz UW. arXiv:nucl-th/0504022
80. Back BB, et al. (PHOBOS Collab.) *Phys. Rev. Lett.* 89:222301 (2002)
81. Back BB, et al. (PHOBOS Collab.) *Phys. Rev. C* 72:051901 (2005)
82. Staszel P. (BRAHMS Collab.) arXiv:nucl-ex/0510061; Johnson EB. arXiv:nucl-ex/0601010
83. Adler C, et al. (STAR Collab.) *Phys. Rev. C* 66:034904 (2002)
84. Back BB, et al. (PHOBOS Collab.) *Phys. Rev. Lett.* 91:052303 (2003)
85. Hirano T. *Phys. Rev. C* 65:011901 (2002)
86. Hanbury Brown R, Twiss RQ. *Nature* 178:1046 (1956)
87. Wiedemann UA, Heinz UW. *Phys. Rep.* 319:145 (1999)
88. Lisa M, Pratt S, Soltz R, Wiedemann UA. *Annu. Rev. Nucl. Part. Sci.* 55:357 (2005)
89. Tomasik B, Wiedemann UA. In *Quark-Gluon Plasma 3*, ed. RC Hwa, XN Wang, pp. 715–77. Singapore: World Sci. (2004)
90. Kolb PF, Heinz U. In *Quark-Gluon Plasma 3*, ed. RC Hwa, XN Wang, pp. 634–714. Singapore: World Sci. (2004)
91. Rischke DH, Gyulassy M. *Nucl. Phys.* A 608:479 (1996)
92. Soff S, Bass SA, Dumitru A. *Phys. Rev. Lett.* 86:3981 (2001); Soff S. arXiv:hep-ph/0202240
93. Adams J, et al. (STAR Collab.) *Phys. Rev. C* 71:044906 (2005)
94. Adler SS, et al. (PHENIX Collab.) *Phys. Rev. Lett.* 93:152302 (2004)
95. Morita K, Muroya S, Nonaka C, Hirano T. *Phys. Rev. C* 66:054904 (2002)
96. Zschiesche D, Schramm S, Stocker H, Greiner W. *Phys. Rev. C* 65:064902 (2002)
97. Grassi F, Hama Y, Padula SS, Socolowski OJ. *Phys. Rev. C* 62:044904 (2000); Sinyukov YM, et al. *Phys. Rev. Lett.* 89:052301 (2002)
98. Dumitru A. arXiv:nucl-th/0206011
99. Arleo F, et al. *CERN Yellow Report on Hard Probes in Heavy Ion Collisions at the LHC*, CERN, Geneva [arXiv:hep-ph/0311131] (2003)
100. Kapusta JI, Lichard P, Seibert D. *Phys. Rev. D* 44:2774 (1991). Erratum. *Phys. Rev. D* 47:4171 (1993)
101. Baier R, Nakkagawa H, Niegawa A, Redlich K. *Z. Phys. C* 53:433 (1992)
102. Aurenche P, Gelis F, Kobes R, Petitgirard E. *Z. Phys. C* 75:315 (1997); Aurench P, et al. *Phys. Rev. D* 58:085003 (1998); Aurenche P, et al. *JHEP* 0205:043 (2002)
103. Steffen FD, Thoma MH. *Phys. Lett. B* 510:98 (2001)
104. Arnold P, Moore GD, Yaffe LG. *JHEP* 0111:057 (2001)
105. Arnold P, Moore GD, Yaffe LG. *JHEP* 0112:009 (2001)
106. Gale C, Haglin KL. In *Quark-Gluon Plasma 3*, ed. RC Hwa, XN Wang, pp. 364–429. Singapore: World Sci. (2004)
107. Xiong L, Shuryak E, Brown GE. *Phys. Rev. D* 46:3798 (1992)
108. Song C. *Phys. Rev. C* 47:2861 (1993)
109. Gao S, Gale C. *Phys. Rev. C* 57:254 (1998)
110. Turbide S, Rapp R, Gale C. *Phys. Rev. C* 69:014903 (2004)
111. Haglin KL. *J. Phys. G* 30:L27 (2004)
112. Wong CY. *Introduction to Heavy Ion Collisions*. Singapore: World Sci. (1994)
113. Cleymans J, Fingberg J, Redlich K. *Phys. Rev. D* 35:2153 (1987)
114. Braaten F, Pisarski RD, Yuan TC. *Phys. Rev. Lett.* 64:2242 (1990)
115. Altherr T, Ruuskanen PV. *Nucl. Phys. B* 380:377 (1992)
116. Aurenche P, Gelis F, Moore GD, Zaraket H. *JHEP* 0212:006 (2002)
117. Karsch F, et al. *Phys. Lett. B* 530:147 (2002)
118. Agakishiev G, et al. (CERES/NA45 Collab.) *Phys. Lett. B* 422:405 (1998); Lenkeit B, et al. (CERES Collab.) *Nucl. Phys. A* 661:23 (1999); Marin A. (CERES Collab.) *J. Phys. G* 30:S709 (2004); Agakichiev G, et al. (CERES Collab.) *Eur. Phys. J. C* 41:475 (2005)

119. Rapp R, Wambach J. *Adv. Nucl. Phys.* 25:1 (2000)
120. Gale C, Lichard P. *Phys. Rev. D* 49:3338 (1994); Lichard P. *Phys. Rev. D* 49:5812 (1994)
121. Rapp R, Chanfray G, Wambach J. *Nucl. Phys. A* 617:472 (1997); Rapp R. *Phys. Rev. C* 63:054907 (2001)
122. Eletsky VL, Belkacem M, Ellis PJ, Kapusta JI. *Phys. Rev. C* 64:035202 (2001)
123. Huovinen P, Belkacem M, Ellis PJ, Kapusta JI. *Phys. Rev. C* 66:014903 (2002)
124. Brown GE, Rho M. *Phys. Rep.* 269:333 (1996)
125. Aggarwal MM, et al. (WA98 Collab.) *Phys. Rev. Lett.* 85:3595 (2000); Aggarwal MM, et al. (WA98 Collab.) arXiv:nucl-ex/0006007
126. Srivastava DK, Sinha B. *Phys. Rev. C* 64:034902 (2001)
127. Alam J, et al. *Phys. Rev. C* 63:021901 (2001); Alam J, Roy P, Sarkar S, Sinha B. *Phys. Rev. C* 67:054901 (2003)
128. Peressounko DY, Pokrovsky YE. hep-ph/0009025
129. Chaudhuri AK. *J. Phys. G* 29:235 (2003)
130. Huovinen P, Ruuskanen PV, Räsänen SS. *Phys. Lett. B* 535:109 (2002)
131. Huovinen P, Ruuskanen PV, Sollfrank J. *Nucl. Phys. A* 650:227 (1999)
132. Wong C, Wang H. *Phys. Rev. C* 58:376 (1998)
133. Bathe S. (PHENIX Collab.) arXiv:nucl-ex/0511042
134. Räsänen SS. *Nucl. Phys. A* 715:717 (2003)
135. Gelis F, Niemi H, Ruuskanen PV, Räsänen SS. *J. Phys. G* 30:S1031 (2004)
136. d'Enterria D, Peressounko D. arXiv:nucl-th/0503054
137. Hammon N, Dumitru A, Stoecker H, Greiner W. *Phys. Rev. C* 57:3292 (1998)
138. Srivastava DK. *Eur. Phys. J. C* 10:487 (1999). Erratum. *Eur. Phys. J. C* 20:399 (2001)
139. Peressounko DY, Pokrovsky YE. *Nucl. Phys. A* 669:196 (2000)
140. Fries RJ, Muller B, Srivastava DK. *Phys. Rev. Lett.* 90:132301 (2003)
141. Eskola KJ, Kajantie K, Ruuskanen PV. *Eur. Phys. J. C* 1:627 (1998)
142. Peitzmann T, Thoma MH. *Phys. Rep.* 364:175 (2002)
143. Shuryak EV. *Phys. Rev. Lett.* 68:3270 (1992)
144. Mustafa MG, Thoma MH. *Phys. Rev. C* 62:014902 (2000). Erratum. *Phys. Rev. C* 63:069902 (2001)
145. Agakishiev G, et al. (CERES Collab.) *Phys. Rev. Lett.* 75:1272 (1995)
146. Abreu MC, et al. (NA38/NA50 Collab.) *Eur. Phys. J. C* 14:443 (2000)
147. Srivastava DK, Sinha B, Gale C. *Phys. Rev. C* 53:567 (1996)
148. Hung CM, Shuryak EV. *Phys. Rev. C* 56:453 (1997)
149. Huovinen P, Prakash M. *Phys. Lett. B* 450:15 (1999)
150. Kvasnikova I, Gale C, Srivastava DK. *Phys. Rev. C* 65:064903 (2002)
151. Miskowiec D. (CERES Collab.) arXiv:nucl-ex/0511010
152. Damjanovic S, et al. (NA60 Collab.) arXiv:nucl-ex/0510044
153. Brown GE, Rho M. arXiv:nucl-th/0509001
154. Shuryak EV. *Phys. Lett. B* 78:150 (1978); Kajantie K, Kapusta JI, McLerran LD, Mekjian A. *Phys. Rev. D* 34:2746 (1986)
155. Rapp R. *J. Phys. G* 31:S217 (2005)
156. Shuryak EV. *Phys. Rev. C* 55:961 (1997)
157. Turbide S, Gale C, Srivastava DK, Fries RJ. arXiv:hep-ph/0601042
158. Toia A. (PHENIX Collab.) arXiv:nucl-ex/0510006
159. Ravinovich I, et al. arXiv:nucl-ex/0510024

Annual Review of Nuclear and Particle Science
Volume 56, 2006

CONTENTS

CERN-TH-2020-099

Temperature dependence of η/s of strongly interacting matter: effects of the equation of state and the parametric form of $(\eta/s)(T)$

Jussi Auvinen,[1,*] Kari J. Eskola,[2,3] Pasi Huovinen,[1,4] Harri Niemi,[2,3] Risto Paatelainen,[5] and Péter Petreczky[6]

[1] *Institute of Physics Belgrade, 11080 Belgrade, Serbia*
[2] *University of Jyvaskyla, Department of Physics, P.O. Box 35, FI-40014 University of Jyvaskyla, Finland*
[3] *Helsinki Institute of Physics, P.O. Box 64, FI-00014 University of Helsinki, Finland*
[4] *Institute of Theoretical Physics, University of Wroclaw, 50-204 Wrocław, Poland*
[5] *Theoretical Physics Department, CERN, CH-1211 Geneve 23, Switzerland*
[6] *Physics Department, Brookhaven National Laboratory, Upton, NY 11973, USA*

We investigate the temperature dependence of the shear viscosity to entropy density ratio η/s using a piecewise linear parametrization. To determine the optimal values of the parameters and the associated uncertainties, we perform a global Bayesian model-to-data comparison on Au+Au collisions at $\sqrt{s_{\rm NN}} = 200$ GeV and Pb+Pb collisions at 2.76 TeV and 5.02 TeV, using a 2+1D hydrodynamical model with the EKRT initial state. We provide three new parametrizations of the equation of state (EoS) based on contemporary lattice results and hadron resonance gas, and use them and the widely used $s95p$ parametrization to explore the uncertainty in the analysis due to the choice of the equation of state. We found that η/s is most constrained in the temperature range $T \approx$ 150–220 MeV, where, for all EoSs, $0.08 < \eta/s < 0.23$ when taking into account the 90% credible intervals. In this temperature range the EoS parametrization has only a small $\sim 10\%$ effect on the favored η/s value, which is less than the $\sim 30\%$ uncertainty of the analysis using a single EoS parametrization. Our parametrization of $(\eta/s)(T)$ leads to a slightly larger minimum value of η/s than the previously used parametrizations. When we constrain our parametrization to mimic the previously used parametrizations, our favored value is reduced, and the difference becomes statistically insignificant.

I. INTRODUCTION

The main goal of the ultrarelativistic heavy-ion collisions at the Large Hadron Collider (LHC) and the Relativistic Heavy-Ion Collider (RHIC) is to understand the properties of the strongly interacting matter produced in these collisions. In recent years the main interest has been in extracting the dissipative properties of this QCD matter from the experimental data (e.g. [1–5]), in particular its specific shear viscosity: the ratio of shear viscosity to entropy density η/s (for a review, see Refs. [6–9]). The field has matured to a level where a global Bayesian analysis of the parameters can provide statistically meaningful credibility ranges to the temperature dependence of η/s [10–12]. These credibility ranges agree with earlier results like those obtained using the EKRT model [13].

However, with the exception of papers like Refs. [14–16], the equation of state (EoS) is taken as given in the models used to extract the η/s ratio from the data. In particular, the EoS parametrization $s95p$ [17] was used in many studies in the literature. This parametrization is based on by now outdated lattice data [18], and recent studies have reported an approximate 60% [16] or 30% increases [19] in the extracted value of η/s when switching from $s95p$ to a contemporary lattice-based EoS. Furthermore, even if the errors of the contemporary lattice QCD calculations overlap, there is still a small tension between the trace anomalies obtained using the HISQ [20, 21] and stout [22, 23] discretization schemes. Consequently the EoSs differ, and if the procedure to extract η/s from the data is as sensitive to the details of the EoS as Refs. [16, 19] claim, this tension may lead to additional uncertainties in the η/s values extracted from the heavy-ion collision data.

In the Bayesian analysis mentioned previously [10, 11], the temperature dependence of η/s was assumed to be monotonously increasing above the QCD transition temperature T_c. In a Bayesian analysis the slope parameter of such parametrization is always constrained to be non-negative, and limiting the final slope parameter to zero would require extremely strong constraints from the experimental data. Therefore, by construction, the analysis leads to an η/s increasing with temperature above T_c, even if there is no physical reason to exclude a scenario where η/s is constant in a broad temperature range above T_c. A more flexible parametrization, which does not impose such constraints, is thus needed to determine the temperature dependence of η/s.

In this work we address both the sensitivity of the extracted η/s to the EoS used in the model calculation, and the temperature dependence of η/s in the vicinity of the QCD transition temperature. We perform a Bayesian analysis of the results of EKRT + hydrodynamics calculations [13, 24], and the data obtained in $\sqrt{s_{\rm NN}} = 200$

* auvinen@ipb.ac.rs

GeV Au+Au collisions [25–27], and Pb+Pb collisions at 2.76 TeV [28–30] and 5.02 TeV [30, 31]. To study the temperature dependence of η/s we use a piecewise linear parametrization in three parts: linearly decreasing and increasing regions at low and high temperatures are connected by a constant-value plateau of variable range. With this parametrization, data favoring a strong temperature dependence will lead to large slopes and a narrow plateau; conversely, an approximately constant η/s can be obtained with small slope parameter values and a wide plateau. To explore the sensitivity to the EoS, we use four different parametrizations: the well-known $s95p$ parametrization, and three new parametrizations based on contemporary lattice QCD results. A comparison of the final probability distributions of the parameters will tell whether the most probable parameter values depend on the EoS used, and whether that difference is significant when the overall uncertainty in the fitting procedure is taken into account.

II. EQUATION OF STATE

In lattice QCD the calculation of the equation of state (EoS) usually proceeds through the calculation of the trace anomaly, $\Theta(T) = \epsilon(T) - 3p(T)$, where ϵ and p are energy density and pressure, respectively. Thermodynamical variables are subsequently derived from it using so-called integral method [32]. Therefore we base our EoS parametrizations on the trace anomaly and obtain pressure from the integral

$$\frac{p(T)}{T^4} - \frac{p(T_{\rm low})}{T_{\rm low}^4} = \int_{T_{\rm low}}^{T} \frac{{\rm d}T'}{T'^5}\Theta(T'). \qquad (1)$$

Once the pressure is known, the energy and entropy densities can be calculated, $\epsilon(T) = \Theta(T) + 3p(T)$, and $s(T) = [\epsilon(T) + p(T)]/T$, respectively. To make a construction of chemical freeze-out at $T \approx 150$ MeV temperature possible, we use the hadron resonance gas (HRG) trace anomaly at low temperatures instead of the lattice QCD result. Equally important is that this choice allows for energy and momentum conserving switch from fluid degrees of freedom to particle degrees of freedom without any non-physical discontinuities in temperature and/or flow velocity[1]. Furthermore, it gives us a consistent value for the pressure at $T_{\rm low}$ required for the evaluation of pressure (see Eq. (1)).

As a baseline, we use the $s95p$ parametrization [17], where HRG containing hadrons and resonances below $M < 2$ GeV mass from the 2004 PDG summary tables [37] is connected to the parametrized hotQCD data from Ref. [18]. To explore the effects of various developments during the last decade, we first connect the HRG based on the PDG 2004 particle list [37] to parametrized contemporary lattice data obtained using the HISQ discretization scheme [20, 21]. The lattice spacing, a, is related to the temperature and temporal lattice extent, N_t, as $a = 1/(N_t T)$. Since the lattice spacing (N_t) dependence is small for this action, we use these results at fixed lattice spacing $N_t = 8, 10$ and 12. We name our parametrizations according to the convention used to name $s95p$, and label this parametrization $s87h_{04}$. '$s87$' signifies entropy density reaching 87% of its ideal gas value at $T = 800$ MeV, the letter 'h' refers to the HISQ action, and the subscript '04' to the vintage of the PDG particle list (2004). Note that even if our parametrization differs from the lattice trace anomaly in the hadronic phase, it agrees with the contemporary lattice calculations which show that at $T = 800$ MeV the entropy density reaches 87–88% of the ideal gas value (c.f. Fig. 8 of Ref. [21]).

The number of well-established resonances has increased since 2004, so we base our parametrization $s88h_{18}$ on HRG containing all[2] strange and non-strange hadrons and resonances in the PDG 2018 summary tables[3][40], and on the same HISQ lattice data [20, 21] we used for $s87h_{04}$. Furthermore, there is a slight tension in the trace anomaly between the HISQ and stout discretization schemes. To explore whether this difference has any effect on hydrodynamical modeling, we construct the parametrization $s83s_{18}$ using PDG 2018 resonances, and the continuum extrapolated lattice data obtained using the stout discretization [22, 23]. The second letter 's' in the label refers now to the stout action, and the subscript '18' to the vintage of the particle list. The details of these parametrizations are shown in Appendix A.

In the top and middle panels of Fig. 1, we show the parametrized trace anomalies, and the lattice data as used to make them: continuum extrapolated for the stout action, and at fixed lattice spacing for the HISQ action, since its lattice spacing (N_t) dependence is small. As seen in the topmost panel, the most noticable change in the lattice results during the last decade is the reduction of the peak of the trace anomaly (cf. $s95p$ to others). Also, as mentioned, the lattice results obtained using the

[1] Energy and momentum conservation require that the fluid EoS is that of free particles, and that the degrees of freedom are the same in the fluid and particles [33]. If the dissipative corrections are small, switch from fluid consistent with the contemporary lattice QCD results [34] to particles in the UrQMD [35] or SMASH [36] hadron cascades at $T = 150$ MeV temperature leads to roughly 9–10% or 6–7% loss in both total energy and entropy, respectively.

[2] With the exception of $f_0(500)$. See Refs. [38, 39].

[3] Note that PDG Meson Summary Table and Baryon Summary Table contain (almost) all states listed by the PDG, and are different from the PDG Meson Summary Tables and Baryon Summary Tables we use [41]. The PDG Baryon Summary Tables contain the three and four star resonance states. The PDG does not assign stars to meson states, but the Meson Summary Tables contain the states not labeled "Omitted from summary table" in the individual listings.

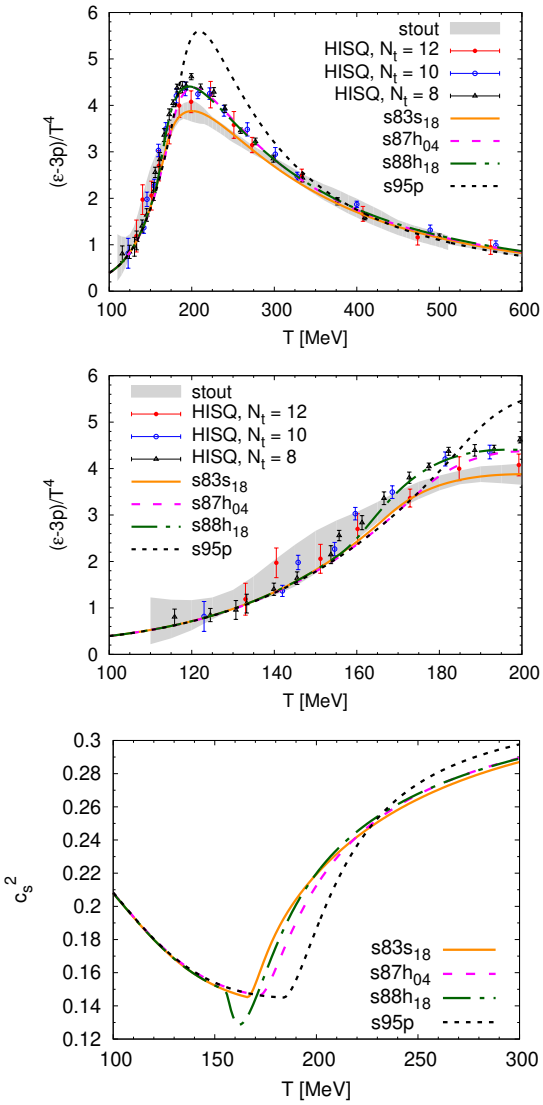

FIG. 1. The trace anomaly (top and middle) and the speed of sound squared (bottom) as functions of temperature in the four parametrizations of the EoS compared to the lattice data obtained using the HISQ [20, 21] and stout [22, 23] discretization schemes.

HISQ and stout actions slightly differ around the peak, and consequently $s83s_{18}$ differs from $s87h_{04}$ and $s88h_{18}$. The higher peak does not, however, mean a lower speed of sound. As shown in the lowest panel of Fig. 1, the speed of sound in the $s95p$ parametrization is not significantly lower than in the other parametrizations, but the temperature region where it is low is broader than in the other parametrizations. Thus we expect $s95p$ to be effectively softer than the other EoSs. On the other hand, the speed of sound in $s88h_{18}$ depicts a characteristic dip below the speed of sound in the other parametrizations. This is a consequence of the parametrization of the trace anomaly in that temperature region.

As known, the HRG trace anomaly is below the lattice results [20, 22, 23] at low temperatures. This difference has been interpreted to indicate the existence of yet unobserved resonance states [34, 42]. The need for further states has also been seen in the study of the strangeness baryon correlations on the lattice [43], and confirmed by the S-matrix based virial expansion [44]. However, we do not include predicted states from any model[4] in this work, since we do not know how they would decay, but use the states from the PDG summary tables only. Consequently the parametrized trace anomaly is slightly below even the most generous error bars of the lattice results around $T \approx 150$–160 MeV temperature, as shown in the middle panel of Fig. 1.

On the other hand, whether we use the PDG 2004 or 2018 particle list causes only a tiny difference in the trace anomaly. The main difference between the $s87h_{04}$ and $s88h_{18}$ parametrizations arises from the connection of the HRG to the lattice parametrization. When parametrizing $s88h_{18}$ we wanted the trace anomaly to reach its lattice values soon above $T_c = 155$ MeV, whereas we allowed $s87h_{04}$ to agree with lattice at larger temperature where the lattice trace anomaly drops below the HRG trace anomaly—for details, see Appendix A. Consequently the $s88h_{18}$ parametrization rises above the HRG values leading to the characteristic dip in the speed of sound (lowest panel in Fig. 1). Note that the $s83s_{18}$ parametrization does not depict a similar dip in the speed of sound, since the lower peak and larger errors of the continuum extrapolated stout action result allow the parametrized trace anomaly to drop below the HRG values immediately.

III. HYDRODYNAMICAL MODEL

We employ a fluid dynamical model used previously in Refs. [13, 24, 46–48]. The spacetime evolution is computed numerically in (2+1) dimensions [49], and the longitudinal expansion is accounted for by assuming longitudinal boost invariance. We also neglect here the bulk viscosity and the small net-baryon number. The evolution of the shear-stress tensor $\pi^{\mu\nu}$ is described by the second-order Israel-Stewart formalism [50], with the coefficients of the non-linear second-order terms obtained by using the 14-moment approximation in the ultrarelativistic limit [51, 52]. The shear relaxation time is related to the shear viscosity by $\tau_\pi = 5\eta/(\epsilon + p)$, where ϵ is energy density in the local rest frame, and p is thermodynamic pressure.

Transverse momentum spectra of hadrons are computed by using the Cooper-Frye freeze-out formalism at a constant-temperature surface, followed by all 2- and 3-body decays of unstable hadrons. The chemical freeze-out is encoded into the EoS as described in Ref. [53],

[4] As done in e.g. Refs. [34, 45].

and the fluid evolves from chemical to kinetic freeze-out in partial chemical equilibrium (PCE)[54]. The kinetic and chemical freeze-out temperatures $T_{\rm dec}$ and $T_{\rm chem}$ are left as free parameters to be determined from the experimental data through the Bayesian analysis. The dissipative corrections δf to the momentum distribution at the freeze-out are computed according to the usual 14-moment approximation $\delta f_{\mathbf{k}} \propto f_{0\mathbf{k}} k^\mu k^\nu \pi_{\mu\nu}$, where $f_{0\mathbf{k}}$ is the equilibrium distribution function, and k^μ is the four-momentum of the hadron.

The remaining input to fluid dynamics are the EoS, initial conditions, and the shear viscosity. The different options for EoS were discussed in the previous section, and the initial conditions will be detailed in the next section. The temperature dependence of the shear viscosity η/s is parametrized in three parts, controlled by $T_{\rm H}$, the lower bound of the temperature range where η/s has its minimum value, $(\eta/s)_{\rm min}$, and the width of this temperature range, $W_{\rm min}$:

$$(\eta/s)(T) = \begin{cases} S_{\rm HG}(T_{\rm H} - T) + (\eta/s)_{\rm min}, & T < T_{\rm H} \\ (\eta/s)_{\rm min}, & T_{\rm H} \leq T \leq T_{\rm Q} \\ S_{\rm QGP}(T - T_{\rm Q}) + (\eta/s)_{\rm min}, & T > T_{\rm Q}, \end{cases} \quad (2)$$

where the additional parameters are the linear slopes below $T_{\rm H}$ and above $T_{\rm Q} = T_{\rm H} + W_{\rm min}$, denoted by $S_{\rm HG}$ and $S_{\rm QGP}$, respectively.

We note that bulk viscosity and chemical non-equilibrium are related [55, 56]. Even if we ignore the bulk viscosity, some of its effects are accounted for by the fugacities in a chemically frozen fluid: At temperatures below $T_{\rm chem}$ the isotropic pressure is reduced compared to the equilibrium pressure due to the different chemical composition. Thus introducing the chemical freeze-out changes not only the particle yields w.r.t. evolution in equilibrium, but similarly to the bulk viscosity, reduces the average transverse momentum of hadrons too. However, this affects the evolution only when temperature is below $T_{\rm chem}$, and in contrast to the bulk viscosity, there is e.g. no entropy production associated with the chemical freeze-out and subsequent chemical non-equilibrium [58].

Finally, we emphasize that we solve the spacetime evolution from the hot QGP all the way to the kinetic freeze-out as a single continuous fluid dynamical evolution. This is different from the hybrid models used e.g. in Refs. [10–12] where the evolution below some switching temperature is solved with a microscopic hadron cascade. The advantage of the fluid dynamical evolution without a cascade stage is that the transport properties are continuous in the whole temperature range. Note that in the hybrid models the switching from fluid dynamics to hadron cascade introduces an unphysical discontinuity in e.g. η/s that is $\mathcal{O}(1)$ in the cascade [57], but $\mathcal{O}(0.1)$ in fluid dynamical simulations at switching. Another advantage of our approach is that we can freely parametrize the viscosity in the hadronic matter too, and constrain it using the experimental data.

IV. INITIAL CONDITIONS

The initial energy density profiles are determined using the EKRT model [59–61] based on the NLO perturbative QCD computation of the transverse energy, and a gluon saturation conjecture. The latter controls the transverse energy production through a local semi-hard scale $p_{\rm sat}(T_A T_A, \sqrt{s_{\rm NN}}, A, K_{\rm sat})$, where $T_A(x,y)$ is a nuclear thickness function at transverse location (x,y). The essential free parameters in the EKRT model are the proportionality constant $K_{\rm sat}$ in the saturation condition, and the constant β controlling the exact definition of the minijet transverse energy at NLO [60]. The setup used here is identical to the one used in Refs. [13, 24, 48], where $\beta = 0.8$, and $K_{\rm sat}$ is left as a free parameter to be determined from the data. We note that $K_{\rm sat}$ is independent of the collision energy $\sqrt{s_{\rm NN}}$ and nuclear mass number A, so that once $K_{\rm sat}$ is fixed the $\sqrt{s_{\rm NN}}$ and A dependence of the initial conditions is entirely determined from the QCD dynamics of the EKRT model. With a given $p_{\rm sat}$ the local energy density at the formation time $\tau_p = 1/p_{\rm sat}$ can be written as

$$\epsilon(x,y,\tau_p) = \frac{K_{\rm sat}}{\pi} \left[p_{\rm sat}(x,y)\right]^4 . \quad (3)$$

This we further evolve to the same proper time $\tau_0 = 1/p_{\rm min}$, where $p_{\rm min} = 1$ GeV, at every point in the transverse plane where $p_{\rm sat} > p_{\rm min}$ by using 0+1 dimensional Bjorken hydrodynamics with the assumption $\epsilon = 3p$.

In the EKRT model, fluctuations in the product of the nuclear thickness functions, $T_A T_A$, give rise to the event-by-event fluctuations in the energy density through $p_{\rm sat}$ in Eq. (3). Moreover, the centrality dependence of the initial conditions arises from the centrality dependence of $T_A T_A$. A full treatment of the dynamics in heavy-ion collisions would take the event-by-event fluctuations into account by evolving each event separately. However, to make the present study computationally feasible, we omit the evolution of such fluctuations here; instead, for each centrality class, we average a large number of these fluctuating initial states, and compute the fluid dynamical evolution only for the averaged initial distributions.

The computed energy densities are not linear in $K_{\rm sat}$ nor in $T_A T_A$, and different averaging procedures can lead to significantly different event-averaged initial conditions. In the previous event-by-event EKRT studies [13, 24, 48] a fair agreement was obtained between the data and the computed $\sqrt{s_{\rm NN}}$, A, and centrality dependencies of the charged hadron multiplicity. To preserve as much as possible of this agreement, we average the initial conditions by averaging the initial entropy distributions: We compute first a large set of initial energy density profiles using the procedure detailed in Ref. [13]. Each of the generated energy density profiles is converted to an entropy density profile by using the EoS which will be used later during the evolution. The entropy density profiles are then averaged, and the average entropy density profile is converted to an average energy density profile using the

same EoS.

In the event-by-event framework the centrality classes were determined from the final multiplicity distribution. However, this way of classifying events is not available here, as it would require fluid dynamical evolution of each of the fluctuating initial conditions. Instead, we predetermine the centrality classes according to the number of wounded nucleons in the sampled Monte-Carlo nuclear configurations, which were used to construct the event-by-event initial conditions. The number of wounded nucleons are computed using the nucleon-nucleon cross section $\sigma_{\rm NN} = 42$, 64, and 70 mb for 200 GeV, 2.76 TeV, and 5.02 TeV collisions, respectively. We note that the nucleon-nucleon cross section does not enter in the computation of the initial conditions, but they are used here only in the centrality classification. In the context of the full event-by-event modeling we have tested that the final results are only weakly sensitive to the precise way of the centrality classification.

V. STATISTICAL ANALYSIS

The eight free parameters of our model, $\{K_{\rm sat}, (\eta/s)_{\rm min}, T_{\rm H}, W_{\rm min}, S_{\rm HG}, S_{\rm QGP}, T_{\rm dec}, T_{\rm chem}\}$, were introduced in Secs. III and IV. We want to tune them to achieve the best possible fit to an experimental data set of 90 data points. This set consists of the following observables at (10–20)%, (20–30)%, (30–40)%, (40–50)% and (50–60)% centrality classes[5]:

- The charged particle multiplicity at midrapidity, $\mathrm{d}N_{\rm ch}/\mathrm{d}\eta$, and 4-particle cumulant p_T-averaged elliptic flow, $v_2\{4\}$, in Au+Au collisions at $\sqrt{s_{\rm NN}} =$ 200 GeV (RHIC) [25, 27] and Pb+Pb collisions at $\sqrt{s_{\rm NN}} = 2.76$ [28, 30] and $\sqrt{s_{\rm NN}} = 5.02$ TeV [30, 31] (LHC).
- The multiplicities at midrapidity, $\mathrm{d}N_i/\mathrm{d}y$, and average transverse momenta $\langle p_T\rangle_i$, of pions (π^+), kaons (K^+) and protons[6] (p) in Au+Au collisions at RHIC [26] and in Pb+Pb collisions at the lower LHC energy [29].

Let us consider each combination of the free parameters as a point $\vec{x}$ in the 8-dimensional input (parameter) space, the model output $\vec{y}(\vec{x})$ as a corresponding point in the 90-dimensional output space (space of observables), and the experimental data $\vec{y}^{\rm exp}$ as the target point in the space of observables. With these definitions we can formulate the posterior probability distribution $P(\vec{x}|\vec{y}^{\rm exp})$ of the best-fit parameter values by utilizing Bayes' theorem:

$$P(\vec{x}|\vec{y}^{\rm exp}) \propto P(\vec{y}^{\rm exp}|\vec{x})P(\vec{x}), \tag{4}$$

where $P(\vec{x})$ is the prior probability distribution of input parameters and $P(\vec{y}^{\rm exp}|\vec{x})$ is the likelihood function

$$P(\vec{y}^{\rm exp}|\vec{x}) \tag{5}$$
$$= \frac{1}{\sqrt{|2\pi\Sigma|}} \exp\left(-\frac{1}{2}(\vec{y}(\vec{x}) - \vec{y}^{\rm exp})^T \Sigma^{-1} (\vec{y}(\vec{x}) - \vec{y}^{\rm exp})\right).$$

Here Σ is the covariance matrix representing the uncertainties related to the model-to-data comparison.

As a function with an eight-dimensional domain, the posterior probability distribution $P(\vec{x}|\vec{y}^{\rm exp})$ is too complicated to evaluate and analyze fully. Instead, we produce samples of it with a parallel tempered Markov chain Monte Carlo [62] based on the EMCEE sampler [63]. An ensemble of random walkers is initialized in the input parameter space based on the prior probability[7] and each proposed step in parameter space is accepted or rejected based on the change in the value of the likelihood function. At a large number of steps, the distribution of the taken steps is expected to converge to the posterior distribution.

Evaluating the output $\vec{y}(\vec{x})$ of the fluid dynamical model at every point $\vec{x}$ where the random walker might enter is a computationally impossible task. Therefore we approximate the output using Gaussian process (GP) emulators [64] (see Appendix B). Each GP is able to provide estimates for only one observable, so to keep the number of required emulators manageable, we perform a principal component analysis (PCA) to reduce the dimension of the output space from 90 observables into $k = 6$ most important principal components. Further details about the PCA are described in Appendix C. We utilize the `scikit-learn` Python module [65] and in particular the submodules `sklearn.gaussian_process` and `sklearn.decomposition.PCA` in the model emulation.

Thus, in our likelihood function (5), we replace $\vec{y}(\vec{x})$ with the GP estimate in the principal component space $\vec{z}^{\rm GP}(\vec{x})$ (likewise $\vec{y}^{\rm exp}$ is transformed to $\vec{z}^{\rm exp}$), and include the emulator estimation error into the covariance matrix:

$$\Sigma_z = \Sigma_z^{\rm exp} + \Sigma_z^{\rm GP}, \tag{6}$$

where $\Sigma_z^{\rm exp}$ is the (originally diagonal) experimental error matrix transformed to principal component space, and

$$\Sigma_z^{\rm GP} = \mathrm{diag}(\sigma_{z,1}^{\rm GP}(\vec{x})^2, \sigma_{z,2}^{\rm GP}(\vec{x})^2, ..., \sigma_{z,k}^{\rm GP}(\vec{x})^2) \tag{7}$$

[5] Charged particle multiplicities at RHIC are averages over two adjacent PHENIX centrality classes; for example, at (10–20)% centrality $N_{\rm ch}$ is an average over (10–15)% and (15–20)% classes, (20–30)% is an average over (20–25)% and (25–30)% classes, and so on. This applies also for RHIC identified particle data at (10–20)% centrality.

[6] We consider an average of measured protons and antiprotons as the target value for the proton multiplicity at RHIC.

[7] In the present case, the shape of the prior is a uniform hypercube with an additional restriction $T_{\rm dec} < T_{\rm chem}$. The prior ranges are shown in Figs. 3 and 4.

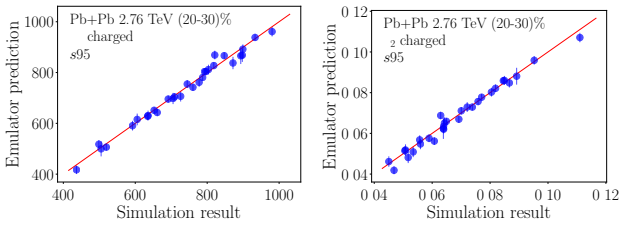

FIG. 2. Illustration of the quality of the Gaussian process emulation for 30 test points for simulations with the $s95p$ EoS. Left panel: Charged particle multiplicity in (20-30)% most central Pb+Pb collisions at $\sqrt{s_{\rm NN}} = 2.76$ TeV. Right panel: Elliptic flow $v_2\{\rm RP\}$ in (20-30)% most central Pb+Pb collisions at $\sqrt{s_{\rm NN}} = 2.76$ TeV.

is the GP emulator covariance matrix obtained from the emulator (see Appendix B).

To work, the GP emulators must be conditioned with a set of training points, $\{\vec{z}(\vec{x}_i)\}$, created by running the fluid dynamical model with several different parameter combinations $\{\vec{x}_i\}$. For the present investigation, we have produced 170 training points for each EoS, distributed evenly in the input parameter space[8] using min-max Latin hypercube sampling [66]. The emulation quality was then checked by using the trained emulator to predict the results at 30 additional test points, which were not part of the training data. An example of the results of this confirmation process is shown in Fig. 2 for 2.76 TeV Pb+Pb collisions using the $s95p$ parametrization.

VI. RESULTS

The marginal posterior probability distributions for each parameter are obtained from the full 8-dimensional probability distribution (see Section V) by integrating over the other seven parameters. The resulting distributions when using the four investigated EoSs are shown in Figs. 3 and 4. In these figures the range of the x-axis illustrates the prior range of values, with the exception of $T_{\rm chem}$ which range depends on the EoS[9]. The median values of these distributions provide a good approximation for the most probable values, and are listed both in the legends of the figures, and in Table I. The 90% credible intervals—i.e. the range which covers 90% of the distribution around the median—are shown as errors in Table I. Two dimensional projections of the probability distribution depicting correlations between parameter pairs are shown in Appendix D.

[8] The restriction $T_{\rm dec} < T_{\rm chem}$ does not apply to the training points.

[9] For $s83s_{18}$, $s87h_{04}$, and $s88h_{18}$, the prior range is 120 MeV $< T_{\rm chem} < T_0$, where T_0 is the temperature where the parametrization deviates from the HRG (see Appendix A). For $s95p$ the range is $120 < T_{\rm chem}/{\rm MeV} < 180$.

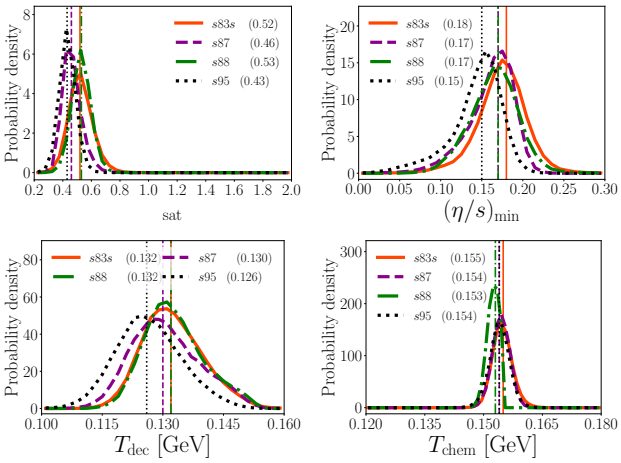

FIG. 3. Comparison of $K_{\rm sat}$, $(\eta/s)_{\rm min}$, $T_{\rm dec}$, and $T_{\rm chem}$ marginal posterior probability distributions for the four investigated EoSs. Vertical lines (bracketed numbers in legend) indicate median values for the distributions. With the exception of $T_{\rm chem}$, the range of the x-axis in the plots is the original prior range.

A. Nuisance parameters

The analysis involves three parameters which are not directly related to the transport properties of produced matter: $K_{\rm sat}$, $T_{\rm dec}$, and $T_{\rm chem}$. The probability distributions for these three "nuisance" parameters, shown in Fig. 3, are nicely peaked, and the parameters have well defined constraints. For the chemical freeze-out temperature, the median is $T_{\rm chem} = 153$–155 MeV, which is compatible with the values obtained using the statistical hadronization model [67]. Note that the difference in the median is not due to the resonance content of the EoS, but due to a complicated interplay of the softness of the EoS, shear, and build-up of the flow. Nevertheless, the particle ratios are the dominant factor in constraining $T_{\rm chem}$.

For $K_{\rm sat}$ and $T_{\rm dec}$, we see a common trend where $s95p$ gives a distribution which peaks at the lowest value of the four EoSs, followed by $s87h_{04}$, and the highest peak values are shared by $s83s_{18}$ and $s88h_{18}$ with almost identical distributions. The obtained values for the EKRT normalization parameter, $K_{\rm sat} \approx 0.5$, are compatible with the values found previously [13], and the small differences between different EoS parametrizations result from slightly different entropy production during the evolution. Differences seen in the kinetic freeze-out temperature $T_{\rm dec} = 126$–132 MeV are also small, and seem to follow the conventional rule of thumb: a softer EoS requires a lower freeze-out temperature to create hard enough proton $p_{\rm T}$ distributions. On the other hand, differences in the median values of all these three parameters are smaller than the credibility limits, and thus not statistically meaningful.

TABLE I. Estimated parameter values (medians) and uncertainties (90% credible intervals) from the posterior distributions.

Parameter		$s83s_{18}$	$s87h_{04}$	$s88h_{18}$	$s95p$
$K_{\rm sat}$		$0.52^{+0.15}_{-0.12}$	$0.46^{+0.12}_{-0.09}$	$0.53^{+0.11}_{-0.10}$	$0.43^{+0.10}_{-0.09}$
$(\eta/s)_{\rm min}$		$0.18^{+0.04}_{-0.06}$	$0.17^{+0.03}_{-0.07}$	$0.17^{+0.04}_{-0.06}$	$0.15^{+0.03}_{-0.07}$
T_H	[GeV]	$0.13^{+0.05}_{-0.03}$	$0.13^{+0.06}_{-0.03}$	$0.13^{+0.06}_{-0.03}$	$0.15^{+0.06}_{-0.04}$
$W_{\rm min}$	[GeV]	$0.19^{+0.10}_{-0.17}$	$0.12^{+0.15}_{-0.11}$	$0.14^{+0.13}_{-0.12}$	$0.12^{+0.10}_{-0.10}$
$S_{\rm HG}$	[GeV^{-1}]	$2.9^{+4.0}_{-2.7}$	$3.0^{+4.5}_{-2.8}$	$3.4^{+4.2}_{-3.2}$	$3.9^{+3.7}_{-3.6}$
$S_{\rm QGP}$	[GeV^{-1}]	$2.4^{+4.9}_{-2.1}$	$3.1^{+4.2}_{-2.5}$	$3.2^{+4.1}_{-2.7}$	$5.2^{+2.5}_{-3.5}$
$T_{\rm dec}$	[MeV]	132^{+14}_{-11}	130^{+16}_{-12}	132^{+15}_{-10}	126^{+15}_{-12}
$T_{\rm chem}$	[MeV]	155^{+4}_{-4}	154^{+4}_{-3}	153^{+2}_{-3}	154^{+4}_{-4}

B. $(\eta/s)(T)$

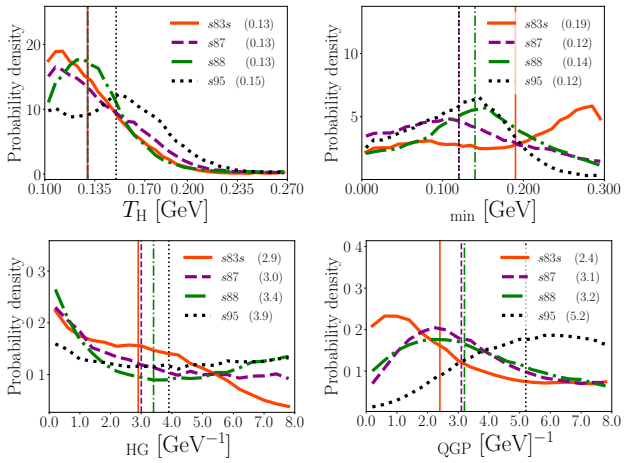

FIG. 4. As Fig. 3, but showing the marginal posterior probability distributions of $T_{\rm H}$, $W_{\rm min}$, $S_{\rm HG}$, and $S_{\rm QGP}$.

At first sight $(\eta/s)_{\rm min}$ depicts the behavior described in Refs. [16, 19]: the favored value is lower for $s95p$ than for the newer parametrizations (see Fig. 3 and Table I). However, the effect is noticeably smaller than seen in those studies—only $\sim$ 10–20%—and well within the 90% credible intervals ($\pm \sim 30\%$) of the analysis. The comparison of η/s for different EoSs is further complicated by the large number of parameters controlling the temperature dependence of η/s. The probability distributions of parameters $T_{\rm H}, W_{\rm min}, S_{\rm HG}$, and $S_{\rm QGP}$, shown in Fig. 4, are very broad extending to the whole prior range in most cases, and thus do not possess any clearly favored values. However, the wide posterior distributions of the $(\eta/s)(T)$ parameters are partly caused by the inherent ambiguity in the chosen parametrization: for a given temperature T, multiple parameter combinations can generate similar values of η/s. For example, at low temperatures $(\eta/s)(T)$ is mostly determined by $S_{\rm HG}$ and $T_{\rm H}$, but it is better constrained than either of these parameters. The reason is that $S_{\rm HG}$ and $T_{\rm H}$ are not independent, but slightly anti-correlated—the correlations between the pairs of parameters are shown in Appendix D. Thus it is more illustrative to construct the probability distribution for η/s values w.r.t. temperature, and plot the median and credibility intervals of this distribution as shown in Figs. 5 and 6.

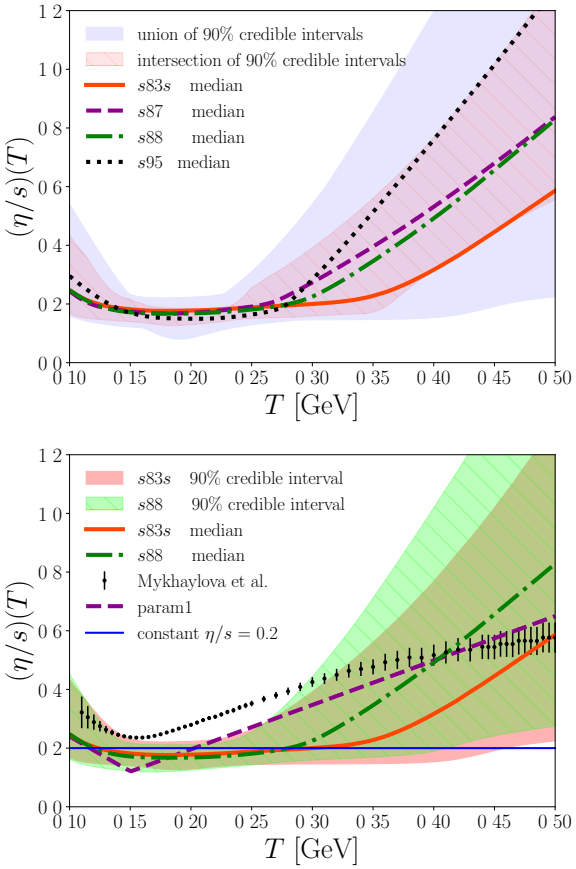

FIG. 5. Temperature dependence of η/s. Upper figure: Median of η/s w.r.t. T for each EoS with the union and intersection of the 90% credible intervals of the distributions. Lower figure: Median of η/s w.r.t. T for the $s83s_{18}$ and $s88h_{18}$ parametrizations with corresponding credibility intervals compared with two results from Ref. [13] ($\eta/s = 0.2$ and param1) and a recent quasiparticle model prediction by Mykhaylova *et al.* [68].

In the upper panel of Fig. 5 we show the median of $(\eta/s)(T)$ for each EoS parametrization, and the union and intersection of the 90% credible intervals of all four distributions. The union of the credibility intervals provides insight on the total uncertainty in the analysis including the uncertainty from the EoS parametrization, whereas the difference between the union and intersection illustrates how much of the uncertainty comes from the EoS parametrizations. To emphasize the result using state-of-the-art EoSs, the lower panel of Fig. 5 depicts the median and credibility intervals for the parametriza-

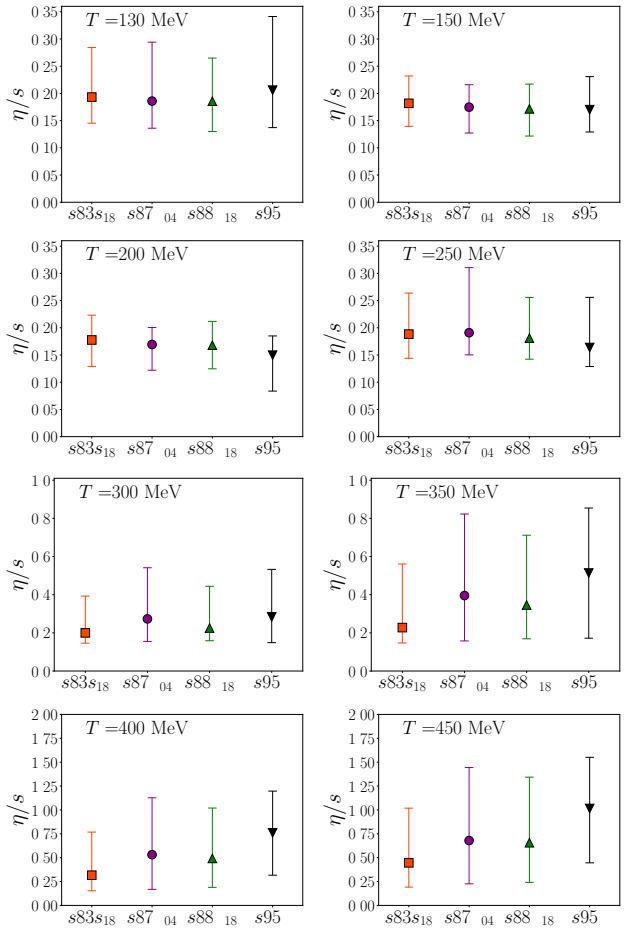

FIG. 6. Median values (filled markers) and 90% credible intervals (error bars) for η/s at temperatures $T = 130, 150, 200, 250, 300, 350, 400$, and 450 MeV.

tions $s83s_{18}$ and $s88h_{18}$ only. In the same panel two older results from Ref. [13], and a recent theoretical prediction from Ref. [68] are shown as well. To make it possible to distinguish the credibility intervals for each EoS separately, η/s for each EoS at various temperatures with associated uncertainties is shown in Fig. 6.

We obtain well constrained η/s in a temperature range $150 \lesssim T/\text{MeV} \lesssim 220$, where the median values of η/s are practically constant for all contemporary EoSs, and $s95p$ leads to modest temperature dependence well within the credibility intervals. Within this temperature range η/s is constrained between 0.08 and 0.23 by the 90% credible intervals. In particular, for the state-of-the-art EoSs ($s83s_{18}$ and $s88h_{18}$), we obtain even tighter limits $0.12 < \eta/s < 0.23$ within this range, and the well constrained region extends to slightly higher temperature. For further details see Fig. 5 and Table II. Interestingly η/s at 130 MeV (or at 150 MeV in case of $s95p$) temperature differs from the favored value (median) of the $(\eta/s)_{\text{min}}$ parameter (compare Tables I and II), even if the favored value of the T_{H} parameter is 130 MeV (or 150 MeV) (see Fig. 4 and Table I). This seemingly counterintuitive behavior is due to the fat tails of T_{H} distributions extending to larger temperatures, and thus broadening the region where S_{HG} affects the η/s values. Consequently we see the lowest η/s values at $T \approx 200$ MeV temperature (Fig. 5 and Table II), where the effect of the lower $(\eta/s)_{\text{min}}$ value of the $s95p$ parametrization is also visible.

TABLE II. Median values of η/s at various temperatures with associated uncertainties (90% credible intervals) from the posterior distributions. Values rounded to two significant figures.

T [MeV]	$s83s_{18}$	$s87h_{04}$	$s88h_{18}$	$s95p$
130	$0.19^{+0.09}_{-0.04}$	$0.19^{+0.10}_{-0.05}$	$0.19^{+0.07}_{-0.06}$	$0.21^{+0.13}_{-0.07}$
150	$0.18^{+0.05}_{-0.04}$	$0.17^{+0.05}_{-0.04}$	$0.17^{+0.05}_{-0.05}$	$0.17^{+0.06}_{-0.04}$
200	$0.18^{+0.04}_{-0.05}$	$0.17^{+0.03}_{-0.05}$	$0.17^{+0.04}_{-0.05}$	$0.15^{+0.04}_{-0.07}$
250	$0.19^{+0.07}_{-0.05}$	$0.19^{+0.12}_{-0.04}$	$0.18^{+0.08}_{-0.04}$	$0.16^{+0.10}_{-0.03}$
300	$0.20^{+0.19}_{-0.05}$	$0.27^{+0.27}_{-0.11}$	$0.23^{+0.21}_{-0.07}$	$0.28^{+0.25}_{-0.13}$
350	$0.23^{+0.33}_{-0.08}$	$0.40^{+0.42}_{-0.24}$	$0.35^{+0.36}_{-0.18}$	$0.51^{+0.34}_{-0.34}$

It is not surprising that we get the best constraints on η/s in the temperature range $150 \lesssim T/\text{MeV} \lesssim 220$. As was shown in Ref. [46], the temperature range where v_2 is most sensitive to the shear viscosity is only slightly broader than this, and higher order anisotropies are sensitive to shear at even narrower temperature ranges[10].

Even if the uncertainties remain large, we can see qualitative differences in the high temperature behavior of η/s, where $s95p$ seems to favor earlier and more rapid rise of η/s with increasing temperature (Figs. 5 and 6), a difference which is visible in the S_{QGP} parameter as well (Fig. 4).

Considering earlier results in the literature this is intriguing. Alba *et al.* [16] used an EoS based on contemporary stout action data called PDG16+/WB2+1, and observed that the reproduction of the LHC data ($\sqrt{s_{\text{NN}}} = 5.02$ TeV) required larger constant η/s for this EoS than for $s95p$. On the other hand, they were able to use the same value of constant η/s for both EoSs to reproduce the RHIC data. They interpreted this to mean that at large temperatures $s95p$ would necessitate lower values of η/s, but we see an opposite behavior. In a similar fashion we see a difference between the high temperature behavior obtained using the HISQ ($s88h_{18}$ and $s87h_{04}$) and stout action based EoSs ($s83s_{18}$), but the differences are way smaller than the credibility intervals, and thus cannot be considered meaningful.

At temperatures below 150 MeV we again see expanding credibility intervals, and a tendency of η/s to increase with decreasing temperature, but hardly any sensitivity to the EoS. Anisotropies measured at RHIC en-

[10] Note that the studies in Ref. [46] were carried out using the $s95p$ EoS. We haven't checked how sensitive those results are to the EoS parametrization.

ergy are sensitive to the shear viscosity in the hadronic phase [46, 47], and since Schenke *et al.* in Ref. [19] saw sensitivity to the EoS using RHIC data only, we would have expected some sensitivity to the EoS at low temperatures. The difference may arise from the bulk viscosity which depended on the EoS as well in Ref. [19], or from a different EoS in the hadronic phase. As mentioned, our EoSs are based on known resonance states, whereas the EoSs in Refs. [16, 19] follow the lattice results closely. Better fit to lattice results can be obtained by including predicted but unobserved resonance states in the HRG. We plan to study how the inclusion of these states might affect the results, once we have concocted a plausible scheme for their decays, so that we can evaluate their contribution to the EoS after chemical freeze-out in a consistent manner.

Furthermore, unlike in Ref. [19] where a hadron cascade was used to describe the evolution in the hadronic phase, in our approach the change in the EoS can also be partly compensated by a change in the freeze-out temperature instead of shear viscosity. As shown in Appendix D, there is indeed an anti-correlation between $T_{\rm dec}$ and $(\eta/s)_{\rm min}$. Therefore forcing the system to freeze out at the same temperature, independent of the EoS, would increase the difference in $(\eta/s)_{\rm min}$. However, the anti-correlation is rather weak $\sim -0.4(-0.2)$ for $s88h_{18}$ ($s95p$), and thus requiring EoS independent $T_{\rm dec}$ would not change $(\eta/s)_{\rm min}$ a lot.

Our result of a very slowly rising η/s with decreasing temperature in the hadronic phase (i.e., below $T \approx 150$ MeV) may look inconsistent with microscopic calculations predicting relatively large $\eta/s \sim 1$ in the hadronic phase [57, 69, 70]. However, our result is for a chemically frozen HRG, while the microscopic calculations usually give η/s in chemical equilibrium. At a given temperature the entropy density $s_{\rm PCE}$ in a chemically frozen HRG can be significantly larger than the entropy density in chemical equilibrium $s_{\rm CE}$, and as a consequence $\eta/s_{\rm PCE}$ can be way smaller than $\eta/s_{\rm CE}$. We may obtain an approximation for the η/s in a chemically equilibrated system as $\eta/s_{\rm CE} = (\eta/s_{\rm PCE})(s_{\rm PCE}/s_{\rm CE})$ [13], since, as a first order approximation, η depends only weakly on the chemical non-equilibrium [71]. In our case, where $T_{\rm chem} = 154$ MeV, the ratio of entropies in a chemically frozen to a chemically equilibrated system is ~ 3.5 at $T = 100$ MeV (~ 1.8 at $T = 130$ MeV) which is sufficient to bring our results to the level described in Ref. [70].

In Fig. 5 we also made a comparison to the earlier results of Ref. [13] and the recent quasiparticle model prediction from Ref. [68]. As expected, the earlier results from Ref. [13, 24] are not far from the present analysis, and param1 is practically within the 90% credible interval in the whole temperature range. On the other hand, constant $\eta/s = 0.2$ is below the $s95p$ limits at high temperatures, but as discussed, the overall sensitivity to η/s at high temperatures is low. Interestingly the prediction of the quasiparticle model of Ref. [68] comes very close to our values for η/s around T_c, although the region where η/s is low is narrower than what we found here. This is intriguing, since the quasiparticle model was tuned to reproduce the stout action EoS, i.e., our EoS $s83s_{18}$, which in our analysis leads to the broadest region where η/s is almost constant.

The small value of η/s and its weak temperature dependence in the temperature range $150 \lesssim T/{\rm MeV} \lesssim 220$ may indicate that the QGP is strongly coupled not only in the immediate vicinity of T_c, but in a broader temperature region. This was first proposed in Ref. [72], and agrees with the lattice QCD calculations that indicate the presence of hadronlike resonances in QGP in a similar or slightly broader temperature interval [73–76]. The strongly coupled nature of QGP can also be seen in the large value of the coupling constant defined in terms of the free energy of static quark anti-quark pairs [77]. In any case, our result for $(\eta/s)(T)$ is compatible with the lattice QCD calculations, which indicate that weakly coupled QGP picture may be applicable only for $T > 350$ MeV [77–80].

C. The effect of the parametric form

When we use the state-of-the-art EoSs ($s88h_{18}$ and $s83s_{18}$), our result for the minimum value of η/s is higher than the result obtained in an earlier Bayesian analysis of Ref. [10]: $0.12 < \eta/s < 0.23$ vs. $\eta/s = 0.07^{+0.05}_{-0.04}$. An important difference in these analyses is that Ref. [10] assumed the minimum of η/s to occur at fixed $T = 154$ MeV temperature, and η/s to rise linearly above that temperature. Moreover, below $T = 154$ MeV they used a hadron cascade to model the evolution, and the transport properties of the hadronic phase were thus fixed.

To explore how much the results depend on the form of the $(\eta/s)(T)$ parametrization, we mimic the parametrization used in Ref. [10] by constraining the plateau in our parametrization to be very small ($0 < W_{\rm min}/{\rm MeV} < 2$), and the minimum to appear close to T_c ($150 < T_{\rm H}/{\rm MeV} < 160$). The resulting temperature dependence of η/s for the $s88h_{18}$ and $s95p$ parametrizations is shown in Fig. 7, and compared to our full result (the behavior of the $s87h_{04}$ and $s83s_{18}$ parametrizations is similar to $s88h_{18}$).

The change in parametrization reduces the minimum value of η/s to $0.12^{+0.03}_{-0.03}$ for $s88h_{18}$ and $0.06^{+0.04}_{-0.04}$ for $s95p$, which are consistent with the value obtained in Ref. [10]. Another interesting change is seen in the high-temperature behavior. In the full analysis the $s95p$ parametrization leads to the largest η/s at large temperatures, but the restricted parametrization causes $s95p$ to favor the lowest η/s at large temperatures. As seen previously, $s95p$ favors the lowest η/s at $200 < T/{\rm MeV} < 250$ temperatures (see Fig. 6 and Table II), which in the restricted parametrization dictates the behavior at much higher temperatures as well.

Nevertheless, even if the results depend on the form of the parametrization, the credibility intervals overlap

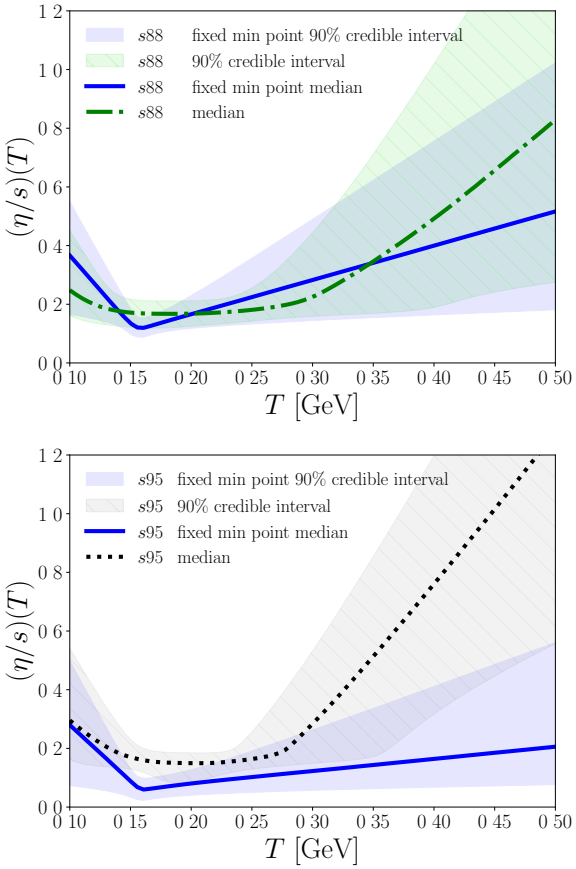

FIG. 7. Temperature dependence of η/s for the $s88h_{18}$ (top) and $s95p$ (bottom) EoSs using the full parametrization and a parametrization constrained to have a minimum at a fixed point in temperature ("fixed min point").

and the results are consistent. The only deviation from this rule is for the $s95p$ parametrization around $T = 160$ MeV temperature where the difference is statistically significant (see Fig. 7). We have also checked that when we use the favored parameter values, the typical differences in the fit to the data due to different parametric forms are only $\sim (1-3)\%$.

Similarly, we can mimic temperature independent η/s by constraining the priors of the $S_{\rm HG}$ and $S_{\rm QGP}$ parameters close to zero. We have checked that such a choice does not increase the sensitivity of η/s to the EoS parametrization, and that the median values of the constant $\eta/s = (\eta/s)_{\rm min}$ were only $\approx 10\%$ larger than the median values for η/s at $T = 200$ MeV for the full parametrization. Again, a sign of v_2 being most sensitive to shear viscosity in the $150 \lesssim T/\text{MeV} \lesssim 220$ temperature range [46].

Thus, in the Bayesian analysis the parametric form of η/s does affect the results, and is therefore a kind of prior whose effects are difficult to quantify. On the other hand, the credibility intervals overlap in all the cases, which emphasizes their importance: The "true" value could be anywhere within the credibility interval, and there is still a 10% chance it is outside of it.

D. Comparison with the data

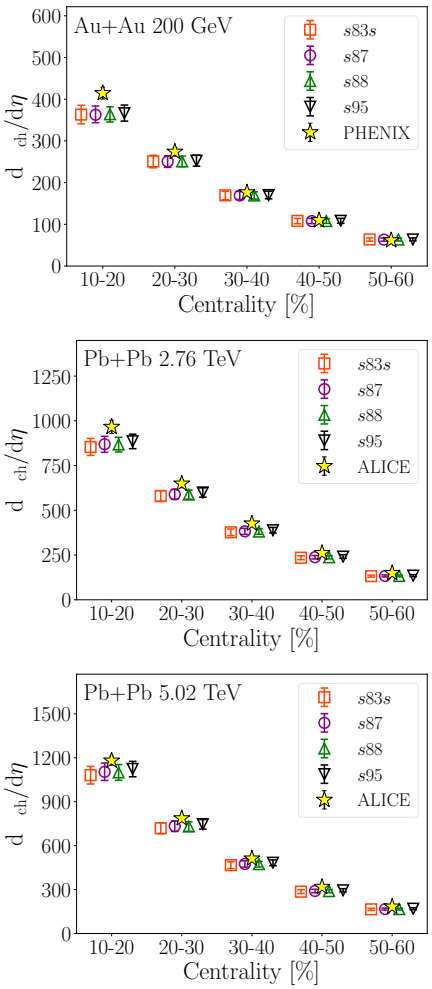

FIG. 8. Charged particle multiplicity at various centralities using 1000 samples from the posterior distribution of each EoS. Marker centers indicate median values, and error bars 90% credible intervals. Top panel: Au+Au at $\sqrt{s_{\rm NN}} = 200$ GeV compared to PHENIX data [25]. Middle panel: Pb+Pb at $\sqrt{s_{\rm NN}} = 2.76$ TeV compared to ALICE data [28]. Bottom panel: Pb+Pb at $\sqrt{s_{\rm NN}} = 5.02$ TeV compared to ALICE data [31].

Finally, as an overall quality check, we show how well the favored parameter combinations reproduce the experimental data. This is done by drawing 1000 samples from each posterior distribution and using the Gaussian process emulator to predict the simulation output for these values. The results for charged and identified particle multiplicities, identified particle $\langle p_T \rangle$, and the elliptic flow $v_2\{4\}$ are shown in Figs. 8, 9, 10, and 11, respec-

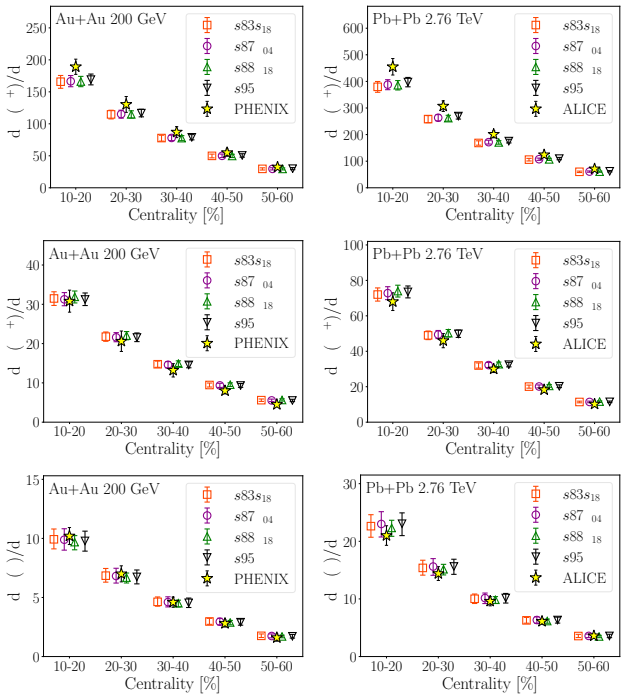

FIG. 9. Pion (upper panels), kaon (middle panels), and proton (lower panels) multiplicities at various centralities using 1000 samples from the posterior distribution of each EoS. Marker centers indicate median values, and error bars 90% credible intervals. Left panels: Au+Au at $\sqrt{s_{\rm NN}} = 200$ GeV compared to PHENIX data [26]. Right panels: Pb+Pb at $\sqrt{s_{\rm NN}} = 2.76$ TeV compared to ALICE data [29]

.

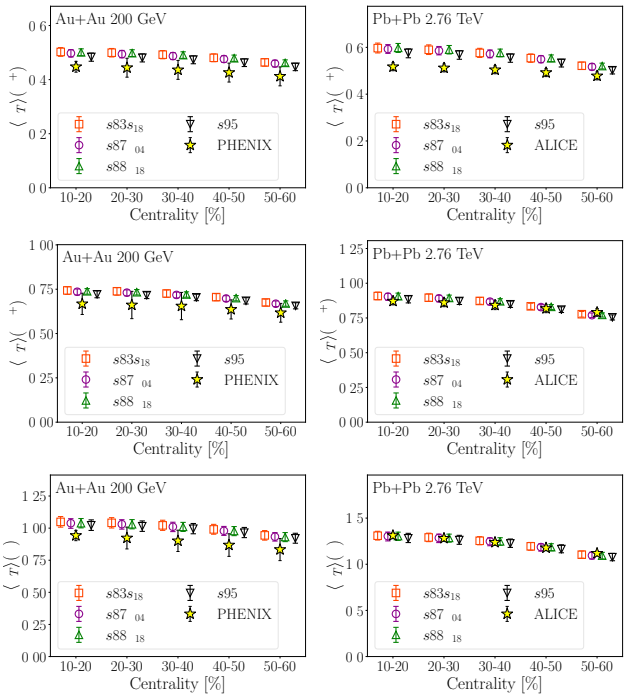

FIG. 10. As Fig. 9 but for the mean transverse momentum.

tively.

The overall agreement with the data is quite good for all observables, and the analysis is able to find equally good data fits for all four EoSs. As normal for thermal models, the charged particle multiplicities tend to be underestimated due to the tension between pion multiplicity on one hand, and kaon and proton multiplicities on the other hand. As the analysis makes a compromise between too few pions and too many kaons and protons, the overall charged particle multiplicity (which is dominated by pions) will remain below the data. Also the mean transverse momentum of pions is slightly too large, which may prove difficult to alleviate without the introduction of bulk viscosity [4] and/or improved treatment of resonances during the hadronic phase [81].

VII. SUMMARY

In this work, we have introduced three new parametrizations of the equation of state based on the contemporary lattice data:

- $s87h_{04}$ connects the HRG based on the PDG 2004 particle list to parametrized lattice data obtained using the HISQ discretization scheme.
- $s88h_{18}$ is based on the HRG containing all strange and non-strange hadrons and resonances in the PDG 2018 summary tables, and the same HISQ lattice data as $s87h_{04}$.
- $s83s_{18}$ is constructed using the PDG 2018 resonances, and the continuum extrapolated lattice data obtained using the stout discretization.

We used these new parametrizations and the older $s95p$ parametrization to examine how sensitive the shear viscosity over entropy density ratio η/s is to the equation of state. We assumed a piecewise linear parametrization for $(\eta/s)(T)$, and determined the probability distributions of the best-fit parameter values within the EKRT framework using a Bayesian statistics approach.

Using charged and identified particle multiplicities, identified particle mean transverse momenta, and elliptic flow at three different collision energies as calibration data, we were able to constrain the value of η/s to be between 0.08 and 0.23 with 90% credibility in the temperature range $150 \lesssim T/\text{MeV} \lesssim 220$ when all EoS parametrizations are taken into account. When we constrain the EoSs to the most contemporary parametrizations $s83s_{18}$ and $s88h_{18}$, we obtain $0.12 < \eta/s < 0.23$ in the above mentioned temperature range. As the differences between the EoSs are well covered by the 90% credible intervals, the earlier results obtained using the $s95p$ parametrization remain valid. The weak sensitivity to the EoS is consistent with the old ideal fluid results

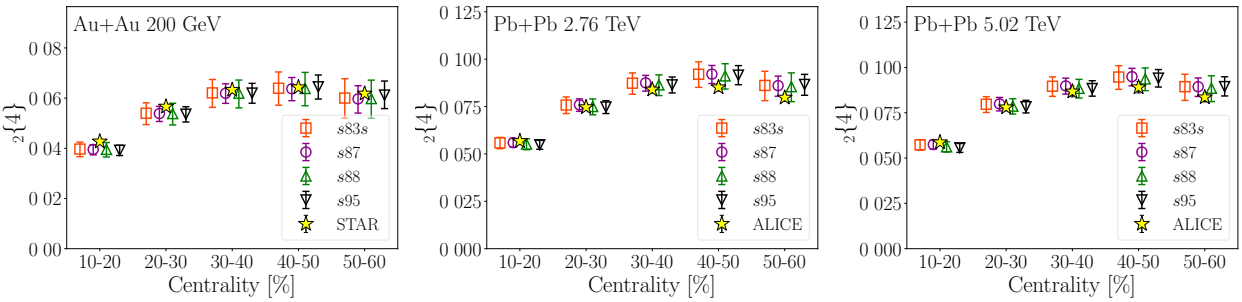

FIG. 11. Charged particle elliptic flow $v_2\{4\}$ at various centralities using 1000 samples from the posterior distribution of each EoS. Marker centers indicate median values, and error bars 90% credible intervals. Left panel: Au+Au at $\sqrt{s_{\rm NN}} = 200$ GeV compared to STAR data [27]. Middle panel: Pb+Pb at $\sqrt{s_{\rm NN}} = 2.76$ TeV compared to ALICE data [30]. Right panel: Pb+Pb at $\sqrt{s_{\rm NN}} = 5.02$ TeV compared to ALICE data [30].

for flow and EoS: Based on flow alone, it is difficult to distinguish an EoS with a smooth crossover from an EoS without phase transition [82]. Thus when the differences between EoSs are just details in the crossover, the differences in flow, which should be compensated by different shear viscosity, are small, and consequently differences in the extracted η/s are small.

The overall agreement with the data is quite good, and similar to Refs. [13, 24], where event-by-event fluctuations were included to the framework of EKRT initial conditions and fluid dynamics, albeit without the Bayesian analysis. The good agreement achieved here is partly due to the EKRT initial conditions. In particular the centrality and $\sqrt{s_{\rm NN}}$ dependence of hadron multiplicities follow mainly from the QCD dynamics of the EKRT model. A noticeable difference to the earlier event-by-event analysis is that here we used identified hadron multiplicities as constraint, which led to the chemical freeze-out temperature $T_{\rm chem} \sim 154$ MeV, and a slight overshoot of the pion average p_T compared to the data. In the earlier analysis $T_{\rm chem} \sim 175$ MeV was used to reproduce the average p_T data, which in turn led to too large proton multiplicity. It is possible to solve this tension by introducing bulk viscosity [4], but that is left for a future work. We emphasize that compared to the (in principle) more detailed hydro + cascade models our hydro + partial chemical equilibrium approach has two major advantages: It allows us to parametrize $\eta/s(T)$ so that it is continuous in the whole temperature range, and at the same time it gives us a possibility to constrain the viscosity also in the hadronic phase.

Inclusion of event-by-event fluctuations to the analysis would provide access to several new flow observables such as higher flow harmonics v_n, and flow correlations, which may give tighter constraints in broader temperature interval on $\eta/s(T)$. However, within the current uncertainties of the fitting procedure, we cannot exclude the possibility that the effect of the EoS remains negligible even when η/s at $T > 220$ MeV becomes better under control.

Since the sensitivity of flow to shear viscosity at high temperatures is low, observables based on high p_T particles may be useful to constrain, not only the pre-equilibrium dynamics [83–85], but also the properties of the fluid when it is hottest.

ACKNOWLEDGMENTS

We thank V. Mykhaylova for sharing her quasiparticle results with us. JA and PH were supported by the European Research Council, Grant No. ERC-2016-COG:725741, PH was also supported by National Science Center, Poland, under grant Polonez DEC-2015/19/P/ST2/03333 receiving funding from the European Union's Horizon 2020 research and innovation program under the Marie Skłodowska-Curie grant agreement No. 665778; KJE and HN were supported by the Academy of Finland, Project No. 297058; and PP was supported by U.S. Department of Energy under Contract No. de-sc0012704. We acknowledge the CSC – IT Center for Science in Espoo, Finland, for the allocation of the computational resources.

Appendix A: EoS parametrization

At high temperature the trace anomaly can be well parametrized by the inverse polynomial form. Therefore we will use the following Ansatz for the high temperature region:

$$\frac{\epsilon - 3p}{T^4} = d_0 + \frac{d_1}{T^2} + \frac{d_2}{T^4} + \frac{d_3}{T^{n_3}} + \frac{d_4}{T^{n_4}} + \frac{d_5}{T^{n_5}}. \quad \text{(A1)}$$

This form does not have the right asymptotic behavior in the high temperature region, where we expect $(\epsilon - 3p)/T^4 \sim g^4(T) \sim 1/\ln^2(T/\Lambda_{QCD})$, but it works well in the temperature range of interest. Furthermore, it is flexible enough to match to the HRG result in the low temperature region. We match this Ansatz to the HRG model at temperature T_0 by requiring that the trace

TABLE III. The values of parameters for different fits of the trace anomaly.

	d_0	$d_1(\mathrm{GeV}^2)$	$d_2(\mathrm{GeV}^4)$	$d_3(\mathrm{GeV}^{n_3})$	$d_4(\mathrm{GeV}^{n_4})$	$d_5(\mathrm{GeV}^{n_5})$	n_3	n_4	n_5	T_0(MeV)
$s83s_{18}$	$5.688{\cdot}10^{-3}$	0.3104	$-6.217{\cdot}10^{-3}$	$-6.680{\cdot}10^{-32}$	$1.071{\cdot}10^{-32}$	–	41	42	–	166
$s87h_{04}$	$5.669{\cdot}10^{-2}$	0.2974	$-4.184{\cdot}10^{-3}$	$-5.146{\cdot}10^{-8}$	$1.420{\cdot}10^{-33}$	–	10	42	–	172
$s88h_{18}$	$4.509{\cdot}10^{-2}$	0.3082	$-5.136{\cdot}10^{-3}$	$-1.150{\cdot}10^{-10}$	$2.076{\cdot}10^{-32}$	$-3.021{\cdot}10^{-33}$	13	41	42	155
$s95p$	–	0.2660	$2.403{\cdot}10^{-3}$	$-2.809{\cdot}10^{-7}$	$6.073{\cdot}10^{-23}$	–	10	30	–	183.8

TABLE IV. The values of parameters for different fits of the HRG trace anomaly.

	$a_1(\mathrm{GeV}^{-m_1})$	$a_2(\mathrm{GeV}^{-m_2})$	$a_3(\mathrm{GeV}^{-m_3})$	$a_4(\mathrm{GeV}^{-m_4})$	m_1	m_2	m_3	m_4	T_{high}(MeV)
$s83s_{18}$	0.1850	$1.985{\cdot}10^4$	$1.278{\cdot}10^5$	$-1.669{\cdot}10^7$	0	5	7	10	170
$s87h_{04}$	4.654	-879	8081	$-7.039{\cdot}10^6$	1	3	4	10	190
$s88h_{18}$	0.1844	$2.043{\cdot}10^4$	$8.550{\cdot}10^5$	$-2.434{\cdot}10^7$	0	5	8	10	169
$s95p$	4.654	-879	8081	$-7.039{\cdot}10^6$	1	3	4	10	190

anomaly, and its first and second derivatives are continuous. This requirement provides constraints for three parameters, d_0, d_1, and d_2, and leaves the remaining seven, $d_3, d_4, d_5, n_3, n_4, n_5$, and T_0 to be fixed by minimizing a χ^2 fit to the data. Fitting the powers n_3–n_5 would be a highly non-linear problem, but we simplify the problem by requiring that the powers are integers, and using brute force: We make a fit with all the integer values $5 \le n_3 \le 40$, $n_3 < n_4 \le 41$, and $n_4 < n_5 \le 42$, and choose the values n_3, n_4, and n_5 which lead to the smallest χ^2. When the powers and T_0 are kept fixed, minimizing χ^2 requires only a simple matrix inversion. Thus to fix T_0 we are able to cast χ^2 as a function of only a single parameter, T_0. We require that $155 \le T_0/\mathrm{MeV} \le 190$, and search for the value of T_0 which minimizes χ^2.

To obtain the continuum limit in the lattice calculations of the trace anomaly, one has to perform interpolation in the temperature, and then perform continuum extrapolations (see e.g. [23]). This procedure can introduce additional uncertainties when providing parametrization of the lattice results. As mentioned in the main text, the lattice spacing (N_t) dependence of the lattice results on the trace anomaly is small in the case of the HISQ discretization scheme for $N_t \ge 8$. In fact, for $T > 230$ MeV and $T < 170$ MeV there is no statistically significant N_t dependence, so in these temperature ranges we can use the HISQ lattice results with $N_t = 8, 10$ and 12. In the peak region, $170 < T/\mathrm{MeV} < 230$, the $N_t = 8$ HISQ results are slightly higher than the $N_t = 10$ and $N_t = 12$ results, and therefore have been omitted from the fits. At temperatures above 800 MeV only lattice results with $N_t = 6$ and 4 are available [20, 21]. To take the larger discretization errors of the $N_t = 6$ and 4 results into account, we follow Ref. [21], scale them by factors 1.4 and 1.2, and include systematic errors of 40% and 20%, respectively. Contrary to the HISQ action results, we employ the continuum extrapolated stout action results [22, 23] for simplicity. The resulting parameters are shown in Table III. We find that only the parametrization $s88h_{18}$ requires the use of all six terms in Eq. A1. In the cases of $s83s_{18}$ and $s87h_{04}$ we are able to obtain equally good fits with only five terms, and thus set d_5 to zero by hand.

For the sake of completeness, we also parametrize the HRG part of the trace anomaly as

$$\frac{\epsilon - 3p}{T^4} = a_1 T^{m_1} + a_2 T^{m_2} + a_3 T^{m_3} + a_4 T^{m_4}. \quad \text{(A2)}$$

To carry out the fit we evaluate HRG trace anomaly in temperature interval $70 < T/\mathrm{MeV} < T_{\mathrm{high}}$, where T_{high} depends on the parametrization, with 1 MeV steps assuming that each point has equal "error". The limits have entirely utilitarian origin: in hydrodynamical applications the system decouples well above 70 MeV temperature and only a rough approximation of the EoS, $p = p(\epsilon)$, is needed at lower temperatures. On the other hand we expect to switch to the lattice parametrization below T_{high}, and the HRG EoS above that temperature is not needed either. We fix the powers in Eq. (A2) again using brute force. We require them to be integers, go through all the combinations $0 \le l_1 < l_2 < l_3 < l_4 \le 10$, fit the parameters a_1, a_2, a_3, a_4 to the HRG trace anomaly evaluated with 1 MeV intervals, and choose the values l_1, l_2, l_3 and l_4 which minimize the χ^2. We end up with parameters shown in Table IV. To obtain the EoS, one also needs the pressure at the lower limit of the integration (see Eq.(1)) $T_{\mathrm{low}} = 0.07$ GeV: $p(T_{\mathrm{low}})/T_{\mathrm{low}}^4 = 0.1661$. Our EoSs are available in a tabulated form at arXiv as ancillary files for this paper, and at Ref. [86]. These tables also include the option of a chemically frozen hadronic stage, and a list of resonances included in the hadronic stage with their properties and decay channels.

Appendix B: Predicting model output with Gaussian processes

Let us assume that we do not know exactly what the model's output y for a particular input parameter $\vec{x}$ is, but we know its most probable value $\mu(\vec{x})$. We postulate that the probability distribution for the output value

$P(y)$ is a normal distribution with mean $\mu(\vec{x})$ and so far unknown width σ. Thus the probability distribution for a set Y_a of N model outputs for observable a, corresponding to a set X of N points in the parameter space, is a multivariate normal distribution:

$$\mathcal{G} : X \to Y_a \sim \mathcal{N}(\boldsymbol{\mu}, \boldsymbol{C}) \tag{B1}$$

where $\boldsymbol{\mu} = \mu(X) = \{\mu(\vec{x}_1), \ldots, \mu(\vec{x}_N)\}$ is the mean of the distribution, and $\boldsymbol{C}$ is the covariance matrix defined by the covariance function $c(\vec{x}, \vec{x}')$:

$$\boldsymbol{C} = \mathcal{C}_{X,X} = \begin{pmatrix} c(\vec{x}_1, \vec{x}_1) & \ldots & c(\vec{x}_1, \vec{x}_N) \\ \vdots & \ddots & \vdots \\ c(\vec{x}_N, \vec{x}_1) & \ldots & c(\vec{x}_N, \vec{x}_N) \end{pmatrix}. \tag{B2}$$

As we are only interested in interpolating within the training data, we may set $\mu(X) \equiv 0$, and construct the covariance function $c(\vec{x}, \vec{x}')$ in such a way that the probability distribution is narrow at the training points nevertheless. This way we minimize our *a priori* assumptions about the model behavior in regions of parameter space not covered by the training data[11]. Our chosen covariance function is a radial-basis function (RBF) with a noise term

$$c(\vec{x}, \vec{x}') = \theta_0 \exp\left(-\sum_{i=1}^{n} \frac{(x_i - x_i')^2}{2\theta_i^2} \right) + \theta_{\text{noise}} \delta_{\vec{x}\vec{x}'} \tag{B3}$$

The hyperparameters $\vec{\theta} = (\theta_0, \theta_1, \ldots, \theta_n, \theta_{\text{noise}})$, where n is the dimension of the input parameter space, are not known a priori and must be estimated from training data, consisting of simulation output U computed at training points T, by maximizing the log-likelihood (see Chapter 5 of [64])

$$\begin{aligned} \log P(U|T, \vec{\theta}) = &-\frac{1}{2} U^T \boldsymbol{C}^{-1}(T, \vec{\theta}) U \\ &-\frac{1}{2} \log |\boldsymbol{C}(T, \vec{\theta})| \\ &-\frac{N}{2} \log(2\pi). \end{aligned} \tag{B4}$$

Emulator prediction for the model output y_0 at a point $\vec{x_0}$ can then be determined by writing a joint probability distribution for the output at various points in parameter space:

$$\begin{pmatrix} y_0 \\ U \end{pmatrix} \sim \mathcal{N}\left(\begin{pmatrix} 0 \\ \vec{0} \end{pmatrix}, \begin{pmatrix} \mathcal{C}_{0,0} & \mathcal{C}_{0,T} \\ \mathcal{C}_{T,0} & \mathcal{C}_{T,T} \end{pmatrix} \right) \tag{B5}$$

from which we can derive the conditional predictive mean $y^{\text{GP}}(\vec{x_0})$ and associated variance $\sigma^{\text{GP}}(\vec{x_0})^2$ as (see e.g. Appendix A.2 of [64])

$$\begin{aligned} y^{\text{GP}}(\vec{x_0}) &= \mathcal{C}_{0,T} \mathcal{C}_{T,T}^{-1} U, \\ \sigma^{\text{GP}}(\vec{x_0})^2 &= \mathcal{C}_{0,0} - \mathcal{C}_{0,T} \mathcal{C}_{T,T}^{-1} \mathcal{C}_{T,0}. \end{aligned} \tag{B6}$$

Note that we use the training data U twice: First in Eq. (B4) to determine the hyperparameters $\vec{\theta}$ of the covariance function $c(\vec{x}, \vec{x}')$ and then in Eq. (B6) as a condition for the GP prediction.

Appendix C: Principal component analysis

We reduce the number of Gaussian processes needed for model emulation with principal component analysis (PCA), which transforms the data in the directions of maximal variance.

We represent the model output with a N x m matrix Y, where N is the number of simulation points and m the number of observables. In preparation for the PCA, the data columns are normalized with the corresponding experimental values to obtain dimensionless quantities, and centered by subtracting the mean of each observable from the elements of each column; we denote this scaled and shifted data matrix by $\hat{Y}$.

We then want to find an eigenvalue decomposition of the covariance matrix $\hat{Y}^T \hat{Y}$:

$$\hat{Y}^T \hat{Y} = V \Lambda V^T, \tag{C1}$$

where Λ is the diagonal matrix containing the eigenvalues $\lambda_1, ..., \lambda_m$ and V is an orthogonal matrix containing the eigenvectors of the covariance matrix.

The eigenvalue decomposition is found by factorizing $\hat{Y}$ via the singular value decomposition:

$$\hat{Y} = U S V^T, \tag{C2}$$

where S is a diagonal matrix containing the singular values (square roots of the eigenvalues of $\hat{Y}^T \hat{Y}$) and V contains the right-singular vectors of $\hat{Y}$ (eigenvectors of $\hat{Y}^T \hat{Y}$); these are the principal components (PCs). Matrix U contains the left-singular vectors of $\hat{Y}$, which are eigenvectors of $\hat{Y} \hat{Y}^T$.

The eigenvalues are proportional to the total variance of the data. Since $\lambda_1 \geq \lambda_2 \geq ... \geq \lambda_m$, the fraction of the total variance explained by the kth principal component, $\lambda_k / (\sum_{j=1}^{m} \lambda_j)$, becomes negligible starting from some index $k < m$. This allows us to define a lower-rank approximation of the original transformed data matrix $Z = \hat{Y} V$ as $Z_k = \hat{Y} V_k$, where V_k contains the first k columns of V.

The transformation of a vector $\vec{y}$ from the space of observables to a vector $\vec{z}$ in the reduced-dimension principal component space is thus defined as

$$\vec{z} = \vec{y} V_k, \tag{C3}$$

[11] Note that we use Gaussian process to estimate the model output of the principal components, not the actual observables, see Appendix C.

while for matrices (such as the covariance matrix in the likelihood function (5)) the transformation is

$$\Sigma_z = V_k^T \, \Sigma_y \, V_k. \tag{C4}$$

To compare an emulator prediction $\vec{z}^{\,\mathrm{GP}}$ against physical observables, we use the inverse transformation

$$\vec{y}^{\,\mathrm{GP}} = \vec{z}^{\,\mathrm{GP}} \, V_k^T. \tag{C5}$$

Appendix D: Correlations between the model parameters

Figure 12 provides a more detailed view of the 8-dimensional posterior probability distribution, using the analysis results for the $s88h_{18}$ and $s95p$ EoSs as an example. The diagonal panels show the marginalized one-dimensional distributions for each parameter, which were summarized in Figs. 3–4 in Section VI. The off-diagonal panels illustrate the correlations between each parameter pair (X, Y). The correlation strength is quantified with the Spearman rank correlation coefficient [87], which is the Pearson correlation coefficient between the rank values r_X and r_Y:

$$\rho = \frac{C(r_X, r_Y)}{\sigma(r_X)\sigma(r_Y)}, \tag{D1}$$

where C refers to covariance and σ to standard deviation. This relaxes the assumption of a linear relationship, present in the Pearson correlation coefficient, and is instead a measure of the monotonic relationship between the two parameters.

[1] M. Luzum and P. Romatschke, Phys. Rev. C **78**, 034915 (2008) Erratum: [Phys. Rev. C **79**, 039903 (2009)] [arXiv:0804.4015 [nucl-th]].
[2] P. Bozek, Phys. Rev. C **81**, 034909 (2010) [arXiv:0911.2397 [nucl-th]].
[3] H. Song, S. A. Bass and U. Heinz, Phys. Rev. C **83**, 054912 (2011) Erratum: [Phys. Rev. C **87**, 019902 (2013)] [arXiv:1103.2380 [nucl-th]].
[4] S. Ryu, J.-F. Paquet, C. Shen, G. S. Denicol, B. Schenke, S. Jeon and C. Gale, Phys. Rev. Lett. **115**, 132301 (2015) [arXiv:1502.01675 [nucl-th]].
[5] I. A. Karpenko, P. Huovinen, H. Petersen and M. Bleicher, Phys. Rev. C **91**, 064901 (2015) [arXiv:1502.01978 [nucl-th]].
[6] U. Heinz and R. Snellings, Ann. Rev. Nucl. Part. Sci. **63**, 123 (2013) [arXiv:1301.2826 [nucl-th]].
[7] C. Gale, S. Jeon and B. Schenke, Int. J. Mod. Phys. A **28**, 1340011 (2013) [arXiv:1301.5893 [nucl-th]].
[8] P. Huovinen, Int. J. Mod. Phys. E **22**, 1330029 (2013) [arXiv:1311.1849 [nucl-th]].
[9] C. Shen, [arXiv:2001.11858 [nucl-th]].
[10] J. E. Bernhard, J. S. Moreland, S. A. Bass, J. Liu and U. Heinz, Phys. Rev. C **94**, 024907 (2016) [arXiv:1605.03954 [nucl-th]].
[11] S. A. Bass, J. E. Bernhard and J. S. Moreland, Nucl. Phys. A **967**, 67 (2017) [arXiv:1704.07671 [nucl-th]].
[12] J. E. Bernhard, J. S. Moreland and S. A. Bass, Nature Phys. **15**, no. 11, 1113 (2019).
[13] H. Niemi, K. J. Eskola and R. Paatelainen, Phys. Rev. C **93**, 024907 (2016) [arXiv:1505.02677 [hep-ph]].
[14] S. Pratt, E. Sangaline, P. Sorensen and H. Wang, Phys. Rev. Lett. **114**, 202301 (2015) [arXiv:1501.04042 [nucl-th]].
[15] J. S. Moreland and R. A. Soltz, Phys. Rev. C **93**, 044913 (2016) [arXiv:1512.02189 [nucl-th]].
[16] P. Alba, V. Mantovani Sarti, J. Noronha, J. Noronha-Hostler, P. Parotto, I. Portillo Vazquez and C. Ratti, Phys. Rev. C **98**, 034909 (2018) [arXiv:1711.05207 [nucl-th]].
[17] P. Huovinen and P. Petreczky, Nucl. Phys. A **837**, 26 (2010) [arXiv:0912.2541 [hep-ph]].
[18] A. Bazavov *et al.*, Phys. Rev. D **80**, 014504 (2009) [arXiv:0903.4379 [hep-lat]].
[19] B. Schenke, C. Shen and P. Tribedy, Phys. Rev. C **99**, 044908 (2019) [arXiv:1901.04378 [nucl-th]].
[20] A. Bazavov *et al.* [HotQCD Collaboration], Phys. Rev. D **90**, 094503 (2014) [arXiv:1407.6387 [hep-lat]].
[21] A. Bazavov, P. Petreczky and J. H. Weber, Phys. Rev. D **97**, 014510 (2018) [arXiv:1710.05024 [hep-lat]].
[22] S. Borsanyi, G. Endrodi, Z. Fodor, A. Jakovac, S. D. Katz, S. Krieg, C. Ratti and K. K. Szabo, JHEP **1011**, 077 (2010) [arXiv:1007.2580 [hep-lat]].
[23] S. Borsanyi, Z. Fodor, C. Hoelbling, S. D. Katz, S. Krieg and K. K. Szabo, Phys. Lett. B **730**, 99 (2014) [arXiv:1309.5258 [hep-lat]].
[24] H. Niemi, K. J. Eskola, R. Paatelainen and K. Tuominen, Phys. Rev. C **93**, 014912 (2016) [arXiv:1511.04296 [hep-ph]].
[25] S. Adler *et al.* [PHENIX], Phys. Rev. C **71**, 034908 (2005). [arXiv:nucl-ex/0409015 [nucl-ex]].
[26] S. S. Adler *et al.* [PHENIX Collaboration], Phys. Rev. C **69**, 034909 (2004) [nucl-ex/0307022].
[27] J. Adams *et al.* [STAR Collaboration], Phys. Rev. C **72**, 014904 (2005) [nucl-ex/0409033].
[28] K. Aamodt *et al.* [ALICE Collaboration], Phys. Rev. Lett. **106**, 032301 (2011) [arXiv:1012.1657 [nucl-ex]].
[29] B. Abelev *et al.* [ALICE Collaboration], Phys. Rev. C **88**, 044910 (2013) [arXiv:1303.0737 [hep-ex]].
[30] J. Adam *et al.* [ALICE Collaboration], Phys. Rev. Lett. **116**, 132302 (2016) [arXiv:1602.01119 [nucl-ex]].
[31] J. Adam *et al.* [ALICE Collaboration], Phys. Rev. Lett. **116**, 222302 (2016) [arXiv:1512.06104 [nucl-ex]].
[32] G. Boyd, J. Engels, F. Karsch, E. Laermann, C. Legeland, M. Lutgemeier and B. Petersson, Nucl. Phys. B **469**, 419 (1996) [arXiv:hep-lat/9602007].
[33] C. Anderlik *et al.*, Phys. Rev. C **59**, 3309 (1999) [arXiv:nucl-th/9806004].
[34] P. Huovinen and P. Petreczky, PoS Confinement **2018**, 145 (2018) [arXiv:1811.09330 [nucl-th]].
[35] S. A. Bass *et al.*, Prog. Part. Nucl. Phys. **41**, 255 (1998) [Prog. Part. Nucl. Phys. **41**, 225 (1998)] [nucl-th/9803035]; M. Bleicher *et al.*, J. Phys. G **25**, 1859

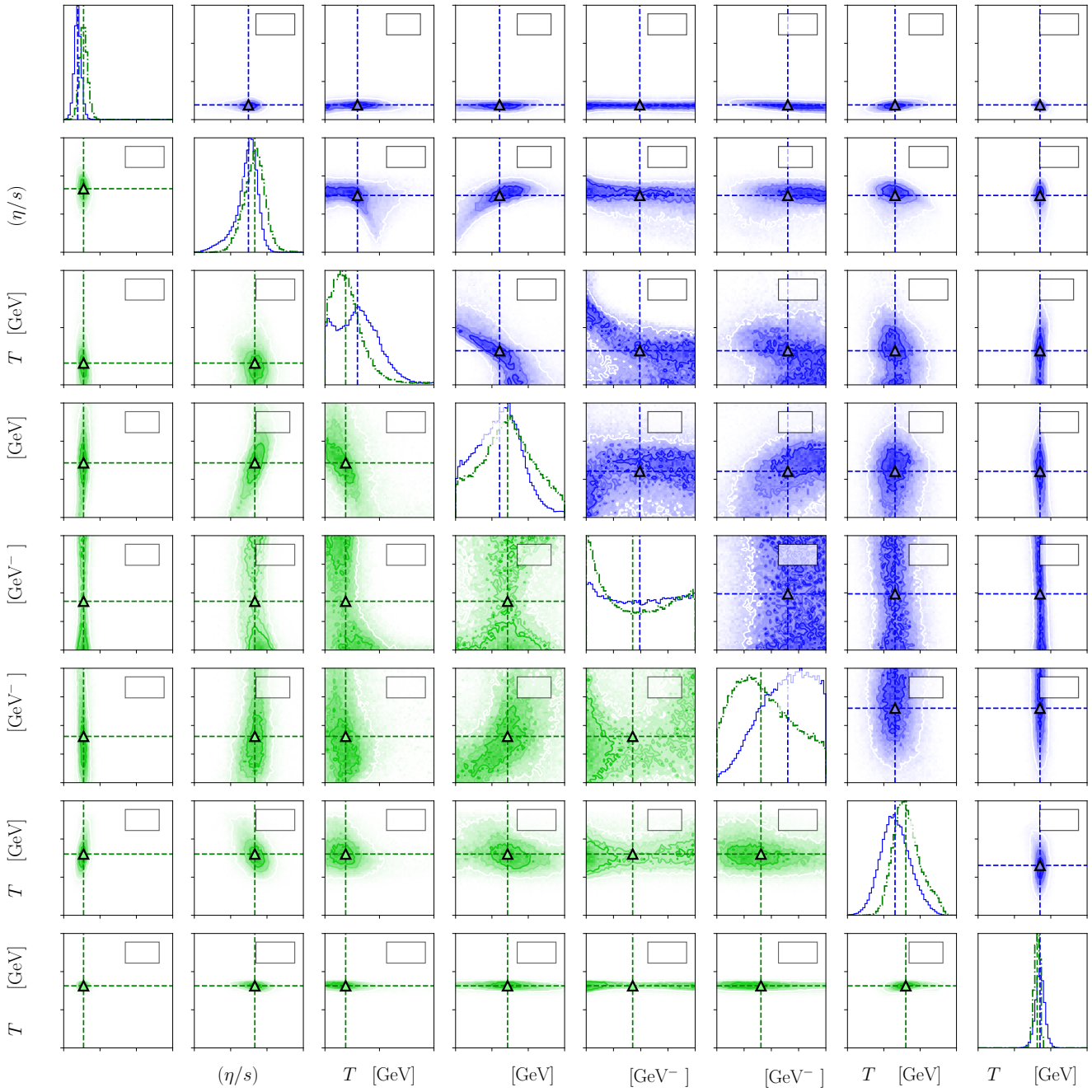

FIG. 12. Posterior probability distribution for the $s88h_{18}$ (lower triangle, green color) and $s95p$ (upper triangle, blue color) EoSs. Diagonal panels: Marginalized 1-D distributions for each parameter. Solid blue line: $s95p$. Dash-dotted green line: $s88h_{18}$. Dashed lines and numbers indicate median value, with upper number corresponding to $s95p$ and lower number to $s88h_{18}$. Off-diagonal panels: 2-D projections of the posterior distributions. Dashed lines indicate median values for each parameter, while the framed numbers refer to Spearman rank correlation coefficients for each parameter pair.

(1999) [hep-ph/9909407].
[36] J. Weil *et al.*, Phys. Rev. C **94**, 054905 (2016) [arXiv:1606.06642 [nucl-th]].
[37] S. Eidelman *et al.* [Particle Data Group], Phys. Lett. B **592**, 1 (2004).
[38] R. Venugopalan and M. Prakash, Nucl. Phys. A **546**, 718-760 (1992).
[39] W. Broniowski, F. Giacosa and V. Begun, Phys. Rev. C **92**, 034905 (2015) [arXiv:1506.01260 [nucl-th]].
[40] M. Tanabashi *et al.* [Particle Data Group], Phys. Rev. D **98**, 030001 (2018).
[41] Non-strange meson summary tables: `http://pdg.lbl.gov/2018/tables/rpp2018-tab-mesons-light.pdf`; Strange mesons: `http://pdg.lbl.gov/2018/tables/`

rpp2018-tab-mesons-strange.pdf;
p, n, and N resonances: http://pdg.lbl.gov/2018/tables/rpp2018-tab-baryons-N.pdf;
Lambda, Lambda resonances: http://pdg.lbl.gov/2018/tables/rpp2018-tab-baryons-Lambda.pdf;
Sigma, Sigma resonances: http://pdg.lbl.gov/2018/tables/rpp2018-tab-baryons-Sigma.pdf;
Xi, Xi resonances: http://pdg.lbl.gov/2018/tables/rpp2018-tab-baryons-Xi.pdf;
Omega, Omega resonances: http://pdg.lbl.gov/2018/tables/rpp2018-tab-baryons-Omega.pdf.

[42] A. Majumder and B. Muller, Phys. Rev. Lett. **105**, 252002 (2010) [arXiv:1008.1747 [hep-ph]].

[43] A. Bazavov *et al.*, Phys. Rev. Lett. **113**, 072001 (2014) [arXiv:1404.6511 [hep-lat]].

[44] C. Fernández-Ramírez, P. M. Lo and P. Petreczky, Phys. Rev. C **98**, 044910 (2018) [arXiv:1806.02177 [hep-ph]].

[45] P. Alba, V. M. Sarti, J. Noronha-Hostler, P. Parotto, I. Portillo-Vazquez, C. Ratti and J. Stafford, Phys. Rev. C **101**, 054905 (2020) [arXiv:2002.12395 [hep-ph]].

[46] H. Niemi, G. S. Denicol, P. Huovinen, E. Molnar and D. H. Rischke, Phys. Rev. C **86**, 014909 (2012) [arXiv:1203.2452 [nucl-th]].

[47] H. Niemi, G. S. Denicol, P. Huovinen, E. Molnar and D. H. Rischke, Phys. Rev. Lett. **106**, 212302 (2011) [arXiv:1101.2442 [nucl-th]].

[48] K. J. Eskola, H. Niemi, R. Paatelainen and K. Tuominen, Phys. Rev. C **97**,, 034911 (2018) [arXiv:1711.09803 [hep-ph]].

[49] E. Molnar, H. Niemi and D. H. Rischke, Eur. Phys. J. C **65**, 615 (2010) [arXiv:0907.2583 [nucl-th]].

[50] W. Israel and J. M. Stewart, Annals Phys. **118**, 341 (1979).

[51] G. S. Denicol, H. Niemi, E. Molnar and D. H. Rischke, Phys. Rev. D **85**, 114047 (2012) Erratum: [Phys. Rev. D **91**, 039902 (2015)] [arXiv:1202.4551 [nucl-th]].

[52] E. Molnar, H. Niemi, G. S. Denicol and D. H. Rischke, Phys. Rev. D **89**, 074010 (2014) [arXiv:1308.0785 [nucl-th]].

[53] P. Huovinen, Eur. Phys. J. A **37**, 121 (2008) [arXiv:0710.4379 [nucl-th]].

[54] T. Hirano and K. Tsuda, Phys. Rev. C **66**, 054905 (2002) [arXiv:nucl-th/0205043 [nucl-th]].

[55] K. Paech and S. Pratt, Phys. Rev. C **74**, 014901 (2006) [arXiv:nucl-th/0604008 [nucl-th]].

[56] K. Dusling and T. Schäfer, Phys. Rev. C **85**, 044909 (2012) [arXiv:1109.5181 [hep-ph]].

[57] J. B. Rose, J. Torres-Rincon, A. Schäfer, D. Oliinychenko and H. Petersen, Phys. Rev. C **97**, 055204 (2018) [arXiv:1709.03826 [nucl-th]].

[58] H. Bebie, P. Gerber, J. Goity and H. Leutwyler, Nucl. Phys. B **378**, 95-128 (1992).

[59] K. J. Eskola, K. Kajantie, P. V. Ruuskanen and K. Tuominen, Nucl. Phys. B **570**, 379 (2000) [hep-ph/9909456].

[60] R. Paatelainen, K. J. Eskola, H. Holopainen and K. Tuominen, Phys. Rev. C **87**, 044904 (2013) [arXiv:1211.0461 [hep-ph]].

[61] R. Paatelainen, K. J. Eskola, H. Niemi and K. Tuominen, Phys. Lett. B **731**, 126 (2014) [arXiv:1310.3105 [hep-ph]].

[62] W. D. Vousden, W. M. Farr and I. Mandel, Mon. Not. Roy. Astron. Soc. **455**, 1919 (2016) [arXiv:1501.05823 [astro-ph.IM]].

[63] D. Foreman-Mackey, D. W. Hogg, D. Lang and J. Goodman, Publ. Astron. Soc. Pac. **125**, 306 (2013) [arXiv:1202.3665 [astro-ph.IM]].

[64] C. E. Rasmussen and C. K. I. Williams, "Gaussian Processes for Machine Learning", MIT Press, Cambridge, MA, USA, 2006.

[65] F. Pedregosa *et al.*, J. Machine Learning Res. **12**, 2825 (2011) [arXiv:1201.0490 [cs.LG]].

[66] "pyDOE: Design of Experiments for Python", https://pythonhosted.org/pyDOE/randomized.html.

[67] A. Andronic, P. Braun-Munzinger, K. Redlich and J. Stachel, Nature **561**, no.7723, 321-330 (2018) [arXiv:1710.09425 [nucl-th]].

[68] V. Mykhaylova, M. Bluhm, K. Redlich and C. Sasaki, Phys. Rev. D **100**, 034002 (2019) [arXiv:1906.01697 [hep-ph]].

[69] M. Prakash, M. Prakash, R. Venugopalan and G. Welke, Phys. Rept. **227**, 321 (1993).

[70] L. P. Csernai, J. I. Kapusta and L. D. McLerran, Phys. Rev. Lett. **97**, 152303 (2006) [nucl-th/0604032].

[71] A. Wiranata, M. Prakash, P. Huovinen, V. Koch and X. Wang, J. Phys. Conf. Ser. **535**, 012017 (2014).

[72] E. V. Shuryak and I. Zahed, Phys. Rev. C **70**, 021901 (2004) [arXiv:hep-ph/0307267 [hep-ph]].

[73] I. Wetzorke, F. Karsch, E. Laermann, P. Petreczky and S. Stickan, Nucl. Phys. B Proc. Suppl. **106**, 510-512 (2002) [arXiv:hep-lat/0110132 [hep-lat]].

[74] F. Karsch, S. Datta, E. Laermann, P. Petreczky, S. Stickan and I. Wetzorke, Nucl. Phys. A **715**, 701-704 (2003) [arXiv:hep-ph/0209028 [hep-ph]].

[75] M. Asakawa, T. Hatsuda and Y. Nakahara, Nucl. Phys. B Proc. Suppl. **119**, 481-483 (2003) [arXiv:hep-lat/0208059 [hep-lat]].

[76] S. Mukherjee, P. Petreczky and S. Sharma, Phys. Rev. D **93**, 014502 (2016) [arXiv:1509.08887 [hep-lat]].

[77] A. Bazavov *et al.* [TUMQCD], Phys. Rev. D **98**, 054511 (2018) [arXiv:1804.10600 [hep-lat]].

[78] A. Bazavov, H. T. Ding, P. Hegde, F. Karsch, C. Miao, S. Mukherjee, P. Petreczky, C. Schmidt and A. Velytsky, Phys. Rev. D **88**, 094021 (2013) [arXiv:1309.2317 [hep-lat]].

[79] R. Bellwied, S. Borsanyi, Z. Fodor, S. Katz, A. Pasztor, C. Ratti and K. Szabo, Phys. Rev. D **92**, 114505 (2015) [arXiv:1507.04627 [hep-lat]].

[80] H. T. Ding, S. Mukherjee, H. Ohno, P. Petreczky and H. P. Schadler, Phys. Rev. D **92**, 074043 (2015) [arXiv:1507.06637 [hep-lat]].

[81] P. Huovinen, P. M. Lo, M. Marczenko, K. Morita, K. Redlich and C. Sasaki, Phys. Lett. B **769**, 509 (2017) [arXiv:1608.06817 [hep-ph]].

[82] P. Huovinen, Nucl. Phys. A **761**, 296 (2005) [nucl-th/0505036].

[83] J. Noronha-Hostler, B. Betz, J. Noronha and M. Gyulassy, Phys. Rev. Lett. **116**, 252301 (2016) [arXiv:1602.03788 [nucl-th]].

[84] C. Andres, N. Armesto, H. Niemi, R. Paatelainen and C. A. Salgado, Phys. Lett. B **803**, 135318 (2020) [arXiv:1902.03231 [hep-ph]].

[85] D. Zigic, B. Ilic, M. Djordjevic and M. Djordjevic, arXiv:1908.11866 [hep-ph].

[86] https://osf.io/thazn/wiki/home doi:10.17605/osf.io/thazn

[87] C. Spearman, The American Journal of Psychology **15**, 72 (1904).

acceptace letter of item [12]

Placeholder for the acceptance letter from PRC.

Rapid Communications

Shape of the quark gluon plasma droplet reflected in the high-$p_\perp$ data

Magdalena Djordjevic,[1,*] Stefan Stojku,[1] Marko Djordjevic,[2] and Pasi Huovinen[1]
[1]*Institute of Physics Belgrade, University of Belgrade, Serbia*
[2]*Faculty of Biology, University of Belgrade, Serbia*

(Received 19 April 2019; revised manuscript received 1 August 2019; published 12 September 2019)

We show, through analytic arguments, numerical calculations, and comparison with experimental data, that the ratio of the high-$p_\perp$ observables $v_2/(1-R_{\rm AA})$ reaches a well-defined saturation value at high $p_\perp$, and that this ratio depends only on the spatial anisotropy of the quark gluon plasma (QGP) formed in ultrarelativistic heavy-ion collisions. With expected future reduction of experimental errors, the anisotropy extracted from experimental data will further constrain the calculations of initial particle production in heavy-ion collisions and thus test our understanding of QGP physics.

DOI: 10.1103/PhysRevC.100.031901

Introduction. The major goal of relativistic heavy-ion physics [1–4] is understanding the properties of the new form of matter called quark gluon plasma (QGP) [5,6], which, in turn, allows the understanding of properties of QCD matter at its most basic level. Energy loss of rare high-momentum partons traversing this matter is known to be an excellent probe of its properties. Different observables such as the nuclear modification factor $R_{\rm AA}$ and the elliptic flow parameter v_2 of high-$p_\perp$ particles, probe the medium in different manners, but they all depend not only on the properties of the medium, but also on the density, size, and shape of the QGP droplet created in a heavy-ion collision. Thus drawing firm conclusions of the material properties of QGP is very time consuming and requires simultaneous description of several observables. It would therefore be very useful if there were an observable, or combination of observables, which would be sensitive to only one or just a few of all the parameters describing the system.

For high-$p_\perp$ particles, spatial asymmetry leads to different paths, and consequently to different energy losses. Consequently, v_2 (angular differential suppression) carries information on both the spatial anisotropy and material properties that affect energy loss along a given path. On the other hand, $R_{\rm AA}$ (angular average suppression) carries information only on material properties affecting the energy loss [7–10], so one might expect to extract information on the system anisotropy by taking a ratio of expressions which depend on v_2 and $R_{\rm AA}$. Of course, it is far from trivial whether such intuitive expectations hold, and what combination of v_2 and $R_{\rm AA}$ one should take to extract the spatial anisotropy. To address this, we here use both analytical and numerical analysis to show that the ratio of v_2 and $1-R_{\rm AA}$ at high $p_\perp$ depends only on the spatial anisotropy of the system. This approach provides a complementary method for evaluating the anisotropy of the QGP fireball, and advances the applicability of high-$p_\perp$ data to a new level as, up to now, these data were mainly used to study the jet-medium interactions, rather than inferring bulk QGP parameters.

Anisotropy and high-$p_\perp$ observables. In [10,11], we showed that at very large values of transverse momentum $p_\perp$, the fractional energy loss $\Delta E/E$ (which is very complex, both analytically and numerically, due to inclusion of multiple effects, see *Numerical results* for more details) shows asymptotic scaling behavior

$$\Delta E/E \approx \chi(p_\perp)\langle T\rangle^a\langle L\rangle^b, \tag{1}$$

where $\langle L\rangle$ is the average path length traversed by the jet, $\langle T\rangle$ is the average temperature along the path of the jet, χ is a proportionality factor (which depends on initial jet $p_\perp$), and a and b are proportionality factors which determine the temperature and path-length dependence of the energy loss. Based on Refs. [12–15], we might expect values like $a=3$ and $b=1$ or 2, but a fit to a full-fledged calculation yields values $a\approx 1.2$ and $b\approx 1.4$ [11,16]. Thus the temperature dependence of the energy loss is close to linear, while the length dependence is between linear and quadratic. To evaluate the path length we follow Ref. [17]:

$$L(x,y,\phi)=\frac{\int_0^\infty d\lambda\,\lambda\,\rho(x+\lambda\cos(\phi),y+\lambda\sin(\phi))}{\int_0^\infty d\lambda\,\rho(x+\lambda\cos(\phi),y+\lambda\sin(\phi))}, \tag{2}$$

which gives the path length of a jet produced at point (x,y) heading to direction ϕ, and where $\rho(x,y)$ is the initial density distribution of the QGP droplet. To evaluate the average path length we take average over all directions and production points.

If $\Delta E/E$ is small (i.e., for high $p_\perp$ and in peripheral collisions), we obtain [7,10,11]

$$R_{\rm AA}\approx 1-\xi\langle T\rangle^a\langle L\rangle^b, \tag{3}$$

*magda@ipb.ac.rs

where $\xi = (n-2)\chi/2$, and n is the steepness of a power-law fit to the transverse momentum distribution, $dN/dp_\perp \propto 1/{p_\perp}^n$. Thus $1 - R_{\rm AA}$ is proportional to the average size and temperature of the medium. To evaluate the anisotropy we define the average path lengths in the in-plane and out-of-plane directions,

$$\langle L_{\rm in}\rangle = \frac{1}{\Delta\phi}\int_{-\Delta\phi/2}^{\Delta\phi/2} d\phi\,\langle L(\phi)\rangle,$$
$$\langle L_{\rm out}\rangle = \frac{1}{\Delta\phi}\int_{\pi/2-\Delta\phi/2}^{\pi/2+\Delta\phi/2} d\phi\,\langle L(\phi)\rangle, \tag{4}$$

where $\Delta\phi = \pi/6$ [18] is the acceptance angle with respect to the event plane (in-plane) or orthogonal to it (out-of-plane), and $\langle L(\phi)\rangle$ the average path length in the ϕ direction. Note that the obtained calculations are robust with respect to the precise value of the small angle $\pm\Delta\phi/2$, but we still keep a small cone ($\pm\pi/12$) for $R_{\rm AA}^{\rm in}$ and $R_{\rm AA}^{\rm out}$ calculations, to have the same numerical setup as in our Ref. [10]. Now we can write $\langle L\rangle = (\langle L_{\rm out}\rangle + \langle L_{\rm in}\rangle)/2$ and $\Delta L = (\langle L_{\rm out}\rangle - \langle L_{\rm in}\rangle)/2$. Similarly, the average temperature along the path length can be split to average temperatures along paths in in- and out-of-plane directions, $\langle T_{\rm in}\rangle = \langle T\rangle + \Delta T$ and $\langle T_{\rm out}\rangle = \langle T\rangle - \Delta T$. When applied to an approximate way to calculate v_2 of high-$p_\perp$ particles [19], we obtain[1]

$$v_2 \approx \frac{1}{2}\frac{R_{\rm AA}^{\rm in} - R_{\rm AA}^{\rm out}}{R_{\rm AA}^{\rm in} + R_{\rm AA}^{\rm out}} \approx \frac{\xi\langle T_{\rm out}\rangle^a\langle L_{\rm out}\rangle^b - \xi\langle T_{\rm in}\rangle^a\langle L_{\rm in}\rangle^b}{4}$$
$$\approx \xi\langle T\rangle^a\langle L\rangle^b\left(\frac{b}{2}\frac{\Delta L}{\langle L\rangle} - \frac{a}{2}\frac{\Delta T}{\langle T\rangle}\right), \tag{5}$$

where we have assumed that $\xi\langle T\rangle^a\langle L\rangle^b \ll 1$, and that $\Delta L/\langle L\rangle$ and $\Delta T/\langle T\rangle$ are small as well.

By combining Eqs. (3) and (5), we obtain

$$\frac{v_2}{1-R_{\rm AA}} \approx \left(\frac{b}{2}\frac{\Delta L}{\langle L\rangle} - \frac{a}{2}\frac{\Delta T}{\langle T\rangle}\right). \tag{6}$$

This ratio carries information on the anisotropy of the system, but through both spatial ($\Delta L/\langle L\rangle$) and temperature ($\Delta T/\langle T\rangle$) variables. From Eq. (6), we see the usefulness of the (approximate) analytical derivations, since the term $(1 - R_{\rm AA})$ in the denominator could hardly have been deduced intuitively or pinpointed by numerical trial and error. Figure 1 shows a linear dependence $\Delta L/\langle L\rangle \approx c\Delta T/\langle T\rangle$, where $c \approx 4.3$, with the temperature evolution given by one-dimensional (1D) Bjorken expansion, as sufficient to describe the early evolution of the system. Equation (6) can thus be simplified to

$$\frac{v_2}{1-R_{\rm AA}} \approx \frac{1}{2}\left(b - \frac{a}{c}\right)\frac{\langle L_{\rm out}\rangle - \langle L_{\rm in}\rangle}{\langle L_{\rm out}\rangle + \langle L_{\rm in}\rangle} \approx 0.57\varsigma,$$
$$\text{where}\quad \varsigma = \frac{\langle L_{\rm out}\rangle - \langle L_{\rm in}\rangle}{\langle L_{\rm out}\rangle + \langle L_{\rm in}\rangle}\quad\text{and}\quad \frac{1}{2}\left(b - \frac{a}{c}\right) \approx 0.57, \tag{7}$$

[1]Note that the first approximate equality in Eq. (5) can be shown to be exact if the higher harmonics v_4, v_6, etc., are zero, and the opening angle where $R_{\rm AA}^{\rm in}$ and $R_{\rm AA}^{\rm out}$ are evaluated is zero [cf. definitions of $\langle L_{\rm out}\rangle$ and $\langle L_{\rm in}\rangle$, Eq. (4)].

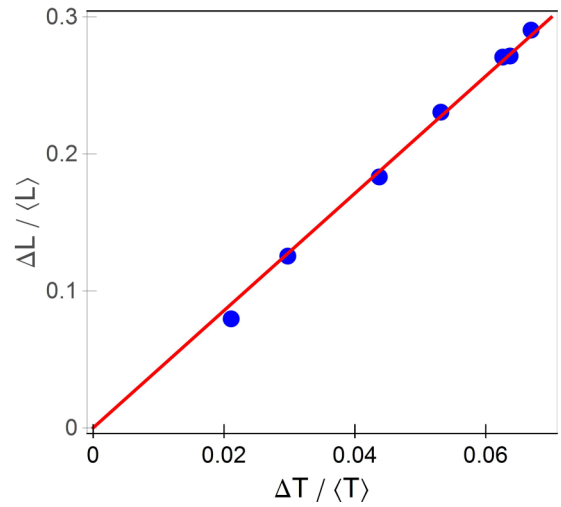

FIG. 1. $\Delta T/\langle T\rangle$ vs $\Delta L/\langle L\rangle$ in Pb+Pb collisions at $\sqrt{s_{NN}} = 5.02$ TeV collision energy at various centralities [7,10]. The more peripheral the collision, the larger the values. The red solid line depicts linear fit to the values.

when $a \approx 1.2$ and $b \approx 1.4$. Consequently, the asymptotic behavior of observables $R_{\rm AA}$ and v_2 is such that at high $p_\perp$, their ratio is dictated solely by the geometry of the fireball. Therefore, the anisotropy parameter ς can be extracted from the high-$p_\perp$ experimental data.

Regarding the parametrization used to derive Eq. (7) (constants a, b, and c), we note that a and b are well established within our dynamical energy-loss formalism and follow from $R_{\rm AA}$ predictions that are extensively tested on experimental data [11,16] and do not depend on the details of the medium evolution. Regarding c, it may (to some extent) depend on the type of implemented medium evolution, but this will not affect the obtained scaling, only (to some extent) the overall prefactor in Eq. (7).

Numerical results. To assess the applicability of the analytically derived scaling in Eq. (7), we calculate $v_2/(1 - R_{\rm AA})$ using our full-fledged numerical procedure for calculating the fractional energy loss. This procedure is based on our state-of-the-art dynamical energy-loss formalism [20,21], which has several unique features in the description of high-$p_\perp$ parton medium interactions: (i) The formalism takes into account a *finite-size, finite-temperature* QCD medium consisting of *dynamical* (that is, moving) partons, contrary to the widely used static scattering approximation and/or medium models with vacuum-like propagators (e.g., [12–15]). (ii) The calculations are based on the finite-temperature generalized hard-thermal-loop approach [22], in which the infrared divergences are naturally regulated [20,21,23]. (iii) Both radiative [20] and collisional [21] energy losses are calculated under *the same* theoretical framework, applicable to both light and heavy flavor. (iv) The formalism is generalized to the case of finite magnetic [24] mass and running coupling [25] and towards removing the widely used soft-gluon approximation [26]. The formalism was further embedded into our recently developed DREENA-B framework [10], which integrates initial momentum distribution of leading partons [27], energy

loss with path-length [17] and multigluon [28] fluctuations and fragmentation functions [29], in order to generate the final medium modified distribution of high-$p_\perp$ hadrons. The framework was recently used to obtain joint $R_{\rm AA}$ and v_2 predictions for 5.02 TeV Pb+Pb collisions at the LHC [10], showing a good agreement with the experimental data.

We have previously shown [30] that all the model ingredients noted above have an effect on the high-$p_\perp$ data, and thus should be included to accurately explain it. In that respect, our model is different from many other approaches, which use a sophisticated medium evolution, but an (over)simplified energy-loss model. Our previous work, however, shows that for explaining the high-$p_\perp$ data, an accurate description of high-$p_\perp$ parton-medium interactions is at least as important as an advanced medium evolution model. For example, the dynamical energy-loss formalism, embedded in 1D Bjorken expansion, explains well the v_2 puzzle [10], i.e., the inability of other models to jointly explain $R_{\rm AA}$ and v_2 measurements. To what extent the dynamical energy-loss predictions will change when embedded in full three-dimensional evolution is at the time of this writing still unknown, but our previous results nevertheless make it plausible that calculations employing simple one-dimensional expansion can provide valuable insight into the behavior of jets in the medium.

Our results for the longitudinally expanding system (1D Bjorken) and the corresponding data are shown in Fig. 2. The gray band shows our full DREENA-B result (see above) with the band resulting from the uncertainty in the magnetic to electric mass ratio μ_M/μ_E [31,32]. The red line corresponds to the 0.57ς limit from Eq. (7), where ς is the anisotropy of the path lengths used in the DREENA-B calculations [7,10]. Importantly, for each centrality, the asymptotic regime—where the $v_2/(1-R_{\rm AA})$ ratio does not depend on $p_\perp$, but is determined by the geometry of the system—is already reached from $p_\perp \approx 20$–30 GeV; the asymptote corresponds to the analytically derived Eq. (7), within $\pm 5\%$ accuracy. It is also worth noticing that our prediction of asymptotic behavior was based on approximations which are not necessarily valid in these calculations, but the asymptotic regime is nevertheless reached, telling us that those assumptions were sufficient to capture the dominant features. If, as we suspect, the high-$p_\perp$ parton-medium interactions are more important than the medium evolution model in explaining the high-$p_\perp$ data, this behavior reflects this importance and the analytical derivations based on a static medium may capture the dominant features seen in Fig. 2.

Furthermore, to check if the experimental data support the derived scaling relation, we compare our results to the ALICE [33,34], CMS [35,36], and ATLAS [37,38] data for $\sqrt{s_{NN}} = 5.02$ TeV Pb+Pb collisions. The experimental data, for all three experiments, show the same tendency, i.e., the independence on the $p_\perp$ and a consistency with our predictions, though the error bars are still large. Therefore, from Fig. 2, we see that at each centrality both the numerically predicted and experimentally observed $v_2/(1-R_{\rm AA})$ approach the same high-$p_\perp$ limit. This robust, straight line, asymptotic value carries information about the system's anisotropy, which is, in principle, simple to infer from the experimental data.

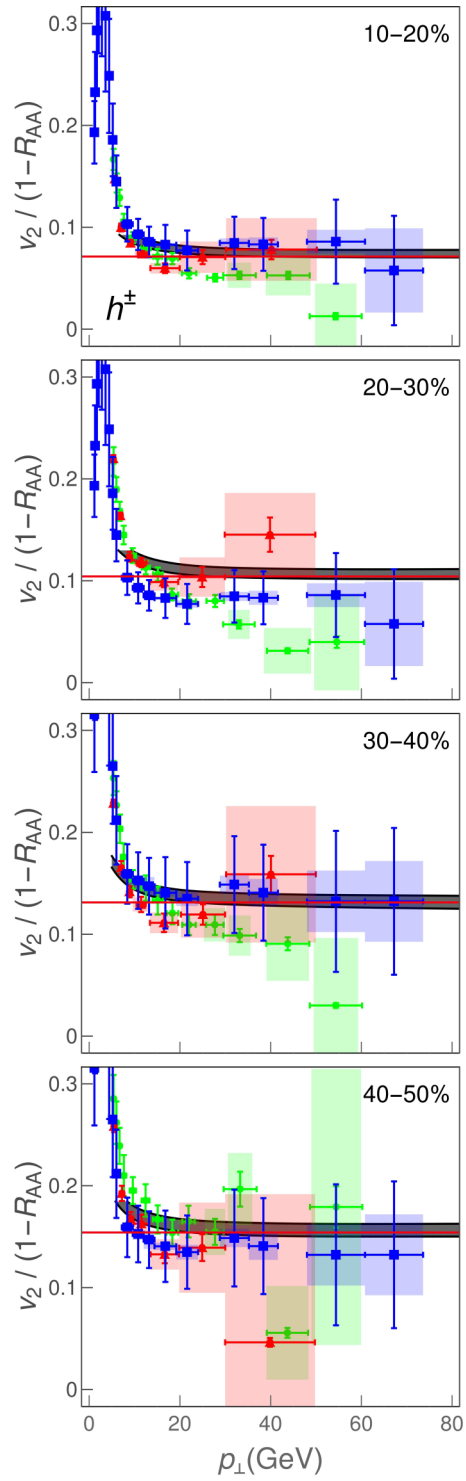

FIG. 2. Theoretical predictions for $v_2/(1-R_{\rm AA})$ ratio of charged hadrons as a function of transverse momentum $p_\perp$ compared with 5.02 TeV Pb+Pb ALICE [33,34] (red triangles), CMS [35,36] (blue squares), and ATLAS [37,38] (green circles) data. Panels correspond to 10–20%, 20–30%, 30–40%, and 40–50% centrality bins. The gray band corresponds to the uncertainty in the magnetic to electric mass ratio μ_M/μ_E. The upper (lower) boundary of the band corresponds to $\mu_M/\mu_E = 0.4$ (0.6) [31,32]. In each panel, the red line corresponds to the limit 0.57ς from Eq. (7).

Ideally, the experimental data (here from ALICE, CMS, and ATLAS) would overlap with each other, and would moreover have small error bars. In such a case, the data could be used to directly extract the anisotropy parameter ς by fitting a straight line to the high-$p_\perp$ part of the $v_2/(1-R_{\rm AA})$ ratio. While such direct anisotropy extraction would be highly desirable, the available experimental data are unfortunately still not near the precision level needed to implement this. However, we expect this to change in the upcoming high-luminosity third run at the LHC, where the error bars are expected to be significantly reduced, so that this procedure can be directly applied to experimental data.

It is worth remembering that the anisotropy parameter ς, which can be extracted from the high-$p_\perp$ data, is not the commonly used anisotropy parameter ϵ_2,

$$\epsilon_2 = \frac{\langle y^2 - x^2\rangle}{\langle y^2 + x^2\rangle} = \frac{\int dx\, dy\, (y^2 - x^2)\, \rho(x,y)}{\int dx\, dy\, (y^2 + x^2)\, \rho(x,y)}, \tag{8}$$

where $\rho(x,y)$ is the initial density distribution of the QGP droplet. We may also expect, that once the transverse expansion is included in the description of the evolution, the path-length anisotropy ς reflects the time-averaged anisotropy of the system, and therefore is not directly related to the initial-state anisotropy ϵ_2. Nevertheless, it is instructive to check how the path-length anisotropy in our simple model relates to conventional ϵ_2 values in the literature. For this purpose we construct a variable

$$\epsilon_{2L} = \frac{\langle L_{\rm out}\rangle^2 - \langle L_{\rm in}\rangle^2}{\langle L_{\rm out}\rangle^2 + \langle L_{\rm in}\rangle^2} = \frac{2\varsigma}{1+\varsigma^2}. \tag{9}$$

We have checked that for different density distributions ϵ_2 and ϵ_{2L} agree within $\approx$10% accuracy.

We have extracted the parameters ς from the DREENA-B results shown in Fig. 2; the corresponding ϵ_{2L} results are shown as a function of centrality in Fig. 3 and compared to ϵ_2 evaluated using various initial-state models in the literature [39–42]. Note that conventional (EKRT [40], IP-Glasma [41]) ϵ_2 values trivially agree with our *initial* ϵ_2 (not shown in the figure), i.e., the initial ϵ_2 characterize the anisotropy of the path lengths used as an input to DREENA-B, which we had chosen to agree with the conventional models.[2] It is, however, much less trivial that through this procedure, in which we calculate the ratio of v_2 and $1-R_{\rm AA}$ through full DREENA framework, our *extracted* ϵ_{2L} almost exactly recovers our initial ϵ_2. Note that ϵ_2 is *indirectly* introduced in $R_{\rm AA}$ and v_2 calculations through path-length distributions, while our calculations are performed using full-fledged numerical procedure, not just Eq. (1). Consequently, such direct extraction of ϵ_{2L} and its agreement with our initial (and consequently also conventional) ϵ_2 is highly nontrivial and gives us a good deal of confidence that $v_2/(1-R_{\rm AA})$ is related to the anisotropy of the system only, and not its material properties.

[2]Binary collision scaling calculated using optical Glauber model with additional cutoff in the tails of Woods-Saxon potentials, to be exact.

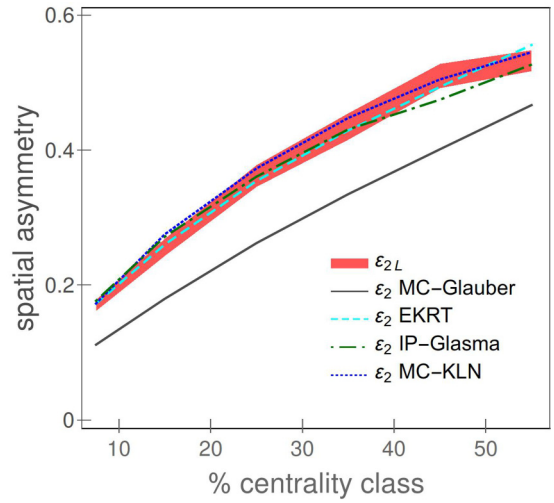

FIG. 3. Comparison of ϵ_{2L} (red band) obtained from our method, with ϵ_2 calculated using Monte Carlo (MC)-Glauber [39] (gray band), EKRT [40] (purple band), IP-Glasma [41] (green dot-dashed curve), and MC-KLN [42] (blue dotted curve) approaches. MC-Glauber and EKRT results correspond to 5.02 TeV, while IP-Glasma and MC-KLN correspond to 2.76 TeV Pb+Pb collisions at the LHC.

Summary. High-$p_\perp$ theory and data are traditionally used to explore interactions of traversing high-$p_\perp$ probes with QGP, while bulk properties of QGP are obtained through low-$p_\perp$ data and the corresponding models. On the other hand, it is clear that high-$p_\perp$ probes are also powerful tomography tools since they are sensitive to global QGP properties. We here demonstrated this in the case of spatial anisotropy of the QCD matter formed in ultrarelativistic heavy-ion collisions. We used our dynamical energy-loss formalism to show that a (modified) ratio of two main high-$p_\perp$ observables, $R_{\rm AA}$ and v_2, approaches an asymptotic limit at experimentally accessible transverse momenta, and that this asymptotic value depends only on the shape of the system, not on its material properties. However, how exactly this asymptotic value reflects the shape and anisotropy of the system requires further study employing full three-dimensional expansion, which is our current work in progress. The experimental accuracy does not yet allow the extraction of the anisotropy from the data using our scheme, but once the accuracy improves in the upcoming LHC runs, we expect that the anisotropy of the QGP formed in heavy-ion collisions can be inferred directly from the data. Such an experimentally obtained anisotropy parameter would provide an important constraint to models describing the early stages of heavy-ion collision and QGP evolution, and demonstrate synergy of high-$p_\perp$ theory and data with more common approaches for inferring QGP properties.

Acknowledgments. We thank Jussi Auvinen, Hendrik van Hees, Etele Molnar, and Dusan Zigic for useful discussions. We also thank Tetsufumi Hirano and Harri Niemi for sharing their MC-KLN and EKRT results with us. This work is supported by the European Research Council, Grant No. ERC-2016-COG: 725741, and by the Ministry of Science and Technological Development of the Republic of Serbia, under Projects No. ON171004 and No. ON173052.

[1] M. Gyulassy and L. McLerran, Nucl. Phys. A **750**, 30 (2005).
[2] E. V. Shuryak, Nucl. Phys. A **750**, 64 (2005).
[3] B. Jacak and P. Steinberg, Phys. Today **63**(5), 39 (2010).
[4] C. V. Johnson and P. Steinberg, Phys. Today **63**(5), 29 (2010).
[5] J. C. Collins and M. J. Perry, Phys. Rev. Lett. **34**, 1353 (1975).
[6] G. Baym and S. A. Chin, Phys. Lett. B **62**, 241 (1976).
[7] D. Zigic, I. Salom, J. Auvinen, M. Djordjevic, and M. Djordjevic, J. Phys. G: Nucl. Part. Phys. **46**, 085101 (2019).
[8] T. Renk, Phys. Rev. C **85**, 044903 (2012).
[9] D. Molnar and D. Sun, Nucl. Phys. A **932**, 140 (2014); **910-911**, 486 (2013).
[10] D. Zigic, I. Salom, J. Auvinen, M. Djordjevic, and M. Djordjevic, Phys. Lett. B **791**, 236 (2019).
[11] M. Djordjevic, D. Zigic, M. Djordjevic, and J. Auvinen, Phys. Rev. C **99**, 061902(R) (2019).
[12] R. Baier, Y. Dokshitzer, A. Mueller, S. Peigne, and D. Schiff, Nucl. Phys. B **484**, 265 (1997).
[13] N. Armesto, C. A. Salgado, and U. A. Wiedemann, Phys. Rev. D **69**, 114003 (2004).
[14] M. Gyulassy, P. Lévai, and I. Vitev, Nucl. Phys. B **594**, 371 (2001).
[15] X. N. Wang and X. f. Guo, Nucl. Phys. A **696**, 788 (2001).
[16] M. Djordjevic and M. Djordjevic, Phys. Rev. C **92**, 024918 (2015).
[17] A. Dainese (ALICE Collaboration), Eur. Phys. J. C **33**, 495 (2004).
[18] S. Afanasiev *et al.* (PHENIX Collaboration), Phys. Rev. C **80**, 054907 (2009).
[19] P. Christiansen, K. Tywoniuk, and V. Vislavicius, Phys. Rev. C **89**, 034912 (2014).
[20] M. Djordjevic, Phys. Rev. C **80**, 064909 (2009); M. Djordjevic and U. Heinz, Phys. Rev. Lett. **101**, 022302 (2008).
[21] M. Djordjevic, Phys. Rev. C **74**, 064907 (2006).
[22] J. I. Kapusta, *Finite-Temperature Field Theory* (Cambridge University, New York, 1989).
[23] M. Djordjevic and M. Gyulassy, Phys. Rev. C **68**, 034914 (2003).
[24] M. Djordjevic and M. Djordjevic, Phys. Lett. B **709**, 229 (2012).
[25] M. Djordjevic and M. Djordjevic, Phys. Lett. B **734**, 286 (2014).
[26] B. Blagojevic, M. Djordjevic, and M. Djordjevic, Phys. Rev. C **99**, 024901 (2019).
[27] Z. B. Kang, I. Vitev, and H. Xing, Phys. Lett. B **718**, 482 (2012).
[28] M. Gyulassy, P. Levai, and I. Vitev, Phys. Lett. B **538**, 282 (2002).
[29] D. de Florian, R. Sassot, and M. Stratmann, Phys. Rev. D **75**, 114010 (2007).
[30] B. Blagojevic and M. Djordjevic, J. Phys. G: Nucl. Part. Phys. **42**, 075105 (2015).
[31] Y. Maezawa, S. Aoki, S. Ejiri, T. Hatsuda, N. Ishii, K. Kanaya, N. Ukita, T. Umeda (WHOT-QCD Collaboration), Phys. Rev. D **81**, 091501(R) (2010).
[32] A. Nakamura, T. Saito, and S. Sakai, Phys. Rev. D **69**, 014506 (2004).
[33] S. Acharya *et al.* (ALICE Collaboration), J. High Energy Phys. 11 (2018) 013.
[34] S. Acharya *et al.* (ALICE Collaboration), J. High Energy Phys. 07 (2018) 103.
[35] V. Khachatryan *et al.* (CMS Collaboration), J. High Energy Phys. 04 (2017) 039.
[36] A. M. Sirunyan *et al.* (CMS Collaboration), Phys. Lett. B **776**, 195 (2018).
[37] ATLAS Collaboration, ATLAS-CONF-2017-012 (unpublished), https://cds.cern.ch/record/2244824.
[38] M. Aaboud *et al.* (ATLAS Collaboration), Eur. Phys. J. C **78**, 997 (2018).
[39] C. Loizides, J. Kamin, and D. d'Enterria, Phys. Rev. C **97**, 054910 (2018).
[40] K. J. Eskola, H. Niemi, R. Paatelainen, and K. Tuominen, Phys. Rev. C **97**, 034911 (2018).
[41] J. E. Bernhard, J. S. Moreland, S. A. Bass, J. Liu, and U. Heinz, Phys. Rev. C **94**, 024907 (2016).
[42] T. Hirano, P. Huovinen, K. Murase, and Y. Nara, Prog. Part. Nucl. Phys. **70**, 108 (2013).

Physics Letters B 777 (2018) 125–130

Contents lists available at ScienceDirect

Physics Letters B

www.elsevier.com/locate/physletb

Hadron resonance gas with repulsive interactions and fluctuations of conserved charges

Pasi Huovinen [a], Peter Petreczky [b]

[a] Institute of Theoretical Physics, University of Wroclaw, 50204 Wrocław, Poland
[b] Physics Department, Brookhaven National Laboratory, Upton, NY 11973, USA

ARTICLE INFO

Article history:
Received 7 August 2017
Received in revised form 30 November 2017
Accepted 1 December 2017
Available online 11 December 2017
Editor: J.-P. Blaizot

ABSTRACT

We discuss the role of repulsive baryon–baryon interactions in a hadron gas using relativistic virial expansion and repulsive mean field approaches. The fluctuations of the baryon number as well as strangeness-baryon correlations are calculated in the hadron resonance gas with repulsive interactions and compared with the recent lattice QCD results. In particular, we calculate the difference between the second and fourth order fluctuations and correlations of baryon number and strangeness, that have been proposed as probes of deconfinement. We show that for not too high temperatures these differences could be understood in terms of repulsive interactions.

1. Introduction

Fluctuations and correlations of conserved charges, e.g. baryon number (B), electric charge (Q) and strangeness (S) have been studied in lattice QCD for some time now. The reason is that they are sensitive probes of deconfinement and can also be used to calculate thermodynamic quantities at non-zero baryon density via Taylor expansion (see Refs. [1,2] for recent reviews and references therein). At sufficiently low temperatures QCD thermodynamics is expected to be fairly well described by a gas of non-interacting hadrons and hadron resonances, by so-called hadron resonance gas (HRG) model [3]. This picture naturally emerges from the S-matrix based relativistic virial expansion, where the interactions are manifested as the phase shifts of two particle scattering [4–7]. In pion–pion and pion–nucleon interactions the repulsive part associated with the negative phase shifts, is largely cancelled by parts of the positive phase shifts associated with attractive interactions. The effect of the remaining attractive interactions on thermodynamics, can be well approximated as a contribution of free resonances with zero widths [5], although some differential observables may require explicit treatment of the interactions [8].

As the temperature increases, particle densities increase, and the virial expansion only up to second virial coefficient becomes less and less reliable. To establish the validity of the HRG model at temperatures close to the QCD transition temperature requires a detailed comparison with the results from lattice QCD. Early comparisons have been discussed in Refs. [9–13], where, however, large cutoff effects and/or unphysical quark masses made a detailed comparison difficult (see e.g. Ref. [13]). In the past several years the fluctuations and correlations of conserved charges have been studied on the lattice using stout and highly improved staggered quark (HISQ) actions, and physical quark masses [14–27]. These lattice formulations significantly reduce the cutoff effects. As the result the comparison between the lattice results and HRG have become straightforward. Second order fluctuations and correlations seem to agree reasonably well with the HRG model. However, higher order fluctuations show deviations from the HRG model close to the transition temperature. In Ref. [18] it was argued that the apparent breakdown of HRG when describing certain differences of fourth and second order fluctuations and correlations is a signal of deconfinement. On the other hand, it has been recently shown that the repulsive interactions modelled by excluded volume can have significant effect on thermodynamic observables, in particular on higher order fluctuations [28–30]. The role of repulsive interaction in the context of statistical hadronization has also been discussed, see e.g. Ref. [31].

The aim of this paper is to study the effect of repulsive baryon–baryon interactions using the S-matrix based virial expansion and the repulsive mean field approach. In this paper we will calculate the fluctuations and correlations of conserved charges defined as

$$\chi_n^X = T^n \frac{\partial^n (p(T,\mu_X)/T^4)}{\partial \mu_X^n}\bigg|_{\mu_X=0}, \tag{1.1}$$

E-mail address: petreczk@bnl.gov (P. Petreczky).

https://doi.org/10.1016/j.physletb.2017.12.001

$$\chi^{XY}_{nm} = T^{n+m} \frac{\partial^{n+m}(p(T,\mu_X,\mu_Y)/T^4)}{\partial\mu_X^n \partial\mu_Y^m}\bigg|_{\mu_X=0,\mu_Y=0}. \quad (1.2)$$

Here $X = B, Q, S$, i.e. we consider fluctuations and correlations of conserved charges corresponding to baryon number, electric charge and strangeness. It may not be easy to disentangle the effects of repulsive interactions from other medium effects such as in-medium mass shift and broadening of width. Therefore it is useful to study the differences of fluctuations and correlations, which are not affected by the latter effects. In particular we evaluate $\chi_2^B - \chi_4^B$, and $\chi_2^B - \chi_6^B$, and show that the inclusion of the repulsive baryon baryon interaction can naturally explain the temperature dependence of these differences.

2. Repulsive interaction in nucleon gas

First we would like to study the role of repulsive interactions in the gas of nucleons at temperature $T = 1/\beta$. The most natural way to do this is to consider the virial expansion. In this case the nucleon pressure can be written as

$$p(T,\mu) = p_0(T)\cosh(\beta\mu) + 2b_2(T)T\cosh(2\beta\mu). \quad (2.1)$$

Here

$$p_0(T) = \frac{4M^2T^2}{\pi^2}K_2(\beta M) \quad (2.2)$$

is the pressure of free nucleon gas at zero chemical potential and the second virial coefficient can be written as

$$b_2(T) = \frac{2T}{\pi^3}\int_0^\infty dE\left(\frac{ME}{2}+M^2\right)K_2\left(2\beta\sqrt{\frac{ME}{2}+M^2}\right) \times \frac{1}{4i}\mathrm{Tr}\left[S^\dagger\frac{dS}{dE} - \frac{dS^\dagger}{dE}S\right], \quad (2.3)$$

with S being the scattering S-matrix and E is the kinetic energy in the lab frame. Furthermore, M is the nucleon mass and $K_2(x)$ is the Bessel function of second kind. The nucleon–nucleon (NN) interactions break the simple factorisation of the pressure into temperature dependent and μ-dependent parts. As the result $\chi_2^B - \chi_4^B$ is not zero as in the case of non-interacting HRG. Even if the effect of NN interactions is small for the pressure when $\mu = 0$, it could be significant for higher order fluctuations as each derivative in μ will multiply b_2 by factor two. Because of the exponential suppression of $K_2(x)$ at large values of the argument, the virial coefficient b_2 is very small for the nucleon gas. Therefore, it makes sense to introduce the reduced virial coefficient

$$\bar{b}_2(T) = \frac{2Tb_2(T)}{p_0(T)K_2(\beta M)}. \quad (2.4)$$

The pressure can now be written as

$$p(T,\mu) = p_0(T)(\cosh(\beta\mu) + \bar{b}_2(T)K_2(\beta M)\cosh(2\beta\mu)). \quad (2.5)$$

To evaluate $b_2(T)$ we need to know the S-matrix for the NN scattering. Through the partial wave analysis we have a good parametrisation of the elastic part of the S-matrix, however, the inelastic part of the S-matrix is not known. The inelastic channels open up for $E > 280$ MeV and become significant for $E > 400$ MeV, and their importance increases with the energy. We estimate $b_2(T)$ using the elastic part of the S-matrix and try to include the effects of the inelastic channel as a systematic uncertainty.

The elastic S-matrix is block diagonal with matrix elements S_J, that are 2×2 matrices for each value of angular momentum J. In the so-called BASQUE parametrisation [32] S_J has diagonal elements

$$S_\pm = \cos^2\rho_\pm^J \cos 2\epsilon^J \exp(2i\delta_\pm^J) \quad (2.6)$$

corresponding to orbital angular momenta $L = J \pm 1$, and off-diagonal elements

$$S_0 = i\cos\rho_+^J\cos\rho_-^J\sin 2\epsilon^J\exp(i(\delta_+^J+\delta_-^J+\phi^J)). \quad (2.7)$$

Here $\delta_\pm^J$ are the phase shifts corresponding to angular momentum J. The parameters $\rho_\pm^J$ describe the in-elasticity of the collisions, while ϵ^J and ϕ^J are the elastic and inelastic mixing parameters of $L = J\pm 1$ states. For $E < 280$ MeV the parameters $\rho_\pm^J$ and ϕ^J are zero. In this case

$$\frac{1}{4i}\mathrm{Tr}\left[S^\dagger\frac{dS}{dE} - \frac{dS^\dagger}{dE}S\right] = \sum_{s=\pm}\sum_J (2J+1)\left(\frac{d\delta_s^{J,I=0}}{dE} + 3\frac{d\delta_s^{J,I=1}}{dE}\right), \quad (2.8)$$

where we distinguish the isospin zero ($I = 0$) and isospin one ($I = 1$) channels in the nucleon–nucleon system. If the parameters $\rho_\pm^J$ and ϕ^J are different from zero, the above equation will become complex, leading to complex value of $b_2(T)$, which is clearly unphysical. The reason for this problem is that S_J is not unitary. If the inelastic channels were included the unitarity would be restored, the imaginary terms in the above equation would drop out and the derivative of inelastic phase shift would appear. This is easy to see for the simple case when the S-matrix has one elastic and one inelastic channel [7]. In the following we will set the parameters $\rho_\pm^J$ and ϕ to zero and use Eq. (2.8) for all energies to evaluate b_2.

In our numerical analysis we use the elastic phase shifts from the SM16 partial wave analysis [33]. We also use SP07 partial wave analysis [34] as well as an old analysis from Ref. [35]. The differences arising from the use of different partial wave analyses are small compared to other uncertainties of our calculations. For $E > 10$ MeV the effects of Coulomb interactions are small, so the $I = 1$ phase shifts are taken from pp scattering data, while the $I = 0$ phase shifts are taken from the np scattering data. At lower energies the electromagnetic effects are important and there is a difference between pp phase shifts and $I = 1$ np phase shifts. Since in our study we do not include electromagnetic interactions for $E < 10$ MeV we use the phase shifts from np scattering data for both $I = 0$ and $I = 1$ channels. Here it is sufficient to consider the lowest partial waves ($^1S_0$ for $I = 1$ and $^3S_1$ for $I = 0$). Finally to obtain the correct threshold behaviour we use effective range expansion for the S-wave np phase shifts: $\cot\delta^I = -1/(a_I k) + r_I^0 k/2$, with $a_{I=1} = -23.7$ fm and $r^0_{I=1} = 2.76$ fm for $I = 1$ [36], and $a_{I=0} = 5.4194$ fm and $r^0_{I=0} = 1.7536$ fm [37]. We checked that the effective range expansion with the above parameters matches smoothly to SM16 analysis for E of about few MeV. We note that there is a large cancellation between the contributions of $I = 0$ and $I = 1$ channels to b_2 at low energies. This is due to different sign of the scattering length a_I in these two channels and unnaturally large value of $a_{I=0}$. At high energies the derivative of the sum of all the phase shifts is negative, which is reflective the repulsive hard core NN interactions.

Finally we need to estimate the uncertainty in b_2 due to the inelastic channels. For this we consider the ratio of the inelastic to total pp cross-section from SM16 partial wave analysis. The inelastic cross-section is very small for $E < 400$ MeV. For 400 MeV $< E <$ 500 MeV the inelastic cross-section is about 10% of the total cross-section. For 500 MeV $< E <$ 600 MeV, 600 MeV $< E <$ 800 MeV

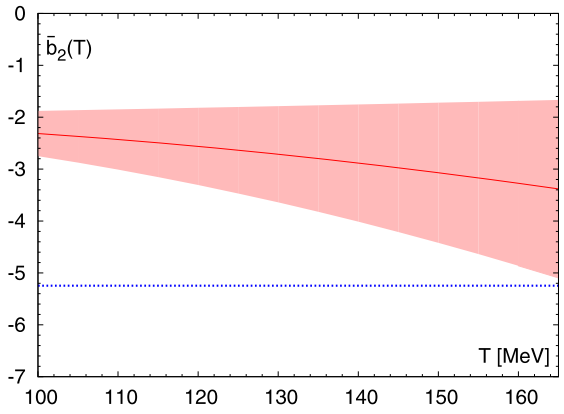

Fig. 1. The reduced virial coefficient as function of the temperature (solid line) together with its uncertainty show as the red band (see text). The dashed line corresponds to KM^2/π^2 with $K = 450$ MeV fm^3. (For interpretation of the references to colour in this figure legend, the reader is referred to the web version of this article.)

and $E > 800$ MeV the inelastic cross-section is about 25%, 40% and 50% of the total cross-section, respectively. Therefore, we estimate that the uncertainty in b_2 that comes from the energy range 400–500 MeV, 500–600, 600–800 MeV and > 800 MeV is 20%, 50%, 80% and 100%, respectively. Here we tried to be conservative and assumed that the contribution of the (unknown) inelastic phase shifts to b_2 is by a factor two larger than to the total cross-section. Our numerical result for the reduced virial coefficient and its uncertainty is shown in Fig. 1.

So far we only considered nucleon–nucleon interactions. Nucleons can also interact with anti-nucleons. Much less is known about the interactions between the nucleons and anti-nucleons, but one may expect that these interactions are significant as well. Fortunately, the nucleon anti-nucleon interactions give a contribution to the pressure, which is independent of the chemical potential. Therefore, these interactions will not affect the fluctuations and correlations that is the main focus of this paper.

Another way to include the repulsive interaction is via a repulsive mean field. In this approach it is assumed that the repulsive interactions lead to shifts in the single particle energies by $U = Kn_b$ and $\bar{U} = K\bar{n}_b$ for nucleons and anti-nucleons, respectively [38,39]. Here n_b and $\bar{n}_b$ are the densities of nucleons and anti-nucleons defined as

$$n_b = 4\int \frac{d^3p}{(2\pi)^3} e^{-\beta(E_p-\mu+U)}, \quad \bar{n}_b = 4\int \frac{d^3p}{(2\pi)^3} e^{-\beta(E_p+\mu+\bar{U})},$$
$$E_p^2 = p^2 + M^2, \tag{2.9}$$

with μ being the chemical potential corresponding to the net nucleon density. We use Boltzmann approximation because the nucleon mass is much larger than the temperature. The phenomenological parameter K characterises the strength of the repulsive interactions and can be related to the integral of the NN potential over the spatial volume [38,39]. The presence of the short distance repulsive core in the NN potential implies that $K > 0$. Requiring, that $\partial p/\partial\mu$ should give the net nucleon density, i.e. $n_b - \bar{n}_b$ one obtains the following expression for the pressure [38,39]

$$p(T,\mu) = T(n_b + \bar{n}_b) + \frac{K}{2}(n_b^2 + \bar{n}_b^2). \tag{2.10}$$

In principle Eq. (2.9) should be solved self-consistently to obtain n_b ($\bar{n}_b$). However, for temperatures below the QCD transition temperature n_b ($\bar{n}_b$) is small, and for typical phenomenological values of K, e.g. $K = 450$ MeV fm^3 [40], βU is small too. For example even for $T = 175$ MeV we get $\beta U = 0.077$. Therefore we can expand the exponential in the equations for n_b and $\bar{n}_b$, and the factor $(1+n_b)^{-1}$ and $(1+\bar{n}_b)^{-1}$ when solving n_b and $\bar{n}_b$, and write

$$n_b = n_b^0(1 - \beta K n_b^0), \ \bar{n}_b = \bar{n}_b^0(1 - \beta K \bar{n}_b^0), \tag{2.11}$$

with n_b^0 and $\bar{n}_b^0$ being the free nucleon and anti-nucleon densities. With this the pressure can be written in terms of n_b^0 and $\bar{n}_b^0$ as follows:

$$p(T,\mu) = T(n_b^0 + \bar{n}_b^0) - \frac{K}{2}\left(\left(n_b^0\right)^2 + \left(\bar{n}_b^0\right)^2\right). \tag{2.12}$$

Taking into account that $n_b^0 = 2TM^2/\pi^2 K_2(\beta M)e^{\beta\mu}$ and $\bar{n}_b^0 = 2TM^2/\pi^2 K_2(\beta M)e^{-\beta\mu}$ we finally get

$$p(T,\mu) = \frac{4T^2M^2}{\pi^2} K_2(\beta M)\cosh(\beta\mu) - 4K\frac{T^2M^4}{\pi^4} K_2^2(\beta M)\cosh(2\beta\mu) \tag{2.13}$$

The structure of the above equation is very similar to the one obtained in the virial expansion. The correction to the free gas result is negative and the factorisation of the pressure in T-dependent part and μ dependent part does not hold. Comparing the above result with the virial expansion result one can determine the value of K at some temperature. To estimate the relative size of the second term in the above equation we write

$$p(T,\mu) = p_0(T)(\cosh(\beta\mu) - \frac{KM^2}{\pi^2} K_2(\beta M)\cosh(2\beta\mu)). \tag{2.14}$$

Comparing this equation with Eq. (2.5) we see that $-KM^2/\pi^2$ corresponds to the reduced virial coefficient $\bar{b}_2(T)$. Therefore, in Fig. 1 we show this combination for the previously used phenomenological value $K = 450$ MeV fm^3. At low temperatures $-\bar{b}_2(T)$ is significantly smaller than KM^2/π^2. However, at the highest temperatures the two agree. We stress again that the smallness of $-\bar{b}_2$ comes from the cancellation of positive and negative contributions in the $I = 0$ and $I = 1$ channels. Such cancellation is a somewhat accidental feature of the NN interactions and may not be present for other baryons. For these reasons we will use the value $K = 450$ MeV fm^3 in what follows.

Finally, we note that the first quantum correction to the pressure of the nucleon gas is $-M^2T^2/\pi^2 K_2(2\beta M)\cosh(2\beta\mu)$. It has the same dependence on μ as the contribution of repulsive interactions but is about 20 times smaller. Therefore, it will be neglected in the following analysis.

3. Repulsive mean field in multi-component hadron gas and fluctuations of conserved charges

It is straightforward to generalise the above repulsive mean field approach to multi-component hadron gas. The baryon density is written as

$$n_B(T,\mu_B,\mu_S,\mu_Q) = \frac{T}{2\pi^2}\sum_i g_i M_i^2 K_2(\beta M_i) e^{\beta\mu_{i,eff}}, \tag{3.1}$$

where M_i is the mass of the ith baryon and g_i is the corresponding degeneracy factor. Furthermore, the effective chemical potential of the ith baryon is given by

$$\mu_{i,eff} = \sum_j q_i^j \mu_j - Kn_B, \tag{3.2}$$

with $(q_i^1, q_i^2, q_i^3) = (B_i, S_i, Q_i)$ being the baryon number, strangeness and electric charge of the ith baryon. Here we assumed that the repulsive interaction is the same for all baryons. This is clearly an oversimplification. While lattice calculations indicate that repulsive core in the central potential is similar for many baryon combinations (e.g. NN, ΛN, $\Lambda\Lambda$, etc.), there are some differences [41]. The hyperon nucleon and hyperon–hyperon interactions have been studied also in chiral effective theory [42,43]. It has been found that these interactions are dominantly repulsive but different from nucleon–nucleon interactions. However, we do not have sufficient information about baryon–baryon interactions to come up with a more sophisticated mean field model. Replacing $\mu_{i,eff}$ in Eq. (3.1) by $\bar{\mu}_{i,eff} = \sum_j \bar{q}_i^j \mu_j - K\bar{n}_B$, we obtain the density of anti-baryons, $\bar{n}_B$. Note that $\bar{q}_i^j = -q_i^j$. Expanding the exponential to leading order in K as in the previous section for the baryon and antibaryon densities, and again requiring that $\partial p/\partial \mu_B = n_B - \bar{n}_B$, we obtain

$$p_B(T,\mu_B,\mu_S,\mu_Q) = T(n_B^0 + \bar{n}_B^0) - \frac{K}{2}\left(\left(n_B^0\right)^2 + \left(\bar{n}_B^0\right)^2\right), \quad (3.3)$$

where n_B^0 and $\bar{n}_B^0$ are the free baryon and anti-baryon densities. The pressure of the free baryon gas can be decomposed into partial baryonic pressure of strangeness one, strangeness two, and strangeness three baryons, and the same is true for anti-baryons. Therefore, we write

$$p_B(T,\mu_B,\mu_S,\mu_Q) = \tilde{p}_B(\mu_S,\mu_Q)e^{\beta\mu_B} + \tilde{p}_B(-\mu_S,-\mu_Q)e^{-\beta\mu_B} - \frac{\beta^2 K}{2}\left(\tilde{p}_B^2\left(\mu_S,\mu_Q\right)e^{2\beta\mu_B} + \tilde{p}_B^2\left(-\mu_S,-\mu_Q\right)e^{-2\beta\mu_B}\right), \quad (3.4)$$

with

$$\tilde{p}_B(\mu_S,\mu_Q) = p_B^{S0} + p_B^{S1}e^{-\beta\mu_S} + p_B^{S2}e^{-2\beta\mu_S} + p_B^{S3}e^{-3\beta\mu_S}, \quad (3.5)$$

and p_B^{Sk} denotes the contribution of $S = -k$ baryons to the free pressure at zero chemical potentials. With this it is straightforward to get the baryon number fluctuations and baryon-strangeness correlations

$$\chi_n^B = \chi_n^{B(0)} - 2^n\beta^4 K\left(N_B^0\right)^2, \qquad (n \text{ even}) \quad (3.6)$$

$$\chi_{n1}^{BS} = \chi_n^{BS(0)} + 2^{n+1}\beta^5 K N_B^0(p_B^{S1} + 2p_B^{S2} + 3p_B^{S3}). \quad (n \text{ odd}) \quad (3.7)$$

Here

$$N_B^0(T) = \frac{T}{2\pi^2}\sum_i g_i M_i^2 K_2(\beta M_i) \quad (3.8)$$

and the subscript "0" in the above equation refers to the non-interacting HRG.

In Ref. [17] it was suggested that certain combinations of fluctuations and correlation of conserved charges can be used as indicators of deconfinement. In particular, the following two combinations

$$\chi_{31}^{BS} - \chi_{11}^{BS}, \qquad \text{and} \qquad \chi_2^B - \chi_4^B \quad (3.9)$$

have been suggested as measures of deconfinement in the light and strange hadron sectors, respectively. In non-interacting HRG these quantities are identically zero, while they have non-zero values for the ideal quark gas. The lattice results show that these quantities quickly rise above zero around the transition temperature and start approaching the ideal gas limit for $T > 200$ MeV.

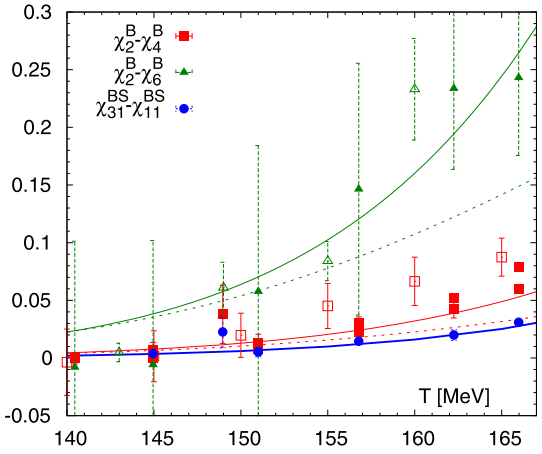

Fig. 2. The differences $\chi_{31}^{BS} - \chi_{11}^{BS}$, $\chi_2^B - \chi_4^B$ and $\chi_2^B - \chi_6^B$ calculated in the HRG model with repulsive mean field (dotted, solid and dashed lines) and in lattice QCD. The filled symbols correspond to lattice calculations of $\chi_2^B - \chi_4^B$ and $\chi_2^B - \chi_6^B$ with HISQ action on $32^3 \times 8$ lattices [27]. The open symbols correspond to lattice results on $\chi_2^B - \chi_4^B$ [22] as well as to lattice results on $\chi_2^B - \chi_6^B$ [26]. For $\chi_{31}^{BS} - \chi_{11}^{BS}$ the lattice results from Ref. [17] are used. The dashed lines correspond to the unexpanded mean field result (see text).

This was interpreted as a transition from non-interacting hadron gas to quark gas [17]. Therefore, it is interesting to see to what extent the increase in $\chi_{31}^{BS} - \chi_{11}^{BS}$, and $\chi_2^B - \chi_4^B$ around the transition temperature can be explained with the repulsive baryon interactions.

We calculated $\chi_2^B - \chi_4^B$, $\chi_2^B - \chi_6^B$ and $\chi_{31}^{BS} - \chi_{11}^{BS}$ in the HRG model with repulsive mean field using Eqs. (3.6) and (3.7). We considered only the contribution of ground state octet and decuplet baryons. The excited baryon states should appear as attractive (resonant) interactions in the hadron gas and thus, they are included in the non-interacting part of HRG. On the other hand, when resonances are interpreted as arising from attractive interactions, they lead to an increase in the density of ground state baryons [6]. We leave creating a proper treatment of heavy resonances for a further study [44], and, as mentioned, concentrate here on the effects of ground state baryons and the lowest resonances.

As discussed before we use the value $K = 450$ MeV fm^3 in our numerical study. Our results are shown in Fig. 2 and compared with the lattice results obtained with HISQ action [17,27] depicted with filled symbols. We also use the lattice results for $\chi_2^B - \chi_6^B$ obtained with stout action [26] as well as continuum extrapolated results for $\chi_2^B - \chi_4^B$ from Ref. [22], depicted with open symbols. As expected the effect of the repulsive interactions is bigger for χ_6^B than for χ_4^B. In our analysis so far we assumed that the density of baryons (anti-baryons) is small and therefore we kept the leading order term of the expansion in baryon density, i.e. the term proportional to K (cf. Eqs. (3.6) and (3.7)). As the temperature is increasing the number density of baryons and anti-baryons also increases and this expansion become less reliable. Therefore, we also calculated $\chi_2^B - \chi_4^B$ and $\chi_2^B - \chi_6^B$ using the unexpanded mean-field expressions and the results are shown in Fig. 2 as dashed lines. The difference between the expanded and un-expanded mean field results is significant at and above the crossover temperature. The full mean field result is below the lattice data. This problem could be cured by taking into account the effect of repulsive interactions for higher baryon resonances, although it is not clear to what extent the HRG model is reliable in this temperature region. Note, that using the full mean field result is more important for the higher order fluctuations and correlations than for the pressure since the effect of the repulsive interactions is enhanced by factor 2^n for the former (cf. Eqs. (3.6) and (3.7)). In Ref. [29] the de-

crease of χ_4^B/χ_2^B from one was described in terms of HRG, where the repulsive interactions are modelled by excluded volume and good agreement with the lattice data was found. The increase in $\chi_2^B - \chi_4^B$ is equivalent to decrease of χ_4^B/χ_2^B from unity, and thus our analysis confirms this result.

In Ref. [17] another combination of strangeness fluctuations and baryon-strangeness correlation has been considered, which is identically zero in the ideal HRG and approaches the free quark gas value at very high temperature, namely

$$v_2 = \frac{1}{3}(\chi_2^S - \chi_4^S) - 2\chi_{13}^{BS} - 4\chi_{22}^{BS} - 2\chi_{31}^{BS}. \tag{3.10}$$

We calculated v_2 in our HRG model with repulsive mean field. We find that it has different sign depending on the value of K and the temperature, while lattice calculation shows that v_2 is positive and monotonically increases with the temperature. So the simplest mean field approach with the same mean-field for all baryons cannot describe this quantity, and the differences in the repulsive baryon interactions in strange and non-strange baryons are important here. This is contrary to the difference $\chi_{31}^{BS} - \chi_{11}^{BS}$ where the repulsive interactions in the different strangeness sectors contribute with the same sign. To understand v_2 in the framework of the hadron gas with repulsive interactions more information on baryon–baryon interactions in different strangeness sectors will be needed.

We also calculated the baryon electric charge correlations χ_{31}^{BQ} and χ_{11}^{BQ} in the repulsive mean field approach. The results are similar to the case of χ_{31}^{BS} and χ_{11}^{BS}. In particular, $\chi_{31}^{BQ} - \chi_{11}^{BQ}$ increases with increasing temperature and the repulsive interactions between different baryons contribute with the same sign. Our results agree with the preliminary lattice results.

4. Conclusions

In this paper we discussed the role of repulsive baryon interactions on the thermodynamics and fluctuations of conserved charges of hadronic matter using relativistic virial expansion and repulsive mean field approach. We showed that the two approaches lead to almost identical results. In particular the reduced virial coefficient $\bar{b}_2(T)$ shows only a mild temperature dependence and corresponds to the combination KM^2/π^2 appearing in the repulsive mean field approach. The deviations from ideal HRG for higher order fluctuations and correlations of conserved charges can be naturally explained by the repulsive interactions. We pointed out that it is useful to study the effect of repulsive interactions in terms of the following differences: $\chi_{31}^{BS} - \chi_{11}^{BS}$, $\chi_2^B - \chi_4^B$ and $\chi_2^B - \chi_6^B$ since the ideal hadron resonance gas part drops out and thus the results are not sensitive to the hadron spectrum. This makes it easy to disentangle the effects of repulsive interactions from other effects such as missing states [19] and in-medium modifications of hadron properties. The size of the deviations from the ideal gas limit for these differences obtained in the simple mean field model is similar to that observed on the lattice, though the former has large uncertainties at and above the QCD crossover temperature. However, not all strangeness baryon correlations can be understood within our simple mean field approach due to the fact that baryon–baryon interactions are different in different strangeness sectors. Therefore, in the future it will be important to refine the treatment of the repulsive interactions of strange baryons using information from lattice QCD and chiral effective theory [42,43] to obtain a better description of the fluctuations and correlation of conserved charges. Nevertheless, it is clear that HRG with repulsive interactions is a useful approach for studying the contribution of baryons to the thermodynamics of hadronic matter at zero and not too high baryon density. It was shown in Ref. [29] that including repulsive interactions by excluded volume affects the equation of state and fluctuations of conserved charges improve the agreement with the lattice data. Along similar lines we plan to study the QCD equation of state and fluctuations of conserved charges at zero and non-zero baryon density using HRG model with repulsive mean field [44] and perform detailed comparisons to the available lattice results. We hope that this study will also clarify the range of applicability of the mean field model.

Acknowledgements

This work was supported by U.S. Department of Energy under Contract No. DE-SC0012704, and by National Science Center, Poland, under grant Polonez DEC-2015/19/P/ST2/03333 receiving funding from the European Union's Horizon 2020 research and innovation programme under the Marie Skłodowska-Curie grant agreement No. 665778. We thank I. Strakovsky for correspondence on partial wave analysis of nucleon–nucleon scattering and for sending the results for the BASQUE parametrisation. We thank Sz. Borsányi, M. D'Elia and G. Gagliardi for sending the lattice results on baryon number fluctuations. PP would like to thank J. Haidenbauer for useful discussions on the application of the chiral effective theory to the baryon–baryon interactions. PH thanks P.M. Lo for illuminating discussions on the S-matrix approach.

References

[1] P. Petreczky, J. Phys. G 39 (2012) 093002, arXiv:1203.5320 [hep-lat].
[2] H.-T. Ding, F. Karsch, S. Mukherjee, Int. J. Mod. Phys. E 24 (2015) 1530007, arXiv:1504.05274 [hep-lat].
[3] R. Hagedorn, Nuovo Cim. Suppl. 3 (1965) 147.
[4] R. Dashen, S.-K. Ma, H.J. Bernstein, Phys. Rev. 187 (1969) 345.
[5] R. Venugopalan, M. Prakash, Nucl. Phys. A 546 (1992) 718.
[6] W. Weinhold, B. Friman, W. Norenberg, Phys. Lett. B 433 (1998) 236, arXiv:nucl-th/9710014.
[7] P.M. Lo, Eur. Phys. J. 77 (2017) 533.
[8] P. Huovinen, P.M. Lo, M. Marczenko, K. Morita, K. Redlich, C. Sasaki, Phys. Lett. B 769 (2017) 509, arXiv:1608.06817 [hep-ph].
[9] F. Karsch, K. Redlich, A. Tawfik, Eur. Phys. J. C 29 (2003) 549, arXiv:hep-ph/0303108.
[10] F. Karsch, K. Redlich, A. Tawfik, Phys. Lett. B 571 (2003) 67, arXiv:hep-ph/0306208.
[11] S. Ejiri, F. Karsch, K. Redlich, Phys. Lett. B 633 (2006) 275, arXiv:hep-ph/0509051.
[12] M. Cheng, et al., Phys. Rev. D 79 (2009) 074505, arXiv:0811.1006 [hep-lat].
[13] P. Huovinen, P. Petreczky, Nucl. Phys. A 837 (2010) 26, arXiv:0912.2541 [hep-ph].
[14] S. Borsanyi, Z. Fodor, C. Hoelbling, S.D. Katz, S. Krieg, C. Ratti, K.K. Szabo, Wuppertal-Budapest, J. High Energy Phys. 09 (2010) 073, arXiv:1005.3508 [hep-lat].
[15] S. Borsanyi, Z. Fodor, S.D. Katz, S. Krieg, C. Ratti, K. Szabo, J. High Energy Phys. 01 (2012) 138, arXiv:1112.4416 [hep-lat].
[16] A. Bazavov, et al., HotQCD, Phys. Rev. D 86 (2012) 034509, arXiv:1203.0784 [hep-lat].
[17] A. Bazavov, et al., Phys. Rev. Lett. 111 (2013) 082301, arXiv:1304.7220 [hep-lat].
[18] A. Bazavov, H.T. Ding, P. Hegde, F. Karsch, C. Miao, S. Mukherjee, P. Petreczky, C. Schmidt, A. Velytsky, Phys. Rev. D 88 (2013) 094021, arXiv:1309.2317 [hep-lat].
[19] A. Bazavov, et al., Phys. Rev. Lett. 113 (2014) 072001, arXiv:1404.6511 [hep-lat].
[20] A. Bazavov, et al., Phys. Lett. B 737 (2014) 210, arXiv:1404.4043 [hep-lat].
[21] S. Borsanyi, Z. Fodor, S.D. Katz, S. Krieg, C. Ratti, K.K. Szabo, Phys. Rev. Lett. 113 (2014) 052301, arXiv:1403.4576 [hep-lat].
[22] R. Bellwied, S. Borsanyi, Z. Fodor, S.D. Katz, A. Pasztor, C. Ratti, K.K. Szabo, Phys. Rev. D 92 (2015) 114505, arXiv:1507.04627 [hep-lat].
[23] H.T. Ding, S. Mukherjee, H. Ohno, P. Petreczky, H.P. Schadler, Phys. Rev. D 92 (2015) 074043, arXiv:1507.06637 [hep-lat].
[24] A. Bazavov, et al., Phys. Rev. D 93 (2016) 014512, arXiv:1509.05786 [hep-lat].
[25] S. Mukherjee, P. Petreczky, S. Sharma, Phys. Rev. D 93 (2016) 014502, arXiv:1509.08887 [hep-lat].
[26] M. D'Elia, G. Gagliardi, F. Sanfilippo, Phys. Rev. D 95 (2017) 094503, arXiv:1611.08285 [hep-lat].

[27] A. Bazavov, et al., Phys. Rev. D 95 (2017) 054504, arXiv:1701.04325 [hep-lat].
[28] M. Albright, J. Kapusta, C. Young, Phys. Rev. C 92 (2015) 044904, arXiv:1506.03408 [nucl-th].
[29] V. Vovchenko, M.I. Gorenstein, H. Stoecker, Phys. Rev. Lett. 118 (2017) 182301, arXiv:1609.03975 [hep-ph].
[30] V. Vovchenko, A. Motornenko, P. Alba, M.I. Gorenstein, L.M. Satarov, H. Stoecker, Phys. Rev. C 96 (2017) 045202.
[31] P. Braun-Munzinger, I. Heppe, J. Stachel, Phys. Lett. B 465 (1999) 15, arXiv:nucl-th/9903010.
[32] D.V. Bugg, Phys. Rev. C 21 (1980) 1004.
[33] R.L. Workman, W.J. Briscoe, I.I. Strakovsky, Phys. Rev. C 94 (2016) 065203, arXiv:1609.01741 [nucl-th].
[34] R.A. Arndt, W.J. Briscoe, I.I. Strakovsky, R.L. Workman, Phys. Rev. C 76 (2007) 025209, arXiv:0706.2195 [nucl-th].
[35] R.A. Arndt, J.S. Hyslop III, L.D. Roper, Phys. Rev. D 35 (1987) 128.
[36] R. Arceo, G. Santos, O. Diaz-Hernandez, World J. Nucl. Sci. Technol. 4 (2014) 16.
[37] J.J. de Swart, C.P.F. Terheggen, V.G.J. Stoks, in: 3rd International Symposium on Dubna Deuteron 95, Dubna, Russia, July 4–7, 1995, 1995, arXiv:nucl-th/9509032.
[38] K.A. Olive, Nucl. Phys. B 190 (1981) 483.
[39] K.A. Olive, Nucl. Phys. B 198 (1982) 461.
[40] J. Sollfrank, P. Huovinen, M. Kataja, P.V. Ruuskanen, M. Prakash, R. Venugopalan, Phys. Rev. C 55 (1997) 392, arXiv:nucl-th/9607029.
[41] T. Doi, et al., in: Proceedings, 34th International Symposium on Lattice Field Theory, Lattice 2016: Southampton, UK, July 24–30, 2016, PoS LATTICE2016 (2017) 110, arXiv:1702.01600 [hep-lat].
[42] H. Polinder, J. Haidenbauer, U.-G. Meissner, Nucl. Phys. A 779 (2006) 244, arXiv:nucl-th/0605050.
[43] J. Haidenbauer, S. Petschauer, N. Kaiser, U.G. Meissner, A. Nogga, W. Weise, Nucl. Phys. A 915 (2013) 24, arXiv:1304.5339 [nucl-th].
[44] P. Huovinen, P. Petreczky, and work in progress.

Physics Letters B 769 (2017) 509–512

Contents lists available at ScienceDirect

Physics Letters B

www.elsevier.com/locate/physletb

Effects of ρ-meson width on pion distributions in heavy-ion collisions

Pasi Huovinen [a], Pok Man Lo [a,b,*], Michał Marczenko [a], Kenji Morita [c,a], Krzysztof Redlich [a,b], Chihiro Sasaki [a]

[a] Institute of Theoretical Physics, University of Wroclaw, PL-50204 Wrocław, Poland
[b] Extreme Matter Institute EMMI, GSI, D-64291 Darmstadt, Germany
[c] Yukawa Institute for Theoretical Physics, Kyoto University, Kyoto 606-8502, Japan

ARTICLE INFO

Article history:
Received 24 August 2016
Received in revised form 25 March 2017
Accepted 25 March 2017
Available online 30 March 2017
Editor: J. Hisano

ABSTRACT

The influence of the finite width of ρ meson on the pion momentum distribution is studied quantitatively in the framework of the S-matrix approach combined with a blast-wave model to describe particle emissions from an expanding fireball. We find that the proper treatment of resonances which accounts for their production dynamics encoded in data for partial wave scattering amplitudes can substantially modify spectra of daughter particles originating in their two body decays. In particular, it results in an enhancement of the low-p_T pions from the decays of ρ mesons which improves the quantitative description of the pion spectra in heavy ion collisions obtained by the ALICE collaboration at the LHC energy.

Recent measurements of the transverse momentum, p_T-distributions of identified particles produced in $\sqrt{s_{NN}} = 2.76$ TeV Pb + Pb collisions at CERN Large Hadron Collider (LHC) [1] revealed an excess of low-momentum ($p_T \lesssim 0.3$ GeV) pions over the conventional fluid-dynamical calculations [1–3].

It is well known that pions originating from decays of resonances have a steeper p_T-distribution than the thermal pions [4], and that they provide a dominant contribution to the spectrum at low transverse momentum. Thus, resonance decays require a particular attention when modeling spectra of particles originating from an expanding thermal fireball.

In fluid-dynamical calculations, the interacting hadrons are usually described by the hadron resonance gas (HRG), where the system is modeled as a gas of free hadrons with resonances considered as particles with vanishing widths. This approximation yields reasonable description of the bulk properties of the hadronic medium [5–8]. The HRG model also provides a very satisfactory description of particle yields measured in heavy ion collisions [9–17], as well as the hadronic equation of state and some fluctuation observables obtained in lattice QCD (LQCD) [18–22]. However, as we show in this letter, when p_T-differential observables are involved, a more refined approach may be necessary.

To properly address the dynamics of hadrons, the effect of resonance width must be included. A conventional way is to impose a Breit–Wigner distribution on the resonance mass. Unfortunately, this approach proves to be too crude in many circumstances. For example, for a broad resonance like the σ meson [23], or the (yet-to-be-confirmed) κ meson [24], the Breit–Wigner approach can give misleading results on the resonance contribution to the thermodynamics.

We thus take a more fundamental approach to evaluate the properties of interacting hadrons based on the S-matrix formulation of Dashen, Ma and Bernstein [25]. For elastic scatterings, the interaction part of the partition function reduces to the Beth–Uhlenbeck form for the second virial coefficient, expressed in terms of the scattering phase shifts [26]. In the context of heavy-ion physics, this approach has been applied to evaluate the contribution of πN [5,27,7], $\pi\pi$ [5,23], and πK interactions [5,24] to the thermodynamics of hadronic matter, and to analyse the resonance production [28].

In this letter, to make the effects of resonance width on particle p_T-spectra more tractable, we concentrate on the $\pi\pi$ system. As shown in Refs. [5,23], the effects of the scalar–isoscalar and the scalar–isotensor channels largely cancel each other. This cancellation remains when the single particle distribution of pions is evaluated. Thus for our purposes it is sufficient to consider only the vector–isovector channel, i.e. the channel of the ρ meson.

In the S-matrix formalism, the density of states per unit volume and unit invariant mass M, assuming thermal equilibrium at temperature T, is given by [26,5,7,28]

* Corresponding author.
E-mail address: pmlo@gsi.de (P.M. Lo).

http://dx.doi.org/10.1016/j.physletb.2017.03.060

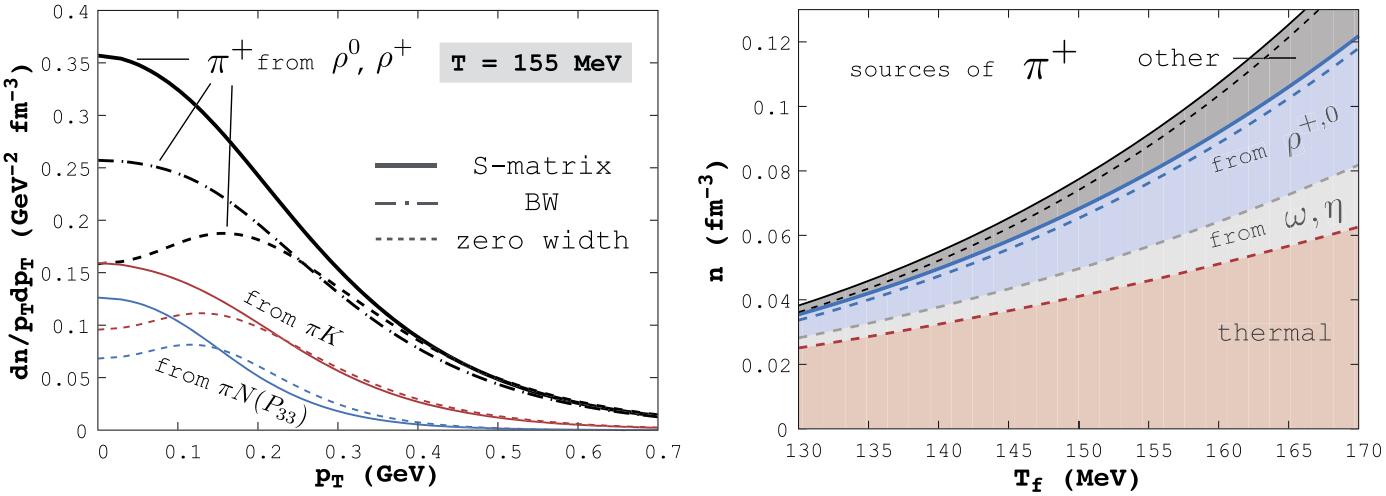

Fig. 1. (Colour online.) Left: p_T spectra of π^+ originating from decays of ρ, the πK (S- and P-wave) system, and the $\Delta(1232)$-channel of πN using both the S-matrix treatment and the zero width approximation at $T = 155$ MeV temperature. The contribution from ρ decays is calculated also using the relativistic Breit–Wigner description of ρ's. Right: Contributions to pion density from various sources as function of freeze-out temperature. In this calculation, the η and ω resonances have zero widths, and the S-matrix treatment has been applied to the system of ρ, and to the processes indicated as "other": the system of $\pi\pi$ (S-wave), πK (S- and P-wave) and the $\Delta(1232)$-channel of πN (see text). In both figures, solid and dashed lines correspond to results of the S-matrix approach and the conventional zero-width approximation, respectively.

$$\frac{\mathrm{d}n_{IJ}}{\mathrm{d}M} = \int \frac{\mathrm{d}^3p}{(2\pi)^3}\,\frac{1}{2\pi}\,\mathcal{B}(M)\,f(E(M,p),T), \tag{1}$$

where f is the Bose–Einstein or Fermi–Dirac distribution, and $\mathcal{B}(M)$ is an effective spectral weight,

$$\mathcal{B}(M) = 2\,\frac{\mathrm{d}\delta_{IJ}}{\mathrm{d}M}, \tag{2}$$

derived from the scattering phase shift δ_{IJ}, of the isospin I and spin J channel.

In the elastic region ($M \lesssim 1$ GeV), the empirical phase shift [29–31] of the $(I = 1, J = 1)$ channel can be effectively described by a phenomenological formula, inspired by a one-loop perturbative calculation of the ρ self-energy [32,33],

$$\delta_{11}(M) = \tan^{-1}\left(-\frac{2}{3M}\,\frac{\alpha_0}{1 + c\,p_{\mathrm{CM}}^2}\,\frac{p_{\mathrm{CM}}^3}{M^2 - m_0^2}\right), \tag{3}$$

where $p_{\mathrm{CM}}(M) = \frac{1}{2}\sqrt{M^2 - 4m_\pi^2}$ is the center-of-mass momentum of the scattering pions, and $\alpha_0 = 3.08$, $m_0 = 0.77$ GeV, and $c = 0.59$ GeV^{-2} are the model parameters chosen to reproduce not only the phase-shift data, but also the known value of the P-wave scattering length. The phase shift and the scattering length are related as

$$a_1^1 = \left.\frac{\delta_{11}}{p_{\mathrm{CM}}^3}\right|_{p_{\mathrm{CM}}\to 0}. \tag{4}$$

We constrain the scattering length to $a_1^1 = 0.038\,m_\pi^{-3}$, matching the experimental value and chiral perturbation theory prediction $a_1^1 = 0.038(2)\,m_\pi^{-3}$ [34] and $0.037(10)\,m_\pi^{-3}$ [35,36], respectively. This requirement is essential for the correct description of the near-threshold behaviour of the density function, introduced in Eq. (2).

An important feature of the current approach is the use of the effective spectral weight $\mathcal{B}(M)$ instead of the standard spectral function. This effective weight includes contributions from both a pure ρ state and the correlated $\pi\pi$ pair. The latter tends to shift the strength of the weight function towards the low invariant-mass region [7]. Such a shift can potentially translate into an enhancement of the low-p_T daughter pions from the decays of ρ mesons.

To quantify this expectation, we evaluate the distribution of ρ's using the Cooper–Frye description [37], with the thermal distribution augmented by the effective spectral weight $\mathcal{B}$ in Eq. (2), as

$$\frac{\mathrm{d}N_\rho}{\mathrm{d}y\,p_T\,\mathrm{d}p_T\,\mathrm{d}\phi} = \int \mathrm{d}M_\rho \int \mathrm{d}\sigma_\mu\,p_\rho^\mu\,\frac{1}{2\pi}\,\mathcal{B}(M_\rho) \times \frac{d_\rho}{(2\pi)^3}\,f_\rho(p\cdot u, T), \tag{5}$$

where f_ρ, d_ρ are respectively the Bose–Einstein distribution and the spin degeneracy for ρ, and u is the flow velocity. In the case of a static source, the integration over the surface, $\int \mathrm{d}\sigma_\mu p^\mu$, becomes a simple multiplication by the volume of the system, V, and by the energy of the particle, E. The momentum spectrum of the decay pions can be evaluated by applying the conventional decay kinematics [4,38,39] to the distribution of ρ's from Eq. (5). For a static source, one gets

$$\frac{\mathrm{d}N_\pi^{de}}{\mathrm{d}y\,p_T\,\mathrm{d}p_T\,\mathrm{d}\phi} = V\int \mathrm{d}M_\rho\,\frac{1}{2\pi}\,\mathcal{B}(M_\rho) \times \frac{M_\rho}{2\,p_\pi\,p_{\mathrm{CM}}}\int_{E_\rho^-}^{E_\rho^+}\mathrm{d}E_\rho\,E_\rho\,\frac{d_\rho}{(2\pi)^3}\,f_\rho(E(M_\rho),T), \tag{6}$$

where

$$E_\rho^\pm = \frac{M_\rho}{2m_\pi^2}(E_\pi M_\rho \pm 2p_\pi p_{\mathrm{CM}}). \tag{7}$$

We evaluate the p_T distributions at $T = 155$ MeV, in the vicinity of the pseudocritical temperature obtained in the lattice formulation of QCD [40,41].

In Fig. 1-left we show the rapidity and azimuthal angle integrated transverse momentum spectra of π^+ originating from ρ decays. The ρ's are treated as zero-width particles, particles with the standard Breit–Wigner width, or according to the S-matrix approach introduced in Eq. (6). The latter description leads to a substantial enhancement of the pion decay spectra. The effect is most prominent in the low-p_T region of the decay pions, where at $p_T \approx 0$ one observes a factor of two increase of the differential pion yield. Note that at larger values of the transverse momentum the spectrum of decay pions is practically unaffected by the width

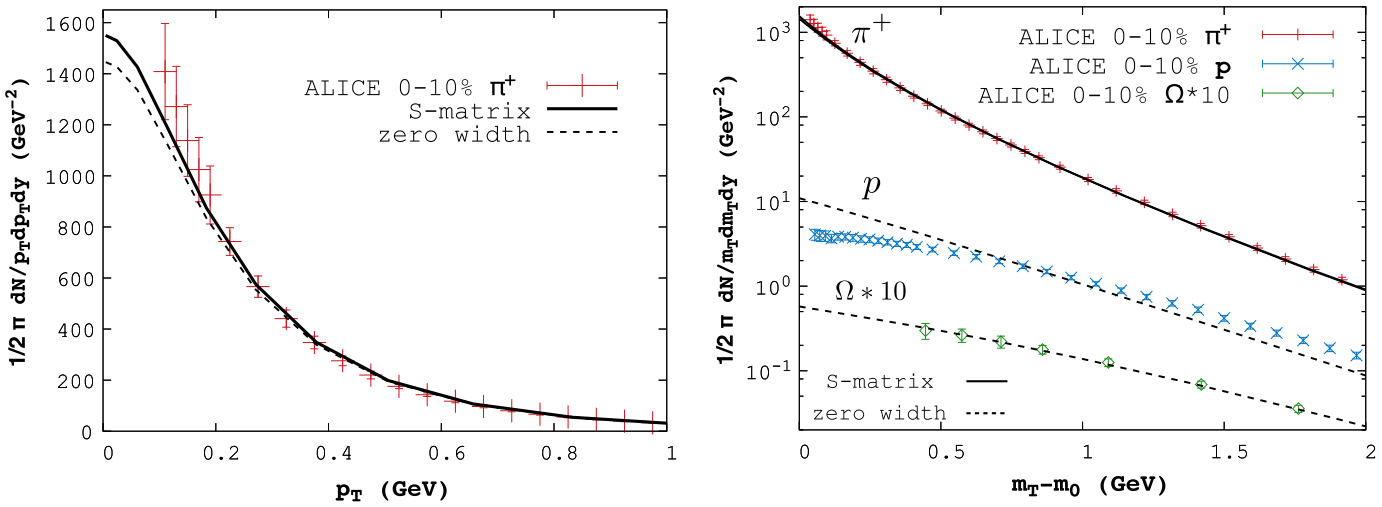

Fig. 2. (Colour online.) Left: The p_T distribution of positive pions in 0–10% most central $\sqrt{s_{NN}} = 2.76$ TeV Pb + Pb collisions as measured by the ALICE collaboration [1,45], and fitted using a blast-wave model. Right: The m_T distribution of positive pions, protons and Ω baryons in 0–10% most central $\sqrt{s_{NN}} = 2.76$ TeV Pb + Pb collisions as measured by the ALICE collaboration [1,45], and fitted using a blast-wave model. In both panels the solid lines correspond to the S-matrix approach result and the dashed lines to the conventional zero-width approximation.

of ρ. For future reference, we also present results on decay π^+ spectra from the system of πK interaction (sum of S- and P-wave) and from πN interaction in the Δ-channel. In all the channels studied we find overall enhancement of low-p_T pions in the S-matrix approach compared to the zero-width results. Nevertheless, the difference is most noticeable in the ρ sector.

To illustrate the effect of leading resonances on the pion yield in the HRG, we show in Fig. 1-right the temperature dependence of the contributions from various sources to pion density after resonance decays. For this analysis, we have included the three-body decays of zero-width η and ω (with branching ratios of 0.228 and 0.893, respectively). Furthermore, we have applied the S-matrix treatment to the $\pi\pi$ (S-wave) and πK (S- and P-wave) systems and the $\Delta(1232)$-channel of πN. At $T = 155$ MeV, when no heavier resonances are included, the relative abundance of π^+ from ρ decay is 25.1%, while the thermal pion yield remains dominant at 49.4%. Three-body decays considered constitute 12.2%, and the sum of the rest of two-body channels we treated give 13.3% of the total yield. The S-matrix treatment significantly affects the yield of pions from ρ decays, resulting in its increase by approximately 15%, whereas the effect is smaller for other channels considered. However, because of the contribution from all the other sources, the overall change in the final pion yield due to the S-matrix approach is only a few per cent.

In general, on the level of particle yields, and at higher temperatures $T > 100$ MeV, the zero-width treatment of resonances gives comparable results to the S-matrix approach [5] despite the fact that the phase shifts in most cases do not resemble a step function and the assumption of a zero (and at times even a narrow) width is strictly speaking not justified. However, as already seen in Fig. 1, essential differences can appear when p_T-differential observables of individual resonance channels are studied. Evidently, the more physical treatment by the S-matrix formulation is needed for precision calculations of particle spectra, as e.g. in modeling data in heavy-ion collisions.

In a realistic heavy-ion collision, however, the situation is further complicated by the expansion of the system, and the presence of all the other resonances. To gauge whether the S-matrix description of ρ mesons would affect the pion distributions observed in heavy-ion collisions, we describe the system using a blast-wave model [42]. There, the thermal source is assumed to be a boost-invariant [43] cylindrically symmetric transversely expanding tube of radius R, from which particles are emitted at constant longitudinal proper time τ with the radial flow velocity $v(r) = v_{max}(r/R)$.

We calculate the distributions of all the resonances in the Particle Data Book up to the 2 GeV mass, apply the two- and three-body decay kinematics, and sum the contributions to the spectrum of thermal pions. We take advantage of the recent finding in the dynamical model calculations in heavy-ion collisions that the pion p_T-distribution changes only very little during the subsequent evolution in the hadronic phase [44]. Thus, we fix the freeze-out temperature at $T = 155$ MeV, which coincides with the chiral crossover in LQCD. The further parameters of the blast-wave model, $\tau = 13.7$ fm, $R = 10$ fm, and $v_{\max} = 0.8$ were chosen to get the best description of spectra for positive pions in 0–10% most central $\sqrt{s_{NN}} = 2.76$ TeV Pb + Pb collisions as measured by the ALICE collaboration. The above freeze-out temperature and the resulting volume of the fireball, $V \simeq 4300$ fm^3, are consistent with that obtained previously in the HRG model description of hadron production yields and some fluctuation observables in heavy-ion collisions at the LHC [10,22].

The resulting pion distribution is shown in the left panel of Fig. 2. In this calculation the conventional zero-width treatment of ρ's leads to a distribution which underestimates the data in the low-p_T region ($p_T \lesssim 200$ MeV). When ρ mesons are treated according to the S-matrix description, there is a clear, up to 7%, increase of the low-p_T pions, which is sufficient to reach the data.

To check further the quality of the model parametrisation, we also show in the right panel of Fig. 2 the pion, proton and Ω baryon distributions in a broader m_T-range. As seen in this figure, the pion data are well described up to $m_T \simeq 2$ GeV, and the model predictions are also consistent with the data for the Ω distribution. These results verify the chosen values for temperature and volume, and they are also consistent with the idea that Ω baryons hardly rescatter in the hadronic phase [47,46], and thus their spectra are fixed at the phase boundary [47]. On the other hand, the proton distribution is steeper than the data, and the overall yield of protons is larger than the experimental value. The observed deviation on the level of proton yield is already discussed in the literature [10]. The deviations in the proton spectrum could be possibly due to their further rescattering during evolution in the hadronic phase [46,48].

In conclusion, we have investigated how the explicit treatment of the ρ-meson width affects the pion yield and p_T distribution

in $\sqrt{s_{NN}} = 2.76$ TeV Pb + Pb collisions at LHC. We have used the S-matrix approach to describe ρ mesons, and found that compared to the conventional zero-width treatment the pion yield increases, particularly at low values of transverse momentum. This indicates that the observed enhancement of low-p_T pions may be possibly explained in fluid-dynamical calculations by a proper implementation of the width of resonances within the S-matrix approach. However, the S-matrix treatment of ρ's alone may not be fully sufficient.

A natural extension of this work is to apply a more complete model for the fluid dynamical calculations [49–53], as well as, to account for a possible medium modification on the phase shifts. Essential in-medium effects for ρ mesons are suggested by studies based on many-body Green's function [33,54–58]. This, together with the S-matrix treatment of three-body decays, can presumably further increase the pion yields in the low-p_T region. We leave this as a matter of future investigation. Nevertheless, even in their present level, our results demonstrate the importance of the proper treatment of resonances in modeling heavy-ion collisions, and the need to improve on the customary hadron resonance gas models for precision calculations of particle spectra at low values of transverse momentum. These studies are also important in hydrodynamics-cascade hybrid models [51,59] for particle production in heavy ion collisions when describing particalization of the fluid as an input to hadronic transport.

Acknowledgements

We acknowledge fruitful discussions with Bengt Friman. K.R. also acknowledges interesting discussions with Peter Braun-Munzinger, Stefen Bass and members of the Nuclear Physics Group at Duke University. P.M.L. acknowledges the support of the Extreme Matter Institute (EMMI). K.M. was supported by the Grants-in-Aid for Scientific Research on Innovative Area from MEXT (No. 24105008) and Grants-in-Aid for Scientific Research from JSPS (No. 16K05349). This work was supported by the National Science Center, Poland under grants: Maestro DEC-2013/10/A/ST2/00106 and Polonez DEC-2015/19/P/ST2/03333, as well as has received funding from the European Union's Horizon 2020 research and innovation programme under the Marie Skłodowska-Curie grant agreement No. 665778.

References

[1] B. Abelev, et al., ALICE Collaboration, Phys. Rev. C 88 (2013) 044910.
[2] V. Begun, W. Florkowski, M. Rybczynski, Phys. Rev. C 90 (2014) 014906.
[3] E. Molnar, H. Holopainen, P. Huovinen, H. Niemi, Phys. Rev. C 90 (2014) 044904.
[4] J. Sollfrank, P. Koch, U.W. Heinz, Z. Phys. C 52 (1991) 593.
[5] R. Venugopalan, M. Prakash, Nucl. Phys. A 546 (1992) 718.
[6] P. Gerber, H. Leutwyler, Nucl. Phys. B 321 (1989) 387.
[7] W. Weinhold, B. Friman, W. Nörenberg, Phys. Lett. B 433 (1998) 236.
[8] D.H. Rischke, Nucl. Phys. A 698 (2002) 153.
[9] P. Braun-Munzinger, K. Redlich, J. Stachel, Particle production in heavy ion collisions, in: R.C. Hwa, X.-N. Wang (Eds.), Quark–Gluon Plasma 3, World Scientific, Singapore, 2004, pp. 491–599, e-Print, arXiv:nucl-th/0304013.
[10] J. Stachel, A. Andronic, P. Braun-Munzinger, K. Redlich, J. Phys. Conf. Ser. 509 (2014) 012019.
[11] M. Floris, Nucl. Phys. A 931 (2014) 103.
[12] A. Andronic, Int. J. Mod. Phys. A 29 (2014) 1430047.
[13] I. Kraus, J. Cleymans, H. Oeschler, K. Redlich, Phys. Rev. C 79 (2009) 014901.
[14] F. Becattini, U.W. Heinz, Z. Phys. C 76 (1997) 269; Z. Phys. C 76 (1997) 578 (Erratum).
[15] F. Becattini, M. Gazdzicki, J. Sollfrank, Eur. Phys. J. C 5 (1998) 143.
[16] A. Kisiel, T. Taluc, W. Broniowski, W. Florkowski, Comput. Phys. Commun. 174 (2006) 669.
[17] M. Chojnacki, A. Kisiel, W. Florkowski, W. Broniowski, Comput. Phys. Commun. 183 (2012) 746.
[18] F. Karsch, K. Redlich, A. Tawfik, Eur. Phys. J. C 29 (2003) 549.
[19] P. Huovinen, P. Petreczky, Nucl. Phys. A 837 (2010) 26.
[20] A. Bazavov, et al., Phys. Rev. Lett. 109 (2012) 192302.
[21] C. Ratti, et al., Wuppertal–Budapest Collaboration, Nucl. Phys. A 855 (2011) 253.
[22] P. Braun-Munzinger, A. Kalweit, K. Redlich, J. Stachel, Phys. Lett. B 747 (2015) 292.
[23] W. Broniowski, F. Giacosa, V. Begun, Phys. Rev. C 92 (2015) 034905.
[24] B. Friman, P.M. Lo, M. Marczenko, K. Redlich, C. Sasaki, Phys. Rev. D 92 (2015) 074003.
[25] R. Dashen, S.K. Ma, H.J. Bernstein, Phys. Rev. 187 (1969) 345.
[26] E. Beth, G. Uhlenbeck, Physica 4 (1937) 915.
[27] K.G. Denisenko, S. Mrowczynski, Phys. Rev. C 35 (1987) 1932.
[28] W. Broniowski, W. Florkowski, B. Hiller, Phys. Rev. C 68 (2003) 034911.
[29] S.D. Protopopescu, et al., Phys. Rev. D 7 (1973) 1279.
[30] P. Estabrooks, A.D. Martin, Nucl. Phys. B 79 (1974) 301.
[31] C.D. Froggatt, J.L. Petersen, Nucl. Phys. B 129 (1977) 89.
[32] C. Gale, J.I. Kapusta, Nucl. Phys. B 357 (1991) 65.
[33] M. Herrmann, B.L. Friman, W. Norenberg, Nucl. Phys. A 560 (1993) 411.
[34] O. Dumbrajs, et al., Nucl. Phys. B 216 (1983) 277.
[35] M. Knecht, B. Moussallam, J. Stern, N.H. Fuchs, Nucl. Phys. B 457 (1995) 513.
[36] X.J. Wang, M.L. Yan, arXiv:hep-ph/0005184.
[37] F. Cooper, G. Frye, Phys. Rev. D 10 (1974) 186.
[38] J. Sollfrank, P. Koch, U.W. Heinz, Phys. Lett. B 252 (1990) 256.
[39] M.I. Gorenstein, M.S. Tsai, S.N. Yang, Phys. Rev. C 51 (1995) 1465.
[40] S. Borsanyi, Z. Fodor, C. Hoelbling, S.D. Katz, S. Krieg, K.K. Szabo, Phys. Lett. B 730 (2014) 99.
[41] A. Bazavov, et al., HotQCD Collaboration, Phys. Rev. D 90 (2014) 094503.
[42] E. Schnedermann, J. Sollfrank, U.W. Heinz, Phys. Rev. C 48 (1993) 2462.
[43] J.D. Bjorken, Phys. Rev. D 27 (1983) 140.
[44] H.j. Xu, Z. Li, H. Song, Phys. Rev. C 93 (2016) 064905.
[45] B.B. Abelev, et al., ALICE Collaboration, Phys. Lett. B 728 (2014) 216; Phys. Lett. B 734 (2014) 409 (Erratum).
[46] S. Takeuchi, K. Murase, T. Hirano, P. Huovinen, Y. Nara, Phys. Rev. C 92 (2015) 044907.
[47] N. Xu, Z.B. Xu, Nucl. Phys. A 715 (2003) 587.
[48] T. Hirano, M. Gyulassy, Nucl. Phys. A 769 (2006) 71.
[49] U.W. Heinz, R. Snellings, Annu. Rev. Nucl. Part. Sci. 63 (2013) 123.
[50] C. Gale, S. Jeon, B. Schenke, Int. J. Mod. Phys. A 28 (2013) 1340011.
[51] T. Hirano, P. Huovinen, K. Murase, Y. Nara, Prog. Part. Nucl. Phys. 70 (2013) 108.
[52] R. Derradi de Souza, T. Koide, T. Kodama, Prog. Part. Nucl. Phys. 86 (2016) 35.
[53] A. Jaiswal, V. Roy, arXiv:1605.08694 [nucl-th].
[54] R. Rapp, G. Chanfray, J. Wambach, Phys. Rev. Lett. 76 (1996) 368.
[55] R. Rapp, G. Chanfray, J. Wambach, Nucl. Phys. A 617 (1997) 472.
[56] F. Klingl, N. Kaiser, W. Weise, Nucl. Phys. A 624 (1997) 527.
[57] S. Leupold, W. Peters, U. Mosel, Nucl. Phys. A 628 (1998) 311.
[58] R. Rapp, J. Wambach, H. van Hees, Landolt-Bornstein 23 (2010) 134.
[59] P. Huovinen, H. Petersen, Eur. Phys. J. A 48 (2012) 171.

Dynamical freeze-out criterion in a hydrodynamical description of Au + Au collisions at $\sqrt{s_{NN}} = 200$ GeV and Pb + Pb collisions at $\sqrt{s_{NN}} = 2760$ GeV

Saeed Ahmad,[1] Hannu Holopainen,[2] and Pasi Huovinen[2,3]
[1]*STEM Division, Eastfield College, 3737 Motley Drive, Mesquite, Texas 75150, USA*
[2]*Frankfurt Institute for Advanced Studies, Ruth-Moufang-Str. 1, D-60438 Frankfurt am Main, Germany*
[3]*Institute of Theoretical Physics, University of Wroclaw, pl. M. Borna 9, PL-50204 Wrocław, Poland*
(Received 20 August 2016; revised manuscript received 28 March 2017; published 19 May 2017)

In hydrodynamical modeling of ultrarelativistic heavy-ion collisions, the freeze-out is typically assumed to take place at a surface of constant temperature or energy density. A more physical approach is to assume that freeze-out takes place at a surface of constant Knudsen number. We evaluate the Knudsen number as a ratio of the expansion rate of the system to the pion-scattering rate and apply the constant Knudsen number freeze-out criterion to the ideal hydrodynamical description of heavy-ion collisions at the Relativistic Heavy Ion Collider at BNL ($\sqrt{s_{\rm NN}} = 200$ GeV) and the Large Hadron Collider ($\sqrt{s_{\rm NN}} = 2760$ GeV) energies. We see that once the numerical values of freeze-out temperature and freeze-out Knudsen number are chosen to produce similar p_T distributions, the elliptic and triangular anisotropies are similar too, in both event-by-event and averaged initial state calculations.

DOI: 10.1103/PhysRevC.95.054911

I. INTRODUCTION

The fluid-dynamical description of heavy-ion collisions at the BNL Relativistic Heavy Ion Collider (RHIC) and the CERN Large Hadron Collider (LHC) has been very successful in reproducing the observed particle distributions and their anisotropies at low values of transverse momentum [1–3]. However, since what is experimentally observed is not a particle fluid, but individual particles, the fluid-dynamical description must break down at some point during the evolution, the interactions must cease, and the particles must start behaving instead like free-streaming particles. The particles decouple from the fluid, and their momentum distributions freeze-out—a process appropriately known as decoupling or freeze-out.

When the freeze-out happens is not described by fluid dynamics but has to be decided by using some other model or theory. Fluid dynamics is considered to be valid when the ratio of the microscopic to macroscopic scales of the system—its Knudsen number—is much smaller than one. In the context of heavy-ion collisions, fluid dynamics has traditionally been considered to be valid until either the mean free path of particles exceeds the size of the system, or the expansion rate exceeds the collision rate of the particles [4,5]. The Knudsen number can be defined in several ways [6], and thus both of these dynamical criteria are equivalent to the requirement that the Knudsen number is less than one. The idea of using the scattering and expansion rates as the limit for the validity of fluid dynamics, and thus as a decoupling criterion, is an old one [7], but it has been used in fluid-dynamical calculations only a couple of times [8–12]. Instead, the freeze-out is assumed to take place on a surface of constant temperature (or density). It has been argued that, since the scattering rate depends strongly on temperature ($\propto T^3$ for a constant cross section), the freeze-out is a very fast process, and thus a constant-temperature surface is a good approximation to the constant-Knudsen-number surface [5,13,14]. It is worth noticing that the well-known Gamow criterion in cosmology—that the time when interaction ceases to be effective is determined by the condition $t_{\rm int} \leqslant t_{\rm expan}$, where $t_{\rm int}$ and $t_{\rm expan}$ are the relevant interaction and expansion timescales [15]—is equivalent to freeze-out at constant Knudsen number and leads to decoupling at a certain temperature only because the expansion of the universe is taken to be uniform.

It was seen in earlier studies with optical Glauber initial profiles that, while the constant-Knudsen-number surface differs significantly from the constant-temperature surface, the effect on observable particle p_T distributions is small [11] and that elliptic flow of charged hadrons shows sensitivity to the freeze-out criterion only at large values of transverse momentum or rapidity, or in peripheral collisions [12]. However, in contemporary event-by-event hydrodynamical calculations, the flow develops more violently and more unevenly than when an averaged initial state is used [16]. Thus it is not obvious whether the two freeze-out conditions lead to similar particle distributions when the initial density fluctuates event by event. Furthermore, the evaluation of the Knudsen number in Refs. [11,12] was based either on pion-pion scattering ignoring all other scattering processes and the chemical nonequilibrium during the hadronic stage [11], or on assumed temperature dependence of the shear viscosity coefficient [12]. Thus it is unknown how more sophisticated calculations of the microscopic scale would affect the results.

In this work we further study whether the freeze-out criterion has any observable effects. We evaluate the p_T differential elliptic flow $v_2(p_T)$ of identified particles (pions and protons) in $\sqrt{s_{\rm NN}} = 200$ GeV Au + Au (RHIC) and $\sqrt{s_{\rm NN}} = 2760$ GeV Pb + Pb collisions (LHC) by using both constant-temperature and constant-Knudsen-number freeze-out criteria. To test our assumption that the large gradients in event-by-event calculations would make the system more sensitive to the freeze-out criterion, we model the collisions at RHIC both event by event and by using the averaged initial

state. We use the pion-scattering rate as the microscopic scale and calculate the rate in a chemically frozen hadron gas from scattering cross sections, including scatterings with all hadron species. Since our aim is not a faithful reproduction of the data, we simplify the description by using a simple boost-invariant ideal fluid model.

Note that, in this work, we use the conventional Cooper–Frye description (see Sec. III B) to evaluate the particle distributions at freeze-out. We do not address the negative contributions,[1] but our approach differs from the conventional freeze-out procedure only by the choice of the decoupling surface.

To some extent the freeze-out problem has been solved in so-called hybrid models, where the late stage of the evolution is described by using a Boltzmann transport model [19,20]. Nevertheless, the results in these models depend on when the switch from fluid to cascade is made [19,21], and therefore it is interesting to study how different criteria for particlization surface affect the particle distributions even in the context of hybrid models.

II. DYNAMICAL FREEZE-OUT CRITERION AND SCATTERING RATE

To maintain kinetic equilibrium in an expanding system the scattering rate must be much larger than the expansion rate. We express this condition as

$$\mathrm{Kn} = \frac{\theta}{\Gamma} \ll 1, \tag{1}$$

where Γ is the scattering rate and θ is the hydrodynamical expansion rate. When Kn approaches one, there are not enough collisions to maintain the kinetic equilibrium, and the system freezes out. Since Kn is a ratio between (an inverse of) a macroscopic length scale and (an inverse of) a microscopic length, it can be identified as a Knudsen number, which should be much smaller than one for fluid dynamics to be valid. Based on these considerations we define a dynamical freeze-out criterion as a surface of constant Knudsen number $\mathrm{Kn} = \mathrm{Kn}_f$, where $\mathrm{Kn}_f \sim 1$.

Before one can apply this criterion, the scattering rate must be known. We evaluate the pion-scattering rate in hadron resonance gas and use it in our freeze-out criterion for all particles. One could argue that we should calculate the scattering rate individually for each particle species and decouple them separately at the corresponding Knudsen number. However, in order to be consistent, one should also remove the decoupled particles from the fluid and model the interaction between the fluid and the decoupled particles,[2] which are not in equilibrium anymore. This cannot be consistently implemented (at least not easily) in the hydrodynamical framework and thus we make the simplifying assumption that the whole system decouples when the most abundant particles (i.e., pions) do.

[1]For a recent discussion, see Refs. [17,18].

[2]See the discussion about "pion wind" in Ref. [9].

Scattering rate of pions

Here we calculate the average scattering rate of pions in hadron resonance gas in kinetic equilibrium. The rate is obtained from [22–25]

$$\Gamma = \frac{1}{n_\pi(T,\mu_\pi)} \sum_i \int d^3p_\pi d^3p_i\, f_\pi(T,\mu_\pi) f_i(T,\mu_i) \times \frac{\sqrt{(s-s_a)(s-s_b)}}{2E_\pi E_i} \sigma_{\pi i}(s), \tag{2}$$

where n_π is the density of pions, $f_\pi(T,\mu_\pi)$ [$f_i(T,\mu_i)$] is the thermal distribution function of pions (particle i), with T being the temperature and μ_π (μ_i) being the chemical potential of pions (particle i). $\sqrt{(s-s_a)(s-s_b)}/(2E_\pi E_i)$ is the relative velocity when s is the square of the center-of-mass energy, $s_a = (m_\pi + m_i)^2$, $s_b = (m_\pi - m_i)^2$, and E_π (E_i) and m_π (m_π) are the energy and mass of pions (particle i). The pion-particle i scattering cross section is labeled $\sigma_{\pi i}$ and the sum runs over all particle species included in the equation of state (EoS) [26].

One can perform most of the integrals analytically and, after some algebra (see Appendix A), one arrives at

$$\Gamma = \frac{T}{n_\pi(T,\mu_\pi)} \sum_i \frac{g_i}{32\pi^4} \sum_{k=1}^{\infty} e^{k\mu_\pi/T} \sum_{n=1}^{\infty} \frac{(\mp 1)^{n+1}}{n} e^{n\mu_i/T} \times \int_{s_a}^{\infty} ds \frac{\sigma_{\pi i}(s)(s-s_a)(s-s_b)}{\sqrt{rs-(r-1)\left(m_i^2 - rm_\pi^2\right)}} \times K_1\left(\frac{n}{T}\sqrt{rs-(r-1)\left(m_i^2-rm_\pi^2\right)}\right), \tag{3}$$

where g_i is the degeneracy of particle i and $r = k/n$.

Cross sections are evaluated as in the UrQMD model [27,28]. Thus the largest contribution comes from resonance formation, which is evaluated by using the Breit–Wigner formula,

$$\sigma_{\pi i \to R}(s) = \frac{2g_R+1}{(2g_\pi+1)(2g_i+1)} \frac{\pi}{[p_{\mathrm{cms}}(\sqrt{s})]^2} \times \frac{\Gamma_{R\to\pi i}(\sqrt{s})\Gamma_{\mathrm{tot}}(\sqrt{s})}{(m_R-\sqrt{s})^2 + \Gamma_{\mathrm{tot}}^2(\sqrt{s})/4}, \tag{4}$$

where g_R, g_π, and g_i are the degeneracies of the resonance, pion, and particle i, and p_{cms} is the center-of-mass momentum of the scattering partners (see Appendix B). $\Gamma_{\mathrm{tot}}(M)$ is the full decay width obtained as a sum of all mass-dependent partial decay widths $\Gamma_{i,j}(M)$ (see Appendix C) given by

$$\Gamma_{R\to\pi i}(M) = \Gamma_R^{\pi i} \frac{m_R}{M} \left(\frac{p_{\mathrm{cms}}(M)}{p_{\mathrm{cms}}(m_R)}\right)^{2l+1} \frac{1.2}{1+0.2\left(\frac{p_{\mathrm{cms}}(M)}{p_{\mathrm{cms}}(m_R)}\right)^{2l}}, \tag{5}$$

where $\Gamma_R^{\pi i}$ is the partial decay width of the resonance into the πi channel at the pole, l is the decay angular momentum of the exit channel, and m_R is the pole mass of the resonance. The pole masses and the decay widths are taken from the Particle Data Book [29] as implemented in the calculation of the EoS [26].

In addition we assume elastic meson-meson scatterings with cross section $\sigma_{mm} = 5$ mb and elastic $\pi\pi$ scatterings with

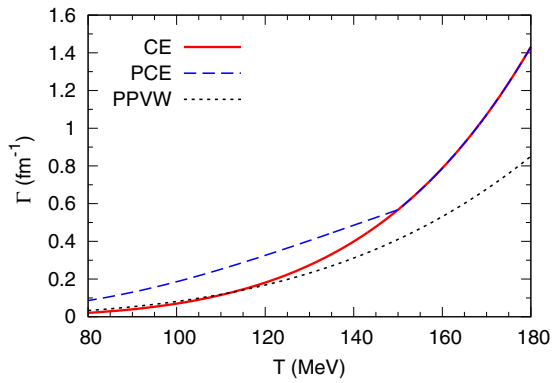

FIG. 1. The scattering rate of pions in both chemically equilibrated (CE, red solid line) and chemically frozen (PCE, blue dashed line) hadron resonance gas compared with the parametrization [30] of the rate evaluated in Ref. [24] (PPVW, black dotted line).

$\sigma_{\pi\pi} = \sigma_0 \exp[-(\sqrt{s} - m_0)^2/w]$ where $\sigma_0 = 15$ mb, $m_0 = 0.65$ GeV, and $w = 0.1$ GeV^2. With these choices we are able to reproduce the measured pion-pion, pion-kaon, and pion-nucleon scattering cross sections reasonably well.

In Fig. 1 we compare the evaluated scattering rates with the rates calculated in Ref. [24]. At low temperatures our simple approach agrees with the more sophisticated calculation of Ref. [24], but above the temperature $T \approx 120$ MeV our rate is larger simply because we include more states in the calculation, and thus the density of scattering partners is larger at large temperatures. Moreover, the scattering rate in a chemically frozen hadron gas is larger than the rate in a chemically equilibrated hadron gas due to larger particle densities.

III. HYDRODYNAMICAL FRAMEWORK

We use an updated version of the event-by-event ideal hydrodynamical framework developed in Ref. [16].

A. Ideal hydrodynamics

We solve the ideal hydrodynamical equations

$$\begin{aligned} \partial_\mu T^{\mu\nu} &= 0, \\ \partial_\mu j^\mu &= 0, \end{aligned} \tag{6}$$

where $T^{\mu\nu} = (\epsilon + P)u^\mu u^\nu - P g^{\mu\nu}$ is the ideal energy-momentum tensor, $j^\mu = n_B u^\mu$ the net-baryon current, ϵ is the energy density, P is the pressure, u^μ is the fluid four-velocity, and n_B is the net-baryon density. We use two different equations of state (EoS): *(i) s95p*-v1, which is always in chemical equilibrium, and *(ii) s95p*-PCE-v1, which has a chemical freeze-out at temperature $T_{\rm chem} = 150$ MeV [26]. Both of these EoSs assume zero net-baryon density.

We concentrate on the midrapidity region, where boost-invariance is a reasonable assumption at the LHC and full RHIC energies. This assumption reduces the number of dimensions in evolution equations to $2 + 1$. We use the sharp and smooth transport algorithm (SHASTA) [31] to solve the equations in hyperbolic coordinates, where one uses $\tau = \sqrt{t^2 - z^2}$ and $\eta_s = \frac{1}{2} \log \frac{t+z}{t-z}$ instead of time t and longitudinal coordinate z. At the antidiffusion stage of SHASTA we use DeVore limiter [32], which is a modified version of the Zalesak multidimensional limiter [33].

B. Freeze-out

We employ two different freeze-out criteria. One is the conventional constant-temperature criterion, and the other is the dynamical criterion, where we assume freeze-out at constant Knudsen number Kn. The hydrodynamical expansion rate is needed to obtain the Knudsen number, and in the boost-invariant case it is calculated as [34]

$$\theta = \partial_\mu u^\mu = \partial_\tau u^\tau + \partial_x u^x + \partial_y u^y + u^\tau/\tau. \tag{7}$$

In both cases the freeze-out surface elements $d\Sigma_\mu$ are obtained using CORNELIUS++ subroutine [21]. After the surface elements are found, we calculate the thermal spectrum of hadron species i by using Cooper–Frye prescription:

$$E\frac{d^3N_i}{d^3p} = \int_\Sigma d\Sigma_\mu p^\mu f_i(x,p), \tag{8}$$

where $f_i(x,p)$ is the thermal distribution function of hadron i and p^μ is the four-momentum of the hadron. At this stage we use the hadron gas EoS at nonzero net-baryon densities to convert the energy and net-baryon density to temperature and chemical potentials. Since the EoS during the fluid-dynamical evolution does not allow finite net-baryon density, this procedure is not fully consistent, but the violation of conservation laws is very small at RHIC and even smaller at the LHC.

After the thermal distributions of all hadron species have been evaluated, we sample individual hadrons as described in Ref. [16]. All strong and electromagnetic two- and three-particle decays are then calculated, and the daughter particles added to the respective thermal ensembles. Note that, unlike in Ref. [16], we no longer use PYTHIA to handle the decays, but evaluate the decays of all the resonances included in the EoS. When evaluating the charged-particle multiplicities we sample hadrons within an interval $|y| < 3$ to make sure that, at midrapidity, the system looks boost invariant after the decays as well. However, when we consider the identified particle p_T spectra and flow coefficients, we take all particles into account regardless of their rapidity to achieve better statistics.

C. Initial-state and centrality class definitions

The initial state and centrality classes are defined by using the Monte Carlo (MC) Glauber model described in Ref. [16]. Nucleons are randomly distributed to nucleus by using a standard two-parameter Woods–Saxon potential. Two nucleons from different nuclei collide if their transverse distance $r_d < \sqrt{\sigma_{NN}/\pi}$, where σ_{NN} is the inelastic nucleon-nucleon cross section. We take $\sigma_{NN} = 42$ mb at $\sqrt{s_{NN}} = 200$ GeV and $\sigma_{NN} = 64$ mb at $\sqrt{s_{NN}} = 2760$ GeV. Here we neglect nucleon-nucleon correlations and finite-size effects since their effects on anisotropies at midcentral collisions were found to be very small [35,36].

Multiplicity is taken to be proportional to the number of ancestors, $N_{\rm anc}$, which is a weighted sum of the number of

participants, $N_{\rm part}$, and the number of binary collisions, $N_{\rm bin}$, and is defined as

$$N_{\rm anc} = (1-f)N_{\rm part} + fN_{\rm bin}, \tag{9}$$

where f is the fraction of the binary collision contribution. This fraction f is chosen to reproduce the centrality dependence of multiplicity.

In principle, when a fit to the multiplicity data is made, one should first generate events with a certain f, sort the events according to their centrality, and then calculate the average number of ancestors in each centrality bin. Unfortunately, this is a very time-consuming procedure because a large number of events must be made for the centrality class definitions. Thus our approach here is to fix the centrality classes by using fixed impact parameter intervals. Because the average number of participants and binary collisions is now known at each centrality bin, a χ-squared fit can be easily made to fit the ratio f. This approximation is well justified, because average $N_{\rm part}$ and $N_{\rm bin}$ values are not sensitive to the centrality class definition.

After the fraction of binary collisions, f, is determined, we convert the centrality classes to the number of ancestors intervals. To fix f, we used the STAR Collaboration data [37] from RHIC, and the ALICE Collaboration data [38] from the LHC. We neglected the most-peripheral centrality classes starting from 60% centrality since we do not expect hydrodynamics to be applicable for peripheral collisions. Our result for RHIC is $f = 0.088$ and at the LHC we obtain $f = 0.17$.

The initial entropy density distribution $s(x,y)$ for a single event is taken to be

$$s(x,y) = \frac{K_{\rm sd}}{\sqrt{2\pi\sigma^2}} \sum w_i \exp\left(-\frac{(x-x_i)^2+(y-y_i)^2}{2\sigma^2}\right), \tag{10}$$

where the sum runs over all participants and binary collisions, w_i is the weight [$(1-f)$ for participant and f for binary collision], x_i and y_i are the transverse coordinates of a participant or a binary collision, and σ is a Gaussian smearing parameter controlling the shape of the distribution. The overall normalization constant $K_{\rm sd}$ is fixed to reproduce the observed multiplicity in the 0%–5% most-central collisions. In this work we use $\sigma = 0.8$ fm. We do not study the dependence of the results on σ because smaller width of the Gaussians leads to a formation of very-small-scale structures on the constant Knudsen number surface; see Ref. [39]. The scale of these structures is smaller than the mean free path of pions, and thus we do not consider them physical. At this stage we do not consider it worth the effort to improve the freeze-out criterion to remove these structures since further studies should be carried out by using viscous hydrodynamics, and dissipation is known to smear small-scale structures, anyway.

To calculate the average initial state, we average 1000 MC Glauber initial states. In this procedure impact parameters in each event are aligned. We first obtain an averaged entropy density profile and then use the EoS to convert it to energy density profile, which is the actual initial condition for hydrodynamics.

IV. RESULTS

We concentrate on the effects of the freeze-out criterion on particle distributions and their anisotropies and do not aim to faithfully reproduce the data. We compare the calculated p_T distributions to the data to show that our parameter choices are reasonable, but do not compare elliptic flow nor triangular flow with the data to avoid the need to evaluate the anisotropy the same way the particular data set was analyzed. It was seen in Ref. [12] that the favored freeze-out temperature and Knudsen number do not depend on centrality in the 0%–50% centrality range where fluid dynamics works best. We do not expect event-by-event fluctuations to change this behavior and therefore do not study the centrality dependence of the p_T spectra or anisotropies in detail. Instead, we mostly concentrate on the 20%–30% centrality bin, and leave the study of $p+A$ and peripheral $A+A$ collisions for a later work.

A. Averaged initial state in $\sqrt{s_{NN}} = 200$ GeV Au + Au collisions at the RHIC

To visualize how the freeze-out surface depends on the freeze-out criterion, we show the constant-temperature and constant-Knudsen-number freeze-out surfaces in Fig. 2. The surfaces are calculated by using an average initial state for a $\sqrt{s_{NN}} = 200$ GeV 20%–30% central Au + Au collision and chemically frozen *s95p*-PCE-v1 EoS. The constant-Knudsen-number surface is closer to the center of the system, and thus the edges of the system are hotter and the maximum flow velocity is lower than on the constant-temperature surface. On the other hand, the system lives longer, and the center decouples at lower temperature. Similar behavior can be seen at the LHC energy as well, and when chemical equilibrium is assumed.

In Fig. 3 we show the transverse momentum spectra of positive pions and protons in 20%–30% centrality class. The calculations were performed either by using the EoS *s95p*-v1, which assumes chemical equilibrium (Fig. 3, top panel), or the *s95p*-PCE-v1 EoS (Fig. 3, bottom panel), which assumes chemical freeze-out at $T_{\rm chem} = 150$ MeV. With the *s95p*-v1 EoS the initial time is the conventional $\tau_0 = 0.6$ fm, and the freeze-out temperature $T_f = 140$ MeV and Knudsen number

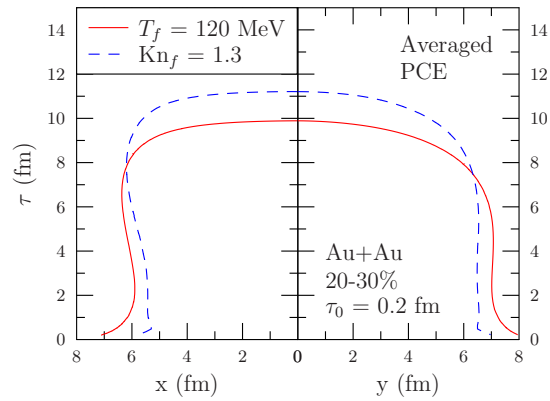

FIG. 2. Constant-temperature (solid red curve) and constant-Knudsen-number (dashed blue curve) freeze-out surfaces in $\sqrt{s_{NN}} =$ 200 GeV 20%–30% central Au + Au collisions. Surfaces are shown along the x and y axes.

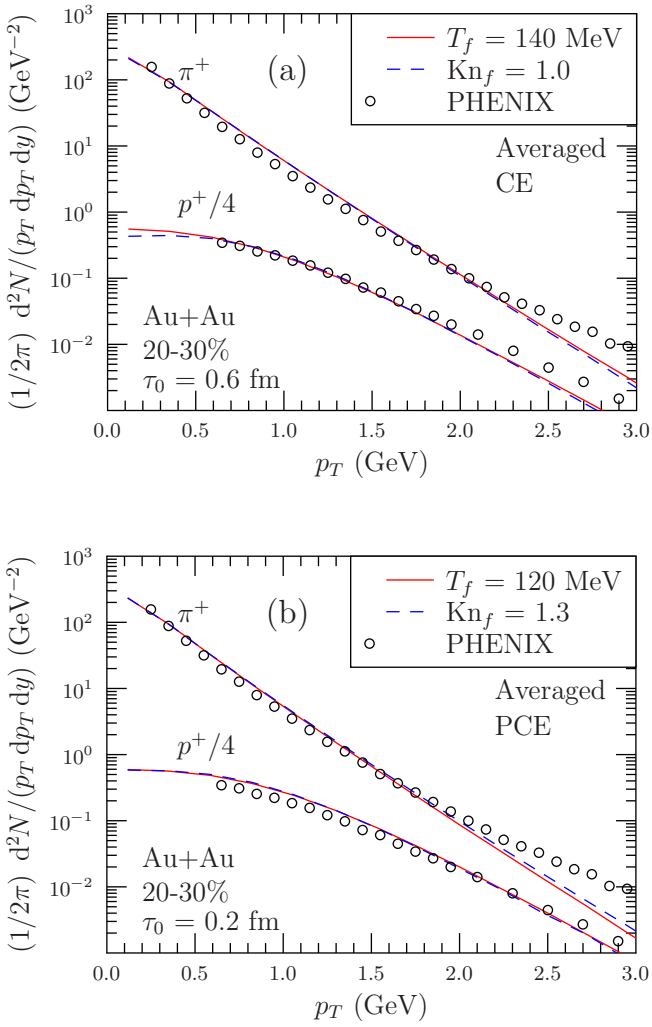

FIG. 3. Transverse momentum spectra of positive pions and protons in $\sqrt{s_{NN}} = 200$ GeV 20%–30% central Au + Au collisions assuming (a) chemically equilibrated or (b) chemically frozen EoS. The solid red line corresponds to the results obtained by using freeze-out at constant temperature and the dashed blue line by using freeze-out at constant Knudsen number. The data are from the PHENIX Collaboration [40].

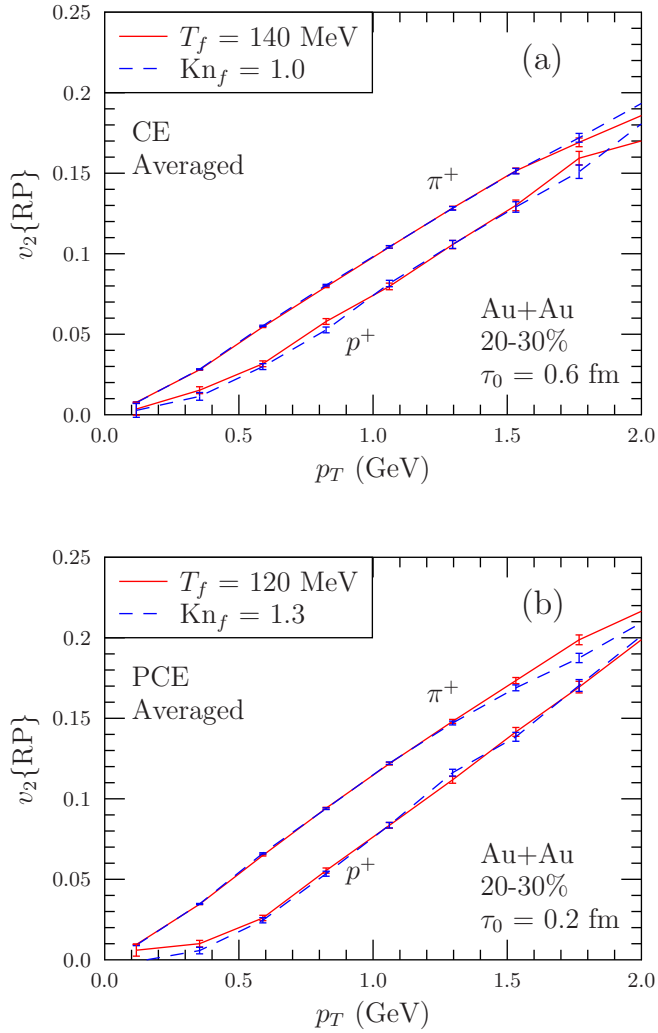

FIG. 4. Elliptic flow of positively charged pions and protons in $\sqrt{s_{NN}} = 200$ GeV 20%–30% central Au + Au collisions assuming (a) chemical or (b) partial chemical equilibrium in the EoS. The solid red line corresponds to the results obtained by using freeze-out at constant temperature and the dashed blue line by using freeze-out at constant Knudsen number. Error bars depict estimated statistical errors.

$\mathrm{Kn}_f = 1$ lead to almost identical pion and proton distributions which reproduce the data reasonably well.

The assumption of separate chemical freeze-out (Fig. 3, bottom) necessitates the use of an earlier initial time $\tau_0 = 0.2$ fm to make the proton spectrum hard enough.[3] When chemical equilibrium has been lost, the temperature decreases faster with decreasing energy density than in chemical equilibrium. This necessitates the use of lower freeze-out temperature $T_f = 120$ MeV, and larger freeze-out Knudsen number $\mathrm{Kn}_f = 1.3$ to get sufficient transverse flow to reproduce the data. Since Kn_f is a free parameter of the order of one, and the assumption of chemical equilibrium until the end of the evolution somewhat unphysical, it is acceptable that Kn_f is different for CE and PCE EoSs.

As shown it is possible to find constant-temperature and constant-Knudsen-number values for freeze-out, which give similar pion and proton spectra. This is a nontrivial result, since the corresponding freeze-out surfaces are different. On a constant-Knudsen-number surface the average flow velocity is lower, and the center decouples at lower temperature. These differences would make the spectra steeper, but their effect is canceled by the edges of the system freezing out at a higher temperature.

Next, in Fig. 4 we plot the p_T-differential elliptic flow $v_2(p_T)$ of pions and protons at $\sqrt{s_{NN}} = 200$ GeV 20%–30% central Au + Au collisions by using both EoSs and freeze-out criteria. Since we use an averaged initial state, we have evaluated the elliptic flow with respect to the reaction plane, $v_2\{\mathrm{RP}\}$.

[3]Later freeze-out, i.e., lower freeze-out temperature or larger freeze-out Knudsen number, would make the pion spectrum too soft; see discussions in Refs. [41,42].

In our earlier proceedings contribution [43], we saw that elliptic flow was sensitive to the freeze-out criterion when *s95p*-PCE-v1 EoS was used. However, in that calculation we had fixed $\mathrm{Kn}_f = 1.0$, and the p_T distributions were different as well. Now, after choosing the freeze-out Knudsen number to reproduce the data and the spectra calculated by using the constant-temperature freeze-out criterion, both freeze-out criteria lead to similar elliptic flow. The same happens also when we keep $\mathrm{Kn}_f = 1.0$ fixed, and adjust the freeze-out temperature instead to $T_f = 140$ MeV to achieve similar spectra.

To study whether the sensitivity to the freeze-out criterion might depend on the initial state, we performed the calculations by using a pure binary-collision profile as well. We used an initial time $\tau_0 = 0.6$ fm, freeze-out temperature $T_f = 120$ MeV, and Knudsen number $\mathrm{Kn}_f = 1.3$ with *s95p*-PCE-v1 and found that the spectra and elliptic flow were again independent of the freeze-out criterion. Thus we suspect that this similarity with both criteria is not due to some property of the initial state but could be a more general phenomenon. Also note that the same pair of constant temperature and constant Knudsen number worked with both initial states.

B. Event-by-event fluctuating initial states in $\sqrt{s_{NN}} = 200$ GeV Au + Au collisions at the RHIC

As argued in the introduction, in event-by-event calculations the two freeze-out criteria might lead to different results, even if the results were similar when averaged initial state was used. To study this assumption, we modeled the collisions at RHIC event by event by using the chemically frozen *s95p*-PCE-v1 EoS. We followed the same procedure than in our calculations using an averaged initial state and treated both the freeze-out temperature and Knudsen number as free parameters to be adjusted to reproduce the observed p_T spectra. It turned out that the same combination of parameters,

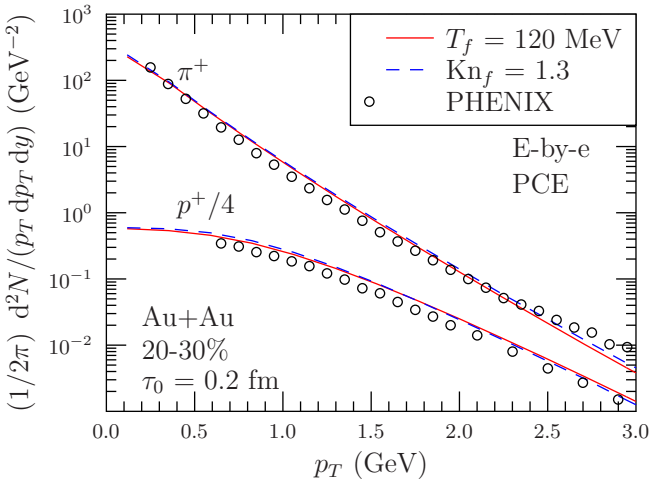

FIG. 5. Transverse momentum spectra of positively charged pions and protons in $\sqrt{s_{NN}} = 200$ GeV 20%–30% central Au + Au collisions from event-by-event hydrodynamical simulations. The solid red line corresponds to the results obtained by using freeze-out at constant temperature and the dashed blue line by using freeze-out at constant Knudsen number. The data are from the PHENIX Collaboration [40].

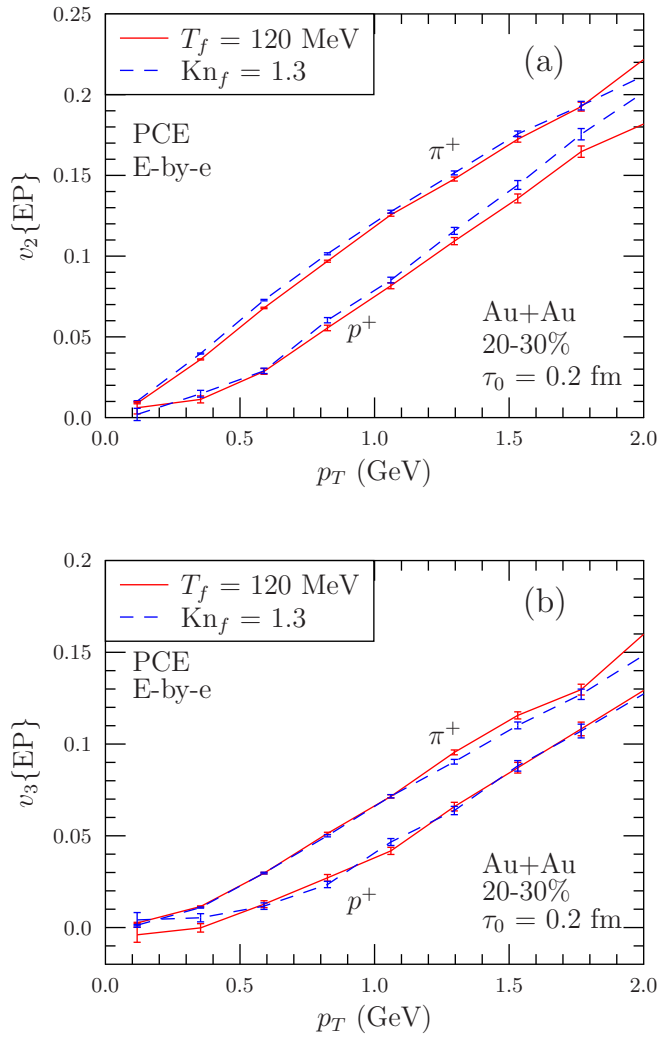

FIG. 6. (a) Elliptic and (b) triangular flow of positive pions and protons in $\sqrt{s_{NN}} = 200$ GeV 20%–30% central Au + Au collisions from event-by-event hydrodynamical simulations. The solid red line corresponds to the results obtained by using freeze-out at constant temperature and the dashed blue line by using freeze-out at constant Knudsen number. Error bars depict estimated statistical errors.

$T_f = 140$ MeV and $\mathrm{Kn}_f = 1.3$, lead to a reasonable reproduction of the data in both event-by-event and averaged initial state calculations; see Figs. 5 and 3, respectively. However, as observed before, e.g., in Ref. [16], the spectra are a little bit flatter in the event-by-event case.

The p_T-differential elliptic and triangular flows are shown in Fig. 6. In event-by-event calculations it makes more sense to calculate the flow coefficients with respect to their event planes, and therefore $v_n\{EP\}$ values are shown in the figures. Consequently, comparison with the averaged initial state case cannot be made, because the definitions of flow are different.

Unlike what we expected, there is no significant difference between the freeze-out criteria. We also checked with a smaller number of events that in the most-central collisions, where both v_2 and v_3 are generated mostly by fluctuations, the situation is the same. Thus both anisotropies seem to be insensitive to the freeze-out criterion in event-by-event calculations, too.

We have also checked that, in individual events, the spectra, elliptic flow, and triangular flow are not necessarily the same with the parameters used, but the difference can be of the order of 10% in each studied variable. This opens up the question of whether the event-by-event distribution of anisotropies [44] might be sensitive to the freeze-out criterion, and how the freeze-out criterion would affect the correlation between the initial-state anisotropy and final momentum anisotropy [44,45]. We have not checked either what would happen if we adjusted the freeze-out criteria event-by-event so that the p_T distributions were similar in each single event.

C. Averaged initial state in $\sqrt{s_{NN}} = 2760$ GeV Pb + Pb collisions at the LHC

At a single collision energy one can always fix the freeze-out temperature to reproduce the p_T spectra, but there is no physical reason why the same freeze-out temperature should work at another collision energy. On the other hand, the dynamical criterion with freeze-out at constant Knudsen number is based on local expansion dynamics and general considerations about the validity of hydrodynamics, and therefore we can expect the freeze-out to take place at the same value of Knudsen number independent of the collision energy. Thus it is worthwhile to check what happens in collisions at the LHC energy.

In Fig. 7 we show the transverse momentum spectra of pions and protons in $\sqrt{s_{NN}} = 2760$ GeV 0%–5% central Pb + Pb collisions using averaged initial state and *s95p*-PCE-v1 EoS. Both in the shown 0%–5% centrality class, and in the semicentral 20%–30% centrality class, the favored freeze-out temperature was the same $T_f = 120$ MeV both at the RHIC and at the LHC, but the data favored lower freeze-out Knudsen number $\mathrm{Kn}_f = 1.0$ at the LHC. Thus, as expected, the freeze-out Knudsen number does not depend on the centrality of the collision, but contrary to expectations, it depends on the collision energy. The dependence on collision energy may be an effect of neglecting dissipation: When the dynamical criterion of freeze-out at constant Knudsen number was used in the context of dissipative hydro [12], the same freeze-out Knudsen number worked both at the RHIC and the LHC. On the other hand, since the slopes of the final p_T distributions depend on the initial pressure gradients, the collision energy dependence of the freeze-out Knudsen number may also indicate that our Glauber-based initial-state model does not properly reproduce the initial gradients. Thus it would be interesting to apply the dynamical freeze-out criterion to more sophisticated EKRT [45–47] and IP-Glasma [48,49] initial states.

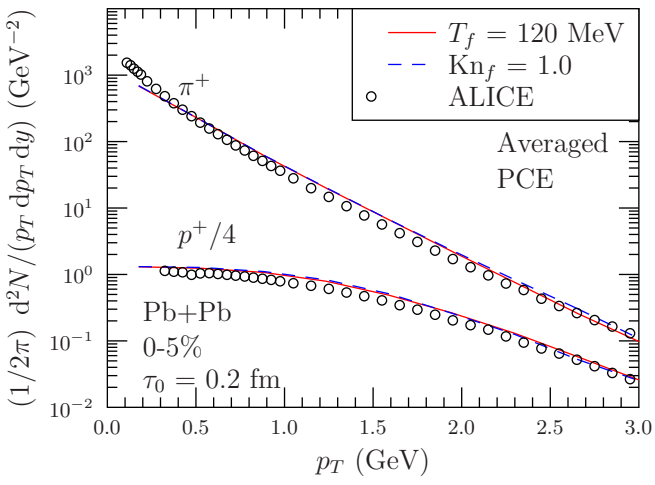

FIG. 7. Transverse momentum spectra of positive pions and protons in $\sqrt{s_{NN}} = 2760$ GeV 0-5% central Pb + Pb collisions. The solid red line corresponds to the results obtained by using freeze-out at constant temperature and the dashed blue line by using freeze-out at constant Knudsen number. The data are from the ALICE Collaboration [50].

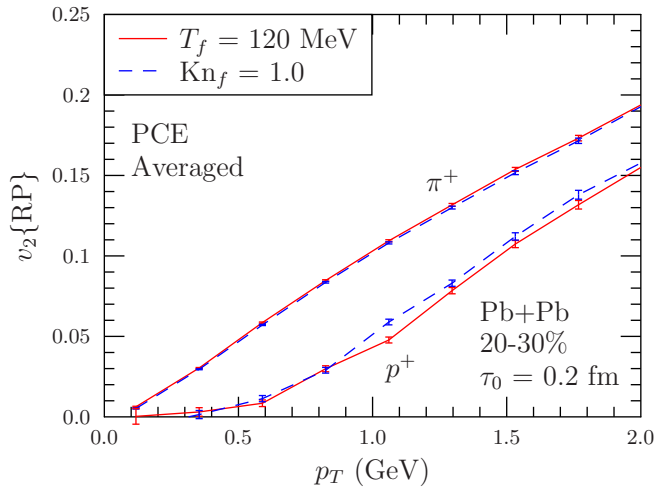

FIG. 8. Elliptic flow of positive pions and protons in $\sqrt{s_{NN}} = 2760$ GeV 20%–30% central Pb + Pb collisions. The solid red line corresponds to the results obtained by using freeze-out at constant temperature and the dashed blue line by using freeze-out at constant Knudsen number. Error bars depict estimated statistical errors.

The p_T-differential elliptic flow of pions and protons shown in Fig. 8 depicts the same pattern at the LHC as at the RHIC: Once the p_T spectra are reproduced, both freeze-out criteria lead to similar elliptic flow.

To be sure, we carried out the event-by-event calculations at the LHC energy too, but saw the very same behavior as at the RHIC and when using the averaged initial state: Once the freeze-out parameters were chosen to reproduce the observed spectra ($T_f = 120$ MeV and $\mathrm{Kn}_f = 1.0$), the elliptic and triangular flows were similar, too.

V. CONCLUSIONS

As argued in the introduction, freeze-out criterion based on freeze-out at a constant temperature is an oversimplification, and a dynamical criterion where freeze-out takes place at constant Knudsen number would be more physical. However, we saw that, in semicentral and central collisions, identified particle spectra and elliptic and triangular flows are not sensitive to the freeze-out criterion.

We evaluated the Knudsen number as the ratio of the expansion rate of the system, and the scattering rate of pions. We applied the freeze-outs at constant temperature and constant Knudsen number to ideal fluid calculations of

Au + Au collisions at the RHIC and Pb + Pb collisions at the LHC at 20%–30% centrality, and fixed the values of freeze-out parameters by fitting the observed pion and proton p_T distributions. The two criteria lead to different freeze-out surfaces: with dynamical freeze-out the edges decouple earlier (i.e., at higher temperature) and the center of the system lives longer, letting the matter cool more compared with the constant-temperature case. However, after the p_T spectra were constrained to be similar, no sign of the different temperatures and flow velocities on the freeze-out surface could be seen in the anisotropies.

We did check that the same insensitivity persists in most-central collisions, but we did not check what might happen when the collision system is much smaller, such as in peripheral $A + A$ or in $p + A$ collisions. The earlier results of Ref. [12] indicate that the sensitivity to the freeze-out criterion increases when the system size or collision energy decreases, and thus the $p + A$ collision system could be very sensitive to the freeze-out criterion. Maybe even to such an extent that the Knudsen number at the very beginning of the evolution is larger than one [6].

Our event-by-event calculations revealed that even if the spectra and anisotropies after averaging over many events were not sensitive to the freeze-out criterion, spectra and anisotropies in individual events were. This leaves open the question of whether event-by-event distributions of average p_T or anisotropy coefficients v_n might be sensitive to the freeze-out criterion. One could also expect that HBT radii would be an observable which is more sensitive than the anisotropies to the exact properties of the freeze-out surface.

Unfortunately, we were unable to study how the value of the smearing parameter σ of the Monte Carlo Glauber model affects the sensitivity to freeze-out, and thus whether small-scale density fluctuations in the initial state might affect the freeze-out. This remains to be explored in a further study, although one may expect that dissipation has largely smeared away small-scale structures by the time of freeze-out.

ACKNOWLEDGMENTS

Fruitful discussions with S. Bass, M. Bleicher, H. van Hees, H. Honkanen, J. I. Kapusta, A. Kurkela, D. Molnar, B. Tomasik, and R. Venugopalan are gratefully acknowledged. We thank J. Jankowski, M. A. R. Kaltenborn, M. Marczenko, and H. Niemi for careful reading of the manuscript and constructive comments. P.H. thanks for hospitality the Iowa State University and Goethe University where part of this work was done. During the long gestation of this project, the work of P.H. has been supported by the National Science Center, Poland, under Grant Polonez DEC-2015/19/P/ST2/03333 funded from the European Union's Horizon 2020 research and innovation programme under the Marie Skłodowska-Curie Grant Agreement No. 665778, the National Science Center, Poland, under Maestro Grant DEC-2013/10/A/ST2/00106, BMBF under Contract No. 06FY9092, the ExtreMe Matter Institute (EMMI), DOE Grant DE-AC02-98CH10886, and the Johannes Råttendahl foundation. The works of S.A. and H.H. have been supported by DOE Grant DE-FG02-01ER41200 and the ExtreMe Matter Institute (EMMI), respectively.

APPENDIX A: INTEGRALS IN CALCULATION OF SCATTERING RATE

The reduction of the number of integrals over momentum in the scattering-rate calculations has been shown in Ref. [25] for equal-mass particles obeying Boltzmann statistics, and generalized for nonidentical particles when the scattering partner has a fixed momentum in Ref. [22]. For the sake of completeness, we repeat the process here and generalize it for quantum statistics.

The total number of times pions scatter with particles i per unit volume per unit time is given by

$$\mathcal{R}_i = 2\int_{s_a}^{\infty} ds\sqrt{(s-s_a)(s-s_b)}\sigma_{\pi i}(s)\int \frac{d^3p_\pi}{2E_\pi}\frac{d^3p_i}{2E_i} f_\pi(T,\mu_\pi) f_i(T,\mu_i)\delta(s-(p_i+p_\pi)^2), \tag{A1}$$

where, compared with Eq. (2), we have added the integration over center-of-mass energy s and the corresponding δ function. To proceed we express the distribution functions f_π and f_i as a series:

$$f_i(T,\mu_i) = \frac{g_i}{(2\pi)^3}\frac{1}{e^{\frac{E-\mu_i}{T}}\pm 1} = \frac{g_i}{(2\pi)^3}\sum_{n=1}^{\infty}(\mp 1)^{n+1}e^{n\mu_i/T}e^{-nE/T}, \tag{A2}$$

where -1 in the series is for fermions and $+1$ for bosons, change the momentum coordinates to spherical coordinates, change the integral over the magnitude of momentum to integral over energy, and rewrite the δ function as

$$\delta(s-(p_i+p_\pi)^2) = \frac{1}{2|\mathbf{p}_\pi||\mathbf{p}_i|}\delta\left(\cos\theta_i + \frac{s-\left(m_\pi^2+m_i^2\right)-2E_\pi E_i}{2|\mathbf{p}_\pi||\mathbf{p}_i|}\right). \tag{A3}$$

The angular integrals can now be carried out, and we get

$$\mathcal{R}_i = \frac{g_i}{2^5\pi^4}\sum_{k=1}^{\infty}e^{k\mu_\pi/T}\sum_{n=1}^{\infty}(\mp 1)^{n+1}e^{n\mu_i/T}\int_{s_a}^{\infty} ds\sqrt{(s-s_a)(s-s_b)}\sigma_{\pi i}(s)$$
$$\times\int_{m_\pi}^{\infty} dE_\pi\int_{m_i}^{\infty} dE_i e^{-\frac{k}{T}\left(E_\pi+\frac{n}{k}E_i\right)}\Theta\left(1-\left|\frac{s-\left(m_\pi^2+m_i^2\right)-2E_\pi E_i}{2|\mathbf{p}_\pi||\mathbf{p}_i|}\right|\right). \tag{A4}$$

We change the integration variables from E_π and E_i to $y = E_\pi + \frac{1}{r}E_i$ and $x = E_\pi - \frac{1}{r}E_i$, where $r = k/n$. The Θ function constraint can now be written as $b < x < c$, where

$$b = \frac{\left(r^2 m_\pi^2 - m_i^2\right)y - d}{rs - (r-1)\left(m_i^2 - r m_\pi^2\right)}, \quad c = \frac{\left(r^2 m_\pi^2 - m_i^2\right)y + d}{rs - (r-1)\left(m_i^2 - r m_\pi^2\right)},$$
$$d = \sqrt{r^2 y^2 - \left[rs - (r-1)\left(m_i^2 - r m_\pi^2\right)\right]}\sqrt{(s-s_a)(s-s_b)}. \tag{A5}$$

It turns out that the integration over x is constrained more by the Θ function than by the integration limits, and we get

$$\mathcal{R}_i = \frac{g_i}{2^6\pi^4}\sum_{k=1}^{\infty} e^{k\mu_\pi/T}\sum_{n=1}^{\infty}(\mp 1)^{n+1}e^{n\mu_i/T} r\int_{s_a}^{\infty} ds\sqrt{(s-s_a)(s-s_b)}\sigma_{\pi i}(s)\int_{\alpha}^{\infty} dy e^{-\frac{ky}{T}}(c-b), \tag{A6}$$

where

$$\alpha = \sqrt{\frac{s}{r} - \frac{r-1}{r^2}\left(m_i^2 - r m_\pi^2\right)}. \tag{A7}$$

The y integral can now be reordered and carried out to be

$$\int_{\alpha}^{\infty} dy e^{-k\frac{y}{T}}\sqrt{y^2-\alpha^2} = \frac{T\alpha}{k}K_1\left(\frac{k\alpha}{T}\right), \tag{A8}$$

where K_1 is the modified Bessel function. Inserting this into Eq. (A6) and keeping the y-independent terms omitted from Eq. (A8), we finally get

$$\mathcal{R}_i = \frac{g_i T}{2^5\pi^4}\sum_{k=1}^{\infty} e^{k\mu_\pi/T}\sum_{n=1}^{\infty}\frac{(\mp 1)^{n+1}}{n}e^{n\mu_i/T}\int_{s_a}^{\infty} ds\frac{(s-s_a)(s-s_b)\sigma_{\pi i}(s)}{\sqrt{rs-(r-1)\left(m_i^2 - r m_\pi^2\right)}}K_1\left(\frac{n}{T}\sqrt{rs-(r-1)\left(m_i^2 - r m_\pi^2\right)}\right). \tag{A9}$$

After summing over all particles i and dividing by the pion density, we get Eq. (3).

APPENDIX B: CENTER-OF-MASS MOMENTUM IN PARTICLE-RESONANCE SCATTERING

If one of the scattering partners is a resonance, the conventional expression for the center-of-mass momentum of the scattering,

$$p_{\rm cms}(\sqrt{s},m_1,m_2) = \frac{\sqrt{[s-(m_1+m_2)^2][s-(m_1-m_2)^2]}}{2\sqrt{s}}, \tag{B1}$$

must be amended to take into account the finite width of the resonance. To do this, we again mostly follow the UrQMD description [27] and include an integral over the mass distribution of the resonance:

$$p_{\rm cms}(\sqrt{s}) = \int_0^{\sqrt{s}-m_\pi} dm\ p_{CMS}(\sqrt{s},m_\pi,m) \times \frac{1}{2\pi}\frac{\Gamma_R}{(m_R-m)^2+\Gamma_R^2/4}, \tag{B2}$$

where we assume the mass distribution to be the Breit–Wigner distribution with mass-independent width Γ_R, and m_R is the pole mass of the resonance.

Note that, in the integrals of Appendix A and in the evaluation of the EoS, the resonances have been assumed to have zero width, and their pole masses have been used as their masses.

APPENDIX C: FULL DECAY WIDTH

The evaluation of the full decay width $\Gamma_{\rm tot}(M)$ in Eq. (4) requires knowledge of partial decay widths of three- and four-body decay channels as well. Unfortunately, Eq. (5) cannot be easily generalized to many-body decays. To treat all decay channels in a similar fashion, we combine the particles in three- and four-body decays into a particle and a particle pair, or two particle pairs, respectively, use the invariant mass(es) of particle pair(s) to evaluate the center-of-mass momentum [Eq. (B1)], and use the available phase space to give the mass distribution of the invariant mass of the pair(s). In particular, for three-body decays we obtain

$$p_{\rm cms}(M) = \frac{8M}{N}\int_{m_1+m_2}^{M-m_3} dm_{\rm pair}\left[p_{\rm cms}\left(M,m_{\rm pair},m_3\right)\right]^2 \times p_{\rm cms}\left(m_{\rm pair},m_1,m_2\right), \tag{C1}$$

where the normalization factor N is given by

$$N = 8M\int_{m_1+m_2}^{M-m_3} dm_{\rm pair}\, p_{\rm cms}\left(M,m_{\rm pair},m_3\right) \times p_{\rm cms}\left(m_{\rm pair},m_1,m_2\right). \tag{C2}$$

If any of the daughter particles in a multiparticle decay is a resonance, we use its pole mass only and neglect its width.

[1] U. W. Heinz and R. Snellings, Annu. Rev. Nucl. Part. Sci. **63**, 123 (2013).
[2] C. Gale, S. Jeon, and B. Schenke, Int. J. Mod. Phys. A **28**, 1340011 (2013).
[3] H. Niemi, Nucl. Phys. A **931**, 227 (2014).
[4] U. W. Heinz, K. S. Lee, and E. Schnedermann, in *Quark-Gluon Plasma*, edited by R. C. Hwa (World Scientific, Singapore, 1990), p. 471.
[5] P. F. Kolb and U. W. Heinz, in *Quark-Gluon Plasma 3*, edited by R. C. Hwa and X.-N. Wang (World Scientific, Singapore, 2004), p. 634.
[6] H. Niemi and G. S. Denicol, arXiv:1404.7327.
[7] J. P. Bondorf, S. I. A. Garpman, and J. Zimanyi, Nucl. Phys. A **296**, 320 (1978).
[8] I. N. Mishustin and L. M. Satarov, Yad. Fiz. **37**, 894 (1983) [Sov. J. Nucl. Phys. **37**, 532 (1983)].
[9] C. M. Hung and E. V. Shuryak, Phys. Rev. C **57**, 1891 (1998).
[10] U. Heinz and G. Kestin, PoS (CPOD2006) 038.
[11] K. J. Eskola, H. Niemi, and P. V. Ruuskanen, Phys. Rev. C **77**, 044907 (2008).
[12] E. Molnar, H. Holopainen, P. Huovinen, and H. Niemi, Phys. Rev. C **90**, 044904 (2014).
[13] D. H. Rischke, Lect. Notes Phys. **516**, 21 (1999).
[14] E. Schnedermann and U. W. Heinz, Phys. Rev. C **50**, 1675 (1994).
[15] D. J. Raine and E. G. Thomas, *An Introduction to the Science of Cosmology* (IoP Publishing, Bristol, 2001).
[16] H. Holopainen, H. Niemi, and K. J. Eskola, Phys. Rev. C **83**, 034901 (2011).
[17] D. Oliinychenko, P. Huovinen, and H. Petersen, Phys. Rev. C **91**, 024906 (2015).
[18] D. Oliinychenko, P. Huovinen, and H. Petersen, J. Phys.: Conf. Ser. **599**, 012017 (2015).
[19] T. Hirano, P. Huovinen, K. Murase, and Y. Nara, Prog. Part. Nucl. Phys. **70**, 108 (2013).
[20] H. Petersen, J. Phys. G **41**, 124005 (2014).
[21] P. Huovinen and H. Petersen, Eur. Phys. J. A **48**, 171 (2012).
[22] B. Tomasik and U. A. Wiedemann, Phys. Rev. C **68**, 034905 (2003).
[23] J. Ftacnik, P. Lichard, N. Pisutova, and J. Pisut, Z. Phys. C: Part. Fields **42**, 139 (1989).
[24] M. Prakash, M. Prakash, R. Venugopalan, and G. Welke, Phys. Rep. **227**, 321 (1993).
[25] B. Zhang, M. Gyulassy, and Y. Pang, Phys. Rev. C **58**, 1175 (1998).
[26] P. Huovinen and P. Petreczky, Nucl. Phys. A **837**, 26 (2010).
[27] S. A. Bass *et al.*, Prog. Part. Nucl. Phys. **41**, 255 (1998).
[28] M. Bleicher *et al.*, J. Phys. G **25**, 1859 (1999).
[29] Particle Data Group, S. Eidelman *et al.*, Phys. Lett. B **592**, 1 (2004).
[30] R. G. Daghigh and J. I. Kapusta, Phys. Rev. D **65**, 064028 (2002).
[31] J. P. Boris and D. L. Book, J. Comput. Phys. **11**, 38 (1973).
[32] C. R. DeVore, J. Comput. Phys. **92**, 142 (1991).
[33] S. T. Zalesak, J. Comput. Phys. **31**, 335 (1979).
[34] A. Dumitru, Phys. Lett. B **463**, 138 (1999).
[35] M. Alvioli, H. Holopainen, K. J. Eskola, and M. Strikman, Phys. Rev. C **85**, 034902 (2012).
[36] G. S. Denicol, C. Gale, S. Jeon, J.-F. Paquet, and B. Schenke, arXiv:1406.7792.
[37] B. I. Abelev *et al.* (STAR Collaboration), Phys. Rev. C **79**, 034909 (2009).
[38] K. Aamodt *et al.* (ALICE Collaboration), Phys. Rev. Lett. **106**, 032301 (2011).
[39] H. Holopainen and P. Huovinen, J. Phys.: Conf. Ser. **389**, 012018 (2012).
[40] S. S. Adler *et al.* (PHENIX Collaboration), Phys. Rev. C **69**, 034909 (2004).
[41] T. Hirano and M. Gyulassy, Nucl. Phys. A **769**, 71 (2006).
[42] P. Huovinen, Eur. Phys. J. A **37**, 121 (2008).
[43] H. Holopainen and P. Huovinen, J. Phys.: Conf. Ser. **509**, 012114 (2014).
[44] H. Niemi, G. S. Denicol, H. Holopainen, and P. Huovinen, Phys. Rev. C **87**, 054901 (2013).
[45] H. Niemi, K. J. Eskola, and R. Paatelainen, Phys. Rev. C **93**, 024907 (2016).
[46] K. J. Eskola, K. Kajantie, P. V. Ruuskanen, and K. Tuominen, Nucl. Phys. B **570**, 379 (2000).
[47] R. Paatelainen, K. J. Eskola, H. Holopainen, and K. Tuominen, Phys. Rev. C **87**, 044904 (2013).
[48] B. Schenke, P. Tribedy, and R. Venugopalan, Phys. Rev. Lett. **108**, 252301 (2012).
[49] B. Schenke, P. Tribedy, and R. Venugopalan, Phys. Rev. C **86**, 034908 (2012).
[50] B. Abelev *et al.* (ALICE Collaboration), Phys. Rev. Lett. **109**, 252301 (2012).

Computer Physics Communications 185 (2014) 3016–3027

Contents lists available at ScienceDirect

Computer Physics Communications

journal homepage: www.elsevier.com/locate/cpc

A 3 + 1 dimensional viscous hydrodynamic code for relativistic heavy ion collisions☆

Iu. Karpenko [a,b,*], P. Huovinen [a,c], M. Bleicher [a,c]

[a] Frankfurt Institute for Advanced Studies, Ruth-Moufang-Straße 1, 60438 Frankfurt am Main, Germany

[b] Bogolyubov Institute for Theoretical Physics, 14-b, Metrolohichna str., 03680 Kiev, Ukraine

[c] Institute for Theoretical Physics, Johann Wolfgang Goethe Universität, Max-von-Laue-Str. 1, 60438 Frankfurt am Main, Germany

ARTICLE INFO

Article history:
Received 10 February 2014
Received in revised form
18 June 2014
Accepted 12 July 2014
Available online 23 July 2014

Keywords:
Quark–gluon plasma
Hydrodynamics
Relativity

ABSTRACT

We describe the details of 3 + 1 dimensional relativistic hydrodynamic code for the simulations of quark–gluon/hadron matter expansion in ultra-relativistic heavy ion collisions. The code solves the equations of relativistic viscous hydrodynamics in the Israel–Stewart framework. With the help of ideal–viscous splitting, we keep the ability to solve the equations of ideal hydrodynamics in the limit of zero viscosities using a Godunov-type algorithm. Milne coordinates are used to treat the predominant expansion in longitudinal (beam) direction effectively. The results are successfully tested against known analytical relativistic inviscid and viscous solutions, as well as against existing 2 + 1D relativistic viscous code.

Program summary

Program title: vHLLE

Catalogue identifier: AETZ_v1_0

Program summary URL: http://cpc.cs.qub.ac.uk/summaries/AETZ_v1_0.html

Program obtainable from: CPC Program Library, Queen's University, Belfast, N. Ireland

Licensing provisions: Standard CPC licence, http://cpc.cs.qub.ac.uk/licence/licence.html

No. of lines in distributed program, including test data, etc.: 13 825

No. of bytes in distributed program, including test data, etc.: 92 750

Distribution format: tar.gz

Programming language: C++.

Computer: any with a C++ compiler and the CERN ROOT libraries.

Operating system: tested on GNU/Linux Ubuntu 12.04 x64 (gcc 4.6.3), GNU/Linux Ubuntu 13.10 (gcc 4.8.2), Red Hat Linux 6 (gcc 4.4.7).

RAM: scales with the number of cells in hydrodynamic grid; 1900 Mbytes for 3D 160 × 160 × 100 grid.

Classification: 1.5, 4.3, 12.

External routines: CERN ROOT (http://root.cern.ch), Gnuplot (http://www.gnuplot.info/) for plotting the results.

Nature of problem:
relativistic hydrodynamical description of the 3-dimensional quark–gluon/hadron matter expansion in ultra-relativistic heavy ion collisions.

Solution method:
finite volume Godunov-type method.

☆ This paper and its associated computer program are available via the Computer Physics Communication homepage on ScienceDirect (http://www.sciencedirect.com/science/journal/00104655).

* Corresponding author at: Frankfurt Institute for Advanced Studies, Ruth-Moufang-Straße 1, 60438 Frankfurt am Main, Germany. Tel.: +49 17639900812.
E-mail addresses: karpenko@fias.uni-frankfurt.de, karpenko@bitp.kiev.ua (Iu. Karpenko).

http://dx.doi.org/10.1016/j.cpc.2014.07.010

Running time:
scales with the number of hydrodynamic cells; typical running times on Intel(R) Core(TM) i7-3770 CPU @ 3.40 GHz, single thread mode, $160 \times 160 \times 100$ grid and $p = \varepsilon/3$ EoS (setup discussed in Sec. 4.4):
7.6 sec/timestep for ideal hydro evolution;
15.7 sec/timestep for viscous hydro evolution;
37 sec/timestep for tabulated EoS and ideal hydro evolution.

1. Introduction

Relativistic fluid dynamics has been applied to various high energy phenomena in astrophysics, nuclear and hadron physics, from collision of galaxies down to the evolution of femtometer-size droplets of dense matter created in ultra-relativistic heavy ion collisions. In astrophysics typical applications of relativistic fluid dynamics are collapse of massive stars, formation of and flow around black holes, collisions of neutron stars and passage of relativistic jets through intergalactic matter [1,2]. On earth relativistic flows appear in ultrarelativistic heavy-ion collisions, where the formed matter depicts collective behavior. Especially the anisotropies of the final particle distribution were described so well using ideal fluid dynamics, that the matter was called almost perfect fluid with the lowest possible viscosity. The determination of the dissipative properties of this matter has became one of the major goals of heavy-ion physics, and requires sophisticated fluid dynamical calculations.

The equations of motion of relativistic fluid dynamics are notoriously difficult to solve. Except in very idealized situations, no analytic solutions exist, and the equations must be solved numerically. Several groups have developed several codes for fluid dynamical modeling of heavy-ion collisions [3–21],[1] but many of these codes assume boost-invariant longitudinal expansion [22] and/or zero net baryon density in the entire system. Neither of these assumptions is a good approximation in collisions at the Beam Energy Scan energies ($\sqrt{s_{\rm NN}} = 6.3$–39 GeV) at BNL RHIC (Relativistic Heavy-Ion Collider) nor in collisions in the forthcoming experiments at FAIR or NICA. We have therefore developed a new code where both of these assumptions have been relaxed. In this paper, we present the results of test simulations of this code.

High-Resolution Shock-Capturing (HRSC) algorithms are particularly suitable for solving the equations of relativistic fluid dynamics, and are applied for a wide variety of problems [2]. HRSC algorithms are designed to treat discontinuous shock configurations in hydrodynamic solution, or shock waves. The methods usually incorporate higher-order schemes which minimize numerical errors. Most of HRSC algorithms are formulated in conservative form, where the time evolution of cell averaged quantities is governed by numerical fluxes evaluated at cell boundaries. The conservative form ensures that the total energy and momentum in the system are conserved during the time evolution. A sub-family of HRSC algorithms are Godunov-type algorithms, which are based on exact or approximate solutions of the Riemann problem at the cell boundaries in order to compute time-averaged fluxes through it.

Our code is based on the Godunov-type relativistic Harten–Lax–van Leer–Einfeldt (HLLE) approximate Riemann solver [23,24]. This particular choice of the approximate Riemann solver is motivated by its simplicity, reliability, and stability for the simulations related to the physics of ultra-relativistic heavy ion collisions. The Riemann problem is formulated for an inviscid fluid, where shock wave solutions are allowed. Basing on the algorithms established for inviscid fluid, we aim to study the evolution of nearly ideal fluid (fluids with close-to-minimal viscosity) like the one presumably created in ultrarelativistic heavy ion collisions. To do this, we employ additional methods to solve the equations of relativistic viscous hydrodynamics in the Israel–Stewart framework [25], keeping the ability to solve the equations of ideal hydrodynamics in the limit of zero shear and bulk viscosities. The use of an (approximate) Riemann solver makes it possible to treat the highly inhomogeneous matter configurations emerging from event-by-event initial conditions as employed in the most recent studies of heavy ion collisions.

The present hydrodynamic code is already being used as a part of EPOS3 event generator for ultra-relativistic heavy ion collisions [26] and as a part of hydrodynamic + cascade model [27] in studies focused on Beam Energy Scan (BES) project at the BNL Relativistic Heavy Ion Collider (RHIC).

The article is organized as follows: in Section 2 the formalism is presented, Section 3 provides the details of the numerical implementation. Section 4 is devoted to the description and results of test simulations, including a comparison for the physical setup for the matter expansion in relativistic A + A collisions, and we summarize in Section 5.

2. Equations

Throughout this work natural units are employed, i.e. the speed of light in vacuum $c = 1$, the Boltzmann constant $k_B = 1$ and the Planck constant $\hbar = 1$.

The equations of relativistic (viscous) hydrodynamics follow from the laws of energy–momentum and charge conservation:

$$\partial_\nu T^{\mu\nu} = 0,$$
$$\partial_\nu N_c^\nu = 0, \qquad (1)$$

with $T^{\mu\nu}$ being the energy–momentum tensor and N_c^ν the charge current, index c enumerates the conserved charges if there are multiple conserved charges in the system.

The Landau definition of flow velocity u^μ (Landau frame) as a flow of energy [28] is adopted, i.e. $\epsilon u^\mu = T^\mu_\nu u^\nu$. In this frame, the energy–momentum tensor for a viscous fluid can be decomposed as:

$$T^{\mu\nu} = \epsilon u^\mu u^\nu - (p + \Pi)\Delta^{\mu\nu} + \pi^{\mu\nu},$$
$$N_c^\mu = n_c u^\mu + V_c^\mu,$$

where

- ϵ and p are energy density in fluid rest frame and equilibrium pressure, respectively;
- $\Delta^{\mu\nu} = g^{\mu\nu} - u^\mu u^\nu$ is the projector orthogonal to u^μ;
- $\pi^{\mu\nu}$ and Π are the shear stress tensor and bulk pressure;
- V_c^μ are charge diffusion currents.

The hydrodynamic equations are closed with the equation of state (EoS) $p = p(\epsilon, n_c)$, which has to be supplied from some external model.

[1] We apologize to our colleagues whose work we forgot to mention.

In the Israel–Stewart framework of relativistic viscous hydrodynamics [25] the shear stress tensor and bulk pressure are independent dynamical variables. Recent studies [29] show that there can be infinitely many choices for the explicit form and coefficients in equations of motion for $\pi^{\mu\nu}$ and Π. In the present work the following choice for the equations of motion for the shear stress tensor and bulk pressure is used, where we neglect vorticity terms:

$$\langle u^\gamma \partial_{;\gamma} \pi^{\mu\nu} \rangle = -\frac{\pi^{\mu\nu} - \pi^{\mu\nu}_{\rm NS}}{\tau_\pi} - \frac{4}{3}\pi^{\mu\nu}\partial_{;\gamma}u^\gamma, \tag{2a}$$

$$u^\gamma \partial_{;\gamma} \Pi = -\frac{\Pi - \Pi_{\rm NS}}{\tau_\Pi} - \frac{4}{3}\Pi\partial_{;\gamma}u^\gamma, \tag{2b}$$

and where $\partial_{;\mu}$ denotes a covariant derivative. This choice has already been widely used in recent simulations of nucleus–nucleus collisions at relativistic energies. For the purpose of the tests and our current applications we do not include the baryon/electric charge diffusion, i.e. $V_c^\mu = 0$. Angle brackets in (2a) are defined as:

$$\langle A^{\mu\nu} \rangle = \left(\frac{1}{2}\Delta^\mu_\alpha \Delta^\nu_\beta + \frac{1}{2}\Delta^\nu_\alpha \Delta^\mu_\beta - \frac{1}{3}\Delta^{\mu\nu}\Delta_{\alpha\beta} \right) A^{\alpha\beta},$$

and denote the symmetric, traceless and orthogonal to u^μ part of $A^{\mu\nu}$.

$$\pi^{\mu\nu}_{\rm NS} = \eta(\Delta^{\mu\lambda}\partial_{;\lambda}u^\nu + \Delta^{\nu\lambda}\partial_{;\lambda}u^\mu) - \frac{2}{3}\eta\Delta^{\mu\nu}\partial_{;\lambda}u^\lambda,$$

$$\Pi_{\rm NS} = -\zeta\,\partial_{;\lambda}u^\lambda, \tag{3}$$

are the values of shear stress tensor and bulk pressure in limiting Navier–Stokes case.

For hydrodynamic simulations related to the physics of ultrarelativistic heavy ion collisions Milne coordinates for the t–z plane in spacetime (z being the collision axis) are chosen. The new coordinates are expressed in terms of Minkowski coordinates $\{t, x, y, z\}$ as $\tau = \sqrt{t^2 - z^2}$, $\eta = \frac{1}{2}\ln((t+z)/(t-z))$, while the definitions of x and y coordinates are unchanged.

The form of hydrodynamic equations in arbitrary coordinate systems is:

$$\partial_{;\nu}T^{\mu\nu} = \partial_\nu T^{\mu\nu} + \Gamma^\mu_{\nu\lambda}T^{\nu\lambda} + \Gamma^\nu_{\nu\lambda}T^{\mu\lambda} = 0, \tag{4}$$
$$\partial_{;\nu}N_c^\nu = \partial_\nu N_c^\nu + \Gamma^\nu_{\nu\lambda}N_c^\lambda = 0,$$

where $\Gamma^\mu_{\nu\lambda}$ are affine connections or Christoffel symbols.

We choose West coast convention $(+,-,-,-)$ for metric tensor in Minkowski spacetime, so in Milne coordinates the invariant interval is: $ds^2 = dt^2 - dx^2 - dy^2 - \tau^2 d\eta^2$, and the metric tensor is $g^{\mu\nu} = diag(1, -1, -1, -1/\tau^2)$

Although spacetime is still flat, there are nontrivial Christoffel symbols, the nonzero components being:

$$\Gamma^\eta_{\tau\eta} = \Gamma^\eta_{\eta\tau} = 1/\tau, \qquad \Gamma^\tau_{\eta\eta} = \tau,$$

which leads to the following explicit form of hydrodynamic equations:

$$\begin{aligned}
&\partial_\nu T^{\tau\nu} + \tau T^{\eta\eta} + \frac{1}{\tau}T^{\tau\tau} = 0,\\
&\partial_\nu T^{x\nu} + \frac{1}{\tau}T^{x\tau} = 0,\\
&\partial_\nu T^{y\nu} + \frac{1}{\tau}T^{y\tau} = 0,\\
&\partial_\nu T^{\eta\nu} + \frac{3}{\tau}T^{\eta\tau} = 0,\\
&\partial_\nu N_c^\nu + \frac{1}{\tau}N_c^\tau = 0.
\end{aligned} \tag{5}$$

In Milne coordinates, $T^{\mu\nu}$ and N^ν keep the same structure, however the velocities are expressed through the longitudinal/transverse rapidities in the Cartesian frame as:

$$u^\mu = \{u^\tau, u^x, u^y, u^\eta\} = \Big(\cosh(\eta_f - \eta)\cosh\eta_T, \sinh\eta_T\{\cos\phi, \sin\phi\}, \frac{1}{\tau}\sinh(\eta_f - \eta)\cosh\eta_T \Big) \tag{6}$$

where $\eta_f = 0.5\ln(1+v_z)/(1-v_z)$ is longitudinal flow rapidity and $\eta_T = \operatorname{arctanh}(v_T/\sqrt{1-v_z^2})$ is transverse flow rapidity. From the equation above one can see that $u^\eta = 0$ when $\eta_f = \eta$, which means that $u^\eta = 0$ corresponds to scaling Bjorken flow in Cartesian coordinates, $v_z = z/t$. Thus, Milne coordinates naturally describe the expansion along z axis from a point-like source.

As one can see, almost all source terms in (5) are proportional to $1/\tau$, which makes them dominant for the hydrodynamic evolution at small τ. This is natural when one remembers that the gradient of the longitudinal scaling flow is inversely proportional to t in the Cartesian frame. The accurate numerical solution would eventually require to apply a higher order numerical time integration scheme. We circumvent this by redefining the variables in Milne coordinates as:

$$T^{\mu\nu} = \tilde{T}^{\mu\nu}, \quad \mu, \nu \neq \eta \tag{7}$$

$$T^{\mu\eta} = \tilde{T}^{\mu\eta}/\tau, \quad \mu \neq \eta \tag{8}$$

$$T^{\eta\eta} = \tilde{T}^{\eta\eta}/\tau^2 \tag{9}$$

$$N_c^\eta = \tilde{N}_c^{\ \eta}/\tau. \tag{10}$$

Rewriting the equations for $\tau T^{\mu\nu}$:

$$\begin{aligned}
&\tilde{\partial}_\nu(\tau\tilde{T}^{\tau\nu}) + \frac{1}{\tau}(\tau\tilde{T}^{\eta\eta}) = 0,\\
&\tilde{\partial}_\nu(\tau\tilde{T}^{x\nu}) = 0,\\
&\tilde{\partial}_\nu(\tau\tilde{T}^{y\nu}) = 0,\\
&\tilde{\partial}_\nu(\tau\tilde{T}^{\eta\nu}) + \frac{1}{\tau}(\tau\tilde{T}^{\eta\tau}) = 0,\\
&\tilde{\partial}_\nu(\tau\tilde{N}_c^\nu) = 0,
\end{aligned} \tag{11}$$

with

$$\tilde{\partial}_\mu \equiv \{\partial/\partial\tau, \partial/\partial x, \partial/\partial y, (1/\tau)\partial/\partial\eta\},$$

all the components of $\tilde{T}^{\mu\nu}$ have the same units as well as $\tilde{\partial}_\mu$ [1/length]. The actual conserved variables used in the code are then $Q = \{\tau\tilde{T}^{\mu\tau}, \tau\tilde{N}^\tau\}$, fluxes are $\{\tau\tilde{T}^{ij}, \tau\tilde{N}^i\}$, so that $\tilde{T}^{\eta\eta} = (\epsilon + p)\tilde{u}^\eta\tilde{u}^\eta + p$ and $\tilde{u}^\eta$ does not include the factor $1/\tau$ (cf. Eq. (6)). Then Eq. (11) provides the explicit form of the energy–momentum and charge conservation equations which are solved numerically.

In the same way as it was done for energy–momentum conservation equations, we separate the factors $1/\tau$ from $\pi^{\mu\nu}$ as follows: $\pi^{\mu\eta} = \tilde{\pi}^{\mu\eta}/\tau$, $\pi^{\eta\eta} = \tilde{\pi}^{\eta\eta}/\tau^2$, as well as $u^\eta = \tilde{u}^\eta/\tau$ and $\partial_\eta \to (1/\tau)\partial_\eta$. Then we rewrite (2a) and (2b) in terms of tilded variables:

$$\tilde{\gamma}\left(\partial_\tau + \tilde{v}^i\tilde{\partial}_i\right)\tilde{\pi}^{\mu\nu} = -\frac{\tilde{\pi}^{\mu\nu} - \tilde{\pi}^{\mu\nu}_{\rm NS}}{\tau_\pi} + I^{\mu\nu}_\pi \tag{12}$$

$$\tilde{\gamma}\left(\partial_\tau + \tilde{v}^i\tilde{\partial}_i\right)\Pi = -\frac{\Pi - \Pi_{\rm NS}}{\tau_\Pi} + I_\Pi \tag{13}$$

and solve the above equations numerically. Here $\tilde{\gamma} = u^0$ and $\tilde{v}^i = \tilde{u}^i/u^0$ $(i = x, y, \eta)$ are the components of 3-velocity. The additional source terms are:

$$I^{\mu\nu}_\pi = -\frac{4}{3}\tilde{\pi}^{\mu\nu}\tilde{\partial}_{;\gamma}\tilde{u}^\gamma - [\tilde{u}^\nu\tilde{\pi}^{\mu\beta} + \tilde{u}^\mu\tilde{\pi}^{\nu\beta}]\tilde{u}^\lambda\tilde{\partial}_{;\lambda}\tilde{u}_\beta - I^{\mu\nu}_{\pi,G}, \tag{14}$$

$$I_\Pi = -\frac{4}{3}\Pi\,\tilde{\partial}_{;\gamma}\tilde{u}^\gamma, \tag{15}$$

where in a given coordinate system all covariant derivatives of the four-velocity are equal to ordinary derivatives, except for:

$$\tilde{\partial}_{;\eta} u^{\tau} = \tilde{\partial}_{\eta} u^{\tau} + \tilde{u}^{\eta}/\tau, \qquad \tilde{\partial}_{;\eta} \tilde{u}^{\eta} = \tilde{\partial}_{\eta} \tilde{u}^{\eta} + u^{\tau}/\tau, \tag{16}$$

so that $\tilde{\partial}_{;\gamma} \tilde{u}^{\gamma} = \tilde{\partial}_{\gamma} \tilde{u}^{\gamma} + u^{\tau}/\tau$. Also, $I^{\mu\nu}_{\pi,G}$ denote geometrical source terms (coming from Christoffel symbols):

$$\begin{aligned}
I^{\tau\tau}_{\pi,G} &= 2\tilde{u}^{\eta}\tilde{\pi}^{\tau\eta}/\tau \qquad & I^{\tau x}_{\pi,G} &= \tilde{u}^{\eta}\tilde{\pi}^{\eta x}/\tau \\
I^{\tau y}_{\pi,G} &= \tilde{u}^{\eta}\tilde{\pi}^{\eta y}/\tau \qquad & I^{\tau\eta}_{\pi,G} &= \tilde{u}^{\eta}(\tilde{\pi}^{\tau\tau} + \tilde{\pi}^{\eta\eta})/\tau \\
I^{\eta x}_{\pi,G} &= \tilde{u}^{\eta}\tilde{\pi}^{\tau x}/\tau \qquad & I^{\eta y}_{\pi,G} &= \tilde{u}^{\eta}\tilde{\pi}^{\tau y}/\tau \\
I^{\eta\eta}_{\pi,G} &= 2\tilde{u}^{\eta}\tilde{\pi}^{\tau\eta}/\tau \qquad & I^{xx}_{\pi,G} &= I^{xy}_{\pi,G} = I^{yy}_{\pi,G} = 0.
\end{aligned} \tag{17}$$

Most of the tests presented below, as well as heavy-ion related simulations, are performed in Milne coordinates. However, to perform shock tube test we use a version of the code which works in Cartesian coordinates. In the latter case we solve the original hydrodynamic equations (1), as well as $I^{\mu\nu}_{\pi,G} = 0$ in (14). As a result, transformations (10) and (11) and tilde notation in general are not used, and z coordinate stands for the third direction in space.

3. Numerical implementation

Let us rewrite Eq. (1) in a form of evolution equations in Minkowski spacetime for simplicity:

$$\frac{\partial Q^{\mu}}{\partial t} + \frac{\partial F^{\mu i}}{\partial x_i} = 0, \tag{18}$$

$$\frac{\partial N^{0}}{\partial t} + \frac{\partial N^{i}}{\partial x_i} = 0, \tag{19}$$

where index i denotes spatial dimensions. $T^{0\mu} \equiv Q^{\mu}$ and N_0 are conventionally called conserved quantities, if the fluxes at the spatial boundaries of the system vanish or compensate each other, then $\int Q^{\mu}(t,x)d^3x$ is conserved. Also, $T^{\mu i} \equiv F^{\mu i}$ and N^i are flux terms.

We use a finite volume method to solve hydrodynamic equations (18), (19). In this method, one works in terms of the averaged values of $T^{\tau\mu}$ in mesh i, which in one dimension reads:

$$\vec{Q}^{n}_{i} = \frac{1}{\Delta x}\int_{x_i-\Delta x/2}^{x_i+\Delta x/2} \{T^{0\mu}(t_i,x), N^{0}_{c}(t_i,x)\}dx,$$

and time-averaged fluxes through left and right facets of the mesh:

$$F^{n}_{i\pm1/2} = \frac{1}{\Delta t}\int_{t_n}^{t_n+\Delta t} \left\{ T^{x\mu}\left(t, x_i \pm \frac{\Delta x}{2}\right), N^{x}\left(t, x_i \pm \frac{\Delta x}{2}\right)\right\} dt.$$

Then, integrating the conservation laws (18) within $[t_n, t_n+\Delta t]$ and $[x_i - \Delta x/2, x_i + \Delta x/2]$, one gets the exact relation between the conserved quantities and the fluxes:

$$\frac{1}{\Delta t}(Q^{n+1}_{i} - Q^{n}_{i}) + \frac{1}{\Delta x_i}(F^{n}_{i+1/2} - F^{n}_{i-1/2}) = 0, \tag{20}$$

which can be used to propagate Q^n to the next timestep. The idea of the Godunov method [30] is to take a piecewise uniform distribution of $T^{0\mu}$, N^0_c on a mesh and to provide an estimate for $F^n_{i\pm1/2}$ based on exact or approximate solution of the Riemann problem at $x = x_i \pm 1/2$ with initial left and right state parameters Q^n_i and Q^n_{i+1}, respectively. In the next timestep, the wave structure from a Riemann problem at the previous timestep is completely discarded and piecewise uniform distributions for Q^{n+1} are used again. One can estimate the criterion of stability for such schemes from the Courant–Friedrichs–Lewy condition [31], which is a necessary condition for numerical scheme to be stable. For the Godunov scheme, the criterion is $2b_{\max}\Delta t < \Delta x$, where $b_{\max}$ is a maximal value of the signal velocity. To be on the safe side, we assume $b_{\max} = c = 1$ and use $2\Delta t \le \Delta x$.

In Milne coordinates the definition of conserved quantities and fluxes are modified as deduced from the transformed energy–momentum conservation equations (11):

$$\vec{Q}^{n}_{i} = \frac{1}{\Delta x}\int_{x_i-\Delta x/2}^{x_i+\Delta x/2} \{\tau_i T^{\tau\mu}(\tau_i,x), \tau_i N^{\tau}_{c}(\tau_i,x)\}dx,$$

$$F^{n}_{i\pm1/2} = \frac{1}{\Delta \tau}\int_{\tau_n}^{\tau_n+\Delta\tau} \{\tau T^{x\mu}(\tau, x_i \pm \Delta x/2), \tau N^{x}(\tau, x_i \pm \Delta x/2)\}d\tau,$$

as well as now there are nonzero source terms in (20). For the case of a viscous fluid one can decompose the conserved quantities and fluxes into their ideal and viscous parts:

$$\begin{aligned}
&\frac{1}{\Delta t}(Q^{n+1}_{\mathrm{id},i} + \delta Q^{n+1}_{i} - Q^{n}_{\mathrm{id},i} - \delta Q^{n}_{i}) \\
&\quad + \frac{1}{\Delta x_i}(\Delta F_{\mathrm{id}} + \Delta\delta F) + S_{\mathrm{id},i} + \delta S_i = 0
\end{aligned} \tag{21}$$

where $\Delta F = F_{i+1/2} - F_{i-1/2}$, and δQ, δF, δS denote viscous corrections to conserved quantities, fluxes and source terms respectively.

Then, the effects of ideal and viscous fluxes/sources in Eq. (21) can be accounted for separately, in the same way as it is done in [32]:

$$\frac{1}{\Delta t}(Q^{*n+1}_{\mathrm{id},i} - Q^{n}_{\mathrm{id},i}) + \frac{1}{\Delta x_i}\Delta F_{\mathrm{id}} + S_{\mathrm{id},i} = 0 \tag{22}$$

$$\frac{1}{\Delta t}(Q^{n+1}_{\mathrm{id},i} + \delta Q^{n+1}_{i} - Q^{*n+1}_{\mathrm{id},i} - \delta Q^{n}_{i}) + \frac{1}{\Delta x_i}\Delta\delta F + \delta S_i = 0. \tag{23}$$

Note that there are only ideal quantities in (22), whereas (23) describes viscous corrections to the evolution.

The full solution (21) for one timestep then proceeds in the substeps:

Substep (1) Q^{*n+1}_{id} is obtained by evolving only the ideal part of the energy–momentum tensor, Eq. (22) over the full timestep Δt using Godunov-type method.

Substep (2) The Israel–Stewart equations (12) and (13) are solved to propagate $\pi^{\mu\nu}$ and Π for the next timestep. Here one has to know the values of shear/bulk terms in the Navier–Stokes limit, $\pi^{\mu\nu}_{\mathrm{NS}}$, Π_{NS}, which depend on velocity gradients. We calculate $\pi^{\mu\nu}_{\mathrm{NS}}$, Π_{NS} at $n+1/2$ (half-step) using $s = s^{*(n+1/2)}$ and

$$\begin{aligned}
\partial_{\tau} u^{\mu} &= ((u^{\mu})^{*n+1}_{i} - u^{\mu,n}_{i})/\Delta\tau \\
\partial_{x_i} u^{\mu} &= ((u^{\mu})^{*(n+1/2)}_{i+1} - (u^{\mu})^{*(n+1/2)}_{i-1})/(2\Delta x_i)
\end{aligned}$$

where central differences are used for second order of accuracy. The asterisk (*) denotes the values obtained from substep 1 (updated with only ideal fluxes/sources).

Substep (3) $Q^{n+1}_{\mathrm{id},i} + \delta Q^{n+1}_{i} = Q^{n+1}_{\mathrm{full}}$ is obtained by evolving Eq. (23) over the full timestep Δt with viscous fluxes/sources only. The initial condition for this substep is $Q_{\mathrm{ini}} = Q^{*n+1}_{\mathrm{id}} + \delta Q^{n}$, the first term obtained from the solution of substep 1.

To update Q_{full} according to Eq. (23), we use edge/half-step values of flux/source terms $\delta F^{n+1/2}_{i\pm1/2}$, $\delta S^{n+1/2}$, saved at substep 2.

Note that for the splitting itself, Eqs. (22) and (23), no assumption of the smallness of the viscous corrections is needed. However, the assumption becomes necessary when we calculate the fluxes in the evolution equations. For example, when one calculates F_{id} for the ideal substep one assumes that the Godunov method works well, which is proven to be the case for hydrodynamics of inviscid fluid. Thus, we can apply the scheme for nearly perfect fluids, keeping in mind that viscosity should only introduce (small) corrections to the evolution.

In what follows we describe substeps 1 and 2 in detail, whereas the application of Eq. (23) for substep 3 is straightforward.

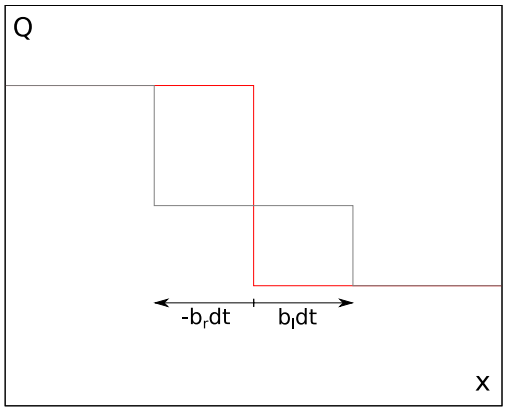

Fig. 1. Evolution of Riemann problem in HLLE approximation. Red line represents the initial discontinuity, gray line represents the intermediate state in HLLE approximation. (For interpretation of the references to colour in this figure legend, the reader is referred to the web version of this article.)

3.1. Ideal substep

For the Godunov-type method employed in substep 1, we use an approximate solution to the Riemann problem constructed with the relativistic extension of the HLLE solver. Below we provide the main points of the method, whereas for a detailed description the reader is referred to [24].

In the HLLE method, the evolution of initial discontinuity (Riemann problem) between left $Q_l = Q_i$ and right $Q_r = Q_{i+1}$ states is approximated by a single uniform intermediate state bounded by two shock waves propagating to the left and to the right from the initial discontinuity, as seen in Fig. 1. Within this approximation, by integrating the hydrodynamic equations over $[b_l \Delta t, b_r \Delta t]$ and $[t^n, t^n + \Delta t]$ one can derive the properties of the intermediate state with the algebraic relations:

$$Q^\kappa_{lr}(Q_l, Q_r) = \frac{b_r Q^\kappa_r - b_l Q^\kappa_l - F^\kappa(Q_r) + F^\kappa(Q_l)}{b_r - b_l} \tag{24}$$

and the corresponding flux:

$$F^\kappa_{lr}(Q_l, Q_r) = \frac{b_r F^\kappa(Q_l) - b_l F^\kappa(Q_r) + b_l b_r (Q^\kappa_r - Q^\kappa_l)}{b_r - b_l}, \tag{25}$$

where κ enumerates the Lorentz index and charge index. For the completeness of the scheme one has to specify the signal velocities b_l, b_r. We take an advanced estimate for signal velocities from [33]:

$$b_r = \max\left\{0, \frac{\bar{v} + \bar{c}_s}{1 + \bar{v}\bar{c}_s}, \frac{v_r + c_{s,r}}{1 + v_r c_{s,r}}\right\}, \tag{26}$$

$$b_l = \min\left\{0, \frac{\bar{v} - \bar{c}_s}{1 - \bar{v}\bar{c}_s}, \frac{v_l - c_{s,l}}{1 - v_l c_{s,l}}\right\}, \tag{27}$$

where $c_{s,r} = c_s(\epsilon_r)$, $c_{s,l} = c_s(\epsilon_l)$, and

$$\bar{v} = \frac{\sqrt{E_l} v_l + \sqrt{E_r} v_r}{\sqrt{E_l} + \sqrt{E_r}}, \tag{28}$$

$$\bar{c}_s^2 = \frac{\sqrt{E_l} c_{s,l}^2 + \sqrt{E_r} c_{s,r}^2}{\sqrt{E_l} + \sqrt{E_r}} + \eta \frac{\sqrt{E_l E_r}}{(\sqrt{E_l} + \sqrt{E_r})^2} (v_r - v_l)^2, \tag{29}$$

together with the suggested value of $\eta = 0.5$.

For cells facing with vacuum, i.e. when $\epsilon_l = 0$ or $\epsilon_r = 0$, we put $b_l = -1$ or $b_r = 1$ respectively.

For the second order accuracy of the scheme in space, a piecewise linear distributions in the cells (`MUSCL` scheme) are introduced. We reconstruct the values at right and left cell boundaries $(i \pm \frac{1}{2})$ as follows:

$$Q_{i\pm} = Q_i \pm \frac{1}{2} \Delta Q. \tag{30}$$

Here we use the so-called `minmod` slope limiter:

$$\Delta Q = \begin{cases} \Delta_l, & \text{if } |\Delta_l| < |\Delta_r| \text{ and } \Delta_l \cdot \Delta_r > 0 \\ \Delta_r, & \text{if } |\Delta_l| > |\Delta_r| \text{ and } \Delta_l \cdot \Delta_r > 0 \\ 0 & \text{if } \Delta_l \cdot \Delta_r < 0 \end{cases}$$

where $\Delta_l = Q_i - Q_{i-1}$, $\Delta_r = Q_{i+1} - Q_i$ are used. The slope limiter chooses the smallest possible slope, and does not introduce new extrema. Therefore, it avoids possible oscillations in the numerical solution.

To employ the piecewise linear distributions we substitute $Q_r \to Q_{(i+1)-}$, $Q_l \to Q_{i+}$ (and correspondingly $v_r \to v(Q_{(i+1)-})$, $v_l \to v(Q_{i+})$ etc.) in Eqs. (24) and (25).

For the second order accuracy in time we use the half-step (or predictor–corrector) method. First, we propagate the evolution for half of timestep:

$$Q_i^{*n+\frac{1}{2}} = Q_i^n + \frac{\Delta t}{2\Delta x}(F^n_{i-\frac{1}{2}} - F^n_{i+\frac{1}{2}}) + \frac{\Delta t}{2} S^n_i,$$

then the propagation is performed for a full timestep, based on fluxes and source terms calculated from $Q^{*n+\frac{1}{2}}$:

$$Q_i^{*n+1} = Q_i^n + \frac{\Delta t}{\Delta x}(F^{n+\frac{1}{2}}_{i-\frac{1}{2}} - F^{n+\frac{1}{2}}_{i+\frac{1}{2}}) + \frac{\Delta t}{2} S^{n+\frac{1}{2}}_i,$$

where $F^{n+\frac{1}{2}} = F(Q^{*n+\frac{1}{2}})$, $S^{n+\frac{1}{2}} = S(Q^{*n+\frac{1}{2}})$ and the propagated Q is marked by an asterisk to keep the notation consistent with (22) and (23).

This completes the description of the scheme in one spatial dimension. To perform the evolution in three dimensions we apply the HLLE solver to calculate the fluxes through the cell boundaries independently for the x, y and η directions. The predictor step reads:

$$\begin{aligned} Q^{*n+\frac{1}{2}}_{ijk} = Q^n_{ijk} &+ \frac{\Delta t}{2\Delta x}(F^n_{i-\frac{1}{2},jk} - F^n_{i+\frac{1}{2},jk}) \\ &+ \frac{\Delta t}{2\Delta y}(F^n_{i,j-\frac{1}{2},k} - F^n_{i,j+\frac{1}{2},k}) + \frac{\Delta t}{2\Delta \eta}(F^n_{ij,k-\frac{1}{2}} - F^n_{ij,k+\frac{1}{2}}) \\ &+ \frac{\Delta t}{2} S^n_{ijk} \end{aligned} \tag{31}$$

and the corrector step reads:

$$\begin{aligned} Q^{*n+1}_{ijk} = Q^n_{ijk} &+ \frac{\Delta t}{\Delta x}(F^{n+\frac{1}{2}}_{i-\frac{1}{2},jk} - F^{n+\frac{1}{2}}_{i+\frac{1}{2},jk}) \\ &+ \frac{\Delta t}{\Delta y}(F^{n+\frac{1}{2}}_{i,j-\frac{1}{2},k} - F^{n+\frac{1}{2}}_{i,j+\frac{1}{2},k}) + \frac{\Delta t}{\Delta \eta}(F^{n+\frac{1}{2}}_{ij,k-\frac{1}{2}} - F^{n+\frac{1}{2}}_{ij,k+\frac{1}{2}}) \\ &+ \frac{\Delta t}{2} S^{n+\frac{1}{2}}_{ijk} \end{aligned} \tag{32}$$

where the half-step updated variables are calculated from the full three dimensional predictor step.

It might happen that in a small amount of cells either $Q^{*n+1/2}_{ijk}$ or Q^{*n+1}_{ijk} do not satisfy the requirement $Q^\tau > \sqrt{(Q^x)^2 + (Q^y)^2 + (Q^\eta)^2}$, which must hold since physical energy density is positive and the velocity $|\vec{v}| < 1$. For these cases we proportionally rescale $\{Q^x, Q^y, Q^\eta\}$ wherever needed for the condition to be satisfied. This results in negligible deviations in a total energy–momentum balance in the system.

3.2. Viscous substep

In parallel to energy–momentum conservation equations, we integrate the equations of motion for the viscous terms, Eqs. (12) and (13). In the following we denote by π either a component of

$\pi^{\mu\nu}$ or Π, since the structure of their evolution equations is the same, except for different geometrical source terms. We split this substep into:

(A) Integration of source terms, which is performed using the predictor–corrector method:

$$\pi^{\dagger n+1/2} = \pi^n + I_{\rm full}(\pi^n) \tag{33}$$

$$\pi^{\dagger n+1} = \pi^n + I_{\rm full}(\pi^{n+1/2}) \tag{34}$$

where $I_{\rm full}(\pi) = -(\pi - \pi_{\rm NS})/\tau_\pi + I_\pi(\pi)$ as defined by (14). Optionally, if τ_π is small enough, following the idea in [32] we use a formal solution to the equation with relaxation part only:

$$\pi^{\dagger n+1} = (\pi^n - \pi_{\rm NS}) \exp\left(-\frac{\Delta t}{\gamma\,\tau_\pi}\right) + \pi_{\rm NS},$$

and integrate I_π separately. This is important since in heavy ion collision scenarios, depending on the ansatz and thermodynamical parameters taken, τ_π may be comparable to the timestep.

(B) Advection using first order upwind method:

$$\pi^{n+1}_{ijk} = \sum_{\Delta i}\sum_{\Delta j}\sum_{\Delta k} w_{\Delta i} w_{\Delta j} w_{\Delta k} \pi^{\dagger n+1}_{i+\Delta i, j+\Delta j, k+\Delta k}$$

where $\Delta i, \Delta j, \Delta k = -1, 0, +1$, and

$$w_{\Delta i} = \{-a_x^-,\ 1 - |a_x|,\ a_x^+\}$$

$$a_x^- = \min(v_x \Delta t/\Delta x, 0), \qquad a_x^+ = \max(v_x \Delta t/\Delta x, 0)$$

with similar expressions for $a_y^\pm$ and $a_\eta^\pm$

The variables propagated for a half step are kept in memory and are used later for the calculation of the viscous fluxes and the source terms in the energy–momentum equations for the full timestep.

We evolve 10 independent components of $\pi^{\mu\nu}$, thus taking into account only that it is a symmetric tensor. This allows to check the consistency of the numerical solution by verification of the achieved accuracy for the resulting orthogonality relations $\pi^{\mu\nu} u_\nu = 0$ and the tracelessness relation $\pi^\mu_\mu = 0$. An additional advantage is the simplicity of the velocity finding procedure, coming from the fact that one does not need to know the velocity to recover all components of $\pi^{\mu\nu}$.

It has been checked that employing the Lax–Wendroff method for advection substep and Strang splitting between advection/source substeps in heavy ion collision scenarios does not alter the evolution significantly. However, the upwind method is more stable for inhomogeneous distributions of $\pi^{\mu\nu}$ emerging from fluctuating initial conditions in event-by-event hydrodynamic simulations for heavy ion collisions.

The Israel–Stewart framework by itself does not restrict the values of the shear stress tensor or the bulk pressure. However, it is required that the viscous corrections are sufficiently small compared to the ideal quantities for the framework to be applicable. Nevertheless, in the practical applications it sometimes happens that $\pi^{\mu\nu}_{\rm NS}$ or $\Pi_{\rm NS}$ are not small due to large gradients of u^μ when the Lorentz-gamma factor is large. As a result, instabilities may develop in the hydrodynamical solution. To prevent this we monitor the conditions:

$$\max_{\mu,\nu} |\pi^{\mu\nu}| < C \cdot \max_{\mu,\nu} |T^{\mu\nu}_{\rm id}| \quad \text{and} \quad |\Pi| < C \cdot p, \tag{35}$$

where C is some constant of the order one, but smaller than one. We rescale $\pi^{\mu\nu}$ and Π where needed, to keep condition (35) satisfied on all hydro grid points. We found that condition (35) may only be violated in the regions with very small density during the matter expansion into the vacuum, as long as the initial conditions for dissipative quantities and values of relaxation times are within reasonable limits. In principle this indicates that in those regions the viscous hydrodynamic approximation becomes inapplicable. However, in heavy ion collision scenarios this does not affect the hydrodynamic evolution of the dense core region.

3.3. Boundary conditions

The cell average Q^n_{ijk} is updated assuming that the values in neighboring cells $Q^n_{i\pm2,j\pm2,k\pm2}$ are known. This is not the case for the cells on the boundary of hydrodynamic grid. Instead of introducing some special algorithm for them which depends on a type of boundary condition, we do somewhat easier procedure and extend the computational grid to include two additional cells on either end (in x, y, η directions), called ghost cells. In applications to heavy ion collisions we study the matter expansion with vacuum. The computational boundary is therefore artificial and there should be no incoming signal, which means outflow (non-reflecting) boundary conditions. To realize it, at the beginning of each timestep the values of conservative variables in ghost cells are reset by the values from the nearest "physical" cell at either end of the grid, e.g. for x direction:

$$Q^n_{N+2,jk} = Q^n_{N+1,jk} = Q^n_{N,jk}, \qquad Q^n_{0,jk} = Q^n_{1,jk} = Q^n_{2,jk},$$

where physical cells are in the range $[2, N]$. Then the fluxes are calculated between *all* cells which have both neighbors in a given direction.

3.4. Final remarks

As was mentioned above, the conserved quantities $Q^\alpha = \{T^{\tau\mu}, N^\tau_c\}$, are used. For the completeness of the algorithm, one has to restore the so-called primitive variables – energy/charge densities and fluid velocity – several times during each timestep for each hydro cell: the fluxes/source terms have no explicit expressions in terms of Q^α. Also the primitive variables are relevant for the output and further physical analysis. Obviously the recovery procedure should be fast. We employ a procedure, based on the one dimensional numerical root search as described in the Appendix.

4. Test results

4.1. Ideal hydrodynamics: analytical solutions vs. numerical solutions

Shock tube: let us start with a one dimensional shock tube problem. We initialize the system with two uniform (left and right) states $\{\epsilon_l = 10\,\text{GeV/fm}^3, v_l = 0\}$ and $\{\epsilon_r = 1\,\text{GeV/fm}^3, v_r = 0\}$, separated at $t < 0$ by an imaginary membrane. The EoS for a relativistic massless gas $p = \epsilon/3$ is used. To extract the temperature or entropy density (for viscous hydro evolution) in this EoS we assume 2.5 massless quark degrees of freedom and $g_q = 2\cdot2\cdot3 = 12$ degeneracy factor and $g_g = 16$ for massless gluons. At $t = 0$ the membrane is removed and the initial discontinuity decays into compression shock wave propagating into the region of smaller density and a rarefaction wave propagating in the opposite direction. For such a case an analytical solution exists. The comparison between the analytical and numerical solution is shown in Fig. 2, upper panel. No scale parameters are present in such setup and the solution is expressed in terms of the dimensionless variable $\xi = x/t$. As it was pointed out in [33], it is essential to explore how many timesteps it takes for the numerical solution to approach the analytical one. The situation does not depend on the cell size provided that the Courant number $\lambda = \Delta t/\Delta x$ is kept the same. Since Eulerian grid is used, the wave profile is being resolved by the number of grid points/cells which increases with time (about 130 hydro cells at $N_t = 200$). From the comparison one can see at the $N_t = 25$th timestep there is substantial smearing of the profile, while at the $N_t = 999$th timestep the profile is practically undistinguishable from the analytical result.

Next, to check the dependence of the simulations on the grid direction (rotational invariance) we rotate the initial discontinuity

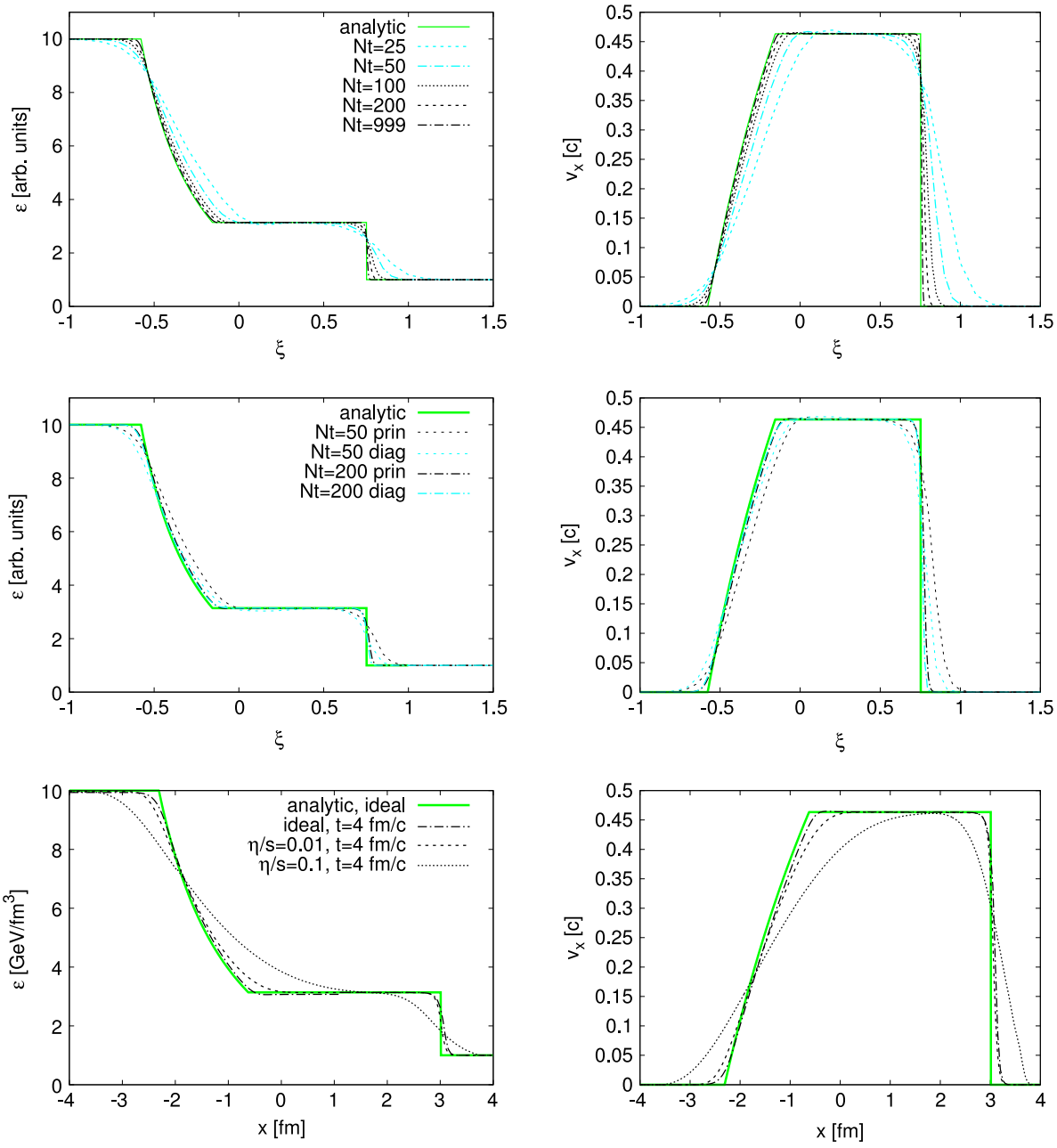

Fig. 2. (Color online) Analytical (solid line) and numerical (dashed lines) solutions to relativistic shock tube problem. Upper panels: comparison of numerical solution at different timesteps. Middle panels: comparison of the 1D numerical solution (denoted as `prin`, for principal direction in hydrodynamic grid) and 2D solution for 45°-rotated initial discontinuity (denoted as `diag`, for diagonal direction in hydrodynamic grid). Lower panels: ideal and viscous numerical solutions of shock tube problem. `Nt` denotes the number of timesteps N_t.

by 45° in the x–y plane and consider the same rarefaction/shock wave profile propagating in diagonal direction. The results are presented in the middle panel of Fig. 2. One can see that the propagation in the diagonal direction is consistent with principal direction at $Nt = 200$, while there are some differences at $Nt = 50$ when the numerical solution still does not approximate the analytical solution well.

Finally, the bottom panels of Fig. 2 compare the simulations with shear viscosity to the solution of Riemann problem in the ideal case.

In Figs. 3 and 4 we consider a special case of the Riemann problem with $\{\epsilon_l = 10\,\mathrm{GeV/fm}^3, v_l = 0\}$ and $\{\epsilon_r = 0, v_r = 0\}$. This corresponds to a matter expansion to vacuum. In this case the analytical solution further depends on the dimensionless variable ξ, however at $t > 0$ left and right (vacuum) states are connected with a rarefaction wave only, while the velocity of matter reaching the speed of light, $v = 1$ at the boundary with vacuum. Fig. 3 shows the results for the energy density profile (top) and the velocity profile (bottom). After $N_t = 200$ timesteps the numerical solution approaches the analytical solution. For this simulation we choose $\lambda_{\mathrm{CFL}} = 0.5$, thus the rarefaction wave at $N_t = 200$ is spread over 100 hydrodynamic cells.

Since we take $\lambda_{\mathrm{CFL}} < 1$, one has to treat the rate of matter expansion to vacuum carefully. In the numerical solution, at each timestep matter from the boundary cells propagates to the next vacuum cells. This makes the effective velocity of the matter front to be $v_{\mathrm{front}} = 1/\lambda_{\mathrm{CFL}}$, i.e. dependent on λ_{CFL}. We prevent this artifact by keeping the relative position of the matter front inside the cell, and allow to propagate to the next vacuum cell only after it crossed the current cell completely.

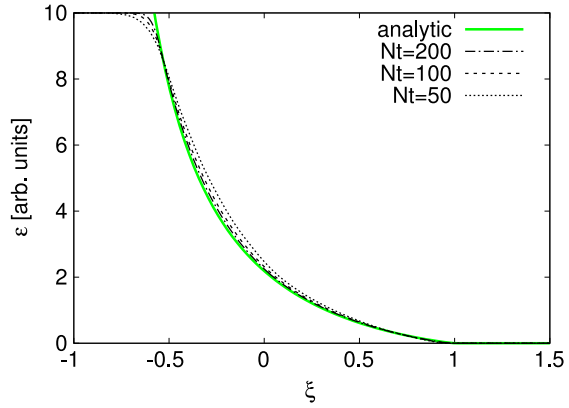

Fig. 3. (Color online) Energy density profile for analytical (solid line) and numerical (dashed lines) solutions to Riemann problem corresponding to matter expansion to vacuum.

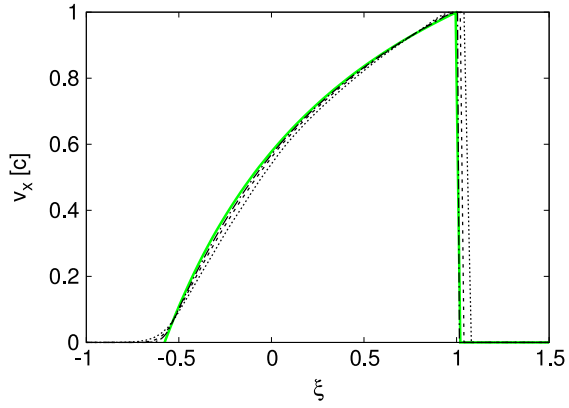

Fig. 4. (Color online) Same as Fig. 3, velocity profile.

Gubser flow. Recently, a family of analytical relativistic hydrodynamic solutions was found for three-dimensional expansion of a conformal fluid, $p = \epsilon/3$. The solution assumes azimuthal symmetry in xy plane and longitudinal scaling flow [34]:

$$\epsilon = \frac{\epsilon_0 (2q)^{8/3}}{\tau^{4/3}} \left[1 + 2q^2(\tau^2 + r_T^2) + q^4(\tau^2 - r_T^2)^2\right]^{4/3}, \tag{36}$$

$$u^\tau = \cosh[k(\tau, r_T)], \qquad u^\eta = 0 \tag{37}$$

$$u^x = \frac{x}{r_T} \sinh[k(\tau, r_T)], \qquad u^y = \frac{y}{r_T} \sinh[k(\tau, r_T)] \tag{38}$$

$$k(\tau, r_T) = \operatorname{arctanh} \frac{2q^2 \tau r_T}{1 + q^2\tau^2 + q^2 x_T^2} \tag{39}$$

where $k(\tau, r_T)$ function has a meaning of transverse flow rapidity in Milne coordinates.

We set the parameters as follows: $\tau_0 = 1$ fm/c. $\epsilon_0 = 1$ (arbitrary units), $q = 1$ (arbitrary units). Figs. 5 and 6 depict the comparison of the numerical solution to the analytical Gubser solution. The parameters correspond to an effective system size in transverse direction on the order of 1 fm, which is much smaller than the typical size of a heavy nucleus. Due to the strong initial transverse flow and persistent longitudinal flow the system expands and cools down very quickly. The evolution of this challenging initial state is reproduced by the numerical solution accurately, even after 10 fm/c time the very rarefied final state is reproduced well.

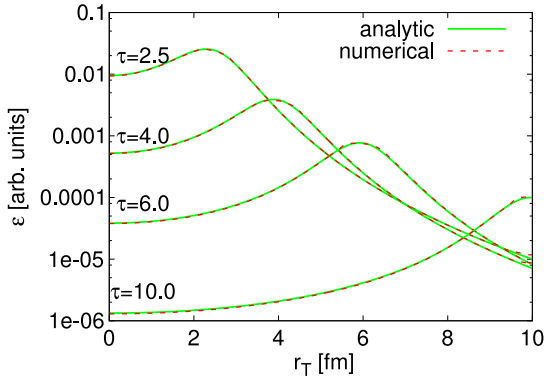

Fig. 5. (Color online) Energy density profile as a function of transverse coordinate at different times in analytical hydrodynamic solution by Gubser [34].

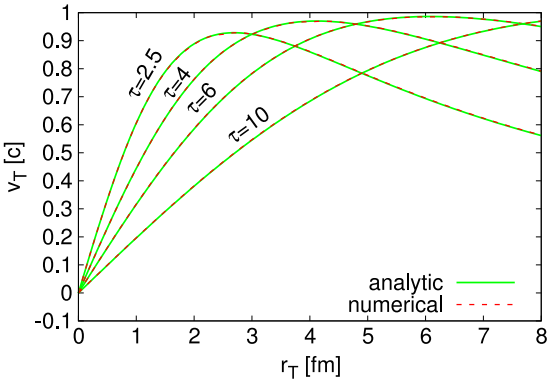

Fig. 6. (Color online) Same as Fig. 5, transverse velocity profile.

4.2. Viscous hydrodynamics: analytical solution vs. numerical solution

It is also important to check the accuracy of the scheme in the viscous case. Viscosity complicates the equations of relativistic hydrodynamics drastically. Thus analytical solutions exist only for very simple scenarios. First, we consider the $(0 + 1)$ dimensional Bjorken case. The system is homogeneous in all space directions with $v_x = v_y = v_\eta = 0$ (which equals to scaling flow $v_z = z/t$) in the Navier–Stokes limit. Then $\pi^{\eta\eta} = -(4/3)\eta/\tau^3 = -(4/3)(\eta/s)s/\tau^3$, and we obtain a modified Bjorken equation for the energy density evolution:

$$\frac{\partial \epsilon}{\partial \tau} + \frac{\epsilon + p + \tau^2 \pi^{\eta\eta}}{\tau} = 0.$$

Assuming an ideal massless gas EoS, $p = \epsilon/3$ and $\epsilon = cT^4$, one obtains the analytical solution for $T(\tau)$ in the viscous case as

$$T(\tau) = \left(\frac{\tau_0}{\tau}\right)^{1/3} \left[T(\tau_0) + \frac{2\eta}{3s\tau_0}\left(1 - \left(\frac{\tau_0}{\tau}\right)^{2/3}\right)\right]. \tag{40}$$

For the ideal fluid case $\eta/s = 0$, the well known cooling law $T \propto \tau^{-1/3}$ for the scaling flow is restored. To compare to the numerical solution, the system is initialized with an energy density of $\epsilon_0 = 30$ GeV/fm^3 at $\tau_0 = \sqrt{t^2 - z^2} = 0.6$ fm/c. Using the EoS for massless particles as described above, the initial temperature is $T_0 = 359$ MeV. We set $\eta/s = 0.2$ and $\tau_\pi = 0.0001$ fm (so that Navier–Stokes limit is well approximated) for the viscous case. Fig. 7 shows the comparison of the numerical solution for temperature to the analytical solution for the inviscid and viscous cases. One observes an agreement between the numerical and the analytical solutions.

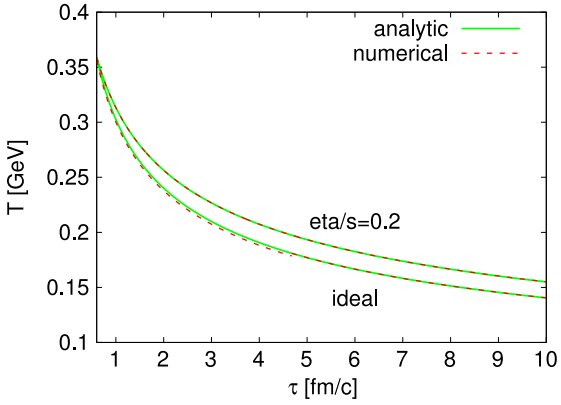

Fig. 7. (Color online) Analytical solutions for the evolution of temperature in 1D Bjorken expansion with and without shear viscosity (solid lines), compared to numerical solution (dashed lines).

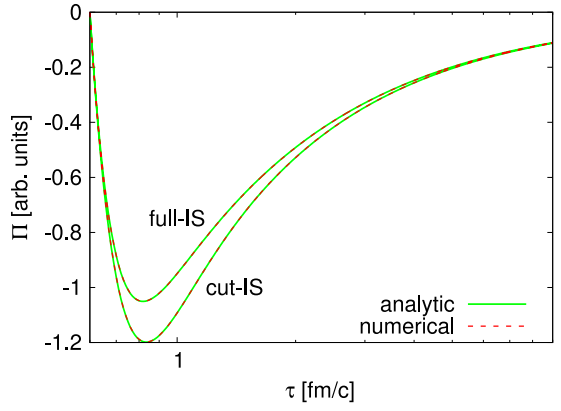

Fig. 8. (Color online) Evolution of bulk pressure Π in analytical 0+1D solution to Israel–Stewart equations (solid lines) with the $(4\Pi)/(3\tau)$ term (indicated as "full IS") and without it (indicated as "cut IS"). Dashed line is numerical solution.

To check how well the integration scheme for viscous fluxes works at finite τ_π, we consider the evolution of the bulk pressure[2] in the same $(0+1)$ dimensional case, but at finite τ_Π. In this case, knowing that $\Pi_{\rm NS} = \zeta/\tau$ one has:

$$\frac{\partial \Pi}{\partial \tau} = -\frac{1}{\tau_\Pi}\left(\Pi - \frac{\zeta}{\tau}\right) - \frac{4\Pi}{3\tau}. \tag{41}$$

Eq. (41), *without* the term $\frac{4\Pi}{3\tau}$ has an analytical solution expressed in terms of exponential integral function $\mathrm{Ei}(x)$:

$$\Pi(\tau) = \Pi(\tau_0)e^{-(\tau-\tau_0)/\tau_\Pi} + \frac{\zeta}{\tau_\Pi}e^{-\tau/\tau_\Pi}\left[\mathrm{Ei}(\tau_0/\tau_\Pi) - \mathrm{Ei}(\tau/\tau_\Pi)\right]. \tag{42}$$

The inclusion of the $\frac{4\Pi}{3\tau}$ term leads to a more complicated analytical solution. In Fig. 8 a comparison between both (with and without the $\frac{4\Pi}{3\tau}$ term) analytical and numerical solutions is given. The specific set of parameters is $\zeta = 1$, $\tau_\pi = 0.1$ fm, $\tau_0 = 0.6$ fm and $\Pi(\tau_0) = 0$. One observes an excellent reproduction of both, the full and the "cut" (with and without $\frac{4\Pi}{3\tau}$ term, respectively) analytical viscous solutions.

[2] The evolution equations for the non-trivial components of the shear stress tensor, π^{xx}, π^{yy} or $\pi^{\eta\eta}$ are all very similar, therefore we only discuss the evolution of the bulk pressure.

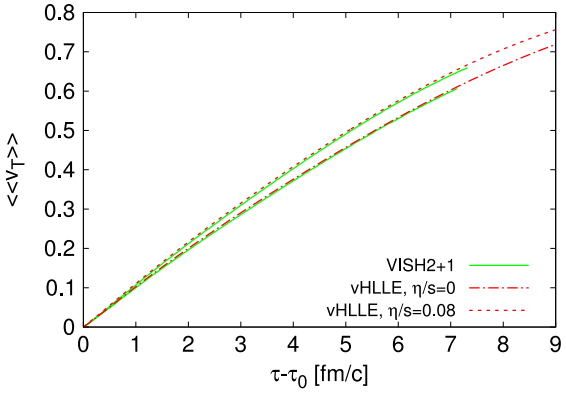

Fig. 9. Averaged radial flow as a function of proper time for our hydro code (vHLLE) compared to VISH2+1 [7].

4.3. Matter expansion in heavy ion collisions

Let us now turn to a more realistic scenario. We compare the present hydrodynamic simulations for a physical scenario related to heavy ion collisions with the open TECHQM results [35]. The initial state has full homogeneity in η direction ($v_\eta = 0$, which corresponds to longitudinal scaling flow $v_z = z/t$) and the initial conditions in the transverse $(x-y)$ plane are taken from the optical Glauber model for symmetric nucleus–nucleus collision:

$$\begin{aligned}\epsilon(\tau_0, r_x, r_y) &= C \cdot n_{WN}(r_x, r_y) \\ &= C \cdot T_A\left(r_x + \frac{b}{2}, r_y\right)\left\{1 - \left[1 - T_A\left(r_x - \frac{b}{2}, r_y\right)\frac{\sigma_{NN}}{A}\right]^A\right\} \\ &\quad + C \cdot T_A\left(r_x - \frac{b}{2}, r_y\right) \\ &\quad \times \left\{1 - \left[1 - T_A\left(r_x + \frac{b}{2}, r_y\right)\frac{\sigma_{NN}}{A}\right]^A\right\},\end{aligned} \tag{43}$$

where the nuclear thickness function $T_A(x, y) = \int dr_z \rho(r_x, r_y, r_z)$ is normalized so that $\int T_A(x, y)dxdy = A$, and $\rho(r_x, r_y) = c/(exp[(r - R_A)/\delta] + 1)$ is the density distribution for nucleons in the nucleus. For Au–Au collision the parameters are $A = 197$, $R_A = 6.37$ fm, $\delta = 0.54$ fm, $\sigma_{NN} = 40$ mb is the inelastic nucleon–nucleon cross section and C is chosen so that $\epsilon_0(0, 0; b = 0) = 30$ GeV/fm^3.

Again we use the EoS for a relativistic massless gas, $p = \epsilon/3$, assuming 2.5 massless quark degrees of freedom. The degeneracy factors are $g_q = 2 \cdot 2 \cdot 3 = 12$ for quarks and $g_g = 16$ for gluons.

For viscous hydrodynamic simulations the bulk viscosity is set to zero, $\pi^{\mu\nu}$ at τ_0 is initialized with the Navier–Stokes values, yielding $\pi^{xx} = \pi^{yy} = -\tau^2\pi^{\eta\eta}/2 = 2\eta/(3\tau_0)$. The relaxation time for the shear is taken as $\tau_\pi = 3\eta/(sT)$.

Fig. 9 shows the comparison between the present simulations and the (2+1) dimensional result by Song and Heinz for the average transverse velocity as a function of evolution time τ for initial conditions with impact parameter $b = 0$. The average is defined as

$$\ll v_T \gg = \int \frac{v_T \cdot \epsilon}{\sqrt{1 - v_T^2}} d^2 r_T$$

where $v_T = \sqrt{v_x^2 + v_y^2}$ and the integration is made for a slice of the system (cells) with rapidity $y = 0$. Shear viscosity works to equalize the expansion in different directions, thus decreasing work in longitudinal direction and accelerating the transverse expansion. This results in an additional acceleration of the transverse radial flow. Our results on the radial expansion for the ideal and viscous

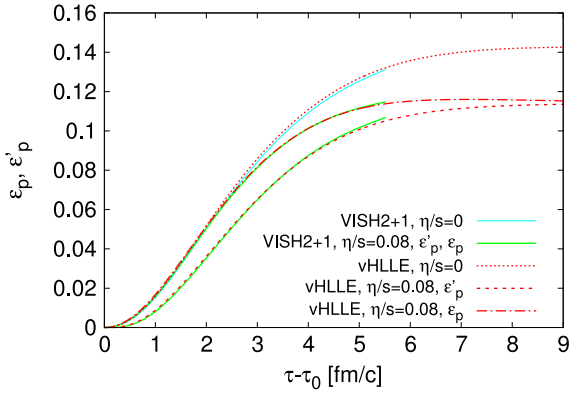

Fig. 10. Flow anisotropies ϵ_p and ϵ_p' (see text for explanation) as a function of proper time for our hydro code (vHLLE) compared to VISH2+1 [7].

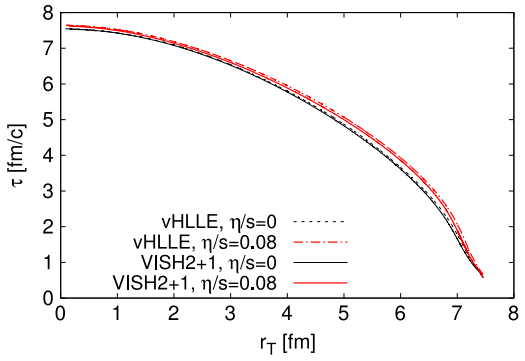

Fig. 11. Iso-thermal surface corresponding to $T_f = 130$ MeV obtained with our hydro code (vHLLE) compared to the results from VISH2+1 [7].

case are consistent with the benchmark results from the VISH2+1 code.

In the same way shear viscosity suppresses the development of flow anisotropies in the transverse plane, the latter being generated by anisotropic pressure gradients in hydrodynamics. To explore this effect, we set the initial conditions to $b = 7$ fm. Fig. 10 shows the corresponding time evolution of the flow anisotropy, defined as

$$\epsilon_p = \frac{\langle T^{xx}_{\rm id} - T^{yy}_{\rm id}\rangle}{\langle T^{xx}_{\rm id} + T^{yy}_{\rm id}\rangle}$$
$$\epsilon_p' = \frac{\langle T^{xx} - T^{yy}\rangle}{\langle T^{xx} + T^{yy}\rangle}$$

where $\langle\cdots\rangle = \int \ldots d^2r_T$. The quantities ϵ_p and ϵ_p' are calculated using the ideal part of the energy–momentum tensor and the full energy–momentum tensor, respectively. The observed suppression of ϵ_p in the viscous case relative to the ideal case comes solely from the rearrangement of collective flow, while ϵ_p' is suppressed stronger due to contributions from $\pi^{\mu\nu}$. The results are consistent with the benchmark results from the VISH2+1 code [7].

Finally, in Fig. 11 we show the iso-thermal surfaces for the case $b = 0$ corresponding to temperature $T_f = 130$ MeV (or $\epsilon_f = 0.516$ GeV/fm^3). The small differences (less than $\Delta x/2 = 0.1$ fm) are related to the details (interpolation scheme) of the freeze-out surface resolution.

4.4. Energy conservation

The present scheme is conservative when Minkowski coordinates are used. However it loses the conservation property in Milne coordinates because the source terms are non-zero, and the accuracy of total energy conservation is determined by the source term integration part. To quantify the numerical accuracy of the energy conservation in a physical scenario, we run the code with initial conditions from the Glauber model (Eq. (43)) with a limited rapidity profile, so that there is no energy/momentum leak through the grid edges in rapidity:

$$\epsilon(\tau_0, r_x, r_y, \eta_s) = CN_{\rm WN}\theta(Y_b - \eta_s) \cdot \exp\left[-\theta(|\eta_s| - \Delta\eta)\frac{(|\eta_s| - \Delta\eta)^2}{\sigma_\eta^2}\right] \quad (44)$$

where $Y_b = 5.3$ corresponds to the beam rapidity, $\sigma_\eta = 2.1$, and $\Delta\eta = 1.3$ is the size of plateau around midrapidity. The hydrodynamic grid consists of $n_x \cdot n_y \cdot n_z = 150 \cdot 150 \cdot 100$ cells with $\Delta x = \Delta y = 0.2$ fm/c, $\Delta\eta = 0.2$ units, and corresponding $\Delta\tau = 0.05$. The total energy on the hypersurface of constant τ is defined as $E_{\rm tot}(\tau) = \int T^{0i} d\sigma_i$, which can be expanded as:

$$E_{\rm tot} = \tau \int d\eta d^2r_T[(\epsilon + p)\tilde{u}^\tau(\tilde{u}^\tau \cosh\eta + \tilde{u}^\eta \sinh\eta) - p\cosh\eta + \tilde{\pi}^{\tau\tau}\cosh\eta + \tilde{\pi}^{\tau\eta}\sinh\eta] \quad (45)$$

$$S_{\rm tot} = \tau \int d\eta d^2r_T \cdot s\tilde{u}^\tau. \quad (46)$$

Numerically $\int d\eta d^2r_T(\ldots) \to \Delta x\Delta y\Delta\eta \sum_{\rm cells}(\ldots)$.

It is important to note that in Israel–Stewart framework the entropy current s^μ includes non-equilibrium corrections:

$$s^\mu = s_{\rm eq} - \left(\frac{\beta_0}{2T}\Pi^2 + \frac{3}{2(\epsilon + p)T}\pi^{\mu\nu}\pi_{\mu\nu}\right)u^\mu$$

where the coefficient in front of $\pi^{\mu\nu}\pi_{\mu\nu}$ is taken consistently with the evolution equation (14), and $\Pi = 0$ since we consider shear viscosity only.

The resulting values of total energy and entropy in the beginning and in the end of hydrodynamic evolution are shown in Table 1. We conclude that energy is conserved on a level better than 3%.

Table 1
Total energy and entropy calculated in the beginning ($\tau = 1$ fm/c) and in the end ($\tau = 10$ fm/c) of 3D hydrodynamic evolution with initial energy density profile (44) for different viscosity/EoS combinations. Small numbers in parentheses denote percentage of increase compared to the value at $\tau = 1$ fm/c.

η/s	0	0	0.1
EoS	$p = \frac{\epsilon}{3}$	Laine [36]	$p = \frac{\epsilon}{3}$
$E_{\rm tot}(\tau = 1)$ (GeV)	68 230	68 230	68 230
$E_{\rm tot}(\tau = 10)$ (GeV)	69 699	69 629	70 126
	(+2.2%)	(+2.1%)	(+2.8%)
$S_{\rm tot}(\tau = 1)$	49 055	45 469	49 994
$S_{\rm tot}(\tau = 10)$	49 206	45 601	54 537
	(+0.3%)	(+0.29%)	(+9.1%)

4.5. Numerical viscosity

Since we study the effects of physical viscosity with the code, the important question which has to be answered is: what amount of numerical viscosity the code has, and how does it depend on the parameters?

To study this, we follow the method used in [19] and examine the sound wave attenuation in numerical hydrodynamic solution. The initial conditions for 1D hydrodynamic simulation in Minkowski coordinates are taken as

$$\epsilon(x) = \epsilon_0 + \delta\epsilon\sin(2\pi x/\lambda), \quad (47)$$

$$v_x(x) = \frac{c_s\delta\epsilon}{\epsilon_0 + p_0}\sin(2\pi x/\lambda), \quad (48)$$

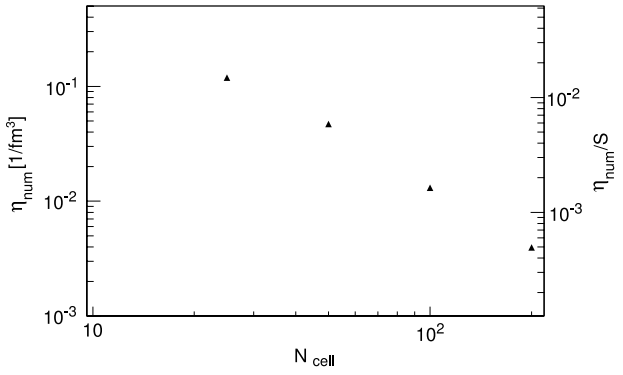

Fig. 12. Numerical viscosity $\eta_{\rm num}$ and corresponding $\eta_{\rm num}/s$ values (the latter using upper estimate for the temperature $T = 0.5$ GeV) observed from sound wave attenuation for different grid sizes.

supplemented by an EoS for an ultrarelativistic gas, $p = \epsilon/3$. Given that $\delta\epsilon \ll \epsilon_0$, this represents a sound wave with length λ propagating on the static uniform background with energy density ϵ_0. We link the last cell in x direction to the first one to set up periodic boundary conditions on the hydro mesh, so that $\epsilon(-\lambda/2) = \epsilon(\lambda/2)$, $v_x(-\lambda/2) = v_x(\lambda/2)$. This setup mimics the propagation of a plain sound wave over an infinite medium. In hydrodynamics the attenuation (or damping) of the sound wave amplitude is only possible due to viscosity. Provided that the damping is not fast (i.e. that the amplitude does not change significantly during one cycle) there is an analytical expression for the amplitude of sound wave after one cycle $t = \lambda/c_s$:

$$\delta\epsilon(\lambda/c_s;\,\eta) = \delta\epsilon(0;\,\eta)\exp\left(-\frac{8\pi^2\eta}{3\lambda c_s(\epsilon_0+p_0)}\right), \tag{49}$$

here and further $c_s = c_s(\epsilon_0)$. However, due to the presence of numerical dissipation, the attenuation of the sound wave is also possible even with zero physical viscosity. To quantify the differences between the solutions we calculate the L1 norm for the energy density function on one-wavelength segment, defined as:

$$L(N_{\rm cell}) = \frac{\lambda}{N_{\rm cell}}\sum_{i=1}^{N_{\rm cell}} |\epsilon_{\rm num}(x_i,\,\lambda/c_s) - \epsilon_{\rm anal}(x_i,\,\lambda/c_s)|$$

which is compared to the same quantity based on the difference between inviscid and viscous solutions:

$$L_{\rm phys}(\eta) = \frac{\lambda}{N_{\rm cell}}\sum_{i=1}^{N_{\rm cell}} \left|\epsilon_{\rm anal}\left(x_i,\,\frac{\lambda}{c_s};\,\eta\right) - \epsilon_{\rm anal}\left(x_i,\,\frac{\lambda}{c_s};\,0\right)\right|.$$

For the latter quantity, in the limit of an infinitely small cell size one gets an analytical result:

$$L_{\rm phys}(\eta) = \frac{2\lambda}{\pi}\delta\epsilon(0)\left(1-\exp\left(-\frac{8\pi^2\eta}{3\lambda c_s(\epsilon_0+p_0)}\right)\right)$$

which is also quite accurate for finite cell size. Comparing the two quantities, $L_{\rm phys}(\eta_{\rm num}) = L(N_{\rm cell})$ one gets:

$$\eta_{\rm num} = -\frac{3\lambda}{8\pi^2}c_s(\epsilon_0+p_0)\ln\left[1-\frac{\pi}{2\lambda\delta\epsilon(0)}L(N_{\rm cell})\right]. \tag{50}$$

We initialize the system with the following parameter values: $\lambda = 10$ fm, $\epsilon_0 = 3$ GeV/fm^3 and $\delta\epsilon(0) = 0.003$ GeV/fm^3. The values of the resulting numerical viscosity for different grid sizes are shown in Fig. 12. Since the shear viscosity coefficient is proportional to density, the relevant (and dimensionless) quantity for relativistic case is the ratio of shear viscosity to entropy density, η/s. Assuming zero chemical potential, one gets:

$$\frac{\eta_{\rm num}}{s} = -\frac{3\lambda T}{8\pi^2}c_s\ln\left[1-\frac{\pi}{2\lambda\delta\epsilon(0)}L(N_{\rm cell})\right]. \tag{51}$$

Note that since $L(N_{\rm cell}) \propto \epsilon_0$, the above expression depends only on λ and T. Assuming $T = 0.5$ GeV as an upper estimate for the initial phase of the hydrodynamic expansion in A + A collisions and $\lambda = 10$ fm, one gets $\eta_{\rm num}/s = 0.015$ for $N_{\rm cell} = 25$. For $N_{\rm cell} = 100$, which is a typical grid size for the physical simulations, $\eta_{\rm num}/s = 0.0016$. I.e., the value of the numerical viscosity to entropy density is about 50 times smaller than the lower bound for the physical viscosity $(\eta/s)_{\rm min} = 1/4\pi$.

We should finally note that the estimate does not guarantee that a similar amount of numerical viscosity is present in full-fledged $(3+1)$ dimensional simulations of matter expansion with the given code. To estimate the numerical viscosity in arbitrary geometry is a rather complicated topic beyond this paper.

5. Conclusions

We have presented a detailed description and test results of a $(3+1)$ dimensional relativistic viscous hydrodynamic code based on the Godunov method and the relativistic HLLE approximation for the solution of the Riemann problem for its inviscid part. This choice ensures that the code is capable of treating shock wave configurations accurately. It has been shown that the code is capable of solving the equations of relativistic viscous hydrodynamics in the Israel–Stewart framework with the help of the ideal–viscous splitting method. We have presented the results of several test problems: the 1 dimensional (2 dimensional) shock tube, Gubser flow and two analytical viscous hydrodynamic solutions. The numerical viscosity of the code in the inviscid case has been estimated and found to be sufficiently small.

The primary application of the code is the simulations of the hydrodynamic expansion of QCD matter created in relativistic heavy ion collisions. For this aim we have also checked the code against the test cases by the TECHQM group.

Acknowledgments

The authors acknowledge the financial support by the ExtreMe Matter Institute EMMI, Helmholtz International Center for FAIR and Hessian LOEWE initiative. The work of P.H. was supported by BMBF under contract no. 06FY9092. Computational resources have been provided by the Center for Scientific Computing (CSC) at the Goethe-University Frankfurt.

Appendix. Velocity finding

An important part of hydrodynamic algorithm is the procedure to find the flow velocity v_i, energy density ϵ and densities of conserved charges n_k in the fluid rest frame from the conserved variables $T^{\tau\mu}$, N^μ.

The procedure is essentially the same for inviscid and viscous cases. In the latter case to account for shear viscosity, one has to subtract the $\pi^{\tau\mu}$ (which are evolved independently with IS equations) from the total energy–momentum tensor: $T^{\tau\mu}_{\rm id} = T^{\tau\mu} - \pi^{\tau\mu}$.

The definition of the energy–momentum tensor of the fluid gives the following system of equations:

$$\begin{aligned}
T^{\tau\tau}_{\rm id} &= E = (\epsilon+p)/(1-v^2) - p,\\
T^{\tau x}_{\rm id} &= M_x = (\epsilon+p)v_x/(1-v^2),\\
T^{\tau y}_{\rm id} &= M_y = (\epsilon+p)v_y/(1-v^2),\\
T^{\tau\eta}_{\rm id} &= M_\eta = (\epsilon+p)v_\eta/(1-v^2),\\
N_c &= n_c/\sqrt{1-v^2}
\end{aligned} \tag{A.1}$$

in terms of ϵ, v_x, v_y, v_η and n_c (c is numbering the conserved charges), which is closed with an equation of state:

$$p = p(\epsilon, n_i).$$

Due to the symmetry of the equations, $v_i(E+p) = M_i$. This allows one to reduce the problem to a one-dimensional equation for the absolute value of the velocity, which has to be solved numerically [33]:

$$v = \frac{|\vec{M}|}{E + p(E - \vec{M}\cdot\vec{v}, N_i\sqrt{1-v^2})} \tag{A.2}$$

then the rest of unknowns are recovered as

$$v_x = M_x/|\vec{M}| \qquad \epsilon = E - \vec{M}\cdot\vec{v}$$
$$v_y = M_y/|\vec{M}| \qquad n_i = N_i\sqrt{1-v^2}$$
$$v_\eta = M_\eta/|\vec{M}|.$$

For non-exotic equation of state Eq. (A.2) has exactly one root in the interval $v = [0\ldots 1)$ and is solved with Newton's method.

In the presence of bulk pressure one has to add it to the equilibrium pressure, $p(\epsilon, n_i) \to p(\epsilon, n_i) + \Pi$ and proceed to solve (A.2) in the same way.

References

[1] http://www.einstein-online.info/spotlights/hydrodynamics_realm.
[2] J.M. Martí, E. Müller, Living Rev. Relativity 6 (2003) 7. http://www.livingreviews.org/lrr-2003-7.
[3] T. Hirano, K. Tsuda, K. Kajimoto, arXiv:nucl-th/0011087;
T. Hirano, Phys. Rev. C 65 (2002) 011901.
[4] P.F. Kolb, J. Sollfrank, U. Heinz, Phys. Rev. C 62 (2000) 054909.
[5] C.E. Aguiar, T. Kodama, T. Osada, Y. Hama, J. Phys. G 27 (2001) 75;
T. Kodama, C.E. Aguiar, T. Osada, Y. Hama, J. Phys. G 27 (2001) 557.
[6] C. Nonaka, S.A. Bass, Phys. Rev. C 75 (2007) 014902;
C. Nonaka, E. Honda, S. Muroya, Eur. Phys. J. C 17 (2000) 663.
[7] H. Song, U. Heinz, Phys. Rev. C 77 (2008) 064901.
[8] R. Baier, P. Romatschke, Eur. Phys. J. C 51 (2007) 677–687.
[9] A. Muronga, Phys. Rev. C 76 (2007) 014909.
[10] S. Pratt, J. Vredevoogd, Phys. Rev. C 78 (2008) 054906.
[11] H. Petersen, J. Steinheimer, G. Burau, M. Bleicher, H. Stöcker, Phys. Rev. C 78 (2008) 044901.
[12] E. Molnar, H. Niemi, D.H. Rischke, Eur. Phys. J. C 65 (2010) 615.
[13] B. Schenke, S. Jeon, C. Gale, Phys. Rev. C 82 (2010) 014903.
[14] K. Werner, et al., Phys. Rev. C 82 (2010) 044904.
[15] Iu.A. Karpenko, Yu.M. Sinyukov, Phys. Rev. C 81 (2010) 054903.
[16] H. Holopainen, H. Niemi, K. Eskola, Phys. Rev. C 83 (2011) 034901.
[17] P. Bozek, Phys. Rev. C 85 (2012) 034901.
[18] J. Gerhard, V. Lindenstruth, M. Bleicher, Comp. Phys. Commun. 184 (2013) 311.
[19] Y. Akamatsu, S. Inutsuka, C. Nonaka, M. Takamoto, J. Comput. Phys. 256 (2014) 34–54.
[20] J. Noronha-Hostler, G.S. Denicol, J. Noronha, R.P.G. Andrade, F. Grassi, Phys. Rev. C 88 (2013) 044916.
[21] L. Del Zanna, et al., Eur. Phys. J. C 73 (2013) 2524.
[22] J.D. Bjorken, Phys. Rev. D 27 (1983) 140.
[23] A. Harten, P.D. Lax, B. van Leer, SIAM Rev. 25 (1983) 35;
B. Einfeldt, SIAM J. Numer. Anal. 25 (1988) 294.
[24] V. Schneider, U. Katscher, D.H. Rischke, B. Waldhauser, J.A. Maruhn, C.D. Munz, J. Comput. Phys. 105 (1993) 92–107.
[25] W. Israel, Ann. Phys. 100 (1976) 310;
Stewart, Proc. R. Soc. Lond. Ser. A Math. Phys. Eng. Sci. 357 (1977) 59;
W. Israel, J.M. Stewart, Ann. Phys. 118 (1979) 341.
[26] K. Werner, M. Bleicher, B. Guiot, Iu. Karpenko, T. Pierog, Phys. Rev. Lett. 112 (2014) 232301. http://dx.doi.org/10.1103/PhysRevLett.112.232301;
K. Werner, B. Guiot, Iu. Karpenko, T. Pierog, Phys. Rev. C 89 (2014) 064903. http://dx.doi.org/10.1103/PhysRevC.89.064903.
[27] Iu. Karpenko, M. Bleicher, P. Huovinen, H. Petersen, J. Phys.: Conf. Ser. 509 (2014) 012067. http://dx.doi.org/10.1088/1742-6596/509/1/012067.
[28] L.D. Landau, E.M. Lifshitz, Fluid Mechanics, Pergamon Press, 1959.
[29] G.S. Denicol, E. Molnár, H. Niemi, D.H. Rischke, Eur. Phys. J. A 48 (11) (2012) 170.
[30] S.K. Godunov, Math. Sbornik 47 (1959) 271. Translated US Joint Publ. Res. Service, JPRS 7226, 1969.
[31] R. Courant, K.O. Friedrichs, H. Lewy, Math. Ann. 100 (1928) 32–74.
[32] M. Takamoto, S. Inutsuka, J. Comput. Phys. 230 (2011) 7002.
[33] D.H. Rischke, S. Bernard, J.A. Maruhn, Nucl. Phys. A 595 (1995) 346–382.
[34] S.S. Gubser, Phys. Rev. D 82 (2010) 85027.
[35] TECHQM working group, https://wiki.bnl.gov/TECHQM/index.php/Bulk_Evolution.
[36] M. Laine, Y. Schroder, Phys. Rev. D 73 (2006) 085009.

Eur. Phys. J. A (2012) **48**: 171
DOI 10.1140/epja/i2012-12171-9

THE EUROPEAN PHYSICAL JOURNAL A

Regular Article – Theoretical Physics

Particlization in hybrid models

Pasi Huovinen[1,a] and Hannah Petersen[2]

[1] Institut für Theoretische Physik, Johann Wolfgang Goethe-Universität, D-60438 Frankfurt am Main, Germany
[2] Department of Physics, Duke University, Durham, NC 27708-0305, USA

Received: 8 June 2012 / Revised: 17 September 2012
Published online: 28 November 2012 –
Communicated by T. Bíró

Abstract. In hybrid models, which combine hydrodynamical and transport approaches to describe different stages of heavy-ion collisions, conversion of fluid to individual particles, particlization, is a non-trivial technical problem. We describe in detail how to find the particlization hypersurface in a 3+1 dimensional model, and how to sample the particle distributions evaluated using the Cooper-Frye procedure to create an ensemble of particles as an initial state for the transport stage. We also discuss the role and magnitude of the negative contributions in the Cooper-Frye procedure.

1 Introduction

In recent years the so-called hybrid models [1–9] have become very popular in describing the expansion and evolution of the hot dense matter created in ultrarelativistic heavy-ion collisions. In these models the different stages of the expansion are described using different models: The early stages of the expansion, when the matter is presumably partonic, are described using ideal or dissipative fluid dynamics, whereas the late dilute stage after hadronization is described using a hadronic transport model like RQMD [10], UrQMD [11,12] or JAM [13,14].

Hybrid models are conceptually attractive since they attempt to combine the best features of fluid dynamics and transport: The complicated microscopic dynamics of hadronization can be sidestepped by assuming it to happen adiabatically, in which case it can be described using fluid dynamics. On the other hand, the dilute hadronic matter is assumed to be highly dissipative and deviate gradually from local equilibrium. Description of such a matter using fluid dynamics is demanding, but is trivial using microscopic transport, which by construction can handle matter arbitrarily far from equilibrium. Also, the transport models describe the last rescattering of particles, so-called freeze-out, based on individual scattering cross-sections. Thus freeze-out is not controlled by a parameter which value is known only after comparison with data.

Furthermore, it has been realised that a consistent comparison with the data is easier if one generates an ensemble of particles event by event, and analyses these ensembles in a similar way than the actual data has been analysed [9,15,16]. In hybrid models this requires no further effort since the transport models are based on propagation of individual particles along their semiclassical trajectories, and thus require the generation of such ensembles to begin with.

However, connecting two approaches with very different degrees of freedom —densities, velocity, and possible dissipative currents in the fluid, and individual particles in the cascade— is highly non-trivial. Instead of running hydro and cascade side by side and using the cascade calculation to provide the boundary conditions for fluid dynamics, all the present hybrid models solve fluid dynamics independently of the cascade taking the boundary condition as vacuum at infinity (see discussion in ref. [17]). The boundary where one switches from fluid dynamical to transport description is then determined a posteriori, once the evolution of the fluid is known. This boundary, or switching surface, is usually chosen to be a surface of constant temperature, energy density, or time. The particle distributions on this surface are evaluated using the Cooper-Frye procedure [18]. These distributions are sampled to generate an ensemble of particles with well-defined positions and momenta, and these ensembles are used as an initial state for the transport stage. Note that even if the transport stage describes the final freeze-out of the particles without additional parameters, the choice of the criterion where to switch from fluid to cascade is an equally free parameter than the freeze-out temperature in a conventional hydrodynamical model. Unfortunately the final results are also somewhat sensitive to this switching criterion as discussed in ref. [9], and as we will discuss later.

We want to emphasise that this switching from fluid dynamics to transport is not freeze-out. By definition,

[a] e-mail: huovinen@th.physik.uni-frankfurt.de

there are no rescatterings, only resonance decays after freeze-out. Thus, if one switches from fluid to transport at freeze-out, the transport stage is unnecessary. It does nothing else but lets the resonances decay. On the other hand, the switching is not necessarily hadronization either. Since the deconfinement transition is a smooth crossover, there is no clear point where hadronization should take place, and it is easier to choose to switch at a stage where the system has already hadronized. In the following we assume that there is no change in the physics nor in the properties of the system on the switching surface. It is only a change in the description of the system. Thus we call the process of changing from fluid dynamics to transport particlization, conversion of fluid to particles.

In this paper we describe some technical aspects of particlization in hybrid models, and how different choices of the switching criterion and constraints imposed to the sampling of the distributions affect the final particle distributions in $E_{\rm lab} = 160A\,\mathrm{GeV}$ Pb+Pb (SPS) and $\sqrt{s_{\rm NN}} = 200\,\mathrm{GeV}$ Au+Au (RHIC) collisions. In particular we discuss finding the particlization surface and its properties in sect. 2, the negative contributions of Cooper-Frye procedure and how to take them into account when sampling the distributions in sect. 3, the actual sampling procedure in sect. 4, and calculations within one specific hybrid approach in sect. 5.

2 Surface finding

The Cooper-Frye procedure [18] for calculating particle distributions on a surface is based on evaluating a particle four-current through a surface, and a kinetic theory decomposition of a four-current j^μ in terms of particle distribution $f(p,x)$,

$$N = \int_\sigma \mathrm{d}\sigma_\mu j^\mu(x) = \int_\sigma \mathrm{d}\sigma_\mu \int \frac{\mathrm{d}^3p}{E}\, p^\mu f(x,p)$$
$$\Longrightarrow E\frac{\mathrm{d}N}{\mathrm{d}p^3} = \int_\sigma \mathrm{d}\sigma_\mu p^\mu f(x,p) \approx \sum_\sigma \Delta\sigma_\mu p^\mu f(x,p). \quad (1)$$

Thus one needs to find not only the location of the surface σ where one applies the Cooper-Frye formula, but also its normal. If we knew the analytic expression for the surface, its normal would be simply given by [19,20]

$$\mathrm{d}\sigma_\mu = \varepsilon_{\mu\alpha\beta\gamma}\frac{\partial x^\alpha}{\partial a}\frac{\partial x^\beta}{\partial b}\frac{\partial x^\gamma}{\partial c}\mathrm{d}a\,\mathrm{d}b\,\mathrm{d}c\,, \quad (2)$$

where a, b, c are the coordinates on the surface and $\varepsilon_{\mu\alpha\beta\gamma}$ is the totally antisymmetric Levi-Cività tensor. However, we do not have an analytic expression since we solve the evolution of the system numerically. Finding the location of an isosurface on a discrete grid is easy, but evaluating the size[1] and normal of each discrete surface element is not, since one has to make sure that the surface elements cover the entire surface without leaving holes or double counting any part of the surface.

In computer graphics and image processing the problem of finding an isosurface of a discrete scalar field is well known, and many algorithms have been proposed for the task, see, *e.g.*, ref. [21] and references therein. One of the best known of these algorithms is the so-called Marching Cubes algorithm [22], a simplified version of which was implemented in a hydrodynamical model by Kataja and Venugopalan [23,24], and subsequently used in AZHYDRO [25–27]. The original Marching Cubes algorithm was extended for hypersurfaces in four dimensional space in ref. [21], and a simplified version implemented in a 3+1 dimensional hydrodynamical model by Schenke [28]. However, it is known that the original Marching Cubes algorithm cannot resolve all possible surface configurations, and may leave holes in the final surface [29,30]. This problem is not serious: As quoted in ref. [28], only 1% of the surface elements in a typical heavy-ion collision calculation are not fully resolved. But, if one is doing event-by-event hydrodynamical calculations with irregular initial conditions, one may expect much more complicated structures to appear, and the Marching Cubes algorithm may leave more holes in the surface. To avoid this problem altogether, we have slightly modified the algorithm proposed in ref. [31], and generalised it for finding a three dimensional hypersurface in four dimensional space[2]. For the lack of a better name, we call it here "disordered lines" algorithm. This algorithm may also have been implemented in ref. [19], but the description there is too vague to tell.

In algorithms solving the equations of motion of fluid dynamics like SHASTA [32–34], a grid point is considered to be in the middle of a corresponding volume element. For purposes of surface finding it is useful to consider the dual of the grid, where the grid points are thought to be at the corners of a volume element, and the values within a volume element can be obtained by interpolation. To find the location of the surface it is practical to "march" through the entire grid and check every volume element whether the values at the corners are all above or all below the isovalue. If not, *i.e.* if some of the corners are above, and some below the isovalue, the surface passes through this volume element.

An alternative to this exhaustive search method is the continuation method [35], which after finding a surface element, checks only the neighbouring volume elements which one of them contains the surface, moves to that element, and continues until it either finds the edge of the grid or returns to the volume element it found first. The continuation method is faster than the exhaustive search, but if the surface is disjoint, it will not necessarily find all parts of the surface, whereas the exhaustive search method by construction finds all parts of the surface.

In the following we call volume elements (hyper)cubes, and explain the algorithm in a 3D case first. Once a cube containing the isosurface is found, the positions of the

[1] The size enters as the length of the discrete normal vector $\Delta\sigma_\mu$.

[2] Fortran and C++ subroutines, cornelius, implementing this algorithm in 3D and 4D, are available at `https://karman.physics.purdue.edu/OSCAR/`.

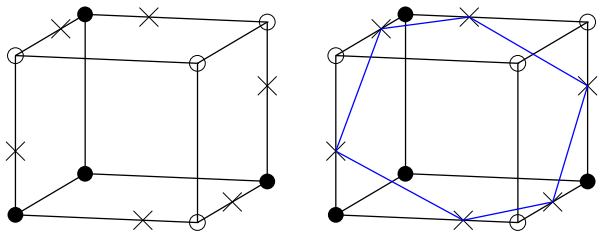

Fig. 1. A 3D volume element, a cube, with four corners above (solid dots) and four below (open dots) the isovalue. In the left panel the points where the interpolated value is the isovalue are marked with crosses. In the right panel these intersection points have been connected to form a polygon. This polygon is a surface element of the isosurface.

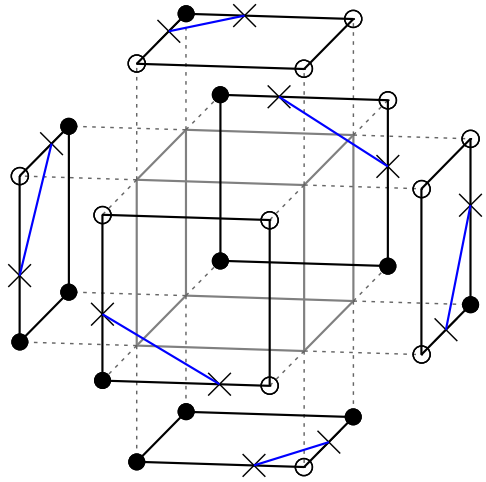

Fig. 2. Reduction of a three-dimensional problem into a series of two-dimensional problems: We find the surface element by looking for its edges on the faces of the cube.

isosurface on the edges of the cube can be found by linear interpolation, see illustration in fig. 1. How to sort these intersection points to form a polygon (or a polyhedron in 4D) which does not cross itself is the crucial part of any algorithm. It can be done in three different ways [36]: By using protomeshes [37], by using a lookup table like in the original Marching Cubes algorithm [21,22,30], or algorithmically [35,38–40] like we do here.

In three or more dimensions the ordering of the intersection points is difficult because of the many possibilities involved, but in two dimensions it is almost trivial. Therefore we reduce the problem of finding the surface into a series of two dimensional problems of finding a line within a square, a line which is an edge of the polygon we want to find, see figs. 1 and 2. If all of the corners of a square are above or below the isovalue, there is of course no edge of the polygon there. If only one of the corners is above or below, we have the configuration shown in fig. 3 a), and if two neighbouring corners are above the isovalue, the configuration is shown in fig. 3 b). The case where two corners above the isovalue are located diagonally is ambiguous. How to choose between configurations shown in figs. 3 c) and d)? We follow the original idea of ref. [31]: If

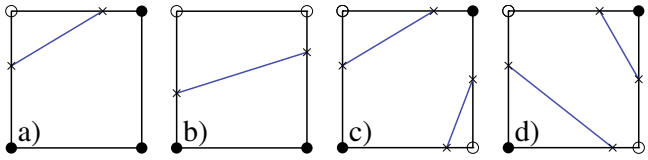

Fig. 3. The non-trivial cases of connecting intersection points at the edges of the face.

the value interpolated at the center of the square is above or equal to the isovalue, the center must be inside of the surface, and if it is below, the center must be outside of the surface. A more sophisticated rule has been suggested in refs. [30,38]: The values on the face are interpolated bilinearly. The isocontours in a bilinear interpolation are hyperbolas, and thus one should interpolate the value at the center of this hyperbola to decide whether the corners above or below the isovalue are linked. A special case occurs when the value in any of the cube corners is the isovalue. In that case we consider such a corner to be within the surface, and place intersection points 10^{-9} times the edgelength away from the corner, on those edges of the cube where the neighbouring corner has a value smaller than the isovalue.

After the intersection points at each face have been found, each edge of the polygon is characterised by two points: its ends. An important difference between our algorithm and that of refs. [31,38] is that in most common cases we do not need to order the edges of the polygon so that the next edge in the list begins where the previous one ends. We may check the faces of the cube in arbitrary order, and keep the edges of the polygon stored in the same arbitrary order. Important exceptions to this rule are the cases where the face by face search returns six or more edges: The surface may consist of two or more disconnected parts, see fig. 4, and we have to sort the edges in sequence to find out whether the surface is disjoint, and which edges belong to which polygon. We group the edges accordingly, and treat the separate polygons independently of each other.

Note that allowing the surface to consist of several parts is necessary for the consistency of the surface. Figure 4 depicts a case when a badly resolved ambiguity on a face may lead to a hole on the surface, or counting parts of the surface twice. Since we solve the ambiguities by using only the information available at the face of a cube, the face is always resolved in the same way, no matter in which cube it is taken to belong to. Thus the surface elements form a consistent surface without holes nor double-counted elements. Furthermore, the rules we described are sufficient to resolve any configuration of values at the cube corners.

After the possible ordering of the edges and dividing them in separate groups if they form two or more disconnected surface elements, we evaluate the area and normal of the polygon(s). The use of Cooper-Frye procedure requires not only the surface area and normal, but also the values of the hydrodynamical fields on the surface. They

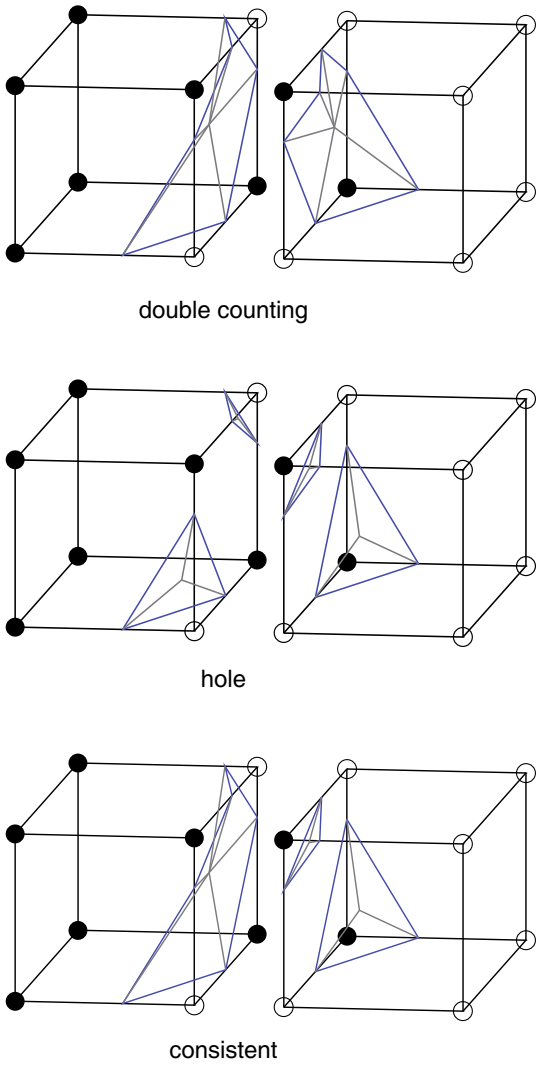

Fig. 4. An example of a configuration where badly resolved ambiguity may lead to double counting or a hole on the surface. The cubes left and right represent neighbouring cubes separated for the sake of clarity.

are best evaluated as interpolated values at the centroid of the surface. Since we have to evaluate the centroid for this purpose anyway, we triangularise the polygon using the centroid: By connecting the ends of each edge of the polygon to the centroid, we obtain a set of triangles which cover the entire polygon. As depicted in fig. 5, the polygon is not necessarily planar. A sum of the areas and normal vectors of the triangles approximates the area and normal of the polygon as

$$\Delta\boldsymbol{\sigma} = \sum_i \frac{1}{2} f_i \mathbf{a}_i \times \mathbf{b}_i, \tag{3}$$

where $\mathbf{a}_i$ and $\mathbf{b}_i$ are vectors from the centroid to the ends of the i-th edge of the polygon, and $f_i = \pm 1$ is chosen so that each of the normal vectors $\frac{1}{2} f_i \mathbf{a}_i \times \mathbf{b}_i$ is directed towards lower values, *i.e.* outside.

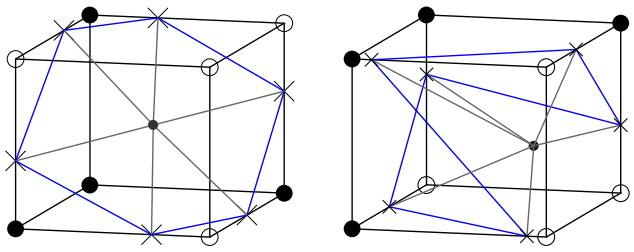

Fig. 5. Examples of triangularisation of the polygon in a simple and a complicated case.

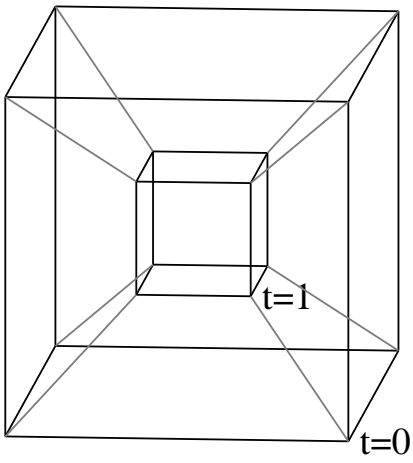

Fig. 6. A 2D projection of a 4D hypercube. In the figure, the cube in the middle is the hyperface of the hypercube at coordinate $t = 1$, the large cube around it is the hyperface at $t = 0$, and the grey lines connecting them are edges with constant values of coordinates x, y, z.

To make the illustrations of the hypersurfaces in a hypercube more understandable, we first show a simple 2D projection of a 4D hypercube in fig. 6, and how an evolving 2D surface in 3D space spans a 3D hypersurface in 4D spacetime in fig. 7. This hypersurface element forms a polyhedron within a hypercube (fig. 8), and like a polygon can be divided into a group of triangles, a polyhedron can be divided into tetrahedra.

We proceed analogously to the 3D case. We first divide the problem into eight three-dimensional problems: As a cube consists of six squares, a hypercube consists of eight cubes, see fig. 9. The surface in each of these is found in the same way than described above. The centroid of these 2D surfaces, which form the faces of the tetrahedra, is calculated, and the corners of the triangles forming these faces are recorded. This is illustrated in fig. 8, where the triangularisation of the face within the $t = 0$ hyperface is shown.

As in 3D the ordering of the edges is not important unless the surface consists of several disconnected parts. If the number of edges and the number of hypercube corners above and below isovalue indicate that this is possible, we order the edges to group them according to the polyhedron they belong to, and treat the groups as separate surfaces.

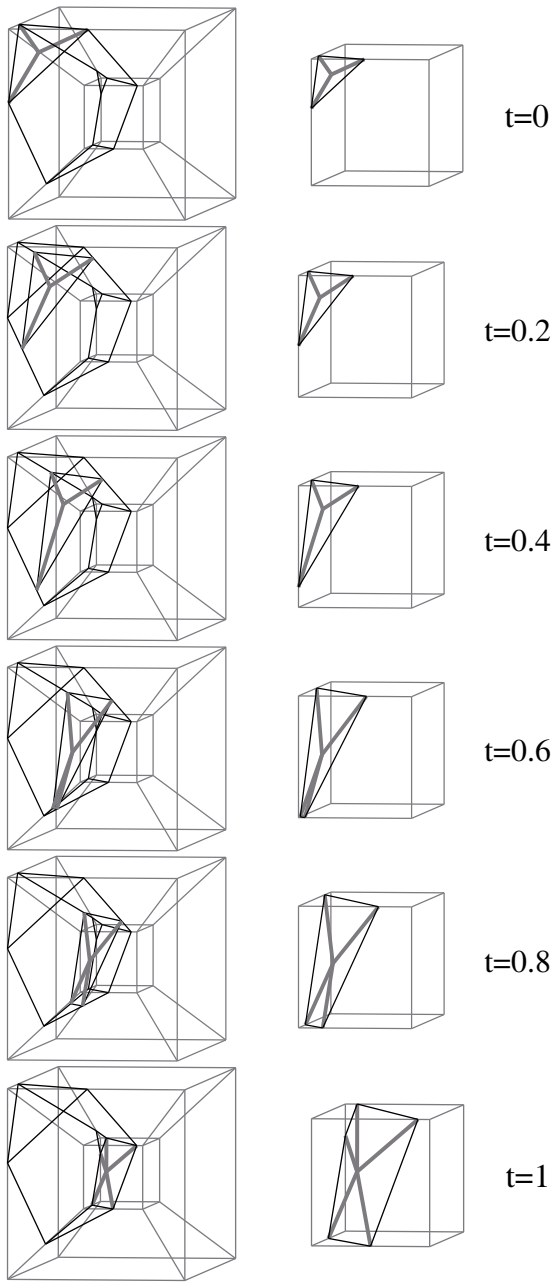

Fig. 7. Time evolution of a surface element in the (left) four- and (right) three-dimensional representation of a volume element. A 2D polygon moving in time spans a 3D polyhedron in a hypercube.

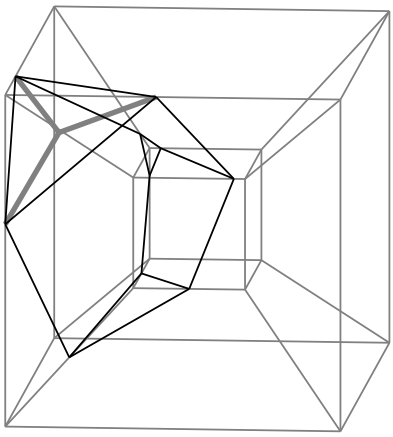

Fig. 8. A hypersurface element, a polyhedron, within a hypercube. A triangularisation of the polyhedron's face with $t = 0$ is shown. We do not show the triangularisation of the other faces for the sake of clarity.

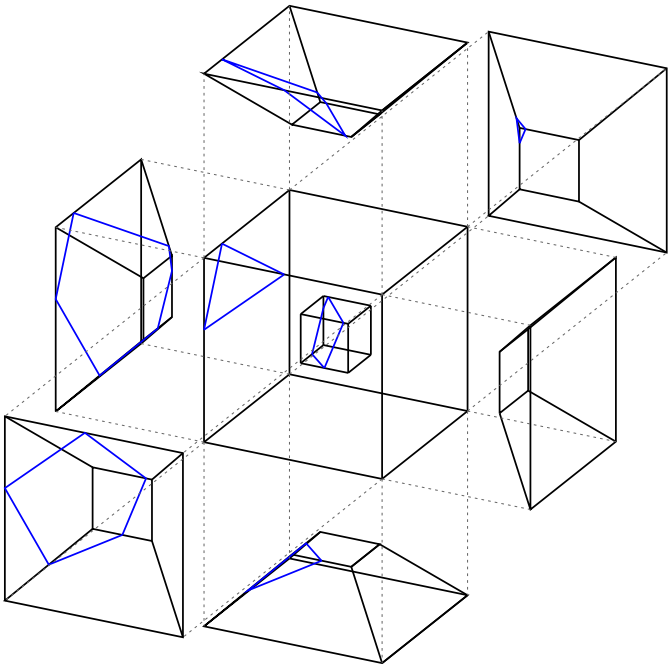

Fig. 9. Reduction of a four-dimensional problem into a series of three-dimensional problems.

We evaluate an approximative centroid for the polyhedron. Analogously to the 2D surface in a 3D space, connecting the centroid to the corners of the triangles forming the faces of the polyhedron, creates a set of tetrahedra which fills the volume of the polyhedron, see fig. 10. The hyperarea, *i.e.* the volume, of the polyhedron and its normal can be calculated as a sum of the volumes and normals of its constituent tetrahedra [28],

$$\Delta\sigma_\mu = \sum_i \varepsilon_{\mu\alpha\beta\gamma} \frac{1}{6} f_i a_i^\alpha b_i^\beta c_i^\gamma, \tag{4}$$

where a_i, b_i and c_i are vectors from the centroid to the corners of the ith triangle, and $f_i = \pm 1$ chosen so that each of the normal vectors of the tetrahedra is directed towards lower values, *i.e.* outside.

We want to emphasise that this algorithm is by no means the only approach for creating consistent surfaces with no holes nor double counting [30,38,39]. Especially Bernd Schlei's VESTA and STEVE algorithms [37], used in ref. [41], are faster than ours and produce even higher-quality surfaces.

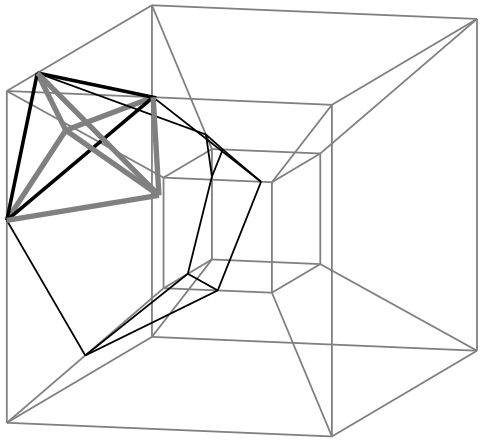

Fig. 10. A part of the tetrahedronisation of the polyhedron based on triangularisation of the faces of the polyhedron. Full tetrahedronisation is not shown for the sake of clarity.

In the recent heavy-ion physics literature two other algorithms for finding a surface in four dimensions have been described. In ref. [9] the surface elements are taken to be the common faces of neighbouring volume elements when the isovalue is reached between them. This algorithm is simple and robust, but it requires very small grid spacing to avoid numerical artefacts (see discussion in refs. [28, 40]). "Very small" in this context means that the volume element for the surface extraction should be the same than the volume element for the fluid evolution, whereas the more sophisticated algorithms discussed here allow significantly larger volume elements for surface evaluation than for fluid evolution. For example, in refs. [42,43] the results were calculated using timestep $\Delta\tau = 0.04\,\mathrm{fm}$ and grid spacing $\Delta x = \Delta y = 0.1\,\mathrm{fm}$, whereas the surface elements were evaluated in cubes 10 times larger in time, and 2 to 4 times larger in both spatial directions (depending on the impact parameter). In the following, however, we play it safe and use the same grid spacing and timestep for both the hydrodynamical evolution and surface extraction to calculate the results shown in sect. 5.

Another algorithm was described in ref. [40] and called a projection method. To our understanding this method insists that there is only one surface element within each volume element. As discussed above this may lead to double counting some parts of the surface.

3 Negative contributions of Cooper-Frye

One of the conceptual problems in using the Cooper-Frye procedure (eq. (1)) to describe freeze-out in hydrodynamical models is that if the surface element of the freeze-out surface is spacelike[3], particles with certain momenta count as a negative contribution to the distribution: These particles move inwards, they are not emitted at the surface but absorbed[4]. However, in a hybrid model, these negative contributions are only a technical, not a conceptual problem. In an ideal case, the switch from fluid to cascade is done in a spacetime region where both descriptions give (approximately) equal solutions [1]. Thus, in the vicinity of the switching surface the particle distributions are close to thermal, and correspond to the hydrodynamical solution on both sides of the surface. Assuming that the system is dilute enough for the kinetic theory decomposition of the fluid variables in terms of particle distributions to be valid, the particle distributions $f(p,x)$ are known on the surface, and there are particles moving inwards through the surface as described by Cooper-Frye. If this is not the case, the particlization takes place in a region where transport and hydro do not give equal solutions, and the switch from hydro to cascade should take place elsewhere.

Thus as an initial state for the cascade, we have to count the particles passing through the switching surface from hydro to cascade. Their distribution is easily obtained by augmenting the distribution in eq. (1) by a Θ-function counting particles going outward,

$$E\frac{\mathrm{d}N(x)}{\mathrm{d}p^3} = \mathrm{d}\sigma_\mu p^\mu f(x,p)\,\Theta(\mathrm{d}\sigma_\mu p^\mu). \tag{5}$$

We have to calculate the number of particles coming from hydro to cascade using this distribution, but we must also have a drain term in the cascade: All the particles crossing the particlization surface from cascade to hydro must be removed from the cascade. Otherwise the conservation laws are not obeyed. It is not possible to remove particles from cascade at the rate described by Cooper-Frye procedure, but we can calculate the distribution of particles which were removed from cascade when they entered the fluid dynamical region. This provides a consistency check: At the end of the evolution we can compare whether the phase-space distribution of particles removed from cascade is (approximately) equal to the negative contributions given by Cooper-Frye. If they are, the calculation was consistent, if not, then the switch from hydro to cascade took place in a wrong place, we have to change the switching criterion, and redo the calculation. Of course this argument assumes that such a spacetime region exists where transport and (dissipative) fluid dynamics give equal spacetime evolution. If this is not the case the whole raison d'être of hybrid models is questionable, since the switching becomes as arbitrary as the freeze-out in hydrodynamical models.

Unfortunately the treatment described above is technically challenging. First, it is numerically expensive to evaluate the number of particles emitted when the distribution is modified by the Θ-function (eq. (5)). Second, we are using UrQMD to describe the hadronic transport, and the present version of UrQMD does not allow tracing

[3] We use the convention to describe a surface as time- or spacelike according to its normal vector. $\mathrm{d}\sigma_\mu \mathrm{d}\sigma^\mu > 0$ is timelike, and $\mathrm{d}\sigma_\mu \mathrm{d}\sigma^\mu < 0$ is spacelike.

[4] In the context of hydrodynamical models, these negative contributions have been discussed, and possible cures proposed, in refs. [17,41,44–51].

the propagation of individual particles in such a way that whenever a particle crosses the boundary between cascade and fluid dynamics, it would be removed from cascade. Such a feature would require extensive rewriting of the code, and is therefore postponed to later. Furthermore, we are using ideal hydro to describe the fluid dynamical part, and we do not expect that there exists a region where UrQMD would lead to ideal fluid dynamical behaviour[5].

Since the correct treatment is at the time of this writing beyond our reach, we have to settle with an approximative solution like in ref. [9]: First, we ignore all the surface elements where the flow is directed inwards, *i.e.* where $\mathrm{d}\sigma_\mu u^\mu < 0$, since the net number of particles passing through such a surface element is negative. There are more particles moving inwards than outwards. Second, on the surface elements where the flow is directed outwards, $\mathrm{d}\sigma_\mu u^\mu > 0$, we use the net number of particles passing the surface, $\mathrm{d}\sigma_\mu j^\mu$, as the number of particles emitted, but we use the thermal distribution with Θ-function, eq. (5) as their momentum distribution. This leads to a small violation of conservation laws. The emitted particles either have too large energy, or we generate too few of them, depending on the constraints we impose on the sampling procedure.

There are approaches in the literature where the problem of negative contributions is solved differently. Instead of sampling the phase-space distributions like we do here, in VISHNU [7,53] and in ref. [15], the momentum distribution of each particle species is calculated by integrating over the particlization surface, eq. (1), like in the conventional calculation of particle spectra in hydrodynamical models [54,55]. The number of particles of species i per unit rapidity, $\mathrm{d}N_i/\mathrm{d}y$, in these boost-invariant distributions is calculated, and the sampling is constrained to produce either $10\mathrm{d}N_i/\mathrm{d}y$ particles in a wide rapidity interval of $-5 < y < 5$ [54], or $\mathrm{d}N_i/\mathrm{d}y$ particles in an interval $-0.5 < y < 0.5$ [15]. These yields are not integers, however. In VISHNU the yield, $10\mathrm{d}N_i/\mathrm{d}y$, is rounded down to the nearest integer [54], whereas in ref. [15] the decimal part is taken as a probability whether to create one additional particle over the rounded down yield [55]. At this stage the sampled particles carry no information of their position. In ref. [15] there are no rescatterings after particlization, and this lack of information is not a problem, whereas in VISHNU each particle is given a position according to the probability given by the Cooper-Frye distribution, neglecting the part where the distribution would be negative, eq. (5). Thus this approach reproduces the Cooper-Frye momentum distribution, but it skews the position distribution of the particles reducing the fraction of particles emitted from timelike surface elements. How this affects the final distribution of particles after rescatterings is unknown. Another disadvantage of this approach is that since it requires evaluating the momentum distributions of all particle species by integrating over the particlization surface, it is slow.

[5] For the difficulties in approaching the ideal fluid limit using transport, see, *e.g.*, ref. [52].

As mentioned in the beginning of this section we want to switch from fluid to cascade in a region where both approaches give similar results, and that there is no physical change in the region where the switch takes place. This means that the solutions to the negative contributions at freeze-out proposed in refs. [41,44–50] are not applicable in our case. In those approaches a non-thermal freeze-out distribution which contains no particles moving inwards is postulated. But since we assume that the distributions are the same on both sides of the switching surface, such a distribution on the particle side would be a contradiction. Furthermore it is perfectly possible that the hadrons in the cascade scatter back to the spacetime region described by fluid dynamics, and assuming that there are no particles entering that region is an oversimplification.

4 Sampling the distributions

Any hadron cascade requires an particle ensemble with well defined particle species, momenta, and positions as an initial state. To generate such ensembles we Monte Carlo sample the particle distributions on the particlization surface. For this purpose we employ two different sampling algorithms. The first one that we call "allcells" sampling, contains a loop over all hypersurface elements and in each of the elements, *i.e.* cells, the particles are sampled according to the steps explained below. In this case the quantum numbers like energy, net baryon number, net strangeness and electric charge are only conserved on the average over many sampled events. The other algorithm that is dubbed "mode" sampling introduces a way to conserve all these quantities event by event, as we will demonstrate in sect. 5.4. The whole sampling algorithm is based on previous work published in [5], but now applied without the assumption of an isochronous transition and with slight improvements.

In general fluctuations in conserved quantum numbers occur in event-by-event studies when only part of the system is described. For example, the spectators are usually not included in the hydrodynamical description of the system. As well fluctuations occur in a rapidity interval which does not contain all the emitted particles. But, once an initial state of the system is defined, and the whole subsequent evolution is considered, the conserved quantum numbers must be conserved. The straightforward "allcells" sampling does not do it, and therefore we have developed the more complicated "mode" sampling approach.

The first step in sampling hadrons on the hypersurface is to decide in which cells a particle has been produced. For example, in a central Au+Au collision at the highest RHIC energy there are roughly 10^7 hypersurface elements, but only ~ 10000 particles produced. Evaluating first, if there is a particle produced in a cell, before doing any of the other steps, results in a speed-up of the calculation, which is essential for the application to event-by-event calculations.

The number of particles of each hadron species produced in one cell is calculated according to the following formula (only the surface elements with $u^\mu \mathrm{d}\sigma_\mu > 0$ are considered):

$$N_i = j^\mu \mathrm{d}\sigma_\mu = n_i u^\mu \mathrm{d}\sigma_\mu \,, \tag{6}$$

where n_i is the particle density in the local rest frame and i is the index of the particle species. It is important to take into account all 150 particle species and their antiparticles implemented in UrQMD to match the equation of state on the particlization surface. Assuming a Boltzmann distribution the integral over momentum space for the particle number density in the local rest frame can be evaluated analytically and the result is

$$n_i = \frac{4\pi g_i m_i^2 T}{(2\pi)^3} e^{\frac{\mu}{T}} K_2\left(\frac{m_i}{T}\right) , \tag{7}$$

where g_i is the degeneracy factor for the respective particle species. All the information about the particle properties is read in directly from the UrQMD tables to avoid any mismatch. The chemical potential includes the baryochemical potential and the strangeness chemical potential in the following way:

$$\mu = B \cdot \mu_B + S \cdot \mu_S \,, \tag{8}$$

where S is the quantum number for strangeness and B is the baryon number. For pions the Bose distribution has to be taken into account because their mass is on the order of the temperature of the system. Expanding the distribution in series and integrating leads to

$$n_\pi = \frac{g_\pi m_\pi^2 T}{(2\pi)^2} \sum_{k=1}^{\infty} \frac{1}{k} K_2\left(\frac{k m_\pi}{T}\right) , \tag{9}$$

where we stop the summation after 10 summands, when it has sufficiently converged.

By summing up all the contributions from different species the total number of particles in this cell $N = \sum N_i$ is known. As long as $N < 0.01$ one can interpret this number directly as a sampling probability and randomly decide, if a particle is produced or not. If N is larger, one needs to sample a Poisson distribution with N as the mean value to decide the actual number of particles produced in this surface element. It turns out that the cases where 2 or more particles per cell are produced are rare. If there is a particle produced the species can be decided by sampling according to their probabilities N_i/N. Isospin is assigned randomly consistent with the isospin symmetry of a system in chemical equilibrium.

The four momenta of the particles are sampled according to the local Cooper-Frye distribution (only the parts where $f(x,p)p^\mu \mathrm{d}\sigma_\mu > 0$ are considered)

$$\frac{\mathrm{d}N(x)}{\mathrm{d}^3 p} = \frac{1}{E} f(x,p) p^\mu \mathrm{d}\sigma_\mu \,, \tag{10}$$

where $f(x,p)$ are the boosted Fermi or Bose distributions corresponding to the respective particle species including again the chemical potentials for baryon number and strangeness. Finding the maximum of the distribution and then applying the rejection method is crucial since the distribution functions in momentum space are highly peaked and dependent on the masses and thermodynamic parameters. Currently, an approximative maximum of

$$\frac{1}{E} p^\mu \mathrm{d}\sigma_\mu f(x,p) \tag{11}$$

is determined by a coarse loop over the three-dimensional momentum space. This approximate maximum is multiplied by 1.2 to make sure it is definitely larger than the function to be sampled.

Then, a momentum vector $\mathbf{p}$ is chosen randomly, and an additional random number between zero and the above mentioned maximum of the distribution is generated. If this random number is smaller than the value of the distribution at this momentum, the momentum is accepted. If not, another momentum and another random number are generated, and the process is repeated until an acceptable momentum is found.

As described in sect. 3 we neglect negative parts of the distribution functions which slightly alters the resulting rapidity and transverse momentum spectra. It is important to sample the momenta according to the boosted distribution function instead of sampling the equilibrium distribution in the local rest frame and then boost the momentum four-vector back to the computational frame. The second procedure leads to a violation of energy conservation since one does not reproduce the whole tensor $T^{\mu\nu}$ in the computational frame correctly [18].

Imposing strict conservation laws on grand canonical distributions on an event-by-event basis is not wholly consistent, and we minimise any bias it creates by the following procedure: To conserve energy, net baryon number, net strangeness and electric charge in all events we do seven subsequent random loops called modes over the hypersurface. During the first mode, cells are randomly chosen and particles are sampled until the total energy is conserved. From this set of particles only the ones containing a $\bar{s}$ quark are kept, and the rest are discarded. In the second mode we produce particles in a similar way, until we have produced as much anti-strangeness as the first mode produced strangeness. We keep the anti-strange particles, and discard the rest. In modes three and four we repeat the same procedure keeping the non-strange baryons and non-strange antibaryons, respectively, but requiring that the net baryon number of these particles is the net baryon number of the system. Modes five and six take care of the conservation of electric charge by keeping the negative and positive non-strange mesons, respectively, and finally mode seven takes care of the energy conservation by sampling neutral non-strange mesons until the energy of the particles corresponds to the energy of the fluid.

5 Results

5.1 Description of the hybrid model

The hypersurface finding and sampling algorithms described in sects. 2 and 4 have been implemented in the hybrid model of ref. [5]. We show here some preliminary results to demonstrate some general trends and overall behavior of the improved model. Note that we have not tried to fine tune any parameters to describe experimental data at this point.

Smooth initial conditions for the hydrodynamic evolution have been generated by averaging over 100 UrQMD events that are run up to the starting time of $t_{\rm start} = 2.83\,{\rm fm}$ for Pb+Pb collisions at $E_{\rm lab} = 160A\,{\rm GeV}$ (SPS) [56] and $t_{\rm start} = 0.5\,{\rm fm}$ for Au+Au collisions at $E_{\rm cm} = 200A\,{\rm GeV}$ [57] (RHIC).

On the constant time surface $t = t_{\rm start}$ the energy, momentum and net baryon number densities are determined by representing each particle in the UrQMD event with a three-dimensional, longitudinally Lorentz-contracted, Gaussian density distribution of thermalised matter, which has the same energy, momentum and baryon number than the particle it represents. Summing up the distributions representing the particles, we obtain a distribution of matter in thermal equilibrium, which has the same energy, momentum and baryon number than the UrQMD event in question. For the RHIC initial state we consider only particles within the rapidity interval $-2 < y < 2$, whereas we include all particles that have interacted at least once when evaluating the initial state for SPS. The mean value of these distributions from 100 events leads to a smooth profile but still includes finite initial velocities in all three directions [58].

The (3+1)D ideal hydrodynamic evolution is solved in Cartesian coordinates using the SHASTA algorithm [59, 60]. The equation of state is calculated within a chiral model coupled to the Polyakov loop to include the deconfinement transition that reproduces nuclear ground state properties and lattice QCD data at zero net baryon chemical potential [61]. This equation of state is also applicable at finite net baryon densities, which allows us to calculate heavy ion collisions at SPS energies to explore the beam energy dependence of our findings. In the hadronic phase this equation of state is equivalent to the effective equation of state of UrQMD, and has the same degrees of freedom than UrQMD. The conservation laws are thus automatically fulfilled on particlization surface when we use Cooper-Frye prescription to calculate the particle distributions.

The hypersurface finder "cornelius" has been implemented in the hydrodynamic code in such a way that the hypersurface for any transition criterion is evaluated while the hydrodynamic evolution is calculated. Then we apply the two sampling algorithms and further calculate resonance decays using UrQMD. To obtain final results that can be compared to experimental data the hadronic transport approach is used in addition to calculate the rescatterings.

Table 1. The conservation of energy (E) and net baryon number (B) in Au+Au collisions at $E_{\rm cm} = 200A\,{\rm GeV}$. The values in the final state are split into two parts: *pos.* is flow through elements where the energy or baryon flow is directed outwards, $d\sigma_\mu T^{\mu 0} > 0$ or $d\sigma_\mu n_B u^\mu > 0$, respectively, whereas *neg.* is flow through elements where energy or baryon flow is directed inwards, $d\sigma_\mu T^{\mu 0} < 0$ or $d\sigma_\mu n_B u^\mu < 0$, respectively, and thus counts as negative. Note that these are not the negative contributions of Cooper-Frye, see the text. The upper two rows are for central ($b < 3.4\,{\rm fm}$) and the lower two rows for mid-central ($b = 7\,{\rm fm}$) collisions.

	E [GeV]			B		
	Total	*pos.*	*neg.*	Total	*pos.*	*neg.*
Initial	5431			93.23		
Final	5430	5861	−431	92.74	97.74	−5.00
Initial	2327			35.84		
Final	2336	2455	−119	35.80	37.10	−1.30

Table 2. The conservation of energy (E) and net baryon number (B) in Pb+Pb collisions at $E_{\rm lab} = 160A\,{\rm GeV}$. The layout is the same as in table 1.

	E [GeV]			B		
	Total	*pos.*	*neg.*	Total	*pos.*	*neg.*
Initial	3117			347.6		
Final	3120	3208	−88.5	345.9	355.8	−9.9
Initial	1528			170.23		
Final	1528	1570	−41.5	169.22	174.26	−5.04

5.2 Structure of the hypersurface

The equations of motion of relativistic hydrodynamics are nothing more than an application of conservation laws for energy, momentum and charge(s). Thus one of the first checks on the accuracy of the numerical solutions of hydrodynamics is to confirm the validity of the conservation laws.

We show the total energy (E) and net baryon number (B) in collisions at two different centralities at RHIC and SPS in tables 1 and 2, respectively. The initial value is evaluated in the beginning of the hydrodynamical evolution by summing over all fluid cells within the particlization surface. With the switching criterion we use here, $\epsilon = 2\epsilon_0$, where ϵ_0 refers to the nuclear ground state energy density of $146\,{\rm MeV/fm^3}$, this means summing over the cells with $\epsilon > 2\epsilon_0$. Since the final state we are interested in is the isosurface with $\epsilon = 2\epsilon_0$, we evaluate the final state energy and net baryon number as energy and baryon number flows through this surface,

$$E = \int_\sigma T^{0\mu} {\rm d}\sigma_\mu \quad \text{and} \quad B = \int_\sigma n_B u^\mu {\rm d}\sigma_\mu, \tag{12}$$

where the energy momentum tensor has been evaluated as $T^{\mu\nu} = (\epsilon + P)u^\mu u^\nu - g^{\mu\nu}P$. As seen in the tables both the energy and baryon number are nicely conserved with better than 0.6% accuracy in all cases.

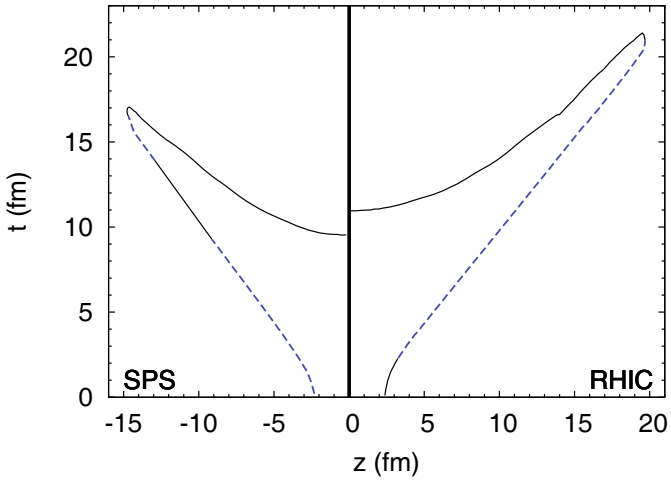

Fig. 11. The position of the $\epsilon = 2\epsilon_0$ isosurface in zt-plane at $x = y = 0$. The left side of the plot (SPS) depicts the surface in central Pb+Pb collisions at $E_{\rm lab} = 160A\,{\rm GeV}$ and the right side (RHIC) in central Au+Au collisions at $E_{\rm cm} = 200A\,{\rm GeV}$. The dashed lines depict regions where the flow may be directed inwards on some surface elements.

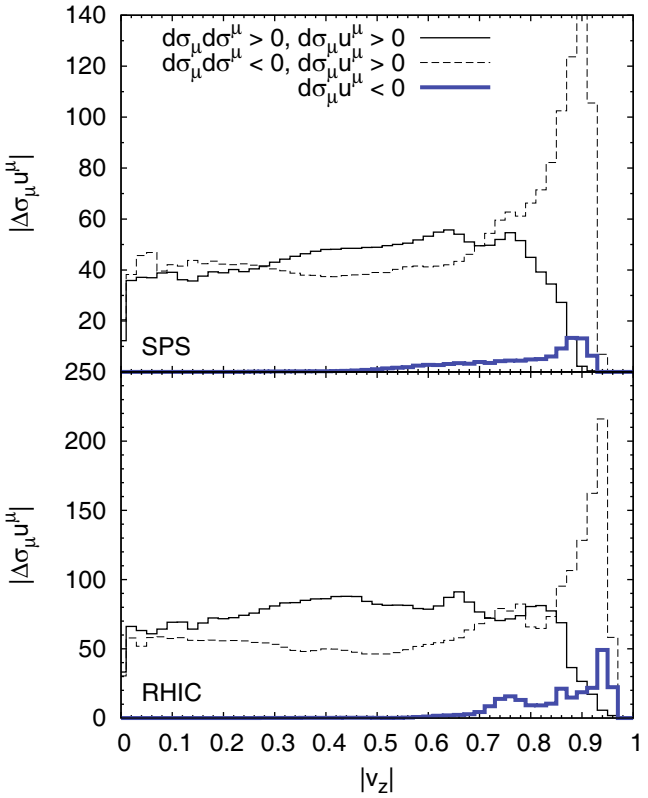

Fig. 12. The magnitude of the fluid flow through different parts of the particlization surface at different longitudinal flow velocities in central Pb+Pb collisions at $E_{\rm lab} = 160A\,{\rm GeV}$ (SPS) and in central Au+Au collisions at $E_{\rm cm} = 200A\,{\rm GeV}$ (RHIC), see the text.

However, a closer look at the properties of the particlization surface reveals that there are surface elements where the flow is directed inwards, $d\sigma_\mu u^\mu < 0$. As described in sect. 4, such elements cannot be used as a source for sampled particles, and thus we check how large uncertainty these elements cause to the total energy and baryon number. In tables 1 and 2, the flows through the surface are also separated in two parts: *pos.* depicts the energy and baryon flows through surface elements where $d\sigma_\mu T^{\mu 0} > 0$ for energy and $d\sigma_\mu n_B u^\mu > 0$ for baryon flow, whereas *neg.* is the flow through elements where $d\sigma_\mu T^{\mu 0} < 0$ for energy and $d\sigma_\mu n_B u^\mu < 0$ for baryons. As seen the surface elements where flow is directed inwards cause a 3–8% uncertainty in the total energy, and a 3–5% uncertainty in the total baryon number of the system. Note that because of the pressure term in T^{00} it is possible that we have an element where energy flow is directed inwards but baryon flow outwards, or vice versa.

To understand this phenomenon we located the surface elements with $d\sigma_\mu u^\mu < 0$ and found out that they are almost entirely located at the edges of the system where the fireball expands longitudinally, see fig. 11, and there are none at midrapidity. Furthermore, the regions depicted by dashed lines in fig. 11 are not regions where the flow is directed inwards, but they are regions where surface elements with inwards directed flow randomly appear among elements where the flow is directed outwards. These are the regions where the longitudinal pressure gradient is still large, the fluid flow is very large, $v_z \sim 0.9$–0.95, and the isosurface moves outwards with a comparable speed as well. It is known that this is a difficult terrain for SHASTA and for any algorithm to solve accurately [59]. Since the flow velocity is almost aligned with the surface, it does not require a large numerical error to flip an outwards flow to inwards. Thus it is possible that these elements with flow directed inwards are just numerical artefacts. However, it is worth remembering that in event-by-event calculations the initial states are highly irregular, and occasionally flow can be directed inwards for physical reasons.

Since the common feature of the elements with inwards directed flow is the large longitudinal flow velocity, we further characterise the surface by it. We bin the surface elements according to the magnitude of the longitudinal flow velocity $|v_z|$, and integrate over the elements in each bin to obtain the magnitude of fluid flow through surface, $|d\sigma_\mu u^\mu|$, at different velocities $|v_z|$. The results are shown in fig. 12. The contribution from elements with flow directed inwards is depicted by the thick curve, and as claimed it is concentrated at large velocities. Furthermore it can be seen that the fluid flow inwards is small compared to the fluid flow outwards, which is depicted by the thin solid and dashed histograms in fig. 12. The 5–8% uncertainties in energy and baryon number listed in tables 1 and 2 are thus concentrated at large longitudinal flow velocities, and can be expected to have only a tiny contribution to observables at midrapidity. The reason why there is a difference between fluid flow $d\sigma_\mu u^\mu$ and energy and baryon number flows, $d\sigma_\mu T^{\mu 0}$ and $d\sigma_\mu j^\mu$, respectively, is that the former has an additional gamma factor and a pressure term, whereas the latter is also sensitive to the baryon chemical potential μ_B which is not uniform on the surface.

5.3 Negative contributions

It is worth remembering that the negative contributions to energy and baryon number discussed above in sect. 5.2 are not the same thing than the negative contributions of Cooper-Frye discussed in the literature (see sect. 3). The former are caused by the collective flow being directed inwards, whereas the negative contributions of Cooper-Frye are caused by individual particles moving inwards through the particlization surface. As discussed in sect. 4, the sampling routine cannot take into account particles moving inwards nor anything emitted on surfaces where flow is directed inwards. Therefore we evaluated these negative contributions to see how much omitting them distorts the spectra.

We evaluated the spectra of thermal pions, kaons and protons on the particlization surface using the conventional Cooper-Frye procedure, eq. (1), *i.e.* we integrated over the surface to obtain distributions, but we divided the contribution into four parts according to whether the flow was directed in- or outwards ($\mathrm{d}\sigma_\mu u^\mu < 0$ or > 0) and whether the particles with the momentum in question were heading in- or outwards ($\mathrm{d}\sigma_\mu p^\mu < 0$ or > 0). It turned out that in general the negative contributions to pion distribution are largest, so we concentrate on them. Some of the actual spectra are shown in sect. 5.5 where we compare the sampled distributions to the integrated ones. Here we emphasise the size of the negative contributions by showing their relative contribution to the total spectrum.

In fig. 13 different negative contributions to the thermal pion rapidity spectrum are shown for collisions at RHIC and SPS. To check how much uncertainty the contribution from elements with flow directed inwards cause, we have calculated the contribution from them (dashed line, $\mathrm{d}\sigma_\mu u^\mu > 0$) even if contribution from them is not negative in the Cooper-Frye sense. It is seen that at midrapidity contribution from them is 2–5%. A modest contribution at midrapidity could be expected, since as shown in fig. 12, the longitudinal flow velocity on these elements is large. Interestingly the contribution from these elements at large rapidities is very different at RHIC and SPS: The magnitude of the relative contribution decreases with increasing rapidity at SPS, but increases at RHIC. Again a result of different flow and emission patterns shown in fig. 12.

We may take the surface and flow pattern as granted, and simply evaluate the fraction of inward moving particles. This is depicted by the solid line, $\mathrm{d}\sigma_\mu p^\mu < 0$, in fig. 13. At midrapidity the contribution of such a particles is surprisingly large, 10–15% with a larger contribution at SPS than at RHIC. That the negative contribution is larger at SPS was already implied in fig. 12 where the fluid flow through the particlization surface was divided into a flow through time- and spacelike surfaces. At SPS the relative fraction of the fluid flow passing through spacelike surfaces is larger than at RHIC. Since negative contributions appear only on spacelike surfaces, the flow pattern at SPS provides a possibility for larger negative contributions than at RHIC. Furthermore, if surfaces are similar,

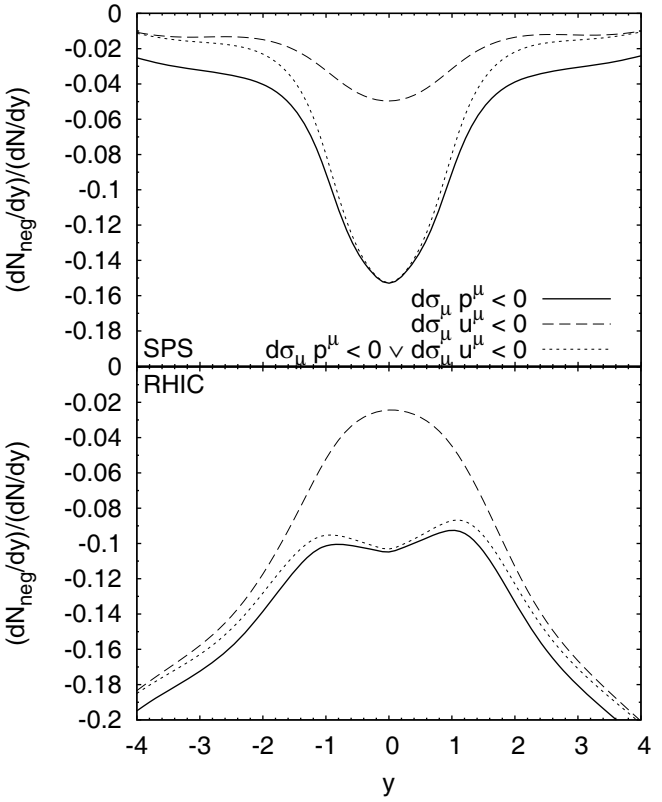

Fig. 13. The ratio of the negative contribution to the total thermal pion rapidity distribution in central Pb+Pb collisions at $E_{\mathrm{lab}} = 160A\,\mathrm{GeV}$ (SPS) and in central Au+Au collisions at $E_{\mathrm{cm}} = 200A\,\mathrm{GeV}$ (RHIC). The curves correspond to different kinds of contributions, see the text.

the lower the flow velocity, the larger the negative contributions. At SPS the flow velocity is lower than at RHIC, and thus it is rather surprising that the difference in negative contributions is not larger than what is shown in fig. 13.

Finally, we want to check how large a contribution our sampling routine misses. Since it cannot sample the particles going inwards nor particles emitted when the flow is directed inwards, sampling misses both contributions. This is shown as the dotted line in fig. 13. At midrapidity the missed part is totally dominated by the conventional negative Cooper-Frye contribution. Thus it is safe to say that what comes to sampling particles at midrapidity, the inwards directed flow is not a problem, but the conventional negative contributions of Cooper-Frye can be.

To further study the effect of negative contributions, we show the contributions to p_T distribution of thermal pions at midrapidity, $-1 < y < 1$, in fig. 14. Again we see that the contribution from the inwards directed flow is smaller than from inwards moving particles. The latter can even reach 40% at low values of transverse momentum! Fortunately the size of the negative contribution decreases rapidly with increasing transverse momentum, and already around 500 MeV it is much more acceptable 8–10%. That the negative contributions are largest at small p_T is understandable since the high p_T particles are

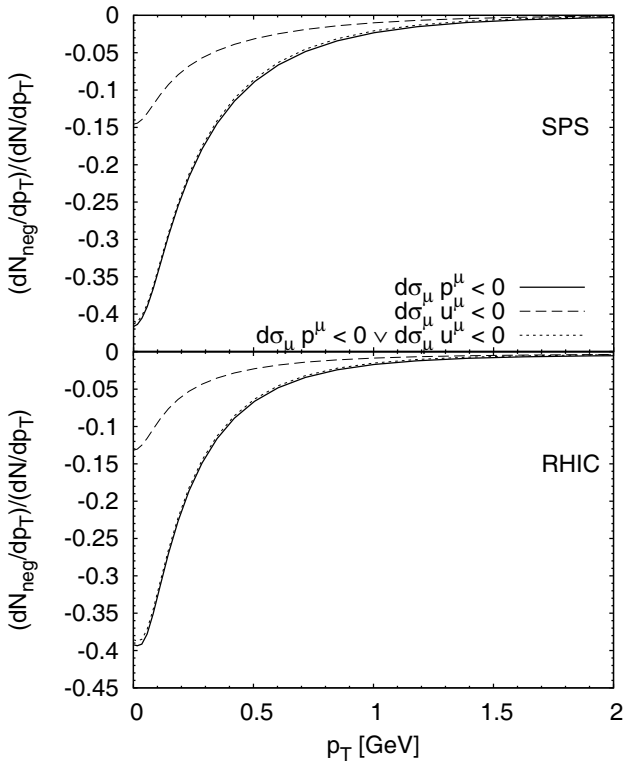

Fig. 14. The ratio of the negative contribution to the total thermal pion p_T-distribution at midrapidity $-1 < y < 1$ in central Pb+Pb collisions at $E_{\rm lab} = 160A$ GeV (SPS) and in central Au+Au collisions at $E_{\rm cm} = 200A$ GeV (RHIC). The curves correspond to different kinds of contributions, see the text.

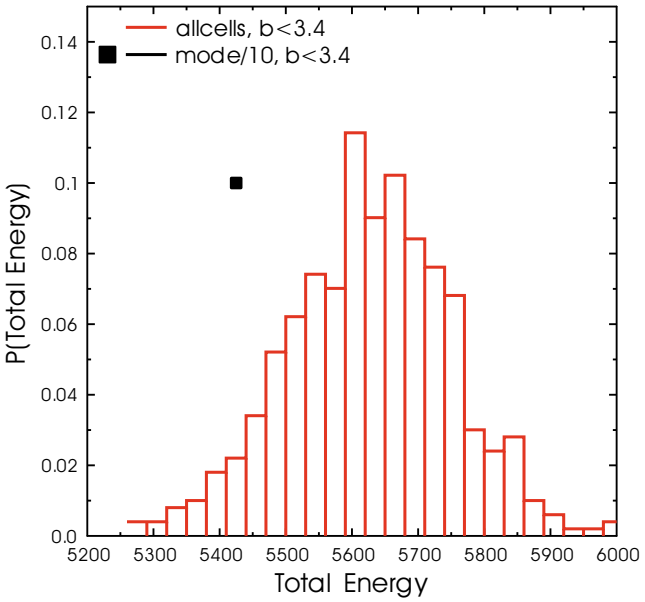

Fig. 15. Probability distribution for the total energy of an event in an ensemble of 500 events created using two different sampling algorithms in central Au+Au collisions at $E_{\rm cm} = 200A$ GeV.

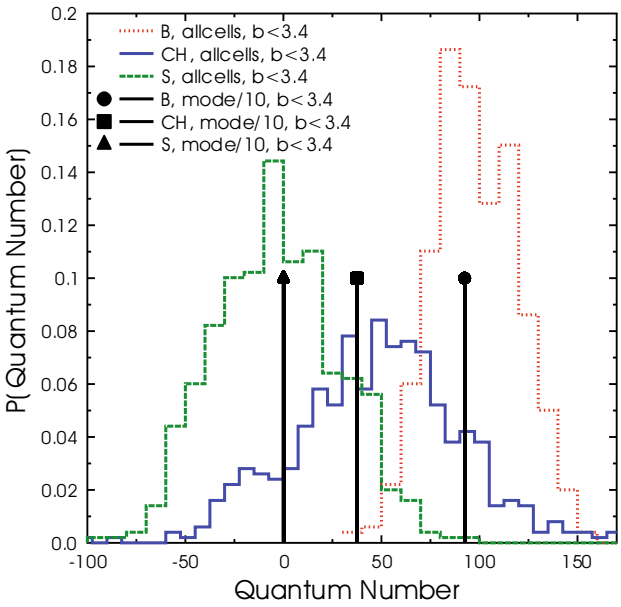

Fig. 16. Probability distribution for the total net baryon number (B), net strangeness (S) and net charge (CH) of an event in an ensemble of 500 events created using two different sampling algorithms in central Au+Au collisions at $E_{\rm cm} = 200A$ GeV.

mostly emitted in regions where the flow velocity is large and parallel to momentum, whereas the negative contributions arise when the momentum is antiparallel to flow velocity.

We also evaluated the p_T averaged v_2 of thermal pions at particlization in mid-central ($b = 7$ fm) collisions at RHIC and SPS. When v_2 was evaluated in a conventional fashion, we got $v_2 = 0.064$ and 0.066 at RHIC and SPS, respectively. When we removed the negative contributions from the distribution, v_2 at RHIC and SPS decreased to 0.058 and 0.06, respectively. If we also removed the remaining positive contribution from elements with flow directed inwards, further change on v_2 was on the level of 10^{-4}. This additional uncertainty of 10% should be kept in mind when discussing the elusiveness of the QGP shear viscosity [62].

5.4 Conservation of quantum numbers

In figs. 15 and 16 we show the probability distributions of relevant quantum numbers using the two sampling algorithms described in sect. 4. As explained, the "mode" sampling is constructed to obey conservation laws event by event, whereas in the simpler sampling of all hypersurface elements the conserved quantities fluctuate around the values given by the positive contributions to the spectra. Note that these values are not those given in tables 1 and 2 as energy and baryon number flow through the parts of surface where flow is directed outwards, but by the distributions of particles coming out through these parts of the surface, eq. (5), after these distributions have been scaled to yield the same number of particles than the local net flow of particles through the surface element, $d\sigma_\mu n u^\mu$.

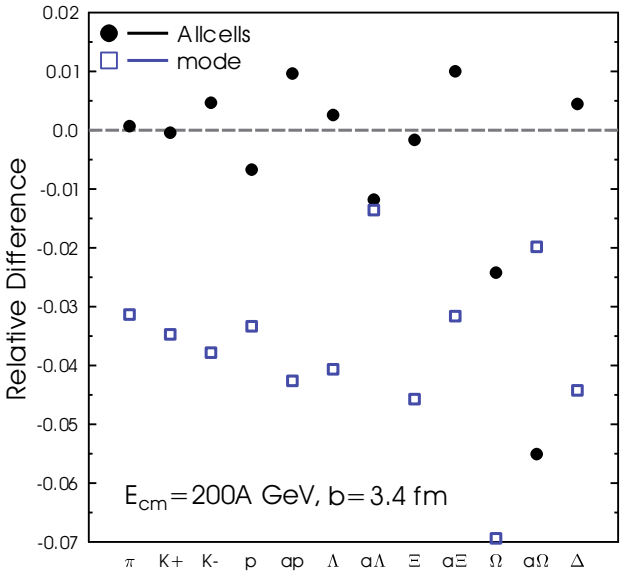

Fig. 17. Relative difference of sampled and integrated particle multiplicities in central Au+Au collisions at $E_{\rm cm} = 200A$ GeV.

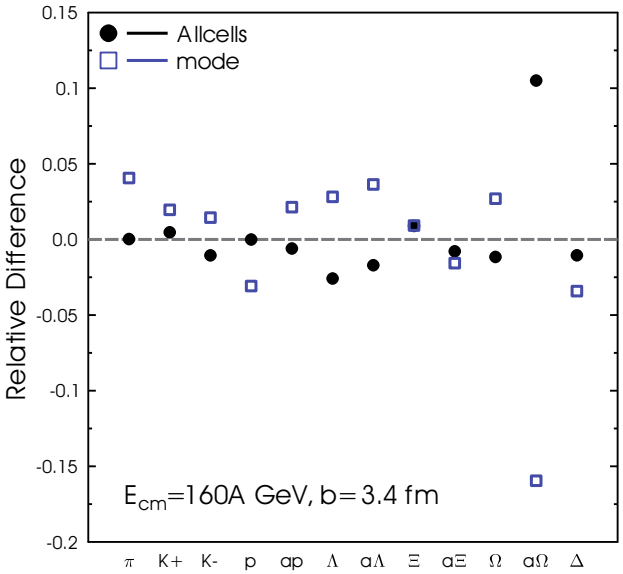

Fig. 18. Relative difference of sampled and integrated particle multiplicities in central Pb+Pb collisions at $E_{\rm lab} = 160A$ GeV.

Therefore, we expect to see a higher mean value in the energy and net baryon number in the allcells sampling compared to the mode setup. One of the reasons to implement the mode sampling was to take into account the distortions caused by different kinds of negative contributions by enforcing the conservation laws[6].

The probability distributions for the different quantities are rather wide in the allcells sampling, so individual events in the more often applied algorithm can have quantum numbers that are far away from their actual values in that event. In a sense this is reasonable since the equation of state used during the hydrodynamical stage, and the particle distributions sampled at particlization assume a grand-canonical ensemble where conservation laws are obeyed only in average. But if we aim at a description of the collisions on an event-by-event basis, we have a contradiction: In nature conservation laws are obeyed in every single event. Thus it makes sense to require that the conservation laws are strictly obeyed during all stages of the model, and check how much the fluctuations created by the sampling procedure affect the observables.

5.5 Tests of sampling algorithm

First of all, we need to check, whether the sampling algorithm reproduces the numbers of particles for each species. In figs. 17 and 18 the multiplicities of selected particle species are compared to the integrated results. Integration means here summing up N_i as defined in eq. (6) for all hypersurface elements where $\mathrm{d}\sigma_\mu u^\mu > 0$. All the results in this section are comparisons of thermal yields for individual species only, the resonance contribution has not been included.

[6] Remember that in event-by-event simulations inwards flow can be physical.

We have plotted in figs. 17 and 18 the relative deviations from the integrated result, (# sampled-# integrated)/# integrated, for the two sampling algorithms. The deviations from zero are within the expected statistical fluctuations for 500 events taking into account their individual abundances for the allcells sampling. Overall, in the allcells sampling the particle multiplicities are nicely reproduced at RHIC and SPS energies, whereas the mode sampling leads to slightly less particles at RHIC. This result is expected, since we enforce a lower value for the total energy of the system. The fluctuations of the particle yields around that lower value are again purely statistical. Since at SPS the inwards directed flow is smaller this difference is also smaller and therefore the difference between allcells and mode sampled yields is smaller. As one can see in the rapidity spectra (figs. 19 and 21), at SPS energies mode sampling produces more particles than allcells sampling.

The next step is to compare the distribution of the particles in momentum space in terms of rapidity and transverse momentum. The different lines in fig. 19 correspond to the integrated result, which is split up into the different contributions depending on the direction of flow and momentum with respect to the particlization surface as described in the legend, see sect. 5.3.

For clarity all the contributions are displayed only for pions while for kaons and protons only the full result and the result from hypersurface elements with flow directed outwards are shown. The full line corresponds to the full result from the complete hypersurface integration that one ideally wants to reproduce. The dashed line shows the result for the contribution from the cells where the flow is directed outward; these are the cells we take into account when sampling the particle number densities. The momentum sampling on the other hand disregards all the negative parts of the distribution function. This treatment slightly

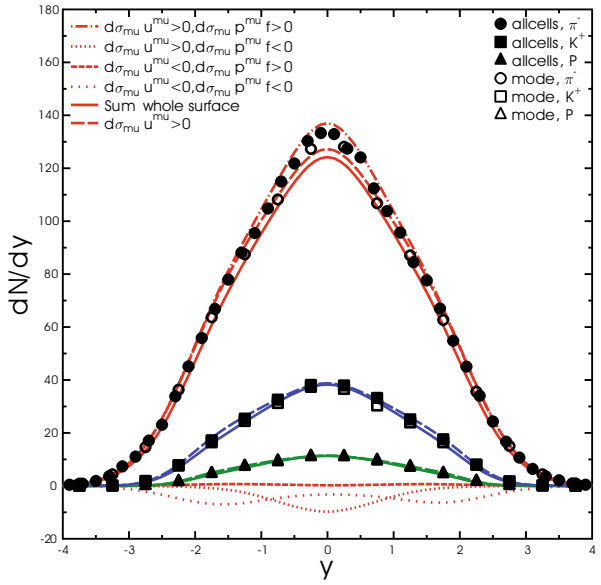

Fig. 19. Comparison of the integrated and sampled rapidity spectra for pions, kaons and protons in central Au+Au collisions at $E_{\mathrm{cm}} = 200A\,\mathrm{GeV}$.

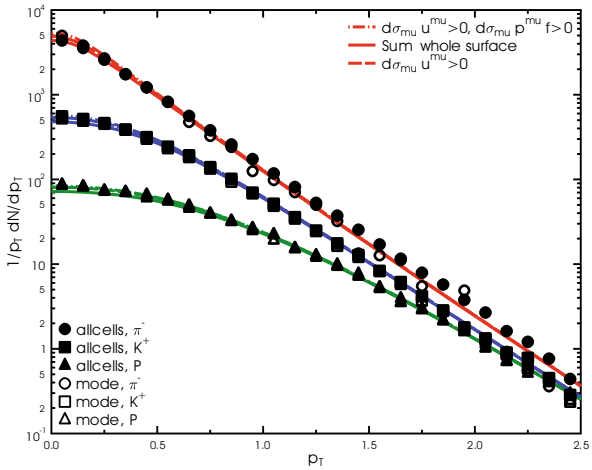

Fig. 20. Comparison of the integrated and sampled transverse momentum spectra for pions, kaons and protons in central Au+Au collisions at $E_{\mathrm{cm}} = 200A\,\mathrm{GeV}$.

skews the spectrum such that we end up with a result that is in between the dashed and the dot-dashed line for the sampled spectra. It may look surprising that the sampling does not reproduce the yield from outward flowing elements at midrapidity. After all, the sampling procedure has been normalised to reproduce the yield from those elements. The reason for this deviation is that the system in our calculations is not boost invariant. If it were, the edges of the system in longitudinal direction would be infinitely far away, and they would not contribute to midrapidity. But in our non-boost invariant system they are close, and we see the same to happen in longitudinal direction than what is depicted in fig. 14 for transverse direction: The low momentum, *i.e.* small rapidity, region is depleted because of the negative contributions. The distributions we sample do not contain this depletion, and thus we end up having too many particles at midrapidity. On the other hand, since the sampling procedure reproduces the total yield of particles as shown in figs. 17 and 18, we must have fewer particles somewhere. A closer look at the spectra reveals that the sampled yield is below the $\mathrm{d}\sigma_\mu u^\mu > 0$ curve at rapidities $1 < |y| < 2.5$, and this deficit is sufficient to cover the excess at midrapidity.

The transverse momentum spectrum is shown in fig. 20. Due to the logarithmic scale in this case, the differences shown in fig. 14 disappear, and only a small difference between the elements with flow directed outwards and the full result is visible at low transverse momentum. The sampled results are in very good agreement with the integrated results. All possible deviations (apart from statistical noise) are smaller than the size of the symbols.

The comparison of rapidity spectra and transverse momentum spectra at SPS, as shown in figs. 21 and 22, leads to very similar results. The only difference is that in the mode sampling there are more pions produced than in the allcells sampling as mentioned above. The reason for this has to be investigated further in the future.

Overall, the sampling algorithms reproduce the particle yields and spectra very well within the expected deviations from the assumptions that are made in the different algorithms. The negative contributions are also smaller than 5% in the regions where most of the particles are emitted and affect heavier particles less than lighter ones.

5.6 Effects of rescattering

In this section we present selected results for multiplicities, spectra and elliptic flow to demonstrate the effect of the hadronic rescattering and the switching criterion. All the results are calculated using the hybrid approach described in sect. 5.1 with mode sampling enforcing exact conservation laws. To obtain the results directly at the switching hypersurface we run UrQMD for 0.1 fm and use it only to calculate the resonance decays ("Hydro"). The second option is to run UrQMD for 200 fm and include all the rescattering dynamics in the hadron transport approach ("After").

In fig. 23 the yields of pions, kaons, protons and Lambdas are shown in central heavy ion collisions at the highest RHIC energy. The final results using allcells sampling are within 3% to the ones shown here (see fig. 17). Therefore, we decided to restrict the number of shown results to mode sampling only. The switching criteria that we have chosen correspond to the following temperatures: $3\epsilon_0 \approx 163\,\mathrm{MeV}$, $2\epsilon_0 \approx 154\,\mathrm{MeV}$ and $1.5\epsilon_0 \approx 149\,\mathrm{MeV}$ and are in the ballpark of switching criteria that are commonly used in other hybrid approaches [1–9]. The energy density ϵ_0 refers to the nuclear ground state energy density $146\,\mathrm{MeV/fm^3}$. The switching criterion needs to be adjusted together with equation of state and parameters defining the initial conditions to achieve a good agreement with experimental data. In this analysis we concentrate on presenting general features of the results and have not searched for the best agreement with the measurements yet.

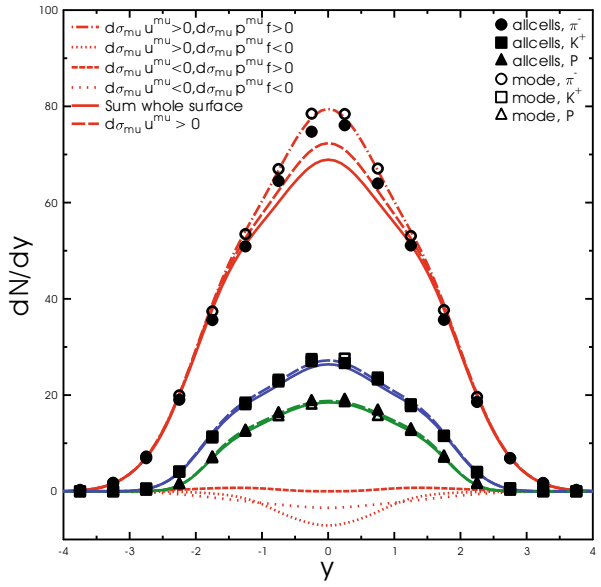

Fig. 21. Comparison of the integrated and sampled rapidity spectra for pions, kaons and protons in central Pb+Pb collisions at $E_{\rm lab} = 160A\,{\rm GeV}$.

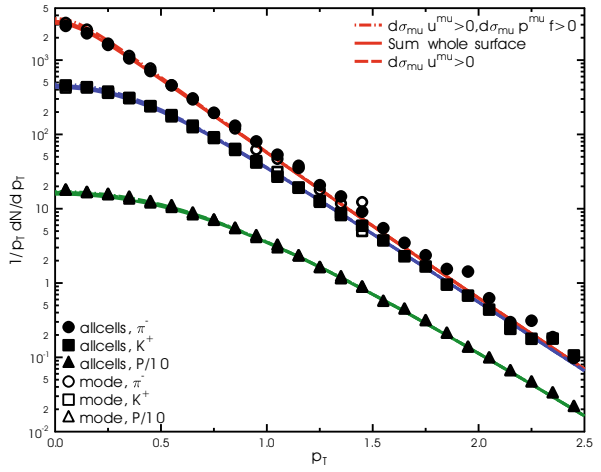

Fig. 22. Comparison of the integrated and sampled transverse momentum spectra for pions, kaons and protons in central Pb+Pb collisions at $E_{\rm lab} = 160A\,{\rm GeV}$.

The yields are slightly higher for higher switching energy densities, because in equilibrium at this temperature range, higher temperatures lead to higher yields. The deviations from equilibrium caused by the sampling procedure are not large enough to break this rule. The rescattering leads to a reduction of the kaon and proton yield, whereas pions and Lambdas are not so much affected. The kaon and proton yields are also higher in the iso-energy density transition scenario than in the previously employed gradual transition, where full transverse slices are sampled on an isochronous surface, when the whole slice has diluted below $5\epsilon_0$. Apart from the fact that the kaon yield is higher than the experimental data our results are in reasonable agreement with the data.

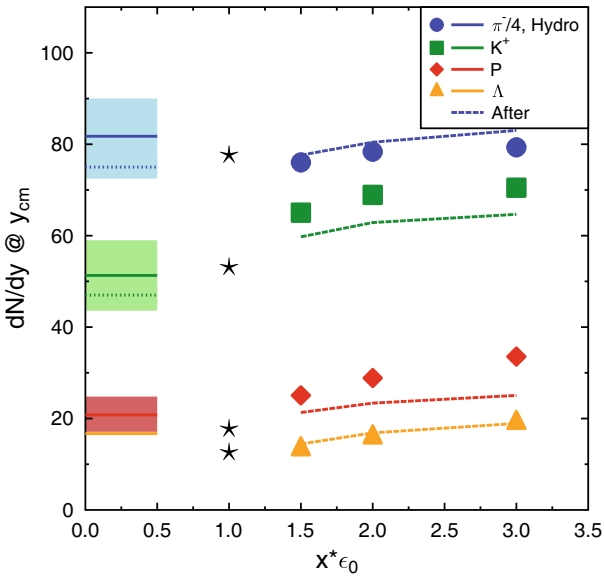

Fig. 23. Yields at midrapidity ($|y| < 0.5$) as a function of switching criterion in multiples of ϵ_0 for four different particle species (π^-, K^+, P, Λ) in central ($b < 3.4\,{\rm fm}$) Au+Au collisions at $\sqrt{s_{\rm NN}} = 200\,{\rm GeV}$. The symbols indicate the result with resonance decays ("Hydro") and the lines show the result after rescattering ("After"). The black stars show the result from the previously used "gradual" transition. The bands on the left indicate data by the STAR and BRAHMS Collaborations [63–66].

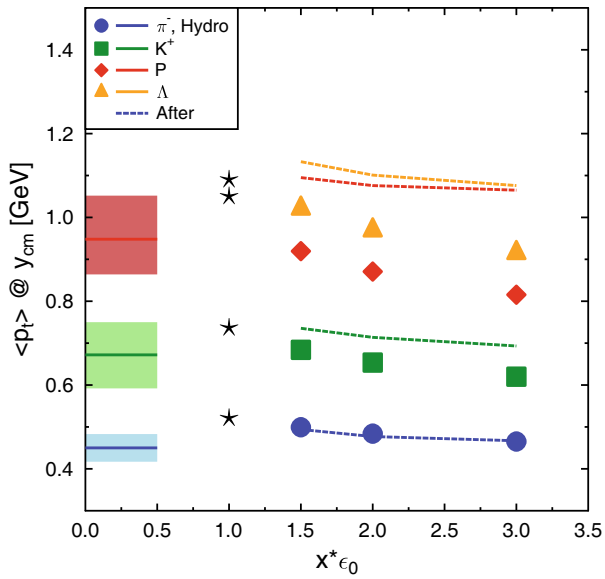

Fig. 24. Mean transverse momentum at midrapidity ($|y| < 0.5$) as a function of switching criterion in multiples of ϵ_0 for four different particle species (π^-, K^+, P, Λ) in central ($b < 3.4\,{\rm fm}$) Au+Au collisions at $\sqrt{s_{\rm NN}} = 200\,{\rm GeV}$. The symbols indicate the result with resonance decays ("Hydro") and the lines show the result after rescattering ("After"). The black stars show the result from the previously used "gradual" transition. The bands on the left indicate data by the PHENIX Collaboration [67].

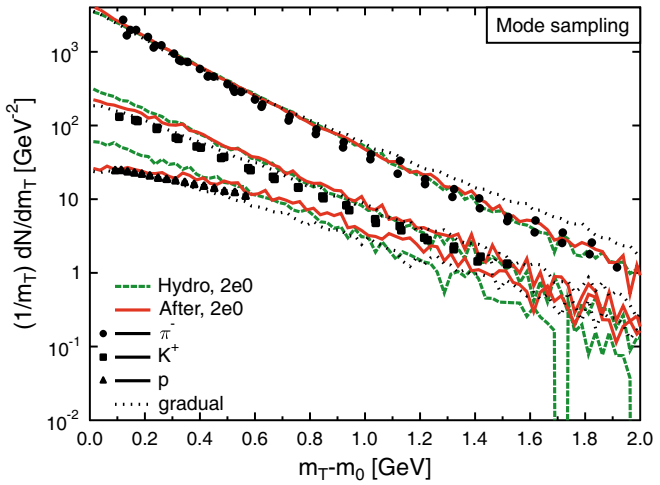

Fig. 25. Transverse mass spectra at midrapidity ($|y| < 0.5$) for pions, kaons and protons in central ($b < 3.4\,\mathrm{fm}$) Au+Au collisions at $\sqrt{s_{\mathrm{NN}}} = 200\,\mathrm{GeV}$. The dashed lines indicate the result with resonance decays ("Hydro") and the full lines show the result after rescattering ("After"). The black dotted line represents the result from the previously used "gradual" transition. The symbols indicate experimental data by the STAR, PHENIX and BRAHMS Collaborations [65,67–69]. The proton data by STAR has been multiplied by 0.6 to correct for the feed-down from Lambdas.

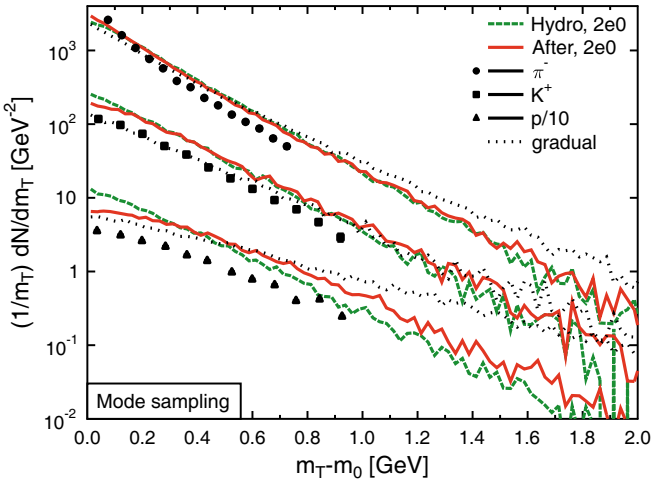

Fig. 26. Transverse mass spectra at midrapidity ($|y| < 0.5$) for pions, kaons and protons in central ($b < 3.4\,\mathrm{fm}$) Pb+Pb collisions at $E_{\mathrm{lab}} = 160A\,\mathrm{GeV}$. The dashed lines indicate the result with resonance decays ("Hydro") and the full lines show the result after rescattering ("After"). The black dotted line represents the result from the previously used "gradual" transition. The symbols indicate experimental data by the NA49 Collaboration [70,71].

The mean transverse momentum as a measure of the radial flow development is shown in fig. 24. In this case the dependence on the switching criterion is opposite to the one of the yields. There are two reasons for this behaviour: The first is that for lower switching energy densities the system stays longer in the hydrodynamic evolution and the particles gain more transverse flow. The second argument is that the total energy needs to be conserved and if there are more particles produced, there is less energy remaining to give them kinetic energy in terms of transverse flow at the switching transition. Depending on their hadronic cross-sections and their mass the particles get pushed a lot (*e.g.*, protons) or almost not at all (pions) during the hadronic rescattering stage.

The transverse mass spectra at RHIC and SPS (shown in figs. 25 and 26, respectively) confirm this behavior. The pion spectra are almost identical before and after the hadronic cascade, but the kaon and proton spectra begin to resemble the experimental data only after the rescattering. The comparison to the previously imposed gradual transition shows that a true iso-energy density switching criterion improves the slope of the spectra at high transverse masses drastically. This can be easily understood, since in the gradual transition scenario the full slice needs to reach the energy density criterion which delays the switching to hadron cascade for the edges in the transverse direction. The edges gain very large transverse flow velocity, which makes the distributions flatter, and even if the edges get very cold, the yield of heavy particles does not drop so much that the effect of large flow velocity would be negated. What comes to the p_T-distributions, the hybrid model based on ideal hydrodynamics works better at high RHIC energies than at high SPS energies. This indicates that the non-equilibrium dynamics gains importance at lower beam energies

In figs. 27 and 28 elliptic flow as a function of transverse momentum is shown for pions and protons at high SPS energy. Quite surprisingly the p_T-differential elliptic flow is quite insensitive to the switching criterion. It is known that in ideal fluid hydrodynamics pion $v_2(p_T)$ is quite insensitive to the freeze-out temperature [42,43]. We presume that the same holds also when one uses the gradual criterion instead of constant temperature/density for particlization, and thus the elliptic flow of pions at particlization is very similar in both cases, and evolves similarly during the cascade. Thus the final $v_2(p_T)$ is similar as well. The proton $v_2(p_T)$ shows more sensitivity than pion $v_2(p_T)$, but the difference is at low p_T, not at high p_T which is influenced by the different evolution of the edges as explained when discussing the p_T spectra. On the other hand, the lower proton v_2 at low p_T is in line with the ideal fluid expectations where lower freeze-out temperature leads to lower proton $v_2(p_T)$ at low p_T. Thus the low p_T range of protons is mostly influenced by the center of the system which evolves hydrodynamically much longer when one uses isodensity switching than when one uses gradual switching. When the hadronic cascade rescattering is taken into account, the proton flow at low transverse momenta seems to even turn negative as recently observed by the CERES Collaboration [73].

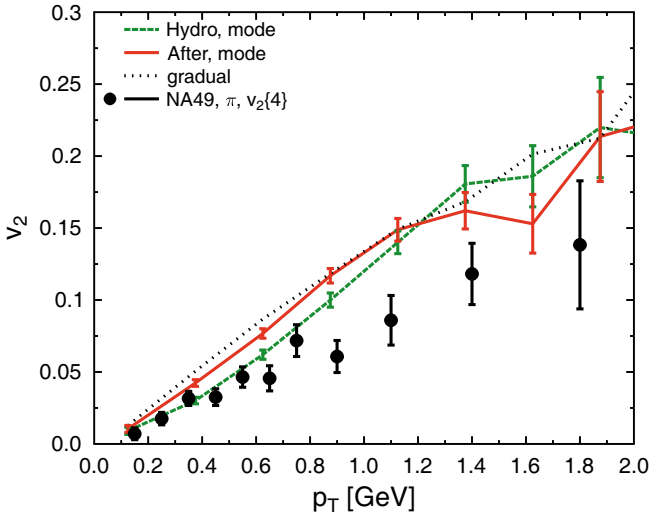

Fig. 27. Elliptic flow of pions as a function of transverse momentum at midrapidity ($|y| < 0.5$) in mid-central ($b = 7$ fm) Pb+Pb collisions at $E_{\rm lab} = 160A$ GeV. The dashed lines indicate the result with resonance decays ("Hydro") and the full lines show the result after rescattering ("After"). The black dotted line represents the result from the previously used "gradual" transition. The symbols indicate experimental data by the NA49 Collaboration [72].

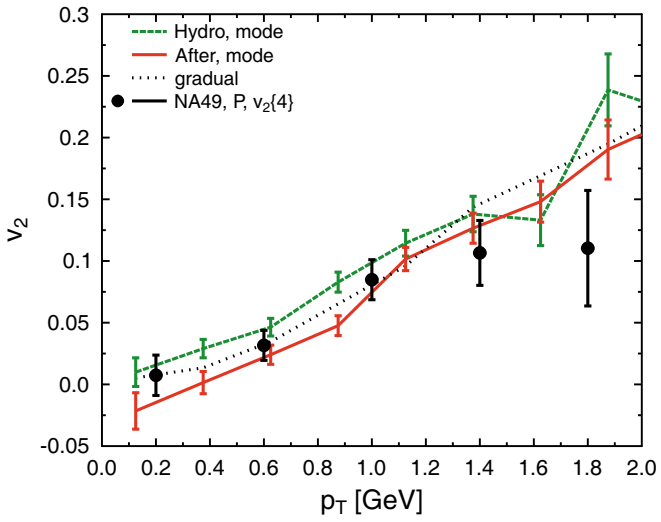

Fig. 28. Elliptic flow of protons as a function of transverse momentum at midrapidity ($|y| < 0.5$) in mid-central ($b = 7$ fm) Pb+Pb collisions at $E_{\rm lab} = 160A$ GeV. The dashed lines indicate the result with resonance decays ("Hydro") and the full lines show the result after rescattering ("After"). The black dotted line represents the result from the previously used "gradual" transition. The symbols indicate experimental data by the NA49 Collaboration [72].

6 Conclusions

In this paper we have discussed a crucial part of hybrid models in detail: How to switch from hydrodynamical description to cascade. We have described an algorithm to find an isovalue surface where the transition takes place, the unavoidable negative contributions of Cooper-Frye procedure on such a surface, and how to make the sampling algorithm, which creates the initial state for the cascade, to work on an arbitrary surface and deal with the negative contributions. We have seen that in realistic calculations the negative contributions are not a large problem, but they create an uncertainty of their own which should be kept in mind when one draws conclusions from the results of the present hybrid or hydrodynamical models. In the long run we hope to develop a model where these negative contributions are properly treated, and not just ignored.

We think that the machinery we have described is particularly suitable for a proper event-by-event analysis of heavy-ion collisions. In event-by-event calculations the initial state of hydrodynamics varies wildly from event to event, and thus one may expect the particlization surface to have a very complicated structure. This poses no problem for the algorithm described here since it can create consistent surfaces without holes nor double counting for any configuration. One of the reasons for studying heavy-ion collisions event by event are fluctuations. In those studies it is important to distinguish at which stage of the evolution fluctuations are created and how. The sampling algorithm we described provides an important check by allowing strict conservation of energy and charges thus guaranteeing that their fluctuations are not caused by the sampling procedure.

All this machinery is not limited to switching from ideal fluid to cascade, but it can be applied at the interface of viscous hydrodynamics and cascade as well. All one needs to do is to modify the particle distributions at particlization accordingly.

However, we presented here preliminary results only without attempting to describe the data well. The next step is to identify the main parameters of the hybrid calculation and perform a multi-parameter analysis compared to bulk observables at RHIC using a sophisticated statistical emulator to limit CPU time. Once a good switching criterion has been identified, the beam energy dependence can be explored. In this context, the framework presented here can easily be even more generalised to other switching criteria based on net baryon density, temperature or combinations of thermodynamic quantities.

We are greatly indebted to Bernd Schlei for many informative discussions about surface finding and related algorithms. We thank Tetsufumi Hirano, Huichao Song and Hannu Holopainen for describing their sampling routines in detail. The work of PH is supported by BMBF under contract no. 06FY9092 and the work of HP by U.S. Department of Energy grant DE-FG02-05ER41367. We are grateful to the Open Science Grid for providing computing resources. HP thanks the J.W. Goethe Universität and HICforFAIR for hospitality during several stages of this work.

References

1. S.A. Bass, A. Dumitru, Phys. Rev. C **61**, 064909 (2000) nucl-th/0001033.
2. D. Teaney, J. Lauret, E.V. Shuryak, nucl-th/0110037.
3. T. Hirano, U.W. Heinz, D. Kharzeev, R. Lacey, Y. Nara, Phys. Lett. B **636**, 299 (2006) nucl-th/0511046.
4. C. Nonaka, S.A. Bass, Phys. Rev. C **75**, 014902 (2007) nucl-th/0607018.
5. H. Petersen, J. Steinheimer, G. Burau, M. Bleicher, H. Stocker, Phys. Rev. C **78**, 044901 (2008) arXiv:0806.1695 [nucl-th].
6. K. Werner, I. Karpenko, T. Pierog, M. Bleicher, K. Mikhailov, Phys. Rev. C **82**, 044904 (2010) arXiv:1004.0805 [nucl-th].
7. H. Song, S.A. Bass, U. Heinz, T. Hirano, C. Shen, Phys. Rev. Lett. **106**, 192301 (2011) arXiv:1011.2783 [nucl-th].
8. I.A. Karpenko, Y.M. Sinyukov, K. Werner, arXiv:1204.5351 [nucl-th].
9. T. Hirano, P. Huovinen, K. Murase, Y. Nara, arXiv:1204.5814 [nucl-th].
10. H. Sorge, Phys. Rev. C **52**, 3291 (1995) nucl-th/9509007.
11. S.A. Bass *et al.*, Prog. Part. Nucl. Phys. **41**, 255 (1998) nucl-th/9803035.
12. M. Bleicher *et al.*, J. Phys. G **25**, 1859 (1999) hep-ph/9909407.
13. Y. Nara, N. Otuka, A. Ohnishi, K. Niita, S. Chiba, Phys. Rev. C **61**, 024901 (2000) nucl-th/9904059.
14. M. Isse, A. Ohnishi, N. Otuka, P. K. Sahu, Y. Nara, Phys. Rev. C **72**, 064908 (2005) arXiv:nucl-th/0502058.
15. H. Holopainen, H. Niemi, K.J. Eskola, Phys. Rev. C **83**, 034901 (2011) arXiv:1007.0368 [hep-ph].
16. H. Petersen, G.-Y. Qin, S.A. Bass, B. Muller, Phys. Rev. C **82**, 041901 (2010) arXiv:1008.0625 [nucl-th].
17. D.H. Rischke, in *Cape Town 1998, Hadrons in dense matter and hadrosynthesis 21-70* nucl-th/9809044.
18. F. Cooper, G. Frye, Phys. Rev. D **10**, 186 (1974).
19. C.M. Hung, E.V. Shuryak, Phys. Rev. C **57**, 1891 (1998) hep-ph/9709264.
20. C.W. Misner, K.S. Thorne, J.A. Wheeler, *Gravitation* (Freeman, San Francisco, 1973) Chapt. 5.
21. J.C. Roberts, S. Hill, Proc. SPIE **3643**, 170 (1999) `http://dx.doi.org/10.1117/12.342833`.
22. W.E. Lorensen, H.E. Cline, SIGGRAPH Computer Graphics **21**, 163 (1987) `http://dx.doi.org/10.1145/37402.37422`.
23. R. Venugopalan, M. Prakash, M. Kataja, P.V. Ruuskanen, Nucl. Phys. A **566**, 473C (1994).
24. J. Sollfrank, P. Huovinen, M. Kataja, P.V. Ruuskanen, M. Prakash, R. Venugopalan, Phys. Rev. C **55**, 392 (1997) nucl-th/9607029.
25. P.F. Kolb, J. Sollfrank, U.W. Heinz, Phys. Rev. C **62**, 054909 (2000) hep-ph/0006129.
26. P.F. Kolb, R. Rapp, Phys. Rev. C **67**, 044903 (2003) hep-ph/0210222.
27. P.F. Kolb, U.W. Heinz, in *Quark gluon plasma*, edited by R.C. Hwa *et al.*, Vol. **3** (World Scientific, Singapore, 2004) pp. 634-714, AZHYDRO is available at `http://www.physics.ohio-state.edu/~froderma/`.
28. B. Schenke, S. Jeon, C. Gale, Phys. Rev. C **82**, 014903 (2010) arXiv:1004.1408 [hep-ph].
29. M.J. Düurst, SIGGRAPH Computer Graphics **22**, 72 (1988).
30. E.V. Chernyaev, technical report CN/95-17 (1995) unpublished, `http://citeseerx.ist.psu.edu/viewdoc/summary?doi=10.1.1.56.7139`
31. G. Wyvill, C. McPheeters, B. Wyvill, The Visual Computer **2**, 227 (1986) `http://dx.doi.org/10.1007/BF01900346` or `www.cpsc.ucalgary.ca/~blob/papers/softobjects.pdf`.
32. J.P. Boris, D.L. Book, J. Comput. Phys. **11**, 38 (1973).
33. D.L. Book, J.P. Boris, K. Hain, J. Comput. Phys. **18**, 248 (1975).
34. J.P. Boris, D.L. Book, J. Comput. Phys. **20**, 397 (1976).
35. J. Bloomenthal, *Graphics Gems IV*, edited by P.S. Heckbert (Academic Press, 1994) `http://www.unchained-geometry.com/jbloom/papers/polygonizer.pdf`.
36. B. Schlei, private communication (2012).
37. B.R. Schlei, Comput. Graph. **36**, 111 (2012) arXiv:1011.1787 [cs.CG].
38. J.-P. Thirion, A. Gourdon, INRIA Research Report RR-1672 (1992) unpublished, `http://hal.inria.fr/inria-00074885/en/`.
39. M. Fidrich, INRIA Research Report RR-2833 (1996) unpublished, `http://hal.inria.fr/inria-00073858/en/`.
40. L. Pang, Q. Wang, X.-N. Wang, Phys. Rev. C **86**, 024911 (2012) arXiv:1205.5019 [nucl-th].
41. Y. Cheng, L.P. Csernai, V.K. Magas, B.R. Schlei, D. Strottman, Phys. Rev. C **81**, 064910 (2010) arXiv:1006.5820 [nucl-th].
42. P.F. Kolb, P. Huovinen, U.W. Heinz, H. Heiselberg, Phys. Lett. B **500**, 232 (2001) hep-ph/0012137.
43. P. Huovinen, P.F. Kolb, U.W. Heinz, P.V. Ruuskanen, S.A. Voloshin, Phys. Lett. B **503**, 58 (2001) hep-ph/0101136.
44. K.A. Bugaev, Nucl. Phys. A **606**, 559 (1996).
45. K.A. Bugaev, M.I. Gorenstein, nucl-th/9903072.
46. K.A. Bugaev, M.I. Gorenstein, W. Greiner, J. Phys. G **25**, 2147 (1999) nucl-th/9906088.
47. C. Anderlik, Z.I. Lazar, V.K. Magas, L.P. Csernai, H. Stöcker, W. Greiner, Phys. Rev. C **59**, 388 (1999).
48. C. Anderlik, L.P. Csernai, F. Grassi, Y. Hama, T. Kodama, Z.I. Lazar, Phys. Rev. C **59**, 3309 (1999).
49. V.K. Magas *et al.*, Heavy Ion Phys. **9**, 193 (1999).
50. K. Tamosiunas, L.P. Csernai, Eur. Phys. J. A **20**, 269 (2004) hep-ph/0403179.
51. S. Bernard, J.A. Maruhn, W. Greiner, D.H. Rischke, Nucl. Phys. A **605**, 566 (1996) nucl-th/9602011.
52. D. Molnar, P. Huovinen, Phys. Rev. Lett. **94**, 012302 (2005) nucl-th/0404065.
53. H. Song, S.A. Bass, U. Heinz, Phys. Rev. C **83**, 024912 (2011) arXiv:1012.0555 [nucl-th].
54. H. Song, private communication (2011).
55. H. Holopainen, private communication (2011).
56. H. Petersen, M. Bleicher, Phys. Rev. C **81**, 044906 (2010) arXiv:1002.1003 [nucl-th].
57. H. Petersen, C. Coleman-Smith, S.A. Bass, R. Wolpert, J. Phys. G **38**, 045102 (2011) arXiv:1012.4629 [nucl-th].
58. H. Petersen, J. Steinheimer, G. Burau, M. Bleicher, Eur. Phys. J. C **62**, 31 (2009).
59. D.H. Rischke, S. Bernard, J.A. Maruhn, Nucl. Phys. A **595**, 346 (1995) nucl-th/9504018.
60. D.H. Rischke, Y. Pursun, J.A. Maruhn, Nucl. Phys. A **595**, 383 (1995) **596**, 717(E) (1996) nucl-th/9504021.
61. J. Steinheimer, S. Schramm, H. Stocker, J. Phys. G **38**, 035001 (2011) arXiv:1009.5239 [hep-ph].

62. C. Shen, S. A. Bass, T. Hirano, P. Huovinen, Z. Qiu, H. Song, U. Heinz, J. Phys. G **38**, 124045 (2011) arXiv: 1106.6350 [nucl-th].
63. BRAHMS Collaboration (D. Ouerdane), Nucl. Phys. A **715**, 478 (2003) arXiv:nucl-ex/0212001.
64. BRAHMS Collaboration (J.H. Lee *et al.*), J. Phys. G **30**, S85 (2004).
65. STAR Collaboration (J. Adams *et al.*), Phys. Rev. Lett. **92**, 112301 (2004) arXiv:nucl-ex/0310004.
66. STAR Collaboration (J. Adams *et al.*), Phys. Rev. Lett. **98**, 062301 (2007) arXiv:nucl-ex/0606014.
67. PHENIX Collaboration (S.S. Adler *et al.*), Phys. Rev. C **69**, 034909 (2004) arXiv:nucl-ex/0307022.
68. BRAHMS Collaboration (I. Arsene *et al.*), Phys. Rev. C **72**, 014908 (2005) arXiv:nucl-ex/0503010.
69. STAR Collaborations and STAR-RICH Collaborations (J. Adams *et al.*), arXiv:nucl-ex/0601042.
70. NA49 Collaboration (S.V. Afanasiev *et al.*), Phys. Rev. C **66**, 054902 (2002) arXiv:nucl-ex/0205002.
71. NA49 Collaboration (C. Alt *et al.*), Phys. Rev. C **73**, 044910 (2006).
72. NA49 Collaboration (C. Alt *et al.*), Phys. Rev. C **68**, 034903 (2003) arXiv:nucl-ex/0303001.
73. CERES Collaboration (D. Adamova *et al.*), Nucl. Phys. A **894**, 41 (2012) arXiv:1205.3692 [nucl-ex].

PHYSICAL REVIEW C **86**, 014909 (2012)

Influence of a temperature-dependent shear viscosity on the azimuthal asymmetries of transverse momentum spectra in ultrarelativistic heavy-ion collisions

H. Niemi,[1,2] G. S. Denicol,[3] P. Huovinen,[3] E. Molnár,[2,4] and D. H. Rischke[2,3]
[1]*Department of Physics, P.O. Box 35 (YFL) FI-40014 University of Jyväskylä, Finland*
[2]*Frankfurt Institute for Advanced Studies, Ruth-Moufang-Str. 1, D-60438 Frankfurt am Main, Germany*
[3]*Institut für Theoretische Physik, Johann Wolfgang Goethe-Universität, Max-von-Laue-Str. 1, D-60438 Frankfurt am Main, Germany*
[4]*MTA Wigner Research Centre for Physics, H-1525 Budapest, P.O.Box 49, Hungary*
(Received 22 March 2012; published 27 July 2012)

We study the influence of a temperature-dependent shear viscosity over entropy density ratio η/s, different shear relaxation times τ_π, as well as different initial conditions on the transverse momentum spectra of charged hadrons and identified particles. We investigate the azimuthal flow asymmetries as a function of both collision energy and centrality. The elliptic flow coefficient turns out to be dominated by the hadronic viscosity at RHIC energies. Only at higher collision energies the impact of the viscosity in the QGP phase is visible in the flow asymmetries. Nevertheless, the shear viscosity near the QCD transition region has the largest impact on the collective flow of the system. We also find that the centrality dependence of the elliptic flow is sensitive to the temperature dependence of η/s.

DOI: 10.1103/PhysRevC.86.014909 PACS number(s): 25.75.Ld, 12.38.Mh, 24.10.Nz

I. INTRODUCTION

Determining the properties of the quark-gluon plasma (QGP) is nowadays one of the most important goals in high-energy nuclear physics. For a system of weakly interacting particles reliable results can be obtained from first-principle quantum field-theoretical calculations. Unfortunately, for strongly interacting matter these tools provide only a limited amount of information. It is, however, possible to calculate the thermodynamical properties of such matter numerically from the theory of strong interactions, quantum chromodynamics (QCD). These lattice QCD calculations show that if the temperature is sufficiently high, the matter undergoes a transition from a confined phase where the relevant degrees of freedom are hadrons, to a deconfined phase where the degrees of freedom are quarks and gluons, the so-called QCD transition [1].

In recent years, experiments at the Relativistic Heavy-Ion Collider (RHIC) at Brookhaven National Laboratory [2] and the Large Hadron Collider (LHC) at CERN have provided a wealth of data from which one could in principle obtain information about the QGP. However, to compare these data with lattice QCD results is not straightforward. So far, lattice calculations have provided reliable results for static thermodynamical properties of QCD matter, e.g., the equation of state (EoS). The system created in heavy-ion collisions is, however, not static but dynamical, because it expands and cools in a very short time span of order 10^{-23} seconds. Obviously, in order to be able to properly interpret the experimental results and infer the properties of QCD matter, we also need a good understanding of the dynamics of heavy-ion collisions.

Fluid dynamics is one of the most commonly used frameworks to describe the space-time evolution of the created fireball, because the complicated microscopic dynamics of the matter is encoded in only a few macroscopic parameters like the EoS and the transport coefficients.

Currently, fluid-dynamical models give a reasonably good quantitative description of transverse momentum spectra of hadrons and their centrality dependence [3–7]. So far, most calculations assume that the shear viscosity to entropy density ratio η/s is constant, and they show that, in order to describe the azimuthal asymmetries of the spectra, e.g., the elliptic flow coefficient v_2, this constant must be very small, of order 0.1. However, for real physical systems, η/s depends (at least) on the temperature [8]. A constant value of η/s can only be justified as an average over the space-time evolution of the system. It is not clear how this average is related to the temperature dependence of η/s.

In previous work [9,10], we have studied the consequences of relaxing the assumption of a constant η/s. We found that the relevant temperature region where the shear viscosity affects the elliptic flow most varies with the collision energy. At RHIC, the most relevant region is around and below the QCD transition temperature, while for higher collision energies the temperature region above the transition becomes more and more important. In this work we shall extend our previous study and provide a more detailed picture of the temperature regions that affect elliptic flow as well as higher harmonics at a given collision energy.

This paper is organized in the following way. In Sec. II, we describe our fluid-dynamical framework and its numerical implementation. In Sec. III, we specify the EoS, the transport coefficients, and the initialization. Sections IV and V contain a detailed compilation of our results, some of which were already shown in Refs. [9,10]. We present the transverse momentum spectra and the elliptic flow of hadrons at various centralities with different parametrizations of η/s as function of temperature. We also study the impact of different initial conditions and of the choice of the relaxation time for the shear-stress tensor. In Sec. VI, we investigate evolution of the elliptic flow in more detail and, in Sec. VII, find the temperature regions where v_2 and v_4 are most sensitive to the value of η/s. Finally, we summarize our results and give some conclusions. We use natural units $\hbar = c = k = 1$ throughout the paper.

II. FLUID DYNAMICS

A. Formalism

In order to describe the evolution of a system on length scales much larger than a typical microscopic scale, for instance the mean-free path, it is sufficient to characterize the state of matter by a few macroscopic fields, namely the energy-momentum tensor $T^{\mu\nu}$ and, possibly, some charge currents N_a^μ. Fluid dynamics is equivalent to the local conservation laws for these fields:

$$\partial_\mu T^{\mu\nu} = 0, \qquad \partial_\mu N_a^\mu = 0. \tag{1}$$

In the absence of conserved charges and bulk viscosity, the energy-momentum tensor $T^{\mu\nu}$ can be decomposed as

$$T^{\mu\nu} = e u^\mu u^\nu - P\Delta^{\mu\nu} + \pi^{\mu\nu}, \tag{2}$$

where $u^\mu = T^{\mu\nu}u_\nu/e$ is the fluid four-velocity, e is the energy density in the local rest frame of the fluid, i.e., in the frame where $u^\mu = (1, 0, 0, 0)$, and P is the thermodynamic pressure. The shear-stress tensor is defined as $\pi^{\mu\nu} = T^{\langle\mu\nu\rangle}$, where the angular brackets $\langle\rangle$ denote the symmetric and traceless part of the tensor orthogonal to the fluid velocity. With the $(+,-,-,-)$ convention for the metric tensor $g^{\mu\nu}$, the projector $\Delta^{\mu\nu} = g^{\mu\nu} - u^\mu u^\nu$.

If the system is sufficiently close to local thermodynamical equilibrium, the energy-momentum conservation equations can be closed by providing the EoS, $P(T)$, the equations determining $\pi^{\mu\nu}$, and the transport coefficients entering these equations, e.g., the shear viscosity $\eta(T)$. The EoS $P(T)$ and the shear viscosity $\eta(T)$ can in principle be computed by integrating out the dynamics on microscopic length scales.

While the conservation laws are exact for any system, the equations determining the shear-stress tensor require certain approximations, so that the only variables entering the equations of motion are those that appear in the energy-momentum tensor, namely e, u^μ, and $\pi^{\mu\nu}$. In the so-called relativistic Navier-Stokes approximation, the shear-stress tensor is directly proportional to the gradients of the four-velocity:

$$\pi^{\mu\nu} = 2\eta\sigma^{\mu\nu} \equiv 2\eta\partial^{\langle\mu}u^{\nu\rangle}. \tag{3}$$

We note that in this approximation the shear-stress tensor is not an independent dynamical variable.

Unfortunately, this approximation results in parabolic equations of motion, and subsequently the signal speed is not limited in this theory. In relativistic fluid dynamics this violation of causality leads to the existence of linearly unstable modes, which make relativistic Navier-Stokes (NS) theory useless for practical applications [11,12].

A commonly used approach that cures these instability and acausality problems is Israel-Stewart (IS) theory [13]. In this approach, the shear-stress tensor, the heat flow, and the bulk viscous pressure are introduced as independent dynamical variables and fulfill coupled, so-called relaxation-type differential equations of motion. Assuming vanishing heat-flow and bulk viscosity, the relaxation equation for the shear-stress tensor can be written as [15]

$$\tau_\pi \dot{\pi}^{\langle\mu\nu\rangle} + \pi^{\mu\nu} = 2\eta\sigma^{\mu\nu} + \lambda_1\pi^{\mu\nu}\theta + \lambda_2\sigma^{\langle\mu}{}_\alpha\pi^{\nu\rangle\alpha} + \lambda_3\pi^{\langle\mu}{}_\alpha\pi^{\nu\rangle\alpha} + \lambda_4\omega^{\langle\mu}{}_\alpha\pi^{\nu\rangle\alpha}, \tag{4}$$

where $\dot{A} = u^\mu\partial_\mu A$ denotes the comoving derivative of A and $\theta = \partial_\mu u^\mu$ is the expansion scalar. The shear-relaxation time τ_π is the slowest time scale of the underlying microscopic theory [14]. Formally, IS theory can be derived by neglecting all faster microscopic time scales [15]. Like τ_π, the coefficients λ_i can in principle be calculated from the underlying microscopic theory, i.e., in our case QCD. Unfortunately, for QCD the transport coefficients appearing in Eq. (4) are still largely unknown. For the sake of simplicity, in this work we use $\lambda_1 = -4/3$, obtained from the Boltzmann equation for a massless gas [13], and $\lambda_2 = \lambda_3 = \lambda_4 = 0$. The shear-relaxation time and the shear viscosity are left as free parameters.

Instead of the full $(3+1)$–dimensional treatment, we consider a simplified evolution where the expansion in the z direction is described by boost-invariant scaling flow [16], i.e., the longitudinal velocity is given by $v_z = z/t$, and the scalar densities are independent of the space-time rapidity $\eta_s = \frac{1}{2}\log(\frac{t+z}{t-z})$. Here, t is the time measured in laboratory coordinates. In this approximation, the full evolution depends only on the coordinates (τ, x, y), where x and y are the transverse coordinates and $\tau = \sqrt{t^2 - z^2}$ is the longitudinal proper time.

B. Numerical implementation

Once the initial values of the components of the energy-momentum tensor are specified at a given initial time τ_0, the space-time evolution of the system is obtained by solving the conservation laws [Eq. (1)] together with the IS equations [Eq. (4)].

The conservation laws are solved using the algorithm developed in Refs. [17] and generalized to more than one dimension in Ref. [18]. This method, known as SHASTA for "sharp and smooth transport algorithm," solves equations of the type

$$\partial_t U + \partial_i(v_i U) = S(t, \mathbf{x}), \tag{5}$$

where $U = U(t, \mathbf{x})$ is, for example, T^{00}, T^{0i}, …, v_i is the ith component of three-velocity, and $S(t, \mathbf{x})$ is a source term; for more details see Ref. [19].

We can further stabilize SHASTA by letting the antidiffusion coefficient $A_{\rm ad}$, which controls the amount of numerical diffusion to be proportional to

$$\frac{1}{(k/e)^2 + 1}, \tag{6}$$

where e is the energy density in the local rest frame, and k is some constant of order 10^{-5} GeV/fm^3. In this way, $A_{\rm ad}$ goes smoothly to zero near the boundaries of the grid, i.e., we increase the amount of numerical diffusion in that region. We have checked that this neither affects the solution nor produces more entropy inside the decoupling surface.

The relaxation Eq. (4) could also be solved using SHASTA. However, we noticed that solving it by replacing the spatial

gradient at grid point i on the left-hand side of Eq. (4) by a centered second-order difference,

$$\partial_x U_i = \frac{U_{i+1} - U_{i-1}}{2\Delta x}, \tag{7}$$

where $U = \pi^{\mu\nu}$, yields a more stable algorithm. Time derivatives in the source terms are simply taken as first-order backward differences. Like in SHASTA, all spatial gradients in the source terms are discretized according to Eq. (7).

C. Freeze-out

We assume that freeze-out, i.e., the transition from the fluid-dynamical system to free-streaming particles happens on a hypersurface of constant temperature. Unless otherwise stated, we assume that the freeze-out temperature is $T_{\rm dec} = 100$ MeV. We include all two- and three-particle decays of hadronic resonances according to Ref. [20].

The transverse momentum distribution of hadrons is calculated using the Cooper-Frye description [21]. For the final spectra we need to know the local single-particle momentum distribution functions of hadrons on the freeze-out surface. Here, we employ the widely used 14-moment ansatz where the correction to the local-equilibrium distribution $f_{0i} = \{\exp[(u_\mu p_i^\mu - \mu_i)/T] \pm 1\}^{-1}$ of a hadron of species i with four-momentum p_i^μ is given by [22]

$$\delta f_i = f_{0i} \frac{p_i^\mu p_i^\nu \pi_{\mu\nu}}{T^2 (e + P)}, \tag{8}$$

where $\pi^{\mu\nu}$ is the solution of Eq. (4). We note that this functional form for δf is merely an ansatz but consistent with Eq. (4). Other forms of δf are also possible, see, e.g., Ref. [23], and a full treatment of the multicomponent system further modifies δf; see Refs. [24,25]. Furthermore, if dissipative fluid dynamics is derived from the Boltzmann equation without assuming the 14-moment approximation, the full expansion of δf contains an infinite number of terms; for details see Ref. [15]. The effect of this will be studied in a future work.

III. PARAMETERS

A. Equation of state

As EoS we use the recent $s95p$-PCE-v1 parametrization of lattice QCD results [26]. In this parameterization, the high-temperature part is matched to recent results of the hotQCD collaboration [27,28] and smoothly connected to the low-temperature part described as a hadron resonance gas. All hadrons listed in Ref. [29] up to a mass of 2 GeV are included in the hadronic part of the EoS. The system is assumed to chemically freeze-out at $T_{\rm chem} = 150$ MeV. Below this temperature the EoS is constructed according to Refs. [30–32]. This construction assumes that the evolution below $T_{\rm chem}$ is isentropic. Strictly speaking this is not the case in viscous hydrodynamics since dissipation causes an increase in entropy. However, we have checked that in our calculations the viscous entropy production from all fluid cells with temperatures below $T_{\rm chem} = 150$ MeV is less than 1% of the initial entropy, whereas the entropy production during the entire evolution ranges from 3 to 14%, depending on the collision energy and the η/s parametrization.

B. Transport coefficients

The temperature-dependent shear viscosity is parametrized as follows. In all cases, we take the minimum of η/s to be at $T_{\rm tr} = 180$ MeV. Unless otherwise stated, the value of η/s at the minimum is assumed to equal the lower bound $\eta/s = 0.08$ conjectured in the framework of the AdS/CFT correspondence [34].

The parametrization of the hadronic viscosity is based on Ref. [35], where the authors consider a hadron resonance gas with additional Hagedorn states. In practice, we use a temperature dependence of η/s of the following functional form [9,36]:

$$\left.\frac{\eta}{s}\right|_{\rm HRG} = 0.681 - 0.0594 \frac{T}{T_{\rm tr}} - 0.544 \left(\frac{T}{T_{\rm tr}}\right)^2. \tag{9}$$

At $T = 100$ MeV this coincides with the η/s value given in Ref. [35] and decreases smoothly to the minimum value $\eta/s = 0.08$ at $T_{\rm tr}$. We note that many authors obtain considerably larger values for the shear viscosity of hadronic matter; see, e.g., Refs. [37]. Our motivation here is to illustrate the effects of hadronic viscosity rather than to use a parametrization that is as realistic as possible. We shall see that even this low η/s leads to considerable effects for hadronic observables in Au + Au collisions at RHIC. We further note that, since we are considering a chemically frozen hadron resonance gas below $T_{\rm chem}$, while in Ref. [35] chemical equilibrium is assumed at all temperatures, the entropy densities, and therefore the values of η, differ between the two calculations at a given value of $T < T_{\rm chem}$.

The high-temperature QGP viscosity is parametrized according to lattice QCD results [38] in such a way that it connects to the minimum of η/s at $T_{\rm tr}$. The functional form used is

$$\left.\frac{\eta}{s}\right|_{\rm QGP} = -0.289 + 0.288 \frac{T}{T_{\rm tr}} + 0.0818 \left(\frac{T}{T_{\rm tr}}\right)^2. \tag{10}$$

We take the following four parametrizations of the shear viscosity:

(1) (LH-LQ) $\eta/s = 0.08$ for all temperatures;
(2) (LH-HQ) $\eta/s = 0.08$ in the hadron gas, and above $T = 180$ MeV η/s increases according to Eq. (10);
(3) (HH-LQ) below $T = 180$ MeV, η/s is given by Eq. (9), and above we set $\eta/s = 0.08$;
(4) (HH-HQ) we use Eqs. (9) and (10) for the hadron gas and the QGP, respectively.

These parametrizations are shown in Fig. 1. Besides these four cases we also study the effect of varying the value of the minimum of η/s; see Secs. V and VII.

In order to complete the description, we also need to specify the relaxation time. In this work we use a functional form

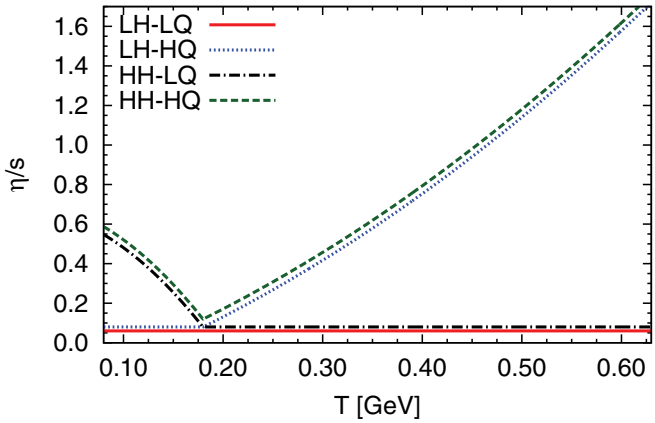

FIG. 1. (Color online) Different parametrizations of η/s as a function of temperature. The LH-LQ line is shifted downwards and the HH-HQ line upwards for better visibility.

suggested by kinetic theory,

$$\tau_\pi = c_\tau \frac{\eta}{e+p}, \tag{11}$$

where c_τ is a constant. Causality requires that $c_\tau \geqslant 2$ [12]. Unless otherwise stated, we shall use the value $c_\tau = 5$, which coincides with the value obtained from the Boltzmann equation in the 14-moment approximation for a massless gas of classical particles [39]. The relaxation times corresponding to the parametrizations above are shown in Fig. 2. The effect of varying the relaxation time separately from η is also studied in Sec. V.

C. Initial state

We still need to specify the initial state at some proper time τ_0. For a boost-invariant system it is sufficient to provide the components of the energy-momentum tensor in the transverse

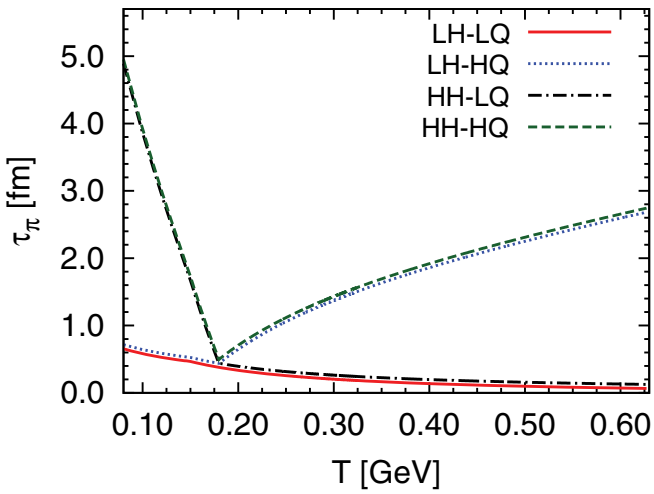

FIG. 2. (Color online) Relaxation times corresponding to the different parametrizations of η/s, for $c_\tau = 5$. The (LH-LQ) line is shifted downward and the (HH-HQ) line is shifted upward for better visibility.

plane at $z = 0$, i.e., $\eta_s = 0$. Within our approximations these are the local energy density, the initial transverse velocity, and the three independent components of the shear-stress tensor. Here, we will assume that the initial transverse velocity is zero and, unless otherwise stated, the initial shear-stress tensor is also assumed to be zero.

For the initial time we choose $\tau_0 = 1$ fm. The energy density $e(\tau_0, x, y)$ is based on the optical Glauber model by assuming that the energy density is a function of the density of binary nucleon-nucleon collisions $n_{\rm BC}$, or the density of wounded nucleons $n_{\rm WN}$, or both,

$$e(\tau_0, x, y) = C_e f(n_{\rm BC}, n_{\rm WN}). \tag{12}$$

The overall normalization, C_e, is fixed in order to reproduce the observed multiplicities in the most central $\sqrt{s_{NN}} = 200$ GeV Au + Au collisions at RHIC, and in $\sqrt{s_{NN}} = 2.76$ GeV Pb + Pb collisions at LHC.

The centrality dependence of the multiplicity is reproduced in this work in two different ways:

(1) BCfit: choosing f to be a polynomial in $n_{\rm BC}$,

$$f(n_{\rm BC}) = n_{\rm BC} + c_1 n_{\rm BC}^2 + c_2 n_{\rm BC}^3. \tag{13}$$

(2) GLmix: using a superposition of $n_{\rm BC}$ and $n_{\rm WN}$,

$$f(n_{\rm BC}, n_{\rm WN}) = d_1 n_{\rm BC} + (1 - d_1) n_{\rm WN}. \tag{14}$$

Here, the coefficient c_2 is introduced in order to guarantee that the parameterizations are monotonically increasing with increasing binary-collision or wounded-nucleon density. This ensures that the highest energy density is in the center of the system, i.e., at $x = y = 0$.

For a given impact parameter, the optical Glauber model yields a different number of participants and different centrality classes than the Monte Carlo Glauber models commonly used by the experimental collaborations. Using the optical Glauber model, we can either choose to reproduce the multiplicity as a function of the number of participants or as a function of centrality classes. In general, this leads to different coefficients c_i and d_1. Here, we choose to determine the initial conditions by requiring that the centrality dependence of the charged particle multiplicity as a function of the number of participants [40,41] is reproduced. We have checked that, if we determine the centrality dependence by matching to the centrality classes given by the optical Glauber model, the elliptic flow is more suppressed in central and enhanced in peripheral collisions at RHIC energies, while at LHC energies it remains practically unchanged. In order to be fully consistent with the experimental determination of the centrality classes, one would need to generate fluctuating initial conditions via a Monte Carlo Glauber model; see, e.g., Refs. [42–44].

For $\sqrt{s_{NN}} = 5.5$ TeV Pb + Pb collisions we use the multiplicity in the most central collisions as predicted by the EKRT model [45]. In this case the centrality dependence is assumed to follow binary scaling, i.e., $c_1 = c_2 = 0$ in Eq. (13). All initialization parameters are shown in Table I.

Different parametrizations of η/s lead to different entropy production and therefore different final multiplicity, even if

TABLE I. Initialization parameters for different collision energies. The maximum temperature $T_{\max}$ is given for the BCfit initialization with the (LH-LQ) parameterization of η/s. For the other initializations $T_{\max}$ differs less than 5%.

$\sqrt{s_{NN}}$ [GeV]	c_1 [fm^{-2}]	c_2 [fm^{-4}]	d_1	$T_{\max}$ [MeV]
200	-0.032	0.00035	0.1	313
2760	-0.01	0.0001	0.7	430
5500	0	0	1.0	504

the initial state is kept the same. This is especially true for different parametrizations of the high-temperature shear viscosity, since most of the entropy is produced during the early stages of the collision [46]. We compensate this using different overall normalizations, e.g., between the (HH-LQ) and (HH-HQ) parametrizations. Entropy production during the hadronic evolution is small and not compensated. The centrality dependence of the entropy production is also different for different η/s parametrizations. Since it leads to at most a 5% difference in the final multiplicities and is hardly visible in the results, it is not corrected here.

IV. RESULTS AND COMPARISON WITH EXPERIMENTAL DATA

In this section we use the initializations and parametrizations of η/s given above and compare the results with experimental data from RHIC and LHC.

A. Transverse momentum spectra and elliptic flow at RHIC

In Fig. 3 we show the p_T-spectra of pions for different centrality classes for RHIC $\sqrt{s_{NN}} = 200$ GeV Au + Au collisions and compare them with PHENIX data [40]. We only show results using the BCfit initialization; those for the GLmix initialization are very similar. The freeze-out temperature is chosen as $T_{\rm dec} = 100$ MeV. This choice reproduces the slopes of the p_T-spectra quite well.

Once we correct the normalization of the initial energy density profile for different entropy production (see discussion at the end of Sec. III C), the slopes of the p_T spectra are practically unaffected by the η/s parametrizations. We note that in our earlier work [9] this correction was not made, and the different η/s parametrizations lead not only to different multiplicities but also to different slopes for the p_T spectra. This effect was even more pronounced at LHC than at RHIC, due to an increase in entropy production caused by larger gradients appearing with an earlier initialization time $\tau_0 = 0.6$ fm.

The kaon spectra are shown in Fig. 4 and the proton spectra in Fig. 5 with the BCfit initialization. Both are compared with PHENIX data [40]. Because we do not consider net-baryon number in our calculations, the proton and antiproton spectra are identical. For this reason we show both the proton and the antiproton data in Fig. 5.

For both kaons and protons, the calculated spectra are slightly more curved than the data and they also lie above the data. As for the pions, the slopes of the spectra are practically independent of the η/s parametrization.

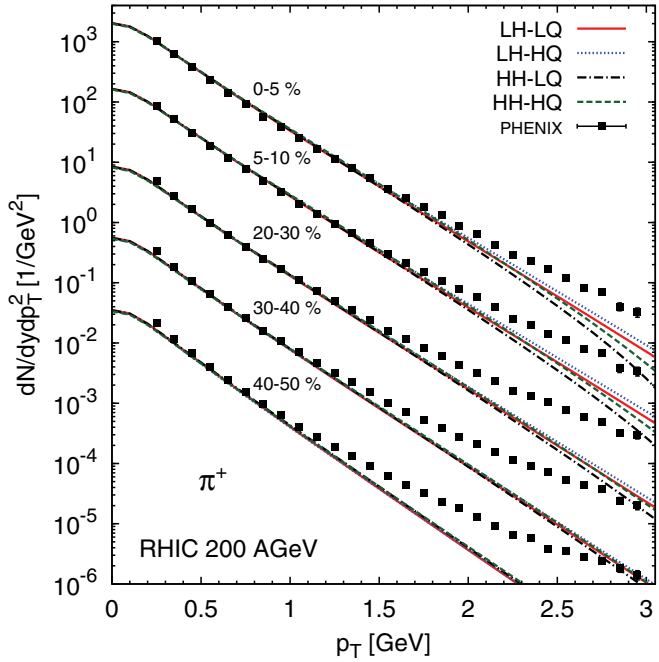

FIG. 3. (Color online) Pion spectra at RHIC, with BCfit initialization.

Figure 6 shows the p_T-differential elliptic flow $v_2(p_T)$ of charged hadrons for different centrality classes using the BCfit initialization. Similarly, Fig. 7 shows the elliptic flow for the GLmix initialization. The calculations are compared with the four-particle cumulant data from the STAR collaboration [47].

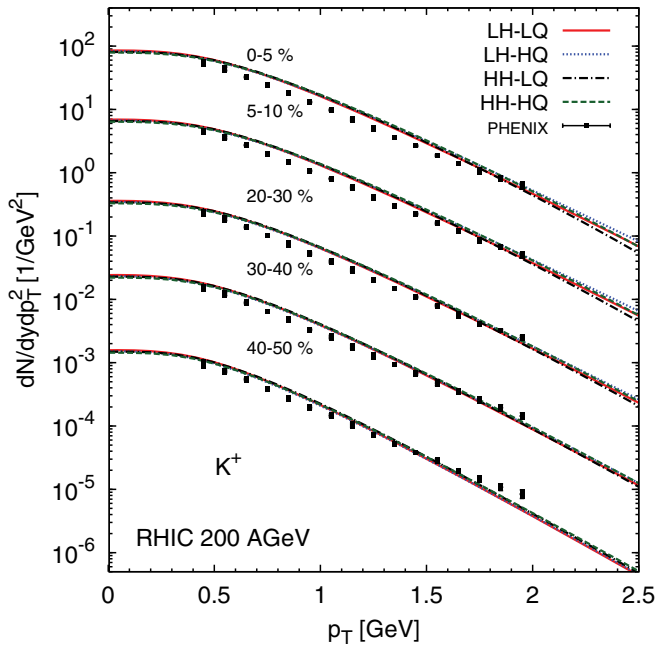

FIG. 4. (Color online) Kaon spectra at RHIC, with BCfit initialization.

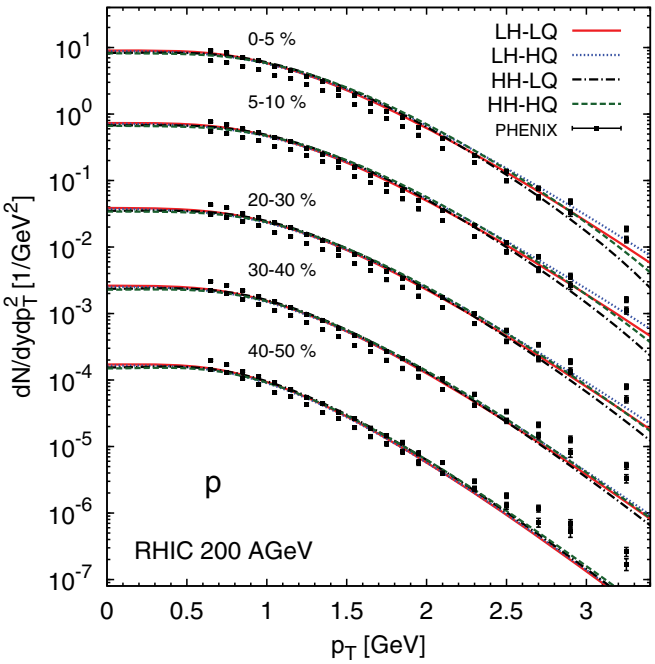

FIG. 5. (Color online) Proton spectra at RHIC, with BCfit initialization.

As was observed in Ref. [9], the differential elliptic flow is largely independent of the high-temperature η/s parameterization, but highly sensitive on the hadronic η/s at RHIC. This holds for all centrality classes. The suppression of the elliptic flow due to the hadronic viscosity is even more enhanced in more peripheral collisions. Note that with the BCfit initialization, the elliptic flow in the most central collision class is reproduced by the parametrizations with a large hadronic viscosity, while with the GLmix initialization the elliptic flow in the same centrality class is better described by taking a constant $\eta/s = 0.08$. However, with the latter choice the elliptic flow tends to be overestimated in more peripheral collisions. On the other hand, the temperature-dependent hadronic η/s gives the centrality dependence correctly down to the 30–40% centrality class. In even more peripheral collisions a large hadronic viscosity tends to suppress the elliptic flow too much.

Figure 8 shows $v_2(p_T)$ for protons with the BCfit initialization compared to the two-particle cumulant data from the STAR collaboration [48]. The protons show qualitatively the same response to the different η/s parametrizations as all charged hadrons, i.e., $v_2(p_T)$ depends strongly on the hadronic viscosity, but is almost independent of the high-temperature η/s. Since we use a smooth initialization, with no initial-state

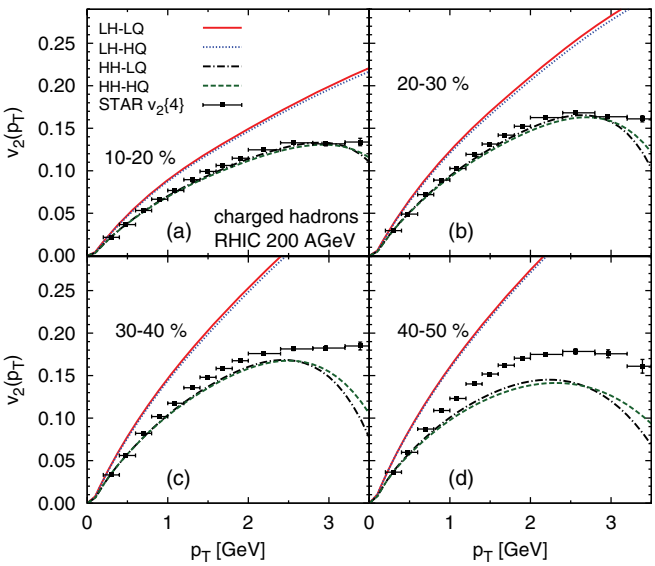

FIG. 6. (Color online) Charged hadron $v_2(p_T)$ at RHIC, with BCfit initialization.

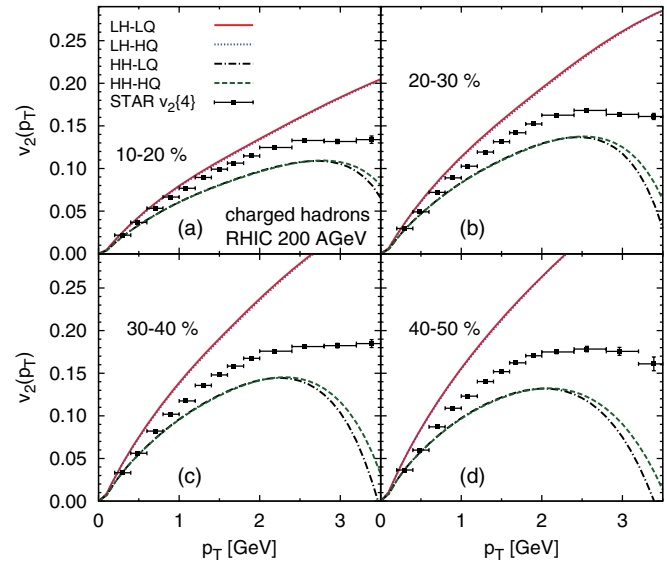

FIG. 7. (Color online) Charged hadron $v_2(p_T)$ at RHIC, with GLmix initialization.

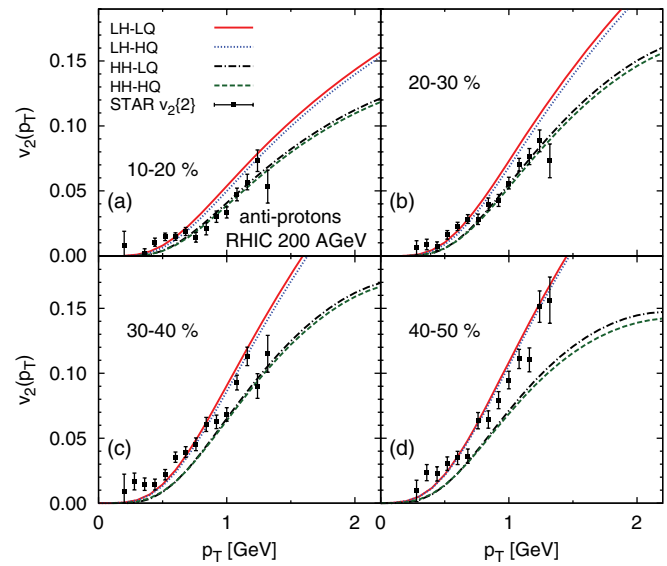

FIG. 8. (Color online) Proton $v_2(p_T)$ at RHIC, with BCfit initialization.

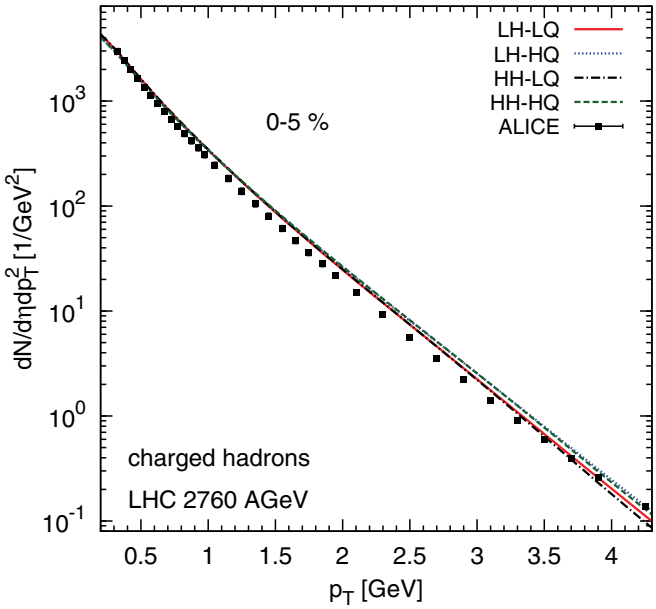

FIG. 9. (Color online) Charged hadron spectra at LHC, with BCfit initialization.

fluctuations included, quantitative comparisons with two- or four-particle cumulant data are not straightforward.

B. Transverse momentum spectra and elliptic flow at LHC

Transverse momentum spectra of charged hadrons in most central Pb + Pb collisions with $\sqrt{s_{NN}} = 2.76$ TeV at LHC are shown in Fig. 9. At LHC, both initializations BCfit and GLmix give very similar results for both elliptic flow and the spectra, because the contribution from binary collisions is large, of order $\sim$70%; see Table I. Therefore, we show only results with the BCfit initialization; these are compared to data from the ALICE collaboration [49]. The calculated spectra are somewhat flatter than the data. Here, we have used the same decoupling temperature as at RHIC, i.e., $T_{\rm dec} = 100$ MeV. We could improve the agreement with the data by decoupling at even lower temperature than at RHIC. Another way to improve the agreement is choosing a larger chemical freeze-out temperature. This would give steeper spectra, but the proton multiplicity at RHIC would then be overestimated. However, we have tested that the dependence of the spectra and the elliptic flow on η/s is unchanged by these details.

As was the case at RHIC, at LHC the slopes of the spectra are practically independent of the η/s parametrization. We note that here we have used the initialization time $\tau_0 = 1.0$ fm, i.e., the same as at RHIC. In Ref. [9] we observed a quite visible correlation between the shear viscosity and the spectral slopes. Here, the later initialization time and the fact that we now compensate for the entropy production between different η/s parametrizations almost completely removes this correlation. However, the earlier the evolution starts, the more the viscosity will affect the slopes.

The p_T-differential elliptic flow for all charged hadrons is shown in Fig. 10 and for protons in Fig. 11. The charged hadron elliptic flow is compared with ALICE four-particle

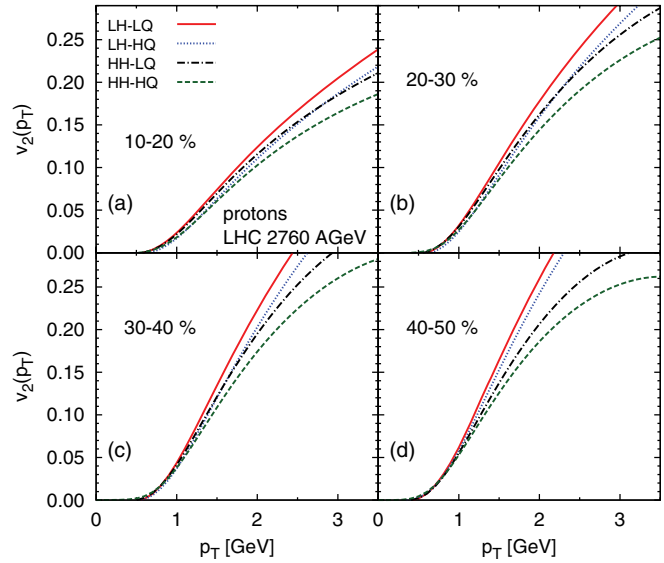

FIG. 10. (Color online) Charged hadron $v_2(p_T)$ at LHC, with BCfit initialization.

cumulant data [50]. We can see that in the 10–20% centrality class, changing the hadronic η/s or changing the high-temperature η/s has quite a similar impact on the elliptic flow; e.g., the difference between the LH-LQ and LH-HQ and between the LH-LQ and HH-LQ curves is nearly the same. However, the more peripheral the collision is, the more the viscous suppression is dominated by the hadronic η/s. This is confirmed by comparing the grouping of the flow curves in the 40–50% centrality class at LHC with that at RHIC; cf. Figs. 6 and 10. As was the case in Au + Au collisions at RHIC, also here the grouping of the curves for the protons is similar to that of all charged hadrons; cf. Fig. 11.

Note that, within our set-up, the best agreement with the ALICE data is obtained with the HH-HQ parametrization,

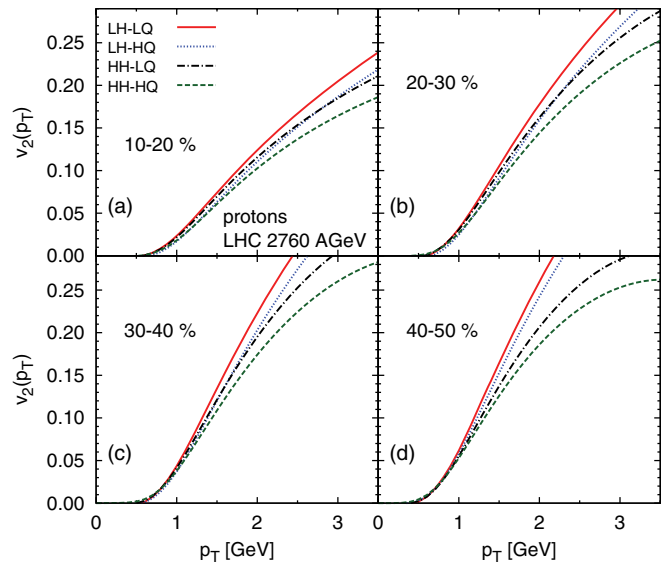

FIG. 11. (Color online) Proton $v_2(p_T)$ at LHC, with BCfit initialization.

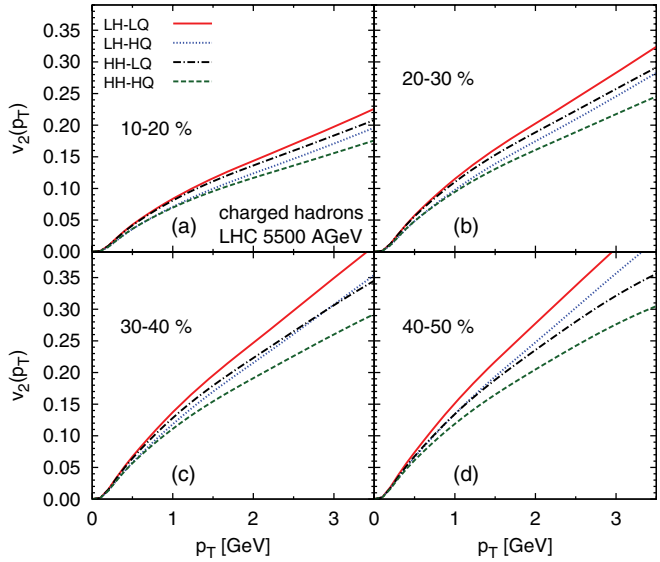

FIG. 12. (Color online) Charged hadron $v_2(p_T)$ at LHC 5.5 A TeV, with BC initialization.

i.e., with a temperature-dependent η/s in both hadronic and high-temperature phases. However, in the low-p_T region our calculations systematically underestimate the elliptic flow in all centrality classes. As was the case with the p_T spectrum, decoupling at a lower temperature and choosing a higher chemical freeze-out temperature would improve the agreement, without changing the grouping of the elliptic flow curves with the η/s parametrizations.

In Fig. 12 we show the p_T-differential elliptic flow for $\sqrt{s_{NN}} = 5.5$ TeV Pb + Pb collisions. In this case the viscous suppression of $v_2(p_T)$ is dominated by the high-temperature η/s in central collisions, while peripheral collisions resemble more the lower-energy central collisions at LHC; i.e., both hadronic and high-temperature viscosity contribute similarly to the suppression. Furthermore, the higher the p_T, the more the hadronic viscosity contributes to the suppression. This happens mainly because δf increases with both viscosity and p_T.

V. EFFECTS OF SHEAR INITIALIZATION, MINIMUM OF η/s AND RELAXATION TIME

One of the main results of Ref. [9] is that, at RHIC, the high-temperature shear viscosity has very little effect on the elliptic flow. In this section we elaborate more on this analysis and explicitly show that this statement holds for an out-of-equilibrium initialization of the shear-stress tensor as well. We also study the effect of varying the relaxation time.

Figure 13 shows the elliptic flow of charged hadrons in the 20–30% centrality class at RHIC. Instead of setting $\pi^{\mu\nu}$ to zero initially, here the so-called Navier-Stokes (NS) initialization where the initial values of the shear-stress tensor are given by the first-order, asymptotic solution of IS theory, Eq. (3). For all η/s parametrizations, the NS initialization increases the entropy production (up to 30%), especially for the parametrizations with a large high-temperature viscosity.

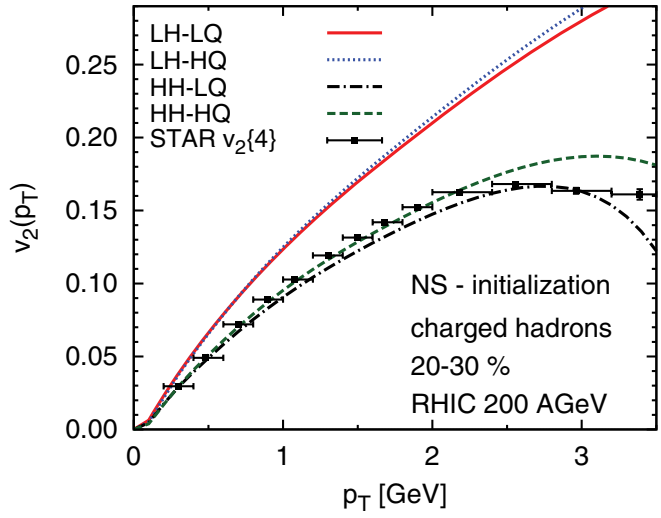

FIG. 13. (Color online) Charged hadron $v_2(p_T)$ at RHIC, with BCfit and NS initialization.

This is corrected by adjusting the initial energy density to produce approximately the same final multiplicity. Although for the parametrizations with a large hadronic η/s the different shear initializations give slightly different $v_2(p_T)$ curves, the grouping of these curves remains intact. We emphasize that the NS initialization gives very different initial conditions for each viscosity parametrization. If we use the same nonzero initial shear stress, e.g., $\pi^{\mu\nu} = \text{const.} \times \sigma^{\mu\nu}$, for each parametrization, the resulting $v_2(p_T)$ curves in each group in Fig. 13 would be even closer to each other.

The NS initialization with a constant $\eta/s = 0.08$ has a relatively short relaxation time; see Fig. 2. Hence, for $\tau_\pi \ll \tau_0$ the NS initialization is not a completely unrealistic assumption for the initial values of $\pi^{\mu\nu}$. However, for larger values of η/s the relaxation times are considerably larger, $\tau_\pi \gtrsim \tau_0$, and there is no reason to assume that the asymptotic solution could have been reached already at very early times.

So far we have changed the shear-viscosity parametrization by keeping the minimum fixed. In Fig. 14 we show the

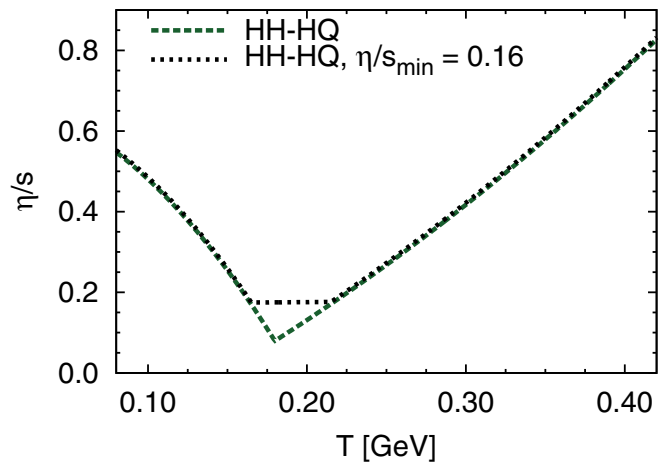

FIG. 14. (Color online) Parameterizations of η/s as a function of temperature. The (HH-HQ) line is the same as in Fig. 1.

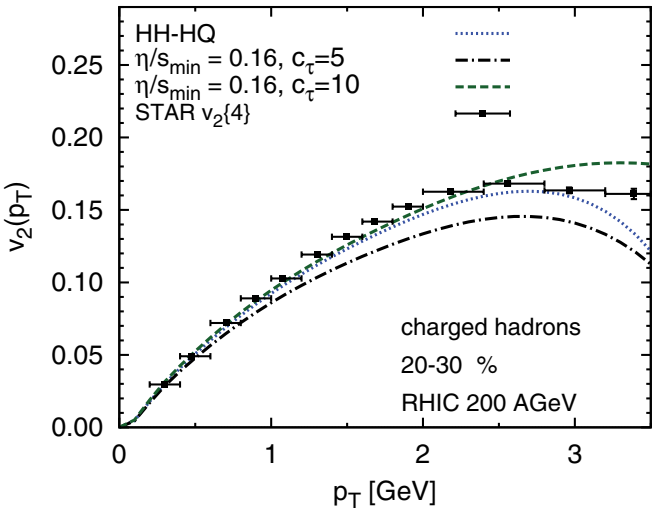

FIG. 15. (Color online) Charged hadron $v_2(p_T)$ at RHIC, with BCfit initialization and for different minima of η/s and relaxation times.

original HH-HQ parameterization and one where η/s around the minimum is twice as large. Figure 15 shows three $v_2(p_T)$ curves for Au + Au collisions at RHIC: one with the original HH-HQ parametrization, one with the larger minimum value of η/s, and the last one with the same large minimum value of η/s, but with a larger relaxation time; i.e., the constant in the relaxation time Eq. (11) is $c_\tau = 10$ instead of $c_\tau = 5$. We note that even a relatively small change in the η/s parameterization near the minimum produces quite a visible change in $v_2(p_T)$. At RHIC, this change can be almost completely compensated by adjusting the relaxation time. This shows that in small, rapidly expanding systems like the one formed in heavy-ion collisions, transient effects have considerable influence on the evolution. In other words, the relaxation time cannot be merely considered as a way to regularize the unstable Navier-Stokes theory: it has real physical effects that cannot be completely distinguished from the effects of η/s. In $\sqrt{s_{NN}} = 2.76$ TeV Pb + Pb collisions at LHC, the effect of changing the minimum or the relaxation time is practically the same.

VI. TIME EVOLUTION OF THE ELLIPTIC FLOW

One way to probe the effects of shear viscosity on the elliptic flow is to calculate the time evolution of the latter. Typically this is done by calculating the so-called momentum-space anisotropy from the energy-momentum tensor,

$$\varepsilon_p = \frac{\langle T^{xx} - T^{yy} \rangle}{\langle T^{xx} + T^{yy} \rangle}, \tag{15}$$

where the $\langle \cdots \rangle$ denotes the average over the transverse plane. The problem is, however, that one cannot make a direct connection of ε_p to the actual value of v_2 obtained from the decoupling procedure. Also, this way of studying the time evolution does not take into account that, at fixed time, part of the matter is already decoupled; i.e., the average over the transverse plane includes also matter that is outside the decoupling surface.

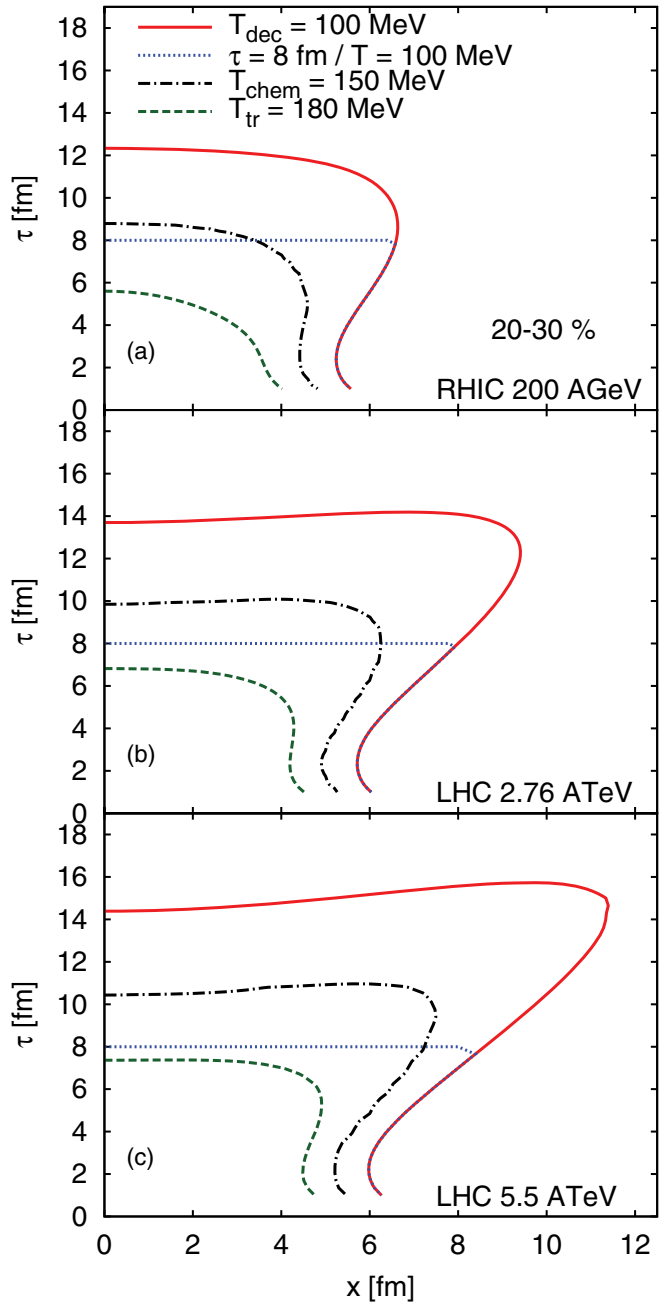

FIG. 16. (Color online) Constant-temperature hypersurfaces at decoupling ($T_{\rm dec} = 100$ MeV), chemical freeze-out ($T_{\rm chem} = 150$ MeV), and at the minimum of η/s ($T_{\rm tr} = 180$ MeV) at different collision energies. Also, examples of surfaces that are used in the calculation of the time evolution of v_2 are shown (dotted lines).

To overcome these two shortcomings of ε_p, we instead calculate the v_2 of pions from a constant-time hypersurface that is connected smoothly to a constant-temperature hypersurface at the edge of the fireball; see Fig. 16 for examples of such hypersurfaces. Although the pions do not exist as real particles before hadronization, the advantage is that the final v_2 we obtain matches the one of thermal pions from the full decoupling calculation.

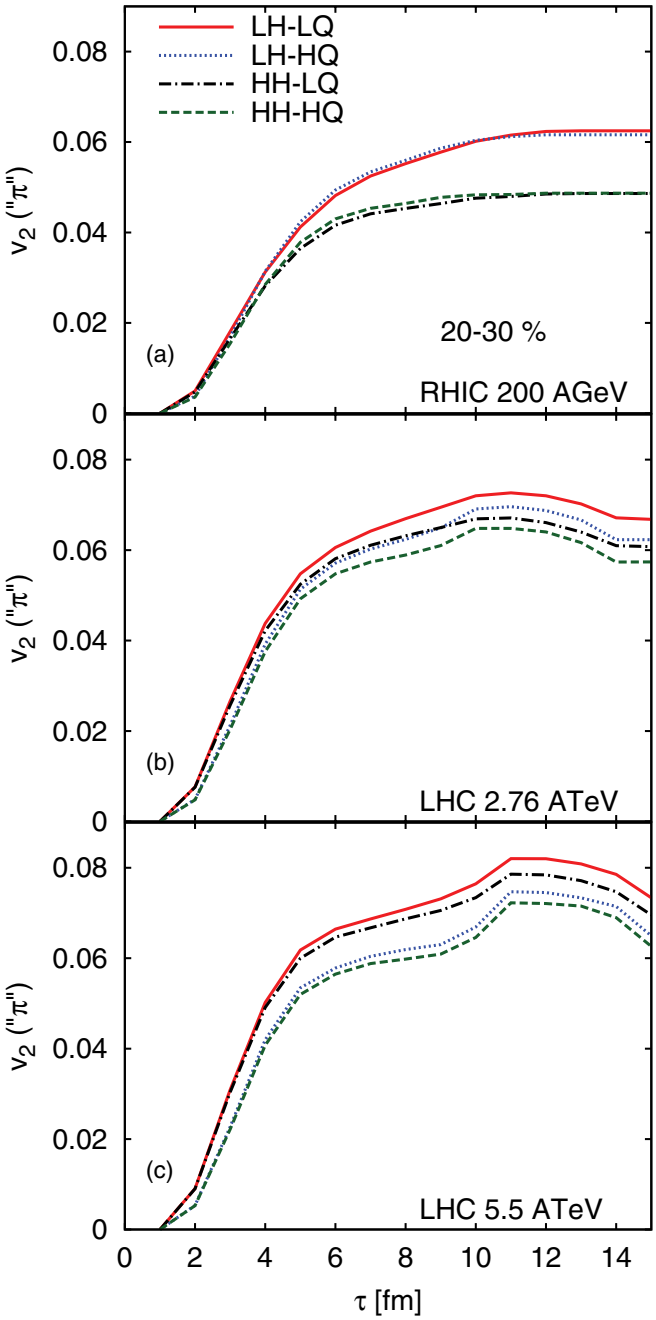

FIG. 17. (Color online) Time evolution of v_2 at different collision energies.

Figure 17 shows the time evolution of v_2 in Au + Au collisions at RHIC, in $\sqrt{s_{NN}} = 2.76$ TeV Pb + Pb collisions at LHC, and in $\sqrt{s_{NN}} = 5.5$ TeV Pb + Pb collisions at LHC. In all cases, the evolution is calculated in the 20–30% centrality class. These results confirm our earlier conjecture: at RHIC, the different η/s parametrizations create very little difference in the elliptic flow in the early stages of the collision, while at later stages the suppression due to the hadronic viscosity takes over and groups the v_2 curves according to the hadronic viscosity. At the intermediate LHC energy the impact of the QGP viscosity is larger, and the final v_2 still has a memory of this difference. The hadronic viscosity has a similar impact on v_2 as the QGP

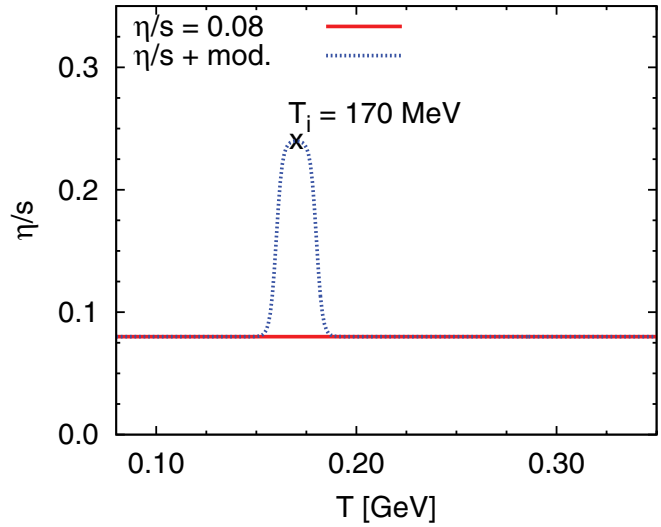

FIG. 18. (Color online) Shear viscosity with a modified temperature dependence.

viscosity. At the highest LHC energy the hadronic suppression is small and the effect of the QGP viscosity clearly dominates the grouping of the v_2 curves. Interestingly, both LHC evolutions show an increase of v_2 around $\tau = 10$ fm/c. This is when the system is going through the chemical decoupling stage. In the chemically frozen system, v_2 tends to increase more rapidly than in chemical equilibrium [32,33]. At RHIC, the chemical decoupling happens earlier, and also the hadronic suppression is stronger, and the increase in v_2 is washed out.

VII. PROBING THE EFFECTS OF A TEMPERATURE-DEPENDENT η/s ON THE v_n's

In this section, we try to probe the effects of a temperature-dependent η/s on the azimuthal asymmetries in a more detailed way. To this end, we introduce a modified η/s. Our baseline is a constant $\eta/s|_c = 0.08$ that we then modify near some temperature T_i according to

$$\frac{\eta}{s}(T) = \frac{\eta}{s}\Big|_c \left\{1 + 2\left[\exp\left(\frac{|T - T_i| - \delta T}{\Delta}\right) + 1\right]^{-1}\right\}, \quad (16)$$

where the parameters are taken to be $\delta T = 10$ MeV and $\Delta = 1.5$ MeV. One example of this η/s parametrization is shown in Fig. 18. We note that, although we use smooth initial conditions from the optical Glauber model, we still get nonzero v_n for all even n. Although these are much smaller than the ones obtained with the fluctuations included, we can still probe the effects of viscosity on these coefficients. In general, one expects that the viscosity affects higher harmonics more than the elliptic flow [43,51]. By changing the temperature T_i and comparing the simulations with a constant η/s we can find the temperature regions where v_2 or v_4 are most sensitive to changes of η/s at different collision energies.

Figure 19 shows the results for v_2 and v_4 in the 20–30% centrality class for RHIC and for both LHC energies considered earlier. We plot the relative difference $\delta v_n/v_n$, where $\delta v_n = v_n[\eta/s(T)] - v_n(\eta/s|_c)$. Each point in the figure

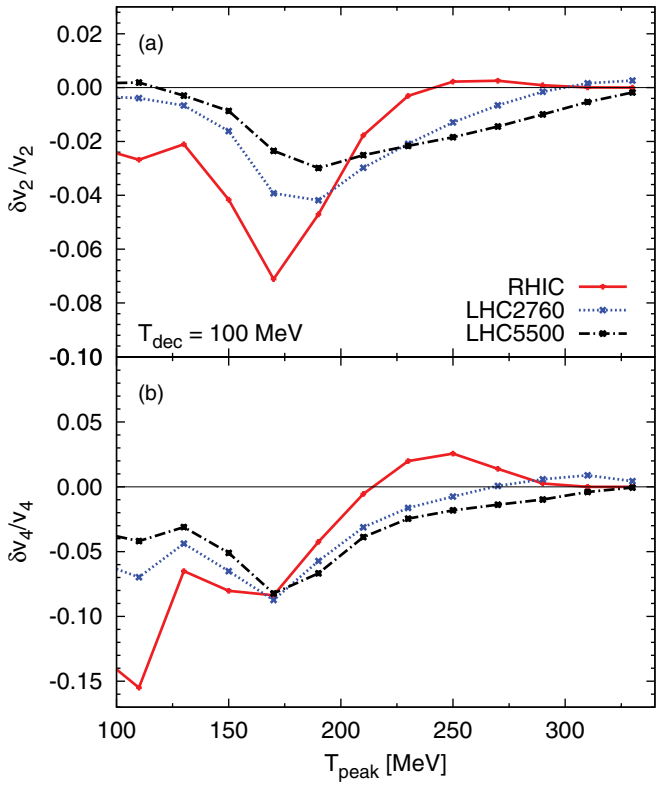

FIG. 19. (Color online) Effects of modified η/s on v_2 and v_4.

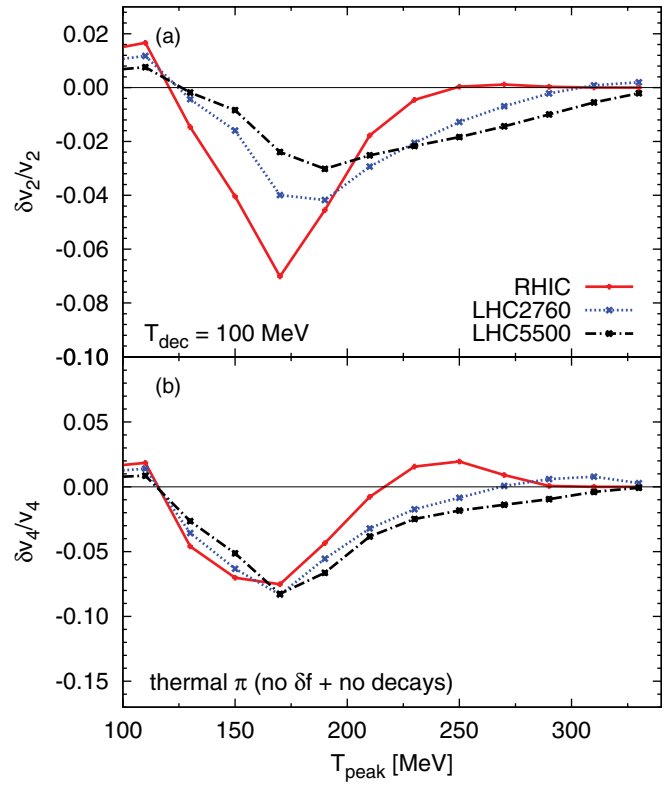

FIG. 20. (Color online) Same as Fig. 19 but without the δf contribution.

corresponds to a different calculation, with a different value of T_i in Eq. (16). Similarly, Fig. 20 shows the same result but without the δf contribution to the freeze-out.

The viscosity can affect v_n in two ways: by changing the space-time evolution of the integrated quantities like the energy density or by changing the local particle-distribution function at freeze-out. With our small baseline viscosity, the effect on the local distribution function is quickly washed out during the evolution below the temperature T_i. Therefore, in these simulations, in most of the temperature points, the change in η/s affects v_n through the space-time evolution, except at the lowest-temperature point $T_i = 110$ MeV, where the peak in η/s is close to the freeze-out temperature $T_{\rm dec} = 100$ MeV. If we exclude the lowest temperature point in v_4 at RHIC, we can read off from the figures that the temperature region where viscosity affects both v_2 and v_4 most is around the transition region $T \sim 150 \ldots 200$ MeV. For v_2 this temperature region shifts slightly toward higher temperatures with increasing collision energy, while for v_4 the temperature where the effect is maximal is practically unchanged. Other than this, the overall behavior of v_2 and v_4 is quite similar. At high temperatures, the effect of η/s increases with increasing collision energy, while at low temperatures the viscous suppression decreases with increasing collision energy, which is most notable for the $T_i = 110$ MeV point where the viscosity effects on the freeze-out distribution are strongest.

For v_2 we observed earlier that the suppression due to the hadronic viscosity practically vanishes at the highest-energy LHC collisions. This is again confirmed in Fig. 19. This is, however, not true for higher harmonics. For v_4 there is still a significant contribution from hadronic viscosity at the full LHC energy. In this sense, higher harmonics do not give direct access to the high-temperature viscosity but can rather help in constraining the hadronic dynamics and viscosity as well as the correct form of δf. This is also important since the hadronic evolution always tends to shadow the effects of the properties of the high-temperature matter.

VIII. CONCLUSIONS

We have studied the effects of a temperature-dependent η/s on the azimuthal asymmetries of hadron transverse momentum spectra. We found earlier [9] that the viscous suppression of the elliptic flow is dominated by the hadronic viscosity in $\sqrt{s_{NN}} = 200$ GeV Au + Au collisions at RHIC, while in Pb + Pb collisions at the full LHC energy $\sqrt{s_{NN}} = 5.5$ TeV the suppression is mostly due to the high-temperature shear viscosity. In this work we have supplemented these earlier studies with more details.

First, we found that the suppression of the elliptic flow due to the shear viscosity becomes more important in more peripheral collisions. At least in our set-up, for RHIC energies a temperature-dependent shear viscosity improves the centrality dependence of the elliptic flow compared to the data, similarly to what was found in the hybrid approach of Ref. [5]. With a constant $\eta/s = 0.08$ and with the GLmix initialization, the measured $v_2(p_T)$ is reproduced in the most central collisions, but the calculations give a too large elliptic flow for peripheral collisions. However, with the BCfit initialization

the elliptic flow in the most central collisions is reproduced with a temperature-dependent viscosity and also the centrality dependence is reproduced down to the 30–40% centrality class. Similarly, in Pb + Pb collisions at LHC both a temperature-dependent hadronic η/s as well as an increasing η/s in the high-temperature phase help in reproducing the centrality dependence. Although there are lots of uncertainties associated with the decoupling and the initial state, at RHIC the centrality dependence of $v_2(p_T)$ may give access to the temperature dependence of η/s in hadronic matter.

Furthermore, we have studied the effects of a temperature-dependent η/s in a more detailed way. We found that for a given collision energy both v_2 and v_4 are most sensitive to the shear viscosity near the transition temperature, i.e., $T \sim$ 150–200 MeV. For v_2, this region moves slightly to higher temperature and widens with increasing collision energy, while for v_4 it remains practically unchanged. Other than that, the dependence of v_2 and v_4 on η/s is similar with increasing collision energy: the effect of the hadronic viscosity decreases and the effect of the high-temperature viscosity increases.

For v_2 the effect of δf almost vanishes at the highest collision energies, but for v_4 it always remains significant. At RHIC the δf corrections clearly dominate v_4, and even at the highest collision energies this effect is comparable to the effects due to the modified space-time evolution. In this sense, higher harmonics give access to the δf corrections and the hadronic viscosity rather than the high-temperature viscosity.

ACKNOWLEDGMENTS

This work was supported by the Helmholtz International Center for FAIR within the framework of the LOEWE program launched by the State of Hesse. G.S.D., P.H., E.M., and D.H.R. acknowledge the hospitality of the Department of Physics of Jyväskylä University where part of this work was done. The work of H.N. was supported by the ExtreMe Matter Institute (EMMI) and the Academy of Finland, Project No. 133005, that of P.H. by BMBF under Contract No. 06FY9092, and that of E.M. by the Hungarian National Development Agency OTKA/NFÜ 81655. We acknowledge CSC – IT Center for Science in Espoo, Finland, for the allocation of computational resources.

[1] P. Petreczky, Nucl. Phys., Proc. Suppl. **140**, 78 (2005); C. E. DeTar, PoS LATTICE **2008**, 001 (2008).
[2] I. Arsene *et al*., Nucl. Phys. A **757**, 1 (2005); B. B. Back *et al*., *ibid*. **757**, 28 (2005); J. Adams *et al*., *ibid*. **757**, 102 (2005); K. Adcox *et al*., *ibid*. **757**, 184 (2005).
[3] For a review, see, for instance, P. Huovinen and P. V. Ruuskanen, Annu. Rev. Nucl. Part. Sci. **56**, 163 (2006).
[4] P. Romatschke and U. Romatschke, Phys. Rev. Lett. **99**, 172301 (2007); M. Luzum and P. Romatschke, Phys. Rev. C **78**, 034915 (2008); P. Bozek, *ibid*. **81**, 034909 (2010); B. Schenke, J. Phys. G **38**, 124009 (2011); J. Peralta-Ramos and E. Calzetta, Phys. Rev. C **82**, 054905 (2010); T. Hirano, U. W. Heinz, D. Kharzeev, R. Lacey, and Y. Nara, *ibid*. **77**, 044909 (2008); Y. Hama, T. Kodama, and O. Socolowski Jr., Braz. J. Phys. **35**, 24 (2005).
[5] H. Song, S. A. Bass, U. Heinz, T. Hirano, and C. Shen, Phys. Rev. C **83**, 054910 (2011).
[6] C. Shen, U. Heinz, P. Huovinen, and H. Song, Phys. Rev. C **82**, 054904 (2010).
[7] H. Song, S. A. Bass, U. Heinz, T. Hirano, and C. Shen, Phys. Rev. Lett. **106**, 192301 (2011).
[8] L. P. Csernai, J. I. Kapusta, and L. D. McLerran, Phys. Rev. Lett. **97**, 152303 (2006).
[9] H. Niemi, G. S. Denicol, P. Huovinen, E. Molnar, and D. H. Rischke, Phys. Rev. Lett. **106**, 212302 (2011).
[10] H. Niemi, G. S. Denicol, P. Huovinen, E. Molnar, and D. H. Rischke, J. Phys. **G38**, 124050 (2011); Acta Phys. Polon. Supp. **5**, 305 (2012).
[11] W. A. Hiscock and L. Lindblom, Ann. Phys. (NY) **151**, 466 (1983); Phys. Rev. D **31**, 725 (1985); **35**, 3723 (1987); Phys. Lett. A **131**, 509 (1988); G. S. Denicol, T. Kodama, T. Koide, and Ph. Mota, J. Phys. G **35**, 115102 (2008).
[12] S. Pu, T. Koide, and D. H. Rischke, Phys. Rev. D **81**, 114039 (2010).
[13] W. Israel and J. M. Stewart, Proc. R. Soc. London A **365**, 43 (1979); Ann. Phys. **118**, 341 (1979).
[14] G. S. Denicol, J. Noronha, H. Niemi, and D. H. Rischke, Phys. Rev. D **83**, 074019 (2011); J. Phys. G **38**, 124177 (2011); G. S. Denicol, H. Niemi, J. Noronha, and D. H. Rischke, arXiv:1103.2476 [hep-th].
[15] G. S. Denicol, H. Niemi, E. Molnar, and D. H. Rischke, arXiv:1202.4551 [nucl-th].
[16] J. D. Bjorken, Phys. Rev. D **27**, 140 (1983).
[17] J. P. Boris and D. L. Book, J. Comp. Physiol. A **11**, 38 (1973); D. L. Book, J. P. Boris, and K. Hain, *ibid*. **18**, 248 (1975).
[18] S. T. Zalesak, J. Comp. Physiol. A **31**, 335 (1979).
[19] E. Molnar, H. Niemi, and D. H. Rischke, Eur. Phys. J. C **65**, 615 (2010).
[20] J. Sollfrank, P. Koch, and U. W. Heinz, Z. Phys. C **52**, 593 (1991).
[21] F. Cooper and G. Frye, Phys. Rev. D **10**, 186 (1974).
[22] D. Teaney, Phys. Rev. C **68**, 034913 (2003).
[23] K. Dusling, G. D. Moore, and D. Teaney, Phys. Rev. C **81**, 034907 (2010).
[24] A. Monnai and T. Hirano, Nucl. Phys. A **847**, 283 (2010).
[25] D. Molnar, J. Phys. G **38**, 124173 (2011).
[26] P. Huovinen and P. Petreczky, Nucl. Phys. A **837**, 26 (2010).
[27] M. Cheng *et al*., Phys. Rev. D **77**, 014511 (2008).
[28] A. Bazavov *et al*., Phys. Rev. D **80**, 014504 (2009).
[29] S. Eidelman *et al*. (Particle Data Group Collaboration), Phys. Lett. B **592**, 1 (2004).
[30] H. Bebie, P. Gerber, J. L. Goity, and H. Leutwyler, Nucl. Phys. B **378**, 95 (1992).
[31] T. Hirano and K. Tsuda, Phys. Rev. C **66**, 054905 (2002).
[32] P. Huovinen, Eur. Phys. J. A **37**, 121 (2008).
[33] T. Hirano and M. Gyulassy, Nucl. Phys. A **769**, 71 (2006).
[34] P. K. Kovtun, D. T. Son, and A. O. Starinets, Phys. Rev. Lett. **94**, 111601 (2005).
[35] J. Noronha-Hostler, J. Noronha, and C. Greiner, Phys. Rev. Lett. **103**, 172302 (2009); C. Greiner, J. Noronha-Hostler, and J. Noronha, arXiv:1105.1756 [nucl-th].

[36] G. S. Denicol, T. Kodama, and T. Koide, J. Phys. G **37**, 094040 (2010).
[37] K. Itakura, O. Morimatsu, and H. Otomo, Phys. Rev. D **77**, 014014 (2008); M. I. Gorenstein, M. Hauer, and O. N. Moroz, Phys. Rev. C **77**, 024911 (2008); N. Demir and S. A. Bass, Phys. Rev. Lett. **102**, 172302 (2009).
[38] A. Nakamura and S. Sakai, Phys. Rev. Lett. **94**, 072305 (2005).
[39] G. S. Denicol, T. Koide, and D. H. Rischke, Phys. Rev. Lett. **105**, 162501 (2010).
[40] S. S. Adler *et al*. (PHENIX Collaboration), Phys. Rev. C **69**, 034909 (2004).
[41] K. Aamodt *et al*. (ALICE Collaboration), Phys. Rev. Lett. **106**, 032301 (2011).
[42] H. Holopainen, H. Niemi, and K. J. Eskola, Phys. Rev. C **83**, 034901 (2011).
[43] B. Schenke, S. Jeon, and C. Gale, Phys. Rev. C **85**, 024901 (2012).
[44] Z. Qiu, C. Shen, and U. Heinz, Phys. Lett. B **707**, 151 (2012)
[45] K. J. Eskola, H. Honkanen, H. Niemi, P. V. Ruuskanen, and S. S. Räsänen, Phys. Rev. C **72**, 044904 (2005).
[46] A. Dumitru, E. Molnar, and Y. Nara, Phys. Rev. C **76**, 024910 (2007).
[47] Y. Bai, Ph.D. Thesis, Nikhef and Utrecht University (2007); A. Tang (STAR Collaboration), arXiv:0808.2144 [nucl-ex].
[48] J. Adams *et al*. (STAR Collaboration), Phys. Rev. C **72**, 014904 (2005).
[49] K. Aamodt *et al*. (ALICE Collaboration), Phys. Lett. B **696**, 30 (2011).
[50] K. Aamodt *et al*. (The ALICE Collaboration), Phys. Rev. Lett. **105**, 252302 (2010).
[51] B. H. Alver, C. Gombeaud, M. Luzum, and J.-Y. Ollitrault, Phys. Rev. C **82**, 034913 (2010).

Quark polarization in a viscous quark-gluon plasma

Xu-Guang Huang,[1,2] Pasi Huovinen,[2] and Xin-Nian Wang[3,4,2]
[1]*Frankfurt Institute for Advanced Studies, D-60438 Frankfurt am Main, Germany*
[2]*Institut für Theoretische Physik, Goethe-Universität, D-60438 Frankfurt am Main, Germany*
[3]*Institute of Particle Physics, Central China Normal University, Wuhan, 430079, China*
[4]*Nuclear Science Division, MS 70R0319, Lawrence Berkeley National Laboratory, Berkeley, California 94720, USA*
(Received 21 September 2011; published 21 November 2011)

Quarks produced in the early stage of noncentral heavy-ion collisions could develop a global spin polarization along the opposite direction of the reaction plane due to the spin-orbital coupling via parton interaction in a medium that has finite longitudinal flow shear along the direction of the impact parameter. We study how such polarization evolves via multiple scattering in a viscous quark-gluon plasma with an initial laminar flow. The final polarization is found to be sensitive to the viscosity and the initial shear of local longitudinal flow.

DOI: 10.1103/PhysRevC.84.054910 PACS number(s): 13.88.+e, 12.38.Mh, 25.75.Nq

I. INTRODUCTION

The observed jet quenching and collective phenomena in high-energy heavy-ion collisions at the Relativistic Heavy Ion Collider (RHIC) provide strong evidence of the formation of strongly coupled quark-gluon plasma (QGP) [1,2]: The strong quenching of high transverse momentum jets is understood to be caused by parton energy loss induced by multiple collisions of the leading parton with color charges in the thermal medium [3–8]; the observed collective flow in the final bulk hadron spectra indicates a hydrodynamic behavior of the initial dense matter as an almost perfect fluid with a very small shear viscosity [9,10], $\eta/s \lesssim 0.5$. The large jet transport parameter from the observed strong jet quenching and small shear viscosity inferred from the collective flow can be connected to each other through a transport process in a strongly coupled system [11]. They both describe the ability of the medium partons to transfer momentum via strong interaction in QCD and maintain local equilibrium. Globally, such transport processes help to dissipate variations of flow velocities and thus will reduce the anisotropic flow, which is driven by the initial geometric anisotropy [9,10]. In this paper, we discuss the possibility of global quark spin polarization caused by such transport processes in noncentral high-energy heavy-ion collisions.

It was first proposed by Liang and Wang [12] that global quark polarization could occur in the QGP formed in a noncentral heavy-ion collision. They argued that at a finite impact parameter, the initial partons produced in the collision can develop a longitudinal fluid shear distribution representing local relative orbital angular momentum (OAM) in the same direction as the global OAM of the noncentral nucleus-nucleus collisions. Since interaction via one-gluon exchange in QCD contains a spin-orbital coupling, the OAM could cause a global spin polarization of quarks and antiquarks in the direction parallel to the OAM. Such a global (anti)quark polarization should have many observable consequences such as global hyperon polarization [12,13], vector meson spin alignment [12,14], and the emission of circularly polarized photons [15]. Predictions have been made [12,14–17] for these measurable quantities as functions of the global quark polarization P_q. Experimental measurements of the Λ hyperon polarization with respect to the reaction plane at RHIC [18–25] place a limit $|P_{\Lambda,\bar{\Lambda}}| \lesssim 0.02$ [19,24]. Such a limit puts a stringent test on both the initial shear of longitudinal flow in noncentral heavy-ion collisions [17] as well as the time evolution of the polarization through transport processes.

The estimates of the global quark polarization in Ref. [12] and in subsequent studies [16,17,26,27] were all obtained by considering the polarization process for a single scattering between quarks and thermal partons. However, one should consider the effect of the multiple scattering and expect that the quarks will be progressively polarized through multiple scattering. Furthermore, with the minimum values of shear viscosity $\eta/s \geqslant 1/4\pi$ in QGP imposed by the quantum limit, the local momentum shear, dp_z/dx, of the fluid, that is, the local OAM of interacting parton pairs, will decay with time. This will lead to a nontrivial time evolution of quark polarization P depending on the shear viscosity of the QGP matter and the final state observed global polarization could serve as a viscometer of QGP. In this paper, we focus on these two issues with a simple and yet interesting hydrodynamic evolution of a relativistic laminar flow between two frictionless impenetrable walls.

The rest of the paper is organized as follows. In Sec. II, we extend the calculation in Ref. [12] to the case of scattering of an initially polarized quark in a static potential model. In Sec. III, we study the relativistic laminar flow and compute the decay of the longitudinal momentum gradient. The results of Secs. II and III are applied to Sec. IV to study the time evolution of the quark polarization.

II. POLARIZATION OF INITIALLY POLARIZED QUARKS

We consider two colliding nuclei with the beam projectile moving in the direction of $\hat{\mathbf{z}}$ and the impact parameter $\mathbf{b}$ defined as the transverse distance of the projectile from the target nucleus along the $\hat{\mathbf{x}}$ direction as illustrated in the upper panel of Fig. 1. The direction $\hat{\mathbf{y}}$ defines the reaction plane, $\hat{\mathbf{y}} \propto \hat{\mathbf{z}} \times \hat{\mathbf{x}}$. The initial OAM of these two colliding nuclei is along the direction opposite to the reaction plane and could be very large. Given $1\,\text{fm} < b < 10\,\text{fm}$, the initial

OAM $L_0 \simeq Ab\sqrt{s}/2$ is roughly $10^5 \lesssim L_0 \lesssim 10^6$ for Au-Au collisions at RHIC energy $\sqrt{s} = 200$ GeV and $3 \times 10^6 \lesssim L_0 \lesssim 3 \times 10^7$ for Pb-Pb collision at Large Hadron Collider energy $\sqrt{s} = 5.5$ TeV. Because of the unequal local number density of the participant projectile and target nucleons at various transverse positions, some fraction of this large OAM could be transferred into the produced QGP matter in the overlapping region. Such global angular momentum, however, would never lead to a collective rotation of the system since there is no strong binding or attractive interaction in the partonic interaction at high energy. Instead, it could be manifested in the finite transverse (along $\hat{\mathbf{x}}$) gradient of the average longitudinal momentum p_z per produced parton due to the partonic interaction at high energy (see the lower panel of Fig. 1). Given the range of interaction Δx, two colliding partons will have relative longitudinal momentum $\Delta p_z = \Delta x dp_z/dx$ with relative OAM $L_y \sim -\Delta x \Delta p_z$. This relative OAM will lead to global quark polarization along $-\hat{\mathbf{y}}$ through the spin-orbital coupling in QCD. This is essentially the argument that was first proposed in Ref. [12]. It was found that the quark polarization via a single scattering with given relative momentum p reads

$$P \equiv \frac{\Delta\sigma}{\sigma} \equiv \frac{\sigma_\uparrow - \sigma_\downarrow}{\sigma_\uparrow + \sigma_\downarrow} = -\frac{\pi\mu p}{2E(E+m)}, \tag{2.1}$$

where $\sigma_s, s = \uparrow, \downarrow$ is the cross section of final quark with spin s along $\hat{\mathbf{y}}$, m is the mass of interacting quark, and μ is the Debye screening mass of longitudinal gluon, $\mu^2 = g^2(N_c + N_f/2)T^2/3$. The initial relative momentum p can be estimated as $p \simeq \Delta x dp_z/dx$ with $\Delta x \sim \mu^{-1}$ being the characteristic range of interaction. Then p/μ is nothing but the relative orbital angular momentum between the scattering quarks, $L_y \sim -p/\mu$. In the nonrelativistic limit for massive quarks, P is proportional to the spin-orbital coupling energy $P \propto E_{LS}/\mu$, where $E_{LS} = (\vec{L}\cdot\vec{S})(dV_0/dr)/rm^2$ and $(dV_0/dr)/r \sim \mu^3$ with typical interaction range $r \sim 1/\mu$.

The estimates in Refs. [12,16] and [17] were based on the assumption that the initial quarks are not polarized. In order to discuss the time evolution of the quark polarization via multiple scattering, one must calculate the quark-quark cross section of initially polarized quarks. Let the fraction of initial quarks of spin $\lambda_i/2$ along $\hat{\mathbf{y}}$ be $R_{\lambda_i} = (1 + \lambda_i P_i)/2$ with P_i being the initial polarization. The identity $R_+ + R_- = 1$ must hold. Consider a quark with initial relative four-momentum $p^\mu = (E, \mathbf{p})$ and spin $\lambda_i/2$ scattering with a virtual gluon and resulting in final spin $\lambda_f/2$; the cross section with fixed impact parameter $\mathbf{x}_T$ is

$$\begin{aligned}
\frac{d\sigma_{\lambda_f}}{d^2\mathbf{x}_T} &= C_T \sum_{\lambda_i} \int \frac{d^2\mathbf{q}_T}{(2\pi)^2} \int \frac{d^2\mathbf{k}_T}{(2\pi)^2} e^{i(\mathbf{k}_T - \mathbf{q}_T)\cdot\mathbf{x}_T} \\
&\quad \times R_{\lambda_i} \mathcal{I}_{\lambda_f\lambda_i}(\mathbf{k}_T, \mathbf{q}_T, E), \\
\mathcal{I}_{\lambda_f\lambda_i} &\equiv \mathcal{M}_{\lambda_f\lambda_i}(\mathbf{q}_T, E)\mathcal{M}^*_{\lambda_f\lambda_i}(\mathbf{k}_T, E), \\
\mathcal{M}_{\lambda_f\lambda_i}(\mathbf{q}_T, E) &= \frac{g}{2E}\bar{u}_{\lambda_f}(p_q)\not{A}(\mathbf{q}_T)u_{\lambda_i}(p),
\end{aligned} \tag{2.2}$$

where $C_T = 2/9$ is the color factor associated with the target, $\mathbf{q}_T$ ($\mathbf{k}_T$) is the transverse momentum transfer from the virtual gluon to quark, and $p^\mu_{q(k)}$ is the final four-momentum of quark, $p^\mu_{q(k)} = p^\mu + [0, \mathbf{q}_T(\mathbf{k}_T)]$. We use the screened static potential model to calculate $\mathcal{M}_{\lambda_f\lambda_i}$ in which $A^\mu = (A^0, \mathbf{0})$ with $A^0(q_T) = g/(q_T^2 + \mu^2)$ [3].

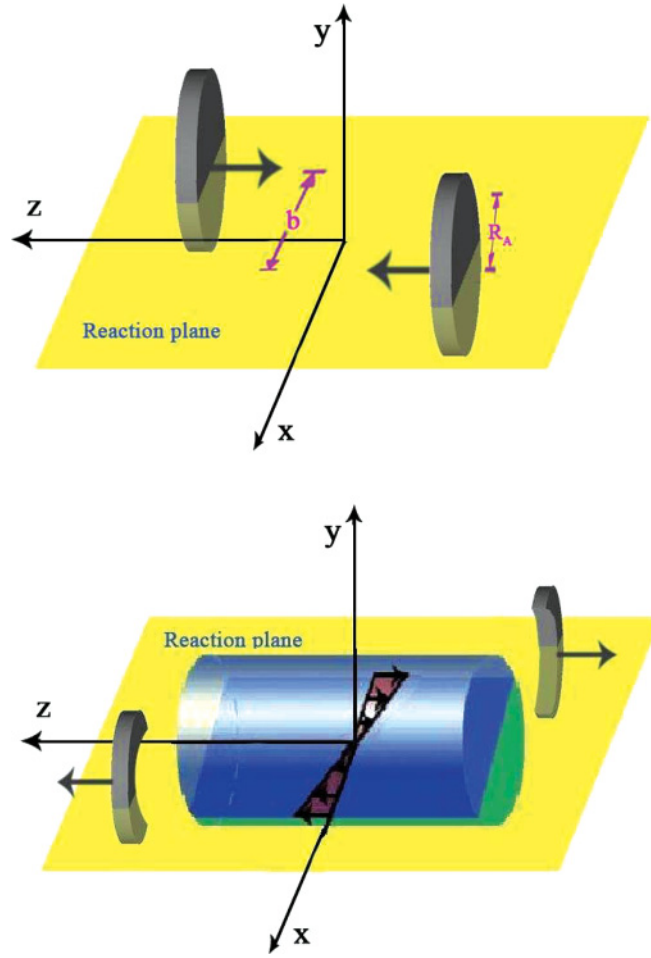

FIG. 1. (Color online) Illustration of noncentral collisions with impact parameter $\mathbf{b}$ of two heavy nuclei with radii R_A. The global angular momentum of the produced matter is along $-\hat{\mathbf{y}}$, opposite to the reaction plane.

For small angle scattering (which is justified when the relative longitudinal momentum $\mathbf{p}$ is large), $q_T, k_T \sim \mu \ll E$, one finds

$$\begin{aligned}
\mathcal{I}_{\lambda_f\lambda_i} \approx \frac{g^2}{2} A_0(q_T)A_0(k_T)\Big\{ & 1 + \lambda_i\lambda_f \\
& + \frac{1}{2E(E+m)}[(1+\lambda_i\lambda_f)\mathbf{p}\cdot(\mathbf{q}_T + \mathbf{k}_T) \\
& + i(\lambda_i + \lambda_f)\mathbf{p}\cdot\hat{\mathbf{y}}\times(\mathbf{k}_T - \mathbf{q}_T)]\Big\}.
\end{aligned} \tag{2.3}$$

From Eqs. (2.2) and (2.3), it is evident that the polarization will not change if one averages the cross section over all the possible directions of the parton impact parameter $\mathbf{x}_T$. However, in noncentral heavy-ion collisions, the local relative OAM L_y provides a preferred average reaction plane for parton collisions. This will lead to a global quark polarization opposite to the reaction plane of nucleus-nucleus collisions. This conclusion should not depend on our perturbative treatment of

parton scattering as far as the effective interaction is mediated by the vector coupling in QCD. Therefore, we average over the upper half-xy-plane with $x > 0$, that is, average over the relative angle between parton $\mathbf{x}_T$ and the nuclear impact parameter $\mathbf{b}$ from $-\pi/2$ to $\pi/2$ and over x_T. To do this, we use the identity

$$\int_{x>0} d^2\mathbf{x}_T e^{i(\mathbf{k}_T-\mathbf{q}_T)\cdot\mathbf{x}_T} = \frac{2\pi i\delta(k_y-q_y)}{k_x-q_x+i0^+}. \tag{2.4}$$

Then the total unpolarized cross section reads

$$\begin{aligned}\sigma &\equiv \int_{x>0} d^2\mathbf{x}_T \frac{d\sigma}{d^2\mathbf{x}_T} \equiv \int_{x>0} d^2\mathbf{x}_T \left(\frac{d\sigma_+}{d^2\mathbf{x}_T}+\frac{d\sigma_-}{d^2\mathbf{x}_T}\right)\\ &= \int_0^\infty dq_T q_T \frac{C_T g^4}{4\pi\left(q_T^2+\mu^2\right)^2}\\ &\quad\times\left[1-P_i\frac{p\sqrt{q_T^2+\mu^2}K\left(q_T/\sqrt{q_T^2+\mu^2}\right)}{\pi E(E+m)}\right]\\ &= \frac{C_T g^4}{8\pi\mu^2}\left[1-P_i\frac{\pi\mu p}{2E(E+m)}\right],\end{aligned} \tag{2.5}$$

and the polarized cross section reads

$$\begin{aligned}\Delta\sigma &\equiv \int_{x>0} d^2\mathbf{x}_T \frac{d\Delta\sigma}{d^2\mathbf{x}_T} \equiv \int_{x>0} d^2\mathbf{x}_T \left(\frac{d\sigma_+}{d^2\mathbf{x}_T}-\frac{d\sigma_-}{d^2\mathbf{x}_T}\right)\\ &= \int_0^\infty dq_T q_T \frac{C_T g^4}{4\pi\left(q_T^2+\mu^2\right)^2}\\ &\quad\times\left[P_i-\frac{p\sqrt{q_T^2+\mu^2}K\left(q_T/\sqrt{q_T^2+\mu^2}\right)}{\pi E(E+m)}\right]\\ &= \frac{C_T g^4}{8\pi\mu^2}\left[P_i-\frac{\pi\mu p}{2E(E+m)}\right],\end{aligned} \tag{2.6}$$

where $K(x)$ is the complete elliptic integral of the first kind. The final global quark polarization is then

$$P_f = P_i - \frac{\left(1-P_i^2\right)\pi\mu p}{2E(E+m)-P_i\pi\mu p}. \tag{2.7}$$

It is also useful to get the transverse momentum dependence of the quark polarization. From Eqs. (2.5) and (2.6), we read out the differential cross sections,

$$\begin{aligned}\frac{d\Delta\sigma}{dq_T} &= q_T\frac{C_T g^4}{4\pi\left(q_T^2+\mu^2\right)^2}\\ &\quad\times\left[P_i-\frac{p\sqrt{q_T^2+\mu^2}K\left(q_T/\sqrt{q_T^2+\mu^2}\right)}{\pi E(E+m)}\right],\end{aligned} \tag{2.8}$$

$$\begin{aligned}\frac{d\sigma}{dq_T} &= q_T\frac{C_T g^4}{4\pi\left(q_T^2+\mu^2\right)^2}\\ &\quad\times\left[1-\frac{P_i p\sqrt{q_T^2+\mu^2}K\left(q_T/\sqrt{q_T^2+\mu^2}\right)}{\pi E(E+m)}\right].\end{aligned} \tag{2.9}$$

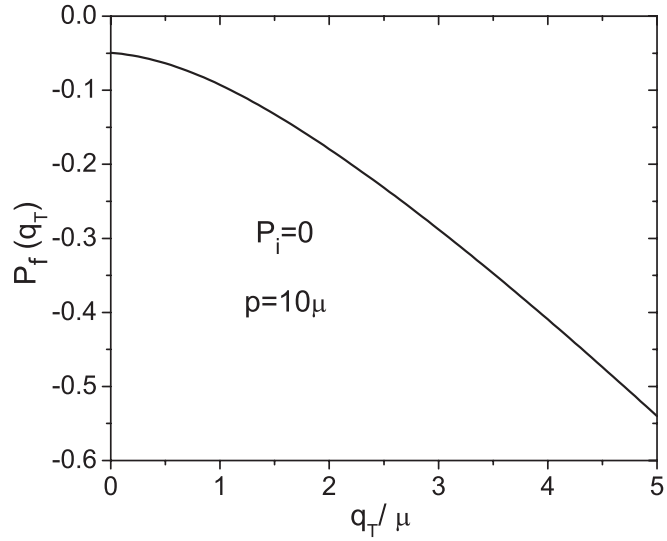

FIG. 2. The TMDP as a function of transverse momentum in unit of μ. The initial relative longitudinal momentum is chosen to be $p = 10\mu$.

The transverse-momentum-dependent polarization (TMDP) defined as $P_f(q_T) \equiv (d\Delta\sigma/dq_T)/(d\sigma/dq_T)$ now reads

$$P_f(q_T) = \frac{\pi E(E+m)P_i - p\sqrt{q_T^2+\mu^2}K\left(q_T/\sqrt{q_T^2+\mu^2}\right)}{\pi E(E+m) - P_i p\sqrt{q_T^2+\mu^2}K\left(q_T/\sqrt{q_T^2+\mu^2}\right)}. \tag{2.10}$$

Some discussions are in order. (i) If the initial quark is unpolarized, $P_i = 0$, we recover the result of Ref. [12]. (ii) Because the denominator is always positive in the right-hand side (RHS) of Eq. (2.7) for high relative longitudinal momentum (i.e., when small angle approximation is applicable), we always have $P_f \leqslant P_i$. Therefore, scattered quarks always prefer to be polarized along $-\hat{\mathbf{y}}$ direction. (iii) The scattering matrix elements $\mathcal{I}_{\lambda_f\lambda_i}$ with spin flipping ($\lambda_f = -\lambda_i$) are zero according to Eq. (2.3), so there is no flipping of quark's spin via the scattering under this small angle approximation. The polarization in the final state is caused by the larger cross section of quarks with spin up relative to quarks with spin down. This will lead to the conclusion that if the initial quark is completely polarized, $P_i = \pm 1$, we must have $P_f = P_i$. This is indeed the case expressed in Eq. (2.7) when $P_i = \pm 1$. (iv) The quark polarization has a remarkable transverse momentum dependence, as shown in Eq. (2.10). Figure 2 shows the typical behavior of TMDP as a function of the transverse momentum with given $p = 10\mu$. The polarization grows with the transverse momentum due to quark-quark scattering. In principle, the Λ-hyperon polarization should have similar transverse momentum dependence, although as we mentioned in Sec. I it is not trivial to construct a correspondence between quark polarization and hadron polarization.

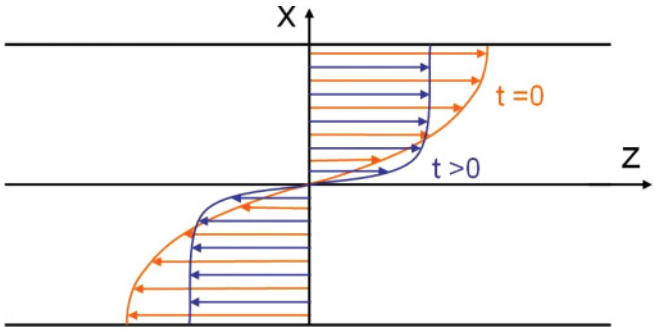

FIG. 3. (Color online) Illustration of the velocity profiles of the relativistic laminar flow.

III. RELATIVISTIC LAMINAR FLOW

Before discussing how the quark polarization evolves in a viscous QGP due to multiple scattering, we have to know how the QGP itself evolves through either transport model or viscous hydrodynamical model [9,10,28–32], Moreover, we also have to know the initial profile of the longitudinal flow field. In the discussion in Sec. II, we simply followed Ref. [12] and assumed that nothing depends on the longitudinal position in the system. In such a case, the finite angular momentum must lead to a velocity profile depicted in Fig. 3 (see Ref. [33] for a discussion of possible consequences of such a profile). On the other hand, another extreme is to assume that $dv_z/dx \equiv 0$ everywhere, but the angular momentum is carried by the matter distribution in the reaction plane; see Ref. [34] for illustration.

To study the effect of viscosity on the decay of the local angular momentum, we consider a simple laminar flow without driving force between two frictionless (free-slip flow) impenetrable walls. We assume the walls are infinitely large and separated by a distance $2h$. To make dimensions relevant for a heavy-ion collision, we set $h = 5$ fm. Such a scenario might be far from the real longitudinal flow profile in high-energy heavy-ion collisions, but it will be very illustrative for our study here. We further assume that the flow profile has no longitudinal variation and the system has a reflection symmetry respect to the yz plane. We study two cases: One with no expansion, and another with boost-invariant expansion in y direction, that is, with flow profile $v_y = y/t$. In both cases, the flow four-velocity in the reaction plane has the general form $u^\mu = (\gamma, \gamma v_x, 0, \gamma v_z)$ with $\gamma \equiv 1/\sqrt{1 - v_x^2 - v_z^2}$ and $v_{x,z}(t, x)$ being the x and z components of the three-velocity.

As is well known, the relativistic Navier-Stokes hydrodynamics is unstable and provides a possibility for acausal signal velocities [35]. Therefore, we use the second-order theory by Israel and Stewart [36] instead. Although hydrodynamics has been widely used to model the heavy-ion collisions, as far as we know, there is no literature discussing the relativistic laminar flow.

If there are no conserved charges, the hydrodynamical equations of motion are given by the conservation of energy and momentum

$$\partial_\mu T^{\mu\nu} = 0, \tag{3.1}$$

where $T^{\mu\nu} \equiv (\varepsilon + \Theta)u^\mu u^\nu - \Theta g^{\mu\nu} + \pi^{\mu\nu}$ is the energy-momentum tensor, ε is the energy density, Θ is the pressure,[1] and $\pi^{\mu\nu}$ is the shear stress tensor. To close the set of differential equations, one also needs to specify an equation of state (EOS) $\varepsilon = \varepsilon(\Theta)$. For simplicity, we use the ideal gas EOS $\varepsilon = 3\Theta$.

In its simplest form, Israel-Stewart hydrodynamics means that instead of being directly proportional to the velocity gradients, the shear stress tensor is a dynamical variable, which relaxes toward the Navier-Stokes value on its relaxation time τ_π:

$$D\pi^{\mu\nu} = -\frac{1}{\tau_\pi}(\pi^{\mu\nu} - 2\eta\nabla^{\langle\mu}u^{\nu\rangle}) - 2\pi^{\kappa(\mu}u^{\nu)}Du_\kappa, \tag{3.2}$$

where $D \equiv u^\lambda\partial_\lambda$, $A^{(\mu\nu)} \equiv (A^{\mu\nu} + A^{\nu\mu})/2$, $A^{\langle\mu\nu\rangle} \equiv [\Delta_\alpha^{(\mu}\Delta_\beta^{\nu)} - \frac{1}{3}\Delta^{\mu\nu}\Delta_{\alpha\beta}]A^{\alpha\beta}$, $\nabla^\mu \equiv \partial^\mu - u^\mu u^\nu\partial_\nu$, $\Delta^{\mu\nu} \equiv g^{\mu\nu} - u^\mu u^\nu$, and η is the shear viscosity coefficient. The last term is required to keep the shear stress tensor orthogonal to the flow velocity in all circumstances. This is the so-called truncated Israel-Stewart equation. Although there are more terms in a complete Israel-Stewart equation, for our purpose here, the truncated one is sufficient.

The relaxation time is given by [36]

$$\tau_\pi = 2\eta\beta_2, \tag{3.3}$$

which is dependent on the shear viscosity and another coefficient β_2. For massless Boltzmann particles, the kinetic theory gives [36]

$$\beta_2 = \frac{3}{4\Theta}. \tag{3.4}$$

If there is no phase transition, it is expected that β_2 for Fermion and Boson gases have only minor modification from β_2 for Boltzmann gas at high temperature [37–42]. Taking temperature $T \sim 350$ MeV, the relaxation time is around $\tau_\pi \sim 0.27$–1.35 fm if using $\eta/s = 1/(4\pi) - 5/(4\pi)$, where s is the entropy density, and for free gluon gas it is

$$s = \nu_g\frac{2\pi^2T^3}{45}, \tag{3.5}$$

with the degeneracy factor $\nu_g = 2(N_c^2 - 1)$.

Since the system has reflection symmetry with respect to the yz plane, and there are no particle, momentum, or heat flow through the hard walls, the system obeys the following boundary conditions:

$$\begin{aligned} v_z(t, 0) = v_x(t, 0) = v_x(t, \pm h) = 0, \\ \partial v_z(t, \pm h)/\partial x = 0. \end{aligned} \tag{3.6}$$

As the initial state we choose uniform initial temperature of 355 MeV (corresponding to RHIC initial temperature), no flow in x direction, and a simple sine-type longitudinal flow velocity profile

$$\begin{aligned} v_x(t_0, x) = 0, \\ v_z(t_0, x) = v_0\sin(\pi x/2h), \end{aligned} \tag{3.7}$$

[1]Note that since we used P to denote polarization, to avoid confusion we do not use it to denote pressure.

where v_0 is the magnitude of the initial velocity at the two boundaries. In the following numerical calculation, we consider two cases: $v_0 = 0.7$ and 0.9. In the expanding case, we use the initial time $\tau_0 = 1$ fm. Since the shear stress tensor is a dynamical variable in Israel-Stewart hydrodynamics, we need its initial value too. A natural choice is the Navier-Stokes value, but its exact evaluation is difficult. It contains the time derivative of the flow velocity, which is unknown before the hydrodynamic equation is solved. To avoid this problem, we initialize the shear stress, not to its exact Navier-Stokes, but to a "static Navier-Stokes" value; that is, we ignore all the time derivatives in the Navier-Stokes definition of the shear stress tensor and calculate the value based on spatial derivatives only. In practice this means that some components of the tensor are slightly larger and some slightly smaller than their exact Navier-Stokes values.

In Fig. 4, we depict the time evolution of the gradient of the longitudinal momentum per particle averaged over $x \in [0, h]$,

$$\left\langle \frac{dp_z}{dx} \right\rangle \equiv \int_0^h dx J^0(x) \frac{d}{dx} \frac{T^{0z}(x)}{J^0(x)} \Big/ \int_0^h dx J^0(x), \qquad (3.8)$$

where $J^0 = \gamma\rho$ is the proper particle number density. As expected, the shear viscosity dissipates the average gradient of the longitudinal momentum, especially for larger values of shear viscosity. The transverse expansion accelerate this degradation, since strong transverse expansion means larger shear (shear tensor).

In the case of transverse expansion and large viscosity, there appear to be a "shoulder" in the time evolution of the longitudinal momentum gradient $\langle dp_z/dx \rangle$ as shown in the lower panel of Fig. 4, where the gradient drops very fast initially and then slows down for a while before it decreases again. The temporary slowdown is caused by the oscillatory behaviors of the induced transverse flow in the x direction, and the particle number density J^0, which is used as a weight in the calculation of the average longitudinal momentum gradient in Eq. (3.8). The oscillations are an artifact of the fixed-wall boundary conditions in our simple scenario. When there is no transverse expansion, the degradation is slower and there is no shoulder because of the smaller shear (in shear tensor).

In Fig. 5, we show the profiles of velocity v_z at different times with viscosity $\eta/s = 5/4\pi$ with (lower panel) and without (upper panel) transverse expansion. One of the functions of the shear viscosity is to transform the kinetic energy of the fluid to internal energy, hence damping the fluid shear (as shown in Fig. 5) and heating up the fluid. This can be explicitly seen in the upper panel of Fig. 6, where the temperature evolution is shown for the nonexpanding system. The transverse Bjorken expansion in our problem, however, will dilute the system and cool the system down, overcoming the slight heating up by the shear viscosity, as shown in the lower panel of Fig. 6. The transverse expansion will also accelerate the degradation of the longitudinal velocity as shown in the lower panel of Fig. 5 as compared to the upper panel for the case of no transverse expansion.

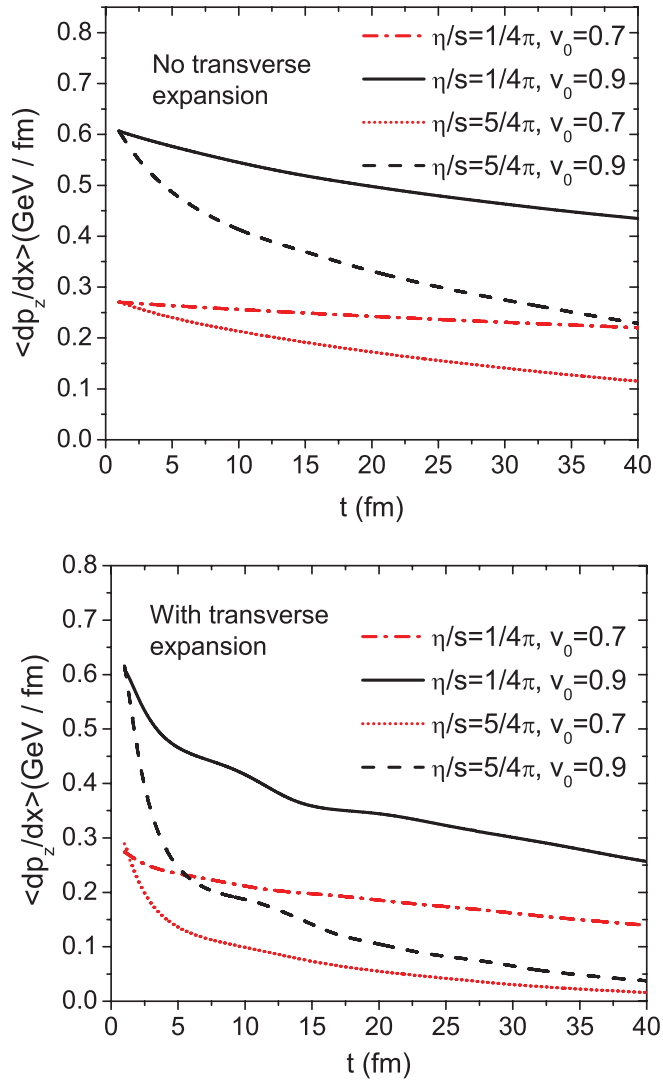

FIG. 4. (Color online) Evolution of the average gradient of the longitudinal momentum per particle, dp_z/dx, at different shear viscosities. Upper panel: the system has no transverse expansion. Lower panel: the system has Bjorken expansion in the $\hat{\mathbf{y}}$ direction.

IV. EVOLUTION OF THE GLOBAL QUARK POLARIZATION

With the model of time evolution of the longitudinal momentum gradient of the medium partons, we can now study the time evolution of the quark polarization when it is progressively polarized due to multiple scattering.

According to Eq. (2.7), the change of polarization caused by one scattering is

$$\Delta P \equiv P_f - P_i = -\frac{(1 - P_i^2)\pi\mu p}{2E(E + m) - P_i \pi \mu p}. \qquad (4.1)$$

For convenience, we denote $P = P_i$. Then we get the following evolution equation for the polarization:

$$\frac{dP}{dt} \equiv \frac{\Delta P}{\tau_q} = -\frac{1}{\tau_q} \frac{(1 - P^2)\pi\mu p}{2E(E + m) - P\pi\mu p}, \qquad (4.2)$$

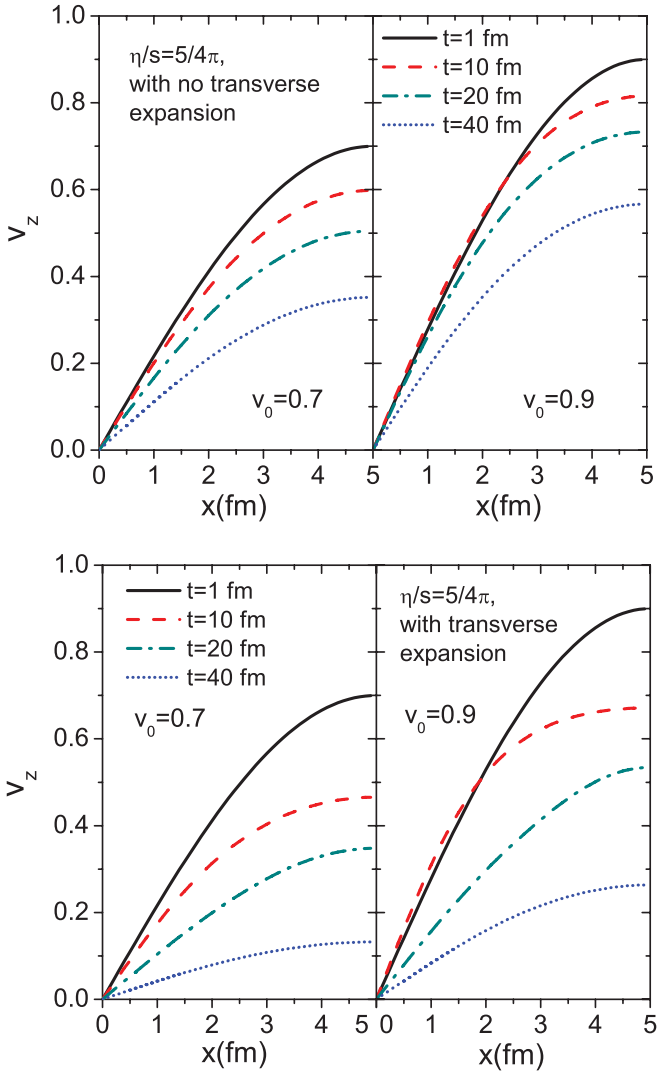

FIG. 5. (Color online) The profile of longitudinal velocity v_z at different times with $\eta/s = 5/4\pi$.

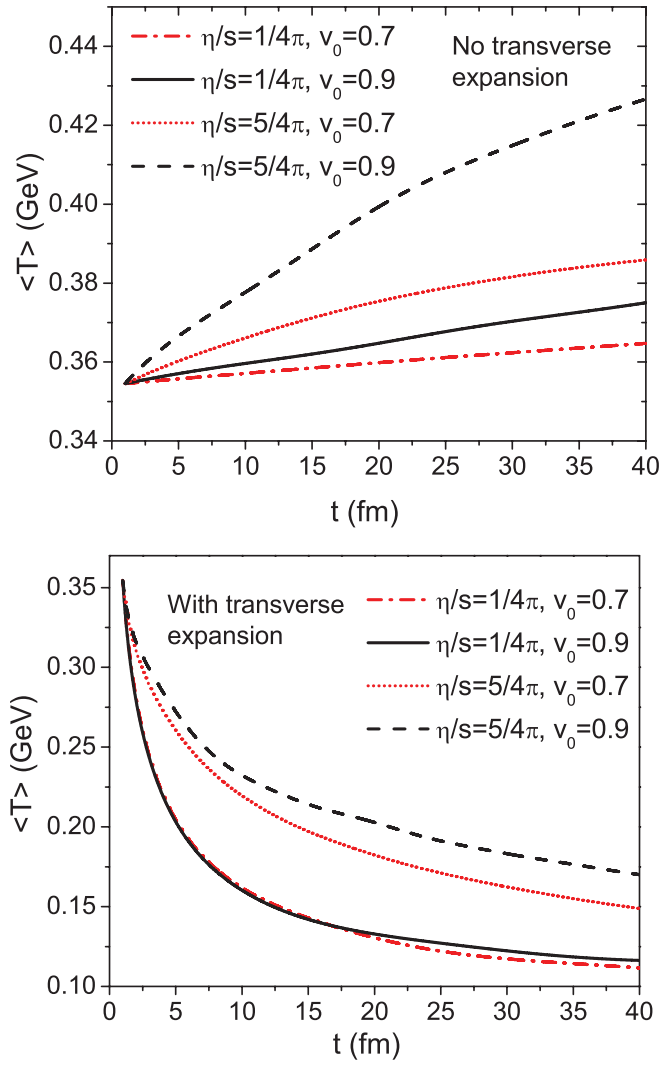

FIG. 6. (Color online) Evolution of the average temperature $\langle T \rangle$ with different shear viscosities and different initial velocities. Upper panel: the system has no transverse expansion. Lower panel: the system is Bjorken expanding in the $\hat{\mathbf{y}}$ direction.

where τ_q is the mean free path of quark, which is related to the transport cross section $\sigma_{\rm tr}$ of the interacting partons though $\tau_q \simeq 1/(\rho\sigma_{\rm tr})$, where $\rho = \nu_g \zeta(3) T^3/\pi^2$ is the density of medium gluons, assuming gluons are the dominant degrees of freedom in the medium. The shear viscosity for a thermal ensemble of gluons is roughly [43]

$$\eta \simeq \tfrac{1}{3}\rho\langle p_{\rm tr}\rangle \tfrac{4}{9}\tau_q \approx T\tfrac{4}{9}\rho\tau_q. \tag{4.3}$$

We have then the final rate equation for the time evolution of the quark polarization,

$$\frac{dP}{dt} = -\frac{4T\rho}{9s}\frac{s}{\eta}\frac{(1-P^2)\pi\mu p}{2E(E+m)-P\pi\mu p}. \tag{4.4}$$

From Eq. (4.4), the rate dP/dt is inversely proportional to the viscosity. This is evidently shown in the upper panel of Fig. 7, in which the evolutions of the quark polarizations are shown for the initial polarizations $P(0) = 0$ and for a system without transverse expansion. With transverse expansion, the mean free path increases more rapidly with time and therefore slows down the polarization rate. The transverse expansion also accelerates the degradation of the longitudinal momentum gradient, reducing the polarization in each scattering. Both effects slow down the time evolution of the polarization in an expanding system as shown by comparison between the upper and lower panels of Fig. 7.

Because of the reheating by viscous interaction, the initial cooling of the system due to transverse expansion is significantly slower for a larger value of shear viscosity, as shown in Fig. 6. This speeds up the polarization according to Eq. (4.4). However, a larger shear viscosity also slows down the polarization because the polarization rate is inversely proportional to the shear viscosity. During the early stage of evolution, the second effect dominates, leading to a slower polarization process with a larger value of shear viscosity. At a later time, effect of reheating becomes more dominant and a larger shear viscosity leads to a faster polarization process.

The polarization is also sensitive to the initial condition of the longitudinal flow shear. In our simple laminar flow model, the initial longitudinal flow shear is proportional to the value

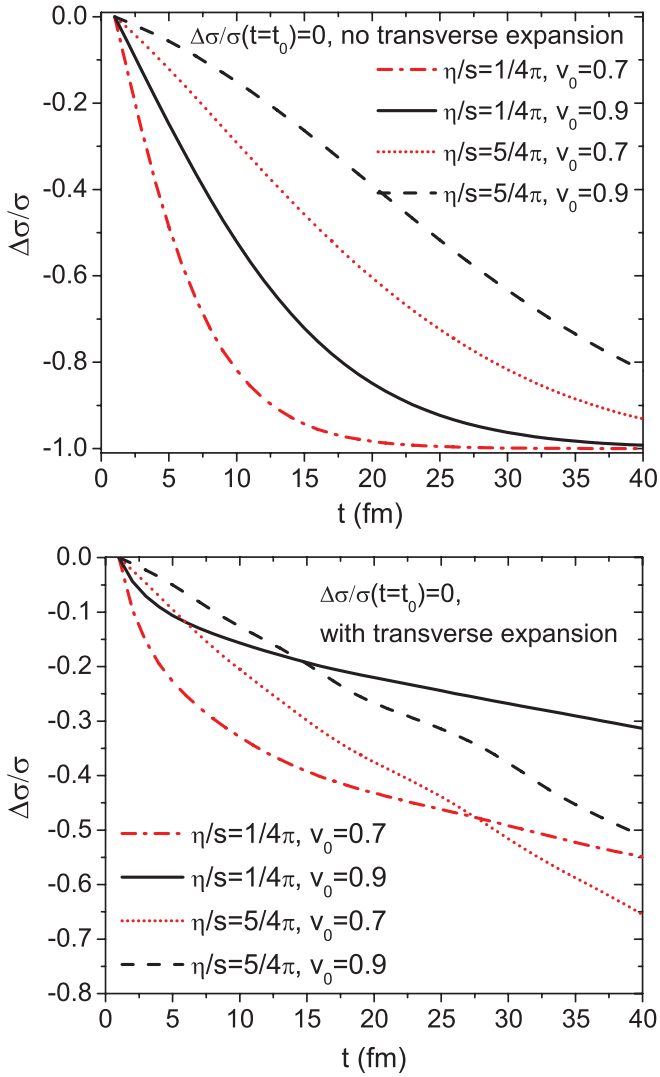

FIG. 7. (Color online) Evolution of the average polarization $P = \Delta\sigma/\sigma$ with initial polarization $P(t_0) = 0$ with different values of viscosities without (upper panel) and with (lower panel) transverse expansion.

of v_0. The nonlinear dependence of the polarization rate on the relative momentum p in Eq. (4.4) determines the nontrivial dependence of the polarization on the values of v_0 as shown in Fig. 7.

Note that the polarization rate we used are derived with the approximation of small angle scattering, which is only valid when the longitudinal momentum gradient is large. For large shear viscosity η/s and at late time, the longitudinal momentum gradient can become too small. One can no longer use the rate equation derived here. However, one can assume that the polarization process will stop at this point when there is not significant local orbital angular momentum.

V. SUMMARY

In conclusion, we have calculated the polarization cross section for quarks with initial polarization within the frame of perturbative QCD, which we use to study the time evolution of the quark polarization via multiple scattering in a medium with nonvanishing local orbital angular momentum. We considered the simple case of laminar flow as governed by viscous hydrodynamics with given shear viscosity η/s and a simple illustrative initial condition. Such a simple hydrodynamic model provides the dynamic evolution of the longitudinal flow shear as the polarization mechanism for quarks via parton scattering. Because the values of the shear viscosity influence the degradation of the longitudinal flow shear with time and the cooling of the system, it also determines the time evolution of the quark polarization. Since the polarization rate is inversely proportional to the shear viscosity and depends nonlinearly on the average longitudinal momentum shear, the final quark polarization is found to be sensitive to the shear viscosity but has a nontrivial dependence. In this sense, one can use the final-state polarization as a possible viscometer of the QGP.

For more realistic studies, one should employ a full scale $3 + 1D$ viscous hydrodynamics [32] with initial conditions from Monte Carlo models such as HIJING [44]. The initial parton production from this kind of model has approximate Bjorken scaling, which will give rise to very small initial local longitudinal flow shear [17] except at very large rapidity regions. Such small initial local longitudinal flow shear comes from the violation of the Bjorken scaling, which one can use as the initial condition. Furthermore, one should also extend the current calculation of the quark polarization beyond the small angle approximation.

ACKNOWLEDGMENTS

We thank G. Torrieri, D. Rischke, and Z. Xu for helpful discussions. This work is supported by the Helmholtz International Center for FAIR within the framework of the LOEWE (Landesoffensive zur Entwicklung Wissenschaftlich-Ökonomischer Exzellenz) program launched by the State of Hesse, by the ExtreMe Matter Institute (EMMI), and by BMBF under Contract No. 06FY9092 and by the director, Office of Energy Research, Office of High Energy and Nuclear Physics, Divisions of Nuclear Physics, of the US Department of Energy under Contract No. DE-AC02-05CH11231. X.-N. Wang thanks the hospitality of the Institut für Theoretische Physik, Johann Wolfgang Goethe-Universität, and support by EMMI in the framework of the Helmholtz Alliance Program of the Helmholtz Association (HA216/EMMI) during the beginning of this work.

[1] M. Gyulassy and L. McLerran, Nucl. Phys. A **750**, 30 (2005).
[2] P. Jacobs and X. N. Wang, Prog. Part. Nucl. Phys. **54**, 443 (2005).
[3] M. Gyulassy and X. N. Wang, Nucl. Phys. B **420**, 583 (1994).
[4] B. G. Zakharov, JETP Lett. **63**, 952 (1996).
[5] U. A. Wiedemann, Nucl. Phys. B **588**, 303 (2000).

[6] M. Gyulassy, P. Levai, and I. Vitev, Nucl. Phys. B **594**, 371 (2001).
[7] R. Baier, Y. L. Dokshitzer, A. H. Mueller, S. Peigne, and D. Schiff, Nucl. Phys. B **483**, 291 (1997).
[8] X. F. Guo and X. N. Wang, Phys. Rev. Lett. **85**, 3591 (2000).
[9] M. Luzum and P. Romatschke, Phys. Rev. C **78**, 034915 (2008); **79**, 039903(E) (2009).
[10] H. Song, S. A. Bass, U. Heinz, T. Hirano, and C. Shen, Phys. Rev. Lett. **106**, 192301 (2011).
[11] A. Majumder, B. Muller, and X. N. Wang, Phys. Rev. Lett. **99**, 192301 (2007).
[12] Z. T. Liang and X. N. Wang, Phys. Rev. Lett. **94**, 102301 (2005); **96**, 039901 (2006).
[13] B. Betz, M. Gyulassy, and G. Torrieri, Phys. Rev. C **76**, 044901 (2007).
[14] Z. T. Liang and X. N. Wang, Phys. Lett. B **629**, 20 (2005).
[15] A. Ipp, A. Di Piazza, J. Evers, and C. H. Keitel, Phys. Lett. B **666**, 315 (2008).
[16] Z. T. Liang, J. Phys. G **34**, S323 (2007).
[17] J. H. Gao, S. W. Chen, W. T. Deng, Z. T. Liang, Q. Wang, and X. N. Wang, Phys. Rev. C **77**, 044902 (2008).
[18] STAR Collaboration, I. V. Selyuzhenkov *et al*., Rom. Rep. Phys. **58**, 49 (2006).
[19] STAR Collaboration, I. Selyuzhenkov *et al*., J. Phys. G **32**, S557 (2006).
[20] STAR Collaboration, I. Selyuzhenkov *et al*., AIP Conf. Proc. **870**, 712 (2006).
[21] STAR Collaboration, I. Selyuzhenkov *et al*., J. Phys. G **34**, S1099 (2007).
[22] STAR Collaboration, B. I. Abelev *et al*., Phys. Rev. C **76**, 024915 (2007).
[23] STAR Collaboration, B. I. Abelev *et al*., Phys. Rev. C **77**, 061902 (2008).
[24] STAR Collaborations, J. H. Chen *et al*., J. Phys. G **34**, S331 (2007).
[25] STAR Collaboration, J. H. Chen *et al*., J. Phys. G **35**, 044068 (2008).
[26] S. W. Chen, J. Deng, J. H. Gao, and Q. Wang, Front. Phys. China **4**, 509 (2009).
[27] J. H. Gao, High Energy Phys. Nucl. Phys. **31**, 1181 (2007).
[28] K. Dusling and D. Teaney, Phys. Rev. C **77**, 034905 (2008).
[29] H. Song and U. W. Heinz, Phys. Lett. B **658**, 279 (2008).
[30] D. Molnar and P. Huovinen, J. Phys. G **35**, 104125 (2008).
[31] G. S. Denicol, T. Kodama, T. Koide, and Ph. Mota, Phys. Rev. C **80**, 064901 (2009).
[32] B. Schenke, S. Jeon, and C. Gale, Phys. Rev. Lett. **106**, 042301 (2011).
[33] F. Becattini, F. Piccinini, and J. Rizzo, Phys. Rev. C **77**, 024906 (2008).
[34] A. Adil and M. Gyulassy, Phys. Rev. C **72**, 034907 (2005).
[35] W. A. Hiscock and L. Lindblom, Ann. Phys. **151**, 466 (1983).
[36] W. Israel and J. M. Stewart, Ann. Phys. **118**, 341 (1979).
[37] R. Baier, P. Romatschke, D. T. Son, A. O. Starinets, and M. A. Stephanov, J. High Energy Phys. **0804**, 100 (2008).
[38] M. Natsuume and T. Okamura, Phys. Rev. D **77**, 066014 (2008); **78**, 089902(E) (2008).
[39] M. A. York and G. D. Moore, Phys. Rev. D **79**, 054011 (2009).
[40] B. Betz, D. Henkel, and D. H. Rischke, Prog. Part. Nucl. Phys. **62**, 556 (2009); G. S. Denicol, T. Koide, and D. H. Rischke, Phys. Rev. Lett. **105**, 162501 (2010).
[41] T. Koide, E. Nakano, and T. Kodama, Phys. Rev. Lett. **103**, 052301 (2009).
[42] G. S. Denicol, X. G. Huang, T. Koide, and D. H. Rischke, arXiv:1003.0780 [hep-th]; X. G. Huang and T. Koide, arXiv:1105.2483 [hep-th].
[43] P. Danielewicz and M. Gyulassy, Phys. Rev. D **31**, 53 (1985).
[44] X. N. Wang and M. Gyulassy, Phys. Rev. D **44**, 3501 (1991).

Radial and elliptic flow in Pb + Pb collisions at energies available at the CERN Large Hadron Collider from viscous hydrodynamics

Chun Shen,[1,*] Ulrich Heinz,[1,†] Pasi Huovinen,[2,‡] and Huichao Song[3,§]

[1]*Department of Physics, The Ohio State University, Columbus, Ohio 43210-1117, USA*

[2]*Institut für Theoretische Physik, Johann Wolfgang Goethe-Universität, Max-von-Laue-Straße 1, D-60438 Frankfurt am Main, Germany*

[3]*Lawrence Berkeley National Laboratory, 1 Cyclotron Road, Berkeley, California 94720, USA*

(Received 19 June 2011; published 7 October 2011)

A comprehensive viscous hydrodynamic fit of spectra and elliptic flow for charged hadrons and identified pions and protons from Au + Au collisions of all centralities measured at the Relativistic Heavy Ion Collider (RHIC) is performed and used as the basis for predicting the analogous observables for Pb + Pb collisions at the Large Hadron Collider (LHC) at $\sqrt{s} = 2.76$ and $5.5A$ TeV. Comparison with recent measurements of the elliptic flow of charged hadrons by the ALICE experiment shows that the model slightly overpredicts the data if the same (constant) specific shear viscosity η/s is assumed at both collision energies. In spite of differences in our assumptions for the equation of state, the freeze-out temperature, the chemical composition at freeze-out, and the starting time for the hydrodynamic evolution, our results agree remarkably well with those of Luzum [Phys. Rev.C **83**, 044911 (2011)], indicating robustness of the hydrodynamic model extrapolations. Future measurements of the centrality and transverse momentum dependence of spectra and elliptic flow for identified hadrons predicted here will further test the model and shed light on possible variations of the quark-gluon transport coefficients between RHIC and LHC energies.

DOI: 10.1103/PhysRevC.84.044903 PACS number(s): 25.75.Ld, 12.38.Mh, 24.10.Nz

I. INTRODUCTION

The first measurement of elliptic flow in Pb + Pb collisions at the Large Hadron Collider (LHC) has just been reported [1]. The elliptic flow coefficient v_2 characterizes the momentum anisotropy of final particle emission in noncentral heavy-ion collisions relative to the event plane, defined by the beam direction and the minor axis of the nuclear overlap region in the collision. It describes the efficiency of the medium generated in the collision to generate from an initial spatial deformation of its density distribution an asymmetry in the final momentum distribution, through interactions of the medium constituents. This efficiency increases with the coupling strength between those constituents and becomes maximal for an infinitely strongly coupled medium. In this limit the mean free path of the constituents becomes as small as allowed by the uncertainty relation [2], and the medium very quickly reaches a state of approximate local thermal equilibrium, which allows us to describe its evolution with fluid dynamics. For given initial spatial deformation of the collision fireball, ideal fluid dynamics (in which zero mean free path is assumed) is expected to generate the largest possible elliptic flow [3]. Shear viscosity, a consequence of nonzero mean free paths and limited from below by quantum mechanics [2,4], will lead to a suppression of v_2 [5,6].

Compelling evidence for fluid dynamical behavior of the collision fireballs created in ultrarelativistic heavy-ion collisions, with a very small ratio of shear viscosity to entropy density, η/s, has been found in heavy-ion collisions at the Relativistic Heavy Ion Collider (RHIC) [7–10]. The new data from the LHC confirm this picture [1,11,12] and agree, at least qualitatively, with hydrodynamic predictions of elliptic flow for Pb + Pb collisions at the LHC [13–19].

The purpose of the present paper is to explore how good this agreement is quantitatively and to gauge to what extent the present and future LHC elliptic flow data can tell us novel facts about the transport behavior of hot QCD matter at temperatures that exceed those accessible at the RHIC but are within reach at the LHC. Similar to the analyses in [11,14,16,19], but different from recent hybrid model studies in [18,20], we base our analysis on a purely hydrodynamic approach. While this ignores the fact that the late dilute hadronic stage of the expansion is very dissipative and not well described by fluid dynamics (neither ideal [21] nor viscous [22]), the importance of the hadronic phase for the development of elliptic flow is expected to be much reduced at the LHC relative to the RHIC [18,23]. As in Refs. [11,16,19,20], but different from Refs. [14,18], we use *viscous* hydrodynamics with a nonzero (but constant, i.e., temperature independent) specific shear viscosity η/s, adjusted to spectra and elliptic flow measurements at the RHIC. Our fitted value $\eta/s = 0.20$ (for Color Glass Condensate (CGC) initial conditions, see below) is 25% larger than that used by Luzum and Romatschke [11,16] but agrees well with the value for the quark-gluon plasma (QGP) viscosity $(\eta/s)_{\mathrm{QGP}}$ recently extracted from RHIC data by using a hybrid viscous hydrodynamic + Boltzmann approach (VISHNU [10,22]). Calculations with such a hybrid approach are numerically much more demanding than purely hydrodynamic simulations; a generalization of the present analysis using VISHNU will follow soon and should further improve the reliability of the LHC predictions.

*shen@mps.ohio-state.edu
†heinz@mps.ohio-state.edu
‡huovinen@th.physik.uni-frankfurt.de
§HSong@LBL.gov

II. HYDRODYNAMIC FIT OF RHIC Au + Au DATA

In this work, we employ (2 + 1)-dimensional viscous hydrodynamics [24] with the lattice QCD-based equation of state s95p-PCE [25,26], which accounts for chemical freeze-out before thermal decoupling at $T_{\rm chem} = 165$ MeV, to simulate the expansion of the collision fireball. From the analysis [10] of charged hadron spectra and elliptic flow in 200A GeV Au + Au collisions at the RHIC we take over a value of $\eta/s = 0.20$ (corresponding to initial conditions from a Monte Carlo version of the Kharzeev-Levin-Nardi model; see below) for the effective specific shear viscosity of the strongly interacting fluid. Using the insights obtained from the systematic parameter study presented in [26], we initialize the hydrodynamic expansion at time $\tau_0 = 0.6$ fm/c and decouple at $T_{\rm dec} = 120$ MeV at both RHIC and LHC energies. For Au + Au collisions at RHIC energies these parameters allow for a good global description of the hadron p_T spectra and differential elliptic flow (see below). Lacking strong theoretical or phenomenological guidance on how to adjust their values for Pb + Pb collisions at the LHC, we here decided to keep them unchanged.

At thermalization time τ_0, we assume that the shear stress tensor is given by its Navier-Stokes value $\pi^{\mu\nu} = 2\eta\sigma^{\mu\nu}$ (where $\sigma^{\mu\nu} = \nabla^{\langle\mu}u^{\nu\rangle}$ is the symmetric and traceless velocity shear tensor) and that the initial expansion flow is entirely longitudinal with Bjorken profile $v_z = z/t$ and zero transverse flow velocity. In Milne coordinates (τ, x, y, η) this corresponds to an initial flow four-velocity $(u^\tau, u^x, u^y, u^\eta) = (1, 0, 0, 0)$. Kinetic freeze-out is implemented by converting the hydrodynamic output to particle spectra with the Cooper-Frye prescription [27] on a decoupling surface of constant temperature $T_{\rm dec}$. We use a quadratic ansatz $\delta f(x, p) \sim p^\mu p^\nu \pi_{\mu\nu}(x)$ [6] for the viscous deviation from local thermal equilibrium of the local phase-space distribution function on the freeze-out surface. Our final hadron spectra include decay products from strong decays of all particles and resonances up to 2 GeV mass [28], using the resonance decay program from the AZHYDRO package.[1]

For the initial density profile we here use a Monte Carlo version [29,30] of the Kharzeev-Levin-Nardi [31] model (MC-KLN).[2] The specific implementation used in this work is described in [18,32]. The model gives for each event the gluon density distribution in the transverse plane. We assume it to thermalize by time τ_0 and convert the gluon density into entropy density [21]. Over one million Monte Carlo events are recentered to the beam axis and rotated in the transverse plane such that their minor axis aligns with the impact parameter (i.e., their "participant plane" coincides with the reaction plane). After sorting them into collision centrality bins according to their number $N_{\rm part}$ of participating ("wounded") nucleons, we average them to obtain a smooth average initial entropy density, which is then converted to energy density using the equation of state. Using this smooth energy density as a weight, we compute the initial eccentricity $\bar{\varepsilon} = \frac{\langle y^2 - x^2\rangle}{\langle y^2 + x^2\rangle}$ and overlap area $S = \pi\sqrt{\langle x^2\rangle\langle y^2\rangle}$ of the reaction zone; these represent the corresponding mean values of events in this centrality class.[3]

The KLN model involves a couple of parameters that need to be adjusted to obtain the correct final charged hadron multiplicity $dN_{\rm ch}/d\eta$ in central Au + Au collisions at the RHIC. In [32] this adjustment was performed for ideal fluid dynamics (which conserves entropy) coupled to a hadron cascade. The model then correctly predicts the charged hadron multiplicities at all other collision centralities. In our viscous hydrodynamic model, viscous heating produces additional entropy, leading to somewhat larger final multiplicities. We thus perform an iterative renormalization of the initial entropy density profile until the measured charged hadron multiplicity in the 0%–5% most central 200A GeV Au + Au collisions at the RHIC is once again reproduced. The lower panel of Fig. 1 shows that, after this renormalization, the model again correctly describes the measured [34] centrality dependence of charged hadron production. The centrality dependence of viscous entropy production (which is relatively larger in peripheral than in central collisions [24]) is (at least at RHIC energies) sufficiently weak to not destroy the agreement of the model with experimental observations.

The ability of the MC-KLN model to describe the centrality dependence of charged hadron production without additional parameters is the main reason for choosing it over the MC-Glauber model as our basis for extrapolation from RHIC to LHC energies. It was recently shown [35] that this centrality dependence is robust against running coupling corrections [36–38] in the Balitsky-Kovchegov evolution (on which the KLN model is based) which were found to hardly affect its shape. They do, however, modify the collision energy dependence of particle production, with the LHC Pb + Pb data being better described if running coupling corrections are included [39]. Our version of the MC-KLN model does not include running coupling corrections,[4] and we must normalize the initial entropy density profile for Pb + Pb collisions at the LHC separately from Au + Au collisions at the RHIC. Without such an independent renormalization, we overpredict the measured charged multiplicity from central 2.76 A TeV Pb + Pb collisions [39,40] by about 10%.

After renormalization we obtain the solid lines bounding the shaded region in the upper panel of Fig. 1, with the lower (upper) bound corresponding to Pb + Pb collisions at 2.76 (5.5)A TeV, respectively. The data in that panel are from the ALICE Collaboration for Pb + Pb at 2.76A TeV [39,40]. [For 5.5A TeV Pb + Pb collisions we assumed $dN_{\rm ch}/dy = 2280$ (corresponding to $dN_{\rm ch}/d\eta = 1972$), based on an extrapolation of Fig. 3 in Ref. [40].] One sees that, even without running coupling corrections, but including viscous entropy production, the MC-KLN model does a good job in describing the measured centrality dependence

[1] AZHYDRO is available at http://www.physics.ohio-state.edu/~froderma/.

[2] The Monte Carlo code is available at http://www.aiu.ac.jp/~ynara/mckln/.

[3] Note that about 10% larger overlap areas are obtained when using the entropy density as a weight [10,18], whereas for all but the most central collisions the eccentricities of the energy and entropy densities are nearly identical [33].

[4] The rcBK code in [35] includes running coupling corrections but it has not been renormalized to take into account viscous entropy production at RHIC energies.

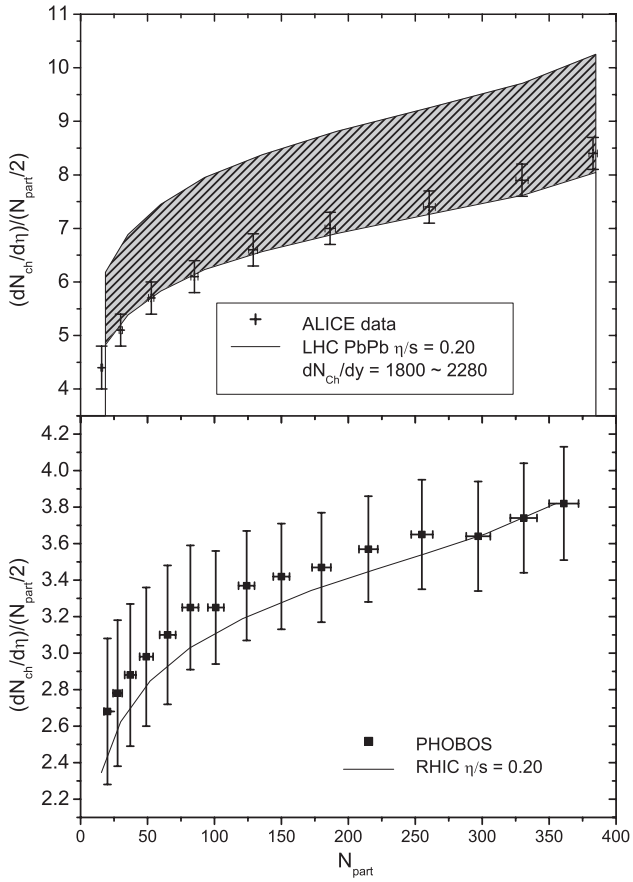

FIG. 1. Centrality dependence of the charged hadron multiplicity per unit pseudorapidity, $dN_{\rm ch}/d\eta/(N_{\rm part}/2)$, as a function of $N_{\rm part}$, in 200A GeV Au + Au collisions at the RHIC (bottom panel) and in (2.76–5.5) A TeV Pb + Pb collisions at the LHC (top panel). Experimental data are from the PHOBOS Collaboration [34] for Au + Au collisions at $\sqrt{s} = 200A$ GeV and from the ALICE Collaboration [39] for Pb + Pb collisions at $\sqrt{s} = 2.76$ A TeV. The lines are from the MC-KLN model (see text). For Au + Au at the RHIC the MC-KLN model was normalized to the measured multiplicity in the 0%–5% centrality bin; at the LHC, the lines bounding the shaded region were normalized to $dN_{\rm ch}/d\eta = 1548$ and 1972 (or $dN_{\rm ch}/dy = 1800$ and 2280) at 0%–5% centrality, respectively.

of charged hadron production in Pb + Pb collisions at the LHC. This gives us hope that the successful description of the centrality dependence of hadron spectra and elliptic flow at RHIC energies (see below and [10]) translates into a reliable prediction of the corresponding centrality dependencies in Pb + Pb collisions at the LHC.

Figures 2 and 3 establish our baseline for the extrapolation to LHC energies. In Fig. 2 we show our purely hydrodynamic fit (obtained with parameters τ_0, η/s, $T_{\rm chem}$, and $T_{\rm dec}$ set as described above[5]) of the hadron spectra measured in

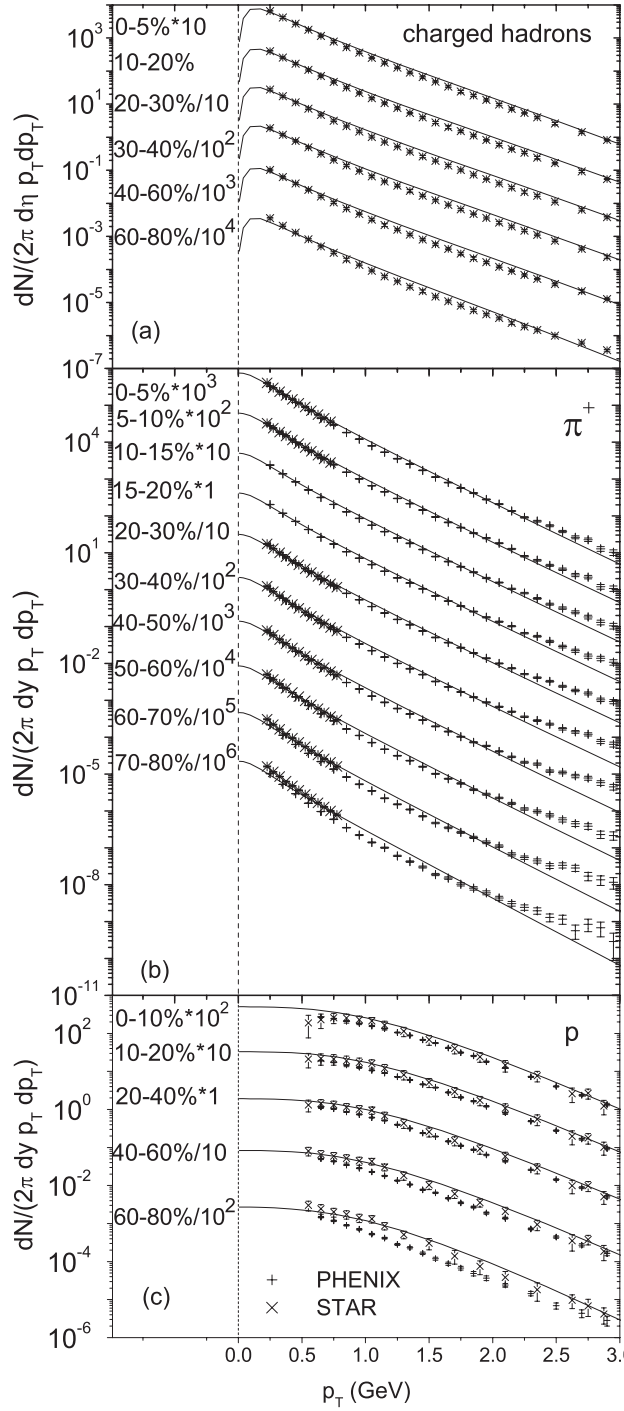

FIG. 2. p_T spectra of all charged hadrons (a), positive pions (b), and protons (c) for 200A GeV Au + Au collisions of different centralities as indicated. The symbols show data from the STAR ([41,43,44], ×) and PHENIX ([42,45], +) experiments. The lines are results from the viscous hydrodynamic model for constant $\eta/s = 0.20$ and MC-KLN initial conditions. See text for other model parameters.

[5]Note that our value $\tau_0 = 0.6$ fm/c is 45% smaller than the value of 1.05 fm/c used for $\eta/s = 0.2$ in the VISHNU simulations in [10]. The earlier evolution of hydrodynamic transverse flow arising from this smaller τ_0 value compensates for the lack of a highly dissipative hadronic phase in the purely hydrodynamic approach. Hadronic dissipation leads to a significant broadening in particular of the proton p_T spectra during the hadronic stage which (given the constraints from the elliptic flow data which prohibit us from simply lowering $T_{\rm dec}$) viscous hydrodynamics with temperature-independent $\eta/s = 0.2$ cannot replicate.

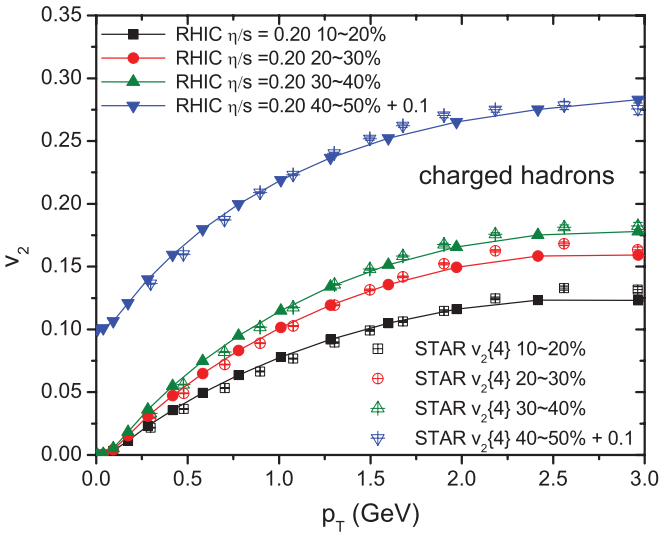

FIG. 3. (Color online) Differential elliptic flow $v_2(p_T)$ for charged hadrons from 200A GeV Au + Au collisions of different centralities as indicated. Open symbols are experimental data from the STAR experiment for $v_2\{4\}(p_T)$ [46,47]; lines with filled symbols of the same shape are the corresponding hydrodynamic fits with the same model as in Fig. 1. For the 40%–50% centrality bin, data and theory are vertically offset by 0.1 for better visibility.

200A GeV Au + Au collisions at the RHIC. Figure 2(a) shows the mid-rapidity transverse momentum spectra per unit pseudorapidity for unidentified charged hadrons from the STAR [41] and PHENIX [42] experiments compared with the hydrodynamical model. Figures 2(b) and 2(c) show a similar comparison for the p_T spectra per unit rapidity of identified pions and protons from STAR [43,44] and PHENIX [45]. In the experimental spectra, protons from weak decays were removed; STAR quotes a large systematic error associated with this feed-down correction, and within that large error band the two data sets agree with each other, even if the central values of the STAR proton data appear to be up to 50% higher than PHENIX data. Our results agree well with the STAR protons for $p_T > 0.6\text{GeV}/c$ but overpredict the PHENIX protons by up to a factor of 2.

Figure 3 shows the hydrodynamically calculated differential elliptic flow for unidentified charged hadrons in comparison with STAR $v_2\{4\}(p_T)$ data [46,47], for four centrality classes ranging from semi-central to mid-peripheral collisions (10%–50% centrality). With $\eta/s = 0.20$, viscous hydrodynamics gives an excellent description of the STAR $v_2\{4\}$ data, even up to 3 GeV/c in transverse momentum (i.e., beyond the p_T range where the hydrodynamic description is expected to begin to break down, due to the increasing influence of hard production processes and large uncertainties in the viscous correction δf to the local phase-space distribution at kinetic freeze-out [48]). Looking more carefully one sees that our model slightly overestimates the elliptic flow at low $p_T < 1$ GeV while underestimating it in the high-p_T region, $p_T > 2$ GeV.

In [26] we noted a tension in trying to simultaneously fit within a purely viscous hydrodynamic approach the proton p_T spectra and the charged hadron differential elliptic $v_2^{\text{ch}}\{2\}(p_T)$ when using the equation of state s95p-PCE. Even a temperature-dependent $\eta/s(T)$ that has a larger shear viscosity in the hadronic phase could not resolve this tension: In [48] two of us found that the RHIC Au + Au hadron spectra are insensitive to a temperature-dependent increase of the shear viscosity in the hadron gas phase, as was previously seen in [49]. Figures 2 and 3 demonstrate that this problem is largely resolved when using the $v_2\{4\}(p_T)$ data (Fig. 3) instead of $v_2\{2\}$ (see Fig. 8 further below): We obtain an excellent description of the differential elliptic flow, together with an acceptable description (within large experimental uncertainties) of the p_T spectra.

Overall, the viscous fluid dynamic description of the hadron spectra and charged hadron elliptic flow $v_2(p_T)$ shown here is of similar quality to the hybrid model description with VISHNU presented in [10]. Since purely hydrodynamic simulations are numerically much less costly than calculations with VISHNU, we will now use them to generate a broad range of predictions for soft hadron production in Pb + Pb collisions at the LHC.

III. PREDICTIONS FOR Pb + Pb COLLISIONS AT THE LHC

As discussed above, the extrapolation from RHIC to LHC is done by keeping τ_0, T_{chem}, T_{dec}, and η/s fixed. When comparing the resulting viscous hydrodynamic predictions with experimental data from the recently started LHC heavy-ion collision program, we will search for indications from experiment that would motivate changing these parameters. The first results for p_T spectra [50] as well as both the p_T-differential and p_T-integrated elliptic flow of unidentified charged hadrons [1] have already been published and will be compared with the theoretical predictions below. Additional experimental information on spectra and elliptic flow of identified hadrons will become available soon; the relevant hydrodynamic predictions are presented in this section.

In Fig. 4 we show the transverse momentum spectra for all charged hadrons, as well as for identified pions and protons, for minimum-bias collisions of Au + Au at the RHIC and Pb + Pb at the LHC.[6] For the RHIC we compare with data from the PHENIX Collaboration [45]. The upper and lower bounds of the shaded areas are predictions for minimum-bias Pb + Pb collisions at collision energies of 5.5 and 2.76 TeV per nucleon pair, respectively. The LHC spectra are visibly flatter than at RHIC energies, reflecting stronger radial flow. For central collisions (0%–5% centrality), the fireball lifetime increases from Au + Au at the RHIC to Pb + Pb at the LHC by about 19% and 24%, respectively, for 2.76 and 5.5 A TeV collision energy; for peripheral collisions at 70%–80% centrality, the corresponding lifetime increases are even larger (34% and 41%, respectively). The average radial flow velocity increases

[6]To simulate minimum-bias collisions, we compute the spectra for the centrality classes shown in Figs. 2(b) and 6 and average them. Any additional observables, such as the minimum-bias elliptic flow in Fig. 8 below, are calculated from these minimum-bias spectra.

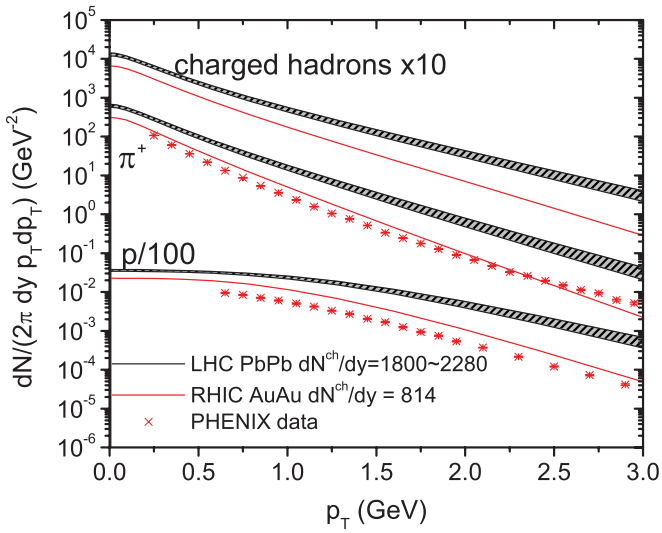

FIG. 4. (Color online) p_T spectra of all charged hadrons, positive pions, and protons for minimum bias 200A GeV Au + Au (thin red lines and data points) and (2.76–5.5) A TeV Pb + Pb collisions (black lines with shaded area). The RHIC data are from the PHENIX experiment [45]. The shaded bands for the LHC predictions are limited at the bottom (top) by lines for $\sqrt{s} = 2.76$ (5.5) A TeV, corresponding to $dN_{\rm ch}/dy = 1800$ (2280) [$dN_{\rm ch}/d\eta = 1548$ (1972)]. In the calculations the same constant $\eta/s = 0.2$ is assumed at all shown collision energies.

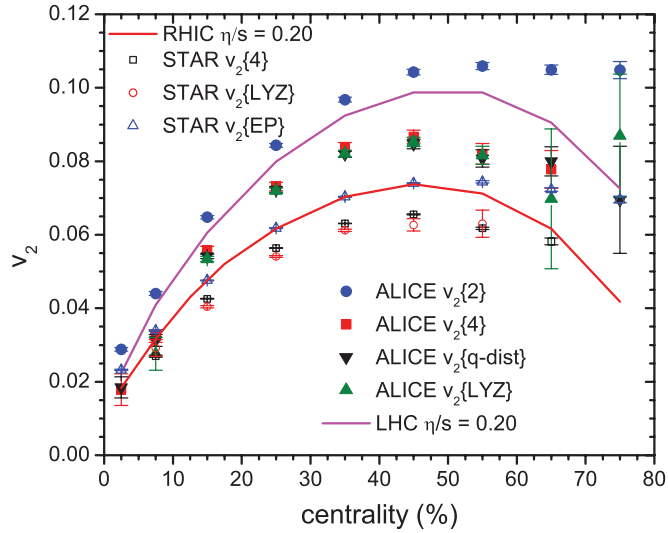

FIG. 5. (Color online) p_T-integrated elliptic flow of charged hadrons for 200A GeV Au + Au collisions at the RHIC (open symbols: STAR data [46,47]; lower red line: the result from viscous hydrodynamics) and for 2.76 A TeV Pb + Pb collisions at the LHC (filled symbols: ALICE data [1]; upper magenta line: the viscous hydrodynamic prediction). In both experiment and theory the differential elliptic flow $v_2(p_T)$ (see Figs. 3 and 7) was integrated over the range $0.15 < p_T < 2$ GeV/c for Au + Au at the RHIC and over $p_T > 0.2$ GeV/c for Pb + Pb at the LHC.

in central collisions (0%–5% centrality) by 5% and 7%, respectively, and in peripheral collisions (70%–80% centrality) by 9% and 11%.

Figure 5 shows the integrated charged hadron elliptic flow v_2 as a function of collision centrality for Au + Au collisions at the RHIC and Pb + Pb collisions at the LHC. At RHIC energy, our results (lower red line) overestimate the STAR $v_2\{4\}$ data by about 11% in mid-central collisions but agree nicely with $v_2\{\rm EP\}$ except for the most peripheral collisions.[7]

At first sight the overprediction of the p_T-integrated $v_2\{4\}$ at the RHIC is surprising, given the excellent description of the differential elliptic flow $v_2\{4\}(p_T)$ shown in Fig. 3. The apparent paradox is resolved by observing that the hydrodnamically computed charged hadron p_T spectra shown in Fig. 2 are somewhat harder than measured, thereby giving too much weight in the p_T integral to the range $0.75 < p_T < 2$ GeV/c where $v_2\{4\}(p_T)$ is large.[8]

At LHC energy ($\sqrt{s} = 2.76$ A TeV) our integrated v_2 lies between $v_2\{2\}$ and $v_2\{4\}$ values measured by the ALICE Collaboration [1]. Again, we overpredict the p_T-integrated $v_2\{4\}$ by about 10%–15%. We note that from RHIC to LHC the hydrodynamically computed integrated v_2 in mid-central to mid-peripheral collisions increases by about 30%, in agreement with the experimental observations. This is due to reduced viscous suppression effects in the larger and denser fireballs created at the LHC and a longer fireball lifetime which allows the momentum flow anisotropy to approach saturation more closely than at lower energies [23,53]. In very peripheral collisions, even at LHC energies such a saturation of v_2 does not happen; this is the reason why in Fig. 5 the integrated v_2 is seen to decrease at large collision centralities, at both the RHIC and the LHC.

In Fig. 6 we present hadron transverse momentum spectra for Pb + Pb collisions at LHC energies, for a range of collision centralities. In panel (a) we compare the hydrodynamic predictions with initial data from the ALICE experiment [50]. Overall, the theoretical description of these experimental data is of similar quality to that for Au + Au collisions at the RHIC (see Fig. 2). In the most central collisions, the hydrodynamical model describes the charged hadron spectrum somewhat better

[7]In very peripheral collisions, the fireball lifetime decreases dramatically, cutting short the buildup of anisotropic hydrodynamic flow and thereby prohibiting v_2 from saturating. In addition, viscous effects are stronger in the small fireballs created in peripheral collisions than in the larger central collision fireballs. Both effects together cause the theoretical v_2 values to decrease sharply at large collision centralities, in apparent conflict with the experimental data. The experimental $v_2\{2\}$ and $v_2\{\rm EP\}$ measurements are, however, contaminated by nonflow effects, in particular in very peripheral collisions. Once nonflow effects are corrected for [51], the experimental v_2 values decrease at large collision centralities much in the same way as predicted by hydrodynamics.

[8]The agreement with the $v_2\{\rm EP\}$ data is fortuitous and should, in fact, not happen since the measured $v_2\{\rm EP\}$ includes a positive contribution from event-by-event v_2 fluctuations [52] while our hydrodynamic calculation yields the average elliptic flow $\langle v_2 \rangle$, which is smaller.

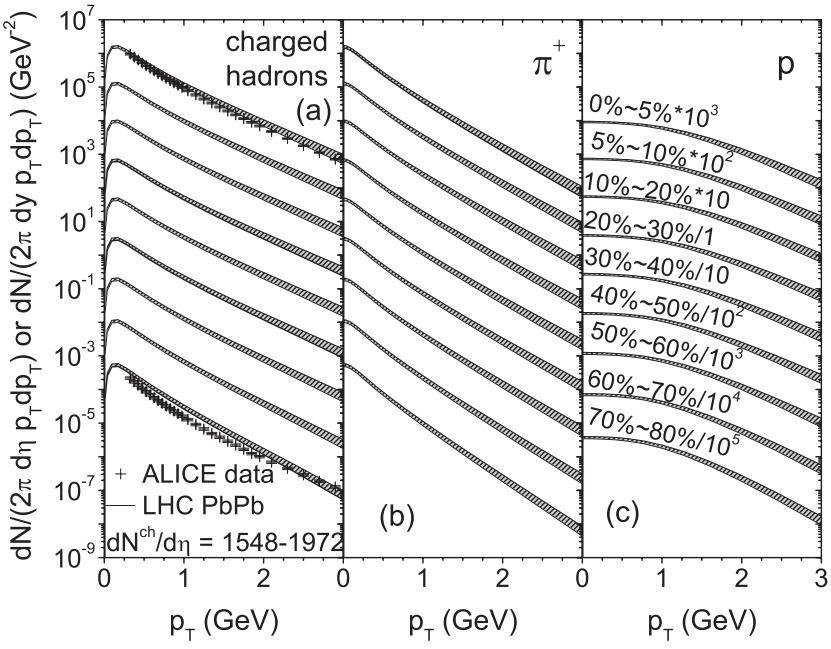

FIG. 6. p_T spectra per unit pseudorapidity for charged hadrons (a) and per unit rapidity for pions (b) and protons (c) for Pb + Pb collisions at the LHC. The lower and upper ends of the shaded bands represent viscous hydrodynamic predictions for $\sqrt{s} = 2.76$ and 5.5 A TeV (corresponding to $dN_{\rm ch}/d\eta = 1548$ and 1972, or $dN_{\rm ch}/dy = 1800$ and 2280), respectively. Experimental data in panel (a) are from the ALICE experiment [50].

than at the RHIC, whereas in the very peripheral collisions the hydrodynamic spectra are too flat, presumably due to large viscous shear pressure effects. Future comparison with the measured spectra at other collision centralities and for identified hadrons, shown here in panels (b) and (c) as predictions, should shed further light on the origin of the discrepancy in peripheral collisions.

Figure 7(a) shows a comparison of the hydrodynamically generated differential $v_2^{\rm ch}(p_T)$ for charged hadrons with the ALICE $v_2\{4\}$ data [1], for four different collision centralities. For the most peripheral of these, we also show the measured $v_2\{2\}$ for comparison. The hydrodynamic predictions agree nicely with the data at low $p_T < 1$ GeV/c, but they overshoot the experimental values by 10%–20% at larger p_T, especially in the more peripheral bins. In the 40%–50% centrality bin, the theoretical prediction happens to agree nicely with $v_2\{2\}(p_T)$ even though the latter should be shifted upward by flow fluctuations that are not included in the theoretical calculation. We note that the theoretical overshoot is less severe in the VISHNU hybrid model (see Fig. 3 in [20]) than in the purely hydrodynamic simulations shown here. This suggests that the excess of $v_2(p_T)$ over the measured values at $p_T > 1$ GeV/c in Fig. 7(a) may be caused by an inadequate description of the late hadronic stage and its freeze-out.

We can summarize Figs. 2(a), 3, 5, 6, and 7(a) by observing that the hydrodynamic model overpredicts the p_T-integrated charged hadron v_2 by 10%–15% at both the RHIC and the LHC, but for different reasons: At the RHIC the differential elliptic flow $v_{2,\rm ch}(p_T)$ is correctly reproduced while the inverse slope of the theoretical p_T spectra is slightly too large, while the LHC p_T spectra are described a bit better (at least in the most central collisions where published data are available) but the slope of $v_{2,\rm ch}(p_T)$ at the LHC is slightly overpredicted.

Panels (b) and (c) of Fig. 7 give predictions for the differential $v_2(p_T)$ of identified pions and protons. Note the different shape of the proton $v_2(p_T)$ from that of the pions at low p_T: Radial flow pushes the proton elliptic flow to larger values of p_T. Comparing the curves for $\sqrt{s} = 2.76$ and 5.5 A TeV, we see that this "radial push" of the proton v_2 increases with collision energy, so for higher $\sqrt{s}$ the rise of $v_2(p_T)$ is shifted to larger transverse momenta, while at fixed $p_T < 1.5$ GeV/c the proton elliptic flow *decreases* with increasing collision energy. This happens only for heavy hadrons but not for the much lighter pions [see panel (b)].

In Figs. 8 and 9 we pursue this theme further, by directly comparing the differential elliptic flows at RHIC and LHC energies. In Fig. 8 we show results for minimum-bias collisions; the RHIC predictions are compared with available data from STAR [54]. We see that at low p_T, the elliptic flow for unidentified charged hadrons (which are strongly pion dominated) and for identified pions increases from the RHIC to the LHC whereas the opposite is true for protons. At higher p_T ($p_T > 1.5$ GeV/c), on the other hand, $v_2(p_T)$ increases for *both* pions and protons as we increase the collision energy. Figure 9 shows this for a few more hadron species, for the 10%–20% and 40%–50% centrality bins: the heavier the hadron, the stronger a push of v_2 toward higher p_T is observed. At sufficiently large p_T, $v_2(p_T)$ is larger at the LHC than at the RHIC for all particle species, but at low p_T this holds only for pions whereas all heavier hadrons show a decrease of $v_2(p_T)$ from the RHIC to the LHC at fixed p_T. As the hadron rest mass grows, the crossing point where the decrease of v_2 at fixed p_T with rising collision energy turns into an increase shifts to larger p_T values. In view of Fig. 9, the experimental observation [1] that for unidentified charged hadrons $v_2^{\rm ch}(p_T)$ hardly changes at all from the RHIC to

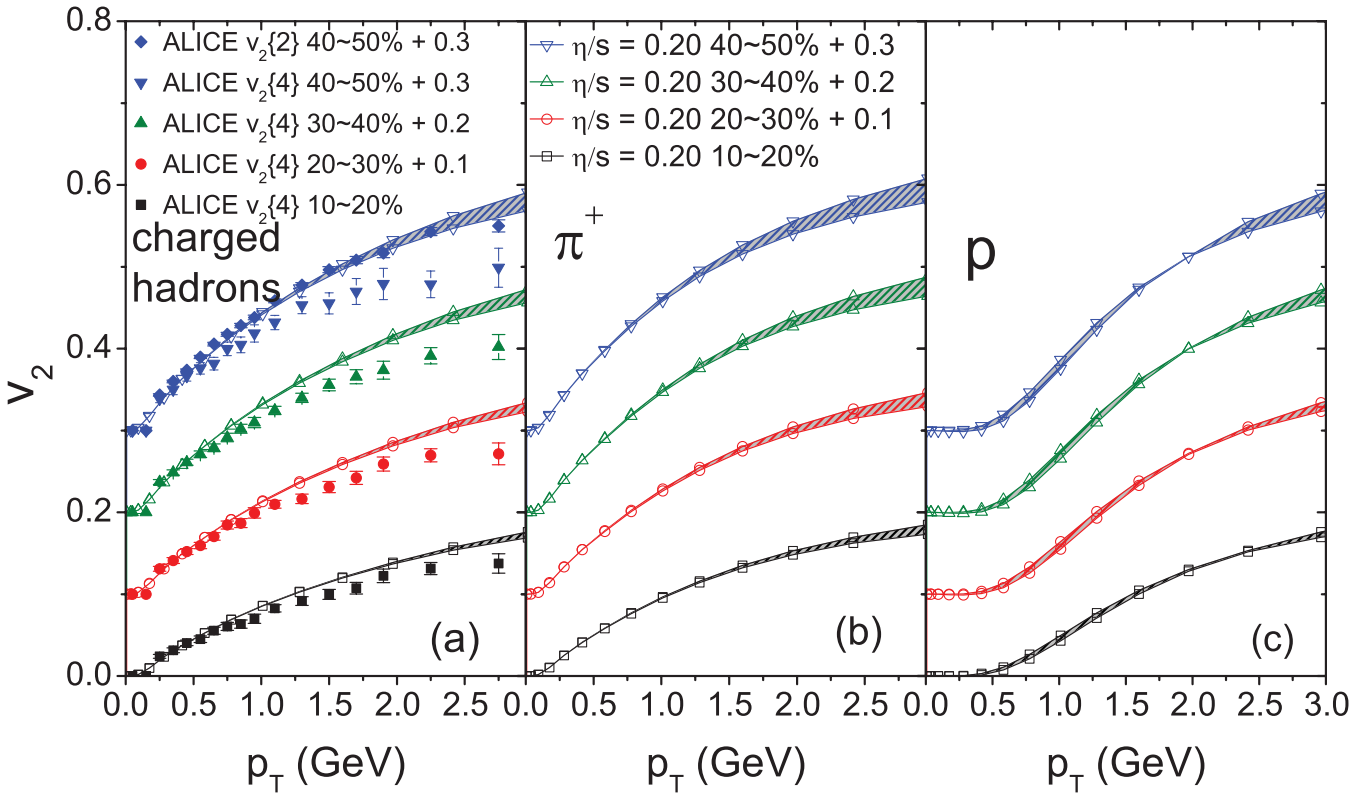

FIG. 7. (Color online) Differential elliptic flow $v_2(p_T)$ for unidentified charged hadrons (a) and identified pions (b) and protons (c), for Pb + Pb collisions of different centralities at the LHC. Experimental data for charged hadron $v_2(p_T)$, denoted by solid symbols, are from the ALICE experiment [1]; they should be compared with theoretical lines carrying open symbols of the same shape and color. The shaded bands show the variation of the hydrodynamic predictions with collision energy between $\sqrt{s} = 2.76$ and 5.5 A TeV (corresponding to $dN_{\rm ch}/dy = 1800$ and 2280, respectively). The lines corresponding to the lower collision energy ($\sqrt{s} = 2.76\ A$ TeV) define the lower end of the shaded regions at $p_T = 3$ GeV/c.

the LHC appears accidental:[9] The increase of $v_2(p_T)$ at fixed p_T for pions is balanced by a corresponding decrease for all heavier hadrons leaving, as it happens, no visible net effect once all charged hadrons are lumped together.

In Refs. [10] it was argued that a robust method for extracting the QGP shear viscosity is to fit the collision centrality dependence of the eccentricity-scaled charged hadron elliptic flow $v_2^{\rm ch}/\bar{\varepsilon}$ with a viscous hydrodynamic + hadron cascade hybrid code. In that study it was found that, at fixed collision energy,[10] plotting $v_2^{\rm ch}/\bar{\varepsilon}$ against the charged hadron multiplicity density per unit overlap area, $(1/S)(dN_{\rm ch}/dy)$, yields "universal" curves that depend only on the QGP shear viscosity but not on the model for the initial energy density distribution (in particular its eccentricity). In Fig. 10 we show such a plot for 200A GeV Au + Au collisions at the RHIC together with Pb + Pb collisions at two LHC energies. The four panels show this scaling in terms of distributions in pseudorapidity (η, left column) or rapidity (y, right column) and also compare it for our default choice of using the initial *energy* density as weight for the calculation of the average eccentricity $\bar{\varepsilon}$ and overlap area S (top row) with what one obtains by evaluating these quantities with the initial *entropy* density instead (as is done in Refs. [10,18]) (bottom row). We see that, independent of these choices of representation, the universality of $v_2^{\rm ch}/\bar{\varepsilon}$ versus $(1/S)(dN_{\rm ch}/dy)$ or $(1/S)(dN_{\rm ch}/d\eta)$ does not carry over to different collision energies (at least not for the purely hydrodynamic simulations studied in the present work): At the same multiplicity density $(1/S)(dN_{\rm ch}/dy)$ or $(1/S)(dN_{\rm ch}/d\eta)$, more peripheral higher energy collisions produce less elliptic flow per initial eccentricity than more central lower energy collisions. At fixed $\eta/s = 0.2$, the difference between 200A GeV Au + Au and 2.76 A TeV Pb + Pb collisions (red circles versus green upward triangles in Fig. 10) is as large as the difference between $\eta/s = 0.16$ and $\eta/s = 0.20$ for Au + Au collisions at fixed $\sqrt{s} = 200A$ GeV (red circles versus black squares).

[9]Contrary to the claim made in [12], the observation that the ratio between $v_2^{\rm ch}(p_T)$ measured at the LHC and at the RHIC is approximately independent of p_T cannot be directly used to conclude that $(\eta/s)_{\rm QGP}$ does not change from RHIC to LHC. If that argument were correct, this ratio should be independent of p_T, not only for the sum of all charged hadrons, but also for each identified hadron species separately. Our hydrodynamic calculations show that the latter does not hold even if η/s remains unchanged from RHIC to LHC.

[10]We recently checked that this multiplicity scaling carries over to other collision systems such as Cu + Cu *at the same collision energy* [55].

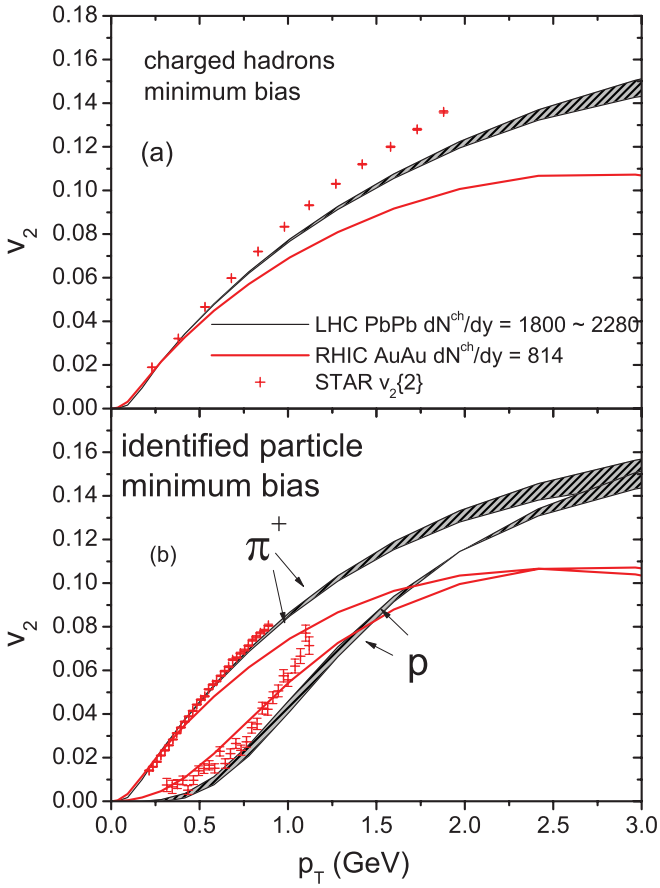

FIG. 8. (Color online) Differential elliptic flow $v_2(p_T)$ for all charged hadrons (a) and identified pions and protons (b), for minimum bias 200A GeV Au + Au collisions at the RHIC and (2.76–5.5) A TeV Pb + Pb collisions at the LHC. Experimental data for $v_2\{2\}$ from Au + Au collisions at the RHIC are from the STAR experiment [54]. Solid lines are viscous hydrodynamic results for 200A GeV Au + Au collisions with the same hydrodynamic parameters as in Figs. 1–4; note their disagreement with the $v_2\{2\}$ data shown here (in contrast to their excellent agreement with $v_2\{4\}$ data shown in Fig. 3). The shaded bands are LHC predictions and show the variation of the theoretical expectations for Pb + Pb collisions at collision energies ranging from $\sqrt{s} = 2.76$ to 5.5 A TeV (corresponding to $dN_{\rm ch}/dy = 1800$ and 2280, respectively). As in Fig. 7, the lines defining the lower end of the shaded region at $p_T = 3$ GeV/c correspond to the lower LHC energy $\sqrt{s} = 2.76$ A TeV.

We note that the tendency in Fig. 10 of higher energy collisions producing less $v_2^{\rm ch}/\bar{\varepsilon}$ at fixed $(1/S)(dN_{\rm ch}/dy)$ than lower energy ones contradicts the opposite tendency observed by Hirano *et al.* in Fig. 3 of Ref. [18] where an ideal hydro + hadron cascade hybrid code was employed.[11] The authors of [18] presented strong arguments that their observation of larger $v_2^{\rm ch}/\bar{\varepsilon}$ at fixed $(1/S)(dN_{\rm ch}/d\eta)$ in higher energy collisions is not related to their use of a hadron cascade for describing the late hadronic stage. Our opposite finding, on the other hand, is supported by the earlier purely hydrodynamic scaling studies presented in the last two works of [24] whose authors came to the same conclusion as we do here. At present this discrepancy remains unresolved; we suspect, however, that the origin of the difference between our work and that of Hirano *et al.* could be in their use of a more realistic (3 + 1)-dimensional hydrodynamic evolution [56], although in the earlier ideal fluid hydrodynamical studies at the full RHIC energy, the differences between boost-invariant and non-boost-invariant results were small [3,57]. Possible consequences of the violation of boost invariance in RHIC and LHC heavy-ion collisions are presently being studied [55].

Before moving on, let us comment on the different shape at the high-multiplicity end of the curves shown in Fig. 10 when using entropy instead of energy density as the weight for calculating the initial eccentricity $\bar{\varepsilon}$ overlap area S: It is caused by the different centrality dependence of the energy- and entropy-density-weighted eccentricities in near-central collisions observed in Ref. [33], whose authors showed that in the most central collisions (where $\bar{\varepsilon}$ is dominated by event-by-event shape fluctuations) the entropy-weighted participant eccentricity decreases faster with decreasing impact parameter than the energy-weighted one.

IV. TEMPERATURE-DEPENDENT $(\eta/s)(T)$

Shear viscosity is known to suppress the buildup of elliptic flow. Naively, the systematic overprediction of $v_2\{4\}(p_T)$ in Pb + Pb collisions at the LHC seen in Fig. 7(a), together with the excellent description of the same quantity in Au + Au collisions at the RHIC seen in Fig. 3, thus suggests that the fireball liquid formed in LHC collisions might be slightly more viscous (i.e., possess larger average η/s) than at RHIC energies [20,49]. In this section we present some results using a temperature-dependent specific shear viscosity, $(\frac{\eta}{s})(T)$, that were motivated by such considerations.

Figure 11 illustrates the following three trial functions explored in this section:

$$\left(\frac{\eta}{s}\right)_1 = 0.2 + 0.3\,\frac{T - T_{\rm chem}}{T_{\rm chem}}, \tag{1}$$

$$\left(\frac{\eta}{s}\right)_2 = 0.2 + 0.4\,\frac{(T - T_{\rm chem})^2}{T_{\rm chem}^2}, \tag{2}$$

$$\left(\frac{\eta}{s}\right)_3 = 0.2 + 0.3\,\sqrt{\frac{T - T_{\rm chem}}{T_{\rm chem}}}. \tag{3}$$

Here $T_{\rm chem} = 165$ MeV is the chemical decoupling temperature and stands for the "transition temperature" at which the hadronization of quarks and gluons is complete.

In principle, the value of η/s should exhibit a minimum near $T_{\rm chem}$ and increase again in the hadronic phase below $T_{\rm chem}$ [58–60]. The authors of [49] pointed out, however, that at the full LHC collision energy of 5.5 A TeV the behavior of η/s at temperatures below $T_{\rm chem}$ has very little effect on the final hadron spectra and their elliptic flow. At 2.76 A TeV the

[11] The careful reader will notice that for 200A GeV Au + Au collisions, our maximal values for $(1/S)(dN_{\rm ch}/d\eta)$ in Fig. 10(b) are significantly larger than those shown in Fig. 3 of Ref. [18]. This is due to a lower normalization of the initial entropy density in [18], corresponding to $dN_{\rm ch}/d\eta \sim 600$ instead of our $dN_{\rm ch}/d\eta \sim 700$ in central Au + Au collisions (T. Hirano, private communication).

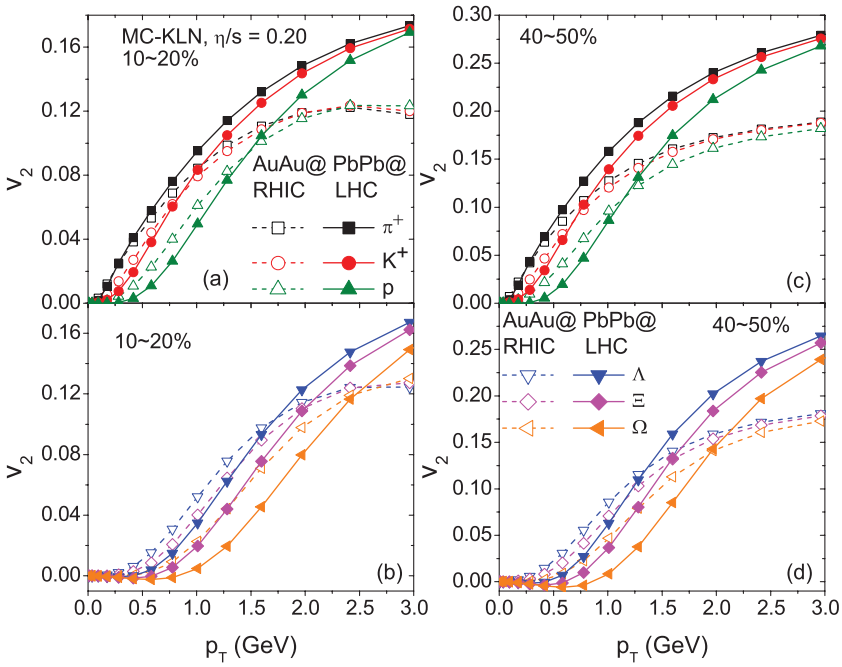

FIG. 9. (Color online) Comparison of the differential elliptic flow $v_2(p_T)$ for 200A GeV Au + Au collisions at the RHIC (dashed lines) and 2.76 A TeV Pb + Pb collisions at the LHC (solid lines), at 10%–20% (a and b) and 40%–50% (c and d) centrality, for a variety of different hadron species. Note the slightly negative elliptic flow for the heavy Ω hyperons at low p_T.

effect on elliptic flow was moderate, and it was negligible on the spectra. Here we will concentrate on qualitative aspects of effects arising from a temperature-dependent growths of η/s in the high-temperature region that can be explored at LHC energies but is beyond the reach of the RHIC, and we continue to set $\eta/s = 0.2$ at $T < T_{\rm chem}$ for simplicity.

As pointed out in [49], the spectra and elliptic flow in Au + Au collisions at RHIC energies are most sensitive to the average value of η/s in the temperature region below 220–230 MeV. We have checked that altering η/s at higher temperatures as shown in Fig. 11 has little influence on the results at RHIC energies shown in Sec. II.

Figure 12 illustrates the influence of a linear temperature dependence of η/s as in Eq. (1) on the centrality dependence of charged hadron production. The solid black line is the same as shown in the upper part of Fig. 1, where it forms the lower bound of the shaded region; it corresponds to constant $\eta/s = 0.2$ and Navier-Stokes initial conditions for the shear stress tensor, $\pi^{\mu\nu} = 2\eta\sigma^{\mu\nu}$ at $\tau_0 = 0.6$ fm/c. The dashed and dash-dotted lines in Fig. 12 use $(\eta/s)_1(T)$ with either Navier-Stokes (dashed) or zero (dash-dotted) initial conditions for $\pi^{\mu\nu}$. These last two lines were normalized to the ALICE point for the 0%–5% most central Pb + Pb collisions ($dN_{\rm ch}/d\eta = 1584 \pm 80$ [40]), whereas the black line was normalized to our best guess before the ALICE data became available ($dN_{\rm ch}/dy = 1800$, corresponding to $dN_{\rm ch}/d\eta = 1548$). The centrality dependence is then controlled by the predictions from the MC-KLN model, modified by viscous entropy production during the hydrodynamic evolution.

We see that even a relatively modest temperature-dependent increase of η/s in the QGP phase leads to a significantly stronger nonlinearity in the dependence of charged particle production on the number of wounded nucleons. The reason for this nonlinearity is that an increase of η/s with temperature leads to more viscous heating in central collisions (which probe higher initial temperatures and larger effective shear viscosities) than in peripheral ones (whose initial temperatures are lower). Since the entropy production rate is given by

$$\partial_\mu S^\mu = \frac{\pi^{\mu\nu}\pi_{\mu\nu}}{2\eta T}, \tag{4}$$

this effect is stronger for Navier-Stokes initial conditions (where $\pi^{\mu\nu}$ is proportional to the velocity shear tensor $\sigma^{\mu\nu}$, which at early times diverges like $1/\tau$) than for zero initial shear stress (where $\pi^{\mu\nu}$ starts from zero and approaches its Navier-Stokes value $2\eta\sigma^{\mu\nu}$ only after several relaxation times τ_π when, due to its $1/\tau$ decay, it has already decreased to much smaller values).[12]

If one were to postulate the validity of the MC-KLN model as the correct description of the initial particle production, the ALICE data shown in Fig. 12 would exclude a temperature dependence of η/s as given in Eqs. (1) and (2) for Naver-Stokes initial conditions. While we are not prepared to make such a statement on the basis of Fig. 12 alone, we believe that it is important to point out this relatively strong sensitivity of the centrality dependence of $dN_{\rm ch}/d\eta$ to the transport properties of the expanding fireball medium and to emphasize the constraints it thus places on possible models for the QGP shear viscosity.

We now turn to the discussion of the influence of a possible temperature dependence of η/s on the charged hadron p_T spectra and elliptic flow. Figure 13 shows LHC predictions

[12]For reference we list the fractions of the finally measured entropy in the most central and most peripheral centrality bins shown in Fig. 12 that are generated by viscous heating during the hydrodynamic expansion: constant $\eta/s = 0.2$: $\Delta S/S_{\rm final} = 26\%$ (0%–5%) and 33% (70%–80%); $(\eta/s)_1(T)$ with $\pi_0^{\mu\nu} = 0$: $\Delta S/S_{\rm final} = 25\%$ (0%–5%) and 15% (70%–80%); $(\eta/s)_1(T)$ with $\pi_0^{\mu\nu} = 2\eta\sigma^{\mu\nu}$: $\Delta S/S_{\rm final} = 60\%$ (0%–5%) and 49% (70%–80%).

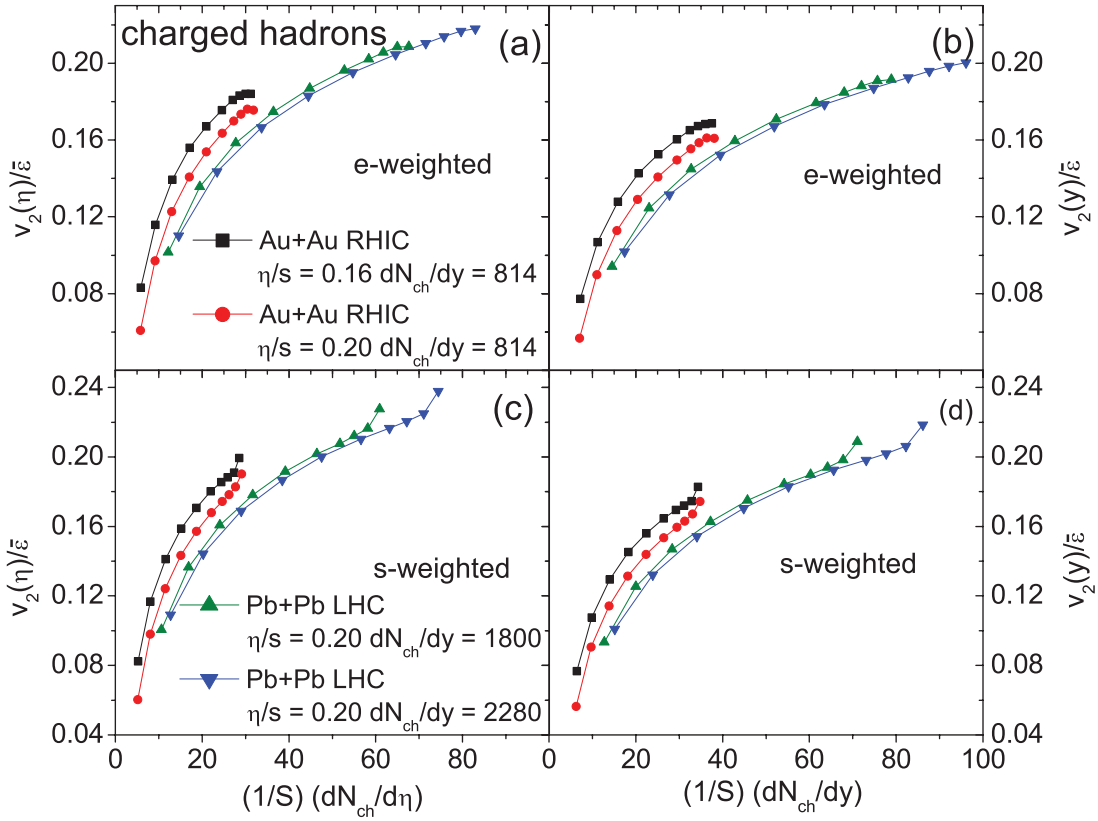

FIG. 10. (Color online) Eccentricity-scaled elliptic flow $v_2/\bar{\varepsilon}$ as a function of the charged hadron multiplicity density per unit overlap area S from viscous hydrodynamic calculations at $\sqrt{s} = 0.2,\ 2.76$, and 5.5 A TeV (corresponding to $dN_{\rm ch}/dy = 814$ (Au + Au) and 1800 and 2280 (Pb + Pb), respectively). Each line corresponds to one collision system at fixed collision energy but different collision centralities. (From right to left, the symbols correspond to 0%–5%, 5%–10%, 10%–15%, 15%–20%, 20%–30%, 30%–40%, 40%–50%, 50%–60%, 60%–70%, and 70%–80% centrality.) The four panels show $v_2(\eta)/\bar{\varepsilon}$ vs $(1/S)(dN_{\rm ch}/d\eta)$ (where η is pseudorapidity) (a and c) and $v_2(y)/\bar{\varepsilon}$ vs $(1/S)(dN_{\rm ch}/dy)$ (where y is rapidity) (b and d), with $\bar{\varepsilon}$ and S evaluated with the participant-plane averaged energy density $\bar{e}(\boldsymbol{r}_\perp, \tau_0)$ as a weight function (a and b) (default option; see Sec. II) or (for comparison with other work) with the corresponding entropy density $\bar{s}(\boldsymbol{r}_\perp, \tau_0)$ as a weight (c and d). The RHIC curves for $\eta/s = 0.16$ (black squares) illustrate the effect of changing the value of the specific shear viscosity by 0.04. The LHC calculations are done for $\eta/s = 0.20$ as obtained from the hydrodynamic fit to RHIC data.

for 2.76 A TeV Pb + Pb collisions of 20%–30% centrality. To ensure comparability of the different cases studied in this figure we simply normalized the initial entropy density profile such that we always obtain $dN_{\rm ch}/dy = 770$, i.e., the same value that we had obtained before for constant $\eta/s = 0.2$ at this centrality. We first note that for constant $\eta/s = 0.2$, we do not observe any significant difference in the charged hadron spectra and elliptic flow between zero and Navier-Stokes initialization for $\pi^{\mu\nu}$. Turning to the temperature-dependent parametrizations $(\eta/s)_i(T)$, we note that for zero initialization of $\pi^{\mu\nu}$ (solid lines) our results agree with those reported in [49]: An increase of η/s at higher QGP temperatures leads to somewhat harder charged hadron p_T spectra (i.e., somewhat stronger radial flow, caused by the larger tranverse effective pressure gradients at early times) and a suppression of the differential elliptic flow (due to an increase of the time-averaged effective shear viscosity of the fluid). It is interesting to observe the hierarchy of the curves in Fig. 13 corresponding to the three parametrizations (1)–(3): For the p_T spectra, all three T-dependent viscosities lead to almost identical hardening effects on the spectral slope, while for the differential elliptic flow $v_2^{\rm ch}(p_T)$ the curves are ordered not according to the η/s values at the initial central fireball temperature (see Table I) but according to their hierarchy in the $165 < T < 280$ MeV

TABLE I. Initial central entropy densities s_0 and temperatures T_0 for the viscous hydrodynamic simulations of 20%–30% centrality Pb + Pb collisions at the LHC ($\sqrt{s} = 2.76$ A TeV) shown in Fig. 13. The different models for the T dependence of η/s are defined in Eqs. (1)–(3). "0" stands for $\pi_0^{\mu\nu} = 0$ at τ_0; "NS" stands for Navier-Stokes initialization of the shear stress tensor, $\pi_0^{\mu\nu} = 2\eta\sigma^{\mu\nu}$, at τ_0.

η/s model	$\pi_0^{\mu\nu}$	s_0 (fm^{-3})	T_0 (MeV)
$\eta/s = 0.2$	0	191.6	427.9
	NS	172.4	413.9
$(\eta/s)_1(T)$	0	179.6	419.2
	NS	119.3	368.7
$(\eta/s)_2(T)$	0	179.6	419.2
	NS	115.6	365.1
$(\eta/s)_3(T)$	0	175.2	416.0
	NS	116.6	366.1

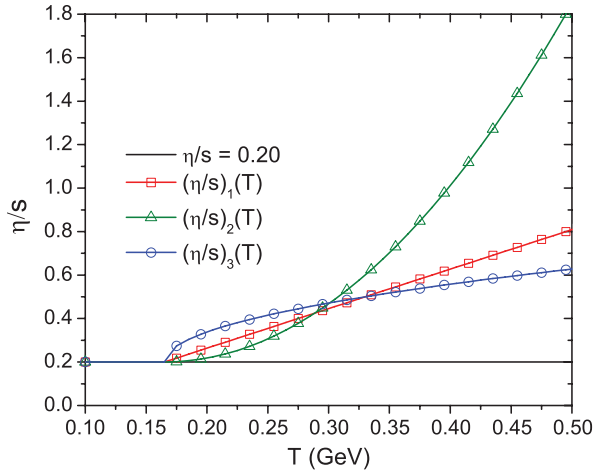

FIG. 11. (Color online) Three temperature-dependent parametrizations $(\eta/s)(T)$ studied in this section. In all cases, $\eta/s = 0.2$ for $T < T_{\rm chem} = 165$ MeV.

range. In fact, the observed magnitudes of the viscous v_2 suppression for the three $(\eta/s)(T)$ functions suggest that, at this beam energy and collision centrality, the buildup of elliptic flow is dominated by the QGP transport properties at $200 \lesssim T \lesssim 250$ MeV. (At RHIC energies, the transport properties for $T \lesssim 200-220$ MeV dominate the generation of v_2 [49].)

For Navier-Stokes initial conditions (dashed lines in Fig. 13), the increase in radial flow caused by an increase of η/s at high temperature is stronger and the viscous v_2 suppression is weaker than for zero initial $\pi^{\mu\nu}$. This is caused by the much larger initial shear stress tensor components in the Navier-Stokes case, compared to the case of $\pi_0^{\mu\nu} = 0$ where $\pi^{\mu\nu}$ approaches its (by that time already much smaller)

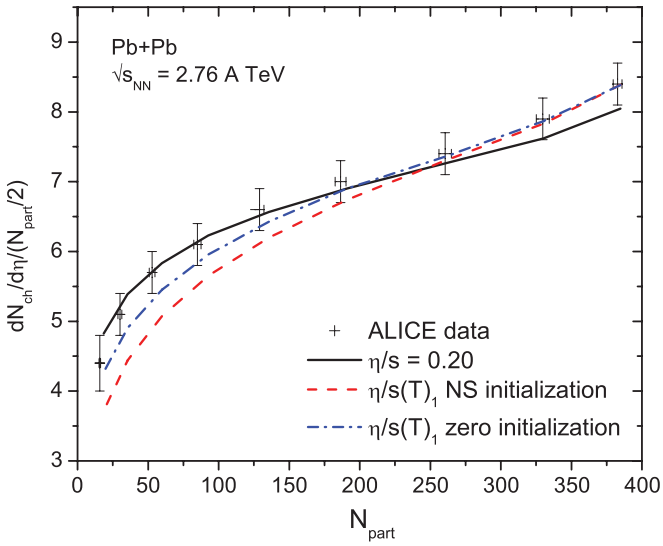

FIG. 12. (Color online) Final charged multiplicity per wounded nucleon pair as a function of number of participant nucleons in Pb + Pb collisions at $\sqrt{s} = 2.76$ A TeV, for different functional forms of $(\eta/s)(T)$ and initial conditions for the shear stress tensor $\pi^{\mu\nu}$ (see text).

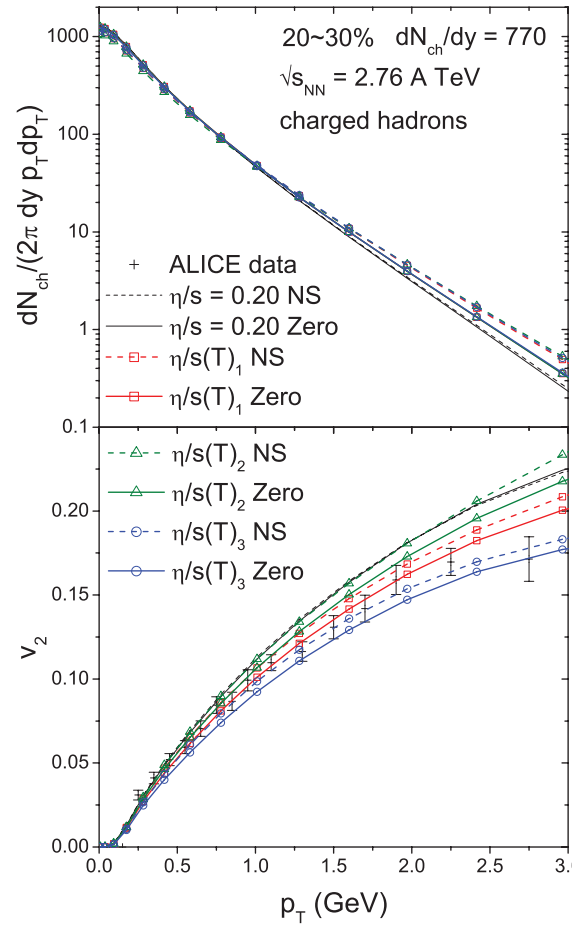

FIG. 13. (Color online) Charged hadron transverse momentum spectra (top) and differential elliptic flow (bottom) for 2.76 A TeV Pb + Pb collisions at 20%–30% centrality, for different models for the temperature dependence of η/s and different initial conditions for $\pi^{\mu\nu}$ [Navier-Stokes ("NS") or 0 ("Zero")]. The ALICE data in the bottom panel are from Ref. [1].

Navier-Stokes limit only after several relaxation times τ_π [24]. The increase of η/s with temperature generates a steeper initial transverse effective pressure gradient (since $\pi^{\mu\nu}$ grows faster than the entropy density s when η/s increases with temperature), and this generates stronger radial flow. It also causes a larger spatial eccentricity of the initial effective pressure profile, which (when compared to the case of $\pi_0^{\mu\nu} = 0$) generates stronger elliptic flow. In fact, we found that for earlier starting times τ_0 (where the Navier-Stokes values for $\pi^{\mu\nu}$ are even larger), the quadratic parametrization $(\eta/s)_2(T)$ with Navier-Stokes initial conditions can lead to *more* elliptic flow than a constant $\eta/s = 0.2$, in spite of the larger mean viscosity of the fluid.

We conclude from this exercise that a firm determination of whether or not the ALICE data point toward a temperature-dependent growth of η/s with increasing T, as expected from perturbative QCD [61] and (perhaps) from lattice QCD [62], is not possible without a better understanding of the initial conditions for the energy momentum tensor (in particular the shear stress components) at the beginning of the hydrodynamic evolution. Whereas generically larger viscosities

cause a suppression of the elliptic flow, temperature-dependent viscosities can influence the initial effective pressure profile and its eccentricity in a way that counteracts this tendency and, for some models such as Navier-Stokes initial conditions, can even overcompensate it.

V. CONCLUSIONS

Based on an successful global fit of soft hadron production data in 200A GeV Au + Au collisions at the RHIC with a pure viscous hydrodynamic model with Cooper-Frye freeze-out, presented in Sec. II, we generated hydrodynamic predictions for the p_T spectra and differential elliptic flow of unidentified charged hadrons and identified pions and protons for Pb + Pb collisions at the LHC. Where available, these predictions were compared with available experimental data from the ALICE Collaboration. Our extrapolation from RHIC to LHC energies was based on the assumption that the QGP shear viscosity η/s does not change with increasing fireball temperature and stays fixed at the value $\eta/s = 0.2$ extracted from the RHIC data, assuming MC-KLN initial conditions. The start time τ_0 for the hydrodynamic evolution and the freeze-out temperature $T_{\rm dec}$ were held fixed, too. We found that, using the beam energy scaling implicit in the MC-KLN model, such an extrapolation gives a good description of the centrality dependence of charged hadron production and the charged hadron p_T spectra in central Pb + Pb collisions, but it overpredicts the slope of the p_T-differential elliptic flow and the value of its p_T-integrated value by about 10%–15% in mid-central to mid-peripheral collisions. In the most peripheral collisions, the predicted charged hadron p_T spectra are too flat, and the integrated elliptic flow is too small compared to the experimental data. A preliminary study of possible temperature-dependent variations of η/s in the high-temperature region explored for the first time at the LHC remained inconclusive but pointed to a clear need for better theoretical control over the initial conditions for the hydrodynamic energy-momentum tensor, in particular its shear stress components. The development of detailed dynamical models for the pre-thermal evolution of the collision fireball and their matching to the viscous hydrodynamic stage is a matter of priority for continued progress toward quantifying the transport properties of the quark-gluon plasma at different temperatures and densities.

ACKNOWLEDGMENTS

We would like to thank R. Snellings and A. Tang for providing us with tables of the experimental data from the ALICE experiment and for helpful discussions. This work was supported by the US Department of Energy under Contracts No. DE-AC02-05CH11231, No. DE-FG02-05ER41367, No. DE-SC0004286, and (within the framework of the JET Collaboration) No. DE-SC0004104. P.H.'s research was supported by the ExtreMe Matter Institute (EMMI) and by BMBF under Contract No. 06FY9092.

[1] K. Aamodt *et al.* (ALICE Collaboration), Phys. Rev. Lett. **105**, 252302 (2010).
[2] P. Danielewicz and M. Gyulassy, Phys. Rev. D **31**, 53 (1985).
[3] U. Heinz and P. F. Kolb, Nucl. Phys. A **702**, 269 (2002).
[4] G. Policastro, D. T. Son, and A. O. Starinets, Phys. Rev. Lett. **87**, 081601 (2001); P. K. Kovtun, D. T. Son, and A. O. Starinets, *ibid.* **94**, 111601 (2005).
[5] U. Heinz and S. M. H. Wong, Phys. Rev. C **66**, 014907 (2002).
[6] D. Teaney, Phys. Rev. C **68**, 034913 (2003).
[7] I. Arsene *et al.* (BRAHMS Collaboration), Nucl. Phys. A **757**, 1 (2005); B. B. Back *et al.* (PHOBOS Collaboration), *ibid.* **757**, 28 (2005); J. Adams *et al.* (STAR Collaboration), *ibid.* **757**, 102 (2005); K. Adcox *et al.* (PHENIX Collaboration), *ibid.* **757**, 184 (2005).
[8] R. A. Lacey and A. Taranenko, PoS **CFRNC2006**, 021 (2006); R. A. Lacey *et al.*, Phys. Rev. Lett. **98**, 092301 (2007); A. Adare *et al.*, *ibid.* **98**, 172301 (2007); H.-J. Drescher, A. Dumitru, C. Gombeaud, and J.-Y. Ollitrault, Phys. Rev. C **76**, 024905 (2007); K. Dusling and D. Teaney, *ibid.* **77**, 034905 (2008); Z. Xu, C. Greiner, and H. Stöcker, Phys. Rev. Lett. **101**, 082302 (2008); D. Molnar and P. Huovinen, J. Phys. G **35**, 104125 (2008); R. A. Lacey, A. Taranenko and R. Wei, in *Proceedings 25th Winter Workshop on* Nuclear Dynamics, edited by W. Bauer, R. Bellwied, and J. W. Harris (EP Systema, Budapest, 2009), p. 73; K. Dusling, G. D. Moore, and D. Teaney, Phys. Rev. C **81**, 034907 (2010); A. K. Chaudhuri, J. Phys. G **37**, 075011 (2010); R. A. Lacey *et al.*, Phys. Rev. C **82**, 034910 (2010).
[9] P. Romatschke and U. Romatschke, Phys. Rev. Lett. **99**, 172301 (2007); M. Luzum and P. Romatschke, Phys. Rev. C **78**, 034915 (2008).
[10] H. Song, S. A. Bass, U. Heinz, T. Hirano, and C. Shen, Phys. Rev. Lett. **106**, 192301 (2011); Phys. Rev. C **83**, 054910 (2011).
[11] M. Luzum, Phys. Rev. C **83**, 044911 (2011).
[12] R. A. Lacey, A. Taranenko, N. N. Ajitanand, and J. M. Alexander, Phys. Rev. C **83**, 031901 (2011).
[13] N. Armesto *et al.*, J. Phys. G **35**, 054001 (2008).
[14] H. Niemi, K. J. Eskola, and P. V. Ruuskanen, Phys. Rev. C **79**, 024903 (2009)
[15] G. Kestin and U. Heinz, Eur. Phys. J. C **61**, 545 (2009); U. Heinz, Nucl. Phys. A **830**, 287c (2009).
[16] M. Luzum and P. Romatschke, Phys. Rev. Lett. **103**, 262302 (2009).
[17] P. Bozek, M. Chojnacki, W. Florkowski, and B. Tomasik, Phys. Lett. B **694**, 238 (2010); P. Bozek, *ibid.* **699**, 283 (2011).
[18] T. Hirano, P. Huovinen, and Y. Nara, Phys. Rev. C **83**, 021902 (2011).
[19] B. Schenke, S. Jeon, and C. Gale, Phys. Lett. B **702**, 59 (2011).
[20] H. Song, S. A. Bass, and U. Heinz, Phys. Rev. C **83**, 054912 (2011).
[21] T. Hirano, U. Heinz, D. Kharzeev, R. Lacey, and Y. Nara, Phys. Lett. B **636**, 299 (2006).
[22] H. Song, S. A. Bass, and U. Heinz, Phys. Rev. C **83**, 024912 (2011).

[23] T. Hirano, U. Heinz, D. Kharzeev, R. Lacey, and Y. Nara, J. Phys. G **34**, S879 (2007).
[24] H. Song and U. Heinz, Phys. Lett. B **658**, 279 (2008); Phys. Rev. C **77**, 064901 (2008); **78**, 024902 (2008); H. Song, Ph.D thesis, Ohio State University, 2009, arXiv:0908.3656 [nucl-th].
[25] P. Huovinen and P. Petreczky, Nucl. Phys. A **837**, 26 (2010).
[26] C. Shen, U. Heinz, P. Huovinen, and H. Song, Phys. Rev. C **82**, 054904 (2010).
[27] F. Cooper and G. Frye, Phys. Rev. D **10**, 186 (1974).
[28] J. Sollfrank, P. Koch, and U. Heinz, Phys. Lett. B **252**, 256 (1990); Z. Phys. C **52**, 593 (1991); J. Sollfrank, P. Huovinen, M. Kataja, P. V. Ruuskanen, M. Prakash, and R. Venugopalan, Phys. Rev. C **55**, 392 (1997).
[29] A. Adil, H. J. Drescher, A. Dumitru, A. Hayashigaki, and Y. Nara, Phys. Rev. C **74**, 044905 (2006).
[30] H. J. Drescher and Y. Nara, Phys. Rev. C **76**, 041903 (2007).
[31] D. Kharzeev, M. Nardi, Phys. Lett. B **507**, 121 (2001); D. Kharzeev and E. Levin, *ibid*. **523**, 79 (2001).
[32] T. Hirano and Y. Nara, Phys. Rev. C **79**, 064904 (2009); Nucl. Phys. A **830**, 191c (2009).
[33] Z. Qiu and U. W. Heinz, Phys. Rev. C **84**, 024911 (2011).
[34] B. B. Back *et al*. (PHOBOS Collaboration), Phys. Rev. C **70**, 021902 (2004); B. Alver *et al*. (PHOBOS Collaboration), *ibid*. **80**, 011901 (2009).
[35] J. L. Albacete and A. Dumitru, arXiv:1011.5161.
[36] I. Balitsky, Phys. Rev. D **75**, 014001 (2007).
[37] J. L. Albacete, Phys. Rev. Lett. **99**, 262301 (2007).
[38] Y. V. Kovchegov and H. Weigert, Nucl. Phys. A **784**, 188 (2007); **807**, 158 (2008).
[39] K. Aamodt *et al*. (ALICE Collaboration), Phys. Rev. Lett. **106**, 032301 (2011).
[40] K. Aamodt *et al*. (ALICE Collaboration), Phys. Rev. Lett. **105**, 252301 (2010).
[41] J. Adams *et al*. (STAR Collaboration), Phys. Rev. Lett. **91**, 172302 (2003).
[42] S. S. Adler *et al*. (PHENIX Collaboration), Phys. Rev. C **69**, 034910 (2004).
[43] J. Adams *et al*. (STAR Collaboration), Phys. Rev. Lett. **92**, 112301 (2004); B. I. Abelev *et al*. (STAR Collaboration), *ibid*. **97**, 152301 (2006).
[44] B. I. Abelev *et al*. (STAR Collaboration), Phys. Rev. C **79**, 034909 (2009).
[45] S. S. Adler *et al*. (PHENIX Collaboration), Phys. Rev. C **69**, 034909 (2004).
[46] Y. Bai, Ph.D. thesis, NIKHEF and Utrecht University, The Netherlands, 2007.
[47] B. I. Abelev *et al*. (STAR Collaboration), Phys. Rev. C **77**, 054901 (2008).
[48] C. Shen and U. Heinz, Phys. Rev. C **83**, 044909 (2011).
[49] H. Niemi, G. S. Denicol, P. Huovinen, E. Molnar, and D. H. Rischke, Phys. Rev. Lett. **106**, 212302 (2011).
[50] K. Aamodt *et al*. (ALICE Collaboration), Phys. Lett. B **696**, 30 (2011).
[51] K. Aamodt *et al*. (ALICE Collaboration), Phys. Rev. Lett. **107**, 032301 (2011); R. Snellings *et al*. (ALICE Collaboration), J. Phys. G (in press), arXiv:1106.6284 [nucl-ex].
[52] J. Y. Ollitrault, A. M. Poskanzer, and S. A. Voloshin, Phys. Rev. C **80**, 014904 (2009).
[53] P. F. Kolb and U. Heinz, in *Quark-Gluon Plasma 3*, edited by R. C. Hwa and X.-N. Wang (World Scientific, Singapore, 2004), p. 634, arXiv:nucl-th/0305084.
[54] J. Adams *et al*. (STAR Collaboration), Phys. Rev. C **72**, 014904 (2005).
[55] C. Shen, B. Schenke, and U. Heinz (private communication).
[56] A. Monnai and T. Hirano, Phys. Lett. B **703**, 583 (2011).
[57] T. Hirano and K. Tsuda, Phys. Rev. C **66**, 054905 (2002).
[58] L. P. Csernai, J. I. Kapusta, and L. D. McLerran, Phys. Rev. Lett. **97**, 152303 (2006).
[59] J. W. Chen, M. Huang, Y. H. Li, E. Nakano, and D. L. Yang, Phys. Lett. B **670**, 18 (2008).
[60] J. I. Kapusta, in *Relativistic Heavy Ion Physics*, Landolt-Börnstein New Series, Vol. I/23, edited by R. Stock (Springer Verlag, New York, 2010), arXiv:0809.3746 [nucl-th].
[61] P. B. Arnold, G. D. Moore, and L. G. Yaffe, J. High Energy Phys. 05 (2003) 051.
[62] H. B. Meyer, Phys. Rev. D **76**, 101701 (2007).

PHYSICAL REVIEW C **84**, 011901(R) (2011)

Elliptic flow in Pb+Pb collisions at $\sqrt{s_{NN}} = 2.76$ TeV: Hybrid model assessment of the first data

Tetsufumi Hirano,[1,2,*] Pasi Huovinen,[3,†] and Yasushi Nara[4,‡]

[1]*Department of Physics, The University of Tokyo, Tokyo 113-0033, Japan*

[2]*Nuclear Science Division, Lawrence Berkeley National Laboratory, Berkeley, California 94720, USA*

[3]*Institut für Theoretische Physik, Johann Wolfgang Goethe-Universität, D-60438 Frankfurt am Main, Germany*

[4]*Akita International University, Yuwa, Akita-city 010-1292, Japan*

(Received 20 December 2010; published 7 July 2011)

We analyze the elliptic flow parameter v_2 in Pb+Pb collisions at $\sqrt{s_{NN}} = 2.76$ TeV and in Au+Au collisions at $\sqrt{s_{NN}} = 200$ GeV using a hybrid model in which the evolution of the quark gluon plasma is described by ideal hydrodynamics with a state-of-the-art lattice QCD equation of state, and the subsequent hadronic stage by a hadron cascade model. For initial conditions, we employ Monte Carlo versions of the Glauber and the Kharzeev-Levin-Nardi models and compare results with each other. We demonstrate that the differential elliptic flow $v_2(p_T)$ hardly changes when the collision energy increases, whereas the integrated v_2 increases due to the enhancement of mean transverse momentum. The amount of increase of both v_2 and mean p_T depends significantly on the model of initialization.

DOI: 10.1103/PhysRevC.84.011901 PACS number(s): 25.75.Nq, 12.38.Mh, 12.38.Qk

The recently started heavy-ion program at Large Hadron Collider (LHC) in CERN opens up opportunities to explore the deconfined matter, the quark gluon plasma (QGP), in a wider temperature region. Elliptic flow [1], which played an essential role to establish the new paradigm of the strongly coupled QGP [2,3] at Relativistic Heavy-Ion Collider (RHIC) in Brookhaven National Laboratory (BNL) [4], is one of the key observables at LHC to investigate the bulk and transport properties of the QGP. First elliptic flow data in Pb+Pb collisions at $\sqrt{s_{NN}} =$ 2.76 TeV were recently published by the ALICE Collaboration [5]. The first goal of flow measurements is to see whether hydrodynamic models reproduce the flow as well at LHC as at RHIC, and thus whether the QGP depicts similar strong coupling nature at LHC.

This Rapid Communication is a sequel to our previous work [6] where we predicted the elliptic flow parameter v_2 before any LHC data was available. In this publication we take the advantage of the first LHC data [5,7] to fix the final particle multiplicity, which removes the main uncertainty in our prediction, and allows us to use a Glauber type initialization too. We calculate the elliptic flow parameter v_2 and its transverse momentum (p_T) dependence in Pb+Pb collisions at LHC and compare them with the data. Our model for the space-time evolution of the matter is the same we used in Ref. [6]: A hybrid model where the expansion of the QGP is described by ideal hydrodynamics [8], and the subsequent evolution of hadronic matter below switching temperature $T_{\rm sw} = 155$ MeV, is described using a hadronic cascade model JAM [9]. During the fluid dynamical stage, we employ EoS $s95p$-v1.1, which interpolates between hadron resonance gas at low temperatures and recent lattice QCD results by the hotQCD collaboration [10,11] at high temperatures in the same way as $s95p$-v1 [12], but the hadron resonance gas part contains the same hadrons and resonances as the JAM hadron cascade [9]. The details of the interpolating procedure are explained in Ref. [12] and the parametrization and EoS tables are available at Ref. [13].

Initial time of hydrodynamic simulations is fixed to be $\tau_0 =$ 0.6 fm/c throughout this work. For initial conditions in the longitudinal direction, we assume the Bjorken scaling solution [14]. To initialize the density distributions in the transverse plane, we utilize two Monte Carlo approaches: Monte Carlo–Glauber (MC-Glauber) model [15] and Monte Carlo–Kharzeev-Levin-Nardi (MC-KLN) model [16]. Using these Monte Carlo models, we calculated initial conditions for hydrodynamic simulations in the transverse plane with respect to the *participant plane* in our previous work [6]. These initial density profiles contain effects of eccentricity fluctuation on average. However, the ALICE Collaboration mainly obtained v_2 using the four-particle cumulant method $v_2\{4\}$ [17]. If the event-by-event distribution of eccentricity in the reaction plane is a two-dimensional Gaussian, and if v_2 is proportional to the participant eccentricity, then $v_2\{4\}$ yields the value of v_2 in the reaction plane [18,19]. Therefore we calculate in this Rapid Communication initial profiles with respect to the *reaction plane*: We average over many events using Monte Carlo calculations instead of shifting and rotating a distribution event by event to match the main and subaxes of the ellipsoids as was done in the previous work [6,20]. It should be noted that the distributions obtained in this way are not identical to the ones from the optical Glauber model or the factorized KLN (fKLN) model [21] because of finite nucleon size effects [16,22]: The collision points in the transverse plane are smeared using an inelastic cross section of $p + p$ collisions in the "mean-field" option in the Monte Carlo approach [16] to obtain smooth initial conditions for hydrodynamic simulations.

In the MC-KLN model, we calculate distribution of gluons at each transverse grid using the k_t-factorized formula [23]. Using the thickness function T_A, we parametrize the saturation

*hirano@phys.s.u-tokyo.ac.jp
†huovinen@th.physik.uni-frankfurt.de
‡nara@aiu.ac.jp

scale for a nucleus A as

$$Q^2_{s,A}(x;\boldsymbol{x}_\perp) = 2\ \mathrm{GeV}^2 \frac{T_A(\boldsymbol{x}_\perp)}{1.53\ \mathrm{fm}^{-2}} \left(\frac{0.01}{x}\right)^\lambda, \qquad (1)$$

and similarly for a nucleus B. We choose $\lambda = 0.28$ and a proportionality constant in the unintegrated gluon distribution in the k_t-factorized formula to reproduce centrality dependence of p_T spectra obtained by the PHENIX Collaboration [24]. As a default parameter set at LHC, we use the same parameters except for colliding energy and mass number of incident nuclei. This predicted $dN_{\mathrm{ch}}/d\eta \sim 1600$ at 5% most central collisions [6], which turns out to be consistent with the recent ALICE measurement [7,25].

In the MC-Glauber model, one calculates the number distributions of participants ρ_{part} and of binary collisions ρ_{coll} for a given nuclear density distribution. We model the initial entropy distribution in hydrodynamic simulations as a linear combination of ρ_{part} and ρ_{coll} in the transverse plane:

$$\frac{dS}{\tau_0 d\eta_s d^2\boldsymbol{x}_\perp} = \frac{C}{\tau_0}\left(\frac{1-\alpha}{2}\rho_{\mathrm{part}}(\boldsymbol{x}_\perp) + \alpha\rho_{\mathrm{coll}}(\boldsymbol{x}_\perp)\right). \qquad (2)$$

At the RHIC energy, the mixing parameter $\alpha = 0.18$ and the proportionality constant $C = 15.0$ in Eq. (2) are chosen to reproduce the centrality dependence of p_T spectra at RHIC [24]. We tune these two parameters in Pb+Pb collisions at LHC to reproduce the centrality dependence of charged hadron multiplicity [25]. For both initializations we do the centrality cuts according to the N_{part} distribution from the MC-Glauber model [6].

In Fig. 1, we calculate $dN_{\mathrm{ch}}/d\eta/(N_{\mathrm{part}}/2)$ as a function of N_{part} for initial conditions from the MC-Glauber and the MC-KLN models and compare them with data. The experimental data point in inelastic $p+p$ collisions at $\sqrt{s_{NN}} = 2.36$ TeV [26] is plotted at $N_{\mathrm{part}} = 2$. The MC-KLN initialization leads to remarkable agreement with the ALICE data. On the other hand, it is difficult to fit the data within the current two-component picture in the MC-Glauber model: The results from the MC-Glauber initialization with $\alpha = 0.08$ and $C = 41.4$ almost

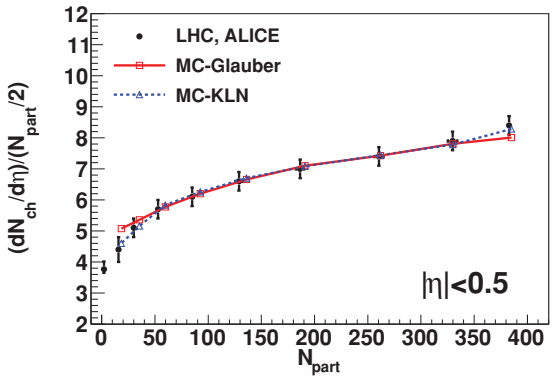

FIG. 1. (Color online) Centrality dependence of charged hadron multiplicity in the MC-Glauber and the MC-KLN initialization is compared with ALICE data [25,26]. A data point from inelastic events at $\sqrt{s_{NN}} = 2.36$ TeV in $p+p$ collisions [26] is shown at $N_{\mathrm{part}} = 2$. Each point in theoretical results from right to left corresponds to 0%–5%, 5%–10%, 10%–20%, 20%–30%, 30%–40%, 40%–50%, 50%–60%, 60%–70%, and 70% –80% centrality, respectively.

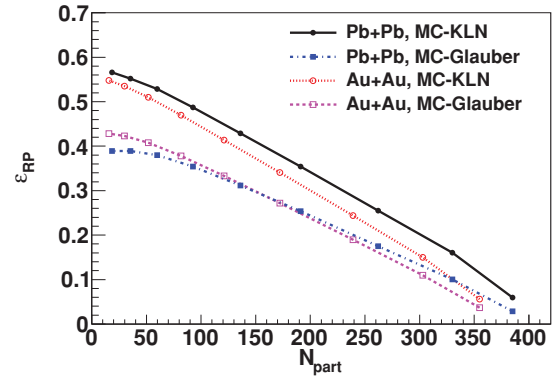

FIG. 2. (Color online) Eccentricity with respect to the reaction plane as a function of N_{part} in Pb + Pb collisions at $\sqrt{s_{NN}} = 2.76$ TeV and in Au+Au collisions at $\sqrt{s_{NN}} = 200$ GeV. Each point from right to left corresponds to 0%–5%, 5%–10%, 10%–20%, 20%–30%, 30%–40%, 40%–50%, 50%–60%, 60%–70%, and 70%–80% centrality, respectively.

trace the ones from the MC-KLN initialization and the ALICE data except for 0%–5% and 70%–80% centrality.

Shown in Fig. 2 is the initial eccentricity with respect to reaction plane as a function of N_{part} in Pb+Pb collisions at $\sqrt{s_{NN}} = 2.76$ TeV and in Au+Au collisions at $\sqrt{s_{NN}} = 200$ GeV. As previously known, the k_t-factorized formula of KLN model generates larger eccentricity than the Glauber model does [21,27]. In the MC-KLN model, eccentricity in Pb+Pb collisions at $\sqrt{s_{NN}} = 2.76$ TeV is slightly larger than that in Au+Au collisions at $\sqrt{s_{NN}} = 200$ GeV when the centrality is fixed [6]. On the other hand, in the MC-Glauber model, eccentricity in Pb+Pb collisions at $\sqrt{s_{NN}} = 2.76$ TeV is slightly smaller than that in Au+Au collisions at $\sqrt{s_{NN}} = 200$ GeV for a fixed centrality.

This is because of the smearing process we use to obtain a smooth initial profile for hydrodynamic evolution. As mentioned, we use the inelastic cross section in $p+p$ collisions, σ_{in}, to smear the distribution of collision points. This cross section is $\sim$1.5 times larger at LHC than at RHIC, and thus the smearing area, $S = \sigma_{\mathrm{in}}$ [16], is also larger at LHC, and the eccentricity is reduced. Our smearing procedure also leads to a smaller eccentricity than the conventional value of the MC-Glauber model.[1] The effect of smearing is smaller in the MC-KLN initialization, and we have checked that the eccentricity at LHC turns out to be essentially the same as at RHIC when the smearing area is the same. Systematic studies of initialization and its effects will be shown in a later publication [28].

Figure 3 shows comparison of transverse momentum distributions of charged hadrons between RHIC and LHC energies at 10%–20% and 40%–50% centralities. As clearly seen from figures, the slope of p_T spectra becomes flatter as collision energy and, consequently, pressure of produced matter increases. To quantify this, we calculate mean p_T of

[1]In the MC-Glauber model in the literature [15], one assumes δ function profile for each collision point in ρ_{part} distribution rather than a boxlike profile in the present work

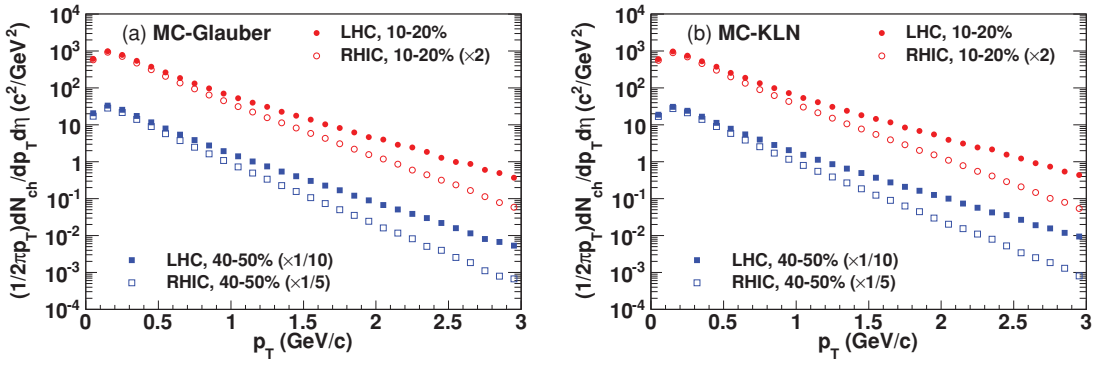

FIG. 3. (Color online) Transverse momentum distribution of charged hadrons at 10%–20% (circles) and 40%–50% (squares) centralities in Pb+Pb collisions at $\sqrt{s_{NN}} = 2.76$ TeV (solid symbols) and in Au + Au collisions at $\sqrt{s_{NN}} = 200$ GeV (open symbols). Results from (a) the MC-Glauber initialization and (b) the MC-KLN initialization. For the sake of comparison and visibility, the spectra are scaled by 2, 1/10, and 1/5 for 10%–20% at RHIC, 40%–50% at LHC, and 40%–50% at RHIC, respectively.

charged hadrons. In the MC-Glauber initialization, mean p_T increases from RHIC to LHC by 21% and 19% in 10%–20% and 40%–50% centrality, respectively. On the other hand, the corresponding fractions are 25% and 24% in the MC-KLN initialization. Because our calculations at RHIC were tuned to reproduce the p_T spectra, this means that at LHC the spectra calculated using the MC-KLN initialization are slightly flatter than those calculated using the MC-Glauber initialization.

We compare integrated v_2 for charged hadrons with respect to the reaction plane with the ALICE [5] and STAR [29] $v_2\{4\}$ data in Fig. 4. When evaluating the integrated v_2, we take account of both transverse momentum and pseudorapidity acceptance as done in the experiments (i.e., $0.2 < p_T < 5.0$ GeV/c and $|\eta| < 0.8$ for ALICE, and $0.15 < p_T < 2.0$ GeV/c and $|\eta| < 1.0$ for STAR). We want to emphasize that not only the p_T cut [30], but also the pseudorapidity cut plays an important role in a consistent comparison with the data. Because of the Jacobian for the change of variables from rapidity y to pseudorapidity η, $v_2(y = 0) < v_2(\eta = 0)$ for positive elliptic flow [31].[2] In the case of the MC-Glauber (MC-KLN) initialization in 40%–50% centrality, v_2 integrated over the whole p_T region is ∼14% (∼10%) larger at $\eta = 0$ than at $y = 0$.

When the MC-Glauber model is employed for initial profiles, centrality dependence of integrated v_2 from the hybrid approach almost agrees with both ALICE and STAR data. Because eccentricity fluctuation contributes little and negatively to $v_2\{4\}$ in non-Gaussian distribution of eccentricity fluctuation [18,19], this indicates there is only little room for the QGP viscosity in the model calculation. On the other hand, apparent discrepancy between the results from the MC-KLN initialization and the ALICE and STAR data means that viscous corrections during the hydrodynamic evolution are required.

From RHIC to LHC, the p_T-integrated $v_2(|\eta| < 0.8)$ increases by 24% and 25% in 10%–20% and 40%–50% centrality, respectively, in the MC-Glauber initialization. On the other hand, in the MC-KLN initialization, the increase reaches 42% and 44% in 10%–20% and 40%–50% centrality, respectively. Because eccentricity does not change significantly (at most ±6% in 40%–50% centrality) from RHIC to LHC as shown in Fig. 2, the significant increase of integrated v_2 must be attributed to a change in transverse dynamics.

Finally, we compare $v_2(p_T)$ of charged hadrons with ALICE [5] and STAR [29] data in 10%–20% [Fig. 5(a)] and 40%–50% [Fig. 5(b)] centrality. Interestingly, the data at LHC agree with the data at RHIC within errors. The calculated $v_2(p_T)$ shows similar independence of collision energy when MC-Glauber initialization is used, whereas MC-KLN initialization leads to a slightly larger $v_2(p_T)$ at the larger energy. For MC-Glauber results, the fit to data is fair below $p_T \sim 1.5$ GeV/c and $p_T \sim 0.8$ GeV/c momenta in the 10%–20% and 40%–50% centralities, respectively. Results from the MC-KLN initialization at both energies are significantly larger than experimental data in the whole p_T region, which again indicates necessity of viscous corrections in hydrodynamic evolution. For both initializations the difference between the data and the calculated $v_2(p_T)$ is larger in more peripheral collisions. This, too, can be understood as an indication of viscosity, because the more peripheral the collision, the smaller the system and the more anisotropic its shape, and both of these qualities enhance the dissipative effects.

Because of the relationships among the p_T spectrum, p_T averaged v_2, and p_T differential $v_2(p_T)$, the flatter the p_T spectrum, the larger the v_2 even if $v_2(p_T)$ stays the same. It is also worth noticing that the steeper the slope of $v_2(p_T)$, the larger the increase in v_2 for the same increase in mean p_T. This is the main reason why quite a similar increase of mean p_T for both MC-Glauber and MC-KLN initializations leads to a much larger increase of v_2 for MC-KLN than for MC-Glauber initialization.

At the time of this writing, the initial state of the fluid dynamical expansion of heavy-ion collisions at ultrarelativistic energies is quite uncertain. This has been a longstanding issue in the physics of heavy-ion collisions which must be by all means resolved. If color glass condensate (CGC) [32] initial conditions, like the ones obtained using the MC-KLN model

[2]Notice that even if one assumes the Bjorken scaling solution, one has to consider the pseudorapidity acceptance because $v_2(\eta)$ is not constant even if $v_2(y)$ is [31]

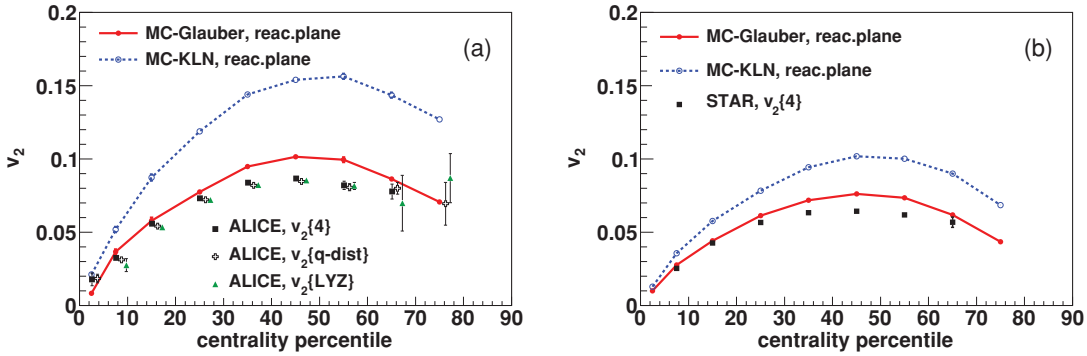

FIG. 4. (Color online) Centrality dependencies of v_2 for charged hadrons with respect to reaction plane (a) in Pb+Pb collisions at $\sqrt{s_{NN}} = 2.76$ TeV ($|\eta| < 0.8$, $0.2 < p_T < 5$ GeV/c) and (b) in Au+Au collisions at $\sqrt{s_{NN}} = 200$ GeV ($|\eta| < 1.0$, $0.15 < p_T < 2$ GeV/c) are compared with ALICE [5] and STAR [29] v_2 data, respectively. ALICE data points are shifted horizontally for visibility.

in the present work, are realized in nature at both RHIC and LHC energies, the larger deviation of v_2 from the data at LHC than at RHIC in Figs. 4 and 5 could mean that viscous effects are larger at LHC than at RHIC. This can indicate a larger specific shear viscosity, η/s, at larger temperatures. For a better interpretation of current experimental data, the issue should be clarified in the near future by determining the initial conditions better and by a more detailed analysis using a hybrid model of viscous hydrodynamics and hadron cascade [33].

In summary, we calculated transverse momentum distribution of charged hadrons, centrality dependence of integrated elliptic flow parameter v_2, and differential elliptic flow $v_2(p_T)$ in Pb+Pb collisions at $\sqrt{s_{NN}} = 2.76$ TeV and in Au+Au collisions at $\sqrt{s_{NN}} = 200$ GeV. We compared v_2 and $v_2(p_T)$ with respect to the reaction plane from the hybrid model with v_2 data mainly obtained from the four-particle cumulant method. Transverse momentum distributions become harder, whereas the shape of $v_2(p_T)$ does not change so much as the collision energy increases. Thus the increase in p_T-integrated v_2 is from the increase in mean p_T. However, the intrinsic slope of $v_2(p_T)$ depends on the initialization: The slope from the MC-KLN initialization is steeper than that from the MC-Glauber initialization, and thus essentially the same change of mean p_T leads to a larger increase of p_T-integrated v_2 for MC-KLN initialization than for MC-Glauber initialization. The larger difference between the data and our MC-KLN result at LHC than at RHIC may indicate larger dissipative effects at LHC than at RHIC. All this emphasizes the importance of understanding initial conditions in relativistic heavy-ion collisions toward extracting the bulk and transport properties of the QGP. In the future, it would be interesting to compare our results with data obtained using a more sophisticated elliptic flow analysis [19], in which both nonflow and eccentricity fluctuation effects are removed.

We thank R. Snellings for providing us with the experimental data. The work of T.H. and Y.N. was partly supported by Grant-in-Aid for Scientific Research (Grants No. 22740151 and No. 20540276, respectively). T.H. is also supported under Excellent Young Researchers Oversea Visit Program (Grant No. 21-3383) by Japan Society for the Promotion of Science. The work of P.H. is supported by the ExtreMe Matter Institute (EMMI) and BMBF (Contract No. 06FY9092). T.H. thanks X. N. Wang and H. Song for fruitful discussion, and members in the nuclear theory group at Lawrence Berkeley National Laboratory for kind hospitality during his sabbatical stay.

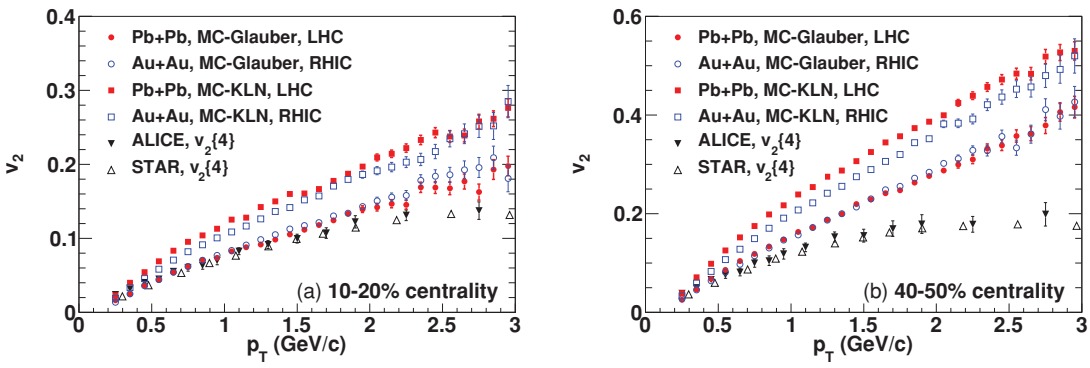

FIG. 5. (Color online) Transverse momentum dependencies of v_2 for charged hadrons in the MC-Glauber (circles) and the MC-KLN (squares) initialization are compared with ALICE [5] (triangles) and STAR [29] (band) $v_2\{4\}$ data in (a) 10%–20% centrality and (b) 40%–50% centrality. We take account of pseudorapidity cut, $|\eta| < 0.8$ (1.0), in the ALICE (STAR) data.

[1] J. Y. Ollitrault, Phys. Rev. D **46**, 229 (1992).
[2] M. Gyulassy, arXiv:nucl-th/0403032.
[3] T. D. Lee, Nucl. Phys. A **750**, 1 (2005); M. Gyulassy and L. McLerran, *ibid.* **750**, 30 (2005); E. V. Shuryak, *ibid.* **750**, 64 (2005).
[4] [http://www.bnl.gov/bnlweb/pubaf/pr/PR_display.asp?prID=05-38].
[5] K. Aamodt *et al.* (The ALICE Collaboration), arXiv:1011.3914 [nucl-ex].
[6] T. Hirano, P. Huovinen, and Y. Nara, Phys. Rev. C **83**, 021902 (2011).
[7] K. Aamodt *et al.* (The ALICE Collaboration), Phys. Rev. Lett. **105**, 252301 (2010).
[8] T. Hirano, Phys. Rev. C **65**, 011901 (2001); T. Hirano and K. Tsuda, *ibid.* **66**, 054905 (2002).
[9] Y. Nara, N. Otuka, A. Ohnishi, K. Niita, and S. Chiba, Phys. Rev. C **61**, 024901 (1999) [http://quark.phy.bnl.gov/∼ynara/jam/].
[10] M. Cheng *et al.*, Phys. Rev. D **77**, 014511 (2008).
[11] A. Bazavov *et al.*, Phys. Rev. D **80**, 014504 (2009).
[12] P. Huovinen and P. Petreczky, Nucl. Phys. A **837**, 26 (2010).
[13] [https://wiki.bnl.gov/hhic/index.php/Lattice_calculatons_of_Equation_of_State] and [https://wiki.bnl.gov/TECHQM/index.php/QCD_Equation_of_State].
[14] J. D. Bjorken, Phys. Rev. D **27**, 140 (1983).
[15] M. L. Miller, K. Reygers, S. J. Sanders, and P. Steinberg, Ann. Rev. Nucl. Part. Sci. **57**, 205 (2007).
[16] H. J. Drescher and Y. Nara, Phys. Rev. C **75**, 034905 (2007); **76**, 041903(R) (2007); [http://www.aiu.ac.jp/∼ynara/mckln/].
[17] N. Borghini, P. M. Dinh, and J. Y. Ollitrault, Phys. Rev. C **63**, 054906 (2001); **64**, 054901 (2001).
[18] S. A. Voloshin, A. M. Poskanzer, A. Tang, and G. Wang, Phys. Lett. B **659**, 537 (2008).
[19] J. Y. Ollitrault, A. M. Poskanzer, and S. A. Voloshin, Phys. Rev. C **80**, 014904 (2009).
[20] T. Hirano and Y. Nara, Phys. Rev. C **79**, 064904 (2009).
[21] A. Adil, H. J. Drescher, A. Dumitru, A. Hayashigaki, and Y. Nara, Phys. Rev. C **74**, 044905 (2006).
[22] P. Sorensen, B. Bolliet, A. Mocsy, Y. Pandit, and N. Pruthi, arXiv:1102.1403 [nucl-th].
[23] D. Kharzeev and M. Nardi, Phys. Lett. B **507**, 121 (2001); D. Kharzeev and E. Levin, *ibid.* **523**, 79 (2001); D. Kharzeev, E. Levin, and M. Nardi, Phys. Rev. C **71**, 054903 (2005); Nucl. Phys. A **730**, 448 (2004).
[24] S. S. Adler *et al.* (PHENIX Collaboration), Phys. Rev. C **69**, 034909 (2004).
[25] K. Aamodt *et al.* (The ALICE Collaboration), Phys. Rev. Lett. **106**, 032301 (2011).
[26] K. Aamodt *et al.* (ALICE Collaboration), Eur. Phys. J. C **68**, 89 (2010).
[27] T. Hirano, U. W. Heinz, D. Kharzeev, R. Lacey, and Y. Nara, Phys. Lett. B **636**, 299 (2006).
[28] T. Hirano, P. Huovinen, and Y. Nara (in preparation).
[29] J. Adams *et al.* (STAR Collaboration), Phys. Rev. C **72**, 014904 (2005).
[30] M. Luzum, Phys. Rev. C **83**, 044911 (2011).
[31] P. F. Kolb, Heavy Ion Phys. **15**, 279 (2002).
[32] F. Gelis, E. Iancu, J. Jalilian-Marian, and R. Venugopalan, Ann. Rev. Nucl. Part. Sci. **60**, 463 (2010).
[33] H. Song, S. A. Bass, U. W. Heinz, T. Hirano, and C. Shen, Phys. Rev. Lett. **106**, 192301 (2011).

PHYSICAL REVIEW C **83**, 021902(R) (2011)

Elliptic flow in U+U collisions at $\sqrt{s_{NN}} = 200$ GeV and in Pb+Pb collisions at $\sqrt{s_{NN}} = 2.76$ TeV: Prediction from a hybrid approach

Tetsufumi Hirano,[1,2,*] Pasi Huovinen,[3,†] and Yasushi Nara[4,‡]
[1]*Department of Physics, the University of Tokyo, Tokyo 113-0033, Japan*
[2]*Nuclear Science Division, Lawrence Berkeley National Laboratory, Berkeley, California 94720, USA*
[3]*Institut für Theoretische Physik, Johann Wolfgang Goethe-Universität, D-60438 Frankfurt am Main, Germany*
[4]*Akita International University, Yuwa, Akita City 010-1292, Japan*
(Received 8 November 2010; revised manuscript received 20 December 2010; published 10 February 2011)

We predict the elliptic flow parameter v_2 in U+U collisions at $\sqrt{s_{NN}} = 200$ GeV and in Pb+Pb collisions at $\sqrt{s_{NN}} = 2.76$ TeV using a hybrid model in which the evolution of the quark gluon plasma is described by ideal hydrodynamics with a state-of-the-art lattice QCD equation of state and the subsequent hadronic stage is described by a hadron cascade model.

DOI: 10.1103/PhysRevC.83.021902 PACS number(s): 25.75.Nq, 12.38.Mh, 12.38.Qk, 25.75.Ld

One of the major discoveries at the Relativistic Heavy Ion Collider (RHIC) in Brookhaven National Laboratory (BNL) was that for the first time in relativistic heavy-ion collisions, the elliptic flow appeared to be as large as an ideal hydrodynamic prediction [1]. Since viscosity and any other dissipative effects vanish in ideal hydrodynamics, and tiny viscosity requires a strong coupling of constituents (quarks and gluons in our case), this discovery established the new paradigm of strongly coupled quark gluon plasma (QGP) [2,3].

In noncentral collisions, rescatterings of the created particles convert the initial spatial anisotropy of the reaction zone to anisotropic particle distribution [4]. Ideal hydrodynamics predicts that the ratio of these anisotropies is $v_2/\varepsilon \sim 0.2$, almost independent of centrality at the RHIC energies [5]. Here, v_2 is the second Fourier coefficient of the azimuthal distribution of final particles, and ε is the initial eccentricity of the produced matter. On the other hand, in the dilute regime, kinetic theory predicts v_2 to be proportional to the particle multiplicity per unit rapidity, dN/dy [6,7]. Thus, the response of the system, v_2/ε, provides information about the transport properties of the QGP. Experimentally v_2/ε is seen to increase with increasing transverse density $(1/S)dN/dy$ [8,9], where S is the transverse area of the collision zone, until it reaches the so-called hydrodynamic limit, $v_2/\varepsilon \sim 0.2$, in central Au+Au collisions at RHIC. With the agreement of the hydrodynamical prediction of the particle mass dependence of $v_2(p_T)$ [10] with the data [11,12], this is considered as evidence for the discovery of the perfect-fluid nature of the QGP [1].

After observing the increase of v_2/ε with increasing transverse density, it is natural to ask what happens if the transverse density increases beyond that achieved at RHIC [13]. Will it saturate to the value observed at RHIC, as expected if the system behaves like a perfect fluid, or will it keep increasing? One suggested way to extend the transverse density is to perform uranium-uranium collisions [13]. Since uranium nuclei are deformed and larger than gold nuclei, one can expect large transverse density with finite eccentricity in the body-body collisions at vanishing impact parameter.[1] Some Monte Carlo studies show that even though one cannot control the orientation of colliding nuclei, events with high multiplicity though finite eccentricity can be selected in the usual triggering process [13,15–18]. Another way to extend the transverse energy is to increase the collision energy to generate more particles in collisions. This is going to happen very soon in the Large Hadron Collider (LHC) heavy-ion program. In this Rapid Communication, we predict elliptic flow parameters both in U+U collisions at RHIC and Pb+Pb collisions at LHC using a hybrid model based on ideal hydrodynamics and hadron cascade.

We describe space-time evolution of the QGP by ideal hydrodynamics [19] with the recent lattice QCD equation of state [20]. After expansion and cooling, the system turns into hadronic matter. We switch from hydrodynamics to a kinetic approach at a switching temperature $T_{\rm sw}$ and employ a hadronic cascade model, JAM [21], to describe the subsequent space-time evolution of hadronic matter.

Our equation of state (EoS), $s95p$-v1.1, is a slightly modified version of the $s95p$-v1 EoS presented in Ref. [20]. It interpolates between hadron resonance gas at low temperatures and recent lattice QCD results by the hotQCD Collaboration [22,23] at high temperatures in the same way as $s95p$-v1, but the hadron resonance gas part contains the same hadrons and resonances as the JAM hadron cascade [21]. The details of the interpolating procedure are explained in Ref. [20], and the parametrization and EoS tables are available in Ref. [24].

For initial conditions, we employ two Monte Carlo approaches to simulate collisions of two energetic nuclei: Monte Carlo Glauber (MC-Glauber) model [25] and Monte Carlo Kharzeev-Levin-Nardi (MC-KLN) model [26]. In the MC-Glauber model, one calculates the number of participants $N_{\rm part}$ and the number of binary collisions $N_{\rm coll}$ for a given nuclear density distribution. We model the initial entropy distribution in hydrodynamic simulations as a linear combination of the

*hirano@phys.s.u-tokyo.ac.jp
†huovinen@th.physik.uni-frankfurt.de
‡nara@aiu.ac.jp

[1]The idea of collisions of deformed nuclei is not new, and one can find literature on this subject. See, e.g., Refs. [5,14].

number distribution of participants $\rho_{\rm part} = \frac{dN_{\rm part}}{d^2\boldsymbol{x}_\perp}$ and that of binary collisions $\rho_{\rm coll} = \frac{dN_{\rm coll}}{d^2\boldsymbol{x}_\perp}$ in the transverse plane:

$$\frac{dS}{d^2\boldsymbol{x}_\perp} \propto \frac{1-\alpha}{2}\rho_{\rm part}(\boldsymbol{x}_\perp) + \alpha\rho_{\rm coll}(\boldsymbol{x}_\perp). \quad (1)$$

We generate the number distributions on an event-by-event basis, align them to match the main axes and subaxes of the ellipsoids, and average over many events for a given centrality bin to obtain a smooth distribution [27]. The eccentricity of the initial profile is then evaluated with respect to participant plane, $\varepsilon_{\rm part}$ [28]. We do the centrality cuts according to the $N_{\rm part}$ distribution from the MC Glauber model instead of using the optical Glauber limit as was done in Ref. [27]. The free parameters of the model, the mixing parameter $\alpha = 0.18$ and the proportionality constant in Eq. (1), are chosen to reproduce transverse momentum spectra for pions, kaons, and protons from central (0–5%) to peripheral (70–80%) events in Au+Au collisions at $\sqrt{s_{NN}} = 200$ GeV obtained by the PHENIX Collaboration [29]. We also choose the switching temperature as $T_{\rm sw} = 155$ MeV to describe the relative yields for pions, kaons, and protons in these data.

The MC-KLN model is a Monte Carlo version of the factorized Kharzeev-Levin-Nardi (fKLN) model [30]. In the MC-KLN model, gluon production is obtained by numerical integration of the k_t-factorized formula [31] at each transverse grid. The fluctuation of gluon distribution due to the position of hard sources (nucleons) in the transverse plane is taken into account in MC-KLN. Using the thickness function T_A, we parametrize the saturation scale for a nucleus A as

$$Q^2_{s,A}(x;\boldsymbol{x}_\perp) = 2\ {\rm GeV}^2 \frac{T_A(\boldsymbol{x}_\perp)}{1.53\ {\rm fm}^{-2}} \left(\frac{0.01}{x}\right)^\lambda \quad (2)$$

and similarly for a nucleus B. We choose $\lambda = 0.28$ and a proportionality constant in the unintegrated gluon distribution in the k_t-factorized formula to reproduce centrality dependence of p_T spectra for pions, kaons, and protons as before.

Using this parameter set, we calculate initial entropy distribution in U+U collisions by changing the nuclear density from gold to uranium. To take account of the prolate deformation of uranium nuclei, we parametrize the radius parameter in the Woods-Saxon distribution as

$$R(\theta,\phi) = R_0[1 + \beta_2 Y_{20}(\theta,\phi) + \beta_4 Y_{40}(\theta,\phi)], \quad (3)$$

where Y_{lm} is the spherical harmonic function, $R_0 = 6.86$ fm, $\beta_2 = 0.28$, and $\beta_4 = 0.093$ [32]. Note that to account for the finite size of nucleons in the Monte Carlo approach, we have adjusted R_0 and the diffuseness parameter $\delta r = 0.44$ to retain the nuclear density as in the original Woods-Saxon distribution [27]. We also take into account that colliding uranium nuclei are randomly oriented in each event.

Figure 1(a) shows initial eccentricity with respect to participant plane in Au+Au and U+U collisions at $\sqrt{s_{NN}} = 200$ GeV as a function of the number of participants. At each of the ten centrality bins, the average eccentricity and the average number of participants $\langle N_{\rm part}\rangle$ were calculated using both the MC-Glauber and the MC-KLN models. Since the eccentricity is measured in the participant plane, it is finite even in the very central (0–5%) Au+Au collisions. As previously known, the MC-KLN model leads to ∼20–30% larger eccentricity than the MC-Glauber model except in the most central events [30,33]. In the most central 5% of U+U collisions, eccentricity reaches 0.146 in the MC-Glauber model and 0.148 in the MC-KLN model. The eccentricity is larger in U+U than in Au+Au collisions. Because of the deformed shape of uranium nucleus, this holds not only at fixed number of participants but also at fixed centrality. However, the difference decreases with decreasing centrality, and there is almost no difference in the very peripheral events (70–80%).

In Fig. 1(b), v_2 in Au+Au collisions is compared with the v_2 in U+U collisions. Since the rule of thumb is that larger eccentricity leads to larger momentum anisotropy and v_2, the systematics of $v_2(N_{\rm part})$ is similar to that of $\varepsilon_{\rm part}(N_{\rm part})$: v_2 is larger in U+U collisions than in Au+Au collisions, and MC-KLN initialization leads to larger v_2 than MC-Glauber initialization. As well, v_2 first increases with decreasing $N_{\rm part}$, which reflects increasing initial eccentricity, but once $N_{\rm part}$ falls to less than ∼50, v_2 begins to decrease. This is due to the short lifetime of the system, which does not allow the flow to fully build up, and to the large fraction of the lifetime spent in the hadronic phase where dissipative effects are large.

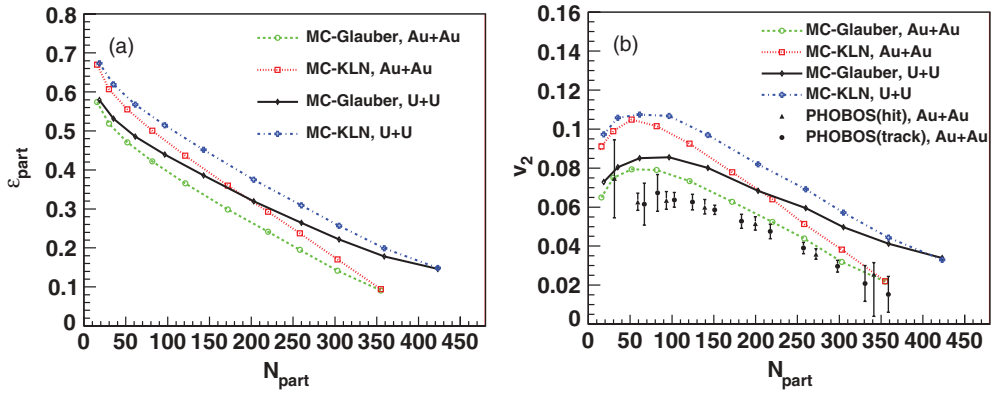

FIG. 1. (Color online) (a) Initial-state eccentricity $\varepsilon_{\rm part}$ and (b) v_2 as a function of $N_{\rm part}$ in Au+Au and U+U collisions at $\sqrt{s_{NN}} = 200$ GeV. Experimental data of v_2 in Au+Au collisions were obtained by the PHOBOS Collaboration [34].

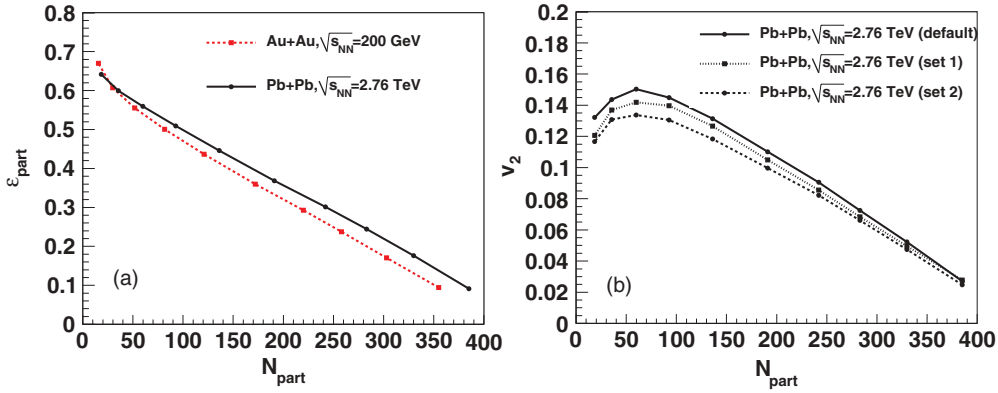

FIG. 2. (Color online) (a) $\varepsilon_{\rm part}$ as a function of $N_{\rm part}$ in Au+Au collisions at $\sqrt{s_{NN}} = 200$ GeV (dashed line) and in Pb+Pb collisions at $\sqrt{s_{NN}} = 2.76$ TeV (solid line); (b) v_2 as function of number of participants $N_{\rm part}$ in Pb+Pb collisions at $\sqrt{s_{NN}} = 2.76$ TeV for three different multiplicities in 0–5% centrality: $dN_{\rm ch}/d\eta \sim 1600$ (solid), 1400 (dotted), and 1200 (dashed). Each point from right to left corresponds to 0–5%, 5–10%, 10–15%, 15–20%, 20–30%, 30–40%, 40–50%, 50–60%, 60–70%, and 70–80% centrality, respectively.

Results from the MC-Glauber initialization almost reproduce the PHOBOS data [34] in Au+Au collisions. This indicates that there is little room for QGP viscosity in the model calculations. On the other hand, the apparent discrepancy between the results from the MC-KLN initialization and the PHOBOS data means that viscous corrections during the plasma phase are required.

Within the color glass condensate picture, the collision energy dependence is taken into account through the saturation scale, Q_s. This allows us to simulate the Pb+Pb collisions at $\sqrt{s_{NN}} = 2.76$ TeV by using the MC-KLN model, adjusting the collision energy parameter and the nuclear density parametrization, and keeping all the other parameters unchanged. This is a consistent way to study the differences between collisions at $\sqrt{s_{NN}} = 62.4$ GeV and 2.76 TeV energies, but it may be too naive, because the MC-KLN model does not take into account running coupling corrections to the evolution equation [35]. At RHIC energies, these effects are known to be small, but at LHC they lead to a clearly lower multiplicity [35,36]. On the other hand, these effects hardly affect the eccentricity [36], which allows us to study the effects of the uncertainty in the final particle multiplicity simply by adjusting the overall factor in the unintegrated gluon distribution function. Our default approach is to use the MC-KLN model with the same factor as in the RHIC calculations. In the most central 5% of Pb+Pb collisions, this leads to multiplicity $dN_{\rm ch}/d\eta \sim 1600$ at midrapidity ($|\eta| < 1$). We also reduce the factor to obtain multiplicities $dN_{\rm ch}/d\eta \sim 1400$ (set 1), as predicted in Ref. [35], and ∼1200 (set 2).[2]

Our result for the initial-state eccentricity as function of the number of participants in Au+Au collisions at $\sqrt{s_{NN}} = 200$ GeV and in Pb+Pb collisions at $\sqrt{s_{NN}} = 2.76$ TeV is shown in Fig. 2(a). As mentioned, the uncertainty in the multiplicity in collisions at $\sqrt{s_{NN}} = 2.76$ TeV does not affect the eccentricity, and we show the result obtained using our default setting. For a fixed $N_{\rm part}$, eccentricity at LHC is apparently larger than that at RHIC. However, this is due solely to the larger size of colliding nuclei. If one compares the eccentricity at a fixed *centrality* (see each point in the figure), eccentricities are essentially the same.

In Fig. 2(b), v_2 in Pb+Pb collisions at $\sqrt{s_{NN}} = 2.76$ TeV is shown as a function of the number of participants for three different multiplicities in central collisions. The larger the multiplicity, the larger the v_2, but even at the lowest setting of multiplicity, v_2 is clearly larger than in the Au+Au collisions at $\sqrt{s_{NN}} = 200$ GeV.

This behavior is clearly visible in Fig. 3, where we plot $v_2/\varepsilon_{\rm part}$ as a function of the transverse charged-particle density $(1/S)dN_{\rm ch}/d\eta$ at midrapidity ($|\eta| < 1$) for various collision systems and energies. First, as expected, the system in U+U

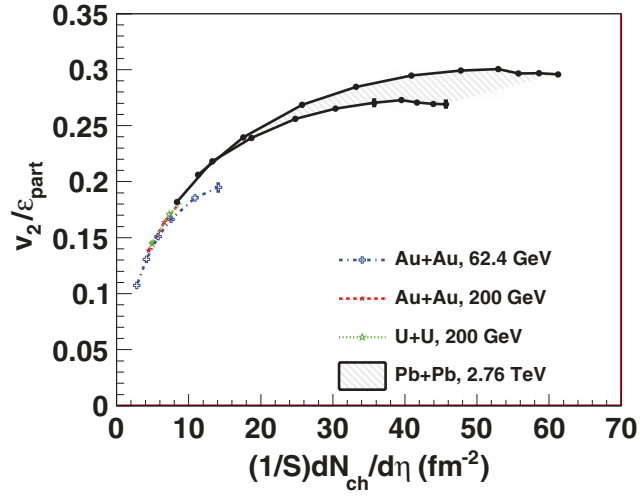

FIG. 3. (Color online) The $v_2/\varepsilon_{\rm part}$ as a function of transverse density in Au+Au collisions at $\sqrt{s_{NN}} = 62.4$ (dash-dotted line) and 200 GeV (dashed line), in U+U collisions at $\sqrt{s_{NN}} = 200$ GeV (dotted line), and in Pb+Pb collisions at $\sqrt{s_{NN}} = 2.76$ TeV (band). The band depicting the Pb+Pb collisions spans the results obtained using the multiplicities $1200 < dN_{\rm ch}/d\eta < 1600$ in the most central 5% of collisions.

[2] η is not the shear viscous coefficient but the pseudorapidity.

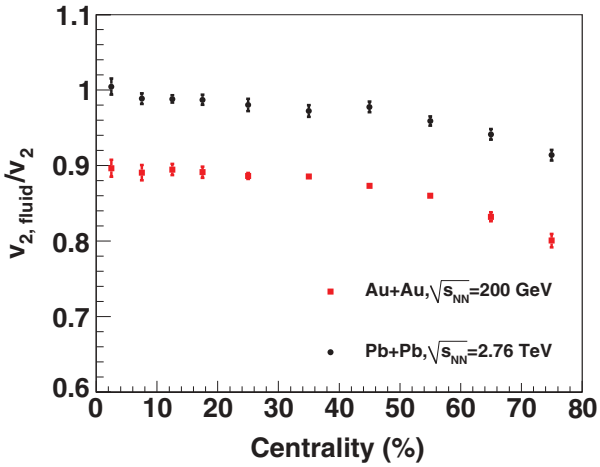

FIG. 4. (Color online) Ratio of v_2 generated during the hydrodynamical evolution to the final v_2, $v_{2,\mathrm{fluid}}/v_2$, in Au+Au and Pb+Pb collisions at $\sqrt{s_{NN}} = 200$ GeV and 2.76 TeV, respectively.

collisions at $\sqrt{s_{NN}} = 200$ GeV is denser than in Au+Au collisions at the same energy. At initial time $\tau_0 = 0.6$ fm/c, the maximum temperature (energy density) in the most central 5% of U+U collisions is $T_0 = 367$ MeV ($e_0 = 33.4$ GeV/fm^3) and $T_0 = 361$ MeV ($e_0 = 31.4$ GeV/fm^3) in the Au+Au collisions of the same centrality. This corresponds to charged-particle transverse densities of 25.4 and 24.1, respectively, which means that the transverse density in U+U collisions is indeed larger, but only by ∼6%.[3] In spite of the differences in the colliding systems, results for various centralities in U+U collisions almost trace the ones in Au+Au collisions, which would suggest existence of scaling behavior in $v_2/\varepsilon_{\mathrm{part}}$ versus $(1/S)dN_{\mathrm{ch}}/d\eta$.

However, the behavior of $v_2/\varepsilon_{\mathrm{part}}$ in Pb+Pb collisions at $\sqrt{s_{NN}} = 2.76$ TeV is very different. In these collisions, the system is much denser than in the collisions at RHIC energies. The maximum temperatures at the initial time $\tau_0 = 0.6$ fm/c are $T_0 = 475, 457, 436$ MeV ($e_0 = 97.0, 82.4, 68.4$ GeV/fm^3) for $dN_{\mathrm{ch}}/d\eta \sim 1600, 1400, 1200$ in the most central 5% of collisions, respectively, which corresponds to roughly 2–2.5 times larger transverse density than in most central Au+Au collisions at $\sqrt{s_{NN}} = 200$ GeV. As can be seen, $v_2/\varepsilon_{\mathrm{part}}$ no longer follows the scaling curve seen at the top RHIC energy, but it reaches ∼0.26–0.3 in central collisions. This value is ∼20–35% larger than the value at RHIC, which is often considered a hydrodynamical upper limit in the literature [37].

The reason for this breaking of the scaling is not in the cascade treatment of the hadronic phase. If anything, dissipation should reduce v_2, so hadron cascade cannot be responsible for the large value of $v_2/\varepsilon_{\mathrm{part}}$ seen here. We have also checked that at LHC, the major part of v_2 is generated during the hydrodynamical stage, and the effects of hadronic cascade are less important than at RHIC. The ratio of v_2 generated during the hydrodynamical evolution to the final v_2, $v_{2,\mathrm{fluid}}/v_2$, in collisions at RHIC and LHC is shown in Fig. 4. As can be seen, the contribution of hadronic cascade to the total v_2 with default setting at LHC is less than 5% at most centralities. However, the effect on the p_T spectra of heavy particles is significant, and one should not ignore the late hadronic effects. On the other hand, the contribution reaches 10–20% of the total v_2 in Au+Au collisions at the top RHIC energy.

To further study the collision energy dependence of $v_2/\varepsilon_{\mathrm{part}}$, we do the calculation using the lower RHIC energy $\sqrt{s_{NN}} = 62.4$ GeV. As seen in Fig. 3, the ratio in central collisions (0–30%) deviates from the scaling curve seen at $\sqrt{s_{NN}} = 200$ GeV, but the amount of the deviation might be too small to be experimentally observable. The collision energy independence of $v_2/\varepsilon_{\mathrm{part}}$ is seen in $(1/S)dN_{\mathrm{ch}}/d\eta \lesssim 10$ (fm^{-2}), which corresponds to $dN_{\mathrm{ch}}/d\eta \lesssim 50$ where hadronic cascading plays a major role in the whole evolution. Note that the collision energy dependence of $v_2/\varepsilon_{\mathrm{part}}$ is consistent with the early calculations where v_2 continuously increases with total pion multiplicity dN_π/dy at midrapidity up to 3000 at a fixed impact parameter ($b = 7$ fm) [5]. See also Ref. [38] for a previous calculation in which the bag model equation of state and a higher switching temperature $T_{\mathrm{sw}} = 169$ MeV were used. The agreement with previous hydrodynamical results means that our result does not break any hydrodynamical upper limit for v_2/ε. It corroborates the old results and shows that the hydrodynamical limit for v_2/ε depends on collision energy.

Recently, a prediction of elliptic flow as a function of transverse charged-particle density up to the LHC energies was made using viscous hydrodynamics in Ref. [39]. To avoid the uncertainties associated with the freeze-out process, v_2 was evaluated in that paper by calculating the momentum anisotropy

$$e_p = \frac{\int dxdy(T^{xx} - T^{yy})}{\int dxdy(T^{xx} + T^{yy})} \tag{4}$$

and relying on an empirical formula $v_2 \approx e_p/2$ [40]. We have checked the validity of this formula in our calculations and found that in the collisions at the LHC energy, the ratio is $v_2/e_p \approx 2/3$, not 1/2. This discrepancy is not surprising. First, it is known that the ratio strongly depends on the freeze-out temperature [41]. The momentum anisotropy depicts the anisotropy of the collective motion, whereas v_2 reflects the anisotropy of the momenta of individual particles, which includes thermal motion and the effects due to resonance decays [42] and the shape of the source [43]. Second, the formula was found to hold in ideal fluid calculations. There is no reason why it should be the same for viscous hydrodynamics.

To summarize, we predicted elliptic flow parameter v_2 in U+U collisions at $\sqrt{s_{NN}} = 200$ GeV and in Pb+Pb collisions at $\sqrt{s_{NN}} = 2.76$ TeV using a hybrid approach that combines ideal hydrodynamic description of the QGP fluid and kinetic description of the hadronic gas. Because of deformation of uranium, eccentricity is larger in U+U collisions than

[3]With sufficient statistics, one may make a more severe centrality cut (e.g., 0–3%) to obtain larger transverse particle density. Multiplicity fluctuation in the centrality cut, which we do not take into account, could also enhance the transverse particle density.

in Au+Au collisions. We found the maximum transverse particle density is ∼6% larger in the 0–5% most central U+U collisions. The $v_2/\varepsilon_{\rm part}$ in U+U collisions follows the results in Au+Au collisions, which suggests a scaling behavior between $v_2/\varepsilon_{\rm part}$ and $(1/S)dN_{\rm ch}/d\eta$. However, at the LHC energy, $v_2/\varepsilon_{\rm part}$ does *not* follow the same scaling curve and reaches the maximum value of ∼0.26–0.30 depending on the final particle multiplicity. This is clearly larger than the corresponding maximum value at the top RHIC energy, $v_2/\varepsilon_{\rm part} \sim 0.22$, and the so-called hydrodynamic limit for v_2/ε is not the same at RHIC and LHC energies.

Acknowledgments. The work of T.H. (Y.N.) was partly supported by Grant-in-Aid for Scientific Research No. 22740151 (No. 20540276). T.H. is also supported under the Excellent Young Researchers Oversea Visit Program (No. 21-3383) by Japan Society for the Promotion of Science. P.H.'s work is supported by the ExtreMe Matter Institute (EMMI). We acknowledge fruitful discussion with A. Dumitru. T.H. thanks members in the nuclear theory group at Lawrence Berkeley National Laboratory for their kind hospitality during his sabbatical stay and M. Gyulassy for his suggestion to calculate v_2 at the LHC energies.

[1] [http://www.bnl.gov/bnlweb/pubaf/pr/PR_display.asp?prID=05-38].
[2] M. Gyulassy, arXiv:nucl-th/0403032.
[3] T. D. Lee, Nucl. Phys. A **750**, 1 (2005); M. Gyulassy and L. McLerran, *ibid.* **750**, 30 (2005); E. V. Shuryak, *ibid.* **750**, 64 (2005).
[4] J. Y. Ollitrault, Phys. Rev. D **46**, 229 (1992).
[5] P. F. Kolb, J. Sollfrank, and U. W. Heinz, Phys. Rev. C **62**, 054909 (2000).
[6] H. Heiselberg and A.-M. Levy, Phys. Rev. C **59**, 2716 (1999).
[7] P. F. Kolb, P. Huovinen, U. W. Heinz, and H. Heiselberg, Phys. Lett. B **500**, 232 (2001).
[8] C. Adler *et al.* (STAR Collaboration), Phys. Rev. C **66**, 034904 (2002).
[9] C. Alt *et al.* (NA49 Collaboration), Phys. Rev. C **68**, 034903 (2003).
[10] P. Huovinen, P. F. Kolb, U. W. Heinz, P. V. Ruuskanen, and S. A. Voloshin, Phys. Lett. B **503**, 58 (2001).
[11] J. Adams *et al.* (STAR Collaboration), Phys. Rev. Lett. **92**, 052302 (2004).
[12] S. S. Adler *et al.* (PHENIX Collaboration), Phys. Rev. Lett. **91**, 182301 (2003).
[13] U. W. Heinz and A. Kuhlman, Phys. Rev. Lett. **94**, 132301 (2005).
[14] C. Nonaka, E. Honda, and S. Muroya, Eur. Phys. J. C **17**, 663 (2000).
[15] A. J. Kuhlman and U. W. Heinz, Phys. Rev. C **72**, 037901 (2005).
[16] C. Nepali, G. Fai, and D. Keane, Phys. Rev. C **73**, 034911 (2006).
[17] C. Nepali, G. I. Fai, and D. Keane, Phys. Rev. C **76**, 051902 (2007); **76**, 069903(E) (2007).
[18] H. Masui, B. Mohanty, and N. Xu, Phys. Lett. B **679**, 440 (2009).
[19] T. Hirano, Phys. Rev. C **65**, 011901 (2001).
[20] P. Huovinen and P. Petreczky, Nucl. Phys. A **837**, 26 (2010).
[21] Y. Nara, N. Otuka, A. Ohnishi, K. Niita, and S. Chiba, Phys. Rev. C **61**, 024901 (1999).
[22] M. Cheng *et al.*, Phys. Rev. D **77**, 014511 (2008).
[23] A. Bazavov *et al.*, Phys. Rev. D **80**, 014504 (2009).
[24] [https://wiki.bnl.gov/hhic/index.php/Lattice_calculaton_of_Equation_of_State] and [https://wiki.bnl.gov/TECHQM/index.php/QCD_Equation_of_State].
[25] M. L. Miller, K. Reygers, S. J. Sanders, and P. Steinberg, Ann. Rev. Nucl. Part. Sci. **57**, 205 (2007).
[26] H. J. Drescher and Y. Nara, Phys. Rev. C **75**, 034905 (2007); **76**, 041903(R) (2007).
[27] T. Hirano and Y. Nara, Phys. Rev. C **79**, 064904 (2009).
[28] B. Alver *et al.*, Phys. Rev. C **77**, 014906 (2008).
[29] S. S. Adler *et al.* (PHENIX Collaboration), Phys. Rev. C **69**, 034909 (2004).
[30] A. Adil, H. J. Drescher, A. Dumitru, A. Hayashigaki, and Y. Nara, Phys. Rev. C **74**, 044905 (2006).
[31] D. Kharzeev and M. Nardi, Phys. Lett. B **507**, 121 (2001); D. Kharzeev and E. Levin, *ibid.* **523**, 79 (2001); D. Kharzeev, E. Levin, and M. Nardi, Phys. Rev. C **71**, 054903 (2005); Nucl. Phys. A **730**, 448 (2004).
[32] P. Filip, R. Lednicky, H. Masui, and N. Xu, Phys. Rev. C **80**, 054903 (2009).
[33] T. Hirano, U. W. Heinz, D. Kharzeev, R. Lacey, and Y. Nara, Phys. Lett. B **636**, 299 (2006).
[34] B. B. Back *et al.* (PHOBOS Collaboration), Phys. Rev. C **72**, 051901 (2005).
[35] J. L. Albacete, Phys. Rev. Lett. **99**, 262301 (2007).
[36] A. Dumitru (private communication); [http://physics.baruch.cuny.edu/node/people/adumitru/res_cgc].
[37] S. A. Voloshin, A. M. Poskanzer, and R. Snellings, arXiv:0809.2949 [nucl-ex].
[38] T. Hirano, U. W. Heinz, D. Kharzeev, R. Lacey, and Y. Nara, J. Phys. G **34**, S879 (2007).
[39] M. Luzum and P. Romatschke, Phys. Rev. Lett. **103**, 262302 (2009).
[40] P. F. Kolb, J. Sollfrank, and U. W. Heinz, Phys. Lett. B **459**, 667 (1999).
[41] P. Huovinen, in *Quark-Gluon Plasma 3*, edited by R. C. Hwa and X. N. Wang (World Scientific, Singapore, 2004), p. 600.
[42] T. Hirano, Phys. Rev. Lett. **86**, 2754 (2001).
[43] P. Huovinen, P. F. Kolb, and U. W. Heinz, Nucl. Phys. A **698**, 475 (2002).

Systematic parameter study of hadron spectra and elliptic flow from viscous hydrodynamic simulations of Au + Au collisions at $\sqrt{s_{NN}} = 200$ GeV

Chun Shen* and Ulrich Heinz†
Department of Physics, The Ohio State University, Columbus, Ohio 43210-1117, USA

Pasi Huovinen‡
Institut für Theoretische Physik, Johann Wolfgang Goethe-Universität, Max-von-Laue-Straße 1, D-60438 Frankfurt am Main, Germany

Huichao Song§
Department of Physics, The Ohio State University, Columbus, Ohio 43210-1117, USA and
Lawrence Berkeley National Laboratory, 1 Cyclotron Road, MS70R0319, Berkeley, California 94720, USA
(Received 9 October 2010; published 12 November 2010)

Using the $(2+1)$-dimensional viscous hydrodynamic code VISH2 + 1 [H. Song and U. Heinz, Phys. Lett. B **658**, 279 (2008); H. Song and U. Heinz, Phys. Rev. C **77**, 064901 (2008); H. Song, Ph. D. thesis, The Ohio State University, 2009], we present systematic studies of the dependence of pion and proton transverse-momentum spectra and their elliptic flow in 200A GeV Au + Au collisions on the parameters of the hydrodynamic model (thermalization time, initial entropy density distribution, decoupling temperature, equation of state, and specific shear viscosity η/s). We identify a tension between the slope of the proton spectra, which (within hydrodynamic simulations that assume a constant shear viscosity to entropy density ratio) prefer larger η/s values, and the slope of the p_T dependence of charged hadron elliptic flow, which prefers smaller values of η/s. Changing other model parameters does not appear to permit dissolution of this tension.

DOI: 10.1103/PhysRevC.82.054904 PACS number(s): 25.75.Dw, 25.75.Ld, 24.10.Nz, 47.75.+f

I. INTRODUCTION

After experiments at the Relativistic Heavy Ion Collider (RHIC) [1–4] and their theoretical analysis [5–7] established that the quark-gluon plasma (QGP) created in ultrarelativistic heavy-ion collisions is strongly coupled and behaves like an almost ideal fluid ("perfect liquid") with very small viscosity, interest in the theoretical and phenomenological determination of the QGP transport parameters, in particular its specific shear viscosity η/s (i.e., the ratio between its shear viscosity η and entropy density s), soared (see Refs. [8,9] for recent reviews). In principle, it should be possible to extract this quantity from heavy-ion collision experiments by comparing the measured hadron spectra and their azimuthal anisotropies (in particular their elliptic flow) with theoretical simulations of the collision dynamics which treat the QGP shear viscosity as an adjustable parameter [10,11]. In practice, this is a complex and difficult task that requires careful and highly constrained simulations of all dynamical stages of the collision that sandwich the viscous hydrodynamic expansion of the QGP between nonequilibrium phases describing (i) the initial geometry and early evolution of the fireball before its thermalization and (ii) the final kinetic hadron rescattering stage after its hadronization [12,13].

The present work is a contribution to help prepare the path for such a phenomenological extraction of $(\eta/s)_{\rm QGP}$. It employs viscous hydrodynamics to describe the fireball evolution, side-stepping the issues related to early and late nonequilibrium evolution by replacing the output from the (hypothetical) early nonequilibrium evolution model by initial conditions for the hydrodynamic stage (to be adjusted *post facto* to final hadron spectra and multiplicities in central collisions [6]), and the late-stage hadronic rescattering and kinetic freeze-out by a sudden transition from viscous fluid to free-streaming particles, using the Cooper-Frye algorithm [14] along a hypersurface of constant temperature $T_{\rm dec}$. This generalizes analogous attempts to describe experimental data from 200A GeV Au + Au collisions at RHIC with ideal fluid dynamics [6,15–21] to the case of viscous fluid dynamics. Related work has already been reported in Refs. [10,22]; what distinguishes the present study from these earlier articles is that we use a state-of-the-art equation of state that matches the latest lattice QCD data [23,24] at high temperatures to a realistic, chemically nonequilibrated hadron resonance gas at low temperatures. The construction of this equation of state (EOS) is described in Ref. [25], except that we here implement chemical freeze-out of the stable hadron yield ratios at $T_{\rm chem} = 165$ MeV by imposing appropriate temperature dependent nonequilibrium chemical potentials for each hadron species below $T_{\rm chem}$ [15,16,19,26,27]. This ensures that the final hadron yield ratios from our simulations are consistent with their measured values which indicate chemical equilibrium at temperature $T_{\rm chem} \approx 160$–170 MeV [3,28,29].

The purpose of this study is *not* a detailed viscous hydrodynamic fit to the RHIC data; its goal is rather to build intuition for systematic trends and parameter dependences that will be useful in forthcoming more ambitious fit attempts. One feature that disqualifies the present model study from being taken too seriously in comparison with the experimental data

*Corresponding author: shen@mps.ohio-state.edu
†heinz@mps.ohio-state.edu
‡huovinen@th.physik.uni-frankfurt.de
§HSong@LBL.gov

is our assumption of a constant (i.e., temperature independent) specific entropy η/s. While η/s is probably small in the QGP phase [10,11,30], possibly close to the Kovtun-Starinets-Son (KSS) bound $(\frac{\eta}{s})_{\rm KSS} = \frac{1}{4\pi}$ [31,32], it is expected to increase dramatically in the late dilute hadronic phase [33,34]. This can have important consequences for the evolution of flow in relativistic heavy-ion collisions [35] which will be studied in a separate article [36].

II. HYDRODYNAMIC EQUATIONS, INITIAL AND FINAL CONDITIONS

In this work, we use viscous hydrodynamics to simulate the collision system by solving the second-order Israel-Stewart equations as described in Ref. [37]. The energy-momentum tensor of the fluid is decomposed as

$$T^{\mu\nu} = eu^\mu u^\nu - (p + \Pi)\Delta^{\mu\nu} + \pi^{\mu\nu}, \tag{1}$$

where e is the local energy density, p is the thermal equilibrium pressure [given by the equation of state $p(e)$, see below], u^μ is the local flow four-velocity, $\Delta^{\mu\nu} = g^{\mu\nu} - u^\mu u^\nu$ is the spatial projector in the local fluid rest frame, Π is the bulk viscous pressure (which we set to zero in this article, assuming that effects from bulk viscosity can be ignored relative to those caused by shear viscosity [38]), and $\pi^{\mu\nu}$ is the traceless and symmetric shear pressure tensor satisfying $u_\mu \pi^{\mu\nu} = 0$. The equations of motion are the hydrodynamic equations

$$d_\mu T^{\mu\nu} = 0, \tag{2}$$

where d_μ denotes the covariant derivative in curvilinear (τ, x, y, η) coordinates (see Refs. [37,39] for details), coupled to the Israel-Stewart [37,40–42] evolution equations for the viscous pressure components:

$$\Delta^{\mu\alpha}\Delta^{\nu\beta}\dot{\pi}_{\alpha\beta} = -\frac{\pi^{\mu\nu} - 2\eta\sigma^{\mu\nu}}{\tau_\pi} - \frac{\pi^{\mu\nu}}{2}\frac{\eta T}{\tau_\pi} d_\lambda\left(\frac{\tau_\pi}{\eta T}u^\lambda\right). \tag{3}$$

The dot on the left-hand side stands for the local comoving time derivative $D = u^\mu d_\mu$, η is the shear viscosity, $\sigma^{\mu\nu} = \nabla^{\langle\mu} u^{\nu\rangle}$ is the velocity shear tensor (see Refs. [37,39] for notation), and τ_π is the microscopic relaxation time that controls the evolution of $\pi^{\mu\nu}$ (we take $\tau_\pi = 3\frac{\eta}{sT}$ [37]).

The equations are solved numerically in the two transverse spatial directions and time, using the $(2+1)$-dimensional hydrodynamic code VISH2+1 [13,43,44], assuming boost-invariant longitudinal expansion along the beam direction. The net baryon density and heat conductivity are set to zero.

To initialize the hydrodynamic evolution we must specify the starting time τ_0 at which the system is sufficiently close to local thermal equilibrium for viscous hydrodynamics to be applicable, initial energy density and velocity profiles, and the initial viscous pressure tensor $\pi^{\mu\nu}$. We here consider τ_0 as a tunable parameter and vary it between 0.2 and 0.8 fm/c in order to study how it affects the final hadron spectra and elliptic flow.

For the initial energy density profile we study both Glauber [44–47] and color glass condensate (CGC-fKLN) initializations [48–51] in the optical limit (i.e., without accounting for event-by-event fluctuations [52–57]). Figure 1 shows a comparison of typical initial energy density profiles generated

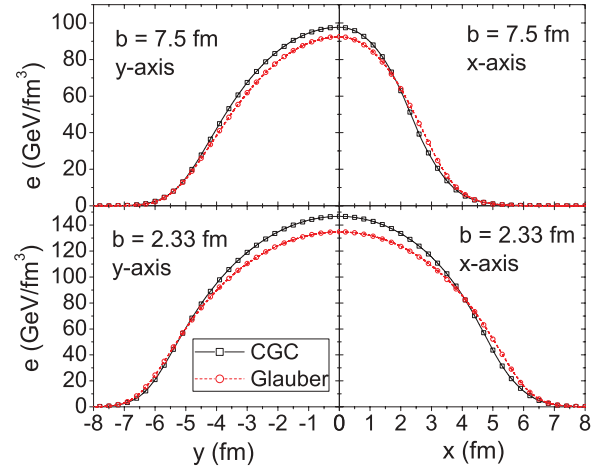

FIG. 1. (Color online) A comparison of initial energy density profiles at $\tau_0 = 0.4$ fm/c for "central" ($b = 2.33$ fm, bottom) and "peripheral" ($b = 7.5$ fm, top) Au + Au collisions from the Glauber and CGC-fKLN models. Shown are cuts along the x axis (right panels) and y axis (left panels). The two profiles are normalized to the same total entropy at $b = 2.33$ fm, using the EOS s95p-PCE to convert energy to entropy density.

from Glauber and CGC initializations. In the Glauber model we assume a mixture of 85% wounded nucleon and 15% binary collision contributions to the entropy production [58]. For the CGC model we assume that the energy density is proportional to the produced gluon energy density distribution, computed with the publicly available fKLN code [59]. In central Au + Au collisions, both profiles are normalized to the same total entropy (adjusted to reproduce the total final charged hadron multiplicity $dN_{\rm ch}/dy$ in these collisions) and converted to energy density using the equation of state s95p-PCE (see next section). With this normalization, both initializations correctly describe the centrality dependence of $dN_{\rm ch}/dy$ for *ideal* fluid dynamics (i.e., for isentropic expansion).

In the viscous case, viscous heating produces additional entropy, resulting in larger final multiplicities which we must correct for by renormalizing the initial entropy density profile in such a way that the final multiplicity is held fixed. We perform this renormalization for the 5% most central Au + Au collisions (i.e., at $b = 2.33$ fm) and then keep the resulting normalization constant fixed for noncentral collisions, i.e., we again assume that the models produce the correct dependence of initial entropy production on collision geometry. It is known, however, that the fractional increase of the final entropy over its initial value due to viscous heating depends on the size of the collision fireball [37] and is therefore expected to be larger in peripheral than central Au + Au collisions. For the results presented in this article, we have checked that the centrality dependence of viscous entropy production is sufficiently weak so that it does not strongly modify the centrality dependence of $dN_{\rm ch}/dy$.

Figure 1 shows that the energy density profile from the CGC initialization has a steeper surface gradient than the Glauber profile. This leads to larger radial acceleration (i.e., radial flow develops more quickly) and is also in part responsible for the larger spatial eccentricity of the CGC profiles at

nonzero impact parameters when compared to the Glauber eccentricities [58,60].

The shear viscous pressure tensor $\pi^{\mu\nu}$ is initialized with its Navier-Stokes value $\pi^{\mu\nu} = 2\eta\sigma_0^{\mu\nu}$, where $\sigma_0^{\mu\nu}$ is the velocity shear tensor at time τ_0, calculated from the initial Bjorken velocity profile, $u^\mu = (u^\tau, u^x, u^y, u^\eta) = (1, 0, 0, 0)$.

For the medium's viscous properties the shear viscosity η/s is the key parameter. According to perturbative and lattice QCD, the temperature dependence of η/s is weak over the range explored in heavy-ion collisions at RHIC energies. This suggests use of a constant ratio η/s. In this work, the value of η/s is tuned from 0.08 to 0.24 in order to study the effects of shear viscosity on the hadron spectra and elliptic flow. The influence of a temperature-dependent η/s will be explored in a forthcoming article [36].

Final-state hadron spectra are calculated from the hydrodynamics output via the Cooper-Frye procedure [14]

$$E\frac{d^3N_i}{d^3p} = \frac{g_i}{(2\pi)^3}\int_\Sigma p\cdot d^3\sigma(x) f_i(x,p), \tag{4}$$

where Σ is the freeze-out surface with normal vector $d^3\sigma_\mu(x)$. We take for Σ an isothermal surface; calculations for different freeze-out temperatures are presented in Sec. IV B. After computing the spectra of all hadronic resonances included in EOS s95p-PCE from Eq. (4), we use the resonance decay program [61,62] from the AZHYDRO package[1] to let the unstable resonances decay. The pion and proton spectra shown in this work include all decay products from strong decays.

The distribution function on the freeze-out surface can be decomposed as $f = f_{\rm eq} + \delta f$ into a local equilibrium part

$$f_{\rm eq}(p,x) = \frac{1}{e^{p\cdot u(x)/T(x)} \pm 1} \tag{5}$$

and a (small) deviation δf from local equilibrium due to shear viscous effects for which we make the quadratic ansatz [63,64] (for other possibilities see Ref. [65]) using

$$\delta f(x,p) = f_{\rm eq}(p,x)[1\mp f_{\rm eq}(p,x)]\frac{p^\mu p^\nu \pi_{\mu\nu}(x)}{2T^2(x)[e(x)+p(x)]} \tag{6}$$

[the upper (lower) sign is for fermions (bosons)] for all particle species. δf is proportional to the shear viscous pressure tensor $\pi^{\mu\nu}(x)$ on the freeze-out surface and increases (in our case) quadratically with the particle momentum.

III. EQUATION OF STATE

To solve Eqs. (2) and (3) one has to know the equation of state $p(e)$ (EOS) of the medium. In this work we compare three different equations of state to study how the EOS affects the hadron spectra and elliptic flow. Two of them, SM-EOS Q [44] and EOS L [37], are well known in the literature; the former implements a (slightly smoothed) first-order phase transition between an ideal massless parton gas and a hadron resonance gas (HRG), and the second is a rough attempt to match lattice QCD (LQCD) data [66] above T_c to the HRG in a smooth crossover transition, as seen in LQCD (see also Ref. [67]). In both cases, the system is assumed to be in chemical equilibrium all the way down to kinetic freeze-out at temperature $T_{\rm dec}$.

Our third equation of state, s95p-PCE, also interpolates between the HRG at low temperature and the lattice EOS at high temperatures, but the matching procedure is more sophisticated than the one used to construct EOS L, and the lattice EOS is based on the recent results by the hotQCD collaboration [23,24]. Furthermore, below $T_{\rm chem} = 165$ MeV, the EOS is that of a *chemically frozen* HRG. The matching procedure using a chemically equilibrated HRG is explained in detail in Ref. [25]. The procedure for the chemically frozen HRG is identical since the chemical freeze-out temperature is below the temperature where the interpolated EOS deviates from the HRG EOS.

However, the version of s95p-PCE used here deviates slightly from the s95p-PCE-v1 EOS shown in Appendix C of Ref. [25]. First, we have chosen $T_{\rm chem} = 165$ MeV for the chemical freeze-out temperature, as fitted to experimental data using thermal models [3,28,29], and we have considered as stable particles those with a half-life larger than 40 fm/c instead of 10 fm/c. Second, our s95p-PCE corresponds to a historically slightly earlier stage of the parametrization of the EOS than the final version published in Ref. [25]: The fit to the lattice data was done without the $T = 630$ MeV data point. This causes at most 0.4% difference between this version and the final version of the EOS. We have checked that such a small difference does not cause observable consequences in the fluid-dynamical evolution.[2]

We have built the EOS of the chemically frozen hadron gas using the standard procedure in the literature: Below $T_{\rm chem}$ the ratios of stable hadron yields are fixed to their chemical equilibrium values at $T_{\rm chem}$ by finite nonequilibrium chemical potentials $\mu_i(T)$ [15,16,19,26,27]. It is worth noting that the ratios of individual particle densities are not conserved. What is conserved are the ratios of the *total densities* of stable particles, $\bar{n}_i$, where total density means the sum of the actual density of species i and the additional density of the same species that would arise if all unstable resonances in the system were allowed to immediately and irreversibly decay. The rapid processes that form and decay resonances through strong interactions are still in equilibrium, and thus the resonance populations are in equilibrium with the populations of their daughter particles (see Refs. [15,26] for a detailed discussion). Thus the chemically frozen system is in a state of partial chemical equilibrium (PCE).

In practice the chemically frozen EOS is evaluated assuming that the evolution is isentropic and the ratios $\bar{n}_i/s$ stay constant. Strictly speaking this is not the case in viscous hydrodynamics since dissipation causes an increase in entropy. However, we have checked that in our calculations the viscous entropy production from fluid cells with temperatures below $T_{\rm chem} = 165$ MeV is small (see also the right panel of

[1] AZHYDRO is available at the URL [http://www.physics.ohio-state.edu/~froderma/].

[2] For a discussion of the uncertainties in parametrizing the lattice data and its effect on fluid dynamics see Ref. [25].

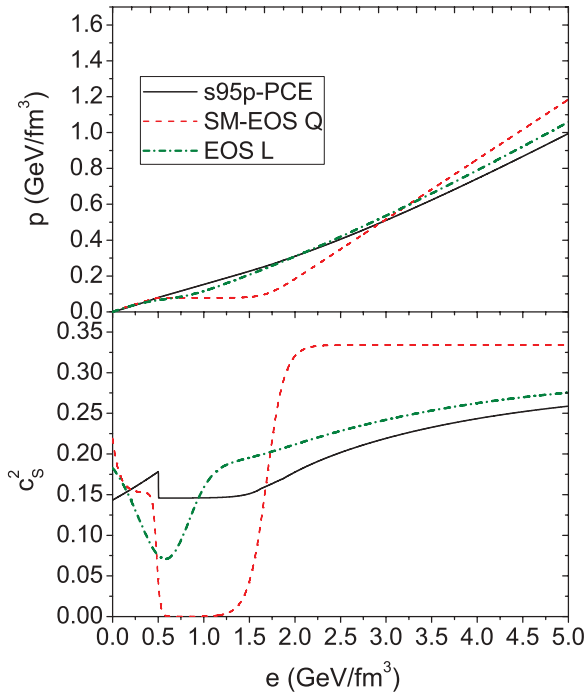

FIG. 2. (Color online) The three equations of state, s95p-PCE, SM-EOS Q, and EOS L, used in this article. The lower panel shows the squared speed of sound $c_s^2 = \frac{\partial p}{\partial e}$ as a function of energy density e, whereas $p(e)$ is shown in the upper panel.

Fig. 8 in Ref. [37]) and our EOS is a good approximation of the physical EOS.

An analytic parametrization of s95p-PCE is given in Appendix; the EOS can be obtained in a tabulated form at Ref. [68], where the particles included in the hadron resonance gas are also listed. (We included all resonances listed in the summary of the 2004 edition of the *Review of Particle Physics* [69] up to 2 GeV mass. Note that our s95p-PCE is called s95p-PCE165-v0 at Ref. [68] to differentiate it from other versions of the parametrization.)

The three equations of state are compared in Fig. 2. The upper panel shows the pressure and the lower panel the squared speed of sound as a function of e. The spike in $c_s^2(e)$ at $e \sim 0.5$ GeV/fm^3 results from the sudden breaking of chemical equilibrium at $T_{\rm chem} = 165$ MeV. It has negligible consequences for the expansion dynamics. Figure 2 shows that s95p-PCE is a much softer EOS than SM-EOS Q in the QGP phase above T_c but much harder in the phase transition region around T_c. Contrary to SM-EOS Q and EOS L, the rapid crossover transition between quarks and hadrons that is realized by nature does not have a well-defined "softest point" [70] which would cause the fireball to spend an extended time period in the critical region. Instead, the speed of sound never drops much below its value in the HRG, causing the fireball to cool rapidly through the phase transition [71].

IV. SPECTRA AND ELLIPTIC FLOW

In this section, we discuss the dependence of the transverse-momentum spectra in central 200A GeV Au + Au collisions (0–5% centrality, $b = 2.33$ fm) and the elliptic flow $v_2(p_T)$ in semiperipheral collisions (20–30% centrality, $b = 7.5$ fm) for pions, protons, and (for v_2) all charged hadrons on the EOS and various input parameters discussed in Secs. II and III. We have also checked that everything we say below about the central collision spectra also applies, at the same level of precision, to the ϕ-averaged spectra in semiperipheral collisions.

Since the amount of viscous heating depends on the input parameters, for each case we retune the normalization of the initial energy density profile *in central collisions* so the same final π^+ multiplicity density dN_{π^+}/dy is obtained. Its value is adjusted by eye such that an optimal fit to the measured pion spectrum is obtained in the low-p_T region, $p_T < 1.5$ GeV/c. As there are slight discrepancies between the published data from the STAR and PHENIX Collaborations, and these experiments give their results in different centrality bins, we have decided to concentrate on PHENIX results [72–74] when comparing the theoretical curves with experimental data. Since we do not attempt to fit these data but use the comparison only to illustrate trends, this procedure is acceptable. A future serious dynamical model fit to the data will require proper accounting for systematic uncertainties and discrepancies among the different experiments.

Since viscous heating effects are relatively more important in peripheral than in central collisions, our renormalization to constant multiplicities at $b = 2.33$ fm leads to slightly different pion multiplicities at larger impact parameters. For a given EOS, ensuring the same final pion multiplicity is equivalent to ensuring the same final total multiplicity. For different equations of state (see Sec. IV D) identical pion multiplicities correspond to slightly different total multiplicities.

In the following we show hadron spectra and elliptic flow up to transverse momenta of 3 GeV/c. We emphasize that this is for illustrative purposes only and does not imply that we believe hydrodynamics to provide a valid description up to such large p_T. When comparing model results with experimental data, we judge the quality of agreement by focusing on the region $p_T < 1.5$ GeV/c for pions and $p_T < 2.5$ GeV/c for protons (which is where we believe hydrodynamics is a reliable approach [75]). Specifically for pions, if the calculated spectra drop off more steeply than the measured ones above $p_T = 1.5$ GeV/c, we discount this discrepancy, noting that this is the region where the experimental spectra begin to change from an exponential to a power-law shape due to the onset of hard physics.

A. η/s dependence at fixed $\tau_0 = 0.4$ fm/c and $T_{\rm dec} = 140$ MeV

Transverse-momentum spectra of pions and protons in the most central Au + Au collision are shown in Fig. 3 and in the upper left panel of Fig. 4. The spectra include all strong resonance decays. Here we hold initial and final conditions fixed (except for a renormalization of the initial peak energy density to ensure the same final multiplicity in all calculations) and vary the specific shear viscosity η/s (see figure captions for details). One sees that under these conditions larger η/s values result in flatter spectra; the effect is particularly strong for protons at low p_T. The main reason is that larger shear viscosity leads to larger radial flow, due to a positive contribution from

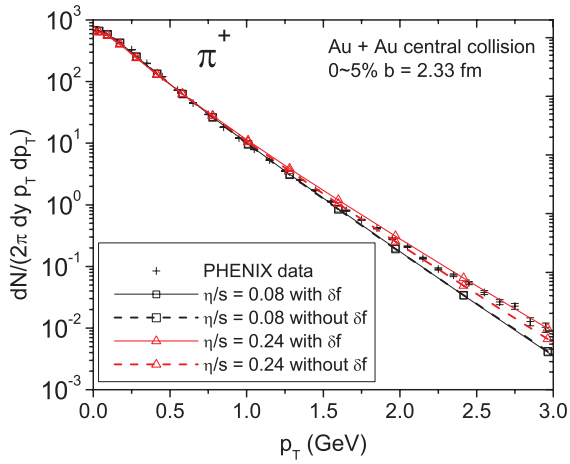

FIG. 3. (Color online) Pion spectra for 200A GeV Au + Au collisions at 0–5% centrality from VISH2+1 compared with PHENIX data [72]. Results for two different constant values of η/s (0.08 and 0.24) are shown; strong resonance decays are included. Solid and dashed lines show the spectra calculated from the full distribution function $f = f_{\rm eq} + \delta f$ ("with δf") and from the equilibrium part only ("without δf"). The hydrodynamic evolution starts at $\tau_0 = 0.4$ fm/c with an initial CGC energy density profile and ends at $T_{\rm dec} = 140$ MeV. The EOS is s95p-PCE.

$\pi^{\mu\nu}$ to the effective transverse pressure gradients at early times [39,76,77].

Figure 3 identifies, however, a second contribution to the viscous hardening of the spectra: For $\eta/s = 0.16$ and 0.24 and evolution with s95p-PCE, we find that the viscous correction due to the nonequilibrium deviation δf of the distribution function on the freeze-out surface, Eq. (6), is *positive* for $p_T \gtrsim 0.5$–1 GeV/c,[3] thus adding to the hardening of the spectra from radial flow.[4] This is the same sign for δf as found in Ref. [78] (for a different EOS) but opposite to what had been found earlier with VISH2+1 for smaller values of η/s using SM-EOS Q (i.e., a first order phase transition) [44]. (For $\eta/s = 0.08$ Fig. 3 shows a *negative* δf correction for pions at large p_T of the *same* sign but much smaller magnitude than found earlier [44] with Glauber initial conditions and SM-EOS Q). Our finding confirms the fragility of the sign of δf that was already discussed in Ref. [44].[5]

We note in passing that the positive δf at large p_T found here with s95p-PCE is found to be largest in near-central collisions ($b \approx 0$) where it can even lead to a *positive* δf correction to the differential elliptic flow $v_2(p_T)$. At larger b, the δf contribution to $v_2(p_T)$ remains negative here (see right panels of Fig. 4), as has been consistently observed in other work [10,43,44,78,79].

The time-integrated effect of the shear viscous pressure on the radial flow and the "instantaneous" effect of the viscous correction δf to the distribution function on the freeze-out surface together give the total shear viscous correction to the hadron spectra. For $\eta/s = 0.08$ we see in Fig. 3 that with s95p-PCE the δf correction to the pion spectrum is almost negligible, but the upper left panel in Fig. 4 shows that the pion and proton spectra are still flatter than for the ideal fluid, reflecting the larger radial flow caused by the shear viscous increase of the transverse pressure gradients [44]. Thus both the effect of viscosity on radial flow *and* δf contribute to the flattening of the hadron spectra.

Comparing with the experimental data we find that both pion and proton spectra favor a relatively large shear viscosity, $\eta/s = 0.16 \sim 0.24$. We caution that this conclusion is based on calculations done with constant (i.e., temperature independent) η/s and may be subject to revision once one properly accounts for the increase of η/s in the dilute late hadronic stage.

Proceeding to the elliptic flow, we start with a discussion of the charged hadron v_2 in the lower left panel of Fig. 4. Here, larger shear viscosity values are seen to lead to a stronger suppression of elliptic flow. The right panels in Fig. 4 show that this suppression is again the consequence of two additive effects: shear viscosity reduces the buildup of anisotropic collective flow, reflected in the equilibrium part $f_{\rm eq}$ of the distribution function on the freeze-out surface (dotted lines in Fig. 4), but the viscous correction δf causes an additional suppression of v_2. For T-independent η/s, both suppression effects increase monotonically with shear viscosity; however, the increase of the δf correction with rising η/s is weaker than that of the viscous suppression of the collective flow anisotropy. The stronger suppression of v_2 for larger η/s is thus mostly due to the viscous suppression of anisotropic flow.

Since elliptic flow data for identified pions and protons in the particular centrality bin shown in Fig. 4 are not yet available, we compare in the lower left panel with experimental data for unidentified charged hadrons. This plot suggests that, even for CGC initial conditions which produce more eccentric fireballs than the Glauber model [10,58], the v_2 data suggest a smaller value for η/s, $\eta/s = 0.08$–0.16, than obtained from the p_T spectra for central collisions.

This tension between the slope of the p_T spectra (which tends to favor larger η/s values) and the p_T dependence of v_2

[3]The Landau matching conditions require the δf correction to integrate to zero when summing over all momenta, so a positive δf contribution at high p_T implies a negative δf contribution at low and/or intermediate p_T. In Ref. [44] we found that it typically changes sign twice.

[4]We checked that for all equations of state studied here that the sign of δf at high p_T does not depend on whether we use CGC or Glauber initial conditions.

[5]For EOS L and SM-EOS Q and $\eta/s > 0.08$, we find a negative sign of the δf contribution to both pion and proton spectra at high p_T, while the corresponding contribution is positive in the case of s95p-PCE. The negative sign appears to be correlated with the use of an EOS with a "softest point." From ideal fluid dynamic simulations with such first-order or almost-first-order phase transitions we know that the rapid change of c_s^2 in the transition region generates strong structures in the radial velocity profile in fireball regions that are close to the critical temperature [46] and that these structures partially survive until the matter has reached decoupling. We suspect that velocity gradients associated with these structures play an important role in generating for EOS L and SM-EOS Q a negative δf contribution to the spectra at high p_T.

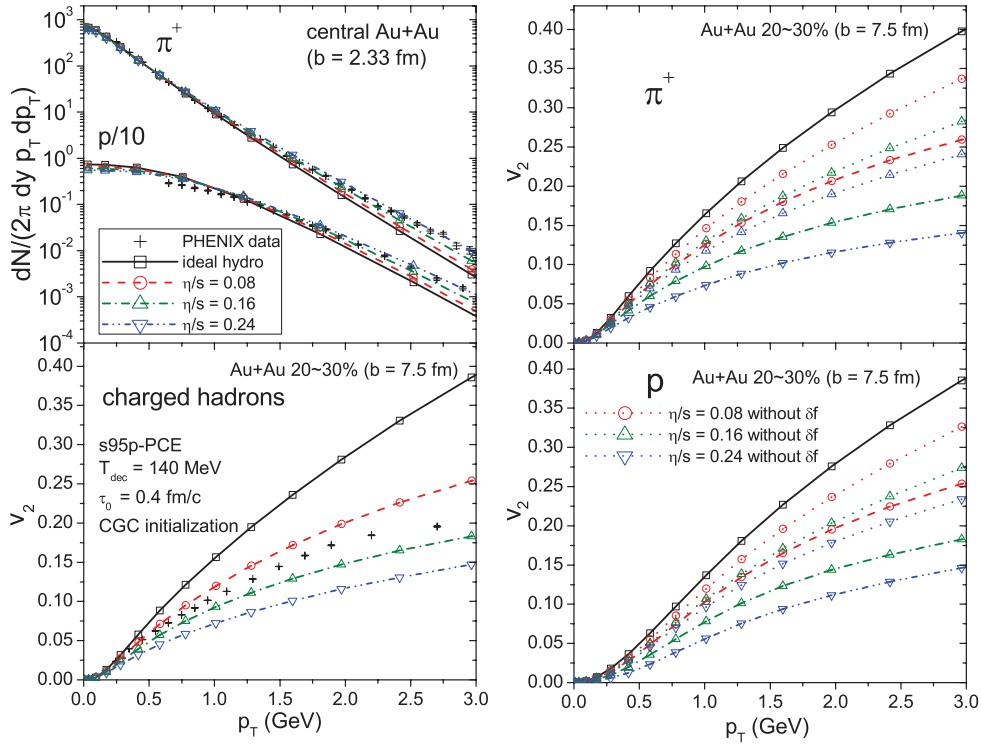

FIG. 4. (Color online) (Upper left panel) Transverse-momentum spectra $dN/(dyd^2p_T)$ for pions and protons from VISH2+1 for the 5% most central Au + Au collisions ($b = 2.33$ fm) compared with experimental data from the PHENIX Collaboration [72]. (Lower left panel) Differential elliptic flow $v_2(p_T)$ for charged hadrons from Au + Au collisions at 20–30% centrality ($b = 7.5$ fm) compared with PHENIX data [73]. (Right panels) $v_2(p_T)$ for pions (top) and protons (bottom). In these panels we compare the elliptic flow computed from the full distribution function $f = f_{\rm eq} + \delta f$ (dashed, dot-dashed, and double-dot-dashed lines) with the contribution from the equilibrium part only (dotted lines, "without δf"). Lines with different symbols show calculations for different constant values of the specific shear viscosity η/s, ranging from 0 (ideal hydro, solid lines) to 0.24 as indicated. All strong resonance decays are included; charged hadrons comprise $\pi^{\pm}$, $K^{\pm}$, p, $\overline{p}$, $\Sigma^{\pm}$, $\overline{\Sigma}^{\mp}$, Ξ^{-}, $\overline{\Xi}^{+}$, Ω^{-}, and $\overline{\Omega}^{+}$. The EOS and initial and final conditions are the same as in Fig. 3.

(which favors smaller values) is generic and, as far as we were able to ascertain, cannot be resolved with purely hydrodynamic calculations that assume constant η/s. A possible solution of this problem will likely involve accounting for temperature dependence of η/s and/or the transition to a microscopic kinetic description for the late hadronic stage.

B. $T_{\rm dec}$ dependence at fixed $\tau_0 = 0.4$ fm/c and $\eta/s = 0.16$

In Fig. 5 we explore the sensitivity of spectra and elliptic flow on the value of the decoupling temperature, holding all other parameters fixed. For the constant η/s we select $\eta/s = 0.16$ as a compromise between the values preferred by the proton spectra and charged hadron v_2, respectively, in Fig. 4.

The left upper panel shows that lower freeze-out temperatures lead to flatter proton spectra. This is a consequence of additional radial flow built up during the extra time the fireball needs to cool down to lower $T_{\rm dec}$. As is well known [80,81], the heavier protons receive a larger push to higher p_T from radial flow than the lighter pions. Indeed, Fig. 4 shows that the pion spectra become *steeper* as $T_{\rm dec}$ is lowered [82]. Since pions are almost massless on the scale of measured transverse momenta, the inverse slope of their p_T spectrum can be approximated by the relativistic blueshift formula [80,81] $T_{\rm slope} = T_{\rm dec}\sqrt{\frac{1+\langle v_\perp\rangle}{1-\langle v_\perp\rangle}}$, where $\langle v_\perp\rangle$ is the average radial flow at $T_{\rm dec}$. For pions, the steepening effects on their spectrum from decreasing $T_{\rm dec}$ overwhelm the flattening effects resulting from the associated increase of $\langle v_\perp\rangle$, causing a net softening of the pion spectra for lower freeze-out temperatures.

From the lower left panel of Fig. 5 one sees that lower decoupling temperatures lead to larger elliptic flow $v_2(p_T)$ for charged hadrons. To fully understand this systematics it is worth comparing charged hadrons to the p_T spectra and $v_2(p_T)$ of pions (upper left and right panels, respectively) which dominate the charged hadron yield. The observed tendency reflects a combination of three effects:

(i) Since the p_T spectrum of pions (which dominate the charged hadrons) gets steeper, even the same hydrodynamic momentum anisotropy would lead to a larger slope of $v_2(p_T)$, to compensate for the lower yield at high p_T.

(ii) Since the fireball has not lost all of its eccentricity by the time the QGP converts to hadrons [44], additional momentum anisotropy is generated during the hadronic stage. Lower decoupling temperatures give the system time to develop more momentum anisotropy, leading to a larger v_2. If the p_T spectrum stays unchanged or gets

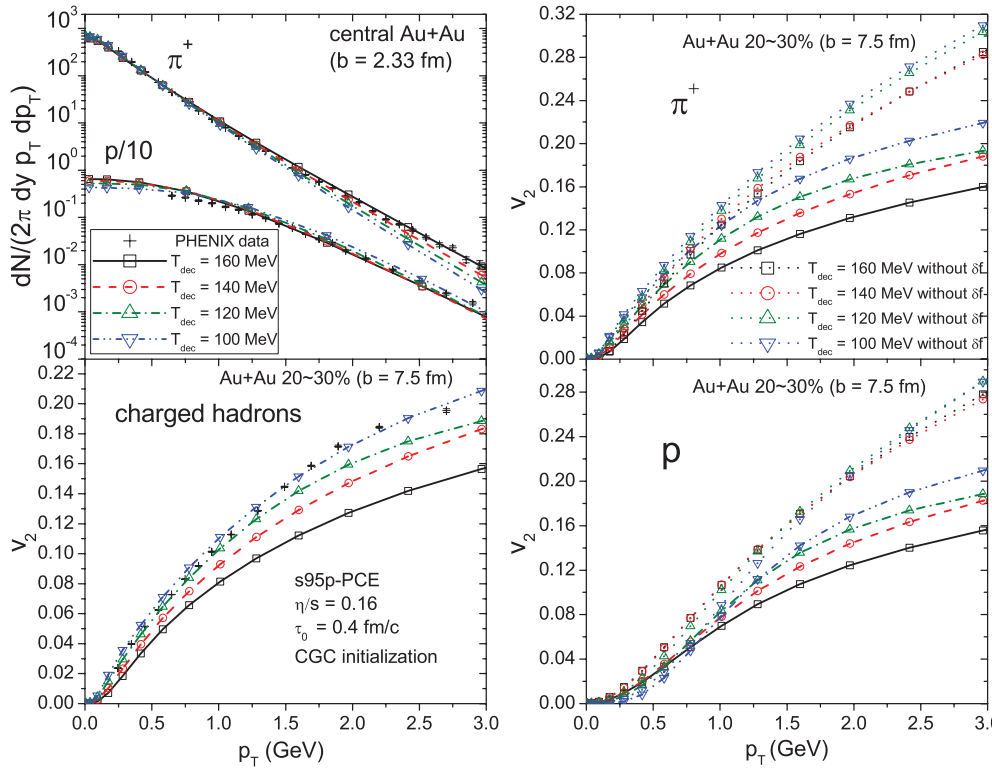

FIG. 5. (Color online) Similar to Fig. 4 but for fixed $\eta/s = 0.16$ and varying decoupling temperature $T_{\rm dec}$ ranging from 100 to 160 MeV as indicated.

steeper (as is the case for pions in Fig. 5), a larger v_2 must lead to a larger $v_2(p_T)$. The combination of effects (i) and (ii) is seen in the dotted lines in the upper right panel, which reflect the hydrodynamic flow anisotropy at decoupling, undistorted by viscous corrections δf to the local equilibrium distributions at freeze-out. The effect (ii) decreases with increasing η/s in the hadronic phase (not shown here), so the combined effect may be weaker than seen in Fig. 5 if viscous hydrodynamics is replaced by a microscopic hadron cascade such as UrQMD in the hadronic phase.

(iii) The (negative) viscous corrections from δf to v_2 are smaller at lower temperatures, due to the general decrease of the viscous pressure components [44]. This contributes the largest fraction of the observed increase of $v_2(p_T)$ with decreasing $T_{\rm dec}$, especially at large p_T.

Combining the information from the two left panels in Fig. 5 we conclude that both the proton spectra in central collisions and charged hadron $v_2(p_T)$ in peripheral collisions favor decoupling temperatures near the lower end of the window studied here (i.e., $T_{\rm dec} = 100$ MeV works better than $T_{\rm dec} = 140$ MeV). The pion spectra are affected by variations of $T_{\rm dec}$ mostly at $p_T \gtrsim 1$–1.5 GeV/c where they fall increasingly below the experimental data as we lower $T_{\rm dec}$. However, this is also the region where the hydrodynamic description of the pion spectra is known to begin to break down [75], due to the gradual transition from soft to hard physics which causes the pion spectrum to change from an exponential to a power-law shape. Focusing therefore on the region $p_T < 1.5(2.5)$ GeV/c for pions (protons), we conclude that a purely hydrodynamic description of the experimental data favors freeze-out temperatures near 100 MeV.

The right panels of Fig. 5 show how $T_{\rm dec}$ affects the elliptic flow of different identified hadrons. Charged hadrons mostly reflect the behavior of the dominating pions whose $v_2(p_T)$ increases with decreasing freeze-out temperature. But protons behave differently: At low $p_T < 1$ GeV, their elliptic flow decreases with decreasing decoupling temperature, while at high p_T it increases with decreasing $T_{\rm dec}$. The latter feature reflects the increasing hydrodynamic momentum anisotropy and decreasing magnitude of the δf correction, just like it is reflected in the pion and charged hadron v_2. The decrease of proton v_2 at low p_T, on the other hand, is a consequence of having larger radial flow at lower $T_{\rm dec}$ which pushes the protons to larger p_T. So rather than thinking of this effect as a decrease of proton v_2 at fixed p_T, we should think of it as shifting the elliptic flow to larger p_T.

C. τ_0 dependence at fixed $\eta/s = 0.16$ and $T_{\rm dec} = 140$ MeV

The upper left panel of Fig. 6 shows that the pion and proton spectra react similarly to a change of the starting time τ_0 of the hydrodynamic evolution: Smaller τ_0 values lead to more high-p_T particles, reflecting more radial flow. Starting hydrodynamics earlier allows it to generate radial flow earlier, and even though this also causes the fireball to cool down to $T_{\rm dec}$ sooner and freeze out earlier, the net effect is still a slight increase of the average radial flow at freeze-out.

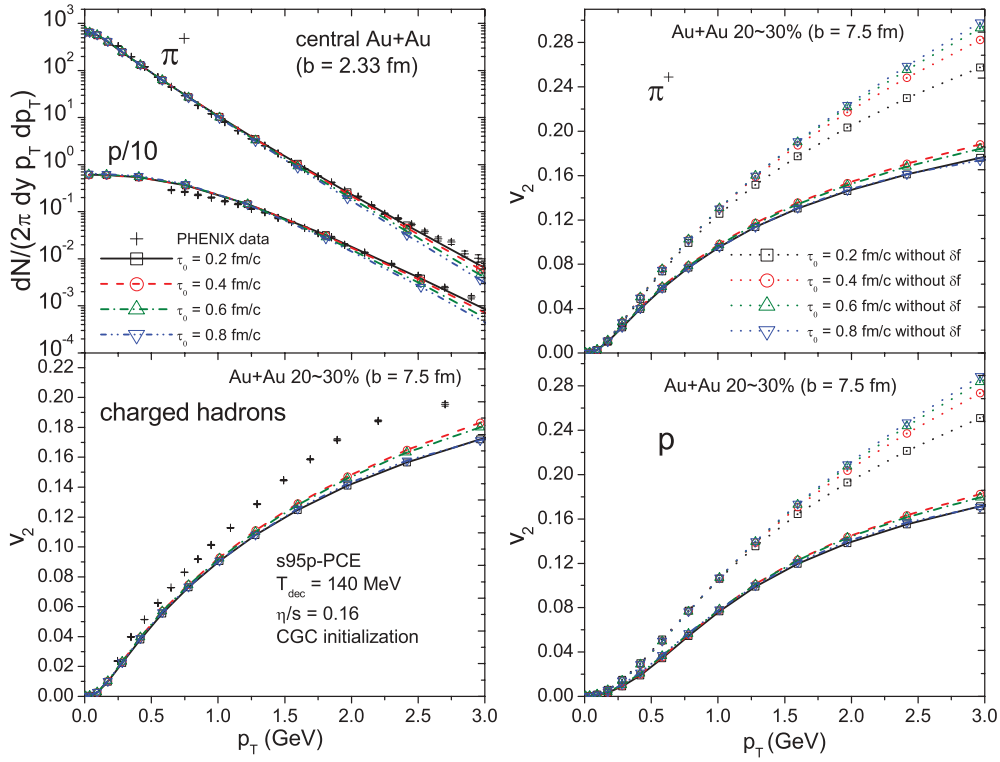

FIG. 6. (Color online) Similar to Fig. 4 but for fixed $\eta/s = 0.16$ and varying starting time τ_0 for the hydrodynamic evolution, ranging from 0.2 to 0.8 fm/c as indicated.

For soft momenta $p_T < 1.5$ GeV/c, the effect of τ_0 on $v_2(p_T)$ is negligible. This is true even for protons, showing that the increase of radial flow with decreasing τ_0 is a small effect and not enough to visibly push the proton v_2 to larger p_T. At higher p_T, the dependence of the charged hadron, pion and proton v_2 on τ_0 is nonmonotonic. The right panels of Fig. 6 show that this nonmonotonic behavior is the result of two counteracting tendencies which both depend on τ_0 monotonically: (i) The elliptic flow computed from the local equilibrium part $f_{\rm eq}$ of the distribution function at freeze-out increases monotonically with increasing τ_0, reflecting the longer total fireball lifetime (and thus the longer time available to build up momentum anisotropy) when the hydrodynamic evolution starts later. (ii) The v_2 suppression resulting from the viscous correction δf at freeze-out also increases monotonically with increasing τ_0. We don't have a complete understanding of why starting (and thus also ending) the hydrodynamics later leads to a larger δf on the decoupling surface; we suspect that since the hydrodynamical flow would eventually settle into a three-dimensional spherically symmetric Hubble flow with no shear stress, starting earlier leads to a stronger transverse flow, and thus to a flow profile which is closer to a spherically symmetric flow at the time of decoupling.

D. EOS dependence at fixed $\tau_0 = 0.4$ fm/c, $\eta/s = 0.16$, and $T_{\rm dec} = 140$ MeV

In Fig. 7 we study the sensitivity of hadron spectra and elliptic flow on the equation of state, holding all other hydrodynamic parameters fixed (except for the normalization of the initial energy density profile which is again adjusted to ensure constant final multiplicity in central Au + Au collisions). We first note that, due to the different chemical composition at hadron freeze-out, the proton yields for EOS L and SM-EOS Q are below those of s95p-PCE if we hold the pion mulitiplicity fixed: In s95p-PCE we prohibit protons from annihilating on antibaryons while such annihilation processes are allowed in the other two equations of state which assume hadrons in chemical equilibrium. To explore flow effects we should concentrate on the *shape* (i.e., inverse slopes) of the pion and proton spectra. We see that EOS L produces the flattest spectra, followed by SM-EOS Q, whereas the spectra from s95p-PCE are steepest. Since all three curves correspond to the same (constant) freeze-out temperature $T_{\rm dec} = 140$ MeV, these differences can only arise from different amounts of radial flow or different δf corrections (i.e., different viscous pressure components $\pi^{\mu\nu}$) along the freeze-out surface. To separate these two effects we plotted the spectra calculated without the δf correction and found the same hierarchy. We conclude that, for fixed freeze-out temperature, s95p-PCE produces the weakest radial flow averaged over the freeze-out surface and EOS L generates the strongest flow, with SM-EOS Q falling in between.

The reasons for s95p-PCE generating less radial flow than the other two equations of state are complex and subtle. The differences in speed of sound during the evolution largely cancel out (see Ref. [25]). The key difference is that, at a fixed freeze-out temperature, the chemically frozen HRG embodied in s95p-PCE has a considerably larger energy density ($e_{\rm dec} = 0.301$ GeV/fm^3 at $T_{\rm dec} = 140$ MeV) than the chemically

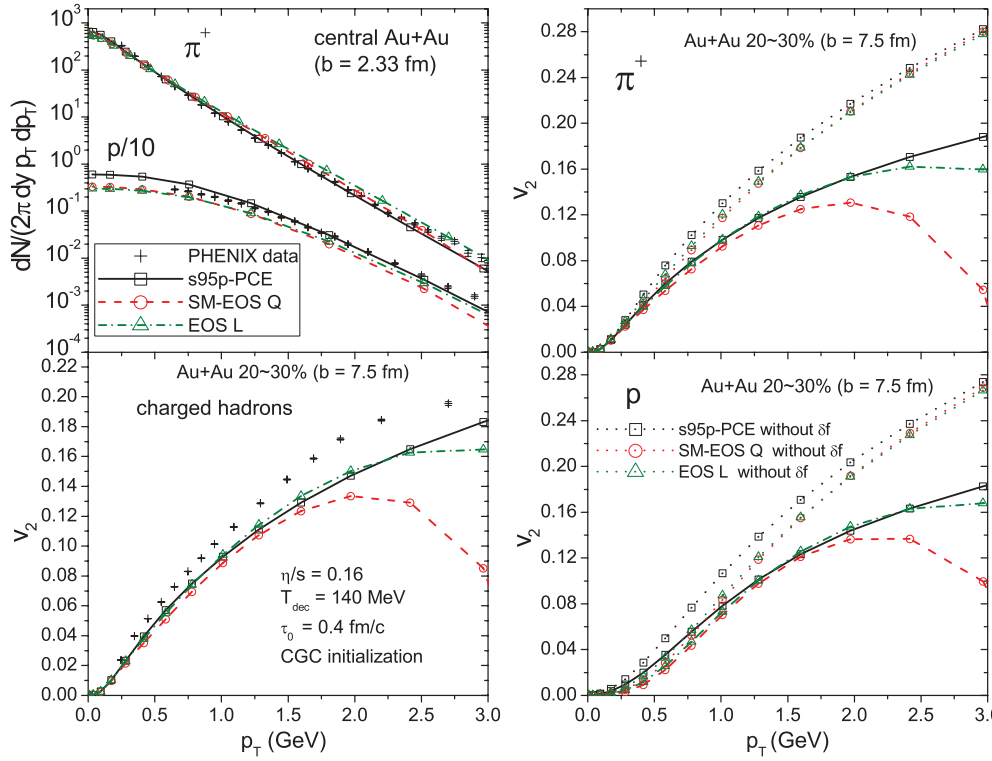

FIG. 7. (Color online) Similar to Fig. 4 but for fixed $\eta/s = 0.16$ and different equations of state (SM-EOS Q, EOS L, and s95p-PCE) as indicated. Since SM-EOS Q and EOS L have different chemical composition than s95p-PCE at $T_{\rm dec} = 140$ MeV, they yield fewer protons than s95p-PCE when normalized to the same pion yield.

equilibrated HRG used in EOS L and SM-EOS Q (which has $e_{\rm dec} = 0.143$ GeV/fm^3 at the same temperature) [15], due to the larger-than-equilibrium abundances of baryon-antibaryon pairs and mesons that are prohibited from annihilating as the system cools below $T_{\rm chem}$. So with s95p-PCE the fireball reaches the freeze-out point earlier, and it has a smaller freeze-out radius. It is this latter feature which causes the average radial flow along the freeze-out surface to be smaller for s95p-PCE than for the other two EOS: when plotting the radial velocity profiles along the decoupling surface, we found that all profiles are approximately linear functions of the radial distance r from the center (qualitatively similar to the profiles shown in Fig. 4 of Ref. [83]) and that the profile for s95p-PCE has the *largest* slope. However, the average radial flow is *smallest* because for s95p-PCE the average over the freeze-out surface is truncated at a smaller maximal r value.

The charged hadron, pion and proton elliptic flows $v_2(p_T)$ show quite large sensitivity to the EOS, especially at high p_T. (We repeat that the hydrodynamic spectra should probably not be trusted beyond $p_T \sim 2$–2.5 GeV/c, but plotting them out to 3 GeV/c makes it easier to see what is going on in the calculation.) But we see that most of this sensitivity comes in through the δf correction at freeze-out which is particularly large for SM-EOS Q. The reason for this is that the first-order phase transition leads to large velocity gradients at the QGP-to-mixed-phase and mixed-phase-to-HRG interfaces [46] which are largely but not completely washed out by viscous effects [44] and leave traces on the decoupling surface. δf effects are weaker with the smoother EOS L than with SM-EOS Q even though EOS L generates on average more radial flow.

To discuss the contribution from collective flow anisotropies to pion and proton $v_2(p_T)$ we focus on the dotted lines in the right panels of Fig. 7. We see that, while s95p-PCE creates less radial flow, it generates a larger flow *anisotropy* (we checked this by direct computation), resulting in larger $v_2(p_T)$ for *both* pions and protons than with the other two equations of state. For EOS Q it was found in Refs. [15,16,19] that if the kinetic freeze-out temperature $T_{\rm dec}$ is adjusted to reproduce the p_T spectra, the correct implementation of chemical freeze-out at $T_{\rm chem}$ in the HRG phase increases the mass splitting between $v_2(p_T)$ of pions and protons at low p_T. On the other hand, if the freeze-out temperature is kept constant, the mass splitting at low p_T decreases [15]. Since we have kept the freeze-out temperature fixed in our calculations, we see a similar phenomenon here: The elliptic flow mass splitting between pions and protons is weaker for the chemically frozen s95p-PCE than for the chemically equilibrated EOS L and SM-EOS Q. This is a consequence of the weaker radial flow generated by s95p-PCE.

E. Dependence on the shape of the initial energy density profile (CGC vs. Glauber)

We close with a discussion of the influence of the shape of the initial energy density profile on the hadron spectra and elliptic flow, using the Glauber and CGC-fKLN models

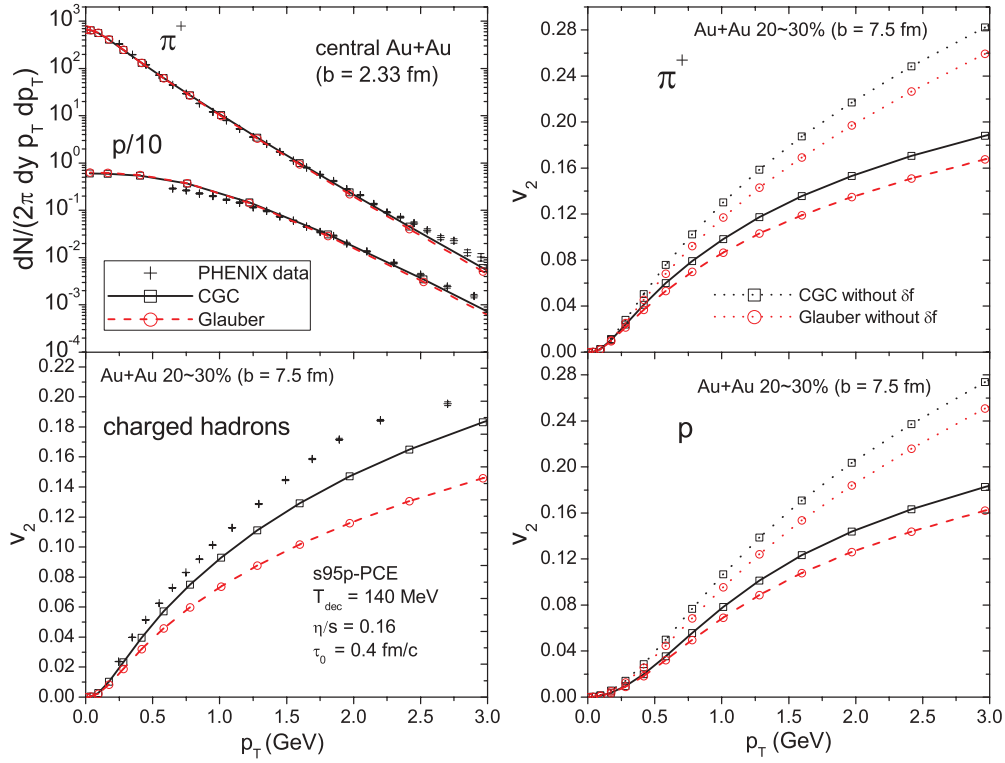

FIG. 8. (Color online) Similar to Fig. 4 but for fixed $\eta/s = 0.16$ and different initial energy density profiles (Glauber vs. CGC) as indicated. The elliptic flow from an initial CGC density profile is larger than for the Glauber initialization, due its larger initial eccentricity.

as examples. For an illustration of these profiles see Fig. 1.

The CGC profile is characterized by slightly steeper normalized energy density gradients than the Glauber profile. According to the Euler equation for ideal fluids

$$\dot{u}_\nu = \frac{c_s^2}{1+c_s^2}\frac{\nabla_\nu e}{e} \tag{7}$$

this leads to larger radial acceleration. Indeed, the upper left panel of Fig. 8 exhibits slightly flatter pion and proton spectra for CGC-initialized simulations than for Glauber initial conditions.

The elliptic flow coefficients for charged hadrons, pions, and protons are all significantly larger for the CGC-initialized runs than for Glauber initial conditions. This is a direct consequence of the well-known larger eccentricity of the CGC density profiles [10,50,58,60] which drives a larger momentum anisotropy. The effect is qualitatively similar for all hadron species. The small amount of added radial flow from the CGC initialization that we see in the spectra has very little influence on the p_T dependence of the proton v_2 when compared to the much larger effects coming from the larger source eccentricity. The suppression of v_2 by viscous δf corrections at freeze-out is similar for CGC and Glauber initial conditions, being slightly larger in the CGC case. This is presumably caused by the slightly larger flow velocities (and flow velicity gradients) generated by the CGC profile.

V. CONCLUSIONS

We have performed a systematic study of the dependence of the pion and proton transverse momentum spectra and their p_T-dependent elliptic flow on the thermalization time τ_0, initial energy density profile, equation of state, freeze-out temperature, and specific shear viscosity in $(2+1)$-dimensional viscous hydrodynamic simulations. Assuming a temperature-independent shear viscosity to entropy ratio and CGC initial conditions for the energy density profile, we find that the proton p_T spectra measured in 200A GeV central Au + Au collisions at RHIC favor η/s values between 2 and 3 times the KSS bound $(\frac{\eta}{s})_{\rm KSS} = \frac{1}{4\pi}$ while the p_T slope of the charged hadron elliptic flow prefers smaller values between 1 and 2 times the KSS bound. This tension cannot be resolved by different choices for the other paramaters whose variation we studied. Of course, the η/s values extracted from a comparison with simulations using the less eccentric Glauber model for the initial energy density profile are smaller, but the comparison with the experimental data gets worse (the proton spectra come out steeper) and tension between the η/s values preferred by spectra and v_2 gets stronger. Lower freeze-out temperatures improve the agreement with the data, in particular with the heavy-particle (proton) spectra. We saw very little sensitivity to the choice of the termalization time τ_0, but for larger values of τ_0 we did not allow for the evolution of pre-equilibrium radial and elliptic flow, contrary to what is expected to happen in reality. The main reason for not doing so was that, at this point, we have no theoretical

control over this pre-equilibrium flow, and we did not want to clutter our study by introducing still further parameters. If there is a tendency worth mentioning in the context of varying τ_0 it is that smaller τ_0 values lead to somewhat larger radial flow which helps with the description of heavy hadron spectra. This may, however, also be achievable by starting hydrodynamics later, but with nonzero initial transverse flow [21,84,85].

The main objective of this study was to gain an intuitive understanding what reasonable changes in the key parameters of a viscous hydrodynamic simulation will do to the final hadron spectra and elliptic flow. By also keeping an eye on the available experimental data we come to the conclusion that a purely hydrodynamic description of the experimental spectra will probably not work, at least not with temperature-independent η/s. Realistic variations of η/s with temperature are the subject of a separate study [36]. Based on that study combined with the one presented here we believe that giving up on a (viscous) hydrodynamic description of the hadron resonance gas stage and replacing it with a more reliable microscopic approach is unavoidable for a quantitative description of the experimental data.

ACKNOWLEDGMENTS

This work was supported by the US Department of Energy under contracts DE-SC0004286 and DE-AC02-05CH11231 and within the framework of the JET Collaboration under Grant No. DE-SC0004104. P.H.'s research was supported by the ExtreMe Matter Institute (EMMI). We thank Thomas Riley for helping us with the analytic parametrization of the EOS tables for s95p-PCE.

APPENDIX: ANALYTIC PARAMETRIZATION OF EOS s95p-PCE [68]

We used the following analytic parametrization for the equation of state s95p-PCE (energy density e and pressure p in GeV/fm^3, entropy density s in fm^{-3}, temperature T in GeV):

1. Pressure

$$p(e) = \begin{cases} 0.3299[\exp(0.4346e) - 1] & : \quad e < e_1 \\ 1.024 \times 10^{-7} \exp(6.041e) + 0.007273 + 0.14578e & : \quad e_1 < e < e_2 \\ 0.30195 \exp(0.31308e) - 0.256232 & : \quad e_2 < e < e_3 \\ 0.332e - 0.3223e^{0.4585} - 0.003906e \exp(-0.05697e) + 0.1167e^{-1.233} + 0.1436e \exp(-0.9131e) & : \quad e_3 < e < e_4 \\ 0.3327e - 0.3223e^{0.4585} - 0.003906e \exp(-0.05697e) & : \quad e > e_4 \end{cases} \tag{A1}$$

where $e_1 = 0.5028563305441270$ GeV/fm^3, $e_2 = 1.62$ GeV/fm^3, $e_3 = 1.86$ GeV/fm^3, and $e_4 = 9.9878355786273545$ GeV/fm^3.

2. Entropy density

$$s^{\frac{4}{3}}(e) = \begin{cases} 12.2304e^{1.16849} & : \quad e < e_1 \\ 11.9279e^{1.15635} & : \quad e_1 < e < e_2 \\ 0.0580578 + 11.833e^{1.16187} & : \quad e_2 < e < e_3 \\ \left.\begin{array}{l} 18.202e - 62.021814 - 4.85479 \exp(-2.72407 \times 10^{-11} e^{4.54886}) \\ +65.1272e^{-0.128012} \exp(-0.00369624e^{1.18735}) - 4.75253e^{-1.18423} \end{array}\right\} & : \quad e_3 < e < e_4 \\ \left.\begin{array}{l} 18.202e - 63.0218 - 4.85479 \exp(-2.72407 \times 10^{-11} e^{4.54886}) \\ +65.1272e^{-0.128012} \exp(-0.00369624e^{1.18735}) \end{array}\right\} & : \quad e > e_4 \end{cases} \tag{A2}$$

where $e_1 = 0.1270769021427449$ GeV/fm^3, $e_2 = 0.4467079524674040$ GeV/fm^3, $e_3 = 1.9402832534193788$ GeV/fm^3, and $e_4 = 3.7292474570977285$ GeV/fm^3.

3. Temperature

$$T(e) = \begin{cases} 0.203054e^{0.30679} & : \quad e < 0.5143939846236409 \text{ GeV/fm}^3 \\ (e + p)/s & : \quad e > 0.5143939846236409 \text{ GeV/fm}^3 \end{cases} \tag{A3}$$

[1] BRAHMS, I. Arsene *et al.*, Nucl. Phys. A **757**, 1 (2005).
[2] B. B. Back *et al.*, Nucl. Phys. A **757**, 28 (2005).
[3] J. Adams *et al.* (STAR Collaboration), Nucl. Phys. A **757**, 102 (2005).
[4] K. Adcox *et al.* (PHENIX Collaboration), Nucl. Phys. A **757**, 184 (2005).
[5] U. Heinz and P. F. Kolb, Nucl. Phys. A **702**, 269 (2002).
[6] P. F. Kolb and U. Heinz, Hydrodynamic description of ultrarelativistic heavy-ion collisions, in *Quark-Gluon Plasma 3*, edited by R. Hwa and X.-N. Wang (World Scientific, Singapore, 2004), p. 634.
[7] M. Gyulassy and L. McLerran, Nucl. Phys. A **750**, 30 (2005).
[8] P. Romatschke, Int. J. Mod. Phys. E **19**, 1 (2010).
[9] U. Heinz, Early collective expansion: Relativistic hydrodynamics and the transport properties of QCD matter, in *Relativistic Heavy Ion Physics*, edited by R. Stock, Landolt-Börnstein (Springer-Verlag, New York, 2010), Vol. I 23, chap. 5-1, arXiv:0901.4355 [nucl-th].
[10] M. Luzum and P. Romatschke, Phys. Rev. C **78**, 034915 (2008); **79**, 039903(E) (2009).
[11] R. A. Lacey *et al.*, Phys. Rev. C **82**, 034910 (2010).
[12] H. Song and U. Heinz, J. Phys. G: Part. Nucl. Phys. **36**, 064033 (2009).
[13] H. Song, Ph.D. thesis, The Ohio State University, 2009, arXiv:0908.3656 [nucl-th].
[14] F. Cooper and G. Frye, Phys. Rev. D **10**, 186 (1974).
[15] T. Hirano and K. Tsuda, Phys. Rev. C **66**, 054905 (2002).
[16] P. F. Kolb and R. Rapp, Phys. Rev. C **67**, 044903 (2003).
[17] P. Huovinen, Nucl. Phys. A **761**, 296 (2005).
[18] P. Huovinen and P. V. Ruuskanen, Annu. Rev. Nucl. Part. Sci. **56**, 163 (2006).
[19] P. Huovinen, Eur. Phys. J. A **37**, 121 (2008).
[20] K. J. Eskola, H. Niemi, and P. V. Ruuskanen, Phys. Rev. C **77**, 044907 (2008).
[21] W. Broniowski, M. Chojnacki, W. Florkowski, and A. Kisiel, Phys. Rev. Lett. **101**, 022301 (2008).
[22] P. Bozek and I. Wyskiel, Phys. Rev. C **79**, 044916 (2009).
[23] M. Cheng *et al.*, Phys. Rev. D **77**, 014511 (2008).
[24] A. Bazavov *et al.*, Phys. Rev. D **80**, 014504 (2009).
[25] P. Huovinen and P. Petreczky, Nucl. Phys. A **837**, 26 (2010).
[26] H. Bebie, P. Gerber, J. L. Goity, and H. Leutwyler, Nucl. Phys. B **378**, 95 (1992).
[27] D. Teaney, arXiv:nucl-th/0204023.
[28] P. Braun-Munzinger, D. Magestro, K. Redlich, and J. Stachel, Phys. Lett. B **518**, 41 (2001).
[29] A. Andronic, P. Braun-Munzinger, and J. Stachel, Phys. Lett. B **673**, 142 (2009); **678**, 516 (2009).
[30] R. A. Lacey and A. Taranenko, PoS **CFRNC2006**, 021 (2006).
[31] G. Policastro, D. T. Son, and A. O. Starinets, Phys. Rev. Lett. **87**, 081601 (2001).
[32] P. K. Kovtun, D. T. Son, and A. O. Starinets, Phys. Rev. Lett. **94**, 111601 (2005).
[33] L. P. Csernai, J. I. Kapusta, and L. D. McLerran, Phys. Rev. Lett. **97**, 152303 (2006).
[34] N. Demir and S. A. Bass, Phys. Rev. Lett. **102**, 172302 (2009).
[35] P. Bozek, Phys. Rev. C **81**, 034909 (2010).
[36] C. Shen *et al.* (to be published).
[37] H. Song and U. Heinz, Phys. Rev. C **78**, 024902 (2008).
[38] H. Song and U. Heinz, Phys. Rev. C **81**, 024905 (2010).
[39] U. Heinz, H. Song, and A. K. Chaudhuri, Phys. Rev. C **73**, 034904 (2006).
[40] W. Israel and J. M. Stewart, Ann. Phys. **118**, 341 (1979).
[41] A. Muronga, Phys. Rev. Lett. **88**, 062302 (2002).
[42] A. Muronga, Phys. Rev. C **69**, 034903 (2004).
[43] H. Song and U. Heinz, Phys. Lett. B **658**, 279 (2008).
[44] H. Song and U. Heinz, Phys. Rev. C **77**, 064901 (2008).
[45] P. F. Kolb, J. Sollfrank, and U. Heinz, Phys. Lett. B **459**, 667 (1999).
[46] P. F. Kolb, J. Sollfrank, and U. Heinz, Phys. Rev. C **62**, 054909 (2000).
[47] P. F. Kolb, U. Heinz, P. Huovinen, K. J. Eskola, and K. Tuominen, Nucl. Phys. A **696**, 197 (2001).
[48] D. Kharzeev and M. Nardi, Phys. Lett. B **507**, 121 (2001).
[49] D. Kharzeev, E. Levin, and M. Nardi, Nucl. Phys. A **730**, 448 (2004).
[50] A. Adil, H.-J. Drescher, A. Dumitru, A. Hayashigaki, and Y. Nara, Phys. Rev. C **74**, 044905 (2006).
[51] H. J. Drescher and Y. Nara, Phys. Rev. C **75**, 034905 (2007).
[52] R. P. G. Andrade, F. Grassi, Y. Hama, T. Kodama, and W. L. Qian, Phys. Rev. Lett. **101**, 112301 (2008).
[53] T. Hirano and Y. Nara, Phys. Rev. C **79**, 064904 (2009).
[54] H. Petersen and M. Bleicher, Phys. Rev. C **81**, 044906 (2010).
[55] H. Holopainen, H. Niemi, and K. J. Eskola, arXiv:1007.0368.
[56] B. Schenke, S. Jeon, and C. Gale, arXiv:1009.3244.
[57] H. Petersen, G.-Y. Qin, S. A. Bass, and B. Muller, arXiv:1008.0625.
[58] T. Hirano, U. Heinz, D. Kharzeev, R. Lacey, and Y. Nara, Phys. Lett. B **636**, 299 (2006).
[59] H.-J. Drescher, fKLN code, available at [http://th.physik.uni-frankfurt.de/∼drescher/CGC/].
[60] U. Heinz, J. S. Moreland, and H. Song, Phys. Rev. C **80**, 061901 (2009).
[61] J. Sollfrank, P. Koch, and U. Heinz, Phys. Lett. B **252**, 256 (1990).
[62] J. Sollfrank, P. Koch, and U. Heinz, Z. Phys. C **52**, 593 (1991).
[63] D. Teaney, Phys. Rev. C **68**, 034913 (2003).
[64] R. Baier, P. Romatschke, and U. A. Wiedemann, Phys. Rev. C **73**, 064903 (2006).
[65] K. Dusling, G. D. Moore, and D. Teaney, Phys. Rev. C **81**, 034907 (2010).
[66] Y. Aoki, Z. Fodor, S. D. Katz, and K. K. Szabo, J. High Energy Phys. 01 (2006) 089.
[67] M. Chojnacki and W. Florkowski, Acta Phys. Pol. B **38**, 3249 (2007).
[68] The EOS tables (by P. Huovinen), their analytic parametrizations (by T. Riley and C. Shen) and the list of included hadrons are available at the URLs [https://wiki.bnl.gov/hhic/index.php/Lattice_calculatons_of_Equation_of_State] and [https://wiki.bnl.gov/TECHQM/index.php/QCD_Equation_of_State].
[69] Particle Data Group, S. Eidelman *et al.*, Phys. Lett. B **592**, 1 (2004).
[70] C. M. Hung and E. V. Shuryak, Phys. Rev. Lett. **75**, 4003 (1995).
[71] D. Zschiesche, H. Stöcker, W. Greiner, and S. Schramm, Phys. Rev. C **65**, 064902 (2002).
[72] S. S. Adler *et al.* (PHENIX Collaboration), Phys. Rev. C **69**, 034909 (2004).
[73] S. Afanasiev *et al.* (PHENIX Collaboraton), Phys. Rev. C **80**, 024909 (2009).
[74] A. Adare *et al.* (PHENIX Collaboraton), Phys. Rev. Lett. **105**, 062301 (2010).
[75] U. Heinz, AIP Conf. Proc. **739**, 163 (2005).

[76] D. A. Teaney, J. Phys. G **30**, S1247 (2004).
[77] A. K. Chaudhuri and U. Heinz, J. Phys. Conf. Ser. **50**, 251 (2006).
[78] K. Dusling and D. Teaney, Phys. Rev. C **77**, 034905 (2008).
[79] P. Romatschke and U. Romatschke, Phys. Rev. Lett. **99**, 172301 (2007).
[80] E. Schnedermann, J. Sollfrank, and U. Heinz, NATO Adv. Study Inst. Ser. B Phys. **303**, 175 (1993).
[81] E. Schnedermann, J. Sollfrank, and U. Heinz, Phys. Rev. C **48**, 2462 (1993).
[82] T. Hirano and M. Gyulassy, Nucl. Phys. A **769**, 71 (2006).
[83] D. Teaney, J. Lauret, and E. V. Shuryak, arXiv:nucl-th/0110037.
[84] J. Vredevoogd and S. Pratt, Phys. Rev. C **79**, 044915 (2009).
[85] S. Pratt, Phys. Rev. Lett. **102**, 232301 (2009).

Applicability of causal dissipative hydrodynamics to relativistic heavy ion collisions

Pasi Huovinen
Department of Physics, University of Virginia, Charlottesville, Virginia 22904, USA and
Physics Department, Purdue University, West Lafayette, Indiana 47907, USA

Denes Molnar
Physics Department, Purdue University, West Lafayette, Indiana 47907, USA and
RIKEN BNL Research Center, Brookhaven National Laboratory, Upton, New York 11973, USA
(Received 19 August 2008; published 28 January 2009)

We utilize nonequilibrium covariant transport theory to determine the region of validity of causal Israel-Stewart (IS) dissipative hydrodynamics and Navier-Stokes (NS) theory for relativistic heavy ion physics applications. A massless ideal gas with $2 \to 2$ interactions is considered in a Bjorken scenario in $0 + 1$ dimension (D) appropriate for the early longitudinal expansion stage of the collision. In the scale-invariant case of a constant shear viscosity to entropy density ratio $\eta/s \approx$ const, we find that IS theory is accurate within 10% in calculating dissipative effects if *initially* the expansion time scale exceeds half the transport mean free path $\tau_0/\lambda_{\mathrm{tr},0} \gtrsim 2$. The same accuracy with NS requires three times larger $\tau_0/\lambda_{\mathrm{tr},0} \gtrsim 6$. For dynamics driven by a constant cross section, on the other hand, about 50% larger $\tau_0/\lambda_{\mathrm{tr},0} \gtrsim 3$ (IS) and 9 (NS) are needed. For typical applications at energies currently available at the BNL Relativistic Heavy Ion Collider (RHIC), i.e., $\sqrt{s_{NN}} \sim$ 100–200 GeV, these limits imply that even the IS approach becomes marginal when $\eta/s \gtrsim 0.15$. In addition, we find that the "naive" approximation to IS theory, which neglects products of gradients and dissipative quantities, has an even smaller range of applicability than Navier-Stokes. We also obtain analytic IS and NS solutions in $0 + 1$D, and present further tests for numerical dissipative hydrodynamics codes in $1 + 1$, $2 + 1$, and $3 + 1$D based on generalized conservation laws.

DOI: 10.1103/PhysRevC.79.014906 PACS number(s): 25.75.−q, 24.10.Nz, 24.10.Lx

I. INTRODUCTION

The realization that shear viscosity is likely nonzero in general [1–3], and therefore the perfect (Euler) fluid paradigm [4–7] of nuclear collisions at the BNL Relativistic Heavy Ion Collider (RHIC) could have significant viscous corrections [8], has fueled great interest in studying dissipative hydrodynamics [9–18]. Causality and stability problems [19] exhibited by standard first-order relativistic Navier-Stokes (NS) hydrodynamics [20,21] steered most effort toward application of the second-order Israel-Stewart (IS) approach [22,23].

However, unlike the NS approach, which comes from a rigorous expansion [24] in small gradients near equilibrium, the IS formulation is *not* a controlled expansion in some small parameter (see Sec. II). Moreover, though causality is restored in a region of hydrodynamic parameters, the stability of IS solutions is not necessarily guaranteed [25]. Therefore it is imperative to test the applicability of the IS approach against a stable, nonequilibrium theory.

In this work we perform such a test utilizing the fully stable and causal covariant transport approach [26–29]. We focus on the special case of $2 \to 2$ transport and a longitudinally boost-invariant system [30] with transverse translational symmetry, i.e., $0 + 1$ dimension (D). Follow-up studies in higher dimensions, such as our earlier comparison between transport and ideal hydrodynamics in $2 + 1$D [8], will be pursued in the future.

A similar study by Gyulassy, Pang, and Zhang [27] compared kinetic theory and Navier-Stokes results. Here we compare kinetic theory to the causal IS solutions. In addition, we provide a series of tests and semianalytic approximations that demonstrate the general behavior of IS solutions, which can be utilized to verify the accuracy of numerical IS solutions.

The paper is structured as follows. We start with reviewing the relationship between hydrodynamics and covariant transport (Sec. II), then proceed to discuss the Israel-Stewart equations (Sec. III). The basic observables studied here are introduced in Sec. IV, while the main results from the hydro-transport comparison are presented in Sec. V, together with implications for heavy ion collisions. Many details are deferred to Appendixes A–D. We highlight here the generalized conservation laws derived in Appendix B and the detailed study of IS and NS solutions in Appendix C utilizing numerical and analytic methods.

II. HYDRODYNAMICS AND COVARIANT TRANSPORT

Hydrodynamics describes a system in terms of a few local, macroscopic variables [20], such as energy density $\varepsilon(x)$, pressure $p(x)$, charge density $n(x)$, and flow velocity $u^\mu(x)$. The equations of motion are energy-momentum and charge conservation

$$\partial_\mu T^{\mu\nu}(x) = 0, \quad \partial_\mu N^\mu(x) = 0, \tag{1}$$

and the equation of state $p(\varepsilon, n)$. *Ideal* (Euler) hydrodynamics assumes local equilibrium, in which case,

$$\begin{aligned} T^{\mu\nu}_{\mathrm{LR,id}} &= \mathrm{diag}(\varepsilon, p, p, p), \\ N^\mu_{\mathrm{LR,id}} &= (n, \mathbf{0}) \quad \left[u^\mu_{\mathrm{LR}} = (1, \mathbf{0})\right], \end{aligned} \tag{2}$$

in the fluid rest frame LR. Extension of the theory with additive corrections *linear* in flow and temperature gradients [20]

$$\delta T^{\mu\nu}_{\mathrm{NS}} = \eta_s\left(\nabla^\mu u^\nu + \nabla^\nu u^\mu - \tfrac{2}{3}\Delta^{\mu\nu}\partial^\alpha u_\alpha\right) + \zeta\,\Delta^{\mu\nu}\partial^\alpha u_\alpha, \tag{3}$$

$$\delta N^{\mu}_{\rm NS} = \kappa_q \left(\frac{nT}{\varepsilon + p}\right)^2 \nabla^{\mu}\left(\frac{\mu}{T}\right) \quad (\Delta^{\mu\nu} \equiv g^{\mu\nu} - u^{\mu}u^{\nu},\ \Delta^{\mu} \equiv \Delta^{\mu\nu}\partial_{\nu}), \tag{4}$$

leads via Eq. (1) to the relativistic NS equations. (We use the Landau frame convention $u_{\mu}\delta T^{\mu\nu} \equiv 0$ throughout this paper, i.e., the flow velocity is chosen such that momentum flow vanishes in the LR frame.) Here $\eta_s(\varepsilon, n)$ and $\zeta(\varepsilon, n)$ are the shear and bulk viscosities, while $\kappa_q(\varepsilon, n)$ is the heat conductivity of the matter. The most notable feature of NS theory relative to the ideal case is dissipation, i.e., entropy production. For consistency, the dissipative corrections (3)–(4) must be small, otherwise nonlinear terms and higher gradients should also be considered.

It is crucial that the above hydrodynamic equations can indeed be obtained from a general nonequilibrium theory, namely, on-shell covariant transport [21,27–29]. For a one-component system, the covariant transport equation reads

$$p^{\mu}\partial_{\mu} f(x, \mathbf{p}) = S(x, \mathbf{p}) + C[f, f](x, \mathbf{p}), \tag{5}$$

where the source term S specifies the initial conditions, and C is the collision term. Throughout this paper, we consider the Boltzmann limit[1] with binary $2 \to 2$ rates

$$C[f, g](x, \mathbf{p}_1) \equiv \int_2 \int_3 \int_4 (f_3 g_4 - f_1 g_2) W_{12\to 34} \delta^4(p_1 + p_2 - p_3 - p_4), \tag{6}$$

where $f_i \equiv f(x, \mathbf{p}_i)$ and $\int_i \equiv \int d^3p_i/(2E_i)$. For dilute systems, f is the phase-space distribution of quasiparticles, while the transition probability $W = (1/\pi)s(s - 4m^2)d\sigma/dt$ is given by the scattering matrix element [21]. Our interest here, on the other hand, is the theory *near its hydrodynamic limit*, $W \to \infty$. In this case, "particles" and "interactions" do not necessarily have to be physical but could simply be mathematical constructs adjusted to reproduce the transport properties of the system near equilibrium [31]. The main advantage of transport theory is its ability to dynamically interpolate between the dilute and opaque limits.

The Euler and Navier-Stokes hydrodynamic equations follow from a rigorous expansion of Eq. (5) in small gradients near local equilibrium

$$f(x, \mathbf{p}) = f_{\rm eq}(x, \mathbf{p})[1 + \phi(x, \mathbf{p})], \quad |\phi| \ll 1, \quad |p^{\mu}\partial_{\mu}\phi| \ll |p^{\mu}\partial_{\mu} f_{\rm eq}|/f_{\rm eq}, \tag{7}$$

and substitution of moments of the solutions

$$N^{\mu}(x) \equiv \int \frac{d^3p}{p_0} p^{\mu}\ f(x, \mathbf{p}),$$

$$T^{\mu\nu}(x) \equiv \int \frac{d^3p}{p_0} p^{\mu}p^{\nu}\ f(x, \mathbf{p}), \tag{8}$$

into Eq. (1). The zeroth order $\phi = 0$ reproduces ideal hydrodynamics. The first-order result is the solution to the linear integral equation

$$p^{\mu}\partial_{\mu} f_{\rm eq}(x, \mathbf{p}) = C[f_{\rm eq}, f_{\rm eq}\phi_{\rm NS}](x, \mathbf{p}) + C[f_{\rm eq}\phi_{\rm NS}, f_{\rm eq}](x, \mathbf{p}) \tag{9}$$

and leads to the NS equations.

Unfortunately, the relativistic Navier-Stokes equations are parabolic and therefore acausal. A solution proposed by Mueller [32] and later extended by Israel and Stewart [22,23] converts the NS equations into relaxation equations for the shear stress $\pi^{\mu\nu}$, bulk pressure Π, and heat flow q^{μ}. The dissipative corrections

$$\delta T^{\mu\nu} \equiv \pi^{\mu\nu} - \Pi\Delta^{\mu\nu}, \quad \delta N^{\mu} \equiv -\frac{n}{\varepsilon + p}q^{\mu} \quad \left(u_{\mu}q^{\mu} = 0, u_{\mu}\pi^{\mu\nu} = u_{\mu}\pi^{\nu\mu} = 0, \pi^{\mu}_{\mu} = 0\right), \tag{10}$$

dynamically relax on microscopic time scales $\tau_{\pi}(\varepsilon, n)$, $\tau_{\Pi}(\varepsilon, n)$, $\tau_q(\varepsilon, n)$ toward values dictated by gradients in flow and temperature. Causality is satisfied in a region of parameter space; however, stability is not guaranteed [25].

More importantly, unlike the Euler and NS equations, the Israel-Stewart approach is not a controlled approximation to the transport theory of Eq. (5). Instead of an expansion in some small parameter, it corresponds to a quadratic ansatz [23,33] for the deviation from local equilibrium

$$\phi_G(x, \mathbf{p}) = D^{\mu}(x)\frac{p_{\mu}}{T} + C^{\mu\nu}(x)\frac{p_{\mu}p_{\nu}}{T^2}, \tag{11}$$

where D^{μ} and $C^{\mu\nu}$ are determined by the local dissipative corrections $\pi^{\mu\nu}$, Π, and q^{μ}.[2] In contrast, the Chapman-Enskog solution (9) contains all orders in momentum. An evident pathology of the quadratic form (11) is that, in general, ϕ_G is not bounded from below, and thus the phase-space density becomes negative at large momenta [cf. Eqs. (7) and (62)]. Furthermore, the two approaches give different results not only for the relaxation times [21,23], e.g.,

$$\tau_{\pi}^{\rm NS} = 0, \quad \tau_{\pi}^{\rm IS} = \frac{3\eta_s}{2p}, \tag{12}$$

but also for the transport coefficients themselves. For an energy-independent isotropic cross section and ultrarelativistic particles ($T \gg m$), the difference is small [21], e.g.,

$$\eta_s^{\rm NS} \approx 0.8436\frac{T}{\sigma_{\rm tr}}, \quad \eta_s^{\rm IS} = \frac{4T}{5\sigma_{\rm tr}}, \tag{13}$$

but can be large for more complicated interactions. Here $\sigma_{\rm tr} \equiv \int d\Omega_{\rm c.m.} \sin^2\theta_{\rm c.m.} d\sigma/d\Omega_{\rm c.m.}$ is the transport cross section (for isotropic, $\sigma_{\rm tr} = 2\sigma_{\rm TOT}/3$).

In the following sections, we analyze IS hydrodynamic solutions analytically and numerically and test the accuracy of the IS approximation via comparison with solutions from full $2 \to 2$ transport theory.

[1] Bose (+) or Fermi (−) statistics can be included in a straightforward manner by substituting $f_1 g_2 \to f_1 g_2(1 \pm \tilde{f}_3)(1 \pm \tilde{g}_4)$ and $f_3 g_4 \to f_3 g_4(1 \pm \tilde{f}_1)(1 \pm \tilde{g}_2)$ in the collision term of Eq. (6) where $\tilde{f} \equiv (1/\gamma)(2\pi)^3 f$ and $\tilde{g} \equiv (1/\gamma)(2\pi)^3 g$ for particles of degeneracy γ. The various hydrodynamic limits can then be derived analogously to the Boltzmann case, if one makes the convenient replacement $\phi \to (1 \pm \tilde{f}_{\rm eq})\phi$ in Eq. (7).

[2] The alternative formulation based on transient thermodynamics [22,23] also lacks a small expansion parameter.

III. ISRAEL-STEWART HYDRODYNAMICS AND BOOST INVARIANCE

A. Israel-Stewart equations

There seems to be some confusion regarding IS theory [22, 23] in the recent literature; therefore, we start with reviewing the key ingredients. The starting point of IS theory is an entropy current that includes terms up to quadratic order in dissipative quantities[3]

$$S^\mu = u^\mu\left[s_{\rm eq} - \frac{1}{2T}(\beta_0\Pi^2 - \beta_1 q_\nu q^\nu + \beta_2\pi^{\lambda\nu}\pi_{\lambda\nu})\right] + \frac{q^\mu}{T}\left(\frac{\mu n}{\varepsilon+p} + \alpha_0\Pi\right) - \frac{\alpha_1 q_\nu \pi^{\nu\mu}}{T} \tag{14}$$

(we follow the Landau frame convention). Here μ is the chemical potential, and $s_{\rm eq}$ is the entropy density in local equilibrium. The coefficients $\{\alpha_i(\varepsilon,n)\}$ and $\{\beta_i(\varepsilon,n)\}$ encode additional matter properties that complement the equation of state the transport coefficients. Most importantly, the parameters $\{\beta_i\}$ control the relaxation times for dissipative quantities:

$$\tau_\Pi = \zeta\beta_0, \quad \tau_q = \kappa_q T\beta_1, \quad \tau_\pi = 2\eta_s\beta_2. \tag{15}$$

The entropy current and relaxation times in NS theory are recovered when all the coefficients are set to zero $\beta_0 = \beta_1 = \beta_2 = 0 = \alpha_0 = \alpha_1$ (but as discussed previously, the IS and NS transport coefficients differ in general).

The requirement of entropy nondecrease ($\partial_\mu S^\mu \geqslant 0$), which IS satisfies via a positive semidefinite[4] quadratic ansatz

$$T\partial_\mu S^\mu = \frac{\Pi^2}{\zeta} - \frac{q_\mu q^\mu}{\kappa_q T} + \frac{\pi_{\mu\nu}\pi^{\mu\nu}}{2\eta_s} \geqslant 0, \tag{16}$$

leads to the identification of the dissipative currents:

$$\Pi = \zeta\left[-\nabla_\mu u^\mu - \frac{1}{2}\Pi T\partial_\mu\left(\frac{\beta_0 u^\mu}{T}\right) - \beta_0 D\Pi + \alpha_0\partial_\mu q^\mu - a_0' q^\mu Du_\mu\right], \tag{17}$$

$$q^\mu = -\kappa_q T\Delta^{\mu\nu}\left[\frac{Tn}{\varepsilon+p}\nabla_\nu\left(\frac{\mu}{T}\right) + \frac{1}{2}q_\nu T\partial_\lambda\left(\frac{\beta_1 u^\lambda}{T}\right) + \beta_1 Dq_\nu + \alpha_0\nabla_\nu\Pi - \alpha_1\partial^\lambda\pi_{\lambda\nu} - a_0\Pi Du_\nu + a_1\pi_{\lambda\nu}Du^\lambda\right], \tag{18}$$

$$\pi^{\mu\nu} = 2\eta_s\left[\nabla^{\langle\mu}u^{\nu\rangle} - \frac{1}{2}\pi^{\mu\nu}T\partial_\lambda\left(\frac{\beta_2 u^\lambda}{T}\right) - \beta_2\langle D\pi^{\mu\nu}\rangle - \alpha_1\nabla^{\langle\mu}q^{\nu\rangle} + a_1' q^{\langle\mu}Du^{\nu\rangle}\right], \tag{19}$$

$$a_i' \equiv \left.\frac{\partial(\alpha_i/T)}{\partial(1/T)}\right|_{\mu/T=\rm const} - a_i. \tag{20}$$

[3]Unlike us here, Israel and Stewart choose $g^{\mu\nu} = {\rm diag}(-1,1,1,1)$, $\Delta^{\mu\nu} = g^{\mu\nu} + u^\mu u^\nu$.

[4]Positive semidefiniteness follows from the general properties $q^\mu q_\mu \leqslant 0$ and $\pi^{\mu\nu}\pi_{\mu\nu} \geqslant 0$.

Here $D \equiv u^\mu\partial_\mu$, and the $\langle\rangle$ brackets denote traceless symmetrization and projection orthogonal to the flow

$$A^{\langle\mu\nu\rangle} \equiv \tfrac{1}{2}\Delta^{\mu\alpha}\Delta^{\nu\beta}(A_{\alpha\beta} + A_{\beta\alpha}) - \tfrac{1}{3}\Delta^{\mu\nu}\Delta_{\alpha\beta}A^{\alpha\beta}. \tag{21}$$

The new matter coefficients $\{a_i(\varepsilon,n)\}$ are needed to describe how contributions from the $q^\mu\Pi$ and $q_\nu\pi^{\mu\nu}$ terms in Eq. (14) are split between the bulk pressure and heat flow, and the heat flow and shear stress evolution equations, respectively (in other words, a whole class of equations of motion generates the same amount of entropy; see Appendix A).

Notice that the time derivatives of heat flow q^μ and shear stress tensor $\pi^{\mu\nu}$ are not expressed *explicitly* in Eqs. (18)–(19); instead, orthogonal projections to the flow velocity vector appear [cf. Eqs. (8a)–(8c) in Ref. [22]]. Reordering the equations explicitly for the time derivatives gives rise to the terms $-u^\mu q_\nu Du^\nu$ and $-(\pi^{\lambda\mu}u^\nu + \pi^{\lambda\nu}u^\mu)Du_\lambda$. There is therefore no need for a kinetic theory treatment [34] to derive these terms. They were missed in Ref. [12], but they are already present in standard IS theory as a trivial consequence of the product rule of differentiation and the orthogonality of the flow velocity and shear stress/heat flow.

As we saw above, the Israel-Stewart procedure only determines the equations of motion up to nonequilibrium terms that do not contribute to entropy production. In kinetic theory, more such terms arise [23] when the vorticity

$$\omega^{\mu\nu} \equiv \tfrac{1}{2}\Delta^{\mu\alpha}\Delta^{\nu\beta}(\partial_\beta u_\alpha - \partial_\alpha u_\beta) \tag{22}$$

is nonzero. Including the vorticity terms, the complete set of evolution equations for the dissipative currents are

$$D\Pi = -\frac{1}{\tau_\Pi}\left(\Pi + \zeta\nabla_\mu u^\mu\right) - \frac{1}{2}\Pi\left(\nabla_\mu u^\mu + D\ln\frac{\beta_0}{T}\right) + \frac{\alpha_0}{\beta_0}\partial_\mu q^\mu - \frac{a_0'}{\beta_0}q^\mu Du_\mu, \tag{23}$$

$$Dq^\mu = -\frac{1}{\tau_q}\left[q^\mu + \kappa_q\frac{T^2 n}{\varepsilon+p}\nabla^\mu\left(\frac{\mu}{T}\right)\right] - u^\mu q_\nu Du^\nu - \frac{1}{2}q^\mu\left(\nabla_\lambda u^\lambda + D\ln\frac{\beta_1}{T}\right) - \omega^{\mu\lambda}q_\lambda - \frac{\alpha_0}{\beta_1}\nabla^\mu\Pi + \frac{\alpha_1}{\beta_1}(\partial_\lambda\pi^{\lambda\mu} + u^\mu\pi^{\lambda\nu}\partial_\lambda u_\nu) + \frac{a_0}{\beta_1}\Pi Du^\mu - \frac{a_1}{\beta_1}\pi^{\lambda\mu}Du_\lambda, \tag{24}$$

$$D\pi^{\mu\nu} = -\frac{1}{\tau_\pi}\left(\pi^{\mu\nu} - 2\eta\nabla^{\langle\mu}u^{\nu\rangle}\right) - (\pi^{\lambda\mu}u^\nu + \pi^{\lambda\nu}u^\mu)Du_\lambda - \frac{1}{2}\pi^{\mu\nu}\left(\nabla_\lambda u^\lambda + D\ln\frac{\beta_2}{T}\right) - 2\pi_\lambda^{\langle\mu}\omega^{\nu\rangle\lambda} - \frac{\alpha_1}{\beta_2}\nabla^{\langle\mu}q^{\nu\rangle} + \frac{a_1'}{\beta_2}q^{\langle\mu}Du^{\nu\rangle}. \tag{25}$$

We will refer to these equations as "complete IS." If we ignore their tensorial structure, the equations have the general form

$$\dot{X} = -\frac{1}{\tau_X}(X - X_{\rm NS}) + X\,Y_X + Z_X \tag{26}$$

for each dissipative quantity X, where $X_{\rm NS}$ is the value of X in NS theory and Y_X, Z_X are given by the ideal hydrodynamic fields and dissipative quantities other than X. Therefore, IS theory describes relaxation toward Navier-Stokes on a

characteristic time τ_X, provided $|Y_X|\tau_X \ll 1$ and $|Z_X|\tau_X \ll |X_{\rm NS}|$. If Y_X and/or Z_X are not small, the effective relaxation times in IS theory differ from τ_X; moreover, the relaxation of dissipative quantities is no longer toward their NS values. This has been discussed in Ref. [12], which, however, argued for dropping all $XY_X + Z_X$ terms for the very same reason.

In the last step of their derivation, Israel and Stewart neglect the terms with the factor 1/2 (this gives the equivalent to [23]), because they expect to study astrophysical systems with small gradients $|\partial^\mu u^\nu + \partial^\nu u^\mu|/T \ll 1$, $|\partial^\mu \varepsilon|/(T\varepsilon) \ll 1$, $|\partial^\mu n|/(Tn) \ll 1$, near a global (possibly rotating) equilibrium state. The neglected terms are then products of small gradients and the dissipative quantities. We will refer to this approximation as "naive IS."[5]

In heavy ion physics applications, on the other hand, gradients $\partial^\mu u^\nu/T$, $|\partial^\mu \varepsilon|/(T\varepsilon)$, and $|\partial^\mu n|/(Tn)$ at early times $\tau \sim 1$ fm are large $\sim\mathcal{O}(1)$, and therefore cannot be ignored. Nevertheless, hydrodynamics may still be applicable, provided the viscosities are unusually small, i.e., $\eta_s/s_{\rm eq} \sim 0.1$, $\zeta/s_{\rm eq} \sim 0.1$, where $s_{\rm eq}$ is the entropy density in local equilibrium. In this case, dissipative effects are still moderate, for example, the pressure corrections from NS theory [Eq. (3)] are

$$\frac{\delta T^{\mu\nu}_{\rm NS}}{p} \approx \left(2\frac{\eta_s}{s_{\rm eq}}\frac{\nabla^{\langle\mu}u^{\nu\rangle}}{T} + \frac{\zeta}{s_{\rm eq}}\frac{\nabla_\alpha u^\alpha}{T}\right)\frac{\varepsilon+p}{p} \sim \mathcal{O}\left(\frac{8\eta_s}{s_{\rm eq}}, \frac{4\zeta}{s_{\rm eq}}\right) \tag{27}$$

Heat flow effects can also be estimated based on Eq. (4):

$$\frac{\delta N^\mu_{\rm NS}}{n} \approx \frac{\kappa_q T}{s_{\rm eq}}\frac{n}{s_{\rm eq}}\frac{\nabla^\mu(\mu/T)}{T}. \tag{28}$$

For RHIC energies and above, at midrapidity, the correction is rather small even for large κ_q because the baryon density and therefore μ_B/T is very low. For example, in a recent ideal fluid calculation at RHIC energy [36], these ratios were $n_B/s \approx 2.2\times10^{-3}$ and $\mu_B/T \approx 0.2$ in order to reproduce the observed net baryon spectra. These choices are also supported by thermal model analyses of particle ratios which lead to $\mu_B/T \approx 0.17$ [37].

B. Viscous equations of motion for longitudinally boost-invariant 0 + 1D dynamics

At this point, we specialize the equations of motion to a viscous, longitudinally boost-invariant[6] system with transverse translation invariance and vanishing bulk viscosity:

$$\dot{n} + \frac{n}{\tau} = 0 \quad\Leftrightarrow\quad n(\tau) = \frac{\tau_0 n(\tau_0)}{\tau}, \tag{29}$$

$$\dot{\varepsilon} + \frac{\varepsilon+p}{\tau} = -\frac{\pi_L}{\tau}, \tag{30}$$

$$\tau_\pi\dot{\pi}_L + \pi_L\left[1 + \frac{\tau_\pi}{2\tau} + \frac{\eta_s T}{2}\left(\frac{\dot{\tau}_\pi}{\eta_s T}\right)\right] = -\frac{4\eta_s}{3\tau}, \tag{31}$$

$$\pi_T = -\frac{\pi_L}{2}. \tag{32}$$

This special case is well known in the literature [9,34,38] as a useful approximation to the early longitudinal expansion stage of a heavy ion collision for observables near midrapidity $\eta \approx 0$. Here $\tau \equiv \sqrt{t^2 - z^2}$ is the Bjorken proper time, and the 'dot' denotes $d/d\tau$. π_L and π_T are the viscous corrections to the longitudinal and transverse pressure, i.e., the π_{zz} and $\pi_{xx} = \pi_{yy}$ components of the shear stress tensor evaluated in the local rest frame,[7] respectively. All the other components of the stress tensor are zero due to symmetry. There is no equation for heat flow, because the symmetries of the system—longitudinal boost-invariance, axial symmetry in the transverse plane, and $\eta \to -\eta$ reflection symmetry—force the heat flow to be zero everywhere. We have chosen to ignore bulk viscosity, since shear viscosity is expected to dominate at RHIC. In the following, we also concentrate on a system of massless particles, where bulk viscosity is zero in general. It is worth noticing that these equations are identical in both Eckart and Landau frames; but in less restricted systems where heat flow is nonzero, Eckart and Landau frames differ.

To simplify the discussion and facilitate comparison with transport results, from here on we concentrate on a system of massless particles with only elastic $2 \to 2$ interactions. Particle number is then conserved, and the equation of state is

$$\varepsilon = 3p, \quad T = \frac{p}{n}. \tag{33}$$

Now the density equation decouples entirely, and we end up with two coupled equations for the equilibrium pressure and the viscous correction π_L. The shear stress relaxation time of Eq. (12) and the shear viscosity of Eq. (13) can be recast with the *transport* mean free path $\lambda_{\rm tr} \equiv 1/(n\sigma_{\rm tr})$ as

$$\eta_s = CnT\lambda_{\rm tr}, \quad \tau_\pi = \frac{3C}{2}\lambda_{\rm tr}, \quad C \approx \frac{4}{5}, \tag{34}$$

and Eqs. (30) and (31) can then be written as

$$\dot{p} + \frac{4p}{3\tau} = -\frac{\pi_L}{3\tau}, \tag{35}$$

$$\dot{\pi}_L + \frac{\pi_L}{\tau}\left(\frac{2\kappa(\tau)}{3} + \frac{4}{3} + \frac{\pi_L}{3p}\right) = -\frac{8p}{9\tau}, \tag{36}$$

where

$$\kappa(\tau) \equiv \frac{K(\tau)}{C} = \frac{nT\tau}{\eta_s}, \quad K(\tau) \equiv \frac{\tau}{\lambda_{\rm tr}(\tau)}. \tag{37}$$

The ratio of expansion and scattering time scales K controls how well ideal and/or dissipative hydrodynamics applies. This is essentially the *inverse* of the ratio of shear stress relaxation time to hydrodynamic time scales $\tau_\pi/\tau = 3/(2\kappa)$. K is also a generalization of the inverse Knudsen number L/λ, since the shortest spatial length scale is given by gradients in the longitudinal direction $L \sim 1/(\partial_z u_z) \sim \tau$. It is also a measure

[5] Note that in Ref. [35], the equivalent sets of equations are called "full IS" and "simplified IS."

[6] By a boost-invariant system we mean a system that obeys the scaling flow, $v = (0, 0, z/t)$, where all scalar quantities are independent of coordinate rapidity $\eta \equiv (1/2)\ln[(t+z)/(t-z)]$, and where all vector and tensor quantities can be obtained from their values at $\eta = 0$ by an appropriate Lorentz boost.

[7] That is, in the often employed curvilinear τ-η-x-y coordinates, we have $\pi_{\eta\eta} = \tau^2\pi_L$.

of the shear viscosity to entropy density ratio, because for a system in chemical equilibrium, $s_{\rm eq} = 4n$ and thus

$$\frac{\eta_s}{s_{\rm eq}} = \frac{T\tau}{4\kappa}. \tag{38}$$

(See Sec. V E for the general case.)

Similar treatment to relativistic NS theory leads to

$$\pi_L = -\frac{4\eta_s}{3\tau} = -\frac{4p}{3\kappa} \tag{39}$$

and the equation of motion

$$\dot{p} + \frac{4p}{3\tau} = \frac{4}{9\kappa(\tau)}\frac{p}{\tau}. \tag{40}$$

As discussed in the previous section, the viscosities in NS and IS theories differ; therefore, κ in Eq. (40) is not identical to the one in Eq. (36). We will ignore the difference, because in our case it is only ≈5%.

Finally, we note that in the "naive" Israel-Stewart approximation, Eq. (36) changes to

$$\dot{\pi}_L + \frac{2\kappa(\tau)\pi_L}{3\tau} = -\frac{8p}{9\tau}. \tag{41}$$

IV. BASIC OBSERVABLES

Here we introduce the basic observables investigated in this study and discuss their evolution based on the analytic IS and NS solutions of Appendix C. It is important to emphasize that our observations will hold only during the longitudinal expansion stage of heavy ion collisions. After some time $\tau \sim R/c_s$, transverse expansion sets in, and hydrodynamics, whether IS or NS, eventually breaks down, because for expansion in three dimensions, $\lambda_{\rm tr} \sim \tau^3/\sigma$, i.e., $\kappa \sim \sigma/\tau^2 \to 0$ in the hadronic world where cross sections are bounded. It is interesting to note that $\eta_s/s_{\rm eq} \approx$ const would not decouple even for a three-dimensional expansion (because in that case $T \propto 1/\tau$, and thus $\lambda_{\rm tr} \propto \eta/p \propto \tau$, while $\tau_{\rm exp} \equiv 1/(\partial_\mu u^\mu) \propto \tau$, i.e., $\kappa \sim$ const).

Throughout this section and the rest of the paper, the subscript 0 refers to the value of quantities at the initial time τ_0 [e.g., $A_0 \equiv A(\tau_0)$]. The most important parameters in the problem are the initial inverse Knudsen number K_0, or the corresponding κ_0, and the initial shear stress to pressure ratio $\xi_0 \equiv \pi_{L,0}/p_0$.

A. Pressure anisotropy

The magnitude of dissipative corrections can be quantified through the ratio of viscous longitudinal shear and equilibrium pressure

$$\xi \equiv \frac{\pi_L}{p}. \tag{42}$$

A suitable equivalent measure is the pressure anisotropy coefficient

$$R_p \equiv \frac{p_L}{p_T} = \frac{1+\xi}{1-\xi/2}, \tag{43}$$

which is the ratio of the transverse and longitudinal pressures $p_T \equiv p - \pi_L/2$ and $p_L \equiv p + \pi_L$. In the ideal hydrodynamic limit, the anisotropy is unity, $R_p \to 1$.

The time evolution of the anisotropy coefficient is given by the equations of motion (35) and (36):

$$\dot{R}_p = -\frac{4}{3\tau}\frac{4+3\kappa\xi}{(2-\xi)^2}. \tag{44}$$

Thus, in IS theory the pressure anisotropy is a constant of motion when the viscous stress is equal to its NS value [Eq. (39)], or at asymptotically late times $\tau \to \infty$. In contrast, from NS theory,

$$R_p^{\rm NS} = \frac{3\kappa - 4}{3\kappa + 2}, \tag{45}$$

which is only constant for $\kappa(\tau) =$ const (constant cross section), or in the ideal hydrodynamic limit $\kappa \to \infty$ (in which case, $R_p \to 1$). From the above, it also follows that in the special case of our boost-invariant scenario, if the cross section is constant and the shear stress starts from its NS value, then NS and IS theory *coincide*.

B. Longitudinal work

Dissipation also affects the evolution of the equilibrium (or average) pressure. From Eq. (35), for ideal hydrodynamic evolution, the pressure drops as $p(\tau) \propto \tau^{-4/3}$ because of longitudinal work. In the viscous case, the work done by the system is smaller, because the viscous correction to the longitudinal pressure is usually negative $\pi_L < 0$. Therefore, pressure decreases slower than in ideal hydrodynamics, and deviations from the ideal evolution, such as the ratio

$$\frac{p(\tau)}{p_{\rm ideal}(\tau)} \equiv \frac{T(\tau)}{T_{\rm ideal}} \quad \text{(for conserved particle number)}, \tag{46}$$

can be used to quantify dissipative effects.

Studies in the past [27,28] have analyzed a closely related quantity, the transverse energy per unit rapidity, $dE_T/d\eta$. This is simply a combination of the pressure anisotropy and deviation from ideal pressure

$$\begin{aligned}\frac{dE_T}{d\eta} &= \frac{3\pi T}{4}\frac{dN}{d\eta}\left(1 - \frac{5}{16}\xi\right) \\ &= \frac{3\pi T_0}{4}\frac{dN}{d\eta}\left(\frac{\tau_0}{\tau}\right)^{-1/3}\frac{p(\tau)}{p_{\rm ideal}(\tau)}\frac{3[7+R_p(\tau)]}{8[2+R_p(\tau)]}\end{aligned} \tag{47}$$

provided the quadratic ansatz (11) is applicable (see Appendix D1).

We can make a few generic observations based on the analytic IS and NS results of Eqs. (C4), (C8), (C21), (C22), and (C29) from Appendix C. For a constant cross section, $p/p_{\rm ideal}$ grows without bound, dissipative corrections keep accumulating forever. The influence of the initial shear stress, or equivalently shear stress to pressure ratio $\xi_0 \equiv \xi(\tau_0)$, is of $\mathcal{O}(\xi_0/\kappa_0)$ and thus vanishes in the large κ_0 limit. At late times $\tau \gg \tau_0$, for $K_0 \gtrsim 2$ and not too large initial shear stress to pressure ratio $|\xi_0| \ll 2\kappa_0$,

$$\begin{aligned}\left(\frac{p}{p_{\rm ideal}}\right)_{\sigma=\rm const} &\approx N\left(\frac{\tau}{\tau_0}\right)^{\beta}, \quad \beta \approx \frac{4}{9\kappa_0}\left(1 - \frac{2}{3\kappa_0^2}\right), \\ N &\approx 1 - \frac{2}{3\kappa_0^2} + \frac{4}{3\kappa_0^4} - \frac{\xi_0}{2\kappa_0},\end{aligned} \tag{48}$$

i.e., for $\tau \approx 10\tau_0$ and $K_0 = 2$ the accumulated pressure increase is $p/p_{\rm ideal} \approx 1.3$, while $p/p_{\rm ideal} \approx 1.15$ if $K_0 = 5$. For a scale-invariant system with $\eta_s/s_{\rm eq} \approx$ const, on the other hand, dissipative effects are more moderate for the same K_0 and at late times approach a finite upper bound

$$\left(\frac{p}{p_{\rm ideal}}\right)_{\eta/s\approx{\rm const}} \approx \left[1 - \frac{2}{3\kappa_0}\left(\frac{\tau_0}{\tau}\right)^{2/3}\right]\left(1 + \frac{2}{3\kappa_0} - \frac{\xi_0}{2\kappa_0}\right) \to 1 + \frac{2}{3\kappa_0} - \frac{\xi_0}{2\kappa_0}. \quad (49)$$

This is because scale-invariant systems turn more and more ideal hydrodynamically as they evolve (as long as their expansion is only longitudinal). For the same $K_0 = 2$ and 5 with $\xi_0 \approx 0$, the bounds are modest: $p/p_{\rm ideal} \lesssim 1.25$ and $\lesssim 1.1$, respectively.

C. Entropy

Another quantitative measure of the importance of dissipative effects is entropy production. Here we consider an ultrarelativistic system [thus $\Pi = 0$ and $\beta_2 = 3/(4p)$], with $2 \to 2$ interactions, 1D Bjorken boost invariance, and transverse translational, axial, and $\eta \to -\eta$ reflectional symmetries (imply $q^\mu = 0$). Therefore, the entropy current of Eq. (14) simplifies to

$$S^\mu = \bar{s}u^\mu, \quad \bar{s} = s_{\rm eq} - \frac{9\pi_L^2}{16pT}, \quad (50)$$

where

$$s_{\rm eq} = n(4 - \chi), \quad \chi \equiv \ln\frac{n}{n_{\rm eq}(T)} = \frac{\mu}{T}, \quad (51)$$

and

$$n_{\rm eq}(T) = \frac{g}{\pi^2}T^3 \quad (52)$$

is the particle density in chemical equilibrium at temperature T for massless particles of degeneracy g in the Boltzmann limit. Dissipative contributions in the entropy density $\bar{s}$ are *negative*, in accordance with the fundamental principle of maximal entropy in equilibrium.

The equations of motion (35) and (36) imply an entropy production rate of

$$\partial_\mu S^\mu = \frac{1}{\tau}\partial_\tau(\tau\bar{s}) = \frac{3\kappa n}{4\tau}\xi^2 \geqslant 0. \quad (53)$$

Equivalently, the entropy per unit rapidity

$$\frac{dS}{d\eta} \equiv \tau A_T \bar{s} \quad (54)$$

never decreases, that is,

$$\partial_\tau\left(\frac{dS}{d\eta}\right) = \frac{3\kappa}{4\tau}\frac{dN}{d\eta}\xi^2 \geqslant 0. \quad (55)$$

Here A_T is the transverse area of the system, and in the last step we substituted the rapidity density $dN/d\eta = \tau A_T n$. Equation (54) is a special case of a *generalized conservation law* [Eq. (B7)] applied to the entropy current S^μ, that is,

$$\tau\int dx_T^2\,\partial_\mu S^\mu = \partial_\tau\left(\tau\int dx_T^2\,S_0^{\rm LR}\right) - \partial_\eta\int dx_T^2\,S_3^{\rm LR}. \quad (56)$$

Analogous relations can be obtained for the energy, momentum, and charge density. In 0 + 1D these are quite trivial; they, respectively, reproduce Eq. (35), give identically zero, and yield $dN/d\eta =$ const. In higher dimensions, however, the generalized conservation laws present important constraints that *any* solution must satisfy at *all* times; therefore, they are ideal for testing the accuracy of numerical solutions at each time step (see Appendix B).

Only the complete set of IS equations gives the correct rate of entropy production. The naive approximation does not guarantee a monotonically increasing entropy

$$(\partial_\mu S^\mu)^{\rm naive\ IS} = \frac{3\kappa n}{4\tau}\xi^2\left(1 - \frac{\xi + 4}{2\kappa}\right) \quad (57)$$

unless κ is sufficiently large; and, away from equilibrium, it underpredicts for a given ξ the entropy production rate[8] (since $\xi < -1$ is unphysical). In contrast, the second law of thermodynamics does hold for Navier-Stokes:

$$(\partial_\mu S^\mu)^{\rm NS} = \frac{3\kappa n}{4\tau}\xi_{\rm NS}^2 \geqslant 0. \quad (58)$$

The NS result is the same as Eq. (53) but with the shear stress restricted to its NS value. We note that in IS theory, the naive entropy per unit rapidity, defined using the *equilibrium* entropy density

$$\frac{dS'}{d\eta} = s_{\rm eq}\tau A_T \quad (59)$$

does *not* increase monotonically. Rather, it increases (decreases) for negative (positive) π_L.

Based on the analytic IS and NS results in Appendix C, we can outline general expectations for the entropy evolution. For a constant cross section by late times $\tau \gg \tau_0$, the entropy increase relative to the initial entropy is logarithmic with time, i.e.,

$$\left[\frac{(dS/d\eta)}{(dS/d\eta)_0}\right]_{\sigma={\rm const}} - 1 \approx \frac{1}{4 - \chi_0}\left(3\ln\frac{p}{p_{\rm ideal}} - \frac{9\xi^2}{16}\right) \approx \frac{1}{4 - \chi_0}\left(3\beta\ln\frac{\tau}{\tau_0} - \frac{3}{\kappa_0^2} + \frac{16}{3\kappa_0^4} - \frac{3\xi_0}{2\kappa_0}\right), \quad (60)$$

where we considered initial conditions not too far from local equilibrium. For example, by $\tau \approx 10\tau_0$ with $K_0 = 2$ and chemical equilibrium initial conditions, ≈20% entropy is produced, while ≈10% with $K_0 = 5$. For a scale-invariant system with

[8] This, however, does *not* imply that the naive IS equations always underpredict the *total* integrated entropy change over a finite time interval. The time evolution of $\xi(\tau)$ in the naive approach differs in general from that in the complete theory.

$\eta_s/s_{\rm eq} = {\rm const}$, on the other hand, entropy production is slower for the same K_0 and saturates at late times, i.e.,

$$\left[\frac{(dS/d\eta)}{(dS/d\eta)_0}\right]_{\eta/s\approx{\rm const}} - 1 \approx \frac{1}{4-\chi_0}\frac{2}{\kappa_0}\left[1-\left(\frac{\tau_0}{\tau}\right)^{2/3}-\frac{3\xi_0}{4}\right] \to \frac{1}{4-\chi_0}\frac{2}{\kappa_0}\left(1-\frac{3\xi_0}{4}\right) = \frac{2}{T_0\tau_0}\frac{\eta_s}{s_{\rm eq}}\left(1-\frac{3\xi_0}{4}\right). \quad (61)$$

For the same $K_0 = 2$ and 5 (and $\xi_0 \approx 0$), the entropy increase by $\tau = 10\tau_0$ is smaller, ≈15% and ≈6%, respectively. Based on this simple analytic formula for entropy production, we also confirm the results of Ref. [38], which considered IS hydrodynamics with a unique initial condition $\xi_0 \approx -16/(9T_0\tau_0) \times \eta_s/s_{\rm eq}$, where $T_0 \approx 0.39$ GeV $\times$ (0.14 fm/τ_0)$^{1/3}$ and τ_0 was varied between 0.5 and 1.5 fm.

V. REGION OF VALIDITY FOR DISSIPATIVE HYDRODYNAMICS

Here we determine the region of validity of dissipative hydrodynamics by comparing it with full nonequilibrium two-body transport theory [26–29]. We consider two scenarios: scenario I with a constant cross section, which is least favorable for hydrodynamics; and scenario II with a growing $\sigma \propto \tau^{2/3}$, which is the most optimistic for applicability of hydrodynamics and is very close to $\eta_s/s_{\rm eq} = {\rm const}$, as we show in Appendix C. In the same appendix, we also study a scenario with $\sigma \propto 1/T^2$, which turns out to be close to scenario II but with stronger dissipative effects, and we discuss analytic NS and (approximate) IS solutions.

Because of scalings of the equations of motion, the results presented here are rather general. Equations (35) and (36) are invariant under rescaling of time, and/or joint rescaling of the pressures p and π_L, provided the dimensionless κ depends only on p, π_L, τ/τ_0, and no additional scales (all solutions studied here satisfy this condition). The same scalings are exhibited by the transport theory [28]. For a physically reasonable $p_0 > 0$, it is therefore convenient to consider dimensionless pressure variables $\tilde{p}(\tau) \equiv p(\tau)/p_0$ and $\pi_L(\tau)/p_0$, for which the solutions only depend on $\tilde{\tau} \equiv \tau/\tau_0$, $\kappa_0 \equiv K_0/C$, and the initial condition $\xi_0 \equiv \pi_{L,0}/p_0$.

Unless stated otherwise, we initialize the transport based on the quadratic form in Eq. (11). In our case of an ultrarelativistic system ($\varepsilon = 3p$) in the Boltzmann limit with vanishing bulk pressure and heat flow

$$D^\mu = 0, \quad C^{\mu\nu} = \frac{\pi^{\mu\nu}}{8p} \Rightarrow \phi_G(\eta=0,\mathbf{p}) = \frac{\xi}{16}\frac{2p_z^2 - p_\perp^2}{T^2}, \quad (62)$$

where $p_\perp \equiv \sqrt{p_x^2 + p_y^2}$ is the transverse momentum. We ensure non-negativity of the phase-space distribution via the Θ function

$$f(\eta=0,\mathbf{p},\tau=\tau_0) = \frac{F(\xi)}{A_T\tau_0}\frac{dN}{d\eta}\frac{e^{-p/T}}{8\pi T^3}[1+\phi_G(\eta,\mathbf{p})] \times \Theta(1+\phi_G(\eta,\mathbf{p})), \quad (63)$$

where A_T is the transverse area of the system (with the elimination of negative phase-space contributions, a normalization factor $F(\xi) \leqslant 1$ is needed to set a given $dN/d\eta$). The cutoff does not affect the general scalings of transport solutions but does influence the initial pressure anisotropy [for example, values $R_p = 0.3$ and 1.75 set based on Eq. (62) change to $R_p \approx 0.476$ and 1.693 when the cutoff is applied]. Therefore, we initialize hydrodynamics with a shear stress π_L that gives the same initial pressure anisotropy as the transport.

The transport solutions were obtained using the MPC algorithm [39], which employs the particle subdivision technique to maintain covariance [26,28]. Transverse translational invariance was maintained in the calculation through periodic boundary conditions in the two transverse directions. A longitudinally boost-invariant system was initialized in a coordinate rapidity interval $-5 < \eta < 5$, and observables were calculated by averaging over $-2 < \eta < 2$ with proper Lorentz boosts of local quantities to $\eta = 0$.

A. Pressure anisotropy

Figure 1 shows the pressure anisotropy p_L/p_T evolution as a function of the rescaled proper time $\tilde{\tau} = \tau/\tau_0$ from the transport and Israel-Stewart hydrodynamics with the local equilibrium initial condition. The left panel shows calculations

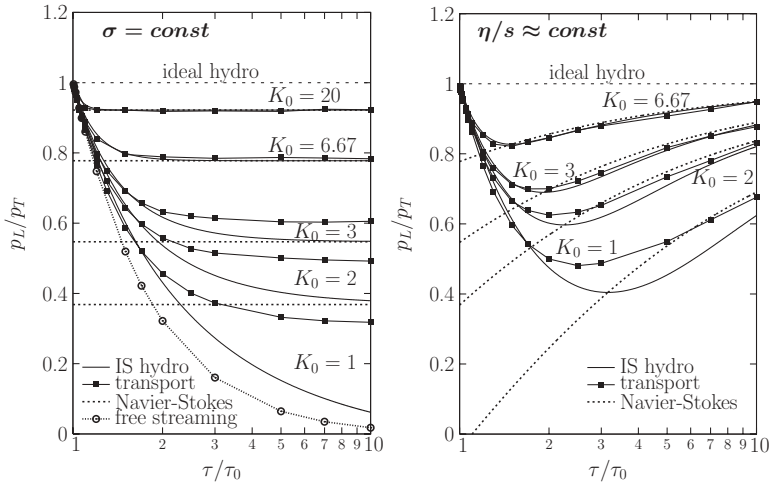

FIG. 1. Time evolution of pressure anisotropy $R_p \equiv p_L/p_T$ from covariant transport and Israel-Stewart dissipative hydrodynamics as a function of $K \equiv \tau/\lambda_{\rm tr}(\tau)$, from local equilibrium initial conditions $\pi_L(\tau_0) = 0$. Results for Navier-Stokes and free streaming are also shown. Left: $\sigma = {\rm const}$ scenario, for which the curves are labeled by $K(\tau) = {\rm const} = K_0 = 1, 2, 3, 6.67$, and 20. For $K = 1$, the Navier-Stokes result is negative and therefore not visible. Right: $\sigma \propto \tau^{2/3}$ scenario, for which $\eta_s/s_{\rm eq} \approx {\rm const}$ and the curves are labeled by the initial $K_0 = K(\tau_0) = 1, 2, 3$, and 6.67.

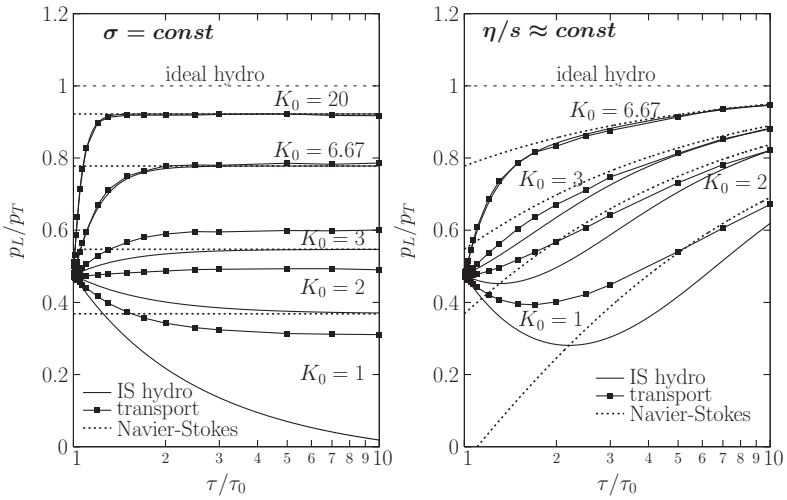

FIG. 2. Same as Fig. 1, but for an initial pressure anisotropy $R_p(\tau_0) = 0.476$ ($\xi_0 = -0.423$). In the $\sigma =$ const scenario, the NS curve for $K_0 = 1$ is negative and therefore not visible.

for the $\sigma =$ const scenario. For $K_0 = 1$, the anisotropy from IS hydro starts to fall rapidly below the transport above $\tau \gtrsim 2\tau_0$, and it is a factor of $\sim$5 smaller by late $\tau \sim 10\tau_0$. Clearly, the system cannot stay near equilibrium when the rate of scatterings equals the expansion rate. With increasing K_0, the undershoot becomes smaller and gradually vanishes as $K_0 \to \infty$. The difference is only $\sim$10% already at $K_0 = 3$ and is rather small by $K_0 \approx 7$.

The right panel shows the same but for the growing cross section scenario with $\eta_s/s_{\rm eq} \approx$ const. The situation of course improves because in this case K increases with time. For $K_0 = 1$, IS hydro undershoots the pressure anisotropy from the transport only by $\sim$20%, and the differences vanish at late times (since in this case both theories converge to $R_p = 1$ as $\tau \to \infty$). About 10% accuracy is achieved already for $K_0 = 2$, while for $K_0 = 3$, IS hydro is accurate to a few percent.

Moreover, the above findings hold for a wide range of initial conditions, including large initial pressure anisotropies, as shown in Figs. 2 and 3. These figures are for the same calculation but with $R_p(\tau_0) = 0.476$ and 1.693, respectively (which correspond to $\xi_0 = -0.423$ and 0.375). We emphasize that the results hold only if nonequilibrium corrections are close to the form (11) suggested by Grad. For such a class of initial conditions, however, we find that IS hydrodynamics can well approximate the transport ($\sim$10% accuracy) provided $K_0 \gtrsim 3$, even for the most pessimistic constant cross section scenario. If $\eta_s/s_{\rm eq} =$ const, only $K_0 \gtrsim 2$ is needed. We stress that in either case, there is no need for the initial conditions to be near the NS limit.

This is quite remarkable, because from Figs. 1–3 it is clear that already the early evolution differs between IS hydrodynamics and transport. For example, for an equilibrium initial condition ($\xi(\tau_0) = 0$), IS hydrodynamics of Eq. (44) gives

$$R_p^{\rm IS}(\tau) = 1 - \frac{4(\tau - \tau_0)}{3\tau_0} + \mathcal{O}((\tau - \tau_0)^2) \qquad (64)$$

for any initial value and evolution scenario for κ. From covariant transport, on the other hand (see Appendix D2),

$$R_p^{\rm transp}(\tau) = 1 - \frac{8(\tau - \tau_0)}{5\tau_0} + \mathcal{O}((\tau - \tau_0)^2). \qquad (65)$$

That is, pressure anisotropy develops, universally, 20% faster from the transport than from IS hydrodynamics (if the evolution starts from equilibrium).

This illustrates a limitation of the hydrodynamic description of transport solutions. Similar discrepancies were observed in Ref. [8] in the early evolution of differential elliptic flow

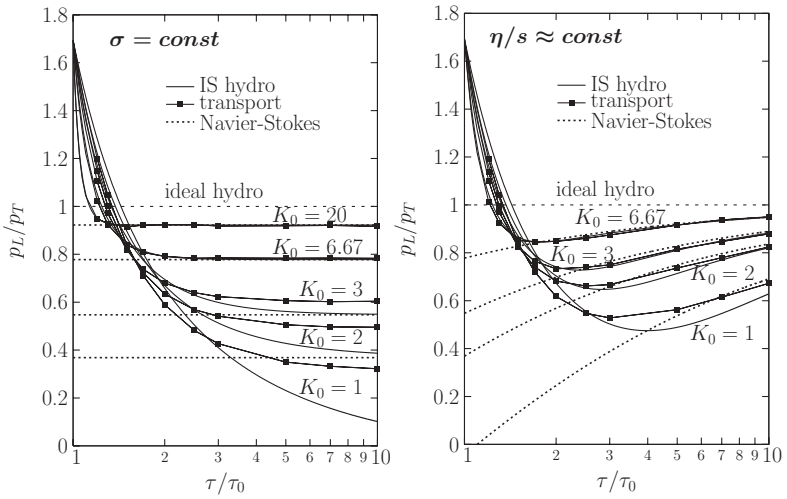

FIG. 3. Same as Fig. 1, but for an initial pressure anisotropy $R_p(\tau_0) = 1.693$ ($\xi_0 = 0.375$). In the $\sigma =$ const scenario, the Navier-Stokes curve for $K_0 = 1$ is negative and therefore not visible.

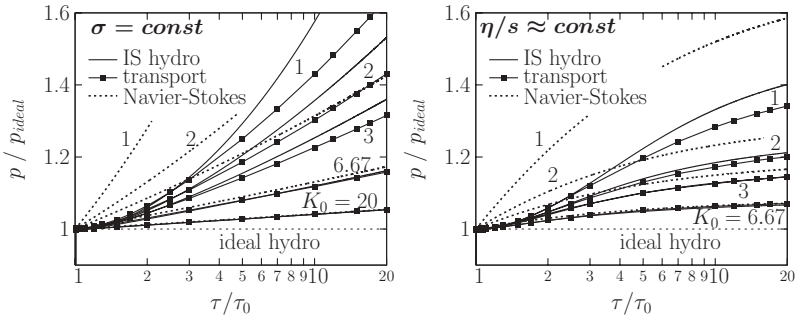

FIG. 4. Same as Fig. 1, except for the time evolution of the (average) pressure. The pressure is plotted normalized to the pressure $p_{\rm ideal}(\tau) = p_0(\tau_0/\tau)^{4/3}$ in ideal hydrodynamics.

$v_2(p_T)$. Remarkably, in our case, though the transport develops deviations from equilibrium faster, its rate of departure slows down quicker, which at intermediate times results in *smaller* accumulated dissipative corrections to the pressure anisotropy than from IS hydrodynamics. Eventually, the hydrodynamic evolution "catches up" to the transport, except for low $K \lesssim 3$ in the $\sigma =$ const scenario.

Figures 1–3 also show the Navier-Stokes approximation for each of the Israel-Stewart results. By late times, the NS and IS solutions converge for both cross section scenarios, independently of the initial pressure anisotropy (for $\sigma =$ const and $K_0 = 1$, the NS anisotropy is negative and therefore not visible in the plots). However, the applicability of NS theory at early times depends, besides on the value of K_0, strongly on how far the initial shear stress is from its NS value [Eq. (39)]. Navier-Stokes assumes that shear stress and, therefore, the pressure anisotropy relax immediately, but relaxation happens over a finite time. The approach toward the Navier-Stokes limit is governed by $\tau_\pi = 3\tau/(2\kappa)$, therefore *Navier-Stokes becomes applicable only after some time* $\Delta\tau \sim |R_0 - R_{\rm NS}|\tau_0/\kappa$. Note that the initial slope of the $R(\tau)$ curves does not always reflect τ_π directly, because it is given by the initial derivative of ξ

$$\dot{R}(\tau) \sim \frac{3}{2}\dot{\xi}(\tau) = -\frac{3}{2\tau_\pi}(\xi - \xi_{\rm NS}) + \mathcal{O}(1)\frac{\xi}{\tau}, \qquad (66)$$

where we combined Eqs. (26) and (35), incorporated the observations that $Y_\pi \sim \mathcal{O}(1)/\tau$ and $Z_\pi = 0$, and assumed ξ is small. For local equilibrium initial conditions, the slope of $R(\tau)$ is therefore $\sim\mathcal{O}(1)\xi_{\rm NS}/\tau_\pi \sim \mathcal{O}(1)/\tau$, independently of K_0 [cf. Fig. 1 and Eq. (64)]. For initial shear stresses far from the NS limit, on the other hand, the slope $\sim\mathcal{O}(1)\xi/\tau_\pi \propto \kappa$ steepens with increasing K as seen in Figs. 2 and 3.

The inaccurate description of early shear stress evolution in Navier-Stokes has a cumulative effect on the evolution of thermodynamic quantities, such as the pressure and the entropy, as we show in the next two sections. Of course, the errors are proportional to the ratio of the time the system spends away from the NS limit and the hydrodynamic time scale, i.e., $\Delta\tau/\tau_0 \sim 1/\kappa$.

B. Pressure evolution

Now we turn to the evolution of the (average) pressure. In ideal hydrodynamics ($K_0 \to \infty$), the pressure drops rapidly with time $p_{\rm id} \propto \tau^{-4/3}$. Therefore it is more convenient to study dissipative effects *relative* to ideal hydrodynamics through the ratio $p(\tau)/p_{\rm id}(\tau)$.

Figure 4 shows the pressure relative to that in ideal hydrodynamics as a function of the rescaled proper time $\tilde{\tau} = \tau/\tau_0$ from the transport and IS hydrodynamics with the local equilibrium initial condition. For the $\sigma =$ const scenario, for all K_0 values, the evolution starts out the same between IS hydrodynamics and transport but then the IS starts to accumulate deviations, because it follows the shear stress evolution only approximately. For $K_0 = 1$, IS hydrodynamics maintains 10% accuracy in the magnitude of dissipative *corrections* (i.e., $p/p_{\rm id} - 1$) only up to $\tau \approx 4\tau_0$. As K_0 increases, the situation improves gradually: for $K_0 = 3$, 10% accuracy holds up to $\tau \approx 10\tau_0$, and by $K_0 \approx 7$ the IS stays within a few percent of the transport even until $\tau = 20\tau_0$.

For the growing cross section scenario with $\eta_s/s_{\rm eq} \approx$ const, we see in Fig. 4 that hydrodynamic has a wider range of applicability. This is because $K \sim \tau^{2/3}$ grows with time. For $K_0 = 1$, the error in the dissipative correction $(p/p_{\rm id} - 1)$ is less than 10% up to $\tau \approx 5\tau_0$, and already for $K_0 = 2$, IS hydrodynamics is accurate to within better than 10% throughout the whole range $\tau \leqslant 20\tau_0$ studied. The pressure evolution results therefore reinforce the regions of validity found in the previous section ($K_0 \gtrsim 3$ for $\sigma =$ const, and $K_0 \gtrsim 2$ for $\eta_s/s_{\rm eq} \approx$ const).

Clearly, the region of applicability for Navier-Stokes is more limited (Fig. 4). For low K_0, it overestimates the pressure corrections not only at late times but also at early $\tau \sim$ few $\times\ \tau_0$. $K_0 \approx 7$ is barely sufficient for 10% accuracy in viscous corrections for $\eta_s/s_{\rm eq} \approx$ const, but it is not enough in the case of $\sigma =$ const. Based on the trends with increasing K_0, we estimate that $K_0 \gtrsim$ 9–10 is needed for Navier-Stokes with $\sigma =$ const to deviate less than 10% from the viscous effects calculated with the transport. Therefore, for local equilibrium initial conditions, Navier-Stokes theory becomes applicable at about three times shorter mean free paths, or equivalently three times larger longitudinal proper time τ (i.e., three times slower longitudinal expansion), than Israel-Stewart theory.

C. Entropy

Now we proceed with results on entropy production. In transport theory, the entropy current is defined as

$$S^\mu(x) = -\int \frac{d^3p}{p^0} p^\mu f(x,\mathbf{p}) \left[\ln\left(\frac{(2\pi)^3}{g} f(x,\mathbf{p})\right) - 1\right], \qquad (67)$$

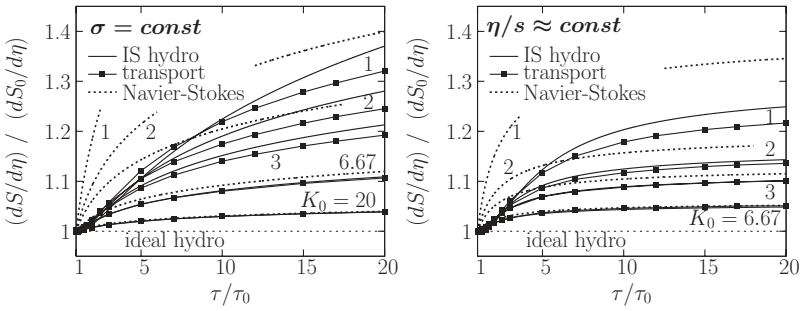

FIG. 5. Same as Fig. 1 except for the time evolution of the entropy per unit rapidity, normalized by its initial value (note the linear time axis used this time). For the transport solutions, entropy was calculated approximately using the IS entropy expression (50). Chemically equilibrated initial conditions (i.e., $\chi_0 = 0$) were assumed.

where g is the number of internal degrees of freedom. This nonlinear function of the phase-space density f is cumbersome to evaluate with the MPC code, and therefore we here opt for an approximate result based on the truncated IS expression (50), evaluated using the pressure and shear stress from the transport. This includes dissipative corrections to the entropy up to quadratic order in ϕ.

In the most dissipative $\sigma = \text{const}$ scenario with $K_0 = 1$, there is about 30% additional entropy produced by late times $\tau/\tau_0 \sim 10$–20, as can be seen in Fig. 5. For $\eta_s/s_{\text{eq}} \approx \text{const}$, the same $K_0 = 1$ yields only about 20% extra entropy. With increasing K_0, entropy generation gradually weakens, and by $K_0 \sim 7$ it is only 10% and 5%, respectively.

The Israel-Stewart results are within 15% of the approximate transport results already for $K_0 = 1$, and about 10% accuracy in the calculated dissipative effect is achieved for $K_0 \gtrsim 3$ (for $\sigma = \text{const}$) and $K_0 \gtrsim 2$ (for $\eta_s/s_{\text{eq}} \approx \text{const}$). In contrast, the Navier-Stokes strongly overpredicts the entropy, unless K_0 exceeds about 6 for $\sigma = \text{const}$ or ≈ 3 for $\eta_s/s_{\text{eq}} \approx \text{const}$. The bounds for 10% accuracy are in agreement with those found previously in Sec. V B.

D. Limitations of the naive Israel-Stewart approximation

Now we discuss the applicability of the "naive" Israel-Stewart equations. Figure 6 compares the pressure evolution in complete Israel-Stewart theory to that in the naive approximation, for local equilibrium initial conditions ($\xi_0 = 0$), as a function of the rescaled proper time τ/τ_0. Clearly, the naive result overshoots the pressure both for the constant cross section scenario and for $\eta_s/s_{\text{eq}} \approx \text{const}$, unless K_0 is large. This confirms expectations based on the analytic solutions in Appendix C. Though the naive theory converges to the correct result at large enough $K_0 \sim 7$–20, comparison with Fig. 4 tells us that it is even less accurate than Navier-Stokes theory.

Similar behavior has also been observed in a 2 + 1D calculation [35] that found that the naive approximation leads to larger dissipative effects on the *transverse* momentum anisotropy than the complete Israel-Stewart theory.

The reason for the large errors is that away from local equilibrium the naive approach drives the shear stress more negative [compare Eqs. (36) and (41), and note that typically $\pi_L < 0$]. For the 0 + 1D expansion studied here ($Y_\pi < 0$ and $Z_\pi = 0$), at early times, complete IS theory drives shear stress toward a value that is less negative than shear stress in Navier-Stokes; whereas at late times, the complete theory can keep the system closer to local equilibrium, because its effective shear stress relaxation time is shorter [see discussion in Ref. [12], or cf. Eq. (26)]. This is demonstrated in Fig. 7 where we plot the pressure anisotropy R_p, which is a monotonic function of $\xi = \pi_L/p$. For $\sigma = \text{const}$, we find that the naive approach saturates the anisotropy at a lower value than the complete theory, confirming the analytic expectations in Appendix C1. For $\eta_s/s_{\text{eq}} \approx \text{const}$, the system does approach ideal hydrodynamic behavior eventually; however, that occurs on a much longer time scale than from complete IS theory. This is in agreement with the expectation based on the analytic solutions (C35)–(C38).

The pressure anisotropy results further reinforce our conclusion that the naive Israel-Stewart approximation is poorer than Navier-Stokes (cf. Fig. 1). In heavy ion collisions, gradients are large, at least initially, and therefore cannot be ignored even if dissipative corrections (e.g., π_L/p) are small.

E. Implications for heavy ion physics

Having determined the region of validity (defined as 10% accuracy in dissipative effects) for IS and NS hydrodynamics in terms of the initial ratio of the expansion and scattering time scales $K_0 = \tau_0/\lambda_{\text{tr},0}$

$$K_0^{\text{IS}} \gtrsim 3, \quad K_0^{\text{NS}} \gtrsim 9 \quad (\sigma = \text{const}), \tag{68}$$

$$K_0^{\text{IS}} \gtrsim 2, \quad K_0^{\text{NS}} \gtrsim 6 \quad (\eta_s/s_{\text{eq}} \approx \text{const}), \tag{69}$$

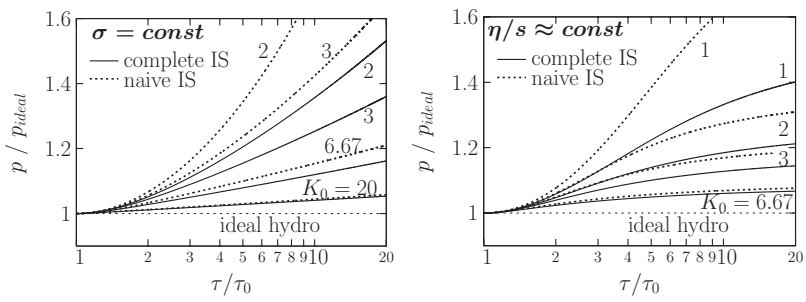

FIG. 6. Time evolution of the (average) pressure from complete IS theory and the naive IS approximation as a function of $K \equiv \tau/\lambda_{\text{tr}}(\tau)$, for local equilibrium initial conditions $\pi_L(\tau_0) = 0$. The pressure is plotted normalized to the pressure $p_{\text{id}}(\tau) = p_0(\tau_0/\tau)^{4/3}$ in ideal hydrodynamics. In the $\sigma = \text{const}$ scenario, $K(\tau) = \text{const} = K_0 = 2, 3, 6.67$, and 20. In the $\sigma \propto \tau^{2/3}$ scenario, $\eta_s/s_{\text{eq}} \approx \text{const}$ and the curves are labeled by the initial $K_0 = K(\tau_0) = 1, 2, 3$, and 6.67.

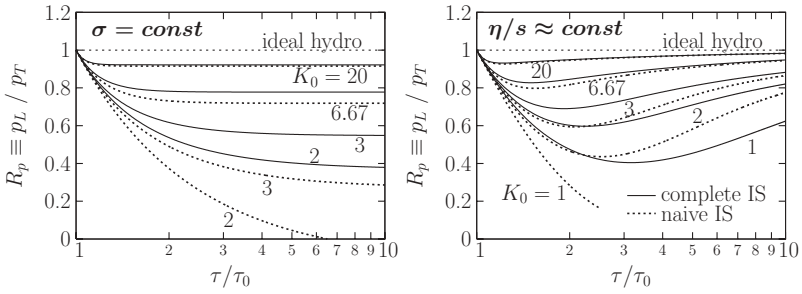

FIG. 7. Same as Fig. 6, but for the time evolution of the pressure anisotropy.

we now turn to implications for heavy ion collisions. From Eqs. (37), (51), and (52),

$$\kappa_0 = \frac{T_0\tau_0}{4-\chi_0}\frac{s_0}{\eta_{s,0}} \approx 15.9 \times \frac{1}{1-\chi_0/4}\left(\frac{T_0}{1\ \text{GeV}}\right)\left(\frac{\tau_0}{1\ \text{fm}}\right)\left(\frac{1/(4\pi)}{\eta_{s_0}/s_0}\right), \quad K_0 \approx 0.8\kappa_0. \tag{70}$$

Therefore, we can place an upper limit on the (initial) shear viscosity for which IS or NS reproduces with better than 10% accuracy the viscous corrections to basic observables such as pressure and entropy: for $\sigma = \text{const}$,

$$\left.\frac{4\pi\eta_{s,0}}{s_{\text{eq},0}}\right|_{\text{IS}} \lesssim 0.8T_0\tau_0, \qquad \left.\frac{4\pi\eta_{s,0}}{s_{\text{eq},0}}\right|_{\text{NS}} \lesssim 0.25T_0\tau_0, \tag{71}$$

while for $\eta_s/s_{\text{eq}} \approx \text{const}$,

$$\left.\frac{4\pi\eta_s}{s_{\text{eq}}}\right|_{\text{IS}} \lesssim 1.2T_0\tau_0, \qquad \left.\frac{4\pi\eta_s}{s_{\text{eq}}}\right|_{\text{NS}} \lesssim 0.4T_0\tau_0, \tag{72}$$

where we assumed chemical equilibrium initial conditions ($\chi_0 = 0$). If the shear viscosity of dense quark-gluon matter is bounded from below by $4\pi\eta_s/s_{\text{eq}} \gtrsim 1$, as has been conjectured recently, then the situation for Israel-Stewart theory is close to marginal. For $\eta_s/s_{\text{eq}} = 1/(4\pi)$, typical parton transport initial conditions ($T_0 = 0.7$ GeV, $\tau_0 = 0.1$ fm) translate into $K_0 \lesssim 1$, for which IS is not applicable for either scenario I or II; whereas for typical hydrodynamic initial conditions ($T_0 \sim 0.38$ GeV, $\tau_0 = 0.6$ fm), we have $K_0 \lesssim 3$, sufficient for both scenarios (barely for $\sigma = \text{const}$).

On the other hand, Navier-Stokes may be marginally applicable only if $\eta_s/s_{\text{eq}} \lesssim 0.5/(4\pi)$ throughout the whole evolution, at least based on this 0 + 1D study, where acausal artifacts and instabilities do not arise. We emphasize that the bound quoted here is for initial conditions close to local equilibrium. The accuracy of the NS approximation strongly depends on how far the initial shear stress is from the NS value. If the evolution starts out near the NS limit, we expect Navier-Stokes to be accurate up to higher viscosities.

Within the region of applicability of the Israel-Stewart theory, dissipative corrections to the average pressure and the entropy are modest and stay below ∼20% even up to late times $\tau \leqslant 10\tau_0$. This may serve as a useful "rule of thumb" applicability condition for hydrodynamics: if dissipative corrections to average pressure and the entropy calculated from hydrodynamics are significantly larger than 20%, the validity of hydrodynamics is questionable.

The above findings reinforce a recent calculation [18] in 2 + 1D that found good agreement between IS hydrodynamics and 2 → 2 transport, for conditions expected in Au + Au at $\sqrt{s_{NN}} \sim 200$ GeV/nucleon at RHIC, in the case of a small shear viscosity to entropy density ratio $\eta_s/s_{\text{eq}} \approx 1/(4\pi)$ (on average). The same study also found good agreement between the two theories for a large constant transport cross section $\sigma_{\text{tr}} \approx 13$ mb. That is also in line with our results here, because it corresponds to $4\pi\eta_s/s_{\text{eq}}(\tau_0) \approx 0.25$ in the center of the collision zone, i.e., initially $\eta_s/s_{\text{eq}} \lesssim 1/(4\pi)$ in most of the system.

Finally we note that the applicability of the hydrodynamic approach on very short time and length scales is another important question. In typical real-life problems, $T_0\tau_0 \gg 1$ because the hydrodynamic expansion time scale τ is by orders of magnitude larger than the quantum (energy) time scale $1/T$. This also leaves ample room to make hydrodynamics applicable ($\kappa_0 \gg 1$) even for appreciable viscosities. In the heavy ion case, however, the two time scales are comparable $T_0\tau_0 \sim \mathcal{O}(1)$, and therefore a macroscopic treatment may be marginal.

VI. CONCLUSIONS

Based on comparison to covariant transport theory, we explore the region of validity of Israel-Stewart and Navier-Stokes hydrodynamics in heavy-ion physics applications. We follow the evolution of the average pressure, pressure anisotropy, and entropy for a massless ideal gas in 0 + 1D longitudinally expanding Bjorken geometry. Binary 2 → 2 interactions are considered for two main scenarios, a fixed cross section $\sigma = \text{const}$ (scenario I, pessimistic for hydrodynamics) and a scale-invariant system with $\eta_s/s_{\text{eq}} \approx \text{const}$ (scenario II, optimistic for hydrodynamics).

We find (Sec. V) that dissipative effects calculated from IS hydrodynamics reproduce those from the transport solutions to within 10%, provided initially the expansion time scale is three (for scenario I) or two (for scenario II) times larger than the transport mean free path, i.e., the initial inverse Knudsen number $K_0 = \tau_0/\lambda_{\text{tr},0} \gtrsim 3$ or 2. When this criterion is fulfilled, Israel-Stewart is accurate even if initial pressure anisotropies are large $p_L/p_T \sim 0.4$–1.7, there is no need to start near the Navier-Stokes limit. On the other hand, the same accuracy from Navier-Stokes requires three times larger K_0, if the expansion starts from the local thermal equilibrium (unlike for Israel-Stewart, the applicability of Navier-Stokes depends strongly on how far the initial shear stress is from its NS

value). We emphasize that these findings apply only when *initial* viscous corrections are of the quadratic form suggested by Grad [Eq. (11)].

These results imply that (Sec. V E) for typical heavy ion initial conditions at RHIC energies, Israel-Stewart hydrodynamics is accurate up to $\eta_s/s_{\rm eq} \lesssim 1.5/(4\pi)$, while for Navier-Stokes, $\eta_s/s_{\rm eq} \lesssim 0.5/(4\pi)$ is needed. This is supported by a recent 2 + 1D calculation [18] that finds good agreement between IS and transport for $\eta_s/s_{\rm eq} \approx 1/(4\pi)$, and also for a large $\sigma_{\rm tr} \approx 13$ mb.

In addition, we test the accuracy of the naive IS approximation (Sec. V D) that neglects products of gradients and dissipative quantities in the equations of motion and find that it has an even more limited applicability than Navier-Stokes.

We also compare in detail (Appendix C) the IS and NS solutions in 0 + 1D for four scenarios, $\sigma = \text{const}, \sigma \propto 1/T^2, \sigma \propto \tau^{2/3}$, and $\eta_s/s_{\rm eq} = \text{const}$, and find that results for the latter two are almost identical, even at low initial Knudsen numbers $\sim$1. Moreover, we obtain analytic IS and NS solutions in 0 + 1D, which are useful for quick estimates (Secs. IV B and IV C) and to test numerical solution techniques. We also derive additional tests (Appendix B) based on generalized conservation laws for conserved currents, energy-momentum, and entropy, which can be utilized to verify the accuracy of numerical IS solvers in 1 + 1, 2 + 1, and 3 + 1 dimensions.

Finally we emphasize that the current study is limited to a massless ideal gas with particle number conserving interactions in 0 + 1D Bjorken geometry. The influence of the transverse expansion will be quantified in a future paper (requires at minimum a 1 + 1D approach). It will also be important to check how the results depend on the equation of state and the presence of particle nonconserving processes, such as radiative $2 \leftrightarrow 3$. For a nonconformal equation of state, bulk viscosity may become important [40,41]. Ideally, one should also test the accuracy of the hydrodynamic approximation for nonequilibrium theories other than covariant transport.

ACKNOWLEDGMENTS

We thank RIKEN, Brookhaven National Laboratory, and the US Department of Energy [DE-AC02-98CH10886] for providing facilities essential for the completion of this work. We also thank the hospitality of INT/Seattle (D.M., P.H.), KFMI/RMKI (D.M.), and Iowa State University (P.H.) where parts of this work were completed. Computational resources managed by RCAC/Purdue are also gratefully acknowledged.

APPENDIX A: ORIGIN OF a_0, a_1, a_0', a_1' IN THE IS EQUATIONS OF MOTION

The equations of motion (23)–(25) reproduce the entropy production rate of Eq. (16) only approximately, up to typically small quartic and higher-order corrections in dissipative quantities. With $a_i \equiv 0 \equiv a_i'$, a contribution

$$\Pi q^\mu T\nabla_\mu(\alpha_0/T) - q_\nu \pi^{\nu\mu} T\nabla_\mu(\alpha_1/T) \tag{A1}$$

would be *missing* from $T\partial_\mu S^\mu$ in Eq. (16). These terms are bilinear in the dissipative quantities and, therefore, can be split arbitrarily between the bulk pressure and heat, and heat and shear equations of motion. That is, with

$$T\nabla^\mu(\alpha_i/T) \equiv a_i^\mu + a_i'^\mu \tag{A2}$$

Eq. (16) is identically satisfied but contributions to the equations of motion depend on a_i

$$\beta_0 D\Pi = (\cdots) + a_0'^\mu q_\mu, \tag{A3}$$

$$\beta_1 Dq^\mu = (\cdots) + \Delta^\mu_\nu a_0{}^\nu \Pi - a_1^\nu \pi^\mu_\nu, \tag{A4}$$

$$\beta_2 D\pi^{\mu\nu} = (\cdots) - a_1'^{\langle\nu} q^{\mu\rangle}. \tag{A5}$$

Only components orthogonal to u^μ contribute, but apart from that constraint, a_0^μ and a_1^μ are arbitrary functions of the hydrodynamic fields and their derivatives and potentially new scalar functions $\{a_i^{(k)}(\varepsilon, n)\}$ characterizing an isotropic matter. However, ignoring the dependence on the dissipative quantities is consistent with the truncation of the entropy current [Eq. (14)] at quadratic order in those. Moreover, for small deviations from equilibrium, one may seek to include only the leading contributions coming from first derivatives of the ideal hydrodynamic fields, i.e.,

$$a_i^\nu = a_i^{(1)} Du^\nu + a_i^{(2)} T\nabla^\nu \frac{1}{T} + a_i^{(3)} \nabla^\nu \frac{\mu}{T}, \tag{A6}$$

where we chose $1/T$ and μ/T as the two independent variables instead of ε and n. But the three terms are not independent: energy-momentum conservation [Eq. (1)] and the Gibbs-Duhem relation $s\,dT = dP - n\,d\mu$ provide one constraint

$$\frac{1}{T}\Delta^{\nu\alpha} Du_\alpha + \nabla^\nu \frac{1}{T} = \frac{n}{\varepsilon + p}\nabla^\nu \frac{\mu}{T}, \tag{A7}$$

and $\nabla^\nu(\mu/T)$ may be ignored, at least parametrically, because it is proportional to the heat flow [Eq. (4)] in the first-order (Navier-Stokes) theory. Therefore, to leading accuracy only one scalar function enters, and we can write

$$a_i^\mu = -a_i(\varepsilon, n) Du^\mu. \tag{A8}$$

Analogous arguments give

$$T\nabla^\nu(\alpha_i/T) \approx T\frac{\partial(\alpha_i/T)}{\partial(1/T)}\nabla^\nu \frac{1}{T} \approx -\frac{\partial(\alpha_i/T)}{\partial(1/T)}\nabla^{\nu\alpha} Du_\alpha, \tag{A9}$$

from which Eq. (20) follows.

We plan to revisit the above approximations in a future study. In any case, they do not influence our 0 + 1D calculations here, because the a_i terms do not play a role (heat flow vanishes by symmetry).

APPENDIX B: GENERALIZED CONSERVATION LAWS

Here we present general relations of the form

$$\frac{d\mathcal{A}(\tau)}{d\tau} = \mathcal{B}(\tau), \tag{B1}$$

which can be used to test the accuracy of numerical dissipative hydrodynamics solutions in any dimensions. $\mathcal{A}$ and $\mathcal{B}$ only

depend on the hydrodynamic fields at the given τ. Evaluating them at each time step, one can either numerically differentiate $\mathcal{A}(\tau)$ or integrate $\mathcal{B}(\tau)$ and check how accurately the solutions satisfy Eq. (B1).

Consider a four-divergence $\partial_\mu A^\mu(x)$ (in regular Minkowski coordinates). Integration over a four-volume V_4 gives

$$\int_{V_4} d^4x \partial_\mu A^\mu(x) = \int_{\sigma(V_4)} d\sigma_\mu(x) A^\mu(x), \tag{B2}$$

where $\sigma(V_4)$ is the three-dimensional boundary ("surface") of V_4. Now take the special case of a Bjorken "box" $V_4 = \Delta\tau \times \Delta\eta \times A_T$ with an infinite transverse area $A_T \to \infty$ but infinitesimal proper time and finite coordinate rapidity extensions $\Delta\tau \to 0$, $\Delta\eta = \eta_2 - \eta_1$. Assuming $A^\mu(x)$ drops faster than $1/x_T^2$ at large $|\mathbf{x}_T|$, we can neglect surface terms at $|\mathbf{x}_T| \to \infty$ and keep only contributions on $\tau = \text{const}$ and $\eta = \text{const}$ hypersurfaces:

$$\begin{aligned}\int d\tau\, \tau d\eta\, dx_T^2\, \partial_\mu A^\mu(x) &= \left[\int_{\sigma(\tau+d\tau)} d\sigma_\mu^{(\tau)} - \int_{\sigma(\tau)} d\sigma_\mu^{(\tau)}\right. \\ &\quad \left. + \int_{\sigma(\eta_2)} d\sigma_\mu^{(\eta)} - \int_{\sigma(\eta_1)} d\sigma_\mu^{(\eta)}\right] A^\mu(x)\end{aligned} \tag{B3}$$

where the surface normals are

$$\begin{aligned} d\sigma^\mu_{(\tau)} &= \tau\, dx_T^2\, d\eta u_B^\mu, \quad d\sigma^\mu_{(\eta)} = -d\tau\, dx_T^2\, u_3^\mu, \\ \text{with} \quad u_B^\mu &\equiv (\text{ch}\,\eta, \mathbf{0}, \text{sh}\,\eta), \quad u_3^\mu \equiv (\text{sh}\,\eta, \mathbf{0}, \text{ch}\,\eta), \end{aligned} \tag{B4}$$

and we used $d^4x = d\tau\, \tau\, d\eta\, dx_T^2$. Here, u_B is the longitudinal Bjorken flow velocity, while u_3 is its orthonormal counterpart in the t-z plane. Note that the actual flow velocity does *not* need to be u_B. Dividing by $\Delta\tau$ and taking the limit, we arrive at

$$\begin{aligned}\tau \int d\eta\, dx_T^2\, \partial_\mu A^\mu &= \partial_\tau \left(\tau \int d\eta\, dx_T^2\, u_B^\mu A_\mu\right) \\ &\quad - \int dx_T^2\, u_3^\mu (A_\mu(\eta_1) - A_\mu(\eta_2)),\end{aligned} \tag{B5}$$

which is a generalized conservation law for the quantity

$$\mathcal{A} \equiv \tau \int d\eta dx_T^2\, u_B^\mu A_\mu. \tag{B6}$$

If $\partial_\mu A^\mu \equiv 0$, and the surface term $u_3^\mu(A_\mu(\eta_1) - A_\mu(\eta_2))$ vanishes, we have $\mathcal{A}(\tau) = \text{const}$.

In a boost-invariant calculation, the longitudinal extension of the system is formally infinite, and thus a generalized conservation law for a quantity per unit rapidity is more practical. It can be obtained in a similar fashion if one divides by $\Delta\eta$ and takes the limit $\Delta\eta \to 0$. The result is

$$\tau \int dx_T^2\, \partial_\mu A^\mu = \partial_\tau \frac{d\mathcal{A}}{d\eta} - \partial_\eta \int dx_T^2\, u_3^\mu A_\mu, \tag{B7}$$

where

$$\frac{d\mathcal{A}}{d\eta} = \tau \int dx_T^2\, u_B^\mu A_\mu. \tag{B8}$$

Again, if $\partial_\mu A^\mu \equiv 0$ and the η-derivative term vanishes, we have $d\mathcal{A}/d\eta = \text{const}$.

1. Charge/particle number

We first apply Eq. (B5) to a *conserved* current in the Eckart frame: $N^\mu = n_{\text{eq}} u^\mu$, where $u^\mu = \gamma(\text{ch}\,\theta, v\mathbf{e}_R, \text{sh}\,\theta)$ is the flow four-velocity and θ is the flow rapidity. Now $u_B^\mu u_\mu = \gamma\, \text{ch}(\eta - \theta)$ and $u_3^\mu u_\mu = \gamma\, \text{sh}(\eta - \theta)$. If the rapidity interval is so large that $N^\mu(\eta_1) = N^\mu(\eta_2) = 0$, or the system is boost invariant, $\eta \equiv \theta$, the surface terms are zero, and we get a simple conservation law

$$N = \tau \int d\eta\, dx_T^2\, \gamma n\, \text{ch}(\eta - \theta) = \text{const}. \tag{B9}$$

In a boost-invariant case, the coordinate rapidity integral is trivial, and we obtain

$$\frac{dN}{d\eta} = \tau \int dx_T^2 \gamma n = \text{const}. \tag{B10}$$

2. Entropy

Second, we apply Eq. (B5) to the entropy current of Eq. (14) and its divergence in Eq. (16). If $S^\mu(\eta_1) = S^\mu(\eta_2) = 0$, we get

$$\partial_\tau S = \tau \int d\eta\, dx_T^2 \left(\frac{\Pi^2}{\zeta T} - \frac{q_\mu q^\mu}{\kappa_q T^2} + \frac{\pi_{\mu\nu}\pi^{\mu\nu}}{2\eta_s T}\right) \geqslant 0, \tag{B11}$$

where the entropy of the system is

$$S = \tau \int d\eta\, dx_T^2\, u_B^\mu S_\mu, \tag{B12}$$

and the last inequality follows from the general properties $q^\mu q_\mu \leqslant 0$ and $\pi^{\mu\nu}\pi_{\mu\nu} \geqslant 0$.

For longitudinally boost-invariant dynamics, it is more natural to follow entropy per unit rapidity:

$$\begin{aligned}\frac{dS}{d\eta} &= \tau \int dx_T^2 u_B^\mu S_\mu, \\ \partial_\tau \left(\frac{dS}{d\eta}\right) &= \tau \int dx_T^2 \left(\frac{\Pi^2}{\zeta T} - \frac{q_\mu q^\mu}{\kappa_q T^2} + \frac{\pi_{\mu\nu}\pi^{\mu\nu}}{2\eta_s T}\right) \geqslant 0.\end{aligned} \tag{B13}$$

3. Energy-momentum

Finally we derive the conservation equation corresponding to energy-momentum conservation $\partial_\mu T^{\mu\nu} = 0$. Contraction of the energy-momentum tensor with u_B^μ gives the conservation of energy. When the entire system is within the interval $[\eta_1, \eta_2]$, then

$$\partial_\tau E \equiv \partial_\tau \left(\tau \int d\eta\, dx_T^2\, u_B^\mu T_{\mu\nu}\, u_B^\nu\right) = 0. \tag{B14}$$

Contraction with $u_R^\mu \equiv (0, \mathbf{e}_R, 0)$ gives the change in transverse radial momentum. Substituting

$$\partial_\mu (T^{\mu\nu} u_{R,\nu}) = 0 + T^{\mu\nu} \partial_\mu u_{R,\nu} \tag{B15}$$

into Eq. (B5) results in

$$\begin{aligned}\partial_\tau M_r &\equiv \partial_\tau \left(\tau \int d\eta\, dx_T^2\, u_B^\mu T_{\mu\nu} u_R^\nu\right) \\ &= \tau \int d\eta\, dx_T^2 T^\mu{}_\nu \partial_\mu u_R^\nu.\end{aligned} \tag{B16}$$

To be more specific, we also show as an example a boost-invariant, cylindrically symmetric case. In the Landau frame,

$$T^{\mu\nu} = (\varepsilon + p + \Pi)u^\mu u^\nu - (p + \Pi)g^{\mu\nu} + (-\tilde{\pi}_2 - \tilde{\pi}_3)u_1^\mu u_1^\nu + \tilde{\pi}_2 u_2^\mu u_2^\nu + \tilde{\pi}_3 u_3^\mu u_3^\nu, \tag{B17}$$

where u_1 is the orthonormal counterpart of the flow velocity in the time-radial plane, while u_2 and u_3 are orthonormal counterparts of these in the axial and beam (rapidity) direction:

$$u^\mu = \gamma(\mathrm{ch}\,\eta, v\,\mathbf{e}_R, \mathrm{sh}\,\eta), \quad u_1^\mu = \gamma(v\,\mathrm{ch}\,\eta, \mathbf{e}_R, v\,\mathrm{sh}\,\eta),$$
$$u_2^\mu = (0, \mathbf{e}_\phi, 0), \quad u_3^\mu = (\mathrm{sh}\,\eta, \mathbf{0}, \mathrm{ch}\,\eta). \tag{B18}$$

These vectors are normalized to $u^2 = 1, u_1^2 = u_2^2 = u_3^2 = -1$. The viscous pressure tensor components in the fluid rest frame are $\pi^{\mu\nu}_{\mathrm{LR}} = \mathrm{diag}(0, -\tilde{\pi}_2 - \tilde{\pi}_3, \tilde{\pi}_2, \tilde{\pi}_3)$. It is important to notice that the surface terms in Eq. (B5) or the η-derivative term in Eq. (B7) are now nonzero. Contraction by u_B^μ as above and substitution into Eq. (B7) gives the evolution of the energy per unit rapidity:

$$\partial_\tau\left(\frac{dE}{d\eta}\right) \equiv \partial_\tau\left(\tau\int dx_T^2 T^{00}(\eta{=}0)\right) = -\int dx_T^2 (p + \Pi + \tilde{\pi}_3). \tag{B19}$$

Contraction by u_R^μ gives the evolution of transverse radial momentum per unit rapidity:

$$\partial_\tau\left(\frac{dM_r}{d\eta}\right) \equiv \partial_\tau\left(\tau\int dx_T^2 T^{01}(\eta{=}0, \phi{=}0)\right) = \tau\int dx_T^2 \frac{p + \Pi + \tilde{\pi}_2}{R}, \tag{B20}$$

where we have used the relations

$$u_B^\mu T_{\mu\nu} u_R^\nu = -T^{01}(\eta{=}0, \phi{=}0), \quad \partial_\mu u_R^\nu = -\frac{1}{R}u_{2,\mu}u_2^\nu. \tag{B21}$$

The above results reflect general expectations. Particle number per unit rapidity $dN/d\eta$ is strictly conserved in both the ideal and the dissipative case. Entropy per unit rapidity $dS/d\eta$ is conserved for an ideal fluid but increases if there is dissipation. In both cases, the energy per unit rapidity $dE/d\eta$ decreases because of longitudinal work, while the radial momentum per unit rapidity $dM_r/d\eta$ increases as a result of the buildup of radial flow, *as long as the system stays near equilibrium* (i.e., the total pressure is dominated by the ideal part).

APPENDIX C: VISCOUS SOLUTIONS FOR VARIOUS CROSS-SECTION SCENARIOS

Next we analyze viscous Israel-Stewart and Navier-Stokes solutions for four different types of cross section: constant, $\sigma \propto 1/T^2$, $\sigma \propto \tau^{2/3}$, and $\eta_s/s_{\mathrm{eq}} = \mathrm{const}$. For convenience, we will often use normalized quantities

$$\tilde{A}(\tau/\tau_0) \equiv \frac{A(\tau)}{A(\tau_0)}. \tag{C1}$$

We will show that for typical observables of interest (average pressure, pressure anisotropy, entropy, and shear viscosity to entropy ratio), $\eta_s/s_{\mathrm{eq}} = \mathrm{const}$ dynamics is well approximated by $\sigma \propto \tau^{2/3}$ already for $K_0 = 1$.

In analytic considerations, it will be often convenient to drop the π_L^2 term in the equations of motion (35) and (36), which is a good approximation for $|\pi_L| \ll p$, i.e., the general region of validity of viscous hydrodynamics. This should not be confused with the naive Israel-Stewart approximation, which also ignores the 4/3 factor in Eq. (36). For the $\sigma \propto \tau^{2/3}$ and $\sigma = \mathrm{const}$ scenarios, we obtain in this way accurate approximate analytic IS solutions. We also derive analytic NS solutions for $\sigma = \mathrm{const}$, $\sigma \propto \tau^{2/3}$, and $\sigma \propto 1/T^2$.

1. Solutions for ultrarelativistic gas with constant $2 \to 2$ cross section

For a *constant* cross section,

$$\lambda_{\mathrm{tr}}(\tau) \propto \tau \Rightarrow K(\tau) = \frac{\tau_0}{\lambda_{\mathrm{tr}}(\tau_0)} \equiv K_0 = \mathrm{const}. \tag{C2}$$

If we ignore the π_L^2 term, the *linear* equations of motion (35) and (36) can be solved in a straightforward manner:

$$\pi_L(\tilde{\tau}) = \tilde{\tau}^{-\frac{4}{3}-\frac{\kappa_0}{3}}\left[\frac{\pi_{L,0}}{2}T_+(\tilde{\tau}) - \frac{1}{2D}\left(\kappa_0\pi_{L,0} + \frac{8p_0}{3}\right)T_-(\tilde{\tau})\right], \tag{C3}$$

$$p(\tilde{\tau}) = \tilde{\tau}^{-\frac{4}{3}-\frac{\kappa_0}{3}}\left[\frac{p_0}{2}T_+(\tilde{\tau}) + \frac{1}{2D}(\kappa_0 p_0 - \pi_{L,0})T_-(\tilde{\tau})\right], \tag{C4}$$

where

$$\kappa_0 \equiv \frac{K_0}{C}, \quad D \equiv \sqrt{\frac{8}{3} + \kappa_0^2}, \quad T_\pm(x) \equiv x^{D/3} \pm x^{-D/3},$$
$$p(\tau_0) \equiv p_0, \quad \pi_L(\tau_0) \equiv \pi_{L,0}. \tag{C5}$$

For a practical approximate formula for the pressure evolution, see Eq. (48).

In the ideal hydrodynamic ($\eta_s \to 0$, or equivalently $\kappa_0 \to \infty$) limit, we recover

$$\pi_L(\tau > \tau_0) = 0, \quad p(\tau) = p_0\left(\frac{\tau_0}{\tau}\right)^{4/3}. \tag{C6}$$

At late times, the pressure anisotropy, regardless of its initial value $R_{p,0}$, approaches a *constant* determined solely by the parameter κ_0, i.e.,

$$R_\infty \equiv R_p(\tau \to \infty) = \frac{12\kappa_0 - 10}{9D + 3\kappa_0 + 14} < 1. \tag{C7}$$

For a finite κ_0, the final anisotropy is below unity.

Therefore, with a constant cross section, at late times the system does *not* behave like an ideal fluid, but instead the

Navier-Stokes limit applies [cf. Eqs. (44) and (45)]. Indeed, for large κ_0, Eqs. (C3)–(C4) reproduce the NS solution

$$p^{\rm NS}(\tau) = p_0 \left(\frac{\tau_0}{\tau}\right)^{4/3-4/(9\kappa_0)}, \quad \pi_L^{\rm NS}(\tau) = -\frac{4p^{\rm NS}(\tau)}{3\kappa_0}, \tag{C8}$$

and the final IS and NS anisotropies of Eqs. (C7) and (45) agree, that is, $R_\infty = 1 - 2/\kappa_0 + 4/(3\kappa_0^2) + \mathcal{O}(1/\kappa_0^3)$.

Because R_∞ is a monotonically increasing function of κ_0, the final pressure anisotropy is a measure of the viscosity. Inverting Eq. (C7),

$$\kappa_0 = \frac{5 + 14R_\infty - R_\infty^2}{6 - 3R_\infty - 3R_\infty^2}, \tag{C9}$$

i.e., near equilibrium ($\kappa_0 \gg 1$),

$$\begin{aligned} \frac{\eta_s(\tau)}{n(\tau)} = \frac{T\tau}{\kappa} &\approx \frac{1-R_\infty}{2} T_0\tau_0 \left(\frac{\tau}{\tau_0}\right)^\gamma, \\ \gamma &= \frac{2}{3} + \frac{4}{9}\frac{\eta_s(\tau_0)}{n_0}\frac{1}{T_0\tau_0}, \end{aligned} \tag{C10}$$

where in the last step we approximated the temperature evolution using the leading NS term (C8). It is natural to measure viscosity relative to the density, which up to a factor $(4-\chi)$ is the same as $\eta_s/s_{\rm eq}$.

The exact analytic solutions to the naive IS equations are analogous to Eqs. (C4) and (C3) but involve different powers of $\tilde\tau$

$$\tilde\tau^{\delta_\pm}, \quad \delta_\pm^{\rm naive} = -\frac{2}{3} - \frac{\kappa_0}{3} \pm \frac{\sqrt{\kappa_0^2 - 4\kappa_0 + \frac{20}{3}}}{3}. \tag{C11}$$

The late time behavior is governed by the exponent

$$\delta_+^{\rm naive} = -\frac{4}{3} + \frac{4}{9\kappa_0} + \frac{8}{9\kappa_0^2} + \mathcal{O}\left(\frac{1}{\kappa_0^3}\right), \tag{C12}$$

which does incorporate correctly the ideal hydrodynamic limit ($-4/3$) and the NS correction $4/(9\kappa_0)$ but is in general higher, the smaller the κ_0, than the complete IS result $\delta_+ = -4/3 + 4/(9\kappa_0) - 8/(27\kappa_0^3) + \mathcal{O}(1/\kappa_0^5)$. Therefore, the naive approach overestimates the pressure. In addition, it underestimates the asymptotic pressure anisotropy $R_\infty^{\rm naive} = 1 - 2/\kappa_0 - 8/(3\kappa_0^2) + \mathcal{O}(1/\kappa_0^3)$, and therefore, overpredicts the magnitude of the shear stress to pressure ratio $|\xi|$.

2. Solutions for ultrarelativistic gas with $\sigma_{2\to2} \propto 1/T^2$

A constant cross section implies the existence of some external scale in the problem. For a scale-invariant system, however, the only scale available (in thermal and chemical equilibrium) is the temperature, and therefore the cross section behaves as $\sigma \propto 1/T^2$. Equations (37), (33), and (29) then give

$$K(\tau) = K_0 \frac{T_0^2}{T^2} = \frac{K_0}{\tilde p^2 \tilde\tau^2}, \tag{C13}$$

i.e., even without the π_L^2 term, the equations of motion become nonlinear (but are easy to solve numerically).

For ideal hydrodynamic evolution, $p \propto \tau^{-4/3}$ and thus, unlike for the case of a constant cross section,

$$K(\tau) = K_0 \tilde\tau^{2/3} \tag{C14}$$

increases with increasing τ. $K(\tau)$ must grow in general in the viscous hydrodynamic case as well, because dissipative corrections, namely, the π_L/τ term in Eq. (35), are assumed to be small (or else hydrodynamics is no longer applicable). Consequently, the system gets *closer and closer* to ideal hydrodynamic behavior as time evolves (as long as the expansion is only one dimensional). For example, the pressure anisotropy approaches unity at late times, for *any* $\kappa_0 > 0$ and initial $\pi_{L,0}/p_0$,

$$R_p(\tau \to \infty) \to 1. \tag{C15}$$

The exact Navier-Stokes solution

$$p^{\rm NS}(\tau) = \left(\frac{\tau_0}{\tau}\right)^{4/3} \frac{p_0}{\sqrt{1 + \frac{4}{3\kappa_0}\left[\left(\frac{\tau_0}{\tau}\right)^{2/3} - 1\right]}} \tag{C16}$$

behaves similarly. At late times, $p \propto \tau^{-4/3}$ as in the ideal case, therefore, $\kappa(\tau\to\infty) = \kappa_0/(\tilde p^2\tilde\tau^2) \to \infty$, i.e., $R_\infty = 1$. The rate of approach to unity is controlled by the viscosity

$$\begin{aligned} R_p^{\rm NS}(\tau) &= 1 - \frac{2}{\kappa_0}\left(\frac{\tau_0}{\tau}\right)^{2/3}\left[1 + \mathcal{O}\left(1/\kappa_0^2\right) + \mathcal{O}((\tau_0/\tau)^{2/3})\right] \\ &\approx 1 - \frac{2}{T_0\tau_0}\frac{\eta_s}{n}\left(\frac{\tau_0}{\tau}\right)^{2/3}. \end{aligned} \tag{C17}$$

Viscosity also increases the pressure relative to the ideal case

$$\frac{p^{\rm NS}}{p_{\rm id}}(\tau \gg \tau_0) \to \frac{1}{\sqrt{1 - \frac{4}{3\kappa_0}}} \approx 1 + \frac{2}{3T_0\tau_0}\frac{\eta_s}{n}. \tag{C18}$$

3. Solutions for ultrarelativistic gas with $\sigma_{2\to2} \propto \tau^{2/3}$

Near the ideal hydrodynamic limit (i.e., for small viscosities and $\pi_{L,0}/p_0$), one may directly substitute the approximate result (C14) in the equations of motion (35) and (36). Provided we drop the π_L^2 term, these can be converted to a second-order linear differential equation, e.g., for $p(\tau)$,

$$\tau\ddot p + \frac{11}{3}\dot p + \frac{40}{27}\frac{p}{\tau} + \frac{2K(\tau)}{3C}\left(\dot p + \frac{4}{3}\frac{p}{\tau}\right) = 0, \tag{C19}$$

with initial conditions

$$p(\tau_0) = p_0, \quad \dot p(\tau_0) = -\frac{4p_0 + \pi_{L,0}}{3\tau_0}. \tag{C20}$$

The general solution with $K(\tau)$ from Eq. (C14) is[9]

$$p(\tilde\tau) = \tilde\tau^{-4/3}\left[C_-\tilde\tau^{-\frac{2\sqrt6}{9}}F_-(\kappa_0\tilde\tau^{2/3}) + C_+\tilde\tau^{\frac{2\sqrt6}{9}}F_+(\kappa_0\tilde\tau^{2/3})\right], \tag{C21}$$

$$\pi_L(\tilde\tau) = -3\,\tilde\tau^{-1/3}\frac{d[\tilde\tau^{4/3}p(\tilde\tau)]}{d\tilde\tau}, \tag{C22}$$

[9]First substitute $p(\tilde\tau) \equiv \bar p(\tilde\tau)\tilde\tau^{-4/3}$, then switch to a new variable $x \equiv -\kappa_0\tilde\tau^{2/3}$, finally look for the solution in the form $\bar p(x) \equiv x^a q(x)$, and choose a suitable a.

where

$$F_\pm(x) \equiv {}_1F_1(\pm a, 1 \pm 2a; -x), \quad a = \sqrt{\frac{2}{3}} \tag{C23}$$

are short-hand for confluent hypergeometric functions of the first kind, while $C_\pm$ are matched[10] to the initial conditions in Eq. (C20):

$$C_\pm = \pm\frac{e^{\kappa_0}}{4a}[p_0 G_\mp(\kappa_0) - \pi_{L,0} F_\mp(\kappa_0)], \tag{C24}$$

$$G_\pm(x) \equiv \pm 2a\left[\frac{x}{1 \pm 2a}\,{}_1F_1(1 \pm a, 2 \pm 2a, -x) - {}_1F_1(\pm a, 1 \pm 2a, -x)\right]. \tag{C25}$$

A very practical approximate formula for the pressure evolution is given by Eq. (49), which comes from the asymptotic forms [cf. Eq. (13.5.1) in Ref. [42]]

$${}_1F_1(a, b; -x) = \frac{\Gamma(b)}{\Gamma(b-a)} x^{-a} S(a, 1 + a - b, x) + \frac{\Gamma(b)}{\Gamma(a)} e^{-x}(-x)^{a-b} S(b - a, 1 - a, -x), \tag{C26}$$

where

$$S(c, d, x) \equiv 1 + \frac{c\,d}{1!x} + \frac{c(c+1)d(d+1)}{2!\,x^2} + \frac{c(c+1)(c+2)d(d+1)(d+2)}{3!\,x^3} + \cdots \tag{C27}$$

Note that the e^{-x} term in Eq. (C26) is crucial. For large κ_0, $C_\pm$ are exponentially large; however, the e^{κ_0} factors drop out[11] in linear combinations relevant for the pressure and shear stress.

[10]Note that

$$\frac{d}{dx}{}_1F_1(a, b, x) \equiv \frac{a}{b}{}_1F_1(a + 1, b + 1, x),$$

and from the Wronskian,

$$G_-(x)F_+(x) - G_+(x)F_-(x) = 4a\,e^{-x}$$

[cf. $W\{1, 2\}$ in Eq. (13.1.20) in Ref. [42]].

[11]For example,

$$\frac{\Gamma(1+2a)}{\Gamma(1+a)}F_-(\kappa_0)\kappa_0^{-a} - \frac{\Gamma(1-2a)}{\Gamma(1-a)}F_+(\kappa_0)\kappa_0^{a} = 2a\frac{e^{-\kappa_0}}{\kappa_0}\left[1 - \frac{1}{3\kappa_0} + \mathcal{O}\left(\frac{1}{\kappa_0^2}\right)\right]$$

and

$$\frac{\Gamma(1+2a)}{\Gamma(1+a)}G_-(\kappa_0)\kappa_0^{-a} - \frac{\Gamma(1-2a)}{\Gamma(1-a)}G_+(\kappa_0)\kappa_0^{a} = 4ae^{-\kappa_0}\left[1 + \frac{2}{3\kappa_0} - \frac{1}{9\kappa_0^2} + \mathcal{O}\left(\frac{1}{\kappa_0^3}\right)\right]$$

($a = \sqrt{2/3}$).

At late times $\tau \gg \tau_0/\kappa_0^{3/2}$, the IS solutions recover ideal hydrodynamics for any initial condition,

$$p(\tau) \propto \left(\frac{\tau_0}{\tau}\right)^{4/3}, \quad \pi_L(\tau) \propto \left(\frac{\tau_0}{\tau}\right)^2 \Rightarrow \frac{\pi_L}{p}(\tau) \propto \left(\frac{\tau_0}{\tau}\right)^{2/3} \to 0, \quad \text{for} \quad \tau \gg \frac{\tau_0}{\kappa_0^{3/2}}, \tag{C28}$$

as can be inferred from Eq. (C26). The NS solution

$$p^{\rm NS}(\tau) = p_0\left(\frac{\tau_0}{\tau}\right)^{4/3} \exp\left\{\frac{2}{3\kappa_0}\left[1 - \left(\frac{\tau_0}{\tau}\right)^{2/3}\right]\right\} \tag{C29}$$

exhibits the same features (as the reader can easily verify). For the late-time evolution, this scenario gives smaller viscous corrections to the pressure and the pressure anisotropy than $\sigma \propto 1/T^2$. However, in the large κ_0 limit, we recover the same results in Eqs. (C17) and (C18).

Analogous derivation gives the exact solutions in the naive IS case:

$$p(\tilde\tau) = C'_-\tilde\tau^{-2(1+a')/3}F'_-(\kappa_0\tilde\tau^{2/3}) + C'_+\tilde\tau^{-2(1-a')/3}F'_+(\kappa_0\tilde\tau^{2/3}), \tag{C30}$$

$$a' = \sqrt{\frac{5}{3}},$$

$$\pi_L(\tilde\tau) = -3\tilde\tau^{-1/3}\frac{d[\tilde\tau^{4/3}p(\tilde\tau)]}{d\tilde\tau}, \tag{C31}$$

where

$$C'_\pm = \pm\frac{e^{-\kappa_0}}{4a'}[p_0 G'_\mp(\kappa_0) - \xi_0 F'_\mp(\kappa_0)], \tag{C32}$$

$$F'_\pm(x) \equiv {}_1F_1(1 \pm a', 1 \pm 2a', -x), \tag{C33}$$

$$G'_\pm(x) \equiv 2x\frac{1 \pm a'}{1 \pm 2a'}F'_\pm(x) - 2(1 \pm a')F'_\pm(x). \tag{C34}$$

With the help of Eq. (C26), it is straightforward (but somewhat lengthy) to determine the late-time behavior

$$\frac{p}{p_{\rm id}} = T(\tilde\tau)[P(\kappa_0) + \xi_0 X(\kappa_0)], \tag{C35}$$

where in the naive case,

$$T^{\rm naive}(\tilde\tau) = 1 - \frac{2}{3\kappa_0\tilde\tau^{2/3}} - \frac{7}{9\kappa_0^2\tilde\tau^{4/3}} + \mathcal{O}\left(\frac{1}{\kappa_0^3\tilde\tau^2}\right), \tag{C36}$$

$$P^{\rm naive}(\kappa_0) = 1 + \frac{2}{3\kappa_0} + \frac{5}{9\kappa_0^2} + \mathcal{O}\left(\frac{1}{\kappa_0^3}\right), \tag{C37}$$

$$X^{\rm naive}(\kappa_0) = -\frac{1}{2\kappa_0} - \frac{5}{6\kappa_0^2} + \mathcal{O}\left(\frac{1}{\kappa_0^3}\right). \tag{C38}$$

Comparing to the complete Israel-Stewart result of Eq. (C21) (obtained in the small ξ limit),

$$T^{\rm IS}(\tilde\tau) \approx 1 - \frac{2}{3\kappa_0\tilde\tau^{2/3}} - \frac{1}{9\kappa_0^2\tilde\tau^{4/3}} + \mathcal{O}\left(\frac{1}{\kappa_0^3\tilde\tau^2}\right), \tag{C39}$$

$$P^{\rm IS}(\kappa_0) \approx 1 + \frac{2}{3\kappa_0} - \frac{1}{9\kappa_0^2} + \mathcal{O}\left(\frac{1}{\kappa_0^3}\right), \tag{C40}$$

$$X^{\rm IS}(\kappa_0) \approx -\frac{1}{2\kappa_0} + \frac{1}{6\kappa_0^2} + \mathcal{O}\left(\frac{1}{\kappa_0^3}\right), \tag{C41}$$

we see that for the naive approximation, the evolution approaches ideal hydrodynamic $p/p_{\rm id} \sim$ const behavior *later*

(deviation of T from unity is larger), and for near-equilibrium initial conditions ($\xi_0 \approx 0$), the pressure saturates at a *higher* value (P is larger).

4. Solutions for ultrarelativistic gas with $2 \to 2$ cross section and $\eta_s/s_{\rm eq} = {\rm const}$

The last scenario we consider is when the cross section is dynamically adjusted to maintain a *constant* shear viscosity to equilibrium entropy density ratio $\eta_s/s_{\rm eq}$, such as the conjectured lower bound of $1/(4\pi)$. From Eqs. (29), (33), (51), and (52),

$$\tilde{s}_{\rm eq} = \frac{1}{\tilde{\tau}}\left(1 + \frac{\ln[\tilde{\tau}^4\tilde{p}^3(\tilde{\tau})]}{4-\chi_0}\right), \tag{C42}$$

and thus

$$\frac{\eta_s}{s_{\rm eq}} = \frac{\eta_{s,0}}{s_{eq,0}}\frac{\tilde{p}(\tilde{\tau})\tilde{\tau}^2}{\tilde{K}(\tilde{\tau})}\frac{4-\chi_0}{4-\chi_0+\ln[\tilde{\tau}^4\tilde{p}^3(\tilde{\tau})]}, \tag{C43}$$

where

$$\frac{\eta_{s,0}}{s_{eq,0}} = \frac{T_0\tau_0}{\kappa_0(4-\chi_0)}. \tag{C44}$$

Therefore, $\eta_s/s_{\rm eq} = {\rm const}$ requires

$$K(\tilde{\tau}) = K_0\tilde{p}(\tilde{\tau})\tilde{\tau}^2\frac{4-\chi_0}{4-\chi_0+\ln[\tilde{\tau}^4\tilde{p}^3(\tilde{\tau})]}. \tag{C45}$$

Within the generic region of validity for viscous hydrodynamics, $|\pi_L| \ll p$, this scenario also implies a growing $K(\tau) \sim \tau^{\approx 2/3}$ and therefore convergence to the ideal limit at late times. Note that the double ratio $(\eta_s/s_{\rm eq})/(\eta_{s,0}/s_{eq,0})$ as a function of τ/τ_0 depends only on $\pi_{L,0}/p_0$, κ_0, the type of cross section (encoded in $\tilde{K}$), and χ_0.

We now analyze the time evolution of $\eta_s/s_{\rm eq}$ in the three earlier scenarios. Compared to the entropy density, $\eta_s/s_{\rm eq}$ contains an additional multiplicative term that comes from the time evolution of the shear viscosity. Assume first, for simplicity, that we are very close to the ideal hydrodynamic limit, in which case, $\eta_s/s_{\rm eq} \propto \tau^{2/3}/K(\tau)$. For a constant cross section, this results in a *growing* $\eta_s/s_{\rm eq} \propto \tau^{2/3}$; while for the other two cases, $\sigma \propto \tau^{2/3}$ or $\sigma \propto 1/T^2$, we obtain $\eta_s/s_{\rm eq} \approx$ const.

In reality, there are of course viscous effects. Because

$$\frac{\tilde{p}(\tilde{\tau})\tilde{\tau}^2}{\tilde{K}(\tilde{\tau})} = \begin{cases} \tilde{p}(\tilde{\tau})\tilde{\tau}^{4/3} \times \tilde{\tau}^{2/3} & \text{for} \quad \sigma = \text{const}, \\ [\tilde{p}(\tilde{\tau})\tilde{\tau}^{4/3}]^3 & \text{for} \quad \sigma \propto 1/T^2, \\ \tilde{p}(\tilde{\tau})\tilde{\tau}^{4/3} & \text{for} \quad \sigma \propto \tau^{2/3}, \end{cases} \tag{C46}$$

the relevant quantity that determines the evolution of $\eta_s/s_{\rm eq}$ is $\tilde{p}\tilde{\tau}^{4/3}$. The last term in Eq. (C43) is only a logarithm. Therefore, the first term, Eq. (C46), dominates the behavior. Typically, $\pi_L < 0$ and thus dissipation generates an increasing $\tilde{p}\tilde{\tau}^{4/3}$. The increase in $\eta_s/s_{\rm eq}$ is then fastest for the constant cross section case. The other two cases, $\sigma \propto 1/T^2$ and $\sigma \propto \tau^{2/3}$, are not equivalent when there is dissipation, because for the latter the prefactor in Eq. (C46) is only linear in $\tilde{p}(\tilde{\tau})\tilde{\tau}^{4/3}$ and, therefore, $\eta_s/s_{\rm eq}$ grows much slower.

5. Comparison of the various cross section scenarios

After exploring the general behavior, we compare numerical solutions for the four scenarios. Unless stated otherwise, for the $\eta_s/s_{\rm eq} = {\rm const}$ case, we start the evolution from chemical equilibrium, i.e., take $\chi_0 = 0$. For the other three scenarios, the pressure and shear stress evolution does not depend on χ_0. For simplicity, we start the evolution from $\pi_L(\tau_0) = 0$, and consider two extremes $K_0 = 1$, i.e., equal expansion and scattering time scales, and $K_0 = 6.67$, i.e., 6.67 times slower expansion than the time scale for scattering. On all figures, the dotted curves correspond to the approximation when the π_L^2 term in Eq. (36) is ignored.

Figure 8 shows the evolution of the pressure relative to the ideal hydrodynamic $p \sim \tau^{-4/3}$ result (for a comparison of the same observable between hydrodynamics and transport, see Fig. 4). Dissipation increases the pressure because it reduces the pdV work. The effect is largest for the $\sigma = {\rm const}$ scenario, while it is smallest for $\eta_s/s_{\rm eq} = {\rm const}$ and $\sigma \propto \tau^{2/3}$, which two scenarios give basically the same result. For $K_0 = 1$, the fourth scenario $\sigma \propto 1/T^2$ is in between these limits; but by $K_0 = 6.67$, it becomes equivalent to $\sigma \propto \tau^{2/3}$. Dropping the π_L^2 terms in Eq. (36) (thin dotted lines) is a fair 10–15% approximation for $\sigma = {\rm const}$ and $\sigma \propto 1/T^2$ at $K_0 = 1$, which improves to an essentially exact one by $K_0 = 6.67$. For the other two scenarios, $\eta_s/s_{\rm eq} = {\rm const}$ and $\sigma \propto \tau^{2/3}$, the nonlinear term can be safely ignored already for $K_0 = 1$. Note that for $K_0 = 6.67$, dissipative corrections to the pressure are still very modest 10–15% at late $\tau/\tau_0 \sim$ 10–20 in all four cases studied.

Now we turn to the evolution of the viscous stress π_L shown in Fig. 9. All four scenarios give very similar results for the early $\tau/\tau_0 \lesssim 1.5$–2 growth in magnitude, but they differ in late-time relaxation. As inferred from the pressure evolution already, $\eta_s/s_{\rm eq} = {\rm const}$ and $\sigma \propto \tau^{2/3}$ are largely identical and relax quickly toward the ideal limit. $\sigma = {\rm const}$ is the one that stays farthest from equilibrium. For low $K_0 = 1$, the $\sigma \propto 1/T^2$ case lies in between; but by $K_0 = 6.67$, it becomes identical to $\eta_s/s_{\rm eq} = {\rm const}$ and $\sigma \propto \tau^{2/3}$. The π_L^2 term in the equation

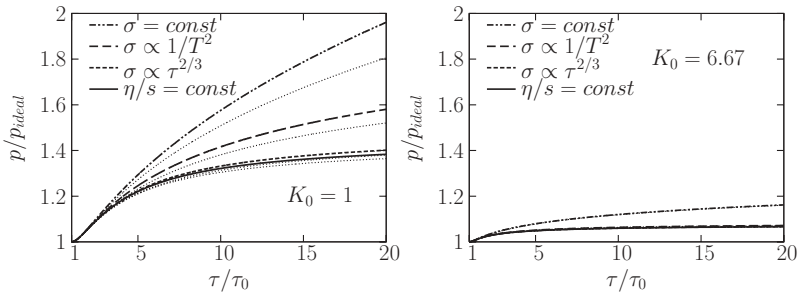

FIG. 8. Pressure evolution from viscous hydrodynamics relative to the ideal hydrodynamic $p = p_0(\tau_0/\tau)^{-4/3}$ result in 0 + 1D Bjorken geometry for an ultrarelativistic gas with $2 \to 2$ interactions. Four scenarios are compared for $K_0 = 1$ and 6.67: $\sigma = {\rm const}$, $\sigma \propto 1/T^2$, $\sigma \propto \tau^{2/3}$, and $\eta_s/s_{\rm eq} = {\rm const}$. Approximate results with dropping π_L^2 terms in the equation of motion are also shown (thin dotted lines).

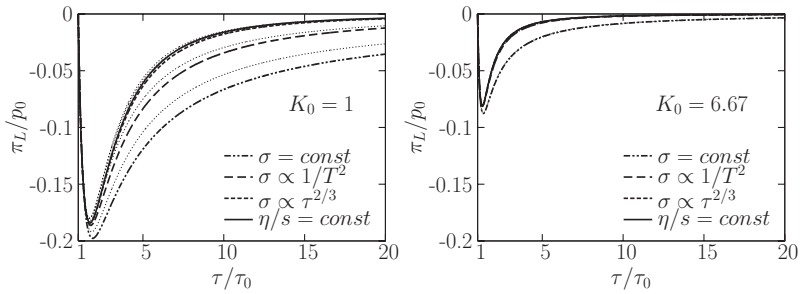

FIG. 9. Same as Fig. 8, but for the longitudinal viscous shear π_L normalized by the *initial* pressure.

of motion affects the pressure and the viscous stress similarly and can be ignored for $K_0 = 6.67$ in all cases and for $\sigma \propto \tau^{2/3}$ and $\eta_s/s_{\rm eq} = \text{const}$ even at $K_0 = 1$.

The same observations carry over to the pressure anisotropy $R_p = p_L/p_T$ shown in Fig. 10. We plot this quantity because it is the same one shown in Fig. 1 for the hydrodynamics vs. transport theory comparison in Sec. V (but note the logarithmic time axis there). These results further confirm that $\sigma \propto \tau^{2/3}$ is a very good approximation to $\eta_s/s_{\rm eq} = \text{const}$ already for $K_0 = 1$.

Figure 11 shows entropy production $dS/d\eta$ as a function of proper time for the four scenarios, with local thermal ($\xi_0 = 0$) and chemical ($\chi_0 = 0$) equilibrium initial conditions. Due to scalings, only entropy relative to the initial one plays a role, i.e.,

$$\frac{(dS/d\eta)}{(dS_0/d\eta)} = \tilde{\tau}\tilde{s} = 1 + \frac{1}{4-\chi_0}\left[\ln(\tilde{\tau}^4\tilde{p}^3) - \frac{9\xi^2(\tau)}{16}\right]. \quad \text{(C47)}$$

For $K_0 = 1$, a constant cross section generates about 35% extra entropy by late $\tau \sim (15\text{–}20)\tau_0$. With $\sigma \propto 1/T^2$, the increase is only ~30%; whereas $\sigma \propto \tau^{2/3}$ and $\eta_s/s_{\rm eq} = \text{const}$ give the smallest increase of about 25%. For a larger $K_0 \sim 7$, the system is much closer to ideal hydrodynamics and therefore entropy generation is slower, about 10% for $\sigma = \text{const}$, while only 5% for the other three cases. Note that these results also depend on χ_0 but almost entirely through the explicit $1/(4-\chi_0)$ factor in Eq. (C47). Therefore, results for arbitrary $\chi_0 \neq 0$ can be obtained via straightforward rescaling. In the $\eta_s/s_{\rm eq} = \text{const}$ case, the shear stress and pressure evolution also depend on χ_0 but only very weakly, as we show later below (cf. Fig. 13).

Figure 12 shows the evolution of the shear viscosity to equilibrium entropy density ratio $\eta_s/s_{\rm eq}$, normalized by the initial value of the ratio. The entropy is calculated for a system starting from chemical equilibrium ($\chi_0 = 0$). The rough expectations that $\eta_s/s_{\rm eq} \sim \tau^{2/3}$ for a constant cross section, while $\eta_s/s_{\rm eq} \sim \text{const}$ for both $\sigma \propto 1/T^2$ and $\sigma \propto \tau^{2/3}$, hold within a factor of 3 already for $K_0 = 1$ and up to $\tau = 20\tau_0$ (note that the $\tau^{2/3}$ growth in the $\sigma = \text{const}$ case has been scaled out in the plots). Relative to this zeroth-order behavior, for all three scenarios, $\eta_s/s_{\rm eq}$ grows with time, reinforcing the general results in Sec. C4. The relative growth decreases with increasing K_0. The K_0 dependence is strongest for the constant cross section scenario: the factor of 3 gain by $\tau = 20\tau_0$ for $K_0 = 1$ is tamed to about a 25% increase for $K_0 \sim 7$. For the other two scenarios, $\sigma \propto 1/T^2$ and $\sigma \propto \tau^{2/3}$, the ratio stays nearly constant much more robustly. As expected (cf. end of Appendix C 4), of all cases studied, $\sigma \propto \tau^{2/3}$ approximates $\eta_s/s_{\rm eq} = \text{const}$ the best, with only ~10% deviation accumulated by late $\tau = 20\tau_0$ even for a small $K_0 = 1$.

Finally, in Fig. 13, we show that the results for $\eta_s/s_{\rm eq} = \text{const}$ depend only weakly on the initial density, i.e., χ_0. Density dependence in shear stress and pressure evolution arises in this case because the cross section is a function of the initial density [see Eq. (C45)]. The dependence is weaker the closer the system is to ideal hydrodynamics, because in that case $p \propto \tau^{-4/3}$ and χ_0 drops out from $K(\tau)$. But even for a pessimistic $K_0 = 1$, the pressure anisotropy $R_p = p_L/p_T$, varies less than 10% as we change the density by a factor of 4 around chemical equilibrium density ($\chi_0 = \pm \ln 4$). In fact, a decrease in the density has a much weaker effect than an increase. The right plot shows the effect of the same initial density variation on entropy $dS/d\eta$ production normalized to the initial entropy. Most of the density dependence in the entropy change comes from the trivial $1/(4-\chi_0)$ prefactor in Eq. (C47), which is there in any cross section scenario even if the shear stress and pressure evolution are independent of the density. To highlight dynamical density effects, we therefore plot, again for a pessimistic $K_0 = 1$, the normalized change in entropy

$$\frac{4-\chi_0}{4}\frac{\Delta(dS/d\eta)}{(dS_0/d\eta)} \equiv \frac{4-\chi_0}{4}\left(\frac{(dS/d\eta)}{(dS_0/d\eta)} - 1\right). \quad \text{(C48)}$$

(The scaling factor is chosen such that it has no effect for chemical equilibrium initial conditions $\chi_0 = 0$.) The results show practically no density dependence, apart from few-percent changes, even for such a low K_0.

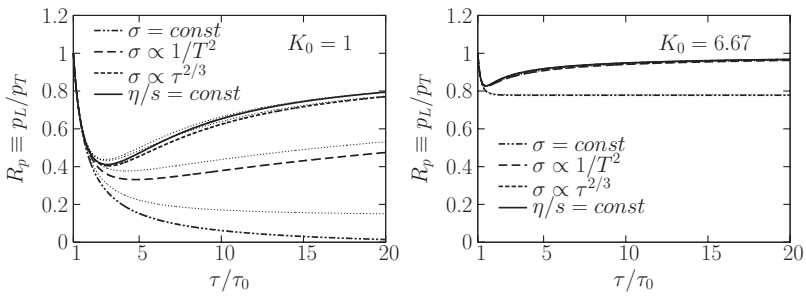

FIG. 10. Same as Fig. 8, but for the pressure anisotropy evolution.

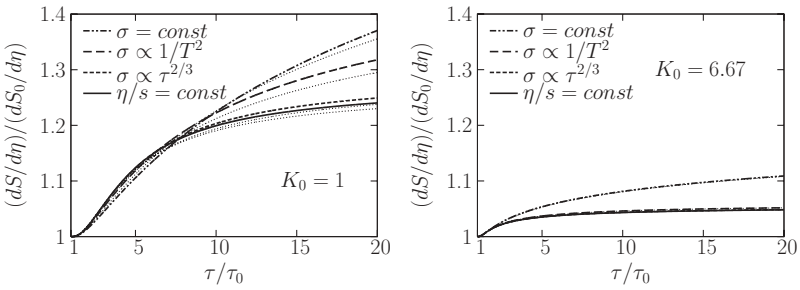

FIG. 11. Same as Fig. 8, but for the normalized entropy per unit rapidity $(dS/d\eta)/(dS_0/d\eta)$.

APPENDIX D: USEFUL RELATIONS FROM COVARIANT TRANSPORT

1. Particle number and transverse energy

The particle number and transverse energy distributions for particles crossing a three-dimensional hypersurface $\sigma(x) =$ const are given by

$$dN = dy\, dp_T^2 \int p^\mu d\sigma_\mu(x) f(x, \mathbf{p}), \tag{D1}$$

$$dE_T = dy\, dp_T^2 \int p^\mu d\sigma_\mu(x) m_T f(x, \mathbf{p}), \tag{D2}$$

where $m_T \equiv \sqrt{p_T^2 + m^2}$, $p_T \equiv \sqrt{p_x^2 + p_y^2}$ is the transverse momentum, and $d\sigma_\mu(x)$ is the normal to the hypersurface at space-time coordinate x. For our boost-invariant scenario, it is natural to follow quantities per *unit coordinate rapidity* as a function of the proper time τ. For $\tau =$ const, hypersurfaces $p^\mu d\sigma_\mu = m_T \tau \operatorname{ch}\omega\, d^2x_T\, d\eta$, and in our $0+1$D case, f only depends on $\operatorname{sh}\omega$, $p_\perp$, and τ, where $\omega \equiv y - \eta$. Thus,

$$\frac{dN(\tau)}{d\eta} = \tau A_T \int d^2p_T\, d\omega\, m_T \operatorname{ch}\omega\, f(\tau, \operatorname{sh}\omega, p_T), \tag{D3}$$

$$\frac{dE_T(\tau)}{d\eta} = \tau A_T \int d^2p_T\, d\omega\, m_T^2 \operatorname{ch}\omega\, f(\tau, \operatorname{sh}\omega, p_T), \tag{D4}$$

A_T is the transverse area of the system. With the local thermal equilibrium distribution for ultrarelativistic particles

$$f(\operatorname{sh}\omega, p_\perp) = \mathcal{N} e^{-p_\perp \operatorname{ch}\omega/T}, \quad \mathcal{N} = \frac{n}{8\pi T^3}, \tag{D5}$$

and the quadratic form (62), straightforward integration gives

$$\frac{dN}{d\eta} = n\,\tau A_T = \text{const}, \tag{D6}$$

$$\frac{dE_T(\tau)}{d\eta} = \frac{3\pi T}{4}\frac{dN}{d\eta}\left(1 - \frac{5\xi}{16}\right). \tag{D7}$$

Clearly, dissipation slows the decrease of transverse energy (for typical $\pi_L < 0$), and $2 \to 2$ interactions, of course, conserve the particle number.

Note that $dE_T/d\eta/(\tau A_T)$ is almost identical to the transverse pressure of Eq. (D10) but has an extra $\operatorname{ch}\omega$ factor in the integrand.

2. Early pressure evolution

Here we evaluate the early transverse and longitudinal pressure evolution from the transport for a local equilibrium initial condition. The results hold for *any* interaction, not only $2 \to 2$.

In local equilibrium, the collision term vanishes; thus in the vicinity of $\tau = \tau_0$, the evolution is governed by *free streaming*.[12] In our $0+1$D case, free streaming

$$\left[\operatorname{ch}\omega\, \partial_\tau - \frac{\operatorname{sh}\omega}{\tau}\partial_\omega\right] f(\operatorname{sh}\omega, p_\perp, \tau) = 0 \quad (\omega \equiv y - \eta) \tag{D8}$$

implies

$$f(\operatorname{sh}\omega, p_\perp, \tau) = f(\tau \operatorname{sh}\omega/\tau_0, p_\perp, \tau_0). \tag{D9}$$

[12]The approach followed here is equivalent to a direct computation of the coefficient $\dot{R}_0$ in the Taylor expansion $R(\tau) = 1 + \dot{R}_0(\tau - \tau_0) + \ddot{R}_0(\tau - \tau_0)^2/2 + \cdots$. In the direct approach, one would differentiate Eq. (43) to obtain

$$\dot{R}_0 = \frac{\dot{T}_{zz}(\tau_0) - \dot{T}_{xx}(\tau_0)}{p_0},$$

then substitute T_{zz} and T_{xx} from Eq. (D10), and replace $\dot{f}(\operatorname{ch}\omega, p_\perp, \tau_0)$ with $\partial_\omega f(\operatorname{ch}\omega, p_\perp, \tau_0)$ using the Boltzmann equation. For locally equilibrated initial conditions of Eq. (D5), the collision term vanishes, and the problem is then reduced to straightforward integration, which yields $\dot{R}_0 = -8/(5\tau_0)$.

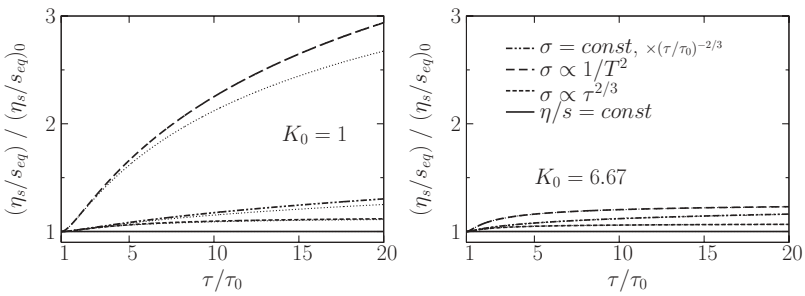

FIG. 12. Same as Fig. 8, but for the shear viscosity to equilibrium entropy density ratio $\eta_s/s_{\rm eq}$. The results for $\sigma =$ const are divided by $(\tau/\tau_0)^{2/3}$, otherwise they would quickly grow off the plot.

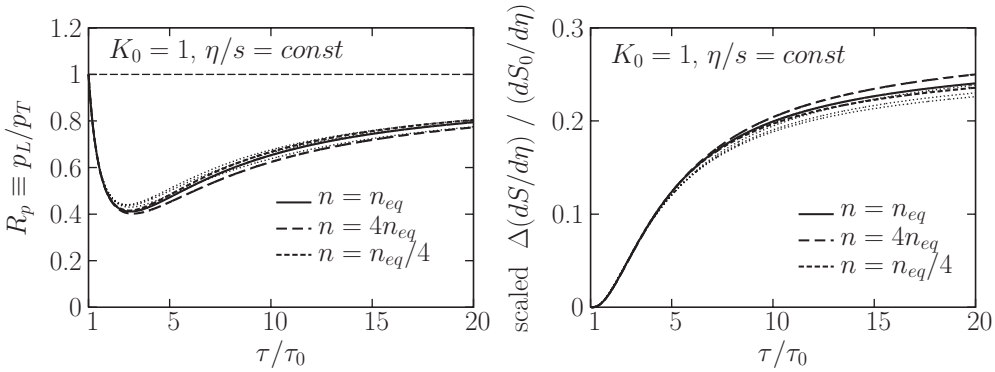

FIG. 13. Initial density dependence of Israel-Stewart viscous hydrodynamic solutions for an ultrarelativistic gas expanding longitudinally in 0 + 1D Bjorken geometry with $2 \to 2$ interactions that maintain $\eta_s/s_{\rm eq} = \text{const}$. To amplify density effects, the initial expansion time scale to mean free path ratio is chosen to be low, $K_0 = 1$. Three different *initial* densities are considered: chemical equilibrium $n = n_{\rm eq}$, oversaturation at $n = 4n_{\rm eq}$, and undersaturation at $n = n_{\rm eq}/4$. Left: time evolution of the pressure anisotropy $R_p = p_L/p_T$. Right: time evolution of the *produced* entropy per unit rapidity, normalized to the initial entropy per unit rapidity. The produced entropy is scaled by $(4 - \chi_0)/4$ to eliminate trivial density effects that do not come from the shear stress and pressure evolution (see text). Approximate results with dropping π_L^2 terms in the equation of motion are also shown (thin dotted lines).

Substituting a local thermal initial distribution for ultrarelativistic particles [Eq. (D5)], the definition of the energy-momentum tensor

$$T^{\mu\nu}(\eta = 0, \tau) = \int \frac{d^3p}{p_0} p^\mu p^\nu f$$

$$= \int d^2p_\perp dy p^\mu p^\nu f(\text{sh}y, p_\perp, \tau) \quad \text{(D10)}$$

gives the transverse pressure

$$p_T(\tau) \equiv T^{xx}(\eta = 0, \tau) = \mathcal{N} \int dp_\perp p_\perp d\phi dy (p_\perp \cos\phi)^2$$

$$\times \exp\left[-\frac{p_\perp}{T_0}\sqrt{1 + a^2 \text{sh}^2 y}\right]$$

$$= \frac{3T_0 n}{2} \int_0^\infty \frac{dy}{(1 + a^2 \text{sh}^2 y)^2}. \quad \text{(D11)}$$

Here $a \equiv \tau/\tau_0$. Change of variables to $q = a\,\text{sh}\,y$ leads to

$$p_T(\tau) = \frac{3T_0 n}{2} \int_0^\infty \frac{dq}{(1 + q^2)^2 \sqrt{q^2 + a^2}}$$

$$= T_0 n \frac{3\left[\sqrt{a^2 - 1} + (a^2 - 2)\text{acos}\frac{1}{a}\right]}{4(a^2 - 1)^{3/2}}. \quad \text{(D12)}$$

Analogous calculation gives for the longitudinal pressure,

$$p_L(\tau) \equiv T^{zz}(\eta = 0, \tau) = 3T_0 n \int \frac{dy\,\text{sh}^2 y}{(1 + a^2 \text{sh}^2 y)^2}$$

$$= T_0 n \frac{3}{2(a^2 - 1)} \left[\frac{\text{acos}\frac{1}{a}}{\sqrt{a^2 - 1}} - \frac{1}{a^2}\right]. \quad \text{(D13)}$$

Expanding near $a = 1$,

$$p_T(\tau) = T_0 n \left[1 - \frac{4(\tau - \tau_0)}{5\tau_0} + \mathcal{O}((\tau - \tau_0)^2)\right], \quad \text{(D14)}$$

$$p_L(\tau) = T_0 n \left[1 - \frac{12(\tau - \tau_0)}{5\tau_0} + \mathcal{O}((\tau - \tau_0)^2)\right], \quad \text{(D15)}$$

and thus Eq. (65) follows.

[1] P. Danielewicz and M. Gyulassy, Phys. Rev. D **31**, 53 (1985).
[2] G. Policastro, D. T. Son, and A. O. Starinets, Phys. Rev. Lett. **87**, 081601 (2001); P. K. Kovtun, D. T. Son, and A. O. Starinets, *ibid*. **94**, 111601 (2005).
[3] M. Brigante, H. Liu, R. C. Myers, S. Shenker, and S. Yaida, Phys. Rev. Lett. **100**, 191601 (2008).
[4] P. F. Kolb and U. W. Heinz, arXiv:nucl-th/0305084.
[5] M. Gyulassy and L. McLerran, Nucl. Phys. **A750**, 30 (2005).
[6] E. V. Shuryak, Nucl. Phys. **A750**, 64 (2005).
[7] H. Stoecker, Nucl. Phys. **A750**, 121 (2005).
[8] D. Molnar and P. Huovinen, Phys. Rev. Lett. **94**, 012302 (2005).
[9] A. Muronga, Phys. Rev. Lett. **88**, 062302 (2002); **89**, 159901(E) (2002).
[10] D. A. Teaney, J. Phys. G **30**, S1247 (2004).
[11] R. Baier, P. Romatschke, and U. A. Wiedemann, Nucl. Phys. **A782**, 313 (2007).
[12] U. W. Heinz, H. Song, and A. K. Chaudhuri, Phys. Rev. C **73**, 034904 (2006).
[13] P. Romatschke, Eur. Phys. J. C **52**, 203 (2007).
[14] T. Koide, G. S. Denicol, Ph. Mota, and T. Kodama, Phys. Rev. C **75**, 034909 (2007).
[15] P. Romatschke and U. Romatschke, Phys. Rev. Lett. **99**, 172301 (2007).
[16] H. Song and U. W. Heinz, Phys. Lett. **B658**, 279 (2008).
[17] K. Dusling and D. Teaney, Phys. Rev. C **77**, 034905 (2008).
[18] D. Molnar and P. Huovinen, J. Phys. G **35**, 104125 (2008).

[19] W. A. Hiscock and L. Lindblom, Phys. Rev. D **31**, 725 (1985).
[20] E. M. Lifshitz and L. D. Landau, *Fluid Mechanics* (Butterworth-Heinemann, Oxford, 1987).
[21] S. R. de Groot, W. A. van Leeuwen, and Ch. G. van Weert, *Relativistic Kinetic Theory—Principles and Applications* (North-Holland, Amsterdam, 1980).
[22] W. Israel, Ann. Phys. (NY) **100**, 310 (1976).
[23] W. Israel and J. M. Stewart, Ann. Phys. (NY) **118**, 349 (1979).
[24] See Chapter V of Ref. [21].
[25] L. Lindblom, Ann. Phys. (NY) **247**, 1 (1996); P. Geroch, J. Math. Phys. **36**, 4226 (1995).
[26] B. Zhang, Comput. Phys. Commun. **109**, 193 (1998).
[27] M. Gyulassy, Y. Pang, and B. Zhang, Nucl. Phys. **A626**, 999 (1997).
[28] D. Molnar and M. Gyulassy, Phys. Rev. C **62**, 054907 (2000).
[29] D. Molnar and M. Gyulassy, Nucl. Phys. **A697**, 495 (2002); **A703**, 893(E) (2002); **A698**, 379 (2002).
[30] J. D. Bjorken, Phys. Rev. D **27**, 140 (1983).
[31] D. Molnar, arXiv:0806.0026.
[32] I. Müller, Z. Phys. **198**, 329 (1967).
[33] See Chapter VI of Ref. [21].
[34] R. Baier, P. Romatschke, and U. A. Wiedemann, Phys. Rev. C **73**, 064903 (2006).
[35] H. Song and U. W. Heinz, Phys. Rev. C **78**, 024902 (2008).
[36] P. Huovinen, Eur. Phys. J. A **37**, 121 (2008).
[37] J. Manninen and F. Becattini, Phys. Rev. C **78**, 054901 (2008).
[38] A. Dumitru, E. Molnar, and Y. Nara, Phys. Rev. C **76**, 024910 (2007).
[39] D. Molnar, MPC 1.8.5 transport code, http://karman.physics.purdue.edu/OSCAR.
[40] D. Kharzeev and K. Tuchin, J. High Energy Phys. 09 (2008) 093; F. Karsch, D. Kharzeev, and K. Tuchin, Phys. Lett. **B663**, 217 (2008).
[41] R. J. Fries, B. Muller, and A. Schafer, Phys. Rev. C **78**, 034913 (2008).
[42] M. Abramowitz and I. A. Stegun, *Handbook of Mathematical Functions* (Dover, New York, 1972).

ELSEVIER

Available online at www.sciencedirect.com

ScienceDirect

Nuclear Physics A 00 (2020) 1–4

Nuclear Physics A

www.elsevier.com/locate/procedia

XXVIIIth International Conference on Ultrarelativistic Nucleus-Nucleus Collisions (Quark Matter 2019)

From high $p_\perp$ theory and data to inferring anisotropy of Quark-Gluon Plasma

Magdalena Djordjevic[a], Stefan Stojku[a], Dusan Zigic[a], Bojana Ilic[a], Jussi Auvinen[a], Igor Salom[a], Marko Djordjevic[b] and Pasi Huovinen[a]

[a] *Institute of Physics Belgrade, University of Belgrade, Serbia*

[b] *Faculty of Biology, University of Belgrade, Serbia*

Abstract

High $p_\perp$ theory and data are commonly used to study high $p_\perp$ parton interactions with QGP, while low $p_\perp$ data and corresponding models are employed to infer QGP bulk properties. On the other hand, with a proper description of high $p_\perp$ parton-medium interactions, high $p_\perp$ probes become also powerful tomography tools, since they are sensitive to global QGP features, such as different temperature profiles or initial conditions. This new role of high $p_\perp$ probes is used here to assess the spatial anisotropy of the QCD matter. With our dynamical energy loss formalism, we show that a (modified) ratio of R_{AA} and v_2, presents a reliable and robust observable for straightforward extraction of initial state anisotropy. We analytically estimated the proportionality between the $v_2/(1 - R_{AA})$ and anisotropy coefficient ϵ_{2L}, and found surprisingly good agreement with full-fledged numerical calculations. Within the current error-bars, the extraction of the anisotropy from the existing data using this approach is still inaccessible. However, with the expected accuracy improvement in the upcoming LHC runs, the anisotropy of the QGP formed in heavy ion collisions can be straightforwardly derived from the data. Such a data-based anisotropy parameter would present an important test to models describing the initial stages of heavy-ion collision and formation of QGP, and demonstrate the usefulness of high $p_\perp$ theory and data in obtaining QGP properties.

Keywords: Quark-gluon plasma, High $p_\perp$ probes, Initial anisotropy

1. Introduction

Understanding the properties of the new form of matter named Quark-Gluon Plasma (QGP) is the major goal of relativistic heavy ion physics [1, 2]. However, to explore the properties of QGP, one needs good probes. With regards to that, it is commonly assumed that high $p_\perp$ theory and data are good probes for exploring the high $p_\perp$ parton interactions with QGP, while low $p_\perp$ theory and data are considered as good probes for bulk QGP properties. Contrary to this common assumption, the goal of this contribution is to demonstrate that high $p_\perp$ particles can also be useful independent probes of *bulk* QGP properties.

To put it simply, the main idea is that when high $p_\perp$ particles transverse QGP, they lose energy, where this energy loss is sensitive to bulk QGP properties, such as its temperature profiles or initial conditions.

Consequently, with realistic and sophisticated high $p_\perp$ parton energy loss model, high $p_\perp$ probes can indeed become powerful tomographic tools. So, in this contribution, we will present if and how we can use these probes to infer some of the bulk QGP properties, i.e., for precision QGP tomography. Note that only the main results are presented here; for a more detailed version, see [3], and references therein.

2. DREENA framework

To achieve the goal of utilizing high $p_\perp$ theory and data for inferring the bulk QGP properties, as previously implied, a reliable high $p_\perp$ parton energy loss model is necessary. With this goal in mind, we developed a dynamical energy loss formalism [4, 5], which takes into account some more realistic and unique features, such as: i) The calculations are performed within finite temperature field theory and generalized Hard-Thermal-Loop [6] approach, in which the infrared divergences are naturally regulated, excluding the need for artificial cutoffs. ii) The formalism assumes QCD medium of a finite size and a finite temperature, consisting of dynamical partons (i.e., energy exchange with medium constituents is included), in distinction to commonly considered static scatterers approximation and/or models with vacuum-like propagators. iii) Both radiative [4] and collisional [5] energy losses are calculated within the same theoretical framework, and are equally applicable to light and heavy flavors. iv) The formalism is generalized to include a finite chromomagnetic mass [7], running coupling, and extend beyond widely used soft-gluon approximation [8]. Finally, the formalism is integrated in a numerical framework DREENA (Dynamical Radiative and Elastic ENergy loss Approach) [9, 10], to provide predictions for high $p_\perp$ observables.

Within this framework, we generated a wide set of high $p_\perp$ predictions using 1D Bjorken expansion [11] (i.e., DREENA-B framework [10]). Thus we obtained a good joint agreement with a wide range of high $p_\perp$ R_{AA} and v_2 data, by applying the same numerical procedure, the same parameter set, and no fitting parameters in model testing. That is, there is no v_2 puzzle [12] within our model, which then strongly suggests that the model provides a realistic description of high $p_\perp$ parton-medium interactions. Moreover, our preliminary findings suggest that, within our formalism, moving from 1D Bjorken to full 3D hydrodynamical expansion does not significantly affect agreement of our predictions with high $p_\perp$ R_{AA} and v_2 data [13]. Consequently, in order to adequately address the high $p_\perp$ measurements, a proper description of high $p_\perp$ parton interactions with the medium appears to be much more important than an advanced medium evolution description. Furthermore, we have also analyzed the sensitivity of high $p_\perp$ R_{AA} and v_2 to different initial stages, giving an additional insigth in the usefullness of both high $p_\perp$ observables in the precision QGP tomography [14].

3. Inferring QGP anisotropy through high $p_\perp$ theory and data

As one example of QGP tomography, in this contribution, we will address how to infer the QGP anisotropy from high $p_\perp$ R_{AA} and v_2 data. The initial state anisotropy is one of the main properties of QGP and a major limiting factor for precision QGP tomography. However, despite its essential importance, it is still not possible to directly infer the initial anisotropy from experimental measurements. Several theoretical studies [15, 16, 17, 18] have provided different methods for calculating the initial anisotropy, leading to notably different predictions, with a notable effect in the resulting predictions for both low and high $p_\perp$ data. Therefore, approaches for inferring anisotropy from the data are necessary. Optimally, these approaches should be complementary to existing predictions, i.e., based on a method that is fundamentally different to models of early stages of QCD matter.

To this end, we here propose a novel approach to extract the initial state anisotropy. Our method is based on inference from high $p_\perp$ data, by using already available R_{AA} and v_2 measurements, which will moreover be measured with much higher precision in the future. Such approach is substantially different from the existing approaches, as it is based on the inference from experimental data (rather than on calculations of early stages of QCD matter) exploiting the information from interactions of rare high $p_\perp$ partons with the QCD medium. This also presents an improvement/optimization in utilizing high $p_\perp$ data as, to date, these data were mostly constrained on studying the parton-medium interactions, rather than assessing bulk QGP parameters, such as spatial asymmetry.

In the literature, the initial state anisotropy is quantified in terms of eccentricity parameter ϵ_2

$$\epsilon_2 = \frac{\langle y^2 - x^2 \rangle}{\langle y^2 + x^2 \rangle} = \frac{\int \mathrm{d}x\,\mathrm{d}y\,(y^2 - x^2)\rho(x,y)}{\int \mathrm{d}x\,\mathrm{d}y\,(y^2 + x^2)\rho(x,y)}, \tag{1}$$

where $\rho(x, y)$ denotes the initial density distribution of the formed QGP. Regarding high $p_\perp$ observables, we note that v_2 is sensitive to both the anisotropy of the system and its size, while R_{AA} is sensitive only to the size of the system. Therefore, it is plausible that the adequate observable for extracting eccentricity from high $p_\perp$ data depends on both v_2 and R_{AA}, and the question is how.

To address this question, we will use the dynamical energy loss formalism, and DREENA-B framework outlined above. For high $p_\perp$, the fractional energy loss scales as [3] $\Delta E/E \sim \chi \langle T \rangle^a \langle L \rangle^b$, where $\langle T \rangle$ stands for the average temperature along the path of high $p_\perp$ parton, $\langle L \rangle$ is the average path-length traversed by the parton, χ is a proportionality factor that depends on the initial parton transverse momentum, and a and b are exponents which govern the temperature and path-length dependence of the energy loss. Within our model, $a \approx 1.2$ and $b \approx 1.4$, which is contrary to simpler models, and consistent with a wide range of experimental data [19, 20]. From this simple scaling arguments, we can straightforwardly obtain the following expressions for R_{AA} and v_2 (for more details we refer the reader to [3]):

$$R_{\mathrm{AA}} \approx 1 - \xi(\chi)\langle T \rangle^a \langle L \rangle^b, \qquad v_2 \approx \frac{1}{2}\frac{R_{\mathrm{AA}}^{in} - R_{\mathrm{AA}}^{out}}{R_{\mathrm{AA}}^{in} + R_{\mathrm{AA}}^{out}} \approx \xi(\chi)\langle T \rangle^a \langle L \rangle^b \left(\frac{b}{2}\frac{\Delta L}{\langle L \rangle} - \frac{a}{2}\frac{\Delta T}{\langle T \rangle} \right), \tag{2}$$

where we see that $\xi(\chi)\langle T \rangle^a \langle L \rangle^b$ corresponds to $1 - R_{AA}$. Therefore, if we divide v_2 by $(1 - R_{AA})$, we see that this ratio is given by the following simple expression:

$$\frac{v_2}{1 - R_{\mathrm{AA}}} \approx \left(\frac{b}{2}\frac{\Delta L}{\langle L \rangle} - \frac{a}{2}\frac{\Delta T}{\langle T \rangle} \right). \tag{3}$$

Note that, while this ratio exposes the dependence on the asymmetry of the system (through spatial $(\Delta L/\langle L \rangle)$ and temperature $(\Delta T/\langle T \rangle)$ parts), the dependence only on spatial anisotropy is still not isolated. However, by plotting together spatial and temperature anisotropy, we obtain a linear dependence [3], with a proportionality factor given by $c \approx 4.3$. Therefore, $v_2/(1 - R_{AA})$ reduces to the following expression:

$$\frac{v_2}{1 - R_{\mathrm{AA}}} \approx \frac{1}{2}\left(b - \frac{a}{c} \right) \frac{\langle L_{out} \rangle - \langle L_{in} \rangle}{\langle L_{out} \rangle + \langle L_{in} \rangle} \approx 0.57\varsigma, \quad \text{where} \quad \varsigma = \frac{\langle L_{out} \rangle - \langle L_{in} \rangle}{\langle L_{out} \rangle + \langle L_{in} \rangle} \quad \text{and} \quad \frac{1}{2}(b - \frac{a}{c}) \approx 0.57. \tag{4}$$

Consequently, the asymptotic scaling behavior of observables v_2 and R_{AA}, at high $p_\perp$, reveals that their (moderated) ratio is determined only by the geometry of the initial QGP droplet. Therefore, the anisotropy parameter ς could, in principle, be directly obtained from the high $p_\perp$ experimental data.

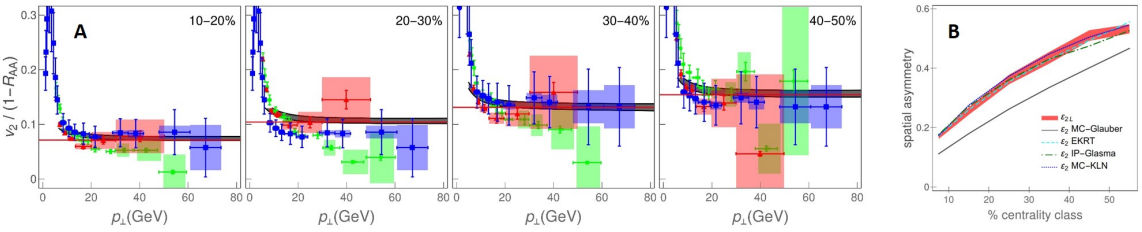

Fig. 1. **A)** Comparison of theoretical predictions for charged hadron $v_2/(1 - R_{AA})$ as a function of $p_\perp$ with 5.02 TeV *Pb* + *Pb* CMS [21, 22] (blue squares), ALICE [23, 24] (red triangles) and ATLAS [25, 26] (green circles) data. Each panel corresponds to different centrality range, as indicated in the upper right corners, while red lines denote the limit 0.57ς from Eq. (4). **B)** Comparison of ϵ_{2L} (red band) extracted from our full-fledged calculations, with ϵ_2 obtained from MC-Glauber [15] (gray full curve), EKRT [16] (cyan dashed curve), IP-Glasma [17] (green dot-dashed curve) and MC-KLN [18] (blue dotted curve) models. MC-Glauber and EKRT curves correspond to 5.02 TeV, whereas IP-Glasma and MC-KLN curves correspond to 2.76 TeV *Pb* + *Pb* collisions at the LHC.

To test the adequacy of the analytical estimate given by Eqs. (2)-(4), Fig. 1A is displayed, which comprises our $v_2/(1 - R_{AA})$ predictions (gray bands), stemming from our full-fledged recently developed

DREENA-B framework (outlined in the previous section), the ALICE, CMS and ATLAS data, and analytically derived asymptote 0.57ς (red lines). Importantly, for each centrality range and for $p_\perp \gtrsim 20$ GeV, $v_2/(1-R_{AA})$ is independent on $p_\perp$, and approaches the asymptote, i.e., is determined by the geometry of the system - depicted by the solid red line, up to 5% accuracy. Moreover, the experimental data for all three experiments also display the independence on the $p_\perp$ and agree with our predictions, although the error bars are rather large. Therefore, we conclude that our scaling estimates are valid and that $v_2/(1-R_{AA})$ indeed carries the information about the anisotropy of the fireball, which can be simply (from the straight line fit to data at high $p_\perp$ limit) and robustly (in the same way for each centrality) inferred from the experimental data.

However, note that the anisotropy parameter ς is not the widely-considered anisotropy parameter ϵ_2 (given by Eq. (1)). To facilitate comparison with ϵ_2 values in the literature, we define $\epsilon_{2L} = \frac{\langle L_{out}\rangle^2 - \langle L_{in}\rangle^2}{\langle L_{out}\rangle^2 + \langle L_{in}\rangle^2} = \frac{2\varsigma}{1+\varsigma^2}$, and in Fig. 1B compare it with the results from different initial-state models [15, 16, 17, 18]. First, we should note that as a starting point, our initial ϵ_2, through which we generate our path-length distributions, agrees with EKRT and IP-Glasma. However, what is highly non-trivial is that, as an outcome of this procedure, in which $v_2/(1-R_{AA})$ is calculated (based on the full-fledged DREENA-B framework), we obtain ϵ_{2L} which practically coincide with our initial ϵ_2 and also with some of the conventional initial-state models. As an overall conclusion, the straightforward extraction of ϵ_{2L} and its agreement with values of the prevailing initial-state models' eccentricity (and our initial ϵ_2) is highly non-trivial and supports $v_2/(1-R_{AA})$ as a reliable and robust observable for anisotropy. Additionally, the width of our ϵ_{2L} band is smaller than the difference in the ϵ_2 values obtained by using different models (e.g., MC-Glauber vs. MC-KLN). Therefore, our approach provides genuine resolving power to distinguish between different initial-state models, although it may not be possible to separate the finer details of more sophisticated models. This resolving power, moreover, comes from entirely different perspective, i.e., from high $p_\perp$ theory and data, supporting the usefulness of utilizing high $p_\perp$ theory and data for inferring the bulk QGP properties.

Acknowledgements: This work is supported by the European Research Council, grant ERC-2016-COG: 725741, and by the Ministry of Science and Technological Development of the Republic of Serbia, under project numbers ON171004, ON173052 and ON171031.

References

[1] M. Gyulassy and L. McLerran, Nucl. Phys. A **750**, 30 (2005); E. V. Shuryak, Nucl. Phys. A **750**, 64 (2005).
[2] B. Jacak and P. Steinberg, Phys. Today **63**, 39 (2010); C. V. Johnson and P. Steinberg, Phys. Today **63**, 29 (2010).
[3] M. Djordjevic, S. Stojku, M. Djordjevic and P. Huovinen, Phys. Rev. C **100**, no. 3, 031901 (2019).
[4] M. Djordjevic, Phys. Rev. C **80**, 064909 (2009); M. Djordjevic and U. Heinz, Phys. Rev. Lett. **101**, 022302 (2008).
[5] M. Djordjevic, Phys. Rev. C **74**, 064907 (2006).
[6] J. I. Kapusta, *Finite-Temperature Field Theory* (Cambridge University Press, 1989).
[7] M. Djordjevic and M. Djordjevic, Phys. Lett. B **709**, 229 (2012).
[8] B. Blagojevic, M. Djordjevic and M. Djordjevic, Phys. Rev. C **99**, 024901 (2019).
[9] D. Zigic, I. Salom, J. Auvinen, M. Djordjevic and M. Djordjevic, J. Phys. G **46**, 085101 (2019).
[10] D. Zigic, I. Salom, M. Djordjevic and M. Djordjevic, Phys. Lett. B **791**, 236 (2019).
[11] J. D. Bjorken, Phys. Rev. D **27**, 140 (1983).
[12] J. Noronha-Hostler, B. Betz, J. Noronha and M. Gyulassy, Phys. Rev. Lett. **116**, no. 25, 252301 (2016).
[13] D. Zigic, *et al.*, to be submitted.
[14] D. Zigic, B. Ilic, M. Djordjevic and M. Djordjevic, arXiv:1908.11866 [hep-ph].
[15] C. Loizides, J. Kamin and D. d'Enterria, Phys. Rev. C **97**, 054910 (2018).
[16] K. J. Eskola, H. Niemi, R. Paatelainen and K. Tuominen, Phys. Rev. C **97**, 034911 (2018).
[17] J. E. Bernhard, J. S. Moreland, S. A. Bass, J. Liu and U. Heinz, Phys. Rev. C **94**, 024907 (2016).
[18] T. Hirano, P. Huovinen, K. Murase and Y. Nara, Prog. Part. Nucl. Phys. **70**, 108 (2013).
[19] M. Djordjevic and M. Djordjevic, Phys. Rev. C **92**, 024918 (2015).
[20] M. Djordjevic, D. Zigic, M. Djordjevic and J. Auvinen, Phys. Rev. C **99**(R), 061902 (2019).
[21] V. Khachatryan *et al.* [CMS Collaboration], JHEP **1704**, 039 (2017).
[22] A. M. Sirunyan *et al.* [CMS Collaboration], Phys. Lett. B **776**, 195 (2018).
[23] S. Acharya *et al.* [ALICE Collaboration], JHEP **1811**, 013 (2018).
[24] S. Acharya *et al.* [ALICE Collaboration], JHEP **1807**, 103 (2018).
[25] [ATLAS Collaboration], ATLAS-CONF-2017-012.
[26] M. Aaboud *et al.* [ATLAS Collaboration], Eur. Phys. J. C **78**, no. 12, 997 (2018).

acceptance letter of item [26]

Subject: Decision on NPA-D-20-00137
Date: 2020-04-27 11:24
From: "Nuclear Physics A" <em@editorialmanager.com>
To: "Magdalena Djordjevic" <magda@ipb.ac.rs>
Reply-To: "Nuclear Physics A" <npa@elsevier.com>

Ms. Ref. No.: NPA-D-20-00137
Title: From high pT theory and data to inferring anisotropy of Quark-Gluon Plasma
Nuclear Physics, Section A

Dear Dr. Djordjevic,

I am pleased to inform you that your paper "From high pT theory and data to inferring anisotropy of Quark-Gluon Plasma" has been accepted for publication in Nuclear Physics, Section A.

Comments from the Editor and Reviewers can be found below.

Thank you for submitting your work to this journal.

Yours sincerely,

Katherine Jane Parr
on behalf of the Editors of Nuclear Physics A

Editorial Office Nuclear Physics A
E-mail: npa@elsevier.com

Comments from the Editors and Reviewers:

Reviewer #1: It is interesting for the authors to propose an approach to extract the initial state anisotropy by the theory and experimental data comparison of the high p_T observables. As I understand any jet-medium interaction framework should incorporate a medium evolution process with a certain initial state. They argue that the ratio of the v_2 and (1-R_AA) will only be determined by the geometry of the initial QGP droplet, and can be approximately expressed as a function of \varsigma. Therefore the anisotropy parameter can be directly obtained from fitting such high p_T observables. And the authors later compare their extracted \epsilon_2L with their initial state's eccentricity \epsilon_2 and many other initial-state models. The ratio of the v_2 and (1-R_AA) may inherit the initial property (initial \epsilon_2)through out the in-medium evolution. The study brings our attention to how the high p_T observables of jet quenching can reflect the initial state geometry. I suggest the manuscript should be published in NPA.

Available online at www.sciencedirect.com

ScienceDirect

Nuclear Physics A 956 (2016) 457–460

NUCLEAR PHYSICS A

www.elsevier.com/locate/nuclphysa

Violation of mass ordering for multi-strange hadrons at RHIC and LHC

Shiori Takeuchi[a], Koichi Murase[a,b,c], Tetsufumi Hirano[a], Pasi Huovinen[d,e,f], Yasushi Nara[g]

[a] *Department of Physics, Sophia University, Tokyo 102-8554, Japan*
[b] *Department of Physics, The University of Tokyo, Tokyo 113-0033, Japan*
[c] *Theoretical Research Division, Nishina Center, RIKEN, Wako 351-0198, Japan*
[d] *Institut für Theoretische Physik, Johann Wolfgang Goethe-Universität, 60438 Frankfurt am Main, Germany*
[e] *Frankfurt Institute for Advanced Studies, 60438 Frankfurt am Main, Germany*
[f] *Institute of Theoretical Physics, University of Wroclaw, 50-204 Wroclaw, Poland*
[g] *Department of International Liberal Arts, Akita International University, Yuwa, Akita-city 010-1292, Japan*

Abstract

We study effects of the hadronic rescattering on final observables especially for multi-strange hadrons such as ϕ, Ξ and Ω in high-energy heavy-ion collisions within an integrated dynamical approach. In this approach, (3+1)-dimensional ideal hydrodynamics is combined with a microscopic transport model, JAM. We simulate the collisions with or without hadronic rescatterings and compare observables between these two options so that we quantify the effects of the hadronic rescattering. We find that the mean transverse momentum and the elliptic flow parameter of multi-strange hadrons are less affected by hadronic rescattering and, as a result, the mass ordering of the p_T-differential elliptic flow parameter $v_2(p_T)$ is violated: At the RHIC and the LHC energies the $v_2(p_T)$ for ϕ-mesons is larger than that for protons in the low-p_T regions.

Keywords: high-energy heavy-ion collisions, multi-strange hadrons, elliptic flow

1. Introduction

The main purpose in the physics of high-energy heavy-ion collisions at the Relativistic Heavy Ion Collider (RHIC) and the Large Hadron Collider (LHC) is to extract properties of the quark gluon plasma (QGP), the deconfined nuclear matter consisting of strongly interacting quarks and gluons. In particular, transport properties of nearly perfect QGP fluids attract a great deal of attention.

The QGP created in the collisions expands, cools down and finally turns into a hadron gas. Hadrons rescatter with each other in this late stage of the collision, thus information about the QGP is usually contaminated by the hadronic rescatterings. This fact makes it difficult to observe the QGP directly. For this reason it is suggested that multi-strange hadrons can be utilised as direct probes of the QGP. Since the multi-strange hadrons have small cross sections with pions, the dominant constituents of a hadron gas, their distributions reflect the state of the system just after hadronization [1, 2, 3, 4, 5, 6, 7, 8]. Unlike conventional penetrating probes such as photons and dileptons which are emitted during the entire evolution of the system, the multi-strange hadrons provide information about this specific stage of the collisions.

http://dx.doi.org/10.1016/j.nuclphysa.2016.01.024

Hydro + cascade calculations predicted several years ago that the elliptic flow coefficient $v_2(p_T)$ for protons and ϕ-mesons violates the mass ordering of this coefficient. This phenomenon reflects the small scattering cross section of ϕ-meson, and was recently observed by the STAR collaboration [7].

In this contribution, we study the violation of mass ordering more systematically and quantitatively by focusing on p_T distributions and elliptic flow of hadrons, in particular for Ξ- and Ω-baryons and ϕ-mesons. An integrated dynamical model, a more sophisticated version of the hydro + cascade approach, is employed here to make the investigation more realistic.

2. Model

We simulate Au + Au collisions at $\sqrt{s_{\rm NN}}$ = 200 GeV and Pb + Pb collisions at $\sqrt{s_{\rm NN}}$ = 2.76 TeV on an event by event basis by employing an integrated dynamical approach [9]. This approach consists of three stages. In the initial stage, entropy-density distribution after the collision is calculated by using a Monte Carlo Glauber model. The subsequent QGP fluid expansion is described by fully (3+1) dimensional ideal hydrodynamics. After we switch the description from fluids to particles, we utilise a hadron cascade model, JAM [10], to describe the evolution of hadron gas. As for an equation of state (EOS), we employ *s95p*-v1.1 [11], in which the lattice EOS at high temperature is connected to the hadron resonance gas EOS at low temperature. Note that this particular version of the model EOS is designed to include all the hadrons in JAM. Switching from hydrodynamics to JAM is done by using the Cooper-Frye formula on the isothermal hypersurface at the temperature of 155 MeV. This temperature is chosen to reproduce the experimentally observed pion-to-kaon and pion-to-proton ratios in low p_T regions at the RHIC energy.

Hadronic reactions in JAM are described as two-particle scatterings with experimental hadronic cross section if available. When there are no experimental data, we employ the additive quark model for the corresponding scatterings. In this model, reactions involving (hidden-)strange hadrons have smaller cross sections than non-strange hadrons due to a phenomenological strangeness suppression factor. Furthermore, the experimentally known scattering cross sections of multi-strange hadrons are small, since they form very few (or not at all) resonances. Thus multi-strange hadrons have smaller cross sections than non-strange hadrons. Note here that, in order to study the effects of hadronic rescattering on ϕ-meson efficiently, we switch off the decay channel $\phi \to K^+K^-$. This does not affect the kinetic evolution of the system because the lifetime of ϕ-mesons ($\sim$ 47 fm/c) [12] is larger than typical lifetime of the system ($\sim$ 10 fm/c). For further details, see Ref. [9].

3. Results

To investigate the effects of hadronic rescattering on final observables, we simulate the collisions with two options in JAM. One of them is the default setting, in which the rescatterings occur until all hadrons have decoupled, and resonances decay according to their lifetimes and decay channels. By using this option, we are able to reasonably reproduce final experimental observables such as the p_T-spectra and differential v_2 at both the RHIC [14] and the LHC energies. In the other option, the hadronic rescatterings are deactivated but resonances decay. These calculations serve the information just after the fluid-dynamical stage. Comparisons of observables calculated using these two options show how much the hadronic rescattering affects final observables.

The phenomenon of violation of mass ordering in $v_2(p_T)$ can be interpreted as a result of interplay between hadronic rescattering effects on mean transverse momentum, $\langle p_T \rangle$, and those on p_T-averaged v_2 because the slope of $v_2(p_T)$ is roughly approximated by the relation [13], $dv_2(p_T)/dp_T \approx v_2/\langle p_T \rangle$. Therefore we quantify the effects on $\langle p_T \rangle$ and v_2 for each hadron by taking ratio of the observables just after the fluid stage to the final observables. As shown in Fig. 8 (a) in Ref. [14], the ratio of $\langle p_T \rangle$ for pions, kaons and protons follow the tendency obtained from m_T scaling ansatz, in which it is assumed that all the hadrons flow with common velocity. However multi-strange hadrons obviously deviate from this pattern. From this observation, multi-strange hadrons do not fully participate in the radial flow during the hadronic stage and therefore freeze out earlier than non-strange hadrons. As for v_2 shown in Fig. 8 (b) in Ref. [14],

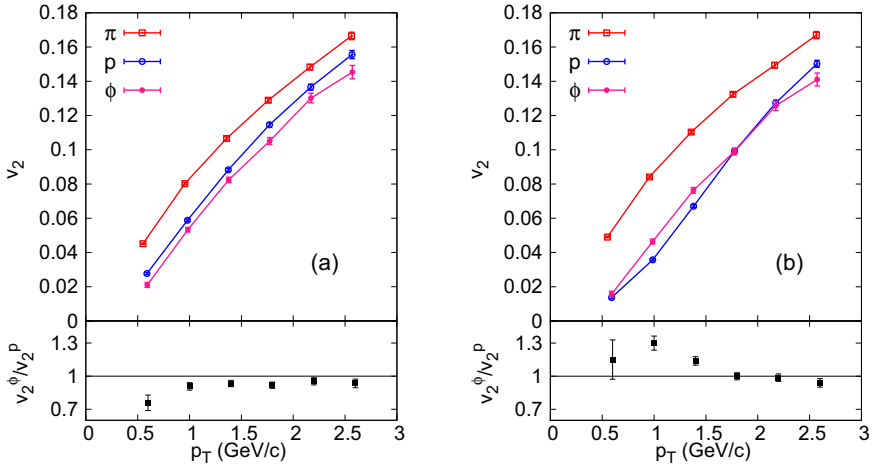

Fig. 1. Transverse momentum dependencies of elliptic flow parameter v_2 for pions (open square), protons (open circle) and ϕ-mesons (filled circle) near midrapidity $|\eta| < 2.0$ obtained from the integrated dynamical approach (a) without hadronic rescattering and (b) with hadronic rescattering in minimum bias Pb+Pb collisions at $\sqrt{s_{\rm NN}} = 2.76$ TeV. The lower panels of the plots show the ratio of v_2^ϕ to v_2^p.

pion v_2 increases by about 20% during the hadronic stage, whereas the v_2 of all the other hadrons shows much smaller increase of 0-5% . By combining the results of these two observables, we see that both $\langle p_T \rangle$ and v_2 for multi-strange hadrons are hardly affected by hadronic rescatterings, but either one of these two observables is affected for all the other particles. This fact is reflected in $v_2(p_T)$ for each hadron. In Fig. 6 in Ref. [14], we showed $v_2(p_T)$ with or without hadronic rescatterings to see how rescatterings affect it. ϕ-meson $v_2(p_T)$ is almost identical in both cases since the hadronic rescatterings do not change its slope. However the situation is different in the case for non-strange hadrons. Pion $v_2(p_T)$ goes up because p_T-averaged v_2 increases but $\langle p_T \rangle$ remains almost unchanged in the hadronic stage. On the other hand, for protons, p_T-averaged v_2 does not change a lot, but $\langle p_T \rangle$ increases. Consequently, proton $v_2(p_T)$ shifts to higher p_T region and crosses ϕ-meson $v_2(p_T)$ at ~ 1.5 GeV violating the conventional mass ordering.

At the LHC energy, this phenomenon appears in the same way. Figure 1 shows $v_2(p_T)$ for pions, protons and ϕ-mesons in minimum bias Pb+Pb collisions at $\sqrt{s_{\rm NN}} = 2.76$ TeV from the integrated dynamical approach. To see this behaviour clearly, we also plot the ratio v_2^ϕ/v_2^p in lower panels of the figures. In the case without hadronic rescatterings shown in Fig. 1 (a), the mass ordering behaviour, $v_2^\pi(p_T) > v_2^p(p_T) > v_2^\phi(p_T)$ for $m_\pi < m_p < m_\phi$, appears due to the collective flow in the fluid stage. However, in Fig. 1 (b), this pattern is reversed below about 2 GeV between protons and ϕ-mesons: $v_2^p(p_T) < v_2^\phi(p_T)$ even though $m_p < m_\phi$. These are qualitatively the same results to those at the RHIC energy but quantitatively the crossing point between these two shown in Fig. 1 (b) shifts to higher p_T region compared to that at the RHIC energy as shown in Fig. 6 (b) in Ref. [14].

In addition to these results, we also show the normalised freeze-out time distributions for identified hadrons. In Figs. 2 (a) and (b), we show the results for mesons and for baryons in separate panels for clarity. Also switching time distributions from fluids to particles are shown with shaded areas. Prominent peaks around 10 fm/c for ϕ-mesons and Ω-baryons can be seen and look quite similar to the ones of the switching time distributions. The distribution for Ξ-baryons has also a peak in the early time but its height is lower than for ϕ-mesons and Ω-baryons. This is because the decay contribution from long-lived resonance $\Xi(1530)$ to Ξ forms a long tail in the late time. Therefore primordial Ξ-baryons freeze out as early as ϕ-mesons and Ω-baryons. These results prove that the multi-strange hadrons freeze out soon after the fluid stage since they rarely rescatter in the hadronic stage.

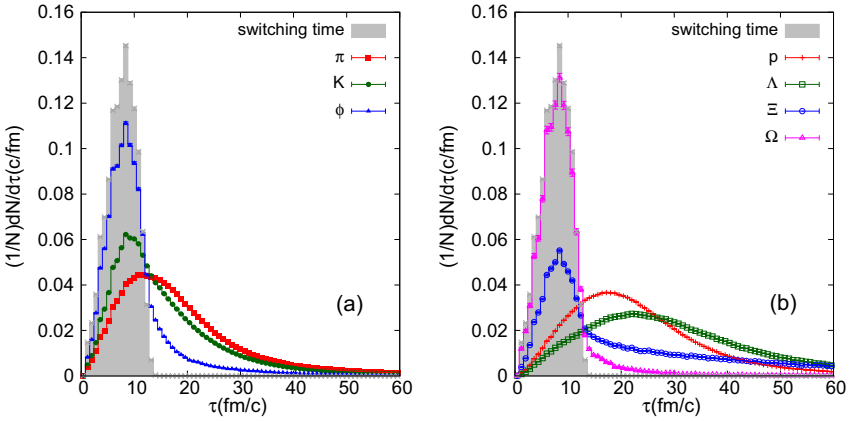

Fig. 2. Normalised freeze-out time (τ) distributions for (a) mesons (π, K and ϕ) and (b) baryons (p, Λ, Ξ and Ω) near midrapidity $|y| < 1.0$ in minimum bias Pb+Pb collisions at $\sqrt{s_{\rm NN}} = 2.76$ TeV. The shaded areas represent the distributions of charged hadrons at the time switching from fluids to particles.

4. Summary

We have studied the effects of the hadronic rescattering on observables especially for multi-strange hadrons. We have used an integrated dynamical approach, a model combining the ideal hydrodynamics with a hadronic cascade model, JAM. In order to investigate the hadronic rescattering effects within this approach, we have compared p_T-distributions and elliptic flow with hadronic rescatterings to the ones without rescatterings. By studying the effects on mean transverse momentum and integrated elliptic flow parameters, we have found that these observables for the multi-strange hadrons are less affected by the rescatterings. Furthermore theoretically and experimentally suggested phenomenon indicating the less rescatterings of ϕ-mesons, violation of mass ordering in $v_2(p_T)$, has been interpreted as a results of the effects on mean p_T and v_2. These results at the RHIC energy had been discussed in Ref. [14]. Now we have shown that this behaviour also appears at the LHC energy. By considering these results, we claim that the multi-strange hadrons can be utilised as "penetrating" probes of the QGP in high-energy heavy-ion collisions.

Acknowledgement

This work was supported by JSPS KAKENHI Grant Numbers 12J08554 (K.M.) and 25400269 (T.H.), by BMBF under contract no. 06FY9092 (P.H.) and by the Polish Science Foundation (NCN), under Maestro grant DEC-2013/10/A/ST2/00106 (P.H.).

References

[1] A. Shor, Phys. Rev. Lett. **54** (1985) 1122.
[2] H. van Hecke, H. Sorge and N. Xu, Phys. Rev. Lett. **81** (1998) 5764.
[3] S. A. Bass and A. Dumitru, Phys. Rev. C **61** (2000) 064909.
[4] Y. Cheng, F. Liu, Z. Liu, K. Schweda and N. Xu, Phys. Rev. C **68** (2003) 034910.
[5] T. Hirano, U. W. Heinz, D. Kharzeev, R. Lacey and Y. Nara, Phys. Rev. C **77** (2008) 044909.
[6] M. He, R. J. Fries and R. Rapp, Phys. Rev. C **85** (2012) 044911.
[7] M. Nasim [STAR Collaboration], Nucl. Phys. A **904-905** (2013) 413c.
[8] X. Zhu, F. Meng, H. Song and Y. X. Liu, Phys. Rev. C **91** (2015) 3, 034904.
[9] T. Hirano, P. Huovinen, K. Murase and Y. Nara, Prog. Part. Nucl. Phys. **70** (2013) 108.
[10] Y. Nara, N. Otuka, A. Ohnishi, K. Niita and S. Chiba, Phys. Rev. C **61** (2000) 024901.
[11] P. Huovinen and P. Petreczky, Nucl. Phys. A **837** (2010) 26.
[12] K. A. Olive *et al.* [Particle Data Group Collaboration], Chin. Phys. C **38** (2014) 090001.
[13] T. Hirano and M. Gyulassy, Nucl. Phys. A **769** (2006) 71.
[14] S. Takeuchi, K. Murase, T. Hirano, P. Huovinen and Y. Nara, Phys. Rev. C **92** (2015) 4, 044907.

Available online at www.sciencedirect.com

ScienceDirect

Nuclear Physics A 956 (2016) 834–837

NUCLEAR PHYSICS A

www.elsevier.com/locate/nuclphysa

Effects of EoS in viscous hydro+cascade model for the RHIC Beam Energy Scan

Iu. Karpenko[a,b,c], M. Bleicher[c,d], P. Huovinen[c,d,e], H. Petersen[c,d,f]

[a] *INFN - Sezione di Firenze, Via G. Sansone 1, I-50019 Sesto Fiorentino (Firenze), Italy*
[b] *Bogolyubov Institute for Theoretical Physics, 14-b, Metrolohichna st., 03680 Kiev, Ukraine*
[c] *Frankfurt Institute for Advanced Studies, Ruth-Moufang-Straße 1, D-60438 Frankfurt am Main, Germany*
[d] *Institute for Theoretical Physics, Johann Wolfgang Goethe Universität, Max-von-Laue-Str. 1, D-60438 Frankfurt am Main, Germany*
[e] *Institute of Theoretical Physics, University of Wroclaw, pl. Maxa Borna 9, PL-50204 Wroclaw, Poland*
[f] *GSI Helmholtzzentrum für Schwerionenforschung GmbH, Planckstr. 1, D-64291 Darmstadt, Germany*

Abstract

A state-of-the-art 3+1 dimensional cascade + viscous hydro + cascade model vHLLE+UrQMD has been applied to heavy ion collisions in RHIC Beam Energy Scan range $\sqrt{s_{\rm NN}} = 7.7, \ldots, 200$ GeV. Based on comparison to available experimental data it was estimated that an effective value of shear viscosity over entropy density ratio η/s in hydrodynamic stage has to decrease from $\eta/s = 0.2$ to 0.08 as collision energy increases from $\sqrt{s_{\rm NN}} = 7.7$ to 39 GeV, and to stay at $\eta/s = 0.08$ for $39 \leq \sqrt{s} \leq 200$ GeV.

In this work we show how an equation of state with first order phase transition affects the hydrodynamic evolution at those collision energies and changes the results of the model as compared to "default scenario" with a crossover type EoS from chiral model.

Keywords: quark-gluon plasma, relativistic hydrodynamics, hadron cascade

1. Introduction

The goal of ongoing Beam Energy Scan (BES) program at RHIC facility and future experimental programs at GSI FAIR and JINR NICA is to explore the high-μ_B region of phase diagram of QCD matter and the phase transition from hadron gas to quark-gluon plasma by colliding heavy nuclei at different energies.

Following the success of hydrodynamic description of heavy ion reactions at full RHIC and LHC energies, we have reported on creation of a state-of-the-art viscous hydro+cascade model and its application to heavy ion collisions in the BES collision energy range [1]. In the context of this model, reproduction of available experimental data requires a finite collision energy dependent shear viscosity over entropy density ratio η/s in the hydrodynamic stage. This ratio was found to decrease from $\eta/s = 0.2$ to 0.08 as collision energy increases from $\sqrt{s_{\rm NN}} = 7.7$ to 39 GeV, and to stay at $\eta/s = 0.08$ for $39 \leq \sqrt{s} \leq 200$ GeV. The found collision energy dependence of the effective η/s indicates that the physical η/s-ratio may depend on baryochemical potential, and that η/s increases with increasing μ_B.

However, only one version of the equation of state (EoS) was used throughout the analysis in [1], namely the chiral model EoS [2]. The question remains: how sensitive the obtained results are to the hydrodynamic EoS and whether it is possible to discriminate between EoSs using experimental data. In this work we show

http://dx.doi.org/10.1016/j.nuclphysa.2016.02.030

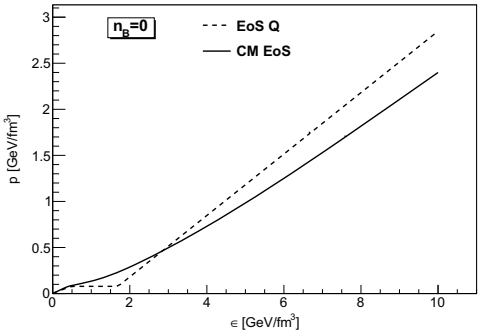

Fig. 1. Pressure as a function of energy density at zero baryon density, for the two EoSs used in the simulations: chiral model EoS (solid curve) and EoS Q (dashed curve).

sensitivity of hadronic observables in RHIC BES collision energy range to the choice of the equation of state (EoS) in the fluid stage.

2. The equations of state in the viscous hydro+cascade model

Since the model has been described in detail in Ref. [1], we summarise here its main features only. The initial stage of evolution is described with UrQMD cascade [3, 4]. At a hypersurface of constant Bjorken proper time $\tau = \sqrt{t^2 - z^2} = \tau_0$ the system is fluidized, *i.e.* the energy and momentum of individual hadrons are converted into energy and momentum of fluid. The τ_0 is a parameter of the model. At lower RHIC BES energies its value is set to the time when all initial nucleon-nucleon scatterings have happened. The hydrodynamic stage which follows is modelled with a 3+1 dimensional numerical solution of relativistic viscous hydrodynamics in Israel-Stewart framework using recently developed `vHLLE` code [5]. Particlization is set to happen when energy density $\epsilon = \epsilon_{\rm sw}$ is reached. The following hadronic stage is described again with UrQMD cascade.

It is worth to note that at BES collision energies local baryon or charge densities can be large. Therefore a consistent hydrodynamic description requires an EoS which is defined at all physical energy/baryon densities. Presently we have only two such EoSs at hand. One is the chiral model EoS (CM EoS), used in our previous analysis, whereas another is so called "EoS Q" [6].

The chiral model (CM) EoS has correct asymptotic degrees of freedom at the high and low temperature limits – quarks and hadrons – and is in qualitative agreement with lattice QCD results at $\mu_B = 0$. However, deconfinement transition appears in it as a (wide) crossover where medium modified hadrons coexist with free quarks. The crossover happens at all values of baryon chemical potential.

The EoS Q comprises hadron resonance gas (HG) and quark-gluon plasma (QGP) phases. HG phase is constructed from contributions of hadron resonances with masses up to 2 GeV and includes repulsive interactions via a mean-field potential. QGP phase is described as an ideal gas of massless quarks and gluons inside a large bag with bag constant B. The value of the latter is taken to be $B^{1/4} = 230$ MeV. The two phases are matched via Maxwell construction, which results in first order phase transition between the phases also at all values of baryon chemical potential. With the given value of the bag constant the transition temperature is $T_c(n_B = 0) = 164$ MeV at zero baryon density.

The particlization (transition from fluid to individual hadrons) is set to happen at fixed energy density $\epsilon_{\rm sw} = 0.5$ GeV/fm^3 for both EoS scenarios. At this energy density the system is firmly on the hadronic side for both EoS. We apply conventional Cooper-Frye prescription for hadron distributions on the particlization hypersurface:

$$p^0 \frac{d^3 N_i(x)}{d^3 p} = d\sigma_\mu p^\mu f(p \cdot u(x), T(x), \mu_i(x)), \tag{1}$$

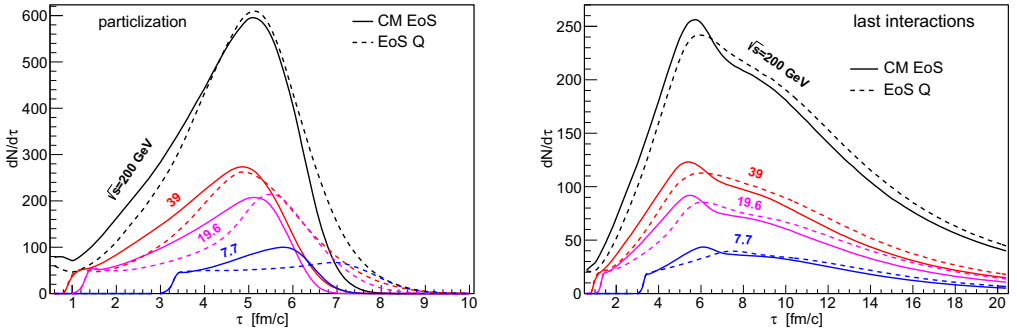

Fig. 2. Longitudinal proper time distribution of hadrons sampled at particlization surface (left) and their last interaction points (right). All distributions correspond to midrapidity region of 20-30% central Au-Au collisions at different collision energies, simulated with CM EoS (solid curves) and EoS Q (dashed curves) in the fluid phase.

where the phase space distribution function f is taken to correspond to free hadron resonance gas close to local equilibrium with non-equilibrium corrections proportional to the shear stress tensor:

$$f = f_{\rm eq}(p^\nu u_\nu; T, \mu_i)\left[1 + (1 \mp f_{\rm eq})\frac{p_\mu p_\nu \pi^{\mu\nu}}{2T^2(\epsilon + p)}\right]. \tag{2}$$

Such distribution function is inconsistent with mean fields included in hadron phase of both EoS used in fluid phase. Therefore we recalculate the energy density, pressure, flow velocity u^μ, temperature, and chemical potentials from the ideal parts of the energy-momentum tensor and charge currents using a free hadron resonance gas EoS and use these values to evaluate the particle distributions on the switching surface.

3. Results and conclusions

To set up the calculations for the Beam Energy Scan range we take collision energy dependent values of the parameters of the model, used to approach the experimental data with CM EoS. Then we perform two sets of simulations: with CM EoS and EoS Q respectively. First of all we like to see how the hydrodynamic evolution itself is affected by the choice of the EoS. It is difficult to compare individual hydro evolutions with irregular initial conditions and different EoSs. Therefore we visualise the effects of the change of the EoS by using the event-averaged proper time distributions of the hadrons sampled at particlization surfaces, see Fig. 2, right. From the plot one can find that EoS Q results in longer average duration of the particle emission. This implies that the average duration of the fluid stage (which is defined as a space-time region where $\tau > \tau_0$ and $\epsilon > \epsilon_{\rm sw} = 0.5$ GeV/fm^3) is longer. Also, the relative change in the average duration of the fluid stage increases with decreasing collision energy and is maximal for lowest collision energy simulated, $\sqrt{s_{\rm NN}} = 7.7$ GeV. We assume that the prolongation is the effect of the mixed phase in EoS Q, since at higher energy densities it is even harder than CM EoS, see Fig. 1.

However, after being sampled at the particlization surface, hadrons decay and rescatter in the cascade. From Fig. 2, left, one can see that the resulting proper time distributions of the last interaction points of hadrons are much wider than the distributions of points of their creation, and differences between the two EoSs in fluid stage are largely smeared. This brings one to the question how much the EoS in the fluid phase affects the final observables.

We found that change in EoS has no impact on the shapes of rapidity distributions of produced particles. There is, however, some impact on the transverse dynamics of the system, which influence transverse momentum distributions of hadrons. From Fig. 3, left, one can conclude that EoS Q results in some suppression of the average radial flow, which decreases mean p_T of hadrons (larger effect for heavier protons and smaller

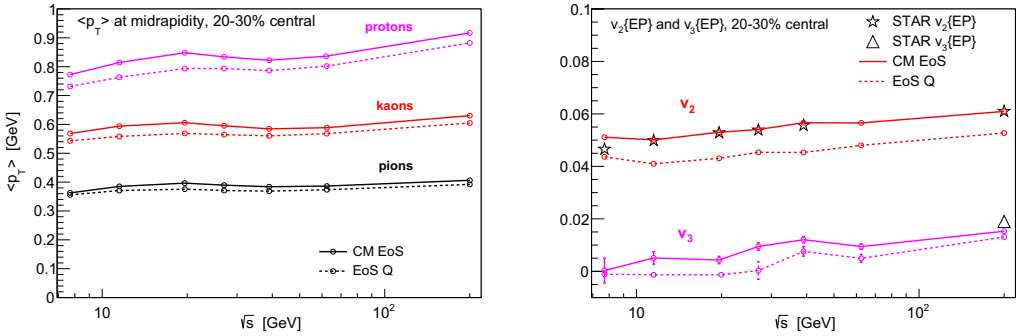

Fig. 3. Mean p_T of pions, kaons and protons at midrapidity (left), elliptic and triangular flow components of all charged hadrons (right) in 20-30% central Au-Au collisions, obtained from model simulations with collision energy dependent values of the parameters and two different equations of state in the fluid stage: chiral model EoS (solid curves) and EoS Q (dashed curves). The experimental data points are from the STAR collaboration [7, 8].

effect for lighter pions). The largest effect is seen in the p_T integrated elliptic flow, which turns out to be suppressed in EoS Q case by the same amount for all collision energies.

In the previous analysis we have shown that elliptic flow, as well as other observables, can be varied by varying free model parameters. Therefore it remains an open question whether it is possible to readjust the parameters of the model in order to compensate such changes in excitation functions of the elliptic flow and mean transverse momentum while keeping same rapidity distributions.

4. Acknowledgements

The simulations have been performed at the Center for Scientific Computing (CSC) at the Goethe-University Frankfurt. The authors acknowledge the financial support by the Helmholtz International Center for FAIR and Hessian LOEWE initiative. HP acknowledges funding by the Helmholtz Young Investigator Group VH-NG-822. The work of PH was supported by BMBF under contract no. 06FY9092.

References

[1] I. A. Karpenko, P. Huovinen, H. Petersen and M. Bleicher, Phys. Rev. C **91** (2015) 6, 064901 [arXiv:1502.01978 [nucl-th]].
[2] J. Steinheimer, S. Schramm and H. Stocker, J. Phys. G **38** (2011) 035001 doi:10.1088/0954-3899/38/3/035001 [arXiv:1009.5239 [hep-ph]].
[3] S. A. Bass *et al.*, Prog. Part. Nucl. Phys. **41** (1998) 255 [nucl-th/9803035].
[4] M. Bleicher *et al.*, J. Phys. G **25** (1999) 1859 [hep-ph/9909407].
[5] I. Karpenko, P. Huovinen and M. Bleicher, Comput. Phys. Commun. **185** (2014) 3016 doi:10.1016/j.cpc.2014.07.010 [arXiv:1312.4160 [nucl-th]].
[6] P. F. Kolb, J. Sollfrank and U. W. Heinz, Phys. Rev. C **62** (2000) 054909 doi:10.1103/PhysRevC.62.054909 [hep-ph/0006129].
[7] L. Adamczyk *et al.* [STAR Collaboration], Phys. Rev. C **86** (2012) 054908 doi:10.1103/PhysRevC.86.054908 [arXiv:1206.5528 [nucl-ex]].
[8] L. Adamczyk *et al.* [STAR Collaboration], Phys. Rev. C **88** (2013) 1, 014904 doi:10.1103/PhysRevC.88.014904 [arXiv:1301.2187 [nucl-ex]].

Available online at www.sciencedirect.com

ScienceDirect

Nuclear Physics A 931 (2014) 769–773

NUCLEAR PHYSICS A

www.elsevier.com/locate/nuclphysa

Equation of state at finite net-baryon density using Taylor coefficients up to sixth order

Pasi Huovinen [a,b,*], Péter Petreczky [c], Christian Schmidt [d]

[a] *Institut für Theoretische Physik, Johann Wolfgang Goethe-Universität, 60438 Frankfurt am Main, Germany*
[b] *Frankfurt Institute for Advanced Studies, 60438 Frankfurt am Main, Germany*
[c] *Physics Department, Brookhaven National Laboratory, Upton, NY 11973, USA*
[d] *Fakultät für Physik, Universität Bielefeld, 33615 Bielefeld, Germany*

Received 1 August 2014; accepted 22 August 2014

Available online 28 August 2014

Abstract

We employ the lattice QCD data on Taylor expansion coefficients up to sixth order to construct an equation of state at finite net-baryon density. When we take into account how hadron masses depend on lattice spacing and quark mass, the coefficients evaluated using the p4 action are equal to those of hadron resonance gas at low temperature. Thus the parametrised equation of state can be smoothly connected to the hadron resonance gas equation of state. We see that the equation of state using Taylor coefficients up to second order is realistic only at low densities, and that at densities corresponding to $s/n_B \gtrsim 40$, the expansion converges by the sixth order term.

Keywords: Lattice QCD; Equation of state; Hadron resonance gas

One of the methods to extend the lattice QCD calculations to non-zero chemical potential is Taylor expansion of pressure in chemical potentials:

$$\frac{P}{T^4} = \sum_{ij} c_{ij}(T) \left(\frac{\mu_B}{T}\right)^i \left(\frac{\mu_S}{T}\right)^j . \tag{1}$$

* Corresponding author.

http://dx.doi.org/10.1016/j.nuclphysa.2014.08.069

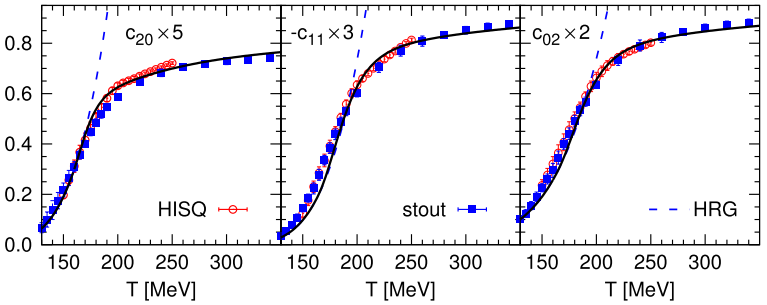

Fig. 1. The parametrised (solid line) second order Fourier coefficients compared to HRG values (dashed) and the continuum extrapolated HISQ [2] and stout [1] data.

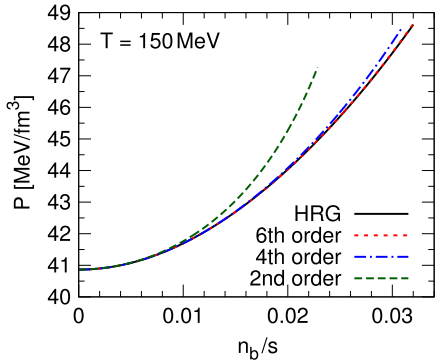

Fig. 2. Pressure at constant temperature $T = 150$ MeV in hadron resonance gas (HRG) and using Taylor coefficients of HRG up to second, fourth and sixth order in Eq. (1).

The coefficients of this expansion are derivatives of pressure, P, with respect to baryon and strangeness chemical potentials, μ_B and μ_S, respectively:

$$c_{ij}(T) = \frac{1}{i!j!}\frac{T^{i+j}}{T^4}\frac{\partial^i}{\partial\mu_B^i}\frac{\partial^j}{\partial\mu_S^j}P(T,\mu_B=0,\mu_S=0), \tag{2}$$

where T is temperature.[1] The lattice QCD calculations of these coefficients have matured to a level where both Budapest–Wuppertal [1] and hotQCD [2] Collaborations have published the final continuum extrapolated results for the second order Taylor coefficients, see Fig. 1.

As seen in Fig. 1, at low temperatures the coefficients evaluated using the hadron resonance gas (HRG) model agree with the lattice QCD results. Thus we may expect that HRG is an acceptable approximation of the physical equation of state also at finite net-baryon densities. To check how soon one may truncate the expansion in Eq. (1), we calculate the Taylor coefficients in HRG up to sixth order, evaluate the pressure using up to second, fourth or sixth order Taylor coefficients, and compare to the actual HRG pressure. The result is shown in Fig. 2, where the pressure at constant $T = 150$ MeV temperature is shown as a function of inverse of entropy per baryon, n_B/s. We use n_B/s as variable to facilitate easy comparison to heavy-ion collisions at

[1] We use natural units where $c = \hbar = k_B = 1$ throughout the text.

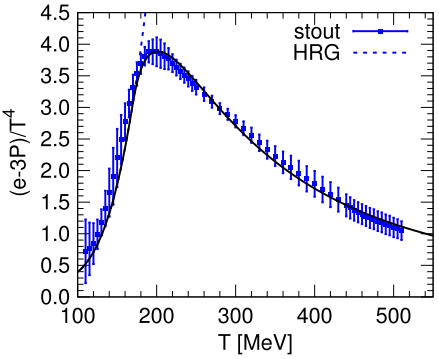

Fig. 3. The fitted trace anomaly (solid curve) compared to the HRG trace anomaly (dotted) and the continuum extrapolated lattice QCD result using stout action [11].

various energies since, unlike net-baryon density n_B, or baryon chemical potential μ_B, s/n_B is (approximately) constant during the entire expansion stage of the collision. We remind that at midrapidity the relevant entropy per baryon is $s/n_B = 400, 100, 65,$ and 40 at collision energies $\sqrt{s_{NN}} \approx 200, 64, 39,$ and 17 GeV/fm^3, respectively. Thus an equation of state based on second order Taylor coefficients only [3] can be expected to be realistic only at relatively low net-baryon densities, $s/n_B \gtrsim 100$, *i.e.*, at collisions with collision energy $\sqrt{s_{NN}} \gtrapprox 64$ GeV.

The Taylor coefficients have been evaluated on lattice up to sixth order [4,5], but unfortunately the fourth and sixth order coefficients suffer from large discretisation errors. As we have argued previously [6–9], these errors are mostly due to the lattice discretisation effects on hadron masses: When the hadron mass spectrum is modified accordingly (for details see [10]), the HRG model reproduces the lattice data, see Fig. 1 of Ref. [8]. Interestingly this change can be accounted for by shifting the modified HRG result of purely baryonic coefficients towards lower temperature by 30 MeV [8,9]. Based on this finding, and because the lattice data agree so well with the modified HRG, we suggest that cutoff effects can be accounted for by shifting the p4 lattice data by 30 MeV. The fourth and sixth order coefficients are shown in Fig. 4, where the data below 206 MeV has been shifted by 30 MeV, the data point at 209 MeV by 15 MeV (open symbol), and the points above 209 MeV have not been shifted. At low temperatures the shifted data now agrees with the unmodified HRG.

We parametrise the shifted p4 data, and the unshifted, continuum extrapolated stout and HISQ data, using an inverse polynomial of five (second order) or six (fourth and sixth order coefficients) terms:

$$c_{ij}(T) = \sum_{k=1}^{m} \frac{a_{kij}}{\hat{T}^{n_{kij}}} + c_{ij}^{\mathrm{SB}}, \tag{3}$$

where c_{ij}^{SB} is the Stefan–Boltzmann value of the particular coefficient, a_{kij} are the parameters, and the powers n_{kij} are required to be integers between 1 and 23. $\hat{T} = (T - T_s)/R$ with scaling factors $T_s = 0$ and $R = 0.15$ GeV for the second order coefficients and $T_s = 0.1$ GeV and $R = 0.05$ GeV for all other coefficients. We match the parametrisation of second order coefficients to the HRG value at temperature $T_{\mathrm{SW}} = 160$ MeV, and the fourth and sixth order coefficients at $T_{\mathrm{SW}} = 155$ MeV by requiring that the Taylor coefficient and its first, second, and third derivatives are continuous. The switching temperatures have been chosen to optimise the fit and lead to smooth behaviour of the speed of sound (see Fig. 5). These constraints fix four (or five) of the

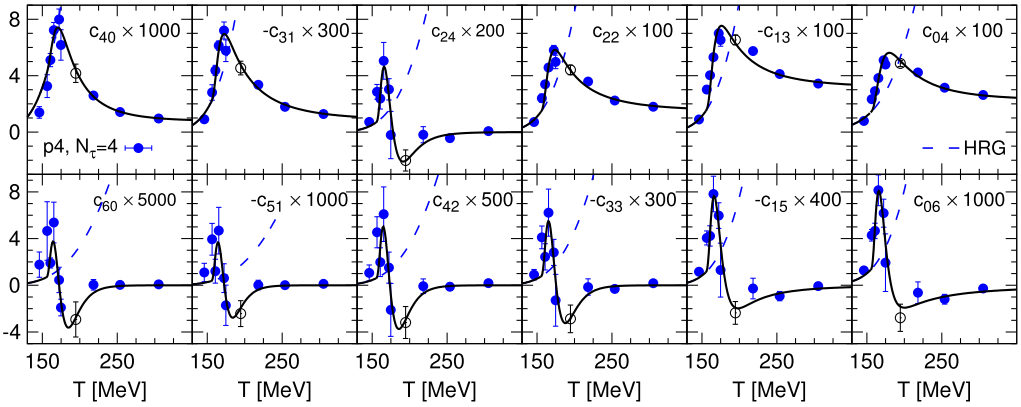

Fig. 4. The parametrised (solid line) fourth and sixth order Fourier coefficients compared to HRG values (dashed line) and the shifted p4 data [4,5] (see the text).

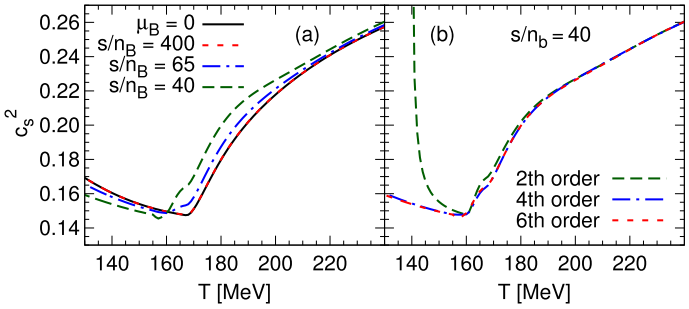

Fig. 5. The square of the speed of sound, c_s^2, as a function of temperature on various isentropic curves with constant entropy per baryon (a), and on $s/n_B = 40$ curve evaluated using Fourier coefficients up to second, fourth or sixth order (b).

parameters a_{kij}. The remaining parameters are fixed by a χ^2 fit to the lattice data. The resulting parameterisations are shown as solid curves in Figs. 1 and 4.

We obtain the pressure at $\mu_B = 0$, *i.e.* the coefficient c_{00}, from the continuum extrapolated stout data for the trace anomaly $(\epsilon - 3P)/T^4$ [11], which agree with the very recent HISQ data [12] within errors. As in our earlier parametrisation of trace anomaly [7], we fit the lattice result using an inverse polynomial with four terms, and connect it to the HRG trace anomaly at $T_{\rm SW} = 167$ MeV temperature, see Fig. 3.

We characterise the equation of state in Fig. 5a by showing the square of the speed of sound, $c_s^2 = \partial P/\partial\epsilon|_{s/n_B}$, on various isentropic curves with constant entropy per baryon. The curves at $s/n_B = 400, 65,$ and 40 are relevant at collision energies $\sqrt{s_{NN}} = 200, 39$ and 17 GeV, respectively. At $s/n_B = 400$ (dotted line), the equation of state is basically identical to the equation of state at $\mu_B = 0$ (thin solid line). At larger baryon densities the effect of finite baryon density is no longer negligible. The larger the density, the stiffer the equation of state above, and softer below the transition temperature. We see some ripples forming in the transition region with decreasing s/n_B. These ripples grow fast with increasing density when one goes beyond $s/n_B = 40$, and therefore we consider $s/n_B = 40$ to give a practical maximum density for our parametrisation.

In Fig. 5b we have evaluated the square of the speed of sound along the isentropic $s/n_B = 40$ curve using Taylor coefficients up to second, fourth and sixth order. At temperatures above the transition region they all lead to very similar speed of sound, but below $T \approx 150$ MeV, the second order result deviates strongly from the fourth and sixth order results. This shows that at low temperatures equation of state based on the second order coefficients only is not sufficient. Furthermore, the small difference between the fourth and sixth order equation of state indicates that if $s/n_B \gtrsim 40$, the expansion has basically converged by the sixth order term.

To summarise we have argued that an equation of state based on the Taylor expansion up to second order, is realistic only in collisions with larger collision energy than at the RHIC beam energy scan. We argue that the temperature shift of 30 MeV is a good approximation of the discretisation effects in the lattice QCD data obtained using p4 action. We have constructed an equation of state for finite baryon densities based on hadron resonance gas and lattice QCD data. In such an equation of state, the Taylor expansion essentially converges by the sixth order term if $s/n_B \gtrsim 40$.

Acknowledgements

This work was supported by BMBF under contract No. 06FY9092, and by the U.S. Department of Energy under contract DE-AC02-98CH1086.

References

[1] S. Borsanyi, Z. Fodor, S.D. Katz, S. Krieg, C. Ratti, K. Szabo, J. High Energy Phys. 1201 (2012) 138.
[2] A. Bazavov, et al., HotQCD Collaboration, Phys. Rev. D 86 (2012) 034509.
[3] S. Borsanyi, G. Endrodi, Z. Fodor, S.D. Katz, S. Krieg, C. Ratti, K.K. Szabo, J. High Energy Phys. 1208 (2012) 053.
[4] C. Miao, et al., RBC–Bielefeld Collaboration, PoS LATTICE2008 (2008) 172.
[5] M. Cheng, et al., Phys. Rev. D 79 (2009) 074505.
[6] P. Petreczky, PoS ConfinementX (2012) 028.
[7] P. Huovinen, P. Petreczky, Nucl. Phys. A 837 (2010) 26.
[8] P. Huovinen, P. Petreczky, J. Phys. G 38 (2011) 124103.
[9] P. Huovinen, P. Petreczky, C. Schmidt, Cent. Eur. J. Phys. 10 (2012) 1385.
[10] P. Huovinen, P. Petreczky, J. Phys. Conf. Ser. 230 (2010) 012012.
[11] S. Borsanyi, Z. Fodor, C. Hoelbling, S.D. Katz, S. Krieg, K.K. Szabo, Phys. Lett. B 730 (2014) 99.
[12] A. Bazavov, et al., arXiv:1407.6387 [hep-lat].

Available online at www.sciencedirect.com

ScienceDirect

Nuclear Physics A 926 (2014) 109–114

NUCLEAR PHYSICS A

www.elsevier.com/locate/nuclphysa

Fluid dynamical response to initial state fluctuations

H. Niemi [a,b,*], G.S. Denicol [c], H. Holopainen [d], P. Huovinen [d,e]

[a] *Department of Physics, P.O. Box 35, FI-40014, University of Jyväskylä, Finland*
[b] *Helsinki Institute of Physics, P.O. Box 64, FI-00014, University of Helsinki, Finland*
[c] *Department of Physics, McGill University, 3600 University Street, Montreal, QC, H3A 2T8, Canada*
[d] *Frankfurt Institute for Advanced Studies, Ruth-Moufang-Str. 1, D-60438 Frankfurt am Main, Germany*
[e] *Institut für Theoretische Physik, Johann Wolfgang Goethe-Universität, Max-von-Laue-Str. 1, D-60438 Frankfurt am Main, Germany*

Received 10 January 2014; received in revised form 19 March 2014; accepted 19 March 2014

Available online 27 March 2014

Abstract

We investigate a fluid dynamical response to the fluctuations and geometry of the initial state density profiles in ultrarelativistic heavy ion collisions.

Keywords: Initial state fluctuations; Relativistic fluid dynamics

1. Introduction

The aim of the experiments in ultrarelativistic heavy ion collisions is to understand the properties of nearly thermalized strongly interacting matter. In extracting these properties a good understanding of the dynamics of the formed system is essential, as almost none of the characteristics of the matter can be understood directly from the data, but some degree of theoretical interpretation is necessary. Relativistic fluid dynamics has become a standard tool in describing the spacetime evolution of the formed matter. For example finding constraints for the shear viscosity of the matter is largely based on the systematics of the azimuthal asymmetries of the hadron transverse momentum spectra, generated by the secondary interactions in the created system [1]. A magnitude of the asymmetries depend on the transport properties of the matter, and

* Corresponding author.

http://dx.doi.org/10.1016/j.nuclphysa.2014.03.014
0375-9474/

the evolution of the matter with non-zero viscosity is relatively straightforward to describe with fluid dynamics.

In the fluid dynamical picture the azimuthal asymmetries of the spectra are generated by initially asymmetric density or pressure gradients. The asymmetries of the final spectra then depend not only on the properties of the matter like equation of state and transport coefficients, but also on the asymmetries in the initial state. The initial state remains one of the largest uncertainties in extracting e.g. the shear viscosity of the strongly interacting matter.

In the recent years it has become evident that the initial density profiles fluctuate from collision to collision, even with a fixed impact parameter. Understanding these fluctuations does not only provide more information on the collisions, but it has become clear that even in describing the average properties of the system it is necessary to take into account the event-by-event nature of the collisions. Therefore it is essential to understand how the fluctuations in the initial state are reflected into the final observable hadron spectra.

2. Fluid dynamics and hadron spectra

A basic quantity in fluid dynamics is the energy–momentum tensor $T^{\mu\nu}$ that can be decomposed as

$$T^{\mu\nu} = eu^{\mu}u^{\nu} - (p + \Pi)\Delta^{\mu\nu} + \pi^{\mu\nu}. \tag{1}$$

In the fluid dynamical limit the evolution of the system can be described in terms of $T^{\mu\nu}$ alone, and a starting point for describing the evolution are the conservation laws

$$\partial_{\mu} T^{\mu\nu} = 0. \tag{2}$$

The conservation laws are completely general, but not sufficient to close the system. The fluid dynamical approximation comes into play when one writes the evolution equations for the viscous parts of the energy–momentum tensor. For example in the Israel–Stewart type of theories [2] the shear-stress tensor satisfies the equations of motion of the form

$$\tau_{\pi} \frac{\mathrm{d}}{\mathrm{d}\tau} \pi^{\langle\mu\nu\rangle} + \pi^{\mu\nu} = 2\eta \nabla^{\langle\mu} u^{\nu\rangle} + (\text{non-linear terms}), \tag{3}$$

where η is the shear viscosity coefficient and τ_{π} is the corresponding relaxation time, for further details see Ref. [3]. If one further specifies an equation of state, the spacetime evolution of $T^{\mu\nu}$ can be solved from the above equations provided that the initial values of $T^{\mu\nu}$ are given.

Once the full spacetime evolution is known, it can be converted to the hadron spectra e.g. via the Cooper–Frye procedure [4]. The resulting transverse momentum (p_T) spectra are then usually characterized in terms of its Fourier components v_n with respect to the azimuthal angle ϕ,

$$\frac{\mathrm{d}N}{\mathrm{d}y\,\mathrm{d}p_T^2\,\mathrm{d}\phi} = \frac{\mathrm{d}N}{\mathrm{d}y\,\mathrm{d}p_T^2}\big[1 + 2v_1(p_T)\cos(\phi - \psi_1) + 2v_2(p_T)\cos\big[2(\phi - \psi_2)\big] + \cdots\big], \tag{4}$$

where the event-plane angle ψ_n can be defined as

$$\psi_n = (1/n)\arctan\big(\langle p_T \sin n\phi\rangle / \langle p_T \cos n\phi\rangle\big). \tag{5}$$

A characterization of an ensemble of collisions requires also probabilities for observing $\mathrm{d}N/\mathrm{d}y$, v_n, ψ_n, …, not only their averages. In addition, the full characterization requires in principle all the possible correlations as well. Here we consider the probability distributions of the Fourier coefficients $\mathcal{P}(v_n)$ and correlations between them $c(v_i, v_j)$.

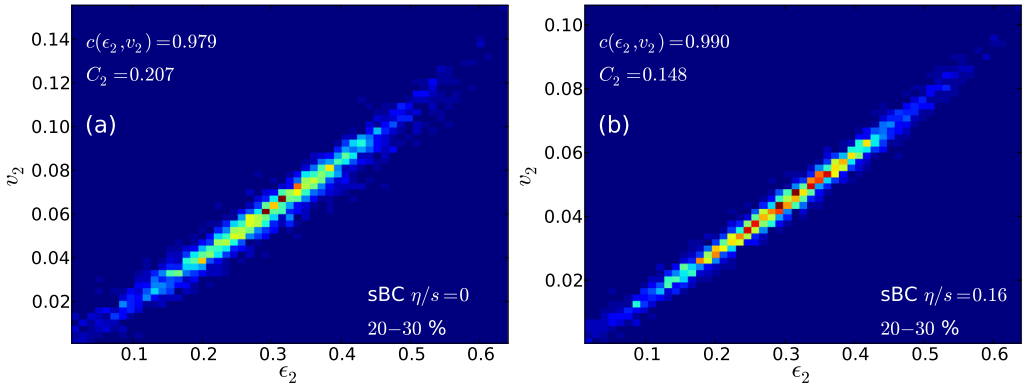

Fig. 1. Eccentricity and elliptic flow correlation [6].

3. Initial state and its fluctuations

An essential input to the fluid dynamical models is the initial density of the matter. A convenient way to characterize the initial density profile $\rho(x, y, \tau_0)$ is to decompose each initial entropy or energy density profile into its eccentricities

$$\epsilon_{m,n} = -\frac{\int \mathrm{d}x\,\mathrm{d}y\, r^m \cos[n(\phi - \Psi_{m,n})]\rho(x, y, \tau_0)}{\int \mathrm{d}x\,\mathrm{d}y\, r^m \rho(x, y, \tau_0)} \tag{6}$$

where r is the distance to the system's center of mass, $\rho(x, y, \tau_0)$ is the entropy or energy density at initial time τ_0, and the angle $\Psi_{m,n}$ is defined as

$$\Psi_{m,n} = \frac{1}{n} \arctan \frac{\int \mathrm{d}x\,\mathrm{d}y\, r^m \sin(n\phi)\rho(x, y, \tau_0)}{\int \mathrm{d}x\,\mathrm{d}y\, r^m \cos(n\phi)\rho(x, y, \tau_0)} + \pi/n. \tag{7}$$

Similarly to the particle spectra, a full description of the possible initial densities needs also the probability distributions and correlations among the eccentricities.

Although the eccentricities provide a relatively simple way of decomposing the initial density, an accurate representation of a density profile requires quite many terms in the expansion. An expansion based on the Bessel–Fourier decomposition was suggested in Ref. [5], where the authors show that with this expansion relatively few terms can reproduce even quite complex initial density profiles.

4. Fluid dynamical response to the initial geometry

If we start from a given initial condition, characterized by the eccentricities $\varepsilon_{m,n}$, the fluid dynamical evolution tends to convert them to the momentum space asymmetries, which then result in azimuthally asymmetric hadron spectra, i.e. non-zero v_n's. The conversion efficiency depends on the properties of the matter and also on the lifetime of the fluid dynamical system.

In principle, there are no apparent reasons to expect a simple relation between $\varepsilon_{m,n}$'s and v_n's as the fluid dynamical equations of motion are non-linear even in the ideal fluid limit. However, it turns out that there is a strong linear correlation between $\varepsilon_{2,2}$ and p_T integrated v_2 so that $v_2 \simeq C_2 \varepsilon_{2,2}$, where the proportionality constant depends on the properties of the matter, but not on the initial state itself. This is demonstrated in Fig. 1 which shows the full correlation between

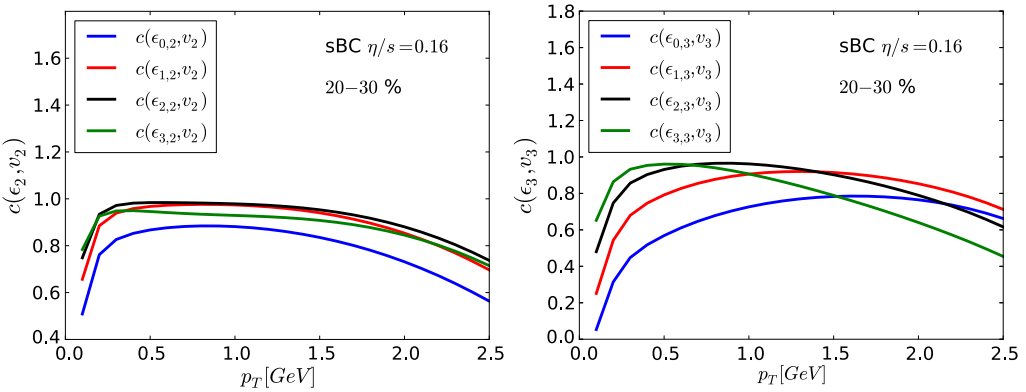

Fig. 2. $\varepsilon_{m,n}$ and $v_n(p_T)$ correlations.

$\varepsilon_{2,2}$ and v_2 from the fluid dynamical calculation with two different shear viscosity to entropy density ratio $\eta/s = 0$ and $\eta/s = 0.16$ [6]. At a fixed eccentricity there is only a small variation of v_2 and the non-zero viscosity even enhances the correlation. In these examples, as well as in all the examples below, the initial state is from the Monte-Carlo Glauber model, with the entropy density proportional to the density of binary collisions (sBC).

For the higher harmonics the situation is not as simple. There is still a linear correlation between v_3 and the corresponding eccentricity $\varepsilon_{m,3}$, although not nearly as strong as for v_2. For even higher harmonics the simple correlation ceases to exist [7–9], but the cross-correlations between different v_n's start to play a significant role [10].

A degree of linear correlation between the quantities a and b can be quantified by using a linear correlation coefficient defined as

$$c(a,b) = \left\langle \frac{(a - \langle a\rangle_{\mathrm{ev}})(b - \langle b\rangle_{\mathrm{ev}})}{\sigma_a \sigma_b} \right\rangle_{\mathrm{ev}}, \tag{8}$$

where the angular brackets $\langle\ \rangle_{\mathrm{ev}}$ denote an average over an ensemble of events, and σ_i is a standard deviation. For a perfect linear (anti-)correlation $c(a,b) = 1(-1)$.

Fig. 2 shows the correlation coefficients between $\varepsilon_{m,n}$ and $v_n(p_T)$ for $n = 2, 3$ as function of p_T from the same calculation as above. In principle one could hope to get an access to the r dependence of the initial density (different m's in the definition of $\varepsilon_{m,n}$) by studying v_n's at different p_T ranges. However, as seen from the figure, $v_2(p_T)$ has the strongest correlation with $\varepsilon_{2,2}$ in whole p_T range. The correlation between v_3 and $\varepsilon_{m,3}$ shows some degree of separation into different p_T ranges as a function of the power m, but even in this case the separation is not particularly strong.

5. Distributions

A detailed description of the evolution should not only reproduce the event averaged v_n, but also their event-by-event probability distributions. Fig. 3(a) shows examples of such distributions from Ref. [6] with two different η/s values. Although, the different cases give different distributions, the strong linear correlation $v_2 \simeq C_2\varepsilon_{2,2}$ means that $\varepsilon_{2,2}$ is in practice the only characteristics of the initial condition that determines v_2. It then follows that if one considers a distribution of relative fluctuations $\delta v_2 = (v_2 - \langle v_2\rangle)/\langle v_2\rangle$ the proportionality constant drops

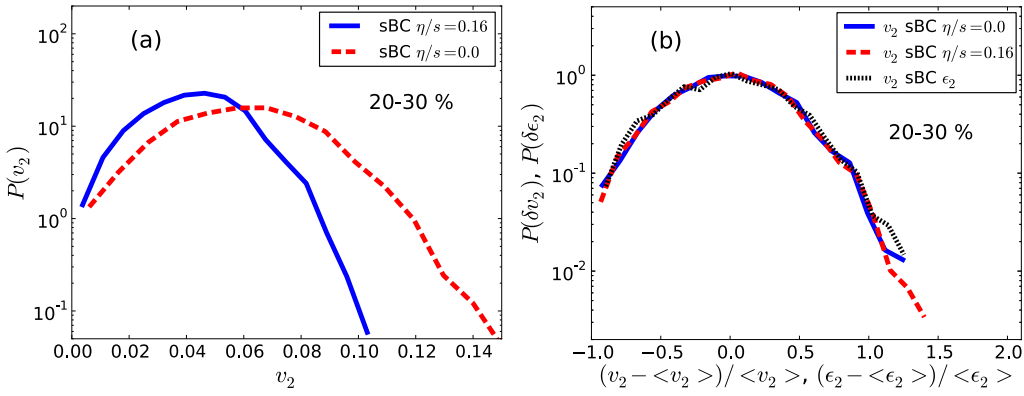

Fig. 3. v_2 (a) and δv_2 (b) distributions [6].

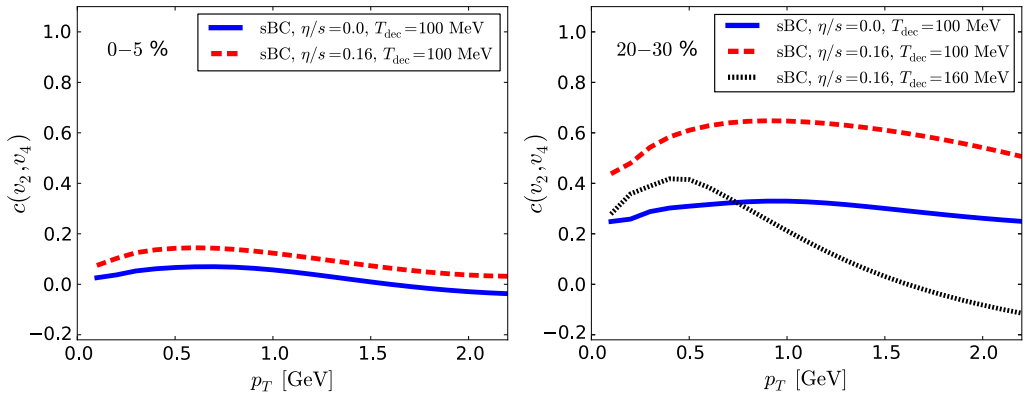

Fig. 4. v_2 and v_4 correlations as a function of transverse momentum [6].

out and the distribution of δv_2 is determined by the initial condition alone, i.e. it is independent of the fluid dynamical evolution. This is demonstrated in Fig. 3(b) which shows that the two cases above collapse into a one distribution that follows the underlying distribution of the scaled eccentricity.

Thus, the scaled v_2 distributions follow directly from the scaled $\varepsilon_{2,2}$ distributions, and the recently measured v_2 distributions [11,12] give direct constraints to the possible initial state models. These constraints can be used to rule out several simple Glauber model based initial conditions [13]. On the other hand the IP-Sat based initial conditions reproduce the distributions quite well [14].

6. Correlations

Even more details about the evolution is provided by the correlations between v_n's. Figs. 4(left) and 4(right) show the correlation coefficient between v_2 and v_4 as a function of p_T in 0–5% and 20–30% centrality class, respectively.

As seen from the figure, a non-zero shear viscosity strongly affects the correlation in peripheral collisions, as does the decoupling temperature. This shows that there is at least a large

contribution to the correlation form the (non-linear) fluid dynamical evolution, i.e. it is not only a result of correlation between the eccentricities in the initial conditions. In the central collisions the (v_2, v_4) correlation almost vanishes. The other correlations, i.e. (v_2, v_3) and (v_3, v_4) are also almost zero in the both centrality classes [6].

Acknowledgements

The work of H.N. was supported by the Academy of Finland, project No. 133005, G.S.D. acknowledges the support of a Banting fellowship provided by the Natural Sciences and Engineering Research Council of Canada, and the work of P.H. was supported by BMBF under contract No. 06FY9092.

References

[1] For a recent review and references, see U.W. Heinz, R. Snellings, Annu. Rev. Nucl. Part. Sci. 63 (2013) 123, arXiv:1301.2826 [nucl-th].
[2] W. Israel, J.M. Stewart, Phys. Lett. A 58 (1976) 213;
W. Israel, J.M. Stewart, Ann. Phys. (N.Y.) 118 (1979) 341;
W. Israel, J.M. Stewart, Proc. R. Soc. Lond. Ser. A 365 (1979) 43.
[3] G.S. Denicol, H. Niemi, E. Molnar, D.H. Rischke, Phys. Rev. D 85 (2012) 114047, arXiv:1202.4551 [nucl-th].
[4] F. Cooper, G. Frye, Phys. Rev. D 10 (1974) 186.
[5] S. Floerchinger, U.A. Wiedemann, Phys. Rev. C 88 (2013) 044906, arXiv:1307.7611 [hep-ph].
[6] H. Niemi, G.S. Denicol, H. Holopainen, P. Huovinen, Phys. Rev. C 87 (2013) 054901, arXiv:1212.1008 [nucl-th].
[7] G.-Y. Qin, H. Petersen, S.A. Bass, B. Muller, Phys. Rev. C 82 (2010) 064903, arXiv:1009.1847 [nucl-th].
[8] Z. Qiu, U.W. Heinz, Phys. Rev. C 84 (2011) 024911, arXiv:1104.0650 [nucl-th].
[9] F.G. Gardim, F. Grassi, M. Luzum, J.-Y. Ollitrault, Phys. Rev. C 85 (2012) 024908, arXiv:1111.6538 [nucl-th].
[10] D. Teaney, L. Yan, Phys. Rev. C 86 (2012) 044908, arXiv:1206.1905 [nucl-th].
[11] J. Jia, ATLAS Collaboration, Nucl. Phys. A 904–905 (2013) 421c, arXiv:1209.4232 [nucl-ex], 2013.
[12] A.R. Timmins, ALICE Collaboration, J. Phys. Conf. Ser. 446 (2013) 012031, arXiv:1301.6084 [nucl-ex].
[13] T. Renk, H. Niemi, arXiv:1401.2069 [nucl-th].
[14] B. Schenke, P. Tribedy, R. Venugopalan, arXiv:1312.5588 [hep-ph].

Progress in Particle and Nuclear Physics 70 (2013) 108–158

Contents lists available at SciVerse ScienceDirect

Progress in Particle and Nuclear Physics

journal homepage: www.elsevier.com/locate/ppnp

Review

Integrated dynamical approach to relativistic heavy ion collisions

T. Hirano [a,b,*], P. Huovinen [c,d], K. Murase [b,a], Y. Nara [e]

[a] Department of Physics, Sophia University, Tokyo 102-8554, Japan
[b] Department of Physics, The University of Tokyo, Tokyo 113-0033, Japan
[c] Frankfurt Institute for Advanced Studies, 60438 Frankfurt am Main, Germany
[d] Institut für Theoretische Physik, Johann Wolfgang Goethe-Universität, 60438 Frankfurt am Main, Germany
[e] Akita International University, Yuwa, Akita-city 010-1292, Japan

ARTICLE INFO

Keywords:
Quark gluon plasma
Relativistic heavy ion collisions
Relativistic hydrodynamic model
Event-by-event initial fluctuation
Anisotropic flow
Colour glass condensate

ABSTRACT

We review integrated dynamical approaches to describe heavy ion reaction as a whole at ultrarelativistic energies. Since final observables result from all the history of the reaction, it is important to describe all the stages of the reaction to obtain the properties of the quark–gluon plasma from experimental data. As an example of these approaches, we develop an integrated dynamical model, which is composed of a fully $(3+1)$ dimensional ideal hydrodynamic model with a state-of-the-art equation of state based on lattice QCD, and subsequent hadronic cascade in the late stage. Initial conditions are obtained employing Monte Carlo versions of the Kharzeev–Levin–Nardi model (MC-KLN) or the Glauber model (MC-Glauber). Using this integrated model, we first simulate relativistic heavy ion collisions at the RHIC and LHC energies starting from conventional smooth initial conditions. We next utilise each Monte Carlo sample of initial conditions on an event-by-event basis and perform event-by-event dynamical simulations to accumulate a large number of minimum bias events. A special attention is paid to performing the flow analysis as in experiments towards consistent comparison of theoretical results with experimental data.

Contents

* Corresponding author at: Department of Physics, Sophia University, Tokyo 102-8554, Japan.
E-mail address: hirano@sophia.ac.jp (T. Hirano).

0146-6410/$ – see front matter © 2013 Elsevier B.V. All rights reserved.
doi:10.1016/j.ppnp.2013.02.002

1. Introduction

Heavy ion programs at Large Hadron Collider (LHC) in European Organisation for Nuclear Research (CERN) and at Relativistic Heavy Ion Collider (RHIC) in Brookhaven National Laboratory (BNL) have focused on the physics of strongly interacting matter of quarks and gluons under extreme conditions, namely, on the physics of the quark–gluon plasma (QGP) [1]. By colliding two heavy nuclei at relativistic energies, the matter formed in the collision is expected to be in the state of QGP in temperatures up to 400 MeV $\sim 4 \times 10^{12}$ K. Such a high temperature was reached in the early universe about ten microseconds after the Big Bang. One of the main goals of the heavy ion programs is to extract bulk and transport properties of the QGP from analyses of experimental data.

So far, a vast body of experimental data have been obtained at RHIC and LHC. Among them, the azimuthal anisotropy of the emitted particles, so-called elliptic flow [2–13] is one of the main observables to provide information of the bulk properties of the QGP. In particular, the large observed value of elliptic flow at RHIC was one of the main reasons to conclude that the matter produced in the collisions at RHIC does indeed thermalise and form QGP [14,15].

In a non-central collision of two spherical nuclei, the reaction zone has an almond-like shape in the plane perpendicular to the collision axis, so called transverse plane. Because of this geometry, pressure gradient within the reaction zone is not azimuthally isotropic, but it is larger along the impact parameter than to the direction orthogonal to it. This leads to anisotropic expansion of the system with more particles being emitted along the impact parameter than orthogonal to it. It is customary to call the plane spanned by the beam and the impact parameter a reaction plane, and thus we say that larger emission along the impact parameter means larger emission "in-plane" than "out-of-plane". This anisotropic particle emission can be quantified by Fourier expanding the azimuthal distribution of observed particles. In particular, this kind of anisotropy is quantified by the second Fourier coefficient of the expansion, v_2. Since a finite v_2 in a Fourier expansion corresponds to an elliptic shape, this anisotropy is commonly called *elliptic flow* [16]. Quite surprisingly ideal hydrodynamics, which neglects all the dissipative effects, gave a good description of the elliptic flow observed at RHIC [17–22]. Given a fact that the expansion rate of the system formed in a heavy ion collision is tremendously large ($\sim 10^{24}$/s), it is far from obvious that dissipative effects can be neglected. Since in ideal hydrodynamics perfect local equilibrium is assumed to hold at any instant, couplings among constituents of the fluid must be so strong that relaxation of the system against any thermodynamic forces happens extremely quickly. Thus, from the agreement of hydrodynamic prediction with the elliptic flow data, an announcement of the "discovery of perfect fluidity" was made [23], and a new paradigm of the strongly coupled QGP (sQGP) was established [14,15,24–27].

However, the described shape of the reaction zone is realistic only as an average over many collisions. Since the nuclei are not uniform but consist of separate nucleons, we may expect the reaction zone in a single event to depict similar granular structure to the nuclei. For example, according to the Monte-Carlo Glauber model [28–30] the reaction zone consists of several peaks (*a.k.a.* hot spots) and valleys originating from the configuration of nucleons in the colliding nuclei. This irregular structure means that even if the underlying shape of the reaction zone in a non-central collision is almond-like, it has been distorted and tilted. Thus, if one fits an ellipse to the reaction zone, its minor axis no longer aligns with the impact parameter. As described, elliptic flow is generated by the anisotropy of pressure gradient. Now, if the thermodynamic language of pressure gradients is applicable in an individual event, the largest gradient and thus the largest emission of particles is not along the reaction plane. It is along the participant plane,[1] which is spanned by the beam and the minor axis of the reaction zone. Thus, the particle distribution should not be Fourier expanded with respect to the reaction plane, but to the participant plane.

The importance of these event-by-event fluctuations of the shape and orientation of reaction zone was discovered when trying to understand the behaviour of v_2 in Cu + Cu collisions. It had been found that when experimentally measured v_2 was divided by the modelled eccentricity of the reaction zone,[2] ε, the ratio v_2/ε scales with transverse density $(1/S)dN/dy$, where S is the modelled transverse area of the overlap region and dN/dy is the measured final particle multiplicity at midrapidity [3,31]. However, the measured v_2 in Cu + Cu collisions did not obey such a scaling, but when the eccentricity ε was replaced by the participant eccentricity $\varepsilon_{\mathrm{part}}$, the scaling was restored [32]. The main difference is that ε is always evaluated with respect to the reaction plane, whereas the participant eccentricity $\varepsilon_{\mathrm{part}}$ is evaluated with respect to the participant plane in each individual event, and thus takes into account the fluctuations in the orientation of the reaction zone [33].

1 Also called event plane is some of the literature.

2 Sometimes called standard eccentricity $\varepsilon_{\mathrm{std}}$. For definitions, see Section 2.6.

Since the reaction zone has a complicated azimuthal structure, and the elliptic flow was explained as a result of the azimuthal variation of the pressure gradient, it is natural to expect that the Fourier coefficients beyond v_2 would be non-zero as well. The third coefficient in the Fourier expansion, v_3, is called triangular flow [34]. It is generated by the triangular component of the shape of the fluctuating reaction zone, and some puzzling phenomena in intermediate transverse momentum regions can be interpreted as manifestation of triangular flow. For example, Mach-cone like structure was discovered in the away-side region in di-hadron correlation functions at RHIC [35–37] when one subtracts background elliptic flow component from it. Recently, it was found that these di-hadron correlation functions can be reproduced by a sum of independently analysed higher harmonic components [38,39], which indicates that Mach-cone like structure would be caused simply by collective triangular flow.

If one Fourier-decomposes the azimuthal particle distribution, one can obtain information how the system responds to the initial fluctuating profile and from this response one may deduce what the properties of the system itself are [40–44]. This reminds an analysis in observational cosmology: Through decomposition of power spectrum of cosmic microwave background radiation into spherical harmonics, one can constrain important cosmological constants and even mass/energy budget of the universe [45].

In the observational cosmology, analysis tools [46] played important roles in extracting cosmological parameters. The situation in the physics of relativistic heavy ion collisions is quite similar to this [47]: One has to develop analysis tools to extract the properties of the QGP from experimental data. From this point of view, let us overview the dynamics of heavy ion collisions. High energy heavy ion collisions contain rich physics and exhibit many aspects of dynamics according to relevant energy and time scales. Two energetic, Lorentz-contracted, heavy nuclei collide with each other. These nuclei can be described by the colour glass condensate (CGC), a universal form of hadrons and nuclei at extremely high energies [48–50]. These collisions can be viewed as collisions of two bunches of highly coherent and dense gluons. Just after the collisions, longitudinal colour electric and magnetic fields, which are also known as the colour flux tubes [51] are formed between two passing nuclei. Subsequent non-equilibrium evolution of these colour fields towards locally thermalised QGP is called "glasma" [52]. Once local thermalisation is achieved, a QGP fluid expands hydrodynamically, cools down and turns into a hadronic gas. Hadrons continue to rescatter until the system is so dilute that interactions become very rare, and hadrons stream freely towards the detectors.

Since the final observables are the result of all these various stages of the collision, it is important to describe the heavy ion collision as a whole. So far, we have developed the following integrated dynamical model [53,54] to describe the dynamics of relativistic heavy ion collisions. For the initial stage, initial conditions are calculated using the CGC picture [55–57]. Using these initial conditions, we describe fully three dimensional ideal hydrodynamic expansion of the QGP fluid [21,22] using a realistic equation of state from lattice QCD simulations [58–60]. The late stage evolution of the hadron gas is described using microscopic kinetic theory [61]. Technical details about numerical simulations of ideal hydrodynamics and hadronic cascades can be found in Ref. [62].

In this paper, we discuss experimental observables, in particular anisotropic flow, at RHIC and LHC energies using an integrated dynamical model. A special emphasis will be put on discussion about initial conditions and final flow analysis methods from an event-by-event analysis point of view. In theoretical calculations both the reaction plane and the participant plane are trivially known, but in experiments it is impossible to measure the reaction plane, and it is quite hard to precisely determine the participant plane from the finite number of observed particles. Thus, several flow analysis methods have been proposed [63–65] to experimentally measure anisotropic flow. Hence, a *consistent* comparison of hydrodynamic results with experimental observables is non-trivial. In this paper we demonstrate the differences of several experimental methods of flow analysis by using them to analyse the output of the integrated dynamical model.

The paper is organised as follows. In Section 2 we describe and review the hybrid models, in which hydrodynamics is combined with hadronic cascade, and hydrodynamic simulations on an event-by-event basis. In particular we describe each module and the interfaces between them of our integrated dynamical model. In Section 3, we first summarise the results obtained using smooth initial profiles, which are the conventional initial conditions employed in hydrodynamic simulations. We next show results from event-by-event hydrodynamic simulations in Section 4 emphasising the importance of employing the same flow analysis method as in experiment. Section 5 is devoted to the conclusion and outlook.

2. Model

Integrated dynamical models, in general, consist of three separate stages: Initial conditions, hydrodynamics and hadronic cascade. In our version, the initial particle production in the collision of the nuclei is either described by the MC-KLN version of the colour glass condensate, or parametrised using the MC-Glauber model. These models provide the initial state for the subsequent expansion of the matter, which we describe by relativistic ideal hydrodynamics. As for the equation of state, we employ results from the state-of-the-art lattice QCD simulations [58,59]. Once the matter is dilute enough to form hadrons, we switch the description of the system from fluid dynamics to microscopic hadron cascade. In this section we describe all these stages of the integrated model, and how we connect hydrodynamics to cascade. We also review current status of the equation of state and its application, hybrid models, and event-by-event hydrodynamic simulations.

2.1. Hydrodynamic equations

To describe a system in length scales much larger than a typical microscopic length scale, like the mean free path, it is sufficient to characterise it in terms of a few macroscopic fields: the energy–momentum tensor $T^{\mu\nu}$, and conserved charge currents j_i^μ (if any). In relativistic fluid dynamics, the equations of motion are given by the conservation laws for these fields

$$\partial_\mu T^{\mu\nu} = 0 \quad \text{and} \quad \partial_\mu j_i^\mu = 0. \tag{1}$$

Without any additional constraints these $4+n$ (n is the number of conserved currents) equations contain $10+4n$ unknown variables. To close the system of equations, one either has to provide further equations in the form of constituent equations for dissipative currents (shear stress tensor $\pi^{\mu\nu}$, bulk pressure Π and energy flow/particle number diffusion q_i^μ), or to eliminate some of the variables by further approximations. In the following we apply the latter approach and reduce the number of unknowns by assuming that the fluid is in exact local thermodynamical equilibrium.

In a local thermodynamical equilibrium, the single particle phase-space distribution for non-interacting fermions or bosons is

$$f_0(p,x) = \frac{g}{(2\pi)^3} \frac{1}{\exp(p\cdot u(x) - \mu(x))/T(x) \pm 1}. \tag{2}$$

When one applies this to the kinetic theory definitions of the energy–momentum tensor and charged currents, one obtains

$$T^{\mu\nu}(x) = [\epsilon(x) + P(x)]\, u^\mu(x) u^\nu(x) - P(x) g^{\mu\nu}, \quad \text{and} \quad j_i^\mu(x) = n_i(x) u^\mu(x), \tag{3}$$

respectively, where ϵ is the energy, and n_i are the charge densities in the local rest frame of the fluid, P is the thermodynamic pressure and u^μ is the fluid flow four-velocity. The Eqs. (3) imply that for a fluid in local thermodynamical equilibrium the dissipative currents are zero. This consideration of a non-interacting gas in local equilibrium is the starting point of the ideal fluid approximation: One postulates that the energy–momentum tensor and charge currents are of the form of Eqs. (3), and thus the dissipative currents are zero by definition.

Such an approximation reduces the number of unknown variables in Eqs. (1) to $5+n$: the above mentioned densities, pressure and three components of the flow four-velocity (note that the usual normalisation $u_\mu u^\mu = 1$ reduces the number of unknowns by one). To finally close the system of equations, an additional equation is usually provided in the form of the equilibrium equation of state (EoS) of the matter, which expresses the pressure and densities in terms of thermodynamical parameters temperature T and chemical potentials $\{\mu_i\}$, $P = P(T, \{\mu_i\})$. However, to solve the Eqs. (1), it is often practical to provide the EoS in the form $P = P(\epsilon, \{n_i\})$ connecting the pressure directly to the densities. The knowledge of temperature and chemical potentials is not necessarily required to calculate the evolution of the fluid itself.

Note that once the EoS, and boundary conditions (usually referred to as initial conditions) for the set of differential equations in Eqs. (1) are fixed, the evolution is determined by Eqs. (1). In the ideal fluid approximation, the only place where information about the nature of the constituents of the fluid and their microscopic interactions enters, is the EoS.

In the implementation of our model, we solve Eqs. (1) numerically in all three spatial dimensions. We employ the Milne coordinates (τ, x, y, η_s), where $\tau = \sqrt{t^2 - z^2}$ is proper time and $\eta_s = \frac{1}{2}\log\frac{t+z}{t-z}$ is space–time rapidity.

Since we are mostly interested in the observables at midrapidity in the collider energies,[3] we can ignore the baryon current [66–69]. [4] As usual in hydrodynamical models, we take the spatial boundary condition to be vacuum at infinity [70], *i.e.* the hydrodynamical evolution proceeds independently without any feedback from the cascade. The temporal boundary, *i.e.* the initial value(s) for the differential equations are described in Section 2.6. We employ the Piecewise Parabolic Method (PPM) [71] as an algorithm to solve the equations of ideal hydrodynamics (Eqs. (1)). PPM is known to be robust against strong shocks, therefore it is suitable to apply for bumpy initial conditions in event-by-event hydrodynamic simulations. For details on PPM, see Ref. [62].

2.2. Equation of state

The equation of state (EoS) of strongly interacting matter can be obtained either by using various models or by lattice QCD calculations [72]. Even if the recent lattice QCD calculations of the EoS have provided continuum extrapolated results [73], there is a practical reason to use the hadron resonance gas (HRG) model for the EoS at low temperatures. When converting fluid to particles using the Cooper–Frye procedure as described in Section 2.3, the conservation laws are obeyed without any further considerations if the degrees of freedom are the same before and after particlisation. In other words, if the emitted particles are the same particles the fluid consists of. If the fluid is described as hadron resonance gas, the degrees of freedom and their properties are well known, and these degrees of freedom are the experimentally observable hadrons which distributions we eventually want to calculate. HRG has also been shown to provide a reasonably good approximation of the EoS of interacting hadron gas in temperatures slightly below the pion mass [74], and its use is therefore justified.

[3] $\sqrt{s_{\rm NN}} = 200$ GeV at RHIC and $\sqrt{s_{\rm NN}} = 2.76$ TeV at LHC.

[4] The other conserved currents relevant for heavy ion collisions; electric charge, isospin and strangeness are in general either tiny or zero.

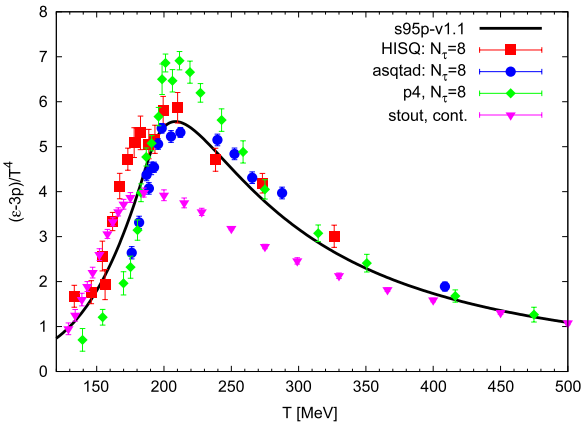

Fig. 1. The parametrised trace anomaly compared with lattice results calculated with *p4* [76], *asqtad* and *HISQ/tree* [77] actions as well as the continuum extrapolated result obtained using *stout* action [73].

To show how an EoS combining a hadron resonance gas at low temperatures, and lattice QCD results at high temperatures can be made, we briefly review the construction of the *s*95*p*-v1.1 parametrisation [53,60]. The high temperature part of this EoS is based on the lattice QCD results of the hotQCD collaboration [58,59], and its low temperature part contains the same hadrons and resonances as the JAM hadron cascade [61]. We have also used this EoS to calculate the results discussed in Sections 3 and 4.

The starting point of the construction of the *s*95*p* EoS is the trace anomaly $\Theta(T) = \epsilon(T) - 3P(T)$ evaluated on lattice, see Fig. 1. The lattice results are parametrised and connected to the trace anomaly of HRG preserving the smooth crossover nature of the transition. The trace anomaly is then converted to pressure via

$$\frac{P(T)}{T^4} - \frac{P(T_{\rm low})}{T_{\rm low}} = \int_{T_{\rm low}}^{T} \frac{dT'}{T'^5}\Theta(T), \tag{4}$$

where pressure at the lower integration limit, $T_{\rm low}$, is given by HRG. Energy and entropy densities are subsequently obtained via laws of thermodynamics. By construction such an EoS is limited to zero net baryon density and zero net strangeness, but as mentioned zero charge is a good approximation when describing the system at midrapidity in collisions at RHIC and LHC.

The trace anomaly of the *s*95*p*-v1.1 EoS is shown in Fig. 1, and compared to recent lattice QCD results. It differs considerably from the continuum extrapolated result by the Budapest–Wuppertal collaboration [73]. However, the Budapest–Wuppertal EoS deviates from HRG already at $T \approx$ 130–140 MeV, which necessitates switching from fluid to cascade below this temperature leading to much worse reproduction of data in our calculations. The *s*95*p* parametrisation follows HRG up to $T = 183$ MeV temperature providing much more freedom in choosing the switching temperature, and therefore we prefer to use it. To estimate the uncertainty our choice of EoS produces in the particle anisotropies, we have calculated the elliptic flow anisotropy v_2 in impact parameter $b = 7$ fm Au + Au collisions at the full RHIC energy ($\sqrt{s_{NN}} = 200$ GeV), see Fig. 2. In this calculation we follow the procedure used in Ref. [60] to test various parametrisations of the EoS. We use ideal fluid hydrodynamical model and assume chemical equilibrium until kinetic freeze-out. The model is initialised using an optical Glauber model with components proportional to the number of participants and binary collisions (see Section 2.6 and Refs. [14,75]). The parameters are chosen to reproduce the centrality dependence of charged particle multiplicity. The usual procedure requires choosing the freeze-out temperature to reproduce the particle spectra in most central collisions, but that would require the use of temperature $T_{\rm fo} \approx 140$ MeV. As mentioned, the Budapest–Wuppertal EoS deviates from HRG below that temperature, and thus converting fluid to free particles in such a temperature violates conservation of energy. Therefore we used freeze-out temperature $T_{\rm fo} = 125$ MeV for both EoSs even if it leads to slightly flatter p_T distributions of pions and protons than experimentally observed. Both EoSs, Budapest–Wuppertal and *s*95*p* lead to very similar p_T distributions at that temperature. As can be seen in Fig. 2, the difference in p_T-differential elliptic flow is tiny as well, and smaller than the experimental errors. Thus we consider the use of *s*95*p*-v1.1 EoS a reasonable approximation.

Similar insensitivity to the details of the EoS was seen in Ref. [60] where different parametrisations of lattice EoS were tested. Even if the EoS governs the expansion of the fluid and buildup of collective motion, the details of the EoS have tiny observable consequences. The rule of thumb is that the stiffer the EoS, *i.e.*, the larger the speed of sound in the fluid, the larger the flow velocity generated during the expansion. But, even if larger flow velocity mean flatter p_T spectrum (see f.ex. Ref. [78]), this effect can be negated by choosing the fluid to freeze-out earlier at larger temperature, by assuming later thermalisation time and thus later start of the hydrodynamical evolution, by changing the initial shape of the density distribution (if the model allows) or by any combination of these three. The integrated dynamical models discussed in this paper have no freeze-out temperature, but the final particle distributions are sensitive to the switching temperature from hydro to cascade, and all these problems hamper these models as well.

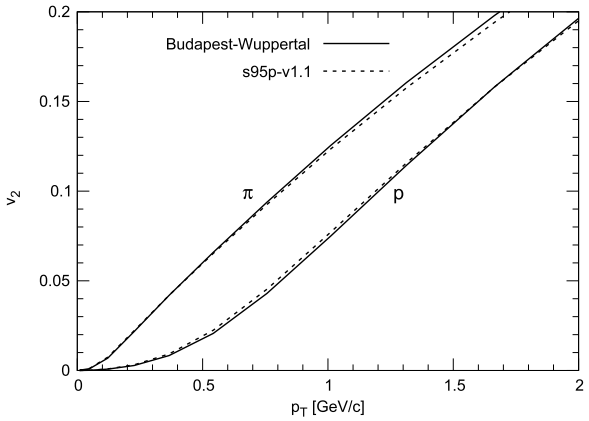

Fig. 2. The p_T-differential elliptic flow of pions and protons in $b = 7$ fm Au + Au collisions at $\sqrt{s_{NN}} = 200$ GeV evaluated using ideal fluid hydrodynamical model using EoS *s*95*p*-v1 [60] and the parametrised Budapest–Wuppertal EoS [73].

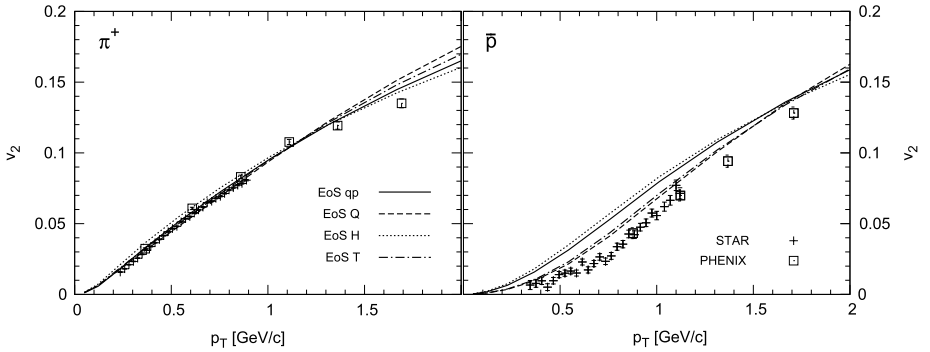

Fig. 3. Elliptic flow of pions and antiprotons vs. transverse momentum in minimum bias Au + Au collisions at $\sqrt{s_{NN}} = 200$ GeV calculated using four different EoSs [79] and compared with the data by the STAR [80] and PHENIX [6] collaborations. The labels stand for a lattice QCD inspired quasiparticle model (qp), EoS with a first order phase transition (Q), a parametrised smooth but rapid crossover (T) and pure hadron resonance gas with no phase transition (H).

Based on the p_T distributions on particles alone, we can basically only say that the EoS must contain a large number of degrees of freedom. Otherwise the p_T distributions come too flat, see discussion and Fig. 5 in Ref. [81], nor does the EoS contain all the observed particles and resonances. To say anything beyond the large number of degrees of freedom requires the use of more sophisticated observables like the azimuthal anisotropy v_2 or the HBT-radii, a.k.a. femtoscopy. In general the changes in v_2 due to different EoSs can be compensated by changing the freeze-out temperature. There is, however, an exception. The p_T differential anisotropy of protons, $v_2(p_T)$, is to some extent sensitive to the order of phase transition [79]. This is demonstrated in Fig. 3 where pion and proton $v_2(p_T)$ in minimum bias Au + Au collisions at $\sqrt{s_{NN}} = 200$ GeV are calculated using ideal fluid hydrodynamical model, and four different EoSs. The EoSs are the bag model based EoS with a first order phase transition between HRG and ideal parton gas (EoS Q), pure hadron resonance gas with no phase transition (EoS H), a lattice inspired quasiparticle model EoS (EoS qp, which is quite close to the present lattice QCD EoSs) by Schneider and Weise [82], and an EoS with a parametrised smooth crossover from HRG to ideal parton gas (EoS T). As seen in the figure, the sensitivity of pion $v_2(p_T)$ on the EoS is tiny, but proton $v_2(p_T)$ shows clear sensitivity to EoS. Surprisingly it is the EoS Q with the first order phase transition which provides the best fit to the data—a construction ruled out by the lattice QCD calculations. The lattice inspired EoS qp leads to proton $v_2(p_T)$ which is clearly above the data, and almost as large as the $v_2(p_T)$ obtained using the purely hadronic EoS H. The EoS T, which has a very rapid crossover leads to proton $v_2(p_T)$ which is almost as close to the data than the one obtained using EoS Q. This means that the order of the phase transition does not affect the build up of anisotropy, but how rapid the transition is does have an effect. Nevertheless, EoS T is ruled out by the present lattice data.

On the other hand, it can be argued that a soft EoS leads to a long lifetime of the system, which is excluded by the HBT measurements [83]. It has also been shown that if one assumes a relatively hard, lattice inspired EoS, it is possible to reproduce the measured HBT radii [84], although in that case the proton $v_2(p_T)$ is not reproduced. This apparent contradiction appears when using ideal fluid dynamics. When dissipative corrections are applied, the proton $v_2(p_T)$ can be reproduced also when a lattice based hard EoS is used, see Fig. 36 in Section 3.1, or Ref. [85]. Thus there is no contradiction between lattice QCD EoS and the observed particle anisotropies.

The previous discussion about the sensitivity of the particle distributions to EoS is based on ideal fluid dynamics, since so far there has been no systematic study addressing what we can learn about the EoS of strongly interacting matter using either dissipative hydrodynamics or integrated models. But since dissipative corrections are supposed to be small in the fluid dynamical stage, it is highly unlikely that adding dissipation would make the fluid evolution more sensitive to the details of the EoS. Thus we may expect that what we have learned about the effects of EoS on flow using ideal fluid dynamics, holds for dissipative fluids as well.

2.3. Fluid to particles

The QGP produced in relativistic heavy ion collisions expands, cools down and goes through a transition to a hadronic gas.[5] At this late stage, the hadronic system is so diluted that it would be hard to maintain equilibrium during the evolution. Thus, we switch from a macroscopic fluid dynamical picture to a microscopic kinetic picture at a switching temperature $T_{\rm sw}$. In this subsection, we discuss how to change from hydrodynamic description to kinetic description. We will discuss dynamics of hadron cascade in the next subsection.

We employ the Cooper–Frye formula [86] to calculate the single particle phase-space distribution for all hadrons in the hadronic equation of state. For a hadron of species i, the contribution to the distribution from a single fluid element located at x is

$$f_i(p,x)d^3x = \frac{d\Delta N_i}{d^3p}(x) = \frac{g_i}{(2\pi)^3 E}\frac{p\cdot\Delta\sigma(x)}{\exp[(p\cdot u(x)-\mu_i(x))/T(x)]\pm 1}. \tag{5}$$

Here $\Delta\sigma$ is a normal vector of a surface element of a constant temperature hypersurface $T(x) = T_{\rm sw}$.[6]

In the actual calculations, we Monte-Carlo sample the distributions of hadrons emitted from individual surface elements [22]. Regarding this, some comments on the conservation laws are in order here:

1. The Cooper–Frye formula counts the *net* number of emitted particles [86]. Here the net number means the number of particles moving outwards through the surface minus the number of particles moving inwards. Thus the number obtained from Eq. (5) could be negative in a case of a fluid element with either a space-like normal vector $(\Delta\sigma)^2 < 0$ or a time-like normal vector having a negative time component. This so-called negative contribution problem of Cooper–Frye, is a long-standing problem in hydrodynamical modelling of relativistic heavy ion collisions. Note that the *total* number of particles obtained by summing the contribution given by Eq. (5) over *all* surface elements is positive for all initial states relevant for heavy ion collisions. Although the in-coming particles are necessary to ensure the energy–momentum conservation, it is conceptually difficult to treat the negative number in the subsequent kinetic approach.[7] However, at the time of particlisation at $T = T_{\rm sw}$ the collective flow is large, and thus the particle distributions are boosted to the direction of the flow, i.e. outwards. Therefore the yield of the in-coming particles is much smaller than the yield of out-going particles, and they form only a small correction of the order of 5% to the total multiplicity and the energy of the system.[8] As a first order approximation, we may thus ignore these in-coming particles without violating the conservation laws significantly.
2. By sampling we create an integer number of particles from a tiny fluid element whose three dimensional volume is typically ~ 0.1 fm^3. An expectation value of the number of particles from this fluid element in the grand canonical ensemble is, of course, not an integer and in our calculations less than unity. Therefore energy, momentum and charges are not conserved in each individual sampling, but only in average—as is customary for a grand canonical ensemble. This issue could be resolved by an oversampling method: At each fluid element, N times larger number of particles is sampled with N being large and, the subsequent dynamics of hadrons is simulated with the cross section divided by N to ensure the original Boltzmann equation [88,89]. This procedure can maintain energy–momentum conservation of the order of $\mathcal{O}(1/N)$ at the particlisation. However, this would be numerically expensive and neglect the effect of fluctuations because different events are averaged over in the oversampling method. A faster method which is called "local-ensemble" method has been proposed in Refs. [90–92]. An alternative approach is to impose the requirement of the conservation of energy and charges on the sampling procedure as done in Refs. [87,93]. This approach maintains the effect of fluctuations, but requires generating several ensembles of particles, where only parts are kept to avoid bias.

[5] It is not necessarily a phase transition. As mentioned in the previous section, the recent lattice QCD simulations predict a crossover rather than a phase transition between the QGP phase and the hadron phase.

[6] Note that this is not a freezeout hypersurface since in the subsequent stage hadrons still interact with each other.

[7] One possible solution would be to provide the cascade with the information of the location of the particlisation hypersurface, and remove from the cascade the hadrons which enter the space–time region within the hypersurface.

[8] Somewhat larger corrections of the order of 10% were reported in Ref. [87]. We believe that the reason is the different longitudinal structure of the system in these approaches.

3. In principle one should switch from a macroscopic fluid picture to a microscopic particle picture in a temperature region where both descriptions give similar results. However, the single particle distribution under *local* equilibrium never becomes a solution of the Boltzmann equation: One needs viscous corrections to the local equilibrium distribution to match the two solutions. Since we use ideal fluid hydrodynamics without any dissipative corrections, the hydrodynamical evolution always differs from the cascade. Thus we cannot expect to find a region where the solutions of both models would agree, and simply regard the single particle phase-space distribution obtained using hydrodynamics as an initial condition for the hadron cascade.

Keeping these issues and assumptions in mind, we calculate a discrete single particle phase-space distribution on an event-by-event basis. First, we need the information of the particlisation hypersurface to apply the Cooper–Frye formula (Eq. (5)). We approximate the surface normal $\Delta\sigma^\mu$ in the following way:

Bulk emission: At each time step τ_i in a hydrodynamic simulation, we scan all the fluid elements to check whether particlisation condition for bulk emission (a) $T(\tau_{i-1}) > T_{\rm sw} > T(\tau_i)$ or (b) $T(\tau_{i-1}) < T_{\rm sw} < T(\tau_i)$ is satisfied. When this condition is satisfied, information about a surface element vector (a) $\Delta\sigma^\tau = \tau_{\rm sw}\Delta x\Delta y\Delta\eta_s$ or (b) $\Delta\sigma^\tau = -\tau_{\rm sw}\Delta x\Delta y\Delta\eta_s$ together with flow velocity $u^\mu_{\rm sw}$ at this point are stored. Here particlisation time τ, flow velocities v^x and v^y and flow rapidity $Y_f = \tanh^{-1} v_z$ are linearly interpolated between τ_i and τ_{i-1} such that

$$w^0_i = \left|\frac{T(\tau_i) - T_{\rm sw}}{T(\tau_i) - T(\tau_{i-1})}\right|, \qquad w^0_{i-1} = \left|\frac{T_{\rm sw} - T(\tau_{i-1})}{T(\tau_i) - T(\tau_{i-1})}\right|, \tag{6}$$

$$\tau_{\rm sw} = \tau_{i-1}w^0_i + \tau_i w^0_{i-1}, \tag{7}$$

$$v^x_{\rm sw} = v^x(\tau_{i-1})w^0_i + v^x(\tau_i)w^0_{i-1}, \tag{8}$$

$$v^y_{\rm sw} = v^y(\tau_{i-1})w^0_i + v^y(\tau_i)w^0_{i-1}, \tag{9}$$

$$Y_{f,{\rm sw}} = Y_f(\tau_{i-1})w^0_i + Y_f(\tau_i)w^0_{i-1}. \tag{10}$$

Surface emission: At each time step τ_i, we scan all the fluid elements in each direction to check whether particlisation condition for surface emission (a) $T(x_{i-1}) > T_{\rm sw} > T(x_i)$ or (b) $T(x_{i-1}) < T_{\rm sw} < T(x_i)$ is satisfied for an adjacent pair of surface elements. Here, for simplicity, we denote only one dimensional dependence, say x coordinate. When this condition is satisfied, information about surface vector (a) $\Delta\sigma^x = \tau_i\Delta\tau\Delta y\Delta\eta_s$ or (b) $\Delta\sigma^x = -\tau_i\Delta\tau\Delta y\Delta\eta_s$ together with flow velocity $u^\mu_{\rm sw}$ at this point are stored. Here flow velocities v^x and v^y and flow rapidity Y_f are linearly interpolated between x_i and x_{i-1} at τ_i such that

$$w^x_i = \left|\frac{T(x_i) - T_{\rm sw}}{T(x_i) - T(x_{i-1})}\right|, \qquad w^x_{i-1} = \left|\frac{T_{\rm sw} - T(x_{i-1})}{T(x_i) - T(x_{i-1})}\right|, \tag{11}$$

$$v^x_{\rm sw} = v^x(x_{i-1})w^x_i + v^x(x_i)w^x_{i-1}, \tag{12}$$

$$v^y_{\rm sw} = v^y(x_{i-1})w^x_i + v^y(x_i)w^x_{i-1}, \tag{13}$$

$$Y_{f,{\rm sw}} = Y_f(x_{i-1})w^x_i + Y_f(x_i)w^x_{i-1}. \tag{14}$$

Unlike more sophisticated algorithms (see Ref. [87]), which give relatively smooth surfaces, this simple algorithm constructs a granular surface consisting of "cubes". At the limit of infinitely small elements, however, the surfaces are equal. As well, for Cooper–Frye procedure the components of the normal vectors of the surface elements are needed, and those come out similarly in this approach and in the more sophisticated approaches. The main difference is in the positions where the velocity and densities are interpolated on the surface. This causes differences proportional to the grid spacing, which defines the accuracy of the numerics in general as well.

Using this information, we generate a hadron from the surface element. We first calculate an expectation value of the number of hadrons of species i out-going or in-coming through a hypersurface element

$$\Delta N^i_\pm = g^i \int \frac{d^3p}{(2\pi)^3 E} \frac{\Theta(\pm p\cdot\Delta\sigma)|p\cdot\Delta\sigma|}{\exp[(p\cdot u - \mu_i)/T_{\rm sw}] - \epsilon}, \tag{15}$$

where $\epsilon = 1$ for bosons and -1 for fermions. $\Delta N_\pm$ are always positive by construction. In the following, we neglect ΔN_- for simplicity as we mentioned before. We next create a hadron of species i only when a randomly generated number r_1 ($0 < r_1 < 1$) is less than ΔN^i_+. Note that ΔN^i_+ is always less than unity in the usual setting of simulations and its typical values are $\sim$0.01. Such a low value allows us to interpret ΔN^i_+ as a probability to create a particle, instead of sampling a Poisson distribution to decide whether and how many particles are created.

If we create a hadron, we choose a momentum for it by sampling the Lorentz invariant distribution

$$\frac{d^3p'}{E'} \frac{1}{\exp[(E' - \mu_i)/T_{\rm sw}] - \epsilon}. \tag{16}$$

This is a momentum in the local rest frame of the fluid. We next Lorentz-boost it by flow velocity u^μ to obtain momentum in the centre-of-mass frame of the system. By construction the boosted momentum p obeys the distribution

$$\frac{d^3p}{E}\frac{1}{\exp[(p\cdot u-\mu_i)/T_{\rm sw}]-\epsilon}. \tag{17}$$

We repeat this procedure until the obtained momentum satisfies $p\cdot\Delta\sigma > 0$. Next we consider an weight $p\cdot\Delta\sigma$ in Eq. (15). Suppose $r_{\rm max}$ is the maximum value of $p\cdot\Delta\sigma$, which varies from hypersurface element to element. We generate another random number r_2, $0 < r_2 < r_{\rm max}$, and require that the momentum of the hadron fulfils $r_2 < p\cdot\Delta\sigma$. If that is not the case, we discard the momentum, and start the process again by sampling the thermal momentum distribution. Finally, we choose a position for this particle from a uniform distribution inside the surface element. The emission time is either $\tau_{\rm sw}$ for bulk emission or τ_i for surface emission.

We go through all the elements of the particlisation surface, and generate in this way an ensemble of hadrons and resonances with well defined positions x^i_μ and momenta p^i_μ.[9] We use this ensemble as the initial condition for the hadron cascade JAM, which we use to model the rest of the hadronic rescattering stage. This will be discussed in the next section.

The switching procedure, namely calculating the contribution to the particle distributions of *all* hadrons in the EoS from *all* hypersurface elements of the particlisation surface is numerically expensive. Among all the constituents of hybrid calculations – initial conditions, hydrodynamic simulation, switching process and hadronic cascade – it has been the bottleneck. In event-by-event hybrid simulations, this rather practical issue must be resolved to gain high statistics. In Appendix, we show in detail how to integrate the Cooper–Frye formula at less numerical costs [94].

2.4. Hadronic cascade

Hadronic transport models can be used to describe the system in the low density hadronic phase of the evolution. In this work we use the microscopic transport model JAM [61,95] for that purpose. In JAM, the trajectories of all hadrons and resonances, including those produced in resonance or string decays, are propagated along their classical trajectories like in other microscopic hadronic transport models such as RQMD [96–99], and UrQMD [100–102]. To achieve a more sophisticated hadronic EoS, a mean field can be included within a framework of either Boltzmann–Uehling–Uhlenbeck (BUU) model [103], or Quantum Molecular Dynamics (QMD) [104] approach. However, all results in this work are obtained without any mean field.

In the hadronic transport models, time evolution of system is described by a sum of incoherent binary hadron–hadron (hh) collisions. Two body collisions are realised by the closest distance approach: Two particles collide if their minimum distance b in the centre-of-mass (c.m.) flame of two colliding particles is smaller than the distance given by the geometrical interpretation of cross section:

$$b \le \sqrt{\frac{\sigma_{\rm tot}}{\pi}}, \tag{18}$$

where $\sigma_{\rm tot}$ denotes the total cross section at the energy $\sqrt{s}$. For two particles with their positions x_1 and x_2, and four momenta p_1 and p_2, the Lorentz invariant expression for impact parameter b is given by

$$b^2 = -(x_1-x_2)^2 + \frac{[P\cdot(x_1-x_2)]^2}{P^2} + \frac{[q\cdot(x_1-x_2)]^2}{q^2}, \tag{19}$$

where $P = p_1+p_2$, and $q = (p_1-p_2) - \frac{[P\cdot(p_1-p_2)]^2}{P^2}P$.

Inelastic hh collisions are modelled by resonance formation at low energies and by formation of colour strings at high energies. Threshold between resonance and string formation is set to about 4 GeV for baryon–baryon (BB), 3 GeV for meson–baryon (MB) and 2 GeV for meson–meson (MM) collisions. In the string formation process, we use the same distribution for the light-cone momentum transfer as in the HIJING model [105–108]. Quark content of a string is assumed to be the same as the quark content of a corresponding hadron before excitation, as in the Fritiof model [109,110].

The string decays are performed by the Lund string model [111–113]. Formation points and times for newly produced particles are determined from string decay by yo-yo formation point [114]. Formation time is about 1 fm/c with the string tension $\kappa = 1$ GeV/fm. In a baryon-like string, hadrons are produced by the quark–antiquark pair creation in the colour flux-tube between the quark and diquark. The antiquark from the pair creation is combined with the constituent quark in the string to form a first rank hadron. This hadron has an original constituent quark. We assign a formation time for the quarks from the quark–antiquark pair creation, but not for the original constituent quark. Thus, for example, the original constituent quark inside a newly formed meson can scatter, but with a reduced cross section $1/2\sigma_{MM}$. In general, leading hadrons which contain original constituent quarks can scatter during their formation time with cross sections reduced according to the

[9] Note that JAM allows different initial times t_i for each hadron. Thus hadrons enter the cascade and begin interacting at the time when they are emitted from the fluid.

additive quark model. The importance of this quark(diquark)-hadron interaction for the description of baryon stopping at CERN/SPS energies has been reported by Frankfurt group [97–101].

Experimentally well-known total and elastic cross sections, such as pp, pn, $\pi^+ p$, $K^- p$ and $\bar{p}p$, are parametrised in JAM. Cross sections involving the resonances are assumed to be the same as the corresponding stable hadron cross sections with the same quark content. For example, ρp cross section is the same as πp cross section.

In nucleon–nucleon scattering, non-strange baryonic resonance excitation channels

$$NN \to NR, \qquad NN \to RR, \tag{20}$$

where R means a nucleon resonance ($N(1440)$–$N(1990)$) or a Δ resonance ($\Delta(1232)$–$\Delta(1950)$) up to 2 GeV, are implemented. These resonance formation cross sections are fixed by pion production cross sections. Inverse processes such as $NR \to NN$ are computed employing the detailed balance formula where the finite width of the resonance is taken into account [91,115,116]. The lifetime of resonance, t, is randomly chosen according to an exponential decay law $\exp(-t\gamma\Gamma(M))$, where $\Gamma(M)$ is the energy-dependent width of the resonance and $\gamma = E/M$ is the Lorentz factor.

As an example of a meson–baryon scattering, the total cross section for the πN incoming channel is decomposed to

$$\sigma_{\rm tot}(s) = \sigma_{\rm el} + \sigma_{\rm ch}(s) + \sigma_{\rm BW}(s) + \sigma_{s-S}(s) + \sigma_{t-S}(s), \tag{21}$$

where $\sigma_{\rm el}$, $\sigma_{\rm ch}(s)$, $\sigma_{\rm BW}(s)$, $\sigma_{s-S}(s)$, and $\sigma_{t-S}(s)$ denote the elastic, charge exchange, s-channel resonance formation, s-channel string formation and t-channel string formation cross section, respectively. Resonance formation cross section $\sigma_{BW}(s)$ is computed using the Breit–Wigner formula [98] by summing up cross sections to form resonances $R = N(1440)$–$N(1990)$, $\Delta(1232)$–$\Delta(1950)$, $\Lambda(1405)$–$\Lambda(2110)$, $\Sigma(1385)$–$\Sigma(2030)$ and $\Xi(1535)$–$\Xi(2030)$.

In the case of $\bar{K}N$ incoming channel, we add t-channel hyperon production cross sections such as $K^- p \to \pi^0 \Lambda$. The cross section of the inverse process $\pi Y \to \bar{K}N, Y = \Lambda, \Sigma$ is calculated using the detailed balance formula. The kaon–nucleon (KN) incoming channel does not have s-channel resonance formation, but t-channel resonance production processes $KN \leftrightarrow K\Delta$, $KN \leftrightarrow K(892)N$, $KN \leftrightarrow K(892)\Delta$ are included. The Breit–Wigner formula is used to evaluate the cross section for resonance production in meson–meson scatterings as well. Meson resonance states are included up to about 1800 MeV.

Additive quark model [97,98,101,102] is used for the experimentally unknown cross sections such as an incoming channel involving multi-strange hadrons, *e.g.* ϕ meson–pion scattering. Strangeness suppression factor is correctly included in the additive quark model: we have $\sigma_{\pi N} \approx 26$ mb and $\sigma_{KN} \approx 21$ mb consistent with the experimental data above resonance region.

2.5. Brief overview of hydro + hadronic cascade models

In this subsection, we briefly overview the current status of hydro + hadronic cascade model (sometimes called the "hybrid" model).

The very first work of hydro + cascade approaches was done by Dumitru et al. [119]. Motivation in this first study was to describe particle species dependence of freezeout process in a consistent manner. They solved hydrodynamic equations by assuming boost invariant longitudinal flow and cylindrical symmetry. As for the equation of state, a bag model which exhibits the first order phase transition was employed with $T_c = 160$ MeV. They switched description of dynamics from hydrodynamics to hadronic cascade at hadronisation. The m_T inverse slope parameters for various hadrons including multi-strange ones were calculated both in pure hydrodynamics (with $T_{\rm fo} = 130$ MeV) and in the hydro + cascade approach as shown in Fig. 4. In pure hydrodynamics, it is known that the inverse slope parameter increases monotonically with the hadron mass. On the other hand, the slope parameter of multi-strange hadrons from the hadron cascade approach are almost identical regardless of the mass difference [119], which is clearly different from a tendency of the pure hydrodynamic result mentioned above. They made a further analysis of kinetic freezeout in the subsequent papers [123,124] within this hybrid approach.

A systematic analysis of SPS and RHIC data was done by Teaney et al. within a (2 + 1) dimensional hydro + cascade model [19,20], where an event generator, RQMD, was employed for the hadronic cascade model. The importance of hadronic dissipation in interpreting the elliptic flow data was first demonstrated in this study. In the SPS and RHIC energy regions, pure ideal hydrodynamics predicts $v_2/\varepsilon \sim 0.2$–0.25 depending on the equation of state employed in the simulations. This is sometimes called "hydrodynamic limit". Experimental data of v_2/ε increase with the transverse particle density $(1/S)dN_{\rm ch}/d\eta$ [31], where S is the transverse area, and reach the "hydrodynamic limit" of $\sim$0.2 in central collisions at the top RHIC energy. As mentioned, ideal hydrodynamics predicts roughly constant v_2/ϵ, and does not reproduce this data. On the other hand, as shown in Fig. 5, this monotonic increase is described by the hydro + RQMD model [19,20] in which finite cross sections of hadronic interactions lead to dissipation and, consequently, integrated v_2 is considerably reduced in comparison with pure ideal hydrodynamic calculations.

Fig. 6 shows a compilation of hydrodynamic results made by the PHENIX Collaboration [122] as of year 2004. Among several hydrodynamic approaches, it was only the hydro + RQMD model that reproduced particle identified spectra and $v_2(p_T)$ data at the same time. p_T spectra for pions and $v_2(p_T)$ for pions and protons are reproduced using ideal hydrodynamics where the fluid is in chemical equilibrium. However, such a model fails to reproduce the yield of protons since the freeze-out temperature required to fit the slopes of the p_T distributions is well below the temperature required to fit the observed

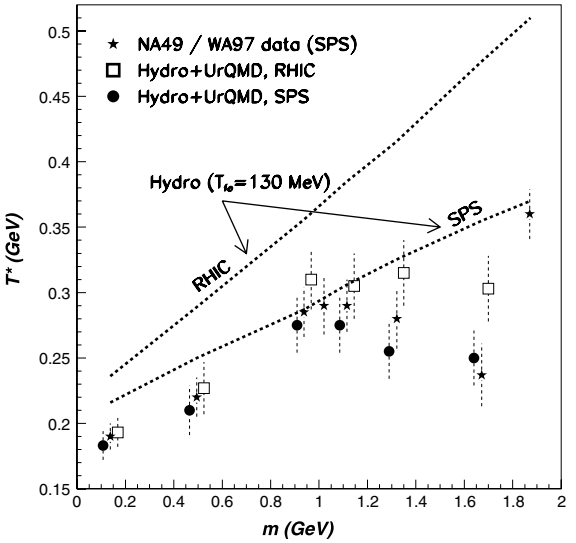

Fig. 4. Inverse slopes of the m_T spectra for various strange and non-strange hadrons at midrapidity from the $(1+1)$-D hybrid model are compared with SPS data (star symbols) [117,118]. lines are results from pure hydrodynamic simulations with freezeout temperature $T_{\rm fo} = 130$ MeV. Open squares and closed circles are results from the hybrid model at RHIC and SPS, respectively. Figure is taken from Ref. [119].

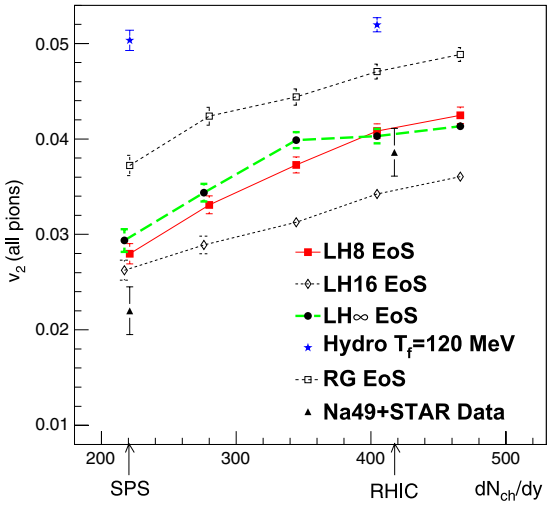

Fig. 5. Elliptic flow parameters v_2 from four different equations of state as functions of the charged particle multiplicity from the $(2+1)$-D hybrid model is compared with SPS [120] and RHIC [121] data (triangle symbols). Impact parameter in the simulations is taken to be $b = 6$ fm. Star symbols are results from pure hydrodynamic simulations with freezeout temperature $T_f = 120$ MeV. Figure is taken from Ref. [19].

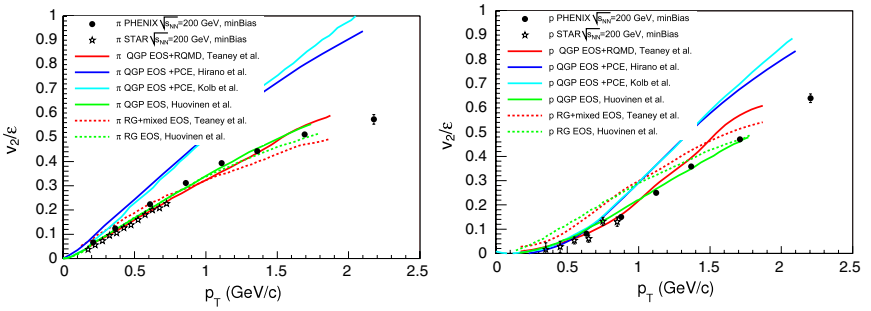

Fig. 6. A compilation of hydrodynamic results as of year 2004. v_2/ε as a function of transverse momentum for pions (left) and for protons (right) from hydrodynamic models are compared with STAR and PHENIX minimum bias data. For details, see text and Ref. [122].

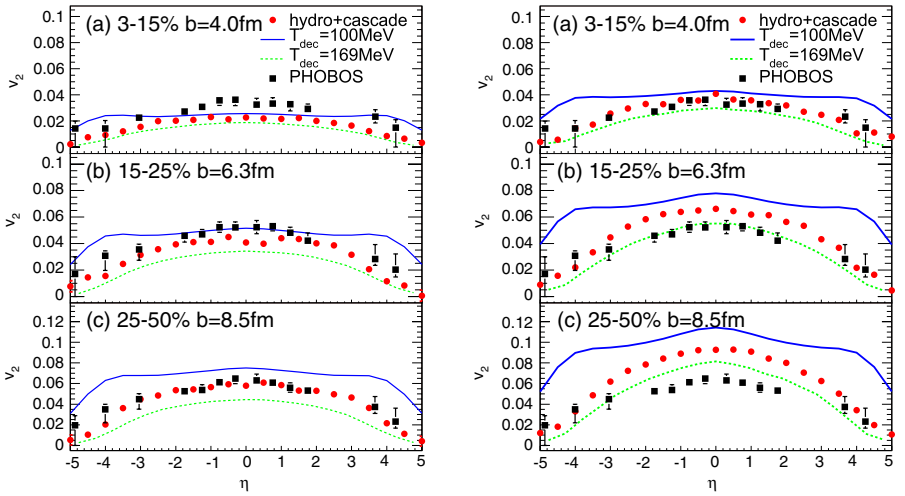

Fig. 7. Pseudorapidity dependence of v_2 in 3–15%, 15–25% and 25–50% centralities from Glauber-BGK (left) and KLN (right) initial conditions are compared with the PHOBOS data [10]. Plots are results from the full 3D hybrid model. Solid and dashed curves are results from pure hydrodynamic simulations with freezeout (decoupling) temperature $T_{\rm dec} = 100$ MeV and 169 MeV, respectively. Since the temperature of the boundary between the QGP and hadron phases in these calculations is $T = 170$ MeV, results with $T_{\rm dec} = 169$ MeV correspond to the ones just after complete hadronisation. Figures are taken from Ref. [125].

particle ratios. To solve this issue, a partial chemical equilibrium (PCE) model [22] is employed. In this case, chemical freezeout is incorporated in the equation of state and the system is in kinetic but not in chemical equilibrium below a chemical freeze-out temperature. Such a model leads to successful reproduction of yields and spectra for pions and protons, but a slope of pion $v_2(p_T)$ is steeper than that of the data [22] as shown in Fig. 6(left). The importance of the hadronic dissipative effects in simultaneous reproduction of yields, spectra and differential v_2 was discussed in detail later in Ref. [27].

Hirano et al. [125,126] combined a fully $(3 + 1)$ dimensional ideal hydrodynamics with a hadronic cascade model, JAM. Our integrated dynamical approach presented in this paper is based on this model. One of the advantages of the fully three dimensional simulations without assuming Bjorken scaling solution is to be able to obtain elliptic flow parameter as a function of pseudorapidity, $v_2(\eta)$. The charged hadron $v_2(\eta)$ has been measured by the PHOBOS Collaboration and it has a maximum at midrapidity and decreases as moving away from midrapidity [8,9]. In a full three dimensional ideal hydrodynamic simulation with $T_{\rm fo} = 100$ MeV [22], v_2 does not depend strongly on rapidity. Thus the main dependence on pseudorapidity comes from the Jacobian between rapidity and pseudorapidity [127], and the calculated $v_2(\eta)$ is flatter than the measured, whereas the three dimensional hybrid approach reproduces the observed $v_2(\eta)$ in the whole rapidity region in non-central collisions when the Glauber initial conditions are used [125], see Fig. 7. The space–time rapidity dependence of life time of the QGP fluid plays an important role in understanding the (pseudo-)rapidity dependence of v_2 since it takes time for the system to fully develop elliptic flow. Since $dN_{\rm ch}/d\eta$ decreases with increasing η, initial entropy and, in turn, initial temperature decreases with increasing η_s. Consequently, the lifetime of the QGP also decreases with increasing η_s, and we may expect lower values of v_2 at large η_s if we evaluate v_2 immediately after hadronisation. In these calculations phase transition took place at $T_c = 170$ MeV, and the evaluation of $v_2(\eta)$ on a $T = 169$ MeV surface leads to a shape peaking at midrapidity as expected, see Fig. 7, although the overall magnitude is less than the PHOBOS data [8,9]. Additional generation of elliptic flow during the hadronic cascading stage fills this gap to reproduce the PHOBOS data. Compared with a purely ideal hydrodynamic treatment of the hadronic gas, the hadron cascade contains dissipative effects through finite mean free path. This indicates the importance of hadronic dissipative effects in particular in forward/backward regions.

It is interesting to note the deviations of the 3D hybrid model results from the PHOBOS data as well [125]. First, $v_2(\eta)$ from the full 3D hybrid model is smaller than the data at 3%–15% centrality when the Glauber type initial conditions are employed (see top panel of Fig. 7(left)), which implies the necessity of eccentricity fluctuations in the initial conditions. Second, the hybrid model with the KLN initialisation leads to larger v_2 than the data in semi-central to peripheral collisions (see Fig. 7(right)), which leaves room for finite although very small QGP viscosity.

Another important finding from this full 3D hybrid model is a violation of mass ordering in differential elliptic flow parameter $v_2(p_T)$ [126]. Because of the interplay of thermal and collective motion, we expect that $m_1 < m_2 \Rightarrow v_2(p_T, m_1) > v_2(p_T, m_2)$ [18]. This mass ordering, however, holds only for particles frozen out in the same temperature having the same collective flow velocity. We expect that particles like ϕ mesons, which have very small cross sections and thus hardly rescatter, freeze-out earlier. Such a particle's $v_2(p_T)$ would be typical for larger temperature and smaller flow velocity. For particles with mass around 1 GeV mass, like ϕ mesons, freezing out earlier would mean larger $v_2(p_T)$ at small p_T. The hybrid model calculations predicted this kind of behaviour for the ϕ meson [126], and this violation of mass ordering was recently confirmed by the STAR collaboration [128] (See also Fig. 8).

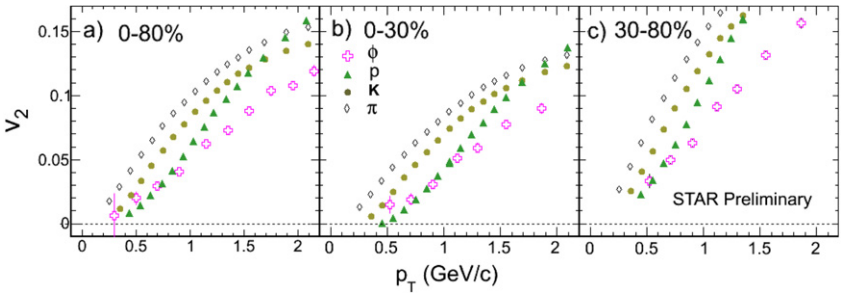

Fig. 8. Transverse momentum dependence of particle identified elliptic flow parameters in 0%–80%, 0%–30% and 30%–80% centrality from STAR Collaboration. Violation of mass ordering is clearly seen below ∼0.8 GeV/c in 0%–30% centrality. Figures are taken from Ref. [128].

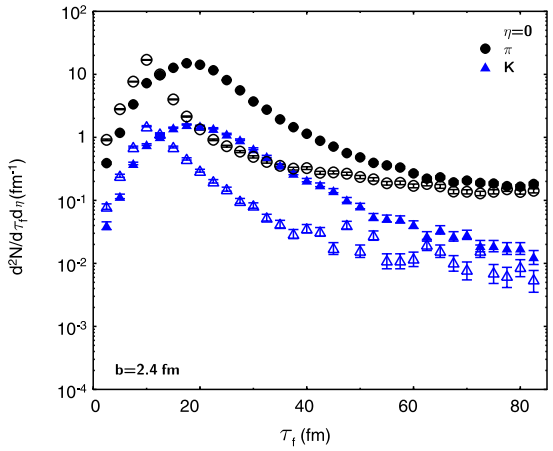

Fig. 9. Freezeout-time distribution for pions (circles) and kaons (triangles) at an impact parameter $b = 2.4$ fm at the RHIC energy. Open (closed) symbols correspond to results without (with) hadronic rescatterings. Figure is taken from Ref. [129].

The ideas of the Frankfurt group's first work were taken over by Nonaka and Bass [129] who used a fully three dimensional ideal hydrodynamic model coupled to UrQMD. Similar reduction of v_2 in forward/backward rapidity regions as shown in Fig. 7 was found in their results as well. Hadronic rescattering effects are seen in Fig. 9 as shifts of the peaks of freeze-out time distributions from ∼10 fm/c to ∼18 fm/c. The effect is similar for pions and kaons.

Petersen et al. combined full three dimensional ideal hydrodynamics in the Cartesian coordinate with UrQMD [93,130–135]. This is the first hybrid simulation on an event-by-event basis, which will be discussed later. One of the distinct features of this model is to employ isochronous particlisation when energy density of all fluid elements drops below 5 times ground state energy density (∼730 MeV/fm^3). They also discussed all fluid elements in one transverse slice rather than the whole region dropping below this value as an alternative criterion [130]. By using this (called gradual freezeout), one can take account of time dilatation in the forward rapidity region where the fluid moves faster in the Cartesian coordinate. An advantage of this method is to be able to avoid negative contribution in the Cooper–Frye formula since the hypersurface element is always time-like vector $d\sigma^\mu = (d^3x, \boldsymbol{0})$ and $p^\mu d\sigma_\mu$ term in this formula is positive definite. On the other hand, it may happen that freezeout occurs in some fluid elements only when the temperature becomes very small ($T < 100$ MeV) and the system is already diluted sufficiently. In the context of hadronic rescattering effects, they mainly focused on collisions at SPS energies and lower and found that their hybrid model can nicely describe elliptic flow at those energies [93,130,131], see Fig. 10. Recently this model has been extended to allow isothermal or iso density particlisation as well [87].

Pratt and Vredevoogd [136] were the first to develop a hybrid model based on viscous hydrodynamics. Their goal was to understand femtoscopic observables at RHIC, and they assumed radial symmetry and boost invariance both in hydrodynamical calculation and hadron cascade. In their model particlisation happens at a switching energy density $e_{\rm sw} =$ 400 MeV/fm^3 instead of a constant temperature. They kept information about particlisation hypersurface and a hadron which returns to the interior of the surface ($e > e_{\rm sw}$) during the cascade description is deleted from simulations. This would correspond to negative contribution to the Cooper–Frye formula. According to their estimation, a percentage of the absorbed particles is only about one percent. Fig. 11 shows positions of last interaction points for pions with $p_x = 300$, $p_y = 0$ MeV/c. Modestly positive correlation between the outward position and the emission time is seen, which would result in $R_{\rm out}/R_{\rm side}$ to be close to unity.

Werner et al. combined an event generator, EPOS, full $(3+1)$ dimensional ideal hydrodynamics and an hadronic cascade, UrQMD [138–141]. In addition to nuclear collisions, they also applied their hybrid model to proton–proton collisions at the

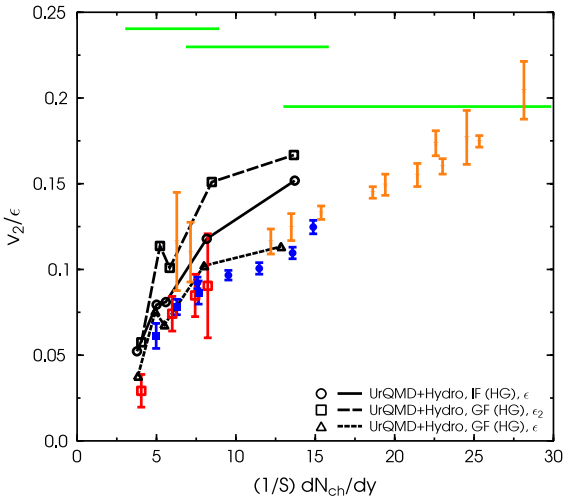

Fig. 10. v_2/ε as a function of transverse density $(1/S)dN_{ch}/dy$ from a full 3D hybrid model is compared with experimental data at AGS, SPS and RHIC energies. Results with isochronous freezeout and gradual freezeout are shown as open circles and triangles, respectively. Results with gradual freezeout using event-by-event ε averaged over many events is shown as open squares. Figure is taken from Ref. [130].

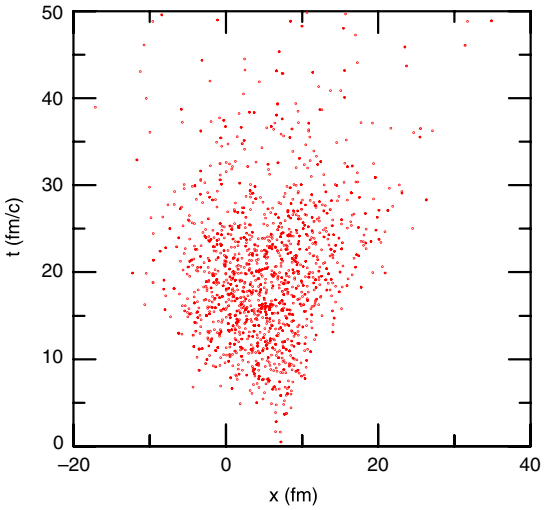

Fig. 11. Positions of last interaction points for pions with $p_x = 300$, $p_y = 0$ MeV/c. Figure is taken from Ref. [136].

LHC energies. They concluded there exists collective flow even in pp collisions. Their results on ridge phenomenon will be discussed later in Section 2.7.

Detailed analyses of elliptic flow parameters based on a $(2 + 1)$ dimensional hybrid model combining viscous hydrodynamics with UrQMD have been made by Song et al. [85,137,142,143]. They mainly focused on extraction of η/s from a comparison of v_2/ε results with data and found η/s is not larger than twice the conjectured minimum bound, $1/4\pi$ [144] (See Fig. 12). From a hybrid model viewpoint, a systematic analysis of switching temperature dependence was made. They concluded that there exists no safe window of temperature below $T_{\rm ch} = 165$ MeV to switch from viscous hydrodynamics to UrQMD [85]. This means that below 165 MeV UrQMD describes expanding matter far from equilibrium. On the other hand they did not test switching temperatures larger than 165 MeV, and thus it is not possible to say whether a temperature range exists in their model where the exact value of the switching temperature does not affect the results.

The χ^2-fitting to spectra, v_2 and HBT radii in 0%–10% central collisions at the RHIC energy was done by Soltz et al. using $(2+1)$ dimensional viscous hydrodynamic simulations combined with the UrQMD cascade code [145]. Although the fit was done to a relatively small number of data sets, they were able to exclude two sets of initial conditions, namely $N_{\rm part}$ density without pre-equilibrium flow and $N_{\rm coll}$ density with pre-equilibrium flow, and to constrain initial temperature and the ratio of shear viscosity to entropy density for the other two sets of initial conditions, $N_{\rm part}$ density with pre-equilibrium flow and $N_{\rm coll}$ density without pre-equilibrium flow.

The simultaneous implementation of full three dimensionality, viscosity, hadronic cascade and event-by-event initialisation was first made by Ryu et al. [146]. Their results are preliminary at the moment, since they do not take into

Table 1
Current status of the hydro + cascade models.

Authors and references	Hadronic cascade	Hydrodynamics	T_{sw} [MeV]
Bass et al. [119,123,124]	UrQMD	(1 + 1)-D ideal	160
Teaney et al. [19,20]	RQMD	(2 + 1)-D ideal	160
Hirano et al. [125,126]	JAM	(3 + 1)-D ideal	169, 155
Nonaka and Bass [129]	UrQMD	(3 + 1)-D ideal	150
Petersen et al. [93,130–135]	UrQMD	(3 + 1)-D ideal	[a]
Pratt and Vredevoogd [136]	[b]	(1 + 1)-D viscous	[c]
Werner et al. [138–141]	UrQMD	(3 + 1)-D ideal	166
Song et al. [85,137,142,143]	UrQMD	(2 + 1)-D viscous	165[d]
Soltz et al. [145]	UrQMD	(2 + 1)-D viscous	165
Ryu et al. [146]	UrQMD	(3 + 1)-D viscous	170

[a] Switching energy density is taken to be ∼730 MeV/fm^3.
[b] A rather simple hadronic cascade model is employed here [136].
[c] Switching energy density is taken to be 400 MeV/fm^3.
[d] Sensitivity of the results to the value of T_{sw} is also investigated.

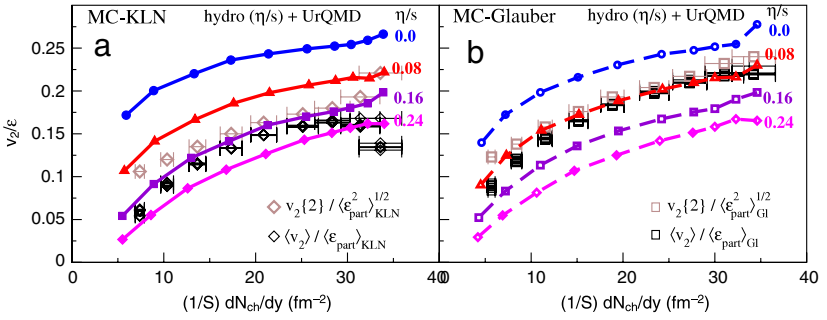

Fig. 12. Comparison of v_2/ε vs. $(1/S)(dN_{ch}/dy)$ curves with experimental data from the STAR Collaboration. (a) the MC-KLN model and (b) the MC-Glauber model. Figures are taken from Ref. [137].

account the dissipative corrections to particle distributions at particlisation, and the statistics in their calculations is so far limited leading to large statistical error bars. Nevertheless, this is one of the promising approaches to investigate the transport properties of the QGP.

Table 1 summarises the current hydro+cascade models by focusing on the cascade model and the switching temperature.

2.6. Initial conditions

The results of hydrodynamic calculations depend strongly on initial conditions since hydrodynamics requires solving initial value problems of partial differential equations. In principle one should obtain the initial conditions for hydrodynamic evolution by solving the non-equilibrium evolution of the matter created in the primary collision of nuclei, but unfortunately this is one of the outstanding problems in heavy-ion physics. Therefore we skip the description of how the matter equilibrates, and rely on models assuming that the matter has equilibrated, and that the densities are given by the density of produced gluons immediately after the primary collision (MC-KLN) or by the density of participating nucleons or binary collisions (MC-Glauber). Due to the lack of models, it is very difficult to quantify how pre-equilibrium dynamics would affect the interpretation of data and our understanding of the initial state of hydrodynamical evolution. It has been argued that flow built up during thermalisation would strongly affect the femtoscopic data [136], but so far we do not know the mechanism creating pre-equilibrium flow, and thus do not know how large it could be. As well, it has been argued that the pre-equilibrium processes affect the granularity of the initial state in event-by-event calculations [85], but we cannot calculate how large this smearing effect should be.

The Glauber model [28–30] has been widely used to fix the initial conditions of hydrodynamic simulations. In the various implementations of Glauber model, one either initialises the energy or entropy density, and assumes it to be proportional to the number density of participants, binary collisions, or some combination of those two [14,75]. On the other hand, one expects highly coherent dense gluon system, called colour glass condensate (CGC) [48–50], to appear in high energy hadronic and nuclear collisions. One may describe the dynamics of gluon fields before local equilibration by solving classical Yang–Mills equation [147–154]. The k_T-factorisation formulation is widely used to compute the inclusive cross section for produced gluons [155–170] in hadronic collisions. Here we shall employ the Monte-Carlo implementations of k_T-factorisation formulation (MC-KLN) [171–173] and Glauber model (MC-Glauber) [28–30] to obtain initial conditions of hydrodynamical simulations. These Monte-Carlo approaches include fluctuations of the positions of nucleons inside

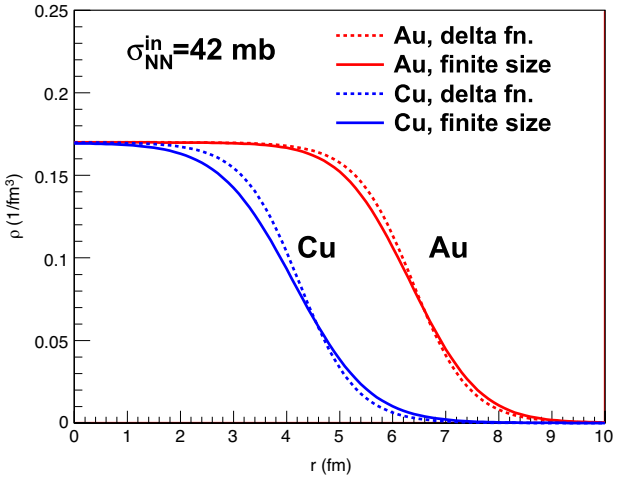

Fig. 13. Nuclear density as a function of nuclear radius. Solid lines show nuclear density distribution for gold and copper nuclei in which a finite nucleon profile is implemented and positions of nucleons are sampled according to the Woods–Saxon distribution with default parameter sets. Dashed lines show the Woods–Saxon distribution with default parameter sets.

colliding nuclei, which allows us to generate a set of initial conditions which fluctuate event-by-event. We do not include fluctuations of energy deposition/entropy generation per collisions [174], which results in negative binomial distribution of multiplicity [133,166,167,175], since rapidity dependence of this kind of fluctuation is not known well.

In MC-Glauber model, for each event the positions of nucleons inside the two colliding nuclei are randomly sampled according to a nuclear density distribution (*e.g.*, Woods–Saxon function). One of the nuclei, and nucleons within, is shifted by a randomly-chosen impact parameter b with probability $b\,db$. A nucleon–nucleon collision is assumed to take place if their distance d in the transverse plane orthogonal to the beam axis fulfils the condition

$$d \leq \sqrt{\frac{\sigma_{\rm in}(\sqrt{s})}{\pi}}, \tag{22}$$

where $\sigma_{\rm in}(\sqrt{s})$ denotes the inelastic nucleon–nucleon cross section at the c.m. energy $\sqrt{s}$. Incident energy dependent total pp cross section is parametrised based on Regge theory, which parameters have been determined by the Particle Data Group [176]:

$$\sigma_{\rm tot}(\sqrt{s}) = Xs^{\epsilon} + Ys^{-\eta} \tag{23}$$

with $X = 22, Y = 56.1, \epsilon = 0.079$ and $\eta = 0.46$ for pp collision. Elastic cross section is computed using PYTHIA parametrisation [113,177,178]:

$$\sigma_{\rm el} = \frac{\sigma^2_{\rm tot}}{16\pi B_{\rm el}(s)}, \qquad B_{\rm el}(s) = 4b_p + 4s^{0.0808} - 4.2\ ({\rm GeV}^{-2}), \tag{24}$$

where $b_p = 2.3$. This parametrisation leads to the following values for the inelastic cross section: $\sigma_{\rm in} = \sigma_{\rm tot} - \sigma_{\rm el} = 39.53$, 41.94 and 61.36 mb at $\sqrt{s} = 130$, 200 and 2760 GeV, respectively.

It should be noted that the standard Woods–Saxon parameters shown in, *e.g.*, Ref. [179] cannot be directly used to distribute nucleons inside a nucleus because of the finite interaction range in our approach. We need to modify nuclear density parameters so that a convolution of nucleon profiles leads to the measured Woods–Saxon profile [57]:

$$\rho(\vec{x}) = \int \Delta(\vec{x} - \vec{x}_0)\rho_{\rm WS}(\vec{x}_0)d^3x_0, \tag{25}$$

$$\Delta(\vec{x} - \vec{x}_0) = \frac{\theta(r_N - |\,\vec{x} - \vec{x}_0\,|)}{V_N}, \tag{26}$$

$$V_N = \frac{4\pi r_N^3}{3}, \qquad r_N = \sqrt{\frac{\sigma^{\rm in}_{NN}}{\pi}}, \qquad \rho_{\rm WS} = \frac{\rho_0}{\exp\left(\frac{r-r_0}{\delta r}\right) + 1}. \tag{27}$$

Fig. 13 shows the standard Woods–Saxon profile (dashed) and the nuclear density profile taking into account finite interaction ranges above but keeping the standard Woods–Saxon parameters (solid). In both gold and copper nuclei, the finite nucleon profile in Eq. (26) makes the nuclear surface more diffused if one uses the standard Woods–Saxon parameters

to distribute nucleons in a nucleus. Without adjustment of the Woods–Saxon parameters for the finite nucleon profile, eccentricity becomes smaller by ∼10% [55]. So we re-parametrise the distribution of nucleon position to reproduce the Woods–Saxon distribution with default parameters in Eq. (27) [29]. The adjustment of the Woods–Saxon parameters has not been considered in most of Monte Carlo approaches of the collisions including event generators If one wants to discuss eccentricity and elliptic flow coefficient v_2 within ∼10% accuracy, this adjustment should be taken into account. If the Gaussian form is used as a nucleon profile, one obtains better agreement with the measured nucleus charged distribution [180]. However, hard sphere form for the nucleon profile is sufficient for the discussion of v_2 in this work. In our MC-Glauber model, we find the default Woods–Saxon distribution is reproduced by larger radius parameter and smaller diffuseness parameter (*i.e.*, sharper boundary of a nucleus) than the default parameters: $\rho_0 = 0.1695(0.1686)$ fm^{-3}, $r_0 = 6.42$ (4.28) fm and $\delta r = 0.44(0.50)$ fm for a gold (copper) nucleus at $\sqrt{s_{NN}} = 200$ GeV and $\rho_0 = 0.161$ fm^{-3}, $r_0 = 6.68$ fm and $\delta r = 0.38$ for a lead nucleus at $\sqrt{s_{NN}} = 2.76$ TeV. In Ref. [180], one finds the parametrisation in the case of Gaussian shape for nucleons. This kind of effect exists in almost all Monte Carlo approaches to the collisions, including event generators. If one wants to discuss eccentricity and elliptic flow coefficient v_2 within ∼10% accuracy, this effect should be taken into account. We also calculate initial entropy distribution in U + U collisions at $\sqrt{s_{NN}} = 200$ GeV by changing the nuclear density from gold to uranium. To take account of the prolate deformation of uranium nuclei, we parametrise the radius parameter in the Woods–Saxon distribution as

$$R(\theta, \phi) = r_0 \left(1 + \beta_2 Y_{20}(\theta, \phi) + \beta_4 Y_{40}(\theta, \phi)\right), \tag{28}$$

where Y_{lm} is the spherical harmonic function, $r_0 = 6.86$ fm, $\beta_2 = 0.28$ and $\beta_4 = 0.093$ [181]. Note that to account of the finite interaction range of nucleons in the Monte Carlo approach, we have again adjusted R_0 above and the diffuseness parameter $\delta r = 0.44$ fm and the saturation density $\rho_0 = 0.166$ fm^{-3} to retain the nuclear density as in the original Woods–Saxon distribution [57]. We also take into account that colliding uranium nuclei are randomly oriented in each event.

Next, we compute particle production at each grid point in the transverse plane. In the MC-Glauber approach, we assume that the initial entropy profile in the transverse plane is proportional to a linear combination of the number density of participants and that of binary collisions:

$$s_0(\boldsymbol{r}_\perp) \equiv \left.\frac{dS}{\tau_0 d^2 r_\perp d\eta_s}\right|_{\eta_s=0} = \frac{C}{\tau_0}\left(\frac{1-\alpha}{2}\rho_{\rm part}(\boldsymbol{r}_\perp) + \alpha\, \rho_{\rm coll}(\boldsymbol{r}_\perp)\right), \tag{29}$$

where $\tau_0 = 0.6$ fm/c is a typical initial time for the hydrodynamical simulation. Parameters $C = 15.0$ and $\alpha = 0.18$ have been fixed through comparison with the centrality dependence of p_T spectra in Au + Au collisions at RHIC [67]. At the LHC energy, $C = 41.4$ and $\alpha = 0.08$ are chosen [54] so that we reproduce the ALICE data on centrality dependence of multiplicity in Pb + Pb collisions at $\sqrt{s_{NN}} = 2.76$ TeV [182–184].

The participant density, $\rho_{\rm part}(\boldsymbol{r}_\perp)$, and the number density of binary collisions, $\rho_{\rm coll}(\boldsymbol{r}_\perp)$, in Eq. (29) are obtained from the previously described positions of nucleons, and the criterion for their interaction, Eq. (22). At each grid point, the participant density is the sum of the number of those nucleons in both nuclei, which scatter within the radius $r_0 = \sqrt{\sigma_{\rm in}/\pi}$ around the grid point, divided by the area $\sigma_{\rm in}$:

$$\rho_{\rm part}(\boldsymbol{r}_\perp) = \rho_{\rm A}(\boldsymbol{r}_\perp) + \rho_{\rm B}(\boldsymbol{r}_\perp) = \frac{N_{A,w}(\boldsymbol{r}_\perp) + N_{A,w}(\boldsymbol{r}_\perp)}{\sigma_{\rm in}}. \tag{30}$$

Similarly, the density of the number of binary collisions at each grid point is obtained by counting the number of binary collisions $N_{\rm coll}$ within the area $\sigma_{\rm in}$, where the position of a binary collision is assumed to be the average position of the two colliding nucleons:

$$\rho_{\rm coll}(\boldsymbol{r}_\perp) = \frac{N_{\rm coll}(\boldsymbol{r}_\perp)}{\sigma_{\rm in}}. \tag{31}$$

which may be also obtained by the expression $\rho_A(\boldsymbol{r}_\perp)\rho_B(\boldsymbol{r}_\perp)\sigma_{\rm in}$.

Note that we calculate the eccentricity of the initial state based on the densities defined above, whereas in the PHOBOS MC-Glauber model [28–30], eccentricity is computed based on the actual positions of point-like particles. The conversion of positions to densities causes an additional smearing over the region $\sigma_{\rm in}$ [44,185]. Therefore the eccentricities in our calculations are smaller than eccentricities in the PHOBOS MC-Glauber model. In the literature the conversion of positions to densities is often done by replacing each position by a Gaussian density profile [93,186,187]. Such a procedure again leads to slightly different eccentricities.

In the Monte-Carlo KLN (MC-KLN) model [171–173], the number distribution of gluon production at each transverse grid is given by the k_T-factorisation formula [156–158]

$$\frac{dN_g}{d^2 r_\perp dy} = \kappa \frac{4N_c}{N_c^2 - 1}\int \frac{d^2 p_\perp}{p_\perp^2}\int \frac{d^2 k_\perp}{4}\, \alpha_s(Q^2)\phi_A(x_1, (\boldsymbol{p}_\perp + \boldsymbol{k}_\perp)^2/4)\, \phi_B(x_2, (\boldsymbol{p}_\perp - \boldsymbol{k}_\perp)^2/4), \tag{32}$$

with $N_c = 3$ the number of colours. Here, $p_\perp$ and y denote the transverse momentum and the rapidity of the produced gluons, respectively. The light-cone momentum fractions of the colliding gluon ladders are then given by $x_{1,2} = p_\perp \exp(\pm y)/\sqrt{s_{NN}}$,

where $\sqrt{s_{NN}}$ denotes the centre of mass energy. Running coupling $\alpha_s(Q^2)$ is evaluated at the scale $Q^2 = \max((\boldsymbol{p}_\perp - \boldsymbol{k}_\perp)^2/4, (\boldsymbol{p}_\perp + \boldsymbol{k}_\perp)^2/4)$. An overall normalisation factor κ is chosen to fit the multiplicity data in most central Au + Au collisions at RHIC. In the MC-KLN model, saturation momentum is parametrised by assuming that the saturation momentum squared is 2 GeV^2 at $x = 0.01$ in Au + Au collisions at $b = 0$ fm at RHIC where $\rho_{\rm part} = 3.06$ fm^{-2} [156–158,188]:

$$Q_{s,A}^2(x;\boldsymbol{r}_\perp) = 2\ \text{GeV}^2 \frac{\rho_A(\boldsymbol{r}_\perp)}{1.53\ \text{fm}^{-2}} \left(\frac{0.01}{x}\right)^\lambda. \tag{33}$$

λ is a free parameter which is expected to be in the range of $0.2 < \lambda < 0.3$ from Hadron Electron Ring Accelerator (HERA) global analysis for $x < 0.01$ [189,190]. In MC-KLN, we assume the gluon distribution function as

$$\phi_A(x, k_\perp^2; \boldsymbol{r}_\perp) \sim \frac{1}{\alpha_s(Q_{s,A}^2)} \frac{Q_{s,A}^2}{\max(Q_{s,A}^2, k_\perp^2)}. \tag{34}$$

We assume that initial conditions of hydrodynamical simulations are obtained by identifying the gluons' momentum rapidity y with space–time rapidity η_s

$$s_0(\boldsymbol{r}_\perp) \propto \frac{dN}{\tau_0 d^2 r_\perp d\eta_s}. \tag{35}$$

We note that gluon production itself also fluctuates [133,166,167,175], but we do not take those fluctuations into account in our model.

To quantify the anisotropy of the initial distributions, we define the anisotropies ε_n, and the corresponding orientation angles Φ_n [34,44]:

$$\varepsilon_n\{\text{PP}\} = \frac{|\langle \boldsymbol{r}_\perp^2 e^{in\varphi}\rangle_x|}{\langle \boldsymbol{r}_\perp^2\rangle_x} \tag{36}$$

$$n\Phi_n = \arg\langle \boldsymbol{r}_\perp^2 e^{in\varphi}\rangle_x \tag{37}$$

where $\langle\cdots\rangle_x$ represents a weighted average over the transverse plane at a fixed space–time rapidity, with the initial density distribution as a weight. Although one may take other definitions [132,191–195], we restrict our discussion to Eqs. (36) and (37) throughout this paper. As for the initial density, we use the entropy density throughout this work. Here $\boldsymbol{r}_\perp$ is the transverse two dimensional vector measured from the centre of mass defined by $\langle \boldsymbol{r}_\perp\rangle_x = \boldsymbol{0}$ and φ is its coordinate angle. For example, the anisotropy ε_2 becomes

$$\varepsilon_2\{\text{PP}\} = \frac{\sqrt{\langle x_\perp^2 - y_\perp^2\rangle_x^2 + 4\langle x_\perp y_\perp\rangle_x^2}}{\langle x_\perp^2 + y_\perp^2\rangle_x}, \tag{38}$$

$$x_\perp = x - \langle x\rangle_x, \tag{39}$$

$$y_\perp = y - \langle y\rangle_x, \tag{40}$$

which is also known as the participant eccentricity $\varepsilon_{\rm part}$ or eccentricity with respect to the participant plane. To keep our terminology consistent with the terminology in literature, we define participant plane as the plane spanned by a unit vector pointing to direction $\Phi_2 - \pi/2$, and the beam axis. Taking a real part of Eq. (36) instead of its absolute value, one obtains the anisotropy with respect to the reaction plane, also known as the standard eccentricity $\varepsilon_{\rm std}$ (although with an opposite sign),

$$\varepsilon_2\{\text{RP}\} = -\varepsilon_{\rm std} = \frac{\Re\langle \boldsymbol{r}_\perp^2 e^{i2\varphi}\rangle_x}{\langle \boldsymbol{r}_\perp^2\rangle_x} = \frac{\langle x_\perp^2 - y_\perp^2\rangle_x}{\langle x_\perp^2 + y_\perp^2\rangle_x}. \tag{41}$$

MC-KLN and MC-Glauber models create an ensemble of initial distributions for event-by-event calculations, but it is also possible to construct an averaged density profile which includes some effects of fluctuations. This is done by rotating each distribution by its orientation angle Φ_n around its centre of mass, shifting the distributions so that the origin of the coordinates is at its centre of mass, $(\langle x\rangle_x, \langle y\rangle_x)$, and averaging over these shifted and rotated distributions. In the literature the required angle is often defined as in Ref. [196]:

$$\tan 2\psi_2 = \frac{2\sigma_{xy}}{\sigma_y^2 - \sigma_x^2}, \tag{42}$$

$$\sigma_x^2 = \langle x^2\rangle_x - \langle x\rangle_x^2, \tag{43}$$

$$\sigma_y^2 = \langle y^2\rangle_x - \langle y\rangle_x^2, \tag{44}$$

$$\sigma_{xy} = \langle xy\rangle_x - \langle x\rangle_x\langle y\rangle_x, \tag{45}$$

Table 2
Centrality definition using $N_{\rm part}$ in Au + Au, U + U and Cu + Cu collisions at $\sqrt{s_{NN}} = 200$ GeV and in Pb + Pb collisions $\sqrt{s_{NN}} = 2.76$ TeV.

Centrality (%)	0–5	5–10	10–15	15–20	20–30	30–40	40–50	50–60	60–70	70–80
Au + Au $N_{\rm part,max}$	394	327	279	237	202	144	99	65	39	21
Au + Au $N_{\rm part,min}$	327	279	237	202	144	99	65	39	21	10
U + U $N_{\rm part,max}$	476	389	330	281	239	170	117	77	46	25
U + U $N_{\rm part,min}$	389	330	281	239	170	117	77	46	25	12
Cu + Cu $N_{\rm part,max}$	126	102	88	75	65	47	33	22	14	9
Cu + Cu $N_{\rm part,min}$	102	88	75	65	47	33	22	14	9	5
Pb + Pb $N_{\rm part,max}$	416	356	305	261	223	161	112	74	46	25
Pb + Pb $N_{\rm part,min}$	356	305	261	223	161	112	74	46	25	12

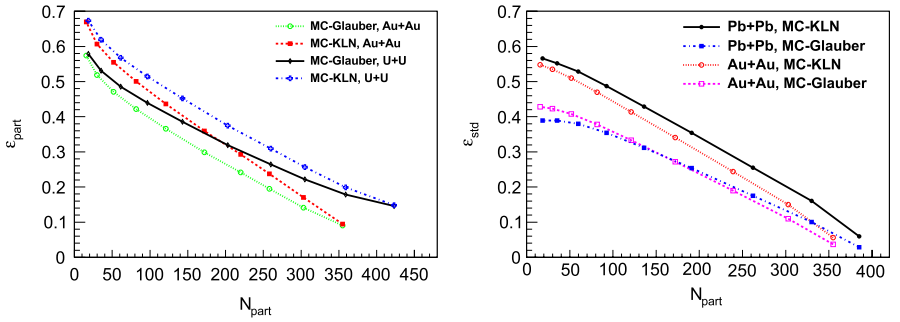

Fig. 14. The second order anisotropy with respect to participant plane (model "B") in Au + Au and U + U collisions at $\sqrt{s_{NN}} = 200$ GeV (left) and with respect to reaction plane (model "A") in Au + Au collisions at $\sqrt{s_{NN}} = 200$ GeV and in Pb + Pb collisions at $\sqrt{s_{NN}} = 2.76$ TeV (right). Results from the MC-KLN and MC-Glauber models are compared with each other. Figures are taken from Refs. [53,54].

where the angle ψ_2 is related to the orientation angle Φ_2 defined in Eq. (37) as $\Phi_2 = -\psi_2$. As was described in the introduction, elliptic flow arises when the system expands preferentially along its participant plane. In this procedure the participant planes of various events are aligned and set equal to the reaction plane. That such an initial state contains some effects of eccentricity fluctuation even though the profile is smooth is manifested in the finite eccentricity even in most central collisions where the impact parameter is zero. We call this initialisation model "B". Compared with this, the procedure averaging over many initial distributions without shift or rotation corresponds to a conventional initialisation without the effect of eccentricity fluctuation and is called model "A". When we use the averaged initial conditions of models "A" and "B", called later the smooth initial profiles, we assume longitudinal boost invariance and calculate observables only at midrapidity. In particular, in the case of the MC-KLN model, we evaluate gluon production at midrapidity using Eq. (32), and assume it to be the same at all rapidities. In actual hydrodynamic simulations, we prepare the lattice in the longitudinal direction up to $\eta_s = 6$ and solve hydrodynamic equations with boost invariant initial conditions. We have checked that the boundary of the lattice does not affect the boost invariant solutions.

In models A and B centrality is defined using the number of events as a function of $N_{\rm part}$. One can categorise the whole events into subevents from top 5%, 5%–10% and so on according to $N_{\rm part}$. In Table 2, we show the maximum and minimum numbers of participants for each centrality bin in Au + Au, U + U, Cu + Cu collisions at the RHIC energy and in Pb + Pb collisions at the LHC energy.

Fig. 14(left) shows the initial eccentricity with respect to participant plane (model "B") in Au + Au and U + U collisions at $\sqrt{s_{NN}} = 200$ GeV as a function of the number of participants. At each of the ten centrality bins the average eccentricity and the average number of participants $\langle N_{\rm part}\rangle$ were calculated using both the MC-Glauber and the MC-KLN models. Since the eccentricity is measured in the participant plane, it is finite even in the very central (0%–5%) Au + Au collisions. As previously known, the MC-KLN model leads to ∼20%–30% larger eccentricity than the MC-Glauber model except in the most central events [125,159]. In most central 5% of U + U collisions eccentricity reaches 0.146 in the MC-Glauber model and 0.148 in the MC-KLN model. The eccentricity is larger in U + U than in Au + Au collisions. Due to the deformed shape of uranium nucleus, this holds not only at fixed number of participants, but also at fixed centrality. The difference, however, decreases with decreasing centrality, and there is almost no difference in the very peripheral events (70%–80%).

Shown in Fig. 14(right) is the initial eccentricity with respect to reaction plane (model "A") as a function of $N_{\rm part}$ in Pb + Pb collisions at $\sqrt{s_{NN}} = 2.76$ TeV and in Au + Au collisions at $\sqrt{s_{NN}} = 200$ GeV. Again, the k_t-factorised formula of KLN model generates larger eccentricity than the Glauber model does [125,159]. In the MC-KLN model, eccentricity in Pb + Pb collisions at $\sqrt{s_{NN}} = 2.76$ TeV is apparently larger than that in Au + Au collisions at $\sqrt{s_{NN}} = 200$ GeV when $N_{\rm part}$ is fixed. However, at a fixed centrality, the difference between them is very small [53]. On the other hand, in the MC-Glauber model, eccentricity in Pb + Pb collisions at $\sqrt{s_{NN}} = 2.76$ TeV is slightly smaller than that in Au + Au collisions at $\sqrt{s_{NN}} = 200$ GeV for a fixed centrality.

This is due to the smearing process we use to obtain a smooth initial profile for hydrodynamic evolution [85]. As mentioned, we use the inelastic cross section in $p + p$ collisions, $\sigma_{\rm in}$, when converting the positions of collision points to

densities, and this effectively smears the distributions. This cross section is ∼1.5 times larger at LHC than at RHIC, and thus the smearing area, $S = \sigma_{\rm in}$ [55,56], is also larger at LHC, and the eccentricity is reduced. Our smearing procedure also leads to a smaller eccentricity than the PHOBOS MC-Glauber model.[10] The effect of smearing is smaller in the MC-KLN initialisation, and we have checked that the eccentricity at LHC turns out to be essentially the same as at RHIC when the smearing area is the same.

Instead of shifting, rotating or averaging transverse profiles, we directly use each individual initial density given by these Monte-Carlo approaches to perform event-by-event hydrodynamic simulations. In these event-by-event calculations, we perform full three dimensional hydrodynamic simulations without assuming boost invariance. In the case of MC-KLN Eq. (32) provides the rapidity distribution of density as well. On the other hand, the Glauber model does not tell the longitudinal structure of the density distribution. Motivated by analyses in Refs. [197,198], we parametrise initial entropy density distribution as [125]

$$s_0(\tau_0, \eta_s, \boldsymbol{r}_\perp) = \frac{dS}{\tau_0 d\eta_s d^2 r_\perp} = \frac{C}{\tau_0}\theta\left(Y_b - |\eta_s|\right) f^{pp}(\eta_s)\left[\frac{1-\alpha}{2}\left(\frac{Y_b-\eta_s}{Y_b}\,\rho_A(\boldsymbol{r}_\perp) + \frac{Y_b+\eta_s}{Y_b}\,\rho_B(\boldsymbol{r}_\perp)\right) + \alpha\,\rho_{\rm coll}(\boldsymbol{r}_\perp)\right], \tag{46}$$

where Y_b is the beam rapidity and f^{pp} is a parametrisation of the shape of rapidity distribution in pp collisions,

$$\frac{dS^{pp}}{d\eta_s} = \int d^2 r_\perp \frac{dS^{pp}}{d\eta_s d^2 r_\perp} = C\theta(Y_b - |\eta_s|) f^{pp}(\eta_s) = C\theta(Y_b - |\eta_s|)\exp\left[-\theta(|\eta_s| - \Delta\eta)\,\frac{(|\eta_s| - \Delta\eta)^2}{\sigma_\eta^2}\right], \tag{47}$$

where $\Delta\eta$ and σ_η are adjustable parameters. Eq. (46) is designed so that the density is independent of the space–time rapidity η_s only around midrapidity when the densities of participating nucleons are the same in both nuclei, $\rho_A(\boldsymbol{r}_\perp) = \rho_B(\boldsymbol{r}_\perp)$. Eq. (46) reduces to Eq. (29) when one plugs in $\eta_s = 0$. We call this parametrisation as the modified BGK model [125]. As mentioned, we do not consider fluctuation of particle production processes and, consequently, longitudinal profile becomes a smooth function. Therefore, there exists some correlation of particle production in the rapidity direction.

Initial parameters in the modified BGK model in Au + Au collisions at $\sqrt{s_{NN}} = 200$ GeV are chosen to reproduce $dN_{\rm ch}/d\eta_s$ measured by PHOBOS Collaboration [199]. The resultant parameters are $\Delta\eta = 1.3$ and $\sigma_\eta = 2.1$. At the time of this writing, the measured pseudorapidity dependence of multiplicity in Pb + Pb collisions at $\sqrt{s_{NN}} = 2.76$ TeV is still preliminary. The parameters $\Delta\eta = 1.9$ and $\sigma_\eta = 3.2$ are chosen to give in central $0 < b < 5$ fm events an average $dN_{\rm ch}/d\eta$ similar to the value obtained using the MC-KLN initialisation. Once the experimental data is finalised, we can adjust these parameters again.

Throughout this work, initial flow velocity is chosen as the Bjorken flow $u^\tau = 1$ and $u^x = u^y = u^{\eta_s} = 0$ [200]. In actual simulations, initial energy density is also needed. One calculates it from the initial entropy density utilising numerical table of EoS, $\epsilon = \epsilon(s)$. Note that we have neglected baryon density in our calculations.

Figs. 15 and 16 show a sample of the initial profile in Pb + Pb collisions at $\sqrt{s_{NN}} = 2.76$ TeV from the MC-KLN model and the MC-Glauber model, respectively. Longitudinal streak-like structures are seen in $y = \langle y\rangle_x$ fm (top-left panel in both figures), where $\langle y\rangle_x$ has been averaged over space–time rapidity. This structure comes simply from smooth longitudinal profiles at the collision point in the transverse plane described in Eq. (32) or (46). Due to this, similar transverse profiles are seen at all space–time rapidities: Hot spots are always located in the same position in the transverse plane.

Fig. 17(left) shows the centrality dependence of the average orientation angle $\cos(n\Phi_n)$. Harmonics with even n do not vanish, which is expected from an almond-like geometry of non-central collisions. The second and the sixth orientation angles negatively correlate with the reaction plane, whereas the fourth orientation angle shows positive correlation. On the other hand, $\langle\cos n\Phi_n\rangle$ for the odd n vanishes, which results from a fact that there is no correlation between $\Phi_n (n = 3, 5)$ and the reaction plane shown in Fig. 17(right). In Fig. 17(right) the number of events as a function of the absolute value of the orientation angle $|n\Phi_n|$ is shown for a sample of 10^5 minimum bias events. These events are binned according to the orientation angle of the initial state measured from the reaction plane. As clearly seen, $|2\Phi_2|$ has a prominent peak at π, which comes from a fact that initial profile looks like an almond shape elongated in the y-direction on average. Note that the angle Φ_2 thus gives the angle between the major axis of the almond and the reaction plane. Other even harmonics, $4\Phi_4$ and $6\Phi_6$, have broad peaks at 0 and π, respectively. Orientation angles with odd n are randomly distributed due to absence of any correlation with respect to the reaction plane. The width of event distribution might be important in understanding the fluctuation of the anisotropies of the particle distribution, δv_n, although we postpone this study to a future work.

Figs. 18 and 19 show space–time rapidity dependences of $\varepsilon_n\{\rm PP\}$ and $\varepsilon_n\{\rm RP\}$, respectively, using the MC-KLN model, and Figs. 20 and 21 using the MC-Glauber model (extended in the longitudinal direction using the BGK model). The anisotropies

[10] In the MC-Glauber model in the literature [28], one assumes δ function profile for each collision point in $\rho_{\rm part}$ distribution rather than a box-like profile in the present work.

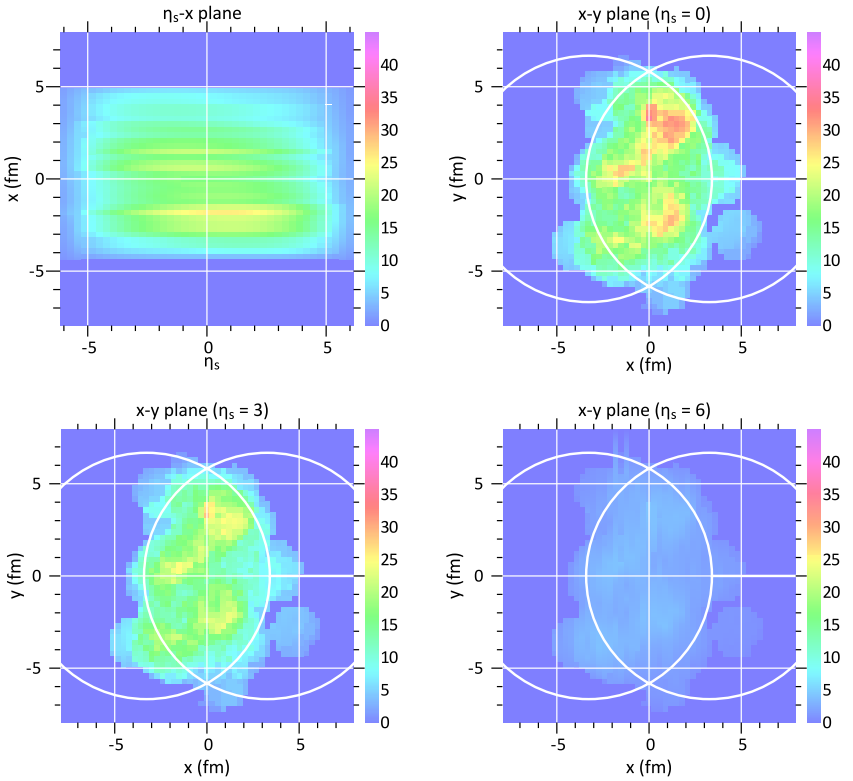

Fig. 15. An example of initial condition in Pb + Pb collisions at $\sqrt{s_{NN}} = 2.76$ TeV from the MC-KLN model. Initial entropy distribution (scaled down by 8.5) is shown in a plane at $y = \langle y \rangle_x$ (top-left), $\eta_s = 0$ (top-right), $\eta_s = 3$ (bottom-left) and $\eta_s = 6$ (bottom-right). Both circles with a radius $r_0 = 6.68$ fm represent a colliding nucleus.

ε_n are evaluated in 0%–10% (left), 30%–40% (middle) and 60%–70% (right) centrality classes in Pb + Pb collisions at $\sqrt{s_{NN}} = 2.76$ TeV. Since the density profiles are smooth and have a streak-like structure in the longitudinal direction as shown in Figs. 15 and 16, $\varepsilon_n\{\mathrm{PP}\}$ are almost independent of η_s. For MC-KLN initialisation $\varepsilon_n\{\mathrm{PP}\}$ for $n = 3$, 5, and 6 are close to each other at all centralities, whereas the values differ for MC-Glauber initialisation. This indicates different origin of fluctuations in these two models. If v_n was roughly proportional to $\varepsilon_n\{\mathrm{PP}\}$, v_n would be independent of rapidity. However, it is not the case at least for $v_2(\eta)$ at RHIC. Even though ε_2 is almost independent of space–time rapidity [21], final v_2 has a broad peak at midrapidity due to relatively larger hadronic dissipative effects in forward/backward rapidity regions [125]. This can be also interpreted as follows. v_2 increases during the QGP evolution and does not so much in the hadronic evolution. So rapidity dependence of v_2 is a key to understand longitudinal structure of the QGP. Since $\varepsilon_n\{\mathrm{PP}\}$ does not depend on space–time rapidity as shown in Fig. 18, $v_n(\eta)$ should contain the direct information about the longitudinal structure of the QGP. We will discuss (pseudo-)rapidity dependence of v_n later. The negative $\varepsilon_2\{\mathrm{RP}\}$ in Figs. 19 and 21 is due to our definition of $\varepsilon_2\{\mathrm{RP}\}$, Eq. (41), which has a different sign than the usual definition of eccentricity. Compared with finite $\varepsilon_n\{\mathrm{PP}\}$, $\varepsilon_n\{\mathrm{RP}\}$ vanishes for odd n since odd harmonics result solely from initial fluctuations and do not correlate with reaction plane. Although longitudinal profiles, Eqs. (46) and (47), in the MC-Glauber model gives similar rapidity and centrality dependence to the MC-KLN model, absolute values of $\varepsilon_n\{\mathrm{PP}\}$ and $\varepsilon_n\{\mathrm{RP}\}$ are different except for $n = 3$ as shown in Fig. 22.

2.7. Brief overview of event-by-event initial conditions

In this subsection, we review hydrodynamic modelling of relativistic heavy ion collisions by focusing particularly on initial conditions on an event-by-event basis.

One of the first works along these lines were the boost-invariant calculations by Gyulassy et al. [201] where HIJING [105–108] event generator was used to evaluate the initial conditions. At collider energies, mini-jets were expected to become one of the dominant sources of fluctuations. In HIJING, particle production is modelled by string excitation and its decay into hadrons by using Lund jet fragmentation scheme for soft processes, and hard pQCD processes are generated based on an eikonal multiple collision formalism and PYTHIA event generator [113].

Another pioneering work was done by the Rio and Sao Paolo groups, who used NeXus event generator [203] to calculate initial condition of fully $(3+1)$ dimensional ideal hydrodynamic simulations [202,204–209]. They were the first to point out the importance of initial state fluctuations when interpreting the elliptic flow data. Namely, the calculated v_2 is different

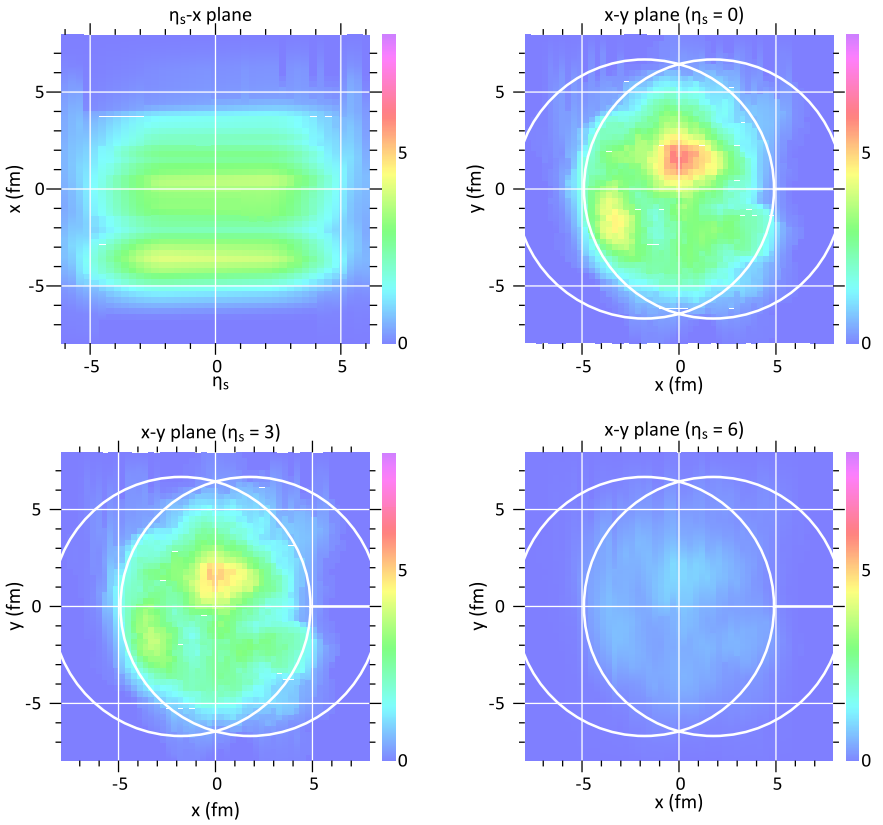

Fig. 16. An example of initial condition in Pb+Pb collisions at $\sqrt{s_{NN}} = 2.76$ TeV from the MC-Glauber model with an extension using the BGK model. Initial entropy distribution (scaled down by 25) is shown in a plane at $y = \langle y \rangle_x$ (top-left), $\eta_s = 0$ (top-right), $\eta_s = 3$ (bottom-left) and $\eta_s = 6$ (bottom-right). Both circles with a radius $r_0 = 6.68$ fm represent a colliding nucleus.

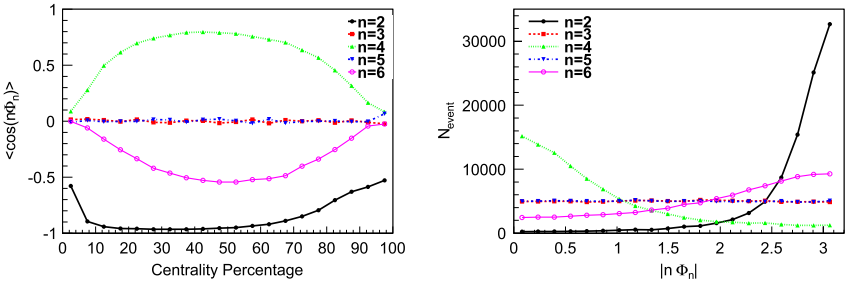

Fig. 17. Centrality dependence of average orientation angle (left) and event distribution of orientation angle (right). The total number of events is 10^5 and the number of bins is 20.

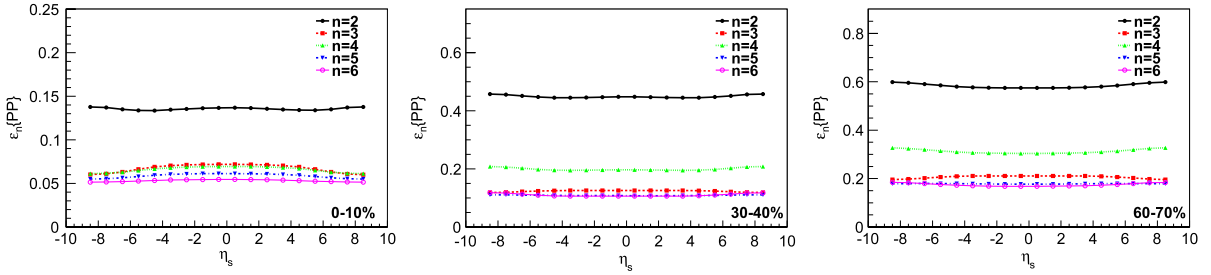

Fig. 18. Space–time rapidity dependences of $\varepsilon_n\{\mathrm{PP}\}$ in 0%–10% (left), 30%–40% (middle) and 60%–70% (right) centrality at LHC energy using the MC-KLN initialisation.

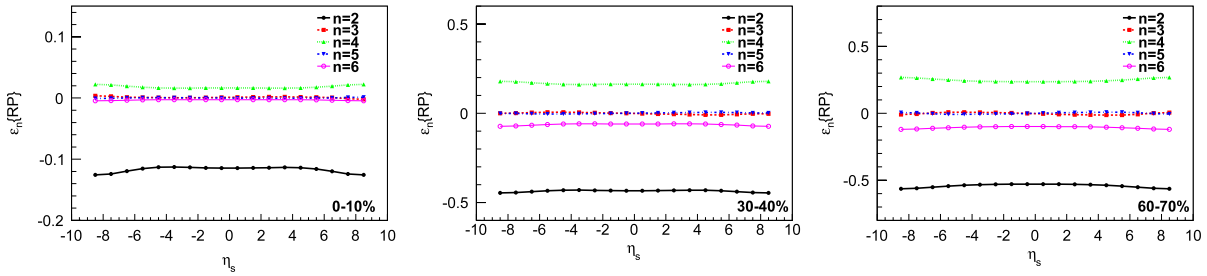

Fig. 19. The same as Fig. 18 but for $\varepsilon_n\{\mathrm{RP}\}$.

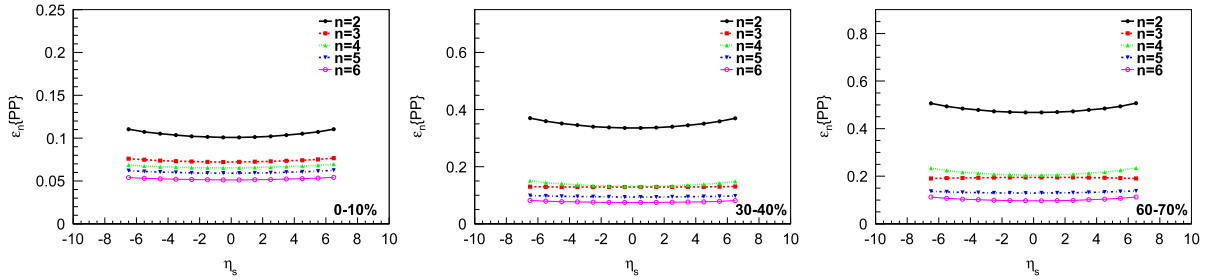

Fig. 20. The same as Fig. 18 but using the MC-Glauber initialisation.

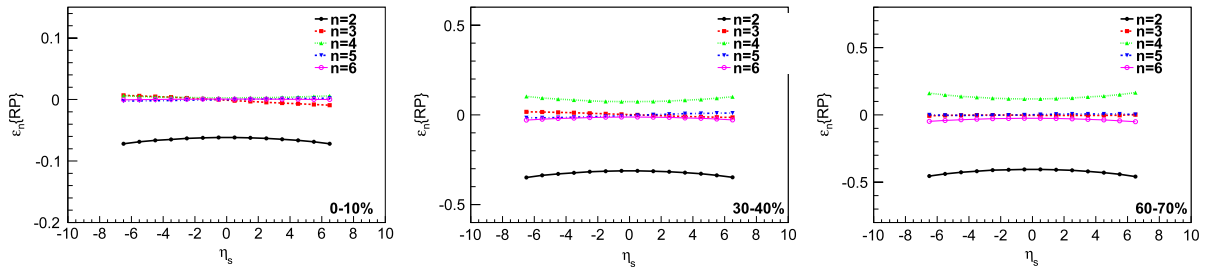

Fig. 21. The same as Fig. 19 but using the MC-Glauber initialisation.

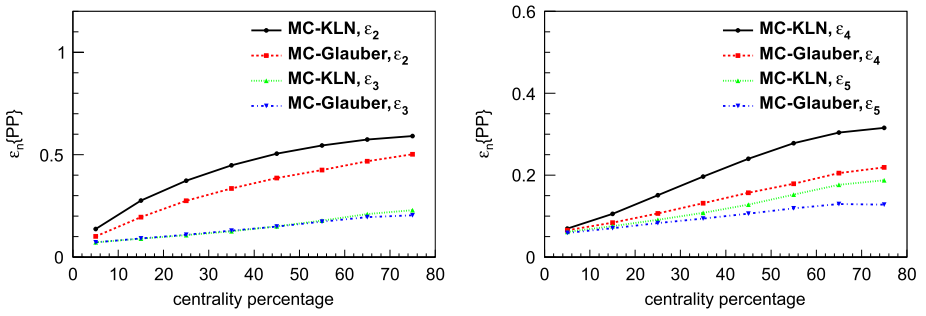

Fig. 22. Centrality dependence of ε_2 and ε_3 (left) and ε_4 and ε_5 (left) for charged hadrons at midrapidity ($0 < \eta_s < 1$) in Pb + Pb collisions at $\sqrt{s_{NN}} = 2.76$ TeV. Results from the MC-KLN model are compared with the ones from the MC-Glauber model.

depending on whether one first evaluates an average initial state, evolves it hydrodynamically, and calculates the v_2, or whether one evolves the initial states event-by-event, calculates v_2 in every event, and averages these calculated values [206,207]. NeXus is a Monte-Carlo event generator based on the Gribov–Regge theory and the pQCD parton model. To convert the output of NeXus to the initial state of hydrodynamic evolution, they calculate the energy–momentum tensor and conserved currents using the kinetic theory definitions. Obviously, energy–momentum tensor obtained in this way is far from the one in equilibrium. Nevertheless, the energy–momentum tensor can be decomposed and energy density and velocity obtained *a. la.* Landau

$$T^{\mu}{}_{\nu}u^{\nu} = \epsilon u^{\mu}. \tag{48}$$

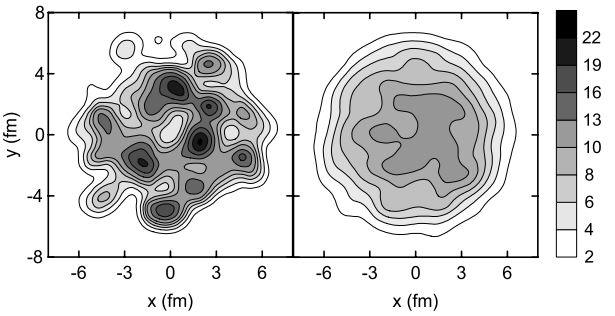

Fig. 23. Examples of initial conditions in central Au + Au collisions given by NeXus at midrapidity. The energy density is plotted in units of GeV/fm^3. (Left) Example of an event. (Right) Average over 30 events. Figure taken from Ref. [202].

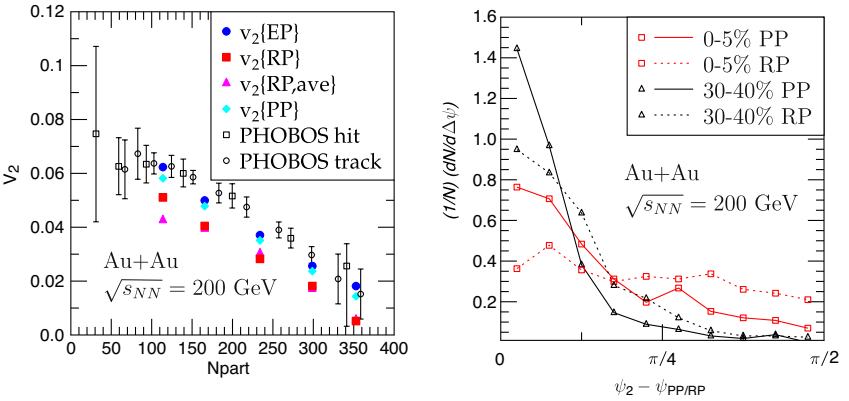

Fig. 24. (Left) Elliptic flow parameter v_2 with $\sigma = 0.4$ fm in Au + Au collisions at $\sqrt{s_{NN}} = 200$ GeV are compared with the PHOBOS data. (Right) Distribution of difference of angles between event and reaction planes and event and participant planes in central (0%–5%) and semi-central (30%–40%) collisions. Figures are taken from Ref. [186].

Using u^μ, one can also obtain baryon density from baryon current $n_B = u_\mu N_B^\mu$. Once ϵ and n_B are obtained, pressure is calculated by using the equation of state $P = P(\epsilon, n_B)$. Energy–momentum tensor for perfect fluids is then based on this energy density, pressure and flow velocity, and the non-ideal terms in the original energy–momentum tensor are ignored. A drawback of this procedure is that energy and momentum are not strictly conserved [210] because the non-ideal terms are ignored and the EoS of the fluid may be different from the EoS of NeXus. Fig. 23 shows initial energy density in a single event (left) and that averaged over 30 events (right). The bumpy structure in a single event is smeared by taking event averages in the initial condition.

The NeXus event generator and hydrodynamic approach was further utilised to evaluate two-pion correlation functions on event-by-event basis by Ren et al. [211]. The main motivation to consider initial fluctuations was to understand RHIC HBT data $R_{\rm out}/R_{\rm side} \sim 1$ [212,213].

Later, the Jyväskylä group performed boost-invariant event-by-event ideal hydrodynamic simulations [186] using Monte-Carlo Glauber initialisation [28], and applied their results to analyse thermal photon spectra [214] and jet quenching [215]. With an option of eWN (energy density using wounded nucleons), initial energy density is calculated as

$$\epsilon(x,y) = \frac{K}{2\pi\sigma^2}\sum_{i=1}^{N_{\rm part}} \exp\left[-\frac{(x-x_i)^2+(y-y_i)^2}{2\sigma^2}\right]. \tag{49}$$

Here (x_i, y_i) is the transverse position of a participant from Monte-Carlo Glauber simulations. σ is a smearing parameter of the collision point being either 0.4 fm or 0.8 fm in this model. A parameter K controls the absolute value of particle yields. In most hydrodynamical calculations the elliptic flow parameter v_2 has been evaluated with respect to either reaction plane or participant plane. The Jyväskylä group were the first to use the event plane method to evaluate the hydrodynamically calculated v_2, and thus to follow the experimental procedure as closely as possible. See, *e.g.*, Fig. 24(left). They also analyse distribution of difference of angle at the second order (elliptic flow) between event and reaction/participant planes as shown in Fig. 24(right).

The Monte-Carlo Glauber and KLN models were employed to initialise ideal [216] and viscous [217] fluid evolution also by the Ohio State group. In their MC-Glauber initialisation they assumed that initial entropy density profile, rather than energy density profile like in Eq. (49), is proportional to linear combination of soft wounded nucleon distribution and

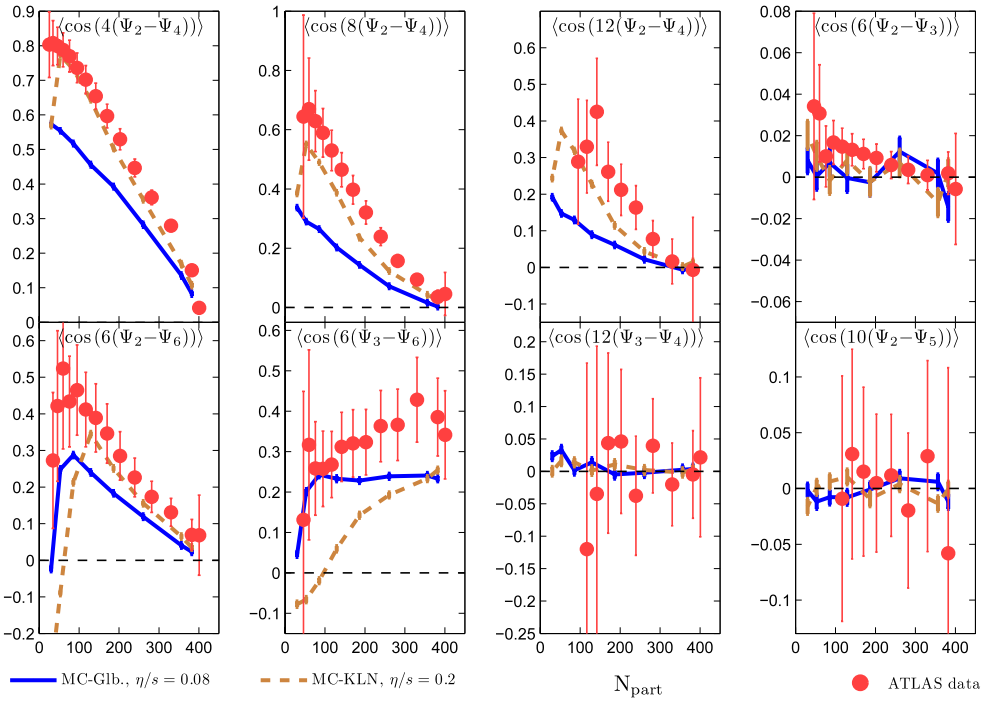

Fig. 25. Centrality dependences of correlation between different order of event plane angles are compared with the ATLAS data [218]. The MC-Glauber (solid) and MC-KLN (dashed) initial profiles are propagated using viscous hydrodynamics with $\eta/s = 0.08$ and 0.2, respectively. Figure is taken from Ref. [217].

hard binary collision distribution. Correlations between the participant and the event plane angles [216], between the two participant plane angles and between the two event plane angles [217] were extensively studied by using event-by-event hydrodynamic simulations in $(2+1)$ dimension assuming boost invariance in the longitudinal direction. Relations between different orders of harmonics were first discussed in Ref. [217] and will be discussed in detail in Section 4. Fig. 25 shows centrality dependences of correlation between different order of event plane angles at the LHC energy using event-by-event viscous hydrodynamic simulations. Although there are small deviations from the ATLAS data [218], overall tendency is reproduced in this approach.

As mentioned in Section 2.5, the Frankfurt group has developed an integrated hybrid model based on fully $(3+1)$ dimensional ideal hydrodynamics and UrQMD. In their model UrQMD is utilised both for generating the initial conditions and for describing the evolution in the hadronic phase [93,130–135]. Hydrodynamic simulations as well as UrQMD are performed in the three-dimensional Cartesian coordinate. At initial time $t_{\rm start}$ at which two colliding nuclei are maximally overlapped, $t_{\rm start} = 2R/\gamma v$, where $R(v)$ is a radius (velocity) of a colliding nucleus, initial energy density in the computational frame is calculated as

$$\epsilon(x,y,z) = \sum_p \frac{\gamma_z}{(2\pi)^{3/2}\sigma^2} E_p \exp\left[-\frac{(x-x_p)^2+(y-y_p)^2+\gamma_z^2(z-z_p)^2}{2\sigma^2}\right], \tag{50}$$

where E_p is the total energy of a particle (also in the computational frame) from string fragmentations and γ_z Lorentz gamma factor in the beam direction. The width of the Gaussian is chosen to be $\sigma = 1$ fm as a default value, which is a little larger compared with other approaches. Consequently the resultant initial energy density distribution is smoother than in other Monte-Carlo approaches requiring smearing. See, *e.g.*, Fig. 26.

Werner et al. [138–141] utilised the EPOS event generator [219] to generate the initial conditions for $(3+1)$ dimensional ideal fluid evolution. EPOS is the successor of NeXus and is based on Pomerons and partons. Nuclear effects such as Cronin effect, parton saturation, and screening are introduced into EPOS. Energy–momentum tensor is calculated from four-momenta of string segments δp^μ

$$T^{\mu\nu}(x) = \sum_i \frac{\delta p_i^\mu \delta p_i^\nu}{\delta p_i^0} g(x-x_i), \tag{51}$$

where the summation is taken over for each i-th segment and g is a Gaussian type smearing function with a width 0.25 fm. The energy–momentum tensor is then converted to energy density and velocity using a similar procedure than what the Rio and Sao Paolo groups use. Since these string segments decayed from flux tubes correlate in the longitudinal direction,

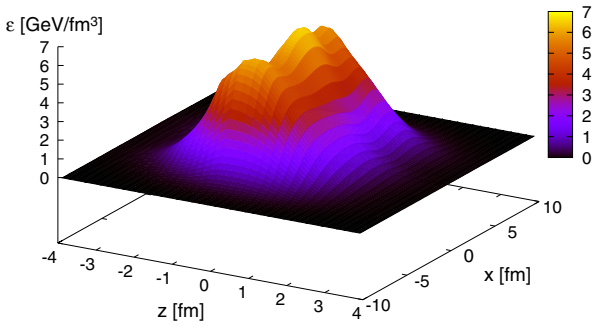

Fig. 26. (Left) Initial energy density distribution in the reaction plane of single central event in Pb + Pb collisions at $E_{\rm lab} = 40A$ GeV from UrQMD. Figure taken from Ref. [93].

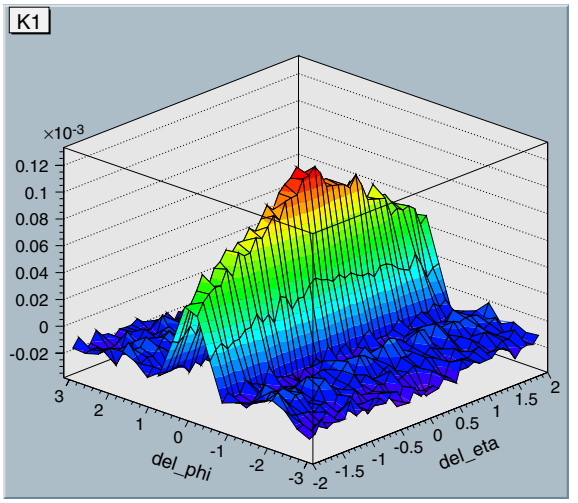

Fig. 27. (Right) Dihadron correlation in $\Delta\eta$–$\Delta\phi$ plane in central Au + Au collisions at $\sqrt{s_{NN}} = 200$ GeV from event-by-event EPOS + ideal hydrodynamic simulations. Figure taken from Ref. [138].

transverse profiles look quite similar at each space–time rapidity. Consequently, this leads to the so-called ridge structure in the di-hadron correlation function as shown in Fig. 27.

Parametrised initial conditions including higher order deformation were used in viscous hydrodynamic simulations to discuss triangular flow by Alver et al. [192]. This is not actually an event-by-event hydrodynamic simulation. Nevertheless, it captures some features of higher order deformation in the initial profiles. An idea behind this is quite similar to the model "B" explained in the previous subsection in our study. Initial energy density in the transverse plane is parametrised as

$$\epsilon(x, y) = \epsilon_0 \exp\left\{-\frac{r^2[1 + \varepsilon_n \cos n(\phi - \psi_n)]}{2\rho^2}\right\}, \tag{52}$$

where $r = \sqrt{x^2 + y^2}$ is radial and ϕ is azimuthal angle in the polar coordinate. ε_n is the magnitude of the deformation and ψ_n is a reference angle. ρ is roughly root-mean-square radius of the produced matter and taken to be 3 fm. The deformation ε_n is estimated by either the MC-Glauber or the MC-KLN model. They tuned η/s to reproduce centrality dependence of v_2 at the RHIC energy. Resultant values are $\eta/s = 0.08$ and 0.16 for the MC-Glauber and the MC-KLN model, respectively. Using this parameter, they could reproduce v_3 as a function of $N_{\rm part}$ in the MC-Glauber model. Whereas, their v_3 using the MC-KLN model with $\eta/s = 0.16$ are significantly smaller than the v_3 data. Thus they concluded v_3 data set a severe constraint to the initialisation model in viscous hydrodynamic simulations.

Fully (3 + 1) dimensional viscous hydrodynamic simulations on an event-by-event basis were performed by Schenke et al. [187,220]. They have also recently evaluated fluctuating Glasma initial conditions by solving classical Yang–Mills equations, and used them as the initial state for hydrodynamical calculations [221,222]. In their first papers they utilise the MC-Glauber model and initialise the energy density distribution in the transverse plane as in Eq. (49) [187]. In the longitudinal direction, they assume the energy density follows Bjorken scaling solution near midrapidity and falls like a half Gaussian near beam rapidity [187]. Recently, the IP-Glasma model [221–223] was employed to initialise energy density in hydrodynamic simulations. The IP-Glasma model solves the classical Yang–Mills equations in which initial charge distributions of two colliding nuclei are sampled from a Gaussian distribution with impact parameter and Bjorken x

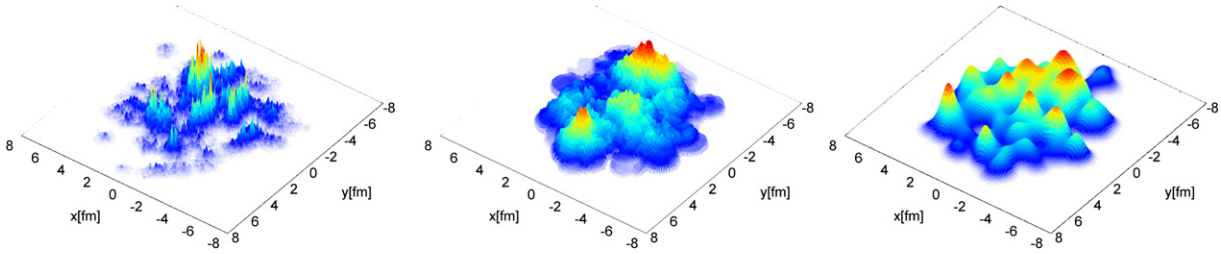

Fig. 28. Examples of initial energy density distribution from the IP-Glasma model at $\tau = 0$ fm (left), the MC-KLN model (middle) and the MC-Glauber model (right). Figures are taken from Ref. [221].

dependent colour charge distributions. Parametrisation of x and impact parameter dependence of saturation scale is taken from the IP-Sat (Impact Parameter Saturation) model [224,225]. In this model event-by-event energy distribution exhibits the expected negative binomial distribution and it described the observed multiplicity distribution up to a constant scaling factor [223]. Quite remarkably it correctly predicts the event-by-event distribution of v_2, v_3 and v_4 [222], which should be important in understanding initial fluctuations. Fluctuations in the IP-Glasma model have a length scale of the order of the inverse of the saturation scale $Q_s^{-1}(\boldsymbol{x}_\perp) \sim 0.1$–$0.2$ fm which is smaller than typical length scales $0.4 \lesssim \sigma \lesssim 1$ fm in other calculations. Fig. 28 shows comparison of initial energy density distribution among the IP-Glasma, MC-KLN and MC-Glauber models. Finer structure is seen in the result from the IP-Glasma model.

A simple parametrisation for initial energy density was employed by Chaudhuri in his $(2 + 1)$-dimensional viscous hydrodynamic simulations [226,227]

$$\epsilon(x, y) = \epsilon_0 \sum_{i=1}^{N_{\rm part}} \exp\left[-\frac{(\boldsymbol{r} - \boldsymbol{r}_i)^2}{2\sigma^2}\right]. \tag{53}$$

The width is set to $\sigma = 1$ fm and ϵ_0 is chosen to reproduce multiplicity in the experimental data. $N_{\rm part}$ is calculated using the optical Glauber model, and the positions of the hotspots, $\boldsymbol{r}_i$, are assumed to be Gaussian distributed. It is noted that, since the hot-spot would originate from a pair of participating nucleons, a scheme to randomly sample independent position of hot-spots using averaged distribution of $N_{\rm part}$ in the transverse plane does not capture the actual distribution of correlated hot-spots from the MC-Glauber model. Later, the effect of choice of smearing profile on final v_2 and v_3 in the context of the MC-Glauber model was examined by choosing the Woods–Saxon profile instead of the Gaussian one [228]. They found that the anisotropy coefficients v_2 and v_3 were not affected by the form of the smearing profile nor by the value of the smearing parameter, whereas coefficients v_4 and v_5 showed some sensitivity to the smearing.

Bozek et al. employed Monte-Carlo Glauber model GLISSANDO [29] for initialisation in their event-by-event full $(3 + 1)$-dimensional viscous hydrodynamic simulations [229]. Initialisation of the entropy profile in the transverse plane is quite similar to others:

$$s(x, y) = \kappa \sum_i g_i(x, y)[(1 - \alpha) + N_i^{\rm coll}\alpha], \tag{54}$$

$$g_i(x, y) = \frac{1}{2\pi w^2} \exp\left[-\frac{(x - x_i)^2 + (y - y_i)^2}{2w^2}\right]. \tag{55}$$

Here the summation is taken over participants and $N_i^{\rm coll}$ is the number of collisions of the i-th participant. Similar to other groups, the transverse position of nucleons is smeared from a point-like source to a Gaussian profile with a width $w = 0.4$ fm. Soft–hard mixture $\alpha = 0.125$ leads to reproduction of centrality dependence of $dN_{\rm ch}/d\eta$ at the top RHIC energy within the full $(3+1)$-dimensional viscous hydrodynamic simulations. Note that, since the Glauber approach tells us only profiles in the transverse plane, longitudinal profiles of the produced matter have to be also modelled by taking account of momentum conservation among colliding nucleons at certain transverse position [229].

$$f_\pm(\eta_s) = \left(1 \pm \frac{\eta_s}{y_{\rm beam}}\right) f(\eta_s), \tag{56}$$

$$f(\eta_s) = \exp\left[-\frac{(\eta_s - \eta_0)^2}{2\sigma_\eta^2}\theta(|\eta_s| - \eta_0)\right], \tag{57}$$

where $y_{\rm beam}$ is the beam rapidity. Using this model, they calculated transverse momentum fluctuations at the RHIC energy and found the experimental data can be explained by the event-by-event fluctuations of initial profiles.

Recently, Pang et al. employed the AMPT event generator for initialisation in event-by-event $(3 + 1)$-dimensional ideal hydrodynamic simulations [230]. Information about phase-space density from the AMPT simulation at some initial time τ_0

Table 3
Event-by-event hydrodynamic simulations.

Authors and references	Initialisation model	Dimension	Ideal/Viscous
Gyulassy et al. [201]	HIJING	(2 + 1)-D	Ideal
Aguiar et al. [202,205–209]	NeXus	(3 + 1)-D	Ideal
Ren et al. [211]	NeXus	(3 + 1)-D	Ideal
Holopainen et al. [186,214,215]	MC-Glauber	(2 + 1)-D	Ideal
Qiu and Heinz [216]	MC-Glauber, MC-KLN	(2 + 1)-D	Ideal
Petersen et al. [93,130–135]	UrQMD	(3 + 1)-D	Ideal
Werner et al. [138–141]	EPOS	(3 + 1)-D	Ideal
Alver et al. [192]	Parametrisation	(2 + 1)-D	Viscous
Schenke et al. [187,220,221]	MC-Glauber, IP-Glasma	(3 + 1)-D	Viscous
Chaudhuri et al. [226,228]	Parametrisation	(2 + 1)-D	Viscous
Bozek and Broniowski [229]	MC-Glauber	(3 + 1)-D	Viscous
Pang et al. [230]	AMPT	(3 + 1)-D	Ideal
Zhang et al. [231]	MC-Glauber	(2 + 1)-D	Ideal
This study	MC-Glauber, MC-KLN	(3 + 1)-D	Ideal

is used to calculate local energy–momentum tensor

$$T^{\mu\nu}(\tau_0, x, y, \eta_s) = K \sum_i \frac{p_i^\mu p_i^\nu}{p_i^\tau} \frac{1}{2\pi\sigma_r^2} \exp\left[-\frac{(x-x_i)^2 + (y-y_i)^2}{2\sigma_r}\right] \frac{1}{\tau_0\sqrt{2\pi\sigma_{\eta_s^2}}} \exp\left[-\frac{(\eta_s - \eta_{s,i})^2}{2\sigma_{\eta_s}^2}\right], \tag{58}$$

where $p^\tau = m_T \cosh(Y - \eta_s)$ for the i-th parton. The widths in transverse and longitudinal directions are chosen as being $\sigma_r = 0.6$ fm and $\sigma_{\eta_s} = 0.6$, respectively. They allowed one parameter K to reproduce experimentally-measured multiplicity at midrapidity. In actual calculations at the LHC energy, $K = 1.6$ and $\tau_0 = 0.2$ fm. Through this approach, one can include fluctuations of the density profile in the longitudinal direction as well as in the transverse plane and of flow velocities in the initial conditions. They found that initial fluctuations in rapidity distributions lead to expanding hot spots in the longitudinal direction and that fluctuations in the initial flow velocities lead to harder transverse momentum spectra of final hadrons due to non-vanishing initial radial flow velocities.

Zhang et al. investigated the effect of initial fluctuation on jet energy loss using (2 + 1) dimensional ideal hydrodynamic model [231]. They found that, compared with smooth initial conditions, a jet loses slightly more energy in the expanding QGP with fluctuating initial conditions.

Table 3 summarises current status of event-by-event hydrodynamic simulations by focusing on initialisation models and dimension of hydrodynamic simulations. Note that there are many more models for initialising the event-by-event calculations than there are hadronic cascade models used in the hydro + cascade models (Table 1).

3. Results from the smooth initial profile

In this section, we show results from the integrated dynamical model starting from conventional smooth initial entropy density distributions to describe a high-energy heavy ion reaction as a whole at LHC and RHIC. We show p_T spectra for pions, kaons and protons, v_2 for charged hadrons as functions of centrality and p_T and $v_2(p_T)$ for identified hadrons. For the models of initialisations, MC-KLN and MC-Glauber models are employed and the results obtained using them are compared with each other. We will compare some of these results with those from event-by-event hydrodynamic simulations later.

3.1. Results at RHIC

In Figs. 29 and 30 we show transverse momentum distributions of positive pions and kaons, and the average of protons and antiprotons around midrapidity ($|\eta| < 0.35$) in $\sqrt{s_{NN}} = 200$ GeV Au + Au collisions. The results calculated using the KLN model and Glauber model initial conditions (Figs. 29 and 30, respectively) are compared with the PHENIX data [67]. Although initial conditions are taken from "Model B" in both cases, results from "Model A" (simple average over many samples) are almost identical to these. In central collisions, we reproduce the PHENIX data [67] well up to $p_T \sim 3$ GeV/c. The p_T region where the model works well becomes smaller as going to peripheral collisions: for example, in 70%–80% centrality, we reproduce p_T spectrum for pions up to $p_T \sim 1$ GeV/c and, beyond this, other components such as recombination and/or jet fragmentation, which are missing in the current integrated model, may be dominant. p_T slopes from the KLN model are a little harder than those from the Glauber model. It should be noted here that we chose the switching temperature $T_{sw} = 155$ MeV to obtain the observed particle ratios of these identified hadrons, not to reproduce p_T slope. Final particle spectra are expected to be independent of a choice of the switching temperature. However, this is not the case in the current calculations: the particle yields depend on the switching temperature and thus it can be fixed using the particle ratios. Similar sensitivity to the value of T_{sw} was seen also in Ref. [85], where a systematic analysis of switching temperature dependence was made.

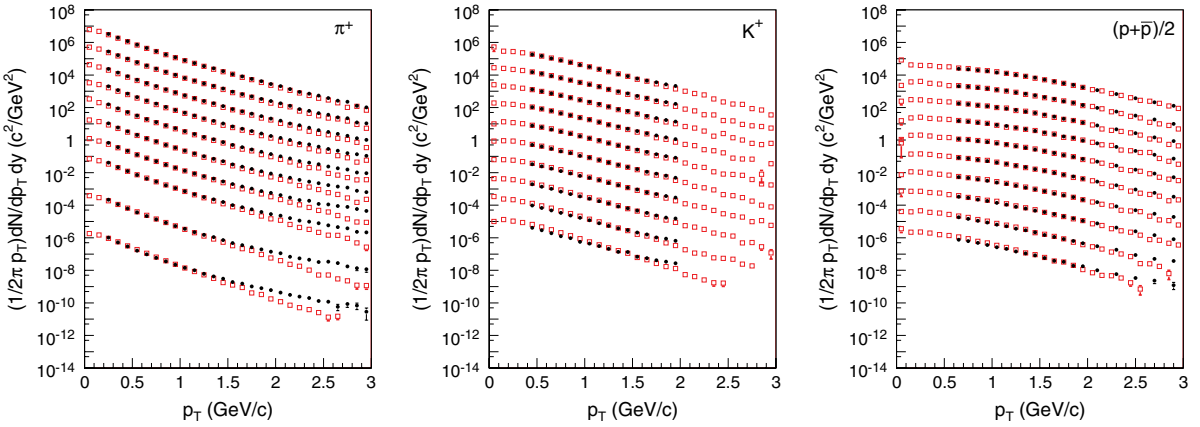

Fig. 29. Transverse momentum distributions of π^+ (left), K^+ (middle) and $(p+\bar{p})/2$ (right) in $\sqrt{s_{NN}} = 200$ GeV Au + Au collisions at 0%–5%, 5%–10%, 10%–15%, 15%–20%, 20%–30%, 30%–40%, 40%–50%, 50%–60%, 60%–70% and 70%–80% centralities from top to bottom. Both the PHENIX data [67] (filled circle) and results calculated using the KLN initial conditions (open square) are shown. To show all these results, each spectrum is multiplied by 10^n with $n = 4, 3, 2, \ldots, -5$ from top to bottom for kaons and protons. For pions, $n = 4, 3, 2, \ldots, -3, -5$ and -7.

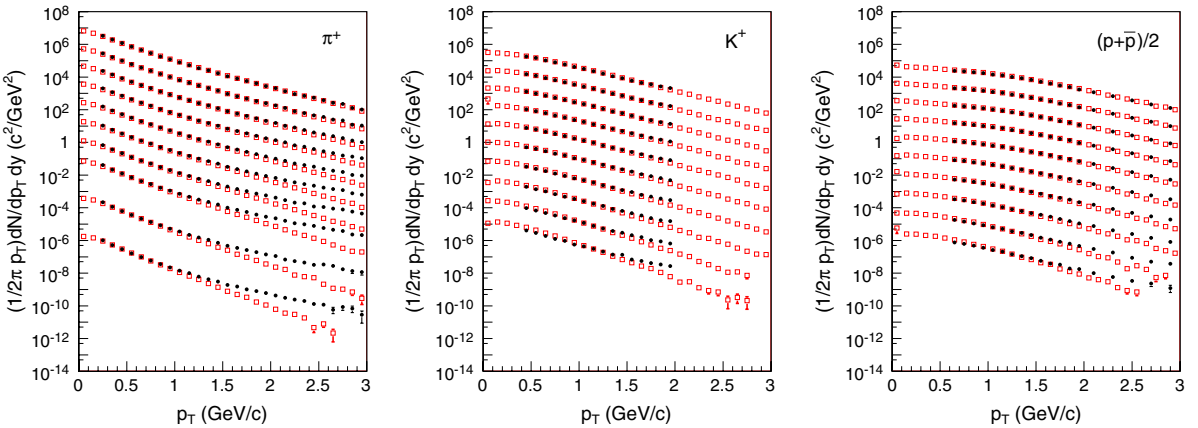

Fig. 30. The same as Fig. 29 but using the Glauber model initial conditions.

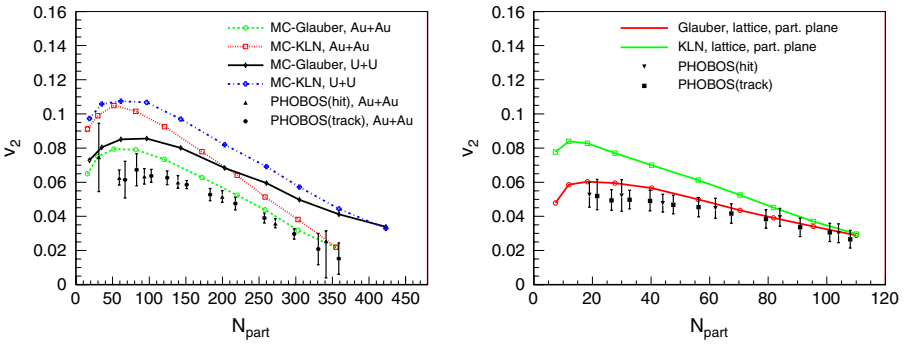

Fig. 31. $N_{\rm part}$ dependence of v_2 evaluated using model "B" (see the text) in Au + Au (left) and Cu + Cu (right) collisions at $\sqrt{s_{NN}} = 200$ GeV are compared with the PHOBOS data [9,32]. Predictions in U + U collisions at $\sqrt{s_{NN}} = 200$ GeV are also shown in the left figure (taken from Ref. [53]).

In Fig. 31(left), v_2 in Au + Au collisions is compared with v_2 in U + U collisions at $\sqrt{s_{NN}} = 200$ GeV. Here initial conditions are taken from "Model B" and the momentum distribution is integrated over $|\eta| < 1$ and the whole p_T region. Since larger eccentricity leads to larger momentum anisotropy and v_2, the systematics of $v_2(N_{\rm part})$ is similar to that of $\varepsilon_{\rm part}(N_{\rm part})$ as shown in Fig. 14(left). v_2 is larger in U + U collisions than in Au + Au collisions, and KLN initialisation leads to larger v_2 than Glauber initialisation. v_2 first increases with decreasing $N_{\rm part}$, which reflects increasing initial eccentricity. When $N_{\rm part}$ falls

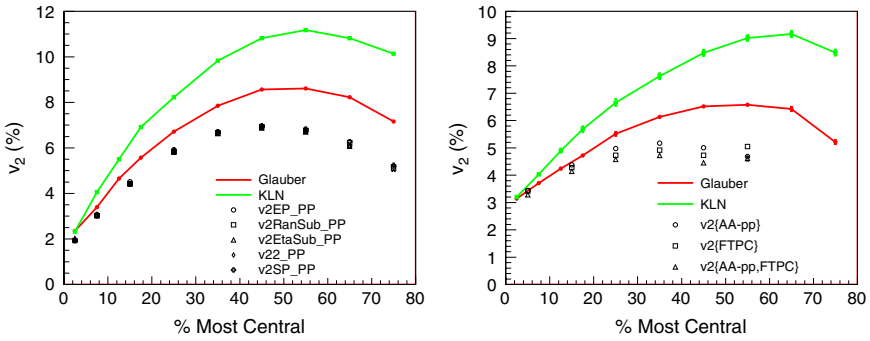

Fig. 32. Centrality dependence of v_2 with respect to participant plane (model "B") in Au + Au (left) and Cu + Cu (right) collisions at $\sqrt{s_{NN}} = 200$ GeV are compared with the STAR data [80,232] ($0.15 < p_T < 2$ GeV/c and $|\eta| < 1$). Experimental data in Au + Au collisions are as corrected in Ref. [233].

below ∼50, v_2, however, begins to decrease. This is due to the short lifetime of the system which does not allow the flow to fully build up, and to the large fraction of the lifetime spent in the hadronic phase where dissipative effects are large.

In Au + Au collisions, results from the Glauber initialisation almost reproduce the PHOBOS data [9]. This indicates that there is little room for QGP viscosity in the model calculations. On the other hand, apparent discrepancy between the results from the KLN initialisation and the PHOBOS data means that viscous corrections during the fluid evolution are required. Fig. 31(right) shows a comparison of results with the PHOBOS data in Cu + Cu collisions [32]. Again, the Glauber model initialisation almost reproduces PHOBOS data, while the KLN initialisation leads to larger v_2 than the PHOBOS data.

As expected, the system in U + U collisions at $\sqrt{s_{NN}} = 200$ GeV is denser than in Au + Au collisions at the same energy. At initial time $\tau_0 = 0.6$ fm/c, the maximum temperature (energy density) in the most central 5% of U + U collisions is $T_0 = 367$ MeV ($e_0 = 33.4$ GeV/fm^3) and $T_0 = 361$ MeV ($e_0 = 31.4$ GeV/fm^3) in the Au + Au collisions of the same centrality. This corresponds to charged particle transverse densities of 25.4 and 24.1, respectively, which means that the transverse density in U + U collisions is indeed larger, but only by ∼ 6%.[11]

Fig. 32 shows again the centrality dependences of v_2 in Au + Au (left) and Cu + Cu (right) collisions at $\sqrt{s_{NN}} = 200$ GeV. Here initial conditions are taken from Model "B" and the momentum distribution is integrated over $|\eta| < 1$ and $0.15 < p_T < 2$ GeV/c according to experimental setup in STAR [80,232]. Experimental data in Au + Au collisions [80] have been corrected to subtract non-flow effects [233] and, thus, all data sets from various flow analysis methods coincide with each other. Notice that the data have not been corrected yet in Cu + Cu collisions [232]. Similar to the results in Fig. 31, the Glauber initialisation little overshoots the STAR data, while the KLN initialisation leads to larger v_2 than the Glauber initialisation clearly overshooting the STAR data.

In Fig. 33 the calculated $v_2(p_T)$ for charged hadrons in $\sqrt{s_{NN}} = 200$ GeV Au + Au collisions is compared with the PHENIX [234] and STAR [80] data in 0%–10% (top left), 10%–20% (top middle), 20%–30% (top right), 30%–40% (bottom left), 40%–50% (bottom middle) and 50%–60% (bottom right) centralities. The calculation was done using the Glauber model initial state in the model "B" setting. In 0%–10% central collisions, results from the model is almost identical to the PHENIX v_2{BBC} data. However, the data deviate from theoretical results as going to peripheral collisions, which suggests the importance of viscous effects in peripheral collisions where the transverse flow is more anisotropic and the size of the system is smaller than in central collisions.

As shown in Fig. 34, $v_2(p_T)$ pattern in Au + Au collisions is quite similar to that in Cu + Cu collisions even though the size of the system in the latter case is smaller than in the former case. Experimental data are taken from PHENIX [235] and STAR [232].

As already seen in the integrated v_2 in Figs. 31 and 32, the KLN model gives a larger v_2 than the Glauber model does. This is again seen in $v_2(p_T)$ in Figs. 33 and 35: The slope of $v_2(p_T)$ from the KLN initialisation is slightly steeper than that from the Glauber initialisation.

In Fig. 36, $v_2(p_T)$ for identified hadrons using the Glauber initialisation are compared with the PHENIX data. Mass splitting pattern, which is known to come mainly from hadronic rescattering effects [126], is seen in both theoretical results and experimental data. In low p_T region up to ∼1 GeV/c, we reasonably reproduce the PHENIX data. However, the data gradually deviate from the theoretical results above $p_T \sim 1$ GeV/c, which suggests again the necessity of viscous corrections. As already seen in the $v_2(p_T)$ for charged hadrons, v_2 for pions overshoots the data in semi-central collisions.

It might be also interesting to analyse v_2 for ϕ mesons in low p_T region: Since ϕ mesons hardly rescatter with pions in the late hadronic stages, these particles do not participate in mass splitting pattern [126]. A hint of this behaviour has been already seen in recent STAR data [236].

[11] With sufficient statistics, one may make more severe centrality cut (e.g., 0%–3%) to obtain larger transverse particle density. Multiplicity fluctuation in the centrality cut, which we do not take into account, could also enhance the transverse particle density.

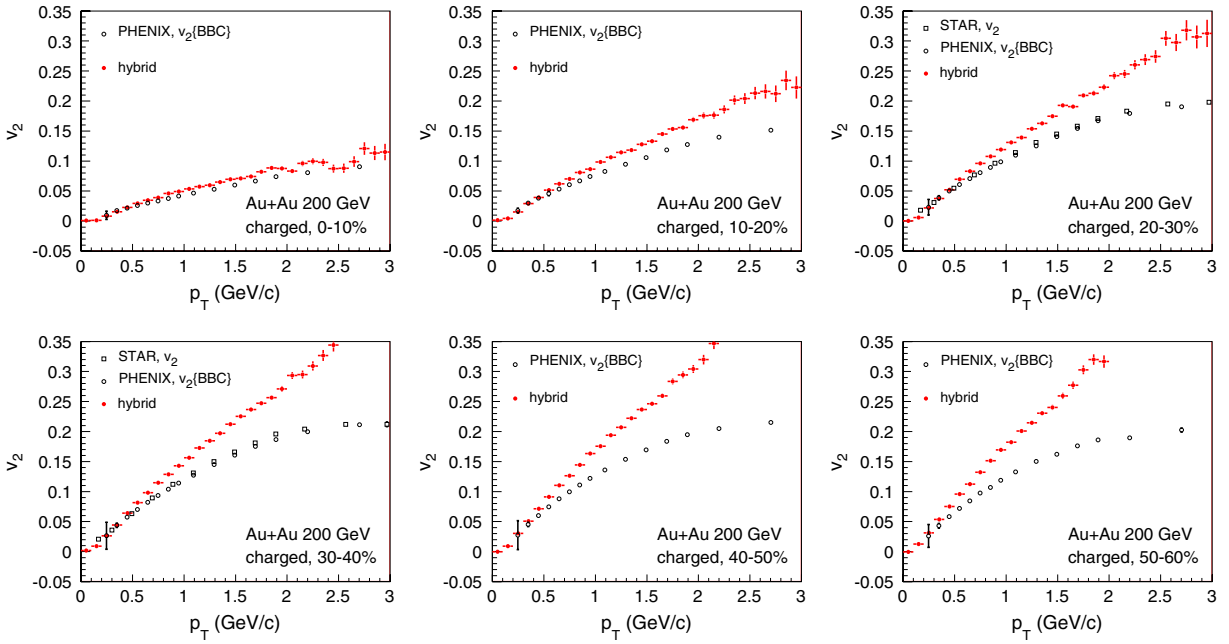

Fig. 33. Transverse momentum dependence of v_2 of charged hadrons in $\sqrt{s_{NN}} = 200$ GeV Au + Au collisions in 0%–10% (top left), 10%–20% (top middle), 20%–30% (top right), 30%–40% (bottom left), 40%–50% (bottom middle) and 50%–60% (bottom right) centralities. Results calculated with respect to the participant plane (model "B") using the Glauber model initial conditions are compared with the PHENIX [234] and STAR data.

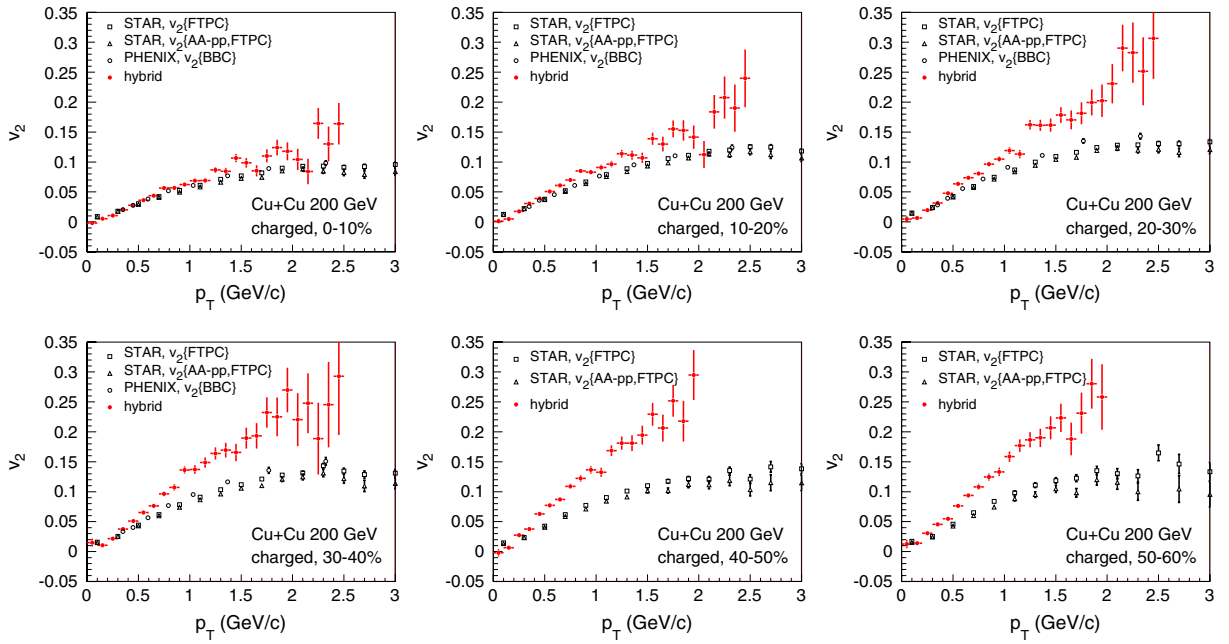

Fig. 34. The same as Fig. 33 but in Cu + Cu collisions. Data are from PHENIX [235] and STAR [232].

3.2. Results at LHC

Fig. 37 shows a comparison of transverse momentum distributions of charged hadrons between RHIC and LHC energies at 10%–20% and 40%–50% centralities. As clearly seen from figures, the slope of the p_T spectra becomes flatter as collision energy and, consequently, pressure of produced matter increases. To quantify this, we calculate mean p_T of charged hadrons. In the MC-Glauber initialisation, mean p_T increases from RHIC to LHC by 21% and 19% in 10%–20% and 40%–50% centrality, respectively. On the other hand, the corresponding relative increases are 25% and 24% in the MC-KLN initialisation. Since

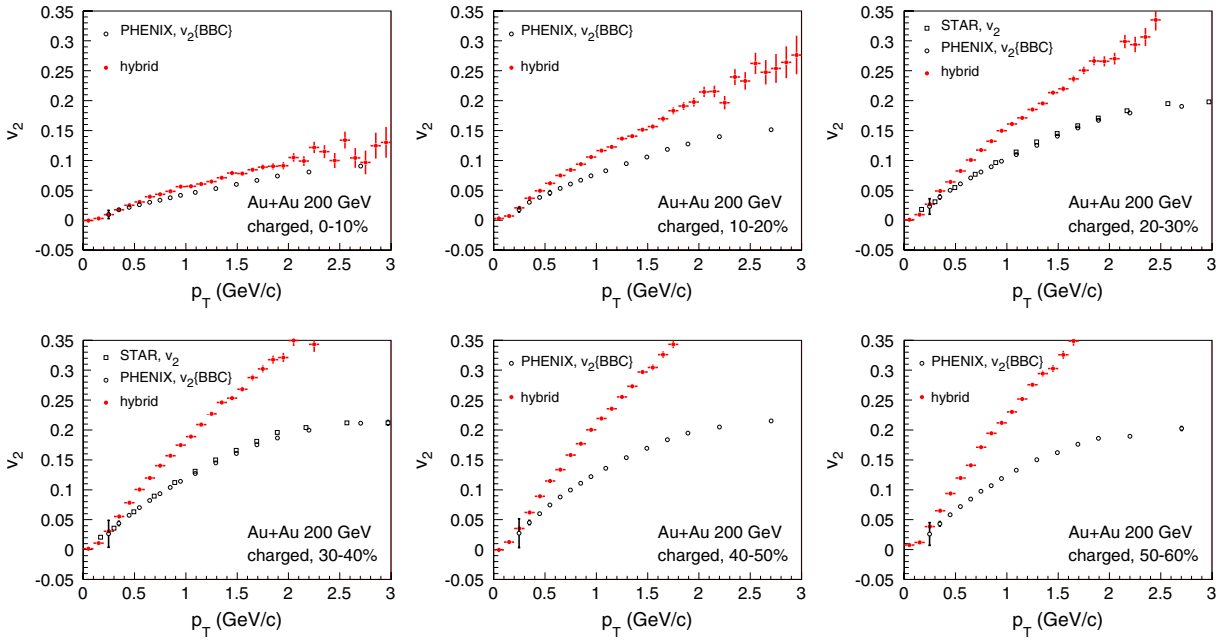

Fig. 35. The same as Fig. 33 but using the KLN model initial conditions.

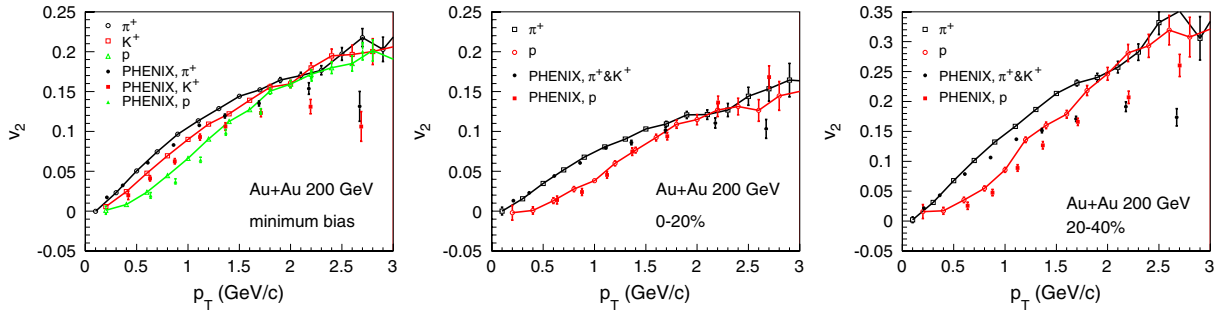

Fig. 36. Transverse momentum dependence of v_2 of identified hadrons with respect to participant plane using the Glauber model initial conditions are compared with the PHENIX data [6] in minimum bias (left), and in 0%–20% (middle) and 20%–40% (right) centralities.

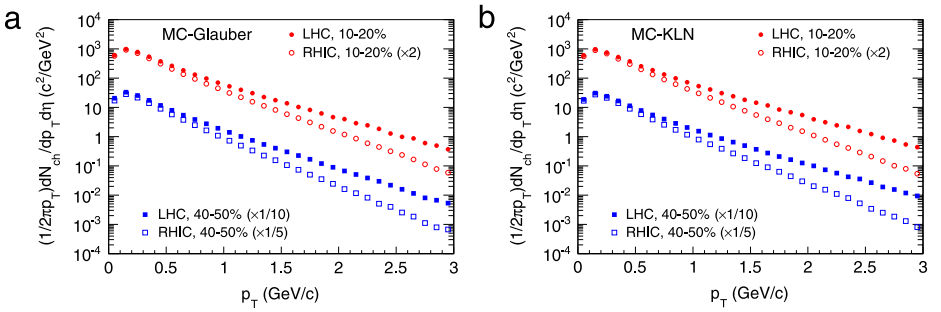

Fig. 37. Transverse momentum distribution of charged hadrons at 10%–20% (circles) and 40%–50% (squares) centralities in Pb + Pb collisions at $\sqrt{s_{NN}} = 2.76$ TeV (filled symbols) and in Au + Au collisions at $\sqrt{s_{NN}} = 200$ GeV (open symbols). Results were calculated using (a) the MC-Glauber initialisation and (b) the MC-KLN initialisation. For the sake of comparison and visibility, the spectra are scaled by 2, 1/10, and 1/5 for 10%–20% at RHIC, 40%–50% at LHC and 40%–50% at RHIC, respectively. Figures are from Ref. [54].

our calculations at RHIC were tuned to reproduce the p_T-spectra, this means that at LHC the spectra calculated using the MC-KLN initialisation are slightly flatter than those calculated using the MC-Glauber initialisation.

We compare the integrated v_2 for charged hadrons with respect to reaction plane with the ALICE [11] and STAR [80] $v_2\{4\}$ data in Fig. 38. When evaluating the integrated v_2, we take account of both transverse momentum and pseudorapidity

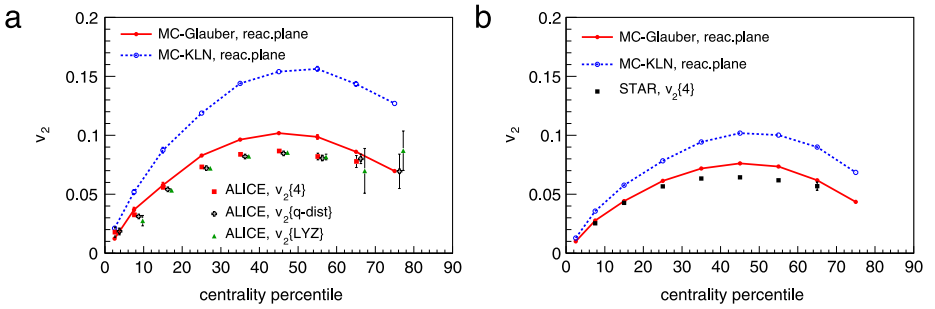

Fig. 38. Centrality dependence of v_2 for charged hadrons with respect to reaction plane (model "A") in Pb + Pb collisions at $\sqrt{s_{NN}} = 2.76$ TeV (left) and in Au + Au collisions at $\sqrt{s_{NN}} = 200$ GeV (right) is compared with the ALICE [11] ($0.2 < p_T < 5$ GeV/c and $|\eta| < 0.8$) and STAR $v_2\{4\}$ data ($0.15 < p_T < 2$ GeV/c and $|\eta| < 1$), respectively. Figures are from Ref. [54].

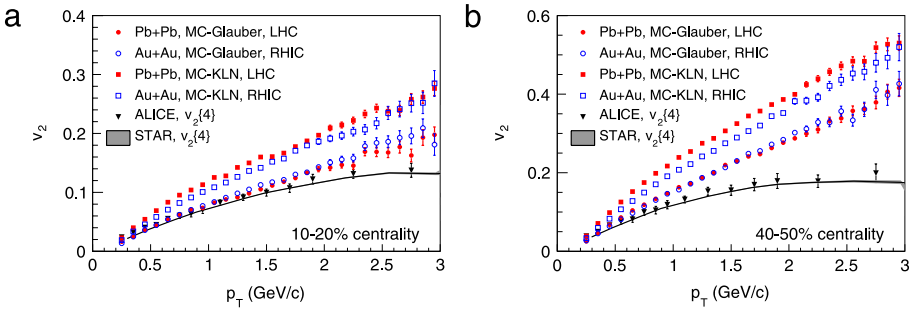

Fig. 39. Transverse momentum dependence of v_2 of charged hadrons with respect to reaction plane in $\sqrt{s_{NN}} = 2.76$ TeV Pb + Pb collisions in 10%–20% (left) and 40%–50% (right) centralities. Figures are from Ref. [54].

acceptance as done in the experiments, *i.e.* $0.2 < p_T < 5.0$ GeV/c and $|\eta| < 0.8$ for ALICE, and $0.15 < p_T < 2.0$ GeV/c and $|\eta| < 1.0$ for STAR. We want to emphasise that, not only the p_T cut [237], but also the pseudorapidity cut plays an important role in a consistent comparison with the data. Due to the Jacobian for the change of variables from rapidity y to pseudorapidity η, $v_2(y = 0) < v_2(\eta = 0)$ for positive elliptic flow [127].[12] In the case of the MC-Glauber (MC-KLN) initialisation in 40%–50% centrality, v_2 integrated over the whole p_T region is ∼14% (∼10%) larger at $\eta = 0$ than at $y = 0$.

When the MC-Glauber model is employed for initial profiles, centrality dependence of integrated v_2 from the hybrid approach almost agrees with both ALICE and STAR data. Since eccentricity fluctuation contributes little and negatively to $v_2\{4\}$ in a non-Gaussian distribution of eccentricity fluctuation [233,238], this indicates there is only little room for the QGP viscosity in the model calculation. On the other hand, apparent discrepancy between the results from the MC-KLN initialisation and the ALICE and STAR data means that viscous corrections during the hydrodynamic evolution are required.

From RHIC to LHC, the p_T-integrated $v_2(|\eta| < 0.8)$ increases by 24% and 25% in 10%–20% and 40%–50% centrality, respectively, in the MC-Glauber initialisation. On the other hand, in the MC-KLN initialisation, the increase reaches 42% and 44% in 10%–20% and 40%–50% centrality, respectively. Since eccentricity does not change significantly (at most ±6% in 40%–50% centrality) from RHIC to LHC as shown in Fig. 14(right), the significant increase of integrated v_2 must be attributed to a change in transverse dynamics.

Finally, we compare $v_2(p_T)$ of charged hadrons with ALICE [11] and STAR [80] data in 10%–20% (Fig. 39(left)) and 40%–50% (Fig. 39(right)) centrality. Interestingly, the data at LHC agrees with the data at RHIC within errors. The calculated $v_2(p_T)$ shows similar independence of collision energy when MC-Glauber initialisation is used, whereas MC-KLN initialisation leads to a slightly larger $v_2(p_T)$ at the larger energy. For MC-Glauber results, the fit to the data is fair below $p_T \sim 1.5$ GeV/c and $p_T \sim 0.8$ GeV/c momenta in the 10%–20% and 40%–50% centralities, respectively. Results from the MC-KLN initialisation at both energies are significantly larger than experimental data in the whole p_T region, which again indicates the necessity of viscous corrections in hydrodynamic evolution. For both initialisations the difference between the data and the calculated $v_2(p_T)$ is larger in more peripheral collisions. This too can be understood as an indication of viscosity, since the more peripheral the collision, the smaller the system and the more anisotropic its shape, and both of these qualities enhance the dissipative effects.

Due to the relationships among the p_T spectrum, p_T averaged v_2, and p_T differential $v_2(p_T)$, the flatter the p_T spectrum, the larger the v_2 even if $v_2(p_T)$ stays the same. It is also worth noticing that the steeper the slope of $v_2(p_T)$, the larger the

[12] Notice that even if one assumes the Bjorken scaling solution, one has to consider the pseudorapidity acceptance since $v_2(\eta)$ is not constant even if $v_2(y)$ is [127].

increase in v_2 for the same increase in mean p_T. This is the main reason why quite a similar increase of mean p_T for both MC-Glauber and MC-KLN initialisations leads to much larger increase of v_2 for MC-KLN than for MC-Glauber initialisation.

Song et al. calculated v_2 as a function of centrality and p_T using viscous hydrodynamics by employing almost the same initial conditions as we did [85,137,142,143] (see also Section 2.7). So it is interesting to see how much viscosity is required to reproduce these data in their analyses. As shown in Fig. 12, $\eta/s \sim 0.08$, which is almost identical to the conjectured minimum value [144], leads to reproduction of the v_2/ε data at RHIC in the MC-Glauber initialisation, whereas $\eta/s \sim 0.16$ in the MC-KLN initialisation [137]. Within the MC-KLN initialisation, they also calculated v_2 at the LHC energy and found that $\eta/s \sim 0.20$–0.24 is required to describe the data. This increase tendency of the specific shear viscosity with temperature is qualitatively consistent with expectation from results based on finite temperature QCD [239]. Temperature dependent shear viscosity was also discussed in [137,240,241]. It turned out that extracting the temperature dependence of η/s from the data is demanding, since at RHIC the value of η/s in the plasma phase does not affect the observed anisotropies. Only the minimum value reached in the transition region and viscosity in the hadronic phase do. At LHC the situation is better, but even there the hadronic viscosity affects the results as much as the plasma viscosity does [240,241].

4. Results from event-by-event hybrid simulations

We perform hydrodynamic simulations on an event-by-event basis and calculate observables using $\sim 10^5$ "minimum bias" events (events with $N_{\rm part} \geq 2$ in our theoretical definition) for each initial parameter set. In this section, we especially focus on higher order harmonics using several flow analysis methods. We first overview the flow analysis methods employed in this study. Using these methods, we analyse final particle distributions to obtain azimuthal anisotropy coefficients. Most of the results are obtained using the MC-KLN initialisation at the LHC energy. We also compare these results with the ones obtained using the MC-Glauber initialisation.

4.1. Event plane method

In the event plane method [63], the event plane is first determined using the anisotropy of the emitted particles. The event plane is in general defined by

$$n\Psi_n^{\rm EP} = \arg \sum_{j \neq i} \omega_j e^{in\phi_j}, \tag{59}$$

where ω_i is an weight and ϕ_i is an azimuthal angle for each particle. The sum is taken over an ensemble of particles which do not coincide with particles which v_n one wants to obtain.

In fact, there have been various event plane methods for the different detector setups. For example, one can randomly divide measured particles in a pseudorapidity region into two subgroups. Then when one wants to obtain flow parameters for particles in one subgroup, particles in the other subgroup are used to determine the event plane. One can also choose two groups of particles separated in pseudorapidity to determine the event plane, which can eliminate short range correlations.

In what follows, we demonstrate the flow analysis according to the event plane method by the ATLAS Collaboration [12].[13] In this analysis method, the event planes are determined using particles in the two regions, A: $3.2 < \eta < 4.8$ and B: $-4.8 < \eta < -3.2$. ω_i is taken as transverse mass m_T^i for each particle. When the harmonics v_n is calculated in positive (negative) rapidity region, particles in the region B (the region A) are used to determine the event plane $\Psi_n^{\rm B}$ ($\Psi_n^{\rm A}$) to avoid the non-flow effect from the autocorrelation. Centrality is defined using the total transverse energy of charged particles deposited in these rapidity regions, as prescribed by the ATLAS Collaboration [12].

In the "η-subevent" method, non-flow effects can be eliminated at midrapidity when event plane angle is determined away from midrapidity. On the other hand, one naively anticipates the correlation between the event plane angle determined in the large rapidity region and the one in the whole rapidity region gets weaker [134]. As will be shown, this can be corrected by taking account of event plane resolution in the "η-subevent" method.

Event plane angles for the n-th harmonics is thus calculated using the particles in the regions A and B as

$$n\Psi_n^{\rm A} = \arg \sum_{\rm A} m_T^i e^{in\phi_i}, \tag{60}$$

$$n\Psi_n^{\rm B} = \arg \sum_{\rm B} m_T^i e^{in\phi_i}. \tag{61}$$

Using these angles, one obtains n-th harmonics

$$v_n^{\rm obs} = \frac{1}{\langle N^{\rm P} + N^{\rm N} \rangle} \left\langle \sum_{\rm P} \cos n(\phi_i - \Psi_n^{\rm B}) + \sum_{\rm N} \cos n(\phi_i - \Psi_n^{\rm A}) \right\rangle \tag{62}$$

[13] The method employed here is categorised in the event plane method in a broad sense. However, this is sometimes called the "η-subevent" method.

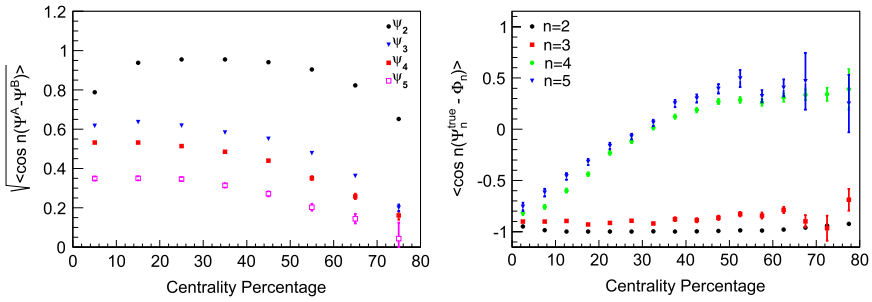

Fig. 40. (Left) Resolution parameter defined in Eq. (67) for $n = 2, 3, 4$ and 5 as a function of centrality. (Right) Correlation $\langle\cos n(\Psi_n^{\rm true} - \Phi_n)\rangle$ between the true event plane and the participant plane as a function of centrality in Pb + Pb collisions at $\sqrt{s_{NN}} = 2.76$ TeV.

where $\langle\cdots\rangle$ denotes the event average. $N^{\rm P}$ ($N^{\rm N}$) is the number of particles in the positive (negative) rapidity region. Since the finite number of measured particles limits resolution in estimating the event plane angle Ψ_n, one has to consider the so-called resolution parameter $\mathcal{R}_n$

$$\mathcal{R}_n = \langle\cos n(\Psi_n - \Psi_n^{\rm true})\rangle, \tag{63}$$

where Ψ_n is the event angle estimated using the measured particle and $\Psi_n^{\rm true}$ is an ideal event plane angle corresponding to the infinite number of measured particles. In this event plane method, the resolution factor can be estimated as

$$\begin{aligned}\langle\cos n(\Psi_n^{\rm A} - \Psi_n^{\rm B})\rangle &= \langle\cos n(\Psi_n^{\rm A} - \Psi_n^{\rm B})\rangle \\ &= \langle\cos n(\Psi_n^{\rm A} - \Psi_n^{\rm true} + \Psi_n^{\rm true} - \Psi_n^{\rm B})\rangle \\ &= \langle\cos n(\Psi_n^{\rm A} - \Psi_n^{\rm true})\cos n(\Psi_n^{\rm B} - \Psi_n^{\rm true})\rangle - \langle\sin n(\Psi_n^{\rm A} - \Psi_n^{\rm true})\sin n(\Psi_n^{\rm B} - \Psi_n^{\rm true})\rangle \\ &= \langle\cos n(\Psi_n^{\rm A} - \Psi_n^{\rm true})\rangle\langle\cos n(\Psi_n^{\rm B} - \Psi_n^{\rm true})\rangle \\ &= \mathcal{R}_n^2. \end{aligned} \tag{64}$$

Here we have assumed that the two groups are symmetrically located with respect to midrapidity like the pseudorapidity regions A and B so that multiplicities in the two groups are almost equal and independent in a sense that two-particle correlation function between a particle from region A and the one from region B can be factorised into two one-particle distribution functions. Thus,

$$\langle\cos n(\Psi_n^{\rm A} - \Psi_n^{\rm true})\rangle = \langle\cos n(\Psi_n^{\rm B} - \Psi_n^{\rm true})\rangle \equiv \mathcal{R}_n. \tag{65}$$

Thus the anisotropic parameters using the event plane method become

$$v_n\{\rm EP\} = \frac{v_n^{\rm obs}}{\mathcal{R}_n}, \tag{66}$$

$$\mathcal{R}_n = \sqrt{\langle\cos n\left(\Psi_n^{\rm A} - \Psi_n^{\rm B}\right)\rangle}. \tag{67}$$

Fig. 40(left) shows the resolution parameter $\mathcal{R}_n$ ($n = 2, 3, 4$ and 5) as a function of centrality. Event plane resolution for the second harmonics reaches almost unity in mid-central collisions (20–30%) and is relatively better than the others as expected from the almond-like geometry on average. The other event plane resolutions become worse as decreasing multiplicity and increasing the order n. To understand the origin of the event plane, we also calculate correlation of angles between the orientation angle Φ_n (see Eg. (37)) and the true event plane

$$\begin{aligned}\mathcal{C}_n(\Psi_n^{\rm true}, \Phi_n) &= \langle\cos n(\Psi_n^{\rm true} - \Phi_n)\rangle \\ &= \frac{\langle\cos n(\Psi_n^{\rm A/B} - \Phi_n)\rangle}{\mathcal{R}_n}. \end{aligned} \tag{68}$$

Since the number of produced particles is finite, the resolution parameter to correct $\Psi_n^{A/B}$ plays again an essential role in evaluating $\mathcal{C}_n$. When the anisotropic flow is generated by anisotropic pressure gradient in the transverse plane, the correlation becomes ~ -1: In the case of positive elliptic flow generated from a conventional smooth almond-like profile elongated in y direction, $\Psi_2^{\rm true} \sim 0$ and $\Phi_2 \sim \pi/2$ and, consequently, $\mathcal{C}_2 \sim -1$. Fig. 40(right) shows $\mathcal{C}_n$ ($n = 2, 3, 4$ and 5) as a function of centrality. $\mathcal{C}_n$ for $n = 2$ and 3 are close to -1. So one can interpret anisotropic flow v_n ($n = 2$ or 3) as generated by the corresponding anisotropy ε_n of the pressure gradient. While $\mathcal{C}_4$ and $\mathcal{C}_5$ start from -1 in very central collisions, increase with centrality percentile and even become positive above 30% centrality. This indicates the possibility of having finite v_n owing to $\varepsilon_m (m \neq n)$.

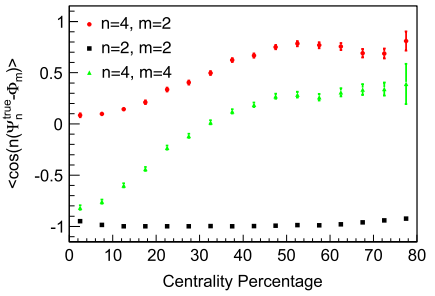

Fig. 41. Mixed correlation between the true event plane $\Psi_n^{\rm true}$ and the orientation angle Φ_m as a function of centrality in Pb + Pb collisions at $\sqrt{s_{NN}} = 2.76$ TeV.

To further investigate the origin of the event plane, we also calculate mixed correlations

$$\mathcal{C}_{nm}(\Psi_n^{\rm true}, \Phi_m) = \langle \cos n(\Psi_n^{\rm true} - \Phi_m)\rangle,$$
$$\mathcal{C}_{nn} = \mathcal{C}_n. \tag{69}$$

Fig. 41 shows $\mathcal{C}_{42}$ together with $\mathcal{C}_2$ and $\mathcal{C}_4$ in Pb + Pb collisions at $\sqrt{s_{NN}} = 2.76$ TeV. If v_4 is generated solely by ε_2, $|\Psi_4 - \Phi_2|$ is expected to be either 0 or $\pi/4$ due to symmetry in the transverse plane and, consequently, $\mathcal{C}_{42} = 1$ or -1. In central collisions where the reaction zone is almost cylindrical on average, there is almost no correlation between Ψ_4 and Φ_2. However, the correlation between them increases towards unity as increasing centrality percentage, which indicates $\Psi_4 \approx \Phi_2 \pm n\pi/2$ (n: integer) and v_4 is partly generated by ε_2 like positive elliptic flow in non-central collisions [133,216,242].

Relations between initial geometry fluctuation and final anisotropic flow were discussed in Ref. [133]. They found that v_4 decreases with increasing ε_2 and changes its sign from positive to negative (see Fig. 17 in Ref. [133]). The behaviour is quite similar to our finding that the centrality dependence of $\mathcal{C}_{42}$ changes also its sign. Distributions of $\Psi_n - \Phi_n$ for $n = 4$ and 5 at the RHIC energy were investigated in Fig. 8 in Ref. [216]. Contrary to the cases for $n = 2$ and 3, the distributions for $n = 4$ and 5 have a peak at $\Psi_n - \Phi_n = 0$ only in central collisions. Peak structure gradually disappears as moving to peripheral collisions and eventually another peak appears at $\Psi_n - \Phi_n = \pi/n$ in the peripheral collisions (50–60% centrality). These results also suggest that v_ns at least $n = 4$ and 5 are generated by other order of initial geometry ε_m ($m \neq n$).

Before showing detailed results from event-by-event hydrodynamic simulations, we make two remarks here: Since the event plane is often determined using particles in forward and backward rapidity regions (also known as "η-subevent method"), full three dimensional dynamical simulations are essential if one wants to do the flow analysis in the same way than in experiments. For example, the PHENIX Collaboration at RHIC utilises the Beam Beam Counter (BBC) or the reaction plane detector (RxNP) in forward and backward rapidity regions to determine event planes. If one assumes boost invariance in dynamical calculations, one cannot perform this kind of flow analysis exactly.

Second, the effect of experimental event plane resolution cannot be properly evaluated unless one samples a finite number of particles at particlisation. The Cooper–Frye formula [86] has been conventionally used to calculate particle spectra in hydrodynamic calculations, but it gives smooth and continuous function of momentum distributions. This corresponds to the N times over-sampling of particles from a fluid element with $N \to \infty$ limit, which is, however, not adequate if event-by-event hydrodynamic simulations are supposed to describe actual events.

4.2. Multi-particle cumulants

In the previous subsection, we described the method to calculate anisotropic parameters with respect to the event plane. In this subsection, we discuss how to calculate anisotropic parameter using the particle ensemble itself, namely, the multi-particle cumulant method [64,65].

We first define a $2p$-particle correlation to calculate the n-th order of higher harmonics as

$$c_n\{2p\} = \langle \exp[in(\phi_1 + \phi_2 + \cdots \phi_p - \phi_{p+1} - \cdots - \phi_{2p})]\rangle \tag{70}$$

where ϕ_i is azimuthal angle of the i-th particle under consideration. In this subsection, $\langle\cdots\rangle$ means an average taken in two steps: First, one averages over all possible permutations of p particles in the same event, then one averages over all events. For example, two-particle correlations can be written as $c_n\{2\} = \langle e^{in(\phi_1-\phi_2)}\rangle$.

We next define the corresponding cumulant. Correlations among $2p$ particles can be in general decomposed into a sum of correlations among smaller number of particles and cumulants. The simplest example is two-particle cumulant

$$\begin{aligned} c_n\{2\} &= d_n\{2\} + \langle e^{in\phi_1}\rangle\langle e^{-in\phi_2}\rangle \\ &= \langle e^{in(\phi_1-\phi_2)}\rangle. \end{aligned} \tag{71}$$

Due to symmetry, a term $\langle e^{in\phi_1}\rangle$ should vanish. As we see, a two-particle cumulant reduces to the corresponding two-particle correlation. This quantity contains correlation from collective flow as well as the so-called non-flow effects such as two-body decays of resonance particles. The next non-trivial and important example is four-particle cumulant:

$$\begin{aligned} c_n\{4\} &= \langle \exp[in(\phi_1+\phi_2-\phi_3-\phi_4)]\rangle \\ &= \langle e^{in(\phi_1-\phi_3)}\rangle\langle e^{in(\phi_2-\phi_4)}\rangle + \langle e^{in(\phi_1-\phi_4)}\rangle\langle e^{in(\phi_2-\phi_3)}\rangle + d_n\{4\} \\ &= 2c_n\{2\}^2 + d_n\{4\}. \end{aligned} \tag{72}$$

Although $d_n\{4\}$ still contains non-flow effects of correlations among four particles, this does not contain non-flow effects from two-particle correlations and, consequently, is expected to contain much information about the anisotropic flow. In fact, it was shown in Ref. [65] that these cumulants are related with higher order anisotropic flow. So one can define higher order anisotropic parameter using $2p$-particle cumulants as

$$v_n\{2\}^2 = d_n\{2\}, \tag{73}$$

$$v_n\{4\}^4 = -d_n\{4\}. \tag{74}$$

Since this method requires many particles to take correlations/cumulates, the statistical errors tend to be large. Even 10^5 events are not enough: It happens that error bars are too large to show the results in our statistics, which indicates the necessity of massive numerical simulations.

In the actual calculations, we evaluate the above correlations as follows: We first calculate the following two quantities:

$$q_n = \frac{1}{\sqrt{M}}\sum_{i=1}^{M} e^{in\phi_i}, \tag{75}$$

$$u_n = \frac{1}{M}\sum_{i=1}^{M} e^{in\phi_i}. \tag{76}$$

q_n is a flow vector and u_n is the one with different normalisation. When the non-flow effects can be neglected, $v_n \approx \sqrt{u_n^* u_n}$. In the case of $2p$-particle correlations, one needs to average over all possible permutations excluding self-correlation terms and take a sum such as

$$\begin{aligned} \sum_{(i,j)} &= \sum_{i=1}^{M}\sum_{j=1}^{M}(1-\delta_{ij}) \\ &= \sum_{i=1}^{M}\sum_{j=1}^{M} - \sum_{i=j=1}^{M}, \end{aligned} \tag{77}$$

$$\begin{aligned} \sum_{(i,j,k)} &= \sum_{(i,j)}\sum_{k=1}^{M}(1-\delta_{ki}-\delta_{kj}) \\ &= \sum_{i}^{M}\sum_{j}^{M}\sum_{k}^{M} - \sum_{i=j=1}^{M}\sum_{k=1}^{M} - \sum_{j=k=1}^{M}\sum_{i=1}^{M} - \sum_{k=i=1}^{M}\sum_{j=1}^{M} + 2\sum_{i=j=k=1}^{M}, \end{aligned} \tag{78}$$

$$\sum_{(i,j,k,l)} = \sum_{(i,j,k)}\sum_{l=1}^{M}(1-\delta_{li}-\delta_{lj}-\delta_{lk}). \tag{79}$$

In this way, correlation functions reduce to [94]

$$\begin{aligned} c_n\{2\} &= \frac{\left\langle \sum_{i=1}^{M} e^{in\phi_i}\sum_{j=1}^{M} e^{in\phi_j} - \sum_{i=j=1}^{M} e^{in(\phi_i-\phi_j)}\right\rangle}{\langle M(M-1)\rangle} \\ &= \frac{\langle |u_n|^2 M^2 - M\rangle}{\langle M^2 - M\rangle}, \end{aligned} \tag{80}$$

$$\begin{aligned} c_n\{4\} &= \frac{\langle U_4 M^4 - 6U_3 M^3 + 11U_2 M^2 - 6M\rangle}{\langle M(M-1)(M-2)(M-3)\rangle}, \\ &= \frac{\langle U_4 M^4 - 6U_3 M^3 + 11U_2 M^2 - 6M\rangle}{\langle M^4 - 6M^3 + 11M^2 - 6M\rangle}, \end{aligned} \tag{81}$$

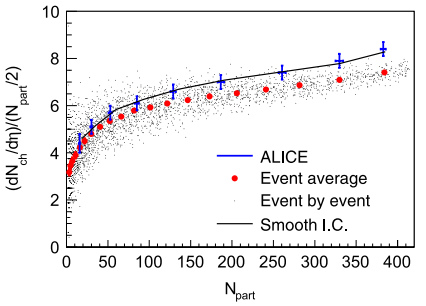

Fig. 42. $(dN_{\rm ch}/d\eta)/(N_{\rm part}/2)$ in $|\eta| < 0.8$ as a function of $N_{\rm part}$ in Pb + Pb collisions at $\sqrt{s_{NN}} = 2.76$ TeV for each event and for events averaged over every 5% centrality. Here we use impact parameter to categorise the centrality for simplicity and plot results at $\langle N_{\rm part}\rangle$ for each centrality. To exhibit how this quantity distributes event-by-event, results from 3000 minimum bias events are shown. Result from the smooth initial condition with the same initial parameter set is also shown in thin solid line. Experimental data are from ALICE Collaboration [183].

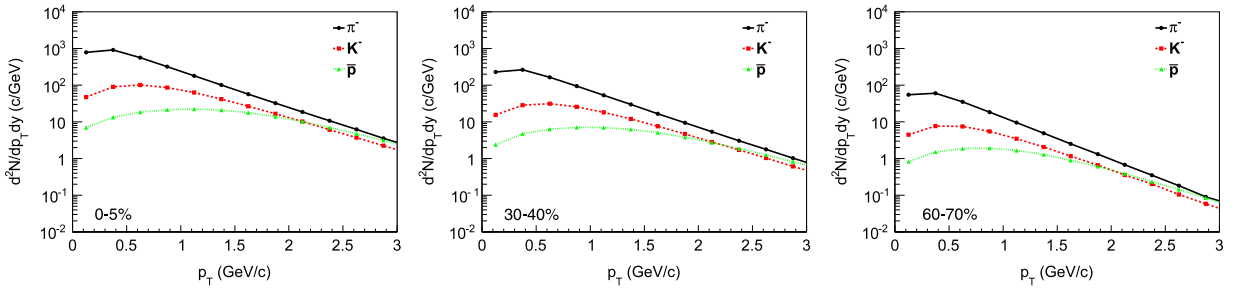

Fig. 43. p_T distribution of identified hadrons at midrapidity in Pb + Pb collisions at $\sqrt{s_{NN}} = 2.76$ TeV at 0–5% (left), 30–40% (middle) and 60–70% (right) centralities.

where

$$U_4 = |u_n|^4, \tag{82}$$

$$6U_3 = 4|u_n|^2 + u_{2n}^* u_n^2 + u_{2n} u_n^{*2}, \tag{83}$$

$$11U_2 = 8|u_n|^2 + |u_{2n}|^2 + 2. \tag{84}$$

4.3. Results

First, in Fig. 42, we show $(dN_{\rm ch}/d\eta)/(N_{\rm part}/2)$ as a function of $N_{\rm part}$ from event-by-event hydrodynamic simulations employing MC-KLN initialisation and compare them with ALICE data [183]. For comparison, we average over these events at every 5% centrality. Although we used the same, adjusted parameter set as in the smooth initial conditions using the MC-KLN initialisation which reproduces the ALICE data reasonably well, results are systematically smaller than the data, in particular, in central events. In this paper, we do not try to fine-tune initial parameters. It would be interesting to see how the effects of the fluctuations of the gluon production itself would change this behaviour. In principle these fluctuations can be included using the negative binomial distribution (N.B.D.) [133,166,167,175], but since the rapidity dependence of the required N.B.D. is not known, it is not clear how to implement these fluctuations in a fully three dimensional calculations.

In Fig. 43, p_T distributions of π^-, K^- and $\bar{p}$ using the MC-KLN initialisation in Pb + Pb collisions at the LHC energy are shown at 0–5%, 30–40% and 60–70% centralities. Antiproton yield becomes comparable with negative pion yields at $p_T \sim 3$ GeV/c in all these results, which is consistent with the preliminary ALICE data [69]. Thus the switching temperature $T_{\rm sw} = 155$ MeV, which affects both particles yields and the slopes of the p_T spectra, and was adjusted to reproduce particle ratios of identified hadrons at RHIC, works reasonably well at the LHC energy too. Detailed comparison of these results with the data would give more precise information about the switching temperature.

We compare the results of v_2 from event-by-event hydrodynamic simulations with those from hydrodynamic simulations with conventional, smooth initial conditions. Fig. 44(left) shows centrality dependence of p_T-integrated v_2 $(0 < \eta < 1)$ of charged hadrons in Pb + Pb collisions at $\sqrt{s_{NN}} = 2.76$ TeV using MC-KLN initialisation. Although the difference between $v_2\{\rm EP\}$ and v_2 from event-averaged initial conditions with shift of the centre of mass and rotation of participant plane discussed in the previous section is hardly seen in central to semi-central collisions (0%–40%), the two results deviate from each other above ∼40%: $v_2\{\rm RP\}$, which is v_2 with respect to the reaction plane in event-by-event simulations (reaction plane method), is slightly smaller than v_2 from event averaged initial conditions and the difference

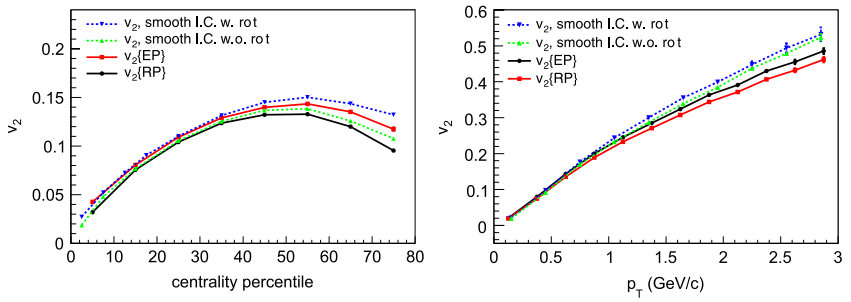

Fig. 44. Centrality (left) and transverse momentum (right) dependences of v_2 of charged hadrons in Pb + Pb collisions at $\sqrt{s_{NN}} = 2.76$ TeV using smooth initial conditions with (inverse triangle) or without (triangle) shifting the centre of mass and rotation to match participant plane angle. These are compared with $v_2\{\mathrm{EP}\}$ (square) and $v_2\{\mathrm{RP}\}$ (circle) (see the text). Transverse momentum dependence is shown at 40%–50% centrality.

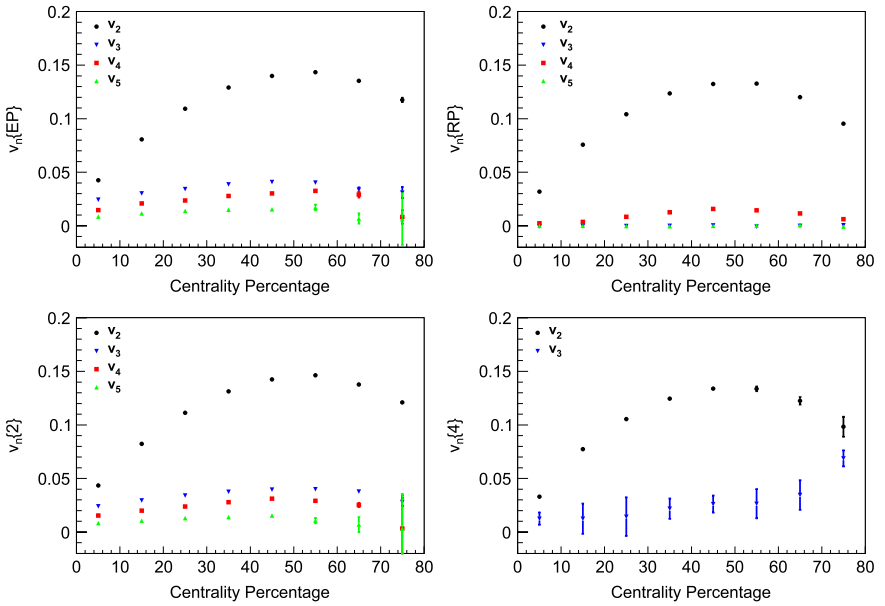

Fig. 45. v_n using the event plane method (upper left), v_n using the reaction plane method (upper right) v_n using the two particle cumulant method (lower right) and v_n using the four particle cumulant method (lower right). $v_4\{4\}$ and $v_5\{5\}$ are omitted due to less statistics.

increases with increasing centrality percentile. This is also the case for the difference between $v_2\{\mathrm{RP}\}$ and v_2 from event-averaged initial conditions without shift of the centre of mass or rotation of participant plane. Fig. 44(right) shows p_T dependence of v_2 for charged hadrons in the same collision system at 40%–50% centrality. In both cases, there is almost no difference between event-by-event simulations and simulations with event-averaged initial conditions in the low p_T region. However, results deviate from each other gradually with increasing p_T above ∼1 GeV/c [207]. From a point of view of conventional hydrodynamic simulations with smooth initial conditions, event-by-event simulations mimic shear viscous effects since shear viscosity reduces p_T-integrated v_2 and v_2 at high p_T [243].

Fig. 45 shows event anisotropies v_n ($n = 2, 3, 4$ and 5) by various flow analysis methods employed in this study. Centrality dependences of $v_n\{\mathrm{EP}\}$ are almost identical to those of $v_n\{2\}$. $v_3\{\mathrm{RP}\}$ and $v_5\{\mathrm{RP}\}$ vanish as they should. $v_4\{\mathrm{RP}\}$ is non-zero only in mid-central collisions (20–70% centrality). Since v_n using the four particle cumulant method demands higher statistics, we only show $v_2\{4\}$ and $v_3\{4\}$. Although $v_3\{4\}$ has large error bars, it seems to increase with increasing centrality percentage. This is contrary to $v_3\{\mathrm{EP}\}$ and $v_3\{2\}$ which first increase up to 50–60% centrality, but begin to decrease in more peripheral collisions. This emphasises the importance of employing the same flow analysis method both in the theory calculations and in the experimental data analysis.

Fig. 46(left) shows the centrality dependence of v_2 compared with the ALICE data [11]. It has been known that ideal hydrodynamics with the CGC based initial state overshoots the data by 50–60%. The deviation could have been understood as viscous effects, which we do not discuss in this paper. It should be noted that the data do not contain charged hadrons below $p_T = 0.15$ GeV/c but that the hydrodynamic results do. If we took account of momentum cut of the ALICE setup, the calculated results would have become larger. Ratios of v_2 to $v_2\{\mathrm{EP}\}$ are shown to see the difference among the various flow analysis methods in Fig. 46(right). $v_2\{2\}$ is almost identical to $v_2\{\mathrm{EP}\}$. On the other hand, $v_2\{\mathrm{RP}\}$ almost traces $v_2\{4\}$. In central (0%–10%) and peripheral (60%–80%) collisions, $v_2\{\mathrm{RP}\}$ and $v_2\{4\}$ are 10%–20% smaller than $v_2\{\mathrm{EP}\}$ and $v_2\{2\}$, which

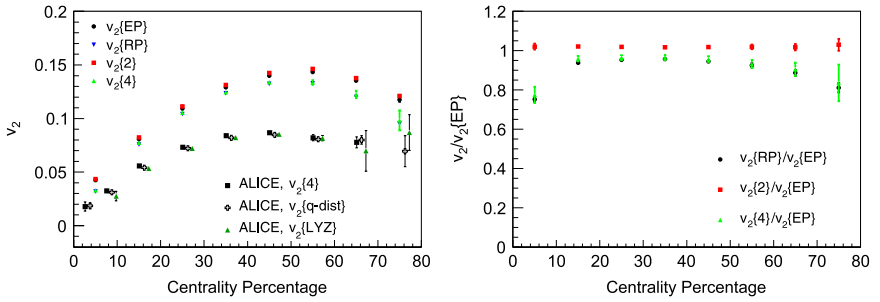

Fig. 46. (Left) Centrality dependence of v_2 using the event plane method, the reaction plane method, the two particle cumulant and the four particle cumulant in MC-KLN initialisation compared with the ALICE data [11]. (Right) Ratio of v_2 to $v_2\{\mathrm{EP}\}$ as a function of centrality.

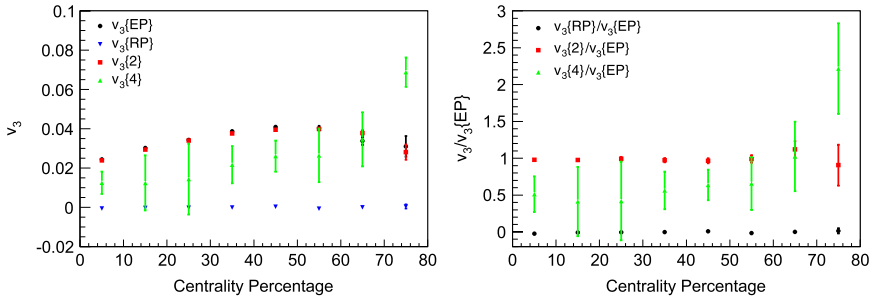

Fig. 47. (Left) Centrality dependence of v_3 using the event plane method, the reaction plane method, the two particle cumulant and the four particle cumulant. (Right) Ratio of v_3 to $v_3\{\mathrm{EP}\}$ as a function of centrality.

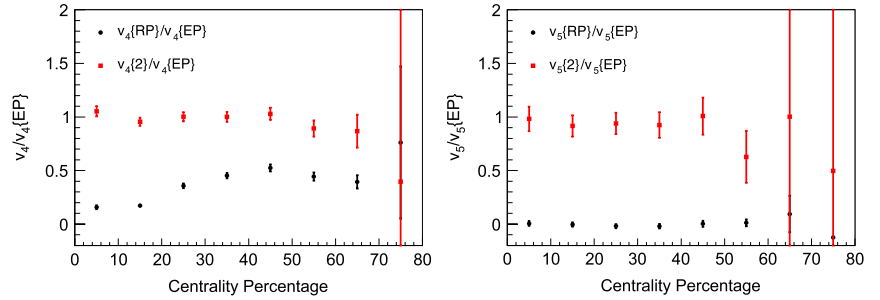

Fig. 48. (Left) Ratio of v_4 to $v_4\{\mathrm{EP}\}$ as a function of centrality. (Right) Ratio of v_5 to $v_5\{\mathrm{EP}\}$ as a function of centrality.

can be understood as a consequence of eccentricity fluctuations shown in Fig. 14. On the other hand, the difference between $v_2\{\mathrm{EP}\}$ and $v_2\{\mathrm{RP}\}$ is ∼5% in semi-central collisions. Correspondences of between $v_2\{2\}$ and $v_2\{\mathrm{EP}\}$ and between $v_2\{4\}$ and $v_2\{\mathrm{RP}\}$ are also discussed using UrQMD in Ref. [244].

Fig. 47 shows centrality dependence of v_3 (left) and its ratio to $v_3\{\mathrm{EP}\}$ (right). If odd harmonics are generated solely by fluctuation in initial transverse profiles, $v_3\{\mathrm{RP}\}$ should vanish since the initial fluctuation does not correlate with the reaction plane. This is, in fact, seen in Fig. 47. As seen in v_2, $v_3\{\mathrm{EP}\}$ is almost identical to $v_3\{2\}$. Due to poor statistics, $v_3\{4\}$ has large errors. Nevertheless, it seems to be finite and smaller than $v_3\{\mathrm{EP}\}$ and $v_3\{2\}$ up to ∼60% centrality: $v_3\{4\}$ is roughly half of $v_3\{2\}$ and $v_3\{\mathrm{EP}\}$ [193,194]. Ratios of v_3 to $v_3\{\mathrm{EP}\}$ as functions of centrality are shown in Fig. 47 to see the dependence of v_3 on flow analysis methods more clearly. It would be interesting to gain more statistics to confirm whether $v_3\{4\}$ differs from the other v_3.

Fig. 48 shows centrality dependence of ratios of fourth (left) and fifth (right) harmonics. Due to poor statistics, harmonics using the four particle cumulant method are omitted. Although $v_4\{2\}$ and $v_5\{2\}$ have large error bars, they seem to agree with the harmonics evaluated using the event plane method, in the same way $v_2\{2\}$ and $v_3\{2\}$ do. $v_4\{\mathrm{RP}\}$ is finite, while $v_5\{\mathrm{RP}\}$ vanishes as already seen in Fig. 45.

Figs. 49–51 show pseudorapidity dependence of higher order harmonics in 0%–10%, 40%–50% and 70%–80% centrality, respectively. The second harmonics v_2, which are shown in the left panels, always have a maximum at midrapidity and decrease as moving away from midrapidity although ε_2 is almost constant as a function of η_s. This triangular shape was also measured at the RHIC energy. As we discussed in Section 2.5 the rapidity dependence is easy to understand as a consequence of the space–time rapidity dependence of the initial energy density even if the initial eccentricity hardly depends on η_s

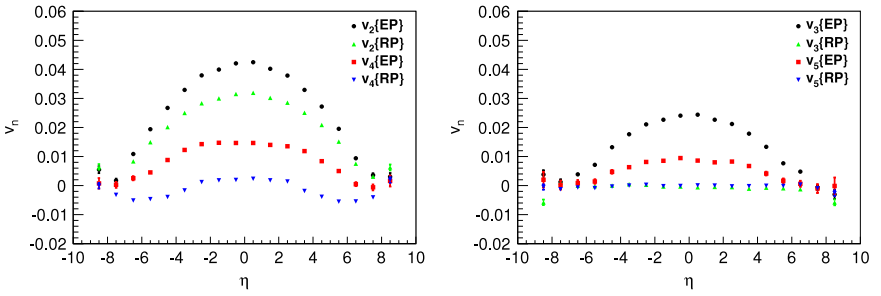

Fig. 49. Pseudorapidity dependence of v_2 and v_4 (left) and v_3 and v_5 (right) at 0%–10% centrality. Harmonics evaluated using the event plane method are compared with those evaluated with respect to the reaction plane.

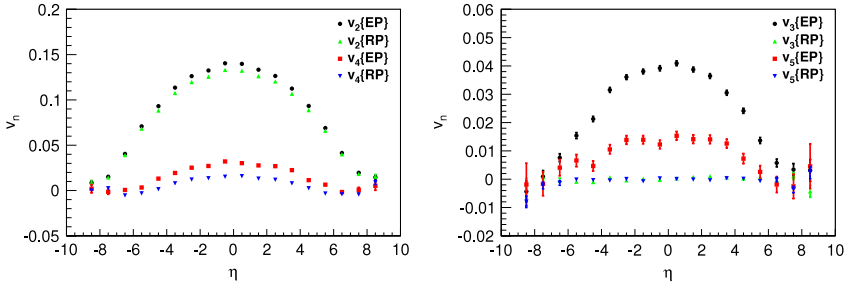

Fig. 50. The same as Fig. 49 but at 40%–50% centrality.

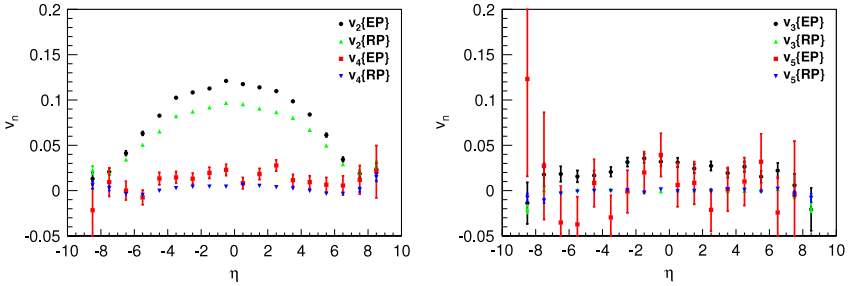

Fig. 51. The same as Fig. 49 but at 70%–80% centrality.

(Fig. 18). The larger the initial density, the longer the lifetime of the low viscosity QGP phase where v_2 is built up much more efficiently than in the highly dissipative hadronic phase, see Fig. 7 and related discussion on page 15.

Difference between $v_2\{\mathrm{EP}\}$ and $v_2\{\mathrm{RP}\}$ is relatively large in central (0%–10%) and peripheral (70%–80%) collisions, whereas the difference is very small in semi-central collisions (30%–40%). This difference at midrapidity was already shown in Fig. 46, but it persists up to $|\ \eta\ | \sim 5$. $v_4\{\mathrm{EP}\}$ also depends on η even if $\varepsilon_4\{\mathrm{PP}\}$ is almost independent of η_s as shown in Fig. 18.

Odd harmonics ($n = 3$ and 5) shown in the right panel are finite near midrapidity when event plane method is used to evaluate them, whereas they vanish when the reaction plane method is used. The $v_3\{\mathrm{EP}\}$ and $v_5\{\mathrm{EP}\}$ have a broad peak at midrapidity, decrease as moving away from midrapidity and eventually vanish near the beam rapidity. Note that v_5 has large error bars in the 70–80% centrality due to small multiplicity. It should be noted that all $v_n\{\mathrm{EP}\}(\eta)$ have almost no boost invariant region which is in good contrast to $\varepsilon_n(\eta_s)$ shown in Fig. 18. As mentioned, this can be understood as the space–time rapidity dependence of the lifetime of the QGP fluid.

Transverse momentum dependences of v_2 evaluated using the four methods described in this study are compared with the ALICE $v_2\{4\}$ data [11] at 40%–50% centrality in Pb + Pb collisions at $\sqrt{s_{NN}} = 2.76$ TeV in Fig. 52. Up to $p_T \sim 1.5$ GeV/c where, in the M-particle cumulant methods, at least M particles are binned in all events in this centrality, the difference among the four methods is very small. Above this, the difference between $v_2\{\mathrm{EP}\}$ and $v_2\{\mathrm{RP}\}$ is visible but still not so significant.

Transverse momentum dependence of v_2 using the event plane method is compared with the ATLAS v_2 data [12] in Pb + Pb central (0%–10%), semi-central (40%–50%) and peripheral (70%–80%) collisions in $0 <|\ \eta\ |< 1$ (top), $1 <|\ \eta\ |< 2$ (middle) and $2 <|\ \eta\ |< 2.5$ (bottom) at $\sqrt{s_{NN}} = 2.76$ TeV in Fig. 53. We emphasise here that we employ the same flow analysis method as the ATLAS Collaboration [12]. v_2 from event-by-event ideal hydrodynamic simulations overshoots the ATLAS data at all centralities regardless of the pseudorapidity regions.

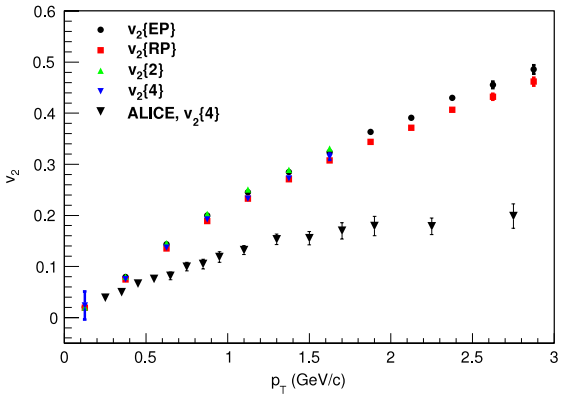

Fig. 52. Transverse momentum dependence of v_2 using the event plane method, the reaction plane method, the two particle cumulant and the four particle cumulant calculated using MC-KLN initialisation compared with the ALICE $v_2\{4\}$ data at 40%–50% centrality [11]. Due to the lack of statistics, results are shown up to 1.625 GeV/c for the two particle cumulant and the four particle cumulant methods.

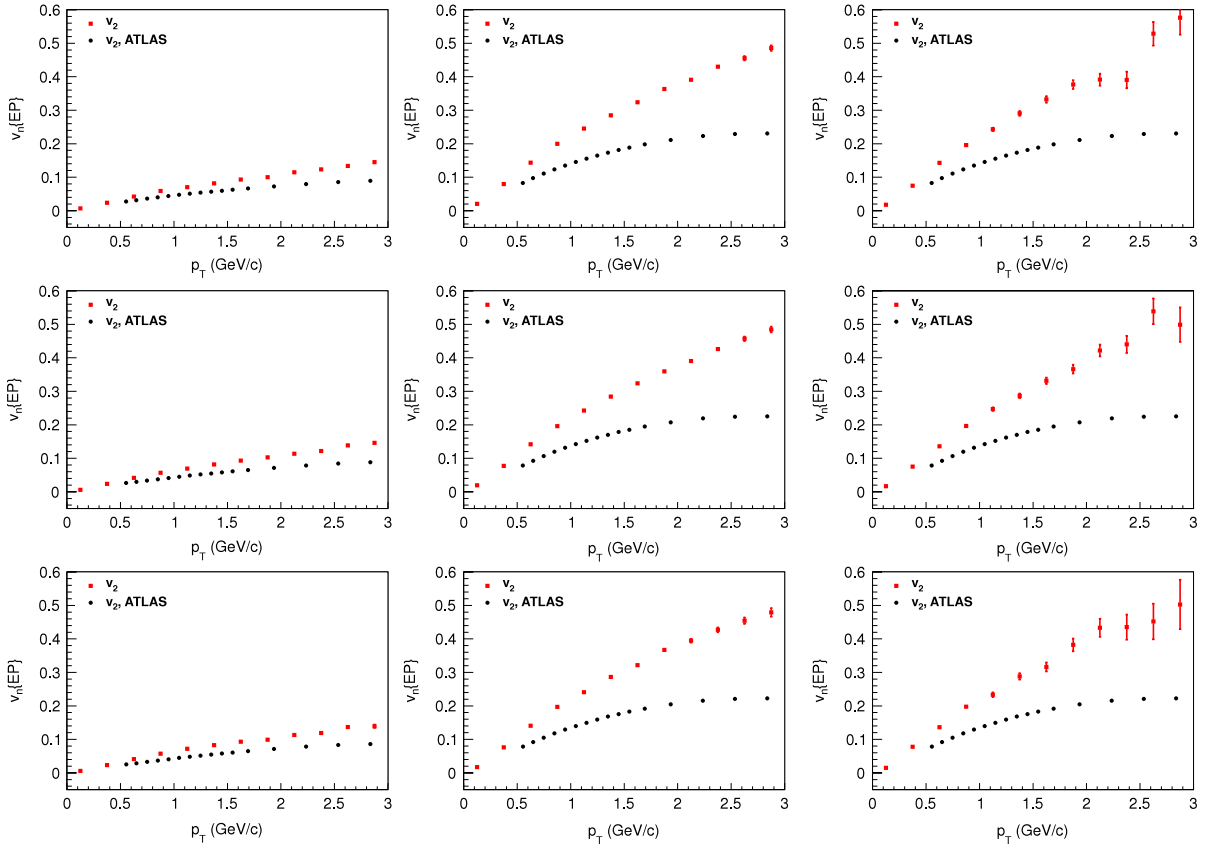

Fig. 53. Transverse momentum dependence of v_2 of charged hadrons in $0 <|\eta|< 1$ (top), $1 <|\eta|< 2$ (middle) and $2 <|\eta|< 2.5$ (bottom) using the event plane method, and compared with the ATLAS data [12] at 0%–10% (left), 40%–50% (middle) and 70%–80% (right) centralities.

Transverse momentum dependences of v_n ($n = 2$, 3, 4 and 5) of charged hadrons at midrapidity are shown at 0%–10% (Fig. 54), 40%–50% (Fig. 55) and 70%–80% (Fig. 56) centralities in Pb + Pb collisions at $\sqrt{s_{NN}} = 2.76$ TeV. In each figure, results using the event plane method, the reaction plane method and the two-particle cumulant method are compared with each other. Due to the poor statistics, we omit the results from the four-particle cumulant method. In central collisions (0%–10% centrality), all $v_n\{\mathrm{EP}\}$ are close to each other. The magnitude and the order of $v_n\{2\}$ are almost identical to those of $v_n\{\mathrm{EP}\}$. However, in the case of the reaction plane method, only v_2 is finite and the other harmonics vanish in $0 < p_T < 3$ GeV/c. In semi-central collisions (40%–50% centrality), v_2 deviates from other harmonics, which reflects the almond like average geometry in non-central collisions. Again, the pattern of $v_n\{2\}$ is quite similar to that of $v_n\{\mathrm{EP}\}$. v_2 using these three

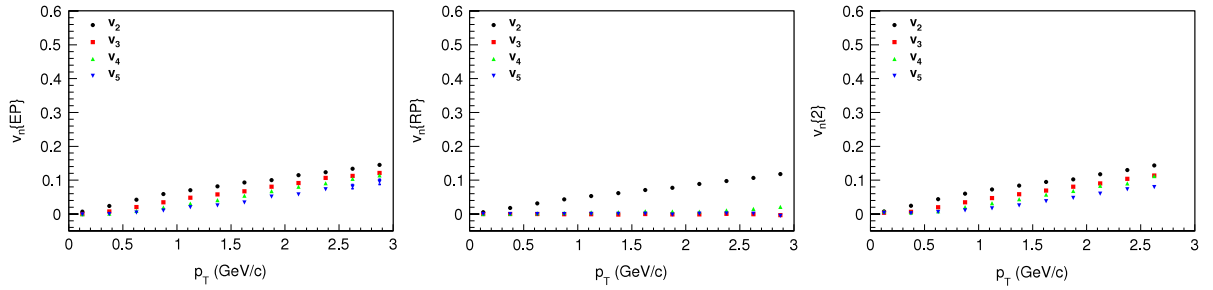

Fig. 54. Transverse momentum dependence of harmonics, v_n ($n = 2$, 3, 4 and 5), using the event plane method (left), the reaction plane method (middle), and the two particle cumulant method (right) at 0%–10% centrality.

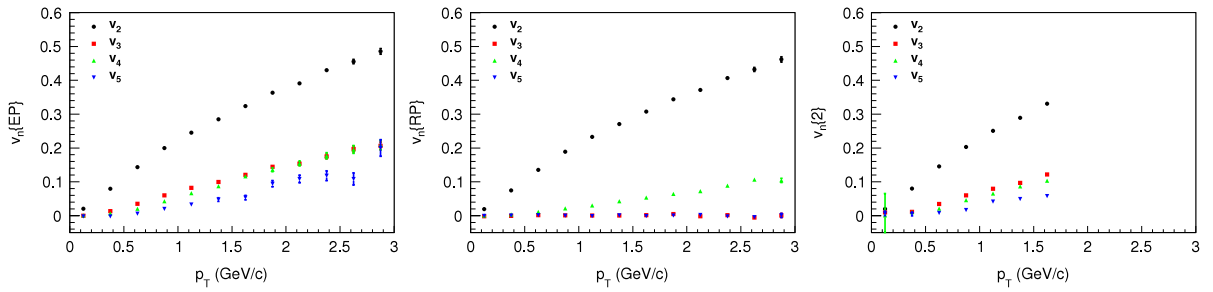

Fig. 55. The same as Fig. 54 but at 40%–50% centrality.

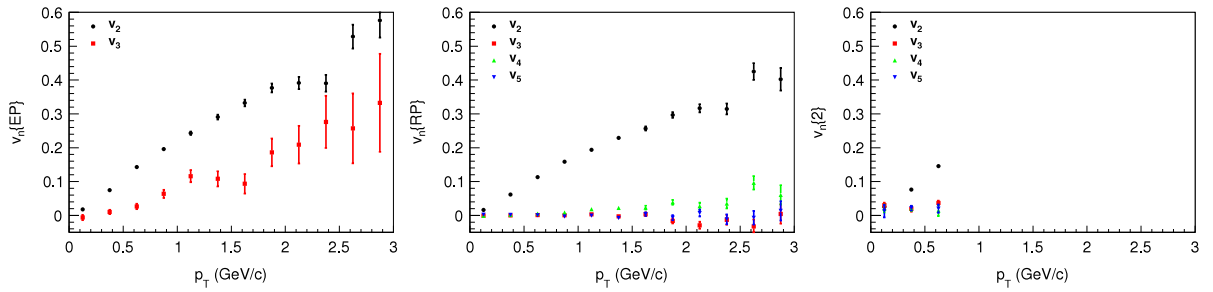

Fig. 56. The same as Fig. 54 but at 70%–80% centrality. v_4 and v_5 are omitted in the event plane method since the errors are too large due to poor resolution of the event plane angle.

methods is almost the same, v_3 and v_5 vanish when the reaction plane method is used as expected from an argument of fluctuating initial conditions,[14] whereas $v_4\{\mathrm{RP}\}$ becomes finite although its magnitude is rather smaller than $v_4\{\mathrm{EP}\}$ and $v_4\{2\}$. The sensitivity of v_4 on the analysis methods indicates that measured v_4 contains both fluctuation and geometry effects. In peripheral collisions, it is quite hard to obtain higher order harmonics with small errors for the given number of events since not only the number of events but also the number of measured particles do matter. In the event plane method, resolution parameter becomes worse with decreasing centrality, which, in turn, increases the errors of v_n^{obs}.

We also show $v_2\{\mathrm{EP}\}$ and $v_3\{\mathrm{EP}\}$ of identified hadrons (π^-, K^- and $\bar{p}$) in Figs. 57 and 58, respectively, at midrapidity ($|\eta| < 0.8$) at three centralities (0–5%, 30–40% and 60–70%) in Pb + Pb collisions at the LHC energy. Mass splitting pattern, namely $v_n^\pi > v_n^K > v_n^p$ for $n = 2$ and 3, is clearly seen in all results except in v_3 at 60–70% centrality where, due to smaller multiplicity, resolution is poor and, consequently, errors are very large. Similar mass splitting pattern was also found in Ref. [135], where it was pointed out that the mass splitting pattern is not necessarily a consequence of the existence of the QGP.

When radial flow is sufficiently large, v_2 of protons could be negative in the low p_T region [18]. However, this cannot be clearly seen even though radial flow at the LHC energy is expected to be larger than that at the RHIC energy. $v_n(p_T)$ for identified hadrons would give further constraints for the dynamical modelling at the LHC energy as well as at the RHIC energy.

So far we have shown the results obtained using the MC-KLN initialisation. We next compare these results with the ones obtained using the MC-Glauber initialisation. As already seen in the previous section, the MC-KLN model gives a larger

[14] Regarding v_5, a more precise reason is still not clear since the correlation between Ψ_5 and Φ_5 is non-trivial as shown in Fig. 40.

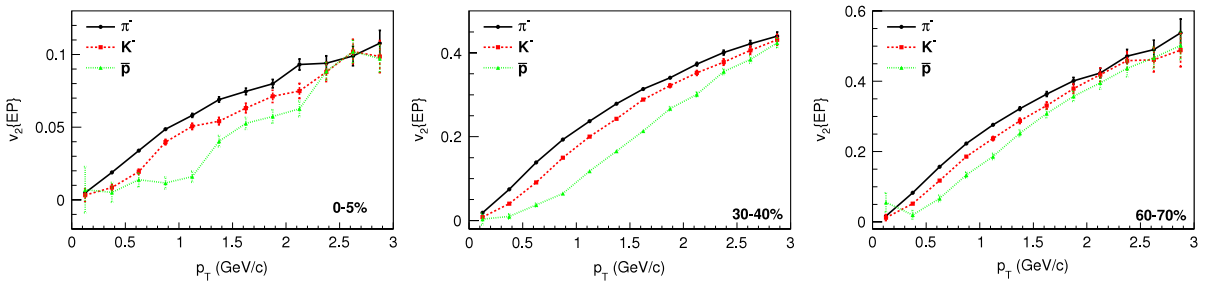

Fig. 57. v_2{EP} of identified hadrons in $|\eta| < 0.8$ in Pb + Pb collisions at $\sqrt{s_{NN}} = 2.76$ TeV. Results at 0–5% (left), 30–40% (middle) and 60–70% (right) centralities are shown.

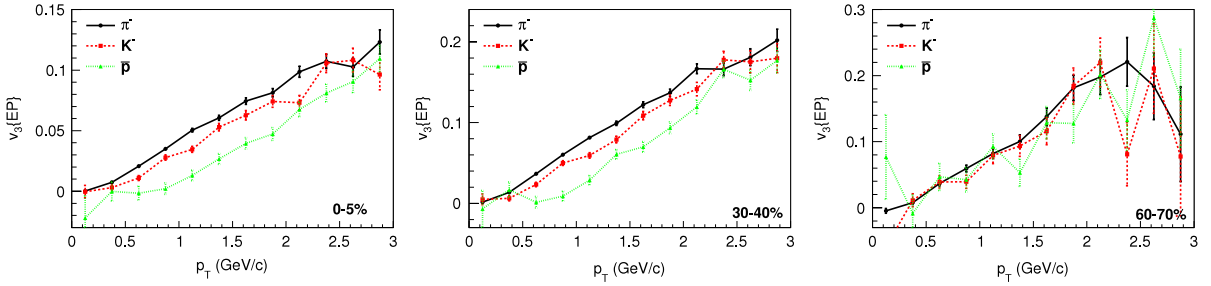

Fig. 58. The same as Fig. 57 but for v_3{EP}.

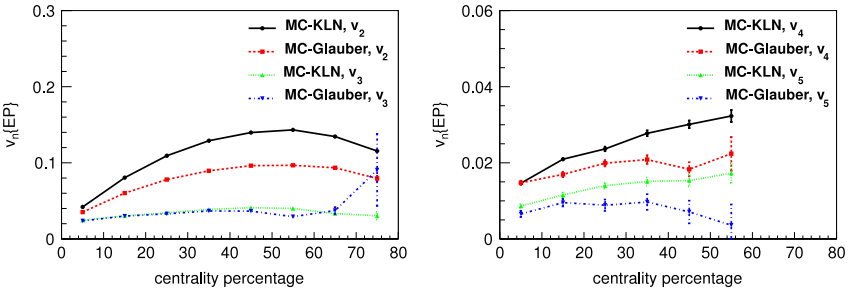

Fig. 59. Centrality dependence of v_2 and v_3 (left) and v_4 and v_5 (left) of charged hadrons at midrapidity ($0 < \eta < 1$) in Pb + Pb collisions at $\sqrt{s_{NN}} = 2.76$ TeV. Results obtained using the MC-KLN model are compared with the ones obtained using the MC-Glauber model.

eccentricity ε_2 than the MC-Glauber model and, consequently, leads to larger v_2. This is again seen in Fig. 59(left). Regardless of different models, v_3 using the MC-KLN model is almost identical to v_3 using the Glauber model. This is due to the fact that, in both models, v_3 is generated by triangular anisotropic shape of the reaction zone, ε_3 and that ε_3 is determined by the granular structure of the colliding nuclei as shown in Fig. 22. On the other hand, one cannot see the similarity of v_n ($n = 4, 5$) between the MC-KLN model and the MC-Glauber model in Fig. 59(right). In semi-central collisions (10–60% centrality) v_n ($n = 4, 5$) using the MC-KLN model are systematically larger than the ones using the MC-Glauber model. In spite of a fact that higher order flow coefficients such as v_4 and v_5 are correlated with lower order flow coefficients as demonstrated in Fig. 41, simultaneous analyses of v_n ($n \lesssim 5$) can be used to discriminate between the CGC and Glauber pictures for the initial conditions and would thus help to provide useful information about the transport properties of the QGP. Although the simultaneous analysis of v_2 and v_3 revealed the MC-KLN model apparently contradicts to the PHENIX data [245], these calculations lack multiplicity fluctuations which would affect ε_n [175] and thus improve the fit to the data.

5. Conclusion

In this paper, we have performed simulations of relativistic heavy ion collisions at RHIC and LHC energies using an integrated approach of dynamical modelling, in which Monte-Carlo calculations of initial collisions based on the colour glass condensate or the Glauber pictures, a fully $(3 + 1)$-dimensional ideal hydrodynamic model with the state-of-the-art lattice QCD equation of state, and a hadronic cascade are combined.

We employed the Monte-Carlo versions of the Kharzeev–Levin–Nardi model and the Glauber model and, using them, generated many events to obtain initial conditions for the subsequent hydrodynamic evolution. We had two options for initial conditions: One is the single smooth initial condition for a given centrality as we take an average of the entropy profiles in each centrality class. By rotating each initial profile to match its participant plane with the reaction plane, we obtained initial conditions containing some fluctuation effects. It turned out that these initial conditions are necessary to obtain large elliptic flow parameter in small systems, such as the matter created in Cu + Cu collisions, and in systems which are almost cylindrical on average, such as central events in Au + Au collisions. However, these initial conditions did not contain higher odd harmonic components and, therefore, could not lead to reproduction of anisotropic flow parameters with odd harmonics. We neglected the longitudinal structure of the created matter in this option and assumed boost invariance. Therefore, we could not discuss (pseudo-) rapidity dependence of observables.

The other option is to utilise each initial profile from the Monte-Carlo calculations on event-by-event basis. Since the entropy production in the primary nucleon–nucleon collision happens when the two nucleons in the colliding nuclei are sufficiently close in the transverse plane, the entropy density profile contains fluctuations from configuration of nucleons in the colliding nuclei. The resultant example of initial conditions exhibits a bumpy structure and contains also odd spatial anisotropies unlike in the first option. In this option, we also considered space–time rapidity dependence of initial conditions. The KLN model gives rapidity distribution of produced gluons through the k_T factorisation formulation. We simply identified the momentum rapidity distribution with the space–time rapidity distribution in the transverse plane to obtain initial conditions in the whole configuration space. The Glauber model does not tell us anything about the longitudinal structure of entropy production. We modelled initial longitudinal structure of entropy profile based on a string picture, which we called a modified BGK (Brodsky–Gunion–Kühn) model. In this model, the space–time rapidity dependence of entropy density was calculated using the numbers of participants and that of binary collisions as given by the Glauber model.

Using these initial conditions, we performed ideal hydrodynamic simulations solving the expansion numerically in all three dimensions using the Milne coordinates (τ, x, y, η_s). For the equation of state, we used a model in which the lattice QCD results in high temperature regions are smoothly connected with a resonance gas equation of state with the same hadrons than the event generator JAM. The resultant equation of states exhibits a crossover behaviour rather than a phase transition. We employed the Piecewise Parabolic Method to solve the hydrodynamic equations. This method has been known as a robust algorithm against strong shock waves, and is thus ideal for simulating fluid evolution starting from bumpy initial conditions on an event-by-event basis. We described the space–time evolution of the QGP fluids all the way down to the switching temperature. The switching temperature was chosen to reproduce the final particle ratios of pions, kaons and protons at the full RHIC energy. With the subsequent hadronic evolution, we found $T_{\rm sw} = 155$ MeV leads to a good description of yields and slopes in transverse momentum distribution for identified hadrons at RHIC. From a macroscopic hydrodynamic picture to a microscopic particle picture at $T_{\rm sw}$, we employed the Cooper–Frye formula rejecting in-coming particles which contribute as a negative number in the phase-space. By sampling hadrons on the particlisation hypersurface according to this prescription, we obtained "initial" phase-space distribution for the subsequent hadronic cascading on an event-by-event basis. We simulated the space–time evolution of hadron gas utilising a hadronic cascade, JAM. Transport models can naturally treat the late low density phase of the system in the heavy ion collision where the system is not expected to be in a local equilibrium any more, and provide a realistic freeze-out which depends on the particle species.

We simulated $\sim 10^5$ "minimum bias" events with $N_{\rm part} \geq 2$ in the event-by-event option for each parameter set. We confirmed the average multiplicity in event-by-event simulations is smaller than the multiplicity using the smooth averaged initial conditions. We also obtained p_T spectra for identified hadrons and found antiproton yields become comparable with negative pion yield at $p_T \sim 3$ GeV/c. So far comparisons of theoretical results using a flow analysis method have been made with experimental data obtained using the different flow analysis method. We analysed the final particle distribution in a spirit of performing (almost) the same procedure as the experimentalists have done. We used particle multiplicity in forward rapidity to perform centrality cuts. When we calculated the anisotropic flow parameters, we employed several typical flow analysis methods such as reaction plane method, event plane method and two- and four-particle cumulant methods.

We found that some of the different flow analysis methods lead to almost the same results. For instance, v_n using the event plane method is almost the same as v_n using the two-particle cumulant method within errors. Notice that contributions from jet fragmentation were missing in our dynamical simulations, which omits one of the major non-flow effects in the two-particle cumulant method. On the other hand, the four-particle cumulant method gives different results. v_2 using the four-particle cumulant method is more like theoretically calculated v_2 with respect to the reaction plane. Although we did not have enough statistics to draw firm conclusions, in our calculations, v_3 using the four particle cumulant method was roughly half of v_3 obtained using the other two methods. v_2 using the event plane method contains effects of participant plane fluctuation: In the limit of vanishing centrality percentage, v_2 using the event plane method stays finite. v_{2n+1} are expected to vanish if measured with respect to the reaction plane. However, v_{2n+1} are finite due to fluctuating initial transverse profiles in the event plane method and the two-particle cumulant method.

We evaluated the correlations between the event plane and the orientation angles to see a possible mechanism of generating higher order anisotropic flow. For v_2 and v_3, these two angles are strongly correlated: Anisotropic flow is generated mainly by pressure gradient in the direction of short axis in each participant anisotropy. On the other hand, non-trivial correlations are seen in v_4 and v_5.v_4 is first driven by the fourth spatial anisotropy in central collisions, but could be driven by *elliptic flow* with respect to reaction plane in mid-central to peripheral collisions. This could be seen in the mixed correlation between Φ_2 and Ψ_4.

We used two models of initial conditions, namely MC-KLN model and MC-Glauber model, and made a systematic comparison between them. Although entropy density profile is different in these two models, both models can lead to almost identical particle yields and p_T spectra. On the other hand, the spatial anisotropy ε_2 from the MC-KLN model is larger than the one from the MC-Glauber model, which leads to discrepancy of v_2 between the MC-KLN model and the MC-Glauber model. Within ideal hydrodynamic simulations, the difference can be seen in all v_2 results. However, ε_3 from the MC-KLN model is almost the same as the one from the MC-Glauber model because it originates from initial fluctuation of transverse profiles, which is treated in a similar fashion in both models. Consequently, there is almost no difference of v_3 between these two models. As claimed by the PHENIX Collaboration [245], one can use this fact to discriminate the MC-KLN model from the MC-Glauber model. Simultaneous analyses of higher order anisotropies such as v_4 and v_5, in addition to v_2 and v_3, would also provide more information about the initial conditions.

In this paper, we restricted our discussion to ideal hydrodynamic description of the QGP fluids. However, to understand the transport properties of the QGP, viscous corrections to both dynamics and particle spectra are mandatory. So far, there have been several viscous hydrodynamic simulations to analyse anisotropic parameters at RHIC and LHC energies. Some of the simulations have been performed in $(2 + 1)$ dimensional space with an assumption of boost invariance. However, given a fact that event planes are determined in forward rapidity regions in some flow analyses experimentally, fully three dimensional simulations are necessary to describe the actual dynamics.

Final higher harmonics were turned out to be sensitive to the flow analysis method. A good example was the triangular flow v_3: although v_3 with respect to the event plane is almost similar to v_3 from the two-particle cumulant method, v_3 from the four-particle cumulant method is roughly a half of them. This has already been confirmed in the experimental data [38]. In the hydrodynamic simulations, one usually obtains smooth distributions using the Cooper–Frye formula. However, Monte-Carlo sampling from these smooth momentum distributions is necessary to perform particle-based analysis method, *i.e.*, event-plane method or multi-particle cumulants methods. Of course, the subsequent hadronic cascading is also important and required to describe the gradual freezeout in the hadronic rescattering stage.

We also showed that, for higher order harmonics ($n \geq 4$), the participant plane defined using initial profiles does not correlate with the event plane defined using final particle samples. This means that calculations using event-averaged initial conditions where the orientation angles of the anisotropy ε_n are matched, are questionable.

The PHENIX Collaboration found [245] that the Glauber initialisation followed by viscous hydrodynamic simulations with $\eta/s = 0.08$ simultaneously reproduced v_2 and v_3 as functions of centrality, while the KLN initialisation with $\eta/s = 0.16$ leads to a reasonable reproduction only of v_2. After that, it was found that fluctuation of particle production obeying KNO scaling at midrapidity enhances initial spatial anisotropy ε_{2n+1} ($n \geq 1$) at all centralities [175]. The initial conditions including this feature could lead to enhancement of v_{2n+1} with keeping v_2. This would change our understanding of v_2 and v_3 as functions of centrality above. Although it would be interesting to consider this KNO scaling idea in the integrated dynamical model, how to formulate it in rapidity direction is an open question.

We assumed that initial entropy production can directly be used as initial conditions in hydrodynamic simulations and neglected the description of any thermalisation processes. As known, thermalisation is one of the outstanding open questions in the physics of relativistic heavy ion collisions.

In the event-by-event hydrodynamic simulations, thermal fluctuations during evolutions might have been important [246]. In this case, hydrodynamic equations (more specifically, constitutive equations) are no longer the deterministic equations, but become the stochastic equations. Since the fluctuation–dissipation relation tells us thermal fluctuation of the energy–momentum tensor is intimately related with viscosity, one should include fluctuation in the dynamical evolution, in particular, in the event-by-event simulations.

Switching from a hydrodynamic picture to a particle picture has several open issues. Some procedures adopted in the present study do not respect energy–momentum conservation. We neglected in-coming particles which contribute as negative number in the phase-space distribution. This could have been resolved partly by simulating hydrodynamics and hadron cascade simultaneously and by explicitly treating absorption of particles coming inside fluid regions. The negative contributions are an issue for the space-like hypersurface elements, but even for the time-like elements, the sampling of the finite number of particles violates the energy–momentum conservation in an individual event. The conservation recovers only when over-sampling of particles is made.

Regarding a switch from a fluid to a gas, one natural question would be when and how hydrodynamic picture breaks down. In the present study, the switching temperature is just an adjustable parameter to reproduce particle ratios among hadrons. It is interesting to note that the switching temperature $T_{\rm sw} = 155$ MeV obtained in this study is very close to the pseudocritical temperature of the chiral phase transition. In fact, it has been claimed [247,248] that bulk viscosity enhanced in the vicinity of cross-over region would trigger this transition from thermalised fluid to individual particles.

Acknowledgements

The authors acknowledge the fruitful discussion with S. Esumi and Y. Hori about the flow analysis methods. T.H. acknowledges a kind hospitality from the nuclear theory group at Lawrence Berkeley National Laboratory where a part of work was done when he visited there on sabbatical. The work of T.H. was supported by Grant-in-Aid for Scientific Research Nos 22740151 and 22340052, the work of P.H. by BMBF under contract no. 06FY9092, the work of K.M. by JSPS Research Fellowships for Young Scientists, and the work of Y.N. by Grant-in-Aid for Scientific Research No. 20540276.

Appendix

In this appendix, we show some technical details about momentum integration of the Cooper–Frye formula [86] for the purpose of less numerical costs [94].

Since the number is Lorentz invariant, Eq. (15) can be Lorentz-transformed to the local rest frame using four flow velocity u^μ and written as

$$\begin{aligned} \Delta N_\pm &= \int \frac{d^3p}{E} \frac{[p\cdot\Delta\sigma]_\pm}{\exp[(p\cdot u-\mu)/T]-\epsilon} \\ &= \int \frac{d^3\bar{p}}{\bar{E}} \frac{[\bar{p}\cdot\Delta\bar{\sigma}]_\pm}{\exp[(\bar{E}-\mu)/T]-\epsilon} \end{aligned} \tag{85}$$

where $[\cdots]_\pm = \Theta(\pm\cdots)|\cdots|$. Hereafter integral variables $\bar{p} = (\bar{E}, \bar{\boldsymbol{p}})$ can be renamed as p. In the following, we discuss only about out-going particles $[\cdots]_+$. Results for in-coming particles $[\cdots]_-$ can be easily obtained by replacing $\Delta\bar{\sigma}$ with $-\Delta\bar{\sigma}$. Taking the z axis being parallel to $\Delta\bar{\boldsymbol{\sigma}}$,

$$\begin{aligned} [p\cdot\Delta\bar{\sigma}]_+ &= [E\Delta\bar{\sigma}^0 - p_z \mid \Delta\bar{\boldsymbol{\sigma}} \mid]_+ \\ &= [E\Delta\bar{\sigma}^0 - p\cos\theta \mid \Delta\bar{\boldsymbol{\sigma}} \mid]_+. \end{aligned} \tag{86}$$

Thus, the above integration becomes

$$\Delta N_+ = \int \frac{dp}{\exp[(E-\mu)/T]-\epsilon} \frac{2\pi p^2 d\cos\theta}{E} [E\Delta\bar{\sigma}^0 - p\cos\theta \mid \Delta\bar{\boldsymbol{\sigma}} \mid]_+. \tag{87}$$

When $\mid \Delta\bar{\boldsymbol{\sigma}} \mid = 0$, we easily integrate the above equation and the results becomes

$$\Delta N_+ = 4\pi \int \frac{p^2 dp}{\exp[(E-\mu)/T]-\epsilon} [\Delta\bar{\sigma}^0]_+. \tag{88}$$

When $\mid \Delta\bar{\boldsymbol{\sigma}} \mid > 0$, a short calculation leads to

$$\begin{aligned} [E\Delta\bar{\sigma}^0 - p\cos\theta|\Delta\bar{\boldsymbol{\sigma}}|]_+ &= p|\Delta\bar{\boldsymbol{\sigma}}| \left[\frac{E\Delta\bar{\sigma}^0}{p|\Delta\bar{\boldsymbol{\sigma}}|} - \cos\theta\right]_+ \\ &= p|\Delta\bar{\boldsymbol{\sigma}}|[A-\cos\theta]_+ \end{aligned} \tag{89}$$

$$A = \frac{E}{|\boldsymbol{p}|} \frac{\Delta\bar{\sigma}^0}{|\Delta\bar{\boldsymbol{\sigma}}|}. \tag{90}$$

First, we integrate the above equation with respect to $\cos\theta$

$$\begin{aligned} \int_{-1}^{1} d\cos\theta [A-\cos\theta]_+ &= \int_{-1}^{1} d\cos\theta (A-\cos\theta)\Theta(A-\cos\theta) \\ &= 2A\Theta(A-1) + \frac{(A+1)^2}{2}\Theta(1-|A|), \end{aligned} \tag{91}$$

where Θ is the Heaviside function. Let us define "velocity" and "momentum" of surface vector as $v_{\bar{\sigma}} = \Delta\bar{\sigma}^0/|\Delta\bar{\boldsymbol{\sigma}}|$ and $p_{\bar{\sigma}} = m|v_{\bar{\sigma}}|/\sqrt{1-v_{\bar{\sigma}}^2}$, respectively.

Finally we obtain

$$\begin{aligned} \Delta N_+ &= 4\pi \int_0^\infty \frac{p^2 dp}{\exp[(E-\mu)/T]-\epsilon} [\Delta\bar{\sigma}^0]_+ \\ &\quad + \Theta(1-|v_{\bar{\sigma}}|) \left(\pi|\Delta\bar{\boldsymbol{\sigma}}| \int_{p_{\bar{\sigma}}}^\infty \frac{p(E^2 v_{\bar{\sigma}}^2 + p^2)dp}{\exp[(E-\mu)/T]-\epsilon} - 2\pi|\Delta\bar{\sigma}^0| \int_{p_{\bar{\sigma}}}^\infty \frac{p^2 dp}{\exp[(E-\mu)/T]-\epsilon} \right). \end{aligned} \tag{92}$$

Remembering that the hypersurface elements have been Lorentz-transformed, we have to Lorentz-transform back to the laboratory frame:

$$\Delta\bar{\sigma}^0 = u\cdot\Delta\sigma \tag{93}$$

$$\begin{aligned} \mid \Delta\bar{\boldsymbol{\sigma}} \mid^2 &= (\Delta\bar{\sigma}^0)^2 - \Delta\bar{\sigma}\cdot\Delta\bar{\sigma} \\ &= -(g_{\mu\nu} - u_\mu u_\nu)\Delta\sigma^\mu \Delta\sigma^\nu. \end{aligned} \tag{94}$$

Now the three-dimensional integral with a complicated integrand such as $[\cdots]_\pm$ reduces to the one-dimensional one and it is easily done numerically.

References

[1] K. Yagi, T. Hatsuda, Y. Miake, Quark-gluon Plasma: From Big Bang to Little Bang, Cambridge, 2005.
[2] C. Adler, et al., [STAR Collaboration], Phys. Rev. Lett. 87 (2001) 182301.
[3] C. Adler, et al., [STAR Collaboration], Phys. Rev. C 66 (2002) 034904.
[4] J. Adams, et al., [STAR Collaboration], Phys. Rev. Lett. 92 (2001) 052302.
[5] K. Adcox, et al., [PHENIX Collaboration], Phys. Rev. Lett. 89 (2002) 212301.
[6] S.S. Adler, et al., [PHENIX Collaboration], Phys. Rev. Lett. 91 (2003) 182301.
[7] S.S. Adler, et al., [PHENIX Collaboration], Phys. Rev. Lett. 94 (2005) 232302.
[8] B.B. Back, et al., [PHOBOS Collaboration], Phys. Rev. Lett. 89 (2002) 222301.
[9] B.B. Back, et al., [PHOBOS Collaboration], Phys. Rev. Lett. 94 (2005) 122303.
[10] B.B. Back, et al., [PHOBOS Collaboration], Phys. Rev. C 72 (2005) 051901.
[11] K. Aamodt, et al., [ALICE Collaboration], Phys. Rev. Lett. 105 (2010) 252302.
[12] G. Aad, et al., [ATLAS Collaboration], Phys. Lett. B 707 (2012) 330.
[13] J. Velkovska, [CMS Collaboration], J. Phys. G 38 (2011) 124011.
[14] U. Heinz, P.F. Kolb, Nuclear Phys. 702 (2002) 269.
[15] M. Gyulassy, Preprint arXiv:nucl-th/0403032.
[16] J.Y. Ollitrault, Phys. Rev. D 46 (1992) 229.
[17] P.F. Kolb, P. Huovinen, U.W. Heinz, H. Heiselberg, Phys. Lett. B 500 (2001) 232.
[18] P. Huovinen, P.F. Kolb, U.W. Heinz, P.V. Ruuskanen, S.A. Voloshin, Phys. Lett. B 503 (2001) 58.
[19] D. Teaney, J. Lauret, E.V. Shuryak, Phys. Rev. Lett. 86 (2001) 4789.
[20] D. Teaney, J. Lauret, E.V. Shuryak, Preprint arXiv:nucl-th/0110037.
[21] T. Hirano, Phys. Rev. C 65 (2002) 011901.
[22] T. Hirano, K. Tsuda, Phys. Rev. C 66 (2002) 054905.
[23] http://www.bnl.gov/bnlweb/pubaf/pr/PR_display.asp?prID=05-38.
[24] T.D. Lee, Nuclear Phys. 750 (2005) 1.
[25] M. Gyulassy, L. Mclerran, Nuclear Phys. 750 (2005) 30.
[26] E.V. Shuryak, Nuclear Phys. 750 (2005) 64.
[27] T. Hirano, M. Gyulassy, Nuclear Phys. 769 (2006) 71.
[28] M.L. Miller, K. Reygers, S.J. Sanders, P. Steinberg, Annu. Rev. Nucl. Part. Sci. 57 (2007) 205.
[29] W. Broniowski, M. Rybczynski, P. Bozek, Comput. Phys. Comm. 180 (2009) 69.
[30] B. Alver, M. Baker, C. Loizides, P. Steinberg, preprint arxiv:0805.4411 [nucl-ex].
[31] C. Alt, et al., [NA49 Collaboration], Phys. Rev. C 68 (2003) 034903.
[32] B. Alver, et al., [PHOBOS Collaboration], Phys. Rev. Lett. 98 (2007) 242302.
[33] M. Miller, R. Snellings, Preprint arXiv:nucl-ex/0312008.
[34] B. Alver, G. Roland, Phys. Rev. C 81 (2010) 054905; Phys. Rev. C 82 (2010) 039903 (erratum).
[35] J. Adams, et al., [STAR Collaboration], Phys. Rev. Lett. 95 (2005) 152301.
[36] S.S. Adler, et al., [PHENIX Collaboration], Phys. Rev. Lett. 97 (2006) 052301.
[37] A. Adare, et al., [PHENIX Collaboration], Phys. Rev. C 78 (2008) 014901.
[38] K. Aamodt, et al., [ALICE Collaboration], Phys. Lett. B 708 (2012) 249.
[39] G. Aad, et al., [ATLAS Collaboration], Phys. Rev. C 86 (2012) 014907.
[40] E. Shuryak, Phys. Rev. C 80 (2009) 054908; Phys. Rev. C 80 (2009) 069902. (erratum).
[41] P. Staig, E. Shuryak, Phys. Rev. C 84 (2011) 034908.
[42] P. Staig, E. Shuryak, Phys. Rev. C 84 (2011) 044912.
[43] A. Mocsy, P. Sorensen, Preprint arxiv:1008.3381 [hep-ph].
[44] P. Sorensen, B. Bolliet, A. Mocsy, Y. Pandit, N. Pruthi, Phys. Lett. B 705 (2011) 71.
[45] E. Komatsu, et al., [WMAP Collaboration], Astrophys. J. Suppl. 180 (2009) 330.
[46] http://lambda.gsfc.nasa.gov/toolbox/.
[47] https://karman.physics.purdue.edu/OSCAR/index.php/Main_Page.
[48] E. Iancu, A. Leonidov, L. Mclerran, Preprint arXiv:hep-ph/0202270.
[49] E. Iancu, R. Venugopalan, in: R.C. Hwa, X.N. Wang (Eds.), Quark Gluon Plasma 3 (QGP3), World Scientific, 2004, p. 249.
[50] F. Gelis, E. Iancu, J. Jalilian-Marian, R. Venugopalan, Annu. Rev. Nucl. Part. Sci. 60 (2010) 463.
[51] G. Gatoff, A.K. Kerman, T. Matsui, Phys. Rev. D 36 (1987) 114.
[52] T. Lappi, L. Mclerran, Nuclear Phys. 772 (2006) 200.
[53] T. Hirano, P. Huovinen, Y. Nara, Phys. Rev. C 83 (2011) 021902.
[54] T. Hirano, P. Huovinen, Y. Nara, Phys. Rev. C 84 (2011) 011901.
[55] H.-J. Drescher, Y. Nara, Phys. Rev. C 75 (2007) 034905.
[56] H.-J. Drescher, Y. Nara, Phys. Rev. C 76 (2007) 041903.
[57] T. Hirano, Y. Nara, Phys. Rev. C 79 (2009) 064904.
[58] M. Cheng, N.H. Christ, S. Datta, J. Van der heide, C. Jung, F. Karsch, O. Kaczmarek, E. Laermann, et al., Phys. Rev. D 77 (2008) 014511.
[59] A. Bazavov, T. Bhattacharya, M. Cheng, N.H. Christ, C. Detar, S. Ejiri, S. Gottlieb, R. Gupta, et al., Phys. Rev. D 80 (2009) 014504.
[60] P. Huovinen, P. Petreczky, Nuclear Phys. 837 (2010) 26.
[61] Y. Nara, N. Otuka, A. Ohnishi, K. Niita, S. Chiba, Phys. Rev. C 61 (2000) 024901.
[62] T. Hirano, Y. Nara, Prog. Theor. Exp. Phys. 1 (2012) 01A203.
[63] A.M. Poskanzer, S.A. Voloshin, Phys. Rev. C 58 (1998) 1671.
[64] N. Borghini, P.M. Dinh, J.-Y. Ollitrault, Phys. Rev. C 63 (2001) 054906.
[65] N. Borghini, P.M. Dinh, J.-Y. Ollitrault, Phys. Rev. C 64 (2001) 054901.
[66] C. Adler, et al., [STAR Collaboration], Phys. Rev. Lett. 90 (2003) 4778; Phys. Rev. Lett. 90 (2003) 119903. (erratum).
[67] S.S. Adler, et al., [PHENIX Collaboration], Phys. Rev. C 69 (2004) 034909.
[68] B.I. Abelev, et al., [STAR Collaboration], Phys. Rev. C 79 (2009) 034909.
[69] M. Floris, Talk at Quark Matter 2011, Annecy, France.
[70] D.H. Rischke, Hadrons in dense matter and hadrosynthesis, Cape Town, 1998, pp. 21–70 [nucl-th/9809044].
[71] P. Colella, P.R. Woodward, J. Comput. Phys. 54 (1984) 174.
[72] P. Petreczky, J. Phys. G 39 (2012) 093002.
[73] S. Borsanyi, G. Endrodi, Z. Fodor, A. Jakovac, S.D. Katz, S. Krieg, C. Ratti, K.K. Szabo, JHEP 1011 (2010) 077.
[74] R. Venugopalan, M. Prakash, Nuclear Phys. 546 (1992) 718.
[75] P.F. Kolb, U.W. Heinz, P. Huovinen, K.J. Eskola, K. Tuominen, Nuclear Phys. 696 (2001) 197.
[76] M. Cheng, et al., Phys. Rev. D 81 (2010) 054504.
[77] A. Bazavov, et al., [HotQCD Collaboration], PoS LATTICE 2010 (2010) 169.
[78] P. Huovinen, P.V. Ruuskanen, Annu. Rev. Nucl. Part. Sci. 56 (2006) 163.
[79] P. Huovinen, Nuclear Phys. 761 (2005) 296.

[80] J. Adams, et al., [STAR Collaboration], Phys. Rev. C 72 (2005) 014904.
[81] J. Sollfrank, P. Huovinen, M. Kataja, P.V. Ruuskanen, M. Prakash, R. Venugopalan, Phys. Rev. C 55 (1997) 392.
[82] R.A. Schneider, W. Weise, Phys. Rev. C 64 (2001) 055201.
[83] M. Chojnacki, W. Florkowski, Acta Phys. Polon. B 38 (2007) 3249.
[84] M. Chojnacki, W. Florkowski, W. Broniowski, A. Kisiel, Phys. Rev. C 78 (2008) 014905.
[85] H. Song, S.A. Bass, U. Heinz, T. Hirano, C. Shen, Phys. Rev. C 83 (2011) 054910.
[86] F. Cooper, G. Frye, Phys. Rev. D 10 (1974) 186.
[87] P. Huovinen, H. Petersen, Eur. Phys. J. A 48 (2012) 171.
[88] G. Welke, R. Malfliet, C. Gregoire, M. Prakash, E. Suraud, Phys. Rev. C 40 (1989) 2611.
[89] D. Molnar, M. Gyulassy, Phys. Rev. C 62 (2000) 054907.
[90] A. Lang, H. Babovsky, W. Cassing, U. Mosel, H-G Reusch, K. Weber, J. Comput. Phys. 106 (1993) 391.
[91] P. Danielewicz, G.F. Bertsch, Nuclear Phys. 533 (1991) 712.
[92] Z. Xu, C. Greiner, Phys. Rev. C 71 (2005) 064901.
[93] H. Petersen, J. Steinheimer, G. Burau, M. Bleicher, H. Stocker, Phys. Rev. C 78 (2008) 044901.
[94] K. Murase, Relativistic Hydrodynamic Model with Event-by-event Fluctuation in High Energy Heavy Ion Collisions, Master Thesis, The University of Tokyo (2012) (in Japanese).
[95] M. Isse, A. Ohnishi, N. Otuka, P.K. Sahu, Y. Nara, Phys. Rev. C 72 (2005) 064908.
[96] H. Sorge, H. Stöcker, W. Greiner, Ann. Physics 192 (1989) 266.
[97] H. Sorge, A. Von keitz, R. Mattiello, H. Stöcker, W. Greiner, Z. Phys. C 47 (1990) 629.
[98] H. Sorge, L. Winckelmann, H. Stöcker, W. Greiner, Z. Phys. C 59 (1993) 85.
[99] H. Sorge, Phys. Rev. C 52 (1995) 3291.
[100] L.A. Winckelmann, et al., Nuclear Phys. 610 (1996) 116c.
[101] S.A. Bass, et al., Prog. Part. Nucl. Phys. 41 (1998) 225.
[102] M. Bleicher, et al., J. Phys. G 25 (1999) 1859.
[103] G.F. Bertsch, S. Das gupta, Phys. Rep. 160 (1998) 189.
[104] J. Aichelin, Phys. Rep. 202 (1991) 233.
[105] X.N. Wang, M. Gyulassy, Phys. Rev. D 44 (1991) 3501.
[106] X.N. Wang, Phys. Rep. 280 (1997) 287.
[107] X.N. Wang, M. Gyulassy, Comp. Phys. Comm. 83 (1994) 307.
[108] http://www-nsdth.lbl.gov/~xnwang/hijing/.
[109] B. Andersson, G. Gustafson, H. Pi, Z. Phys. C 57 (1993) 485.
[110] H. Pi, Comp. Phys. Comm. 71 (1992) 173.
[111] B. Andersson, G. Gustafson, G. Ingelman, T. Sjöstrand, Phys. Rep. 97 (1983) 31.
[112] B. Andersson, The Lund Model, Cambridge, 2005.
[113] T. Sjostrand, S. Mrenna, P.Z. Skands, JHEP 0605 (2006) 026.
[114] A. Bialas, M. Gyulassy, Nuclear Phys. 291 (1987) 793.
[115] Gy. Wolf, W. Cassing, U. Mosel, Nuclear Phys. 552 (1993) 549.
[116] B.-A. Li, Nuclear Phys. 552 (1993) 605.
[117] E. Andersen, et al., [WA97 Collaboration], Phys. Lett. B 433 (1998) 209.
[118] H. Appelshäuser, et al., [NA49 Collaboration], Phys. Lett. B 444 (1998) 523.
[119] A. Dumitru, S.A. Bass, M. Bleicher, H. Stoecker, W. Greiner, Phys. Lett. B 460 (1999) 411.
[120] A.M. Poskanzer, et al., [NA49 Collaboration], Nuclear Phys. 661 (1999) 341c.
[121] K.H. Ackermann, et al., [STAR Collaboration], Phys. Rev. Lett. 86 (2001) 401.
[122] K. Adcox, et al., [PHENIX Collaboration], Nuclear Phys. 757 (2005) 184.
[123] S.A. Bass, A. Dumitru, M. Bleicher, L. Bravina, E. Zabrodin, H. Stoecker, W. Greiner, Phys. Rev. C 60 (1999) 021902.
[124] S.A. Bass, A. Dumitru, Phys. Rev. C 61 (2000) 064909.
[125] T. Hirano, U.W. Heinz, D. Kharzeev, R. Lacey, Y. Nara, Phys. Lett. B 636 (2006) 299.
[126] T. Hirano, U.W. Heinz, D. Kharzeev, R. Lacey, Y. Nara, Phys. Rev. C 77 (2008) 044909.
[127] P.F. Kolb, Heavy Ion Phys. 15 (2002) 279.
[128] M. Nasim, [STAR Collaboration], arxiv:1210.5045 [nucl-ex].
[129] C. Nonaka, S.A. Bass, Phys. Rev. C 75 (2007) 014902.
[130] H. Petersen, M. Bleicher, Phys. Rev. C 79 (2009) 054904.
[131] H. Petersen, M. Bleicher, Phys. Rev. C 81 (2010) 044906.
[132] H. Petersen, G.-Y. Qin, S.A. Bass, B. Muller, Phys. Rev. C 82 (2010) 041901.
[133] G.-Y. Qin, H. Petersen, S.A. Bass, B. Muller, Phys. Rev. C 82 (2010) 064903.
[134] H. Petersen, V. Bhattacharya, S.A. Bass, C. Greiner, Phys. Rev. C 84 (2011) 054908.
[135] H. Petersen, Phys. Rev. C 84 (2011) 034912.
[136] S. Pratt, J. Vredevoogd, Phys. Rev. C 78 (2008) 054906;
S. Pratt, J. Vredevoogd, Phys. Rev. C 79 (2009) 069901 (erratum).
[137] H. Song, S.A. Bass, U. Heinz, T. Hirano, C. Shen, Phys. Rev. Lett. 106 (2011) 192301;
H. Song, S.A. Bass, U. Heinz, T. Hirano, C. Shen, Phys. Rev. Lett. 109 (2012) 139904 (erratum).
[138] K. Werner, I. Karpenko, T. Pierog, M. Bleicher, K. Mikhailov, Phys. Rev. C 82 (2010) 044904.
[139] K. Werner, I. Karpenko, T. Pierog, M. Bleicher, K. Mikhailov, Phys. Rev. C 83 (2011) 044915.
[140] K. Werner, I. Karpenko, T. Pierog, Phys. Rev. Lett. 106 (2011) 122004.
[141] K. Werner, I. Karpenko, M. Bleicher, T. Pierog, S. Porteboeuf-Houssais, Phys. Rev. C 85 (2012) 064907.
[142] H. Song, S.A. Bass, U. Heinz, Phys. Rev. C 83 (2011) 024912.
[143] H. Song, S.A. Bass, U. Heinz, Phys. Rev. C 83 (2011) 054912.
[144] P. Kovtun, D.T. Son, A.O. Starinets, Phys. Rev. Lett. 94 (2005) 111601.
[145] R.A. Soltz, I. Garishvili, M. Cheng, B. Abelev, A. Glenn, J. Newby, L.A.L. Levy, S. Pratt, Preprint. arxiv:1208.0897 [nucl-th].
[146] S. Ryu, S. Jeon, C. Gale, B. Schenke, C. Young, Preprint arxiv:1210.4588 [hep-ph].
[147] A. Krasnitz, R. Venugopalan, Nucl. Phys. B 557 (1999) 237.
[148] A. Krasnitz, R. Venugopalan, Phys. Rev. Lett. 84 (2000) 4309.
[149] A. Krasnitz, R. Venugopalan, Phys. Rev. Lett. 86 (2001) 1717.
[150] A. Krasnitz, Y. Nara, R. Venugopalan, Phys. Rev. Lett. 87 (2001) 192302.
[151] A. Krasnitz, Y. Nara, R. Venugopalan, Nuclear Phys. 717 (2003) 268.
[152] A. Krasnitz, Y. Nara, R. Venugopalan, Nuclear Phys. 727 (2003) 427.
[153] T. Lappi, Phys. Rev. C 67 (2003) 054903.
[154] T. Lappi, Phys. Rev. C 70 (2004) 054905.
[155] L.V. Gribov, E.M. Levin, M.G. Ryskin, Phys. Rep. 100 (1983) 1.
[156] D. Kharzeev, E. Levin, Phys. Lett. B 523 (2001) 79.
[157] D. Kharzeev, E. Levin, M. Nardi, Phys. Rev. C 71 (2005) 054903.

[158] D. Kharzeev, E. Levin, M. Nardi, Nucl. Phys. A 730 (2004) 448.
[159] A. Adil, H.J. Drescher, A. Dumitru, A. Hayashigaki, Y. Nara, Phys. Rev. C 74 (2006) 044905.
[160] F. Gelis, A.M. Stasto, R. Venugopalan, Eur. Phys. J. C 48 (2006) 489.
[161] J.L. Albacete, Phys. Rev. Lett. 99 (2007) 262301.
[162] J.L. Albacete, C. Marquet, Phys. Lett. B 687 (2010) 174.
[163] E. Levin, A.H. Rezaeian, Phys. Rev. D 82 (2010) 014022.
[164] E. Levin, A.H. Rezaeian, Phys. Rev. D 82 (2010) 054003.
[165] E. Levin, A.H. Rezaeian, Phys. Rev. D 83 (2011) 114001.
[166] P. Tribedy, R. Venugopalan, Nucl. Phys. A 850 (2011) 136; Nucl. Phys. A 859 (2011) 185. (erratum).
[167] P. Tribedy, R. Venugopalan, Phys. Lett. B 710 (2012) 125.
[168] A. Dumitru, D.E. Kharzeev, E.M. Levin, Y. Nara, Phys. Rev. C 85 (2012) 044920.
[169] J.L. Albacete, A. Dumitru, Preprint arxiv:1011.5161 [hep-ph]; http://faculty.baruch.cuny.edu/naturalscience/physics/dumitru/CGC_IC.html.
[170] J.L. Albacete, A. Dumitru, Y. Nara, J. Phys. Conf. Ser. 316 (2011) 012011.
[171] H.J. Drescher, Y. Nara, Phys. Rev. C 75 (2007) 034905.
[172] J.L. Albacete, A. Dumitru, H. Fujii, Y. Nara, Nuclear Phys. 897 (2013) 1.
[173] H.J. Drescher, Y. Nara, Phys. Rev. C 76 (2007) 041903(R).
[174] B. Muller, A. Schafer, Phys. Rev. D 85 (2012) 114030.
[175] A. Dumitru, Y. Nara, Phys. Rev. C 85 (2012) 034907.
[176] R.M. Barnett, et al., Phys. Rev. D 54 (1996) 1.
[177] G.A. Schuler, T. Sjostrand, Nucl. Phys. B 407 (1993) 539.
[178] G.A. Schuler, T. Sjostrand, Phys. Rev. D 49 (1994) 2257.
[179] H. De Vries, C.W. De Jager, C. De Vries, At. Data Nucl. Data Tables 36 (1987) 495.
[180] U. Heinz, J.S. Moreland, Phys. Rev. C 84 (2011) 054905.
[181] P. Filip, R. Lednicky, H. Masui, N. Xu, Phys. Rev. C 80 (2009) 054903.
[182] K. Aamodt, et al., [ALICE Collaboration], Phys. Rev. Lett. 106 (2011) 032301.
[183] K. Aamodt, et al., [ALICE Collaboration], Phys. Rev. Lett. 106 (2011) 032301.
[184] K. Aamodt, et al., [ALICE Collaboration], Eur. Phys. J. C 68 (2010) 89.
[185] Y. Nara, Progr. Theoret. Phys. Suppl. 193 (2012) 145.
[186] H. Holopainen, H. Niemi, K.J. Eskola, Phys. Rev. C 83 (2011) 034901.
[187] B. Schenke, S. Jeon, C. Gale, Phys. Rev. Lett. 106 (2011) 042301.
[188] D. Kharzeev, M. Nardi, Phys. Lett. B 507 (2001) 121.
[189] K. Golec-Biernat, M. Wusthoff, Phys. Rev. D 59 (1999) 014017.
[190] K. Golec-Biernat, M. Wusthoff, Phys. Rev. D 60 (1999) 114023.
[191] D. Teaney, L. Yan, Phys. Rev. C 83 (2011) 064904.
[192] B.H. Alver, C. Gombeaud, M. Luzum, J.-Y. Ollitrault, Phys. Rev. C 82 (2010) 034913.
[193] R.S. Bhalerao, M. Luzum, J.-Y. Ollitrault, Phys. Rev. C 84 (2011) 034910.
[194] R.S. Bhalerao, M. Luzum, J.-Y. Ollitrault, Phys. Rev. C 84 (2011) 054901.
[195] F.G. Gardim, F. Grassi, M. Luzum, J.-Y. Ollitrault, Phys. Rev. C 85 (2012) 024908.
[196] B. Alver, et al., Phys. Rev. C 77 (2008) 014906.
[197] S.J. Brodsky, J.F. Gunion, J.H. Kuhn, Phys. Rev. Lett. 39 (1977) 1120.
[198] A. Adil, M. Gyulassy, Phys. Rev. C 72 (2005) 034907.
[199] B.B. Back, et al., Phys. Rev. Lett. 91 (2003) 052303.
[200] J.D. Bjorken, Phys. Rev. D 27 (1983) 140.
[201] M. Gyulassy, D.H. Rischke, B. Zhang, Nuclear Phys. 613 (1997) 397.
[202] Y. Hama, T. Kodama, O. Socolowski Jr., Braz. J. Phys. 35 (2005) 24.
[203] H.J. Drescher, M. Hladik, S. Ostapchenko, T. Pierog, K. Werner, Phys. Rep. 350 (2001) 93.
[204] T. Osada, C.E. Aguiar, Y. Hama, T. Kodama, nucl-th/0102011.
[205] C.E. Aguiar, Y. Hama, T. Kodama, T. Osada, Nuclear Phys. 698 (2002) 639.
[206] R. Andrade, F. Grassi, Y. Hama, T. Kodama, O. Socolowski Jr., Phys. Rev. Lett. 97 (2006) 202302.
[207] R.P.G. Andrade, F. Grassi, Y. Hama, T. Kodama, W.L. Qian, Phys. Rev. Lett. 101 (2008) 112301.
[208] J. Takahashi, B.M. Tavares, W.L. Qian, R. Andrade, F. Grassi, Y. Hama, T. Kodama, N. Xu, Phys. Rev. Lett. 103 (2009) 242301.
[209] F.G. Gardim, F. Grassi, Y. Hama, M. Luzum, J.-Y. Ollitrault, Phys. Rev. C 83 (2011) 064901.
[210] Y. Cheng, L.P. Csernai, V.K. Magas, B.R. Schlei, D. Strottman, Phys. Rev. C 81 (2010) 064910.
[211] Y.-Y. Ren, W.-N. Zhang, J.-L. Liu, Phys. Lett. B 669 (2008) 317.
[212] C. Adler, et al., [STAR Collaboration], Phys. Rev. Lett. 87 (2001) 082301.
[213] K. Adcox, et al., [PHENIX Collaboration], Phys. Rev. Lett. 88 (2002) 192302.
[214] R. Chatterjee, H. Holopainen, T. Renk, K.J. Eskola, Phys. Rev. C 83 (2011) 054908.
[215] T. Renk, H. Holopainen, J. Auvinen, K.J. Eskola, Preprint arxiv:1105.2647 [hep-ph].
[216] Z. Qiu, U.W. Heinz, Phys. Rev. C 84 (2011) 024911.
[217] Z. Qiu, U.W. Heinz, Phys. Lett. B 717 (2012) 261.
[218] J. Jia, ATLAS Collaboration, Preprint arxiv:1208.1427 [nucl-ex].
[219] K. Werner, F.-M. Liu, T. Pierog, Phys. Rev. C 74 (2006) 044902.
[220] B. Schenke, S. Jeon, C. Gale, Phys. Rev. C 85 (2012) 024901.
[221] B. Schenke, P. Tribedy, R. Venugopalan, Phys. Rev. Lett. 108 (2012) 252301.
[222] C. Gale, S. Jeon, B. Schenke, P. Tribedy, R. Venugopalan, Preprint arxiv:1209.6330 [nucl-th].
[223] B. Schenke, P. Tribedy, R. Venugopalan, Phys. Rev. C 86 (2012) 034908.
[224] J. Bartels, K.J. Golec-Biernat, H. Kowalski, Phys. Rev. D 66 (2002) 014001.
[225] H. Kowalski, D. Teaney, Phys. Rev. D 68 (2003) 114005.
[226] A.K. Chaudhuri, Phys. Lett. B 710 (2012) 339.
[227] A.K. Chaudhuri, Phys. Lett. B 713 (2012) 91.
[228] M. Rihan Haque, V. Roy, A.K. Chaudhuri, Phys. Rev. C 86 (2012) 037901.
[229] P. Bozek, W. Broniowski, Phys. Rev. C 85 (2012) 044910.
[230] L. Pang, Q. Wang, X.-N. Wang, Phys. Rev. C 86 (2012) 024911.
[231] H. Zhang, T. Song, C.M. Ko, Preprint arxiv:1208.2980 [hep-ph].
[232] B.I. Abelev, et al., [STAR Collaboration], Phys. Rev. C 81 (2010) 044902.
[233] J.-Y. Ollitrault, A.M. Poskanzer, S.A. Voloshin, Phys. Rev. C 80 (2009) 014904.
[234] S. Afanasiev, et al., [PHENIX Collaboration], Phys. Rev. C 80 (2009) 024909.
[235] A. Adare, et al., [PHENIX Collaboration], Phys. Rev. Lett. 98 (2008) 162301.
[236] X. Zhang, et al., [STAR Collaboration], Acta Phys. Polon. Supp. 5 (2012) 509.
[237] M. Luzum, Phys. Rev. C 83 (2011) 044911.
[238] S.A. Voloshin, A.M. Poskanzer, A. Tang, G. Wang, Phys. Lett. B 659 (2008) 537.

[239] P. Arnold, G.D. Moore, L.G. Yaffe, JHEP 05 (2003) 051.
[240] H. Niemi, G.S. Denicol, P. Huovinen, E. Molnar, D.H. Rischke, Phys. Rev. Lett. 106 (2011) 212302.
[241] H. Niemi, G.S. Denicol, P. Huovinen, E. Molnar, D.H. Rischke, Phys. Rev. C 86 (2012) 014909.
[242] N. Borghini, J.-Y. Ollitrault, Phys. Lett. B 642 (2006) 227.
[243] D. Teaney, Phys. Rev. C 68 (2003) 034913.
[244] X.-l. Zhu, M. Bleicher, H. Stoecker, Phys. Rev. C 72 (2005) 064911.
[245] A. Adare, et al., [PHENIX Collaboration], Phys. Rev. Lett. 107 (2011) 252301.
[246] J.I. Kapusta, B. Muller, M. Stephanov, Phys. Rev. C 85 (2012) 054906.
[247] G. Torrieri, B. Tomasik, I. Mishustin, Phys. Rev. C 77 (2008) 034903.
[248] K. Rajagopal, N. Tripuraneni, JHEP 1003 (2010) 018.

Cent. Eur. J. Phys. • 10(6) • 2012 • 1385-1387
DOI: 10.2478/s11534-012-0110-3

VERSITA

Central European Journal of **Physics**

Equation of state at non-zero baryon density based on lattice QCD

Short Communication

Pasi Huovinen[1]*, Péter Petreczky[2], Christian Schmidt[3]

1 *Institut für Theoretische Physik, Johann Wolfgang Goethe-Universität, 60438 Frankfurt am Main, Germany*

2 *Physics Department, Brookhaven National Laboratory, Upton, NY 11973, USA*

3 *Fakultät für Physik, Universität Bielefeld, 33615 Bielefeld, Germany*

Received 14 February 2012 ; accepted 7 July 2012

Abstract: We employ the lattice QCD data on Taylor expansion coefficients to extend our previous parametrization of the equation of state to finite baryon density. When we take into account lattice spacing and quark mass dependence of the hadron masses, the Taylor coefficients at low temperature are equal to those of hadron resonance gas. Parametrized lattice equation of state can thus be smoothly connected to the hadron resonance gas equation of state at low temperatures.

PACS (2008): 12.38.Gc, 21.65.Qr, 25.75.Nq

Keywords: lattice QCD • equation of state • hadron resonance gas • hydrodynamic models

One of the methods to extend the lattice QCD calculations to non-zero chemical potential is Taylor expansion. In that approach pressure is Taylor expanded in chemical potentials, and the Taylor coefficients are calculated on the lattice at zero chemical potential. In this contribution we use the results of the most comprehensive lattice QCD analysis of the Taylor coefficients to date [1, 2] to construct a parametrisation of an equation of state (EoS) for finite baryon density. As in our earlier parametrisation of the EoS at zero chemical potential [3], we require that our parametrisation matches smoothly to the hadron resonance gas (HRG) at low temperatures.

Taylor coefficients are derivatives of pressure, P, with respect to baryon and strangeness chemical potentials, μ_B and μ_S, respectively:

$$c_{ij}(T) = \frac{1}{i!j!}\frac{T^{i+j}}{T^4}\frac{\partial^i}{\partial\mu_B^i}\frac{\partial^j}{\partial\mu_S^j}P(T,\mu_B=0,\mu_S=0), \qquad (1)$$

where T is temperature[1]. As we discussed in [4], all the coefficients evaluated in Refs. [1, 2] are well below the

*E-mail: huovinen@th.physik.uni-frankfurt.de

[1] *We use natural units where $c = \hbar = k_B = 1$ throughout the text.*

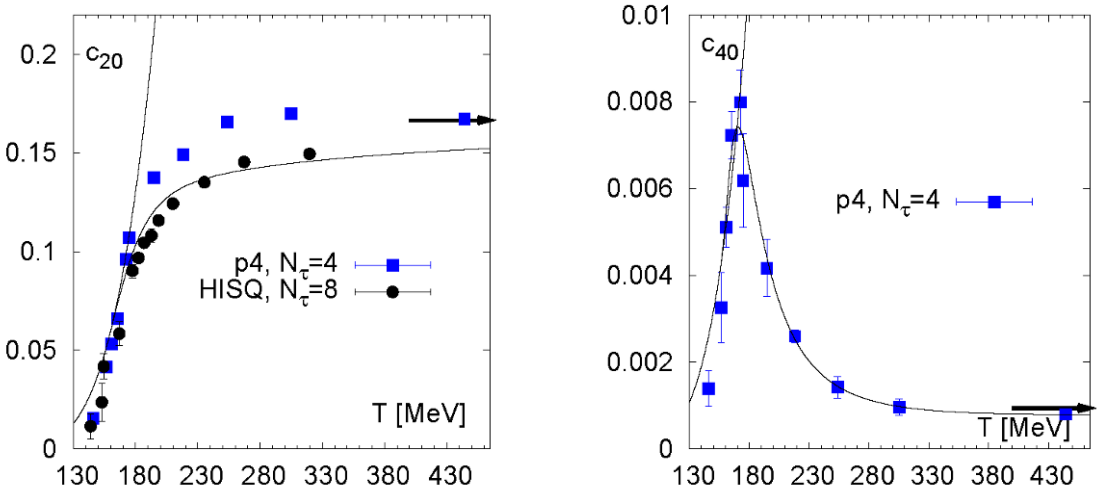

Figure 1. The parametrisation (solid line) and HRG value (dashed) of the c_{20} (left) and c_{40} (right) coefficients compared with the shifted p4 data (see the text). The recent lattice result for c_{20} with the HISQ action [6] is also shown. The arrows depict the Stefan-Boltzmann values.

HRG results. This discrepancy can largely be explained by the lattice discretisation effects on hadron masses: When the hadron mass spectrum is modified accordingly (for details see [5]), the HRG model reproduces the lattice data, see Fig. 1 of Ref. [4]. Interestingly this change can be accounted for by shifting the modified HRG result of purely baryonic coefficients towards lower temperature by 30 MeV. The situation is similar for other Taylor expansion coefficients [5], although the strange coefficients might favour slightly smaller shift. Based on this finding and because the lattice data agree so well with the modified HRG we suggest that cutoff effects can be accounted for by shifting the lattice data by 30 MeV. We show the effect of such a shift in the left panel of Fig. 1, where we plot the HRG curve with physical masses (dashed line) and compare it with the lattice data, where all the points below 206 MeV temperature are shifted by 30 MeV, and the 209 MeV point by 15 MeV. For further confirmation of this procedure we also plot the recent HISQ result of c_{20} [6] in Fig. 1 (right): At low temperatures the shifted p4 data agree with the HISQ data.

We parametrise the shifted data as a function of temperature T using an inverse polynomial of four (c_{20}), five (c_{11} and c_{02}), or six (fourth and sixth order coefficients) terms:

$$c_{ij}(T) = \sum_{k=1}^{m} \frac{a_{kij}}{\hat{T}^{n_{kij}}} + c_{ij}^{\mathrm{SB}}, \qquad (2)$$

where c_{ij}^{SB} is the Stefan-Boltzmann value of the particular coefficient, a_{kij} are the parameters, and the powers n_{kij} are required to be integers between 1 and 42. $\hat{T} = (T - T_s)/R$ with scaling factors $T_s = 0$ and $R = 0.15$ GeV for the second order coefficients and $T_s = 0.1$ GeV and $R = 0.05$ GeV for all the other coefficients. We match this parametrisation to the HRG value at temperature $T_{\mathrm{SW}} = 155$ MeV by requiring that the Taylor coefficient and its first, second, and third derivatives are continuous. Since the recent lattice data obtained using HISQ action [6] shows that the second order coefficients approach their Stefan-Boltzmann limits slowly, we require that their value is 95% of their Stefan-Boltzmann value at 800 MeV temperature. These constraints fix four (or five) of the parameters a_{kij}. The remaining parameters, are fixed by a χ^2 fit to the lattice data. As an example we show the parametrised c_{20}, c_{40}, and c_{60} in Figs. 1 and 2. Once the coefficients are known, pressure can be written as

$$\frac{P}{T^4} = \sum_{ij} c_{ij}(T) \left(\frac{\mu_B}{T}\right)^i \left(\frac{\mu_S}{T}\right)^j, \qquad (3)$$

and all the other thermodynamical quantities can be obtained from Eq. (3) by using the laws of thermodynamics. This kind of an expansion breaks down at large chemical potentials. However, at baryon densities of interest here, the contribution from coefficients of particular order is clearly below (< 20%) the lower order contribution. Thus the approximation of the EoS in terms of fourth- and sixth order expansion looks reasonable. As pressure at $\mu_B = 0$, i.e. the coefficient c_{00}, we use our earlier parametrisation $s95p$-v1 [3]. We describe the EoS in the right panel of Fig. 2 by showing the square of the speed of sound $c_s^2 = \partial P/\partial\epsilon|_{s/n_B}$ [7] on various isentropic curves with constant entropy per baryon s/n_B [8]. The curves at $s/n_B = 400$, 65, and 40 are relevant at collision energies $\sqrt{s_{\mathrm{NN}}} = 200$, 39 and 17 GeV, respectively. At $s/n_B = 400$

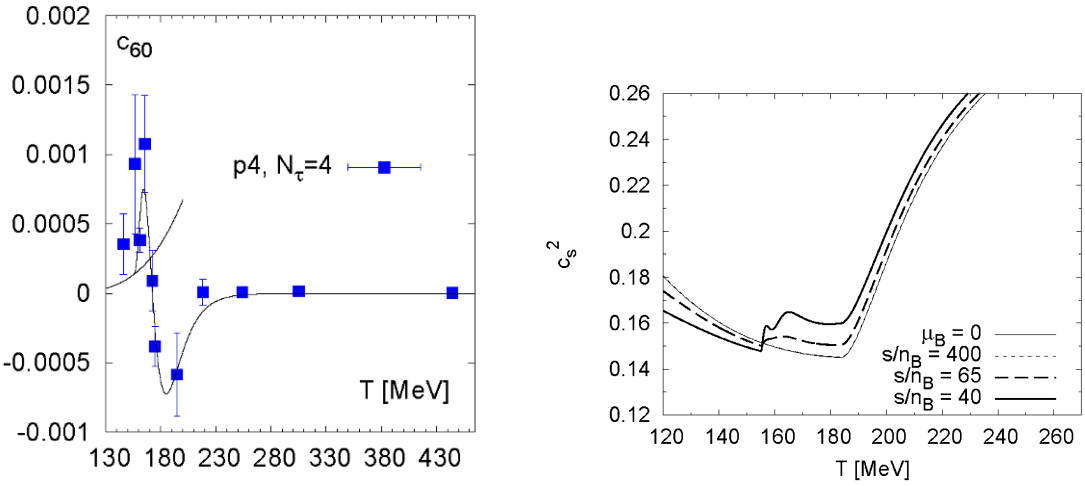

Figure 2. (Left) The parametrisation (solid line) and HRG value (dashed) of the c_{60} coefficient compared with the shifted p4 data (see the text). (Right) The square of the speed of sound c_s^2 as a function of temperature on various isentropic curves with constant entropy per baryon s/n_B (see the text).

(dotted line), the EoS is basically identical to the EoS at $\mu_B = 0$ (thin solid line). At larger baryon densities the effect of finite baryon density is no longer negligible. The larger the density, the stiffer the EoS above, and softer below the transition temperature.

Furthermore, additional structure begins to appear around the transition temperature with increasing density. We expect this structure to be an artifact of our fitting procedure: Our fit is too good and elevates errors to features leading to additional ripples in the speed of sound. Another interesting feature in the equation of state is the rapid change of the speed of sound around $T_{sw} = 155$ MeV and another change around $T \approx 185$ MeV. The latter has its origin in our baseline $\mu_B = 0$ EoS. It follows hadron resonance gas up to $T = 184$ MeV temperature causing a change in the speed of sound at that temperature. Nevertheless, when pressure is plotted as a function of energy density, these structures are hardly visible. Therefore we do not expect them to affect the buildup of flow and the evolution of the system, and consider our parametrisation a reasonable first attempt.

We have studied the effect of the EoS on flow by calculating elliptic flow in Pb+Pb collision at the full SPS collision energy ($\sqrt{s_{NN}} = 17$ GeV). Our results are similar to those we have shown earlier [4]: Even if in an ideal fluid calculation at RHIC energy proton $v_2(p_T)$ is sensitive to the order of phase transition [9], at SPS energy both proton and pion $v_2(p_T)$ are insensitive to it.

To summarise, we have shown that a temperature shift of 30 MeV is a good approximation of the discretisation effects in the lattice QCD data obtained using p4 action. We have constructed an equation of state for finite baryon densities based on hadron resonance gas and lattice QCD data. At the full SPS energy ($\sqrt{s_{NN}} = 17$ GeV) the p_T-differential elliptic flow is almost insensitive to the equation of state. This is bad news for the experimental search of the critical point, since a change from a first order phase transition to a smooth crossover does not cause an observable change in the flow.

Acknowledgements

This work was supported by BMBF under contract no. 06FY9092, and by the U.S. Department of Energy under contract DE-AC02-98CH1086.

References

[1] C. Miao et al. [RBC-Bielefeld Collaboration], PoS LATTICE2008, 172 (2008)
[2] M. Cheng et al., Phys. Rev. D 79, 074505 (2009)
[3] P. Huovinen, P. Petreczky, Nucl. Phys. A 837, 26 (2010)
[4] P. Huovinen, P. Petreczky, J. Phys. G 38, 124103 (2011)
[5] P. Huovinen, P. Petreczky, J. Phys. Conf. Ser. 230, 012012 (2010)
[6] A. Bazavov et al. [HotQCD Collaboration], J. Phys. Conf. Ser. 230, 012014 (2010)
[7] D. Teaney, J. Lauret, E. V. Shuryak, arXiv:nucl-th/0110037
[8] C. Schmidt, Eur. Phys. J. C 61, 537 (2009)
[9] P. Huovinen, Nucl. Phys. A 761 , 296 (2005)

Available online at www.sciencedirect.com
ScienceDirect
Nuclear Physics A 837 (2010) 26–53
NUCLEAR PHYSICS A
www.elsevier.com/locate/nuclphysa

QCD equation of state and hadron resonance gas

Pasi Huovinen [a], Péter Petreczky [b,*]

[a] *Institut für Theoretische Physik, Johann Wolfgang Goethe-Universität, Max-von-Laue-Straße 1, 60438 Frankfurt am Main, Germany*

[b] *Physics Department and RIKEN-BNL Research Center, Brookhaven National Laboratory, Upton, NY 11973, USA*

Received 26 December 2009; received in revised form 5 February 2010; accepted 5 February 2010

Available online 20 March 2010

Abstract

We compare the trace anomaly, strangeness and baryon number fluctuations calculated in lattice QCD with expectations based on hadron resonance gas model. We find that there is a significant discrepancy between the hadron resonance gas and the lattice data. This discrepancy is largely reduced if the hadron spectrum is modified to take into account the larger values of the quark mass used in lattice calculations as well as the finite lattice spacing errors. We also give a simple parametrization of QCD equation of state, which combines hadron resonance gas at low temperatures with lattice QCD at high temperatures. We compare this parametrization with other parametrizations of the equation of state used in hydrodynamical models and discuss differences in hydrodynamic flow for different equations of state.

Keywords: Laticce QCD; Equation of state; Hadron resonance gas; Hydrodynamic models

1. Introduction

Equation of state of hot strongly interacting matter play important role in cosmology [1,2] and hydrodynamic description of heavy ion collisions [3]. In many cases hydrodynamical models which try to describe the collective flow in heavy ion collisions used equation of state (EoS) with first order phase transition, although lattice QCD shows that the transition to the deconfined phase is only a crossover [4]. It is not obvious to what extent the collective flow is sensitive to details of the equation of state (EoS). It turns out, however, that in ideal fluid dynamics the

* Corresponding author.
E-mail address: petreczk@bnl.gov (P. Petreczky).

0375-9474/$ – see front matter
doi:10.1016/j.nuclphysa.2010.02.015

anisotropy of the proton flow is particularly sensitive to the QCD equation of state [5] and using lattice inspired EoS with crossover transition overpredicts proton elliptic flow.

Attempts to calculate EoS on the lattice have been made over the last 20 years (see Refs. [6,7] for reviews). One of the difficulties in calculating EoS on the lattice is its sensitivity to high momentum modes and thus to the effects of finite lattice spacing. This problem is particularly severe in the high temperature limit. Therefore in recent years calculations have been done using improved staggered fermions with higher order discretization of the lattice Dirac operators [8,9] which largely reduce the cutoff dependence in the high temperature region. However, there is another source of discretization effects if staggered quarks are used. The staggered fermion formulation does not preserve the flavor symmetry of continuum QCD. Because of this the spectrum of low lying hadronic states is distorted and this may effect thermodynamic quantities in the low temperature region.

Hadron resonance gas (HRG) turned out to be very successful in describing particle abundances produced in heavy ion collisions [10]. It was also used to estimate QCD transport coefficients [11] as well as chemical equilibration rates [12] close to the transition temperature. Thermodynamic quantities calculated in lattice QCD with rather large quark mass agree well with the HRG model if the masses of the hadrons in the model are tuned appropriately to match the large quark mass used in lattice calculations [13]. Furthermore, the ratio of certain charge susceptibilities are not very sensitive to the details of the hadron spectrum and the lattice calculations of these ratios show a reasonably good agreement with HRG model predictions at low temperatures [14–16]. The purpose of this paper is to confront the results of recent lattice calculations performed with light quark masses with the prediction of the HRG model and clarify its range of applicability. As we will see the HRG model describes thermodynamic quantities quite well up to unexpectedly high temperatures. Therefore lattice EoS can be combined with HRG EoS at low temperatures to get rid of large discretization effects. Such an EoS is also useful for hydrodynamic modeling, and we construct a parametrization for an EoS interpolating between HRG at low temperatures and lattice QCD at high temperatures. The rest of the paper is organized as follows. In Section 2 we discuss the hadron resonance gas model and the effects of finite lattice spacing on hadron masses. Section 3 deals with the comparison of fluctuations of baryon number and strangeness with the prediction of HRG model. In Section 4 we compare the HRG with the lattice results on trace anomaly and construct a parametrization of equation of state which is easy to use in hydrodynamic simulations. In this section we also give a detailed comparison with other parametrizations of EoS in the literature. In Section 5 we discuss hydrodynamic flow for different EoSs discussed in the previous section, and highlight the differences. Finally Section 6 contains our conclusions. In appendices we discuss some technical aspects of the calculations, in particular the fits of the lattice data as well as the hydrodynamic flow for partial chemical equilibrium.

2. Hadron resonance gas and lattice QCD

At sufficiently low temperature thermodynamics of strongly interacting matter at zero baryon number density is dominated by pions. The interaction between pions is suppressed and chiral perturbation theory can be used to estimate the pion contribution to thermodynamic potential [17]. In fact, for temperatures $T \leqslant 150$ MeV, the energy density of pions calculated in 3-loop chiral perturbation theory differs only by less than 15% from the ideal gas value [17]. As temperature increases heavier hadrons start to contribute to thermodynamics. For temperatures $T \geqslant 150$ MeV heavy states dominate the energy density. However, the densities of heavy

particles are still small, $n_i \sim \exp(-M_i/T)$, and their mutual interactions, being proportional to $n_i n_k \sim \exp(-(M_i + M_k)/T)$, are suppressed. Therefore one can use the virial expansion to evaluate the effect of interactions [18]. In the low temperature limit the virial expansion reduces to chiral perturbation theory [17]. The virial expansion together with experimental information on the scattering phase shifts was used by Prakash and Venugopalan to study thermodynamics of low temperature hadronic matter [19]. Their analysis showed that there is an interplay between attractive interactions (characterized by positive phase shifts) and repulsive interactions (characterized by negative phase shifts) such that their net effect can be well approximated by inclusion of free resonances: ρ, K^*, $\Delta(1234)$, etc. Thus the interacting gas of hadrons can be fairly well approximated by a non-interacting gas of resonances corroborating earlier ideas of the statistical bootstrap model [20]. To summarize, the partition function of strongly interacting matter at low temperature can be well approximated by the partition function of non-interacting hadrons and resonances

$$p^{\mathrm{HRG}}/T^4 = \frac{1}{VT^3} \sum_{i\in \text{mesons}} \ln \mathcal{Z}^M_{m_i}(T, V, \mu_{X^a}) + \frac{1}{VT^3} \sum_{i\in \text{baryons}} \ln \mathcal{Z}^B_{m_i}(T, V, \mu_{X^a}), \tag{2.1}$$

where

$$\ln \mathcal{Z}^{M/B}_{m_i} = \mp \frac{V d_i}{2\pi^2} \int_0^\infty dk\, k^2 \ln\bigl(1 \mp z_i e^{-\varepsilon_i/T}\bigr), \tag{2.2}$$

with energies $\varepsilon_i = \sqrt{k^2 + m_i^2}$, degeneracy factors d_i and fugacities

$$z_i = \exp\left(\left(\sum_a X_i^a \mu_{X^a}\right)/T\right). \tag{2.3}$$

Here we consider all possible conserved charges X^a, including the baryon number B, electric charge Q, strangeness S etc. We do not include any repulsive interactions in the form of excluded volume corrections or repulsive mean field [21].

The assumption that thermodynamics in the low temperature region is well described by a gas of non-interacting hadrons and resonances is important for practical applications of hydrodynamic models. At the end of the hydrodynamical evolution, the fluid is usually converted into particles using the Cooper–Frye procedure [22]. This procedure conserves energy, momentum and charge without any specific considerations if, and only if, the equation of state of the fluid is the same than the equation of state of free particles [23]. Therefore it is important to confront the predictions of the hadron resonance gas for different thermodynamical quantities with the available lattice data.

The most extensive lattice calculations of the equation of state have been performed using two versions of improved staggered fermions: the so-called asqtad and p4 formulations [8,9,24]. Calculations have been performed using lattices with temporal extent $N_\tau = 4$ and 6 [8,9] and more recently with temporal extent $N_\tau = 8$ [24]. These correspond to lattice spacings $a = 1/(4T)$, $1/(6T)$ and $1/(8T)$ respectively. The strange quark mass m_s was close to its physical value, while the light (u and d) quark masses were one tenth of the strange quark mass, $m_q = 0.1 m_s$, corresponding to the pion mass in the range 220–260 MeV. The lattice calculations of the equation of state have been compared to the prediction of the hadron resonance gas [9,24]. It turned out that the lattice results fall considerably below the HRG prediction. One obvious reason for this discrepancy is the fact that the quark mass used in lattice calculations is about a factor two

larger then the physical one. However, this fact alone is unlikely to explain the whole discrepancy as the contribution of the pseudo-scalar mesons to the energy density is small and quark mass dependence of other hadron masses in this small quark mass region is relatively weak. On the other hand, the lattice spacing dependence of the hadron masses may play an important role. Since the lattice calculations of the EoS are performed at fixed temporal extent N_τ, the temperature is varied by changing the lattice spacing $T = 1/(N_\tau a)$. As the temperature is decreased the lattice spacing gets larger and the cutoff effects on the hadron masses increase, i.e. the size of cutoff effects on the hadron masses is a function of the temperature.

The hadron masses for asqtad improved staggered fermions have been studied in Refs. [25–28] for several lattice spacings $a \simeq 0.06$, 0.09, 0.125, 0.18 and 0.25 fm. For all of these lattice spacings there are significant deviations in the hadron masses from the experimental values. Of course, after the proper continuum extrapolations all the hadron masses agree with the experiment [25]. The large cutoff dependence of the hadron masses in the staggered formulation is due to large $\mathcal{O}(\alpha_s a^2)$ discretization errors which also break the flavor symmetry. This is not the case for the improved Wilson fermion formulation [29,30], where cutoff dependence of the hadron masses is below 5% already at lattice spacing < 0.2 fm. In the following subsections we discuss the cutoff dependence of the pseudo-scalar meson, vector meson and baryon masses separately.

2.1. Pseudo-scalar mesons in staggered formulation

The staggered formulation of lattice QCD describes four degenerate quark flavors in the continuum limit. To obtain the physical number of flavors, i.e. one relatively heavy strange quark and two light quarks, the so-called rooting procedure is used. The rooting procedure amounts to replacing the fermion determinant in the path integral expression of the partition function with its fourth root. In the continuum limit this procedure is justified [31].[1] At finite lattice spacing, however, the four flavors are not degenerate, but there are flavor changing discretization effects of order $\mathcal{O}(\alpha_s a^2)$. As the result of this the sixteen pseudo-scalar mesons of the 4 flavor theory have unequal masses, and only one of them has a vanishing mass in the limit of the zero quark mass, $m_q \to 0$. The sixteen pseudo-scalar mesons can be grouped into eight multiplets [34]. The multiplets are characterized by the different masses m_{ps_i} and degeneracies d^i_{ps}, $i = 0, 1, \ldots, 7$. The first multiplet contains one Goldstone pseudo-scalar meson, i.e. $m^2_{\mathrm{ps}_0} \sim m_q$ and $d^0_{\mathrm{ps}} = 1$. The flavor generators Γ^F of the 4 flavor theory can be chosen to be the product of the Dirac matrices [34,35]. The masses of other pseudo-scalar mesons are given by

$$m^2_{\mathrm{ps}_i} = m^2_{\mathrm{ps}_0} + \delta m^2_{\mathrm{ps}_i}. \tag{2.4}$$

The quadratic splittings $\delta m^2_{\mathrm{ps}_i}$ are independent of the input quark mass m_q to a very good approximation and are proportional to $(\alpha_s a^2)$ for small lattice spacings, and in general, increase with increasing index i. The correspondence between the index i and the flavor matrix as well as the degeneracies d^i_{ps} for non-Goldstone pseudo-scalar mesons are given in Table 1.

[1] The justification of the rooting procedure at finite lattice spacing is still subject of debate see e.g. Refs. [32,33].

Table 1
The parameters of Eq. (2.5) describing the quadratic pseudo-scalar meson splittings. Also shown are the flavor matrices Γ^F and the degeneracy factors $d^i_{\rm ps}$.

i	Γ^F	$d^i_{\rm ps}$	$a^i_{\rm ps}$	$b^i_{\rm ps}$	$c^i_{\rm ps}$	$\beta^i_{\rm ps}$
1	$\gamma_0\gamma_5$	1	7.96583	45.6265	−0.983624	1.80
2	$\gamma_i\gamma_5$	3	25.9514	129.049	−4.673780	1.45
3	$\gamma_i\gamma_j$	3	19.3047	163.787	−5.675470	1.55
4	$\gamma_i\gamma_0$	3	4.26042	45.0193	−0.489748	2.00
5	γ_i	3	5.43308	79.455	−1.71669	2.00
6	γ_0	1	7.52963	95.2536	−2.24599	1.80
7	1	1	3.76433	70.8311	−0.373003	2.20

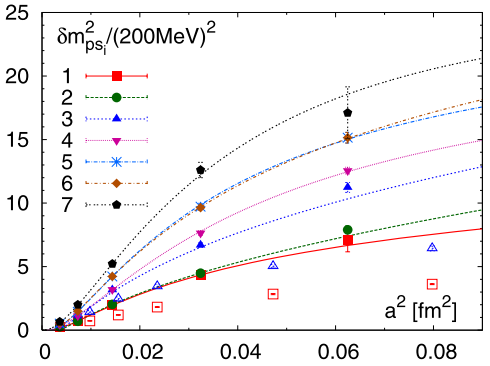

Fig. 1. The quadratic splittings of non-Goldstone pseudo-scalar mesons in the seven different multiplets calculated with asqtad action [25] at different lattice spacings. The lines show the parametrization given by Eq. (2.5). The open symbols refer to the lattice data obtained with the stout action [36].

The quadratic splittings have been calculated in numerical simulations with asqtad action in Refs. [25,27]. For lattice spacings 0.09 fm $< a <$ 0.25 fm the data can be well parametrized by the form

$$r_1^2 \cdot \delta m^2_{{\rm ps}_i} = \frac{a^i_{\rm ps} x + b^i_{\rm ps} x^2}{(1 + c^i_{\rm ps} x)^{\beta_i}}, \quad x = (a/r_1)^2. \tag{2.5}$$

Here and in what follows we use the scale parameter r_1 extracted from the static quark potential $V(r)$ to convert from lattice units to physical units. The scale parameter r_1 is defined as

$$r^2 \frac{dV(r)}{dr}\bigg|_{r=r_1} = 1.0. \tag{2.6}$$

We use the value $r_1 = 0.318$ fm determined from bottomonium splitting [27]. The values of the parameters $a^i_{\rm ps}$, $b^i_{\rm ps}$, $c^i_{\rm ps}$, $\beta^i_{\rm ps}$ are given in Table 1. In Fig. 1 we show the quadratic pseudo-scalar meson splittings calculated by the MILC Collaboration [25,27] as function of the lattice spacing and compared with the parametrization given by Eq. (2.5). As one can see from the Fig. 1, this parametrization gives good description of the data. In Fig. 1 we also show the pseudo-scalar meson splitting for stout action used by the Budapest–Wuppertal group [36]. The splittings are significantly reduced compared to the calculations with asqtad action. To take into account the

flavor symmetry breaking in the pseudo-scalar meson sector, i.e. the fact that pion masses are non-degenerate the contributions of pions and kaons to the pressure is calculated as

$$p^{\pi,K}/T^4 = \frac{1}{16}\frac{1}{VT^3}\sum_{i=0}^{7} d^i_{\rm ps} \ln \mathcal{Z}^M(m_{{\rm ps}_i}), \tag{2.7}$$

where $m_{{\rm ps}_i}$, $i = 1$–7, is calculated according to Eq. (2.4) and $m_{{\rm ps}_0}$ is equal to the pion or kaon mass used in the actual lattice calculations. Fig. 1 shows that the splitting between different pseudo-scalar mesons is quite large for lattice spacings used in calculations of the equation of state ($a = 0.12$–0.18) fm. Even in the calculations with the stout action the mass of the heaviest pion that enters Eq. (2.7) is about 500 MeV if $N_\tau = 8$ lattices are used. As the result the contribution of the pseudo-scalar mesons to thermodynamic quantities at finite lattice spacings is smaller than in the continuum.

2.2. Vector meson masses

In lattice calculations hadron masses are functions of the input quark mass and the lattice spacing. The quark mass dependence of the hadron masses is usually studied in terms of the lightest (Goldstone) pion mass. Since in lattice calculations quark masses are larger than the physical ones, and there is no full flavored chiral symmetry at finite lattice spacing a combined extrapolation in the pion mass and lattice spacing is needed for all hadron masses. We fitted the lattice spacing and pion mass dependence of the vector meson masses with the following simple formula

$$r_1 \cdot m(a, m_\pi) = r_1 m^{phys} + \frac{a_1 (r_1 m_\pi)^2 - a_1 (r_1 m_\pi^{phys})^2}{1 + a_2 x} + \frac{b_1 x}{1 + b_2 x}, \quad x = (a/r_1)^2, \tag{2.8}$$

where m^{phys} is the physical value of the meson mass from the particle data book. It turns out that this formula describes the lattice spacing dependence of the vector meson masses in the interval $0.06\ {\rm fm} < a < 0.18\ {\rm fm}$ for $(r_1 m_\pi)^2 < 0.8$. For strange vector mesons we set $a_2 = 0$ as there is no apparent lattice spacing dependence of the slope in their quark mass dependence. The numerical values of a_1, a_2, b_1 and b_2 are given in Appendix A, where also the lattice data on the vector meson masses are shown.

2.3. Baryon masses

The nucleon and the Ω baryon masses have been calculated by the MILC Collaboration with asqtad action at five different lattice spacings, $a = 0.06, 0.09, 0.12$ and 0.18 fm [25,27,28,37] and several quark masses. We performed a simultaneous fit of their quark mass (pion mass) and the lattice spacing dependence using the Ansatz given by Eq. (2.8), which works well for $(r_1 m_\pi)^2 < 0.8$. The parameters of this fit together with the lattice data on the nucleon and Ω baryon masses are presented in Appendix A. In calculations with asqtad action the value of the strange quark mass was slightly larger than its physical value for each lattice spacing considered. This is due to the fact that the strange quark mass was fixed considering the ratio of the ϕ meson mass to the mass of the unmixed η_{ss} pseudo-scalar meson instead fixing the kaon mass. This gives difference $\mathcal{O}(a^2)$ in the value of the strange quark mass. To take this into account the lattice spacing dependence of the strange quark mass was parametrized as $m_s/m_s^{phys}(a) = 1 + 1.02(a/r_1)^2$. Then to estimate the Ω baryon mass we used the following formula

$$r_1 m_\Omega(a,m_\pi) = r_1 m_\Omega^{phys} + a_1 (r_1 m_\pi)^2 - a_1 \left(r_1 m_\pi^{phys}\right)^2 + b_1 x + \left(m_\Omega^{phys} - m_\Delta^{phys}\right)\cdot 1.02x, \quad x = (a/r_1)^2. \tag{2.9}$$

Here the last term accounts for the small deviation of the strange quark mass from its physical value. For other baryons (Δ, Λ, Σ, and Ξ) no such detailed lattice calculations are available. Therefore to estimate the cutoff dependence of the Δ mass we use the same formula as for nucleon. While to estimate the cutoff dependence of the masses of the strange baryons we used the following formulas

$$r_1 \cdot m_\Lambda(a,m_\pi) = m_\Lambda^{phys} + \frac{2}{3}\frac{a_1 (r_1 m_\pi)^2}{1+a_2 x} + \frac{b_1 x}{1+b_2 x} + \frac{r_1 \cdot (m_\Lambda^{phys} - m_p^{phys})}{1+a_2 x}\left(\frac{m_s}{m_s^{phys}}\right), \tag{2.10}$$

$$r_1 \cdot m_\Sigma(a,m_\pi) = m_\Sigma^{phys} + \frac{1}{3}\frac{a_1 (r_1 m_\pi)^2}{1+a_2 x} + \frac{b_1 x}{1+b_2 x} + \frac{r_1 \cdot (m_\Sigma^{phys} - m_p^{phys})}{1+a_2 x}\left(\frac{m_s}{m_s^{phys}}\right), \tag{2.11}$$

$$r_1 \cdot m_\Xi(a,m_\pi) = m_\Xi^{phys} + \frac{1}{3}\frac{a_1 (r_1 m_\pi)^2}{1+a_2 x} + \frac{b_1 x}{1+b_2 x} + \frac{r_1 \cdot (m_\Xi^{phys} - m_p^{phys})}{1+a_2 x}\left(\frac{m_s}{m_s^{phys}}\right), \quad x = (a/r_1)^2. \tag{2.12}$$

Here again we have taken into account that the strange quark mass in simulations with asqtad was slightly larger than the physical value. In Appendix A we give the comparison of the baryon masses calculated using the above formulas with available lattice results. It turns out that our parametrization of the baryon masses works reasonably well. We will use these parametrizations when calculating different quantities in the HRG model in the following sections.

3. Fluctuations of conserved charges

Derivatives of the pressure with respect to chemical potential of conserved charges, e.g. baryon number (B), electric charge Q and strangeness S can be easily calculated in lattice QCD

$$\chi_n^X = T^n \left.\frac{\partial^n p(T,\mu_B,\mu_Q,\mu_S)}{\partial \mu_X^n}\right|_{\mu_X=0}, \quad X = B, Q, S. \tag{3.1}$$

These are related to quadratic and higher order fluctuations of conserved charges $\chi_2^X = \langle X^2\rangle/(VT^3)$, $\chi_4^X = (\langle N_X^4\rangle - 3\langle N_X^2\rangle^2)/(VT^3)$, etc.[2] Contrary to the pressure itself the evaluation of these derivatives does not involve zero temperature subtraction and integration in the temperature variable starting from some low temperature value. Therefore it is easy to compare them to the prediction of the HRG model. Different fluctuations up to the sixth order have been calculated for p4 and asqtad action [16,38,39] on $N_\tau = 4$ and $N_\tau = 6$ lattices. Quadratic strangeness fluctuations have been also calculated on $N_\tau = 8$ lattices for the p4 and asqtad actions by the HotQCD Collaboration [24]. While there are extensive calculations with p4 action at finite temperature, the zero temperature hadron spectrum was not studied in detail for p4 action. Therefore our analysis of fluctuations and comparison with HRG model will mostly rely on results obtained with asqtad action.

[2] Here we consider the case of zero chemical potential, so $\langle N_X\rangle = 0$.

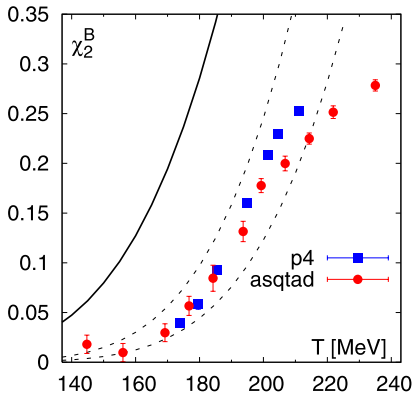

Fig. 2. Baryon number fluctuations calculated with asqtad action on the $N_\tau = 6$ lattices compared with HRG model with physical value of the baryon masses (solid line) and with HRG model with baryon masses calculated according to Eqs. (2.8)–(2.12), $m^B_{cut} = 1.8$ GeV and $m^B_{cut} = 2.5$ GeV (dashed lines). Also shown are the lattice results for the p4 action.

Let us start our discussion with baryon number fluctuations. Baryon number fluctuations for asqtad action have been calculated in Ref. [38] for $m_q = 0.2m_s$ on $N_\tau = 6$ lattices. Eqs. (2.8)–(2.12) describe the quark mass and lattice spacing dependence of ground state baryon masses calculated on lattice with asqtad action. Nothing is known about the lattice spacing dependence of the excited baryon masses which play very important role in baryon number fluctuations in the temperature range of interest. We assume that all the excited baryons up to certain mass threshold m^B_{cut} have the same quark mass and lattice spacing dependence, while the baryon masses above that threshold are not modified by finite lattice spacing. The mass threshold m^B_{cut} is an additional parameter of our model. In Fig. 2 we show the lattice data for baryon number fluctuations for asqtad action compared with hadron resonance gas model with physical value of the baryon masses including all the states up to 2.5 GeV. The lattice data fall considerably below the HRG prediction. The baryon number fluctuations have also been calculated in a HRG model, where all the baryon masses up to the $m^B_{cut} = 1.8$ GeV and $m^B_{cut} = 2.5$ GeV have been modified according to Eqs. (2.8)–(2.12). The corresponding results are shown as dashed lines. As one can see, the HRG overshoots the lattice data with $m^B_{cut} = 1.8$ GeV, while with $m^B_{cut} = 2.5$ GeV it undershoots the lattice data. However, the agreement between lattice data and HRG is greatly improved. For completeness we also show the lattice data for p4 action calculated for $m_q = 0.1m_s$ [16].

Strangeness fluctuations have also been calculated on the lattice using asqtad and p4 action [16,24,38,39] on $N_\tau = 6$ and $N_\tau = 8$ lattices. We have calculated strangeness fluctuations in HRG model, where ground vector state meson masses have been calculated using Eq. (2.8), while baryon masses have been calculated using Eqs. (2.8)–(2.12). The contribution of kaons has been treated in the way discussed in Section 2.1, i.e. for each physical kaon averaging over sixteen staggered flavors have been performed and the mass splitting has been calculated using Eq. (2.5). This turns out to be important for the description of strangeness fluctuation for temperatures $T <$ 165 MeV, where the contribution of kaons is quite significant. In Fig. 3 we show the prediction of the HRG model with modified hadron masses compared to the lattice data for asqtad action for $N_\tau = 8$. In the figure we show the prediction of the HRG model with cutoffs $m^B_{cut} = 1.8$ GeV and $m^B_{cut} = 2.5$ GeV for the baryon masses. Here the effect of using different cutoffs for the modification of the baryon masses is significantly smaller as meson contribution to strangeness fluctuations is large. In the figure we also show the prediction of the HRG model with physical

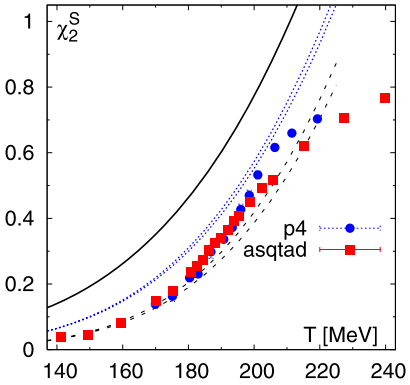

Fig. 3. The strangeness fluctuations calculated on $N_\tau = 8$ lattices for asqtad and p4 actions and compared with the prediction of the HRG model with physical (solid line) and modified (dashed lines) hadron masses. The upper (lower) dashed line corresponds to $m^B_{cut} = 1.8(2.5)$ GeV. The doted lines show the prediction of the HRG with modified hadron masses for $N_\tau = 12$.

hadron masses as well as the lattice results for the p4 action. As one can see the lattice data fall significantly below the predictions of HRG model with physical quark masses, while the HRG model with modified hadron masses gives quite a good description of the lattice data. For completeness we also show the result for HRG model with modified hadron masses for $N_\tau = 12$. As one can see from Figs. 2 and 3, HRG model can describe baryon number and strangeness fluctuations reasonably well up to temperatures as high as T_c.

4. QCD equation of state

4.1. The trace anomaly and parametrization of the equation of state

Available lattice data provide an EoS which is not easy to use in hydrodynamic models because different thermodynamic quantities are suppressed in the low temperature region due to discretization errors. In the previous section we have seen this for baryon number and strangeness fluctuations.

In lattice QCD the calculation of the pressure, energy density and entropy density usually proceeds through the calculation of the trace anomaly $\Theta(T) = \epsilon(T) - 3p(T)$. Using the thermodynamic identity the pressure difference at temperatures T and $T_{\rm low}$ can be expressed as the integral of the trace anomaly

$$\frac{p(T)}{T^4} - \frac{p(T_{\rm low})}{T_{\rm low}} = \int_{T_{\rm low}}^{T} \frac{dT'}{T'^5}\Theta(T). \tag{4.1}$$

By choosing the lower integration limit sufficiently small, $p(T_{\rm low})$ can be neglected due to the exponential suppression. Then the energy density $\epsilon(T) = \Theta(T) + 3p(T)$ and the entropy density $s(T) = (\epsilon + p)/T$ can be calculated. This procedure is known as the integral method [40]. Since the trace anomaly plays a central role in lattice determination of the equation of state, we will discuss it in the HRG model and its comparison with the lattice data in the following. As we will see this helps constructing realistic equation of state that can be used in hydrodynamic models.

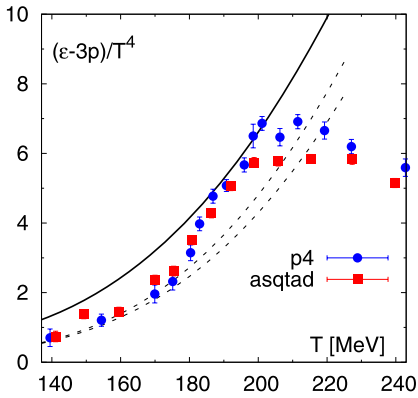

Fig. 4. The trace anomaly calculated in lattice QCD compared with the HRG model with physical hadron masses (solid line) and modified hadron masses (dashed lines). The upper (lower) dashed line corresponds to $m^B_{cut} = 1.8(2.5)$ GeV.

As mentioned before, finite temperature lattice calculations are usually performed at fixed temporal extent N_τ and the temperature is varied by varying the lattice spacing a, $T = 1/(N_\tau a)$. Thus, calculations at low temperatures are performed on coarse lattices, while the lattice spacing gets smaller as the temperature is increased. Consequently the trace anomaly can be accurately calculated in the high temperature region, while in the low temperature region it is affected by possibly large discretization effects. Therefore to construct realistic equation of state we could use the lattice data for the trace anomaly in the high temperature region, $T > 250$ MeV, and use HRG model in the low temperature region, $T \lesssim 180$ MeV. In Fig. 4 we compare the lattice results on trace anomaly obtained on $N_\tau = 8$ lattices with asqtad and p4 action with the HRG model. The HRG model with modified masses appears to describe the lattice data quite well up to temperatures of about 180 MeV. In the intermediate temperature region 180 MeV $\lesssim T < 250$ MeV the HRG model is no longer reliable, whereas discretization effects in lattice calculations could be large. The later can be seen by comparing the lattice data obtained on $N_\tau = 6$ and $N_\tau = 8$ lattices with p4 and asqtad action. Therefore we constrain the trace anomaly in the intermediate region only by the value of the entropy density at high temperatures.

In pure gauge theory, where continuum extrapolation has been performed, the entropy density falls below the ideal gas limit only by 15% at temperatures of about $4T_c$ [40] (T_c is the transition temperature). In QCD the entropy density calculated on $N_\tau = 6$ and 8 lattices is (5–10)% below the ideal gas limit [41] at the highest available temperature. Furthermore, resummed perturbative calculations describe quite well the entropy density in the high temperature region both in pure gauge theory [42] and in QCD [41]. These calculations indicate that deviation from the ideal gas limit is about (5–10)%. The fluctuations of quark number are also close to ideal gas limit and well described by resummed perturbative calculations [41]. Here the deviation from the ideal gas limit is less than 5%. Therefore we will use the guidance from existing lattice QCD calculations and require that the entropy density is below the ideal gas limit by either 5% or 10%, when parametrizing the trace anomaly.

At high temperature the trace anomaly can be well parametrized by the inverse polynomial form (see e.g. Ref. [24]). Therefore we will use the following Ansatz for the high temperature region

$$(e - 3P)/T^4 = d_2/T^2 + d_4/T^4 + c_1/T^{n_1} + c_2/T^{n_2}. \tag{4.2}$$

Table 2
The values of the parameters for different fits of the trace anomaly.

	d_2 (GeV^2)	d_4 (GeV^4)	c_1 (GeV^{n_1})	c_2 (GeV^{n_2})	n_1	n_2	T_0 (MeV)
$s95p$	0.2660	2.403×10^{-3}	-2.809×10^{-7}	6.073×10^{-23}	10	30	183.8
$s95n$	0.2654	6.563×10^{-3}	-4.370×10^{-5}	5.774×10^{-6}	8	9	171.8
$s90f$	0.2495	1.355×10^{-2}	-3.237×10^{-3}	1.439×10^{-14}	5	18	170.0

This form does not have the right asymptotic behavior in the high temperature region, where we expect $(e-3P)/T^4 \sim g^4(T) \sim 1/\ln^2(T/\Lambda_{\rm QCD})$, but works well in the temperature range of interest. Furthermore, it is flexible enough to do the matching to the HRG result in low temperature region. We match to the HRG model at temperature T_0 by requiring that the trace anomaly as well as its first and second derivatives are continuous. The parametrization of the trace anomaly and thus QCD equation of state obtained using these requirements are labeled by $s95p$-v1, $s95n$-v1 and $s90f$-v1. The labels "$s95$" and "$s90$" refer to the fraction of the ideal entropy density reached at $T = 800$ MeV (95% and 90% respectively), whereas the labels p, n and f refer to a specific treatment of the peak of the trace anomaly or its matching to the HRG. The detailed procedure of performing the fit to the lattice data and matching to the HRG model is described in Appendix B, where also the labeling scheme is explained in more detail. The values of the parameters T_0, d_2, d_4, c_1, c_2, n_1 and n_2 in each parametrization are given in Table 2. The HRG result for the trace anomaly can also be parametrized by the simple form

$$\frac{\epsilon - 3P}{T^4} = a_1 T + a_2 T^3 + a_3 T^4 + a_4 T^{10}, \tag{4.3}$$

with $a_1 = 4.654$ GeV^{-1}, $a_2 = -879$ GeV^{-3}, $a_3 = 8081$ GeV^{-4}, $a_4 = -7039000$ GeV^{-10} (see Appendix B for details).

The lattice data for trace anomaly compared to the parametrization given by Eqs. (4.2) and (4.3) is shown in Fig. 5. We show three parametrizations in the figure corresponding to a entropy density at $T = 800$ MeV which is below the ideal gas limit by 5% ($s95p$-v1 and $s95n$-v1, the solid and dotted lines, respectively) and 10% ($s90f$-v1, dashed line). All the parametrizations describe the lattice data for $T > 250$ MeV, while in the low temperature region, $T < 170$ MeV, they are significantly above the lattice results. On the other hand, our parametrizations of the trace anomaly are below the lattice data in the peak region. This comes from the imposed constraint on the entropy density at $T = 800$ MeV. If we would use a parametrization which goes through the $N_\tau = 8$, p4 lattice data and matches the resonance gas model at some temperature near 190 MeV, the entropy density would overshoot the ideal gas limit already at temperatures of about 600–700 MeV. Such a behavior would contradict the available lattice and weak coupling results.

The difference in the $s95n$-v1 and $s95p$-v1 parametrizations is in the treatment of the peak region. When we do the fit only on the lattice data above $T = 250$ MeV ($s95n$-v1, dotted line), the peak value is clearly below the present data. To explore the sensitivity of the EoS to the height of the peak, we also did the fit using one additional point at $T = 205$ MeV close to the present data, and the same entropy constrain ($s95p$-v1, solid line). This forces the trace anomaly almost to reach the data at the peak maintaining a reasonable fit to the data at high temperatures.

The EoSs, obtained by integrating the parametrizations given in Eqs. (4.2) and (4.3) over temperature as shown in Eq. (4.1), are shown in Fig. 6. The clearest difference between our different parametrizations is trivial: The different behavior at high temperatures is due to the different entropy constraint at $T = 800$ MeV, which is of course manifested in energy density and pressure

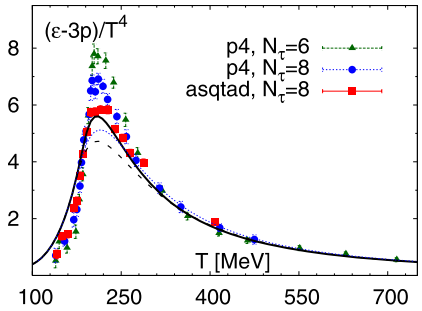

Fig. 5. The trace anomaly calculated in lattice QCD with p4 and asqtad actions on $N_\tau = 6$ and 8 lattices compared with the parametrization given by Eqs. (4.2) and (4.3). The solid, dotted and dashed lines correspond to parametrizations $s95p$-v1, $s95n$-v1 and $s90f$-v1 respectively, as discussed in the text.

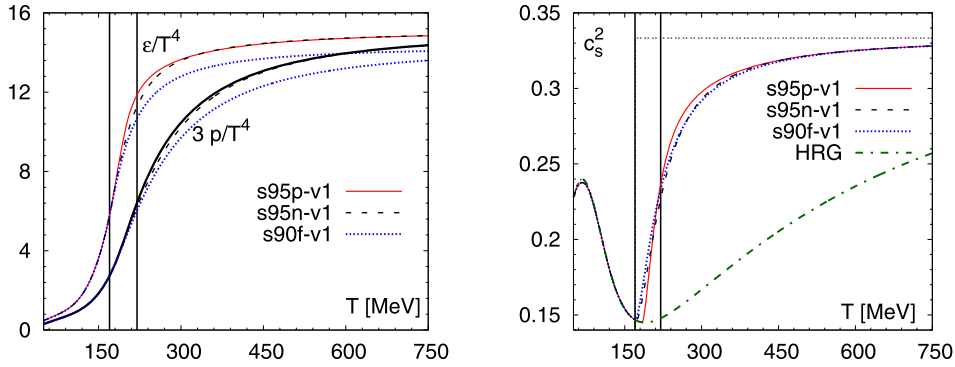

Fig. 6. The pressure, energy density (left panel) and speed of sound (right panel) in the equations of state obtained from Eqs. (4.2) and (4.3). The vertical lines indicate the transition region (see text). In the right panel we also show the speed of sound for the HRG EoS and EoS with first order phase transition (thin dotted) line, the EoS Q.

too. On the other hand, the different height of the peak of the trace anomaly causes only a tiny difference in pressure and energy density around $T = 200$ MeV. This difference is manifested much clearer in the speed of sound: The large peak and larger switching temperature from HRG to lattice causes much more rapid change in the speed of sound in $s95p$-v1 parametrization than in the two others. One could claim that the differences in the speed of sound are due to the different matching temperatures T_0, but we want to remind the reader that we treated T_0 as a fitting parameter in our model, and any changes in T_0 would make the fit to the lattice data worse (see details in Appendix B). In Fig. 6 we show the speed of sound for EoS Q from Refs. [43,44]: An equation of state with a first order phase transition at $T_c = 170$ MeV. Below T_c EoS Q coincides with HRG EoS, while above this temperature it is given by bag equation of state with three massless flavors and bag constant $B = (0.2447\ \text{GeV})^4$. Nevertheless, the most striking feature of the speed of sound in the proposed parametrization of the EoS is that there is no softening below the hadron gas. There is no region where speed of sound would be smaller than in hadron gas, and its minimum value is that of HRG speed of sound.[3] It is quite simple to understand why this happens: To achieve smaller speed of sound than the speed of sound in hadron gas, the

[3] Similar EoS was presented already in Refs. [45,46].

trace anomaly should be larger than in HRG. As one can see in Fig. 4, the present lattice data clearly disfavors such a scenario. In Fig. 6 we indicate the transition region from hadronic matter to deconfined state by vertical lines. We define the transition region as the temperature interval 170 MeV $< T <$ 220 MeV. In view of the crossover nature of the finite temperature QCD transition such definition is ambiguous. The lower temperature limit in our definition comes form the fact that for $T <$ 170 MeV all our EoS agree with HRG EoS. The rapid rise in the energy density and entropy density stops roughly at 220 MeV and starting from this temperature the variation of thermodynamic quantities is quite smooth [24]. Also the Kurtosis of the baryon number becomes compatible with quark gas at temperatures of about 220 MeV [16]. For these reasons we have chosen it as the upper limit for the transition region.

4.2. Comparison with other works

The idea of using HRG in low temperatures and parametrized lattice EoS in high temperatures is by no means new. Laine and Schröder constructed QCD equation of state based on the effective theory approach in the high temperature region, while using the resonance gas equation of state in the low temperature region [47]. In the effective theory approach the contribution of hard modes is treated perturbatively, while the contribution of soft modes is calculated using 3-dimensional lattice simulations of the effective theory called EQCD [48]. This parametrization has been used in recent viscous hydrodynamic calculations [49]. The smooth matching to the resonance gas was done in the temperature interval $T =$ 170–180 MeV.

Two other parametrizations of the EoS [45,46,50] used lattice data of Budapest–Wuppertal (BW) group obtained using so-called stout staggered fermion action [51] and temporal extent $N_\tau = 4$ and 6. Since the stout action does not use higher order difference scheme in the lattice Dirac operator, discretization effects at high temperatures are very large. In the ideal gas limit the pressure calculated on $N_\tau = 4$ and 6 lattices is about twice the continuum value. As the consequence the lattice results of the BW group have large cut-off effects and overshoot the continuum ideal gas at high temperatures, see discussion in Ref. [52]. In an attempt to correct this problem the authors of Ref. [51] divided all their thermodynamic observables by the corresponding ideal gas value calculated on $N_\tau = 4$ and 6. Since cutoff effects are strongly temperature dependent this procedure overestimates cutoff effects in the interesting temperature region and underestimates the pressure and other thermodynamic observables.

The Krakow group used the stout lattice results parametrized in Ref. [53] with $T_c = 167$ MeV and matched the speed of sound to the HRG result at that temperature [45,46]. The procedure of the Krakow group involves extracting all the other thermodynamical quantities from the speed of sound using the relation

$$s(T) = s(T_0) \exp\left[\int_{T_0}^{T} \frac{dT'}{T' c_s^2} \right]. \tag{4.4}$$

Connecting the speeds of sound in HRG and lattice leads in this procedure to a larger entropy density at high temperatures than given by the lattice parametrization of Ref. [53]. To make their EoS to fit the lattice data at $T \approx 1$ GeV, the Krakow group made the speed of sound smaller in the temperature region 28 MeV $< T <$ 118 MeV by hand [54]. This change is below the expected freeze-out temperature, and thus the speed of sound which affects the actual hydrodynamical evolution is unchanged. However, since entropy density is calculated by integrating over the entire temperature range, entropy density is smaller than the original HRG value everywhere in

the range 28 MeV $< T < T_c$. More specifically, in the range 120 MeV $< T <$ 160 MeV, both energy and entropy densities and pressure are $\sim 5\%$ below the HRG value, and energy is not automatically conserved at freeze-out, see the discussion in Section 5.

Heinz and Song also used the BW lattice results, but they parametrized pressure and temperature as function of energy density and matched them to HRG result; they used $T_c = 172$ MeV [50]. As the authors themselves note, their EoS is not exactly thermodynamically consistent, which leads to a violation of entropy conservation in an ideal fluid calculation. However, to our understanding this does not affect the qualitative studies the EoS has been used so far and the conclusions of those papers should be valid.

Here a note concerning T_c in these parametrizations is in order: In Ref. [51] thermodynamic quantities are given as function of T/T_c but the value of T_c is not specified. At lattice spacings corresponding to temporal extent $N_\tau = 4$ and $N_\tau = 6$, used in BW EoS calculations, T_c has large cutoff effects and may deviate considerably from the continuum value $T_c = 170(3)(4)$ MeV determined in Ref. [36] (e.g. calculations of T_c reported at Quark Matter 2005 on $N_\tau = 4$ and 6 lattices gave $T_c = 189(8)$ MeV [55]). The best way to eliminate part of the cutoff effects in the BW EoS is to use the continuum value of the transition temperature T_c, which is interestingly enough appears to agree within errors with the values used in the phenomenological parametrizations discussed above.

The parametrization of the EoS by the HotQCD Collaboration [24] is based on a simple fit of the lattice results on the trace anomaly. For temperatures below 130 MeV, where no lattice data is available, HRG values for the trace anomaly have been used and assigned an artificial error. The resulting parametrization is well below the HRG at temperatures $T > 50$ MeV, see discussion in Ref. [24]. For example, at $T \approx 130$ MeV and $T \approx 170$ MeV temperatures, pressure, energy and entropy densities are roughly 20% and 10% smaller than in HRG, respectively. Therefore, when one uses this parametrization, energy conservation at freeze-out requires additional consideration, see the discussion in Section 5.

In Fig. 7 we show the comparison of our parametrization for EoS with the ones discussed above including the trace anomaly, speed of sound, pressure and energy density as function of the temperature as well as the pressure as function of the energy density. From the figure we see that there are significant differences between different parametrizations. The parametrization based on BW lattice results seem to have different high temperature asymptotic. In the low temperature region the EoS L parametrization by Heinz and Song and the HotQCD parametrization differ significantly from others. It is worth noting that EoS L does not even try to reproduce the HRG below 130 MeV temperature. The authors assumed that the details of the EoS below freeze-out temperature have only a negligible effect on the evolution within the freeze-out surface and a faithful reproduction of the HRG is thus not needed. Finally, for the trace anomaly, the difference between our parametrization and HotQCD parametrization is limited to temperatures $T < 250$ MeV by construction. However, since the pressure, energy density and entropy density is obtained using the integral method the differences in trace anomaly at low temperatures result in differences at all temperatures for these quantities.

5. Effect on hydrodynamical flow

Now we are in a position to use the lattice results on EoS in a hydrodynamical model and compare the results with previous approaches using first order phase transition or the other lattice parametrizations in the literature. We also quantify how present uncertainties in the EoS parametrization affect the hydrodynamical flow. For simplicity we perform our analysis using

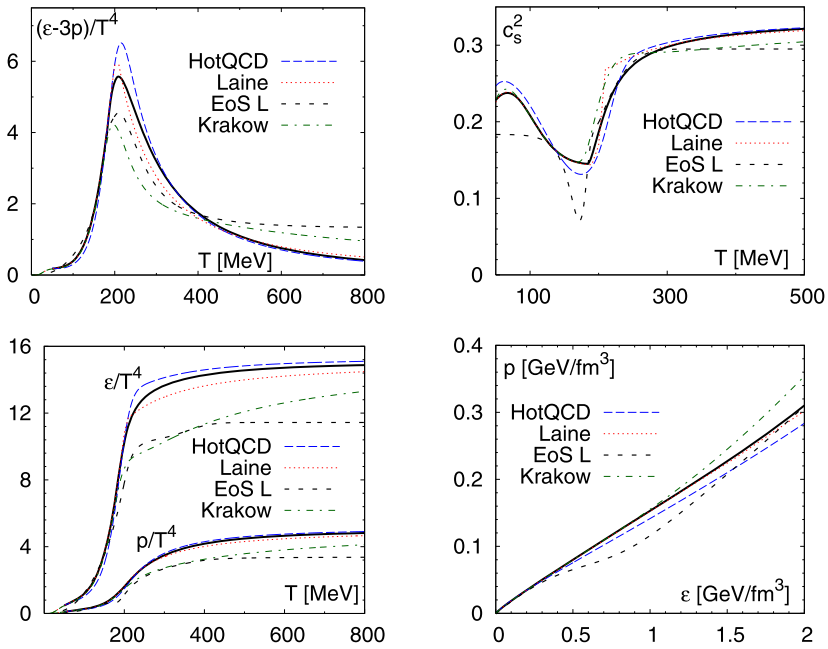

Fig. 7. The trace anomaly, the speed of sound, the pressure and the energy density as function of the temperature for different parametrizations used in hydrodynamic models. Also shown is the pressure as function of the energy density. The solid black line corresponds to $s95p$-v1 parametrization.

ideal hydrodynamics. This is also motivated by the fact that the overall value and temperature dependence of the QCD and HRG transport coefficients is not known and any attempts to parametrize them would introduce additional uncertainties in the analysis.

As the first step we study the sensitivity of the momentum anisotropy ϵ_p on the EoS. This is the cleanest way to address the sensitivity of hydrodynamic flow to the EoS as additional complications due to freezeout do not enter here. The momentum anisotropy is defined as [43]

$$\epsilon_p = \frac{\langle T_{xx} - T_{yy} \rangle}{\langle T_{xx} + T_{yy} \rangle}, \tag{5.1}$$

where T_{xx} and T_{yy} are the diagonal transverse components of the energy–momentum tensor and brackets denote averaging over the entire transverse plane. In Fig. 8 we show the time evolution of momentum anisotropy in Au + Au collisions at $\sqrt{s_{\rm NN}} = 200$ GeV with $b = 7$ fm impact parameter for different EoSs. The left panel shows the anisotropy calculated using our different parametrizations, and EoS Q from Refs. [43,44]. As studied in detail in Ref. [43] the first order phase transition causes the build up of the flow anisotropy to stall when most of the system is in the mixed phase. There is no such a structure when the transition to the hadronic matter is a smooth cross over, but the anisotropy increases monotonously. The hardness of the EoS in plasma phase is also manifested in the early behavior of the anisotropy. EoS Q is much harder in that region than any of the lattice EoSs studied here, and thus the build up of the flow anisotropy is faster. On the other hand, the mixed phase makes the EoS Q much softer in average during the evolution, and the final anisotropy is the smallest of all EoSs studied here. The speed of sound is quite similar in EoSs $s95p$-v1, $s95n$-v1 and $s90f$-v1, and consequently the development of the flow anisotropy is similar. When the system cools, the speed of sound stays large longest for

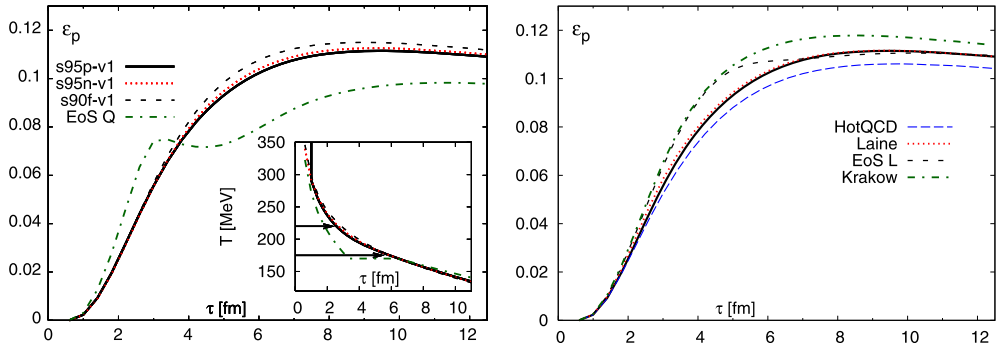

Fig. 8. The time evolution of the momentum anisotropy in $b = 7$ fm Au + Au collisions using the EoSs developed in this paper and the old EoS with a first order phase transition (EoS Q) from Refs. [43,44] (left panel) and the EoS $s95p$-v1 compared to the various lattice EoSs in the literature [24,45–47,50] (right panel). In the right panel the solid black line refers to the result obtained with $s95p$-v1 parametrization. The inset in the right panel shows the temperature evolution in the middle of the system for different EoSs. The horizontal lines indicate the transition region.

$s95p$-v1, but it also drops fastest and stays small longest for $s95p$-v1. These effects cancel, and the evolution of the anisotropy is almost identical to $s95n$-v1. After that argument, the largest anisotropy obtained using $s90f$-v1 may look surprising, but closer inspection of Fig. 6 reveals that $s90f$-v1 has always either larger or equal speed of sound than $s95p$-v1. Thus $s90f$-v1 is harder, and it should lead to a larger anisotropy than $s95p$-v1.

The old wisdom has been that elliptic flow builds up quickly during the early stages of the evolution and is mostly build up during the plasma phase. For example, for EoS Q, three quarters of the final anisotropy has been built up when the center of the system reaches mixed phase. For lattice based EoSs this is no longer as clear: Roughly half of the anisotropy is built up during the transition region, after the first three fm of the evolution, but the hadronic contribution from below $T = 170$ MeV temperatures to ϵ_p is essentially negligible unlike in EoS Q. This difference in the evolution is partly explained by the softer EoS in the plasma phase—anisotropy is built up slower. Another reason is that the transition region in our EoSs reaches up to $\epsilon \approx 3.5$ GeV/fm^3 energy density, whereas EoS Q reaches plasma phase already at $\epsilon \approx 2.15$ GeV/fm^3 density.

In the right panel of Fig. 8 $s95p$-v1 is compared to other lattice EoSs in the literature. The differences in flow are difficult to sort out based on the speed of sound as function of temperature alone, but they are easy to understand when one looks at the pressure as function of energy density (Fig. 7). It can be seen that the gradient $\partial P/\partial\epsilon$, i.e. speed of sound squared, is largest for the Krakow EoS, and EoS L is approximately as stiff as the Krakow EoS above $\epsilon \approx 1$ GeV/fm^3 density. Thus it is not surprising that the Krakow EoS leads to the largest anisotropy, and that the initial build up of the anisotropy is similar for the Krakow EoS and EoS L. The build up of flow deviates when EoS L reaches its softest region which is much softer than in any other EoS, and leads to behavior reminiscent of EoS Q: A sudden stall in the increase of the anisotropy. Unlike in EoS Q, however, there is no subsequent increase in anisotropy after the soft region has been passed. Likewise, even if the speed of sound in the HotQCD EoS at high temperatures is equal or even larger than in $s95p$-v1 or in the EoS by Laine and Schroder, the speed of sound in the transition region is so much smaller than in the other EoSs, that the final anisotropy is the smallest of all. As well, even if the speed of sound as function of temperature look different for $s95p$-v1 and Laine and Schroder's EoS, as a function of energy density they are almost equal, and thus these EoSs lead to basically identical build up of the flow anisotropy.

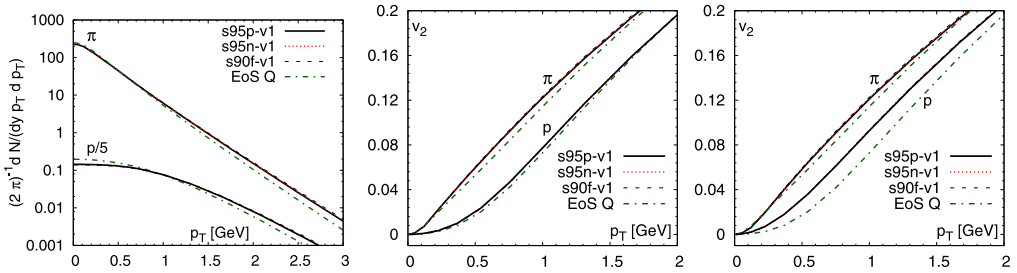

Fig. 9. The proton and pion spectra (left) and differential elliptic flow $v_2(p_T)$ of protons and pions (middle and right) in $b = 7$ fm Au + Au collisions for different EoSs. The results in the left and middle panels are calculated using the same freeze-out temperature $T_{\rm fo} = 125$ MeV for all the EoSs, whereas in the right panel it has been adjusted to produce similar p_T-distributions. $T_{\rm fo} = 125$ MeV for EoS Q, and $T_{\rm fo} = 140$ MeV for EoSs $s95p$-v1, $s95n$-v1 and $s90f$-v1.

As the next step we study the sensitivity of the spectra and elliptic flow on the EoS. We include freeze out into the calculation described above, and use first the same freeze out temperature, $T_{\rm fo} = 125$ MeV, for all EoSs.[4] The pion and proton spectra after resonance decays is shown in the left panel of Fig. 9 for EoSs $s95p$-v1, $s95n$-v1, $s90f$-v1 and EoS Q. As expected the new parametrization lead to flatter spectra than EoS Q, but the differences between the parametrizations themselves are too small to result in significant differences in spectra. The p_T-differential v_2 of pions and protons shown in the middle panel are surprisingly insensitive to the EoS. The larger flow anisotropy shown in Fig. 8 leads to larger p_T averaged v_2, but that is mostly due to flatter spectra weighting $v_2(p_T)$ at higher p_T where it is larger, than due to $v_2(p_T)$ being larger. One must also remember that this result is obtained using the same freeze-out temperature for all the EoSs. Before discussing how the EoS affects elliptic flow, one has to readjust the freeze-out temperature to produce similar spectra. This we have done in the right panel of Fig. 9: When one uses $T_{\rm fo} = 140$ MeV for EoSs $s95p$-v1, $s95n$-v1 and $s90f$-v1, the spectra are similar to those calculated using EoS Q. The pion $v_2(p_T)$ is virtually insensitive to the change in freeze-out temperature, but the higher temperature leads to much larger p_T-differential v_2 for protons. This behavior has already been explained in Ref. [56], where it was argued that the lower the temperature and larger the flow velocity, the smaller the $v_2(p_T)$ at low values of p_T, and that the heavier the particle, the stronger this effect. Note that the three different lattice based parametrizations of EoS give almost identical results for v_2 and spectra. This means that existing uncertainties in the EoS parametrization have negligible effect on the flow.

Unfortunately it is not straightforward to calculate the spectra and v_2 using the various EoSs in the literature discussed earlier. One of the advantages of the Cooper–Frye procedure for freeze-out is that energy, momentum, particle number and entropy are conserved. But, they are conserved only if the equation of state is the same before and after the freeze-out [23], i.e. that the fluid EoS is that of free particles and that the number of degrees of freedom in the fluid is the same than the number of hadrons and resonances which spectrum is calculated. This is not the case with the EoSs discussed here. When calculating the spectra we use the same set of resonances up to 2 GeV mass than what is included in our HRG. Laine and Schroder used resonances up to 2.5 GeV mass, but at, say, $T_{\rm fo} = 125$ MeV freeze-out temperature the difference in energy and entropy is minuscule, about 0.05%. The situation with the other EoSs is more difficult. At the mentioned temperature, the Krakow EoS has 4.5% smaller, EoS L 7% larger, and the HotQCD

[4] This temperature was found to reproduce the spectra when EoS Q is used [5].

Table 3
The freeze-out energy densities (in GeV/fm^3) and corresponding temperatures (in MeV) for fluid and particles for each EoS used in the calculations shown in Fig. 10.

	$\epsilon_{\rm fo}$	$T_{\rm fluid}$	$T_{\rm particles}$	$\epsilon_{\rm fo}$	$T_{\rm fluid}$	$T_{\rm particles}$
$s95p$-v1	0.065	125	125	0.14	140	140
HotQCD	0.065	129	125	0.11	139	135
Laine	0.065	125	125	0.14	140	140
EoS L	0.065	124	126	0.11	134	136
Krakow	0.065	126	125	0.185	146	145

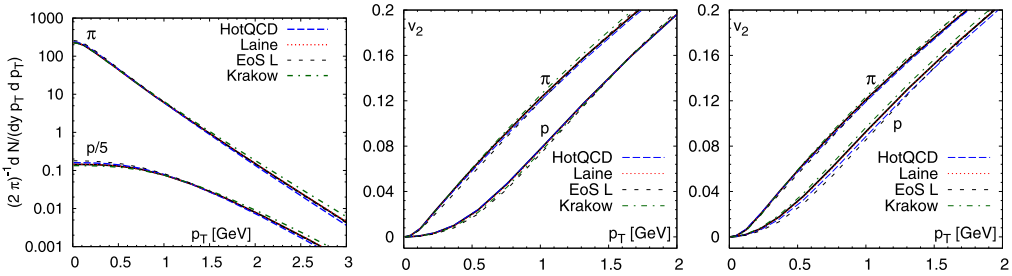

Fig. 10. The proton and pion spectra (left) and differential elliptic flow $v_2(p_T)$ of protons and pions (middle and right) in $b = 7$ fm Au + Au collisions for $s95p$-v1 (solid black line) and different EoSs in the literature [24,45–47,50]. The results in the left and middle panels are calculated using the same freeze-out energy density $\epsilon_{\rm fo} = 0.065$ GeV/fm^3 for all the EoSs, whereas in the right panel it has been adjusted to produce similar p_T-distributions, see text and Table 3.

EoS 22% smaller energy and entropy than hadrons and resonances up to 2 GeV mass. One way to correct this discrepancy is of course to change the number of hadrons and resonances included in the spectra calculation. But, this approach would be tedious since the number of resonances needed to fit the densities in the EoS may depend on temperature. Also there is no telling whether there exists a set of resonances reproducing both densities and pressure at a given temperature, and the number of resonances could be surprisingly small. For example a hadron resonance gas consisting of only pseudo-scalar and vector meson nonets, and baryon octet and decuplet, still has 10% larger energy density at $T = 125$ MeV than HotQCD EoS. Therefore we follow the approach espoused by Csernai [23] and Bugaev [57]: We require that energy and momentum are conserved locally on the freeze-out surface, i.e.

$$d\sigma_\mu T^{\mu\nu}_{\rm fluid} = d\sigma_\mu T^{\mu\nu}_{\rm particles}, \tag{5.2}$$

where $T^{\mu\nu}_{\rm fluid}$ is the energy–momentum tensor of the fluid on the surface, and $T^{\mu\nu}_{\rm particles}$ is the energy–momentum tensor of the emitted particles. To conserve energy and momentum, we allow the temperature and flow velocity of fluid and particles *differ*, i.e. there is a discontinuity on the surface, and freeze-out is a shock-like phenomenon [57]. We have to admit the corrections due to this procedure are small and mostly affect the multiplicity, but consider obeying the conservation laws worth the extra effort.

At first we use the same freeze-out energy density we used when comparing our parametrization to EoS Q, $\epsilon = 0.065$ GeV/fm^3, for all EoSs. The corresponding temperatures for each EoS are listed in Table 3. In the left panel of Fig. 10 we show the p_T distributions of pions and protons in $b = 7$ fm Au + Au collision. The differences in distributions are small, and the general behavior is what can be expected based on the stiffness of the EoSs and the flow anisotropy: The

Krakow EoS is the stiffest, and leads thus to the flattest spectra. The EoS by Laine and Schröder leads to behavior almost identical to $s95p$-v1, and the HotQCD EoS and EoS L are the softest and have slightly steeper spectra than the other EoSs. For the p_T-differential anisotropy of pions and protons the systematics is the same than seen for our parametrizations: when the freeze-out criterion is the same for all the EoSs, $v_2(p_T)$ is basically independent of the EoS, as shown in the middle panel of Fig. 10. After the freeze-out criterion is adjusted to reproduce spectra obtained using EoS Q, the pion $v_2(p_T)$ is independent of the EoS, but the proton anisotropy shows some sensitivity, see the right panel of Fig. 10. The differences between the EoSs are small and thus the differences in $v_2(p_T)$ are small, but an ordering according to the stiffness of the EoS is visible: The Krakow EoS is hardest, and its proton $v_2(p_T)$ is largest at small p_T, whereas the HotQCD EoS and EoS L are softest and lead to lowest $v_2(p_T)$ of protons at low p_T. After all the main results of this comparison are that the differences in the lattice EoS parametrization in the literature are small and not observable in the p_T-differential elliptic flow, and that energy conservation at freeze-out is not trivial if the EoS at freeze out is not that of free hadron resonance gas.

Finally we want to compare the results of our calculations with data. Since all of our parametrizations lead to practically identical spectra and v_2, we use only $s95p$-v1 for simplicity, and compare the results to those obtained using EoS Q in Ref. [5]. First we fix all the parameters by requiring the reproduction of pion and net-proton ($p - \bar{p}$) spectra in the 0–5% most central Au + Au collisions at $\sqrt{s_{\rm NN}} = 200$ GeV energy. The resulting spectra are shown in the left panel of Fig. 11, and the freeze-out temperatures are the same than mentioned before, $T_{\rm fo} = 125$ MeV for EoS Q, and $T_{\rm fo} = 140$ MeV for EoSs $s95p$-v1. Since we assume chemical equilibrium we cannot reproduce both proton and anti-proton yields at such a low temperature. Our parametrization is for zero baryochemical potential, so we cannot calculate net-protons either, but we approximate them by having a finite baryon density in the calculation, and converting this density into a finite chemical potential at freeze-out by using a HRG EoS which allows a finite net baryon density. The right panel of Fig. 11 shows the p_T-differential elliptic flow of pions and anti-protons in minimum bias Au + Au collisions at the same energy. As earlier, the pion $v_2(p_T)$ is very similar for both EoSs, but the anti-proton $v_2(p_T)$ is quite different. In fact for the realistic EoS the anti-proton v_2 is largely overpredicted, while we have a reasonable agreement with the data when the bag model EoS Q is used. This is very similar to the finding of Ref. [5]. Also the Krakow group seem to overpredict the proton v_2 [46] indicating that this could be a general feature of ideal hydrodynamic models using more realistic EoS. The first results indicate that dissipative effects can at least reduce this problem [60].

This analysis has been repeated assuming partial chemical equilibrium in the hadronic phase. The details of this analysis are given in Appendix C. Our main finding did not change. Using different EoS for the same initial conditions and kinetic freeze-out temperature has little effect on v_2 but leads to significant differences in the spectra. If the spectra are fitted to reproduce the experimental data by adjusting the initial conditions, the p_T-differential elliptic flow of anti-protons becomes too large for lattice based EoS, but agrees reasonably well with EoS Q. On the other hand, the p_T-differential elliptic flow of pions is clearly too large for both EoSs requiring substantial dissipation to reduce it to fit the data.

6. Conclusion

In this paper we addressed the question to what extent the Hadron Resonance Gas (HRG) model can describe the thermodynamic quantities calculated on the lattice. As discussed above this question is very important for implementing a consistent freeze-out prescription or a con-

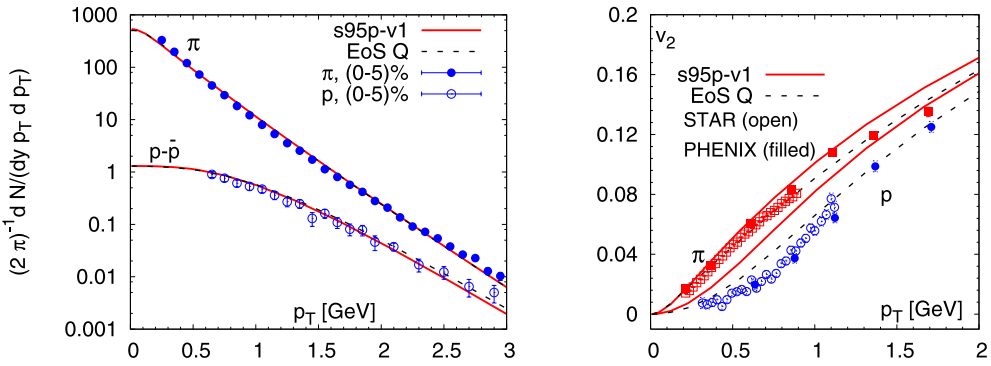

Fig. 11. Pion (π^+) and net-proton ($p-\bar{p}$) spectra in 0–5% most central (left), and pion and anti-proton p_T-differential elliptic flow $v_2(p_T)$ in minimum bias (right) Au + Au collisions at $\sqrt{s_{\rm NN}} = 200$ GeV compared with hydrodynamic calculations using two different EoSs and assuming chemical equilibrium. The data was taken by the PHENIX [58] and the STAR [59] Collaborations.

sistent switch to transport in hydrodynamic or hybrid models, respectively. We have found that lattice data strongly disagree with the HRG model in the low temperature regime. The reason for this disagreement has been identified with large cutoff effects in the lattice calculations. We also showed that taking into account the discretization effects in the hadron spectrum in the HRG model leads to a good agreement with the lattice data. In fact, we find that for some quantities the HRG model works well to unexpectedly high temperatures. Based on this observation we constructed several parametrizations of the equation of state which interpolate between the lattice data at high temperature and the resonance gas in the low temperature region. The central quantity in this analysis was the trace anomaly since it is directly calculated on the lattice and the differences in the proposed parametrizations are found in the temperature region where the trace anomaly reaches its maximal value.

We studied the hydrodynamic evolution using three parametrizations of the EoS that interpolate between HRG EoS and the lattice data and compared the results with the corresponding ones obtained using an EoS with a first order phase transition, the so-called EoS Q, as well as several other parametrizations of the EoS used in the literature. We have analyzed the flow in terms of momentum space anisotropy ϵ_p, p_T-differential elliptic flow $v_2(p_T)$ and proton and pion spectra. The three parametrizations of the EoS proposed in this paper as well the parametrization by Laine and Schröder [47] gave very similar results for all of the above quantities. The effect of using different EoS parametrizations is the most visible in ϵ_p. The difference in the results obtained with EoS Q and other parametrizations is especially large. Quite surprisingly $v_2(p_T)$ is not sensitive to the choice of the EoS if the same freeze-out temperature is used. The particle spectra on the other hand are sensitive to the EoS. However, the change in the EoS can be compensated by change of the freeze-out temperature. If the freeze-out temperature is adjusted to reproduce the particle spectra we see large differences in the proton $v_2(p_T)$ for EoS Q and other EoS parametrizations. However, for all the other parametrizations considered here, the proton $v_2(p_T)$ is quite similar.

The work presented in this paper should be extended in number of different ways. First we should extend the comparison of lattice QCD results with modified HRG to other fluctuations, including electric charge fluctuations as well as fourth and higher order fluctuations of baryon number, strangeness and electric charge. However, since these quantities were studied in detail

only for the p4 action, in the analysis additional assumptions about the cutoff effects in the hadron spectrum have to be made. Furthermore, it would be interesting to study the quark mass effects in the HRG model, especially since recent lattice calculations of the EoS extend to physical values of the light quark masses [61]. We also should consider the effect of finite baryon potential on the EoS. This will become important for application of hydrodynamic models to heavy ion collisions at lower energies, especially to the proposed RHIC energy scan. Finally, it will be interesting to study the effect of the EoS in the framework of viscous hydrodynamics. We plan to address these issues in forthcoming publications.

Acknowledgements

This work was supported by the U.S. Department of Energy under contract DE-AC02-98CH1086 and by the ExtreMe Matter Institute (EMMI). P.H. is grateful for support from Center of Analysis and Theory for Heavy Ion Experiment (CATHIE) which enabled him to stay in BNL where large part of this work was finalized, and for hospitality for Iowa State University where part of this work was done. We thank Larry McLerran for encouraging us to do this work. We also want to thank Mikko Laine, Mikolaj Chojnacki, Wojciech Florkowski, Huichao Song and Ulrich Heinz for providing us with their equations of state for comparison. P.P. thanks the members of the MILC Collaborations, especially Carleton DeTar, Steve Gottlieb, Urs Heller and Bob Sugar for correspondence and for providing their numerical results, including the unpublished data of Ref. [37]. P.P. is also grateful to Zoltán Fodor and Sándor Katz for correspondence and for providing the pion masses for the stout action.

Appendix A. Hadron masses on the lattice

In this appendix we are going to discuss the cutoff and quark mass dependence of hadron masses calculated on the lattice and give the parameters entering Eqs. (2.8)–(2.12). We have fitted the quark (pion) mass and lattice spacing dependence of the ρ, K^*, ϕ, N and Ω masses obtained in Refs. [25–28] by a simple Ansatz

$$r_1 m = r_1 m_0 + \frac{a_1 (r_1 m_\pi)^2}{1 + a_2 x} + \frac{b_1 x}{1 + b_2 x}, \quad x = (a/r_1)^2. \tag{A.1}$$

The values of the fit parameters m_0, a_1, a_2, b_1 and b_2 are given in Table 4. In Figs. 12, 13 and 14 we show the above parametrization against the available lattice data. Here we note that the lattice data for the Ω mass have been corrected to take into account that the physical strange quark mass is slightly smaller that the one used in lattice simulations. It turns out that Eq. (A.1) reproduces the experimental values of the hadron masses in continuum limit at the physical point $r_1 m_\pi = 0.226$. This justifies the use of Eqs. (2.8)–(2.12) for the evaluation of the hadron masses in the HRG model.

As discussed in the main text due to lack of detailed lattice studies we used Eq. (2.8) and Eqs. (2.10)–(2.12) to evaluate the mass of the Δ resonance as well as single and double strange baryons with values of the parameters in Table 4 corresponding to the nucleon. In Fig. 15 we compare our estimates of the Δ, Λ and Ξ baryon masses shown as lines with available lattice data from the MILC Collaboration [27,28].

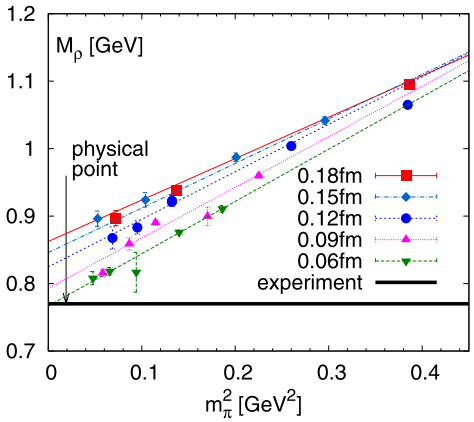

Fig. 12. The ρ-meson (right) masses calculated on the lattice using asqtad action [27,28,37] and compared with Eq. (A.1) (lines).

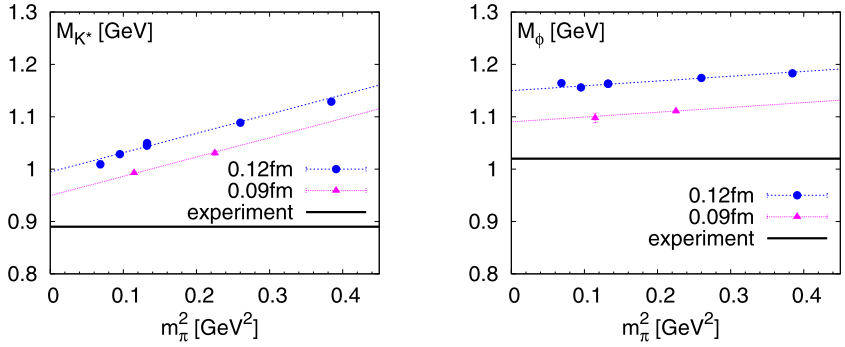

Fig. 13. The K^* (left) and ϕ-meson (right) masses calculated on the lattice using asqtad action [27,28] and compared with Eq. (A.1) (lines).

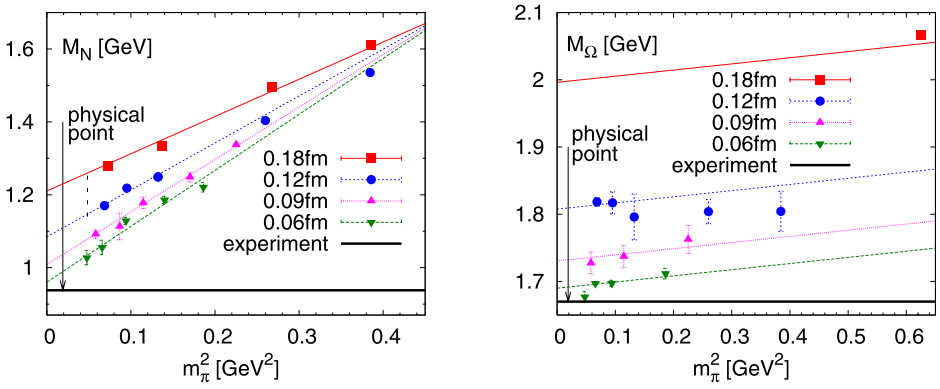

Fig. 14. The nucleon mass [27,28,37] (left) and the Ω baryon mass [25] (right) calculated with asqtad action and compared with our parametrization.

Table 4
The values of the parameters appearing in Eq. (2.8) for different hadrons.

	$r_1 m_0$	a_1	b_1	a_2	b_2
ρ	1.17856	0.496745	2.03538	0.958366	6.39177
K^*	1.41505	0.228217	2.07898	0	0
ϕ	1.60476	0.056901	2.74519	0	0
N	1.51418	0.933405	1.65138	1.27391	1.65138
Ω	2.66589	0.056779	1.74275	0	0

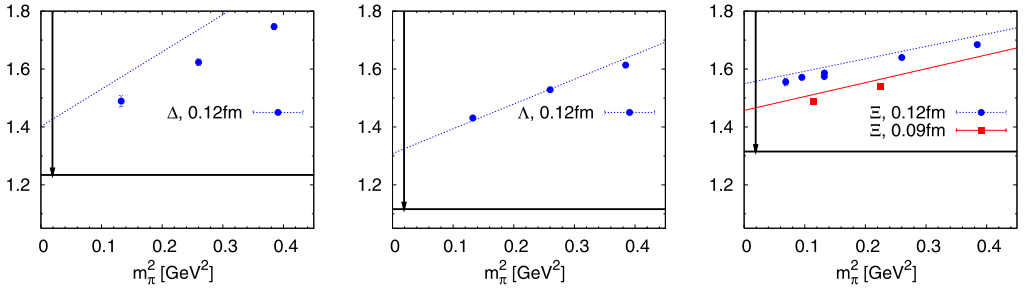

Fig. 15. The baryon masses calculated for asqtad action [27,28,37] and compared with our parametrization.

Appendix B. Fitting procedure

Here we describe in detail how we fit the trace anomaly of lattice and hadron resonance gas. The two first terms of the inverse polynomial Ansatz (Eq. 4.2)

$$(e-3P)/T^4 = d_2/T^2 + d_4/T^4 + c_1/T^{n_1} + c_2/T^{n_2} \tag{B.1}$$

appear to provide good fit of the lattice data at high temperatures, $T > 250$ MeV [24]. We want to join this parametrization to the trace anomaly of hadron resonance gas and require that the trace anomaly and its first and second derivative with respect to temperature are continuous where joined. Thus, we need one additional term with negative coefficient c_1 and exponent $n_1 > 4$ to produce a peak around $T \approx 200$ MeV, and another with positive coefficient c_2 and exponent $n_2 > n_1$ to make the second derivative continuous. We calculate the trace anomaly of hadron resonance gas using all the resonances up to 2 GeV mass[5] in the summary of the 2004 edition of the Review of Particle Physics [63]. We note that including all the resonances up to 2.5 GeV instead of 2 GeV mass gives result for the trace anomaly, which is only 2% larger at $T = 170$ MeV and 3% larger at $T = 180$ MeV. This change is definitely smaller than the expected discrepancies between HRG and lattice at these temperatures.

In the ansatz we have seven unknown parameters: the coefficients d_2, d_4, c_1 and c_2, exponents n_1 and n_2, and the switching temperature T_0. We have four constraints, the continuity of the trace anomaly and its derivatives at T_0, and the requirement $s(T = 800\ \text{MeV}) = 0.95 \cdot s_{\text{SB}}$ or $s(T = 800\ \text{MeV}) = 0.90 \cdot s_{\text{SB}}$. The requirement of the continuity of the derivatives gives two equations to fix the parameters c_1 and c_2:

$$c_2 = \frac{2(n_1-2)}{n_2(n_2-n_1)} T^{n_2-2} d_2 + \frac{4(n_1-4)}{n_2(n_2-n_1)} T^{n_2-4} d_4$$

[5] The list of included resonances and their properties can be found at [62].

$$+\frac{n_1+1}{n_2(n_2-n_1)}T^{n_2+1}G_1(T_0)+\frac{1}{n_2(n_2-n_1)}T^{n_2+2}G_2(T_0),$$

$$c_1=\frac{2(n_2-2)}{n_1(n_1-n_2)}T^{n_1-2}d_2+\frac{4(n_2-4)}{n_1(n_1-n_2)}T^{n_1-4}d_4$$

$$+\frac{n_2+1}{n_1(n_1-n_2)}T^{n_1+1}G_1(T_0)+\frac{1}{n_1(n_1-n_2)}T^{n_1+2}G_2(T_0),$$

where

$$\frac{d}{dT}\frac{\epsilon-3P}{T^4}\bigg|_{HG}\equiv G_1(T)\quad\text{and}\quad\frac{d^2}{dT^2}\frac{\epsilon-3P}{T^4}\bigg|_{HG}\equiv G_2(T).$$

From Eq. (4.1) and $Ts=\epsilon+P$ we obtain

$$\frac{s}{T^3}=d_2\left(\frac{2}{T_0^2}-\frac{1}{T^2}\right)+\frac{d_4}{T_0^4}+\frac{c_1}{n_1}\left(\frac{4}{T_0^{n_1}}+\frac{n_1-4}{T^{n_1}}\right)+\frac{c_2}{n_2}\left(\frac{4}{T_0^{n_2}}+\frac{n_2-4}{T^{n_2}}\right)+\frac{4P(T_0)}{T_0^4}. \tag{B.2}$$

Since entropy at $T=800$ MeV is fixed, we can use the above equation to constrain d_4,

$$d_4=d_4(d_2,n_1,n_2,T_0). \tag{B.3}$$

We can thus express the parameters c_1, c_2 and d_4 in terms of d_2, n_1, n_2 and T_0, and use the continuity of the trace anomaly to fix T_0. We get an equation

$$\frac{\epsilon-3P}{T^4}\bigg|_{HG}(T_0)=\frac{d_2}{T_0^2}+\frac{d_4(d_2,n_1,n_2,T_0)}{T_0^4}+\frac{c_1(d_2,n_1,n_2,T_0)}{T_0^{n_1}}+\frac{c_2(d_2,n_1,n_2,T_0)}{T_0^{n_2}}, \tag{B.4}$$

which can be evaluated numerically to obtain T_0. This procedure leaves us with three unknowns d_2, n_1 and n_2, which are chosen to fit the lattice data. However, such a fitting procedure would be highly nonlinear. We simplify the problem by requiring that the exponents are integers, and use brute force: We make a single parameter (d_2) fit with all the integer values $4<n_1<31$, and $n_1<n_2<43$, and choose the values n_1 and n_2 which lead to the smallest χ^2. Alternatively we can fix T_0 to a prescribed value, use Eq. (B.4) to fix the value of d_2, and use only n_1 and n_2 to perform the fit.

In our fit we use the lattice data for $T>250$ MeV obtained with p4 action on $N_\tau=8$ lattices as they extend to sufficiently high temperature [24]. In addition, we include $N_\tau=6$ p4 data for $T>500$ MeV [9]. The fits in general do not reproduce the lattice data in peak region (190 MeV $<T<$ 250 MeV). On the other hand the height of the peak in the trace anomaly may be affected by discretization effects. This can be seen as a difference between the $N_\tau=6$ and $N_\tau=8$ results. Assuming that discretization effects in the peak height go like $1/N_\tau^2$ we can estimate the trace anomaly at $T=206$ MeV to be 5.7 ± 0.15. We can use this value as an additional data point in our fits. We label different parametrizations of the trace anomaly obtained using different constraints on the entropy density at $T=800$ MeV and its height in the temperature region 190 MeV $<T<$ 250 MeV as $s95p$-v1, $s95n$-v1, $s90f$-v1 etc. The first three characters stand for the constrain on the entropy density (90% or 95% of the ideal gas value). The fourth character stands for additional constraints on the trace anomaly in the peak region. Namely, "n" stands for a fit with no constraints: using data for $T>250$ MeV, and T_0 as a free parameter in the fit. "p" means having an additional data point of 5.7 ± 0.15 at $T=206$ MeV to constrain the

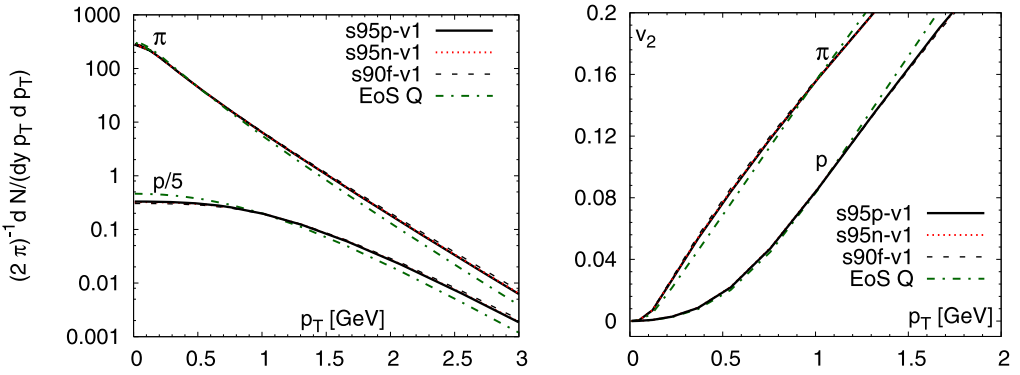

Fig. 16. The p_T-differential elliptic flow $v_2(p_T)$ of protons and pions (left) and proton and pion spectra (right) for different EoSs in $b = 7$ fm Au + Au collision when chemical freeze-out takes place at $T_{\rm chem} = 150$ MeV and kinetic at $T_{\rm kin} = 120$ MeV.

peak, and "f" stands for a fixed value $T_0 = 170$ MeV in the fit. Finally "v1" is the version number of the current parametrization. The value of the parameters d_2, d_4, c_1, c_2, n_1, n_2 and T_0 for different fits are given in Table 2. This procedure was designed for numerical applications when the trace anomaly is numerically evaluated using Eq. (2.1) and laws of thermodynamics. For practical purposes we also provide a parametrized version of the trace anomaly of the hadronic part of our EoS. We choose a polynomial

$$\frac{\epsilon - 3P}{T^4} = a_1 T^{l_1} + a_2 T^{l_2} + a_3 T^{l_3} + a_4 T^{l_4} \tag{B.5}$$

and fit it to the trace anomaly of the hadron resonance gas evaluated in the temperature interval $70 < T/\text{MeV} < 190$ with 1 MeV steps assuming that each point has equal "error". The limits have entirely utilitarian origin: in hydrodynamical applications the system decouples well above 70 MeV temperature and only a rough approximation of the EoS, $P = P(\epsilon)$, is needed at lower temperatures. On the other hand we expect to switch to the lattice parametrization below 190 MeV, and the HRG EoS above that is not needed either. We fix the exponents in Eq. (B.5) again using brute force. We require them to be integers, go through all the combinations $0 \leqslant l_1 < l_2 < l_3 < l_4 \leqslant 10$, fit the parameters a_1, a_2, a_3, a_4 to the HRG trace anomaly evaluated with 1 MeV intervals, and choose the values l_1, l_2, l_3 and l_4 which minimize the χ^2. We end up with $l_1 = 1$, $l_2 = 3$, $l_3 = 4$, $l_4 = 10$, and $a_1 = 4.654\ \text{GeV}^{-1}$, $a_2 = -879\ \text{GeV}^{-3}$, $a_3 = 8081\ \text{GeV}^{-4}$, $a_4 = -7039000\ \text{GeV}^{-10}$. To obtain the EoS, one also needs the pressure at the lower limit of the integration (see Eq. (4.1)) $T_{\rm low} = 0.07$ GeV: $P(T_{\rm low})/T_{\rm low}^4 = 0.1661$. Our EoSs are also available in a tabulated form at [62].

Appendix C. Spectra and elliptic flow for partial chemical equilibrium

In this appendix we discuss the elliptic flow and the spectra of protons and pions and their sensitivity on EoS when partial chemical equilibrium [44,64,65] is assumed to reproduce the observed particle yields. The EoS for the system in partial chemical equilibrium is available in tabulated form [62]. We again calculate the flow in Au + Au collision at $\sqrt{s_{\rm NN}} = 200$ GeV with impact parameter $b = 7$ fm. First we used the same initial condition and the same freeze-out temperature for all EoSs, namely $T_{\rm chem} = 150$ MeV for the chemical freeze-out temperature and

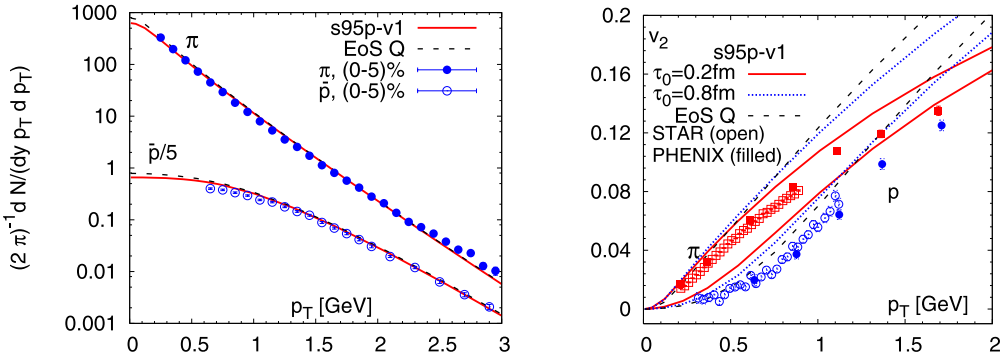

Fig. 17. Pion (π^+) and net-proton ($p-\bar{p}$) spectra in 0–5% most central (left), and pion and anti-proton p_T-differential elliptic flow $v_2(p_T)$ in minimum bias (right) Au + Au collisions at $\sqrt{s_{\rm NN}} = 200$ GeV compared with hydrodynamic calculations using two different EoSs and assuming chemical freeze-out at $T_{\rm chem} = 150$ MeV. The calculation using EoS $s95p$-v1 was done using two different initial states, see the text. The data was taken by the PHENIX [58] and the STAR [59] Collaborations.

$T_{\rm kin} = 120$ MeV for the kinetic freeze-out temperature. The initial time for the hydrodynamic evolution was chosen to be $\tau = 0.6$ fm and the initial entropy density was chosen as for the case of chemical equilibrium. The results are shown in Fig. 16. As one can see the elliptic flow is not very sensitive to the choice of EoS if everything else is kept unchanged, and all three parametrizations used in the analysis give almost the same result. The spectra are much more sensitive to the EoS but again there is no difference for the different lattice parametrizations.

For a proper discussion on the sensitivity of elliptic flow on the EoS, one has to again re-tune the calculation to reproduce the experimental results on the p_T-spectra. We obtained the best results by keeping the chemical and kinetic freeze-out temperatures, $T_{\rm chem} = 150$ MeV and $T_{\rm kin} = 120$ MeV unchanged, and tuned the initial conditions. For EoS Q we used $\tau_0 = 0.2$ fm and initial entropy density which scales with the number of binary collisions (see Ref. [44]). For the $s95p$-v1 parametrization of the EoS we used two different initial conditions. One with $\tau_0 = 0.8$ fm and initial entropy density proportional to the number of binary collisions, and a second one with $\tau_0 = 0.2$ fm and initial entropy density scaling with a combination of binary collisions and number of participants. The corresponding results are shown in Fig. 17. We see again that the lattice based EoS give larger p_T-differential elliptic flow for the protons than EoS Q for both initial conditions. In this case, however, the EoS Q does not do a good job of describing the data either, in agreement with previous findings [44,65]. Especially the pion p_T-differential v_2 is too large for all EoSs, and there is clearly room for significant dissipation to reduce the anisotropy. It is also worth to notice that the uncertainty related to the initial state is at least as large as the effect of the EoS on the proton $v_2(p_T)$ and better theoretical constraints to the initial state are needed.

References

[1] M. Hindmarsh, O. Philipsen, Phys. Rev. D 71 (2005) 087302, arXiv:hep-ph/0501232.
[2] M. Laine, PoS LAT2006 (2006) 014, arXiv:hep-lat/0612023.
[3] P.F. Kolb, U.W. Heinz, arXiv:nucl-th/0305084;
P. Huovinen, arXiv:nucl-th/0305064.
[4] Y. Aoki, G. Endrodi, Z. Fodor, S.D. Katz, K.K. Szabo, Nature 443 (2006) 675, arXiv:hep-lat/0611014.
[5] P. Huovinen, Nucl. Phys. A 761 (2005) 296, arXiv:nucl-th/0505036.

[6] P. Petreczky, Nucl. Phys. B (Proc. Suppl.) 140 (2005) 78, arXiv:hep-lat/0409139.
[7] C. DeTar, PoS LAT2008 (2008) 001, arXiv:0811.2429 [hep-lat].
[8] C. Bernard, et al., Phys. Rev. D 75 (2007) 094505, arXiv:hep-lat/0611031.
[9] M. Cheng, et al., Phys. Rev. D 77 (2008) 014511, arXiv:0710.0354 [hep-lat].
[10] A. Andronic, P. Braun-Munzinger, K. Redlich, J. Stachel, Phys. Lett. B 571 (2003) 36, arXiv:nucl-th/0303036.
[11] J. Noronha-Hostler, J. Noronha, C. Greiner, Phys. Rev. Lett. 103 (2009) 172302, arXiv:0811.1571 [nucl-th].
[12] P. Braun-Munzinger, J. Stachel, C. Wetterich, Phys. Lett. B 596 (2004) 61, arXiv:nucl-th/0311005.
[13] F. Karsch, K. Redlich, A. Tawfik, Eur. Phys. J. C 29 (2003) 549, arXiv:hep-ph/0303108.
[14] F. Karsch, K. Redlich, A. Tawfik, Phys. Lett. B 571 (2003) 67, arXiv:hep-ph/0306208.
[15] S. Ejiri, F. Karsch, K. Redlich, Phys. Lett. B 633 (2006) 275, arXiv:hep-ph/0509051.
[16] M. Cheng, et al., Phys. Rev. D 79 (2009) 074505, arXiv:0811.1006 [hep-lat].
[17] P. Gerber, H. Leutwyler, Nucl. Phys. B 321 (1989) 387.
[18] R. Dashen, S. Ma, H.J. Berstein, Phys. Rev. 187 (1969) 349.
[19] R. Venugopalan, M. Prakash, Nucl. Phys. A 546 (1992) 718.
[20] R. Hagedorn, in: Quark Matter '84, in: Lecture Notes in Physics, vol. 211, Springer, Berlin, 1985;
R. Hagedorn, Riv. Nuovo Cim. 6 (1983) 1;
R. Fiore, R. Hagedorn, F. D'Isep, Nuovo Cim. A 88 (1985) 301.
[21] L.M. Satarov, M.N. Dmitriev, I.N. Mishustin, Phys. Atom. Nucl. 72 (2009) 1390, arXiv:0901.1430 [hep-ph].
[22] F. Cooper, G. Frye, Phys. Rev. D 10 (1974) 186.
[23] C. Anderlik, et al., Phys. Rev. C 59 (1999) 3309, arXiv:nucl-th/9806004.
[24] A. Bazavov, et al., Phys. Rev. D 80 (2009) 014504, arXiv:0903.4379 [hep-lat].
[25] A. Bazavov, et al., arXiv:0903.3598 [hep-lat].
[26] C. Bernard, et al., MILC Collaboration, PoS LAT2007 (2007) 137, arXiv:0711.0021 [hep-lat].
[27] C. Aubin, et al., Phys. Rev. D 70 (2004) 094505, arXiv:hep-lat/0402030.
[28] C.W. Bernard, et al., Phys. Rev. D 64 (2001) 054506, arXiv:hep-lat/0104002.
[29] S. Durr, et al., Science 322 (2008) 1224.
[30] S. Durr, et al., Phys. Rev. D 79 (2009) 014501, arXiv:0802.2706 [hep-lat].
[31] C. Bernard, M. Golterman, Y. Shamir, S.R. Sharpe, Phys. Rev. D 77 (2008) 114504, arXiv:0711.0696 [hep-lat].
[32] M. Creutz, PoS LAT2007 (2007) 007, arXiv:0708.1295 [hep-lat].
[33] A.S. Kronfeld, PoS LAT2007 (2007) 016, arXiv:0711.0699 [hep-lat].
[34] M.F.L. Golterman, Nucl. Phys. B 273 (1986) 663;
M.F.L. Golterman, Nucl. Phys. B 278 (1986) 417.
[35] H. Kluberg-Stern, A. Morel, O. Napoly, B. Petersson, Nucl. Phys. B 220 (1983) 447.
[36] Y. Aoki, Z. Fodor, S.D. Katz, K.K. Szabó, Phys. Lett. B 643 (2006) 46, arXiv:hep-lat/0609068;
Y. Aoki, S. Borsányi, S. Durr, Z. Fodor, S.D. Katz, S. Krieg, K.K. Szabó, JHEP 0906 (2009) 088, arXiv:0903.4155 [hep-lat].
[37] Baryon and vector meson masses for 0.15 fm and 0.18 fm were calculated by the MILC Collaboration but not published.
[38] C. Bernard, et al., MILC Collaboration, Phys. Rev. D 71 (2005) 034504, arXiv:hep-lat/0405029.
[39] S. Basak, et al., MILC Collaboration, PoS LATTICE2008 (2008) 175, arXiv:0910.0276 [hep-lat].
[40] G. Boyd, J. Engels, F. Karsch, E. Laermann, C. Legeland, M. Lutgemeier, B. Petersson, Nucl. Phys. B 469 (1996) 419, arXiv:hep-lat/9602007.
[41] P. Petreczky, Nucl. Phys. A 830 (2009) 11C, arXiv:0908.1917 [hep-ph].
[42] J.P. Blaizot, E. Iancu, A. Rebhan, Phys. Rev. Lett. 83 (1999) 2906, arXiv:hep-ph/9906340;
J.P. Blaizot, E. Iancu, A. Rebhan, Phys. Lett. B 523 (2001) 143, arXiv:hep-ph/0110369;
J.O. Andersen, E. Braaten, M. Strickland, Phys. Rev. Lett. 83 (1999) 2139, arXiv:hep-ph/9902327;
J.O. Andersen, M. Strickland, N. Su, arXiv:0911.0676 [hep-ph].
[43] P.F. Kolb, J. Sollfrank, U.W. Heinz, Phys. Rev. C 62 (2000) 054909, arXiv:hep-ph/0006129.
[44] P. Huovinen, Eur. Phys. J. A 37 (2008) 121, arXiv:0710.4379 [nucl-th].
[45] M. Chojnacki, W. Florkowski, Acta Phys. Polon. B 38 (2007) 3249, arXiv:nucl-th/0702030.
[46] M. Chojnacki, W. Florkowski, W. Broniowski, A. Kisiel, Phys. Rev. C 78 (2008) 014905, arXiv:0712.0947 [nucl-th].
[47] M. Laine, Y. Schroder, Phys. Rev. D 73 (2006) 085009, arXiv:hep-ph/0603048.
[48] K. Kajantie, M. Laine, K. Rummukainen, Y. Schroder, Phys. Rev. Lett. 86 (2001) 10, arXiv:hep-ph/0007109;
K. Kajantie, M. Laine, K. Rummukainen, M.E. Shaposhnikov, Nucl. Phys. B 503 (1997) 357, arXiv:hep-ph/9704416.

[49] P. Romatschke, U. Romatschke, Phys. Rev. Lett. 99 (2007) 172301, arXiv:0706.1522 [nucl-th];
M. Luzum, P. Romatschke, Phys. Rev. C 78 (2008) 034915, arXiv:0804.4015 [nucl-th];
M. Luzum, P. Romatschke, Phys. Rev. C 79 (2009) 039903, Erratum.
[50] H. Song, U.W. Heinz, Phys. Rev. C 78 (2008) 024902, arXiv:0805.1756 [nucl-th].
[51] Y. Aoki, Z. Fodor, S.D. Katz, K.K. Szabó, JHEP 0601 (2006) 089, arXiv:hep-lat/0510084.
[52] P. Petreczky, Nucl. Phys. A 785 (2007) 10, arXiv:hep-lat/0609040.
[53] T.S. Biro, J. Zimányi, Phys. Lett. B 650 (2007) 193, arXiv:hep-ph/0607079.
[54] M. Chojnacki, personal communication.
[55] S. Katz, Plenary talk presented at Quark Matter, http://qm2005.kfki.hu/Talks/Globe/aug5/0930//0930_Katz.pdf, 2005.
[56] P. Huovinen, P.F. Kolb, U.W. Heinz, P.V. Ruuskanen, S.A. Voloshin, Phys. Lett. B 503 (2001) 58, arXiv:hep-ph/0101136.
[57] K.A. Bugaev, M.I. Gorenstein, W. Greiner, J. Phys. G 25 (1999) 2147, arXiv:nucl-th/9906088.
[58] S.S. Adler, et al., PHENIX Collaboration, Phys. Rev. C 69 (2004) 034909, arXiv:nucl-ex/0307022;
S.S. Adler, et al., PHENIX Collaboration, Phys. Rev. Lett. 91 (2003) 182301, arXiv:nucl-ex/0305013.
[59] J. Adams, et al., STAR Collaboration, Phys. Rev. C 72 (2005) 014904, arXiv:nucl-ex/0409033.
[60] P. Bozek, arXiv:0911.2397 [nucl-th];
P. Bozek, H. Song, Ph.D. Thesis, Ohio State University, arXiv:0908.3656 [nucl-th], 2009.
[61] M. Cheng, et al., arXiv:0911.2215 [hep-lat].
[62] https://wiki.bnl.gov/hhic/index.php/Lattice_calculatons_of_Equation_of_State and https://wiki.bnl.gov/TECHQM/index.php/Bulk_Evolution.
[63] S. Eidelman, et al., Particle Data Group, Phys. Lett. B 592 (2004) 1.
[64] H. Bebie, P. Gerber, J.L. Goity, H. Leutwyler, Nucl. Phys. B 378 (1992) 95.
[65] T. Hirano, K. Tsuda, Phys. Rev. C 66 (2002) 054905, arXiv:nucl-th/0205043.

Available online at www.sciencedirect.com
ScienceDirect
Nuclear Physics A 830 (2009) 475c–478c
NUCLEAR PHYSICS A
www.elsevier.com/locate/nuclphysa

Applicability of viscous hydrodynamics at RHIC

Denes Molnar[a,b] and Pasi Huovinen[a,c]

[a] *Physics Department, Purdue University, 525 Northwestern Avenue, West Lafayette, IN 47906, USA*
[b] *RIKEN BNL Research Center, Brookhaven National Laboratory, Upton, NY 11973, USA*
[c] *Institute für Theoretische Physik, Johann Wolfgang Goethe-Universität, Frankfurt am Main, Germany*

Abstract

In an earlier work[1] we established that causal Israel-Stewart viscous hydrodynamics is only accurate in RHIC applications at very low shear viscosities $4\pi\eta_s/s \lesssim 1.5-2$. We show here that the region of applicability is significantly reduced if bulk viscosity plays a role in the dynamics.

1. Introduction

There has been a lot of recent interest in quantifying the effect of viscosity on observables in heavy-ion collisions at the Relativistic Heavy Ion Collider (RHIC) at Brookhaven. Calculations are most commonly performed using causal dissipative hydrodynamics[2, 3, 4, 5], though covariant transport theory can also be utilized[5, 6, 7].

Hydrodynamics assumes that the system is near local thermal equilibrium. Its region of applicability can only be reliably determined with the help of a fully nonequilibrium theory. In a recent work[1] we used covariant transport to establish the region of validity for the causal Israel-Stewart (IS) formulation of viscous hydrodynamics, in a longitudinally boost invariant setting with a massless $e = 3p$ equation of state (EOS) and only shear viscosity. We found that for typical conditions expected in nuclear collisions at RHIC, IS hydrodynamics is a very good approximation (more precisely, 10% accurate in computing dissipative effects) when the shear viscosity (η_s) to entropy density (s) ratio is not too large, $4\pi\eta_s/s \lesssim 1.5-2$. A useful rule of thumb we obtained is that, in order to reach such accuracy, dissipative corrections to pressure and entropy must not exceed about 20%. This is only a necessary condition but its main advantage is that it can be tested directly from the hydrodynamic calculation.

Here we study the region of validity of IS hydrodynamics for systems with shear *and* bulk viscosity. Quantifying bulk effects in covariant transport near the hydrodynamic limit is unfortunately unfeasible, at least for a one-component system with $2 \to 2$ scattering, because bulk viscosity is at least two orders of magnitude smaller than shear viscosity. In order to proceed, we assume that the 20% rule of thumb above applies in the more general "shear+bulk" case as well.

Because for a massless equation of state bulk viscosity identically vanishes, we here use a more realistic result from lattice QCD[8] (we smoothly merge the EOS onto that of a hadron gas at low $T \lesssim 160$ MeV). Reliable calculations of viscosity in QCD are unfortunately not available for temperatures relevant for RHIC. We therefore focus on the "minimal viscosity"[9] paradigm, i.e., set $\eta_s = s/(4\pi)$. For the bulk viscosity, we consider a Lorentzian in temperature $\zeta = \zeta_m\, s/[1 + (T - T_c)^2/\Delta T^2]$, where the peak height and width are adjustable parameters. Matching to the bulk viscosity estimate from Meyer[10] gives our *default parameterization* $\zeta_m = 0.2$, $\Delta T = 0.03$ GeV and $T_c = 0.192$ GeV. Though our approach is similar to an earlier study by

doi:10.1016/j.nuclphysa.2009.10.104

Fries et al[11], *the main difference is that we also ensure thermodynamic consistency because we use the complete set of Israel-Stewart equations of motion*. We also map out a much wider range of initial conditions.

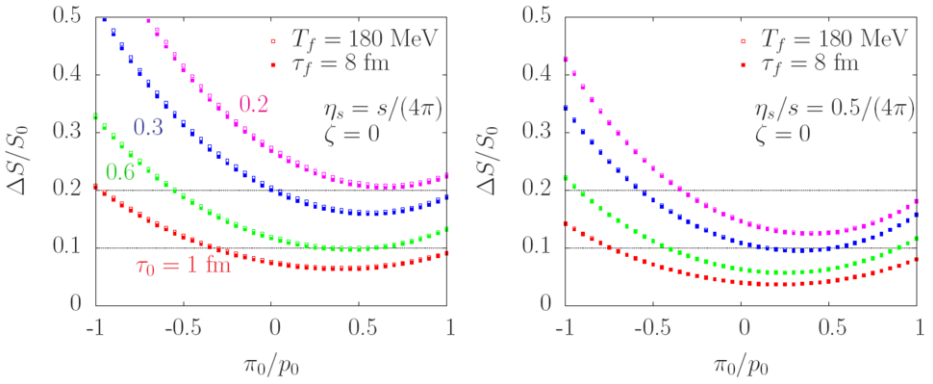

Figure 1: Entropy produced by the time the system cools down to $T = 180$ MeV ($\tau \approx 8$ fm) relative to the initial entropy, plotted as a function of thermalization time and initial shear stress, for $\eta_s/s = 1/(4\pi)$ (left) and $0.5/(4\pi)$ (right).

2. Main results

We solve the complete set of Israel-Stewart equations (cf. [1]) for a boost-invariant Bjorken scenario with axial and transverse translational symmetry. We only highlight here the equation for bulk pressure

$$\tau_\Pi \frac{d\Pi}{d\tau} = -\left(\Pi + \frac{\zeta}{\tau}\right) - \frac{\Pi\,\tau_\Pi}{2}\left(\frac{1}{\tau} + \frac{d}{d\tau}\ln\frac{\zeta}{\tau_\Pi T}\right). \quad (1)$$

Here τ_Π is bulk pressure relaxation time. If the last $\Pi\tau_\Pi$... term is ignored, the entropy generation rate per unit rapidity $d(dS/d\eta)/d\tau = \tau A_T[\Pi^2/(\zeta T) + 3\pi_L^2/(4\eta_s T)]$ becomes inconsistent with the Israel-Stewart expression for entropy $dS/d\eta = \tau A_T[s_{eq} - \Pi^2\tau_\Pi/(2T\zeta) - 3\pi_L^2\tau_\pi/(4T\eta_s)]$ (π_L is the shear correction to the longitudinal pressure, τ_π is the shear stress relaxation time, A_T is the transverse area of the system, and s_{eq} is the entropy density in local equilibrium). *Therefore, entropy production was overestimated in [11].*

Motivated by kinetic theory we set $\tau_\pi = 6\eta_s/(sT)$, but for simplicity take $\tau_\Pi = \tau_\pi$ (in kinetic theory $\tau_\Pi \approx 5\tau_\pi/3$ near the massless limit). Our default initial condition for Au+Au at RHIC is $e_0 = 15$ GeV/fm^3 ($T_0 \approx 0.297$ GeV) at a thermalization time $\tau_0 = 0.6$ fm. For $\tau_0 = 0.3$ and 1 fm, we scale on an isentropic curve $\tau_0 s_0 = const$. For initial shear stress and bulk pressure we map out wide ranges $-p_0 < \pi_0 < p_0$, $-p_0/2 < \Pi_0 < p_0/2$ where p_0 is the initial pressure. Three choices are of special interest: i) local equilibrium (LTE) $\pi_0 = \Pi_0 = 0$; ii) Navier-Stokes (NS) $\pi_0 = -(4/3)\eta_s(T_0)/\tau_0$, $\Pi_0 = -\zeta(T_0)/\tau_0$; and iii) gluon saturation[12] (CGC) $\pi_0 \approx -p_0$, $\Pi_0 \approx 0$.

The main quantity we analyze is the entropy produced relative to the initial entropy $\Delta S/S_0$. We shall impose $\Delta S/S_0 \lesssim 0.2$ as the condition for region of validity. Because we only consider longitudinal expansion, we focus on entropy production until the beginning of the hadronic phase $T_f = 180$ MeV (this is almost identical to entropy production until $\tau_f = 8$ fm). Figure 1(left) shows our results for "minimal" shear and vanishing bulk viscosity. For LTE initial conditions, IS hydrodynamics is applicable when $\tau_0 \gtrsim 0.3$ fm. Good accuracy for NS initial conditions

requires $\tau_0 \gtrsim 0.6$ fm ($\pi_0^{NS}/p_0 \approx -0.846$, -0.585, and -0.488 for $\tau_0 = 0.3$, 0.6, and 1 fm), while for CGC initial conditions even later $\tau_0 \gtrsim 1$ fm.

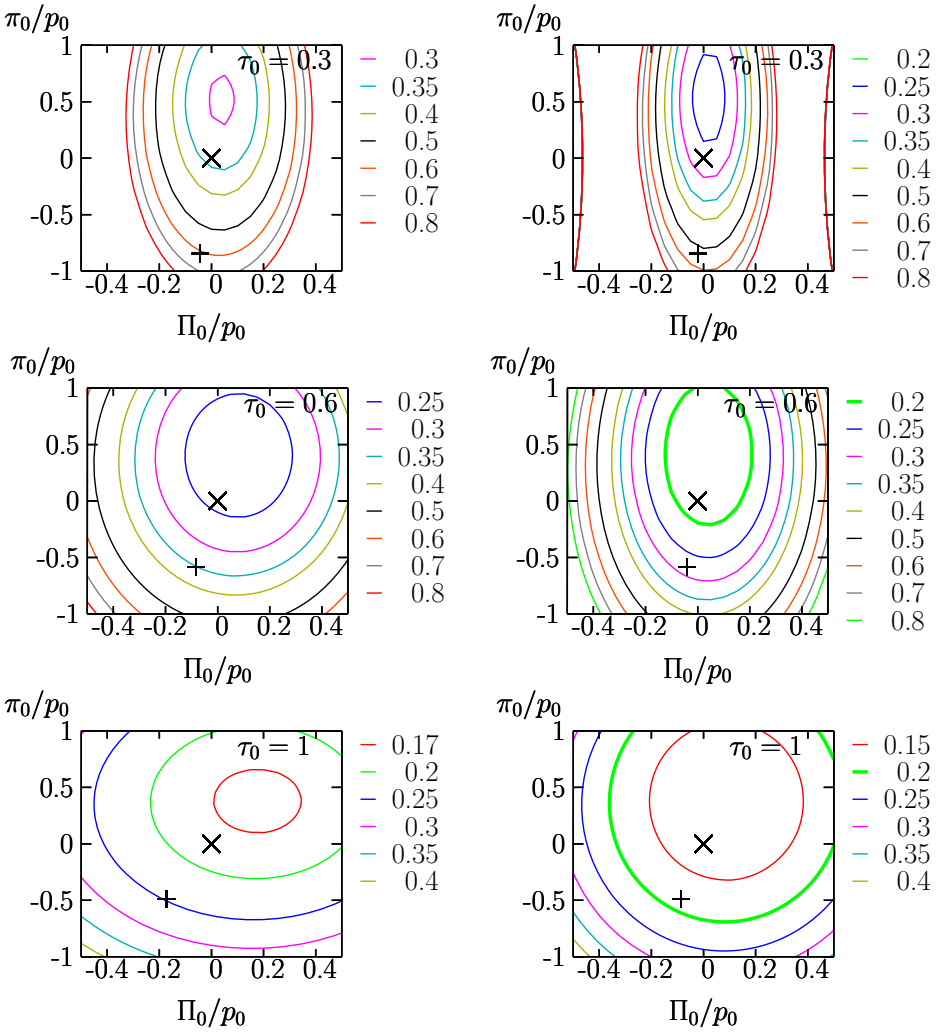

Figure 2: Relative entropy production until $T_f = 180$ MeV as a function of initial shear stress and bulk pressure, for thermalization times $\tau_0 = 0.3$ (top), 0.6 (middle), and 1 fm (bottom). Left column is for $\zeta(T)$ based on Meyer's calculation[10], right column is for half that large $\zeta(T)$. Crosses indicate local equilibrium initial conditions, while pluses are for Navier-Stokes. In all cases $\eta_s/s = 1/(4\pi)$.

Let us now turn on bulk viscosity. The left column of Figure 2 shows $\Delta S/S_0$ for our default $\zeta(T)$ parameterization. Due to the additional entropy produced, LTE initial conditions now require $\tau_0 \gtrsim 1$ fm, while simulations from NS and CGC ones necessitate even later thermalization. The situation improves somewhat if bulk viscosity is half as large as our default ($\zeta_m = 0.1$). As seen in the right column, LTE initial conditions are then suitable when $\tau_0 \gtrsim 0.6$ fm, while NS can be accommodated if $\tau_0 \gtrsim 1$ fm. Results are quite similar if instead the width of the $\zeta(T)$ peak is halved, i.e., $\zeta_m = 0.2$, $\Delta T = 0.015$ GeV. We checked that shorter relaxation times help only a

little, as illustrated in Figure 3(left) for $\tau_0 = 0.6$ fm. On the other hand, the region of applicability widens substantially if the shear viscosity is a factor of two smaller (cf. Fig. 3(right)).

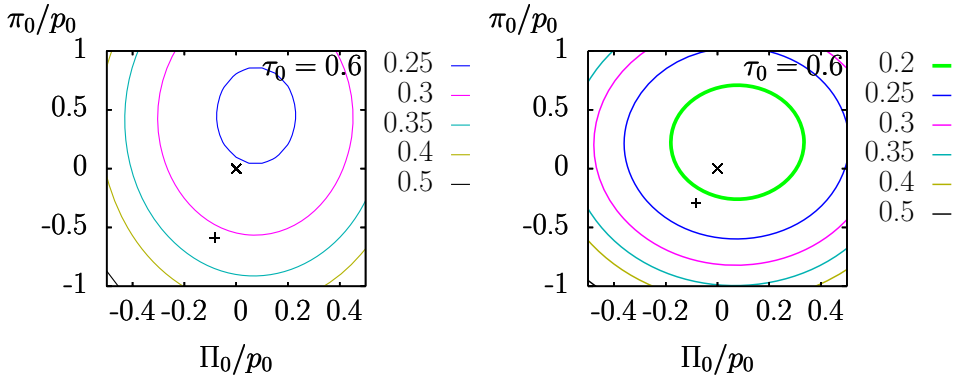

Figure 3: Same as Fig. 2 with our default parameters but halved relaxation times (left), or $\eta_s/s = 0.5/(4\pi)$ (right).

3. Conclusions

We study the region of validity of Israel-Stewart viscous hydrodynamics for conditions expected at RHIC, based on the entropy produced during the evolution when both shear and bulk viscosity are present. Our results indicate that, unlike it was previously hoped, viscous hydrodynamics does not extend the range of dynamical description to proper times earlier than $\tau \approx 0.6$ fm, even for local thermal equilibrium initial conditions - *unless* the influence of bulk viscosity is basically negligible, or the shear viscosity of hot and dense quark-gluon matter is significantly below the conjectured "minimal" value of $\eta_s = s/(4\pi)$.

Acknowledgments

We thank RIKEN, Brookhaven National Laboratory and the US Department of Energy [DE-AC02-98CH10886] for providing facilities essential for the completion of this work.

References

[1] P. Huovinen and D. Molnar, Phys. Rev. C **79**, 014906 (2009) [arXiv:0808.0953 [nucl-th]].
[2] P Romatschke U Romatschke, Phys. Rev. Lett. **99**, 172301 (2007)
[3] H Song and U W Heinz, Phys. Lett. B **658**, 279 (2008)
[4] K Dusling and D Teaney, Phys. Rev. C **77**, 034905 (2008)
[5] D. Molnar and P. Huovinen, J. Phys. G **35**, 104125 (2008) [arXiv:0806.1367 [nucl-th]].
[6] D. Molnar, arXiv:0806.0026 [nucl-th].
[7] A. El, A. Muronga, Z. Xu and C. Greiner, arXiv:0812.2762 [hep-ph].
[8] M. Cheng *et al.*, Phys. Rev. D **77**, 014511 (2008) [arXiv:0710.0354 [hep-lat]].
[9] G. Policastro, D. T. Son and A. O. Starinets, Phys. Rev. Lett. **87**, 081601 (2001); P. Kovtun, D. T. Son and A. O. Starinets, Phys. Rev. Lett. **94**, 111601 (2005)
[10] H. B. Meyer, Phys. Rev. Lett. **100**, 162001 (2008) [arXiv:0710.3717 [hep-lat]].
[11] R. J. Fries, B. Muller and A. Schafer, Phys. Rev. C **78**, 034913 (2008) [arXiv:0807.4333 [nucl-th]].
[12] A. Krasnitz, Y. Nara and R. Venugopalan, Phys. Rev. Lett. **87**, 192302 (2001); Y. V. Kovchegov, Nucl. Phys. A **762**, 298 (2005) [arXiv:hep-ph/0503038].

Eur. Phys. J. A **37**, 121–128 (2008)
DOI 10.1140/epja/i2007-10611-3

THE EUROPEAN PHYSICAL JOURNAL A

Regular Article – Theoretical Physics

Chemical freeze-out temperature in the hydrodynamical description of Au + Au collisions at $\sqrt{s_{NN}} = 200\,\mathrm{GeV}$

P. Huovinen[a]

Department of Physics, University of Virginia, P.O. Box 400714, Charlottesville, VA 22904-4714, USA

Received: 29 October 2007 / Revised: 26 May 2008
Published online: 7 July 2008 –
Communicated by P. Braun-Munzinger

Abstract. We study the effect of separate chemical and kinetic freeze-outs to the ideal hydrodynamical flow in Au + Au collisions at RHIC ($\sqrt{s_{NN}} = 200\,\mathrm{GeV}$ energy). Unlike earlier studies we explore how these effects can be counteracted by changes in the initial state of the hydrodynamical evolution. We conclude that the reproduction of pion, proton and antiproton yields necessitates a chemical freeze-out temperature of $T \approx 150\,\mathrm{MeV}$ instead of $T = 160$–$170\,\mathrm{MeV}$ motivated by thermal models. Contrary to previous reports, this lower temperature makes it possible to reproduce the p_T spectra of hadrons if one assumes very small initial time, $\tau_0 = 0.2\,\mathrm{fm}/c$. However, the p_T differential elliptic flow, $v_2(p_T)$ remains badly reproduced. This points to the need to include dissipative effects (viscosity) or some other refinement to the model.

PACS. 25.75.Dw Particle and resonance production – 25.75.Ld Collective flow

1 Introduction

Ideal fluid hydrodynamical models have been very successful in describing the bulk behaviour of particles formed in heavy-ion collisions at RHIC. The low-p_T single-particle spectra as well as the transverse momentum dependence of elliptic anisotropy ($v_2(p_T)$) are reproduced nicely [1,2]. This success has been one of the reasons to conclude that partonic state of matter with exceptionally low shear viscosity has been formed at RHIC [3].

However, these results have been achieved using ideal fluid hydrodynamical models, which assumed chemical equilibrium until the very end of the evolution of the system. This assumption is questionable, since the cross-sections of inelastic, particle number changing processes, are smaller than the cross-sections of elastic and quasi-elastic processes. Thus it is natural to assume that the system would still maintain local kinetic equilibrium when it begins to deviate from local chemical equilibrium.

This kind of approach is also supported by experimental data. The final hadron abundances in Au + Au collisions at RHIC can be well described by a hadron gas in approximate chemical equilibrium at $T_{\mathrm{ch}} \approx 160$–$175\,\mathrm{MeV}$ [4,5]. The reproduction of the slopes of particle distributions using a blast-wave model requires much lower temperatures around $T_{\mathrm{kin}} \approx 90$–$130\,\mathrm{MeV}$ (depending on centrality) [6]. The hydrodynamical models assuming chemical equilibrium usually require freeze-out temperatures close to the blast-wave fits[1] and cannot reproduce all observed particle yields simultaneously. It is thus reasonable to postulate two separate freeze-outs: first a chemical freeze-out where the yields of various particle species are fixed (frozen out) and somewhat later a kinetic freeze-out where the particles scatter for the last time and the momentum distributions cease to evolve.

The formalism to describe such a chemically frozen hadron gas has been known for quite a long time [9]. There have been several applications of this formalism to the hydrodynamical description of heavy-ion collisions at SPS ($\sqrt{s_{AA}} = 17\,\mathrm{GeV}$) and RHIC ($\sqrt{s_{AA}} = 130$ and $200\,\mathrm{GeV}$) energies [10–13], but the results have been unsatisfactory. The conclusion of these studies has been that if the chemical composition of the hadron gas freezes out at hadronization, an ideal fluid hydrodynamical model can reproduce neither the single-particle spectra nor the p_T differential anisotropy [14,15]. However, these studies are lacking in such a sense that they used the same initial state for both the chemically equilibrated and chemically frozen description. It is known that p_T distributions are sensitive not only to the equation of state and kinetic freeze-out temperature, but also to the initial pressure gradients, *i.e.* to the initial density distribution [16]. Here we redo the hydrodynamic calculations once more to explore whether there is such an initial state which leads to an acceptable reproduction of the p_T spectra and elliptic flow of pions and antiprotons.

[a] *Present address:* Department of Physics, Purdue University, West Lafayette, IN 47907, USA; e-mail: phuovine@purdue.edu

[1] With the notable exception of refs. [7,8].

2 Equation of state

As a baseline, we use an equation of state (EoS) in chemical equilibrium. We construct it in the usual way: the hadronic phase is described by ideal resonance gas consisting of all hadrons and resonances listed in the Particle Data Book [17] with mass below 2 GeV. The plasma phase is described by an ideal massless parton gas consisting of gluons and three-quark flavours. There is a first-order phase transition between these two phases at $T_c = 170$ MeV. Note that this EoS is slightly different from the EoS with a first-order phase transition used in ref. [18] and EoS Q used in ref. [19]. The phase transition temperature in this work is $T_c = 170$ MeV instead of 165 MeV and the number of quark flavours in the plasma phase is 3 instead of 2.5. The latter results in slightly larger latent heat. As can be seen by comparing the results here and in ref. [18], these differences have only a small effect on the particle spectra and anisotropies. In the following we refer to this EoS and the corresponding initial state as CE.

We construct an EoS out of chemical equilibrium in the way outlined in ref. [9] and later applied in refs. [11–13]. Below the chemical freeze-out temperature all inelastic, particle number changing processes have ceased, but elastic and quasielastic scatterings are still frequent enough to keep the system in kinetic equilibrium. The quasielastic scatterings lead to frequent formation and decay of resonances, which means that the yields of resonances and their daughter particles, say ρ-mesons and pions, still are in relative chemical equilibrium. This approach is therefore called partial chemical equilibrium (PCE). The presence of resonances means that the actual particle number of any particle species is not conserved after chemical freeze-out, but the effective particle number is. The effective particle number is defined as $\bar{N}_i = N_i + \sum_j n_j^{(i)} N_j$, where N_i is the actual number of particle species i, $n_j^{(i)}$ is the number of particles i formed in the decay of resonance j including the branching ratios, and N_j is the number of resonances j. The sum is over all the resonances with lifetimes smaller than the characteristic lifetime of the system. We take the characteristic lifetime to be 10 fm/c irrespective of the actual lifetime of the system. The following particles and resonances have lifetimes longer than 10 fm/c and are thus considered stable:

$$\pi,\ K,\ \eta,\ \omega,\ p,\ n,\ \eta',\ \phi,\ \Lambda,\ \Sigma,\ \Xi,\ \Lambda(1520),\ \Xi(1530),\ \Omega,$$

and the corresponding antiparticles. The corresponding effective potential of resonances is obtained in a similar fashion: $\mu_j = \sum_i n_j^{(i)} \mu_i$, where the sum is over all decay products of the resonance j.

We treat each isospin state of each particle species independently. This results in 35 conserved quantities and chemical potentials in the chemically frozen stage. Tabulating the EoS as a function of 36 quantities (35 chemical potentials and temperature) is unpractical, but avoidable by taking the advantage of the isentropic nature of ideal fluid hydrodynamics. Since entropy is conserved, the ratio of the effective particle number density ($\bar{n}_i = \bar{N}_i/V$) and entropy density, $\bar{n}_i/s$, stays constant on streamlines of the flow. The expansion thus traces a trajectory of constant $\bar{n}_i/s$ in the $(T, \{\mu_i\})$-space and we need to evaluate the EoS only on this trajectory. The trajectories in the (T, μ_N)-plane of the chemically frozen (PCE) and equilibrated systems (CE) at RHIC are shown in fig. 1.

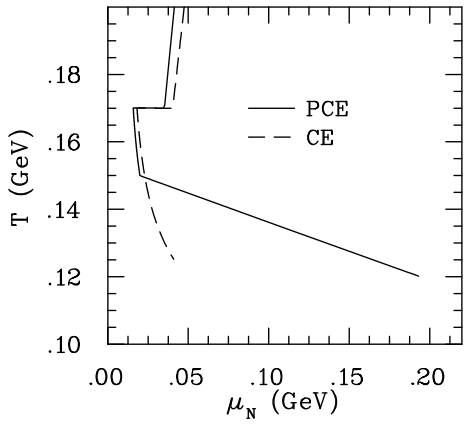

Fig. 1. Isentropic thermodynamic trajectories below 200 MeV at RHIC. PCE corresponds to chemically frozen calculation and CE corresponds to the center of the system in chemically equilibrated calculation. Above the phase transition temperature nucleon chemical potential $\mu_N = 3\mu_q$. The curves terminate at the kinetic freeze-out temperature ($\langle T_{\rm kin}\rangle = 120$ and 125 MeV). Note that the difference above the chemical freeze-out temperature $T_{\rm ch} = 150$ MeV is due to different initial states, see sect. 3. For PCE and CE, $s/n_B = 453.5$ and 395, respectively, where n_B is net baryon density.

Qualitatively our EoS is similar to the EoSs in refs. [11–13]. The relation between pressure and energy density is almost identical in chemically equilibrated and frozen cases whereas at fixed energy density the chemically frozen system is much colder than a system in chemical equilibrium.

3 Initial conditions

We use the same boost-invariant hydrodynamic code as in ref. [18]. In the case of chemical equilibrium (CE) we use the same initial conditions as in ref. [18] for the equation of state with a first-order phase transition: The initial entropy density distribution is a linear combination

Table 1. Initial time, phase transition temperature, chemical freeze-out temperature, kinetic freeze-out energy density and the corresponding average temperature on the kinetic freeze-out surface used in chemical equilibrium (CE) and partial chemical equilibrium (PCE) calculations.

	CE	PCE
τ_0 (fm/c)	0.6	0.2
T_c (MeV)	170	170
$T_{\rm ch}$ (MeV)	–	150
$\epsilon_{\rm kin}$ (GeV/fm^3)	0.065	0.117
$\langle T_{\rm kin}\rangle$ (MeV)	125	120

Table 2. Measured and calculated particle yields at midrapidity in most central (0–5%) Au + Au collisions at $\sqrt{s_{NN}} = 200\,\mathrm{GeV}$. CE stands for chemical equilibrium, $T_{\mathrm{ch}} = 170$ and 150 MeV denote cases where chemical freeze-out takes places at 170 and 150 MeV temperatures, respectively, but the initial state of the system is similar to the case CE. PCE is the final partial chemical equilibrium result where chemical freeze-out takes place at $T_{\mathrm{ch}} = 150\,\mathrm{MeV}$ and the initial conditions are adjusted to reproduce the observed p_T distributions.

$\mathrm{d}N/\mathrm{d}y$	π^+	π^-	K^+	K^-	p	$\bar{p}$
PHENIX [31]	286.4 ± 24.2	281.8 ± 22.8	48.9 ± 5.2	45.7 ± 5.2	18.4 ± 2.6	13.5 ± 1.8
CE	273	273	44	42	10	5
$T_{\mathrm{ch}} = 170\,\mathrm{MeV}$	268	268	52	50	25	20
$T_{\mathrm{ch}} = 150\,\mathrm{MeV}$	265	265	51	49	18	13
PCE	278	278	53	51	18	14

of the density of participants and binary collisions in the transverse plane whereas the initial baryon density is proportional to the number of participants. The parameter values are fixed to reproduce the p_T spectra of pions and net protons ($p - \bar{p}$) in the most central collisions and the centrality dependence of charged hadron multiplicity at midrapidity. The initial time, phase transition temperature and freeze-out criteria for cases CE and PCE are shown in table 1. Note that the freeze-out energy density is slightly lower than in the corresponding calculation of ref. [18] because the EoS is slightly different (see sect. 2).

We find that the same initialization will not work in the chemically frozen case. To reproduce the slopes of the p_T distributions we increase the transverse flow by making the initial pressure gradients steeper and by starting the hydrodynamical evolution earlier. An acceptable result is achieved when the initial entropy density distribution is assumed to be proportional to the number of binary collisions in the transverse plane and the initial time is taken to be $\tau_0 = 0.2\,\mathrm{fm}/c$.

This choice of initial time is bold since it requires hydrodynamics to be applicable almost immediately after the formation time of the partons of the system, but is nevertheless plausible [1,8]. First, in the pQCD + saturation method for calculating the particle production of ref. [8], the average energy and particle number densities are almost equal to those of a system of fixed temperature. Thus there is no need for particle number changing processes to achieve thermalization. Second, for massless particles, the relation between pressure and energy density is $\epsilon = 3P$ for any isotropic momentum distribution. Thus the use of hydrodynamics to describe the build-up of collective flow could be a reasonable assumption even if the momentum distribution differs from thermal equilibrium distribution. Third, this ideal gas EoS may be applicable very rapidly, since isotropization of the momentum distribution occurs much faster than thermal equilibration [20,21]. Finally, the studies of plasma instabilities support the notion of fast thermalization of the system [22].

If the proportionality between the initial entropy density and the number of binary collisions is independent of the centrality of the collision, the centrality dependence of the final particle multiplicity is not reproduced [23]. To correct this, we modify the parametrization given in ref. [23] by assuming an impact parameter-dependent proportionality constant:

$$K_s(\tau_0 = 0.2\,\mathrm{fm}; b) = 0.26942\,\mathrm{fm}^{-6}\, b^3 + 10.9\,\mathrm{fm}^{-4}\, b + 453.5\,\mathrm{fm}^{-3},$$

and parametrize the initial entropy density in the transverse plane as

$$s(\mathbf{s}; \tau_0; \mathbf{b}) = K_s(\tau_0; b)\, T_A\left(\mathbf{s} + \tfrac{1}{2}\mathbf{b}\right) T_B\left(\mathbf{s} - \tfrac{1}{2}\mathbf{b}\right),$$

where T_A is the customary nuclear thickness function [23]. The initial baryon number distribution is obtained in the same way, *i.e.* it is taken to be proportional to the initial entropy density.

4 Particle yields and chemical freeze-out temperature

When separate chemical and kinetic freeze-outs are discussed in recent literature, chemical freeze-out is assumed to take place immediately after hadronization at $T_{\mathrm{ch}} =$ 160–170 MeV [10–13]. Either the ratios of all particle species are taken to be fixed at this temperature [11–13] or only strange particle yields are supposed to freeze-out [10]. The idea of chemical freeze-out at hadronization is conceptually attractive [24,25] and to some extent supported by thermal models which lead to temperatures [4,5] quite similar to the predicted phase transition temperature [26]. However, in the context of the hydrodynamical model, we have found that assuming chemical freeze-out of all particle species at $T \approx 170\,\mathrm{MeV}$, leads to proton and antiproton yields that are too large when the model is tuned to reproduce the observed pion multiplicity. In most central collisions we obtain $\mathrm{d}N_p/\mathrm{d}y = 25$ protons and $\mathrm{d}N_{\bar{p}}/\mathrm{d}y = 20$ antiprotons at midrapidity instead of the experimentally observed yields of $\mathrm{d}N_p/\mathrm{d}y = 18.4 \pm 2.6$ and $\mathrm{d}N_{\bar{p}}/\mathrm{d}y = 13.5 \pm 1.8$ (see table 2 and fig. 2, case $T_{\mathrm{ch}} =$ 170 MeV). This discrepancy is not surprising. Some thermal model fits to RHIC data have actually led to temperatures near or below 160 MeV rather than 170 MeV [27,28]. Thermal models also tend to lead to p/π ratios which are slightly larger than the experimental ratio, although still within experimental errors [27–30]. If the model is required to fit only K/π and p/π ratios, the temperature is lower, $T \approx 152\,\mathrm{MeV}$ [30].

As was argued in [15], the evolution of the average transverse momentum per particle, and thus the observed p_T spectra, is sensitive to pion number changing processes. In a hydrodynamical model it is thus important to describe the pion chemistry correctly and get the pion chemical freeze-out temperature right even if that means a worse reproduction of strange baryon yields. Inspired by the results of ref. [27], we take $T = 150\,\mathrm{MeV}$ as the temperature where the pion number changing processes become negligible and the effective pion number freezes out. We expect that the better reproduction of the pion to proton and the pion to antiproton ratios gives a more realistic description of the temperature evolution and therefore of the evolution of particle distributions. As can be seen in the case $T_{\mathrm{ch}} = 150\,\mathrm{MeV}$ of table 2, this approach gives the expected results: pion, kaon, proton and antiproton yields are almost exactly reproduced. The strange baryon yields, on the other hand, become too small at $T_{\mathrm{ch}} = 150\,\mathrm{MeV}$.

The possible contribution from weak decays of strange particles causes a significant uncertainty in determining the chemical freeze-out temperature [4]. According to the PHENIX Collaboration [31,32], the data has been corrected for the feed-down from weak decays of Λ's and Σ^0's, but whether the pion spectrum contains a contribution from K^0_S decays, is not clearly explained. In these calculations we have assumed that there is no contribution from any weak decays in the PHENIX data. The decay of thermally produced K^0_S's and $\Sigma^{\pm}$'s would increase the pion yield at midrapidity by ~ 40 pions and one proton/antiproton. For the cases $T_{\mathrm{ch}} = 170$ and $150\,\mathrm{MeV}$, the pion yield is thus at the experimental upper limit. The reduction of initial entropy by 5–10% would bring the pion yield closer to the experimental value and reduce the proton/antiproton yield by the same 5–10%. The proton and antiproton yields at $T_{\mathrm{ch}} = 170\,\mathrm{MeV}$ temperature would be too large in this case too. At $T_{\mathrm{ch}} = 150\,\mathrm{MeV}$, the proton and antiproton yields would be within experimental errors, but one can argue that a slightly larger freeze-out temperature $T_{\mathrm{ch}} \approx 155\,\mathrm{MeV}$ is favoured by the data.

In the case PCE the same procedure leads to a pion yield larger than the data, which necessitates a larger adjustment in the initial entropy. However, after the adjustment, the conclusion is the same than for the cases $T_{\mathrm{ch}} = 170$ and $150\,\mathrm{MeV}$: even if the pion yield contains a contribution from K^0_S decays, $T_{\mathrm{ch}} = 170\,\mathrm{MeV}$ chemical freeze-out temperature leads to too large proton and antiproton yields and a temperature around $T_{\mathrm{ch}} = 150$–$155\,\mathrm{MeV}$ is favoured.

On the other hand, if the experimental correction for weak decays is not perfect and the spectra contains a feed-down from strange baryons, the relative increase in the proton/antiproton yields would be larger than in the pion yield. In such a case the favoured freeze-out temperature would be even smaller than what is suggested here.

5 Transverse momentum spectra

The transverse momentum distributions for protons, antiprotons, pions and kaons in the most central collisions

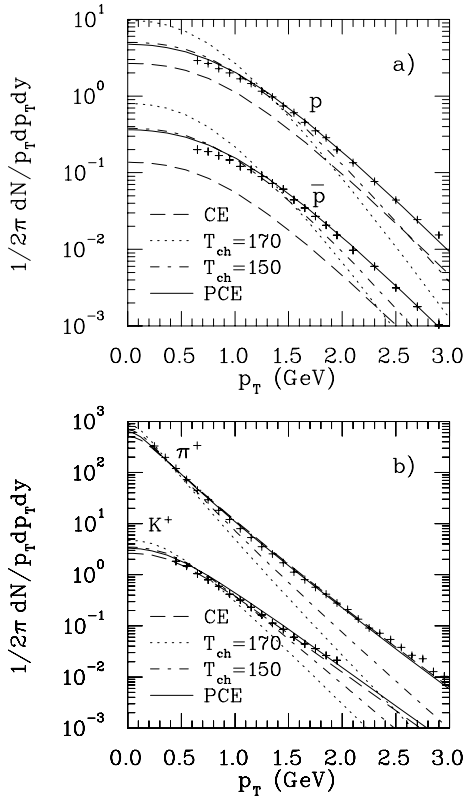

Fig. 2. (a) Proton and antiproton and (b) pion (π^+) and kaon (K^+) p_T spectra in most central (0–5%) Au + Au collisions at $\sqrt{s_{NN}} = 200\,\mathrm{GeV}$ compared with hydrodynamical calculations using different chemical freeze-out descriptions (see the text). The data was taken by the PHENIX Collaboration [31]. For clarity the antiproton and kaon spectra are scaled by a factor 10^{-1}.

are shown in fig. 2. As before [18], the calculation with chemical equilibrium (CE) reproduces the pion and kaon data well, but it reproduces only the slopes of proton and antiproton distributions. If we proceed as in refs. [12,13] and replace the EoS by an EoS with partial chemical equilibrium below $T_{\mathrm{ch}} = 170\,\mathrm{MeV}$, adjust only the kinetic freeze-out density[2], and keep everything else unchanged, the result is a disaster ($T_{\mathrm{ch}} = 170$ in the figure). Even at $\langle T_{\mathrm{kin}} \rangle = 100\,\mathrm{MeV}$ average freeze-out temperature, the slopes of proton and antiproton spectra are far too steep. Decreasing the freeze-out temperature/density does not help the overall fit, since the pion spectrum becomes steeper with decreasing freeze-out temperature. This slightly counterintuitive behaviour was explained in ref. [15]. In the boost-invariant expansion, the transverse energy per unit rapidity, $\mathrm{d}E_T/\mathrm{d}y$, decreases with increasing time. In partial chemical equilibrium the particle number is conserved and the transverse energy has to be distributed among the same number of particles. Consequently, $\langle p_T \rangle$ decreases and the slope of the p_T distribution steepens.

[2] Note that in the actual calculation we use the constant energy density as freeze-out criterion for numerical simplicity. In the following we talk about freeze-out temperature instead.

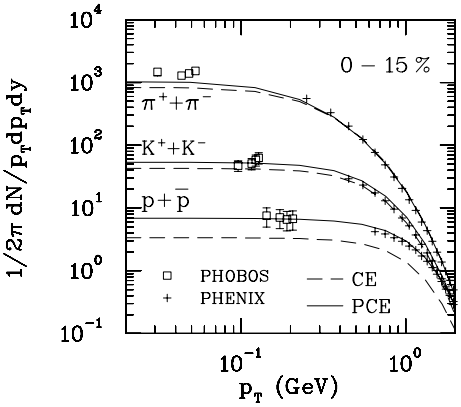

Fig. 3. Transverse momentum spectra of charged pions, charged kaons and protons + antiprotons in 15% most central Au + Au collisions at $\sqrt{s_{NN}} = 200\,\mathrm{GeV}$ in the ultralow-p_T region measured by PHOBOS [33] compared with hydrodynamical calculations. The systematic and statistical errors of the PHOBOS data have been added in quadrature. The PHENIX data [31] are an average of the data in 0–5%, 5–10% and 10–15% centrality bins and have only statistical errors.

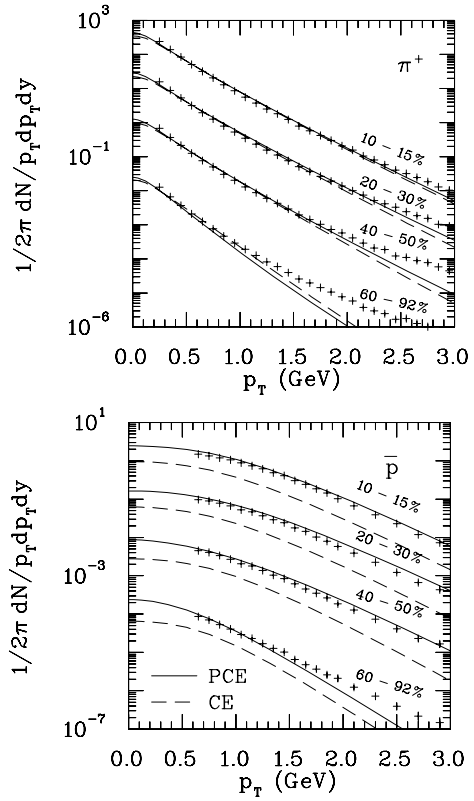

Fig. 4. Pion (π^+) and antiproton ($\bar{p}$) p_T spectra in semi-central to peripheral Au + Au collisions at $\sqrt{s_{AA}} = 200\,\mathrm{GeV}$ compared with hydrodynamical calculations (see text). The data was taken by the PHENIX Collaboration [31]. For clarity the spectra at centralities 20–30%, 40–60% and 60–80% are scaled by factors 10^{-1}, 10^{-2} and 10^{-3}, respectively.

Another problem with $T_{\mathrm{ch}} = 170\,\mathrm{MeV}$ temperature can also be seen in fig. 2: there are too many protons and antiprotons as discussed in the previous section. This can be cured by decreasing the chemical freeze-out temperature to $T_{\mathrm{ch}} = 150\,\mathrm{MeV}$. The calculation labelled $T_{\mathrm{ch}} = 150$ in fig. 2 is performed in the same way as $T_{\mathrm{ch}} = 170$. Only the EoS is changed, but the initial state is kept the same. When the kinetic freeze-out temperature is kept the same, $\langle T_{\mathrm{kin}} \rangle = 100\,\mathrm{MeV}$, as for $T_{\mathrm{ch}} = 170$, the particle distributions are closer to the data, but the slopes are still too steep. The flattening of the spectra is easy to understand. Between $T = 170$ and $150\,\mathrm{MeV}$ the particle number is not conserved but the energy stored in masses of heavy particles is converted to kinetic energy of light particles (mostly pions) when the system cools. Thus $\langle p_T \rangle$ may increase even if $\mathrm{d}E_T/\mathrm{d}y$ decreases, and $\langle p_T \rangle$ is larger at the time of chemical freeze-out when the particle number is fixed and pion $\langle p_T \rangle$ begins its slow decrease.

Neither the steeper initial profile given by the pure binary collision profile nor the small initial time $\tau_0 = 0.2\,\mathrm{fm}/c$ is sufficient alone to create a large enough flow before chemical freeze-out to fit the data. When these two are used together (PCE), the fit to the data is good. The fit to pion data is even better than in the chemical equilibrium case (CE) at low p_T, where PCE depicts a concave curvature typical for a finite pion chemical potential [34]. At low p_T the calculation still suffers from excess of protons and especially antiprotons as if even a larger flow velocity and a smaller chemical freeze-out temperature were necessary. We have checked that the combination of the binary collision profile, the short initial time and an EoS with $T_{\mathrm{ch}} = 170\,\mathrm{MeV}$ does not lead to a satisfactory reproduction of the slopes either, but the extra push created in the hadronic equilibrium stage between $T = 170$ and $150\,\mathrm{MeV}$ temperatures is necessary to fit the data.

Figure 3 shows the results for the very low transverse momentum measured by the PHOBOS Collaboration [33] as well as the spectra measured by the PHENIX Collaboration [31] at larger p_T. The model PCE works well also at this p_T region reproducing the flat behaviour of the data. The spectrum of pions is slightly below the data. This was seen already in table 2 where pion multiplicity was shown to be slightly below the data but still within the experimental error. The increase in the initial entropy of the system to increase pion multiplicity would, however, necessitate even lower chemical freeze-out temperature not to exceed the observed kaon multiplicity.

Pion and antiproton p_T spectra at various centralities are shown in fig. 4. The pattern is familiar from earlier hydrodynamical studies: the more peripheral the collisions, the narrower the p_T range where hydrodynamics can reproduce the spectra. An interesting detail is that antiproton spectra in semi-central collisions (20–30% and 40–50% of total cross-section) are slightly too flat. As mentioned in the introduction, blast-wave fits give higher kinetic freeze-out temperatures in peripheral than in central collisions. Hydrodynamical models have traditionally used fixed freeze-out temperature/density for simplicity, but the overshooting of antiproton spectra here suggests that a slightly larger kinetic freeze-out density in semi-central than in central collisions might lead to better results.

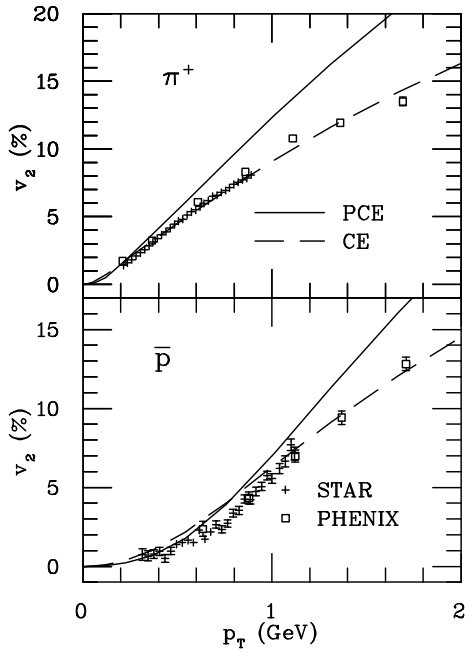

Fig. 5. Elliptic anisotropy of pions and antiprotons *vs.* transverse momentum in minimum bias Au + Au collisions at $\sqrt{s_{NN}} = 200\,\mathrm{GeV}$ calculated using different chemical freeze-out descriptions (see text) and compared with the data by the STAR [35] and PHENIX [36] Collaborations.

6 Elliptic anisotropy

Unfortunately, the success in the previous section cannot be repeated for elliptic anisotropy. Figure 5 shows the p_T differential elliptic anisotropy of pions and antiprotons in minimum bias Au + Au collisions. The trend is similar to that in ref. [12]. The chemical equilibrium result (CE) reproduces the pion data excellently and is slightly above the proton data. Partial chemical equilibrium (PCE) leads to a slope of the pion anisotropy that is too large and the calculated result is clearly above the data. The proton anisotropy is reproduced at $p_T < 600\,\mathrm{MeV}$, but increases too fast at larger momenta.

It is worth noticing that the different p_T differential v_2 is mostly due to the different description of the hadron gas. As shown in ref. [12], the same initial state leads to different v_2 in chemically equilibrated and frozen cases. The basic reason for this is in the different temperature evolution in the hadron gas. When both systems have reached the same density, the collective flow field and its anisotropies are almost identical in both cases. However, the chemically equilibrated system is hotter and thus the random thermal motion is stronger. Thermal motion smears away the underlying anisotropy of the collective flow field, and, therefore, the final v_2 of particles of the chemically equilibrated system is smaller than the v_2 of particles of the corresponding chemically frozen system[3].

Comparison of these results with the recent results obtained using viscous hydrodynamics [37–39] is particularly interesting. Dissipation reduces elliptic flow and it was claimed in ref. [39] that even the postulated minimal shear viscosity $\frac{\eta}{s} = \frac{1}{4\pi}$ causes very large suppression. As shown here, the suppression of the elliptic flow is required to fit the data when chemical equilibrium is lost in the hadron gas. However, the actual size of the allowed viscous correction is unknown since the EoS affects especially the proton anisotropy. At least in the chemically equilibrated case, the lattice QCD-based EoS leads to an even larger proton $v_2(p_T)$ than the EoS used here [18]. Whether finite shear viscosity leads to a correct reproduction of the data remains to be seen as well as how large of a viscosity is allowed in plasma and hadronic phases [40].

7 Summary and discussion

Contrary to previous reports [12–15], we have shown that it is possible to reproduce both (nonstrange) hadron yields and their transverse momentum spectra using ideal fluid hydrodynamics with separate chemical and kinetic freeze-outs. The difference between our approach and the previous studies is that we used a different initial state for the chemically frozen system than for the system in chemical equilibrium, adjusted the initial time to be as small as $\tau_0 = 0.2\,\mathrm{fm}/c$ and changed the chemical freeze-out temperature to be below the phase transition temperature to $T_{\mathrm{ch}} = 150\,\mathrm{MeV}$. However, our success is incomplete. Even after these adjustments of the model, we were not able to reproduce the p_T differential elliptic flow of pions and protons. To describe particle yields, their p_T distributions and anisotropies, the description of expansion has to be amended, most probably by including dissipative effects: viscosity and diffusion.

Nevertheless, our results demonstrate how sensitive the expansion dynamics during the hadronic phase is to hadron chemistry. A good knowledge of hadron chemistry is therefore essential if we wish to extract the viscosity of the QGP from the experimental data using viscous hydrodynamics. The recent method of choice for this purpose has been the so-called hybrid hydro + cascade model where the expansion is described using hydrodynamics until the system is hadronized and the hadronic phase is described using hadronic cascade [40–43]. These models have the advantage that the dissipative effects and hadronic chemistry are included in the model and the kinetic freeze-out is a result of hadronic cross-sections without any free parameters. So far cascade models used in these hybrid models have been limited to two-particle scatterings, but it has been argued that multiparticle processes are essential for reproducing the proton and antiproton yields [44,45]. It is therefore not surprising that hydro + cascade models may have difficulties in reproducing the antiproton spectrum at the lowest values of transverse momentum [43]. On the other hand, multiparticle processes are included in hydrodynamical models and as argued in sect. 5, processes where heavy particles annihilate and form lighter particles, and vice versa, are important for the build-up of flow. For this reason we consider that a hydrodynamical description of the hadronic phase

[3] For a more detailed discussion see ref. [15].

is still worth pursuing as a complementary tool to hybrid models, even if there are transport models where the multiparticle processes are included [45].

Another conclusion of these results is that the final spectra are sensitive to the details of the initial state. As already stated in ref. [40], theoretical constraints to the initial state and especially to its shape are of utmost importance if we wish to extract the properties of the QGP from experimental data.

Some arguments favouring the use of hydrodynamics already at initial time $\tau_0 = 0.2\,\mathrm{fm}/c$ were given in sect. 3. We admit that in a certain sense our result is similar to ref. [13], where Kolb and Rapp claimed that it is not possible to fit the p_T spectra without pre-hydrodynamic transverse flow. Some of our arguments favouring the use of hydrodynamics at $\tau = 0.2\,\mathrm{fm}/c$ centered on the fact that for the relation $\epsilon = 3P$ to hold, it is sufficient that the momentum distribution is isotropic. It does not need to be thermal. Thus one may say that we are using hydrodynamics to calculate the pre-hydrodynamic transverse flow, although the flow field in our case is different from the one used in ref. [13].

The low chemical freeze-out temperature $T_{\mathrm{ch}} = 150\,\mathrm{MeV}$ clearly below the phase transition temperature $T_{\mathrm{c}} = 170\,\mathrm{MeV}$ leads to another problem. The chemical freeze-out temperature is almost independent of centrality [30]. It was argued in ref. [25] that such an independence requires either chemical freeze-out at phase transition or extremely steep temperature dependence of the inelastic scattering rate. One way to solve this apparent discrepancy is to assume that the chemical equilibration in the hadron gas close to T_{c} is very fast indeed due to massive Hagedorn resonances [46]. These resonances couple to multi-pion states and baryon-antibaryon pairs and thus lead to fast chemical equilibration, but they appear only close to the critical temperature.

The treatment of hadronic chemistry and choice of chemical freeze-out used in this paper is by no means the final one. Since the data seem to favour the notion that strange baryon yields are fixed at higher temperature than the yields of pions, kaons and nucleons/antinucleons, it would be relatively easy to use two separate chemical freeze-out temperatures: one for strange baryons and another for everything else. Another relatively straightforward improvement is to redo the calculation of the chemical relaxation rate of pions [47] for the RHIC environment and to use it to dynamically find the local chemical freeze-out temperature by comparing this rate to the expansion rate. This approach is particularly appealing if the kinetic freeze-out surface is also found by comparing the scattering and expansion rates. Finally, it would be useful to calculate the particle yields dynamically during the evolution using actual rate equations for particle number changing processes. For baryons, a preliminary study was already done in ref. [48], but in that work mesons were supposed to be in chemical equilibrium and the EoS was independent of baryon and antibaryon densities. A proper calculation would require the dynamical treatment of mesons and calculating the EoS using actual particle densities.

I thank K. Haglin, T. Hirano, H. Honkanen, S. Pratt, P.V. Ruuskanen, S.S. Räsänen and G. Torrieri for many enlightening discussions. The financial support from Johannes Råttendahl foundation is also gratefully acknowledged.

References

1. P. Huovinen, P.V. Ruuskanen, Annu. Rev. Nucl. Part. Sci. **56**, 163 (2006) [arXiv:nucl-th/0605008].
2. P.F. Kolb, U.W. Heinz, in *Quark-Gluon Plasma 3*, edited by R.C. Hwa, X.N. Wang (World Scientific, Singapore, 2004) p. 634 [arXiv:nucl-th/0305084].
3. M. Gyulassy, L. McLerran, Nucl. Phys. A **750**, 30 (2005) [arXiv:nucl-th/0405013].
4. P. Braun-Munzinger, K. Redlich, J. Stachel, in *Quark-Gluon Plasma 3*, edited by R.C. Hwa, X.N. Wang (World Scientific, Singapore, 2004) p. 491 [arXiv:nucl-th/0304013].
5. STAR Collaboration (J. Adams *et al.*), Nucl. Phys. A **757**, 102 (2005) [arXiv:nucl-ex/0501009].
6. STAR Collaboration (J. Adams *et al.*), Phys. Rev. Lett. **92**, 112301 (2004) [arXiv:nucl-ex/0310004].
7. K.J. Eskola, H. Niemi, P.V. Ruuskanen, S.S. Rasanen, Phys. Lett. B **566**, 187 (2003) [arXiv:hep-ph/0206230].
8. K.J. Eskola, H. Honkanen, H. Niemi, P.V. Ruuskanen, S.S. Rasanen, Phys. Rev. C **72**, 044904 (2005) [arXiv:hep-ph/0506049].
9. H. Bebie, P. Gerber, J.L. Goity, H. Leutwyler, Nucl. Phys. B **378**, 95 (1992).
10. N. Arbex, F. Grassi, Y. Hama, O. Socolowski, Phys. Rev. C **64**, 064906 (2001); W.L. Qian, R. Andrade, F. Grassi, O.J. Socolowski, T. Kodama, Y. Hama, Int. J. Mod. Phys. E **16**, 1877 (2007) [arXiv:nucl-th/0703078]; W.L. Qian, R. Andrade, F. Grassi, Y. Hama, T. Kodama, arXiv:0709.0845 [nucl-th].
11. D. Teaney, arXiv:nucl-th/0204023.
12. T. Hirano, K. Tsuda, Phys. Rev. C **66**, 054905 (2002) [arXiv:nucl-th/0205043].
13. P.F. Kolb, R. Rapp, Phys. Rev. C **67**, 044903 (2003) [arXiv:hep-ph/0210222].
14. PHENIX Collaboration (K. Adcox *et al.*), Nucl. Phys. A **757**, 184 (2005) [arXiv:nucl-ex/0410003].
15. T. Hirano, M. Gyulassy, Nucl. Phys. A **769**, 71 (2006) [arXiv:nucl-th/0506049].
16. A. Dumitru, D.H. Rischke, Phys. Rev. C **59**, 354 (1999) [arXiv:nucl-th/9806003].
17. Particle Data Group (S. Eidelman *et al.*), Phys. Lett. B **592**, 1 (2004).
18. P. Huovinen, Nucl. Phys. A **761**, 296 (2005) [arXiv:nucl-th/0505036].
19. P.F. Kolb, J. Sollfrank, U.W. Heinz, Phys. Rev. C **62**, 054909 (2000) [arXiv:hep-ph/0006129].
20. J. Berges, S. Borsanyi, C. Wetterich, Nucl. Phys. B **727**, 244 (2005) [arXiv:hep-ph/0505182].
21. Y.V. Kovchegov, A. Taliotis, Phys. Rev. C **76**, 014905 (2007) [arXiv:0705.1234 [hep-ph]].
22. S. Mrowczynski, Acta Phys. Pol. B **37**, 427 (2006) [arXiv:hep-ph/0511052].
23. P.F. Kolb, U.W. Heinz, P. Huovinen, K.J. Eskola, K. Tuominen, Nucl. Phys. A **696**, 197 (2001) [arXiv:hep-ph/0103234].

24. B. Muller, arXiv:nucl-th/0508062.
25. U. Heinz, G. Kestin, PoS **CPOD2006**, 038 (2006) [arXiv:nucl-th/0612105].
26. F. Karsch, E. Laermann, in *Quark-Gluon Plasma 3*, edited by R.C. Hwa, X.N. Wang (World Scientific, Singapore, 2004) p. 1 [arXiv:hep-lat/0305025].
27. M. Kaneta, N. Xu, arXiv:nucl-th/0405068.
28. A. Andronic, P. Braun-Munzinger, J. Stachel, Nucl. Phys. A **772**, 167 (2006) [arXiv:nucl-th/0511071].
29. A. Baran, W. Broniowski, W. Florkowski, Acta Phys. Pol. B **35**, 779 (2004) [arXiv:nucl-th/0305075].
30. J. Cleymans, B. Kampfer, M. Kaneta, S. Wheaton, N. Xu, Phys. Rev. C **71**, 054901 (2005) [arXiv:hep-ph/0409071].
31. PHENIX Collaboration (S.S. Adler *et al.*), Phys. Rev. C **69**, 034909 (2004) [arXiv:nucl-ex/0307022].
32. Roy Lacey, private communication.
33. PHOBOS Collaboration (B.B. Back *et al.*), Phys. Rev. C **70**, 051901 (2004) [arXiv:nucl-ex/0401006].
34. M. Kataja, P.V. Ruuskanen, Phys. Lett. B **243**, 181 (1990).
35. STAR Collaboration (J. Adams *et al.*), Phys. Rev. C **72**, 014904 (2005) [arXiv:nucl-ex/0409033].
36. PHENIX Collaboration (S.S. Adler *et al.*), Phys. Rev. Lett. **91**, 182301 (2003) [arXiv:nucl-ex/0305013].
37. A.K. Chaudhuri, arXiv:0704.0134 [nucl-th].
38. P. Romatschke, U. Romatschke, Phys. Rev. Lett. **99**, 172301 (2007) [arXiv:0706.1522 [nucl-th]].
39. H. Song, U.W. Heinz, Phys. Lett. B **658**, 279 (2008) [arXiv:0709.0742 [nucl-th]].
40. T. Hirano, U.W. Heinz, D. Kharzeev, R. Lacey, Y. Nara, Phys. Lett. B **636**, 299 (2006) [arXiv:nucl-th/0511046].
41. S.A. Bass, A. Dumitru, Phys. Rev. C **61**, 064909 (2000) [arXiv:nucl-th/0001033].
42. D. Teaney, J. Lauret, E.V. Shuryak, arXiv:nucl-th/0110037.
43. C. Nonaka, S.A. Bass, Phys. Rev. C **75**, 014902 (2007) [arXiv:nucl-th/0607018].
44. R. Rapp, E.V. Shuryak, Phys. Rev. Lett. **86**, 2980 (2001) [arXiv:hep-ph/0008326]; R. Rapp, Phys. Rev. C **66**, 017901 (2002) [arXiv:hep-ph/0204131].
45. W. Cassing, Nucl. Phys. A **700**, 618 (2002) [arXiv:nucl-th/0105069].
46. J. Noronha-Hostler, C. Greiner, I.A. Shovkovy, arXiv:nucl-th/0703079.
47. S. Pratt, K. Haglin, Phys. Rev. C **59**, 3304 (1999).
48. P. Huovinen, J.I. Kapusta, Phys. Rev. C **69**, 014902 (2004) [arXiv:nucl-th/0310051].

Available online at www.sciencedirect.com
SCIENCE DIRECT®
ELSEVIER
Nuclear Physics A 761 (2005) 296–312
NUCLEAR PHYSICS A

Anisotropy of flow and the order of phase transition in relativistic heavy ion collisions

Pasi Huovinen [a,b]

[a] *Helsinki Institute of Physics, P.O. Box 64, FIN-00014 University of Helsinki, Finland*
[b] *Department of Physics, P.O. Box 35, FIN-40014 University of Jyväskylä, Finland*

Received 24 May 2005; received in revised form 14 July 2005; accepted 21 July 2005

Available online 8 August 2005

Abstract

Using a hydrodynamical model we study how the order of phase transition in the equation of state of strongly interacting matter affects single particle spectra, elliptic flow and higher order anisotropies in Au + Au collisions at RHIC ($\sqrt{s_{\mathrm{NN}}} = 200$ GeV energy). We find that the single particle spectra are independent of the order of phase transition and that the fourth harmonic $v_4(p_T)$ shows only a weak dependence in the p_T region where hydrodynamics is expected to work. The differential elliptic flow, $v_2(p_T)$, of baryons shows the strongest dependence on equation of state. Surprisingly the closest fit to data was obtained when the equation of state had a strong first order phase transition and a lattice inspired equation of state fits the data as badly as a purely hadronic equation of state.

PACS: 25.75.-q; 25.75.Ld; 25.75.Nq

Keywords: Relativistic heavy ion collisions; Elliptic flow; Order of phase transition; Hydrodynamic model

1. Introduction

In non-central heavy ion collisions at the Relativistic Heavy Ion Collider (RHIC) of BNL the particle distributions exhibit quite large anisotropies [1–3]. The second Fourier coefficient of the azimuthal distribution of particles, so-called elliptic flow, has been exten-

E-mail address: pasi.huovinen@phys.jyu.fi (P. Huovinen).

0375-9474/$ – see front matter
doi:10.1016/j.nuclphysa.2005.07.016

sively studied [4] since it is sensitive to the early dense stage of the evolution [5]. Recently also higher harmonics have been measured [3,6]. It has been claimed that they should be even more sensitive to the initial configuration of the system [7].

Ideal fluid hydrodynamics has been particularly successful in describing the observed anisotropy of particles at low p_T in minimum bias collisions [8,9]. This success has been interpreted as a sign of formation of thermalized matter rapidly after the primary collision [10]. Studies of both single particle spectra and anisotropies have also shown that a reasonable reproduction of data favours an Equation of State (EoS) of strongly interacting matter with a phase transition [11,12].

The lattice QCD calculations of the EoS of strongly interacting matter support such a scenario by predicting a phase transition at $T_c \approx 170$ MeV temperature. For a physical scenario of two light and one heavier quark, the phase transition is predicted to be a smooth crossover at small values of baryochemical potential. Contrary to naive expectations, lattice QCD predicts that pressure and energy density do not reach their ideal Stefan–Boltzmann values immediately above the critical temperature, but approach them slowly [13].

At mid-rapidity at collisions at RHIC, the net baryon density is small and the relevant EoS should exhibit a crossover transition. However, so far all hydrodynamical calculations of elliptic flow [10–12,14–19] have used an EoS with a strong first order phase transition and ideal parton gas to describe the plasma phase. The usual point of view has been that it is unlikely that the details of phase transition would lead to significant dynamical effects [9]. This standpoint has been supported by the early calculations [20,21], where it was found that the width of the phase transition region, ΔT, had only little effect on the final flow pattern in one-dimensional flow. Thus it was considered safe to claim that the final particle distributions would not be sensitive to ΔT either.

However, full three-dimensional expansion is more complicated than one-dimensional. It is known that in three-dimensional expansion the differential elliptic anisotropy, $v_2(p_T)$, of (anti)protons is sensitive to the existence of phase transition and its latent heat [11,12,15]. The anisotropy of flow might thus be sensitive to other details of phase transition as well. In this paper we address this possible sensitivity. We use a hydrodynamical model to calculate single particle spectra, elliptic flow and higher order anisotropies in $\sqrt{s_{\mathrm{NN}}} = 200$ GeV Au + Au collisions using four different EoSs with different phase transitions and plasma properties. As a representative of lattice QCD results, we use an EoS based on the thermal quasiparticle model of Schneider and Weise [22] (EoS qp). This model is tuned to reproduce the lattice QCD EoS and provides a method to extrapolate the results to physical quark masses. To facilitate comparison with earlier calculations we use as reference points the EoSs Q and H used in Refs. [10,12,14–16]. EoS Q has a first order phase transition between hadron gas and an ideal parton gas whereas EoS H is a hadron gas EoS without any phase transition. To study the effects of the order of phase transition and slow approach to the Stefan–Boltzmann limits separately we also use a simple parametrisation for an EoS (EoS T) where the hadron gas and ideal parton gas phases are connected using a hyperbolic tangent function. Such an EoS has a smooth crossover transition but the plasma properties approach their ideal values much faster than in EoS qp.

We find that the main sensitivity to the details of an EoS lies in the differential elliptic flow of heavy particles ($m \gtrsim 1$ GeV) where EoS Q with a first order phase transition leads to an anisotropy closest to the data. Surprisingly, the lattice inspired EoS qp re-

produces the data as badly as purely hadronic EoS. EoS T with a crossover transition leads to almost as good results as EoS Q. Thus hydrodynamical description of elliptic flow does not require a strong first order phase transition, but it does require sufficiently large increase in entropy and energy densities within sufficiently small temperature interval.

2. Equation of state

Until recently the lattice QCD calculations were restricted to vanishing net baryon densities, $\mu_B = 0$. Even if there are some recent results for $\mu_B \neq 0$ [13], we limit our discussion to zero net baryon density for the sake of simplicity. Since we are interested in the behaviour of the collision system at midrapidity at RHIC where net baryon density is small, this approximation is unlikely to cause a large effect. Thermal models suggest that around phase transition temperature, the baryon chemical potential is below 50 MeV [23] corresponding to a quark chemical potential of about 15 MeV. At these small values of μ the critical temperature is expected to change by less than a percent from that at $\mu = 0$ [13]. One of our EoSs (EoS Q, see below) also includes extension to non-zero baryon densities. We have checked that for this EoS, the results obtained when the finite baryon density is included in the EoS or approximated by zero, differ by less than two percents. Even if we do not include finite baryon density to the EoS, we still have finite baryon current in our hydrodynamical calculation. This allows us to have different baryon and antibaryon yields at freeze-out and thus finite net proton yields.

So far the lattice QCD calculations with quarks must be done using unphysically large quark masses. The calculated equation of state must therefore be extrapolated to physical quark mass values. For this purpose we use the thermal quasiparticle model of Schneider and Weise [22]. In this model the lattice QCD results are described in terms of quasiparticles with temperature dependent effective masses and effective number of degrees of freedom. In this approach the EoSs obtained in lattice calculations for pure glue [24] and different number of quark flavours [25] are well reproduced. Since the mass of quarks is an explicit parameter in this model, it is easy to extrapolate the results to physical quark masses. Here we use the quasiparticle EoS for two light quark flavours ($m_{u,d} = 0$) and a heavier strange quark ($m_s \simeq 170$ MeV) to describe the plasma phase of an EoS qp.

The quasiparticle model is compared to the lattice results in Fig. 1, where pressure and energy density are shown as a function of temperature. The lattice result for pressure [25] is extrapolated to the continuum limit by assuming a 10% correction, i.e., $p_{\mathrm{cont}} \approx 1.1 p_{\mathrm{lat}}$ [22], whereas the result for energy density is shown without such an extrapolation. When the quark masses in the quasiparticle model are set temperature dependent as in the lattice calculations, $m_q = 0.4T$ (light quarks) and $m_s = 1.0T$ (heavy quark), the lattice pressure is nicely reproduced (PQP, dashed line). When physical quark masses are chosen (EoS qp, thin solid line), the pressure is larger than with temperature dependent masses.

There is no quasiparticle result with temperature dependent masses available for energy density, but comparison of quasiparticle model with physical quark masses (EoS qp) to the

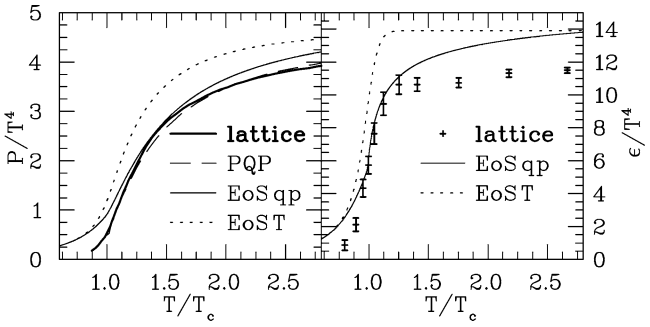

Fig. 1. The lattice results for pressure (left panel) and energy density (right panel) [25] compared to the quasiparticle model with quark masses as used in the lattice calculation (PQP), quasiparticle model with physical quark masses (EoS qp) and a parametrized EoS T (introduced later in the text). The lattice result for pressure is extrapolated to continuum limit by $p_{\rm cont} \approx 1.1 p_{\rm lat}$ [22].

lattice shows nice reproduction of the lattice energy density just above T_c but much larger density above $1.5T_c$. This can be partly explained by the missing extrapolation to continuum limit of the lattice result. If one assumes similar 10% correction than for pressure, the difference between lattice and EoS qp is quite similar for both pressure and energy density at high temperature. The parametrized EoS T (see later in the text) is included for comparison's sake and is shown to lead to much larger pressure and energy density than lattice calculations.

The large difference between EoS qp and lattice below T_c is intentional and not related to the quasiparticle model. In the present lattice simulations pions turn out too heavy and therefore their contribution to pressure and entropy is strongly suppressed. Thus one may expect the lattice calculations to give too small pressure and entropy density in the hadronic phase below T_c. The quasiparticle model reproduces also this feature of the lattice EoS and one has to describe the hadronic phase using another model.

We adopt the usual approach of using an EoS of noninteracting hadron resonance gas to describe the hadronic phase. It has been shown that such an EoS describes interacting hadron gas reasonably well at temperatures around pion mass [26] and that the hadron resonance gas approach reproduces the lattice results below T_c if the same approximations are used in both [27]. The properties of hadron resonance gas depend on the number of particles included in the model. Here we include all the strange and non-strange particles and resonances listed in the Particle data Book up to 2 GeV mass. The details of constructing this EoS can be found in Ref. [28].

To circumvent our ignorance of the behaviour of the EoS around T_c, we use the approach outlined in Ref. [29]: we use the hadron resonance gas EoS up to a temperature $T_c - \Delta T$, the quasiparticle EoS above T_c and interpolate smoothly between these two regimes. In practice we choose the values $T_c = 170$ MeV and $\Delta T = 5$ MeV and connect the entropy densities of both models using a polynomial function. We require that the first, second and third temperature derivatives of entropy density are continuous to approximate a smooth crossover from hadronic to plasma phase. Below $T_c - \Delta T$ we use the hadron resonance gas values for pressure and energy density. Above this limit we obtain $P(T)$ and $\varepsilon(T)$ by

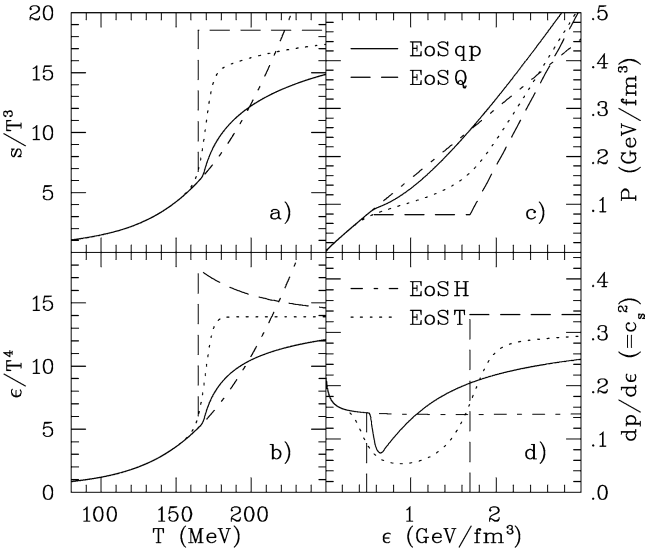

Fig. 2. (a) The entropy density divided by T^3 and (b) the energy density divided by T^4 as functions of temperature, (c) the pressure and (d) velocity of sound squared as functions of energy density in the EoSs qp (quasiparticle EoS), Q (ideal parton gas with first order phase transition), H (hadron resonance gas) and T (ansatz with crossover).

using the thermodynamical relations $\mathrm{d}P = s\,\mathrm{d}T$ and $\varepsilon = Ts - P$. This EoS is called EoS qp in the following.

For comparison's sake we also carry out the calculations using the EoS Q and H used in Refs. [10,12,14–16]. EoS H is a purely hadronic EoS without any phase transition. It is constructed by extending the previously described hadron resonance gas EoS to arbitrarily high temperatures. EoS Q, on the other hand, is inspired by a bag model and contains a first order phase transition from hadron gas to ideal parton gas. The hadron phase is again described by an hadron resonance gas and the plasma phase by a gas of ideal massless quarks and gluons with a bag constant. To approximate the effect of the finite strange quark mass we use the number of quark flavours $N_f = 2.5$. The phase boundary is determined using the Gibbs criterion $p_{\mathrm{HG}}(T_c) = p_{\mathrm{QGP}}(T_c)$ and the two phases are connected using the Maxwell construction at $T_c = 165$ MeV. Details of constructing these two EoSs can be found in Ref. [28].

As can be seen in Fig. 2 the quasiparticle and bag model inspired EoSs (qp and Q, respectively) lead to quite different behaviour around critical temperature. Since we want to study the effects of the order of phase transition and slow approach to ideal Stefan–Boltzmann values separately, we construct yet another EoS. We follow the idea presented in Ref. [20] and connect the hadron and parton phases of the EoS by a hyperbolic tangent function. We refine this approach by using hadron resonance gas EoS instead of ideal pion gas to describe the hadron phase. In Ref. [20] the entropy densities of hadron and parton phases are connected in this way. This leads to similar behaviour of energy density than the Maxwell construction of EoS Q—above T_c energy density rises above the ideal Stefan–Boltzmann limit and approaches the ideal values from above. There is no sign of this kind

of behaviour in the lattice results. Therefore, we use hyperbolic tangent to connect the energy density of the different phases instead of entropy density. Energy density is given by

$$\varepsilon(T) = \frac{1}{2}\left[\varepsilon_{\mathrm{HRG}}(T)\left(1-\tanh\frac{T-T_c}{\Delta T}\right)+\frac{169}{120}\pi^2T^4\left(1+\tanh\frac{T-T_c}{\Delta T}\right)\right], \qquad (1)$$

where the latter term is the energy density of ideal parton gas with 3 colours and 2.5 quark flavours. We use again $T_c = 170$ MeV and make the crossover rapid by choosing $\Delta T = 5$ MeV. After obtaining $\varepsilon(T)$ we again use standard thermodynamical relations, $(\partial S/\partial E)_{N,V} = 1/T$ and $P = Ts - \varepsilon$, to obtain entropy density and pressure as a function of temperature. This EoS is called EoS T in the following.

All four EoSs are compared in Fig. 2 where entropy and energy density are shown as functions of temperature and pressure and the square of the speed of sound are shown as functions of energy density for each EoS. As can be seen the behaviour of the lattice inspired EoS qp is quite different from the previously used EoS Q with a first order phase transition. The latter has a relatively large latent heat of 1.15 GeV/fm^3 whereas in the former the region where the speed of sound is small and the EoS soft is much smaller. The parametrised EoS T is a compromise between these two. It can also be seen that above the phase transition region the EoS Q has the largest speed of sound and is therefore hardest whereas the EoS H without phase transition is softest.

It is worth noticing that EoS qp depicts a smaller rise in both energy and entropy densities around T_c than what could be expected from lattice calculations. This is not a property of the quasiparticle model used here, but due to the use of hadron resonance gas EoS below T_c. As mentioned before, lattice calculations lead to too high pion mass and correspondingly too small densities below T_c. If realistic pion masses are used in hadron resonance gas, its pressure and densities are well above lattice results below T_c.

3. Initialization

We use the same boost-invariant hydrodynamic code than in Refs. [14–16] and described in detail in Ref. [30]. To fix the parameters of the model, we require that the model reproduces the p_T spectra of pions and net protons ($p - \bar{p}$) in most central collisions and the centrality dependence of pion multiplicity at midrapidity. We use net protons instead of protons and/or antiprotons because our model assumes chemical equilibrium to hold down to kinetic freeze-out temperature and is unable to reproduce proton and antiproton yields simultaneously.

Some parametrisations to fix the initial density distributions were explored in Ref. [16]. None of them reproduces the observed centrality dependence of multiplicity, but a linear combination of them does. Here we use the same combination than in Refs. [10,12]. The local entropy density is taken to scale with a linear combination of the density of participants and binary collisions in the transverse plane with weights of 0.75 and 0.25, respectively. This kind of scaling can be interpreted as particle production from "soft" and "hard" processes. For the sake of simplicity, the initial baryon number density is taken to

scale with the number of participants. The initial time of the calculation, $\tau_0 = 0.6$ fm/c, is taken from earlier calculations for $\sqrt{s_{\rm NN}} = 130$ GeV energy [14,15].

The freeze-out energy density is chosen to reproduce the slopes of pion and net proton spectra in most central collisions (see upper left panel of Fig. 3). The stiffer the EoS, the sooner, i.e., at higher density, the necessary flow velocity to fit the spectra has been built up. We find that effectively the EoS qp is stiffest since it requires the highest decoupling energy density $\varepsilon_{\rm fo} = 0.14$ GeV/fm^3 ($\langle T_{\rm fo}\rangle = 141$ MeV) to fit the data. Even if the ideal parton gas EoS is stiff, the mixed phase of the EoS Q makes it effectively the softest EoS here. The stiffening of the phase transition region and softening of the plasma phase in the EoS T cancel each other. It is almost as soft as EoS Q and can use the same freeze-out energy density $\varepsilon_{\rm fo} = 0.08$ GeV/fm^3 ($\langle T_{\rm fo}\rangle = 130$ MeV). The purely hadronic EoS H is in between these extremes and requires $\varepsilon_{\rm fo} = 0.10$ GeV/fm^3 ($\langle T_{\rm fo}\rangle = 135$ MeV) to fit the data. As can be seen in the upper left panel of Fig. 3, these choices of $\varepsilon_{\rm fo}$ allow all EoSs to fit the data equally well.

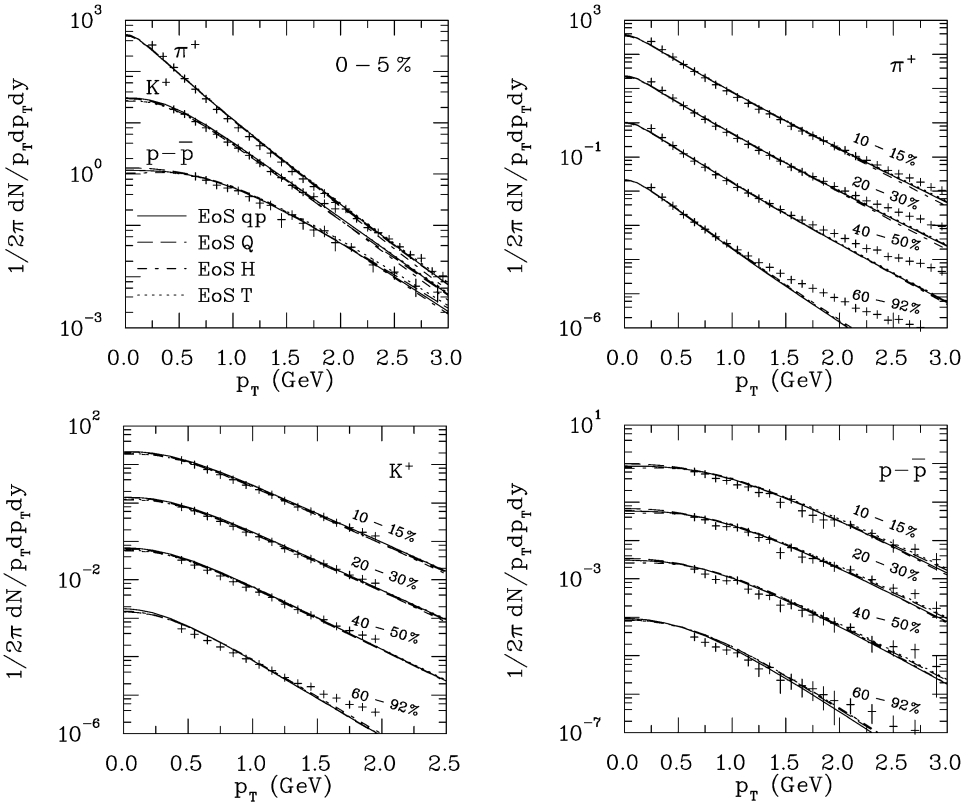

Fig. 3. Pion (π^+), kaon (K^+) and net proton (p–$\bar{p}$) p_T-spectra in most central (top left) and semi-central to peripheral Au + Au collisions at $\sqrt{s_{AA}} = 200$ GeV compared with hydrodynamical calculations using four different EoSs. The data was taken by the PHENIX Collaboration [31]. For clarity the spectra at centralities 20–30%, 40–60% and 60–80% are scaled by factors 10^{-1}, 10^{-2} and 10^{-3}, respectively.

4. Results

4.1. p_T-spectra

The transverse momentum spectra for pions, kaons and net protons for various centralities are shown in Fig. 3. Pion and net proton spectra in most central collisions were used to fix the parameters of the model, but the data are well reproduced at other centralities too. Only at the most peripheral collisions the data tend to favour flatter spectra than calculated.

The kaon spectra was not taken into account when choosing the parameters and the calculated spectra is a prediction in most central collisions too. The fit to data is surprisingly good when one takes into account that the freeze-out temperature is well below the $T_{\rm chem} \approx$ 174 MeV chemical freeze-out temperature where particle yields are fixed [23].

The net proton spectra is well reproduced up to $p_T = 2.5$–3.0 GeV except in the most peripheral collisions, where the data begins to deviate form the calculation at lower p_T. It is worth noticing that we are able to fit the p_T spectra of net protons without any initial transverse velocity field whereas the fit of protons in Ref. [19] required a non-zero initial transverse velocity. One reason for this is that due to larger errors, it is easier to fit the net-proton than proton spectra. The main cause is, however, the different EoS in the hadronic phase. In [19], the authors assumed a separate thermal and kinetic freeze-outs and only a partial chemical equilibrium in the hadronic phase whereas in this work a full chemical equilibrium is assumed. Although the relation between pressure and energy density is almost independent of these assumptions, the relation between temperature and energy density depends strongly on them [18,32]. Thus the relation between collective and thermal motion in a hydrodynamical model depends on the assumption of chemical equilibrium or non-equilibrium and very different initial states can be required to fit the data.

4.2. Elliptic anisotropy

The second Fourier coefficient, v_2, of the azimuthal distribution of charged particles as function of centrality is shown as a histogram in Fig. 4. Note that the data measured by the STAR [6] and PHENIX [1] Collaborations have different pseudorapidity and p_T cuts. After these cuts have been applied to the calculations, the results differ slightly. Therefore, the comparison with the data is done in two separate panels. The agreement with data is similar to that seen in $\sqrt{s_{\rm NN}} = 130$ GeV collisions [11,14,33]: at most central collisions ($< 10\%$ of cross section, $b \lesssim 4.6$ fm) the observed anisotropy is above the hydrodynamical result. At semicentral collisions the calculations fit the data (10–30% of cross section, $4.6 \lesssim b \lesssim 8$ fm, depending on the EoS) and at peripheral collisions the calculated anisotropy is well above the observed. One possible explanation for larger observed than calculated anisotropy in most central collisions is fluctuations in the initial state geometry [34]. The present experimental procedure cannot distinguish between the enhancing and suppressing effects of fluctuations on anisotropy in most central collisions and consequently leads to too large value of v_2.

The sensitivity of the anisotropy to the EoS depends on centrality. In the most central and semi-peripheral collisions EoS Q leads to the lowest anisotropy and EoS H to the largest, but in most peripheral collisions the lowest anisotropy is achieved using EoS qp.

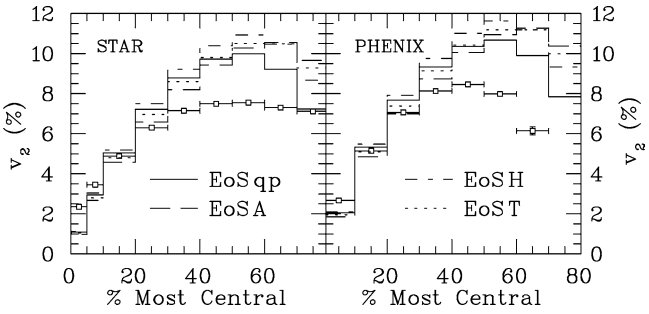

Fig. 4. Centrality dependence of elliptic flow of charged hadrons calculated using three different equations of state and compared with data by the STAR [6] and the PHENIX [1] Collaborations. The STAR data is for $|\eta| < 1.2$ and $p_T > 0.15$ GeV and the PHENIX data is for $|\eta| < 0.35$ and $0.2 < p_T < 10$ GeV. The same cuts have been applied to the hydrodynamic calculations.

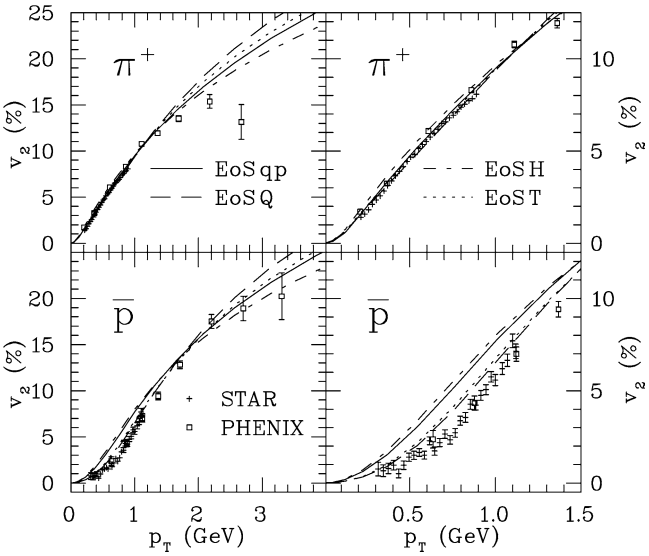

Fig. 5. Elliptic flow of pions and antiprotons vs. transverse momentum in minimum bias Au + Au collisions at $\sqrt{s_{\mathrm{NN}}} = 200$ GeV calculated using four different EoSs and compared with the data by the STAR [3] and PHENIX [1] Collaborations. Feed-down from weak decays of strange baryons is included in the calculations.

The stiffest EoS does not always lead to the largest anisotropy and the softest to smallest because of the interplay of collective and thermal motion. Stiff EoS may necessitate decoupling at higher temperature when larger thermal motion dilutes the flow anisotropy.

The momentum dependence of elliptic flow, $v_2(p_T)$, in minimum bias collisions is shown in Fig. 5 for positive pions and antiprotons and in Fig. 6 for neutral kaons and a sum of lambdas and antilambdas. For pions the behaviour is similar to the charged particle $v_2(p_T)$ at $\sqrt{s_{\mathrm{NN}}} = 130$ GeV collisions [12,14]. Regardless of the EoS the calculated anisotropy reproduces the data up to $p_T \approx 1.5$ GeV where the data begins to saturate but the hydrodynamical curve keeps increasing. Major differences between dif-

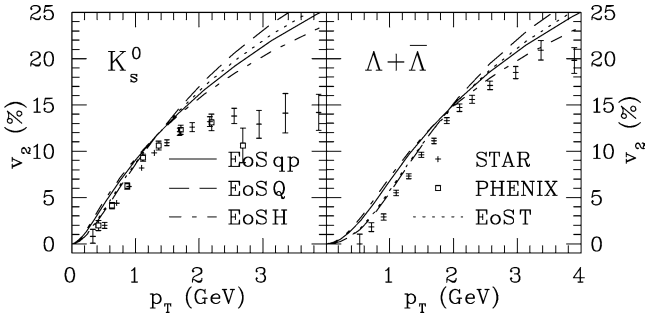

Fig. 6. Elliptic flow of kaons and lambdas vs. transverse momentum in minimum bias Au + Au collisions at $\sqrt{s_{NN}} = 200$ GeV calculated using four different EoSs and compared with the data by the STAR [3] and PHENIX [1] Collaborations.

ferent EoSs are at the high p_T region where no EoS fits the data. Closer look at low p_T region ($p_T < 1$ GeV) reveals that EoS H leads to slightly larger v_2 than the other EoSs, but the difference is equal to the difference between the STAR and PHENIX data.

The antiprotons show much stronger sensitivity to the EoS than pions. Below $p_T = 2$ GeV the results form two groups. EoSs qp and H lead to almost identical $v_2(p_T)$ which is clearly above the data whereas EoSs Q and T lead to anisotropy very close to the data. The phase transition crossover in EoS T is very rapid with $\Delta T = 5$ MeV. We have tested that increase in ΔT leads to larger antiproton $v_2(p_T)$ at low p_T and worse fit with the data. For example, $\Delta T = 17$ MeV moves the $v_2(p_T)$ curve roughly halfway between results for EoS Q and qp. At high values of p_T the order of results is changed with EoS Q leading to highest and EoS H to the lowest anisotropy. The antiproton data follows the hydrodynamical calculation to much higher values of p_T than the pion data. Even the highest data point at $p_T = 3.2$ GeV is fitted while using EoS qp or H.

Even when EoS Q is used, we cannot reproduce the antiproton $v_2(p_T)$ as well as in earlier studies [15]. The main reason is that in Ref. [15] freeze-out temperature was lower $T_f \approx 120$ MeV, but after constraining the freeze-out to fit the p_T spectra we are forced to use higher freeze-out temperature which does not allow as good description of the v_2 data.

The general behaviour of antiproton $v_2(p_T)$ suggests that the larger the latent heat, the smaller the $v_2(p_T)$ at low p_T. However, this is not the case. To test this hypothesis we used also an EoS with a first order phase transition and larger latent heat than EoS Q (2 GeV/fm^3 instead of 1.15 GeV/fm^3). The fit to antiproton anisotropy was no better than for EoS Q (similar behaviour was already seen in Ref. [11] for EoSs with latent heats 0.8 and 1.6 GeV/fm^3).

Comparison with the strange particle data (K^0_s, $\Lambda + \bar{\Lambda}$) in Fig. 6 shows similar trends. The larger the particle mass the larger the differences between EoSs at low p_T. The data deviates from the overall behaviour of hydrodynamical calculation at lower p_T for mesons than for baryons—the kaon data deviates already around $p_T \approx 1.2$ GeV whereas hydrodynamical calculation is close to lambda data up to $p_T \approx 3.5$ GeV. On the other hand, the overall fit to data is worse for strange than non-strange particles. Even EoS Q leads to calculated anisotropy which is above the data also at low p_T. Smaller v_2 at low p_T cannot be interpreted as a sign of strange particles freezing out earlier at higher temperature. For

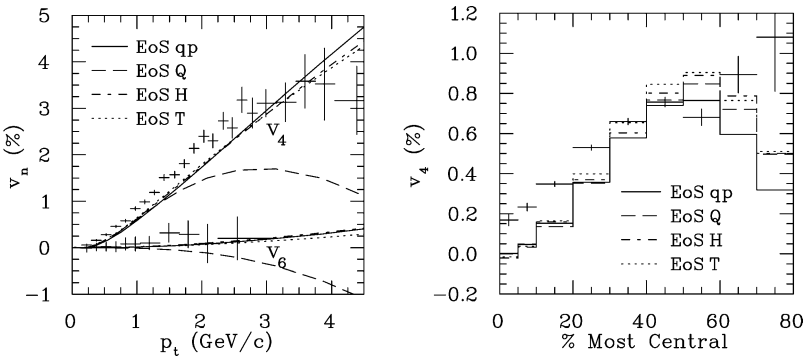

Fig. 7. The fourth and sixth harmonics, $v_4(p_T)$ and $v_6(p_T)$, in minimum bias collisions (left) and p_T-averaged fourth harmonic, v_4, of the azimuthal distribution of charged hadrons as function of centrality (right) calculated using four different EoSs and compared with the STAR data [6].

kaons and lambdas that would mean *larger* v_2 at small p_T. The good fit to kaon p_T spectra is also against a higher kinetic freeze-out temperature for strange particles.

As shown in Ref. [16], the different parametrisations of the initial state can lead to similar pion $v_2(p_T)$ but different proton $v_2(p_T)$ in minimum bias collisions. We have checked if it would be possible to bring the antiproton $v_2(p_T)$ down to fit the data using EoS H but different initial state as speculated in Ref. [8]. To do this we assumed that at each value of impact parameter b, the initial energy density was proportional to the density of binary collisions in the transverse plane (parametrisation eBC of Ref. [16]), but the proportionality constant depended on impact parameter to reproduce the observed centrality dependence of multiplicity. Because this parametrisation led to steeper initial gradients than our usual parametrisation, we had to use freeze-out energy density $\varepsilon_f = 0.12$ GeV/fm^3 instead of $\varepsilon_f = 0.1$ GeV/fm^3 ($\langle T_f \rangle = 138$ MeV and $\langle T_f \rangle = 135$ MeV, respectively) to reproduce the p_T distributions of pions and net-protons. As a result, the earlier decoupling negated the change due to the different initial shape and the final proton $v_2(p_T)$ was almost similar to that shown in Fig. 5 and well above the data. We conclude that the anisotropies shown in Figs. 5 and 6 are typical for each EoS and robust against small variations in the initial parametrisation of the system.

4.3. Higher harmonics

Recently there has been interest in measuring the higher harmonics of the azimuthal distribution of particles [3,6]. It has been proposed that these higher coefficients should be even more sensitive to the initial configuration of the system than the elliptic flow coefficient v_2 [7]. A detailed study of these coefficients would require checking how different initial configurations would affect these coefficients. Instead we calculate the fourth and sixth harmonics of distribution, v_4 and v_6, using the initial state defined above as a first attempt to see how an EoS affects higher harmonics.

The fourth and sixth harmonics of the charged particle distribution in minimum bias collisions, $v_4(p_T)$ and $v_6(p_T)$ as function of transverse momenta are shown in the left panel of Fig. 7. The EoS has significant effect only above $p_T \approx 2$ GeV, i.e., in the re-

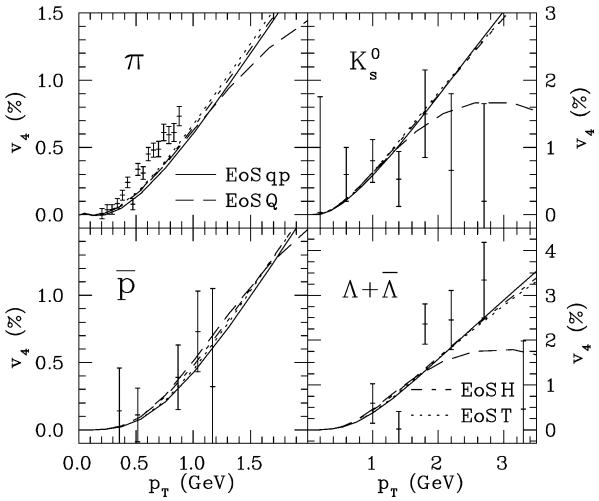

Fig. 8. The fourth harmonic, $v_4(p_T)$, of the azimuthal particle distribution of pions, antiprotons, K^0_S and $\Lambda + \bar{\Lambda}$ for minimum bias Au + Au collisions calculated using four different EoSs and compared with the preliminary STAR data [3].

gion where $v_2(p_T)$ is no longer reproduced by hydrodynamics. EoS Q leads to v_4 peaking around $p_T \approx 3$ GeV whereas all the other EoSs lead to monotonous increase of $v_4(p_T)$ with increasing p_T. The data, on the other hand, increases up to $p_T \approx 3$ GeV and saturates. Except for the high p_T region all the EoSs lead to v_4 which is smaller than the experimentally measured values. The measured values of the sixth harmonics of the distribution, v_6, are consistent with zero, although the errors are large enough not to exclude any of the calculations here. The calculated values of v_6 are also small but show a qualitative dependence on the EoS: EoS Q leads to negative v_6 whereas all the other EoSs lead to positive values of v_6.

The centrality dependence of the p_T averaged fourth harmonic v_4 is shown in the right panel of Fig. 7. It shows qualitatively similar behaviour to $v_4(p_T)$. The EoS has only a weak effect on v_4 except in peripheral collisions. In central and semicentral collisions the calculated values are below the observed ones.

In Fig. 8 the p_T dependence of fourth harmonic v_4 in minimum bias collisions is shown for identified pions, kaons (K^0_s), antiprotons and lambdas. As was the case for charged hadrons, the EoS has only a weak effect on results below $p_T \approx 2$ GeV. The pion data is above the hydrodynamical calculations. The errors for other particles are large and the calculations fit the data except at the highest p_T where kaon data seems to favour EoS Q and lambda data all the other EoSs.

5. Flow on decoupling surface

To understand how different EoSs lead to different anisotropies, we study the properties of the freeze-out surface in Au + Au collision with impact parameter $b = 6$ fm. We try

Table 1
Freeze-out temperature, average transverse flow velocity, spatial eccentricity and flow anisotropy on the decoupling surface in Au + Au collision with impact parameter $b = 6$ fm using four different EoSs

	EoS qp	EoS Q	EoS H	EoS T
$\langle T_{\rm fo}\rangle$ (MeV)	141	130	134	130
$\langle v_r\rangle$	0.47	0.47	0.49	0.49
ϵ_x	0.058	0.033	0.056	0.034
a_2	0.027	0.027	0.025	0.026

to find a set of parameters to describe the surface similar to those presented in Ref. [35] for a blast wave model. Freeze-out temperature, average transverse flow velocity and two anisotropy coefficients are shown in Table 1. To characterise the spatial anisotropy of the surface we generalise the usual spatial anisotropy ϵ_x [30] for hypersurfaces:

$$\epsilon_x = \frac{\int \mathrm{d}\sigma_\mu\, s^\mu (y^2 - x^2)}{\int \mathrm{d}\sigma_\mu\, s^\mu (y^2 + x^2)}, \tag{2}$$

where the usual integral over $\mathrm{d}x\,\mathrm{d}y$ is replaced by an integral over space–time hypersurface and instead of energy density, entropy density is used as a weight. To characterise the azimuthal modulation of the flow field, we first calculate average flow velocity as function of flow angle, $\langle v_r(\phi_v)\rangle$, where $\phi_v = \arctan(v_y/v_x)$. We use the second Fourier coefficient of this distribution as a measure of anisotropy of the flow field:

$$a_2 = \frac{\int \mathrm{d}\phi\, \langle v_r(\phi)\rangle \cos(2\phi)}{\int \mathrm{d}\phi\, \langle v_r(\phi)\rangle}. \tag{3}$$

This allows us to separate the spatial anisotropy from the flow anisotropy.

The average flow velocity and anisotropy of the velocity field are surprisingly similar in all four cases. The main differences at freeze-out are freeze-out temperature and the shape of the surface. As seen in Ref. [36] where the anisotropies are studied using a parametrisation of the freeze-out surface, at this temperature and velocity range the lower temperature should lead to larger anisotropies for both pions and protons. As can be expected, in parametrisation smaller spatial anisotropy is seen to lead to smaller v_2 of particles. This behaviour is different from what we see here where EoS Q leads to lowest $v_2(p_T)$ at low p_T. Smaller spatial anisotropy cannot explain this alone, since its effect should be cancelled by lower temperature. Also the differences between EoS Q and T are such that one would expect EoS T to lead to lower v_2 for both pions and protons, but that is not the case.

Clearly the average values do not characterise the flow well enough. The reason for different anisotropies must lie in the details of the flow profiles. To have a closer look at the properties of flow on the decoupling surface, we have plotted the flow velocity on decoupling surface as a function of radial coordinate in Fig. 9. In the left panel the flow velocity is shown as function of y when $x = 0$ and in the right panel as function of x when $y = 0$.

As expected from very similar spectra and differential anisotropies, the velocity distribution for EoSs qp and H is also close to each other. EoS Q, on the other hand, leads to different flow profile with slower increase of velocity with increasing radius, a distinctive

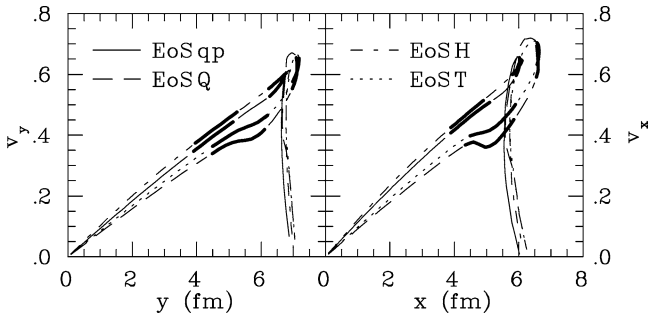

Fig. 9. The transverse flow velocity on decoupling surface of a Au + Au collision with impact parameter $b = 6$ fm using four different EoSs. The left panel shows the velocity as function of y-coordinate when $x = 0$ and the right panel as function of x when $y = 0$. The curves are divided into segments of thin and thick lines where each segment corresponds to 20% of total entropy flowing through freeze-out surface.

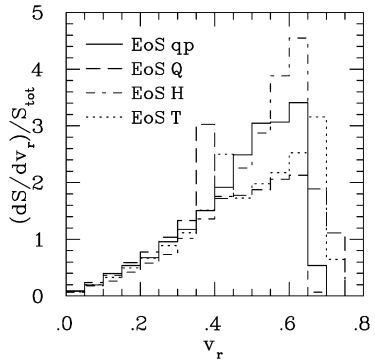

Fig. 10. Entropy flow through fluid elements on decoupling surface as function of the transverse flow velocity of each fluid element.

"shoulder" at $r \approx 5$ fm where the velocity can even slightly decrease with increasing r (in x-direction) and very rapid rise of flow velocity close to maximum radius of the system. EoS T on the other hand is somewhere in between these two with the slow rise at low r and very rapid rise at large r but with much weaker structure around $r \approx 5$ fm.

Even if the flow velocity distributions shown in Fig. 9 do not look too different from each other, the amount of particles emitted from fluid elements at different velocities is very different. To characterise this, the velocity curves in Fig. 9 are divided into segments so that each segment corresponds to 20% of entropy flowing through surface and thus $\sim 20\%$ of particles emitted. Also the entropy flow as function of flow velocity on the decoupling surface is shown in Fig. 10. As can be seen EoS Q leads to very different distribution with much more particles being emitted at small flow velocities. Especially the "shoulder" in flow profile around $r = 5$ fm leads to a peak in entropy distribution at $v_r \approx 0.38$ whereas EoSs qp and H lead to distributions peaking at $v_r \approx 0.6$, close to maximum values of flow velocity. EoS T is again a compromise between these two extremes. The entropy flow has a peak both at the "shoulder" at $v_r \approx 0.42$ and close to maximum velocity at $v_r \approx 0.68$. The largest flow velocity is also larger than for EoSs qp and H and close to the maximum

for EoS Q. The flow on decoupling surface is thus weighted very differently for each EoS and the average values of flow velocity and anisotropy do not completely describe p_T differential anisotropies of particles.

In Ref. [11] similar velocity profiles were considered linear and corroborating the general use of linear velocity profiles in hydrodynamically inspired fits to particle spectra. As seen here the deviations from linear behaviour are important at least in non-central collisions. Thus the parameter values from fits can deviate from values obtained in full-fledged hydrodynamical calculations.

6. Conclusions

In this paper we have examined how the order of deconfinement phase transition affects the anisotropy in a hydrodynamical description of relativistic nuclear collision. We used four different equations of state—one lattice inspired EoS with a crossover transition from hadronic to partonic phase (EoS qp), one where a simple Maxwell construction between different phases creates a first order phase transition (EoS Q), a purely hadronic EoS with no phase transition at all (EoS H) and an EoS where different phases were smoothly connected with a hyperbolic tangent function (EoS T).

The p_T distributions of various particles could be reproduced equally well using each of these EoSs when the freeze-out density was chosen accordingly. Our result is thus different from Ref. [11] where p_T distributions were sensitive to the amount of latent heat of the EoS. This difference is due to different treatment of freeze-out. In Ref. [11], the hadronic stage was described using RQMD cascade model which does not have freeze-out temperature or density as a free parameter.

The main sensitivity to the EoS was seen in the differential anisotropy of heavy particles at low p_T, i.e., antiprotons and lambdas. None of the EoSs was able to reproduce the data, but the EoS with the first order phase transition, EoS Q was closest. Surprisingly the lattice based EoS qp was as far from the proton v_2 data as the EoS H without any phase transition. The basic rule was that the sharper the rapid rise in entropy and energy density at phase transition and the larger the latent heat, the lower the differential anisotropy of antiprotons at low p_T was. This, however, is valid only among the EoSs discussed here.

The results here favour EoS Q and first order phase transition over lattice inspired EoS qp. One should not interpret this to mean that hydrodynamical description of elliptic flow requires a first order phase transition since EoS T with a crossover transition lead to only marginally worse results than EoS Q. The main difference between EoSs qp and T is in the size of the increase in energy and entropy densities around the critical temperature and consequently how wide is the region where the speed of sound is small. Thus the acceptable description of elliptic flow seems to require very fast and sufficiently large increase in entropy and energy densities around T_c.

However, these results must be taken as only preliminary. For simplicity hadron gas was assumed to maintain chemical equilibrium until kinetic freeze-out in these calculations. As mentioned in Section 3, this assumption does not allow the reproduction of observed particle yields but only the slopes of their spectra and approximatively their anisotropies [10, 14]. The recent calculations where this assumption is relaxed and a separate chemical and

kinetic freeze-outs included in the model [18,19], have lead to much worse description of the data [37]. It looks like it is very difficult to describe the data using ideal fluid hydrodynamics while the hadron gas is not in chemical equilibrium [38]. On the other hand, if the hadronic phase is described using RQMD cascade which allows chemical non-equilibrium, the data is again reproduced [11]. Thus the correct treatment of the hadronic phase in a hydrodynamical model is an open question and it is not yet possible to draw final conclusions about the details of the EoS based on the observed anisotropies.

Nevertheless, our results point to that a large and rapid increase in densities around critical temperature is necessary in hydrodynamical description to describe the observed anisotropies. The failure of lattice inspired EoS to do this raises the questions whether the lattice result used here is sufficiently accurate around T_c, whether the hadron resonance gas description of the EoS below T_c is inaccurate or whether some finite size effects make the EoS relevant for heavy ion collisions differ from lattice QCD results.

Acknowledgements

I am grateful for Thorsten Renk and Roland Schneider for allowing us to use a parametrisation of their quasiparticle EoS. Fruitful discussions with P.V. Ruuskanen, R. Snellings and S.S. Räsänen are also thankfully acknowledged. This work was partially supported by the Academy of Finland under project No. 77744.

References

[1] S.S. Adler, et al., PHENIX Collaboration, Phys. Rev. Lett. 91 (2003) 182301, nucl-ex/0305013.
[2] B.B. Back, et al., PHOBOS Collaboration, nucl-ex/0407012.
[3] J. Adams, et al., STAR Collaboration, nucl-ex/0409033.
[4] For reviews see, e.g., J. Ollitrault, Nucl. Phys. A 638 (1998) 195, nucl-ex/9802005;
A.M. Poskanzer, nucl-ex/0110013;
S.A. Voloshin, Nucl. Phys. A 715 (2003) 379, nucl-ex/0210014.
[5] H. Sorge, Phys. Rev. Lett. 78 (1997) 2309, nucl-th/9610026.
[6] J. Adams, et al., STAR Collaboration Phys. Rev. Lett. 92 (2004) 062301, nucl-ex/0310029;
A.M. Poskanzer, STAR Collaboration, J. Phys. G 30 (2004) S1225, nucl-ex/0403019.
[7] P.F. Kolb, Phys. Rev. C 68 (2003) 031902, nucl-th/0306081.
[8] P. Huovinen, in: R.C. Hwa, X.N. Wang, et al. (Eds.), in: Quark–Gluon Plasma, vol. 3, World Scientific, Singapore, 2004, nucl-th/0305064.
[9] P.F. Kolb, U. Heinz, in: R.C. Hwa, X.N. Wang (Eds.), in: Quark–Gluon Plasma, vol. 3, World Scientific, Singapore, 2004, nucl-th/0305084.
[10] U.W. Heinz, P.F. Kolb, Nucl. Phys. A 702 (2002) 269, hep-ph/0111075.
[11] D. Teaney, J. Lauret, E.V. Shuryak, nucl-th/0110037.
[12] U.W. Heinz, P.F. Kolb, hep-ph/0204061.
[13] F. Karsch, E. Laermann, in: R.C. Hwa, X.N. Wang (Eds.), in: Quark–Gluon Plasma, vol. 3, World Scientific, Singapore, 2004, hep-lat/0305025.
[14] P.F. Kolb, P. Huovinen, U.W. Heinz, H. Heiselberg, Phys. Lett. B 500 (2001) 232, hep-ph/0012137.
[15] P. Huovinen, P.F. Kolb, U.W. Heinz, P.V. Ruuskanen, S.A. Voloshin, Phys. Lett. B 503 (2001) 58, hep-ph/0101136.
[16] P.F. Kolb, U.W. Heinz, P. Huovinen, K.J. Eskola, K. Tuominen, Nucl. Phys. A 696 (2001) 197, hep-ph/0103234.

[17] T. Hirano, Phys. Rev. C 65 (2002) 011901, nucl-th/0108004.
[18] T. Hirano, K. Tsuda, Phys. Rev. C 66 (2002) 054905, nucl-th/0205043.
[19] P.F. Kolb, R. Rapp, Phys. Rev. C 67 (2003) 044903, hep-ph/0210222.
[20] J.P. Blaizot, J.Y. Ollitrault, Phys. Rev. D 36 (1987) 916.
[21] D.H. Rischke, M. Gyulassy, Nucl. Phys. A 597 (1996) 701, nucl-th/9509040.
[22] R.A. Schneider, W. Weise, Phys. Rev. C 64 (2001) 055201, hep-ph/0105242.
[23] P. Braun-Munzinger, D. Magestro, K. Redlich, J. Stachel, Phys. Lett. B 518 (2001) 41, hep-ph/0105229.
[24] G. Boyd, J. Engels, F. Karsch, E. Laermann, C. Legeland, M. Lutgemeier, B. Petersson, Nucl. Phys. B 469 (1996) 419, hep-lat/9602007.
[25] F. Karsch, E. Laermann, A. Peikert, Phys. Lett. B 478 (2000) 447, hep-lat/0002003;
F. Karsch, Nucl. Phys. A 698 (2002) 199, hep-ph/0103314.
[26] R. Venugopalan, M. Prakash, Nucl. Phys. A 546 (1992) 718.
[27] F. Karsch, K. Redlich, A. Tawfik, Eur. Phys. J. C 29 (2003) 549, hep-ph/0303108.
[28] J. Sollfrank, P. Huovinen, M. Kataja, P.V. Ruuskanen, M. Prakash, R. Venugopalan, Phys. Rev. C 55 (1997) 392, nucl-th/9607029.
[29] T. Renk, R.A. Schneider, W. Weise, Phys. Rev. C 66 (2002) 014902, hep-ph/0201048.
[30] P.F. Kolb, J. Sollfrank, U.W. Heinz, Phys. Rev. C 62 (2000) 054909, hep-ph/0006129.
[31] S.S. Adler, et al., PHENIX Collaboration, Phys. Rev. C 69 (2004) 034909, nucl-ex/0307022.
[32] D. Teaney, nucl-th/0204023.
[33] P. Huovinen, Nucl. Phys. A 715 (2003) 299, nucl-th/0210024.
[34] M. Miller, R. Snellings, nucl-ex/0312008.
[35] C. Adler, et al., STAR Collaboration, Phys. Rev. Lett. 87 (2001) 182301, nucl-ex/0107003.
[36] F. Retiere, M.A. Lisa, Phys. Rev. C 70 (2004) 044907, nucl-th/0312024.
[37] K. Adcox, et al., PHENIX Collaboration, Nucl. Phys. A 757 (2005) 184, nucl-ex/0410003.
[38] T. Hirano, M. Gyulassy, nucl-th/0506049.

International Journal of Modern Physics E
Vol. 22, No. 12 (2013) 1330029 (24 pages)

DOI: 10.1142/S0218301313300294

World Scientific
www.worldscientific.com

HYDRODYNAMICS AT RHIC AND LHC: WHAT HAVE WE LEARNED?

PASI HUOVINEN

Frankfurt Institute for Advanced Studies, Ruth-Moufang-Straße 1, 60438 Frankfurt am Main, Germany
huovinen@fias.uni-frankfurt.de

Received 28 October 2013
Accepted 31 October 2013
Published 20 November 2013

Fluid dynamical description of elementary particle collisions has a long history dating back to the works of Landau and Fermi. Nevertheless, it is during the last 10–15 years when fluid dynamics has become the standard tool to describe the evolution of matter created in ultrarelativistic heavy-ion collisions. In this paper, I briefly describe the hydrodynamical models, what we have learned when analyzing the RHIC and LHC data using these models, and what the latest developments and challenges are.

Keywords: Heavy-ion collisions; hydrodynamical models; elliptic flow.

PACS Number(s): 25.75.Ld, 25.75.Nq, 24.10.Nz

1. Introduction

The goal of the heavy-ion programs at BNL RHIC[a] and CERN LHC[b] is to observe strongly interacting matter. "Strongly interacting" in a sense that the interactions in the system are not mediated by the electromagnetic, but by the strong interaction, and "matter" in the sense that to describe the system, we do not need to describe every (quasi-)particle individually, but thermodynamic concepts like temperature and pressure are applicable. Thus, it is natural to try to describe the expansion stage of the collision by a macroscopic approach like fluid dynamics. We expect that the system formed in the collision is initially so hot and dense that relevant degrees of freedom are partons, not hadrons. The system expands and cools, undergoes a phase transition to hadrons, and when the system is dilute enough, interactions cease and the particles stream freely to detectors.

[a]Relativistic Heavy-Ion Collider, full collision energy $\sqrt{s_{\rm NN}} = 200$ GeV.
[b]Large Hadron Collider, $\sqrt{s_{\rm NN}} = 2.76$ TeV at the time of this writing, designed $\sqrt{s_{\rm NN}} = 5.5$ TeV.

2. Fluid Dynamics

2.1. *Ideal fluid dynamics*

Relativistic fluid dynamics is basically an application of conservation laws for energy, momentum and conserved charges (if any). When written in differential form,

$$\partial_\mu T^{\mu\nu} = 0 \quad \text{and} \quad \partial_\mu j_x^\mu = 0\,, \tag{1}$$

where $T^{\mu\nu}$ is the energy-momentum tensor, and j_x^μ the charge 4-current of charge x (baryon or electric charge, strangeness, isospin, etc.), the conservation laws provide evolution equations for the system. If there are n conserved charges, there are $4+n$ equations, which contain $10+4n$ unknowns. To make this set of equations solvable, further constraints for the unknowns must be provided. The simplest approach is to assume that the system is in exact local equilibrium. In that case the energy-momentum tensor and charge currents can be expressed as

$$T^{\mu\nu} = (\epsilon + P)u^\mu u^\nu - P g^{\mu\nu} \quad \text{and} \quad j_x^\mu = n_x u^\mu\,, \tag{2}$$

respectively, where ϵ and P are energy density and pressure in the local rest frame, u^μ flow velocity, $g^{\mu\nu}$ is the metric tensor and n_x the charge density of charge x in the local rest frame. Now the number of unknowns is reduced to $5+n$, and the system of equations can be closed by providing the equation of state (EoS) of the fluid in a form $P = P(\epsilon, \{n_i\})$. To model the collisions at RHIC and LHC, the description is usually further simplified by assuming that net baryon density and other conserved charges are zero. After specifying the boundary conditions for this set of partial differential equations the evolution is determined, and all the microscopic physics is contained within the EoS.[c]

However, the simple phrase "after specifying the boundary conditions" contains a lot of physics. Hydrodynamics provides neither the initial distribution of matter nor the criterion for the end of the evolution, but they must be supplied by other models. At ultrarelativistic energies the initial state of the hydrodynamical evolution cannot be two colliding nuclei: The initial collision processes are far from equilibrium and produce large amount of entropy.[3] Thus, the initial state is assumed to be a distribution of thermalized matter soon after the initial collision. The most common approach is so-called Glauber model,[4,5] which is basically a geometrical constraint on the distributions. The Woods–Saxon distributions of nuclear matter in colliding nuclei are projected on a plane orthogonal to the beam (so-called transverse plane), and the resulting densities on this plane, and nucleon–nucleon cross-section at the collision energy, are used to calculate the number density of binary collisions and participants on this plane — participant meaning a nucleon which has interacted at least once (for details, see Ref. 4). The initial energy or entropy density profile is taken to be proportional to the profile of collisions or

[c]For further discussion of fluid dynamics see Refs. 1 and 2.

participants, or to a linear combination of them.[6,7] The proportionality constant is a free parameter chosen to reproduce the observed final particle multiplicity.

Another popular approach is the Kharzeev–Levin–Nardi (KLN) model[8–13] where the initial entropy density distribution is proportional to the distribution of gluons produced in primary collisions. The gluon production is calculated using the Color Glass Condensate (CGC) framework,[14–17] where one applies the feature of QCD that at small-x gluon densities are large. These large densities correspond to classical fields permitting calculations using classical techniques. Another approach to calculate the initial particle production from first principles is so-called EKRT saturation model[18–20] based on perturbative QCD + saturation framework. Besides Glauber and CGC based approaches, one can use event generators like UrQMD,[21–23] AMPT,[24,25] or EPOS[26] to generate the initial state for hydrodynamic expansion. Nevertheless, no model so far describes a dynamical process leading to thermalized matter, but thermalization has to be postulated and imposed by hand.

When the system expands and cools, the mean free paths increase. Ultimately mean free paths become so long that rescatterings cease, and particle distributions no longer evolve. Particle distributions are "frozen" at that stage, and we say that the particles freeze out, or alternatively, that the particles decouple from each other. In practice this freeze-out should be a gradual process, but since implementing a gradual freeze-out is difficult,[d] it is approximated to take place suddenly on a surface of zero thickness. In such a case one can use so-called Cooper–Frye prescription to evaluate particle distributions on this surface[29]:

$$E\frac{dN}{dp^3} = \int_\sigma d\sigma_\mu p^\mu f(T(x), \mu(x), p \cdot u(x)) \,, \tag{3}$$

where σ is the surface where the distribution is to be evaluated, $d\sigma_\mu$ its normal 4-vector, f distribution of particles, and u 4-flow velocity of the fluid. Hydrodynamics does not tell when decoupling should take place, but the criterion is a free parameter, and its value is chosen to reproduce the observed p_T-spectra. Usually a constant temperature or energy density is used as the criterion, although a more realistic criterion would be the ratio of the scattering rate of particles to the expansion rate of the system, i.e. the inverse Knudsen number.[30,31]

2.2. *Dissipative fluid dynamics*

The ideal fluid assumption is extremely strong, and in nature gradients in the system always indicate deviations from equilibrium and thus dissipation. In non-relativistic fluid dynamics Navier–Stokes equations are known to describe viscous fluid well, but unfortunately the relativistic generalization of Navier–Stokes equations is unstable and allows acausal solutions with superluminal signal propagation speeds.[32–34] This undesired behavior can be avoided if one assumes that the dissipative currents (shear stress $\pi^{\mu\nu}$, heat flow q^μ and bulk pressure Π) are not directly

[d]For attempts see Refs. 27 and 28.

proportional to gradients in the system, but are dynamical variables which relax to their Navier–Stokes values on time scales given by corresponding relaxation times τ_π, τ_q and τ_Π. The evolution equations for the dissipative currents can be derived phenomenologically from entropy current,[35,36] from kinetic theory using the Grad 14-moment ansatz,[37–39] or via gradient expansion.[40,41]

The derivation from kinetic theory leads to the commonly used Israel–Stewart equations, but so far it has had a problem: Unlike Chapman–Enskog expansion,[42] which leads to relativistic Navier–Stokes equations, it is not a controlled expansion in some small parameter, in which one could do power counting and improve the approximation if necessary. This problem has recently been solved by rederiving viscous hydrodynamics using the method of moments, and ordering the terms in the expansion according to their (generalized) Reynolds and Knudsen numbers.[43] In lowest order in Knudsen and Reynolds numbers this approach leads to equations identical to the original Israel–Stewart approach, but it has been shown that an adequate description of heat flow would require inclusion of some higher-order terms.[44]

Strictly speaking all these derivations are for a single component system, and the derivation for a multi-component system has not been completed yet.[45–47] For the behavior of the fluid this does not matter — the different components are assumed to behave as a single fluid — but when the fluid is converted to various types of hadrons, this causes an additional uncertainty. The Cooper–Frye prescription (Eq. (3)) is equally valid in dissipative as in ideal system, but dissipation causes the distribution function f to deviate slightly from the thermal equilibrium distribution. If there is only shear, no bulk pressure nor heat flow, in a single component system the Grad 14-moment ansatz leads in Boltzmann approximation to

$$f = f_0 + \delta f, \quad \text{where} \quad \delta f = f_0 \frac{p^\mu p^\nu \pi_{\mu\nu}}{2T^2(\epsilon + P)}\,, \tag{4}$$

and f_0 is the equilibrium distribution function. In a multicomponent system the effect of shear stress on particle distributions should depend on particle properties, but how exactly, is still a work in progress.[48] In practical calculations one has therefore assumed that the dissipative correction to the thermal distribution is given by Eq. (4) for all hadron species. Note that the form of δf in Eq. (4) is only an ansatz. Other forms have been argued for Ref. 49, but if the thermal distribution is expanded differently than in the 14-moment ansatz, the evolution equations and definitions of the dissipative coefficients may change as well.

So far the viscous hydrodynamical calculations have concentrated on studying the effects of shear viscosity, characterized by the shear viscosity coefficient η. In no calculation has heat conductivity been included, and the bulk pressure has usually been omitted as well.[e] When the only dissipative current is shear stress, the energy-

[e]There are some calculations with bulk, like Refs. 50–54.

momentum tensor becomes

$$T^{\mu\nu} = (\epsilon + P)u^\mu u^\nu - Pg^{\mu\nu} + \pi^{\mu\nu}\,, \tag{5}$$

where $\pi^{\mu\nu}$ is the shear stress tensor. Its evolution is usually given by

$$\langle D\pi^{\mu\nu}\rangle = \frac{1}{\tau_\pi}\left(2\eta\sigma^{\mu\nu} - \pi^{\mu\nu}\right) - \frac{4}{3}\pi^{\mu\nu}\partial_\lambda u^\lambda\,, \tag{6}$$

where $D = u^\mu\partial_\mu$, $\sigma^{\mu\nu} = \nabla^{\langle\mu}u^{\nu\rangle}$, and the angular brackets $\langle\ \rangle$ denote the symmetrized and traceless projection, orthogonal to the fluid four-velocity u^μ. Both Israel–Stewart[39,43] and gradient expansion[40,41] approaches lead to some additional terms in the evolution equation, but these terms are usually considered numerically insignificant, although a full analysis of the effect of all terms has not yet been done. It is worth noting that the factor 4/3 in the last term of Eq. (6) is strictly valid for massless particles. Whether modifying this term according to the mass of particles would change any results has not been studied yet. As well, in the original Israel–Stewart papers[36,38] this term was estimated small and omitted in the final equations. In the context of heavy-ion collisions, however, it improves the applicability of viscous hydrodynamics significantly.[55]

2.3. *Hybrid models*

The sudden change from interacting fluid to free streaming particles in the Cooper–Frye description is clearly an oversimplification. We also expect hadron gas to be so dissipative[45,56] that the applicability of dissipative fluid dynamics is questionable.[57] In so-called hybrid models these problems are avoided by using fluid dynamics to describe only the early dense stage of the evolution. The fluid is converted to particles using the Cooper–Frye description, not at freeze-out, but when rescatterings are still abundant, and the individual particles are fed to a hadron cascade model like UrQMD[22,23] or JAM[58,59] to describe the dilute hadronic stage. These models have the advantage that hadron cascades describe freeze-out dynamically without free parameters, all dissipative processes are included, and they can describe a system arbitrarily far from equilibrium. Unfortunately they do not remove all the arbitrariness from the end of the evolution: Like the results of pure hydrodynamical models depend on the freeze-out criterion, the results of hybrid models depend on when the switch from fluid to cascade is done.[57,60] For a detailed discussion of these models see Ref. 60.

3. What We Know

3.1. *There are rescatterings*

The particle production in the primary collisions is azimuthally isotropic, but the distribution of observed particles in $A + A$ collisions is not. The anisotropy can be easily explained in terms of rescatterings of the produced particles: In a noncentral collision of identical nuclei the collision zone has an elongated shape, see Fig. 1. If a

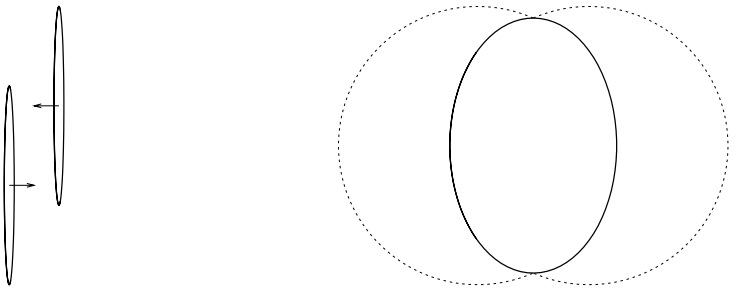

Fig. 1. A schematic representation of the geometry of a noncentral heavy-ion collision. (Left) Two Lorentz-contracted nuclei approaching each other. (Right) A projection of the collision zone onto a plane orthogonal to the beam (so-called transverse plane). The dotted circles depict the target and projectile nuclei.

particle is moving along the long axis of the collision zone, it has a larger probability to scatter and change its direction than a particle moving along the short axis. Thus more particles end up in the direction of the short axis. Or, in the hydrodynamical language, the pressure gradient between the center of the system and the vacuum is larger in the direction of the short axis, the flow velocity is thus larger in that direction, and more particles are emitted along the short than along the long axis.

This anisotropy is quantified in terms of Fourier expansion of the azimuthal distribution. The coefficients of this expansion v_n, and the associated participant angles ψ_n, are defined as[f]

$$v_n = \langle \cos[n(\phi - \psi_n)] \rangle \quad \text{and} \quad \psi_n = \frac{1}{n} \arctan \frac{\langle p_T \sin(n\phi) \rangle}{\langle p_T \cos(n\phi) \rangle} \,. \tag{7}$$

Of these coefficients v_1 is called directed, and v_2 elliptic flow. Elliptic flow of charged hadrons as a function of centrality was one of the first measurements at RHIC.[62] The result is shown in Fig. 2, and compared to early fluid dynamical calculations.[63] As seen, the elliptic flow is quite large and increases with decreasing centrality, as expected if it has the described geometric origin. Thus there must be rescatterings among the particles formed in the collision, and an $A+A$ collision is not just a sum of independent pp collisions.

The observed elliptic flow is also very close to the hydrodynamically calculated one, which is a strong indication of hydrodynamical behavior of the matter. Another signature of hydrodynamical behavior is shown in Fig. 3: It was observed that the heavier the particle, the smaller its p_T-differential v_2 at low p_T. As explained in Refs. 2 and 68, such a behavior arises if all the particles are emitted from the same expanding thermal source. Thus, if the produced matter is not close to kinetic equilibrium, at least it behaves as if it was!

[f]For a detailed discussion of the anisotropy measurements see Ref. 61.

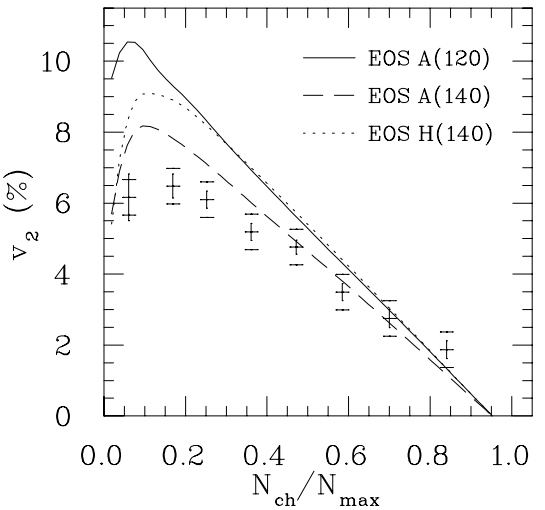

Fig. 2. The elliptic flow parameter v_2 of charged hadrons as function of centrality ($N_{\rm ch}/N_{\rm max} = 1$ is the most central collision) in Au + Au collisions at $\sqrt{s_{\rm NN}} = 130$ GeV. The data are from Ref. 62 and the calculation using different EoSs (labels A and H), and freeze-out temperatures (120 MeV or 140 MeV) from Ref. 63. The figure is from Ref. 64.

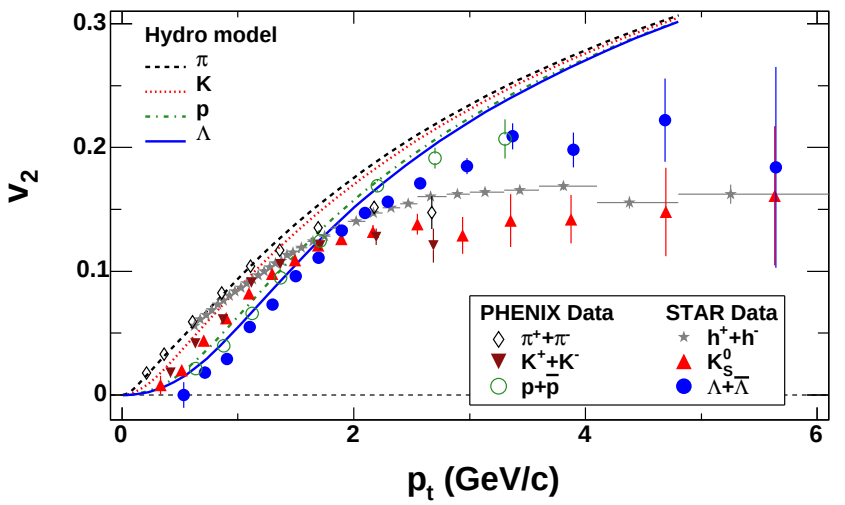

Fig. 3. v_2 versus p_T for identified particles in minimum bias Au + Au collisions at $\sqrt{s_{\rm NN}} =$ 200 GeV. The figure is from Ref. 65 and reprinted with permission. The data are from Refs. 65–67.

It has often been argued that the large observed v_2 and its hydrodynamical reproduction requires that the system reaches thermal equilibrium very fast,[69] within 1 fm/c after the initial collision. The hydrodynamical models fitting the data do indeed use short initial times, $\tau_0 = 0.15 - 1$ fm/c, but in Ref. 70 it was shown that

$\tau_0 = 2$ fm/c works as well. The crucial distinction is what the shape of the initial state is: the larger the deformation, the larger the final momentum anisotropy. During thermalization the matter will not stay put, but begins to expand. This expansion reduces the spatial anisotropy, and unless momentum anisotropy is built up during thermalization, the final anisotropy is smaller.[71] If thermalization is fast, we may assume that changes in matter distribution and flow field during thermalization are tiny, and geometry (Glauber) and/or initial gluon production (color glass, EKRT) give reasonable constraints to the initial state of hydrodynamical evolution. In Ref. 70, the shape of the initial state was assumed to be independent of the thermalization time, but if thermalization time is long, this is no longer a good approximation. Thus, if thermalization is fast, we know that we can reproduce the data using hydrodynamical models, but if thermalization takes long, we do not know, since we do not know a plausible initial state for hydrodynamical evolution.

3.2. *EoS has many degrees of freedom*

The EoS of strongly interacting matter is an explicit input to hydrodynamical models. Thus one might expect hydrodynamical modeling of heavy-ion collisions to tell us a lot about the EoS, but unfortunately that is not the case. The collective motion of the system is directly affected by the pressure gradients in the system, and thus by the EoS, but the effects of the EoS on the final particle p_T distributions can to very large extent be compensated by changes in the initial state of the evolution, and the final decoupling temperature. This makes constraining the properties of the EoS very difficult. However, what we do know is that the number of degrees of freedom has to be large.

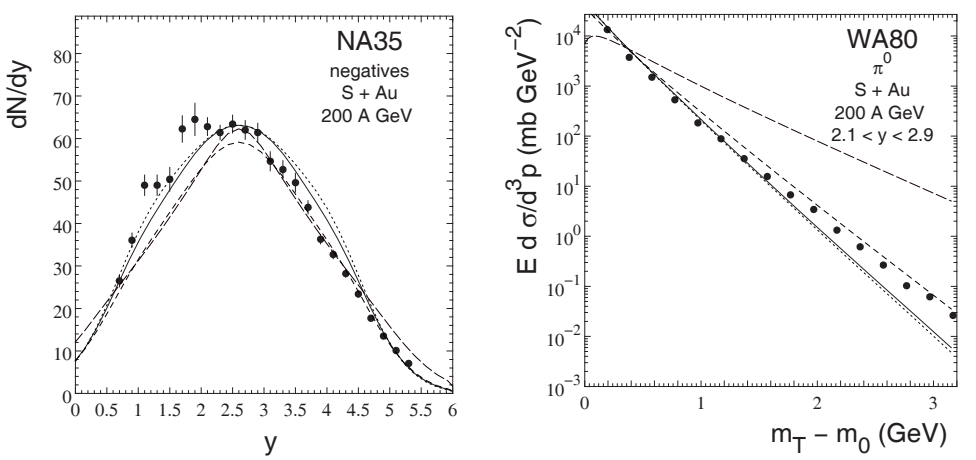

Fig. 4. (Color online) Rapidity distribution of negative hadrons (left) and transverse momentum distribution of neutral pions (right) in S + Au collision at $E_{\rm lab} = 200A$ GeV using four different EoSs. The red long dashed curve corresponds to ideal pion gas EoS, whereas the other curves correspond to hadron resonance gas (HRG) with or without phase transition to ideal parton gas. The figures are from Ref. 72, and the data from Refs. 73 and 74.

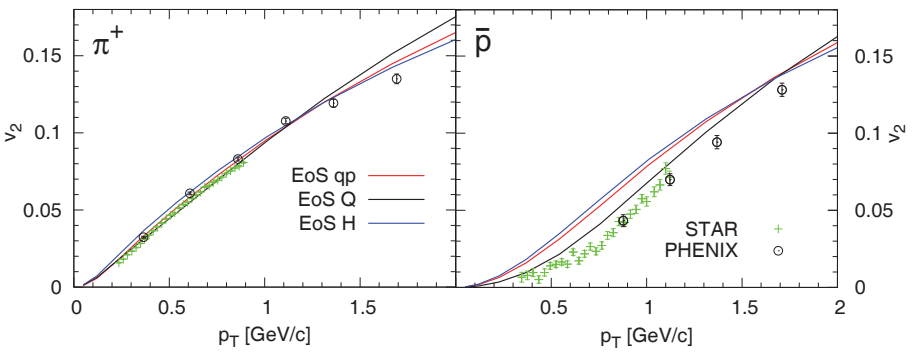

Fig. 5. Elliptic flow of pions and antiprotons versus transverse momentum in minimum bias Au + Au collisions at $\sqrt{s_{\rm NN}} = 200$ GeV calculated using three different EoSs[75] and compared with the data by the STAR and PHENIX collaborations.[65,66] The labels stand for a lattice QCD inspired quasiparticle model (qp), EoS with a first-order phase transition (Q) and pure HRG with no phase transition (H). Figure is from Ref. 64.

It was already seen when modeling S + Au collisions at the CERN SPS at $E_{\rm lab} = 200A$ GeV energy, that if we use ideal pion gas EoS, it is not possible to fit the pion rapidity and p_T-distributions simultaneously. Once the initial state and decoupling temperature are fixed to reproduce the rapidity distribution, the transverse momentum distribution of pions becomes too flat,[72] see Fig. 4. Or if one chooses parameters to fit the p_T-spectrum, the rapidity distribution is not reproduced. On the other hand, if we use an EoS containing several hadrons and resonances, the distributions can be fitted.

One might want to use the elliptic flow to constrain the EoS after the initial state and freeze-out temperature are fixed to reproduce the p_T distributions. Unfortunately elliptic flow is only very weakly sensitive to the details of the EoS[75]: The only flow observable affected by the EoS seems to be the p_T-differential anisotropy of heavy particles, e.g., protons. As shown in Fig. 5, the $v_2(p_t)$ of pions is unchanged within the experimental errors no matter whether one uses an EoS with (EoS A) or without phase transition (EoS H), or an EoS with a first-order phase transition (EoS A) or with a smooth crossover (EoS qp). On the other hand, the proton $v_2(p_t)$ is sensitive to the EoS, but surprisingly the EoS with the first-order phase transition is closest to the data. Consequently distinguishing between different lattice QCD EoS parametrizations is very difficult, see Ref. 76.

3.3. *Softest point of the EoS is quite hard*

The two-particle correlations at low relative momentum provide information about the space-time structure of the source, and thus constraints to dynamical models generating the source. For bosons these correlations are called Bose–Einstein correlations, and for identical particles the method for their interpretation is called Hanbury Brown–Twiss (HBT) interferometry, or, as in general case, femtoscopy.[77–79] To make the measured/calculated three-dimensional correlator easier to understand, it

is often expressed in terms of multi-dimensional Gaussian parametrization, widths of which are called HBT radii. Reproduction of the HBT radii measured at RHIC was surprisingly difficult, and for many years it was not possible to describe simultaneously the particle spectra, their anisotropies and HBT radii. An inconsistency referred to as "HBT puzzle".[80,81] It turned out that this inconsistency was due to several small effects. Successful reproduction of the data required that, (1) the transverse collective expansion begins very early, (2) the EoS is quite hard, (3) dissipative effects are included, and (4) contribution from resonance decays is included.[80–83] When these requirements are taken into account, the present calculations provide an acceptable fit to the data.[26,52,84]

The early build up of collective expansion supports the notion of early thermalization discussed in Sec. 3.1, but the HBT radii provide as ambiguous support as elliptic flow. If sufficient collective motion is build up during thermalization, HBT radii can be fitted also if thermalization takes long (so-called pre-equilibrium flow).[80,81,83] The sufficient hardness of the EoS is fortunately more solid requirement. In practice it means that a bag model EoS with a mixed phase, where the speed of sound is negligible, is disfavored, and thus the softest point of the EoS can hardly be any softer than that of HRG.[85] A notion in line with the lattice QCD EoS calculations.[86]

Nevertheless, since it is so difficult to constrain the EoS, in the present calculations the lattice QCD EoS[86–89] is taken as given, and the main interest is in studying the dissipative properties of the system. At low temperatures the lattice EoS is equivalent to the EoS of noninteracting HRG with all the hadrons and resonances in the Particle Data Book up to $\sim$ 2–2.5 GeV mass. In calculations one often uses an EoS which is a HRG EoS at low temperature, and connected smoothly to a parametrized lattice EoS at high temperature.[76,90]

In the long run a systematic study of collisions at different energies may reveal some sensitivity to EoS and thus allow to test experimentally the lattice QCD prediction. However, since the parameter space and the amount of data to be fitted are vast, such a study requires the use of model emulators to map the parameter space instead of using actual hydrodynamical model to calculate results at all parameter combinations.[91,92]

3.4. *Shear viscosity over entropy density ratio has very low minimum*

Once it became clear that ideal fluid dynamics can describe the particle spectra and their anisotropies quite well, it was reasonable to assume that the shear viscosity coefficient over entropy density ratio η/s of the matter produced in the collision was very low. But how low in particular? To answer that required the development and use of relativistic dissipative hydrodynamics. Of the other dissipative quantities heat conductivity can be ignored since at midrapidity the matter formed in the collisions at RHIC and LHC is almost baryon free. Thus there is no gradient of

chemical potential and no force causing heat flow. The bulk viscosity, on the other hand, is expected to peak around the phase transition, but be small above it. If it is small at lower temperatures too, the effect of bulk viscosity has been evaluated to be smaller than the effect of shear viscosity.[51] Large viscosity in hadronic phase can have a sizable effect[50,53,54] but since bulk viscosity in hadron gas is not well known, and there is no reliable method to distinguish the effects of bulk from the effects of shear, the former is largely ignored, and the calculations concentrate on studying the effects of shear viscosity and on extracting the η/s ratio from the experimental data.[93]

It has been shown that the shear viscosity strongly reduces v_2.[94] Thus in principle extracting the η/s ratio from the data is easy: One needs to calculate the p_T-averaged v_2 of charged hadrons using various values of η/s and choose the value of η/s which reproduces the data. Unfortunately this approach is hampered by our ignorance of the initial state of the evolution. Figure 6 shows a viscous fluid calculation of v_2 of charged hadrons from the first attempt to extract η/s from the data. As seen, a curve corresponding to a finite value of η/s fits the data best, but the preferred value depends on how the initial state of hydrodynamic evolution is chosen: Whether one uses Glauber[4] or KLN approach[10,12] (see Sec. 2.1) causes a factor two difference in the preferred value ($\eta/s = 0.08$–0.16). Furthermore, the approximations in the description of the late hadron gas stage in these calculations caused additional uncertainties, so it was estimated[96] that based on these results $\eta/s < 5/(4\pi)$.

The description of hadronic stage in Ref. 70 was problematic for two reasons. It assumed chemical equilibrium until the very end of the evolution, but at RHIC, the final particle yields correspond to a chemically equilibrated source in $T = 160$–165 MeV temperature.[97,100] The decoupling temperature required to fit the

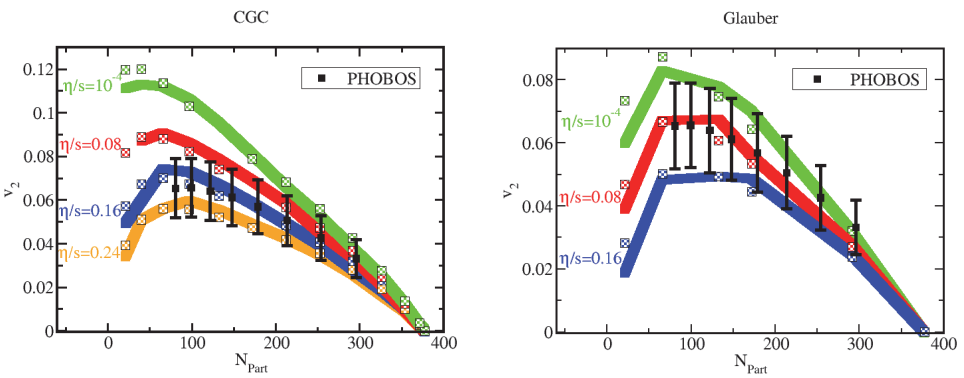

Fig. 6. Charged hadron v_2 as function of centrality in Au + Au collisions at $\sqrt{s_{\rm NN}} = 200$ GeV using different values of η/s and KLN (labeled CGC, left) or Glauber (right) initial conditions. The larger the number of participants, $N_{\rm part}$, the more central the collision. The data are from Ref. 95, the figures from Ref. 70 and reprinted with permission.

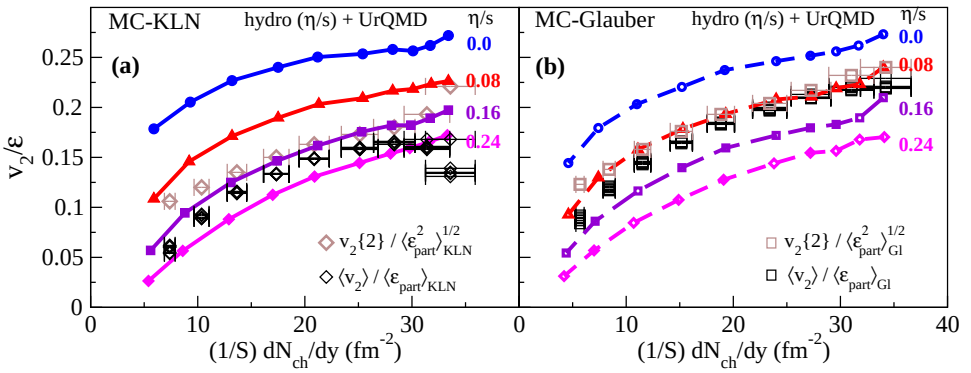

Fig. 7. v_2 scaled by the initial state anisotropy ϵ, v_2/ϵ, as function of centrality, characterized by the final multiplicity per area of the initial state, $(1/S)\,dN/dy$, in Au + Au collisions at $\sqrt{s_{\rm NN}} =$ 200 GeV. The experimental data are from Refs. 102, 65 and 103 for $\langle v_2\rangle$, $v_2\{2\}$ and $dN_{\rm ch}/dy$, respectively. The experimental data used in (a) and (b) are identical, but the normalization factors $\langle\varepsilon_{\rm part}\rangle$, $\langle\varepsilon^2_{\rm part}\rangle^{1/2}$ and S are taken from the MC-KLN model in (a) and from the MC-Glauber model in (b). The viscous hydro + UrQMD hadron cascade hybrid model calculations from Ref. 101 are done using the MC-KLN initial conditions in (a) and MC-Glauber in (b). The figure is from Ref. 101 and reprinted with permission.

p_T-distributions is usually around $T_{\rm dec} = 100$–140 MeV.[g] Thus there must be a stage where the fluid is in local kinetic, but not in chemical equilibrium. Such a "chemically frozen" stage turned out to have surprisingly large effect on the collective flow in general and elliptic flow in particular.[98,99] The second problem was that η/s was constant during the entire evolution, but the theoretical expectation is that hadron gas has much larger viscosity than what the obtained value $\eta/s = 0.08$–0.16 indicates.[45,56]

In subsequent calculations these uncertainties have been addressed. A state-of-the-art calculation of Ref. 101 employs a hybrid viscous hydro + UrQMD hadron cascade model. Such a model reduces the uncertainty related to the description of hadron gas since it provides a dynamical description of chemistry and dissipative properties — including bulk viscosity — based on the scattering cross-sections of various hadron species. Unfortunately some uncertainties still remain: It is uncertain whether hadron cascade is applicable in the vicinity of phase transition where the switch from hydro to cascade is done, the dissipative properties of the system (i.e., η, ζ, τ_π and τ_Π) change abruptly at the switch, and the results also depend on when the switch from hydro to cascade is done.[57] The elliptic flow coefficient v_2 as function of centrality as calculated in Ref. 101 is shown in Fig. 7. In this figure the coefficients v_2 have been scaled by the anisotropy of the initial shape, ϵ, and consequently the resulting v_2/ϵ is almost independent of the initialization. Unfortunately ϵ is not a measurable, but a model dependent quantity. Thus the data has to be scaled by the same ϵ which was used in the calculation, and the data points in Fig. 7 depend on

[g] $T_{\rm dec} = 140$ MeV in Ref. 70.

the model used to initialize the calculation. The result is almost identical to the one shown in Fig. 6 — Glauber initialization favors lower value of viscosity, $\eta/s \approx 0.08$, than KLN initialization, $\eta/s \approx 0.16$. Since the uncertainties are smaller, this result was estimated to provide a limit $1/(4\pi) < \eta/s < 2.5/(4\pi)$ for the effective QGP viscosity.[96,101] For further discussion of evaluating η/s, see Ref. 96.

4. What We are Working With

4.1. $\eta/s(T)$

Calculations discussed in Sec. 3.4 assumed that the η/s-ratio is constant. We know no fluid where η/s would be temperature independent, and there are theoretical reasons to expect it to depend on temperature with a minimum around the phase

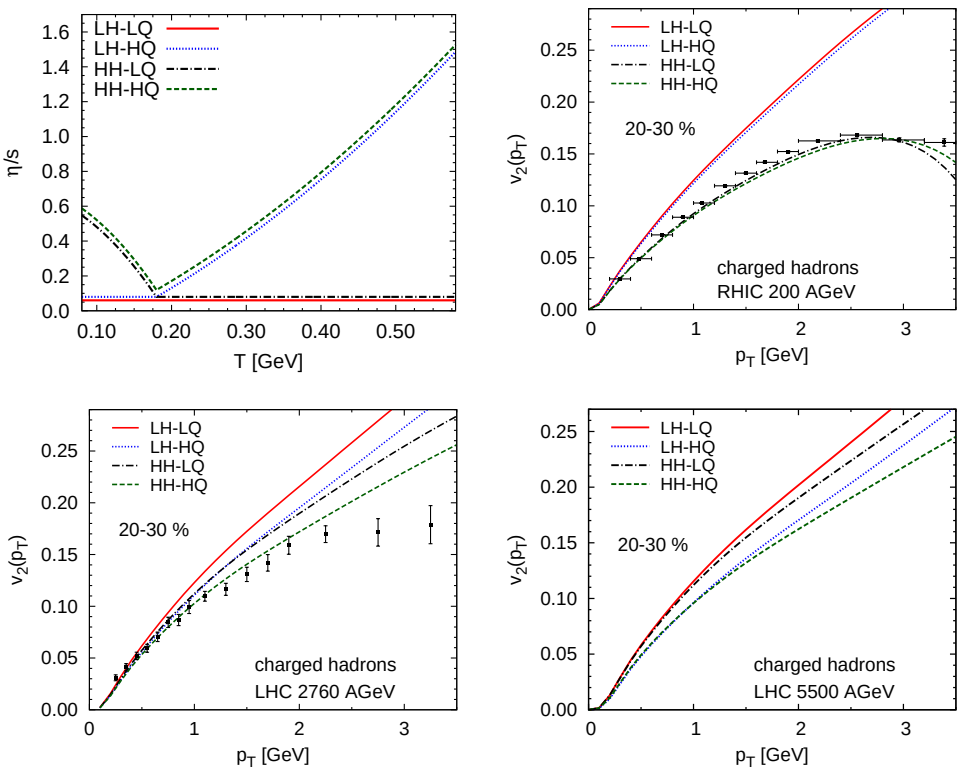

Fig. 8. (top left) Different parametrizations of η/s as a function of temperature. The (LH-LQ) line is shifted downwards and the (HH-HQ) line upwards for clarity. Labels refer to low (L) or high (H) viscosity in the hadronic (H) or partonic (Q) phases. (top right) $v_2(p_T)$ of charged hadrons in the 20–30% Au + Au collisions at $\sqrt{s_{\rm NN}} = 200$ GeV (RHIC). Data are from Refs. 106 and 107. (bottom left) $v_2(p_T)$ of charged hadrons in the 20–30% Pb+Pb collisions at $\sqrt{s_{\rm NN}} = 2.76$ TeV (LHC). Data are from Ref. 108. (bottom right) $v_2(p_T)$ of charged hadrons in the 20–30% Pb+Pb collisions at $\sqrt{s_{\rm NN}} = 5.5$ TeV (LHC). All the figures are from Ref. 109.

transition.[104] Thus the temperature independent η/s is an effective viscosity, and its connection to the physical, temperature dependent, shear viscosity coefficient is unclear. What complicates the determination of the physical shear viscosity coefficient, is that the sensitivity of the anisotropies to dissipation varies during the evolution of the system. As studied in Ref. 105, and illustrated in Fig. 8, at RHIC ($\sqrt{s_{\rm NN}} = 200$ GeV) $v_2(p_T)$ is insensitive to the value of η/s above phase transition, but very sensitive to its value in the hadronic phase. At the present LHC energy ($\sqrt{s_{\rm NN}} = 2.76$ TeV) the shear viscosity in the plasma phase does affect the final $v_2(p_T)$, but not more than the shear viscosity in the hadronic phase. It is only at the full LHC energy, $\sqrt{s_{\rm NN}} = 5.5$ TeV where the viscosity in the plasma phase dominates, and dissipation in the hadronic phase has only a minor effect. Note that a change of the minimum value of η/s would clearly change $v_2(p_T)$ at all energies.

Additional factor complicating the determination of the temperature dependence of η/s is that the effect of viscosity on the anisotropies does not depend only on the ratio η/s, but also on the relaxation time τ_π of the shear stress tensor. This is demonstrated in Fig. 9. If the minimum value of η/s is increased by a factor two, v_2 is reduced as expected, but if the relaxation time is also increased by a factor two, the effect of the increase in η/s is almost completely compensated.[105] The interplay of relaxation time and shear viscosity was discussed also in Refs. 57 and 110 where it was found that to reproduce hybrid model results using viscous hydrodynamics only, it is not sufficient to increase η/s in the hadronic phase, but one should also change the relaxation time.

So far we have seen that calculations with constant η/s require slightly larger value of η/s at LHC than at RHIC.[111,112] This is in line with the increase of $(\eta/s)(T)$ in high temperatures, but as shown in Ref. 112 one cannot uniquely constrain $(\eta/s)(T)$ by fitting the spectra and v_2 alone.

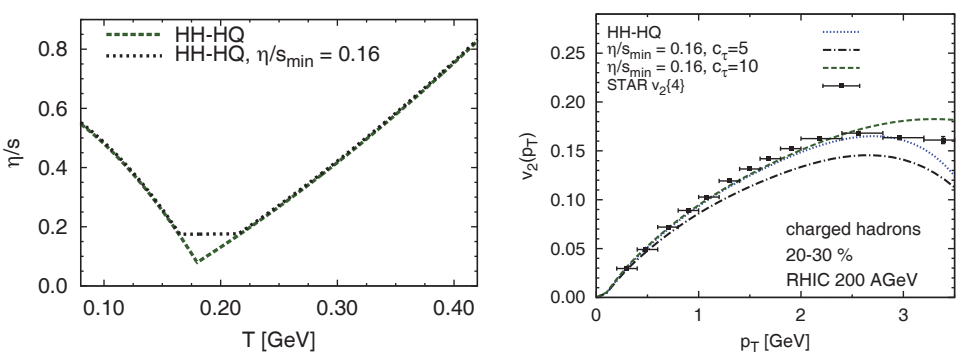

Fig. 9. (left) Parametrizations of η/s as a function of temperature with different minima. The (HH-HQ) line is the same than in Fig. 8. (right) $v_2(p_t)$ of charged hadrons at RHIC using $\eta/s(T)$ with different minima and different relaxation times. Figures are from Ref. 105.

4.2. *Fluctuations*

In the average the matter formed in heavy-ion collisions has a smooth shape as indicated in Fig. 1, but in each event that is not true. Nuclei are not smooth distributions of nuclear matter, but consist of individual nucleons, and thus the collision zone can be expected to have a highly irregular shape which fluctuates event-by-event, see Fig. 10. The initial state models (see Sec. 2.1) can be generalized to so-called Monte Carlo (MC) models to take this into account. In those models the initial Woods–Saxon distributions of nuclear matter are sampled to generate configurations of nucleons in nuclei, and the number of participants/collisions[4] or gluon production[12,13] in an event is calculated based on the positions of individual nuclei.

It was shown already a while ago that the final observables differ whether one first averages the initial state, and evolves it hydrodynamically, or one evolves the event-by-event fluctuating initial states individually, and averages the results.[114,115] This became widely recognized only years later when it was realized that because of the irregular shape of each event, not only even, but also odd anisotropy coefficients v_n are finite and measurable.[116] The higher coefficients are very helpful for extracting the transport coefficients from the data, since the larger the n, the more sensitive the coefficient v_n is to viscosity,[117] see Fig. 11. Thus the study of fluctuations provides a way to distinguish different initializations, and first results for the p_T-dependence of v_2 and v_3 (called triangular flow) seem to favor the MC-Glauber initialization.[118]

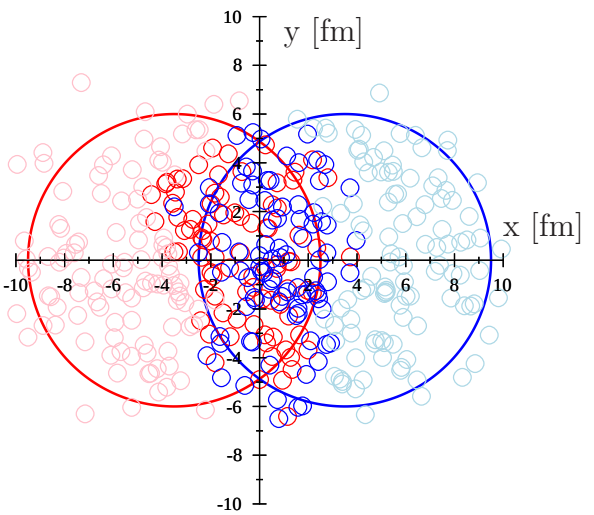

Fig. 10. An example of the positions of interacting nuclei in MC-Glauber model. Figure is from Ref. 113.

It has been suggested that initial fluctuations provide also a way to circumvent our ignorance of the initial shape.[119] In most central collisions the anisotropies are entirely driven by fluctuations, which are better understood than the average shape in semi-central collisions. Thus evaluating η/s using v_n in the most central collisions should be less sensitive to the model used to calculate the initial state. The preliminary result of such an analysis was that $0.07 < \eta/s < 0.43$.[119] This value is again for effective viscosity which does not exclude the possibility that η/s could be even smaller or larger in some temperature region. For a further discussion of flow and viscosity, see Ref. 93.

In event-by-event studies it is not sufficient to reproduce only the average values of v_n, but the fluctuations of the flow coefficients should be reproduced as well.

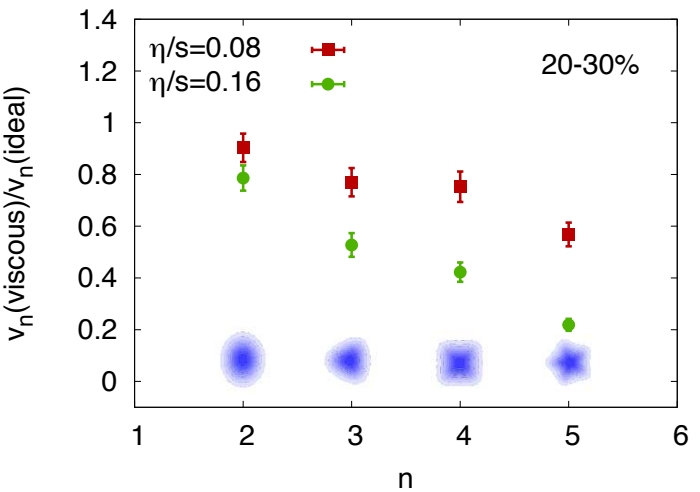

Fig. 11. Ratio of the anisotropy coefficients of charged hadrons in viscous calculation to the coefficients in ideal fluid calculation.[117] Figure shown in Ref. 64 by courtesy of Björn Schenke.

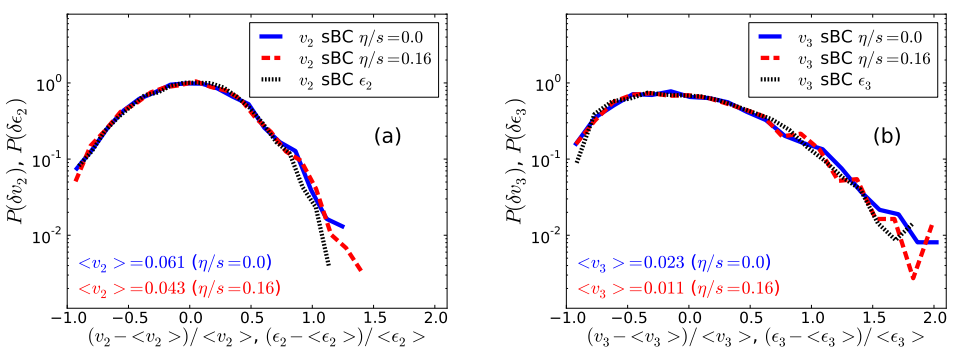

Fig. 12. Probability distributions: (a) $P(\delta v2)$ and $P(\delta\epsilon_2)$ and (b) $P(\delta v3)$ and $P(\delta\epsilon_3)$ in the 20–30% centrality class with sBC Glauber model initialization and two different values of η/s, $\eta/s = 0$ and $\eta/s = 0.16$. $\delta v_n = (v_n - \langle v_n\rangle)/\langle v_n\rangle$ and $\epsilon_n = (\epsilon_n - \langle\epsilon_n\rangle)/\langle\epsilon_n\rangle$. Figures are from Ref. 120.

The distributions of these fluctuations provide a way to constrain the fluctuation spectrum of initial state models independently of the dissipative properties of the fluid. As shown in Fig. 12, once the average v_n has been scaled out, the distributions of these fluctuations, i.e., $(v_n - \langle v_n \rangle)/\langle v_n \rangle$ or $v_n/\langle v_n \rangle$, are almost independent of viscosity. The independence extends to other details of the evolution to such an extent, that the distributions of the fluctuations of initial anisotropies are good approximations of the measured distributions of v_n,[120] and thus it is sufficient to compare the fluctuations of initial shape, ϵ_n, to the observed fluctuations of v_n. Unlike the recently developed IP-Glasma model,[121,122] neither MC-Glauber nor MC-KLN model seems to be able to reproduce the measured fluctuations.[123]

4.3. *Initialization*

During last two years there have been major advances in modeling the initial state of hydrodynamical evolution. So called IP-Glasma model[121,122] is based on CGC and employs the IP-Sat (Impact Parameter dependent Saturation) model[124,125] of nucleon wave functions to generate fluctuating gluon fields in the initial collision, and the classical Yang–Mills dynamics to evolve these fields.[126–131] Unlike most of the initial state models, the IP-Glasma model includes the fluctuations of color charge in colliding nucleons too, not only the fluctuations of nucleon positions. Another advantage is that the model includes some of the pre-equilibrium dynamics of the gluon fields making the model less sensitive on the time when one switches to hydrodynamics.[111] Unfortunately the description is still incomplete: the present IP-Glasma model does not lead to a thermal system, but final thermalization still has to be assumed. Nevertheless, calculations using the IP-Glasma initialization reproduce both the fluctuations and the average values of v_2, v_3 and v_4,[111,132] which makes this approach very promising. For a general overview of IP-Glasma, fluctuations and hydrodynamics, see Ref. 133.

5. What Worries Us

As described in the previous sections, fluid dynamics has been very successful in describing heavy-ion collisions. However, at the time of this writing there are some data which may cause difficulties for the conventional fluid dynamical picture.

5.1. *Photons*

Unlike hadrons and partons, photons and leptons interact only electromagnetically, and hardly scatter at all after being produced. Thus the observed photon and lepton spectra contain contributions from all stages of a heavy-ion collision, and can be used to probe the early hot and dense stage.[134] The yield and p_T-spectrum of photons in heavy-ion collisions is fairly well understood[135–139] — see also Ref. 140 and references therein — but the recent measurements of direct photon v_2 at RHIC[141] and LHC[142] have presented a puzzle: If photons are emitted during all stages of

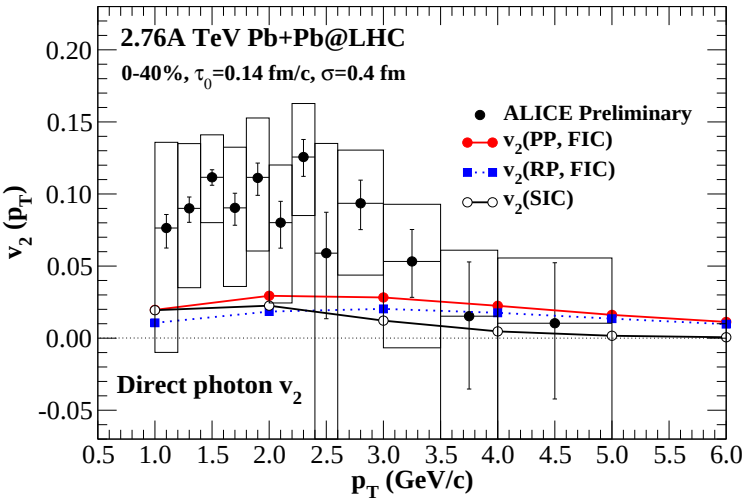

Fig. 13. Thermal photon v_2 versus p_T for 0–40% central collisions at LHC. The figure is from Ref. 144 and reprinted with permission. The preliminary direct photon data are from Ref. 142.

the evolution, and momentum anisotropy increases during the evolution, photon v_2 should be smaller than the hadron v_2. Such a behavior is seen in the theoretical calculations,[143] but not in the data where the photon $v_2(p_T)$ is roughly equal to the observed pion $v_2(p_T)$.[141,142] The further refinements of the calculations, where event-by-event fluctuations[144] and viscosity have been taken into account,[145,146] have not been able to increase the v_2 to the observed level, see Fig. 13. So far the only approach to get close to the data has used parametrized expansion with very strong initial expansion and large photon production rates in the hadronic phase.[147] Thus the reproduction of the data remains a challenge to our understanding of microscopic production rates and/or expansion dynamics.

5.2. *$p + Pb$ collisions*

In $p+Pb$ collisions at $\sqrt{s_{\rm NN}} = 5.02$ TeV, the measured dihadron correlations,[148–151] multiplicity and species dependence of average p_T,[152,153] and elliptic and triangular flows[149–151] all depict features easily explained by using hydrodynamics[154–159] (for a short summary see Ref. 160). Especially striking is the mass ordering of the p_T-differential elliptic flow,[151] see Fig. 14. As discussed in Sec. 3.1, this was taken as a strong indicator of the formation of a thermal system. However, it is questionable whether hydrodynamics is applicable to such a small system. Gradients are so large, that dissipative corrections should be of the same order than equilibrium pressure. As discussed in Ref. 161, large dissipative corrections are a problem even in $Pb+Pb$ collisions, but in $Pb + Pb$ collisions corrections are large only for a small fraction of the lifetime of the system, whereas corrections are large for a significant fraction of the lifetime in $p + Pb$ collision.

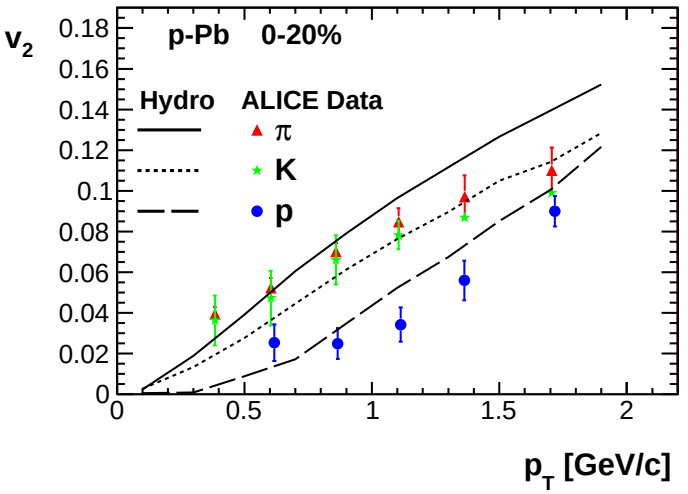

Fig. 14. v_2 versus p_T for identified particles in 0–20% most central $p + Pb$ collisions. Data are from Ref. 151 and the hydrodynamical calculation from Ref. 159. Figure courtesy by Piotr Bozek.

In the CGC framework similar correlations[162–164] and the mass hierarchy of average p_T[165] arise as a result of gluon saturation in the proton and nuclear wave functions. How much of the observed behavior can be explained as such an initial state effect,[h] and how to differentiate initial state effects from hydrodynamical final state effects[161,166] is at the time of this writing under intense study. If it turns out that the apparently hydrodynamical behavior in $p + Pb$ collisions can be explained as an initial state effect, then we may wonder whether the hydrodynamical behavior in $Pb + Pb$ collisions could be explained as an initial state effect as well. On the other hand, if this is not possible, and fluid dynamics is the most viable description of $p + Pb$ collisions, then the properties of QCD matter are even more surprising than thought so far.

6. Summary

Fluid dynamics has been very successful in explaining the features of bulk, i.e., low p_T, particle production in ultrarelativistic heavy-ion collisions. We have seen that in particular anisotropies of particle production can be explained if the rescatterings among particles are so frequent that the system is approximately thermal, that the EoS of such a matter has many degrees of freedom and relatively hard, and that the shear viscosity coefficient over entropy ratio of the produced matter has very low value at some temperature. Providing further experimental constraints on the

[h]Here initial state refers to the initial state of primary collisions, not to the initial state of hydrodynamical evolution.

EoS as well as figuring out the temperature dependence and the precise value of the minimum of η/s will require a lot of work. The present studies in event-by-event fluctuations and recent advances in modeling the pre-equilibrium processes in heavy-ion collisions are very helpful for this goal, but it is not yet clear how the elliptic flow of photons in $A + A$ collisions and the $p + Pb$ collisions at LHC fit in the overall picture. After a few years' work we will know.

Acknowledgments

This review is based on a talk[64] given in the 10th Conference on Quark Confinement and the Hadron Spectrum (Confinement X), October 2012, Münich, Germany. I thank Hannu Holopainen and Iurii Karpenko for helpful discussions. This work was supported by BMBF under contract No. 06FY9092.

References

1. D. H. Rischke, Fluid dynamics for relativistic nuclear collisions, arXiv:nucl-th/9809044.
2. J.-Y. Ollitrault, *Eur. J. Phys.* **29** (2008) 275.
3. B. Muller and A. Schafer, *Int. J. Mod. Phys. E* **20** (2011) 2235.
4. M. L. Miller, K. Reygers, S. J. Sanders and P. Steinberg, *Ann. Rev. Nucl. Part. Sci.* **57** (2007) 205.
5. A. Bialas, M. Bleszynski and W. Czyz, *Nucl. Phys. B* **111** (1976) 461.
6. P. F. Kolb *et al.*, *Nucl. Phys. A* **696** (2001) 197.
7. U. W. Heinz and P. F. Kolb, *Nucl. Phys. A* **702** (2002) 269.
8. D. Kharzeev and M. Nardi, *Phys. Lett. B* **507** (2001) 121.
9. D. Kharzeev and E. Levin, *Phys. Lett. B* **523** (2001) 79.
10. D. Kharzeev, E. Levin and M. Nardi, *Phys. Rev. C* **71** (2005) 054903.
11. D. Kharzeev, E. Levin and M. Nardi, *Nucl. Phys. A* **730** (2004) 448 [Erratum-*ibid.* **743** (2004) 329].
12. H.-J. Drescher and Y. Nara, *Phys. Rev. C* **75** (2007) 034905.
13. H.-J. Drescher and Y. Nara, *Phys. Rev. C* **76** (2007) 041903.
14. E. Iancu, A. Leonidov and L. McLerran, The colour glass condensate: An introduction, arXiv:hep-ph/0202270.
15. E. Iancu and R. Venugopalan, in *Quark-Gluon Plasma 3*, eds. R. C. Hwa and X.-N. Wang (World Scientific, Singapore, 2004), p. 249.
16. F. Gelis, E. Iancu, J. Jalilian-Marian and R. Venugopalan, *Ann. Rev. Nucl. Part. Sci.* **60** (2010) 463.

17. T. Lappi, *Int. J. Mod. Phys. E* **20** (2011) 1.
18. K. J. Eskola, K. Kajantie, P. V. Ruuskanen and K. Tuominen, *Nucl. Phys. B* **570** (2000) 379.
19. R. Paatelainen, K. J. Eskola, H. Holopainen and K. Tuominen, *Phys. Rev. C* **87** (2013) 044904.
20. R. Paatelainen, K. J. Eskola, H. Niemi and K. Tuominen, Fluid dynamics with saturated minijet initial conditions in ultrarelativistic heavy-ion collisions, arXiv:1310.3105 [hep-ph].
21. H. Petersen *et al.*, *Phys. Rev. C* **78** (2008) 044901.
22. S. A. Bass *et al.*, *Prog. Part. Nucl. Phys.* **41** (1998) 255.
23. M. Bleicher *et al.*, *J. Phys. G* **25** (1999) 1859.
24. B. Zhang, C. M. Ko, B.-A. Li and Z.-W. Lin, *Phys. Rev. C* **61** (2000) 067901.
25. L. Pang, Q. Wang and X.-N. Wang, *Phys. Rev. C* **86** (2012) 024911.
26. K. Werner *et al.*, *Phys. Rev. C* **82** (2010) 044904.
27. S. V. Akkelin, Y. Hama, I. A. Karpenko and Y. M. Sinyukov, *Phys. Rev. C* **78** (2008) 034906.
28. I. A. Karpenko and Y. M. Sinyukov, *Phys. Rev. C* **81** (2010) 054903.
29. F. Cooper and G. Frye, *Phys. Rev. D* **10** (1974) 186.
30. J. P. Bondorf, S. I. A. Garpman and J. Zimanyi, *Nucl. Phys. A* **296** (1978) 320.
31. H. Holopainen and P. Huovinen, *J. Phys. Conf. Ser.* **389** (2012) 012018.
32. W. A. Hiscock and L. Lindblom, *Ann. Phys.* **151** (1983) 466.
33. W. A. Hiscock and L. Lindblom, *Phys. Rev. D* **31** (1985) 725.
34. W. A. Hiscock and L. Lindblom, *Phys. Rev. D* **35** (1987) 3723.
35. I. Muller, *Z. Phys.* **198** (1967) 329.
36. W. Israel, *Ann. Phys.* **100** (1976) 310.
37. H. Grad, *Commun. Pure Appl. Math.* **2** (1949) 331.
38. W. Israel and J. M. Stewart, *Ann. Phys.* **118** (1979) 341.
39. G. S. Denicol, E. Molnar, H. Niemi and D. H. Rischke, *Eur. Phys. J. A* **11** (2012) 170.
40. R. Baier *et al.*, *J. High Energy Phys.* **0804** (2008) 100.
41. P. Romatschke, *Class. Quantum Grav.* **27** (2010) 025006.
42. S. Chapman and T. G. Cowling, *The Mathematical Theory of Non-uniform Gases*, 3rd edition (Cambridge University Press, Cambridge, 1970).
43. G. S. Denicol, H. Niemi, E. Molnar and D. H. Rischke, *Phys. Rev. D* **85** (2012) 114047.
44. G. S. Denicol *et al.*, Solving the heat-flow problem with transient relativistic fluid dynamics, arXiv:1207.6811 [nucl-th].
45. M. Prakash, M. Prakash, R. Venugopalan and G. Welke, *Phys. Rep.* **227** (1993) 321.
46. A. Monnai and T. Hirano, *Nucl. Phys. A* **847** (2010) 283.
47. G. S. Denicol and H. Niemi, *Nucl. Phys. A* **904–905** (2013) 369c.
48. D. Molnar, *J. Phys. G* **38** (2011) 124173.
49. K. Dusling, G. D. Moore and D. Teaney, *Phys. Rev. C* **81** (2010) 034907.
50. A. Monnai and T. Hirano, *Phys. Rev. C* **80** (2009) 054906.
51. H. Song and U. W. Heinz, *Phys. Rev. C* **81** (2010) 024905.
52. P. Bozek, *Phys. Rev. C* **85** (2012) 034901.
53. K. Dusling and T. Schäfer, *Phys. Rev. C* **85** (2012) 044909.
54. J. Noronha-Hostler *et al.*, *Phys. Rev. C* **88** (2013) 044916.
55. P. Huovinen and D. Molnar, *Phys. Rev. C* **79** (2009) 014906.
56. N. Demir and S. A. Bass, *Phys. Rev. Lett.* **102** (2009) 172302.
57. H. Song, S. A. Bass and U. Heinz, *Phys. Rev. C* **83** (2011) 024912.

58. Y. Nara *et al.*, *Phys. Rev. C* **61** (2000) 024901.
59. M. Isse *et al.*, *Phys. Rev. C* **72** (2005) 064908.
60. T. Hirano, P. Huovinen, K. Murase and Y. Nara, *Prog. Part. Nucl. Phys.* **70** (2013) 108.
61. S. A. Voloshin, A. M. Poskanzer and R. Snellings, Collective phenomena in noncentral nuclear collisions, arXiv:0809.2949 [nucl-ex].
62. STAR Collab. (K. H. Ackermann *et al.*), *Phys. Rev. Lett.* **86** (2001) 402.
63. P. F. Kolb, P. Huovinen, U. W. Heinz and H. Heiselberg, *Phys. Lett. B* **500** (2001) 232.
64. P. Huovinen, PoS ConfinementX (2012) 165.
65. STAR Collab. (J. Adams *et al.*), *Phys. Rev. C* **72** (2005) 014904.
66. PHENIX Collab. (S. S. Adler *et al.*), *Phys. Rev. Lett.* **91** (2003) 182301.
67. STAR Collab. (J. Adams *et al.*), *Phys. Rev. Lett.* **92** (2004) 052302.
68. P. Huovinen *et al.*, *Phys. Lett. B* **503** (2001) 58.
69. P. F. Kolb and U. W. Heinz, in *Quark-Gluon Plasma 3*, eds. R. C. Hwa and X.-N. Wang (World Scientific, Singapore, 2004), p. 634.
70. M. Luzum and P. Romatschke, *Phys. Rev. C* **78** (2008) 034915 [Erratum-*ibid.* **79** (2009) 039903].
71. P. F. Kolb, J. Sollfrank and U. W. Heinz, *Phys. Rev. C* **62** (2000) 054909.
72. J. Sollfrank *et al.*, *Phys. Rev. C* **55** (1997) 392.
73. NA35 Collab. (M. Gazdzicki *et al.*), *Nucl. Phys. A* **590** (1995) 197C.
74. WA80 Collab. (R. Santo *et al.*), *Nucl. Phys. A* **566** (1994) 61C.
75. P. Huovinen, *Nucl. Phys. A* **761** (2005) 296.
76. P. Huovinen and P. Petreczky, *Nucl. Phys. A* **837** (2010) 26.
77. M. A. Lisa, S. Pratt, R. Soltz and U. Wiedemann, *Ann. Rev. Nucl. Part. Sci.* **55** (2005) 357.
78. M. A. Lisa and S. Pratt, Femtoscopically probing the freeze-out configuration in heavy-ion collisions, arXiv:0811.1352 [nucl-ex].
79. M. A. Lisa *et al.*, *New J. Phys.* **13** (2011) 065006.
80. S. Pratt, *Phys. Rev. Lett.* **102** (2009) 232301.
81. S. Pratt, *Nucl. Phys. A* **830** (2009) 51C.
82. A. Kisiel, W. Florkowski and W. Broniowski, *Phys. Rev. C* **73** (2006) 064902.
83. W. Broniowski, M. Chojnacki, W. Florkowski and A. Kisiel, *Phys. Rev. Lett.* **101** (2008) 022301.
84. I. A. Karpenko, Y. M. Sinyukov and K. Werner, *Phys. Rev. C* **87** (2013) 024914.
85. M. Chojnacki and W. Florkowski, *Acta Phys. Pol. B* **38** (2007) 3249.
86. S. Borsanyi *et al.*, *J. High Energy Phys.* **1011** (2010) 077.
87. O. Philipsen, *Prog. Part. Nucl. Phys.* **70** (2013) 55.
88. P. Petreczky, *J. Phys. G* **39** (2012) 093002.
89. S. Borsanyi *et al.*, Full result for the QCD equation of state with 2+1 flavors, arXiv:1309.5258 [hep-lat].
90. M. Bluhm *et al.*, Lattice QCD-based equations of state at vanishing net-baryon density, arXiv:1306.6188 [hep-ph].
91. H. Petersen, C. Coleman-Smith, S. A. Bass and R. Wolpert, *J. Phys. G* **38** (2011) 045102.
92. J. Novak *et al.*, Determining fundamental properties of matter created in ultrarelativistic heavy-ion collisions, arXiv:1303.5769 [nucl-th].
93. U. W. Heinz and R. Snellings, *Ann. Rev. Nucl. Part. Sci.* **63** (2013) 123.
94. D. Teaney, *Phys. Rev. C* **68** (2003) 034913.
95. PHOBOS Collab. (B. Alver), *Int. J. Mod. Phys. E* **16** (2007) 3331.

96. H. Song, *Eur. Phys. J. A* **48** (2012) 163.
97. A. Andronic, P. Braun-Munzinger and J. Stachel, *Phys. Lett. B* **673** (2009) 142; [Erratum-*ibid.* **678** (2009) 516].
98. P. Huovinen, *Eur. Phys. J. A* **37** (2008) 121.
99. T. Hirano and K. Tsuda, *Phys. Rev. C* **66** (2002) 054905.
100. A. Andronic, P. Braun-Munzinger and J. Stachel, *Acta Phys. Pol. B* **40** (2009) 1005.
101. H. Song *et al.*, *Phys. Rev. Lett.* **106** (2011) 192301 [Erratum-*ibid.* **109** (2012) 139904].
102. J. Y. Ollitrault, A. M. Poskanzer and S. A. Voloshin, *Phys. Rev. C* **80** (2009) 014904.
103. STAR Collab. (B. I. Abelev *et al.*), *Phys. Rev. C* **79** (2009) 034909.
104. L. P. Csernai, J. I. Kapusta and L. D. McLerran, *Phys. Rev. Lett.* **97** (2006) 152303.
105. H. Niemi *et al.*, *Phys. Rev. C* **86** (2012) 014909.
106. Y. Bai, Ph.D. thesis, Nikhef and Utrecht University, Utrecht (2007).
107. STAR Collab. (A. Tang), Flow results and hints of incomplete thermalization, arXiv:0808.2144 [nucl-ex].
108. ALICE Collab. (K. Aamodt *et al.*), *Phys. Rev. Lett.* **105** (2011) 252302.
109. H. Niemi *et al.*, *Acta Phys. Pol. Supp.* **5** (2012) 305.
110. C. Shen and U. Heinz, *Phys. Rev. C* **83** (2011) 044909.
111. C. Gale *et al.*, *Phys. Rev. Lett.* **110** (2013) 012302.
112. H. Song, S. A. Bass and U. Heinz, *Phys. Rev. C* **83** (2011) 054912; [Erratum-*ibid.* **87** (2013) 019902].
113. H. Holopainen, Ph. D. thesis, University of Jyväskylä, Jyväskylä (2011), http://urn.fi/URN:ISBN:978-951-39-4371-4.
114. C. E. Aguiar, Y. Hama, T. Kodama and T. Osada, *Nucl. Phys. A* **698** (2002) 639.
115. O. Socolowski, Jr., F. Grassi, Y. Hama and T. Kodama, *Phys. Rev. Lett.* **93** (2004) 182301.
116. B. Alver and G. Roland, *Phys. Rev. C* **81** (2010) 054905; [Erratum-*ibid.* **82** (2010) 039903].
117. B. Schenke, S. Jeon and C. Gale, *Phys. Rev. C* **85** (2012) 024901.
118. Z. Qiu, C. Shen and U. Heinz, *Phys. Lett. B* **707** (2012) 151.
119. M. Luzum and J.-Y. Ollitrault, *Nucl. Phys. A* **904–905** (2013) 377c.
120. H. Niemi, G. S. Denicol, H. Holopainen and P. Huovinen, *Phys. Rev. C* **87** (2013) 054901.
121. B. Schenke, P. Tribedy and R. Venugopalan, *Phys. Rev. Lett.* **108** (2012) 252301.
122. B. Schenke, P. Tribedy and R. Venugopalan, *Phys. Rev. C* **86** (2012) 034908.
123. ATLAS Collab. (J. Jia), *Nucl. Phys. A* **904–905** (2013) 421c.
124. J. Bartels, K. J. Golec-Biernat and H. Kowalski, *Phys. Rev. D* **66** (2002) 014001.
125. H. Kowalski and D. Teaney, *Phys. Rev. D* **68** (2003) 114005.
126. A. Kovner, L. D. McLerran and H. Weigert, *Phys. Rev. D* **52** (1995) 6231.
127. Y. V. Kovchegov and D. H. Rischke, *Phys. Rev. C* **56** (1997) 1084.
128. A. Krasnitz and R. Venugopalan, *Nucl. Phys. B* **557** (1999) 237.
129. A. Krasnitz and R. Venugopalan, *Phys. Rev. Lett.* **84** (2000) 4309.
130. A. Krasnitz and R. Venugopalan, *Phys. Rev. Lett.* **86** (2001) 1717.
131. T. Lappi, *Phys. Rev. C* **67** (2003) 054903.
132. C. Gale *et al.*, *Nucl. Phys. A* **904–905** (2013) 409c.
133. C. Gale, S. Jeon and B. Schenke, *Int. J. Mod. Phys. A* **28** (2013) 1340011.
134. K. Kajantie and H. I. Miettinen, *Z. Phys. C* **9** (1981) 341.
135. S. Turbide, C. Gale, S. Jeon and G. D. Moore, *Phys. Rev. C* **72** (2005) 014906.
136. S. Turbide, C. Gale, E. Frodermann and U. Heinz, *Phys. Rev. C* **77** (2008) 024909.
137. R. Chatterjee and D. K. Srivastava, *Phys. Rev. C* **79** (2009) 021901.

138. R. Chatterjee, H. Holopainen, T. Renk and K. J. Eskola, *Phys. Rev. C* **83** (2011) 054908.
139. H. Holopainen, S. Rasanen and K. J. Eskola, *Phys. Rev. C* **84** (2011) 064903.
140. C. Gale, *Nucl. Phys. A* **910–911** (2013) 147.
141. PHENIX Collab. (A. Adare *et al.*), *Phys. Rev. Lett.* **109** (2012) 122302.
142. ALICE Collab. (D. Lohner), *J. Phys. Conf. Ser.* **446** (2013) 012028.
143. R. Chatterjee, E. S. Frodermann, U. W. Heinz and D. K. Srivastava, *Phys. Rev. Lett.* **96** (2006) 202302.
144. R. Chatterjee *et al.*, *Phys. Rev. C* **88** (2013) 034901.
145. M. Dion *et al.*, *Phys. Rev. C* **84** (2011) 064901.
146. C. Shen *et al.*, Anisotropic flow of thermal photons as a quark-gluon plasma viscometer, arXiv:1308.2111 [nucl-th].
147. H. van Hees, C. Gale and R. Rapp, *Phys. Rev. C* **84** (2011) 054906.
148. ALICE Collab. (B. Abelev *et al.*), *Phys. Lett. B* **719** (2013) 29.
149. CMS Collab. (S. Chatrchyan *et al.*), *Phys. Lett. B* **724** (2013) 213.
150. ATLAS Collab. (G. Aad *et al.*), *Phys. Lett. B* **725** (2013) 60.
151. ALICE Collab. (B. B. Abelev *et al.*), *Phys. Lett. B* **726** (2013) 164.
152. ALICE Collab. (B. B. Abelev *et al*), Multiplicity dependence of the average transverse momentum in pp, p-Pb, and Pb-Pb collisions at the LHC, arXiv:1307.1094 [nucl-ex].
153. CMS Collab. (S. Chatrchyan *et al.*), Study of the production of charged pions, kaons, and protons in p-Pb collisions at $\sqrt{s_{NN}} = 5.02$ TeV, arXiv:1307.3442 [hep-ex].
154. P. Bozek and W. Broniowski, *Phys. Lett. B* **718** (2013) 1557.
155. P. Bozek and W. Broniowski, *Phys. Rev. C* **88** (2013) 014903.
156. T. Pierog *et al.*, EPOS LHC: Test of collective hadronization with LHC data, arXiv:1306.0121 [hep-ph].
157. G.-Y. Qin and B. Müller, Elliptic and triangular flow anisotropy in deuteron-gold collisions at RHIC and proton-lead collisions at the LHC, arXiv:1306.3439 [nucl-th].
158. K. Werner *et al*, Evidence for flow in pPb collisions at 5 TeV from v2 mass splitting, arXiv:1307.4379 [nucl-th].
159. P. Bozek, W. Broniowski and G. Torrieri, *Phys. Rev. Lett.* **111** (2013) 172303.
160. P. Bozek, W. Broniowski and G. Torrieri, Hydrodynamic models of particle production, arXiv:1309.7782 [nucl-th].
161. A. Bzdak, B. Schenke, P. Tribedy and R. Venugopalan, *Phys. Rev. C* **87** (2013) 064906.
162. K. Dusling, F. Gelis, T. Lappi and R. Venugopalan, *Nucl. Phys. A* **836** (2010) 159.
163. K. Dusling and R. Venugopalan, *Phys. Rev. D* **87** (2013) 094034.
164. K. Dusling and R. Venugopalan, *Phys. Rev. D* **87** (2013) 054014.
165. L. McLerran, M. Praszalowicz and B. Schenke, *Nucl. Phys. A* **916** (2013) 210.
166. P. Bozek, A. Bzdak and V. Skokov, The rapidity dependence of the average transverse momentum in p + Pb collisions at the LHC: The Color Glass Condensate versus hydrodynamics, arXiv:1309.7358 [hep-ph].